

CODEN: JASMAN

The Journal of the Acoustical Society of America

ISSN: 0001-4966

Vol. 109, No. 3

March 2001

ACOUSTICAL NEWS—USA	839
USA Meetings Calendar	840
ACOUSTICAL STANDARDS NEWS	845
Standards Meetings Calendar	845
BOOK REVIEWS	849
ABSTRACTS FROM ACOUSTICS RESEARCH LETTERS ONLINE	851
REVIEWS OF ACOUSTICAL PATENTS	855

GENERAL LINEAR ACOUSTICS [20]

Wave localization on a submerged cylindrical shell with rib aperiodicity	Martin H. Marcus, Brian H. Houston, Douglas M. Photiadis	865
Acoustic scattering by a circular cylinder parallel with another of small radius	John A. Roumeliotis, Agissilaos-Georgios P. Ziotopoulos, Gerassimos C. Kokkorakis	870
Low-frequency scattering of acoustic waves by a bounded rough surface in a half-plane	F. J. Sabina, V. M. Babich	878
Guided waves in a transversely isotropic cylinder immersed in a fluid	Faiz Ahmad	886

NONLINEAR ACOUSTICS [25]

Gas bubble pulsation in a semiconfined space subjected to ultrasound	Boris Krasovitski, Eitan Kimmel	891
--	---------------------------------	-----

AEROACOUSTICS, ATMOSPHERIC SOUND [28]

A computational analysis of sonic booms penetrating a realistic ocean surface	Judith L. Rochat, Victor W. Sparrow	899
---	-------------------------------------	-----

UNDERWATER SOUND [30]

A unified model for reverberation and submerged object scattering in a stratified ocean waveguide	Nicholas C. Makris, Purnima Ratilal	909
---	-------------------------------------	-----

(Continued)

CONTENTS—Continued from preceding page

ULTRASONICS, QUANTUM ACOUSTICS, AND PHYSICAL EFFECTS OF SOUND [35]

- High-amplitude thermoacoustic effects in a single pore G. Petculescu, L. A. Wilen 942

TRANSDUCTION [38]

- Equivalent circuits and directivity patterns of air-coupled ultrasonic transducers Lin Shuyu 949
- Robustness to head misalignment of virtual sound imaging systems Takashi Takeuchi, Philip A. Nelson, Hareo Hamada 958

STRUCTURAL ACOUSTICS AND VIBRATION [40]

- Implication of conservative and gyroscopic forces on vibration and stability of an elastically tailored rotating shaft modeled as a composite thin-walled beam Ohseop Song, Nam-Heui Jeong, Liviu Librescu 972
- A new method for true and spurious eigensolutions of arbitrary cavities using the combined Helmholtz exterior integral equation formulation method I. L. Chen, J. T. Chen, S. R. Kuo, M. T. Liang 982
- Modeling vibrational energy transmission at bolted junctions between a plate and a stiffening rib Ivan Bosmans, Trevor R. T. Nightingale 999

NOISE: ITS EFFECTS AND CONTROL [50]

- Prediction models for sound leakage through noise barriers Hon Yiu Wong, Kai Ming Li 1011
- Community noise exposure and stress in children Gary W. Evans, Peter Lercher, Markus Meis, Hartmut Ising, Walter W. Kofler 1023

ARCHITECTURAL ACOUSTICS [55]

- Relation of acoustical parameters with and without audiences in concert halls and a simple method for simulating the occupied state Takayuki Hidaka, Noriko Nishihara, Leo L. Beranek 1028

ACOUSTICAL MEASUREMENTS AND INSTRUMENTATION [58]

- Simulation of jet-noise excitation in an acoustic progressive wave tube facility Alexander Steinwolf, Robert G. White, Howard F. Wolfe 1043

ACOUSTIC SIGNAL PROCESSING [60]

- Underwater source detection using a spatial stationarity test A. Ephraty, J. Tabrikian, H. Messer 1053
- Feature dependence in the automatic identification of musical woodwind instruments Judith C. Brown, Olivier Houix, Stephen McAdams 1064

PHYSIOLOGICAL ACOUSTICS [64]

- The feasibility of maximum length sequences to reduce acquisition time of the middle latency response S. L. Bell, R. Allen, M. E. Lutman 1073

PSYCHOLOGICAL ACOUSTICS [66]

- Searching for the time constant of neural pitch extraction Lutz Wiegrebe 1082
- Auditory backward recognition masking in children with a specific language impairment and children with a specific reading disability G. M. McArthur, J. H. Hogben 1092
- Informational and energetic masking effects in the perception of two simultaneous talkers Douglas S. Brungart 1101
- Elevation localization and head-related transfer function analysis at low frequencies V. Ralph Algazi, Carlos Avendano, Richard O. Duda 1110

CONTENTS—Continued from preceding page

Performance of an adaptive beamforming noise reduction scheme for hearing aid applications. I. Prediction of the signal-to-noise-ratio improvement	Martin Kompis, Norbert Dillier	1123
Performance of an adaptive beamforming noise reduction scheme for hearing aid applications. II. Experimental verification of the predictions	Martin Kompis, Norbert Dillier	1134
SPEECH PRODUCTION [70]		
The role of the mora in the timing of spontaneous Japanese speech	Natasha Warner, Takayuki Arai	1144
SPEECH PERCEPTION [71]		
Acoustic and linguistic factors in the perception of bandpass-filtered speech	Ginger S. Stickney, Peter F. Assmann	1157
Recognition of spectrally asynchronous speech by normal-hearing listeners and Nucleus-22 cochlear implant users	Qian-Jie Fu, John J. Galvin III	1166
Vowel perception by adults and children with normal language and specific language impairment: Based on steady states or transitions?	Joan E. Sussman	1173
The perceptual consequences of within-talker variability in fricative production	Rochelle S. Newman, Sheryl A. Clouse, Jessica L. Burnham	1181
Relations between intelligibility of narrow-band speech and auditory functions, both in the 1-kHz frequency region	Ingrid M. Noordhoek, Tammo Houtgast, Joost M. Festen	1197
BIOACOUSTICS [80]		
A numerical method to predict the effects of frequency-dependent attenuation and dispersion on speed of sound estimates in cancellous bone	Keith A. Wear	1213
Acoustic nonlinearity parameter tomography for biological tissues via parametric array from a circular piston source—Theoretical analysis and computer simulations	Dong Zhang, Xi Chen, Xiu-fen Gong	1219
Dynamic photoelastic study of the transient stress field in solids during shock wave lithotripsy	Xufeng Xi, Pei Zhong	1226
Characteristics of whistles from the acoustic repertoire of resident killer whales (<i>Orcinus orca</i>) off Vancouver Island, British Columbia	F. Thomsen, D. Franck, J. K. B. Ford	1240
Neural representation of sound amplitude by functionally different auditory receptors in crickets	Kazuo Imaizumi, Gerald S. Pollack	1247
ERRATA		
Erratum: “Thermal diffusion and mixture separation in the acoustic boundary layer” [J. Acoust. Soc. Am. 106, 1794–1800 (1999)]	G. W. Swift, P. S. Spoor	1261
CUMULATIVE AUTHOR INDEX		1262

ACOUSTICAL NEWS—USA

Elaine Moran

Acoustical Society of America, Suite 1N01, 2 Huntington Quadrangle, Melville, NY 11747-4502

Editor's Note: Readers of this Journal are encouraged to submit news items on awards, appointments, and other activities about themselves or their colleagues. Deadline dates for news items and notices are 2 months prior to publication.

The 140th meeting of the Acoustical Society of America held in Newport Beach, CA

The 140th meeting of the Acoustical Society of America was held 3–8 December 2000 at the Newport Beach Marriott Hotel and Tennis Club in Newport Beach, CA. This was the first time the Society has met in this city. The meeting was held jointly with Noise-Con 2000.

The meeting drew a total of 1368 registrants. There were 277 non-members and 224 students in attendance.

Noise-Con 2000 was arranged through the Institute of Noise Control Engineering. Twenty joint Noise-Con/ASA sessions were held from Sunday through Tuesday. A joint meeting Exhibit was sponsored and registrants had the option to purchase a copy of the proceedings of Noise-Con 2000 on CD ROM.

Attesting to the international ties of our organization, 182 of the registrants (that is, about 13%) were from outside North America, the United States, Canada, and Mexico, which accounted for 1120, 61, and 5, respectively. There were 35 registrants from Japan, 26 from the United Kingdom, 20 from Germany, 15 from Korea, 13 from France, 7 from Denmark, 6 each from Italy and Sweden, 5 from Australia, 4 each from Brazil, China, and Poland, 3 each from Malaysia, Norway, Singapore, and Switzerland, 2 each from Belgium, Netherlands, New Zealand, Spain, Thailand, and Ukraine, and 1 each from Argentina, Bangkok, Ecuador, Finland, Greece, India, Ireland, Israel, Russia, South Africa, Taiwan, Turkey, and Uzbekistan.

A total of 873 papers organized into 108 sessions covered the areas of interest of all 12 Technical Committees and 1 Technical Group. The Technical Committee on Biomedical Ultrasound/Bioresponse to Vibration sponsored a Topical Meeting on the Physics of Echo Contrast Agents—a format which was deemed successful as a method to focus attention on a particular topic. A Distinguished Lecture on “Ultrasonic Eyeglasses for the Blind” was presented by Leslie Kay of New Zealand and two ASA History Lectures were presented—one by Leo Beranek on Noise and another by Peter Ladefoged on Speech Communication.

A Gallery of Acoustics was displayed with the winning entry submitted by Dr. Michel Versluis. A Student Design Competition involving the design of a loudspeaker system was held. The winning entry was submitted by Shawn Devantier and Commendation awards were presented to Ara Baghdassarian, Geoffrey Christopherson, and David Tremblay.

The meeting also included 14 different meetings dealing with standards, indicating a healthy level of activity in this area of our endeavors. The Newport Beach meeting was preceded by a meeting of International Electrotechnical Commission Technical Committee 29 and followed by meetings of the International Organization for Standardization TC 43 and TC 43, Subcommittee 1. The ASA provides the representation to these standards committees for the American National Standards Institute.

The local meeting committee arranged the following technical tours: A tour of the Orange County Performing Arts Center featuring the 3000-seat Segerstrom Hall; John Wayne Airport Access and Noise Office; and the Fiske Museum of Musical Instruments.

The tutorial lecture series was continued at the Newport Beach meeting. Julius O. Smith III of the Center for Computer Research in Music, Stanford University, presented “Virtual Musical Instruments” to an audience of about 100. The Short Course on Applied Digital Signal Processing, with James Candy of Lawrence Livermore National Laboratory as the instructor, was filled to capacity and will be repeated at the Spring meeting in Chicago in June 2001.

The equipment exhibit began on Sunday evening with an opening reception and was open through Tuesday afternoon. It included exhibits on computer-based instrumentation and software, sound-level meters, sound intensity systems, signal processing systems, instruments for noise measurement, products and devices for noise and vibration control, and acoustical materials.

Other special events included a concert performance by the Americus Brass Band, a visit by the California State University, Long Beach, Mobile Science Museum, receptions for students in various areas of acoustics, and an all-student reception. The Fellows Luncheon was held and included a presentation by Dr. Peter Narins of the University of California, Los Angeles.

The plenary session included the presentation of awards, announcement of newly elected Fellows of the Society, and recognition of the meeting organizers. The President presented ASA Science Writing Awards, four Society awards (see Figs. 1–4) and announced the election of new Fellows (see Fig. 5).

The Science Writing Award for Professionals in Acoustics was presented to William M. Hartmann for his article in the November 1999 issue of *Physics Today* titled “How We Localize Sound.” The co-winners of the Science Writing Award in Acoustics for Journalists were announced. Kathryn Brown received the award for her series of articles published in *New*



FIG. 1. John V. Bouyoucos, recipient of the Distinguished Service Citation (r), with ASA President Katherine Harris (l).



FIG. 2. Avril Brenig, recipient of the Distinguished Service Citation (r), with ASA President Katherine Harris (l).



FIG. 3. Darrell R. Jackson, recipient of the Pioneers of Underwater Acoustics Medal (r), with ASA President Katherine Harris (l).

Scientist and Roland Pease and Radek Boschetty received the award for their audio program "Soundworks" aired by BBC World Radio Service. The Distinguished Service Citation was presented to two recipients. John Bouyoucos of Hydroacoustics Inc. received the Citation "for service, leadership and foresight in promoting innovative programs and sound financial planning for the Society's future" and Avril Brenig, ASA Standards Manager, received the Citation "for helping to build the Society's leading position in acoustical standardization." The Pioneers of Underwater Acoustics Medal was presented to Darrell R. Jackson of the University of Washington "for work on acoustic time reversal techniques and scattering from the ocean sea floor and sea surface." The Silver Medal in Physical Acoustics was presented to Gregory W. Swift of Los Alamos National Laboratory "for theoretical and experimental contributions to the development of thermoacoustic engines."

Election of the following persons to Fellow grade was announced: R. Dean Ayers, Donald Bray, Peter D'Antonio, Laurent J. D. Demany, John Franks, Oleg A. Godin, Donald E. Hall, Gordon R. Hamilton, Mark A. Holden, W. Jack Hughes, Dennis F. Jones, Richard H. Love, Hari S. Paul, Hans C. Strifors, Charles Thompson, Paul L. Thompson, and Ji-Qing Wang.

The President expressed the Society's thanks to the Local Committee for the excellent execution of the meeting, which clearly required meticulous planning. She introduced the Chair of the Meeting, Sigfrid Soli, who acknowledged the contributions of the members of his committee including: Lynne E. Bernstein, Technical Program Chair; Edward Auer, Audio-Visual; Laurie Eisenberg, Hotel/Facilities; Monita Chatterjee, Registration; Abeer



FIG. 4. Gregory W. Swift, recipient of the Silver Medal in Physical Acoustics (l), with ASA President Katherine Harris (r).



FIG. 5. Newly-elected Fellows of the Acoustical Society of America receive their certificates from ASA Vice President Gilles Daigle (far l) and President Katherine Harris (far r).

Alwan, Signs; David Lubman, Technical Tours; Robert V. Shannon, Plenary Session/Fellows Luncheon; and Shannon Adams, Accompanying Persons Program.

The President also extended thanks to the members of the Technical Program Organizing Committee: Lynne E. Bernstein, Technical Program Chair; D. Vance Holliday and Duncan McGhee, Acoustical Oceanography; Ann E. Bowles, Animal Bioacoustics; Angelo J. Campanella and Lily Wang, Architectural Acoustics; Michael R. Bailey, Biomedical Ultrasound/Bioresponse to Vibration; Joie P. Jones, Education in Acoustics; R. Lowell Smith, Engineering Acoustics; R. Dean Ayers, Musical Acoustics; Richard J. Peppin, Brigitte Schulte-Fortkamp, George C. Maling, Alan H. Marsh, and John J. Van Houten, Noise and Noise-Con; Robert M. Keolian, Physical Acoustics; Bruce G. Berg, Psychological and Physiological Acoustics; James V. Candy and David H. Chambers, Signal Processing in Acoustics; Jody Kreiman and Dani Byrd, Speech Communication; Courtney B. Burroughs, Structural Acoustics and Vibration; and David R. Dowling and Kevin B. Smith, Underwater Acoustics.

KATHERINE S. HARRIS
President 2000–2001

USA Meetings Calendar

Listed below is a summary of meetings related to acoustics to be held in the U.S. in the near future. The month/year notation refers to the issue in which a complete meeting announcement appeared.

2001

- 15–17 March Annual Meeting, American Auditory Society, Scottsdale, AZ [Wayne J. Staab, Ph.D., American Auditory Society, 512 E. Canterbury Ln., Phoenix, AZ 85022, Tel.: 602-789-0755; Fax: 602-942-1486; E-mail: amaudsoc@aol.com; WWW: www.amauditorysoc.org].
- 22–25 March "New Frontiers in the Amelioration of Hearing Loss," St. Louis, MO [Sarah Uffman, CID Department of Research, 4560 Clayton Ave., St. Louis, MO 63110, Tel.: 314-977-0278; Fax: 314-977-0030; E-mail: suffman@cid.wustl.edu].
- 30 April–3 May 2001 SAE Noise & Vibration Conference & Exposition, Traverse City, MI [Patti Kreh, SAE Int'l., 755 W. Big Beaver Rd., Suite 1600, Troy, MI 48084, Tel.: 248-273-2474; Fax: 248-273-2494; E-mail: pkreh@sae.org].
- 4–8 June 141st Meeting of the Acoustical Society of America, Chicago, IL, Palmer House Hilton Hotel [Acoustical Society of America, Suite 1N01, 2 Huntington Quadrangle, Melville, NY 11747-4502, Tel.: 516-576-2360; Fax: 516-576-2377; E-mail: asa@aip.org; WWW: asa.aip.org]. Deadline for receipt of abstracts has passed.

- 7–9 June International Hearing Aid Conference VI. Novel Processing and Fitting Strategies, Iowa City, IA [Rich Tyler, Tel.: 319-356-2471, E-mail: rich-tyler@uiowa.edu, WWW: www.medicine.uiowa.edu/otolaryngology/news/news].
- 9–13 July 2001 SIAM Annual Meeting, San Diego, CA [Society for Industrial and Applied Mathematics (SIAM), Tel.: 215-382-9800; Fax: 215-386-7999; E-mail: meetings@siam.org; WWW: www.siam.org/meetings/an01/].
- 15–19 August ClarinetFest 2001, New Orleans, LA [Dr. Keith Koons, ICA Research Presentation Committee Chair, Music Dept., Univ. of Central Florida, P.O. Box 161354, Orlando, FL 32816-1354, Tel.: 407-823-5116; E-mail: kkoons@pegasus.cc.ucf.edu].
- 19–24 August Asilomar Conference on Implantable Auditory Prostheses, Pacific Gove, CA [Michael Dorman, Dept. of Speech and Hearing Science, Arizona State Univ., Tempe, AZ 85287-0102, Tel.: 480-965-3345; Fax: 480-965-0965; E-mail: mdorman@asu.edu].
- 4–6 October Ninth Annual Conference on the Management of the Tinnitus Patient, Iowa City, IA [Rich Tyler, Tel.: 319-356-2471; E-mail: rich-tyler@uiowa.edu; WWW: www.medicine.uiowa.edu/otolaryngology/news/news].
- 7–10 October 2001 IEEE International Ultrasonics Symposium Joint with World Congress on Ultrasonics, Atlanta, GA [W. O'Brien, Electrical and Computer Engineering, Univ. of Illinois, 405 N. Mathews, Urbana, IL 61801; Fax: 217-244-0105; WWW: www.ieee-uffc.org/2001].
- 3–7 December 142nd Meeting of the Acoustical Society of America, Ft. Lauderdale, FL [Acoustical Society of America, Suite 1N01, 2 Huntington Quadrangle, Melville, NY 11747-4502, Tel.: 516-576-2360; Fax: 516-576-2377; E-mail: asa@aip.org; WWW: asa.aip.org].
- 2002**
- 3–7 June 143rd Meeting of the Acoustical Society of America, Pittsburgh, PA [Acoustical Society of America, Suite 1N01, 2 Huntington Quadrangle, Melville, NY 11747-4502, Tel.: 516-576-2360; Fax: 516-576-2377; E-mail: asa@aip.org; WWW: asa.aip.org].
- 2–6 December Joint Meeting: 144th Meeting of the Acoustical Society of America, 3rd Iberoamerican Congress of Acoustics and 9th Mexican Congress on Acoustics, Cancun, Mexico [Acoustical Society of America, Suite 1N01, 2 Huntington Quadrangle, Melville, NY 11747-4502, Tel.: 516-576-2360; Fax: 516-576-2377; E-mail: asa@aip.org; WWW: asa.aip.org/cancun.html].

Revision List

New Associates

Adachi, Kazunari, Department of Electrical and Electronic Engineering, Yamagata Univ., 4-3-16 Jonan, Yonezawa, Yanagata, 992-8510 Japan

Ali, Sherif F., 3800 West Chandler Blvd., #1118, Chandler, AZ 85226

Anderson, David, Electrical and Computer Engineering, Georgia Institute of Technology, 777 Atlantic Dr., Atlanta, GA 30332-0250

Au-Yeung, James B., Psychology Department, University College London, Gower St., London WC1E 6BT, United Kingdom

Avan, Paul A., Biophysics, School of Medicine, 28 Place Dunant, P.O. Box 38, Clermont-Ferrand 63001, France

Balck, Ralph E., 957 Maxwell Ave., SE, Grand Rapids, MI 49506

Ballesty, Darragh E., DSP Group, Silicon & Software Systems, South County Business Park, Leopardstown, Dublin 18, Ireland

Bartlebaugh, Ronald J., 2636 Cardington Green, Uniontown, OH 44685-7526

Bassett, John, G.P.O. Box 372, Sydney 1043, Australia

Bayon, Ana, Caleruega 97, 5F, Madrid 28033, Spain

Berg, Erik A., Systems Development Div., SRS Technologies, 105 North "H" St., Lompoc, CA 93436

Bettega-Correa, Arthur, Inst. de Pesquisas da Marinha, Grupo de Sonar, Rue Ipiru 2, Rio de Janeiro, RJ 21931-090, Brazil

Bidondo, Carlos A., Freire 3766, Capital Federal, Buenos Aires 1429, Argentina

Brown, Ellen D., SAIC, 10260 Campus Point Dr., San Diego, CA 92121

Bui, Sean K., 25812 Bronte La., Stevenson Ranch, CA 91381

Burghardt, Gunther, Nokia GmBH, P.O. Box 101823, Bochum 44718, Germany

Campbell, Christopher S., IBM Almaden Research Center, 650 Harry Rd., NWE-B2, San Jose, CA 95120

Charette, Francois, 46324 Gainsborough, Canton, MI 48187

Chelf, Roger D., 18569 Foliage Rd., Diamond, MO 64840

Chiu, Peter, Psychology Department, University of Cincinnati, 401A Dyer Hall, ML 0376, Cincinnati, OH 45221-0376

Colman, Jeremy G., New Ventures Div., Woodside Energy Ltd., 1 Adelaide Terrace, Perth WA 6000, Australia

Cowan, Leigh, U.S. Audiology, P.O. Box 5027, Oak Ridge, TN 37830

Crew, Jennifer C., 46 Pine Ridge Rd., East Falmouth, MA 02536

Crockett, Ben H., Management Recruiters of Chicago Farwest, 564 South Washington St., Suite 203, Naperville, IL 60540

Cruz, Rachel J., Hearing and Speech Research Laboratory, University of California, Irvine, 364 Med. Surg. II, Irvine, CA 92697

Dat, Tran H., Institute of Hydromechanics of National Academy of Sciences of Ukraine, Zeliaboya Str. No. 8/4, Kiev 03680, Ukraine

de Castro, Sandro, SAE Technology College, Audio Engineering Diploma, Weena, 732-D7.137, Rotterdam, Zuid Holland, 3013AM, The Netherlands

Deffenbaugh, Max, Exxon Mobil Upstream Research, P.O. Box 2187, Houston, TX 77252

DeMoss, Jeffrey J., Dell Computer, Acoustics Laboratory, One Dell Way, Round Rock, TX 78682

Dickey, Nolan S., Ohio State University, ME/Ctr. for Automotive Research, 930 Kinnear Road, Columbus, OH 43212-1443

Diniz, Solon, Rua Dario Coelho, 45 casa 2, Rio de Janeiro, RJ 22793-270, Brazil

Dugelay, Samantha, DERA, Newton's Road, Weymouth, Dorset DT4 8UR, United Kingdom

Evans, Kirk E., 10105 Mill Wheel La., Vienna, VA 22182

Eysholdt, Ulrich, Department of Phoniatics, University of Erlangen, Bohlenplatz 21, Erlangen D-91054, Germany

Fellner, Maria, Feuerbachgasse 7, Graz A-8020, Austria

Fernandez, Marcos D., Signal Theory and Communications, Telecommunications Engineering, Polytechnic School of Cuenca, University of Castilla—La Mancha, Camino Del Pozvelo, S/N, Cuenca 16071, Spain

Freeberg, Todd M., Audiology and Speech Sciences, Purdue University, Heavilon Hall, West Lafayette, IN 47907

Futa, Kohji, 103 Fudogaoka-Msn, 524 Kameino, Fujisawa-shi, Kanagawa, 252-0813 Japan

Galmarini, Chuck, Building Materials, The Dow Chemical Company, 1605 Joseph Dr., Midland, MI 48674

Gong, Xiu-Fen, Department of Electronics Science and Engineering, Institute of Acoustics, Nanjing University, 22 Hankou Rd., Nanjing 210093, China

Gonneau, Eric, LAMI—Univ. Paul Sabatier, 118 Route de Narbonne, Toulouse 31062, France

Gordon, Jonathan C. D., Sea Mammal Research Unit, Gatty Marine Laboratory, University of St. Andrews, St. Andrews, Fife KY16 8LB, United Kingdom

Guise, Paul E., 551-3535 55th Ave., Red Deer, ON T4N 0W4, Canada

Gumerov, Nail A., 7496 Merrymaker Way, Elkridge, MD 21075

Hammer, Michael J., 2020 West 27th, Apt. #6, Lawrence, KS 66046

Harris, John G., Electrical and Computer Engineering, University of Florida, 353 EB, P.O. Box 116130, Gainesville, FL 32611

Hin, Chow K., Sound & Communication & Acoustics Treatment, Mega Snergy Sdn Bhd, 23A Jalan Helang 13, Bandar Puchong Jaya, Puchong, Selangor, 47100 Malaysia

Hiroshi, Sato, 3-6-401 Hayamamachi, Aoba-Ku, Sendai, Miyagi Pref., 981-0917 Japan

Holm, James P., 2466 Signal Hill Dr., Kalamazoo, MI 49009

Homayounfar, Kambiz, Genista, Aoyama Nozue 301, 2-11-10 Kita Aoyama, Minato-ku, Tokyo, 107-0061 Japan

- Horne, John K., School of Aquatic and Fishery Sciences, University of Washington, Box 355020, Seattle, WA 98195-5020
- Hunsaker, Don II, Hubbs Sea World Research Institute, 2595 Ingraham St., San Diego, CA 92109
- Ishikawa, Keiichi, 25-7 Shiomi-cho, Ashiya-shi, Hyogo, 659-0043 Japan
- Ishiwata, Tsuneo, Oki Electric Industry Co., Ltd., Advanced Technology Research Division, 10-3 Shibaura, 4-chome, Minato-ku, Tokyo, 108-8551 Japan
- Iyer, Shrinivas N., Bint Al Jazeera Electronics, Salam Street, Co-Orp Off. Center, Ground No. 4, Mex. 02, Abu Dhabi 46845, UAE
- Jacewicz, Ewa, Speech and Hearing Science, Ohio State University, 1070 Carmack Rd., Columbus, OH 43210
- Johnson, Mark, Applied Ocean Physics and Engineering, Woods Hole Oceanographic Institute, Water Street, Woods Hole, MA 02543
- Jones, Andrew, Pioneer Electronics Technology, Inc., 1800 West Holt Ave., Pomona, CA 91768
- Jonte, Patrick, Delta Faucet Company, 55 East 111th St., Indianapolis, IN 46280
- Kentaro, Ishizuka, NTT Communication Science Laboratories, Media Information Laboratory, Morinosato-Wakamiya 3-1, Atsugi City, Kanagawa, 243-0198 Japan
- Kerr, Fiona H., Underwater Sensors and Oceanography, Defense Evaluation and Research Agency, Building A22, Winfrith Technology Centre, Dorchester, Dorset DT2 8XJ, United Kingdom
- Lago, Thomas L., 70 Himalaya Ct., Alpine, UT 84004
- Landa, Michal, Institute of Thermomechanics, Czech Academy of Sciences, NDT&E Laboratory, Dolejskova 5, Prague 18200, Czech Republic
- Lane, Steven A., Space Vehicles, Air Force Research Laboratory, 3550 Aberdeen Avenue, SE, VSSV, Kirtland AFB, NM 87117-5776
- Lang, William, Minerals Management Service, 1201 Elmwood Park Blvd., New Orleans, LA 70123
- Larsen, Claus, Sofielundvej 18, Glostrup, Copenhagen, 2600 Denmark
- Larsen, Ole N., Center for Sound Communication, Institute of Biology, University of Southern Denmark, Campusvej 55, Odense DK-5230, Denmark
- Legleiter, Kurt A., EDAW, Inc., Air Quality and Noise Division, 2022 "J" St., Sacramento, CA 95814
- Lenk, Torsten, Chemnitz University of Technology, Informatik/DVS, Strasse der Nationen 62, Chemnitz, Sachsen 09107, Germany
- Lopez-Poveda, Enrique A., Facultad De Medicina, Medical Sciences, Campus Universitario, Albacete 02071, Spain
- Luttrell, Robert S., National Center for Physical Acoustics, 1 Coliseum Drive, Oxford, MS 38677
- Marvit, Peter, 11 Stearns Rd., Watertown, MA 02472
- Medlin, Kathleen, 6660 Curlew Terrace, Carlsbad, CA 92009
- Messerly, Jeffrey D., 3940 Marburg Ave., Cincinnati, OH 45209
- Mihelich, Ryan J., 419 Canal View Circle, Apt. B, Indianapolis, IN 46202
- Mills, Harold G., Bioacoustics Research Program, Cornell Laboratory of Ornithology, 159 Sapsucker Woods Rd., Ithaca, NY 14850
- Morozov, Andrey K., Webb Research Corporation, 82 Technology Park Dr., East Falmouth, MA 02536
- Munson, Benjamin R., Communication Disorders, University of Minnesota, 164 Pillsbury Dr., SE, Minneapolis, MN 55455
- Musser, Chadwyck T., Cambridge Collaborative, Inc., 689 Concord Ave., Cambridge, MA 02138
- Neuhoff, John G., Psychology Department, College of Wooster, Kauke Hall, Wooster, OH 44691
- Noonan, Timothy F., D. L. Adams Associate, Ltd., 970 North Kalaheo Ave., A-311, Kailua, HI 96734
- Nyland David L., WesternGeco, 351 East International Airport Rd., Anchorage, AK 99518
- O'Connell, John, 15 Hancock Ave., Yonkers, NY 10705
- Parkinson, Anthony F., 4 Lomond Ct., West Lakes SA 5021, Australia
- Paul, Donald W., 44 Baltic Ave., North Easton, MA 02356
- Prausnitz, Mark R., School of Chemical Engineering, Georgia Tech, 778 Atlantic Dr., Atlanta, GA 30332-0100
- Rizzi, Stephen A., NASA Langley Research Center, Structural Acoustics Branch, MS 463, 2 North Dryden St., Hampton, VA 23681-2199
- Rodriguez, Gonzalo J., Maryland Sound and Image, Inc., 4900 Wethereds-ville Rd., Baltimore, MD 21207
- Ross, Leslie M., 520 East 14th St., #35, New York, NY 10009
- Rudzinsky, Jason P., 11 Hunter Dr., Derry, NH 03038
- Scandrett, Clyde, Naval Postgraduate School, Mathematics Department, 1411 Cunningham Rd., Monterey, CA 93943
- Schmidt, William B., National Park Service, NRSS, 1849 "C" St., NW, Washington, DC 20240
- Schuhmann, Richard J., Department of Environmental Engineering, Pennsylvania State University, 212 Sackett Building, University Park, PA 16802
- Senzig, David A., Senzig Engineering, 7 Everett St., Boston, MA 02130
- Shinn, Philip E., 1110 B Milo Circle, Lafayette, CO 80026
- Shreves, Joseph W., SPL Services, Inc., 3580 El Paso Alto, Vista, CA 92084
- Smith, Randy W., University of Arkansas for Medical Sciences, Audiology and Speech Pathology, 2801 South University, Little Rock, AR 72204
- Sprague, Mark W., Department of Physics, East Carolina University, Howell Science Complex, Greenville, NC 27858
- Srinivas, Narasimha, 1 Tarangini Apt. Prabhadevi, Mumbai, Maharashtra, 400025 India
- Storey, Brian D., F. W. Olin College of Engineering, 1735 Great Plain Ave., Needham, MA 02492
- Sundermuthy, Sanjay, Starkey Laboratories, Inc., Applications Engineering, 6600 Washington Ave., South, Eden Prairie, MN 55344
- Szyhowski, Amy M., Engineering Dynamics International, 8420 Delmar Blvd., Suite 303, St. Louis, MO 63124
- Tanaka, Akira, Division of Systems and Information Eng., Hokkaido University, Kita-13, Nishi-8, Kita-ku, Sapporo, Hokkaido 060-8628, Japan
- Tanaka, Nobuo, Department of Mechanical Engineering, Tokyo Metropolitan Institute of Technology, 6-6 Asahigaoka, Hino-City, Tokyo 191-0065, Japan
- Teel, Jeffrey D., Acoustical Design Group, 5799 Broadmoor, Suite 108, Mission, KS 66202
- Ternstrom, Sten O., Kungliga Tekniska Hogskolan, Speech, Music and Hearing, Drottning Kristinas Vag 31, Stockholm SE-10044, Sweden
- Tinkle, Mark D., Dynamics Technology, Inc., 21311 Hawthorne Blvd., Suite 300, Torrance, CA 90503-5691
- Tokashiki, Takeshi, Department of Civil Engineering and Architecture, University of the Ryukyus, 1 Senbaru Nishihara-cho, Nakagami-gun, 903-0213 Japan
- Tollefsen, Dag, Forscarets Forskningsinstitut, BM-H, Boks 115, Norten N-3191, Norway
- Turneare, Stefan J., 124 North Gill St., #2, State College, PA 16801
- Vera, Sergio, Belgrano 477, Dpto. 1, Bahia Blanca, Buenos Aires 8000, Argentina
- Wahyudi, Ir., Jl. Setiabudhi 274, Bandung WJ-40143, Indonesia
- Wattanasarn, Thukkapol, ADR Co., Ltd., House 1, Soi Pipat, Convent Road, Bangrak, Bangkok, 10500 Thailand
- Wattrus, Nigel J., Large Lakes Observatory, University of Minnesota, 10 University Dr., Duluth, MN 55812
- Yaeger-Dror, Malcah L., 5252 East 3rd St., Tucson, AZ 85711-1328
- Zhang, Jinmin, Advanced Materials Lab., DSO National Labs., 20 Science Park Dr., S118230 Singapore
- Zimmerman, Eric J., 5980 Chesbro Ave., San Jose, CA 95123-3915
- Zoccola, Paul J., Naval Surface Warfare Center, Carderock Division, Code 725, 9500 MacArthur Blvd., West Bethesda, MD 20817

New Students

- Andrews, Meagan K., 865 Kings Crossing Dr., Concord, NC 28027
- Asmussen, Robert L., 220 Indiana St., Neodesha, KS 66757
- Bajwa, Manjit, Mechanical Engineering, Wayne State University, 5100 Anthony Wayne Dr., Detroit, MI 48202
- Ball, Keenan R., 277 Bumfagon Rd., Loudon, NH 03307
- Barthmaier, Paul T., Department of Linguistics, University of California, Santa Barbara, 3607 South Hall, Santa Barbara, CA 93106
- Boemio, Anthony B., 11206 Snowden Pond Rd., Laurel, MD 20708
- Bourgeois, Paul J., 22910 Bruce Dr., Richton Park, IL 60471
- Bradley, David T., Physics Department, Grinnell College, P.O. Box 01-66, Grinnell, IA 50112
- Campbell, Gregory S., 175 Juniper Ave., Carlsbad, CA 92008
- Chung, Hyunjuo, 1189 Spruce Court, Kent, OH 44240
- Corey, Jason A., Faculty of Music, McGill University, 555 Sherbrooke St., West, Montreal, PQ H3A 1E3, Canada

- Davies, Chris L., 415 South Atherton St., Apt. C-6, State College, PA 16801
del Solar Dorrego, Fernando M., Estancias Lauquen, C. Pellegrini 1163 p12,
Buenos Aires 1009, Argentina
- DeSellier, Cherish, 43 Harmon Ave., Springfield, MA 01118
- Dizon, Roberto M., Hearing Research Center, Boston University, 44 Cum-
mington St., Boston, MA 02144
- Dubaniewicz, Witold, ul. Slaska 57/30, Gdynia, Pomorski 80-304 Poland
- Dugan, Erin L., 821A #7 Southgate Dr., State College, PA 16801
- Edmonds, Barrie A., 118 Arabella St., Cardiff, Wales CF24 4TB, United
Kingdom
- Elias, Jennifer A., 315 South West Ave., Apt. G, Elmhurst, IL 60126
- Fisher, Karen E., Ocean Resources and Ecosystems, Cornell University,
2154 Snee Hall, Ithaca, NY 14853
- Flanagan, Sheila A., Department of Experimental Psychology, University of
Cambridge, Downing Street, Cambridge CB2 3EB, United Kingdom
- Gardner, Glenn C., Mechanical Engineering, University of Delaware, 126
Spencer Laboratory, Newark, DE 19716
- Giordano, Bruno L., Via Sorio 8, Padova PD 35141, Italy
- Grinnip, Roger S., 1011 North 20th St., Lafayette, IN 47904
- Hacopian, Narineh, Linguistics Department, University of Southern Califor-
nia, 3601 Watt Way, GFS 301, Los Angeles, CA 90089-1693
- Hall-Lew, Lauren A., 1421 East Mabel, Tucson, AZ 85719
- Hamilton, Phillip M., 11250 Playa St., 100, Culver City, CA 90230
- Hibbs, Merrill G., 3742 US Hwy. 321, South, Blowing Rock, NC 28605
- Jang, Seung-Ho, NOVIC, Department of Mechanical Engineering, Korea
Advanced Institute of Science and Technology, Science Town, Taejon
305-701, Korea
- John, Krueger S., Engineering, University of Hartford, Box 3781, 200
Bloomfield Ave., West Hartford, CT 06117
- Jones, Jeffery A., Psychology Department, Queen's University, Humphrey
Hall, Kingston, ON K7L 3N6, Canada
- Kelly, Michael C., 48 Westwood Terrace, York, North Yorkshire YO23
1HL, United Kingdom
- Kim, Bumjun, 2909 SW 13th St., #37, Gainesville, FL 32608
- Kim, Byung-Chul, 537 Lincoln Street, 1st Fl., Palisades Park, NJ 07650
- Kim, Wontak, Acoustics, Pennsylvania State University, P.O. Box 30, State
College, PA 16804
- Kim, Youngmoo E., MIT Media Laboratory, 20 Ames St., E15-401, Cam-
bridge, MA 02139
- Kimotsuki, Kayo, 6165 North Winthrop Ave., Apt. 611, Chicago, IL 60660
- Kovacyk, Kristie J., 488 Highbury Rd., Cheswick, PA 15024
- Kraus, Michael A., 4605 Lindell Blvd., Apt. 402, St. Louis, MO 63108
- Larson, Julie C., 87 Rhodes Ct., San Jose, CA 95126
- Lau, Justin Y., 4 Blackberry Lane, Andover, MA 01810
- Lawson, Mark A., Department of Construction Management and Engineer-
ing, Reading University, Room G04, Furs, Whiteknights, P.O. Box 219,
Reading RG6 6AW, United Kingdom
- Lecomte, Christophe, 109 Standish Rd., Watertown, MA 02472
- Lee, Young-A, Architecture, University of Ulsan, Mugeo-dong 29 namgu,
Ulsan 689-749, Korea
- Litvak, Leonid M., Massachusetts Eye and Ear Infirmary, Eaton Peabody
Laboratory, 243 Charles St., Boston, MA 02135
- Liu, Jin, 229 South Sparks St., Apt. 16, State College, PA 16801
- Lussier, Brett A., 3611 University Dr., Apt. 15H, Durham, NC 27707
- Ma, Binbing, School of Oceanography, University of Washington, Boat St.
Turnoff 15 Avenue, NE, Box 357940, Seattle, WA 98195-7940
- Marrone, Nicole L., 608 7th St., SE, #48, Minneapolis, MN 55414
- Megregor, Iain P., 22 Lochrin Buildings, Edinburgh, Lothian EH3 9NB,
Scotland
- Mellody, Maureen, 1843 Pointe Crossing, #304, Ann Arbor, MI 48105
- Munro, Jennifer A., 1230 Massachusetts Ave., #6, Arlington, MA 02476
- Nelson, Brian S., 8475 East Kent Rd., Bloomington, IN 47401
- O'Halloran, Ryan P., 1432 Louisiana St., Lawrence, KS 66044
- Orgar, John E., University of Hartford, Box 346, 200 Bloomfield Ave., West
Hartford, CT 06117
- Oswald, Julie N., Scripps Institute of Oceanography, University of Califor-
nia, San Diego, 9500 Gilman Dr., La Jolla, CA 92123
- Paek, Hyun, 2600 SW Williston Rd., 721, Gainesville, FL 32608
- Park, Duk W., P.O. Box 10111, Calder Square, State College, PA 16805
- Paul, Brent S., 3181 Shellers Bend, #3, State College, PA 16801
- Pauli, Nathan S., 1518 East Beach, Peoria Heights, IL 61614
- Payri, Blas G., UCLA, Head and Neck Surgery, 31-24 Rehabilitation, Los
Angeles, CA 90095-1794
- Pinyard, Michael S., 200 Bloomfield Ave., West Hartford, CT 06117
- Pradhan, Rajdeep S., Graduate Program in Acoustics, Pennsylvania State
University, Applied Science Building, West Campus, State College, PA
16801
- Preissner, Curt A., 9628 West Higgins, Rosemont, IL 60018
- Ramamoorthy, Sripriya, Mechanical Engineering, University of Michigan,
2200 EECS, 1301 Beal Ave., Ann Arbor, MI 48109-2122
- Rapp, Brian M., Campus Box 3860, Wydown Boulevard, St. Louis, MO
63105-2298
- Reilly, Kevin J., University of Washington, Department of Speech and
Hearing Science, 1417 NE 42nd St., Seattle, WA 98105-2406
- Rosso, Pablo Nahuel, C. Lorenzini 4238, Los Polvorines, Buenos Aires,
1613 Argentina
- Sands, Kathy L., 297 Mathilda Dr., #2, Goleta, CA 93117
- Sanford, Chris A., Speech and Hearing Sciences, University of Washington,
1417 NE 42nd St., Seattle, WA 98105
- Sebastian, Ghinet, Genie Mecanique, Univ. de Sherbrooke, 2500 Boul. de
l'Universite, Sherbrooke, PQ J1K 2R1, Canada
- Seresangtakul, Pusadee, International House B201, University of the
Ryukyus, Senbaru, Nishihara, Okinawa 903-0129, Japan
- Shandera, Karen R., 445 Waupelani Dr., Apt. B-10, State College, PA
16801
- Shapley, Kathy L., 1301 Lincoln Mall, #206, Lincoln, NE 68508
- Shin, Jinho, 808 Opal Dr., #2, San Jose, CA 95117
- Smyth, Todd S., 150 Massachusetts Ave., Box 928, Berklee College of
Music, Boston, MA 02115
- Steele, Catriona M., 65 Guthrie Ave., Toronto, Ontario M8Y 3L2, Canada
- Suzuki, Takao, Aeronautics and Astronautics, Stanford University, Durand
Building, Room 364, Stanford, CA 94305-4035
- Takehara, Shinichi, 206 Hyunfuburugu, 4-13-22 Honmachi, Nonoichimachi,
Ishikawagunn, Ishikawa 921-8815, Japan
- Thomas, Liao Y. C., University of Warwick, Claycroft Hall 1, Flat No. 16,
Room No. 3, Coventry, Warwickshire CV4 7AL, United Kingdom
- Treesuwan, Paskorn, Mechanical Engineering Department, Vibration Con-
trol and Smart Material Laboratory, Catholic University of America, 620
Michigan Ave., G-32 Pangbon Hall, Washington, DC 20064
- Tucholski, Edward J., Naval Postgraduate School, Physics Department,
Spanagle Hall, 833 Dyer Rd., Monterey, CA 93940
- Turkovic, Alex F., 1016 West 12th St., Rolla, MO 65401
- Veprek, Peter, Panasonic Speech Technology Laboratory, 3888 State St.,
#202, Santa Barbara, CA 93105
- Verneuil, Andrew C., 811 Madera Place, Fullerton, CA 92835
- Wolfe, Patrick J., Signal Processing Group, Cambridge University, Trump-
ington St., Cambridge, Cambridgeshire CB2 1PZ, United Kingdom
- Wrede, Britta, Faculty of Technology, Applied Computer Science Group,
Bielefeld University, Universitaetsstr. 25, Bielefeld NRW 33615, Ger-
many
- Yang, Xinmai, Aerospace/Medical Engineering, Boston University, 110
Cummington St., Boston, MA 02215
- Yeh, John R., 12406 Silverbitch La., Laurel, MD 20708
- Zagrai, Andrei N., Mechanical Engineering, University of South Carolina,
300 South Main St., Office A236, Columbia, SC 29208
- Zakaria, Ahmad, Applied Physics, Curtin University of Technology, Kent
St. Bentley, Perth WA 6102, Australia
- Zollinger, Sue Anne, Department of Biology, Indiana University, 1001 East
Third St., Bloomington, IN 47405
- Zou, Wei, Theoretical and Applied Mechanics, Cornell University, 212
Kimball Hall, Ithaca, NY 14853

Students to Associates

- N. A. Amos, M. Blau, K. E. Bunton, D. A. Cartes, J. A. Coady, B. C.
Davenny, M. Destrade, B. J. Doust, T. Fitch, A. J. Fredricks, F. M. Guillot,
J.-Y. Jeng, C. D. Jones, M. Kariyasu, M. J. Kiefert, S.-M. Kim, L. M.
Knightly, B. J. Kwon, C. Y. Lee, S. A. Lindemann, B. F. Magill, B. A.
Mulhearn, B. R. Munson, F. R. Pereira, G. R. Potty, A. Sarampalis, R. W.
Schwenke, B. L. Scott, E. J. Terrill, R. J. Tincoff, R. J. Unglenieks, M. B.
Van Dyke, H. K. Vorperian, J. D. Warren, M. Zampolli

Associates Elected Members

D. H. Chambers, R. G. Holt, S. H. R. Hosseini, S. Kawamura, C. T. Kello, J. C. Lacefield, S. Manneville, S. L. Mattys, P. Menounou, R. L. O'Toole, A. Peiffer, M. Salameh, E. A. Stickland, A. M. Sutin, T. R. Waters, I. Yukio

Associate to Student

G. J. Overson

Reinstated

J. R. Franks—*Fellow*

S. A. Africk, K. R. Dickensheets, J. W. Myatt, S. K. Tomar—*Members*

G. P. Smith—*Student*

Resigned

J. R. Pierce, E. L. R. Corliss—*Fellows*

J. L. Baylor, I. W. Campbell, R. Cohen, R. P. Dougherty, A. Eilemann, D. C. Greene, P. C. Kirkland, A. H. Lubell, W. H. Marsh, J. C. Ortega, J. G. Schothorst, E. D. Smith, A. W. Walker, G. H. White III, T. J. Zadnik—*Members*

B. Bhattacharya, J. A. Campbell, C. C. Countryman, R. I. Goodwin, M. G. Imhof, B. J. Kroger, A. K. Kukk, C. C. Matthews, S. R. Mehta, J. Ohman, D. L. Shaffer, I. Stemplinger, A. Stirnemann, D. L. Storm, L. Van Vliet, K. Weninger—*Associates*

G. A. Epling, S. C. Hill, S. A. Kollman, D. E. Rust—*Students*

Deceased

J. H. Dewson III, W. M. Hall, B. Hartmann, S. Labate, S. F. Lybarger, J. G. Woodward—*Fellows*

H. T. Chaudiere, D. D'Eustachio, J. W. Gratian, L. F. Heiner, R. C. Maninger—*Members*

T. J. Carroll—*Associate*

Fellows	969
Members	2763
Associates	2879
Students	<u>905</u>
	7516

BOOK REVIEWS

P. L. Marston

Physics Department, Washington State University, Pullman, Washington 99164

These reviews of books and other forms of information express the opinions of the individual reviewers and are not necessarily endorsed by the Editorial Board of this Journal.

Editorial Policy: *If there is a negative review, the author of the book will be given a chance to respond to the review in this section of the Journal and the reviewer will be allowed to respond to the author's comments. [See "Book Reviews Editor's Note," J. Acoust. Soc. Am. 81, 1651 (May 1987).]*

Hearing: Its Physiology and Pathophysiology

Aage R. Møller

Academic Press, San Diego, 2000.

xv + 515 pp. Price: \$79.95 (hardcover) ISBN: 0125042558.

In the introduction to this book, Møller states that the book "... not only prepares the clinician and the clinical researcher for the challenges of the modern clinical auditory discipline, but the knowledge it provides about the pathophysiology of the auditory system is also essential to individuals engaged in basic research in the auditory field The text thus aims at cross fertilization between clinicians, clinical researchers, and basic scientists." In keeping with this goal, the book provides an extensive and comprehensive overview of the anatomy and physiology of the auditory system and of the physiological basis of various pathologies of the auditory system.

The book is divided into four main sections, each with its own reference section. Also, within the text, references are cited using a numbering system, i.e., the author's name and the date of the reference are not given. I found this a little annoying, as I was constantly skipping to the reference sections to see what piece of work was being cited to support a particular claim, and this task was made more cumbersome by the existence of four separate reference sections.

The first section of the book deals with "The Ear." Within that section there are chapters on The Anatomy of the Ear, Sound Conduction to the Cochlea, Physiology of the Cochlea, and Electrical Potentials in the Cochlea. The second section of the book is concerned with the "Auditory Nervous System." The chapters cover Anatomy of the Auditory Nervous System, Representation of Frequency in the Auditory System, Is Temporal Code or Place Code the Basis for Frequency Discrimination?, Coding of Complex Sounds, Hearing with Two Ears, Electrical Potentials in the Auditory Nervous System and Far-Field Evoked Potentials. Section 3 covers "Acoustic Reflexes" and section 4 covers "Disorders of the Auditory System and Their Pathophysiology." Chapters include Sound-Conducting Apparatus, Disorders of the Cochlea, Auditory Nerve and Auditory Nervous System, and Tinnitus, Hyperacusis, and Phonophobia. Each chapter is preceded by an "Abstract" which lists the key points made in that chapter, which should be useful for students and researchers alike.

The writing is, for the most part, clear, although sometimes anatomical terms and names of disorders are used without explanation, which might lead to difficulties for some readers without a clinical background. Difficult concepts are explained clearly and there are many helpful diagrams. However, there are several figures where one of the axes is not labeled, and some of the figures contain features or information which are not referred to or explained in the text. One diagram (page 33) has axes that are labeled in a language other than English (perhaps Swedish?). There are quite a few minor grammatical errors, which should have been picked up by the copy editor. Perhaps most importantly, the facts presented are accurate, and the interpretations given by Møller are authoritative. In other words, this is a book whose contents can, by and large, be trusted. There are extensive references, especially to Møller's own research, and this makes it easy for the reader to track down original sources and check the evidence for themselves. However, this is much less the case in instances where Møller discusses psychoacoustic and perceptual results; references to such work are few and far between, which is a pity.

There were a few places where I found the text confusing or inaccurate. For example, on page 159, there is a figure reproduced from Johnstone *et al.* (1986) showing responses of the basilar membrane of a guinea pig. The figure appears to show the response magnitude as a function of frequency for four input levels; the y axis is labeled "BM amplitude dB." But, the figure caption states "The amplitude scale is normalized, and the individual curves would have coincided if the basilar membrane motion had been linear." This does not seem to be correct, as the response of the basilar membrane is approximately linear for frequencies well below the characteristic frequency, and the curves clearly do not coincide at these frequencies. On page 162, Møller points out that "... the location on the basilar membrane where the cochlear microphonic response...was largest, shifted more than 4 mm towards the base of the cochlea when the sound intensity was increased from 60 to 100 dB." He goes on to state "This corresponds to a shift in the frequencies (of several octaves) to which a certain point is tuned." In fact, a shift of 4 mm corresponds to a shift in frequency of less than one octave (Greenwood, 1961).

Møller does not distinguish clearly between frequency selectivity (the ability to resolve the simultaneous frequency components in a complex sound) and frequency discrimination (the ability to detect changes in frequency over time). This is unfortunate, and it leads to confusion at times. For example, on page 182 he states "... it is also frequency discrimination that makes it possible to hear the difference between complex sounds with different spectra."

There is some inconsistency in the numbers he gives regarding the ability of humans to detect changes in interaural timing. For example, on page 178 Møller states that $2 \mu\text{s}$ is "about the same time difference as can be discriminated in the arrival time of sounds at the two ears." Few researchers have reported thresholds as low as this. On page 194 he states that "interaural time intervals of approximately $1 \mu\text{s}$ can be detected by the auditory nervous system." In Chap. 9 (page 246), Møller gives a more realistic estimate, stating that "humans can detect interaural time differences of 5–10 μs under ideal conditions."

In discussing the work of Sachs and Young (1980) on the coding of the spectra of vowel-like sounds, Møller ignores the possible role of neurons with low spontaneous rates (and wide dynamic ranges) (Liberman, 1978) and hence concludes "... the place representation of vowel formants cannot be regarded as sufficient to discriminate formant frequencies." Later (page 187) he states "... speech discrimination is more dependent on the time pattern of sounds than on their spectrum." These conclusions seem a bit too strong to me.

The section on disorders of the auditory system seems to be written at a slightly different level from the other sections. There are fewer references, and the writing is less dense. On the whole, this section is easier to read and follow than the other sections. However, there are a few poorly explained points. For example, many audiograms are shown without any statement of the meanings of the symbols used in the audiograms. Clinicians will be familiar with the conventional symbols, but some basic researchers may not be. Loudness recruitment is described (page 397) in these terms: "A person with cochlear hearing loss hears a sound that is slightly above the elevated threshold almost as loud as a person with normal hearing." In fact, for a person with moderate hearing loss, the loudness often does not reach the "normal" value until the sound is 30 to 50 dB above threshold (Moore and Glasberg, 1997), which can hardly be described as "slightly." On page 413 it is stated that "... the amplification caused by outer hair cells ... has little effect for sounds that are more than 50–60 dB above (normal) hearing

threshold." Many researchers believe that the active mechanism mediated by the outer hair cells plays a role over a considerably wider range than this (Ruggero *et al.*, 1997; Russell and Murugasu, 1997).

Although I have dwelled on some minor shortcomings of the book, overall, I regard it as a valuable work, covering a very wide range of materials in a clear and authoritative way. It will be useful both to clinicians and basic researchers, and I am glad to have it on my shelves. I have no doubt that I will refer to it often in the coming years.

Greenwood, D. D. (1961). "Critical bandwidth and the frequency coordinates of the basilar membrane," *J. Acoust. Soc. Am.* **33**, 1344–1356.
 Johnstone, B. M., Patuzzi, R., and Yates, G. K. (1986). "Basilar membrane measurements and the travelling wave," *Hear. Res.* **22**, 147–153.
 Liberman, M. C. (1978). "Auditory-nerve response from cats raised in a low-noise chamber," *J. Acoust. Soc. Am.* **63**, 442–455.

Moore, B. C. J., and Glasberg, B. R. (1997). "A model of loudness perception applied to cochlear hearing loss," *Aud. Neurosci.* **3**, 289–311.
 Ruggero, M. A., Rich, N. C., Recio, A., Narayan, S. S., and Robles, L. (1997). "Basilar-membrane responses to tones at the base of the chinchilla cochlea," *J. Acoust. Soc. Am.* **101**, 2151–2163.
 Russell, I. J., and Murugasu, E. (1997). "Medial efferent inhibition suppresses basilar membrane responses to near characteristic frequency tones of moderate to high intensities," *J. Acoust. Soc. Am.* **102**, 1734–1738.
 Sachs, M. B., and Young, E. D. (1980). "Effects of nonlinearities on speech encoding in the auditory nerve," *J. Acoust. Soc. Am.* **68**, 858–875.

BRIAN C. J. MOORE
Department of Experimental Psychology
University of Cambridge
Downing Street
Cambridge CB2 3EB, England

BOOKS RECEIVED

Master Handbook of Acoustics. F. Alton Everest. McGraw-Hill, New York, 2000. 592 pp. \$34.95 *pb*. ISBN 0071360972.
The Noise Manual, 5th Edition. E. H. Berger, L. H. Royster, J. D. Royster, D. P. Driscoll, and M. Layne, eds. AIHA, Virginia, 2000. 818 pp. \$74.00 *hc* ISBN 0932628029.
Handbook of Multimodal and Spoken Dialogue Systems: Resources, Terminology, and Product Evaluation. Dafydd Gibbon, Inge Mertins, and Roger Moore, eds. Kluwer Academic Publishing, Netherlands, 2000. \$175.00 *hc*. ISBN 0792379047.
The Emergence of the Speech Capacity. D. Kimbrough Oller. Lawrence Erlbaum Assoc., 2000. 441 pp. \$99.95 *hc* (\$39.95 *pb*). ISBN 0805826289 *hc* (0805826297 *pb*).
Emerging Cognitive Abilities in Early Infancy. F. Lacerda, C. von Hofsten, and M. Heimann, eds. Lawrence Erlbaum Associates, New Jersey, 2000. 264 pp. \$59.95 *hc* (\$27.50 *pb*). ISBN 0805826696 *hc* (080582670X *pb*).
Experimental Acoustic Inversion Methods for Exploration of the Shallow Water Environment. A. Caiti, J-P. Hermand, S. M. Jesus, and M. B. Porter, eds. Kluwer Academic Publishers, 2000. 302 pp. \$127.00 *hc*. ISBN 0792363051.
Assessment and Prediction of Speech Quality in Telecommunications. Sebastian Möller. Kluwer Academic Publishers, Boston, 2000. 257 pp. \$115.00 *hc*. ISBN 0792378946.
Science of Percussion Instruments. Thomas D. Rossing. World Scientific

Pub. Co., New Jersey, 2000. 224 pp. *hc* (160 pp. *pb*). \$75.00 *hc* (\$17.00 *pb*). ISBN 9810241585 *hc* (9810241593 *pb*).
Les Phénomènes d'ondes dans les Moteurs. Michel Borel. Editions Technip, Paris, 2000. 352 pp. 640 FF, 97,57 Euros, \$107.00 US *hc*. ISBN 2710807785.
Flow Control: Passive, Active, and Reactive Flow Management. Mohamed Gad-el-Hak. Cambridge University Press, 2000. 442 pp. \$95.00 *hc*. ISBN 0-521-77006-8.
Electromagnetic Noise Quantum Optical Measurements. Hermann A. Haus. Springer-Verlag, New York, 2000. 580 pp. \$79.95 *hc*. ISBN 3540652728.
Advanced Mathematical Methods in Science and Engineering. Sabih I. Hayek. Marcel Dekker, New York, 2000. 749 pp. \$195.00 *hc*. ISBN 0824704665.
Blind Estimation using Higher-Order Statistics. A. K. Nandi, ed. Kluwer Academic Publishers, Boston, 1999. 294 pp. \$120.00 *hc* ISBN 1792384423.
Data Analysis Techniques for High-Energy Physics. R. Fruhwirth, M. Regler, R. K. Bock, H. Grote, and D. Notz. Cambridge University Press, New York, 2000. 408 pp. \$120.00 *hc* (\$54.95 *pb*). ISBN 0521632196 *hc* (0521635489 *pb*).
Video Object Extraction and Representation. I-Jong Lin and S. Y. Kung. Kluwer Academic Publishers, Boston, 2000. 191 pp. \$98.00 *hc*. ISBN 0792379748.

REVIEWS OF ACOUSTICAL PATENTS

Lloyd Rice

11222 Flatiron Drive, Lafayette, Colorado 80026

The purpose of these acoustical patent reviews is to provide enough information for a Journal reader to decide whether to seek more information from the patent itself. Any opinions expressed here are those of reviewers as individuals and are not legal opinions. Printed copies of United States Patents may be ordered at \$3.00 each from the Commissioner of Patents and Trademarks, Washington, DC 20231. Patents are available via the Internet at <http://www.uspto.gov>.

Reviewers for this issue:

GEORGE L. AUGSPURGER, *Perception, Incorporated, Box 39536, Los Angeles, California 90039*
 RONALD B. COLEMAN, *BBN Technologies, 70 Fawcett Street, Cambridge, Massachusetts 02138*
 DAVID PREVES, *Songbird Hearing, Inc., 5 Cedar Brook Drive, Cranbury, New Jersey 08512*
 KEVIN P. SHEPHERD, *M.S. 463, NASA Langley Research Center, Hampton, Virginia 23681*
 ERIC E. UNGAR, *Acentech, Incorporated, 33 Moulton Street, Cambridge, Massachusetts 02138*

6,069,961

43.38.Hz MICROPHONE SYSTEM

Fumihiko Nakazawa, assignor to Fujitsu Limited
 30 May 2000 (Class 381/92); filed in Japan 27 November 1996

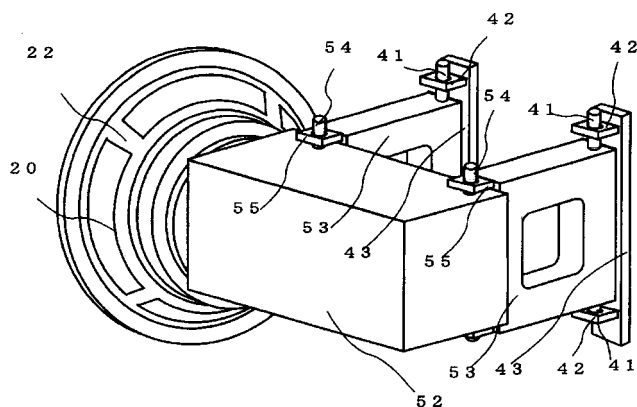
Although designed for computer voice recognition, the invention might also be applied to teleconference systems. The goal is to get the highest possible signal-to-noise ratio from a talker whose location is not known. Prior art has employed an array of microphones whose outputs are analyzed in pairs, allowing the direction of the sound source to be accurately determined. Instead of using this information to select the best microphone for voice pickup, the invention instead chooses the best pair and then electronically tilts the pickup pattern as needed.—GLA

6,058,199

43.38.Ja SPEAKER SYSTEM WITH VIBRATION ISOLATION SPEAKER UNIT MOUNTING STRUCTURE

Shigetomo Umitsu, Yokohama, Japan
 2 May 2000 (Class 381/395); filed 23 March 1998

A conventional moving-coil loudspeaker mounted in a lightweight wood or plastic enclosure can excite panel vibrations by direct, mechanical coupling. High quality loudspeaker enclosures are made of heavy, well braced, internally damped panels to minimize resonances, but this is not a



practical option for something like a portable TV set. The inventor's solution involves couplings, brackets, bearings, and an inertia block. A locking retainer (not shown) immobilizes the assembly for shipping.—GLA

6,059,069

43.38.Ja LOUDSPEAKER WAVEGUIDE DESIGN

Charles Emory Hughes II, assignor to Peavey Electronics Corporation
 9 May 2000 (Class 181/152); filed 25 August 1999

A major advancement in sound reinforcement and motion picture sound was the constant-directivity high frequency horn, invented by D. B. Keele, Jr. more than 20 years ago. Since then, new designs by Keele and others have been patented every other year or so. This latest entry is essentially a truncated, four-sided pyramid joined to the circular throat of its driver by a simple transition arc. The patent includes extensive test results demonstrating that the new design has less distortion than the two "conventional" horns used for comparison.—GLA

6,075,867

43.38.Kb MICROMECHANICAL MICROPHONE

Jesper Bay *et al.*, assignors to Microtronic A/S
 13 June 2000 (Class 381/191); filed in Denmark 23 June 1995

Using micromechanics technology, it is possible to automatically fabricate tiny, high quality microphones in large batches. Although these miniature microphones would seem ideal for use in hearing aids, they tend to be overly sensitive to humidity and dirt. This short patent describes a clever method of encapsulation that does not degrade performance or increase the size of the assembly.—GLA

6,028,943

43.38.Lc AUDIO AMPLIFIER SYSTEM USING A CLASS D AMPLIFIER

Koichiro Nagata, assignor to Matsushita Electric Industrial Company, Limited
 22 February 2000 (Class 381/111); filed in Japan 30 April 1998

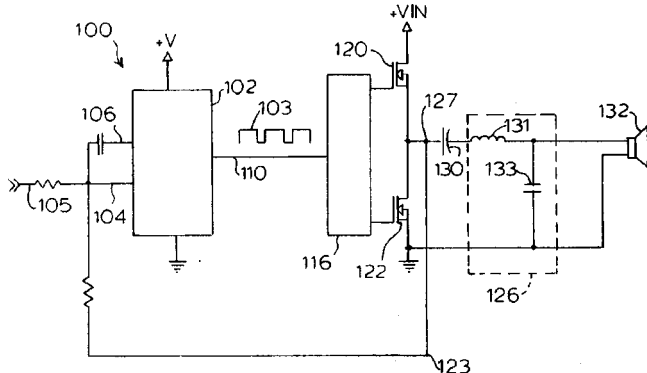
Suppose you try to design a class D stereo amplifier for use in a television receiver. "In this case, the fundamental frequency components of the PWM signal from each of the class D amplifiers not only interfere with surrounding circuits, they also interfere with each other and become superposed as an interference signal on the audio output signal." By properly choosing separate modulation frequencies for the two amplifiers, the difference frequency can be placed outside the bandwidth of the loudspeakers used.—GLA

6,016,075

43.38.Lc CLASS-D AMPLIFIER INPUT STRUCTURE

David J. Hamo, assignor to Lord Corporation
18 January 2000 (Class 330/10); filed 4 June 1997

The patent document includes a good, brief description of class-D audio amplifiers and explains why prior designs require relatively expensive discrete components. The invention utilizes a switching power supply PWM



controller integrated circuit, whose nonideal characteristics are then linearized by a control loop. This drives a simplified, single power supply output stage to further reduce complexity and cost.—GLA

6,064,329

43.38.Lc SYSTEM FOR CREATING AND AMPLIFYING THREE DIMENSIONAL SOUND EMPLOYING PHASE DISTRIBUTION AND DUTY CYCLE MODULATION OF A HIGH FREQUENCY DIGITAL SIGNAL

Eldon A. Byrd, Winchester, Indiana and Alan J. Kacperski, Willoughby, Ohio
16 May 2000 (Class 341/157); filed 2 July 1997

The invention can be described as a kind of audio hologram process which converts conventional stereo signals into "phase distributed monaural." This is done in the digital domain. "Conventional loudspeakers and the brain decode the signal to provide audio signals that contain more information than simply frequency and amplitude changes as a function of time." Stripped of five pages of similar verbiage, the circuit is an electronic processor that attempts to make conventional stereo recordings sound better.—GLA

6,091,826

43.38.Tj METHOD FOR IMPLEMENTING A SOUND REPRODUCTION SYSTEM FOR A LARGE SPACE, AND A SOUND REPRODUCTION SYSTEM

Arvo Olavi Laitinen and Jarkko Tapio Vuori, assignors to Farm Film Oy
18 July 2000 (Class 381/82); filed in Finland 17 March 1995

Consider a large, distributed sound system in an airport or shopping mall. Such systems are typically divided into multiple zones so that local announcements can override general paging or background music. It is also possible to sense background noise in each zone and control the local level accordingly. Individual loudspeakers can even be checked automatically, and malfunctioning units identified at the central control location. The inventors have incorporated all of these features and more in a sophisticated, computerized, wireless network.—GLA

5,987,142

43.38.Vk SYSTEM OF SOUND SPATIALIZATION AND METHOD PERSONALIZATION FOR THE IMPLEMENTATION THEREOF

Maitte Corneau *et al.*, assignors to Sextant Avionique
16 November 1999 (Class 381/17); filed in France 13 February 1996

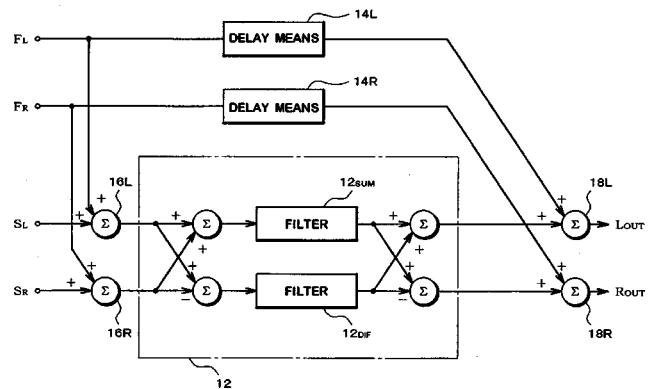
The popularity of computer games has spurred commercial development of virtual reality systems, which usually incorporate a headphone-transmitted sound field that tracks the head movements of the user. This patent, however, is concerned mainly with military applications in which several streams of information plus various alarm signals are individually located in virtual space. The invention includes a method of improving localization by matching left and right transfer functions to the particular user.—GLA

6,067,360

43.38.Vk APPARATUS FOR LOCALIZING A SOUND IMAGE AND A METHOD FOR LOCALIZING THE SAME

Joji Kasai *et al.*, assignors to Onkyo Corporation
23 May 2000 (Class 381/1); filed in Japan 18 November 1997

The invention is one of many signal processing circuits intended to generate a spacious subjective sound field from a pair of closely spaced loudspeakers. In this case, the goal is not only to create virtual left and right



surround sources but also to increase the apparent width of the front stereo image.—GLA

6,072,879

43.38.Vk SOUND FIELD CONTROL UNIT AND SOUND FIELD CONTROL DEVICE

Kunihiro Ouchi *et al.*, assignors to Yamaha Corporation
6 June 2000 (Class 381/61); filed in Japan 17 June 1996

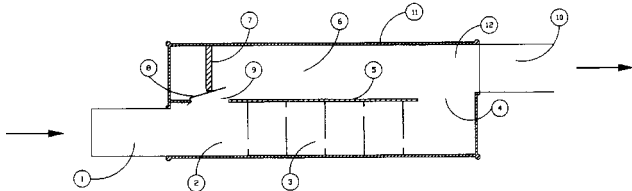
The patent describes an elaborate method for enhancing the acoustical sound field in a performance space. Multiple loudspeaker/microphone assemblies are interconnected. Signals from individual sensing microphones are sampled sequentially rather than mixed, thus minimizing coloration and the onset of howling. Initial setup is automatic, establishing a stable, flat reference function which can then be modified by the user.—GLA

6,079,516

43.50.Gf AUTO-MATIC BACK PRESSURE RELIEF MUFFLER

James E. Pearson, Westchester, California
27 June 2000 (Class 181/254); filed 2 March 1998

A muffler for an internal combustion engine is described which consists of multiple chambers 2, 3, 4, and 6. Under light engine load conditions



flapper valve 8 is closed. Under high load conditions, the valve is opened, thus reducing back pressure and improving engine performance.—KPS

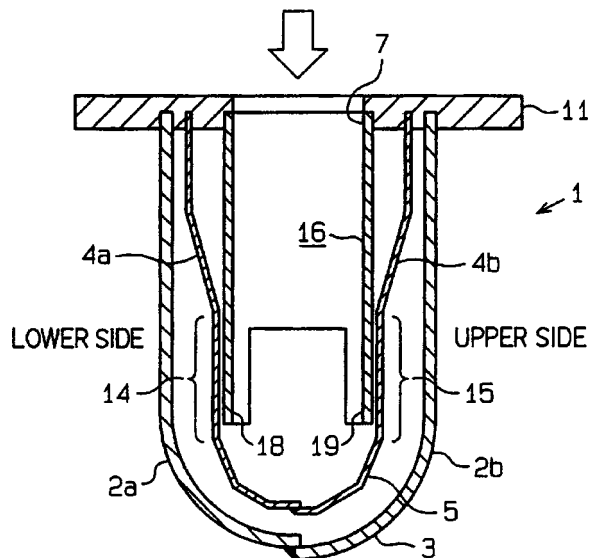
6,082,104

43.50.Gf STAINLESS DOUBLE TUBE EXHAUST MANIFOLD

Tetsuya Hyakutake *et al.*, assignors to Nippon Soken, Incorporated; Toyota Jidosha Kabushiki Kaisha
4 July 2000 (Class 60/323); filed in Japan 8 August 1997

A stainless steel exhaust manifold for an internal combustion engine consists of inner (5) and outer (3) tubes. The inner tube is designed to have low thermal mass to aid in the rapid warming of the catalytic converter. The flat surfaces, 14 and 15, of the inner tube are easily vibrated by the exhaust gas flow, resulting in high-frequency noise. Various methods are described

EXHAUST GAS FLOW



to reduce this vibration and noise. Cover tubes, 16, having high rigidity, reduce excitation of the surfaces 14 and 15. Other methods require the use of perforations in 14 and 15, and also include the deployment of acoustical treatment between the inner and outer tubes.—KPS

6,082,487

43.50.Gf MUFFLERS FOR USE WITH ENGINE RETARDERS; AND METHODS

Theodore G. Angelo *et al.*, assignors to Donaldson Company, Incorporated
4 July 2000 (Class 181/256); filed 13 February 1998

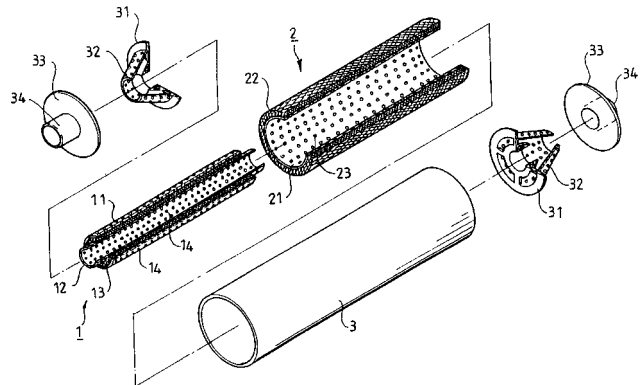
Numerous designs of mufflers intended to suppress noise from engine compression braking systems found on heavy trucks are described. The various designs have combinations of reactive, resistive, and dissipative elements. Extensive geometrical details are provided, along with acoustical performance data for a range of specific engines.—KPS

6,082,488

43.50.Gf MUFFLER FOR VEHICLES

Min-Chyr Lin, Chia Yi Hsien, Taiwan
4 July 2000 (Class 181/256); filed 22 September 1999

The muffler described in this patent consists of three concentric tubes, the inner two of which are perforated. Glass fiber material is placed in the two annular cavities. Supports 31 at both ends of the muffler are also per-



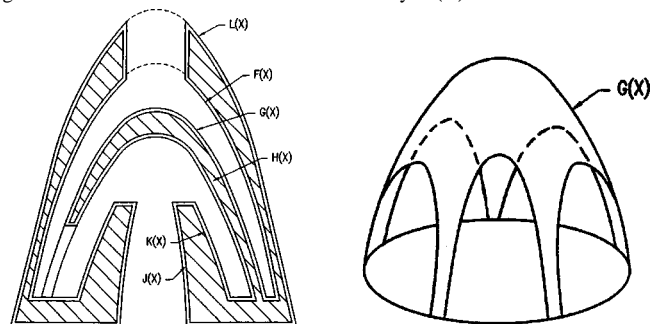
forated, and include elements to guide the exhaust gas flow into both the primary (inner) and secondary exhaust passages.—KPS

6,098,745

43.50.Gf DOME MUFFLER

Jonathan Zalben, Port Washington, New York
8 August 2000 (Class 181/282); filed 19 February 1999

A dome shaped muffler is described in which engine exhaust gases enter at the base and encounter parabolic reflectors, J(X), K(X), and F(X), presumably intended to reflect sound back toward the source. The exhaust gases flow from the inner chamber formed by H(X) to the outer chamber



formed by F(X) via the arches indicated in Fig. 3. Some or all of the hatched region in Fig. 2 contains a vacuum, also intended to enhance the acoustic performance of the muffler, although the responsible physical mechanism is unclear.—KPS

6,118,878

43.50.Ki VARIABLE GAIN ACTIVE NOISE CANCELING SYSTEM WITH IMPROVED RESIDUAL NOISE SENSING

Owen Jones, assignor to Noise Cancellation Technologies, Incorporated
12 September 2000 (Class 381/72); filed 23 June 1993

This patent describes an active noise cancellation headset for use in canceling extraneous noise. Several aspects of the invention are cited that result in the following headset features: less susceptible to instability, conserves power, extends battery life, and operates as a feedback system. These benefits are achieved by a combination of mechanical design (i.e., microphone placement and the location of perforation holes) and control circuitry. The latter includes many features designed to detect the onset of instability and reduce feedback-loop gain accordingly.—RBC

6,122,383

43.50.Ki DEVICE FOR REDUCING NOISE

Wolfgang zum Berge, assignor to Sennheiser electronic KG
19 September 2000 (Class 381/71.6); filed in Germany 7 April 1995

An active headphone is described that is comprised of a microphone, loudspeaker, and feedback control circuitry to reduce extraneous noise entering the ear. The microphone is located within a "balancing element" that reportedly reduces the differences in the transfer functions from the loudspeaker to the microphone from one ear to another. This, in turn, makes the fixed control circuitry more robust. The device does not enclose the ear, but rather rests on the ear. This results in smaller size and weight as compared to conventional headphones.—RBC

6,097,285

43.50.Lj AUTOMOTIVE AUDITORY FEEDBACK OF CHANGING CONDITIONS OUTSIDE THE VEHICLE CABIN

Steven D. Curtin, assignor to Lucent Technologies Incorporated
1 August 2000 (Class 340/436); filed 26 March 1999

A system to alert the driver of a vehicle to the presence of nearby objects is described in which sensors on the exterior of the vehicle are positioned to detect objects in one or more zones. Such zones include "blind spots" on both the left and right sides, as well as behind the vehicle. One or more loudspeakers within the vehicle provide audible signals which indicate the presence of an object and also the zone in which it was detected. For example, a sound generated by a loudspeaker behind and to the left of the driver would indicate the presence of an object in that vicinity. An alternative approach is the use of signals having frequency or temporal characteristics unique to each zone, including the spoken word (e.g., "caution, rear left").—KPS

6,102,465

43.50.Lj NOISE INSULATING STRUCTURE FOR AUTOMOTIVE VEHICLE PASSENGER COMPARTMENT

Kouichi Nemoto *et al.*, assignors to Nissan Motor Company, Limited
15 August 2000 (Class 296/39.3); filed in Japan 16 October 1997

A method to control interior automobile noise consists of deployment of sound absorbing materials on the floor, dashboard, and headliner. Multilayer treatments are designed so that the floor controls low frequencies (0.1–1 kHz), the dashboard the mid-frequencies (0.3–2 kHz), and the headliner the high frequencies (0.8–10 kHz). Each multilayer treatment contains

a layer of sound absorbing material formed of an unshaped polyester fiber mixture composed of polyester (main) fibers and binder fibers, also polyester. Numerous examples are provided in which acoustic performance is determined for a range of treatment characteristics, including surface density, fiber diameter, volume occupied, etc. Acoustic treatment suitable for installation in seat backs, headrests, and other surfaces is also described.—KPS

6,105,443

43.55.Ev DUMMY SOUND ABSORBER REPRESENTING A SEATED HUMAN FOR MEASURING SOUND ABSORPTION POWER OF A THEATER CHAIR

Takeshi Sakai and Kawakami Fukushi, assignors to Yamaha Corporation
22 August 2000 (Class 73/865.6); filed in Japan 1 October 1992

A dummy is provided in order to permit measurement of the absorption characteristics of a theater chair when its upholstery is compressed and partly covered as it would be if a person were seated. The dummy is covered with an acoustic absorption material to simulate the acoustical absorption of a person's clothing and is provided with weights or strapped to the chair seat and back, so that it compresses the upholstery properly. The patent also discusses absorption measurements on a number of chairs in a reverberation chamber.—EEU

6,115,478

43.66.Ts APPARATUS FOR AND METHOD OF PROGRAMMING A DIGITAL HEARING AID

Anthony Todd Schneider, assignor to dspfactory Limited
5 September 2000 (Class 381/314); filed 16 April 1998

A method to program a multi-channel digital hearing aid using audio signals is described. Programming data are distinguished from the desired signals normally processed by a hearing aid by utilizing computer modern modulation methods or by providing the programming signals in alternate frequency bands and no programming signals between the frequency bands of the digital filter.—DAP

6,118,877

43.66.Ts HEARING AID WITH *IN SITU* TESTING CAPABILITY

Eric Lindemann and John L. Melanson, assignors to AudioLogic, Incorporated
12 September 2000 (Class 381/60); filed 12 October 1995

Real world signals are received through an input port or are digitized and stored in the internal memory of a digital hearing aid for assessing hearing aid performance under simulated listening conditions. A tone/noise generator is also provided either by the digital signal processor of the hearing aid or externally for performing *in situ* diagnostic tests using the hearing aid receiver. Use of probe microphones normally required for determining the insertion gain frequency response provided by a hearing aid is said to be eliminated by measuring functional gain (by adjusting the amplitudes of the hearing aid receiver test signal in the frequency bands until they are just barely audible).—DAP

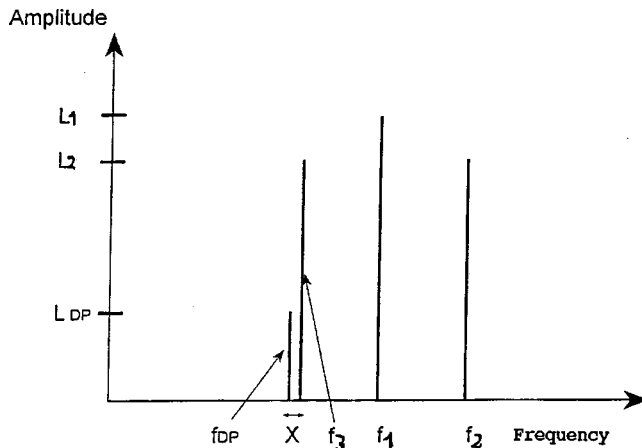
6,123,677

43.66.Yw OBTAINING DATA ON HEARING CAPACITY

Juergen Heitmann and Bernd Waldmann, assignors to Juergen Heitmann; Bernd Waldmann; Peter K. Plinkert; Hans-Ulrich Schnitzler; Hans-Peter Zenner

26 September 2000 (Class 600/559); filed in Germany 29 December 1995

Improved correlation of the $2f_1-f_2$ distortion product otoacoustic emission to conventionally measured hearing thresholds is said to be achieved by adding a third stimulus or suppressor tone at a frequency f_3 as near as possible to the frequency of the distortion product. Preferably, to



L_1 = level of f_1
 L_2 = level of f_2
 L_{DP} = level of distortion product
 f_{DP} = frequency of distortion product
 f_3 = frequency of suppression tone
 x = frequency difference between f_{DP} and f_3
 f_1, f_2 = primary tone frequencies

achieve good suppression, f_3 is presented just above the frequency of the distortion product and at the same level as the second primary tone at frequency f_2 .—DAP

6,085,157

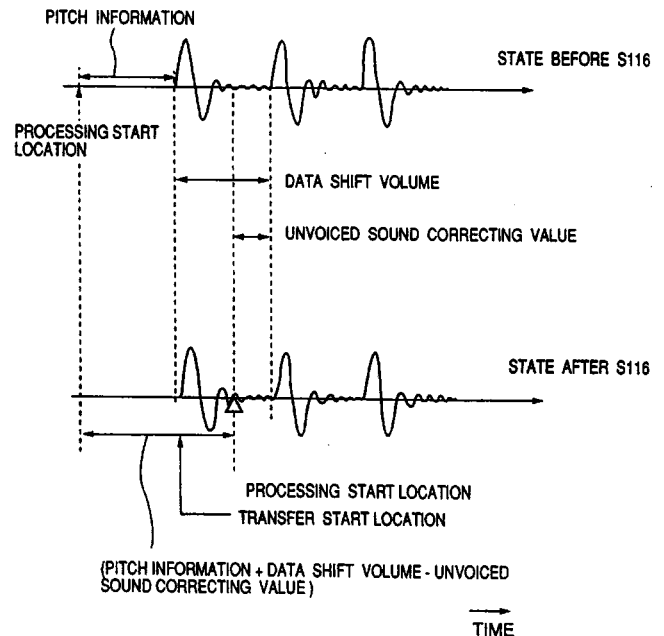
43.72.Ar REPRODUCING VELOCITY CONVERTING APPARATUS WITH DIFFERENT SPEECH VELOCITY BETWEEN VOICED SOUND AND UNVOICED SOUND

Hiroaki Takeda, assignor to Matsushita Electric Industrial Company, Limited

4 July 2000 (Class 704/208); filed in Japan 19 January 1996

The word "velocity" in this patent refers to the speaking rate. The system is a speech rate converter which treats voiced and unvoiced portions of the signal differently so as to minimize distortion. In this case, as seen in the figure, unvoiced refers to the closed glottis portion of the voicing wave-

DATA SHIFT VOLUME $1k \geq$ UNVOICED SOUND CORRECTING VALUE 10 (S115)



form. By treating the open and closed glottal portions separately, it becomes a fairly simple matter to adjust vowel durations with minimal impact on the vowel spectral quality.—DLR

6,088,670

43.72.Ar VOICE DETECTOR

Masashi Takada, assignor to Oki Electric Industry Company, Limited

11 July 2000 (Class 704/233); filed in Japan 30 April 1997

This patent describes a well-known voice detection method which has been patented and repatented many times over. The absolute value of the difference between a long-term energy average and a short-term energy average is smoothed and compared to a threshold. Different threshold values distinguish between onset and offset of the voice signal.—DLR

6,092,040

43.72.Ar AUDIO SIGNAL TIME OFFSET ESTIMATION ALGORITHM AND MEASURING NORMALIZING BLOCK ALGORITHMS FOR THE PERCEPTUALLY-CONSISTENT COMPARISON OF SPEECH SIGNALS

Stephen Voran, Boulder, Colorado

18 July 2000 (Class 704/228); filed 22 September 1997

A speech transmission channel may distort the speech signal in some ways which are readily perceivable, such as severe spectral alterations or nonuniform time delays, and in other ways which are not readily perceivable, such as minor, smooth spectral alterations or uniform time delays. The patented device is a transmission channel tester which processes both the original and the transmitted signals, normalizing both in ways which are not perceptually important, but leaving those discrepancies which would be perceptually detectable.—DLR

6,081,780

43.72.Ja TTS AND PROSODY BASED AUTHORING SYSTEM

Leon Lumelsky, assignor to International Business Machines Corporation
 27 June 2000 (Class 704/260); filed 28 April 1998

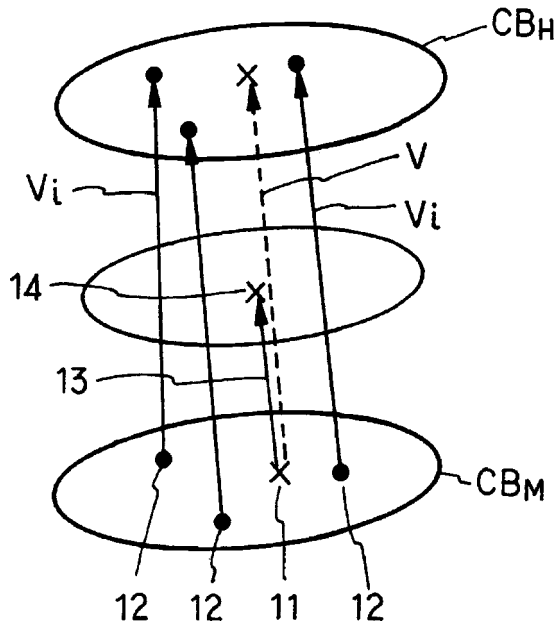
This patent describes an authoring system used to prepare audio material for any of several wireless systems, such as cell phones, digital radio, and personal communication devices. Generally, such systems have very limited spare bandwidth available, usually less than required for high-quality compressed speech. With this authoring system, the service provider may prepare materials by having a person read from text. The text is also available to the system, which performs both recognition and text-to-speech and compares the results. The material is then compressed into a very compact form based on the phonetic structure and prosodic information. The final form is thus suitable for use in the wireless network.—DLR

6,081,781

43.72.Ja METHOD AND APPARATUS FOR SPEECH SYNTHESIS AND PROGRAM RECORDED MEDIUM

Kimihito Tanaka and Masanobu Abe, assignors to Nippon Telegraph and Telephone Corporation
 27 June 2000 (Class 704/268); filed in Japan 11 September 1996

The patent describes a method of synthesizing speech based on the concatenation of prerecorded segments. In order to prevent distortions which occur when there is a large discrepancy between the pitch of the recorded segment and the desired synthetic pitch, this system provides multiple segments of each spectral type having low, medium, and high pitch



ranges. From these segments, a fuzzy vector quantization codebook is prepared for each pitch range. During synthesis, a code mapping is performed to locate the codebook with the pitch range closest to the desired synthesis pitch. This allows resynthesis with a minimum of spectral distortion.—DLR

6,088,673

43.72.Ja TEXT-TO-SPEECH CONVERSION SYSTEM FOR INTERLOCKING WITH MULTIMEDIA AND A METHOD FOR ORGANIZING INPUT DATA OF THE SAME

Jung Chul Lee *et al.*, assignors to Electronics and Telecommunications Research Institute
 11 July 2000 (Class 704/260); filed in Republic of Korea 8 May 1997

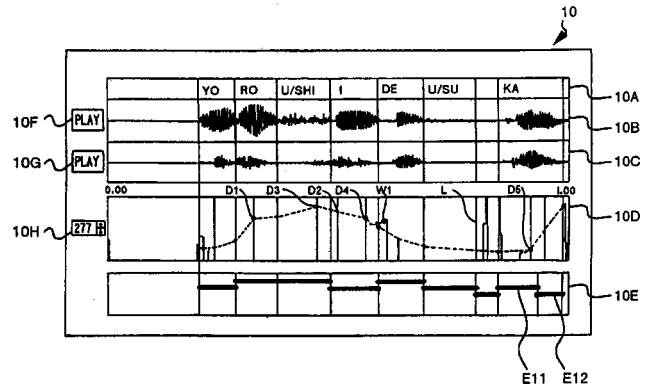
This patent describes a system for text-to-speech (TTS) synthesis in the context of multimedia presentations where the resulting speech should be synchronized in various ways with actions occurring in video or other channels. This would be accomplished by adding control information to the video and other channels. The controls would consist of flags or markers representing lip actions and any physical activity which should be reflected by stress changes in the speech. The TTS system would then interpret these flags and adjust the speech prosodic output accordingly. During operation, the end user can change certain items, such as the speaker's gender. Procedures are described for processing input speech to generate the needed control streams.—DLR

6,088,674

43.72.Ja SYNTHESIZING A VOICE BY DEVELOPING METER PATTERNS IN THE DIRECTION OF A TIME AXIS ACCORDING TO VELOCITY AND PITCH OF A VOICE

Nobuhide Yamazaki, assignor to Justsystem Corporation
 11 July 2000 (Class 704/266); filed in Japan 4 December 1996

This voice processing workstation would allow the operator to edit voice control parameters to improve the output voice quality. It is not entirely clear whether the original parameter data would come from analysis or from a text-to-speech synthesizer. The emphasis is on prosodic controls,



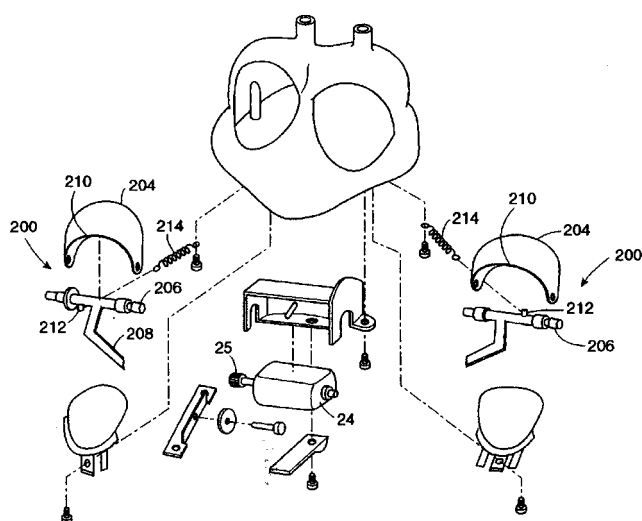
such as timing and pitch, which may be specified in terms of a particular metric pattern. It is said that the resynthesized speech output may be given different speaker characteristics from the original, although there is no discussion of how the formant structure should be adjusted.—DLR

6,089,942

43.72.Ja INTERACTIVE TOYS

Albert W. T. Chan, assignor to Thinking Technology, Incorporated
 18 July 2000 (Class 446/175); filed 9 April 1998

This toy doll or animal is provided with a speech synthesizer and an infrared interface designed to interact with a similar infrared device in a second toy. The two toys can then carry on a simulated conversation in which the real transmission occurs via infrared, but an accompanying voice



output makes the two toys appear to be interacting by verbal conversation. Each toy has a microphone which allows it to coordinate its verbal output in response to external sounds in addition to those of the other toy.—DLR

6,094,633

43.72.Ja GRAPHEME-TO-PHONEME MODULE FOR SYNTHESIZING SPEECH ALTERNATELY USING PAIRS OF FOUR RELATED DATA BASES

Margaret Gaved and James Hawkey, assignors to British Telecommunications public limited company
25 July 2000 (Class 704/260); filed in European Patent Office 26 March 1993

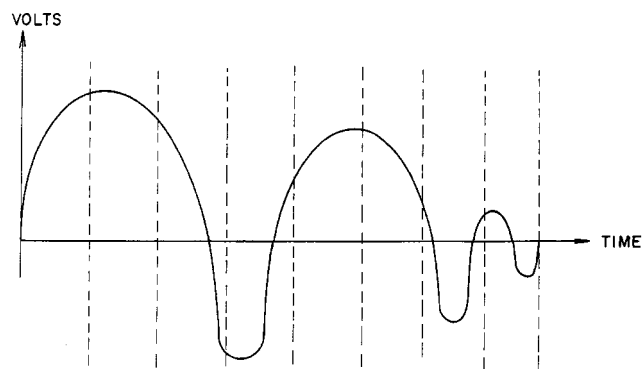
This text-to-speech synthesizer performs a detailed syllable analysis of the entered text words, extracting the initial consonant (onset) and trailing vowel/consonant (rime) patterns from each syllable. Of particular interest is a process for breaking down within-word consonant clusters into a rime portion assigned to the preceding syllable and an onset portion assigned to the following syllable. A number of English-language examples are given which demonstrate the difficulty of this task.—DLR

6,091,813

43.72.Kb ACOUSTIC ECHO CANCELLER

Thomas Harley and Stephen Leese, assignors to Noise Cancellation Technologies, Incorporated
18 July 2000 (Class 379/406); filed 23 June 1998

The echo cancelling method described in this patent works in the reverse of the typical cancellation technique. Instead of subtracting an estimated echo contribution from the received line signal, that estimate is subtracted from the microphone signal before transmission on the outgoing line.



KEY:

----- SINGLE, DIGITIZED SAMPLE OF FAR END LOUDSPEAKER SIGNAL
———— NEAR END MICROPHONE IMPULSE RESPONSE

The actual estimation uses a constrained, orthogonalized, frequency domain, least squares adaptive filter, more or less typical for this sort of application.—DLR

6,078,883

43.72.Ne METHOD FOR TRAINING A SPEECH RECOGNITION SYSTEM AND AN APPARATUS FOR PRACTISING THE METHOD, IN PARTICULAR, A PORTABLE TELEPHONE APPARATUS

Benoit Guilhaumon and Gilles Miet, assignors to U.S. Philips Corporation
20 June 2000 (Class 704/236); filed in European Patent Office 24 December 1996

A procedure is described for training new vocabulary items for a small-vocabulary, template-matching recognizer, such as might be used in a cell phone. When a new item is received, a normal recognition pass is performed to determine whether the score for the new item is sufficiently different from the closest existing item. If the scores are too similar, the user is asked whether the old item should be replaced by the new one.—DLR

6,078,885

43.72.Ne VERBAL, FULLY AUTOMATIC DICTIONARY UPDATES BY END-USERS OF SPEECH SYNTHESIS AND RECOGNITION SYSTEMS

Mark C. Beutnagel, assignor to AT&T Corporation
20 June 2000 (Class 704/258); filed 8 May 1998

This phonetic-based speech recognizer provides a way for the user or a system maintainer to update the dictionary with new phonetic spellings for old or new items based on the pronunciation of the item as processed by the recognition system. The user types in the word to be added or changed and also speaks that word into the recognizer. Using a combination of text-to-phoneme conversion and phoneme extraction from the recognizer, the system generates a new phonetic spelling for the item and updates the dictionary accordingly.—DLR

6,078,887

43.72.Ne SPEECH RECOGNITION SYSTEM FOR NUMERIC CHARACTERS

Stephan Gamm *et al.*, assignors to U.S. Philips Corporation
20 June 2000 (Class 704/275); filed in Germany 11 March 1997

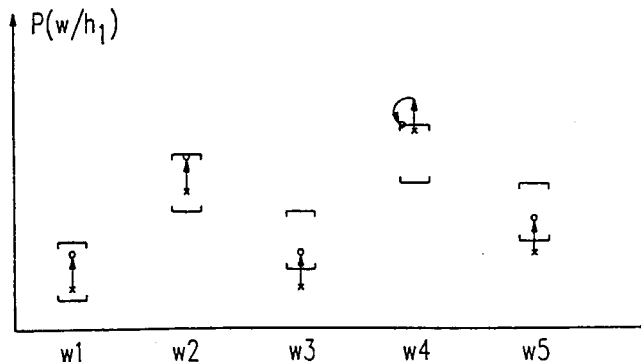
This is a strategy for correcting recognition errors in a spoken number sequence during the use of a small-vocabulary recognizer, such as could be included in a remote control device. The vocabulary includes only the digits and a small number of control words, such as "yes" and "no." After the initial entry, the system repeats the sequence as recognized, asking for confirmation of correctness. If wrong, the user re-enters a portion of the sequence. The recognizer then aligns the old and new sequences to locate the repeated item or items. A scheme for stress labeling of the digits seems mechanical and likely of little help in the process.—DLR

6,081,779

43.72.Ne LANGUAGE MODEL ADAPTATION FOR AUTOMATIC SPEECH RECOGNITION

Stefan Besling and Hans-Gunter Meier, assignors to U.S. Philips Corporation
27 June 2000 (Class 704/257); filed in Germany 28 February 1997

This patent presents a method for updating the language model of a large-vocabulary recognizer. In this case, the language model values represent the long-term frequency of occurrence of the word according to a method known as the CACHE method described in a referenced publication.



When a word is used during recognizer operation, the occurrence probability values are updated as shown in the figure, scaling all values to maintain an overall probability of one.—DLR

6,081,782

43.72.Ne VOICE COMMAND CONTROL AND VERIFICATION SYSTEM

Michael D. Rabin, assignor to Lucent Technologies Incorporated
27 June 2000 (Class 704/275); filed 29 December 1993

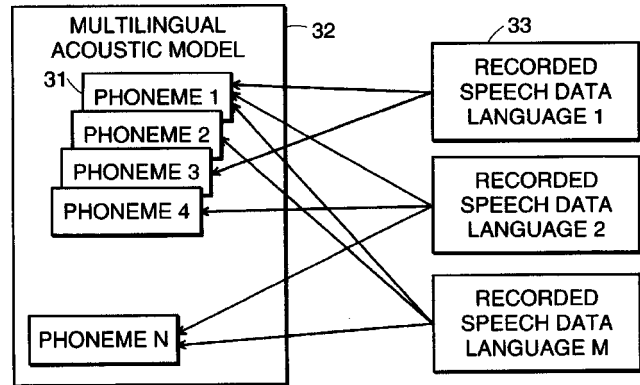
This voice interface system allows the user to enter a short voice command, such as a phone dialing instruction or an ATM operation, and then uses the same voice data to identify and verify the user's identity as well as decoding and executing the command. In general terms, the strategy used by the system is to successively decode different aspects of the signal and at each step, as the system learns more about the signal, it switches to a different model for more specific comparison information. This method provides a more accurate final result for both the command and the user identity.—DLR

6,085,160

43.72.Ne LANGUAGE INDEPENDENT SPEECH RECOGNITION

Bart D'hoore and Dirk Van Compennolle, assignors to Lernout & Hauspie Speech Products N.V.
4 July 2000 (Class 704/256); filed 10 July 1998

This multilanguage speech recognizer is arranged so as to save memory costs by selecting phoneme models from a large set of such models, using just those phoneme models needed for each language. The irony is that the very novelty upon which the patent is based could be the primary factor that would cause the system to perform poorly. It is well known that



even similar phonemes are not quite the same when they are used in different languages. This system gives up the opportunity to capture any such differences, or at least, would do so by using the extra memory it was asked to save.—DLR

6,088,669

43.72.Ne SPEECH RECOGNITION WITH ATTEMPTED SPEAKER RECOGNITION FOR SPEAKER MODEL PREFETCHING OR ALTERNATIVE SPEECH MODELING

Stephane Herman Maes, assignor to International Business Machines Corporation
11 July 2000 (Class 704/231); filed 2 February 1996

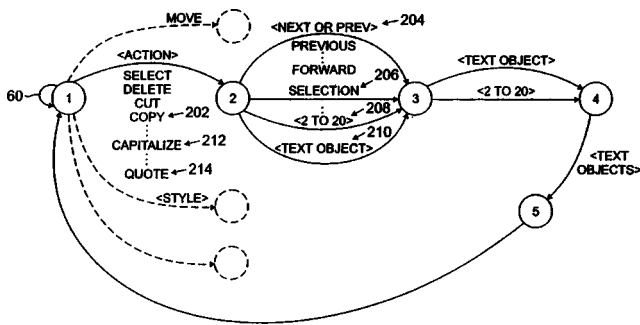
This system attempts to perform simultaneous speech and speaker recognition upon the input of a speech utterance. The preferred method of speaker recognition, based on mel cepstral, delta, and delta-delta coefficients, is performed first. If an enrolled speaker is recognized, then speaker-specific models and vocabulary are loaded for use by the speech recognizer. If no enrolled speaker fits the input data, then a speaker-independent model is loaded.—DLR

6,088,671

43.72.Ne CONTINUOUS SPEECH RECOGNITION OF TEXT AND COMMANDS

Joel M. Gould and Jonathan H. Young, assignors to Dragon Systems
11 July 2000 (Class 704/235); filed 13 November 1995

This dictation recognizer system allows dictated text and editor voice commands to be interspersed during dictation. Single-mode operation may be selected, forcing the processing of subsequent inputs as one or the other entry category. Various "tricks" are used to help discriminate the category.



6,092,043

43.72.Ne APPARATUS AND METHOD FOR TRAINING AND OPERATING SPEECH RECOGNITION SYSTEMS

Steven D. Squires *et al.*, assignors to Dragon Systems, Incorporated
18 July 2000 (Class 704/251); filed 13 November 1992

The patent describes and presents solutions for a number of issues which arise in a voice interface for control of a personal computer, particularly when used for text entry and editing by dictation. There are several methods to simplify the correction of recognition errors. The recognizer adapts by detecting what peripheral resources are available on the machine, what other programs are currently running, and the current location of the graphical focus. Word models are provided for standard speech and spelled words and in several customized forms.—DLR

ries. For example, an editing command should be surrounded by brief pauses. All commands are assumed to begin with action verbs, while dictated text normally begins with a vowel. Let us hope you do not inadvertently pause in mid-sentence.—DLR

6,088,672

43.72.Ne VOICE RECOGNITION SYSTEM CAPABLE OF SORTING PROSPECTIVE RECOGNITION RESULTS OBTAINED FOR A VOICE IN OPTIMIZED ORDER BY A LANGUAGE PROCESSING

Kiyokazu Miki, assignor to NEC Corporation
11 July 2000 (Class 704/246); filed in Japan 8 August 1997

This Japanese-language speech recognition system does template matching, using dynamic programming techniques to compare the input with reference items representing multiple words and multiple speakers' voices. Recognized results are placed into some sort of lattice storage, which appears to be a system for computing syntactic constraints for each recognized item.—DLR

6,092,044

43.72.Ne PRONUNCIATION GENERATION IN SPEECH RECOGNITION

James K. Baker *et al.*, assignors to Dragon Systems, Incorporated
18 July 2000 (Class 704/254); filed 28 March 1997

A method is presented for adding words to the phonetic dictionary of a large-vocabulary speech recognizer. The new word is entered on the keyboard and spoken into the microphone. The spelling is used to generate multiple phonetic forms, represented either as letter-string maps or as a

6,092,039

43.72.Ne SYMBIOTIC AUTOMATIC SPEECH RECOGNITION AND VOCODER

Arthur Richard Zingher, assignor to International Business Machines Corporation
18 July 2000 (Class 704/221); filed 31 October 1997

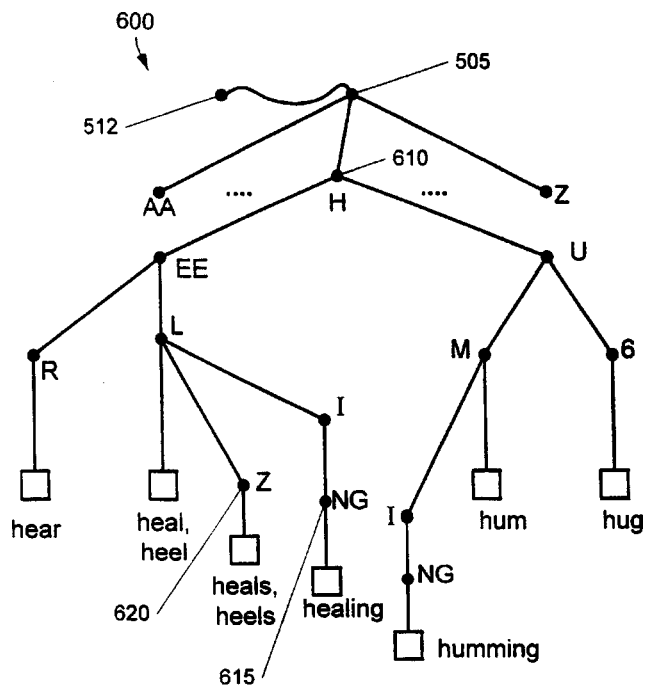
The speech encoding system described here produces a coded form of the speech suitable for simultaneous decoding back to speech and recognition to text. The feature vectors consist of mel cepstral coefficients with delta and delta-delta differences. The encoded speech may be stored in a computer or transmitted via a channel to the receiver. The receiver includes both types of decoding equipment, along with output devices such as loudspeaker and text display.—DLR

6,092,042

43.72.Ne SPEECH RECOGNITION METHOD AND APPARATUS

Kenichi Iso, assignor to NEC Corporation
18 July 2000 (Class 704/240); filed in Japan 31 March 1997

Language problems in the patent text make the exact nature somewhat unclear, but this seems to be a method of replacing triphone probability tables with tables representing single transitions of both feature vectors and phoneme state models. Speaker cluster information is also included in the model, resulting in something described as a single, ergodic hidden Markov model.—DLR



graph of letter patterns. The recognition results are used to search the set of possible phonetic forms. The best match is then inserted into the dictionary.—DLR

6,092,045

**43.72.Ne METHOD AND APPARATUS FOR
SPEECH RECOGNITION**

**Peter R. Stubley *et al.*, assignors to Nortel Networks Corporation
18 July 2000 (Class 704/254); filed in Canada 19 September 1997**

The scheme patented here appears to be a revival of an old and well-known method of word recognition which might be called divide and conquer. The reference word models are divided into subgroups, based on the detection of common elements within a subgroup. New input feature vectors are tested first against the subgroup models, which result in the selection of the most appropriate detailed models for further classification.—DLR

6,094,632

43.72.Pf SPEAKER RECOGNITION DEVICE

**Hiroaki Hattori, assignor to NEC Corporation
25 July 2000 (Class 704/239); filed in Japan 29 January 1997**

This device for speaker recognition and verification performs both speech recognition on a prompted phrase and template comparison of a password phrase. In use, the candidate speaker speaks three items, an ID phrase, a short prompted phrase, and a password phrase. Speaker independent recognition is performed on the ID and the password. If the results of these are consistent, then a speaker verification match is performed on all three phrases.—DLR

Wave localization on a submerged cylindrical shell with rib aperiodicity

Martin H. Marcus, Brian H. Houston, and Douglas M. Photiadis
Naval Research Laboratory, Washington, D.C. 20375-5320

(Received 23 June 2000; revised 30 October 2000; accepted 31 October 2000)

The results of a numerical study of vibration localization due to stiffener variability in a framed shell are reported. An axisymmetric finite element (FE)–infinite element model is used to obtain predictions in good general agreement with previously reported experimental results. Over the frequency band of this study, up to three times the ring frequency, two structural resonances dominate the vibratory response of the shell for high circumferential orders ($n > 10$). Localization is shown to be linked to the sensitivity of the local resonance frequencies of the system to specific geometrical parameters. Specifically, rib thickness variations strongly affect the first pass band, while rib spacing variations strongly affect the second pass band. [DOI: 10.1121/1.1336500]

PACS numbers: 43.20.Ks, 43.40.Dx, 43.40.Ey, 43.40.Rj [CBB]

I. INTRODUCTION

Understanding the structural acoustics of stiffened shells is central to advancing the acoustic design of many aerospace and marine vehicles. Recent experimental and theoretical results^{1–5} have extended our understanding of the mid-frequency behavior of these systems considerably, advancing our understanding of the resonances of the framed-shell system and the role of irregularity in generating spatially localized modes. Thus far, however, direct numerical simulations have been only sparingly employed by researchers. Employing current state-of-the-art finite-element (FE) tools, we have investigated the modes found to be most affected by irregularity in the recent measurements. We have examined the nature of the shell/frame motion in the resonance bands and the dependence of the localization phenomena on different types of irregularity, aspects which are difficult to investigate without using numerical simulations.

Hodges⁶ was among the first to realize that the localization phenomena investigated in the context of electronic transport in impure crystals⁷ might also occur in macroscopic plate and shell structures. He investigated one-dimensional systems and demonstrated the significant effects which can arise due to irregularity. Photiadis showed that such phenomena can persist in the presence of fluid loading on plate structures⁸ and further predicted that localization phenomena would become much stronger on generic framed shell structures, particularly for the higher order azimuthal modes.⁹ Recent measurements³ have borne out the qualitative aspects of these predictions, but quantitative agreement between the measurements and a first principles theory requires more accurate modeling of the frames than was used in Ref. 9.

Predicting Anderson localization phenomena from first principles requires accurate modeling of the resonance bandwidths of the system^{7,10} or, in terms of the basic vibration properties of the system, the bay to bay coupling of vibrational energy.³ The modeling must also correctly capture the sensitivity of the resonance frequencies to variations in system parameters, the other ingredient required to compute localization lengths. Finite-element modeling enables us to do

a fairly good job in both areas, and hence to correctly predict localization phenomena in framed-shell structures.

In Sec. II, the finite-element modeling is described along with the specific geometry we have investigated. We provide some comparisons to the previously reported experimental data, and we find reasonably good agreement for both the band structure and the wave number–frequency response of the system to a localized force. Encouraged by this agreement, we explore the effects of various kinds of geometrical irregularity in Sec. III. We find there that different types of irregularity produce localization in different resonance bands. General theoretical principles regarding localization phenomena³ then imply that the different bands have a different sensitivity to the various geometrical parameters. In Sec. IV, the resonance bands are investigated in some detail and it is indeed found that the nature of the motions is quite different, and hence sensitive to different aspects of the input parameters. Finally, in Sec. V, we summarize our principal results.

II. FINITE-ELEMENT RIBBED SHELL ANALYSIS

The structure is shown in Fig. 1. It is a cylindrical shell made of nickel with 80 straight frames and a cone-sphere endcap. The load is applied at a point halfway between frames 38 and 39 and at 295 evenly spaced frequencies from 122 Hz to 36 kHz. The finite-element program sara2d (Ref.

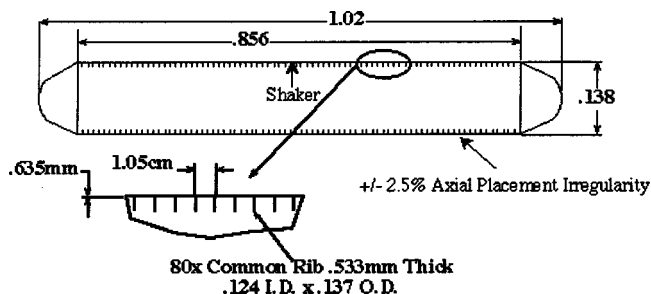


FIG. 1. Framed shell cross-section.

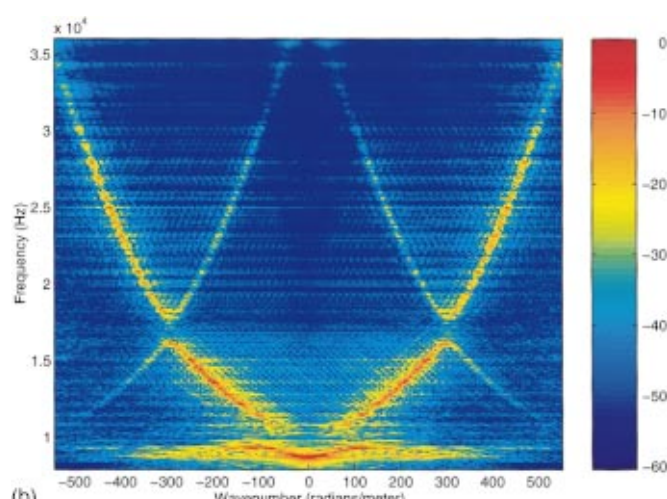
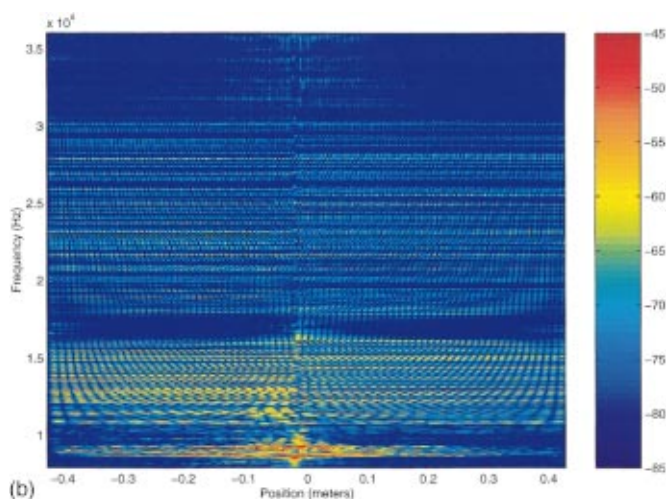
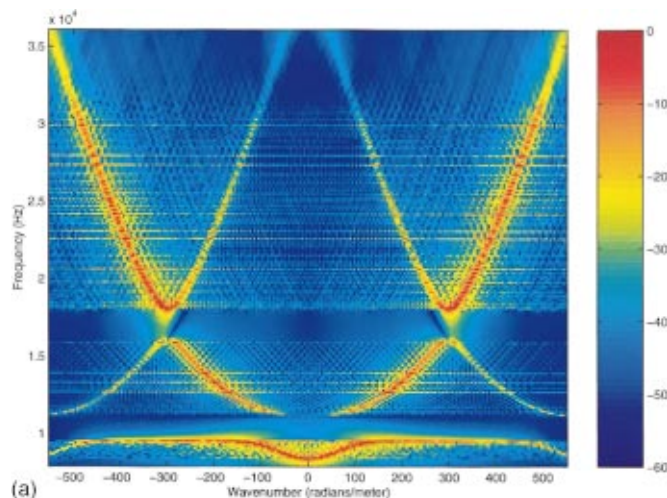
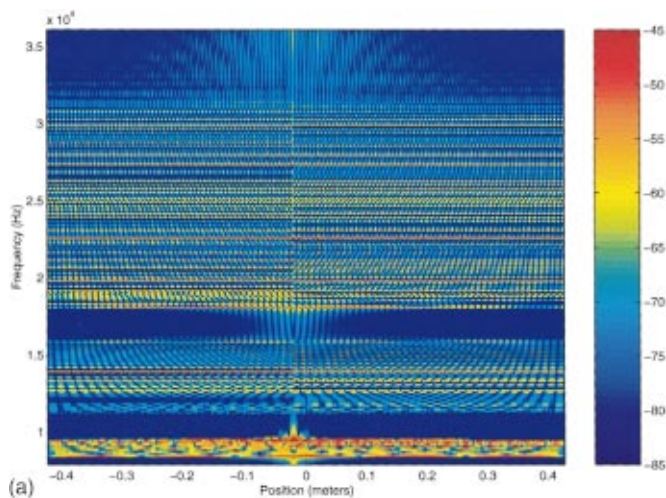


FIG. 2. Circumferential mode seven component of the surface normal velocity of the framed shell from a point load. Colors refer to the dB level *re*: one meter per second for a one Newton load. (a) Calculation. (b) Data.

FIG. 3. Circumferential mode seven component in wave number space for the surface normal velocity of the framed shell from a point load. Colors refer to the dB level *re*: one meter per second for a one Newton load. (a) Calculation. (b) Data.

11) may be used because the shell is axisymmetric, while the nonaxisymmetric load is Fourier analyzed into circumferential modes zero through 30. Consequently, 31 finite-element computations are performed. The shell has six quadratic elements per frame spacing, as well as four elements per frame, to make a total of 914 elements. Including the five layers of quadratic fluid elements, one of which is infinite, the computer model has 3884 elements. The entire model has 10 739 nodes, including 1829 structural nodes. The computations require 6.4 s for one frequency and circumferential mode on a Silicon Graphics power challenge computer. In this section of this paper, the structure has 80 identical frames with the geometry of the shell used in the measurements;³ the frame spacing has a pseudo-random variation of 1.64 percent from the mean frame spacing.

Numerical results for the surface normal velocities are plotted versus frequency and position along the cylindrical length for circumferential mode 7 in Fig. 2(a). The first two pass bands, horizontal stripes at about 9 kHz and 13 kHz, are associated with significant frame motion, an aspect we will investigate in more detail in Sec. IV. The third, much

broader, stripe is associated with flexural shell motion scattered by the frames.^{12–14} In this case, the frames play more of a passive role as scatterers of flexural shell vibration. The corresponding experimental results³ shown in Fig. 2(b) provide qualitative verification of the above results. The same three horizontal stripes appear, albeit at a slightly lower level. The other low order circumferential modes show similar agreement, but mode 7 was selected for display, because at mode 7 all of the interesting phenomena are inside the frequency range of the experimental database.

The wave number space response is shown for the $n = 7$ mode in Fig. 3. The first pass band is seen as a thin horizontal stripe nearly independent of wave number, indicative of single bay frame resonances weakly coupled by the shell. The second pass band has more dispersion, indicating that flexural shell motion is a more important component of the resonant motion. The third pass band's dispersion curves follow those for an unribbed shell, except in the vicinity of the stop bands. In all of the curves, the apparent aliasing of the dispersion curves by $2\pi/a$ (a is the frame spacing) is

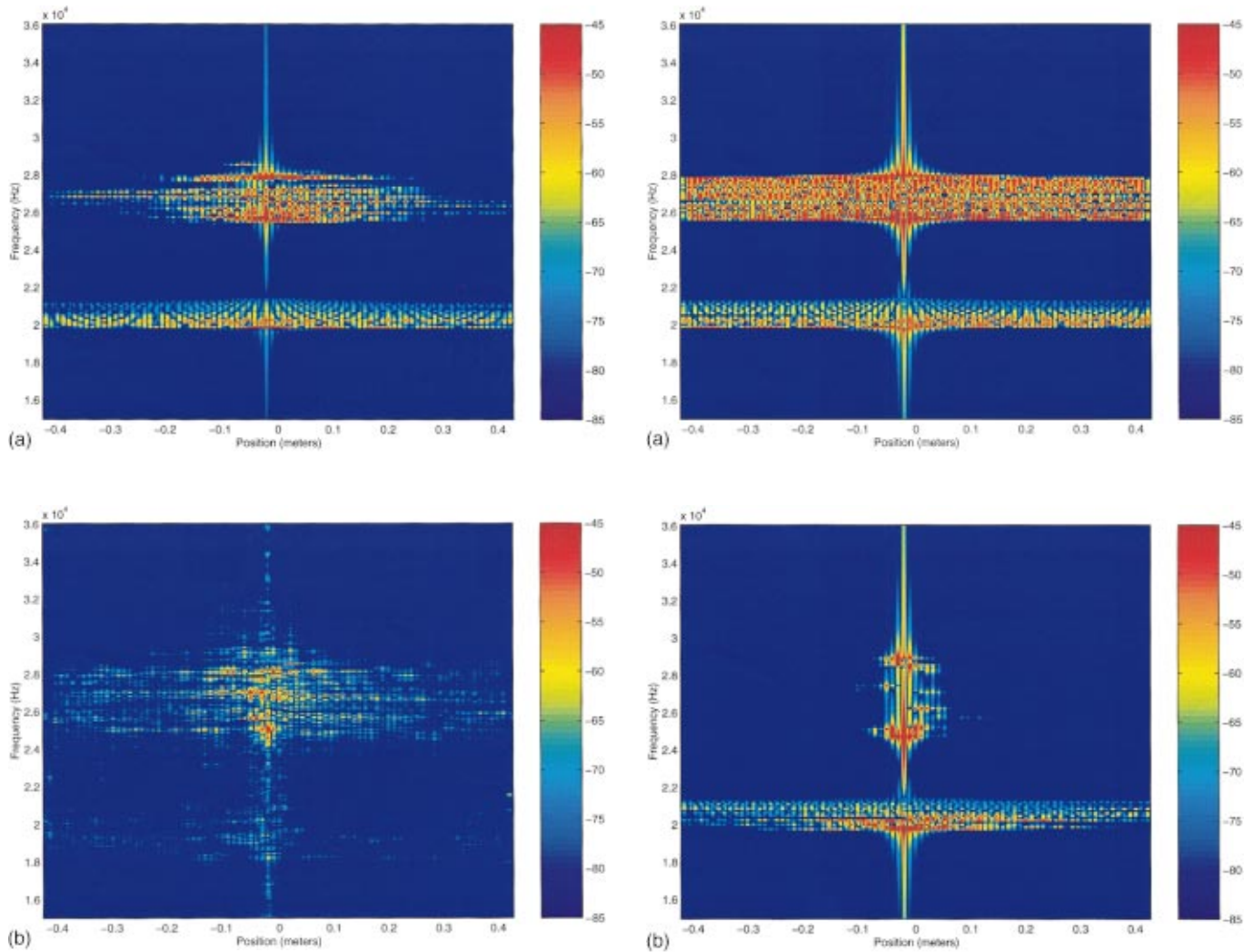


FIG. 4. Circumferential mode 20 component of the surface normal velocity of the framed shell from a point load. Colors refer to the dB level v_r : one meter per second for a one Newton load. (a) Calculation. (b) Data.

Brillouin zone folding of the outer branch, resulting from scattering from the nearly periodic array of ribs. Comparing the numerical and experimental results, Figs. 3(a) and (b), it is clear that the finite-element calculations are capturing the band structure fairly well, a critical ingredient for predicting localization phenomena correctly.

Figure 4 shows the surface normal velocities for a typical large n mode, circumferential mode 20. The numerical results, Fig. 4(a), show two resonance bands in correspondence to the first two pass bands of Fig. 2(a). Figure 4(b) shows the experimental results for mode 20. The numerical results are again in qualitative agreement with the data, particularly with regard to the dominant higher frequency resonance band. Note the clear spatial localization of the response of the $n=20$ mode (Fig. 4) as opposed to the $n=7$ mode (Fig. 2). This general behavior is in accord with theoretical predictions based on Anderson localization.⁹

Observe that the lower frequency resonance band in the experimental data for the $n=20$ mode is suppressed relative to the numerical results, spatially as well as in level. This suggests that additional features of the model beyond irregu-

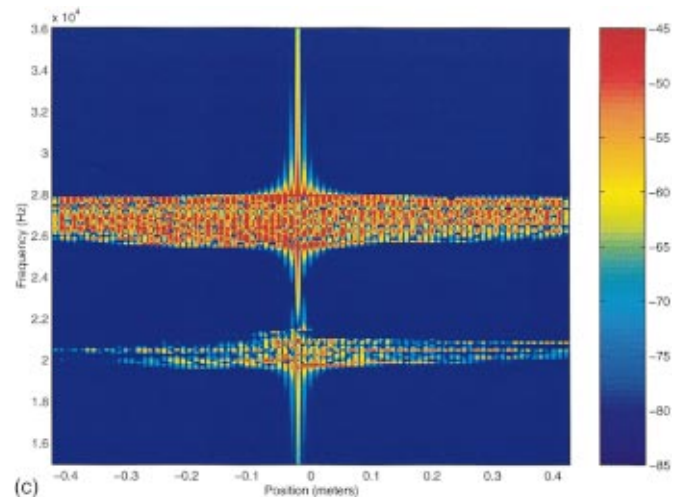


FIG. 5. Circumferential mode 20 component of the surface normal velocity of the framed shell from a point load. Colors refer to the dB level v_r : one meter per second for a one Newton load. (a) No rib nonuniformities. (b) Nonuniformity of frame spacing. (c) Nonuniformity in the rib thickness.

larity in the frame spacing are at work in the measurements. One possible mechanism which could account for this is irregularity in the frame properties, an aspect we will explore in the following section.

III. TWO DIFFERENT TYPES OF APERIODICITY AND THEIR EFFECT ON LOCALIZATION

Comparisons of the simulations and the experiments revealed a significant discrepancy with regard to the lowest resonance band of the large n modes. In this section, numerical simulations are performed to determine whether additional irregularity in the system associated with irregularity in the frames as opposed to the spacing might account for this. Thus numerical simulations are performed with two different types of variations in frame parameters, the frame spacing and the frame thickness. In all cases, the shell is excited at a point near the center midway between two frames, and only results for the $n=20$ mode, a typical large n mode for this shell based on the experimental data,³ are presented.

Figure 5(a) shows the response of the shell for the control case of a periodically framed shell. The parameters of the shell correspond to the mean parameters of the experimental model examined in the above section. The damping factor was chosen to be 0.002 in accord with the experimental results.³ The resonance bands clearly show extended modes; i.e., modes propagating with virtually no attenuation along the length of the shell.

Figure 5(b) shows the surface velocities for a shell with a frame spacing nonuniformity of 6.55 percent of the mean (four times the irregularity of the shell in Fig. 1). The second pass band is highly localized, while the first pass band shows only weak localization. In contrast, variations in the frame thickness (2.15 percent of the mean) with a uniform frame spacing produces the opposite phenomenon as shown in Fig. 5(c); the lower frequency band is significantly localized while the upper band is nearly unattenuated. Hence, variations in the two different geometrical parameters, frame spacing and frame thickness, are shown to cause varying degrees of localization phenomena in different resonance bands.

Although the plots in Figs. 5(b) and (c) show behavior similar to that of the experimental data, Fig. 4(b), their purpose is merely to show the qualitative differences from different types of nonuniformity. A precise reproduction of the data from a finite-element calculation would require a measurement of the frame thickness variation, which was not performed, as well as measurements of other nonuniformities, some of which cannot be included in an axisymmetric computer model.

IV. PARAMETER DEPENDENCE OF LOCALIZATION PHENOMENA

The parameter dependence of localization phenomena in axisymmetric framed shells can be analyzed based on the general expression for the localization factor in the middle of a pass band,³

$$\gamma a \approx \frac{\sigma^2\{\omega_i^2\}}{2\omega^2(\Delta\omega)^2}. \quad (1)$$

Here, γ is the localization factor (i.e., the reciprocal of the spatial attenuation length), a the mean frame spacing, σ^2 the variance of the frequency spread caused by the irregularity,

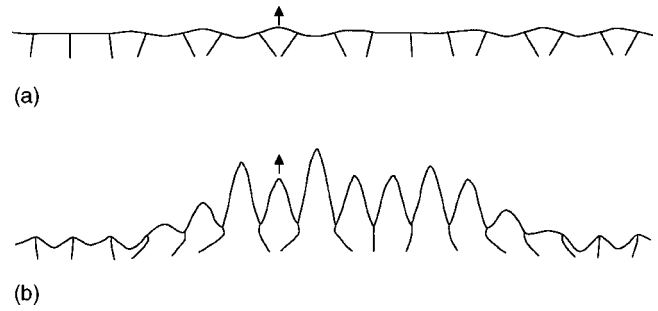


FIG. 6. Circumferential mode 20 response of the framed shell cylindrical section from a point load. (a) 19 890 Hz. (b) 27 940 Hz.

ω the center frequency, $\{\omega_i\}$ the set of frequencies comprising the pass band, and $\Delta\omega$ the width of the particular band under consideration. The parameter dependence of the localization factor is contained solely in the quantity σ^2 , the spread of the natural frequencies caused by the irregularity, and we thus proceed to examine this quantity.

The variance $\sigma^2\{\omega_i^2\}$ results from the variation of the frame parameters via the dependence of the local resonance frequencies on these parameters,

$$\omega_n \approx \omega_n(a, h), \quad (2)$$

where a and h are the frame spacing and thickness, respectively. For a small variation in a single parameter λ , one may easily show³

$$\sigma^2\{\omega_i^2\} \approx \left(2\omega \frac{\partial\omega_i}{\partial\lambda}\right)^2 \sigma^2\{\lambda\}. \quad (3)$$

Therefore, the variation of localization lengths in different resonance bands results from the sensitivity of the local resonance frequencies to changes in the parameters; i.e., γ depends on the parameters through the derivative $\partial\omega_i/\partial\lambda$.

With this perspective, let us reexamine the results in Fig. 5. The case with the irregularity in the frame spacing but not the frame thickness, Fig. 5(b) shows strong localization in the second pass band and very little in the first. Thus from Eq. (3), we may surmise that $\partial\omega_2/\partial a \gg \partial\omega_1/\partial a$, where the subscripts refer to the two passbands. Conversely, the opposite phenomena in Fig. 5(c), resulting from a variation of the frame thickness, lead to the assertion, $\partial\omega_2/\partial h \ll \partial\omega_1/\partial h$. Basically, the observed parameter dependence of the localization lengths implies that the local resonance phenomena underlying the second resonance band are much more sensitive to shell parameters than are the local resonance phenomena underlying the first resonance band, and vice versa.

An intuitive grasp of these results can be obtained by directly examining the resonant responses. Figure 6(a) shows the circumferential mode 20 response of the shell in Fig. 1 from a point load applied at 19 890 Hz, in the first pass band. The ribs appear to move independently from each other, and wave motion on the shell appears to be of little relevance. Figure 6(b) shows the corresponding plot for 27 940 Hz, in the second pass band. Resonant shell vibration is clearly the major component of the motion, with the ribs appearing to be synchronized to the corresponding motion of the shell. These mode shapes from the two different pass bands are typical of all of the circumferential modes and hence confirm, at least

qualitatively, our interpretation above. Finally, some recent theoretical results predicting the resonance frequencies of these modes^{15,16} are also consistent with the conclusions.

V. CONCLUSIONS

We report here the results of a numerical study of the localization due to structural variability associated with a submerged cylindrical shell. An axisymmetric finite-element–infinite-element model is employed for a frequency range up to three times the ring frequency. We find that the FE results are in good general agreement with experiments previously reported. Due to the tendency of large n modes to localize more strongly than do the low circumferential orders, the study was primarily focused on resonances of a typical large n mode, $n = 20$. Over the band of this study, two structural resonances dominate the vibratory response for high circumferential orders. Localization is shown to be linked to the sensitivity of the resonance frequencies of the system to specific geometrical parameters. Specifically, rib thickness variations strongly affect the first pass band and rib spacing variations strongly affect the second pass band.

We have shown that conventional finite element tools can be straightforwardly used to predict localization effects resulting from irregularity in framed shell structures, provided the irregularity preserves the structural axisymmetry. The generality of the approach enables different geometrical aspects of the system to be easily analyzed, and thus enables the investigator to evaluate the importance of various structural idealizations. Bearing in mind the importance of structural irregularity in determining the acoustic response of structures in a variety of applications, we conclude that the inclusion of such detail in FE modeling is of great importance.

ACKNOWLEDGMENT

The authors gratefully acknowledge the Office of Naval Research for support of this work.

- ¹M. L. Rumerman, "Contribution of membrane wave reradiation to scattering from finite cylindrical steel shells in water," *J. Acoust. Soc. Am.* **93**, 55–65 (1993).
- ²Douglas M. Photiadis, Earl G. Williams, and Brian H. Houston, "Wave number response of a near periodically ribbed shell," *J. Acoust. Soc. Am.* **101**, 877–886 (1997).
- ³D. M. Photiadis and B. H. Houston, "Anderson localization of vibration on a framed cylindrical shell," *J. Acoust. Soc. Am.* **106**, 1377–1391 (1999).
- ⁴Douglas M. Photiadis, J. A. Bucaro, and Brian H. Houston, "The effect of internal oscillators on the acoustic response of a submerged shell," *J. Acoust. Soc. Am.* **101**, 87–92 (1997).
- ⁵J. A. Bucaro, Douglas M. Photiadis, and Brian H. Houston, "The effect of internal oscillators on the acoustic response of a submerged shell," in *Proceedings of the ASME, Noise Control and the Acoustics Division* (ASME, New York, 1997).
- ⁶C. H. Hodges and J. Woodhouse, "Vibration isolation from irregularity in a periodic structure: Theory and measurements," *J. Acoust. Soc. Am.* **74**, 894–905 (1983).
- ⁷P. W. Anderson, "Absence of diffusion in certain random lattices," *Phys. Rev.* **109**, 1492–1505 (1958).
- ⁸D. M. Photiadis, "Anderson localization of one-dimensional wave propagation on a fluid-loaded plate," *J. Acoust. Soc. Am.* **91**, 771–780 (1992).
- ⁹D. M. Photiadis, "Localization of helical flexural waves by irregularity," *J. Acoust. Soc. Am.* **96**, 2291–2301 (1994).
- ¹⁰D. J. Thouless, *Ill-Condensed Matter* (North Holland, Amsterdam, 1979), pp. 5–60.
- ¹¹H. Allik, *Sara-2d user's manual, version 95-3*, BBN Systems and Technologies, New London, CT, 1995.
- ¹²A. W. Leissa, *Vibration of shells*, NASA SP-288, Washington, D.C., 1973.
- ¹³D. M. Photiadis, "The effect of irregularity on the scattering of acoustic waves from a ribbed plate," *J. Acoust. Soc. Am.* **91**, 1897–1903 (1992).
- ¹⁴L. Brillouin, *Wave Propagation in Periodic Structures* (Dover, New York, 1946).
- ¹⁵M. H. Marcus and A. Sarkissian, "Rib resonances present in the scattering response of a ribbed cylindrical shell," *J. Acoust. Soc. Am.* **103**, 1864–1866 (1998).
- ¹⁶M. H. Marcus, "The effect of rib resonances on the vibration and wave scattering of a ribbed cylindrical shell," *J. Acoust. Soc. Am.* **103**, 3055 (A) (1998).

Acoustic scattering by a circular cylinder parallel with another of small radius

John A. Roumeliotis,^{a)} Agissilaos-Georgios P. Ziotopoulos, and Gerassimos C. Kokkorakis

Department of Electrical and Computer Engineering, National Technical University of Athens, Athens 15773, Greece

(Received 9 December 1998; accepted for publication 19 December 2000)

The scattering of a plane acoustic wave by an infinite penetrable or impenetrable circular cylinder, parallel with another one, also penetrable or impenetrable, of acoustically small radius, is considered. The method of separation of variables, in conjunction with translational addition theorems for cylindrical wave functions, is used. Analytical expressions are obtained for the scattered pressure field and the various scattering cross sections, for normal incidence. Numerical results are given for penetrable and impenetrable cylinders. © 2001 Acoustical Society of America. [DOI: 10.1121/1.1348296]

PACS numbers: 43.20.Fn [ANN]

LIST OF SYMBOLS

ρ_0, ρ_1, ρ_2	densities in three regions
c_0, c_1, c_2	sound speeds in three regions
k_0, k_1, k_2	wave numbers in three regions
$\lambda_0 = 2\pi/k_0$	wavelength in region 0 (outside the cylinders)
R_1, R_2	radii of the two cylinders
d	distance between the axes of the two cylinders
$r_1, \varphi_1, r_2, \varphi_2$	polar coordinates
φ_0	incidence angle

p_i	incident plane pressure wave
p_{s1}, p_{s2}	scattered pressure fields by the two cylinders
$p_{in,1}, p_{in,2}$	pressure fields inside the two cylinders
J_m	cylindrical Bessel function of the first kind
$H_m \equiv H_m^{(2)}$	cylindrical Hankel function of the second kind
σ_b	backscattering (sonar) cross section
σ_f	forward scattering cross section
Q_t	total scattering cross section

I. INTRODUCTION

Acoustic and electromagnetic scattering by multiple objects is an important problem with various practical applications, such as simulation and modeling of complex bodies, prediction of radiation by reflector antennas, and control of the scattering cross sections of different objects. Applications of this type, in the special case of cylindrical objects simulated by a number of circular cylinders, can be found, among others, in Refs. 1–3. Other problems of acoustic and electromagnetic scattering by two or more circular cylinders, at normal incidence, have been treated by many researchers^{4–13} using a variety of methods. Recent applications concerning cylindrical structures in fluid mechanical problems can be found in Refs. 14–17.

In this paper we examine the scattering of a plane acoustic wave by an infinite penetrable or impenetrable circular cylinder, parallel with another circular cylinder, also penetrable or impenetrable, of acoustically small radius (much smaller than the wavelength). An extension of the special analytical perturbation method applied elsewhere^{18,19} is used, in order to obtain first order approximate analytical solutions for the scattered pressure field and the various scattering

cross sections. Separation of variables, in conjunction with translational addition theorems for cylindrical wave functions, are used for the solution. The plane acoustic wave impinges normally on the axes of the two cylinders.

In Sec. II we examine the scattering by two penetrable cylinders, while in Sec. III we examine the scattering by two cylinders, one of which, at least, is impenetrable (soft or hard). Finally, in Sec. IV, we give numerical results for the various scattering cross sections and for both the former cases.

II. PENETRABLE CYLINDER PARALLEL WITH ANOTHER PENETRABLE ONE OF SMALL RADIUS

The geometry of the problem is shown in Fig. 1. The cylinder radii are R_1 and R_2 , respectively, while d is the distance between their axes. The density, sound speed, and wave number are ρ_0, c_0, k_0 in the space outside the cylinders (region 0), ρ_1, c_1, k_1 inside the first cylinder (region 1), and ρ_2, c_2, k_2 inside the second cylinder (region 2). All materials are fluids or fluidlike, i.e., they do not support shear waves. The incident plane pressure wave impinging normally on the axes of the cylinders (z -axes) has the form^{19,20}

^{a)}Electronic mail: iroumel@cc.ece.ntua.gr

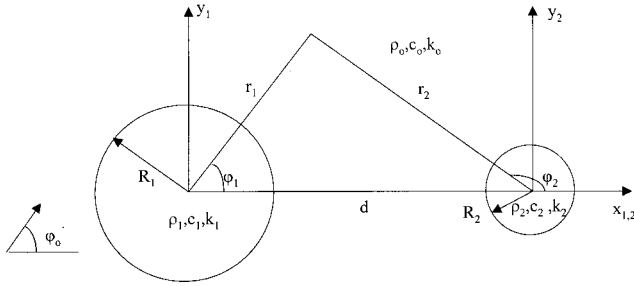


FIG. 1. Geometry of the scatterer.

$$p_i = e^{-jk_0 r_1 \cos(\varphi_1 - \varphi_0)} = \sum_{m=-\infty}^{\infty} j^{-m} J_m(k_0 r_1) e^{jm(\varphi_1 - \varphi_0)}, \quad (1)$$

where r_1 , φ_1 are the polar coordinates, φ_0 defines the direction of incidence, and J_m is the cylindrical Bessel function of the first kind. The time dependence $e^{j\omega t}$ is suppressed throughout.

Let $p_{s1}(0)$ and $p_{in,1}(0)$ be the pressure field scattered by and the field inside the first cylinder, respectively, in the unperturbed problem, i.e., in the absence of the second cylinder. These fields have the expressions

$$p_{s1}(0) = \sum_{m=-\infty}^{\infty} C_m(0) H_m(k_0 r_1) e^{jm\varphi_1}, \quad (2)$$

$$p_{in,1}(0) = \sum_{m=-\infty}^{\infty} A_m(0) J_m(k_1 r_1) e^{jm\varphi_1}, \quad (3)$$

where H_m is the Hankel function of the second kind, with the superscript (2) omitted for simplicity. The expressions for $C_m(0)$ and $A_m(0)$ are¹⁹

$$C_m(0) = j^{-m} \frac{J_m(w_0) J'_m(w_1) - q_1 J'_m(w_0) J_m(w_1)}{q_1 J_m(w_1) H'_m(w_0) - J'_m(w_1) H_m(w_0)} e^{-jm\varphi_0}, \quad (4)$$

$$A_m(0) = j^{-m} \frac{q_1 [J_m(w_0) H'_m(w_0) - J'_m(w_0) H_m(w_0)]}{q_1 J_m(w_1) H'_m(w_0) - J'_m(w_1) H_m(w_0)} e^{-jm\varphi_0}, \quad (5)$$

where we have made the substitutions

$$w_0 = k_0 R_1, \quad w_1 = k_1 R_1, \quad q_1 = \frac{\rho_1 c_1}{\rho_0 c_0}, \quad (6)$$

and the primes denote derivatives with respect to the argument.

In the presence of the second cylinder, Eqs. (2) and (3) are modified taking the form

$$p_{s1} = \sum_{m=-\infty}^{\infty} C_m H_m(k_0 r_1) e^{jm\varphi_1}, \quad (7)$$

$$p_{in,1} = \sum_{m=-\infty}^{\infty} A_m J_m(k_1 r_1) e^{jm\varphi_1}, \quad (8)$$

with C_m and A_m different from $C_m(0)$ and $A_m(0)$, respectively.

In this case there is also a scattered field from the second cylinder and a field inside it, given by the expressions

$$p_{s2} = \sum_{m=-\infty}^{\infty} B_m H_m(k_0 r_2) e^{jm\varphi_2}, \quad (9)$$

$$p_{in,2} = \sum_{m=-\infty}^{\infty} F_m J_m(k_2 r_2) e^{jm\varphi_2}. \quad (10)$$

The various expansion coefficients in Eqs. (7)–(10) can be evaluated by satisfying the boundary conditions at $r_1 = R_1$ and $r_2 = R_2$

$$p_i + p_{s1} + p_{s2} = p_{in,v}, \quad (11)$$

$$\frac{1}{\rho_0} \frac{\partial(p_i + p_{s1} + p_{s2})}{\partial r_v} = \frac{1}{\rho_v} \frac{\partial p_{in,v}}{\partial r_v}, \quad (12)$$

with $v=1$ and 2 corresponding to the first and the second cylinder, respectively. For this purpose the translational addition theorem for the Hankel functions, from the u th to the q th coordinates is used²⁰

$$\begin{aligned} & H_m(kr_u) e^{jm\varphi_u} \\ &= \sum_{n=-\infty}^{\infty} J_n(kr_q) H_{m-n}(kd_{uq}) e^{jn\varphi_q} e^{j(m-n)\varphi_{uq}}, \\ & \quad r_q < d_{uq} \\ &= \sum_{n=-\infty}^{\infty} J_n(kd_{uq}) H_{m-n}(kr_q) e^{jn\varphi_{uq}} e^{j(m-n)\varphi_q}, \\ & \quad r_q > d_{uq}, \end{aligned} \quad (13)$$

where d_{uq} is the distance between the z axes of the two systems, while φ_{uq} is the angle between the positive semi-axis x_u and d_{uq} . If the Hankel functions are replaced by the corresponding Bessel ones on both sides of Eq. (13), the two expressions at the right side of this relation become equal.

Satisfaction of Eqs. (11), (12) at $r_1 = R_1$ ($v=1$), with the use of Eqs. (1), (7)–(9), the addition theorem Eq. (13) to express p_{s2} in terms of r_1 , φ_1 , and the orthogonal property of $e^{jm\varphi_1}$, provides the following set of equations ($m=0, \pm 1, \pm 2, \dots$):

$$\begin{aligned} & j^{-m} J_m(w_0) e^{-jm\varphi_0} + C_m H_m(w_0) \\ & + J_m(w_0) \sum_{p=-\infty}^{\infty} B_p H_{m-p}(k_0 d) = A_m J_m(w_1), \end{aligned} \quad (14)$$

$$\begin{aligned} & j^{-m} J'_m(w_0) e^{-jm\varphi_0} + C_m H'_m(w_0) \\ & + J'_m(w_0) \sum_{p=-\infty}^{\infty} B_p H_{m-p}(k_0 d) = \frac{1}{q_1} A_m J'_m(w_1). \end{aligned} \quad (15)$$

Satisfaction of Eqs. (11), (12) at $r_2 = R_2$ ($v=2$), with the use of Eqs. (1), (7), (9), (10), the addition theorem Eq. (13) to express p_i and p_{s1} in terms of r_2 , φ_2 , and the orthogonal property of $e^{jm\varphi_2}$, provides the set ($m=0, \pm 1, \pm 2, \dots$)

$$J_m(w) \left[j^{-m} e^{-jm\varphi_0} e^{-jk_0d \cos \varphi_0} + \sum_{p=-\infty}^{\infty} C_p H_{p-m}(k_0d) \right] + B_m H_m(w) = F_m J_m(w_2), \quad (16)$$

$$J'_m(w) \left[j^{-m} e^{-jm\varphi_0} e^{-jk_0d \cos \varphi_0} + \sum_{p=-\infty}^{\infty} C_p H_{p-m}(k_0d) \right] + B_m H'_m(w) = \frac{1}{q_2} F_m J'_m(w_2), \quad (17)$$

where

$$w = k_0 R_2, \quad w_2 = k_2 R_2, \quad q_2 = \frac{\rho_2 c_2}{\rho_0 c_0}. \quad (18)$$

In Eqs. (16), (17) we have also used the result

$$\begin{aligned} & \sum_{p=-\infty}^{\infty} j^{-p} e^{-jp\varphi_0} J_{p-m}(k_0d) \\ &= j^{-m} e^{-jm\varphi_0} \sum_{p=-\infty}^{\infty} j^{-(p-m)} e^{-j(p-m)\varphi_0} J_{p-m}(k_0d) \\ &= j^{-m} e^{-jm\varphi_0} \sum_{n=-\infty}^{\infty} j^{-n} e^{-jn\varphi_0} J_n(k_0d) \\ &= j^{-m} e^{-jm\varphi_0} e^{-jk_0d \cos \varphi_0}, \end{aligned} \quad (19)$$

where $p-m$ is replaced by n , while Eq. (1) is used with $r_1 = d$ and $\varphi_1 = 0$.

For general values of R_2 the infinite sets of Eqs. (14)–(17) can be solved only numerically, by truncation. However, for small R_2 an analytical solution can be obtained. As $R_2 \rightarrow 0$, also $w \rightarrow 0$ and $w_2 \rightarrow 0$. In this case the expansion coefficients A_m and C_m can be approximated by the formulas

$$A_m = A_m(0) + \delta A_m, \quad C_m = C_m(0) + \delta C_m, \quad (20)$$

with δA_m and δC_m small perturbations of $A_m(0)$ and $C_m(0)$, respectively.

We substitute from Eq. (20) into Eqs. (14) and (15), thus obtaining the relations

$$\begin{aligned} & \delta C_m H_m(w_0) + J_m(w_0) \sum_{p=-\infty}^{\infty} B_p H_{m-p}(k_0d) \\ &= \delta A_m J_m(w_1), \end{aligned} \quad (21)$$

$$\begin{aligned} & \delta C_m H'_m(w_0) + J'_m(w_0) \sum_{p=-\infty}^{\infty} B_p H_{m-p}(k_0d) \\ &= \frac{1}{q_1} \delta A_m J'_m(w_1), \end{aligned} \quad (22)$$

while from Eqs. (16) and (17), by eliminating F_m , we obtain

$$B_m = M_m \left[j^{-m} e^{-jm\varphi_0} e^{-jk_0d \cos \varphi_0} + \sum_{p=-\infty}^{\infty} C_p H_{p-m}(k_0d) \right], \quad (23)$$

where

$$M_m = \frac{J'_m(w_2) J_m(w) - q_2 J_m(w_2) J'_m(w)}{q_2 J_m(w_2) H'_m(w) - J'_m(w_2) H_m(w)}. \quad (24)$$

In Eqs. (21) and (22) we used the result that the boundary conditions Eqs. (11), (12) at $r_1 = R_1$ ($v=1$) are also valid for the case of the unperturbed problem (i.e., in the absence of the second cylinder), with p_{s2} omitted and p_{s1} , $p_{in,1}$ replaced by $p_{s1}(0)$, $p_{in,1}(0)$, respectively.

From Eqs. (21) and (22), by eliminating δA_m , we obtain

$$\delta C_m = j^m e^{jm\varphi_0} C_m(0) \sum_{p=-\infty}^{\infty} B_p H_{m-p}(k_0d). \quad (25)$$

Also, from the same equations, by eliminating the infinite sums we obtain

$$\begin{aligned} \delta A_m &= \frac{q_1 [J_m(w_0) H'_m(w_0) - J'_m(w_0) H_m(w_0)]}{J_m(w_0) J'_m(w_1) - q_1 J'_m(w_0) J_m(w_1)} \delta C_m \\ &= \frac{A_m(0)}{C_m(0)} \delta C_m. \end{aligned} \quad (26)$$

By using the small argument formulas for the Bessel and Hankel functions as $w \rightarrow 0$ ^{18,21} ($w_2 = wk_2/k_0$) in Eq. (24) we find

$$M_0 = \frac{j\pi w^2}{4} f, \quad M_m = \frac{j\pi w^{2m}}{4^m (m-1)! m!} g, \quad (m \geq 1), \quad (27)$$

where

$$f = 1 - \frac{\rho_0}{\rho_2} \left(\frac{c_0}{c_2} \right)^2, \quad g = \frac{\rho_0 - \rho_2}{\rho_0 + \rho_2}. \quad (28)$$

We substitute B_m from Eq. (23) into Eq. (25) keeping only the dominant terms (for B_m), i.e., those with $|m| = 0, 1$, which are of order w^2 , as is seen from Eq. (27). The omitted terms, with $|m| \geq 2$, are of order w^4 and higher. From Eq. (24) is evident that $M_{-m} = M_m$, because $J_{-m}(x) = (-1)^m J_m(x)$ and $H_{-m}(x) = (-1)^m H_m(x)$. So, we finally obtain, after some manipulation,

$$\begin{aligned} \delta C_m &= j^m e^{jm\varphi_0} C_m(0) \sum_{p=-1}^1 H_{m-p}(k_0d) M_p \left[j^{-p} e^{-jp\varphi_0} e^{-jk_0d \cos \varphi_0} + \sum_{s=-\infty}^{\infty} C_s(0) H_{s-p}(k_0d) \right] \\ &= \frac{j\pi w^2}{4} j^m e^{jm\varphi_0} C_m(0) \left\{ e^{-jk_0d \cos \varphi_0} [f H_m(k_0d) - jg [e^{-j\varphi_0} H_{m-1}(k_0d) - e^{j\varphi_0} H_{m+1}(k_0d)]] \right. \\ &\quad \left. + \sum_{s=-\infty}^{\infty} C_s(0) [f H_s(k_0d) H_m(k_0d) + g [H_{s-1}(k_0d) H_{m-1}(k_0d) + H_{s+1}(k_0d) H_{m+1}(k_0d)]] \right\}. \end{aligned} \quad (29)$$

In Eq. (29) we have omitted the higher order products $M_p \delta C_s$. The total scattered field from both cylinders is $p_s = p_{s1} + p_{s2}$, where p_{s1} and p_{s2} are given in Eqs. (7) and (9). Using Eq. (13) in Eq. (9) we express p_s in terms of r_1, φ_1 :

$$p_s = \sum_{m=-\infty}^{\infty} C_m H_m(k_0 r_1) e^{jm\varphi_1} + \sum_{m=-\infty}^{\infty} \sum_{n=-\infty}^{\infty} B_m J_n(k_0 d) H_{m-n}(k_0 r_1) \times e^{j(m-n)\varphi_1} (-1)^n. \quad (30)$$

In Eq. (30) we have used the second of the expressions Eq. (13), because for the scattered far field $r_1 > d$. Substituting the asymptotic expansions for the Hankel functions into Eq. (30) we obtain, for this far field, the expression

$$p_s = \frac{e^{-jk_0 r_1}}{\sqrt{r_1}} \frac{1+j}{\sqrt{\pi k_0}} G(\varphi_1), \quad (31)$$

where, with the use of Eq. (19)

$$G(\varphi_1) = \sum_{m=-\infty}^{\infty} [C_m + B_m e^{jk_0 d \cos \varphi_1}] j^m e^{jm\varphi_1}. \quad (32)$$

The backscattering or sonar (σ_b), the forward (σ_f), and the total (Q_t) scattering cross sections are¹⁸

$$k_0 \sigma_b = 4 |G(\varphi_0 + \pi)|^2, \quad k_0 \sigma_f = 4 |G(\varphi_0)|^2, \quad (33)$$

$$k_0 Q_t = \frac{2}{\pi} \int_0^{2\pi} |G(\varphi_1)|^2 d\varphi_1 = \frac{2}{\pi} \int_0^{2\pi} G(\varphi_1) G^*(\varphi_1) d\varphi_1 = 4 \sum_{m=-\infty}^{\infty} \left\{ |C_m|^2 + |B_m|^2 + 2 \operatorname{Re} \left[C_m^* \sum_{p=-\infty}^{\infty} B_p J_{m-p}(k_0 d) \right] \right\}, \quad (34)$$

where the asterisk denotes the complex conjugate, while Re represents the real part.

In analogy to Eq. (20) we can set

$$G(\varphi_1) = G_0(\varphi_1) + \delta G(\varphi_1), \quad (35)$$

where

$$G_0(\varphi_1) = \sum_{m=-\infty}^{\infty} C_m(0) j^m e^{jm\varphi_1}, \quad (36)$$

$$\delta G(\varphi_1) = \sum_{m=-\infty}^{\infty} [\delta C_m + B_m e^{jk_0 d \cos \varphi_1}] j^m e^{jm\varphi_1}.$$

From Eq. (35) we obtain, by omitting the second order differential $|\delta G(\varphi_1)|^2$,

$$|G(\varphi_1)|^2 = G(\varphi_1) G^*(\varphi_1) = |G_0(\varphi_1)|^2 + 2 \operatorname{Re} [G_0^*(\varphi_1) \delta G(\varphi_1)]. \quad (37)$$

Substituting Eqs. (23) and (27) into Eq. (36) and keeping only the dominant terms for B_m ($|m|=0,1$) we obtain, after some manipulation,

$$\delta G(\varphi_1) = \sum_{m=-\infty}^{\infty} \delta C_m j^m e^{jm\varphi_1} + \frac{j\pi w^2}{4} e^{jk_0 d \cos \varphi_1} \left\{ e^{-jk_0 d \cos \varphi_0} \times [f + 2g \cos(\varphi_1 - \varphi_0)] + \sum_{p=-\infty}^{\infty} C_p(0) \times [f H_p(k_0 d) + jg [e^{j\varphi_1} H_{p-1}(k_0 d) - e^{-j\varphi_1} H_{p+1}(k_0 d)]] \right\}. \quad (38)$$

In Eq. (38) we have omitted the higher order products $M_m \delta C_p$.

From Eqs. (33), (35)–(38) we easily obtain the zero order (unperturbed) term $\sigma(0)$ and its first order perturbation $\delta\sigma$, for both σ_b and σ_f .

From Eqs. (35)–(37) we find

$$k_0 Q_t = \frac{2}{\pi} \int_0^{2\pi} G_0(\varphi_1) G_0^*(\varphi_1) d\varphi_1 + \frac{4}{\pi} \operatorname{Re} \left[\int_0^{2\pi} G_0^*(\varphi_1) \delta G(\varphi_1) d\varphi_1 \right] = k_0 Q_t(0) + k_0 \delta Q_t, \quad (39)$$

where

$$k_0 Q_t(0) = 4 \sum_{m=-\infty}^{\infty} |C_m(0)|^2 \quad (40)$$

and

$$k_0 \delta Q_t = 8 \operatorname{Re} \left\{ \sum_{m=-\infty}^{\infty} C_m^*(0) \left[\delta C_m + \sum_{p=-1}^1 B_p J_{m-p}(k_0 d) \right] \right\}. \quad (41)$$

The results of Eqs. (40) and (41) can also be obtained from the general relation Eq. (34), in the special case where $R_2 \rightarrow 0$. The small argument formula for the sum $\sum_{p=-1}^1 B_p J_{m-p}(k_0 d)$ is given by Eq. (29), but with $j^m e^{jm\varphi_0} C_m(0)$ omitted and with $H_{m-p}(k_0 d)$ replaced by $J_{m-p}(k_0 d)$ for $p=0, \pm 1$. This is evident by a simple comparison of the aforementioned sum with Eq. (25), for $p=0, \pm 1$.

Our results were checked, to a very good accuracy, by the forward scattering theorem^{19,22} having the form

$$k_0 Q_t(0) = -4 \operatorname{Re} [G_0(\varphi_0)], \quad (42)$$

$$k_0 \delta Q_t = -4 \operatorname{Re} [\delta G(\varphi_0)]$$

for various values of the parameters used.

III. TWO PARALLEL CYLINDERS, NOT BOTH PENETRABLE, ONE OF WHICH HAS SMALL RADIUS

The geometry of the problem is again shown in Fig. 1. In this case at least one of the cylinders is impenetrable (soft or hard). The difference here is that the field inside the impenetrable cylinder is zero, thus modifying the boundary conditions at its surface. We can follow steps analogous to those in the previous section for the solution (we have done it, to verify the results), but, equivalently and more easily, we can use the limiting values $\rho_v \rightarrow 0$ or $\rho_v \rightarrow \infty$ ($v=1,2$), for a soft or a hard cylinder, respectively, keeping c_v ($v=1,2$) fixed in both cases, in the results of that section.

There are three distinct cases: (a) the first cylinder is impenetrable and the second penetrable; (b) the first cylinder is penetrable and the second impenetrable; and (c) both cylinders are impenetrable. We examine them separately.

A. The first cylinder impenetrable and the second, with small radius, penetrable

In this case we use $\rho_1 \rightarrow 0$ ($q_1 \rightarrow 0$) for a soft cylinder and $\rho_1 \rightarrow \infty$ ($q_1 \rightarrow \infty$) for a hard one (c_1 is finite in both cases), in the results of Sec. II. The expressions which turn out to be different from the corresponding ones there, are the following (superscripts s and h stand for a soft and a hard cylinder, respectively, and are used only when differences appear between them):

$$C_m^s(0) = -j^{-m} \frac{J_m(w_0)}{H_m(w_0)} e^{-jm\varphi_0}, \quad (43)$$

$$C_m^h(0) = -j^{-m} \frac{J'_m(w_0)}{H'_m(w_0)} e^{-jm\varphi_0}.$$

Also

$$A_m(0) = 0, \quad A_m = 0 (\delta A_m = 0), \quad (44)$$

because there is no pressure field inside the impenetrable cylinder. Equations (11) (for $v=1$), (14), (21), and (12) (for $v=1$), (15), and (22) are missing for a hard and a soft cylinder, respectively, and Eq. (26) is missing from both, while the others remain the same as in Sec. II, embodying the former changes.

B. The first cylinder penetrable and the second, with small radius, impenetrable

In this case we use $\rho_2 \rightarrow 0$ ($q_2 \rightarrow 0$) for a soft cylinder and $\rho_2 \rightarrow \infty$ ($q_2 \rightarrow \infty$) for a hard one (c_2 is finite in both cases), in the results of Sec. II. The expressions that change will be given in what follows, while the others remain as in Sec. II, embodying these changes:

$$F_m = 0, \quad (45)$$

because there is no pressure field inside the impenetrable cylinder. Equations (11) (for $v=2$), (16), and (12) (for $v=2$), (17) are missing for a hard and a soft cylinder, respectively. Also, Eq. (24) is replaced by

$$M_m^s = -\frac{J_m(w)}{H_m(w)}, \quad M_m^h = -\frac{J'_m(w)}{H'_m(w)}. \quad (46)$$

By using the small argument formulas for the Bessel and Hankel functions as $w \rightarrow 0$ from Refs. 18, 21 in Eq. (46), we obtain

$$M_0^s = -\frac{j\pi}{2\left(\ln\frac{w}{2} + \gamma\right)}, \quad (\gamma=0.57722), \quad M_0^h = \frac{j\pi w^2}{4}, \quad (47)$$

$$M_m^s = -M_m^h = \frac{j\pi w^{2m}}{4^m(m-1)!m!}, \quad (m \geq 1).$$

M_0^s in Eq. (47) cannot be obtained from Eqs. (27), (28) by taking the limit $\rho_2 \rightarrow 0$. On the other hand, M_m^s ($m \geq 1$), as well as M_0^h and M_m^h ($m \geq 1$) can be obtained in the limit $\rho_2 \rightarrow \infty$. The reason is evident after using the small argument formulas of Bessel and Hankel functions in Eq. (24). For $m=0$ and $\rho_2 \neq 0$ ($q_2 \neq 0$), the first term in its denominator is dominant, giving the result Eq. (27), but for $m=0$ and $\rho_2 \rightarrow 0$ ($q_2 \rightarrow 0$, soft cylinder) the second term becomes dominant, giving the result Eq. (47). In all the other cases there is no such a problem, so the remaining formulas in Eq. (47) are obtained as limiting expressions from Eqs. (27) and (28).

From Eq. (47) we see that M_0^s is dominant with respect to M_m^s ($m \geq 1$), which is of order w^2 and higher. This means that in Eq. (25) we keep only the dominant term B_0^s , substituting it from Eq. (23). So

$$\delta C_m^s = -\frac{j\pi}{2\left(\ln\frac{w}{2} + \gamma\right)} j^m e^{jm\varphi_0} C_m^s(0) H_m(k_0 d) \times \left[e^{-jk_0 d \cos \varphi_0} + \sum_{p=-\infty}^{\infty} C_p^s(0) H_p(k_0 d) \right], \quad (48)$$

while δC_m^h is given by Eq. (29), for $\rho_2 \rightarrow \infty$, i.e., for $f^h = 1$ and $g^h = -1$.

For the same reasons only B_0^s is kept in the expressions Eqs. (32) and (36) for $\delta G^s(\varphi_1)$. So, in this case Eq. (38) takes the form

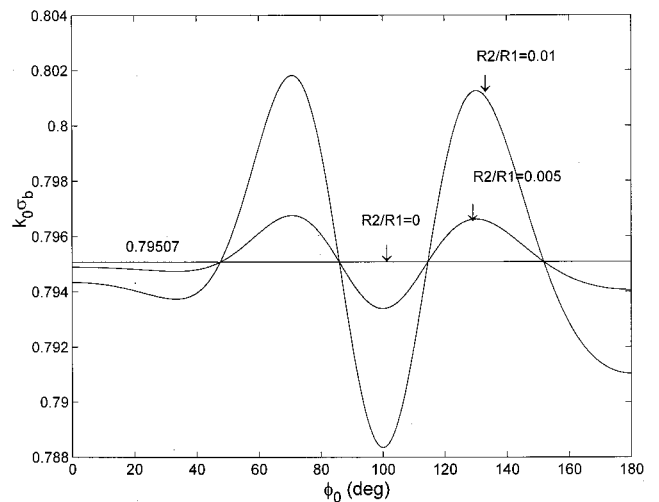


FIG. 2. Backscattering cross section vs φ_0 ($^\circ$) for $R_1/\lambda_0=0.5$, $d/R_1=1.1$, $\rho_1/\rho_0=1.22$, $c_1/c_0=1.27$, $\rho_2/\rho_0=2.7$, $c_2/c_0=4.3$ (penetrable cylinders).

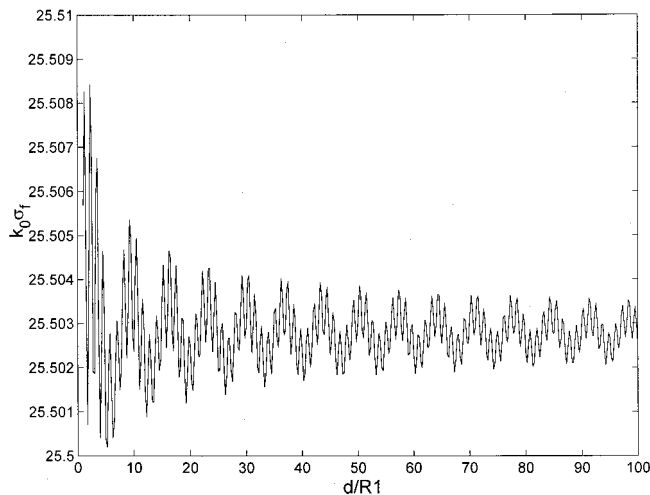


FIG. 3. Forward scattering cross section for $R_1/\lambda_0=0.5$, $R_2/R_1=0.01$, $\varphi_0=45^\circ$, $\rho_1/\rho_0=1.22$, $c_1/c_0=1.27$, $\rho_2/\rho_0=2.7$, $c_2/c_0=4.3$ (penetrable cylinders).

$$\delta G^s(\varphi_1) = \sum_{m=-\infty}^{\infty} \delta C_m^s j^m e^{jm\varphi_1} - \frac{j\pi}{2\left(\ln\frac{w}{2} + \gamma\right)} e^{jk_0d \cos \varphi_1} \left[e^{-jk_0d \cos \varphi_0} + \sum_{p=-\infty}^{\infty} C_p^s(0) H_p(k_0d) \right], \quad (49)$$

while $\delta G^h(\varphi_1)$ is given by Eq. (38) for $f^h=1$ and $g^h=-1$.

Finally, the remarks after Eq. (41) for $\sum_{p=-1}^1 B_p J_{m-p}(k_0d)$ remain valid for the hard cylinder examined here, provided, moreover, that one sets $f^h=1$ and $g^h=-1$ in Eq. (29). For the soft cylinder we only keep B_0^s in Eq. (41), so $B_0^s J_m(k_0d)$ is given by Eq. (48), if we omit there $j^m e^{jm\varphi_0} C_m^s(0)$ and replace $H_m(k_0d)$ by $J_m(k_0d)$.

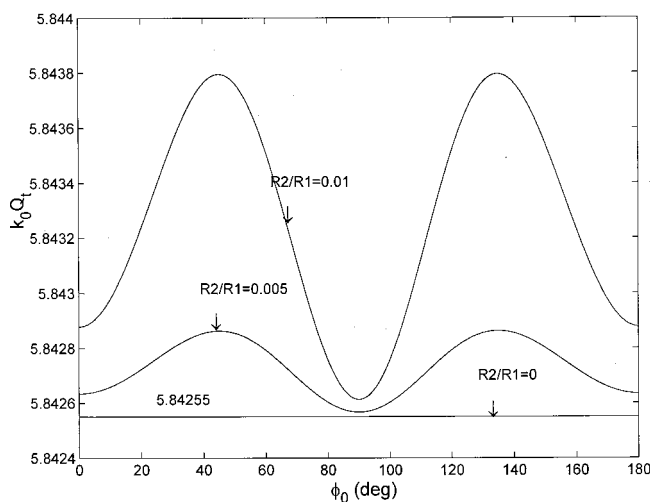


FIG. 4. Total scattering cross section vs $\varphi_0(^\circ)$ for $R_1/\lambda_0=0.5$, $d/R_1=1.1$, $\rho_1/\rho_0=1.22$, $c_1/c_0=1.27$, $\rho_2/\rho_0=2.7$, $c_2/c_0=4.3$ (penetrable cylinders).

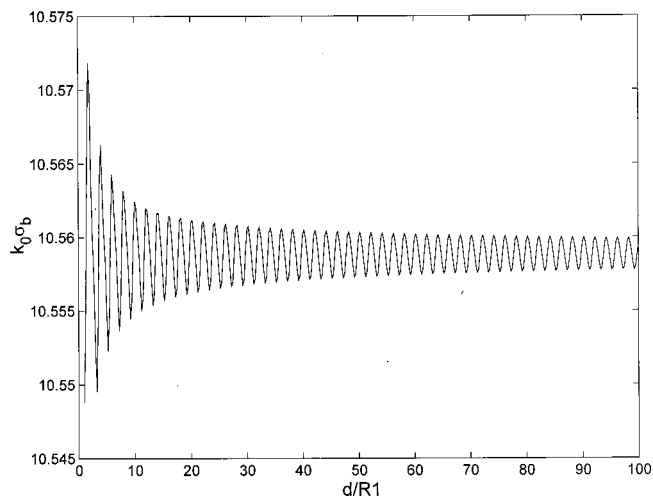


FIG. 5. Backscattering cross section for $R_1/\lambda_0=0.5$, $R_2/R_1=0.01$, $\varphi_0=90^\circ$ (hard impenetrable cylinders).

C. Both cylinders impenetrable

In this case we use $\rho_v \rightarrow 0$ for a soft cylinder and $\rho_v \rightarrow \infty$ for a hard one, with c_v finite in both cases ($v=1,2$). So the changes to the results of Sec. II are all those appearing in the two former cases, (A) and (B).

IV. NUMERICAL RESULTS AND DISCUSSION

In Figs. 2–7 the various scattering cross sections are given for the configuration of Fig. 1, for penetrable and impenetrable (soft or hard) cylinders. Figures 2–4 refer to penetrable cylinders, while Figs. 5–7 refer to impenetrable ones. The wavelength in region 0 is $\lambda_0=2\pi/k_0$. The case $R_2/R_1=0$ corresponds to the unperturbed problem, i.e., when only the first cylinder (of radius R_1) is present.

The results are symmetrical about the xz plane, as it is imposed by the geometry of the scatterer. A result expected from reciprocity and seen in Figs. 4 and 6 is that σ_f and Q_t have the same values for incidence angles with sum equal to

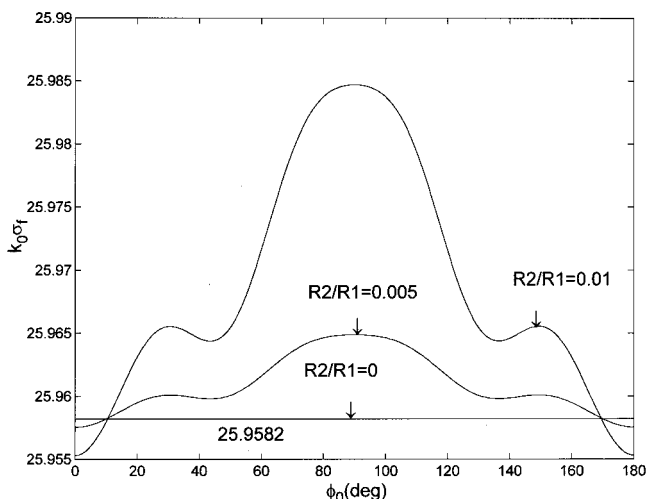


FIG. 6. Forward scattering cross section vs $\varphi_0(^\circ)$ for $R_1/\lambda_0=0.5$, $d/R_1=1.1$ (hard impenetrable cylinders).

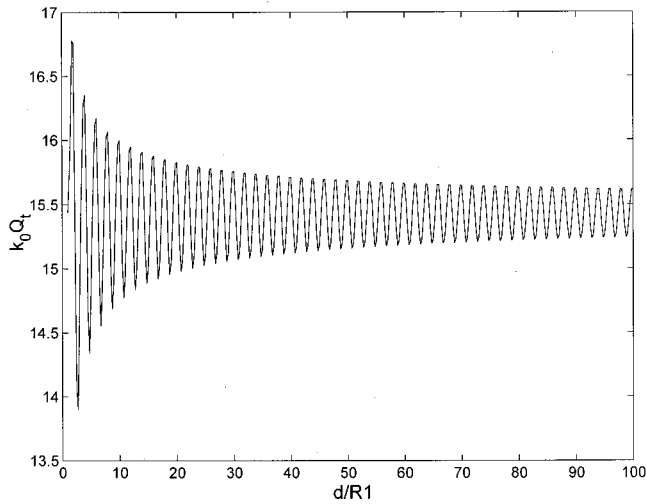


FIG. 7. Total scattering cross section for $R_1/\lambda_0=0.5$, $R_2/R_1=0.01$, $\varphi_0=90^\circ$ (soft impenetrable cylinders).

π . From Figs. 3, 5, and 7 we see that the various scattering cross sections change rapidly with d/R_1 , as is expected.

The results of Figs. 2–7 were verified, to a high degree of accuracy, by comparing to independent results obtained from the numerical solution of the same problems, by truncating the infinite sets of linear equations. In Figs. 8–10 we give the relative absolute errors [(approximate value-exact value)/exact value] for σ_b , σ_f , and Q_t , resulting from the comparison of the approximate results of this paper with the exact numerical ones obtained by truncation. Figure 8 refers to penetrable cylinders, while Figs. 9 and 10 refer to hard and soft impenetrable cylinders, respectively. The values of the parameters used are the same as in Figs. 2–7, with the difference that now $d/R_1=2.0$, while the various errors given are maximum with respect to φ_0 (obtained by using $\varphi_0=0^\circ-180^\circ$ in steps of 1°). It is evident that the error in σ_b is greater than that in σ_f and Q_t , in any case. The errors for soft impenetrable cylinders are much greater than those

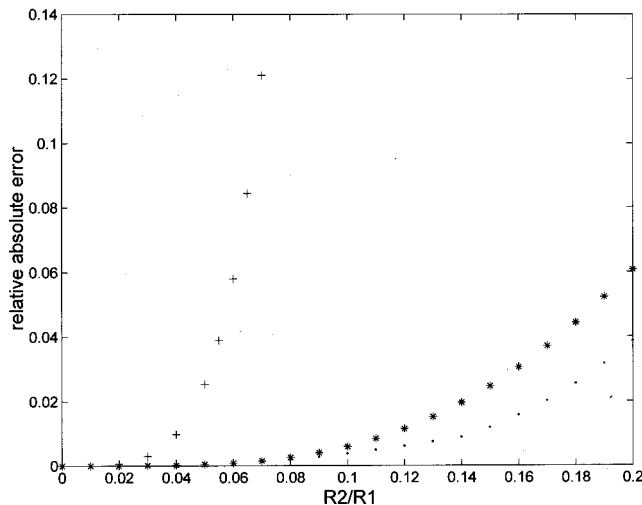


FIG. 8. Relative absolute error for $R_1/\lambda_0=0.5$, $d/R_1=2.0$, $\rho_1/\rho_0=1.22$, $c_1/c_0=1.27$, $\rho_2/\rho_0=2.7$, $c_2/c_0=4.3$ [penetrable cylinders. + + + + (σ_b), \cdots (σ_f), * * * * (Q_t)].

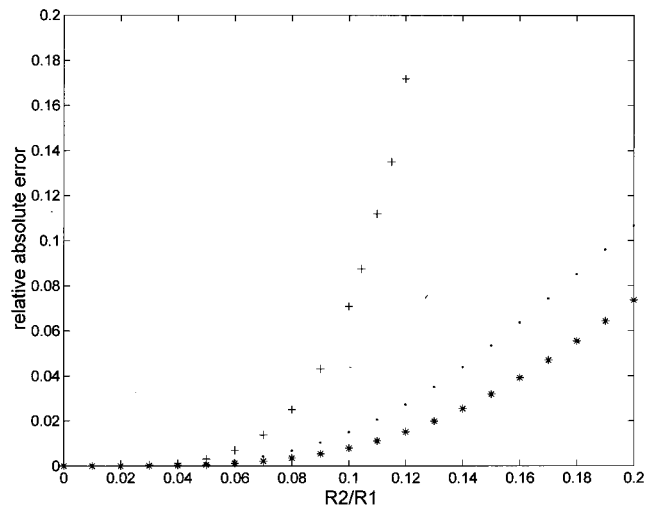


FIG. 9. Relative absolute error for $R_1/\lambda_0=0.5$, $d/R_1=2.0$ [hard impenetrable cylinders. + + + + (σ_b), \cdots (σ_f), * * * * (Q_t)].

for hard, or for penetrable ones, due to the presence of the factor $1/[\ln(w/2) + \gamma]$ in Eqs. (48), (49). This factor becomes small only for very small values of w , as compared to the factor w^2 appearing in the corresponding formulas for hard or penetrable cylinders, which diminishes very faster. This was also true in Refs. 18 and 19. The maximum value of R_2/R_1 used in Figs. 2–7 is 0.01, thus keeping the errors low enough in each case.

By the formulas derived in this paper we can easily calculate the various scattering cross sections for each small value of the ratio R_2/R_1 , if the other parameters remain constant, simply by using the results given in Figs. 2–7. The same is valid for different values of $\rho_2 \neq \rho_0$ when $\kappa_2 = \kappa_0$ [$\kappa_2 \neq \kappa_0$ when $\rho_2 = \rho_0$], with $\kappa = 1/\rho c^2$ the compressibility of the material. In this case $\delta C_m \sim g[\delta C_m \sim f]$, and finally $\delta\sigma$, δQ_t are proportional to these quantities, making simple the calculation of the various scattering cross sections for

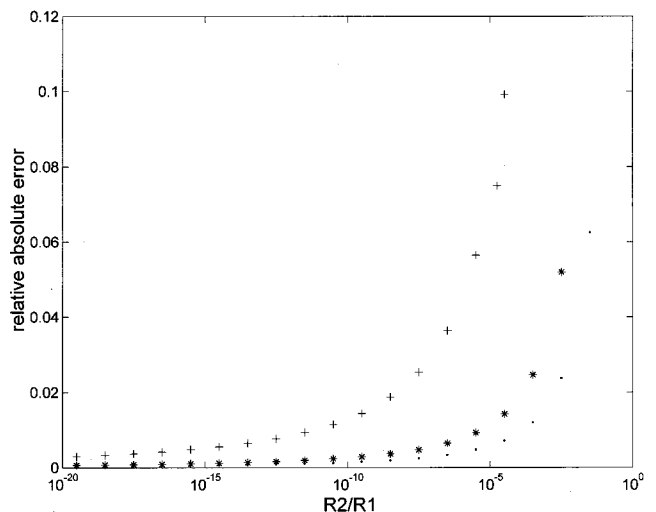


FIG. 10. Relative absolute error for $R_1/\lambda_0=0.5$, $d/R_1=2.0$ [soft impenetrable cylinders. + + + + (σ_b), \cdots (σ_f), * * * * (Q_t)].

each different value of $\rho_2/\rho_0[\kappa_2/\kappa_0]$ as long as the other parameters of the problem remain constant. These remarks also pertain to the inverse problem of calculating the radius R_2 , the density, or the compressibility of the thin cylinder, from the measurement of the scattered field.

- ¹A. Z. Elsherbeni and A. A. Kisk, "Modeling of cylindrical objects by circular dielectric and conducting cylinders," *IEEE Trans. Antennas Propag.* **40**, 96–99 (1992).
- ²H. A. Ragheb and M. Hamid, "Scattering by N parallel conducting circular cylinders," *Int. J. Electron.* **59**, 407–421 (1985).
- ³H. A. Ragheb and M. Hamid, "Simulation of a cylindrical reflector by conducting circular cylinders," *IEEE Trans. Antennas Propag.* **35**, 349–353 (1987).
- ⁴V. Twersky, "Multiple scattering of radiation by an arbitrary configuration of parallel cylinders," *J. Acoust. Soc. Am.* **24**, 42–46 (1952).
- ⁵V. Twersky, "Multiple scattering of radiation by an arbitrary planar configuration of parallel cylinders, and by two parallel cylinders," *J. Appl. Phys.* **23**, 407–414 (1952).
- ⁶J. W. Joungh and J. C. Bertrand, "Multiple scattering by two cylinders," *J. Acoust. Soc. Am.* **58**, 1190–1195 (1975).
- ⁷E. B. Danilla, J. M. Conoir, and J. L. Izbicki, "The generalized Debye series expansion: Treatment of the concentric and nonconcentric cylindrical fluid–fluid interfaces," *J. Acoust. Soc. Am.* **98**, 3326–3342 (1995).
- ⁸E. B. Danilla, J. M. Conoir, and J. L. Izbicki, "Generalized Debye series expansion: Part II, Treatment of eccentric fluid-solid cylindrical interfaces," *Acust. Acta Acust.* **84**, 38–44 (1998).
- ⁹R. V. Row, "Theoretical and experimental study of electromagnetic scattering by two identical conducting cylinders," *J. Appl. Phys.* **26**, 666–675 (1955).
- ¹⁰R. Millar, "The scattering of a plane wave by a row of small cylinders," *Can. J. Phys.* **38**, 272–289 (1960).
- ¹¹G. O. Olaofe, "Scattering by two cylinders," *Radio Sci.* **5**, 1351–1360 (1970).
- ¹²K. Hongo, "Multiple scattering by two conducting circular cylinders," *IEEE Trans. Antennas Propag.* **26**, 748–751 (1978).
- ¹³A. Z. Elsherbeni and M. Hamid, "Scattering by parallel conducting circular cylinders," *IEEE Trans. Antennas Propag.* **35**, 355–358 (1987).
- ¹⁴D. V. Evans and P. Porter, "Trapped multiple cylinders in a channel," *J. Fluid Mech.* **339**, 331–356 (1997).
- ¹⁵H. D. Maniar and J. N. Newman, "Wave diffraction by a long array of cylinders," *J. Fluid Mech.* **339**, 309–330 (1997).
- ¹⁶C. M. Linton and D. V. Evans, "The interaction of waves with a row of circular cylinders," *J. Fluid Mech.* **251**, 687–708 (1993).
- ¹⁷B. Fornberg, "Steady incompressible flow past a row of circular cylinders," *J. Fluid Mech.* **225**, 655–671 (1991).
- ¹⁸J. A. Roumeliotis and N. B. Kakogiannos, "Scattering from an infinite cylinder of small radius embedded into a dielectric one," *IEEE Trans. Microwave Theory Tech.* **42**, 463–470 (1994).
- ¹⁹J. A. Roumeliotis and N. B. Kakogiannos, "Acoustic scattering from an infinite cylinder of small radius coated by a penetrable one," *J. Acoust. Soc. Am.* **97**, 2074–2081 (1995).
- ²⁰J. A. Stratton, *Electromagnetic Theory* (McGraw-Hill, New York, 1941).
- ²¹M. Abramowitz and I. A. Stegun, *Handbook of Mathematical Functions* (Dover, New York, 1972).
- ²²J. J. Bowman, T. B. A. Senior, and P. L. E. Uslenghi, *Electromagnetic and Acoustic Scattering by Simple Shapes* (North-Holland, Amsterdam, 1969).

Low-frequency scattering of acoustic waves by a bounded rough surface in a half-plane

F. J. Sabina

Instituto de Investigaciones en Matemáticas Aplicadas y en Sistemas, Universidad Nacional Autónoma de México, Apartado Postal 20-726, Delegación Alvaro Obregón, 01000 México, D.F., Mexico

V. M. Babich

St. Petersburg Branch of the Steklov Mathematical Institute (POMI), Fontanka 27, St. Petersburg, 191011, Russia

(Received 14 April 2000; revised 9 November 2000; accepted 18 December 2000)

The problem of the scattering of harmonic plane waves by a rough half-plane is studied here. The surface roughness is finite. The slope of the irregularity is taken as arbitrary. Two boundary conditions are considered, those of Dirichlet and Neumann. An asymptotic solution is obtained, when the wavelength λ of the incident wave is much larger than the characteristic length of the roughness l , by means of the method of matched asymptotic expansions in terms of the small parameter $\epsilon = 2\pi l/\lambda$. For the Dirichlet problem, the solution of the near and far fields is obtained up to $O(\epsilon^2)$. The far field solution is given in terms of a coefficient that have a simple explicit expression, which also appears in the corresponding solution to the Neumann problem, already solved. Also the scattering cross section is given by simple formulas to $O(\epsilon^3)$. It is noted that, for the Dirichlet problem, the leading term is of order ϵ^3 which, by contrast, is different from that of the circular cylinder in full space, that is, of order $\epsilon^{-1}(\log \epsilon)^{-2}$. Some examples display the simplicity of the general results based on conformal mapping, which involve arcs of circle, polygonal lines, surface cracks and the like. © 2001 Acoustical Society of America. [DOI: 10.1121/1.1348297]

PACS numbers: 43.20.Fn, 43.20.Bi [ANN]

I. INTRODUCTION

Two scattering problems are considered here which involve either the Dirichlet or Neumann conditions for the rough, but finite, surface of a half-plane. When the roughness is a semicircle or a semiellipse, the method of separation of variables yields an explicit solution of the reduced wave equation in terms of a series.¹⁻³ For other shapes, in the Rayleigh and resonance regime, a numerical scheme that leads to a linear algebraic system of equations is generally used. In these cases, the theoretical method exploits the geometry of the single ridge type scatterer (viz., semielliptical,⁴ rectangular,⁴⁻⁶ triangular⁷ or arbitrarily shaped⁸). Whereas a different asymptotic approach is proposed to deal with shallow rough profiles, which include periodic and nonperiodic ones.⁹ Application of some of the above methods can be found in seismological applications.^{6,7,10} Boundary element methods have also been applied to empty^{11,12} and filled¹³⁻¹⁵ surface scatterers in the earthquake engineering context for wavelengths comparable to the characteristic size of the irregularity and much longer. When the slope of the irregularity is small, a regular asymptotic method arises and the solution can be obtained as an asymptotic series,^{16,17} or see, for instance, the Appendix in Sabina and Willis.¹⁸ If no restriction is imposed on the slope of the roughness, then a singular perturbation problem can be formulated and solved in the low-frequency limit. The Neumann problem has already been solved to the second order in the small parameter.¹⁸ Near and far field expressions were obtained by means of the method of matched asymptotic expansions. The far field asymptotic expression is shown to be the contribution of the

superposition of two sources, a monopole and a dipole, acting at the origin. The amplitude of the former source is equal to the area under the curve defined by the roughness, whereas the latter is related to an integral defined on the rough boundary. In the limit of a small slope, both coefficients are equal. In this paper it will be shown that exactly the same dipole source coefficient appears in the far field expression for the Dirichlet problem. Moreover, it is found that it is given as the product of two coefficients of a related conformal mapping. The scattering cross section to the leading order for both problems, Neumann and Dirichlet, is expressed in terms of the monopole and dipole amplitudes. These formulas are very simple. A similar problem, that of scattering of acoustic waves by bounded inhomogeneities, is also treated as a singular perturbation problem by Kriegsmann and Reiss.¹⁹ Also full two-dimensional scattering problems are dealt with in the low frequency limit by Gotlib.²⁰ More references to related problems can be found in Datta and Sabina.²¹

In Sec. II, the Dirichlet scattering problem is formulated. The method of matched asymptotic expansions is used, in Sec. III to find the near and far field in the low-frequency limit. In Sec. IV, the scattering cross section is calculated to the leading order term. Some examples are explicitly treated in Sec. V, viz., mountain and valley arcs of circle, polygonal surface irregularities: arbitrary triangle, isosceles triangle, one edge crack, two edge cracks. The formulas obtained for these geometries are quite simple. Section VI contains some concluding remarks. The Appendix deals with the polarization tensor which is closely related to these problems.

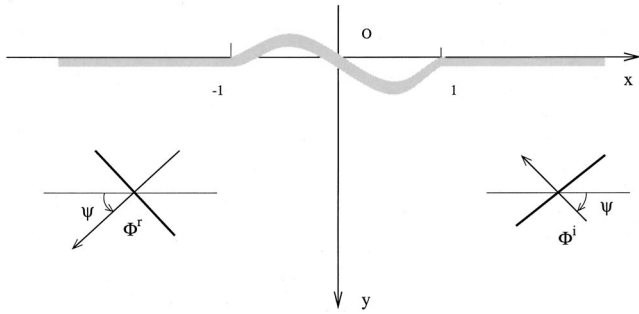


FIG. 1. Finite rough boundary half-plane $y > f(x)$. Unit amplitude incident Φ^i and reflected Φ^r plane waves at an angle ψ . Note that $f(x) = 0$ for $|x| \geq 1$.

II. STATEMENT OF THE SCATTERING PROBLEM

A two-dimensional harmonic wave motion is considered in a homogeneous half-plane $y' > f(x')$, whose boundary $y' = f(x')$ is such that $f(x') \neq 0$ in the finite interval $-l < x' < l$ and $f(x') = 0$ for $|x'| \geq l$. All lengths are nondimensionalized with respect to the half-interval length l . Henceforth $y = f(x)$ is understood to be nonvanishing in the interval $(-1, 1)$; see Fig. 1. The scattering problem is formulated in such a way that the scattered wave $\Phi_D(x, y)e^{i\omega t}$, where ω is the circular frequency, satisfies the Dirichlet boundary value problem:

$$\Delta \Phi_D + \epsilon^2 \Phi_D = 0 \quad \text{in } y > f(x), \quad (1)$$

$$\Phi_D = -\Phi^0 \quad \text{on } y = f(x), \quad (2)$$

$$r^{1/2} \left(\frac{\partial \Phi_D}{\partial r} + i\epsilon \Phi_D \right) = o(1) \quad \text{as } r = (x^2 + y^2)^{1/2} \rightarrow \infty, \quad (3)$$

where $\epsilon = \omega l / c$, the speed of the wave is c and the total wave field Φ_D^t is given by

$$\Phi_D^t = \Phi^0 + \Phi_D \quad \text{in } y > f(x), \quad (4)$$

and

$$\Phi^0 = 2i \sin(\epsilon y \sin \psi) \exp(i\epsilon x \cos \psi) \quad (5)$$

is the sum of the unit amplitude incident and reflected plane waves with the angle of incidence ψ measured with respect to the x -axis. Note that Φ_D vanishes on $y = f(x)$ for $|x| \geq 1$. The factor $\exp(i\omega t)$ is understood and omitted henceforth.

The wave field Φ_D may be the velocity potential in acoustics or the antiplane shear-horizontal displacement in elasticity; $\Phi_D \mathbf{e}_z$ may be a Hertz vector in electromagnetism, where \mathbf{e}_z is the unit vector in the direction of the z -axis. The Dirichlet or Neumann boundary conditions correspond to open or rigid surfaces in acoustics, to fixed rigid or free surfaces in elasticity and to electric or magnetic fields parallel to \mathbf{e}_z for a perfect conductor in electromagnetism.

It is well-known that it is possible to obtain the solution of Eqs. (1)–(3), (5) and its Neumann counterpart in explicit form only if the curve $y = f(x)$, $f(x) < 0, |x| \leq 1$ is a semi-circle or a semiellipse by the method of separation of variables.^{1–3} There are other cases where asymptotic methods are applicable and give quite satisfactory approximate formulas to the solution (see, for instance, the Appendix in

Ref. 18). Here a low-frequency approximation is sought for $\epsilon \ll 1$, so that Eqs. (1)–(3), (5) define a singular perturbation problem.

The corresponding Neumann problem was solved using the method of matched asymptotic expansions¹⁸ (see, also, Datta and Sabina²¹). The far field asymptotic expansion obtained by them is

$$\Phi_N \sim \epsilon^2 [i a_m H_0^{(2)}(\epsilon r) + a_d H_1^{(2)}(\epsilon r) \cos \theta \cos \psi] \quad (6)$$

as ϵ tends to zero for the same incident wave; note that the subindex N refers to the Neumann boundary condition; (r, θ) are the polar coordinates of the point (x, y) ; $H_n^{(2)}(r)$ is the Hankel function of the second class and order n . The coefficients a_m and a_d are real and were found to have simple explicit expressions related to the boundary shape. They can be thought of as the amplitude due to a monopole or the dipole source acting at the origin, respectively. The coefficient a_m is equal to the area under the curve $y = f(x)$. The other one, related to the shape, is given below in Eq. (30) and also appears in the far field expression for the Dirichlet problem, as shown below.

III. SOLUTION OF THE DIRICHLET SCATTERING PROBLEM

In asymptotic problems, a key point is the correct choice of the “ansatz,” i.e., a suitable form of the asymptotic expansion. Here the form of convenient asymptotic expansions of Φ_D is suggested by earlier works.^{18,20,22} Thus, for the near field, let

$$\Phi_D \sim \epsilon \varphi_1(x, y) + \epsilon^2 \varphi_2(x, y) + \epsilon^3 \varphi_3(x, y) + \dots \quad (7)$$

in a domain which includes the finite nonzero part of the boundary curve $y = f(x)$ as ϵ tends to zero and, for the far field, consider the multipole ansatz

$$\Phi_D \sim \epsilon \sum_{j=1}^{\infty} a_j \epsilon^j H_j^{(2)}(\epsilon r) \sin j \theta, \quad (8a)$$

$$a_j = \sum_{l=0}^{\infty} a_{jl} \epsilon^l, \quad (8b)$$

where a_{jl} may be a polynomial in $\ln \epsilon$, in a domain which includes the point at infinity as ϵ tends to zero.

The expansions in Eqs. (7) and (8a) are to be matched in the domain^{23,18}

$$\text{constant } \epsilon^{-\alpha} < r < \text{constant } \epsilon^{-\beta}, \quad 0 < \alpha < \beta < 1 \quad (9)$$

for $y > 0$. In other words, they are equivalent in the domain given by Eq. (9) provided

$$\sum_{j=1}^n \epsilon [(\varphi_j - a_j H_j^{(2)}(\epsilon r) \sin j \theta)] = O(\epsilon^{\gamma_n}), \quad (10)$$

where $\gamma_n \rightarrow \infty$ as $n \rightarrow \infty$. Coefficients a_{jl} and the functions $\varphi_j(x, y)$ shall be sought as follows.

Note that, on the boundary $y = f(x)$, the expansion of Eq. (5) and Eq. (7) yields

$$\varphi_1 = -2iy \sin \psi, \quad (11)$$

$$\varphi_2 = xy \sin 2\psi. \quad (12)$$

To find the φ_j 's everywhere, it is necessary to know their behavior at infinity. This can be found from the possibility of matching the expansions in Eqs. (7) and (8a) in the domain given by Eq. (9). The argument of the Hankel functions is small there and the following expansions take place

$$H_j^{(2)}(\epsilon r) = \sum_{l=0}^{\infty} K_{lj}(\epsilon r)^{2l+j} \ln \epsilon r + \sum_{l=0}^{\infty} L_{lj}(\epsilon r)^{2l-j}, \quad (13)$$

where the coefficients K_{lj} and L_{lj} are known²⁴ (p. 951). Only here

$$L_{01} = -2i/\pi \quad (14)$$

is explicitly needed later on.

It is clear that the expansion

$$\begin{aligned} \Phi_D \sim \epsilon \left(a_{10} L_{01} \frac{\sin \theta}{r} + a_{20} L_{02} \frac{\sin 2\theta}{r^2} + \dots \right) \\ + \epsilon^2 \left(a_{11} L_{01} \frac{\sin \theta}{r} + a_{21} L_{02} \frac{\sin 2\theta}{r^2} + \dots \right) \\ + \epsilon^3 \left[a_{12} L_{01} \frac{\sin \theta}{r} + a_{10} \sin \theta (L_{01} r + K_{01} r \ln \epsilon r) + \dots \right] \\ + \dots \end{aligned} \quad (15)$$

is possible in the domain given by Eq. (9). It can now be deduced that the matching will take place, i.e., the expansions in Eqs. (7) and (8) are asymptotically identical, if and only if

$$\varphi_1 \sim a_{10} L_{01} \frac{\sin \theta}{r} + a_{20} L_{02} \frac{\sin 2\theta}{r^2} + \dots, \quad (16a)$$

$$\varphi_2 \sim a_{11} L_{01} \frac{\sin \theta}{r} + a_{21} L_{02} \frac{\sin 2\theta}{r^2} + \dots, \quad (16b)$$

$$\varphi_3 \sim a_{12} L_{01} \frac{\sin \theta}{r} + a_{10} \sin \theta (L_{01} r + K_{01} r \ln \epsilon r) + \dots, \quad (16c)$$

as r tends to infinity.

Substituting the expansion of Eq. (7) into Eq. (1) yields

$$\Delta \varphi_1 = 0, \quad \Delta \varphi_2 = 0, \quad \Delta \varphi_3 = -\varphi_1, \dots \quad (17)$$

The problem

$$\begin{aligned} \Delta \varphi_1 = 0 \quad \text{in } y > f(x), \quad \varphi_1 = -2iy \sin \psi \quad \text{for } y = f(x), \\ \varphi_1 \rightarrow 0 \quad \text{as } r \rightarrow \infty, \end{aligned} \quad (18)$$

has one and only one solution in $y > 0$. The sine Fourier series of the solution of Eq. (18) for large r has the expansion

$$\varphi_1 = \sum_{l=1}^{\infty} \alpha_{1l} \frac{\sin l\theta}{r^l} \quad (19)$$

when the coefficients α_{1l} are known.

Comparison of Eqs. (16a) and (19) gives

$$a_{10} = \frac{\alpha_{11}}{L_{01}}. \quad (20)$$

After finding φ_1 , it is possible to consider $\Delta \varphi_2 = 0$, the boundary condition for φ_2 given by Eq. (12) and the expansion of Eq. (16b) to obtain $a_{11}, a_{21}, a_{31}, \dots$ in the same manner. Then, the equation $\Delta \varphi_3 = -\varphi_1$, the boundary condition for φ_3 and the expansion of Eq. (16c) give the possibility to find a_{12}, a_{22}, \dots , etc. It is evident that this is the main scheme for finding φ_j and a_{jl} , which depends on the intermediate operation of solving the Dirichlet problem of potential theory in the semi-infinite domain $y > f(x)$. However, it is possible to express the solution of this problem in terms of the conformal mapping of the domain $y > f(x)$ onto the upper half-plane and get formulas for the functions φ_j , the coefficients a_{jl} and other quantities of interest.

Let $z = z(\zeta)$, $z = x + iy$, $\zeta = \xi + i\eta$ be the conformal mapping of the domain $y > f(x)$ into the half-plane $\eta > 0$ and $\zeta = \zeta(z)$ be the inverse mapping. It is assumed that $\zeta(\infty) = \infty$, $\zeta(-1) = \lambda_l$, $\zeta(1) = \lambda_r$, $\lambda_l \leq \lambda_r$. The values of λ_l and λ_r define the mapping completely. The image of the semi-infinite interval $(-\infty, -1)$ is $(-\infty, \lambda_l)$ and the image of $(1, +\infty)$ is $(\lambda_r, +\infty)$. Now it is possible to continue the function $z = z(\zeta)$ using the symmetry principle: $z = z(\zeta)$ is real on the real axis outside the interval (λ_l, λ_r) . The continued function $z = z(\zeta)$ has the property

$$z(\bar{\zeta}) = \overline{z(\zeta)} \quad (21)$$

in accordance with the symmetry principle. The function $z(\zeta)$ is now defined in a neighborhood of infinity and has a simple pole there, because $z(\infty) = \infty$ and the map is conformal. Its Laurent expansion has the form

$$z = z(\zeta) = b_1 \zeta + b_0 + \frac{b_{-1}}{\zeta} + \dots \quad (22)$$

The inequality $b_1 > 0$ follows from the inequality $z(\zeta) > 1$ if $\zeta > \lambda_r$.

In order to solve Eqs. (18) it is sufficient to solve the new problem

$$\begin{aligned} \left(\frac{\partial^2}{\partial \xi^2} + \frac{\partial^2}{\partial \eta^2} \right) \varphi_1(\xi, \eta) = 0 \quad \text{in } \eta > 0, \\ \varphi_1(\xi, 0) = -2i \sin \psi \operatorname{Im} z(\xi), \end{aligned} \quad (23)$$

$$\varphi_1 \rightarrow 0 \quad \text{as } |\zeta| \rightarrow \infty,$$

and to use inverse mapping $\zeta = \zeta(z)$, or to put

$$\varphi_1(x, y) = \varphi_1(\xi(x, y), \eta(x, y)).$$

The solution of Eqs. (23) is known to be²⁵ (p. 568)

$$\varphi_1(\xi, \eta) = -\frac{2i \eta \sin \psi}{\pi} \int_{\lambda_l}^{\lambda_r} \frac{\operatorname{Im} z(\xi') d\xi'}{|\xi' - \zeta|^2}. \quad (24)$$

When $\zeta \rightarrow \infty$,

$$\varphi_1(\xi, \eta) = -\frac{2i \sin \psi \eta}{\pi} \int_{\lambda_l}^{\lambda_r} \operatorname{Im} z(\xi') d\xi' + O(|\zeta|^{-2}).$$

Hence

$$\begin{aligned} \varphi_1(x,y) &= \varphi_1(\xi(x,y), \eta(x,y)) \\ &= -\frac{2i \sin \psi}{\pi} b_1 \frac{y}{x^2+y^2} \int_{\lambda_l}^{\lambda_r} \text{Im } z(\xi) d\xi \\ &\quad + O((x^2+y^2)^{-1}), \end{aligned} \quad (25)$$

because for large $|z|$

$$\zeta = \zeta(z) = \frac{1}{b_1} z - \frac{b_0}{b_1} - \frac{b_{-1}}{z} + \dots \quad (26)$$

The leading term of Eq. (25) can now give the sought coefficient of Eq. (20), i.e.,

$$a_{10} = -a_d \sin \psi, \quad (27)$$

where

$$a_d = b_1 \int_{\lambda_l}^{\lambda_r} \text{Im } z(\xi) d\xi \quad (28)$$

is a real coefficient. It is not difficult to show that $a_d = a_m$ when the slope of the surface irregularity is small, i.e., when $|f'(x)| \ll 1$.

The calculation of the integral in Eq. (28) is not difficult in the general case. It follows immediately that

$$\int_{\lambda_l}^{\lambda_r} \text{Im } z(\xi) d\xi = \frac{1}{2i} \int_{\lambda_l}^{\lambda_r} [z(\xi) - z(\overline{\xi})] d\xi = \frac{1}{2i} \int_L z(\xi) d\xi, \quad (29)$$

where L is a path of integration around the cut $[\lambda_l, \lambda_r]$ in the positive direction. Here the property $z(\xi^-) = z(\overline{\xi^+})$ is used, if ξ^\pm are corresponding points on opposite sides of the cut. The residue theorem for unbounded domains leads to the very simple formula for the dipole amplitude

$$a_d = \pi b_1 b_{-1}. \quad (30)$$

The next term φ_2 can be obtained in the same manner. The results obtained for the near and far field are then given by

$$\Phi_D \sim \frac{\eta}{\pi} \int_{\lambda_l}^{\lambda_r} [-2\epsilon \sin \psi + \epsilon^2 \sin 2\psi \text{Re } z(\xi')] \frac{\text{Im } z(\xi') d\xi'}{|\xi - \xi'|^2}, \quad (31)$$

$$\Phi_D \sim -\epsilon^2 a_d H_1^{(2)}(\epsilon r) \sin \theta \sin \psi \quad (32)$$

as ϵ tends to zero, respectively. Note that Eq. (32) is symmetric relative to θ and ψ , i.e., the reciprocity principle is satisfied to this order.

IV. SCATTERING CROSS SECTION

One measure of the surface irregularity effect upon an incident wave is the scattering cross section Σ of the irregularity. It is defined as the ratio of the average rate at which energy is scattered by the irregularity to the average rate at which the energy of the incident wave crosses a unit length perpendicular to its direction of propagation. It can be obtained from the expression

$$\Sigma = \int_0^\pi |h(\theta)|^2 d\theta, \quad (33)$$

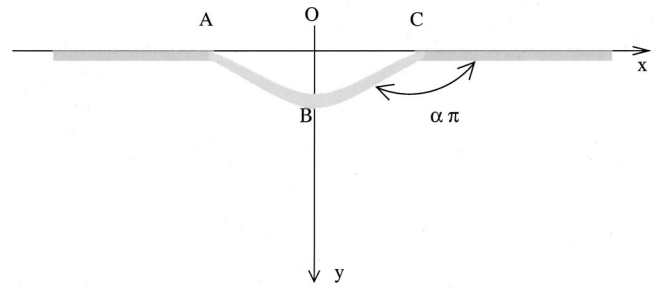


FIG. 2. The rough boundary is a valley, an arc of circle ABC of radius $R = |\sin \alpha\pi|^{-1}$, which intersects $y=0$ at an angle $\alpha\pi$. Coordinates of A $(-1, 0)$, B $(0, -R \cot \alpha\pi)$, C $(1, 0)$.

where $h(\theta)$ is the far field scattering amplitude of the wave

$$\Phi = h(\theta) r^{-1/2} e^{-ir} \quad \text{as } r \rightarrow \infty. \quad (34)$$

Since the Hankel function has the expansion

$$H_n^{(2)}(r) = \left(\frac{2}{\pi r}\right)^{1/2} \exp\left[-ir + i\left(n + \frac{1}{2}\right)\frac{\pi}{2}\right] \quad \text{as } r \rightarrow \infty, \quad (35)$$

it is easy to find that the first term of the scattering cross section is

$$\Sigma_D = \epsilon^3 a_d^2 \sin^2 \psi \quad (36)$$

for the Dirichlet problem and

$$\Sigma_N = \epsilon^3 (2a_m^2 + a_d^2 \cos^2 \psi) \quad (37)$$

for the Neumann problem as ϵ tends to zero.

It is seen that the leading term of the scattering cross section is of order ϵ^3 for both problems. This behavior is the same for a circular cylinder in a full space for the Neumann condition but contrasts with the different one of order $\epsilon^{-1} (\log \epsilon)^{-2}$ for the Dirichlet condition.^{26,27} The different asymptotic behavior arises because the two scattering problems differ in the number of incident waves. In the full two-dimensional case, one is dealing with one incident wave. In the half-plane situation, it is well-known²⁸ that this problem, when the inclusion (of a valley type that can be reflected toward the other half-plane), is reflected, it is equivalent to the full two-dimensional body and two incident waves. Then the scattered waves interfere constructively and destructively in such a way as have the different asymptotic behavior noted above.

V. EXAMPLES

Some specific shapes are now considered which will show the applicability of the above results.

A. Mountain and valley arcs

Let the function $f(x)$ for $|x| < 1$ be an arc of circle ABC , so that $y=f(x)$ consists of the two intervals $(-\infty, 1), (1, +\infty)$ and the arc of circle ABC intersecting $y=0$ at an angle $\alpha\pi$; see Fig. 2. When $1 < \alpha \leq 3/2$, the arc can be thought of as a ridge, and if $1/2 \leq \alpha < 1$, ABC is a valley. This convention is commonly used by geophysicists, who consider that the plane $y=0$ is the surface of the Earth. The radius R of the circle, the arc of which is ABC , can easily be derived, $R = |\sin \alpha\pi|^{-1}$.

The mapping and its inverse function are

$$z(\zeta) = \{[T(\zeta)]^\alpha + 1\} \{[T(\zeta)]^\alpha - 1\}^{-1}, \quad (38)$$

and

$$\zeta(z) = \{[T(z)]^{1/\alpha} + 1\} \{[T(z)]^{1/\alpha} - 1\}^{-1}, \quad (39)$$

respectively, where

$$T(z) = (z+1)/(z-1). \quad (40)$$

It is not difficult to find that

$$b_1 = 1/\alpha; \quad (41a)$$

the residue at the point of infinity of the mapping function, Eq. (38), is

$$b_{-1} = (1 - \alpha^2)/3\alpha; \quad (41b)$$

the monopole and dipole amplitudes:

$$a_m = \pi(1 - \alpha) \csc^2 \alpha \pi + \cot \alpha \pi, \quad (41c)$$

$$a_d = \pi(1 - \alpha^2)/3\alpha^2. \quad (41d)$$

Hence, to the leading order,

$$\Sigma_D = \epsilon^3 \pi^2 (1 - \alpha^2)^2 \sin^2 \psi / 9\alpha^4, \quad (42a)$$

$$\Sigma_N = \epsilon^3 \{ 2[\pi(1 - \alpha) \csc^2 \alpha \pi + \cot \alpha \pi]^2 + \pi^2 (1 - \alpha^2)^2 \cos^2 \psi / 9\alpha^4 \}. \quad (42b)$$

In particular, for a semicircular mountain $\alpha = 3/2$,

$$a_m = -\pi/2, \quad (43a)$$

$$a_d = -5\pi/27, \quad (43b)$$

and, to the leading order,

$$\Sigma_D = \frac{25}{729} \epsilon^3 \pi^2 \sin^2 \psi, \quad (43c)$$

$$\Sigma_N = \epsilon^3 \pi^2 \left(\frac{1}{2} + \frac{25}{729} \cos^2 \psi \right). \quad (43d)$$

For a semicircular valley, $\alpha = 1/2$, the mapping becomes $\zeta = (z + z^{-1})/2$, and

$$a_m = \pi/2, \quad (44a)$$

$$a_d = \pi, \quad (44b)$$

and, to the leading order,

$$\Sigma_D = \epsilon^3 \pi^2 \sin^2 \psi, \quad (44c)$$

$$\Sigma_N = \epsilon^3 \pi^2 (\cos^2 \psi + 1/2). \quad (44d)$$

B. Polygonal surface irregularities

Let the boundary $y = f(x)$ of the half-plane $y > f(x)$ be a piecewise linear function taken as an open polygon of p vertices located at the points $\Lambda_i(x_i, y_i)$, $|x_i| \leq 1$, $i = 1, 2, \dots, p$, with corresponding interior angles $\alpha_i \pi$; $(x_1, y_1) = (-1, 0)$ and $(x_p, y_p) = (1, 0)$. The Schwarz-Christoffel mapping function

$$z(\zeta) = b_1 \int_0^\zeta \prod_{i=1}^p (\zeta - \lambda_i)^{\alpha_i - 1} d\zeta + ih \quad (45)$$

maps conformally the upper half-plane $\eta > 0$ of the ζ -plane into the polygon interior $y > f(x)$ of the z -plane so that the points λ_i on $\eta = 0$ are mapped into the points Λ_i . Here $\lambda_i = \lambda_1$, $\lambda_r = \lambda_p$, b_1 and h are real constants and $\sum_{i=1}^p \alpha_i = p$. The residue at the point of infinity of the mapping of Eq. (45) is

$$b_{-1} = -\frac{1}{2} b_1 \left[\sum_{i=1}^p (\alpha_i - 1)(\alpha_i - 2) \lambda_i^2 + 2 \sum_{i=1}^p \sum_{j=i+1}^p (\alpha_i - 1)(\alpha_j - 1) \lambda_i \lambda_j \right]. \quad (46)$$

Hence

$$a_d = -\frac{1}{2} \pi b_1^2 \left[\sum_{i=1}^p (\alpha_i - 1)(\alpha_i - 2) \lambda_i^2 + 2 \sum_{i=1}^p \sum_{j=i+1}^p (\alpha_i - 1)(\alpha_j - 1) \lambda_i \lambda_j \right]. \quad (47)$$

Various particular choices of the polygonal shape $y = f(x)$ for $|x| \leq 1$ are now considered.

1. Arbitrary triangle

Thus $p = 3$, $\alpha_1 + \alpha_2 + \alpha_3 = 3$, vertices at $\Lambda_1(-1, 0)$, $\Lambda_2(L, H)$ and $\Lambda_3(1, 0)$; a ridge (groove) occurs when H is negative (positive); $\lambda_1 = -1$, $\lambda_2 = 0$ and $\lambda_3 = (\alpha_1 - 1)/(\alpha_3 - 1)$. Then

$$z = b_1 \int_0^\zeta (\zeta + 1)^{\alpha_1 - 1} \zeta^{\alpha_2 - 1} (\zeta - \lambda_3)^{2 - \alpha_1 - \alpha_2} d\zeta + L + iH, \quad (48)$$

$$b_1 = [(1 - L)^2 + H^2]^{1/2} / I, \quad (49)$$

where I is the integral

$$I = \int_0^{\lambda_3} (\xi + 1)^{\alpha_1 - 1} \xi^{\alpha_2 - 1} (\lambda_3 - \xi)^{2\alpha_1 - \alpha_2} d\xi = \lambda_3^{2 - \alpha_1} \Gamma(\alpha_2) \Gamma(3 - \alpha_1 - \alpha_2) \times F_1(1 - \alpha_1, \alpha_2; 3 - \alpha_1; -\lambda_3) / \Gamma(3 - \alpha_1), \quad (50)$$

which is evaluated from Gradshteyn and Ryzhik²⁴ (p. 287), where $\Gamma(x)$ is the Gamma function and ${}_2F_1(a, b; c; z)$ is the hypergeometric function. Then,

$$b_{-1} = (1 - \alpha_2) \lambda_3 b_1 / 2, \quad (51)$$

$$a_m = H, \quad (52)$$

$$a_d = \pi(1 - \alpha_2) \lambda_3^{2\alpha_1 - 3} [(1 - L)^2 + H^2] \Gamma^2(3 - \alpha_1) / [2\Gamma^2(\alpha_2) \times \Gamma^2(3 - \alpha_1 - \alpha_2) {}_2F_1^2(1 - \alpha_1, \alpha_2; 3 - \alpha_1; -\lambda_3)]. \quad (53)$$

2. Isosceles triangle

The above results simplify somewhat. Set $\alpha_1 = \alpha_3 = \alpha$ ($\frac{1}{2} \leq \alpha \leq \frac{3}{2}$) and $L = 0$, then $\lambda_1 = -1$, $\lambda_2 = 0$, $\lambda_3 = 1$. Thus,

$$z = b_1 \int_0^\zeta \left(\frac{\zeta^2 - 1}{\zeta^2} \right)^{\alpha - 1} d\zeta + iH, \quad (54)$$

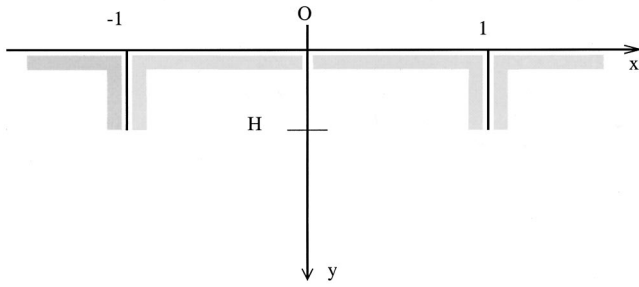


FIG. 3. Two neighboring edge cracks of depth H separated a normalized distance of two.

$$b_1 = \Gamma(\alpha - 1/2) / \pi^{1/2} \Gamma(\alpha), \quad (55)$$

$$b_{-1} = (1 - \alpha) b_1 / 2, \quad (56)$$

$$a_m = H, \quad (57)$$

$$a_d = (\alpha - 1) \Gamma^2(\alpha - 1/2) / \Gamma^2(\alpha). \quad (58)$$

These results were obtained before.¹⁸ The dipole amplitude a_d in Eq. (58) is equal to the expression obtained by Sabina and Willis¹⁸ [Eq. (6.19)] although it is written differently.

3. One edge crack

The limiting case of a vertical surface crack of depth H is interesting: now $\alpha = 1/2$ in Eqs. (54) to (58); then

$$a_m = 0, \quad (59)$$

$$a_d = -\pi/2. \quad (60)$$

The value given in Eq. (60) agrees with a known result,²⁹ which were obtained differently. Thus, the scattering cross sections become

$$\Sigma_N = \epsilon^3 \pi \cos^2 \psi / 4, \quad (61)$$

$$\Sigma_D = \epsilon^3 \pi \sin^2 \psi / 4. \quad (62)$$

4. Two neighboring edge cracks

Another interesting calculation can be done for two vertical neighboring edge cracks of the same size. Their penetration is H and they are separated a dimensionless distance of two; see Fig. 3. The Schwarz–Christoffel transformation, Eq. (45), involves six vertices, i.e., $p = 6$, so that

$$z = b_1 \int_0^\xi (\xi^2 - k_2^2) [(\xi^2 - 1)(\xi^2 - k_1^2)]^{-1/2} d\xi, \quad (63)$$

$$0 < k_1 < k_2 < 1,$$

with

$$b_1 = [(1 - k_2^2)K(k_1) - E(k_1)]^{-1}, \quad (64)$$

where $K(k)$ and $E(k)$ are the complete elliptic integrals of the first and second kind, respectively, with modulus k . The parameters k_1 and k_2 are not independent. They can be shown to be related through the following equation

$$k_2^2 = E'(k_1) / K'(k_1), \quad (65)$$

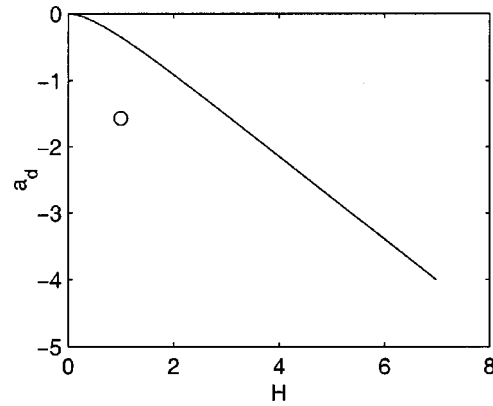


FIG. 4. It shows a plot of the dipole amplitude a_d against crack depth H for two neighboring edge cracks. The amplitude of a simple crack is also shown by the open circle.

where $K'(k)$ and $E'(k)$ are the associated complete elliptic integrals of the first and second kind, respectively. They are given by

$$K'(k) = K(k'), \quad (66a)$$

$$E'(k) = E(k'), \quad (66b)$$

where k' is the complementary modulus related to k , i.e.,

$$k^2 = 1 - k'^2. \quad (67)$$

The residue of Eq. (63) at the point of infinity is simply derived. It is given by

$$b_{-1} = b_1(2k_2^2 - k_1^2 - 1)/2. \quad (68)$$

It can be shown also that

$$b_1 = 4K'^2(k_1) / \pi^2. \quad (69)$$

The monopole and dipole amplitudes are easily computed. Thus

$$a_m = 0, \quad (70)$$

$$a_d = 2(2k_2^2 - k_1^2 - 1)K'^2(k_1) / \pi. \quad (71)$$

Also, it can be shown that the depth H is related to k_1 and k_2 through

$$\pi^2 H = 4k_2 K'^2(k_1) [K'(k_{12}) - E'(k_{12})], \quad k_{12} = k_1 / k_2. \quad (72)$$

Figure 4 shows a plot of the dipole amplitude a_d against depth H . The amplitude a_d of the dipole decreases monotonically with depth H . From about $H = 1.5$, a_d is asymptotically equal to a line of slope corresponding to an angle of, approximately, -29.74° . Also the value of Eq. (60) for a single crack of unit depth is shown there. This amplitude value is seen to be the same as that due to two edge cracks of depth close to 3, because, probably, of constructive and destructive interference. One edge crack is more noticeable in the far field than two neighboring cracks of the same size.

VI. CONCLUDING REMARKS

Near and far field expressions were obtained for the Dirichlet problem of the low-frequency scattering of plane harmonic waves by a compact rough half-plane. The near field problem is solved using a conformal mapping. To the second

order in the small parameter, the near field is given as an integral over the rough boundary only. As for the far field, the leading order term is a dipole of amplitude a_d , the same coefficient which appears in the corresponding expression for the Neumann problem. Moreover, it is shown that it can be calculated as the product of two coefficients of the conformal mapping. Expressions for the leading third order term, of the scattering cross section of both the Dirichlet and Neumann problems are obtained. In the Neumann problem another coefficient, the source monopole of the far field comes into play. Some examples of simple conformal transformations are worked out, that is, formulas for the monopole and dipole amplitudes, and the scattering cross section are explicitly obtained. These include arcs of circle: semicircular valley or ridge, polygonal irregularities: arbitrary triangle, isosceles, one or two edge cracks. Other examples (rectangle, trapezoid) can be found in Ref. 18.

ACKNOWLEDGMENTS

Thanks to Oscar C. Valdiviezo Mijangos for computer graphics and to Ana Pérez Arteaga for computational support.

APPENDIX

It is clear, from a physical point of view, that the coefficients of the expansion Eq. (8a) cannot depend on any local properties of the scatterers surface since a long wavelength situation is dealt with. The coefficients a_{jl} have to be connected with the global characteristics of the scatterers. The product $b_1 b_{-1}$ [see formulas given by Eqs. (26) and (30)] is such a characteristic. If the conformal mapping Eq. (22) were fixed by the condition

$$z = z(\zeta) = \zeta + \tilde{b}_0 + \frac{\tilde{b}_{-1}}{\zeta} + \dots, \quad (\text{A1})$$

the global characteristic $b_1 b_{-1}$ will be equal to \tilde{b}_{-1} , evidently. In the case when $f(x) > 0, -1 < x < 1$, it is possible to express $b_1 b_{-1} = a_{10}/\pi$ in terms of the classical polarization tensor e_{ij} .³⁰ The definition of one such example follows.

Let $\psi_i(x_1, x_2), i = 1, 2$, be the solution of the exterior Dirichlet problem

$$\left(\frac{\partial^2}{\partial x_1^2} + \frac{\partial^2}{\partial x_2^2} \right) \psi_i(x_1, x_2) = 0, \quad \text{in } \Omega, \quad (\text{A2})$$

$$|\psi_i| \leq \text{constant}, \quad \text{in } \Omega, \quad (\text{A3})$$

$$\psi_i = x_i + c_i \quad \text{on } \partial\Omega, \quad (\text{A4})$$

where c_i is a constant, Ω is a compact domain in \mathbb{R}^2 , i.e., $\Omega \subset \mathbb{R}^2$. The constants c_i are fixed in such a way that

$$\psi_i(x_1, x_2) = 0 \quad \text{as } r = (x_1^2 + x_2^2)^{1/2} \rightarrow \infty. \quad (\text{A5})$$

Equations (A2) and (A5) imply

$$\psi_i(x_1, x_2) = \sum_{j=1}^2 e_{ij} \frac{\partial \ln r}{\partial x_j} + O\left(\frac{1}{r^2}\right), \quad (\text{A6})$$

as $r \rightarrow \infty$; by definition the constants e_{ij} are the components of the polarization tensor. The matrix e_{ij} is symmetric and positive definite. The tensor e_{ij} is an important global characteristic of the domain Ω .

Consider now the Dirichlet problem Eq. (18). The symmetry principle of harmonic functions gives the possibility to continue $\varphi(x, y)$ to the half-plane $y < 0$ by means of the formula

$$\varphi(x, y) = -\varphi(x, -y). \quad (\text{A7})$$

The continued function $\varphi(x, y)$ is the solution of the Dirichlet problem

$$\Delta \varphi(x, y) = 0,$$

$$\varphi = -2iy \sin \psi \quad \text{on } |y| = f(x), \quad -1 \leq x \leq 1. \quad (\text{A8})$$

Then, as $r \rightarrow \infty$,

$$\varphi(x, y) = -2i \sin \psi \ b_1 b_{-1} \frac{\partial}{\partial y} \ln r + O\left(\frac{1}{r^2}\right). \quad (\text{A9})$$

Let $x_1 = x, x_2 = y$ in Eqs. (A2) to (A8). From the comparison of Eqs. (A2) to (A6) and Eqs. (A8) to (A9), it is obtained that

$$e_{22} = b_1 b_{-1}, \quad e_{12} = e_{21} = 0, \quad (\text{A10})$$

and the equality

$$a_{10} = -a_d \sin \psi = -\frac{1}{\pi} e_{22}.$$

It is clear from Eqs. (28)–(30) that $a_d = \pi e_{22} > 0$, in accordance with the positiveness of the matrix e_{ij} .

The possibility to express e_{ij} in terms of the conformal mapping is not unexpected. See Babich *et al.*³¹ for results which apply to an analog of e_{ij} to elasticity.

It is possible to apply the symmetry principle to the scattering problem of Eqs. (1)–(3), if $f(x) > 0$. The problem of the scattering of two plane waves by a compact scatterer is obtained. However, this approach, not used here, does not lead to any simplifications.

¹M. D. Trifunac, "Scattering of plane SH waves by a semi-cylindrical canyon," *Int. J. Earthquake Eng. Struct. Dyn.* **1**, 267–281 (1973).

²J. E. Burke and V. Twersky, "On scattering of waves by an elliptic cylinder and by a semielliptic protuberance on a ground plane," *J. Opt. Soc. Am.* **54**, 723–744 (1964).

³H. L. Wong and M. D. Trifunac, "Scattering of plane SH waves by a semi-elliptical canyon," *Int. J. Earthquake Eng. Struct. Dyn.* **3**, 157–169 (1974).

⁴D. E. Barrick, "Low-frequency scatter from a semielliptic groove in a grounded plane," *J. Opt. Soc. Am.* **60**, 625–634 (1970).

⁵W. Wirgin, "Resonance scattering of electromagnetic waves from a rectangular groove on a metallic mirror," *Opt. Commun.* **7**, 70–75 (1973).

⁶L. Kouoh-Bille, F. J. Sánchez-Sesma, and A. Wirgin, "Réponse résonante d'une montagne cylindrique à onde sismique SH," *C.R. Acad. Sci. Paris II* **312**, 849–854 (1991).

⁷L. Kouoh-Bille and A. Wirgin, "Réponse sismique en surface d'une montagne triangulaire soumise à une onde SH," *C.R. Acad. Sci. Paris II* **315**, 1187–1192 (1992).

⁸A. Wirgin, "Resonance scattering from an arbitrarily shaped protuberance on a ground plane," *Opt. Acta* **22**, 47–58 (1975).

⁹D. Maystre, O. Mata Mendez, and A. Roger, "A new electromagnetic theory for scattering from shallow rough surfaces," *Opt. Acta* **30**, 1707–1723 (1983).

¹⁰F. J. Sánchez-Sesma and M. Campillo, "Diffraction of P, SV and Ray-

- leigh waves by topographic features: A boundary integral formulation," Bull. Seismol. Soc. Am. **81**, 2234–2253 (1991).
- ¹¹F. J. Sabina, I. Herrera, and R. England, "Theory of connectivity: Applications to scattering of SH waves: I. SH wave motion," Proc. Intl. Conf. on Microzonation (San Francisco, CA) **2**, 813–824 (1978).
- ¹²R. England, F. J. Sabina, and I. Herrera, "Scattering of SH waves by surface cavities of arbitrary shape using boundary methods," Phys. Earth Planet. Inter. **21**, 148–157 (1980).
- ¹³J. Ize, R. England, and F. J. Sabina, "Theoretical and numerical study of diffraction of waves by inhomogeneous obstacles," Comunicaciones Técnicas, Serie Naranja: Investigaciones, IIMAS, UNAM, No. 291, 48 pp. (1981).
- ¹⁴R. England, J. Ize, and F. J. Sabina, "Scattered SH waves and displacement field over inhomogeneous surface obstacles in a half-space," in *Earthquake Source Modeling Ground Motion, and Structural Response*, edited by S. K. Datta (The American Society of Mechanical Engineers, New York), PVP-80/AMD-60, pp. 81–95 (1984).
- ¹⁵J. Ize, R. England, and F. J. Sabina, "Diffraction of waves by inhomogeneous obstacles," Ann. Matem. Pura Appl. IV **154**, 31–63 (1987).
- ¹⁶J.A. Ogilvy, *Theory of Wave Scattering from Random Surfaces* (Adam Hilger, Bristol, 1981).
- ¹⁷P. Beckmann and A. Spizzichino, *The Scattering of Electromagnetic Waves from Rough Surfaces* (Artech, Norwood, MA, 1987).
- ¹⁸F. J. Sabina and J. R. Willis, "Scattering of SH waves by a rough half-space of arbitrary slope," Geophys. J. R. Astron. Soc. **42**, 685–703 (1975).
- ¹⁹G. A. Kriegsmann and E. L. Reiss, "Low frequency scattering by local inhomogeneities," SIAM (Soc. Ind. Appl. Math.) J. Appl. Math. **43**, 923–943 (1983).
- ²⁰V. Yu Gotlib, "Rayleigh asymptotics of diffraction problems," J. Sov. Math. **11**, 695–699 (1979).
- ²¹S. K. Datta and F. J. Sabina, "Matched asymptotic expansions applied to diffraction of elastic waves," in *Low and High Frequency Asymptotics*, edited by V. K. Varadan and V. V. Varadan (Elsevier Science, Amsterdam, 1986), Vol. 2, Chap. 2, pp. 71–264.
- ²²A. M. Il'in, *Matching of Asymptotic Expansions of Boundary Value Problems* (Nauka, Moscow, 1989) (in Russian).
- ²³M. Van Dyke, *Perturbations Methods in Fluid Mechanics* (Parabolic, Stanford, 1975).
- ²⁴I. S. Gradshteyn and I. M. Ryzhik, *Table of Integrals, Series of Products* (Academic, New York, 1980).
- ²⁵L. V. Kantorovich and V. I. Krylov, *Approximate Methods of Higher Analysis* (Interscience, New York, 1964).
- ²⁶D. S. Jones, *The Theory of Electromagnetism* (Pergamon, Oxford, 1964), p. 454.
- ²⁷P. J. Barrat and W. D. Collins, "The scattering cross-section of an obstacle in an elastic solid for plane harmonic waves," Proc. Cambridge Philos. Soc. **61**, 969–981 (1965).
- ²⁸J. Ch. Bolomey and A. Wirgin, "Sur le comportement du champ électromagnétique aux arêtes," Ann. Inst. Henri Poincaré **14**, 97–112 (1971).
- ²⁹S. K. Datta, A. H. Shah, and C. M. Fortunko, "Diffraction of medium and long wavelength horizontally polarized shear waves by edge cracks," J. Appl. Phys. **53**, 2895–2903 (1982).
- ³⁰G. Pólya and G. Szegő, *Isoperimetric Inequalities in Mathematical Physics* (Princeton University Press, Princeton, NJ, 1951).
- ³¹V. M. Babich, I. S. Zorin, M. I. Ivanov, A. V. Movchan, and S. A. Nazarov, "Integral characteristics in problems of elasticity theory," LOMI Preprint P-6-89, pp. 59–60 (1989) (in Russian).

Guided waves in a transversely isotropic cylinder immersed in a fluid

Faiz Ahmad

Department of Mathematics, Quaid-i-Azam University, Islamabad, Pakistan

(Received 20 January 2000; revised 26 October 2000; accepted 18 December 2000)

Propagation of flexural guided waves in a fluid-loaded transversely isotropic cylinder is studied. Numerical results are presented for a cobalt cylinder immersed in water. The phase velocities are not significantly affected except for several modes in which the energy leakage occurs into the fluid over certain frequency ranges. Attenuation spectra for the leaking modes are plotted. © 2001 Acoustical Society of America. [DOI: 10.1121/1.1348299]

PACS numbers: 43.20.Jr, 43.20.Mv, 43.35.Cg [ANN]

I. INTRODUCTION

Modes of propagation of free time harmonic waves in a homogeneous isotropic cylinder were studied more than a century ago by Pochhammer¹ and Chree.² The frequency equation, determining the frequencies as functions of the wave number, is transcendental and recourse has to be made to numerical techniques. Mindlin and co-workers^{3,4} developed the method of bounds to plot dispersion relations for axially symmetric waves. Meeker and Meitzler⁵ have reviewed wave propagation in free plates and cylinders.

Let u_r , u_θ , and u_z denote components of the displacement, respectively, in the radial, circumferential and axial directions with respect to a polar coordinate system. Three types of waves can exist in a free cylinder:

- (1) A torsional wave in which $u_r \equiv u_z \equiv 0$ and u_θ is independent of θ .
- (2) A longitudinal or an axisymmetric wave in which $u_\theta \equiv 0$ and both u_r and u_z are independent of θ .
- (3) A flexural wave in which all three components exist and depend on the angle θ .

In a fluid-loaded cylinder, the torsional wave is not affected since its displacement is parallel to the fluid surface. On the other hand, both longitudinal and flexural waves have a component normal to the interface and, if their phase velocity exceeds that of sound in the surrounding fluid, energy is transferred from the cylinder to the fluid.

Recently Dayal⁶ studied longitudinal vibrations of a fluid-loaded transversely isotropic (TI) cylinder. However, Nagy⁷ pointed out a flaw in the representation used by Dayal⁶ which invalidates most of his results. Nagy⁷ has presented dispersion curves and attenuation spectra for a glass/epoxy composite rod immersed in water.

In the present paper we shall generalize Nagy's results to include flexural vibrations of a TI cylinder immersed in a fluid. For the potentials we use a representation introduced by Buchwald.⁸ This representation is ideally suited for TI materials and has been used with success in dealing with forced vibrations of a TI cylinder insonified by a harmonic acoustic wave.^{9,10} We introduce the Christoffel matrix for the n -th partial wave, two of whose eigenvalues are identical to those obtained by Nagy⁷ for the axisymmetric case. The free

boundary conditions on the cylinder's surface give a 3×3 matrix which leads to the dispersion relations for a free cylinder. Finally we modify the boundary conditions to take into account fluid-loading and calculate the modified dispersion relations and the attenuation curves for a cobalt cylinder immersed in water.

II. FREE CYLINDER

We consider a cylinder of infinite length and radius " a ", the axis of the cylinder is assumed to coincide with the axis of symmetry of the material. The density of the cylinder is denoted by ρ_1 and is assumed to be surrounded by a fluid of density ρ_0 . The velocity of sound in the fluid is denoted by c . We choose the z -axis of a cylindrical coordinate system (r, θ, z) along the axis of symmetry of the TI material. Let u_r , u_θ , u_z be the components of the displacement. The Buchwald representation⁸

$$u_r = \frac{\partial \varphi}{\partial r} + \frac{1}{r} \frac{\partial \chi}{\partial \theta}, \quad (1a)$$

$$u_\theta = \frac{1}{r} \frac{\partial \varphi}{\partial \theta} - \frac{\partial \chi}{\partial r}, \quad (1b)$$

$$u_z = \frac{\partial \psi}{\partial z}, \quad (1c)$$

reduces the equation of motion for the displacement in a TI material, to the following equations:¹¹

$$c_{11} \left[\frac{\partial^2 \varphi}{\partial r^2} + \frac{1}{r} \frac{\partial \varphi}{\partial r} + \frac{1}{r^2} \frac{\partial^2 \varphi}{\partial \theta^2} \right] + c_{44} \frac{\partial^2 \varphi}{\partial z^2} + (c_{13} + c_{44}) \frac{\partial^2 \psi}{\partial z^2} = \rho_1 \frac{\partial^2 \varphi}{\partial t^2}, \quad (2a)$$

$$(c_{13} + c_{44}) \left[\frac{\partial^2 \varphi}{\partial r^2} + \frac{1}{r} \frac{\partial \varphi}{\partial r} + \frac{1}{r^2} \frac{\partial^2 \varphi}{\partial \theta^2} \right] + c_{44} \left[\frac{\partial^2 \psi}{\partial r^2} + \frac{1}{r} \frac{\partial \psi}{\partial r} + \frac{1}{r^2} \frac{\partial^2 \psi}{\partial \theta^2} \right] + c_{33} \frac{\partial^2 \psi}{\partial z^2} = \rho_1 \frac{\partial^2 \psi}{\partial t^2}, \quad (2b)$$

$$\frac{1}{2}(c_{11}-c_{12})\left[\frac{\partial^2\chi}{\partial r^2}+\frac{1}{r}\frac{\partial\chi}{\partial r}+\frac{1}{r^2}\frac{\partial^2\chi}{\partial\theta^2}\right]+c_{44}\frac{\partial^2\chi}{\partial z^2}=\rho_1\frac{\partial^2\chi}{\partial t^2}, \quad (2c)$$

where c_{11} , etc. are the elastic constants for the material. We assume that, at any point in the cylinder,

$$\varphi=\sum_{n=0}^{\infty}B_nJ_n(\beta r)\cos(n\theta)\exp\{i(kz-\omega t)\}, \quad (3a)$$

$$\psi=\sum_{n=0}^{\infty}C_nJ_n(\beta r)\cos(n\theta)\exp\{i(kz-\omega t)\}, \quad (3b)$$

$$\chi=\sum_{n=0}^{\infty}D_nJ_n(\gamma r)\sin(n\theta)\exp\{i(kz-\omega t)\}, \quad (3c)$$

where J denotes Bessel function of the first kind and β , γ are to be determined. Substitution of Eqs. (3) in Eqs. (2) gives

$$\begin{bmatrix} c_{11}\beta^2-(\rho_1\omega^2-c_{44}k^2) & (c_{13}+c_{44})k^2 & 0 \\ (c_{13}+c_{44})\beta^2 & c_{44}\beta^2-(\rho_1\omega^2-c_{33}k^2) & 0 \\ 0 & 0 & \frac{1}{2}(c_{11}-c_{12})\gamma^2-(\rho_1\omega^2-c_{44}k^2) \end{bmatrix} \begin{bmatrix} B_n \\ C_n \\ D_n \end{bmatrix} = \begin{bmatrix} 0 \\ 0 \\ 0 \end{bmatrix}. \quad (4)$$

The above *Christoffel matrix* contains the matrix pertaining to the axisymmetric waves as a sub-matrix. For a nontrivial solution, β must be determined from the equation

$$c_{11}c_{44}\beta^4-E\beta^2+F=0, \quad (5)$$

where

$$E=(c_{13}+c_{44})^2k^2+c_{11}(\rho_1\omega^2-c_{33}k^2)+c_{44}(\rho_1\omega^2-c_{44}k^2), \quad (6)$$

and

$$F=(\rho_1\omega^2-c_{44}k^2)(\rho_1\omega^2-c_{33}k^2). \quad (7)$$

The parameter γ is found to be

$$\gamma^2=\frac{2(\rho_1\omega^2-c_{44}k^2)}{c_{11}-c_{12}}. \quad (8)$$

Equations similar to Eqs. (5) and (8) were obtained by Ahmad and Rehman⁹ and Honarvar and Sinclair¹⁰ where the response of a TI cylinder to an incident harmonic wave was studied. However, in such a problem the frequency and wave number are related by the equation $\omega=ck$. In the problem under consideration in this paper, our goal is to find a dispersion relation forced by the boundary conditions.

Define $\Delta=\sqrt{E^2-4c_{11}c_{44}F}$. The roots of Eq. (5) can be written as

$$\beta_1^2=(E-\Delta)/(2c_{11}c_{44}), \quad \beta_2^2=(E+\Delta)/(2c_{11}c_{44}). \quad (9)$$

The general solution now takes the form

$$\varphi=\sum_{n=0}^{\infty}[B_nJ_n(\beta_1r)+q_2C_nJ_n(\beta_2r)]\times\cos(n\theta)\exp\{i(kz-\omega t)\}, \quad (10a)$$

$$\psi=\sum_{n=0}^{\infty}[q_1B_nJ_n(\beta_1r)+C_nJ_n(\beta_2r)]\times\cos(n\theta)\exp\{i(kz-\omega t)\}, \quad (10b)$$

$$\chi=\sum_{n=0}^{\infty}D_nJ_n(\gamma r)\sin(n\theta)\exp\{i(kz-\omega t)\}, \quad (10c)$$

where q_1 and q_2 are the *amplitude ratios*

$$q_1=-\frac{c_{11}\beta_1^2+(c_{44}k^2-\rho_1\omega^2)}{(c_{13}+c_{44})k^2}, \quad (11a)$$

$$q_2=-\frac{(c_{13}+c_{44})k^2}{c_{11}\beta_2^2+(c_{44}k^2-\rho_1\omega^2)}. \quad (11b)$$

To find the dispersion relation for the free cylinder, components of the displacement are calculated from Eqs. (1). Components of the strain tensor ϵ , in polar coordinates, are given in Achenbach¹² (p. 74). For a TI material the components σ_{rr} , $\sigma_{r\theta}$ and σ_{rz} of the stress tensor are given by

$$\sigma_{rr}=c_{11}\epsilon_{rr}+c_{12}\epsilon_{\theta\theta}+c_{13}\epsilon_{zz}, \quad (12a)$$

$$\sigma_{r\theta}=(c_{11}-c_{12})\epsilon_{r\theta}, \quad (12b)$$

$$\sigma_{rz}=2c_{44}\epsilon_{rz}. \quad (12c)$$

For a free rod, the boundary conditions, at $r=a$, are

$$\sigma_{rr}=\sigma_{r\theta}=\sigma_{rz}=0. \quad (13)$$

When we insert the potential functions in the boundary conditions Eqs. (13) we get the following system of equations

$$\begin{bmatrix} a_{11} & a_{12} & a_{13} \\ a_{21} & a_{22} & a_{23} \\ a_{31} & a_{32} & a_{33} \end{bmatrix} \begin{bmatrix} B_n \\ C_n \\ D_n \end{bmatrix} = \begin{bmatrix} 0 \\ 0 \\ 0 \end{bmatrix}, \quad (14)$$

where the elements a_{ij} of the matrix $A=(a_{ij})$ are given in the Appendix. The secular equation,

$$\text{Det}(A)=0, \quad (15)$$

is to be solved to find a dispersion relation between ω and k .

III. FLUID-LOADED CYLINDER

Now we consider the cylinder to be immersed in a fluid of density ρ_0 in which the velocity of the acoustic wave is c . The pressure $p(r, \theta, z)$ can be taken in the form

$$p = \sum_{n=0}^{\infty} P_n H_n(\gamma_f r) \cos(n\theta) \exp\{i(kz - \omega t)\}, \quad (16)$$

where H_n denotes the Hankel function of the first kind, of order n . The choice is made because we require Eq. (16) to asymptotically represent an outgoing wave. The radial wave number γ_f is defined as

$$\gamma_f = \sqrt{\left(\frac{\omega}{c}\right)^2 - k^2}. \quad (17)$$

At the interface, $r = a$, the following boundary conditions are applied:

- (1) The normal component of the displacement must be continuous across the interface.
- (2) The pressure in the fluid must be equal to the normal component of stress in the solid.
- (3) The tangential components of stress must vanish at the surface of the solid.

The above conditions lead to the following equations. For $r = a$,

$$-\frac{1}{\rho_0} \frac{\partial p}{\partial r} = \frac{\partial^2 u_r}{\partial t^2}, \quad \sigma_{rr} = -p, \quad \sigma_{r\theta} = 0, \quad \sigma_{rz} = 0. \quad (18)$$

Instead of Eq. (14) we now get the following system of equations:

$$\begin{bmatrix} b_{11} & b_{12} & b_{13} & b_{14} \\ b_{21} & a_{11} & a_{12} & a_{13} \\ 0 & a_{21} & a_{22} & a_{23} \\ 0 & a_{31} & a_{32} & a_{33} \end{bmatrix} \begin{bmatrix} P_n \\ B_n \\ C_n \\ D_n \end{bmatrix} = \begin{bmatrix} 0 \\ 0 \\ 0 \\ 0 \end{bmatrix}, \quad (19)$$

where the 4×4 matrix on the left hand side of Eq. (19), apart from its first row and the first column, is identical with the

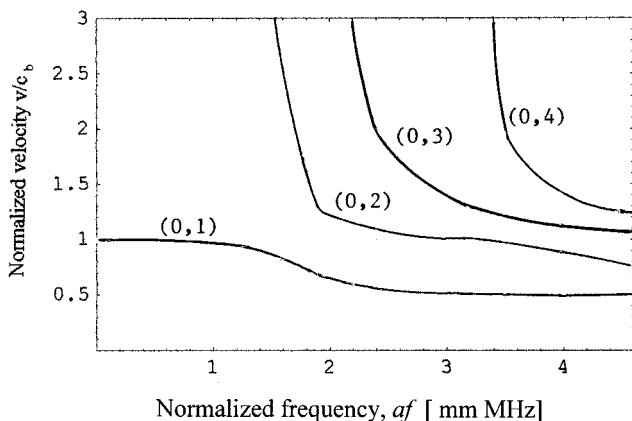


FIG. 1. Dispersion curves for the first four longitudinal modes in a cobalt cylinder.

TABLE I. Material properties of cobalt.

Stiffness 10^{11} N/m ²					Density kg/m ³
c_{11}	c_{12}	c_{13}	c_{33}	c_{44}	ρ_1
2.95	1.59	1.11	3.35	0.71	8900

matrix A which appears in Eq. (14). The elements b_{ij} are

$$\begin{aligned} b_{11} &= \frac{1}{\rho_0 \omega^2} \gamma_f a H_n'(\gamma_f a), & b_{12} &= -\beta_1 a J_n'(\beta_1 a), \\ b_{13} &= -q_2 \beta_2 a J_n'(\beta_2 a), & & \\ b_{14} &= -n J_n(\gamma a), & b_{21} &= H_n(\gamma_f a) a^2. \end{aligned} \quad (20)$$

The dispersion relations for the fluid-loaded cylinder are found by solving the secular equation

$$\det \begin{bmatrix} b_{11} & b_{12} & b_{13} & b_{14} \\ b_{21} & a_{11} & a_{12} & a_{13} \\ 0 & a_{21} & a_{22} & a_{23} \\ 0 & a_{31} & a_{32} & a_{33} \end{bmatrix} = 0. \quad (21)$$

IV. RESULTS AND DISCUSSION

For each value of n , i.e., $n=0,1,2, \dots$, Eq. (15), for a free rod, and Eq. (21) for a fluid-loaded rod, determine an infinite number of dispersion curves. The case $n=0$ is particularly simple. The displacement has only two components, u_r and u_z , which are independent of θ . Thus we have an axisymmetric wave; explicitly

$$u_r = -[B_0 \beta_1 J_1(\beta_1 r) + q_2 C_0 \beta_2 J_1(\beta_2 r)] \times \exp\{i(kz - \omega t)\}, \quad (22)$$

$$u_z = ik[q_1 B_0 J_0(\beta_1 r) + C_0 J_0(\beta_2 r)] \exp\{i(kz - \omega t)\}. \quad (23)$$

When the analysis is carried through, we get Eqs. (7) and (10), respectively, of Nagy.⁷

Figure 1 shows the calculated dispersion curves for the longitudinal modes (i.e., $n=0$) for a cobalt cylinder immersed in water. Material properties for the metal are taken from Landolt and Bornstein¹² and are reproduced in Table I.

The density of water is $\rho_0 = 1000$ kg/m³ and $c = 1475$ m/s.¹⁰ Fluid-loading significantly perturbs the spectrum of the guided waves only when the density ratio (ρ_0/ρ_1) ≈ 1 . In the present case this ratio is 0.11 and the dispersion curves of the fluid-loaded cylinder have not been shown since they essentially overlap the curves for the free cylinder. The phase velocity has been normalized to the bar velocity $c_b = \sqrt{E_a/\rho_1}$, where $E_a = c_{33} - 2c_{13}^2/(c_{11} - c_{12})$. The lowest mode exhibits the expected behavior in that the normalized velocity approaches unity at low frequencies.

Figure 2 shows first six dispersion curves for the first group of flexural modes, i.e., corresponding to $n=1$. It is usual to denote the i -th mode belonging to the index n as (n,i) . Again the curves for the fluid-loaded rod are indistinguishable from those of the free rod. The wave numbers for all modes, $(1,i)$, $i \geq 2$, have a small imaginary part giving

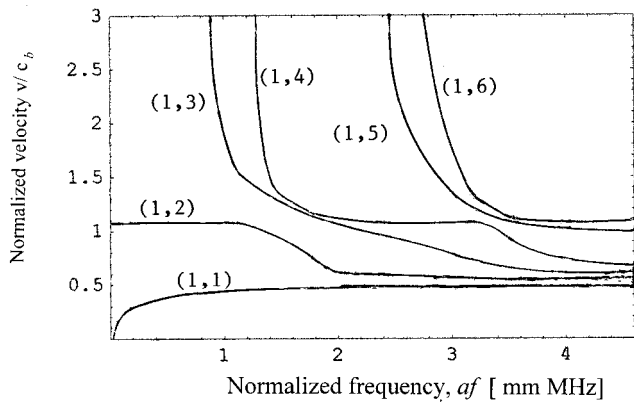


FIG. 2. Dispersion curves for the first six modes belonging to the first group (i.e., $n=1$) of flexural modes.

rise to leakage of energy from the solid to the fluid. The lowest mode (1,1) is undamped as long as its phase speed is less than that of sound in the fluid. For cobalt this corresponds to $v/c_b=0.355$ in Fig. 2. Since all higher modes have speeds greater than $0.5 c_b$, they suffer from attenuation for all frequencies. For the same reason, all axisymmetric modes of Fig. 1 are also damped. In Fig. 2 all modes from (1,3) upward appear to be asymptotically approaching the velocity $\sqrt{c_{44}/\rho_1}$ but the lowest mode will approach the Rayleigh velocity. Such behavior is also exhibited by waves propagating in an isotropic plate; see Fig. 13 in Überall.¹³ Similarity between the two cases is not surprising since for very large radius the effect of curvature on the wave propagation in a cylinder becomes minimal.

Figures 3 and 4 show the attenuation spectra of a cobalt cylinder immersed in water. The normalized attenuation $8.68a \text{Im}(k)$ is plotted as a function of the normalized frequency. In Fig. 3 we have plotted attenuation curves of the first three longitudinal modes of the fluid-loaded rod. For the lowest mode the attenuation increases, first rapidly then almost linearly with frequency. On the other hand, the (0,2) and (0,3) modes are highly damped near their cutoff frequencies but for (0,2) the damping disappears near the normalized frequency $af=2.39$ and the attenuation for the (0,3) mode becomes small when af exceeds 3.98. In Fig. 4 plotted at-

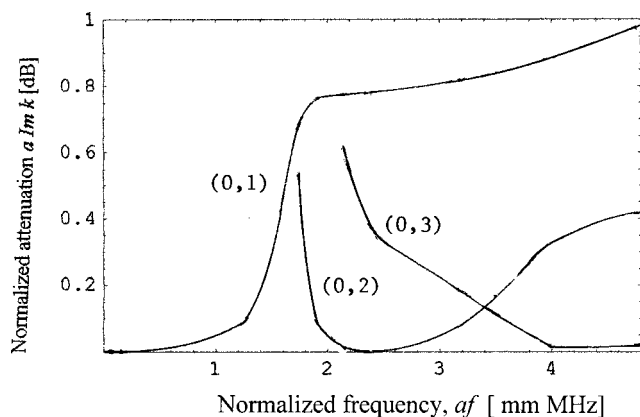


FIG. 3. Leaky attenuation spectra for the longitudinal modes in the fluid-loaded rod.

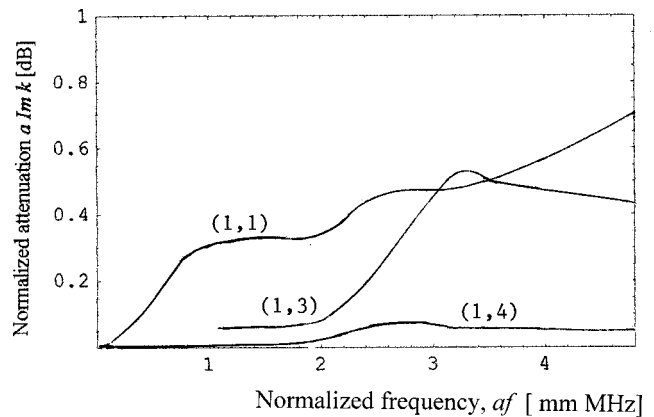


FIG. 4. Leaky attenuation spectra for the flexural modes in the fluid-loaded rod.

tenuation curves are given for the (1,1), (1,3) and (1,4) modes. The attenuation of the mode (1,5) is so small that it cannot be shown on the scale used in Figs. 3 and 4. Its spectrum is shown in Fig. 5 in which the attenuation has been multiplied by a factor of 100. A comparison of Figs. 3 and 4 indicates that the attenuation for the flexural modes is relatively small as compared with the longitudinal ones. For high frequencies, the leaky modes approach the leaky Rayleigh mode and, in this limit, the attenuation is proportional to the normalized frequency af .

V. CONCLUSIONS

We have generalized the results of Nagy⁷ to include the propagation of flexural waves in a fluid-loaded rod of circular cross section. An earlier attempt by Dayal⁶ to solve the problem failed due to an incorrect representation for the potential functions. The representation used in this paper helps to solve the problem conveniently.

The flexural modes for the free rod exhibit the expected asymptotic behavior. Leaky attenuation spectra for the axially symmetric as well as flexural modes have also been plotted.

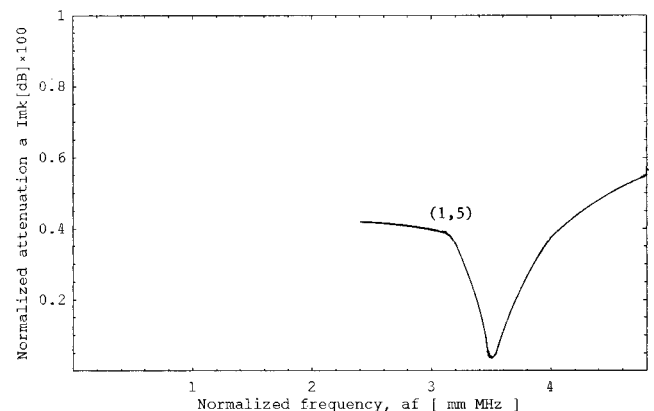


FIG. 5. Leaky attenuation spectrum for the (1,5) mode in the fluid-loaded rod.

ACKNOWLEDGMENT

Financial support for this work was provided by the University Research Fund of the Quaid-i-Azam University.

APPENDIX

$$\begin{aligned}
 a_{11} &= c_{11}J_n''(\beta_1 a)(\beta_1 a)^2 + c_{12}\{J_n'(\beta_1 a)\beta_1 a - n^2J_n(\beta_1 a) \\
 &\quad - c_{13}(ka)^2q_1J_n(\beta_1 a)\}, \\
 a_{12} &= c_{11}q_2J_n''(\beta_2 a)(\beta_2 a)^2 + c_{12}\{q_2J_n'(\beta_2 a)\beta_2 a \\
 &\quad - q_2n^2J_n(\beta_2 a)\} - c_{13}(ka)^2J_n(\beta_2 a), \\
 a_{13} &= -n(c_{11} - c_{12})\{J_n(\gamma a) - (\gamma a)J_n'(\gamma a)\}, \\
 a_{21} &= 2n\{J_n(\beta_1 a) - (\beta_1 a)J_n'(\beta_1 a)\}, \\
 a_{22} &= 2nq_2\{J_n(\beta_2 a) - (\beta_2 a)J_n'(\beta_2 a)\}, \\
 a_{23} &= -J_n''(\gamma a)(\gamma a)^2 + J_n'(\gamma a)\gamma a - n^2J_n(\gamma a), \\
 a_{31} &= (1 + q_1)\beta_1 aJ_n'(\beta_1 a), \\
 a_{32} &= (1 + q_2)\beta_2 aJ_n'(\beta_2 a), \\
 a_{33} &= nJ_n(\gamma a).
 \end{aligned}$$

- ¹L. Pochhammer, "Über die Fortpflanzungsgeschwindigkeiten Schwingungen in einem unbegrenzten isotropen Kreiscylinder," *Z. Math.* **81**, 326–336 (1876).
- ²C. Chree, "Longitudinal vibrations of a circular cylinder," *Q. J. Math.* **21**, 287–298 (1886).
- ³R. D. Mindlin and H. D. McNiven, "Axially symmetric waves in elastic rods," *J. Appl. Mech.* **27**, 145–151 (1960).
- ⁴M. Onoe, H. D. McNiven, and R. D. Mindlin, "Dispersion of axially symmetric waves in elastic rods," *J. Appl. Mech.* **28**, 729–734 (1963).
- ⁵T. R. Meeker and A. H. Meitzler, "Guided wave propagation in elongated cylinders and plates," in *Physical Acoustics*, edited by W. P. Mason (Academic, New York, 1964), Vol. 1.
- ⁶V. Dayal, "Longitudinal waves in homogeneous anisotropic cylindrical bars immersed in fluid," *J. Acoust. Soc. Am.* **93**, 1249–1255 (1993).
- ⁷P. B. Nagy, "Longitudinal guided wave propagation in a transversely isotropic rod immersed in fluid," *J. Acoust. Soc. Am.* **98**, 454–457 (1995).
- ⁸V. T. Buchwald, "Rayleigh waves in transversely isotropic media," *Q. J. Mech. Appl. Math.* **14**, 293–317 (1961).
- ⁹F. Ahmad and A. Rahman, "Acoustic scattering by transversely isotropic cylinders," *Int. J. Eng. Sci.* **38**, 325–335 (2000).
- ¹⁰F. Honarvar and A. N. Sinclair, "Acoustic wave scattering from transversely isotropic cylinders," *J. Acoust. Soc. Am.* **100**, 57–63 (1995).
- ¹¹A. Rahman and F. Ahmad, "Representation of the displacement in terms of the scalar functions for use in transversely isotropic materials," *J. Acoust. Soc. Am.* **104**, 3675–3676 (1998).
- ¹²H. H. Landolt and R. Börnstein, *Zahlenwerte und Funktionen aus Naturwissenschaften und Technik. Neue Serie*, edited by K. H. Hellweg, Vol. 3/11 (Springer-Verlag, Berlin, 1979), p. 40.
- ¹³H. Überall, "Surface waves in acoustics" in *Physical Acoustics*, edited by W. P. Mason and R. N. Thurston (Academic, New York, 1973), Vol. 10.

Gas bubble pulsation in a semiconfined space subjected to ultrasound

Boris Krasovitski^{a)} and Eitan Kimmel

The Department of Agricultural Engineering, Technion, Haifa 32000, Israel

(Received 6 November 1999; accepted for publication 7 December 2000)

In the case of ultrasound application in biological tissues, gas bubbles might form and collapse within cells, in the intercellular spaces and on tissue surfaces. In this work the effect of confined space on the behavior of the gas bubble in the presence of ultrasonic field is studied. A numerical model for bubble pulsation in a planar liquid layer, bounded by two rigid walls, is developed. Surface tension at the interface between the host liquid and the gas in the bubble is considered as well. A mathematical statement and solution technique based on the boundary integral method are presented. In some cases, the bubble divides into two symmetrical parts and high-velocity jets are generated, aimed at the walls. The final velocity of the jets strongly depends on the surface tension of the host liquid. Two new parameters that predict the occurrence of jet formation are developed. © 2001 Acoustical Society of America. [DOI: 10.1121/1.1346683]

PACS numbers: 43.25.Yw [MAB]

I. INTRODUCTION

Ultrasound irradiation in liquid may produce rapidly oscillating and collapsing gas- and vapor-filled bubbles. Patterns of the bubbles formation and collapse significantly depend on the fluid properties, the geometry of the boundaries in the vicinity of the bubbles, and the characteristics of the ultrasound field. Most previous theoretical studies on bubble dynamics have focused on infinite, where no boundaries are considered, or semi-infinite domains where the boundary is a rigid plane.

Single bubbles surrounded by an infinite mass of homogeneous incompressible fluid collapse symmetrically. When placed in the vicinity of a rigid wall, bubbles collapse in a different pattern. The behavior of a pulsating bubble adjacent to a rigid wall was studied numerically by Blake *et al.* (1986), Zhang *et al.* (1993, 1994), Sato *et al.* (1994), assuming that the liquid around the bubble is inviscid, incompressible, and irrotational. They found that wall-directed reentrant jet is formed in the later phase of the collapse. This jet impacts with the side of the bubble closest to the wall, creating a toroidal-shaped bubble and a shear layer develops along the impact interface. In some cases, towards the end of the collapse phase, the gas-filled bubble reaches a minimum volume and then, due to its high internal pressure, begins to grow again (rebound). The pressure on the wall was predicted to reach a maximum value when the bubble starts to rebound. Both the period and the amplitude of the bubble oscillation are related to the bubble distance from a wall.

In the case of ultrasound application to biological tissues, bubbles might form and collapse within cells, in the intercellular spaces and on tissue surfaces.

In this work we studied the effect of confined space on the bubble behavior. In biological tissues there are three types of confinement: (i) a half infinite space relative to the bubble size such as the bladder, heart ventricles, or even the

large blood vessels; (ii) a thin semi-infinite liquid film between two walls such as the cavities of the peritoneum, the pleura, and the dura where the distance between the walls is comparable to a typical diameter of a bubble and the other dimensions are much greater; and (iii) cells where all three dimensions are of the order of a bubble diameter. As described above, the first type of confinement is covered by all studies devoted to a bubble cavitation near a wall in a semi-infinite space. To the best of our knowledge, there are no theoretical or experimental data describing bubble collapse within a bounded domain of the second and third type. Here, we developed a numerical model for bubble pulsation in a tissue volume of the second type (bounded by two parallel planar walls). Surface tension at the interface between the host liquid and the gas in the bubble was considered as well.

II. MATHEMATICAL STATEMENT OF THE PROBLEM

A space between two rigid walls is filled with a liquid. A gas bubble with initial radius R_0 is placed between the walls on equal distances from them (see Fig. 1). The initial pressure in the liquid and inside the bubble is assumed uniform and equal to P_0 . From the initial moment, an oscillatory pressure field with frequency \bar{f} and amplitude A is applied to the liquid

$$\bar{P}_\infty = P_0 [1 + A \sin(\omega \tau + \beta_0)]. \quad (2.1)$$

Here, $\omega = 2\pi\bar{f}$.

The following assumptions are made: (i) viscous effects are neglected on the grounds that the time scale for viscous diffusion is much longer than a typical time scale of bubble collapse; (ii) effects of buoyancy can be neglected due to small lifetime and volume associated with the growth and collapse of a bubble; (iii) liquid compressibility effects are generally negligible. The following dimensionless variables and parameters were introduced:

^{a)}Author to whom correspondence should be addressed.

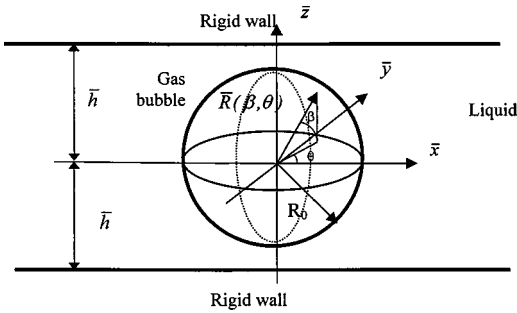


FIG. 1. Schematics of the problem.

$$\begin{aligned}
 x &= \frac{\bar{x}}{R_0}; & y &= \frac{\bar{y}}{R_0}; & z &= \frac{\bar{z}}{R_0}; & t &= \omega \tau; & f &= \frac{\bar{f}}{f_c}; \\
 h &= \frac{\bar{h}}{R_0}; & R &= \frac{\bar{R}}{R_0}; & R_m &= \frac{\bar{R}_m}{R_0}; & V &= \frac{\bar{V}}{V_0}, \\
 \Theta &= \frac{\bar{\Theta}}{R_0^2 \omega}; & \Psi &= \frac{\bar{\Psi}}{R_0 \omega}; & U &= \frac{\bar{U}}{R_0 \omega}; & \sigma &= \frac{\bar{\sigma}}{R_0 P_0}; \\
 D &= \frac{P_0}{\rho_L R_0^2 \omega^2}; & P_v &= \frac{\bar{P}_v}{P_0}; & P_{i,0} &= \frac{\bar{P}_{i,0}}{P_0}.
 \end{aligned}$$

Here, dimensional variables and parameters are denoted by an overbar. The coordinates are \bar{x} , \bar{y} , and \bar{z} , τ is the time, $2\bar{h}$ is the distance between the walls, \bar{R} is the radius vector, \bar{R}_m is the local mean radius of curvature of the bubble surface, V_0 is the initial volume of the bubble, \bar{V} is the current volume of the bubble, $\bar{\Theta}$ is the velocity potential, $\bar{\Psi}$ is the spatial derivative of the potential taken along inner normal to the bubble surface, \bar{U} is the absolute velocity of the bubble surface, $\bar{\sigma}$ is the surface tension, \bar{P}_v is the partial pressure of the water vapor inside the bubble, $\bar{P}_{i,0}$ is the initial pressure in the bubble, ρ_L is the liquid density, f_c is the bubble natural frequency

$$f_c = \frac{1}{2\pi R_0} \sqrt{\frac{3kP_0 - 2\bar{\sigma}/R_0}{\rho_L}},$$

and k is the adiabatic constant of the gas.

The fluid dynamics may be thereafter modeled by considering the fluid to fulfill the Laplace equation for the potential field

$$\nabla^2 \Theta = 0, \quad (2.2)$$

in the domain: $-h \leq z \leq h$; $-\infty < x < \infty$; $-\infty < y < \infty$.

The boundary condition on the bubble surface S_0 is determined from the Bernoulli equation

$$\frac{\partial \Theta}{\partial t} = D \left(P_\infty - P_L + \frac{2\sigma}{R_m} \right) - \frac{U^2}{2}. \quad (2.3)$$

Assuming adiabatic process where the heat transfer between the bubble and the surrounding liquid is neglected, the dimensionless pressure inside the bubble is

$$P_L = P_v + (P_{i,0} + 2\sigma)(V)^{-k}. \quad (2.4)$$

The boundary conditions on the walls are

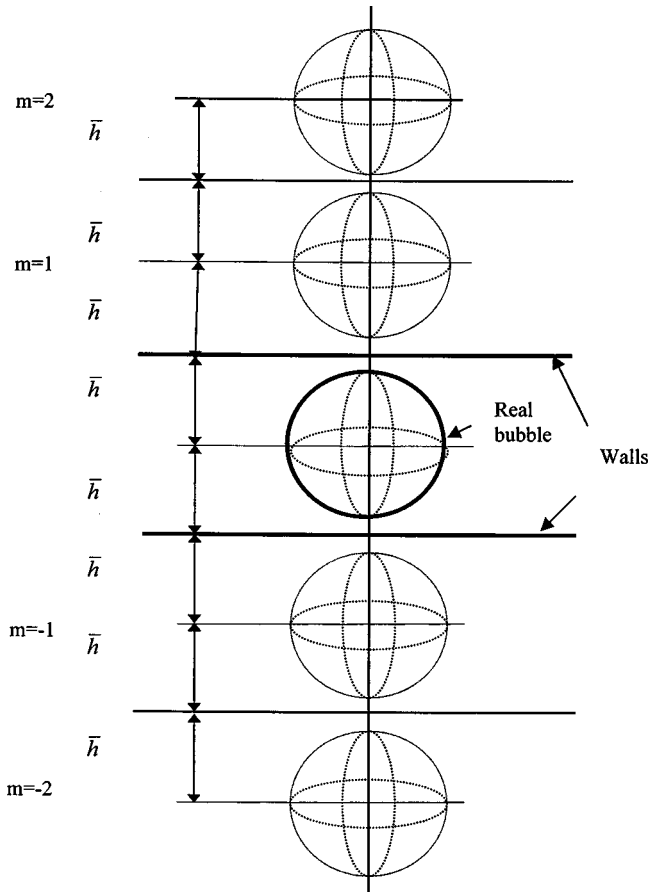


FIG. 2. System of the image bubbles.

$$\frac{\partial \Theta}{\partial z} = 0 \quad \text{at } z = \pm h, \quad (2.5)$$

and the initial conditions are

$$R = 1; \quad \Theta = 0 \quad \text{at } t = 0. \quad (2.6)$$

The problem (2.2)–(2.6) for a bubble between two close walls may be converted to the problem of an array of bubbles in an infinite liquid space. Note that the problem of a bubble near one wall was solved introducing an image bubble, positioned symmetrically to the real bubble relative to the wall. In our case we introduce a system of M image bubble pairs, in addition to the real bubble, in an infinite space (Fig. 2). The image bubbles are placed along the z axis with a distance between two successive bubble centers equal to $2h$. The boundary conditions on the surfaces of the image bubbles are the same as for the real bubble. The solution of the problem (2.2)–(2.6) is obtained when M approaches infinity. Thereafter, we solve the Laplace equation (2.2) in a semi-infinite space, bounded with surfaces of the real and image bubbles $\cup S_m$ $m = 0, \pm 1, \dots, \pm M$ with boundary condition (2.3) on the surfaces. The technique may be easily extended to a bubble located in a different distances from the two walls.

III. THE SOLUTION TECHNIQUE

The solution of the Laplace equation for each point p over the real bubble surface S_0 may be expressed with help of Green's functions [Tikhonov *et al.* (1990)]

$$\Theta(p) = \frac{1}{2\pi} \sum_{m=-M}^M \int \int_{S_m} \left(\Psi G - \Theta \frac{\partial G}{\partial n} \right) ds. \quad (3.1)$$

Here, $p \in S_0$, $\Psi \equiv \partial\Theta/\partial n$, $G = 1/|p-q|$ is the Green function, q is the integration point, and n is the inner normal to the surface in the integration point q . Note that in the sum $m=0$ corresponds to the real bubble surface and $m = \pm 1, \pm 2, \dots, \pm M$ to the image bubble surfaces. In a spherical system of coordinates r, β, θ (see Fig. 1, origin at the center of the real bubble) the real bubble surface is replaced by $N-1$ segments S_{0j} that satisfy at the initial moment the conditions

$$\hat{\beta}_j \leq \beta \leq \hat{\beta}_{j+1}; \quad 0 \leq \theta \leq 2\pi;$$

$$\hat{\beta}_j = -\frac{\pi}{2} + \frac{\pi}{N-1}(j-1); \quad j = 1, 2, \dots, N.$$

After discretization, the solution will locate at each time the disposition and shape of each segment S_{0j} . Based on the integral (3.1) the following expressions may be written:

$$\Theta_i = \frac{1}{2\pi} \sum_{j=1}^{N-1} \sum_{m=-M}^M \int \int_{S_{mj}} \left(\Psi G_i - \Theta \frac{\partial G_i}{\partial n} \right) ds. \quad (3.2)$$

Here, Θ_i is the value of the potential in the surface point $p_i = [R(\beta_i), \beta_i, 0]$; $G_i = 1/|p_i - q(\beta, \theta)|$ is the Green function for this point and the integration point $q = [R(\beta), \beta, \theta]$ on the surface S_{mj} .

Solution of the integral equations (3.2) was carried out numerically. Following Blake *et al.* (1986), unknown functions Θ and Ψ are expressed with their values on the segment boundaries

$$\Theta = \Theta_j(1-\xi) + \Theta_{j+1}\xi; \quad \Psi = \Psi_j(1-\xi) + \Psi_{j+1}\xi, \quad (3.3)$$

where ξ is in the range $[0, 1]$.

The functions $R_j(\xi, t)$ and $\beta_j(\xi, t)$ were approximated inside the j th segment with quadratic Hermite splines with additional internal knots (Späth, 1995)

$$R_j(\xi, t) = c_{01j}(t) + c_{11j}(t)\xi + c_{21j}(t)\xi^2; \quad 0 \leq \xi \leq \zeta_{aj}(t);$$

$$R_j(\xi, t) = c_{02j}(t) + c_{12j}(t)(\xi - \zeta_{aj}) + c_{22j}(t)(\xi - \zeta_{aj})^2; \quad (3.4)$$

$$\zeta_{aj}(t) \leq \xi \leq 1;$$

$$\beta_j(\xi, t) = d_{01j}(t) + d_{11j}(t)\xi + d_{21j}(t)\xi^2; \quad 0 \leq \xi \leq \zeta_{bj}(t);$$

$$\beta_j(\xi, t) = d_{02j}(t) + d_{12j}(t)(\xi - \zeta_{bj}) + d_{22j}(t)(\xi - \zeta_{bj})^2; \quad (3.5)$$

$$\zeta_{bj}(t) \leq \xi \leq 1; \quad 1 \leq j \leq N-1.$$

The coefficients $c_{ikj}(t)$ and $d_{ikj}(t)$ in Eq. (3.5) are determined by fulfilling the continuity and smoothness conditions for the curves on the segment boundaries and the internal knots ζ_{aj} and ζ_{bj} .

Using the interpolations of Eq. (3.5), one converts the integral in Eq. (3.2) to

$$\Theta_i = \frac{1}{2\pi} \sum_{j=1}^{N-1} \sum_{m=-M}^M \int_0^1 \int_0^{2\pi} \left[\{\Psi_j(1-\xi) + \Psi_{j+1}\xi\} G_i - \{\Theta_j(1-\xi) + \Theta_{j+1}\xi\} \frac{\partial G_i}{\partial n} \right] s_j(\xi) d\theta d\xi$$

$$i = 1, 2, \dots, N, \quad (3.6)$$

where

$$s_j(\xi) \equiv R_j(\xi, t) \cos[\beta_j(\xi, t)] \sqrt{R_j^2 + (R_j \dot{\beta}_j)^2};$$

$$\dot{R}_j \equiv (\partial R_j / \partial \xi); \quad \dot{\beta}_j \equiv (\partial \beta_j / \partial \xi).$$

Equations (3.6) may be represented as a system of N linear algebraic equations for the unknown variables Ψ_j , $j = 1, 2, \dots, N$

$$\sum_{j=1}^N B_{ij} \Psi_j = A_i; \quad i = 1, 2, \dots, N; \quad j = 1, 2, \dots, N, \quad (3.7)$$

where $B_{ij} = b_{2,i,j-1} + b_{1,i,j}$ for $i = 1, 2, \dots, N$; $j = 2, 3, \dots, N-1$;

$$B_{i,1} = b_{1,i,1}; \quad B_{i,N} = b_{2,i,N-1}; \quad (3.8)$$

$$A_i = 2\pi \Theta_i + \sum_{j=1}^{N-1} (\Theta_j a_{1,i,j} + \Theta_{j+1} a_{2,i,j}); \quad i = 1, 2, \dots, N; \quad (3.9)$$

$$a_{k,i,j} = \int_0^1 M_k(\xi) s_j(\xi) \int_0^{2\pi} \sum_{m=-M}^M \frac{\partial G_i}{\partial n} d\theta d\xi; \quad (3.10)$$

$$b_{k,i,j} = \int_0^1 M_k(\xi) s_j(\xi) \int_0^{2\pi} \sum_{m=-M}^M G_i d\theta d\xi; \quad (3.11)$$

$$M_k(\xi) \equiv \begin{cases} 1-\xi; & k=1 \\ \xi; & k=2 \end{cases}.$$

For further use, we represent coefficients $a_{k,i,j}$ and $b_{k,i,j}$ as a sum

$$a_{k,i,j} = a_{k,i,j}^r + \sum_{m=-M}^{-1} a_{k,i,j}^{fm} + \sum_{m=1}^M a_{k,i,j}^{fm};$$

$$b_{k,i,j} = b_{k,i,j}^r + \sum_{m=-M}^{-1} b_{k,i,j}^{fm} + \sum_{m=1}^M b_{k,i,j}^{fm},$$

where

$$a_{k,i,j}^r = \int_0^1 M_k(\xi) s_j(\xi) \int_0^{2\pi} \frac{\partial G_i}{\partial n} d\theta d\xi,$$

where $q \in S_{0j}$,

$$a_{k,i,j}^{fm} = \int_0^1 M_k(\xi) s_j(\xi) \int_0^{2\pi} \frac{\partial G_i}{\partial n} d\theta d\xi,$$

where $q \in S_{mj}$, $m = \pm 1, \pm 2, \dots, \pm M$,

$$b_{k,i,j}^r = \int_0^1 M_k(\xi) s_j(\xi) \int_0^{2\pi} G_i d\theta d\xi,$$

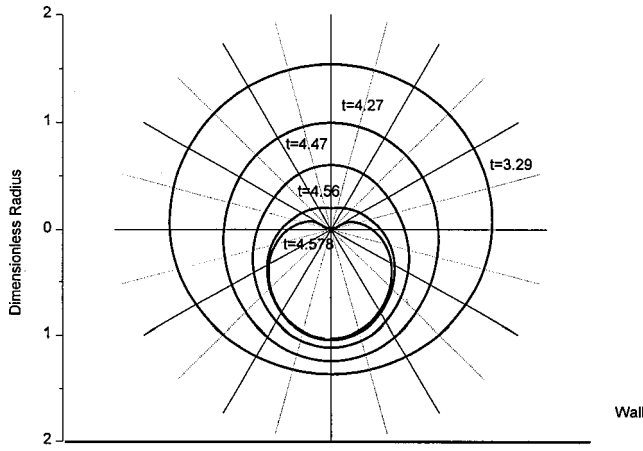


FIG. 3. Evolution of the bubble shape during collapse. Bubble near wall. Initial stage of the collapse. $R_0 = 10 \mu\text{m}$; $f = 0.5$; $h = 2$.

where $q \in S_{0j}$,

$$b_{k,i,j}^{fm} = \int_0^1 M_k(\xi) s_j(\xi) \int_0^{2\pi} G_i d\theta d\xi, \quad (3.12)$$

where $q \in S_{mj}$, $m = \pm 1, \pm 2, \dots, \pm M$.

The surface integrals (3.10) and (3.11) were reduced to ordinary integrals, using the elliptic integrals concept. The integrals were computed numerically except for a close vicinity to the points p_i , where the integrands have singularity and had to be computed analytically (see the Appendix).

A full scheme of the computational algorithm follows below. For a certain moment t with a known set of values Θ_i , R_i , β_i , the coefficients A_i and B_{ij} in Eqs. (3.8) and (3.9), respectively, are calculated. Then, by introducing A_i and B_{ij} into Eq. (3.7), a set of the normal velocities Ψ_i is determined. To continue further, we use the boundary condition (2.3), which is transformed into Lagrange coordinates, in order to calculate the new value of the potential and radius vector of the fluid particle at the next time step. The new value of the potential (Θ'_i) is

$$\Theta'_i = \Theta_i + \left[D \left(P_\infty - P_L + \frac{2\sigma}{R_{mj}} \right) + \frac{U_i^2}{2} \right] \Delta t, \quad (3.13)$$

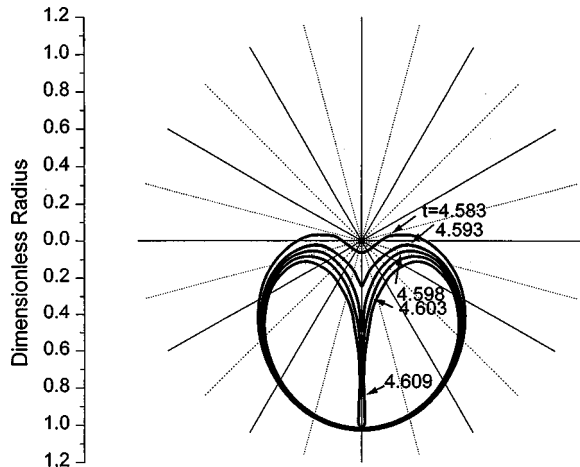


FIG. 4. Evolution of the bubble shape during collapse. Bubble near wall. Final stage of the collapse. $R_0 = 10 \mu\text{m}$; $f = 0.5$; $h = 2$.

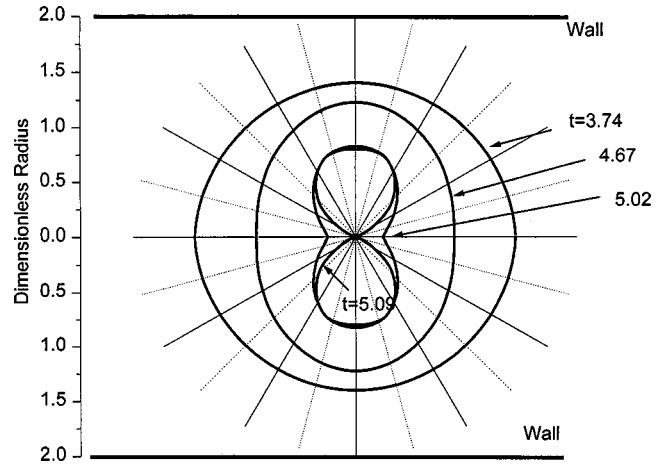


FIG. 5. Evolution of the bubble shape during collapse. Bubble between two walls. Initial stage of the collapse. $R_0 = 10 \mu\text{m}$; $f = 0.5$; $h = 2$.

where U_i is the absolute velocity of the i th point on the surface. $U_i = \sqrt{\Psi_i^2 + T_i^2}$; i —tangential velocities of the i th point.

The fluid particle with coordinates $[\hat{R}_i, \hat{\beta}_i]$ arrives at moment $t + \Delta t$ to the point with coordinates $[\hat{R}'_i, \hat{\beta}'_i]$, where $\hat{R}'_i = \hat{R}_i + \Delta \hat{R}_i$; $\hat{\beta}'_i = \hat{\beta}_i + \Delta \hat{\beta}_i$;

$$\begin{aligned} \Delta \hat{R}_i &= \Delta t [\Psi_i \sin(\hat{\beta}_i - \gamma_{mi}) + T_i \cos(\hat{\beta}_i - \gamma_{mi})]; \\ \Delta \hat{\beta}_i &= \frac{\Delta t}{\hat{R}_i} [\Psi_i \cos(\hat{\beta}_i - \gamma_{mi}) - T_i \sin(\hat{\beta}_i - \gamma_{mi})]. \end{aligned} \quad (3.14)$$

Note that here we use the following notation: $\hat{R}_i \equiv R_i(0, t)$; $\hat{\beta}_i \equiv \beta_i(0, t)$.

The angle γ_{mi} is defined between the tangent to the surface at point p_i (in the plane xoz) and the axis ox . In summary, the new set Θ'_i , \hat{R}'_i , $\hat{\beta}'_i$ for the time $t + \Delta t$ is obtained and the procedure is repeated in the next time step.

In order to increase stability of the algorithm, the values of coefficients $a_{k,i,j}^r$ were normalized in the following way. According to Gauss flux theorem, for the points $p_i \in S$ the integral over the real bubble surface is

$$T_{ri} = \sum_{k=1}^2 \sum_{j=1}^{N-1} a_{k,i,j}^r = \int \int_{S_o} \frac{\partial G_i}{\partial n} ds = 2\pi. \quad (3.15)$$

After calculating the coefficients $a_{k,i,j}^r$ [see Eq. (3.10)] for a given i , the values T_i were calculated and each component $a_{k,i,j}^r$ was multiplied by the correction coefficient $k_i = 2\pi/T_i$ and thus Eqs. (3.15) were satisfied. It worth noting that one can verify the calculations by checking Eqs. (3.15).

IV. RESULTS AND DISCUSSION

The first case is a simulation of a bubble pulsation near a single wall, where the bubble surface contours are shown in Figs. 3 and 4. This case has been solved before [Blake *et al.* (1986), Sato *et al.* (1994)] and is used to test and illustrate the developed technique for $M = 1$ [see Eq. (3.1)]. Here, we considered an air-filled bubble, situated near a flat wall. The distance between the bubble center and the wall was assumed to be equal to the initial bubble diameter ($h = 2$),

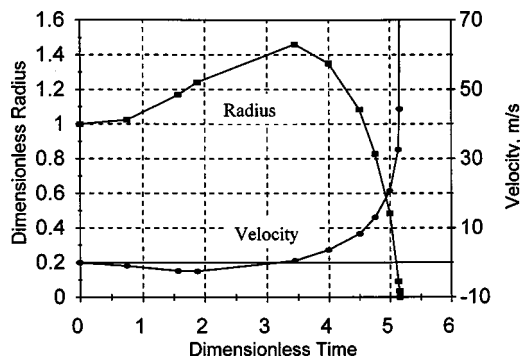


FIG. 6. Displacement and velocity of the bubble equatorial points before dividing. $R_0 = 10 \mu\text{m}$; $f = 0.5$; $h = 2$.

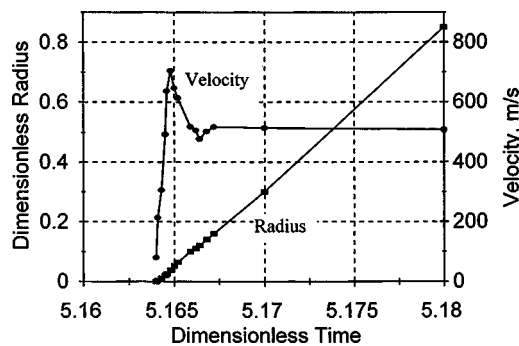


FIG. 8. Displacement and velocity of the bubble polar points after dividing. $R_0 = 10 \mu\text{m}$; $f = 0.5$; $h = 2$.

the dimensionless frequency of the applied ultrasound was $f = 0.5$, amplitude $A = 0.8$. For simplicity, we denote by “north pole” the point on the bubble surface, farthest from the wall, and “south pole” for the point closest to the wall. At the first phase ($0 < t < 3.3$) the bubble expands up to a maximal dimensionless radius of about 1.46 for the north pole and 1.4 for the south pole. Apparently, this difference is attributed to the influence of the wall, which “resists” the bubble expansion. On the next stage the bubble contracts ($3.3 < t < 4.6$), the surface near the north pole moves quickly towards the bubble center while the south pole moves much slower towards the center (see Fig. 3). Then, the surface area near the north pole accelerates and a jet directed towards the wall is being formed (see Fig. 4). In this case the initial radius was $10 \mu\text{m}$, and the velocity of the jet tip approaches some 500 m/s, shortly (about $1.3 \mu\text{s}$) after the contraction starts. The simulation was carried out until the tip of the jet reaches the bubble surface at the south pole. At later times, the solution technique is no longer applicable and the theory of submerged jets should be considered. Our results are in close agreement with those of Sato *et al.* (1994). For instance, the time of maximal expanding differs by about 5% and the time of collapse by about 1%. The values of dimensionless radius for the north and south poles (1.46 and 1.4,

respectively) at the moment of maximal expanding differ from corresponding values of Sato *et al.* (1994) (1.54 and 1.33) by about 5%.

The simulation results of an air-filled bubble, placed in water between two flat walls, are presented in Figs. 5–12. We have varied the number of image bubbles that are required to solve the problem and found that three pairs of image bubbles [$M = 3$ in Eqs. (3.6)] were sufficient to provide good accuracy. Any further increase of the number of image bubbles did not have a significant effect on the results. Some typical features of the bubble evolution are presented in Figs. 5 to 8 for the case of $h = 2$ and $f = 0.5$. At the first stage ($0 < t < 3.45$) the bubble expands up to a maximal dimensionless radius of about 1.5 for the points on the bubble equator (a circle of intersection of the bubble surface with a plane passing through the bubble center and parallel to the walls), and about 1.35 for the poles (the points on the bubble surface, closest to the walls). During the second stage of the process (Fig. 5) the bubble starts to contract. The surface area near the equator moves quickly inward, reaching dimensionless velocities equal to about 50 (Fig. 6). This stage lasts until the equator shrinks to a point at $t \approx 1.7$ and the bubble splits into two bubbles symmetric about the equatorial plane. At the next stage, jets are being formed at each bubble, directed towards the wall, closer to the corresponding bubble (see Fig. 7). Dimensionless velocities of the jet tips reach about 50, which corresponds to about 500 m/s (see Fig. 8) for a bubble with initial radius of $10 \mu\text{m}$. As in the previous case, the simulation run was stopped when the jet tips reached the opposite pole of the bubble.

In order to explore the influence of the host liquid sur-

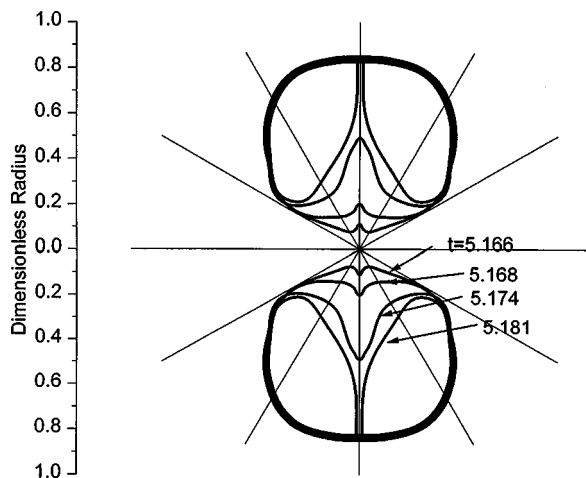


FIG. 7. Evolution of the bubble shape during collapse. Bubble between two walls. Final stage of the collapse. $R_0 = 10 \mu\text{m}$; $f = 0.5$; $h = 2$.

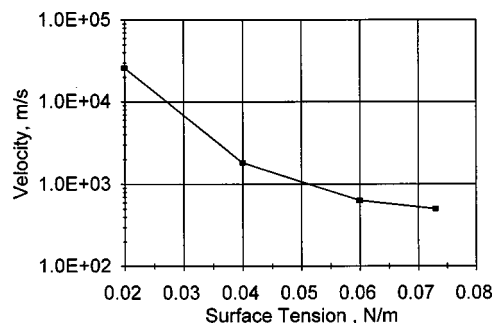


FIG. 9. Dependence of the jet velocity at final stage of collapse on surface tension of the host liquid. $R_0 = 10 \mu\text{m}$; $f = 0.5$; $h = 2$.

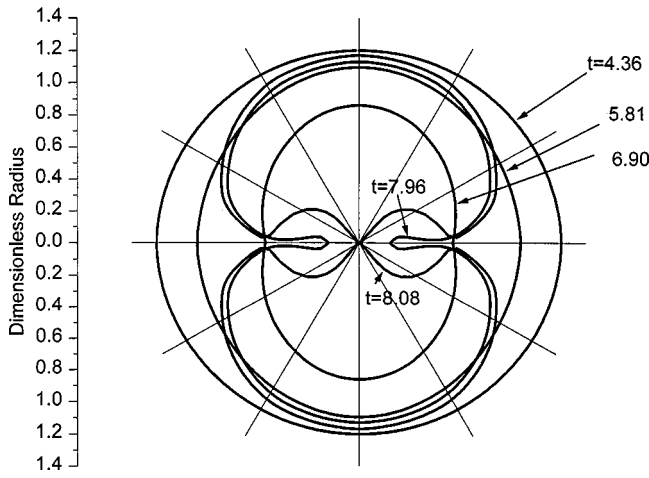


FIG. 10. Evolution of the bubble shape during collapse. Bubble between two walls. Initial stage of the collapse. $R_0 = 10 \mu\text{m}$; $f = 1$; $h = 2$.

face tension ($\bar{\sigma}$) on the intensity of the bubble collapse, we repeated the above process for various values of $\bar{\sigma}$ (0.02; 0.04; 0.06; and 0.073 N/m) and found $\bar{\sigma}$ to have a substantial effect. For instance, for $R_0 = 10 \mu\text{m}$, $f = 0.5$ and $h = 2$, reducing $\bar{\sigma}$ from 0.073 N/m (its value in water) down to 0.02 N/m, resulted in an increase of the final jet velocity from about 500 up to 25 000 m/s.

The frequency of the applied ultrasound has a strong influence on the dividing process of the bubble and the subsequent jet appearance. The above first stage of contraction, shown for $f = 0.5$ in Fig. 5, is repeated for $f = 1$ in Fig. 10. As shown for the greater frequency, the equator shrinks while developing a deep slit around it. Further increase of the frequency results by the situation where the walls of the slit strike each other before the equator shrinks to a point, as shown in Fig. 11. At this point the inward movement of the bubble equator diminishes, probably due to dissipation of the energy during the strike.

The combined effect of the distance between the walls, the frequency, the host liquid properties, and the initial bubble size on the bubble behavior was investigated by running a set of cases. For each case, we determined whether the

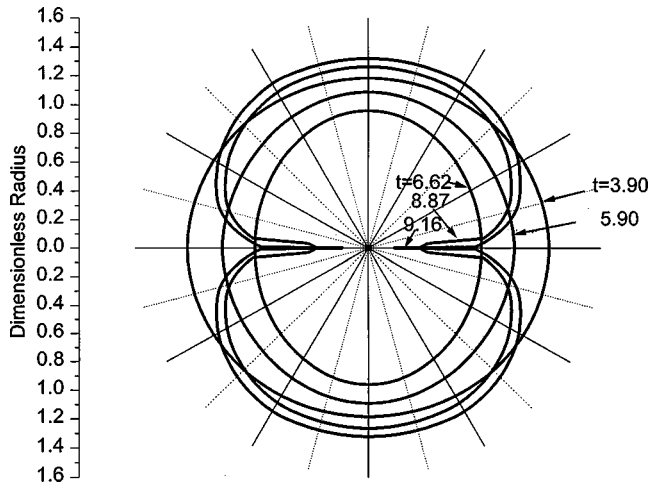


FIG. 11. The bubble shape at the final stage of contraction. No collapse. Bubble between two walls. $R_0 = 10 \mu\text{m}$; $f = 1.1$; $h = 2$.

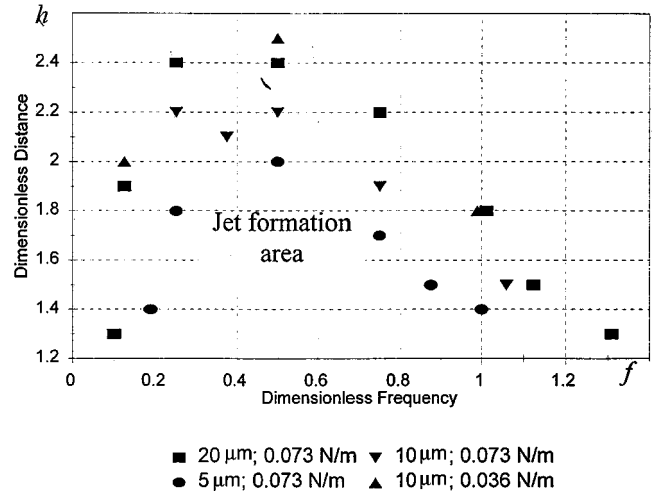


FIG. 12. Jet formation area in coordinates $f-h$.

bubble is divided into two separate parts with the consequent formation of jets aiming at the walls. Such a case is typical of ‘‘jet formation.’’ The case where dividing and jet formation did not take place is denoted by the ‘‘no jet formation’’ term. Many cases were calculated with a special attention given to the boundaries between the areas. As shown in Fig. 12, one possible way of presenting the data is by using parameters h and f as independent variables and R_0 and $\bar{\sigma}$ as parameters. Each point in Fig. 12 is located at the boundary between jet formation and no jet formation areas, for example for $f = 0.5$, and $R_0 = 5 \mu\text{m}$ at $h \leq 2$ jet formation occurs, while for $h > 2$ jet formation does not take place. As a rule, h reach maximum values, for each R_0 and $\bar{\sigma}$, at f about 0.5, and decrease with both increasing and decreasing values of f . It worth noting that the occurrence of the jet formation case is not predetermined by values of f and h only but also by R_0 and $\bar{\sigma}$ as well (see Fig. 12).

We searched for universal parameters that determine the boundaries of the jet formation area. The results of the search are shown in Fig. 13, where by employing the two parameters

$$\Omega = \sigma^{0.1}(f - 0.54\sigma^{0.6}), \quad H = \sigma^{0.24}(h - 1), \quad (4.1)$$

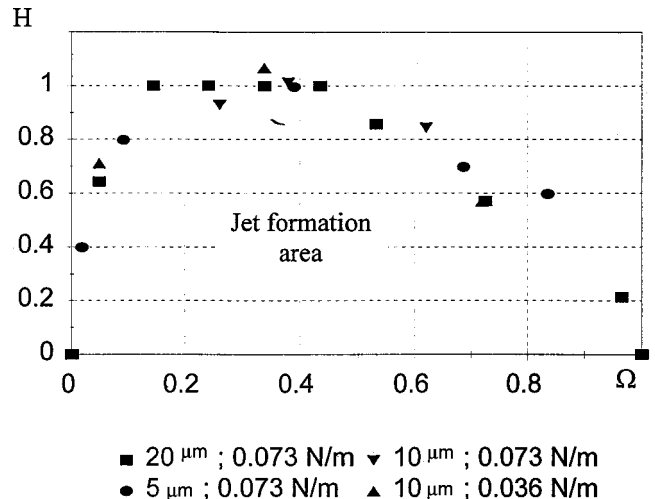


FIG. 13. Jet formation area in coordinates $\Omega-H$.

almost all the data points of the boundaries fall onto a common curve in coordinates $\Omega-H$, that bounds jet formation area (see Fig. 13). Note that the expressions for Ω and H [Eq. (4.1)] were found using only part of the data points, namely those with R_0 values equal to 5 and 20 μm and $\bar{\sigma}$ value 0.073 N/m which corresponds to water. The other data points with R_0 of 10 μm and $\bar{\sigma}$ of 0.073 and 0.036 N/m were used to test the fitting procedure and fall with good approximation on the same curve (Fig. 13).

V. CONCLUSIONS

Our solution describes the features of bubble behavior in a confined space exposed to ultrasound. The bubble is located symmetrically between two rigid walls and surface tension is considered. The technique is applicable to the known case of a bubble near a single wall and may be extended to a bubble located in a different distances from the two walls. Our solution predicts a new phenomenon of a bubble dividing into two symmetrical parts and subsequent formation of two high-speed liquid jets directed towards the walls. This phenomenon resembles bubble collapse near a single wall. The maximum jet velocity, which corresponds to the moment the jet impacts on the liquid surface, depends strongly on the surface tension of the host liquid.

As for the conditions for jet formation, our study predicts that for a given frequency, jets are formed when the distance between the walls is smaller than some limiting value. Decreasing of surface tension increases this limiting value. Also, lower and upper frequencies which bound the jet formation area were found. All these effects are described by two new parameters that were found. The parameters depend on geometry, ultrasound frequency, and host liquid properties, and determine the formation of jets.

Future investigation is required to evaluate the effect of additional tissual properties such as cell shape confined space, non-Newtonian liquid, and wall flexibility.

ACKNOWLEDGMENTS

This research was supported by the Center for Absorption in Science, Ministry of Immigrant Absorption, The State of Israel. We are grateful to Professor Avi Marmor for helpful discussions and support and to Dr. Giora Enden for assistance with the problem statement.

APPENDIX

Expressions (3.10) and (3.11) have singularity at $j=i$ (while $\xi \rightarrow 0$) and at $j=i-1$ (while $\xi \rightarrow 1$). An example of the technique of calculation of the integrals over these areas is presented here for the coefficients $a_{k,i,j}^r$ and $b_{k,i,j}^r$ at $j=i$.

In order to extract a small area where the integrand turns to infinity, we choose on the bubble surface a point q_0 with the coordinates: $[R_0=R_i(\xi_0, t), \beta_0=\beta_i(\xi_0, t), \theta_0=0]$. Here, $\xi_0 \ll 1$. When $\xi_0 \rightarrow 0$, then $q_0 \rightarrow p_i$. We define a curve on the bubble surface l_i : $[R=R_i(\xi(\xi), t), \beta=\beta_i(\xi(\xi), t)]$, in such a way that all the points that belong to the curve have the same distance from point p_i as point q_0 .

The coefficient $a_{k,i,j}^r$ may then be presented as a sum of three integrals:

$$a_{k,i,j}^r = I_{1,k,i} + I_{2,k,i} + I_{3,k,i}. \quad (\text{A1})$$

Here,

$$I_{1,k,j} = \int_0^1 M_k(\xi) s_i(\xi) \int_{\theta_0}^{2\pi-\theta_0} (\partial G_i / \partial n) d\theta d\xi;$$

$$I_{2,k,i} = \int_{\xi(\theta)}^1 M_k(\xi) s_i(\xi) \int_{-\theta_1}^{\theta_1} (\partial G_i / \partial n) d\theta d\xi;$$

$$I_{3,k,i} = \int_0^{\xi(\theta)} M_k(\xi) s_i(\xi) \int_{-\theta_1}^{\theta_1} (\partial G_i / \partial n) d\theta d\xi;$$

and

$$\theta_1 = \sin^{-1} \frac{\sqrt{R_0^2 + \hat{R}_i^2 - 2R_0\hat{R}_i \cos(\beta_0 - \hat{\beta}_i)}}{\hat{R}_i \cos \hat{\beta}_i}.$$

The proper integrals $I_{1,k,i}$ and $I_{2,k,i}$ were calculated numerically. Integrals $I_{3,k,i}$ are improper because their integration area includes the singular point $q=p_i$.

According to Green function theory, the integral

$$J_i = \int_0^{\xi(\theta)} \int_{-\theta_0}^{\theta_0} \frac{\partial G_i}{\partial n} s_i(\xi) d\theta d\xi \quad (\text{A2})$$

is an improper converging integral (Tikhonov, 1990).

While taking into account the definition of the function $M_k(\xi)$, the following approximation takes place in the close vicinity of the point p_i :

$$I_{3,1,i} \approx \left(1 - \frac{\xi_0}{2}\right) J_i; \quad I_{3,2,i} \approx \frac{\xi_0}{2} J_i; \quad \text{while } \xi_0 \rightarrow 0.$$

The value of J_i equals the value of a solid angle with a vertex in p_i and is based on the part of the surface S_i which is restricted to the curve l_i (Arsenin, 1974). For a given case the value is

$$J_i = \begin{cases} \pi \frac{\cos \gamma_0 - \cos \gamma_1}{\gamma_1 - \gamma_0}; & \gamma_0 \neq \gamma_1 \\ \pi \sin \gamma_0; & \gamma_0 = \gamma_1. \end{cases} \quad (\text{A3})$$

Here,

$$\gamma_0 = \tan^{-1} \frac{R_0 \sin \beta_0 - \hat{R}_i \sin \hat{\beta}_i}{R_0 \cos \beta_0 - \hat{R}_i \cos \hat{\beta}_i} - \gamma_i; \quad \gamma_1 = \theta_1 \sin \gamma_i,$$

where γ_i denotes the angle between the positive direction (corresponding to increasing parameter ξ) of the tangent to the bubble surface at point $[\hat{R}_i, \hat{\beta}_i, 0]$ in the plane xOz and the positive direction of the x axis.

Analogously, coefficient $b_{k,i,j}^r$ may be presented as a sum of three integrals

$$b_{k,i,j}^r = U_{1,k,i} + U_{2,k,i} + U_{3,k,i}. \quad (\text{A4})$$

Here,

$$U_{1,k,i} = \int_0^1 M_k(\xi) s_i(\xi) \int_{\theta_0}^{2\pi-\theta_0} G_i d\theta d\xi;$$

$$U_{2,k,i} = \int_{\xi(\theta)}^1 M_k(\xi) s_i(\xi) \int_{-\theta_1}^{\theta_1} G_i d\theta d\xi;$$

$$U_{3,k,i} = \int_0^{\xi(\theta)} M_k(\xi) s_i(\xi) \int_{-\theta_1}^{\theta_1} G_i d\theta d\xi.$$

Integrals $U_{1,k,i}$ and $U_{2,k,i}$ are proper ones and were calculated numerically. Integrals $U_{3,k,i}$ are improper and converging.

Then, the following approximation takes place in the close vicinity of the point p_i :

$$U_{3,1,i} \approx \left(1 - \frac{\xi_0}{2}\right) W_i; \quad U_{3,2,i} \approx \frac{\xi_0}{2} W_i; \quad \text{while } \xi_0 \rightarrow 0.$$

Here,

$$\frac{2.4 \dot{\beta}_1(0,t) \xi_0 \hat{R}_i}{\sin(\beta_{ni} - \hat{\beta}_i)} \quad \text{while } \hat{\beta}_i \neq \beta_{ni} \beta_i; \quad (A5)$$

$$W_i = 2.4 \xi_0 \hat{R}_i \quad \text{while } \hat{\beta}_i = \beta_{ni},$$

and β_{ni} denotes the angle between the inner normal to the bubble surface and z axis.

Arsenin, V. Ya. (1974) *Methods of Mathematical Physics and Special Functions* (Nauka, Moscow) (in Russian).

Blake, J. R., Taib, B. B., and Doherty, G. (1986). "Transient cavities near boundaries. I. Rigid boundary," J. Fluid Mech. **170**, 479–497.

Sato, K., Tomita, Y., and Shima, A. (1994). "Numerical analysis of a gas bubble near a rigid boundary in an oscillatory pressure field," J. Acoust. Soc. Am. **95**, 2416–2424.

Späth, H. (1995). *One Dimensional Spline Interpolation Algorithms* (Peters, Wellesley, MA).

Tikhonov, A. N., and Samarskii, A. A. (1990). *Equations of Mathematical Physics* (Dover, New York).

Zhang, S., Duncan, J. H., and Chahine, G. L. (1993). "The final stage of the collapse of a cavitation bubble near a rigid wall," J. Fluid Mech. **257**, 147–181.

Zhang, S., and Duncan, J. H. (1994). "On the nonspherical collapse and rebound of a cavitation bubble," Phys. Fluids **6**(7), 2352–2362.

A computational analysis of sonic booms penetrating a realistic ocean surface

Judith L. Rochat^{a)}

U.S. Department of Transportation, John A. Volpe National Transportation Systems Center, Cambridge, Massachusetts 02142

Victor W. Sparrow

Graduate Program in Acoustics, The Pennsylvania State University, University Park, Pennsylvania 16802

(Received 27 July 1999; revised 27 November 2000; accepted 11 December 2000)

The last decade has seen a revival of sonic boom research, a direct result of the projected market for a new breed of supersonic passenger aircraft, its design, and its operation. One area of the research involves sonic boom penetration into the ocean, one concern being the possible disturbance of marine mammals from the noise generated by proposed high-speed civil transport (HSCT) flyovers. Although theory is available to predict underwater sound levels due to a sonic boom hitting a homogeneous ocean with a flat surface, theory for a realistic ocean, one with a wavy surface and bubbles near the surface, is missing and will be presented in this paper. First, reviews are given of a computational method to calculate the underwater pressure field and the effects of a simple wavy ocean surface on the impinging sonic boom. Second, effects are described for the implementation of three additional conditions: a sonic boom/ocean “wavelength” comparison, complex ocean surfaces, and bubbles near the ocean surface. Overall, results from the model suggest that the realistic ocean features affect the penetrating proposed HSCT sonic booms by modifying the underwater sound-pressure levels only about 1 decibel or less. © 2001 Acoustical Society of America. [DOI: 10.1121/1.1346684]

PACS numbers: 43.28.Mw, 43.50.Lj [LCS]

I. INTRODUCTION

It is well-known that sonic booms are produced from aircraft traveling faster than the speed of sound. Sound associated with these high-pressure disturbances is a concern when a supersonic airplane flies over inhabited areas; thus, supersonic flight has been restricted to over water or low population areas. Even though humans may not reside in these locations, other animals do.

The 1990s have seen a heightened interest in the impact of noise on marine mammals. One example is research being conducted on marine mammal behavioral response to sonic booms (Bowles, 1995); this research is in response to United States policies detailed in the Marine Mammals Protection Act and the Endangered Species Act (Wilhite and Shaw, 1997). Concern lies in behavioral responses rather than physiological harm (Cummings, 1993). Marine mammals include several different animals, some living in the water, some on land, but all spend time near the surface of the ocean; hence, each has the potential to hear sound created by supersonic aircraft. Those most likely to be affected are ones whose eating grounds, mating grounds, or migration paths coincide with the sonic boom carpet.

Sometime in the next century it is expected that a new breed of supersonic passenger aircraft will be in operation over the world's oceans (Poisson-Quinton, 1994; Williams, 1995). Although the parameters of the sonic booms generated by such new aircraft are not defined, sonic booms from these aircraft will penetrate the ocean surface, causing an

acoustic pressure disturbance underwater. The purpose of the present research is to determine the underwater sound-pressure levels due to sonic booms generated by a new HSCT (high-speed civil transport). It is possible using existing theories to make such calculations for a *homogeneous* ocean with a *flat* surface. What is not yet available are theories which include realistic ocean features: waves on the ocean surface and bubbles beneath the surface (an *inhomogeneous* ocean).

Adding such realistic ocean features to the study of sonic booms penetrating from air into the ocean can be accomplished by formulating a computational model. By use of such a model, each ocean feature can be treated separately to find its individual effects on the incoming sonic boom waveform. The focus or defocus from the curvature of a wavy ocean surface may cause a change in the underwater pressure disturbance. While bubbles near the surface may alter the underwater pressure field, the main concern here is the possible increase in the sound transmission through the air-water interface.

Determining underwater sound levels associated with sonic booms hitting the surface of a realistic ocean surface would allow predictions of the noise that marine mammals will hear. Marine biologists could use this information to predict the impact from the HSCT-generated sonic booms on these animals, treating each animal type according to its unique hearing abilities.

The next section of this paper offers a brief background to this research, followed by sections describing the method of computational analysis applied to the research. The fifth section reviews the effects of a wavy ocean surface on an

^{a)}Electronic mail: rochat@volpe.dot.gov

impinging sonic boom (Rochat and Sparrow, 1996); part of this section reveals the effects of the ratio of sonic boom to ocean “wavelength.” The sixth section reveals the effects of ocean bubbles on an impinging sonic boom. Finally, conclusions are stated. Details of this research can be found in Rochat (1998).

II. BACKGROUND

By the time a sonic boom reaches the earth’s surface, it often approximates an N-shaped plane wave (Plotkin and Sutherland, 1990); it is assumed that the aircraft is flying in steady flight at its cruising altitude and that atmospheric turbulence effects are negligible. It is also assumed that the incident angle at the mean ocean surface is equal to the Mach angle (at the aircraft); although a rough approximation, this is sufficient for the current research. Plane wave theory can then be applied to determine transmission/reflection of the sonic boom at the surface of the ocean. Here, Snell’s law applies. The transmitted wave can be either a propagating wave or an evanescent wave, the result determined by the incident angle.

When interacting with a flat water surface, a sonic boom sees a large impedance change and will be totally reflected if the incident angle θ_1 (from normal) is greater than 13.2° . If it is less than 13.2° , the incident plane wave creates both a transmitted propagating wave into the water and a reflected wave propagating back into the air. This critical angle of 13.2° corresponds to a Mach number of approximately 4.4 [$\theta_1 = \theta_c = \arcsin(1/M)$, M =Mach number]. This implies that the aircraft must be traveling at a speed greater than the speed of sound in water in order for the sonic boom to penetrate as a propagating wave. A foreseeable speed for a supersonic passenger aircraft would be approximately Mach 2.4 (Vartabedian, 1994; Wilhite and Shaw, 1997), which implies the incident angle is 24.6° , an angle associated with total wave reflection. However, when the sonic boom hits the surface of the water, an evanescent wave penetrates the water’s surface. This evanescent wave decays as a function of depth; it is *not* a propagating wave nor does it have an associated propagation angle (angle of refraction), but rather descends in a direction normal to the surface.

In the 1960s and early 1970s, research on supersonic transport (SST) was in full force, incorporating several studies focusing on sonic booms and their corresponding underwater sound (Ribner and Hubbard, 1972). For a general noise source in the air, it was shown that evanescent waves are a definite contribution to the underwater noise and that curvature on the water’s surface enhances this underwater pressure field (Urlick, 1972; Medwin *et al.*, 1973; Lubard and Hurdle, 1976; Meecham, 1978). Theory was developed for a perfect N-shaped sonic boom penetrating a flat air–water interface by Sawyers (Sawyers, 1968) and Cook (Cook, 1970); they theoretically showed that an evanescent sound wave was produced under water. This wave was validated by experiments (Waters and Glass, 1970; Waters, 1971; Intrieri and Malcolm, 1973; Young, 1968).

Research on sonic booms under water has again blossomed, after the U.S. SST program was canceled in 1971. Data have been recorded of underwater sonic booms for a

relatively flat ocean surface (Desharnais and Chapman, 1997); results seem to follow the known theories. Recently, additions to the known theories include effects of aircraft speed (Sparrow, 1995), surface waviness, and shaped sonic booms (Sparrow and Ferguson, 1997).

Another study includes the description of sonic booms under water in relation to the effects on marine mammals (Rochat and Sparrow, 1995; Rochat, 1998). This research can be applied to the current work to obtain underwater sound levels corresponding to hypothetical supersonic aircraft. These flat ocean surface results indicate that a 50-Pa peak pressure, 300-ms duration airborne sonic boom can generate sound levels just under the surface from an A-weighted sound exposure level of 94.4 to 131.0 dB peak pressure *re* 20 μ Pa (120.4–157.0 dB *re* 1 μ Pa), depending on the metric applied. Also metric dependent, the sound levels may decrease rapidly with depth, as much as 91.5 dB for the A-weighted sound exposure level and an average of 15.0 dB for the unweighted level at a depth of 128 m.

The inclusion of more realistic ocean features to underwater sonic boom penetration still needs to be addressed. Research on a wavy ocean surface is ongoing. Cheng *et al.* (1996 AIAA; 1996 Armstrong Laboratories; Cheng and Lee, 1997) have presented initial results using an analytical method, and the current authors have addressed the problem in this paper as well as the effects of an inhomogeneous ocean—containing bubbles near the surface.

III. METHOD OF COMPUTATIONAL ANALYSIS

The remaining work is based on a new method of computational analysis; it incorporates known finite difference schemes into new FORTRAN code. This method was verified with proven theories, higher-order formulations, and recent applications (Rochat, 1998).

Due to its simplicity and efficiency, a second-order two-dimensional centered finite difference scheme is used for wave propagation in the air and in the water, where the density is constant; this scheme is not implemented at the interface. Although the scheme is not a high-order method, it is very stable and has sufficient accuracy for the present problem. The centered difference scheme for the acoustic wave equation, derived from Hirsch (Hirsch, 1988), is

$$p_{i,j}^{n+1} = 2p_{i,j}^n - p_{i,j}^{n-1} + c_o^2(\Delta t)^2 \left[\frac{p_{i+1,j}^n - 2p_{i,j}^n + p_{i-1,j}^n}{(\Delta x)^2} + \left(\frac{p_{i,j+1}^n - p_{i,j}^n}{\Delta z_{j+1}} - \frac{p_{i,j}^n - p_{i,j-1}^n}{\Delta z_j} \right) \times \frac{2}{\Delta z_{j+1} + \Delta z_j} \right], \quad (1)$$

where the index n represents time, and the indices i and j , the grid points in the x and z directions, respectively, represent space. The variable p is the acoustic pressure, c_o is the speed of sound (different for each medium, values stated below), Δt is the time increment, Δx is the spatial increment in the x direction (horizontal), and Δz is the spatial increment in the z direction (vertical). In general, $\Delta z_j = z_j - z_{j-1}$, z_j being the physical location at index j on the grid. As is indicated by

Eq. (1), the computational grid must be uniform in the x direction but allows for nonuniformity in the z direction.

Since the air–water interface signifies a huge impedance change, it is necessary to implement a scheme capable of handling the changes in speed of sound and density. Although finite differences can easily handle the sound speed change, a factor of 4.4 between air and water, most finite difference schemes will go unstable with the huge change in ambient density, a factor of approximately 800. For example, if used alone Eq. (1) will go unstable at the air–water interface.

To overcome this instability, a finite difference method different from Eq. (1), similar to one used in seismology, is applied at all grid points within $\pm \frac{1}{2}\Delta z$ of the air–water interface. The scheme is derived by integrating the acoustic wave equation across the interface; this ensures proper reflection and transmission coefficients. This method was originally applied by Sochacki *et al.* (1991) to a slightly different set of equations. The present interface finite difference scheme is written as

$$p_{i,j}^{n+1} = 2p_{i,j}^n - p_{i,j}^{n-1} + \frac{\Delta t^2}{a_{i,j}} \times \left\{ \frac{1}{\Delta x^2} [b_{i+1/2,j} p_{i+1,j}^n - (b_{i+1/2,j} + b_{i-1/2,j}) p_{i,j}^n + b_{i-1/2,j} p_{i-1,j}^n] + \left[\frac{b_{i,j+1/2}(p_{i,j+1}^n - p_{i,j}^n)}{\Delta z_{j+1}} - \frac{b_{i,j-1/2}(p_{i,j}^n - p_{i,j-1}^n)}{\Delta z_j} \right] \frac{2}{\Delta z_{j+1} + \Delta z_j} \right\}, \quad (2)$$

where p , Δt , Δx , and Δz are the same as in Eq. (1). The additional variables are $a = 1/\rho_o c_o^2$ and $b = 1/\rho_o$, ρ_o being the ambient density for each medium. Both a and b change depending on the location of the calculation. If the calculation is made in air $c_o = 343$ m/s and $\rho_o = 1.21$ kg/m³, in water $c_o = 1500$ m/s and $\rho_o = 1000$ kg/m³. However, at the interface a and b are theoretically complicated (Sochacki *et al.*, 1991) and can be difficult to implement, depending on whether or not the interface line intersects grid blocks or outlines them. Since the current interface is grid-block approximated (the interface line does not intersect a grid block), the functions can be written simply as $a = \frac{1}{2}(a_{\text{air}} + a_{\text{water}})$ and $b = \frac{1}{2}(b_{\text{air}} + b_{\text{water}})$.

IV. PROGRAM PARAMETERS AND FEATURES

There are many different variables to consider in the current problem; these include computational variables (grid parameters and boundary conditions) and physical variables (sonic boom parameters, ocean wave heights, ocean bubbles, and media).

The computational domain is a rectangular grid with hard reflecting boundaries on the left, right, and top sides and an absorbing boundary (Sparrow and Raspet, 1990) on the bottom. Hard reflecting boundaries are implemented wherever possible for simplicity. Since the propagating wave starts from the upper-left-hand corner of the computational domain, the left boundary is of no consequence, and reflec-

tions from the right and top boundaries would not interact with the analysis region until a time later than would cause any interference. Hard reflecting boundaries are therefore suitable for the left, right, and top sides of the domain. However, the sound speed in water is 4.4 times that in air, and false reflections from a rigid bottom boundary would interfere with the present analysis of the sound levels at the interface. Two possible solutions to avoid this interference are: first, to extend the domain by a factor of 4.4 below the water surface or second, to implement an absorbing boundary on the bottom of the domain. The latter was chosen in order to make the program more efficient.

The computational grid physically represents a region with dimensions $x \times z$ of 799×781 m (340 m in height in the air and 441 m in depth in the water); however, there are 800 grid points in both the x and z directions. This nonuniform grid has a refined region surrounding the air–water interface, a necessary feature for the program’s stability. In the refined region a grid block spans 1 m in the x direction and 0.25 m in the z direction; this refined region physically extends 3 m above and 3 m below the midline of any type of ocean interface. Elsewhere in the domain, a grid block spans 1 m in the x direction and also 1 m in the z direction.

A rounded N-shaped sonic boom is inserted in the upper-left-hand corner of the computational domain. Figure 1 shows a typical initial condition with a horizontal slice showing the initial rounded sonic boom waveform. The sonic boom has a specified peak pressure, duration, and angle of incidence which, as previously mentioned, is a function of the Mach number. Using a rounded N-shaped sonic boom instead of a perfect N wave is justified for two reasons. First, realistic sonic booms vary in shape, some roughly appearing as rounded N waves; second, a perfect N wave would require a computationally intensive simulation (possibly using a very fine grid) which is not feasible at this time.

V. EFFECTS OF WAVY OCEAN SURFACE

A. Simple curved surfaces

This section reviews the effects of a simple wavy surface (or swell) on an impinging sonic boom (Rochat and Sparrow, 1995; Rochat, 1998). The previously described computer program is implemented for flat and wavy ocean surfaces; the wavy ocean surface is represented by simple curvature.

The flat ocean surface runs supplied reference pressure values near the ocean surface. These runs also supplied insight into the visualization of an evanescent wave. Shown in Fig. 2, the Mach 2.4, wave height 3.75-m case, is the acoustic intensity field superimposed on the pressure field for a snapshot in time. The incoming waveform is represented by vectors pointing down and to the right and the reflected waveform is represented by vectors pointing up and to the right. Just under the ocean surface, it is seen that two sets of arrows, one for each peak of the sonic boom waveform, each forms a scoop shape which decays with depth; this represents the evanescent wave caused by the impinging sonic boom. The intensity amplitude in the air is actually much greater than in the water, and the intensity vectors in that area of the

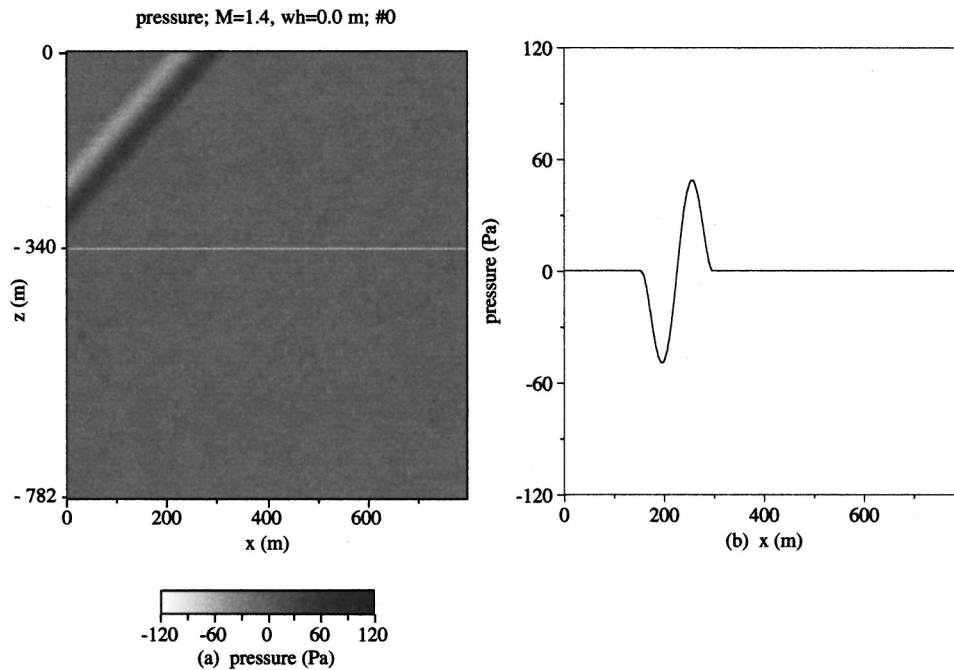


FIG. 1. Initial pulse, Mach number 1.4, wave height 0.0 m; (a) full domain plot; (b) horizontal line intersection.

domain are greatly magnified for visualization. Also, the illustrated density of the air intensity vectors is less than for the ocean vectors which allows showing the incoming and reflected waves more clearly.

Now, the effect of a simple wavy ocean surface profile is explored. The ocean wave height is a function of the wind speed in the air; any wave height, peak to trough, can be specified. It is assumed that the wind is blowing in the x direction; hence, a two-dimensional computational analysis is appropriate. Wavelengths of these wind-driven waves are taken to be 20 times their heights, a common ocean engineer-

ing approximation (Gaythwaite, 1981). Also, several height profiles for the curved interface are chosen. The first type is a sinusoidal ocean surface, and the second more realistic one is a trochoidal ocean surface. A simple expression for the trochoidal surface representing ocean swell is

$$\eta = -A \cos kx + \frac{1}{2}kA^2 \cos 2kx - \frac{3}{8}k^2A^3 \cos 3kx, \quad (3)$$

where η is the vertical displacement of the water surface above the mean water level, A is the wave amplitude (half the wind wave height), and k is the wave number for the ocean surface. An illustration of this surface is seen in Fig. 3.

Even though the grid is refined in the interface region, the ocean surface curve is still approximated by ragged grid blocks; in turn, depending on the ocean wave height, the peaks and dips of the ocean waves can create numerical instabilities. To avoid this problem, a function is inserted into the FORTRAN code which "smooths" any peak or dip with a singular maximum or minimum grid point by adjusting the singular extreme point to match the value of its neighboring grid points.

The Mach 1.4 and 2.4 cases were run for wave heights of 1.0, 1.4, 2.3, and 3.75 m and the Mach 3.0 and 3.5 cases were run for wave heights of 2.3 and 3.75 m. The air and water are considered to be homogeneous media. Qualitatively, results of the computational simulations show that as a sonic boom hits a wavy ocean surface, its energy is focused in the ocean wave troughs and defocused over the ocean wave crests. The amplitude of the underwater pressure just under the troughs is higher, and in the crests lower, than it would be under a flat ocean surface. The sonic boom was seen to penetrate the surface of the water as an evanescent

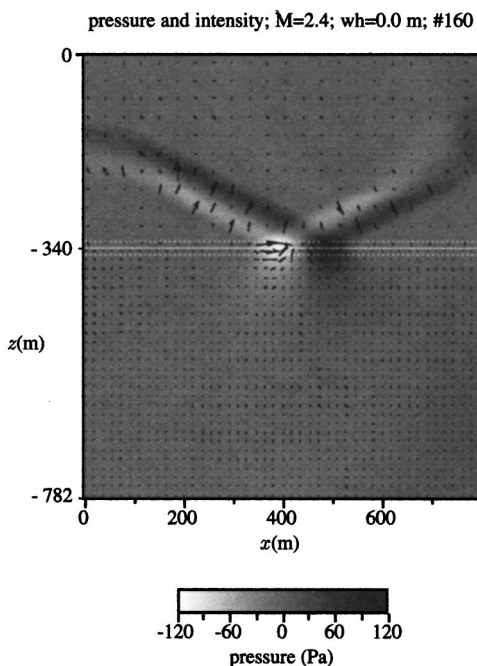


FIG. 2. Mach number 2.4, wave height 0.0 m; incident wave interacting with the air-water interface at $z=340$ m; pressure and intensity fields for $c_{\text{air}}=343$ m/s and $c_{\text{ocean}}=1500$ m/s.



FIG. 3. Trochoidal ocean surface profile.

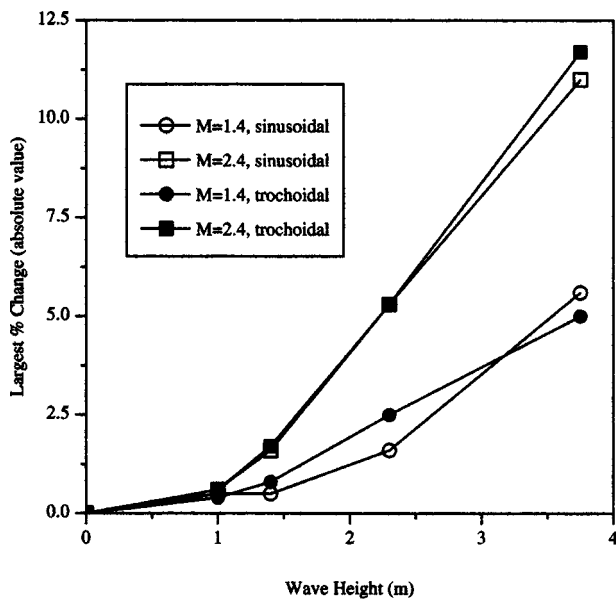


FIG. 4. Largest pressure amplitude percent change from a simple ocean swell to a flat surface as a function of wave height.

wave, not a propagating wave. Examination of the pressure field as well as the associated intensity field helps in this analysis.

Quantitatively, looking at a sonic boom with a peak pressure of 50 Pa and duration of 300 ms, this pressure increase/decrease in the troughs and over the crests is at most 11.7% for a simple ocean surface; the change in sound-pressure level is 1 dB or less. Two trends can be identified when extracting pressure values from just under a simple ocean swell: (1) increasing wind wave heights strengthen the focusing and defocusing of the evanescent acoustic pressure, and (2) increasing the Mach number strengthens the focusing and defocusing due to curvature. Please refer to Fig. 4 for the results. Last, when extracting pressure values as a function of depth for a simple ocean surface simulation, it is found that the effects of curvature on the underwater pressure are stronger near the ocean surface than at greater depths.

B. Complex curved surfaces and wavelength comparisons

Complex ocean surfaces are used to investigate the effects of waves with more complex structure; they are crude approximations to a fully developed sea. Each complex surface adds a higher frequency component in the ocean wave described in Eq. (3). The first complex surface is the trochoidal wave with a sine wave of lower amplitude and half the wavelength superimposed. The second complex surface is the trochoidal wave with a sine wave of lower amplitude and one-third the wavelength superimposed. The Mach 1.4 and 2.4 cases were run for wave heights of 2.3 and 3.75 m, respectively.

As was found for the simple ocean swell, results indicate that as the sonic boom interacts with the complex wavy ocean surface, its energy is being focused in the troughs and defocused over the crests. Effects caused by the curvature are stronger for greater ocean wave heights, consistent with the

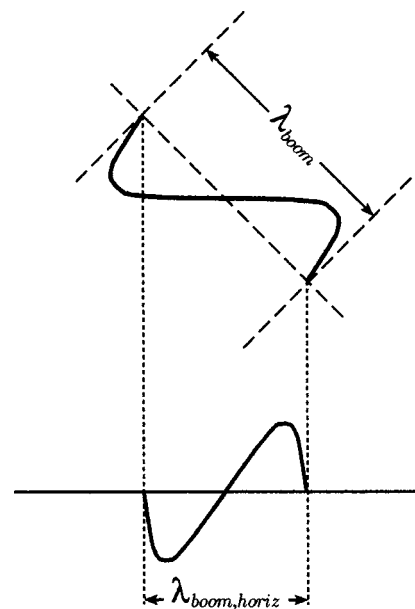


FIG. 5. Illustration of the sonic boom effective wavelength variables.

trend found for the simple curved surface. The largest percent change in peak pressure was 11.2%; this corresponds to less than 1 dB. Results indicate, however, that the complex numerical data do not follow the other simple ocean swell trend, that the highest percent changes increase with increasing Mach number. Inspired by this inconsistency, research was conducted to determine the cause; following are the results of this investigation.

It was thought that perhaps the relationship of the “wavelengths” of the sonic boom and the ocean surface waves reveals the strength of effects due to ocean surface curvature. The term *effective wavelength* describes the physical length associated with the sonic boom duration. For all previous runs the sonic boom duration T was 300 ms; this is associated with a sonic boom effective wavelength λ_{boom} of 102.9 m in air ($\lambda_{boom} = c_{air}T$). The results for the simple and complex ocean profiles indicate that the positive and negative peaks of the sonic boom waveform interact with the ocean waves separately; while one peak is in a trough of the ocean surface the other peak is either on the far side of the neighboring peak or in the next trough. Hence, looking at just one peak of the sonic boom is warranted. The wavelength associated with half the duration of the sonic boom is $\lambda_{1/2boom} \approx 51.5$ m. Since the ocean surface is horizontal in the computational domain, the horizontal component of $\lambda_{1/2boom}$, $\lambda_{1/2boom,horiz}$, is applied when comparing the sonic boom effective wavelength to the ocean surface wavelength. The length of the horizontal component is Mach number dependent. Figure 5 illustrates the sonic boom effective wavelength variables. As a way of comparing the sonic boom effective wavelength with the ocean wavelength, the following ratio is defined: $\lambda\text{-ratio} = \lambda_{1/2boom,horiz} / \lambda_{ocean}$.

For the simulations in this section, a trochoidal ocean profile is applied. Again, a rounded sonic boom with a peak pressure of 50 Pa is the initial waveform. For these runs, however, the duration of the sonic boom varies. Varying the duration allows a systematic evaluation of the wavelength

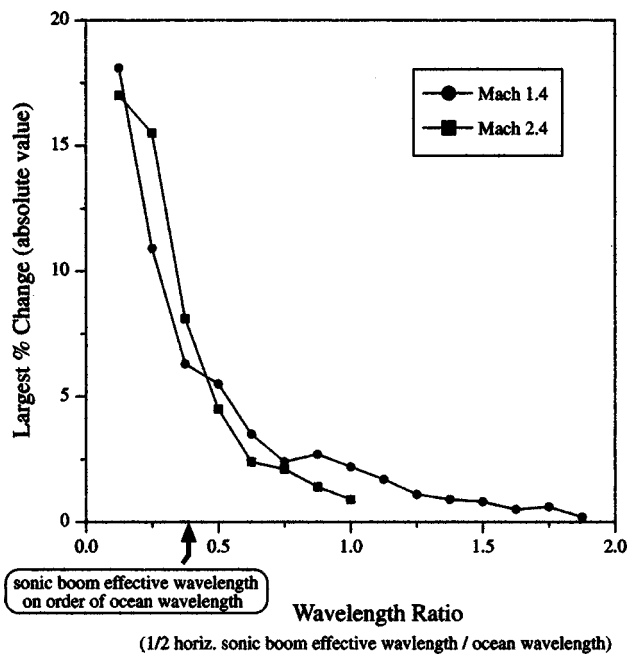


FIG. 6. Largest pressure amplitude percent change from a simple ocean swell to a flat surface for the corresponding wavelength ratio, λ -ratio $= \lambda_{1/2\text{boom,horiz}} / \lambda_{\text{ocean}}$.

ratio λ -ratio and the corresponding effects. The durations are chosen such that the λ -ratio ranges from 0.125 to 1.875 in steps of 0.125; this adds up to 15 ratios or durations. Due to the size of the computational domain the runs are limited; not all cases (combinations of Mach 1.4 and 2.4 and ocean wave heights 2.3 and 3.75 m) were run to completion. The only wave height applied is 2.3 m, since the duration of the sonic boom would have to be quite long in order to accommodate the higher wavelength ratio values for the ocean wave height of 3.75 m. The Mach 1.4, wave height 2.3-m case is run for all wavelength ratios. The Mach 2.4, wave height 2.3-m case is run for all wavelength ratios less than or equal to 1; the higher wavelength ratios cannot be applied because of computational limits. While all of the sonic boom durations used were not realistic, their use helped the understanding of the effect of the wavelength variations.

For every case run, several snapshots in time of the simulation are evaluated. The largest modification of the pressure values just under the surface are then turned into percent change from the flat ocean results. Figure 6 shows the results of this wavelength comparison study. It is a plot of the largest amplitude percent change from a flat surface caused by a simple ocean swell for the corresponding wavelength ratio λ -ratio $= \lambda_{1/2\text{boom,horiz}} / \lambda_{\text{ocean}}$. The Mach 1.4 and the Mach 2.4 curves roughly follow the same path, indicating that for a wavy surface the percent change is governed by the relation between the sonic boom and ocean wavelengths rather than the Mach number. The curves show that the effects of the ocean waviness are more significant when the ocean surface wavelength is larger than half the horizontal component of the sonic boom effective wavelength.

Cheng *et al.* (1996 AIAA, 1996 Armstrong Laboratories) assert that waviness influence will be significant only for swell with wavelengths comparable to or much larger

TABLE I. Largest pressure amplitude percent changes for simulations and predictions from plot in Fig. 6; also the difference between these two results; trochoidal surface.

Mach number	Ocean wave height	λ -Ratio	Simulation % change	Fig. 6 predicted % change	Magnitude of difference in percent
1.4	1.0	1.84	0.4	0.5	0.1
	1.4	1.31	0.8	1.0	0.2
	2.3	0.80	2.5	2.0	0.5
	3.75	0.49	5.0	5.0	0.0
2.4	1.0	1.07	0.6	1.8	1.2
	1.4	0.76	1.7	2.4	0.7
	2.3	0.47	5.3	5.1	0.2
	3.75	0.29	11.7	11.0	0.7
3.0	3.75	0.23	15.4	14.8	0.6
3.5	3.75	0.20	16.9	15.5	1.4

than the sonic boom effective wavelength. The arrow in Fig. 6 indicates where the sonic boom effective wavelength (not the horizontal component) is comparable to the ocean wavelength. It is at this point on the plot where the largest percent change is approximately 7%. Sonic boom effective wavelengths larger than the ocean wavelength would be associated with percent changes larger than 7%. Thus, Fig. 6 supports Cheng *et al.*'s assertion.

Now, it is necessary to go back to the different ocean profile results and see where specific values of λ -ratio fall on the plot and if the percent change predicted by Fig. 6 matches those previously calculated. The simple trochoidal profile and the complex profiles are used to represent the ocean surface, where the larger and smaller components of the complex profiles are examined. It should be noted that the largest percent changes extracted from the plot in Fig. 6 are approximated by taking the average of the two curves.

Table I compares the difference between the results obtained in the simulations and those predicted using Fig. 6 for various Mach numbers and various wave heights. For the trochoidal profile the differences indicate that the approximations using the plot are quite accurate, the largest difference being 1.4%. Thus, when a sonic boom impinges upon an ocean with a simple surface profile, the waveform change is governed by the relation between the sonic boom effective wavelength and the ocean surface wavelength.

For complex profiles the smallest ocean wavelength component does not govern the effects of the curvature, nor does the largest ocean wavelength component. Each is off by more than 6% in some cases. It follows that Fig. 6 cannot be used to predict how much the curvature of the complex ocean surface affects the impinging sonic boom.

In conducting these wavelength comparison studies, a tool was developed to help predict the effect that simple ocean curvature has on an impinging waveform. For a particular Mach number and ocean wave height, the plot in Fig. 6 can be used to estimate the percent change of the acoustic pressure just under the surface from a flat ocean to that with simple ocean swell. For complex surfaces, however, the plot cannot be applied. So, although the complex surface studies prompted the wavelength comparison studies, the resulting prediction plot cannot help in determining the underwater

pressure. The wavelength comparison studies do not explain the unpredictability of the curvature effects felt by a sonic boom interacting with a complex ocean surface. It is concluded that each complex surface case must be treated individually.

VI. EFFECTS OF OCEAN BUBBLES

A. Parameters of ocean bubbles

To isolate the effects of bubbles near the ocean surface, the ocean surface is flat for the simulations including the bubbles. According to Snell's law, the speed of sound in water would have to be less than about 823 m/s for a flat ocean surface to allow propagation of a sonic boom waveform for the Mach 2.4 case. In a flat, homogeneous ocean, the speed of sound is approximately 1500 m/s, so propagation is impossible. However, the presence of bubbles in an ocean changes its sound speed. In an extreme case (Brennen, 1995), the speed of sound in the bubbly water could be as low as 500 m/s; for the Mach 2.4 case, there should then be propagation into this ocean. It is therefore important to add ocean bubbles to the overall analysis.

Bubbles in the ocean are formed when wind-generated waves break. The Beaufort scale reveals that waves start to break when the wind speed is from 7–10 knots (kn) (3.4–5.4 m/s); it is at this sea state that scattered whitecaps appear (Bascomb, 1980; Brown *et al.*, 1989). Large numbers of bubbles are entrained during the breaking wave process; air is trapped or enveloped as the seawater surrounds it (Leighton, 1994). These bubbles are actually seen in groups under the ocean surface as clouds or plumes, their shape and depth dependent on the turbulent motions in the water (Thorpe, 1982).

Even though ocean bubbles dissipate after formation, their existence should not always be considered transient. Studying the bubble plume depth, the maximum lifetime of a bubble plume, and the frequency of wave breaking, it is determined that if the wind speed exceeds 12.6 kn (6.5 m/s), the bubbles will persist from one wave break to the next (Leighton, 1994). The Beaufort scale categorizes this wind speed as a "moderate breeze," where whitecaps are fairly frequent. So while at lower wind speeds bubbles will not exist or may be formed in discrete patches, the bubble plumes will overlap at higher wind speeds forming a continuous bubble layer.

In general, the speed of sound in a bubble plume depends on the size and number of bubbles and on the frequency of the sound (Leighton, 1994). However, if the insonification frequency is much lower than any of the bubbles' resonance frequencies, then the plume can be viewed as a uniform body with an effective acoustic impedance (Leighton, 1994; Crighton, 1992).

Although an N-shaped sonic boom has significant high-frequency content, it can be found that most of its energy is below 400 Hz and most significant below 40 Hz. Extreme bubble radii have been observed to be approximately 300 μm for the largest and 20 μm for the smallest (Thorpe, 1982), the largest having a lower resonance frequency of 9.3 kHz. The lowest bubble resonance (9.3 kHz) is much greater

than the majority of the sonic boom frequency content (<400 Hz).

Applying the assumption, it is possible to look at the portion of the ocean containing bubbles as an area of effective acoustic impedance rather than modeling individual bubbles; its speed of sound and density must be calculated as a function of depth. The speed of sound profile used for an ocean with bubbles resembles the exponential law as a function of depth (Leighton, 1994; Farmer and Vagle, 1989)

$$c_{\text{bub}} = c_{\text{water}} - (c_{\text{water}} - c_{\text{surface}})e^{(\text{depth}/\text{efold})}, \quad (4)$$

where c_{water} is the speed of sound in the ocean without bubbles, c_{surface} is the speed of sound in the bubble layers right near the surface (here taken to be 500 m/s), depth is the depth from the surface (a negative value), and efold determines the shape of the exponential decay. Values for efold here are case specific, for a 20-kn wind, efold=1.05, and for a 30-kn wind, efold=1.5. These efold values were chosen to approximate the shape of the sound-speed profiles found in Farmer and Vagle (1989).

The average depth of a bubble plume can be determined by (Thorpe, 1982)

$$\text{depth}_{\text{ave}} \approx 0.4(\text{wind speed} - 2.5). \quad (5)$$

The wind speed here is in meters/second and the $\text{depth}_{\text{ave}}$ in meters. The maximum depth of a bubble plume is approximately twice the average depth

$$\text{depth}_{\text{max}} \approx B \times \text{depth}_{\text{ave}}, \quad (6)$$

where B is 2.3 for a 20-kn wind and 1.9 for a 30-kn wind. It can be seen from Eqs. (5) and (6) that as the wind speed increases, the maximum depth of the bubble plume increases. For example, for a wind speed of 20 kn (10.28 m/s), the maximum depth of the bubbles is approximately 7 m and 10 m for 30 kn (15.42 m/s). Although the speed of sound is significantly changed due to the bubbles, the density change is determined to be negligible for this work.

B. Bubble models

Two ocean bubble models, one simple and one more complicated, are now incorporated into the computer code. Instead of a continuous change in speed of sound with depth, the part of the ocean containing the bubbles is divided into sections or layers; as depth increases, each layer has an increasing sound speed, but the density remains a constant, 1000 kg/m^3 (the density of the water without the bubbles). A simple model is constructed with several flat bubble layers; a more complicated model consists of one bubble plume also with several bubble layers.

The simple model is used to find the effects of the bubbles (on the sonic boom) just from the different impedance layers and not from the shape of the bubble plumes. Each flat layer with a different sound speed has a specified height or thickness, the sound speed calculated at the layer's average depth using Eq. (4). The layers are thinner near the surface where the sound speed is rapidly changing. The number of layers depends on the maximum depth of the bubbles, which depends on the wind speed.

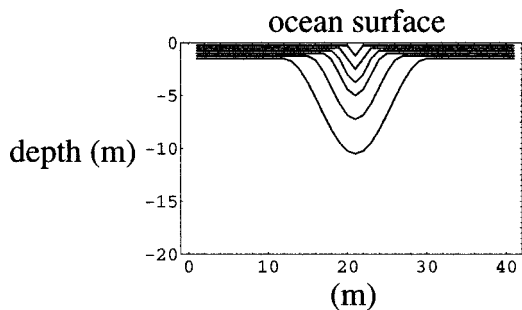


FIG. 7. Profile of bubble plume near the surface of the ocean. The case shown is for a 30-kn wind.

The more realistic model of bubbles in the ocean would include bubble plumes. If sound energy does penetrate the plume, there is the possibility that it may become trapped, forming a concentrated noise source. Therefore, the more complicated model applied here is a single bubble plume. This plume is modeled using a sine-squared function, an approximation to what is actually a constantly changing shape. This function was chosen for its smooth profile, an important feature when approximating its curve with computational grid blocks. The model, seen in Fig. 7, is comprised of bubble layers. The speed of sound for each bubble layer is calculated as if the layers were flat, as in the previous model. However, there are fewer layers used in the bubble plume model than in the flat bubble layer model.

C. Computational simulations

All computational simulations are conducted with the flat ocean surface; while unrealistic for these wind speeds, this separates the bubble effects from the wind wave effects. The air–water interface finite difference scheme is applied at both the flat ocean surface and between each bubble layer. Moreover, the refined grid region is now stretched to include all bubble layers. Since the domain is still 800 grid points in the z direction, this implies that the domain has physically shrunk.

Two runs of the program including the flat bubble layer model were made in order to help assess the impact bubbles have on an impinging sonic boom waveform. In all runs the peak pressure of the sonic boom is 50 Pa and the duration 300 ms; the only Mach number used is 2.4. Calculations were performed for two different wind speeds, 20 kn (10.3 m/s) and 30 kn (15.4 m/s). Each flat bubble layer has an associated thickness: starting from the surface, the first six layers are 0.5 m, the next two layers are 1.0 m, the ninth layer is 2.0 m, and (for the 30-kn wind case) the tenth layer is 3 m. The maximum depth, the total of all thicknesses added together, is determined using Eqs. (5) and (6). The speed of sound in each layer is again calculated using Eq. (4).

The simulation analyzed is for the 30-kn case, since this more extreme case would be more likely to show effects due to the bubbles if there are any. From time snapshots, it was apparent that there is no propagation of the sonic boom into the ocean; the pressure field and especially the intensity field

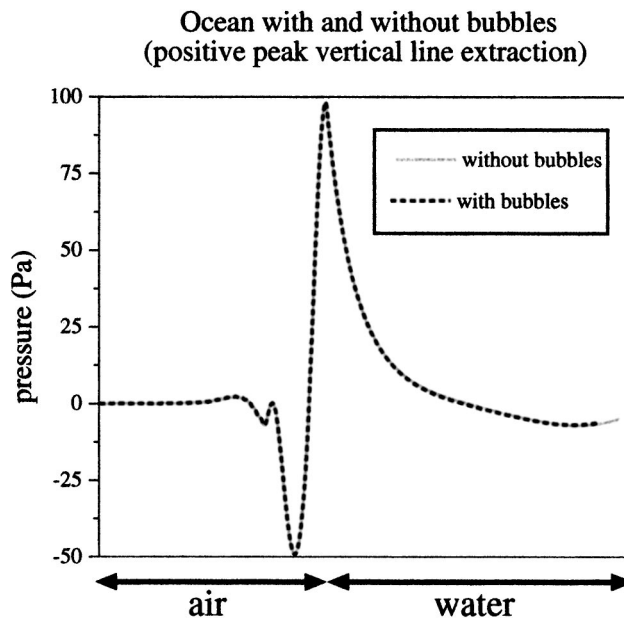


FIG. 8. Vertical intersection of the greatest positive peak pressure of the sonic boom waveform. Lines for ocean with and without bubbles.

indicate that the sonic boom still penetrates the ocean only as an evanescent wave.

As stated before, for the Mach 2.4 case the sound should penetrate the ocean surface as a propagating wave only if the sound speed is less than 823 m/s. Just the top layer of bubbles for both the 20-kn and 30-kn cases has a sound speed less than 823 m/s; the underwater sound field is apparently unaffected by this layer because its thickness is only 0.5 m. Since the sonic boom effective wavelength is quite large in comparison (≈ 103 m in air for the 300-ms-duration sonic boom), the top bubble layer is most likely invisible to the incoming waveform.

While flat layers of bubbles do not allow propagation into the ocean, their effect on the evanescent field is uncertain. Therefore, runs with and without the ocean bubbles were conducted. A vertical slice of data is extracted from the two-dimensional computational domain, at two horizontal locations; these two locations are chosen to be the highest and lowest pressure values just under the ocean surface. Figure 8 shows that vertical pressure profiles at the greatest positive peak pressure for the runs with and without ocean bubbles are essentially identical. This indicates that the ocean bubbles do not have an effect on the evanescent field. Vertical profiles at the greatest negative peak pressure repeat this indication. The effects are less than 1 dB.

Two runs of the program with a layered bubble plume were made to assess the impact bubbles have on an impinging sonic boom waveform. For this bubble plume model, a computer simulation of the more extreme wind speed, 30 kn, was utilized with a Mach number of 1.4. As before, the ocean surface is flat. Each bubble layer has an associated thickness at the location of the bubble plume. The first four layers are 1 m, the fifth layer is 2 m, and the sixth layer is 3 m. Again, the maximum depth is approximated using Eqs. (5) and (6); from these equations, the depth of the bubble plume should be about 10 m.

It was clear from the computed waveform time history that the sonic boom penetrates the ocean as an evanescent wave, the field being relatively unaffected as it passes over the bubble plume. The smaller Mach number (1.4) calculation was performed in order to determine whether or not a sonic boom with a shorter horizontal effective wavelength would more easily penetrate the narrow opening of the bubble plume. The results still indicate that the evanescent field is relatively unaffected by the bubble plume. The greatest percent change from the no bubble case corresponds to less than 1-dB change.

VII. CONCLUSIONS AND DISCUSSION

A study of underwater sound levels due to an impinging airborne sonic boom considered the effects due to a wavy ocean surface and the effects due to ocean bubbles.

Simple ocean surface curvature due to wind waves was shown to affect the impinging sonic boom, its energy being focused in the ocean wave troughs and defocused over the wave crests. For the cases studied, the largest percent change in peak pressure was 11.7%, which corresponds to the sound level being augmented only 1 dB. Also, two trends in the data were exposed: (1) increasing wind wave heights strengthens the focusing and defocusing of the evanescent acoustic pressure, and (2) increasing the Mach number strengthens the focusing and defocusing due to curvature.

An ocean surface with a complex profile revealed the largest effect due to curvature to be an 11.2%-increase in peak pressure; this corresponds to less than 1 dB in sound-pressure level. The first trend found with the simple surface was confirmed in the complex surface simulations, but the second was not. A study of wavelength comparisons, sonic boom effective wavelength relative to the wavy ocean surface wavelength, produced a tool to help predict the magnitude of the effect due to simple curvature. The most significant effects were associated with the sonic boom effective wavelength being on the order of, or less than, the ocean surface wavelength. It was determined that this tool could not be applied to a complex surface, and that each complex case should be treated individually.

In addition to a homogeneous wavy ocean surface, a nonhomogeneous flat ocean was also studied; for the latter, ocean bubbles were included. Two bubble models were formulated. The first consisted of flat layers, where each layer had a different sound speed. The second model consisted of one bubble plume also with layers. Results for both models indicate that the sonic boom penetrates the ocean surface only as an evanescent wave, and that bubbles affect the evanescent pressure field by less than 1 dB.

Studying the effects that realistic ocean features have on impinging sonic booms has revealed that any underwater augmentation due to curvature on the ocean surface or bubbles beneath the surface is minor. This returns us to the basic problem: a sonic boom impinging upon a homogeneous ocean with a flat surface. Having equations for calculating the acoustic pressure as well as having an understanding of the frequency content as a function of depth is important to analyzing the underwater sound field.

It is somewhat remarkable that after all the effects of bubbles and variations in ocean surface profiles have been accounted for that the theory based on the simple two-fluid interface does an excellent job of describing the sonic boom penetration into the ocean. The flat, homogeneous ocean model should be sufficient for most engineering predictions of the sonic boom underwater pressure field.

Using equations developed by Sawyers or by Cook, it is possible to calculate the pressure field as a function of depth; hypothetical HSCT parameters can be used as the input variables. A description of this underwater sonic boom, however, requires further analysis. If interested purely in the frequency content and not in the features of an incident wave form's shape, it is possible to follow the decay of each frequency component as a function of depth ($e^{-|\omega|z/m}$, where ω is the angular frequency, z is the depth, and m is a function of the speed of the aircraft and the speed of sound in the ocean; Sawyers, 1968).

ACKNOWLEDGMENTS

The authors appreciate financial support from the National Aeronautics and Space Administration, Langley Research Center, Grant No. NAG-1-1638, administered by Dr. Gerry L. McAninch. Research for this article was done while J. L. R. was at The Pennsylvania State University. Thanks also to Kevin Shepherd for numerous conversations.

- Bascomb, W. (1980). *Waves and Beaches* (Anchor, Doubleday, New York), Chap. 3.
- Bowles, A. E. (1995). "Responses of wildlife to noise," *Wildlife and Recreationists: Coexistence Through Management and Research*, edited by R. L. Knight and K. J. Gutzwiller (Island, Washington, DC), Chap. 8.
- Brennen, C. E. (1995). *Cavitation and Bubble Dynamics* (Oxford University Press, New York), Chap. 6.
- Brown, J. et al. (1989). *Waves, Tides and Shallow-Water Processes*, edited by Gerry Bearman (The Open University, Paragon, Tarrytown, NY), Chap. 1.
- Cheng, H. K., Lee, C. J., Hafez, M. M., and Guo, W. H. (1996). "Sonic boom propagation and its submarine impact: a study of theoretical and computational issues," AIAA Paper 96-0755, 34th Aerospace Sciences Meeting and Exhibit, Reno, NV.
- Cheng, H. K., Hafez, M. M., Lee, C. J., and Tang, C. Y. (1996). "Assessment of an improved theory for further program development of sonic boom prediction and submarine impact study," Final report submitted to Armstrong Laboratories, OEBN, Noise Effects Branch, 28 November.
- Cheng, H. K., and Lee, C. J. (1997). "Submarine impact of sonic boom: A study comparing and reconciling results from two prediction approaches," Proceedings, Noise-Con 97, pp. 399-404.
- Cook, R. K. (1970). "Penetration of a sonic boom into water," J. Acoust. Soc. Am. Suppl. 1 47, S1430-S1436.
- Crighton, D. G., Dowling, A. P., Ffowcs Williams, J. E., Heckl, M., and Leppington, F. G. (1992). *Modern Methods in Analytical Acoustics* (Springer-London Limited, Berlin), Chap. 21.
- Cummings, W. C. (1993). "Sonic booms and marine mammals: Informational status and recommendations," NASA CP-10132, pp. 219-231.
- Desharnais, F., and Chapman, D. M. F. (1997). "Underwater measurements of a sonic boom," Proceedings, Oceans 97 MTS/IEEE.
- Farmer, D. M., and Vagle, S. (1989). "Waveguide propagation of ambient sound in the ocean-surface bubble layer," J. Acoust. Soc. Am. 86, 1897-1908.
- Gaythwaite, J. (1981). *The Marine Environment and Structural Design* (Van Nostrand Reinhold, New York), Chap. 3.
- Hirsch, C. (1988). *Numerical Computation of Internal and External Flows: Volume 1: Fundamentals of Numerical Discretization* (Wiley, New York), Part II, also Chap. 1.
- Intieri, P., and Malcolm, G. (1973). "Ballistic range investigation of sonic-boom overpressures in water," AIAA J. 11, 510-516.

- Leighton, T. G. (1994). *The Acoustic Bubble* (Academic, San Diego), Chap. 3.
- Lubard, S. C., and Hurdle, P. M. (1976). "Experimental investigation of acoustic transmission from air into a rough ocean," *J. Acoust. Soc. Am.* **60**, 1048–1052.
- Medwin, H., Helbig, R. A., and Hagy, Jr., J. D. (1973). "Spectral characteristics of sound transmission through the rough sea surface," *J. Acoust. Soc. Am.* **54**, 99–109.
- Meecham, W. C. (1978). "Point source transmission through a sinusoidal ocean surface," *J. Acoust. Soc. Am.* **64**, 1478–1481.
- Plotkin, K. J., and Sutherland, L. C. (1990). "Sonic boom: prediction and effects," AIAA Professional Studies Series, Tallahassee, FL, 25–26 October.
- Poisson-Quinton, P. (1994). "Future SSTs, a European approach," *Aerospace America*, pp. 39–43, September.
- Ribner, H. S., and Hubbard, H. H. (1972). "Second sonic boom symposium," *J. Acoust. Soc. Am.* **51**, 671–798.
- Rochat, J. L. (1998). "Effects of realistic ocean features on sonic boom noise penetration into the ocean: A computational analysis," Ph.D. thesis, The Pennsylvania State University, University Park, PA.
- Rochat, J. L., and Sparrow, V. W. (1996). "Two-dimensional focusing of sonic boom noise penetrating an air-water interface," *AIAA J.* **35**(1), 35–39; also AIAA Paper 96–1751, AIAA/CEAS 2nd Aeroacoustics Conference, State College, PA.
- Rochat, J. L., and Sparrow, V. W. (1995). "Sound levels under the ocean due to sonic boom penetration," Proceedings, Inter-Noise 95, pp. 967–970.
- Sawyers, K. N. (1968). "Underwater sound pressure from sonic booms," *J. Acoust. Soc. Am.* **44**, 523–524.
- Sochacki, J. S., George, J. H., Ewing, R. E., and Smithson, S. B. (1991). "Interface conditions for acoustic and elastic wave propagation," *Geophysics* **56**, 168–181.
- Sparrow, V., and Ferguson, T. (1997). "Penetration of shaped sonic boom noise into a flat ocean," AIAA Paper 97–0486, 35th Aerospace Sciences Meeting and Exhibit, Reno, NV.
- Sparrow, V. W. (1995). "The effect of supersonic aircraft on the penetration of sonic boom noise into the ocean," *J. Acoust. Soc. Am.* **97**, 159–162.
- Sparrow, V. W., and Raspet, R. (1990). "Absorbing boundary conditions for a spherical monopole in a set of two-dimensional acoustics equations," *J. Acoust. Soc. Am.* **87**, 2422–2427.
- Stevens, S. S. (1972). "Perceived level of noise by Mark VII and decibels(E)," *J. Acoust. Soc. Am.* **51**, 575–601.
- Thorpe, S. A. (1982). "On the clouds of bubbles formed by breaking wind-waves in deep water, and their role in air-sea gas transfer," *Philos. Trans. R. Soc. London, Ser. A* **304**, 155–210.
- Urlick, R. J. (1972). "Noise signature of an aircraft in level flight over a hydrophone in the sea," *J. Acoust. Soc. Am.* **52**, 993–999.
- Vartabedian, R. (1994). "Launching supersonic dreams," *Los Angeles Times*, 1 June 1994.
- Waters, J. (1971). "Penetration of sonic boom energy into the ocean: An experimental simulation," in *Noise and Vibration Control Engineering*, edited by M. Crocker, Proceedings of the Purdue Noise Control Conference, pp. 554–557, 14–16 July 1971.
- Waters, J., and Glass, R. E. (1970). "Penetration of sonic boom energy into the ocean: An experimental simulation," Hydrospace Research Corp. Final Report on Contract FA70-WAI-185, HRC TR 288, June, available from NTIS/DTIC as AD 711 963.
- Wilhite, A. W., and Shaw, R. J. (1997). "HSCT research picks up speed," *Aerospace America*, pp. 24–29, 41, August.
- Williams, L. J. (1995). "HSCT research gathers speed," *Aerospace America*, pp. 32–37, April.
- Young, R. W. (1968). "Penetration of sonic booms into the ocean," *J. Acoust. Soc. Am.* **44**, 392.

A unified model for reverberation and submerged object scattering in a stratified ocean waveguide

Nicholas C. Makris and Purnima Ratilal

Department of Ocean Engineering, Massachusetts Institute of Technology, Cambridge, Massachusetts 02139

(Received 24 March 2000; revised 14 September 2000; accepted 13 November 2000)

A unified model for reverberation and submerged target scattering in a stratified medium is developed from wave theory. The advantage of the unified approach is that it enables quantitative predictions to be made of the target-echo-to-reverberation ratio in an ocean waveguide. Analytic expressions are derived for both deterministic and stochastic scattering from the seafloor and subseafloor. Asymptotic techniques are used to derive expressions for the scattering of broadband waveforms from distant objects or surfaces. Expressions are then obtained for the scattered field after beamforming with a horizontal line array. The model is applied to problems of active detection in shallow water. Sample calculations for narrow-band signals indicate that the detection of submerged target echoes above diffuse seafloor reverberation is highly dependent upon water column and sediment stratification as well as array aperture, source, receiver, and target locations, in addition to the scattering properties of the target and seafloor. The model is also applied to determine the conditions necessary for echo returns from discrete geomorphologic features of the seafloor and subseafloor to stand prominently above diffuse seafloor reverberation. This has great relevance to the geologic clutter problem encountered by active sonar systems operating in shallow water, as well as to the remote sensing of underwater geomorphology. © 2001 Acoustical Society of America. [DOI: 10.1121/1.1339826]

PACS numbers: 43.30.Gv, 43.30.Hw, 43.30.Vh [DLB]

I. INTRODUCTION

A common problem in the active detection and localization of a radar or sonar target arises when scattered returns from the target become indistinguishable from returns from randomly rough boundaries, volume inhomogeneities, or deterministic features of the environment. The goal of the present article is to investigate the extent to which environmental reverberation limits the ability to detect and localize a target submerged in an ocean waveguide, where methods developed for the radar half-space problem are inapplicable due to the added complications of multi-modal propagation and dispersion.

To this end, a unified model for 3-D reverberation and submerged target scattering in a stratified medium is developed from wave theory. The model is fully *bistatic* and stems directly from Green's theorem, since it generalizes Ingenito's approach^{1,2} for harmonic scattering in a stratified medium by incorporating stochastic scatterers and time-dependent sources. While it is consistent with certain narrow-band results of previous "heuristic" derivations³⁻⁷ for shallow water reverberation measured with an omni-directional receiver that are based on the work of Bucker and Morris,⁴ it offers more insight and generality since it is developed from first principles with explicitly stated assumptions. For example, it clearly obeys reciprocity for source-receiver locations within a layered media, which is important in properly modeling the absolute level of returns from targets or surfaces within the seafloor, and it allows absolute comparison between reverberation and deterministic target returns. Such comparison led to inconsistencies in previous formulations as noted in Ref. 3. It also provides analytic expressions for the three-dimensional (3-D) field scattered bistatically by

both stochastic and deterministic objects from a source with arbitrary time function, as well as the associated spatial and temporal covariances. This enables realistic modeling of the moments of the raw reverberant field received over extended spatial and temporal apertures as well as the output after subsequent processing with standard beamforming and broadband signal processing techniques. In the present article, applications of the theory are restricted to systems which employ the beamforming and temporally incoherent processing widely used in narrow-band signal reception. Analytic expressions for the statistical moments of the scattered field are obtained directly, but can also be obtained by sample averaging over realizations by Monte Carlo simulations, as for example is done for rough surface scattering in Ref. 8. The relative merit of either approach depends on the relative difficulty in evaluating the analytically obtained moments or performing the Monte Carlo simulations for the given problem. The analytic approach has proven to be more advantageous and insightful for the illustrative examples of the present article.

The primary motivation for developing the unified model is to compare the absolute level of target echo returns with those from the seafloor and to investigate how these vary in both absolute and relative level as a function of water column and sediment stratification, receiving array aperture, and source, receiver, and target locations in a shallow water waveguide. Another major focus of the present article is to investigate the manner in which scattering from both extended geomorphologic features and randomly rough patches of the seafloor and subseafloor contribute to measured reverberation. The latter typically makes up the diffuse reverberant background, which has an expected intensity that decays

in time after the arrival of the direct signal waveform. The former typically leads to geological clutter, which is defined as any set of acoustic returns from the seabed that stand significantly above the diffuse and temporally decaying reverberation background. Geological clutter is a primary problem in active sonar operations in shallow water. This is because the clutter can be confused with or camouflage returns intended from a submerged target.

A goal of this work is then to determine plausible physical mechanisms for geological clutter by use of the unified model. To do so, both first-order perturbation theory and empirical Lambert–Mackenzie⁹ models are used to describe stochastic scattering from a randomly rough seafloor. These models, together with deterministic models for scattering from seafloor features, are used to determine scenarios where geologic clutter is significant. The present focus is on seafloor features with mean surfaces that are finite and inclined with the reflection properties of the layer to which they belong, since such features are ubiquitous in continental shelf waters. While a large literature exists for scattering from 2-D features in a waveguide, the focus of the present work is on scattering from 3-D features in a waveguide. Apparently, the only previous work on deterministic scattering from 3-D seafloor features in a waveguide has been for acoustically compact ($ka \ll 1$) protrusions on perfectly reflecting bottoms,¹⁰ but compact targets are too weak to comprise geological clutter in a long-range active sonar system and are not relevant to the present analysis. A review of the general literature on 3-D scattering in an ocean waveguide is given in Ref. 11. All illustrative examples in the present article employ time-windowed cw source waveforms and monostatic geometries to investigate the central detection issues with as simple an approach as possible.

II. THE UNIFIED MODEL

A. The single-scatter approximation for 3-D scattering from an object of arbitrary shape in a layered medium

A number of simplifying conditions¹¹ that apply to a wide variety of active sonar problems in the ocean enable the field scattered from an object submerged in a stratified medium to be approximated, from Green's exact theorem, as a linear function of the object's plane wave scatter function.¹² The plane wave scatter function $S(\theta, \phi; \theta_i, \phi_i)$ at frequency f is defined in Appendix A, where its relationship to Green's theorem and the traditional target strength and scattering strength measures of ocean acoustics is explained.

To formulate the unified model, it is convenient to initially follow Refs. 1, 2, and 11 by placing the object centroid at the center of all coordinate systems. The source coordinates are then defined by (x_0, y_0, z_0) , receiver coordinates by (x, y, z) , and coordinates on the surface of the object by (x_t, y_t, z_t) where the positive z axis points downward and normal to the interfaces between horizontal strata. Spatial cylindrical (ρ, θ, z) and spherical systems (r, θ, ϕ) are defined by $x = r \sin \theta \cos \phi$, $y = r \sin \theta \sin \phi$, $z = r \cos \theta$, and $\rho^2 = x^2 + y^2$. The horizontal and vertical wave number components for the n th mode are respectively $\xi_n = k \sin \alpha_n$ and

$\gamma_n = k \cos \alpha_n$, where $k^2 = \xi_n^2 + \gamma_n^2$ and the wave number magnitude k equals the angular frequency ω divided by the sound speed c in the target layer.

The spectral component of the scattered field for a time-harmonic source of frequency f at \mathbf{r}_0 and a receiver at \mathbf{r} then becomes

$$\Phi_s(\mathbf{r}|\mathbf{r}_0) \approx \sum_{m=1}^{\infty} \sum_{n=1}^{\infty} \Phi_s^{(m,n)}(\mathbf{r}|\mathbf{r}_0), \quad (1a)$$

where

$$\begin{aligned} \Phi_s^{(m,n)}(\mathbf{r}|\mathbf{r}_0) = & \frac{4\pi}{k} [A_m(\mathbf{r})A_n(\mathbf{r}_0)S(\pi - \alpha_m, \phi; \alpha_n, \phi_0 + \pi) \\ & - B_m(\mathbf{r})A_n(\mathbf{r}_0)S(\alpha_m, \phi; \alpha_n, \phi_0 + \pi) \\ & - A_m(\mathbf{r})B_n(\mathbf{r}_0)S(\pi - \alpha_m, \phi; \pi - \alpha_n, \phi_0 + \pi) \\ & + B_m(\mathbf{r})B_n(\mathbf{r}_0)S(\alpha_m, \phi; \pi - \alpha_n, \phi_0 + \pi)], \end{aligned} \quad (1b)$$

and

$$A_m(\mathbf{r}) = \frac{i}{d(0)} (8\pi\xi_m\rho)^{-1/2} u_m(z) N_m^- e^{i(\xi_m\rho + \gamma_m D - \pi/4)}, \quad (2a)$$

$$B_m(\mathbf{r}) = \frac{i}{d(0)} (8\pi\xi_m\rho)^{-1/2} u_m(z) N_m^+ e^{i(\xi_m\rho - \gamma_m D - \pi/4)}, \quad (2b)$$

$$A_n(\mathbf{r}_0) = \frac{i}{d(z_0)} (8\pi\xi_n\rho_0)^{-1/2} u_n(z_0) N_n^- e^{i(\xi_n\rho_0 + \gamma_n D - \pi/4)}, \quad (2c)$$

$$B_n(\mathbf{r}_0) = \frac{i}{d(z_0)} (8\pi\xi_n\rho_0)^{-1/2} u_n(z_0) N_n^+ e^{i(\xi_n\rho_0 - \gamma_n D - \pi/4)}, \quad (2d)$$

are the down- and up-going plane wave amplitudes in the layer of the object, D is the depth of the object center from the sea surface, $d(z)$ is the density at depth z , and $u_n(z)$ are the mode functions. The product of $e^{-i2\pi ft}$ and the right-hand side of Eq. (1a) yields the time-harmonic scattered field. The mode functions are normalized¹³ according to

$$\delta_{nm} = \int_{-D}^{\infty} \frac{u_m^*(z)u_n(z)}{d(z)} dz, \quad (3)$$

and must be decomposable into up- and down-going plane waves via

$$u_n(z) = N_n^- e^{i\gamma_n(z+D)} - N_n^+ e^{-i\gamma_n(z+D)} \quad (4)$$

in the layer of the object, where N_n^- and N_n^+ are the amplitudes of down- and up-going plane waves in this layer. In a Pekeris waveguide, for example,

$$N_n^- = N_n^+ = \frac{\sqrt{2}}{2i} \left[\frac{1}{d} \left(H - \frac{\sin 2\gamma_n H}{2\gamma_n} \right) + \frac{1}{d_b} \frac{\sin^2 \gamma_n H}{\sqrt{\xi_n^2 - (\omega/c_b)^2}} \right]^{-1/2}, \quad (5)$$

where d_b and c_b are the density and sound speed of the bottom. If the mode functions are specified at any two depths, z_1 and z_2 within the target layer, the down- and up-going plane wave amplitudes can be readily obtained as

$$\begin{bmatrix} N_n^- \\ -N_n^+ \end{bmatrix} = \begin{bmatrix} e^{i\gamma_n(z_1+D)} & e^{-i\gamma_n(z_1+D)} \\ e^{i\gamma_n(z_2+D)} & e^{-i\gamma_n(z_2+D)} \end{bmatrix}^{-1} \begin{bmatrix} u_n(z_1) \\ u_n(z_2) \end{bmatrix}. \quad (6)$$

Equations (1)–(6) for the scattered field from an arbitrarily shaped object in a waveguide differ from Ingenito's formulation¹ in a number of ways. The most substantial difference is that, by inclusion of Eqs. (4) and (6), they explicitly show how the scattered field for an arbitrarily shaped object can be computed in a stratified medium. Ingenito also defines the plane wave scatter function differently than most standard texts by describing the incident plane wave in terms of *the direction it comes from* rather than *the direction it goes to*. The latter, standard approach, is adopted here.

Finally, the more standard mode function normalization of Ref. 13 is adopted here, so that Eq. (1) obeys reciprocity as defined in Appendix A2 of Ref. 13, so that $d(z_0)\Phi_s(\mathbf{r}|\mathbf{r}_0) = d(z)\Phi_s(\mathbf{r}_0|\mathbf{r})$. Satisfaction of reciprocity becomes important for an approach if it is to yield accurate estimates of the scattered field when the source, receiver, and target are in layers that have significantly different densities, and is a natural consequence of the use of Green's theorem in the present formulation, but has been left unaddressed as an issue in previous heuristic reverberation formulations.^{3–7} The issue becomes of practical concern in modeling the level of returns from targets or surfaces buried in the seafloor from sonar systems operating in the water column above.

A more general expression than Eqs. (1)–(6), for the scattered field from an arbitrarily shaped object in a stratified medium, is given in Refs. 2 and 11 in terms of wave number integrals. As noted in Ref. 11, the more general wave num-

ber formulation is valid when (1) the propagation medium is horizontally stratified and range independent; (2) the object is contained within an iso-velocity layer; (3) multiple reflections between the *object* and waveguide boundaries make a negligible contribution at the receiver; and (4) the range from the object to source or receiver is large enough that the scattered field can be expressed as a linear function of the object's plane wave scatter function. All of these conditions then must be satisfied for Eqs. (1)–(6) to be valid, with one additional constraint. The ranges involved must be large enough that the Green's functions, from source-to-target and target-to-receiver, are accurately approximated as sums of discrete modes. The latter is an expected consequence of the Riemann–Lebesgue lemma.¹⁴ The present formulation and its spectral equivalent have been implemented for target scattering in a waveguide over the full 360-degree span of bistatic angles in Refs. 1, 2 and 11. It is noteworthy that this formulation includes the scattering of evanescent waves by analytic continuation of the scatter function, as has been previously discussed and implemented in Refs. 2 and 11, as well as in Ref. 8 which uses a formulation similar to Ingenito's.

B. The field scattered from general stochastic targets

By allowing the scatter function for the object to be a random variable, the single-scatter formulation of the previous section applies to the more general problem of scattering from a stochastic target submerged in a waveguide. This approach is particularly valuable in modeling scattering from targets of unknown shape or orientation, randomly rough surface interfaces, or stochastic volume heterogeneities, all of which can contribute significantly to the reverberant field measured in shallow water.

The moments of the scattered field can be derived analytically to determine its expected behavior. The mean field, for example, becomes

$$\langle \Phi_s(\mathbf{r}|\mathbf{r}_0) \rangle \approx \sum_{m=1}^{\infty} \sum_{n=1}^{\infty} \langle \Phi_s^{(m,n)}(\mathbf{r}|\mathbf{r}_0) \rangle, \quad (7)$$

where

$$\begin{aligned} \langle \Phi_s^{(m,n)}(\mathbf{r}|\mathbf{r}_0) \rangle &= \frac{4\pi}{k} [A_m(\mathbf{r})A_n(\mathbf{r}_0)\langle S(\pi - \alpha_m, \phi; \alpha_n, \phi_0 + \pi) \rangle - B_m(\mathbf{r})A_n(\mathbf{r}_0)\langle S(\alpha_m, \phi; \alpha_n, \phi_0 + \pi) \rangle \\ &\quad - A_m(\mathbf{r})B_n(\mathbf{r}_0)\langle S(\pi - \alpha_m, \phi; \pi - \alpha_n, \phi_0 + \pi) \rangle + B_m(\mathbf{r})B_n(\mathbf{r}_0)\langle S(\alpha_m, \phi; \pi - \alpha_n, \phi_0 + \pi) \rangle] \end{aligned} \quad (8)$$

while the mutual intensity of the field scattered for receivers at \mathbf{r} and \mathbf{r}' becomes

$$\langle \Phi_s(\mathbf{r}|\mathbf{r}_0)\Phi_s^*(\mathbf{r}'|\mathbf{r}_0) \rangle \approx \sum_{m=1}^{\infty} \sum_{n=1}^{\infty} \sum_{m'=1}^{\infty} \sum_{n'=1}^{\infty} \langle \Phi_s^{(m,n)}(\mathbf{r}|\mathbf{r}_0)\Phi_s^{(m',n')}(\mathbf{r}'|\mathbf{r}_0) \rangle, \quad (9)$$

where

$$\begin{aligned} \langle \Phi_s^{(m,n)}(\mathbf{r}|\mathbf{r}_0)\Phi_s^{(m',n')}(\mathbf{r}'|\mathbf{r}_0) \rangle &= \left(\frac{4\pi}{k} \right)^2 [A_m(\mathbf{r})A_n(\mathbf{r}_0)A_{m'}^*(\mathbf{r}')A_{n'}^*(\mathbf{r}_0)\langle S(\pi - \alpha_m, \phi; \alpha_n, \phi_0 + \pi)S^*(\pi - \alpha_{m'}, \phi'; \alpha_{n'}, \phi_0 + \pi) \rangle \\ &\quad - A_m(\mathbf{r})A_n(\mathbf{r}_0)B_{m'}^*(\mathbf{r}')A_{n'}^*(\mathbf{r}_0)\langle S(\pi - \alpha_m, \phi; \alpha_n, \phi_0 + \pi)S^*(\alpha_{m'}, \phi'; \alpha_{n'}, \phi_0 + \pi) \rangle \\ &\quad - A_m(\mathbf{r})A_n(\mathbf{r}_0)A_{m'}^*(\mathbf{r}')B_{n'}^*(\mathbf{r}_0)\langle S(\pi - \alpha_m, \phi; \alpha_n, \phi_0 + \pi)S^*(\pi - \alpha_{m'}, \phi'; \pi - \alpha_{n'}, \phi_0 + \pi) \rangle \\ &\quad - A_m(\mathbf{r})A_n(\mathbf{r}_0)B_{m'}^*(\mathbf{r}')B_{n'}^*(\mathbf{r}_0)\langle S(\pi - \alpha_m, \phi; \alpha_n, \phi_0 + \pi)S^*(\alpha_{m'}, \phi'; \pi - \alpha_{n'}, \phi_0 + \pi) \rangle] \end{aligned}$$

$$\begin{aligned}
& + A_m(\mathbf{r})A_n(\mathbf{r}_0)B_m^*(\mathbf{r}')B_n^*(\mathbf{r}_0)\langle S(\pi-\alpha_m, \phi; \alpha_n, \phi_0+\pi)S^*(\alpha_{m'}, \phi'; \pi-\alpha_{n'}, \phi_0+\pi)\rangle \\
& - B_m(\mathbf{r})A_n(\mathbf{r}_0)A_m^*(\mathbf{r}')A_n^*(\mathbf{r}_0)\langle S(\alpha_m, \phi; \alpha_n, \phi_0+\pi)S^*(\pi-\alpha_{m'}, \phi'; \alpha_{n'}, \phi_0+\pi)\rangle \\
& + B_m(\mathbf{r})A_n(\mathbf{r}_0)B_m^*(\mathbf{r}')A_n^*(\mathbf{r}_0)\langle S(\alpha_m, \phi; \alpha_n, \phi_0+\pi)S^*(\alpha_{m'}, \phi'; \alpha_{n'}, \phi_0+\pi)\rangle \\
& + B_m(\mathbf{r})A_n(\mathbf{r}_0)A_m^*(\mathbf{r}')B_n^*(\mathbf{r}_0)\langle S(\alpha_m, \phi; \alpha_n, \phi_0+\pi)S^*(\pi-\alpha_{m'}, \phi'; \pi-\alpha_{n'}, \phi_0+\pi)\rangle \\
& - B_m(\mathbf{r})A_n(\mathbf{r}_0)B_m^*(\mathbf{r}')B_n^*(\mathbf{r}_0)\langle S(\alpha_m, \phi; \alpha_n, \phi_0+\pi)S^*(\alpha_{m'}, \phi'; \pi-\alpha_{n'}, \phi_0+\pi)\rangle \\
& - A_m(\mathbf{r})B_n(\mathbf{r}_0)A_m^*(\mathbf{r}')A_n^*(\mathbf{r}_0)\langle S(\pi-\alpha_m, \phi; \pi-\alpha_n, \phi_0+\pi)S^*(\pi-\alpha_{m'}, \phi'; \alpha_{n'}, \phi_0+\pi)\rangle \\
& + A_m(\mathbf{r})B_n(\mathbf{r}_0)B_m^*(\mathbf{r}')A_n^*(\mathbf{r}_0)\langle S(\pi-\alpha_m, \phi; \pi-\alpha_n, \phi_0+\pi)S^*(\alpha_{m'}, \phi'; \alpha_{n'}, \phi_0+\pi)\rangle \\
& + A_m(\mathbf{r})B_n(\mathbf{r}_0)A_m^*(\mathbf{r}')B_n^*(\mathbf{r}_0)\langle S(\pi-\alpha_m, \phi; \pi-\alpha_n, \phi_0+\pi)S^*(\pi-\alpha_{m'}, \phi'; \pi-\alpha_{n'}, \phi_0+\pi)\rangle \\
& - A_m(\mathbf{r})B_n(\mathbf{r}_0)B_m^*(\mathbf{r}')B_n^*(\mathbf{r}_0)\langle S(\pi-\alpha_m, \phi; \pi-\alpha_n, \phi_0+\pi)S^*(\alpha_{m'}, \phi'; \pi-\alpha_{n'}, \phi_0+\pi)\rangle \\
& + B_m(\mathbf{r})B_n(\mathbf{r}_0)A_m^*(\mathbf{r}')A_n^*(\mathbf{r}_0)\langle S(\alpha_m, \phi; \pi-\alpha_n, \phi_0+\pi)S^*(\pi-\alpha_{m'}, \phi'; \alpha_{n'}, \phi_0+\pi)\rangle \\
& - B_m(\mathbf{r})B_n(\mathbf{r}_0)B_m^*(\mathbf{r}')A_n^*(\mathbf{r}_0)\langle S(\alpha_m, \phi; \pi-\alpha_n, \phi_0+\pi)S^*(\alpha_{m'}, \phi'; \alpha_{n'}, \phi_0+\pi)\rangle \\
& - B_m(\mathbf{r})B_n(\mathbf{r}_0)A_m^*(\mathbf{r}')B_n^*(\mathbf{r}_0)\langle S(\alpha_m, \phi; \pi-\alpha_n, \phi_0+\pi)S^*(\pi-\alpha_{m'}, \phi'; \pi-\alpha_{n'}, \phi_0+\pi)\rangle \\
& + B_m(\mathbf{r})B_n(\mathbf{r}_0)B_m^*(\mathbf{r}')B_n^*(\mathbf{r}_0)\langle S(\alpha_m, \phi; \pi-\alpha_n, \phi_0+\pi)S^*(\alpha_{m'}, \phi'; \pi-\alpha_{n'}, \phi_0+\pi)\rangle].
\end{aligned} \tag{10}$$

The spatial covariance, or cross spectral density, of the scattered field,

$$\begin{aligned}
& \langle \Phi_s(\mathbf{r}|\mathbf{r}_0)\Phi_s^*(\mathbf{r}'|\mathbf{r}_0)\rangle - \langle \Phi_s(\mathbf{r}|\mathbf{r}_0)\rangle\langle \Phi_s^*(\mathbf{r}'|\mathbf{r}_0)\rangle \\
& \approx \sum_{m=1}^{\infty} \sum_{n=1}^{\infty} \sum_{m'=1}^{\infty} \sum_{n'=1}^{\infty} \langle \Phi_s^{(m,n)}(\mathbf{r}|\mathbf{r}_0)\Phi_s^{(m',n')*}(\mathbf{r}'|\mathbf{r}_0)\rangle \\
& \quad - \langle \Phi_s^{(m,n)}(\mathbf{r}|\mathbf{r}_0)\rangle\langle \Phi_s^{(m',n')*}(\mathbf{r}'|\mathbf{r}_0)\rangle,
\end{aligned} \tag{11}$$

follows directly from Eqs. (7)–(10), and has been implemented for fluctuating targets submerged in an ocean waveguide.¹⁵

C. When scattering statistically decorrelates the waveguide modes

Many useful scattering properties of a random target are described by the covariance of its scatter function, which couples incident modes with n and n' subscripts together with scattered modes with m and m' subscripts in the cross spectral density of Eq. (11). Under many situations of practical interest in the scattering from fluctuating targets or randomly rough surfaces, the n and n' incident modes decouple as do the scattered m and m' modes.

Assume that the random target's characteristic dimension L is large compared to the wavelength λ and that for any realization it has complicated structure with significant variations on the wavelength scale. These assumptions are used extensively in radar to describe fluctuating targets,^{16,17} such as aircraft of unknown shape and orientation, and in radar, statistical optics, and acoustics to describe scattering from randomly rough surfaces.^{18–20} They typically lead to circular complex Gaussian random (CCGR) fluctuations in the scattered field over different statistical realizations of the

target.^{16–21} When the target is a randomly rough surface, these assumptions are equivalent to restricting the correlation length of the surface roughness to be much smaller than the dimension L of the targeted surface. In this case the scattered field is usually termed *diffuse* or *incoherent* “because of its wide angular spread and lack of phase relationship with the incident wave.”¹⁸

For any realization of such a random surface or target, say for example the k th realization, its scatter function $S_k(\Omega; \Omega_i)$ will be highly oscillatory in magnitude and phase over both incident $\Omega_i = (\theta_i, \phi_i)$ and scattered $\Omega = (\theta, \phi)$ directions and will have a complicated lobe pattern. This lobe pattern will vary significantly over random realizations of the surface or target due to changes in constructive and destructive interference, making the scatter function representing all realizations $S(\Omega; \Omega_i)$ a random variable with zero expected value, $\langle S(\Omega; \Omega_i) \rangle = 0$. Due to the complicated structure of the target, the angular width of any lobe in the scatter function will be on the order of the minimum width set by diffraction of λ/L , which is small by assumption. The second moment of the scatter function $\langle S(\Omega; \Omega_i)S^*(\Omega'; \Omega'_i) \rangle$ for incident angles Ω_i, Ω'_i and scattered angles Ω, Ω' can be thought of as an ensemble average of $S_k(\Omega; \Omega_i)S_k^*(\Omega'; \Omega'_i)$ over realizations of the random surface. This product will oscillate about zero across realizations k for $|\Omega_i - \Omega'_i| > \lambda/L$ and $|\Omega - \Omega'| > \lambda/L$ so that the ensemble average will tend to zero due to term by term cancellation. Here λ/L behaves as an angular correlation width of the scatter function over variations in both incident and scattered angle. The product will tend to become positive definite for $|\Omega_i - \Omega'_i| \leq \lambda/L, |\Omega - \Omega'| \leq \lambda/L$, however, so that the ensemble average will approach $\langle |S(\Omega; \Omega_i)|^2 \rangle$.

Applying this reasoning to stochastic targets or surface

patches in a waveguide, the covariance of the scatter function can be written as

$$\begin{aligned} & \langle S(\alpha_m, \phi; \alpha_n, \phi_0 + \pi) S^*(\alpha_{m'}, \phi'; \alpha_{n'}, \phi_0 + \pi) \rangle - \langle S(\alpha_m, \phi; \alpha_n, \phi_0 + \pi) \rangle \langle S^*(\alpha_{m'}, \phi'; \alpha_{n'}, \phi_0 + \pi) \rangle \\ & = \delta_{nn'} \delta_{mm'} C_{mn}(\mathbf{r}, \mathbf{r}' | \mathbf{r}_0), \end{aligned} \quad (12a)$$

where

$$C_{mn}(\mathbf{r}, \mathbf{r}' | \mathbf{r}_0) = \langle S(\alpha_m, \phi; \alpha_n, \phi_0 + \pi) S^*(\alpha_m, \phi'; \alpha_n, \phi_0 + \pi) \rangle - \langle S(\alpha_m, \phi; \alpha_n, \phi_0 + \pi) \rangle \langle S^*(\alpha_m, \phi'; \alpha_n, \phi_0 + \pi) \rangle, \quad (12b)$$

when the angular separation $|\alpha_n - \alpha_{n'}|$ between modes n and n' is greater than the angular correlation width λ/L set by diffraction. In practical scenarios, this criterion will apply most stringently to the dominant modes, where full decorrelation will occur for $|\alpha_{n+1} - \alpha_n|$ on the order or greater than λ/L . For trapped modes, $|\alpha_{n+1} - \alpha_n|$ is less than the critical angle of the bottom.

Insertion of Eq. (12a) into Eq. (11) then leads to a great simplification in the spatial covariance of the scattered field

$$\begin{aligned} & \langle \Phi_s(\mathbf{r} | \mathbf{r}_0) \Phi_s^*(\mathbf{r}' | \mathbf{r}_0) \rangle - \langle \Phi_s(\mathbf{r} | \mathbf{r}_0) \rangle \langle \Phi_s^*(\mathbf{r}' | \mathbf{r}_0) \rangle \\ & \approx \sum_{m=1}^{\infty} \sum_{n=1}^{\infty} \langle \Phi_s^{(m,n)}(\mathbf{r} | \mathbf{r}_0) \Phi_s^{(m,n)*}(\mathbf{r}' | \mathbf{r}_0) \rangle \\ & \quad - \langle \Phi_s^{(m,n)}(\mathbf{r} | \mathbf{r}_0) \rangle \langle \Phi_s^{(m,n)*}(\mathbf{r}' | \mathbf{r}_0) \rangle, \end{aligned} \quad (13)$$

where the quadrupole modal sum reduces to a double modal sum.

D. The field scattered from a randomly rough or inhomogeneous seabed

When the scattering is due to a randomly rough seafloor patch, a great simplification occurs in the form of the mutual intensity. Of the 16 parenthetical terms of Eq. (10), only 1 represents a down-going incident wave coupling to an up-going scattered wave. Accordingly, the field scattered into the waveguide from a randomly rough seafloor patch of area ΔA , as defined in Appendix A, must have mutual intensity given by Eq. (9) with

$$\begin{aligned} & \langle \Phi_s^{(m,n)}(\mathbf{r} | \mathbf{r}_0) \Phi_s^{(m',n')*}(\mathbf{r}' | \mathbf{r}_0) \rangle \\ & = \left(\frac{4\pi}{k} \right)^2 [B_m(\mathbf{r}) A_n(\mathbf{r}_0) B_{m'}^*(\mathbf{r}') A_{n'}^*(\mathbf{r}_0) \\ & \quad \times \langle S(\alpha_m, \phi; \alpha_n, \phi_0 + \pi) S^*(\alpha_{m'}, \phi'; \alpha_{n'}, \phi_0 + \pi) \rangle], \end{aligned} \quad (14)$$

and cross spectral density given by Eq. (11) with

$$\begin{aligned} & \langle \Phi_s^{(m,n)}(\mathbf{r} | \mathbf{r}_0) \Phi_s^{(m',n')*}(\mathbf{r}' | \mathbf{r}_0) \rangle - \langle \Phi_s^{(m,n)}(\mathbf{r} | \mathbf{r}_0) \rangle \langle \Phi_s^{(m',n')*}(\mathbf{r}' | \mathbf{r}_0) \rangle \\ & = \left(\frac{4\pi}{k} \right)^2 B_m(\mathbf{r}) A_n(\mathbf{r}_0) B_{m'}^*(\mathbf{r}') A_{n'}^*(\mathbf{r}_0) \{ \langle S(\alpha_m, \phi; \alpha_n, \phi_0 + \pi) S^*(\alpha_{m'}, \phi'; \alpha_{n'}, \phi_0 + \pi) \rangle \\ & \quad - \langle S(\alpha_m, \phi; \alpha_n, \phi_0 + \pi) \rangle \langle S^*(\alpha_{m'}, \phi'; \alpha_{n'}, \phi_0 + \pi) \rangle \}. \end{aligned} \quad (15)$$

The cross spectral density is more useful in describing the stochastic scattering properties of a randomly rough seafloor patch than the mutual intensity because deterministic effects, such as specular reflection, coherent beaming, and forward scattering, are removed with the expected field. In diffuse surface scattering problems, where the surface scattering patch must be much larger than the wavelength, the expected value of the scattered field is typically negligible away from the specular direction due to random interference. The cross spectral density and mutual intensity then become effectively indistinguishable.

With the assumption of diffuse scattering described in the previous section, which is supported by a large amount of experimental evidence,^{18,22} application of Eq. (12a) yields

$$\begin{aligned} & \langle \Phi_s^{(m,n)}(\mathbf{r} | \mathbf{r}_0) \Phi_s^{(m',n')*}(\mathbf{r}' | \mathbf{r}_0) \rangle \\ & \quad - \langle \Phi_s^{(m,n)}(\mathbf{r} | \mathbf{r}_0) \rangle \langle \Phi_s^{(m',n')*}(\mathbf{r}' | \mathbf{r}_0) \rangle \\ & = \delta_{mm'} \delta_{nn'} C_{mn}(\mathbf{r}, \mathbf{r}' | \mathbf{r}_0) B_m(\mathbf{r}) A_n(\mathbf{r}_0) B_{m'}^*(\mathbf{r}') A_{n'}^*(\mathbf{r}_0) \\ & \quad \times \left(\frac{4\pi}{k} \right)^2, \end{aligned} \quad (16)$$

which leads to a great simplification in the scattered field covariance:

$$\begin{aligned} & \langle \Phi_s(\mathbf{r} | \mathbf{r}_0) \Phi_s^*(\mathbf{r}' | \mathbf{r}_0) \rangle - \langle \Phi_s(\mathbf{r} | \mathbf{r}_0) \rangle \langle \Phi_s^*(\mathbf{r}' | \mathbf{r}_0) \rangle \\ & = \left(\frac{4\pi}{k} \right)^2 \sum_{m=1}^{\infty} \sum_{n=1}^{\infty} B_m(\mathbf{r}) B_m^*(\mathbf{r}') |A_n(\mathbf{r}_0)|^2 C_{mn}(\mathbf{r}, \mathbf{r}' | \mathbf{r}_0). \end{aligned} \quad (17)$$

If the seafloor is taken as an aggregate of range-dependent scattering patches and if these are each small enough to have little effect on the mean forward field, Eq. (17) provides a good approximation to the cross spectral density after forward propagating through this mildly range-dependent waveguide and then scattering in a specified direction from the given patch.

It is noteworthy that a formulation in terms of wave number integrals is not convenient in describing the statistical equipartition of energy associated with diffuse scattering since the modes are the entities that describe the system's degrees of freedom rather than the wave number components.

E. General saddle point approximation for the scattered field in time from a distant object

For a source with general time dependence

$$q(t) = \int_{-\infty}^{\infty} Q(f) e^{-i2\pi ft} df, \quad (18)$$

and spectrum

$$Q(f) = \int_{-\infty}^{\infty} q(t) e^{i2\pi ft} dt, \quad (19)$$

the scattered field as a function of time from an object with center at the origin becomes

$$\Psi_s(\mathbf{r}|\mathbf{r}_0|t) = \int_{-\infty}^{\infty} Q(f) \Phi_s(\mathbf{r}|\mathbf{r}_0) e^{-i2\pi ft} df, \quad (20)$$

where Eq. (1) can be rewritten as

$$\Phi_s(\mathbf{r}|\mathbf{r}_0) = \sum_{m=1} \sum_{n=1} \Lambda_{mn}(\mathbf{r}|\mathbf{r}_0, f) e^{i\rho_0 \xi_n + i\rho \xi_m}, \quad (21)$$

so that

$$\Psi_s(\mathbf{r}|\mathbf{r}_0|t) = \sum_{m=1} \sum_{n=1} \int_{-\infty}^{\infty} Q(f) \Lambda_{mn}(\mathbf{r}|\mathbf{r}_0, f) e^{i\rho \psi_{mn}(f)} df, \quad (22)$$

where

$$\Lambda_{mn}(\mathbf{r}|\mathbf{r}_0, f) = \Phi_s^{(m,n)}(\mathbf{r}|\mathbf{r}_0) e^{-i\rho_0 \xi_n - i\rho \xi_m}, \quad (23)$$

and

$$\psi_{mn}(f) = \frac{\rho_0}{\rho} \xi_n + \xi_m - 2\pi f \frac{t}{\rho}. \quad (24)$$

By application of the saddle point method, for large ρ , assuming ρ_0/ρ and t/ρ are fixed,

$$\begin{aligned} \Psi_s(\mathbf{r}|\mathbf{r}_0|t) \approx & \sum_{l=1} \sum_{m=1} \sum_{n=1} \sqrt{\frac{2\pi}{\rho \psi''(f_{lmn})}} \\ & \times Q(f_{lmn}) \Lambda_{nm}(\mathbf{r}|\mathbf{r}_0, f_{lmn}) \\ & \times e^{i\rho \psi_{mn}(f_{lmn}) + (\pm i\pi/4)_{lmn}}, \end{aligned} \quad (25)$$

where the relevant saddle points f_{lmn} are determined by solving the equation

$$\left. \frac{d\psi_{mn}(f)}{df} \right|_{f=f_{lmn}} = 0, \quad (26)$$

and choosing the complex roots that lead to a finite solution of Eq. (24) as ρ and ρ_0 increase, where l is the index for multiple roots given n and m . Such solutions do not exist before the wave packet has arrived or after it has passed the receiver. Equation (24) can also be written more conveniently as

$$\begin{aligned} \Psi_s(\mathbf{r}|\mathbf{r}_0|t) \approx & \sum_{l=1} \sum_{m=1} \sum_{n=1} Q(f_{lmn}) \sqrt{\frac{2\pi}{\rho \psi''(f_{lmn})}} \\ & \times \Phi_s^{(n,m)}(\mathbf{r}|\mathbf{r}_0)|_{f=f_{lmn}} e^{-i2\pi t f_{lmn} + (\pm i\pi/4)_{lmn}}, \end{aligned} \quad (27)$$

where the frequencies f_{lmn} for each n to m mode conversion must be evaluated at each time and source and receiver range. Equation (27) is also obtained if, analogously, ρ_0 is made large and t/ρ_0 held fixed in Eqs. (22)–(24). Typically, both ρ and ρ_0 will be sufficiently large for the saddle point method approximation to hold whenever the modal formulation of Sec. II A, which also requires large ρ and ρ_0 , is valid.

The covariance of the scattered field at time t from a distant stochastic target then becomes

$$\begin{aligned} & \langle \Psi_s(\mathbf{r}|\mathbf{r}_0|t) \Psi_s^*(\mathbf{r}'|\mathbf{r}_0|t) \rangle - \langle \Psi_s(\mathbf{r}|\mathbf{r}_0|t) \rangle \langle \Psi_s^*(\mathbf{r}'|\mathbf{r}_0|t) \rangle \\ & \approx \sum_{l=1} \sum_{m=1} \sum_{n=1} \sum_{l'=1} \sum_{m'=1} \sum_{n'=1} Q(f_{lmn}) Q^*(f_{l'm'n'}) \\ & \times \frac{2\pi}{\sqrt{\rho \rho' \psi''(f_{lmn}) \psi''^*(f_{l'm'n'})}} \\ & \times e^{-i2\pi t(f_{lmn} - f_{l'm'n'}^*) + (\pm i\pi/4)_{lmn} - (\pm i\pi/4)_{l'm'n'}} \\ & \times \{ \langle \Phi_s^{(m,n)}(\mathbf{r}|\mathbf{r}_0)|_{f=f_{lmn}} \Phi_s^{(m',n')*}(\mathbf{r}'|\mathbf{r}_0)|_{f=f_{l'm'n'}} \rangle \\ & - \langle \Phi_s^{(m,n)}(\mathbf{r}|\mathbf{r}_0)|_{f=f_{lmn}} \rangle \langle \Phi_s^{(m',n')*}(\mathbf{r}'|\mathbf{r}_0)|_{f=f_{l'm'n'}} \rangle \} \end{aligned} \quad (28)$$

by substitution of Eq. (1a) as appropriate for the given scattering scenario.

It can now be seen that the basic equation of Ref. 3, Eq. (9), which appears without stated restrictions, is not generally valid, except under certain narrow-band conditions. Also, the present analysis indicates that the group velocity cannot generally be treated as a frequency-independent quantity as it is in the development of Ref. 3, where a number of narrow-band assumptions have apparently been made implicitly, as may be seen by also consulting Refs. 7 and 23, for example.

F. An absolute reference frame

To compute reverberation from wide and heterogeneous areas of seafloor or a number of distributed scatterers, it is convenient to recast Eq. (1) in terms of an absolute, rather than target-centered, spatial coordinate system. Let this system be defined by coordinates $\mathbf{R}=(X, Y, Z)$ whose axes are

parallel to those of the x, y, z target-centered system, where the positive Z axis is again downward pointing, but whose origin lies at the ocean surface, for example, where $z = -D$ in the target-oriented frame. In this more general frame, the source position is defined by $\mathbf{R}_0 = (X_0, Y_0, Z_0)$, the receiver positions by $\mathbf{R}_r = (X_r, Y_r, Z_r)$ and $\mathbf{R}'_r = (X'_r, Y'_r, Z'_r)$, and the center of a given scattering patch by $\mathbf{R} = (X, Y, Z)$, where, for example, $X = R \sin \vartheta \cos \varphi$, $Y = R \sin \vartheta \sin \varphi$, $Z = R \cos \vartheta$, and $R^2 = X^2 + Y^2 + Z^2$. The origin of all these coordinate systems are colocated and the axes are parallel. Spatial coordinates are translated from the target-oriented to the absolute frame by substituting $\mathbf{r} = \mathbf{R}_r - \mathbf{R}$, $\mathbf{r}' = \mathbf{R}'_r - \mathbf{R}$, and $\mathbf{r}_0 = \mathbf{R}_0 - \mathbf{R}$ in Eqs. (1) and (2). This leads, for example, to

$$A_m(\mathbf{R}_r - \mathbf{R}) = \frac{i u_m (Z_r - Z) N_m^-}{d(Z) (8 \pi \xi_m \sqrt{(X_r - X)^2 + (Y_r - Y)^2})^{1/2}} \times e^{i(\xi_m \sqrt{(X_r - X)^2 + (Y_r - Y)^2} + \gamma_m Z - \pi/4)}, \quad (29a)$$

$$B_m(\mathbf{R}_r - \mathbf{R}) = \frac{i u_m (Z_r - Z) N_m^+}{d(Z) (8 \pi \xi_m \sqrt{(X_r - X)^2 + (Y_r - Y)^2})^{1/2}} \times e^{i(\xi_m \sqrt{(X_r - X)^2 + (Y_r - Y)^2} - \gamma_m Z - \pi/4)} \quad (29b)$$

by making the substitutions

$$\begin{aligned} x_0 &= (X_0 - X), & y_0 &= (Y_0 - Y), \\ x &= (X_r - X), & y &= (Y_r - Y), \\ \rho_0 &= \sqrt{(X_0 - X)^2 + (Y_0 - Y)^2}, \\ \rho &= \sqrt{(X_r - X)^2 + (Y_r - Y)^2}, \\ z_0 &= Z_0 - Z, & z &= Z_r - Z, \end{aligned} \quad (30a)$$

in Eqs. (1) and (2), where

$$\begin{aligned} \cos \phi_0 &= x_0 / \rho_0, & \sin \phi_0 &= y_0 / \rho_0, \\ \cos \phi &= x / \rho, & \sin \phi &= y / \rho. \end{aligned} \quad (30b)$$

It must be stressed that the plane wave amplitudes and vertical wave numbers are evaluated in the layer of the scattering patch. The covariance of the scattering function for a given patch in the absolute, rather than object-oriented frame then becomes

$$C_{mn}(\mathbf{R}_r - \mathbf{R}, \mathbf{R}'_r - \mathbf{R} | \mathbf{R}_0 - \mathbf{R}) = C_{mn}(\mathbf{r}, \mathbf{r}' | \mathbf{r}_0). \quad (31)$$

III. SHALLOW WATER REVERBERATION

A. Reverberation in time

Reverberation, as measured with an active sonar system, is taken to be any and all echoes returning from the environment rather than the intended target. The characteristics of reverberation then depend not only on the environment but also the geometry of the source and receiver as well as the signal waveform. In field measurements, reverberation is measured as a function of time. It can often be decomposed into two components. The most prevalent is a diffuse component. This has instantaneous intensity that typically undergoes random fluctuations that obey the central limit theorem about an expected value that decays uniformly with time. For

reverberation to be diffuse, the scattering region that contributes to the intensity measured at a given instant must be large compared to the mean wavelength. This region, referred to as the system resolution footprint, will be considerably smaller for data beamformed with a high-resolution array than for data received by an omni-directional receiver. The second component, known as clutter, is here defined as any discrete temporal event, caused by an anomalous scatterer, that stands significantly above the diffuse reverberation background. Here ‘‘significantly above’’ means much more than one standard deviation in sound pressure level. For certain systems that employ high-resolution temporal processing and operate in weakly dispersive waveguides, there may be no diffuse component to the reverberation. In this case coherent temporal oscillations may be found in reverberant intensity measurements²⁴ that are due to modal interference as noted by Ellis.³ Lepage has recently investigated similar coherent effects under a narrow-band approximation for an omni-directional receiver.⁷

When the single-scatter approximation is valid, the total reverberant field measured at any time t for a time-harmonic source is simply the sum of the scattered fields from all environmental scatterers

$$\begin{aligned} \Phi_T(\mathbf{R}_r, \mathbf{R}_0) e^{-i2\pi f t} \\ = e^{-i2\pi f t} \int \int \int_V \Phi_s(\mathbf{R}_r - \mathbf{R} | \mathbf{R}_0 - \mathbf{R}) dX dY dZ. \end{aligned} \quad (32)$$

For a source with general time dependence $q(t)$, the total reverberant field becomes

$$\Psi_T(\mathbf{R}_r, \mathbf{R}_0 | t) = \int_{-\infty}^{\infty} Q(f) \Phi_T(\mathbf{R}_r, \mathbf{R}_0) e^{-i2\pi f t} df, \quad (33)$$

or equivalently

$$\Psi_T(\mathbf{R}_r, \mathbf{R}_0 | t) = \int \int \int_V \Psi_s(\mathbf{R}_r - \mathbf{R} | \mathbf{R}_0 - \mathbf{R} | t) dX dY dZ, \quad (34)$$

where $\Psi_s(\mathbf{R}_r - \mathbf{R} | \mathbf{R}_0 - \mathbf{R} | t)$ can be obtained directly from Eq. (25) for distant scatterers. The simplicity of this equation is deceptive. While it can be evaluated in a relatively straightforward manner for deterministic targets, its interpretation and implementation become far more difficult for stochastic targets. The covariance

$$\begin{aligned} \langle \Psi_T(\mathbf{R}_r, \mathbf{R}_0 | t) \Psi_T^*(\mathbf{R}'_r, \mathbf{R}_0 | t') \rangle \\ - \langle \Psi_T(\mathbf{R}_r, \mathbf{R}_0 | t) \rangle \langle \Psi_T^*(\mathbf{R}'_r, \mathbf{R}_0 | t') \rangle, \end{aligned}$$

for example, provides a second moment characterization of the reverberant field that is sufficient for most remote sensing applications, where a statistical correlation between scatterers over the volume V is implicitly required to evaluate the covariance. This quantity is most useful for investigating the performance of systems that employ pulse compression in an attempt to attain high temporal resolution. If all scatterers are independent, the covariance of the total reverberant field in

time can be obtained directly by summing the covariances of the individual scatterers using Eq. (28).

A difficulty arises, however, in any *analytic* representation for $\langle \Psi_T(\mathbf{R}_r, \mathbf{R}_0|t) \Psi_T^*(\mathbf{R}'_r, \mathbf{R}_0|t') \rangle$ when expectation values are brought within the modal sums and spatial and Fourier integrals. Even for a single random scattering patch, one finds that the second moment of the scatter-function, $\langle S(\theta, \phi; \theta_i, \phi_i) |_{f} S^*(\theta', \phi'; \theta'_i, \phi'_i) |_{f'} \rangle$, is required for *joint* correlation across both wave number and frequency. We are only aware of analytic derivations existing for this second moment when $\theta = \theta'$, $\phi = \phi'$, $\theta_i = \theta'_i$, $\phi_i = \phi'_i$, and $f = f'$, as noted in the definition of the expected bistatic scattering cross section of a random target or rough surface patch in Appendix A. This difficulty is circumvented when $\langle \Psi_T(\mathbf{R}_r, \mathbf{R}_0|t) \Psi_T^*(\mathbf{R}'_r, \mathbf{R}_0|t') \rangle$ is estimated by Monte Carlo simulation since $\Psi_T(\mathbf{R}_r, \mathbf{R}_0|t) \Psi_T^*(\mathbf{R}'_r, \mathbf{R}_0|t')$ is averaged across independent realizations of the rough surface. Broadband scattering statistics can then be obtained by either the saddle point method of Sec. II E or the Fourier synthesis of Eq. (20) since only the deterministic scatter function need be known to compute the scattered field for a given realization of the rough surface. In this way, by Monte Carlo simulations, $\langle \Psi_T(\mathbf{R}_r, \mathbf{R}_0|t) \Psi_T^*(\mathbf{R}'_r, \mathbf{R}_0|t') \rangle$ can be readily obtained using the theory developed in Sec. II to investigate the performance of systems that employ high-resolution temporal processing such as pulse compression.

B. Charting diffuse reverberation when system integration time spans dominant signal energy

A simpler analytic approach than the saddle point approximation or Fourier synthesis can be employed to investigate system performance when the integration time of the measurement system T is sufficiently long to include the dominant signal energy returned from the target or scattering patch. In this case, Parseval's theorem can be applied to the Fourier integral of Eq. (20), converted to absolute coordinates, to obtain the time-averaged mutual intensity expected at \mathbf{R}_r from a target or scattering patch at \mathbf{R} due to a source at \mathbf{R}_0 ,

$$\begin{aligned} I(\mathbf{R}, \mathbf{R}_r, \mathbf{R}_0, t) &= \frac{1}{T} \int_{t-T/2}^{t+T/2} \langle |\Psi_s(\mathbf{R}_r - \mathbf{R} | \mathbf{R}_0 - \mathbf{R} | t_0)|^2 \rangle dt_0 \\ &\approx \frac{1}{T} \int_{-\infty}^{\infty} \langle |\Psi_s(\mathbf{R}_r - \mathbf{R} | \mathbf{R}_0 - \mathbf{R} | t_0)|^2 \rangle dt_0 \\ &= \frac{1}{T} \int_{-\infty}^{\infty} |Q(f)|^2 \langle |\Phi_s(\mathbf{R}_r - \mathbf{R} | \mathbf{R}_0 - \mathbf{R})|^2 \rangle df, \end{aligned} \quad (35)$$

where $t - T/2$ is less than or equal to the arrival time of the scattered signal.

This type of incoherent integration is typically used in the reception of narrow-band source waveforms, and is also often used in the analysis of broadband returns from explosive sources such as SUS²² where the exact time function of the source is unknown. While it is equally valid for waveforms of arbitrary bandwidth, it does not take advantage of

the full pulse compression possible for broadband waveforms. However, it is often unclear in practice whether or not pulse compression can be meaningfully exploited with signals received after dispersive waveguide propagation. For the type of incoherent time average specified in Eq. (35), the problems mentioned in Sec. III A are alleviated since only $\langle S(\theta, \phi; \theta_i, \phi_i) |_{f} S^*(\theta', \phi'; \theta'_i, \phi'_i) |_{f'} \rangle$ need be evaluated for a given random scatterer, so that Eqs. (9) and (10) can be directly applied, since frequency cross terms vanish as a result of Parseval's theorem. A center frequency approximation to Eq. (35) can often be made for narrow-band signals as discussed in Appendix B.

If the time spread of the signal due to dispersion in the waveguide $\Delta \tau_s$ is small compared to the time duration T_s of the source signal, the expected horizontal range resolution $\Delta \rho$ of the system will take roughly the same form as in free space $\Delta \rho = \bar{c} T_s / 2$, for narrow-band signals, where \bar{c} is the mean horizontal propagation speed of the signal between source and receiver in the waveguide. In this case, the integration time T of the system can be set to its minimum value of T_s . Both $\Delta \tau_s$ and \bar{c} can be quantitatively defined in terms of the received field as in Ref. 25. They depend on the acoustic properties of the waveguide, the signal time dependence, and source-receiver geometry. For the narrow-band examples of Sec. IV, simulations show that $\bar{c} \approx 1500$ m/s, $t\bar{c} \approx \rho + \rho_0$, and $\Delta \tau_s / T_s$ is small, where ρ and ρ_0 are defined in Eq. (30a).

A typical bistatic sonar system will resolve a patch of seafloor $A(\mathbf{R}, \mathbf{R}_r, \mathbf{R}_0)$, the dimensions of which depend on the receiving array aperture, frequency, and the bistatic geometry of the source, receiver, and seafloor patch as discussed in Appendix C of Ref. 26 and Refs. 27 and 28. For a monostatic measurement $A = \rho \Delta \rho \Delta \varphi$, where $\Delta \varphi = \lambda / L_A$ is the Rayleigh resolution of the horizontal aperture of length L_A .

For convenience, assume that the *horizontal* origin in an absolute reference frame is chosen to be at the center of the receiving array $\mathbf{Z}_r = (0, 0, Z_r)$. Let the beamformed output of a receiving array located along the Y_r -axis, obtained by spatial Fourier transform of the time-harmonic scattered field across the array aperture, be denoted by

$$\begin{aligned} \Phi_B(\phi_s, Z_r, \mathbf{R}, \mathbf{R}_0) &= \int_{-\infty}^{\infty} T(Y_r) Q(f) \Phi_s(\mathbf{R}_r - \mathbf{R} | \mathbf{R}_0 - \mathbf{R}) \\ &\quad \times e^{ik \sin \varphi_s Y_r} dY_r, \end{aligned} \quad (36)$$

where φ_s is the azimuth the array is steered towards, φ is the azimuth of the scattering patch, and $T(Y_r)$ is the array taper function. Suppose a uniform rectangular taper function is used with $T(Y_r) = 1/L_A$ for $-L_A/2 \leq Y_r \leq L_A/2$ and zero elsewhere, and the seafloor scattering patch is in the far field of the array, such that $|\mathbf{R}| > L_A^2 / \lambda$, and the scattering patch behaves as a point target to the array so that the angle it subtends at the array is less than λ / L_A . Under these assumptions, the spectral density or field variance received from this patch can be well approximated by

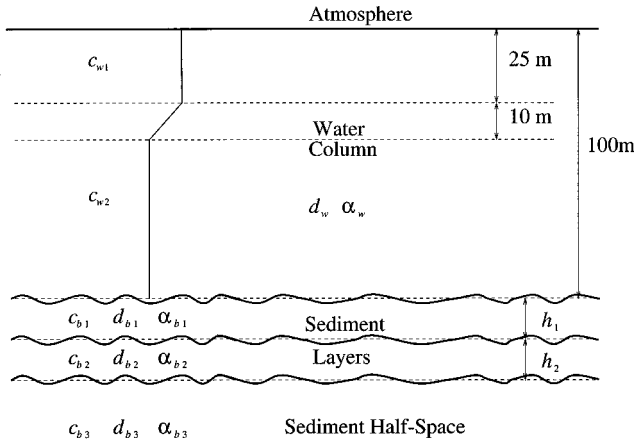


FIG. 1. The geometry of the waveguide which has a water column comprised of upper layer sound speed c_{w1} for $0 < Z < 25$, lower layer sound speed c_{w2} for $35 < Z < 100$, and transition layer sound speed $c_{w1} - (c_{w1} - c_{w2})(Z - 25)/10$ for $25 \leq Z \leq 35$. The water column density is $d_w = 1000 \text{ kg/m}^3$ and the attenuation is $\alpha_w = 6.0 \times 10^{-5} \text{ dB}/\lambda$. The bottom can have up to two sediment layers. The upper and middle sediment layers have respective thicknesses, sound speeds, densities, and attenuations of h_1 , c_{b1} , d_{b1} , α_{b1} and h_2 , c_{b2} , d_{b2} , α_{b2} , overlying a sediment half-space of sound speed c_{b3} , density d_{b3} , and attenuation α_{b3} . The monopole source is collocated with receiving array center, with array axis normal to the range-depth plane of the sketch. Source and receiver may be placed anywhere in the water column. The submerged target may be placed in the upper or lower layers of the water column where sound speed is constant as indicated in Fig. 2. Seafloor and buried riverbank features may also be included at the water-sediment and sediment-layer to sediment half-space interfaces as indicated in Fig. 6. Squiggly lines indicate statistically rough interfaces.

$$\begin{aligned}
 & \langle |\Phi_B(\varphi, Z_r, \mathbf{R}, \mathbf{R}_0)|^2 \rangle - \langle \Phi_B(\varphi, Z_r, \mathbf{R}, \mathbf{R}_0) \rangle^2 \\
 &= \left(\frac{4\pi}{k} \right)^2 |Q(f)|^2 \sum_{m=1}^{\infty} \sum_{n=1}^{\infty} |B_m(\mathbf{Z}_r - \mathbf{R})|^2 \\
 & \quad \times |A_n(\mathbf{R}_0 - \mathbf{R})|^2 C_{mn}(\mathbf{Z}_r - \mathbf{R}, \mathbf{Z}_r - \mathbf{R} | \mathbf{R}_0 - \mathbf{R}) \\
 & \quad \times \left| \frac{\sin\{(L_A/2) \sin \varphi [k - \text{Re}\{\xi_m\}]\}}{(L_A/2) \sin \varphi [k - \text{Re}\{\xi_m\}]} \right|^2 \quad (37)
 \end{aligned}$$

upon substitution of Eq. (17) into Eq. (36) with $\phi_s = \phi$ so the array is steered toward the patch. With the assumption that the resolution footprint A is much larger than ΔA , the area of a given patch, and all patches are statistically independent, the total variance of the received field from seafloor within the system resolution footprint can be written as the sum of the variances of each patch via

$$\begin{aligned}
 V_B(X, Y) &= \iint_{A(\mathbf{R}, Z_r, \mathbf{R}_0)} \langle |\Phi_B(\varphi, Z_r, \mathbf{R}', \mathbf{R}_0)|^2 \rangle \\
 & \quad - \langle \Phi_B(\varphi, Z_r, \mathbf{R}', \mathbf{R}_0) \rangle^2 \frac{1}{n_z' \Delta A} dX' dY', \quad (38)
 \end{aligned}$$

where $\hat{n} = (n_x, n_y, n_z)$ is the surface normal at \mathbf{R} . Since the differential area $dX' dY'$ must be normalized by the horizontal projected area of each potentially inclined patch at \mathbf{R}' to allow horizontal integration, Eq. (38) does not allow vertical patches.

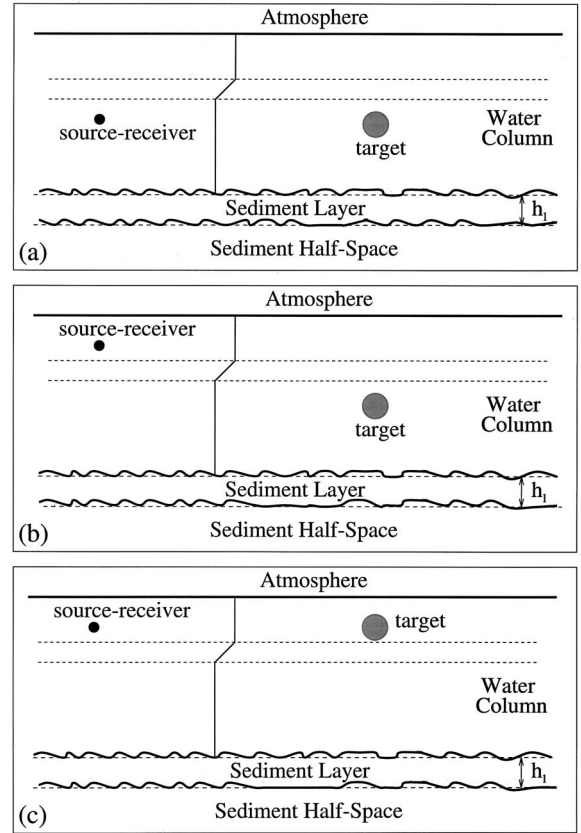


FIG. 2. Three scenarios for the active detection of a submerged pressure release sphere of radius $a = 10 \text{ m}$. The water column is modeled as either having constant sound speed or as downward refracting. The bottom is composed of either a pure sediment half-space or a single sediment layer over a sediment half-space. (a) Monopole source and horizontal receiving array center are collocated at 50-m depth with target at 50-m depth also. (b) Source and receiving array center are collocated at 10-m depth with target at 50-m depth. (c) Source and receiving array center are collocated at 10-m depth with target at 15-m depth.

When Parseval's theorem is invoked again under the assumption that the integration time of the measurement system includes the dominant energy returned from the resolved patch of seafloor, after time-domain beamforming and finite time averaging by the receiver over period T , the field variance from seafloor within the system resolution footprint of area $A(\mathbf{R}, \mathbf{R}_r, \mathbf{R}_0)$ centered at (X, Y) becomes

$$\bar{V}_B(X, Y) = \frac{1}{T} \int_{-\infty}^{\infty} V_B(X, Y) df. \quad (39)$$

Equations (37)–(39) imply a reduction in reverberation level for off-broadside beams due solely to modal dispersion. Only at broadside does the phase speed of the incident waves match that expected under the nondispersive assumptions of plane wave beamforming. Only broadside beamforming is considered in the simulations of the present article to eliminate this effect from the analysis. The effects of modal dispersion on beamformed reverberation are investigated in Ref. 25.

Under the present assumptions, reverberation measured in time can be charted in space for any bistatic geometry using a look-up table comprised of the mean time delay from source to scattering patch $\bar{\tau}(\mathbf{r}_t, \mathbf{r}_0)$ and scattering patch to

receiver $\bar{r}(\mathbf{r}, \mathbf{r}_r)$.²⁵ Similarly, reverberation modeled with the spatial formulation of Eqs. (38) and (39) can be made a function of time by reversing the procedure.

C. Lambert–Mackenzie scattering and reverberation

A number of simplifications are possible when the scattering surface has *Lambertian*²⁹ behavior. The covariance of the scattering function for a Lambertian scattering patch of area ΔA with albedo ε takes the form of Eq. (12a) with

$$C_{lm}(\mathbf{R}_r - \mathbf{R}, \mathbf{R}'_r - \mathbf{R} | \mathbf{R}_0 - \mathbf{R}) = k^2 \frac{\varepsilon}{\pi} |\hat{i}_{sl} \cdot \hat{n}| |\hat{i}_{im} \cdot \hat{n}| \Delta A, \quad (40)$$

where \hat{i}_{im} and \hat{i}_{sl} are the directions in which the down-going component of the m th incident and up-going component of the l th scattered modes propagate and \hat{n} is the seafloor normal, pointing away from the water column, in a scattering-patch-centered coordinate system where the positive- z axis points downward. The differential scattering cross section of the surface patch is then given by the product of $4\pi/k^2$ and the right-hand side of Eq. (40).

Under Lambertian scattering, the cross spectral density of the scattered field given in Eq. (17) then becomes expressible in terms of single summations

$$\begin{aligned} & \langle \Phi_s(\mathbf{r}) \Phi_s^*(\mathbf{r}') \rangle - \langle \Phi_s(\mathbf{r}) \rangle \langle \Phi_s^*(\mathbf{r}') \rangle \\ &= 16\pi\varepsilon\Delta A \left(\sum_{l=1}^{\infty} B_l(\mathbf{r}) B_l^*(\mathbf{r}') |\hat{i}_{sl} \cdot \hat{n}| \right) \\ & \quad \times \left(\sum_{m=1}^{\infty} |A_m(\mathbf{r}_0)|^2 |\hat{i}_{im} \cdot \hat{n}| \right). \end{aligned} \quad (41)$$

The surface projection factors can be written in terms of the incident and scattered wave number components, the measurement geometry, and the orientation of the surface patch via

$$|\hat{i}_{sl} \cdot \hat{n}| = \left| \frac{\xi_l}{k} [n_x \cos \varphi + n_y \sin \varphi] + \frac{\gamma_l}{k} n_z \right|, \quad (42a)$$

$$|\hat{i}_{im} \cdot \hat{n}| = \left| \frac{\xi_m}{k} [n_x \cos(\varphi_0 + \pi) + n_y \sin(\varphi_0 + \pi)] - \frac{\gamma_m}{k} n_z \right|. \quad (42b)$$

The scattered field covariance from a given seafloor patch in a target-oriented frame is

$$\begin{aligned} & \langle \Phi_s(\mathbf{r} | \mathbf{r}_0) \Phi_s^*(\mathbf{r}' | \mathbf{r}_0) \rangle - \langle \Phi_s(\mathbf{r} | \mathbf{r}_0) \rangle \langle \Phi_s^*(\mathbf{r}' | \mathbf{r}_0) \rangle \\ &= 16\pi\varepsilon\Delta A \left(\sum_{l=1}^{\infty} B_l(\mathbf{r}) B_l^*(\mathbf{r}') \left| \frac{\xi_l}{k} [n_x \cos \varphi + n_y \sin \varphi] \right. \right. \\ & \quad \left. \left. + \frac{\gamma_l}{k} n_z \right| \right) \left(\sum_{m=1}^{\infty} |A_m(\mathbf{r}_0)|^2 \left| \frac{\xi_m}{k} [n_x \cos(\varphi_0 + \pi) \right. \right. \\ & \quad \left. \left. + n_y \sin(\varphi_0 + \pi)] - \frac{\gamma_m}{k} n_z \right| \right), \end{aligned} \quad (43)$$

where $n_x = n_y = 0$ for a bottom with zero mean inclination. In an absolute frame it becomes

$$\begin{aligned} & \langle \Phi_s(\mathbf{R}_r - \mathbf{R} | \mathbf{R}_0 - \mathbf{R}) \Phi_s^*(\mathbf{R}'_r - \mathbf{R} | \mathbf{R}_0 - \mathbf{R}) \rangle - \langle \Phi_s(\mathbf{R}_r - \mathbf{R} | \mathbf{R}_0 - \mathbf{R}) \rangle \langle \Phi_s^*(\mathbf{R}'_r - \mathbf{R} | \mathbf{R}_0 - \mathbf{R}) \rangle \\ &= 16\pi\varepsilon\Delta A \left(\sum_{l=1}^{\infty} B_l(\mathbf{R}_r - \mathbf{R}) B_l^*(\mathbf{R}'_r - \mathbf{R}) \left| \frac{\xi_l}{k} \frac{n_x(X_r - X) + n_y(Y_r - Y)}{\sqrt{(X_r - X)^2 + (Y_r - Y)^2}} + \frac{\gamma_l}{k} n_z \right| \right) \\ & \quad \times \left(\sum_{m=1}^{\infty} |A_m(\mathbf{R}_0 - \mathbf{R})|^2 \left| \frac{\xi_m}{k} \frac{n_x(X_0 - X) + n_y(Y_0 - Y)}{\sqrt{(X_0 - X)^2 + (Y_0 - Y)^2}} + \frac{\gamma_m}{k} n_z \right| \right), \end{aligned} \quad (44)$$

where the components of the surface normal \hat{n} are now a function of the X, Y, Z position of the surface patch center. Under far-field assumption, the field variance received from seafloor within the system resolution footprint centered at (X, Y) and averaged over time period T can be well approximated by

$$\begin{aligned} \bar{V}_B(X, Y) &= \frac{16\pi\varepsilon}{T} \int_{-\infty}^{\infty} |Q(f)|^2 \int \int_{A(\mathbf{R}, \mathbf{Z}_r, \mathbf{R}_0)} \left(\sum_{l=1}^{\infty} |B_l(\mathbf{Z}_r - \mathbf{R}')|^2 \left| \frac{\xi_l}{k} \frac{n_x(X_r - X') + n_y(Y_r - Y')}{\sqrt{(X_r - X')^2 + (Y_r - Y')^2}} + \frac{\gamma_l}{k} \right| \right. \\ & \quad \left. \times \left| \frac{\sin((L_A/2) \sin \varphi [k - \text{Re}\{\xi_l\}])}{(L_A/2) \sin \varphi [k - \text{Re}\{\xi_l\}]} \right|^2 \right) \left(\sum_{m=1}^{\infty} |A_m(\mathbf{R}_0 - \mathbf{R}')|^2 \left| \frac{\xi_m}{k} \frac{n_x(X_0 - X') + n_y(Y_0 - Y')}{\sqrt{(X_0 - X')^2 + (Y_0 - Y')^2}} + \frac{\gamma_m}{k} \right| \right) dX' dY' df, \end{aligned} \quad (45)$$

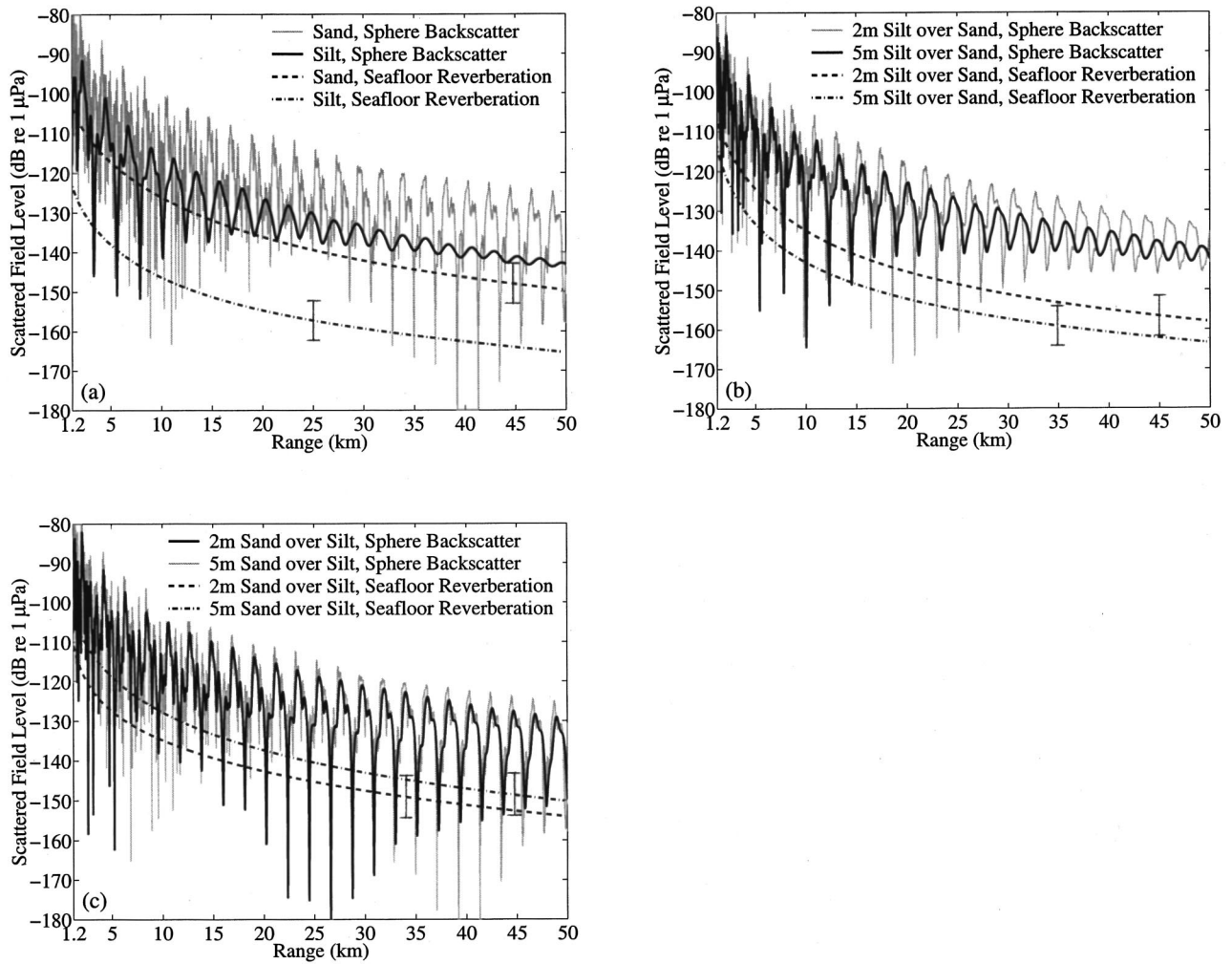


FIG. 3. The scattered field from a submerged pressure-release sphere of radius $a = 10$ m, at $f = 300$ Hz and center at 50-m depth, and Lambert–Mackenzie reverberation from the seafloor within the broadside resolution footprint of the monostatic system as a function of range for a water column with constant sound speed of 1500 m/s, i.e., $c_{w1} = c_{w2} = 1500$ m/s. Monopole source and receiving array center are collocated at 50-m depth. Range increases along the x -axis and depth along the z -axis, with the array axis along the y -axis. Source strength is 0 dB re 1 μ Pa @ 1 m. Reverb modeled with $T = 1/2$ s duration cw source signal at 300 Hz and receiving array resolution $\lambda/L = 3.7$ degrees. (a) Pekeris waveguide examples for bottom half-spaces composed of either sand or silt, i.e., $h_1 = h_2 = 0$. (b) Bottom has a silt layer of either $h_1 = 2$ m or $h_1 = 5$ m overlying a sand half-space, and $h_2 = 0$. (c) Bottom has a sand layer of either $h_1 = 2$ m or $h_1 = 5$ m overlying a silt half-space, and $h_2 = 0$. Error bars show the 5.6 dB standard deviation in reverb level.

when T is sufficiently large for the dominant energy of the scattered field to be received. This result for the Lambertian seafloor offers significant advantages in implementation through the separation of the incident and scattered modal summations. For narrow-band waveforms, terms within the modal summations of Eq. (45) often vary so slowly that they can be approximated as a constant function of frequency over the dominant portion of the spectral window $Q(f)$. This greatly simplifies computations as shown in Appendix B.

D. Perturbation theory for diffuse rough surface scattering and reverberation

Perturbation theory can also be used to calculate the field scattered by a rough surface. The advantage of perturbation theory, when it is applicable, is that it is derived from first principles and so requires knowledge of only the geoacoustic properties of the media, such as sound speed and density, as well as a second moment characterization of the statistical properties of the scattering surface.

Let the x and y components of the gradient of the surface $z_s(x, y)$ be denoted by

$$p = \frac{\partial z_s}{\partial x}, \quad (46a)$$

$$q = \frac{\partial z_s}{\partial y}. \quad (46b)$$

The surface normal can be expressed as

$$\mathbf{n} = \frac{(-p, -q, 1)}{\sqrt{1 + p^2 + q^2}}, \quad (47a)$$

along with two orthonormal surface tangents

$$\mathbf{t}_1 = \frac{(1, 0, p)}{\sqrt{1 + p^2}}, \quad (47b)$$

and

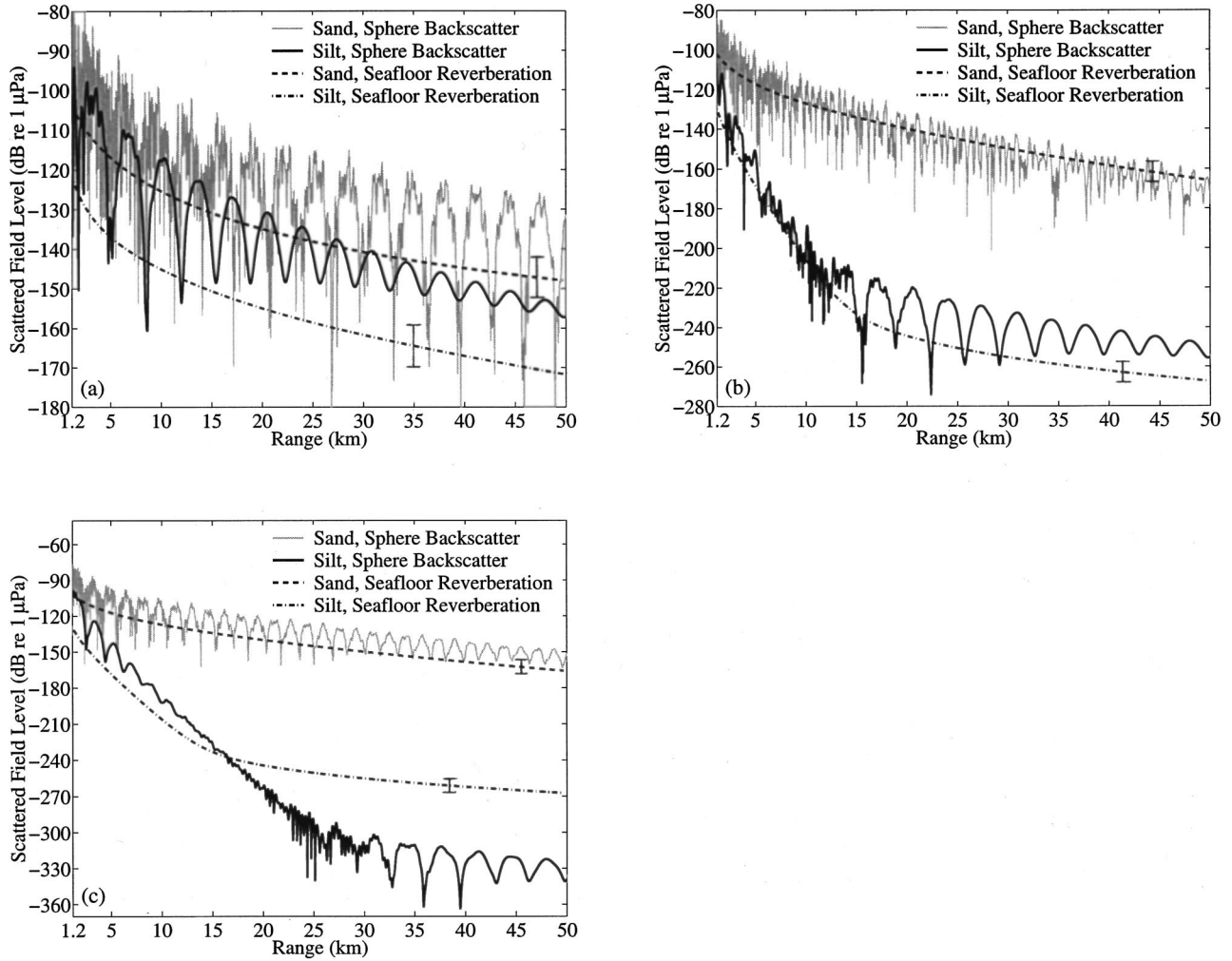


FIG. 4. Same as Fig. 3 except water column is layered with $c_{w1} = 1520$ m/s and $c_{w2} = 1500$ m/s and monostatic source–receiver as well as target sphere are at variable depth. Only the cases of pure sand or pure silt bottom half-spaces are shown. (a) Source–receiver and sphere center are at 50-m depth. (b) Source–receiver are at 10-m depth while sphere center is at 50-m depth. (c) Source–receiver are at 10-m depth while sphere center is at 15-m depth.

$$\mathbf{t}_2 = \frac{(-pq, 1+p^2, q)}{\sqrt{(1+p^2)(1+p^2+q^2)}}, \quad (47c)$$

where \mathbf{t}_1 is obtained by taking an infinitesimal step along the surface on the x axis, and \mathbf{t}_2 is the crossproduct of \mathbf{n} and \mathbf{t}_1 .

The projections of the incident and scattered wave number vectors on the surface then become

$$\mathbf{K}_i = (\mathbf{k}_i \cdot \mathbf{t}_1)\mathbf{t}_1 + (\mathbf{k}_i \cdot \mathbf{t}_2)\mathbf{t}_2, \quad (48a)$$

$$\mathbf{K} = (\mathbf{k} \cdot \mathbf{t}_1)\mathbf{t}_1 + (\mathbf{k} \cdot \mathbf{t}_2)\mathbf{t}_2, \quad (48b)$$

where, for incident mode n and scattered mode m ,

$$\mathbf{k}_i = (\xi_n \cos(\phi_0 + \pi), \xi_n \sin(\phi_0 + \pi), \gamma_n), \quad (49a)$$

$$\mathbf{k} = (\xi_m \cos \phi, \xi_m \sin \phi, \gamma_m), \quad (49b)$$

so that

$$\mathbf{K}_i \cdot \mathbf{K} = (\mathbf{k}_i \cdot \mathbf{t}_1)(\mathbf{k} \cdot \mathbf{t}_1) + (\mathbf{k}_i \cdot \mathbf{t}_2)(\mathbf{k} \cdot \mathbf{t}_2), \quad (50)$$

and, for example,

$$|\mathbf{K}_i|^2 = (\mathbf{k}_i \cdot \mathbf{t}_1)^2 + (\mathbf{k}_i \cdot \mathbf{t}_2)^2, \quad (51a)$$

$$|\mathbf{K}|^2 = (\mathbf{k} \cdot \mathbf{t}_1)^2 + (\mathbf{k} \cdot \mathbf{t}_2)^2. \quad (51b)$$

A plane wave incident from medium 1 half-space that is reflected from strata below has total reflection coefficient³⁰

$$\Gamma(\mathbf{K}_i) = \frac{\Gamma_{12}(\mathbf{K}_i) + \Gamma'(\mathbf{K}_i)e^{i2\gamma^{(2)}h_1}}{1 + \Gamma_{12}(\mathbf{K}_i)\Gamma'(\mathbf{K}_i)e^{i2\gamma^{(2)}h_1}}, \quad (52a)$$

where

$$\Gamma_{12}(\mathbf{K}_i) = \frac{\rho_2 / \sqrt{k_2^2 - K_i^2} - \rho_1 / \sqrt{k_1^2 - K_i^2}}{\rho_2 / \sqrt{k_2^2 - K_i^2} + \rho_1 / \sqrt{k_1^2 - K_i^2}} \quad (52b)$$

is the reflection coefficient from the medium 1 to medium 2 interface, $\Gamma'(\mathbf{K}_i)$ is the total reflection coefficient from all strata below medium 2 for a plane wave incident from medium 2, h_1 is the thickness of the layer containing medium 2, and $\gamma^{(2)}$ is the vertical wave number component of medium 2.

The differential scattering cross section of a surface patch of area ΔA , from first-order perturbation theory, can be expressed as³⁰

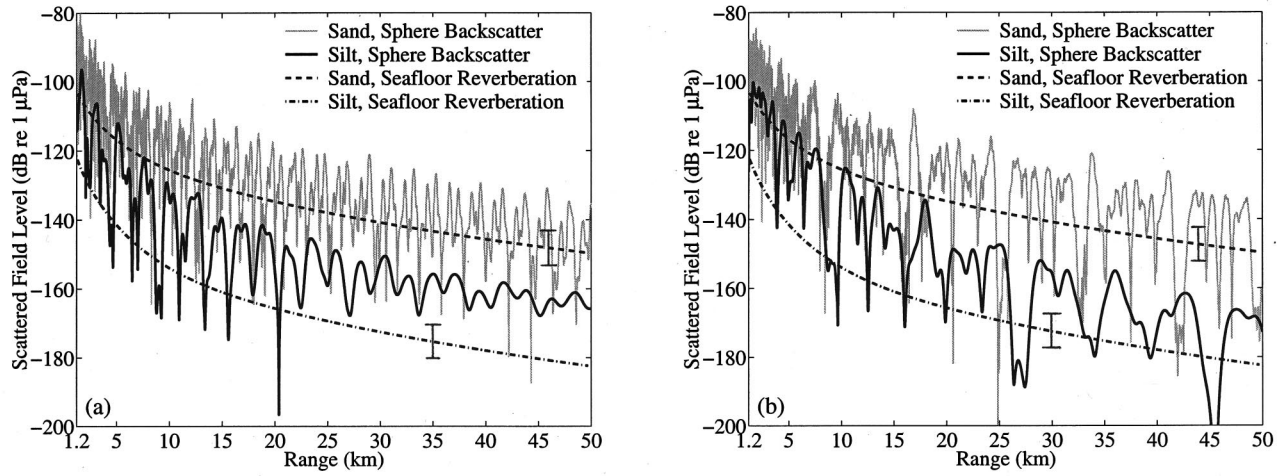


FIG. 5. Pekeris waveguide with varying source–receiver and target depth. (a) Same as Fig. 3(a) except source–receiver is at 10-m depth and target is at 50-m depth. (b) Same as Fig. 3(a) except source–receiver is at 10-m depth and target is at 15-m depth.

$$\sigma_{\text{pert}}(\alpha, \beta; \alpha_i, \beta_i) = 4\pi\Delta A \left(\frac{k_1^4}{4} \right) \left| [\Gamma(\mathbf{K}) + 1][\Gamma(\mathbf{K}_i) + 1] \right|^2 \left| 1 - \frac{\kappa^2}{d_{bt}} + \left(\frac{1}{d_{bt}} - 1 \right) \left(\frac{\mathbf{K} \cdot \mathbf{K}_i}{k_1^2} - \frac{P_g^2(\mathbf{k}, \mathbf{k}_i, \mathbf{n})}{d_{bt}} \right) \right|^2 W(\mathbf{K} - \mathbf{K}_i), \quad (53)$$

where

$$P_g^2(\mathbf{K}, \mathbf{K}_i) = d_{bt}^2 \frac{|\mathbf{k}_i \cdot \mathbf{n}|}{k_i} \frac{|\mathbf{k} \cdot \mathbf{n}|}{k} \left(\frac{1 - \Gamma(\mathbf{K}_i)}{1 + \Gamma(\mathbf{K}_i)} \right) \left(\frac{1 - \Gamma(\mathbf{K})}{1 + \Gamma(\mathbf{K})} \right), \quad (54)$$

and

$$d_{bt} = d_b / d_t, \quad (55)$$

$$\kappa = \kappa_t / \kappa_b, \quad (56)$$

where d_t and d_b are the respective densities above and below the scattering interface and κ_t and κ_b the respective wave number magnitudes above and below the scattering interface.

Following Moe and Jackson,³⁰ the roughness of the given surface patch is assumed to follow the isotropic power law

$$W(\mathbf{K}) = w_2 |\mathbf{K}|^{-\gamma}. \quad (57)$$

With the assumption that the scattering patch is much greater than the wavelength so that the incident and scattered modes are decorrelated by the scattering process, the covariance of the scatter function is given by Eq. (12a) with

$$C_{mn}(\mathbf{r}, \mathbf{r}' | \mathbf{r}_0) = \frac{k^2}{4\pi} \sigma_{\text{pert}}(\alpha_m, \phi; \alpha_n, \phi_0 + \pi). \quad (58)$$

Upon substituting Eq. (58) into Eqs. (17), or (38) after beam-

forming, it is found that the covariance of the field scattered from a rough surface patch that obeys first-order perturbation theory involves a double summation over the waveguide modes. Evaluating this is significantly more computationally intensive than the product of single modal summations found in the Lambert–Mackenzie formulation.

E. Coherent reverberation from deterministic and stochastic geological features

There are two general kinds of seafloor scatterers that do not decorrelate the incident or scattered modes. A seafloor scatterer of the first kind can be modeled as a deterministic feature, with known or computable far-field scatter function, that can have arbitrary size compared to the wavelength so long as it falls within the resolution footprint of the active sonar system. The feature must be distinct from the otherwise range-independent boundaries of the stratified medium in order to induce scattering.

A compelling canonical example of a seafloor scatterer of the first kind is a smooth flat inclined segment of the seafloor, such as a seafloor or subseafloor river channel, iceberg scour, or submerged hillside, that can be modeled as a flat plate with scattering characteristics determined by its size, inclination, and the local geo-acoustic properties of the interface. The 3-D scatter function for a rectangular surface patch with total reflection coefficient $\Gamma(\mathbf{K}_i)$, for example, can be readily determined by applying Green's theorem, Eq. (A1), for a plane wave, with wave number magnitude k_1 , incident in the direction (α_i, β_i) and a far-field receiver in the direction (α, β) with respect to the patch centroid. If the patch is assumed to be at inclination χ from horizontal, where the angle χ comprises a counter-clockwise rotation about the y axis, the scatter function takes the form

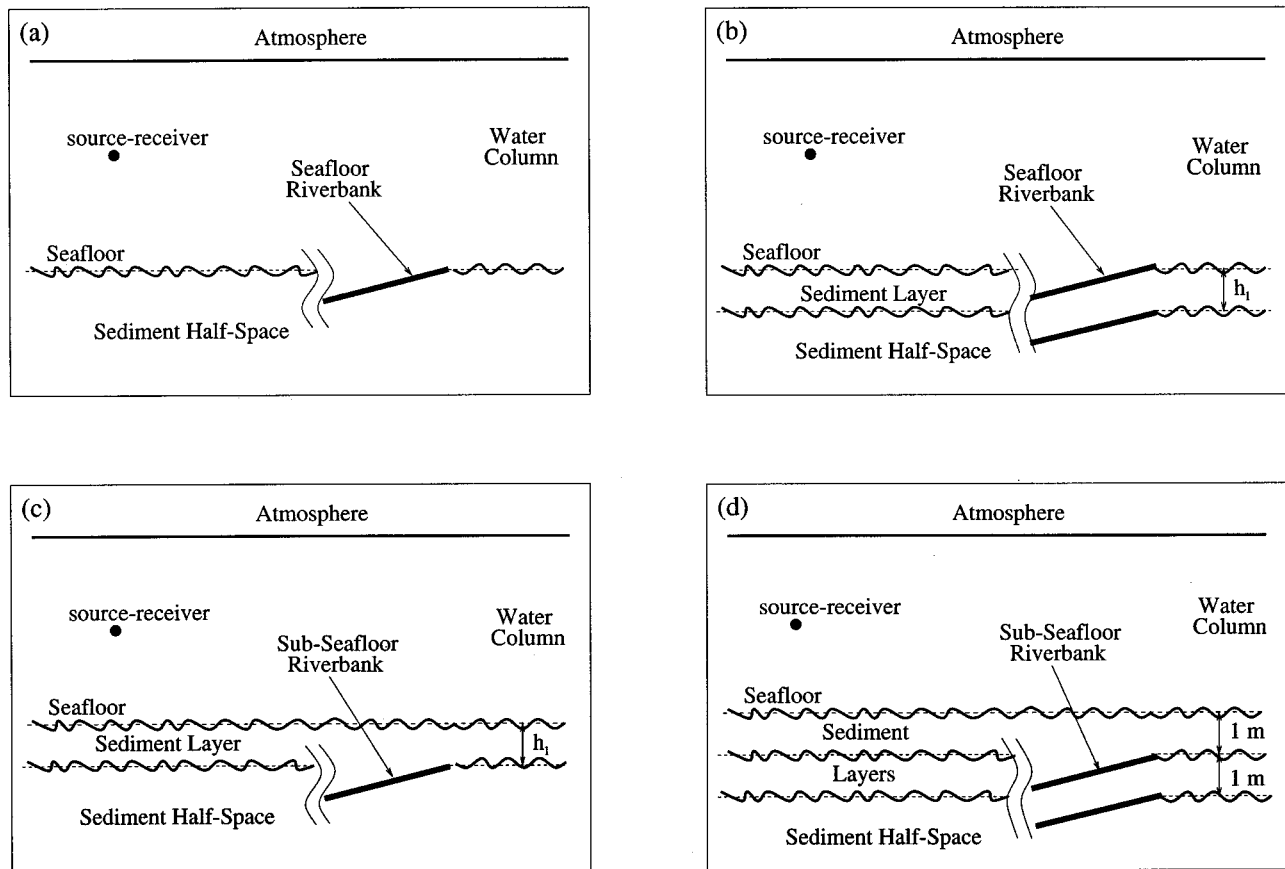


FIG. 6. Scenarios for the active detection of seafloor and subseafloor riverbank features. The water column is modeled as having constant sound speed, i.e., $c_{w1} = c_{w2} = 1500$ m/s, and monopole source and horizontal receiving array center are collocated at 50-m depth in all cases. (a) Bottom is sediment half-space with seafloor feature, i.e., $h_1 = h_2 = 0$. (b) Bottom is composed of a single sediment layer with double-interface seafloor feature, i.e., $h_2 = 0$. (c) Bottom is composed of a single sediment layer with subseafloor feature, i.e., $h_2 = 0$. (d) Bottom is composed of two sediment layers with double-interface subseafloor feature.

$$S(\alpha, \beta; \alpha_i, \beta_i) = i \frac{k_1^2}{4\pi} L_x L_y \left[(1 - \Gamma(\mathbf{K}_i)) \{ \cos \alpha_i \cos \chi + \sin \alpha_i \sin \chi \cos \beta_i \} + (1 + \Gamma(\mathbf{K}_i)) \{ \cos \alpha \cos \chi + \sin \alpha \sin \chi \cos \beta \} \right] \\ \times \text{sinc} \left[\frac{k_1 L_x}{2} \{ (\sin \alpha_i \cos \beta_i \cos \chi - \cos \alpha_i \sin \chi) - (\sin \alpha \cos \beta \cos \chi - \cos \alpha \sin \chi) \} \right] \text{sinc} \left[\frac{k_1 L_y}{2} \{ \sin \alpha_i \sin \beta_i - \sin \alpha \sin \beta \} \right], \quad (59)$$

where $\text{sinc}(x)$ is defined as $\sin x/x$. The reflection coefficient can be determined from Eq. (52) with the understanding that, in the present geometry, the squared magnitude of the transverse component of the incident wave number vector on the inclined surface patch is

$$K_i^2 = k_1^2 - k_1^2 (\cos \alpha_i \cos \chi + \sin \alpha_i \sin \chi \cos \beta_i)^2. \quad (60)$$

Irregularities in the surface can make its scatter function deviate from that given in Eq. (59). For realistic seafloor and subseafloor riverbanks, however, it is reasonable to assume that, for a low-frequency active system²⁸ at long range in a shallow water waveguide where propagation is near horizontal, the product of the amplitude of such irregularities and the normal component of the wave number vector with respect to the surface will be small enough that the irregularities will have a negligible effect on the field from the riverbank.

A seafloor scatterer of the second kind is a randomly rough rather than deterministic feature but is appropriately modeled with completely coherent modes when the ratio of wavelength to system range resolution, $\lambda/\Delta\rho$, is near or greater than the equivalent vertical propagation angle of the highest order trapped mode, which in many shallow water scenarios is roughly the bottom critical angle. This situation occurs for active sonar systems with high range-resolution and can lead to the formation of range-dependent rings in charted reverberant intensity caused by modal interference.²⁴ (Lepage⁷ has recently described scenarios in which such rings can form even in narrow-band reverberation at short ranges.) The level of returns can be estimated by appropriately modeling the seafloor scatter function. If the system resolution footprint extends over many wavelengths in any direction and the correlation length of surface roughness is

much smaller than the system resolution footprint, then the scattering function for the seafloor over this area can be treated as a fluctuating target. If the resolution footprint is on the order of the wavelength or the correlation length of surface roughness, a quasi-deterministic description of the scattering process can be used.

IV. ILLUSTRATIVE EXAMPLES

In all the illustrative examples of this section, a water column of 100-m depth is used to simulate a typical continental shelf environment. The sound speed structure of the water column varies from iso-velocity to downward refracting layers with constant density of 1 g/cm^3 and attenuation of $6.0 \times 10^{-5} \text{ dB}/\lambda$. The seabed is comprised of sand or silt half-spaces, with up to two sediment layers, comprised of sand or silt, over a sand or silt half-space. The density, sound speed and attenuation are taken to be 1.9 g/cm^3 , 1700 m/s , and $0.8 \text{ dB}/\lambda$ for sand, 1.4 g/cm^3 , 1520 m/s , and $0.3 \text{ dB}/\lambda$ for silt, and 1.2 g/cm^3 , 1510 m/s , and $0.3 \text{ dB}/\lambda$ for light-silt. Scattering and reverberation calculations are made for a submerged target, roughness at the water–seabed interface, roughness at the interface between the upper seabed layer and lower half-space, as well as for anomalous features of the seafloor or subseafloor that return geological clutter. The latter are taken to be seafloor river banks at the water–seabed interface or subseafloor riverbanks at the interface between the upper sediment layer and lower half-space. The geometry of the waveguide is sketched in Fig. 1.

A horizontal line array with $N=32$ equally spaced elements of length $L_A=(N-1)\lambda/2$ at $f=300 \text{ Hz}$ is used as a receiver and a cw pulse of $T=\frac{1}{2}$ -s duration centered at f

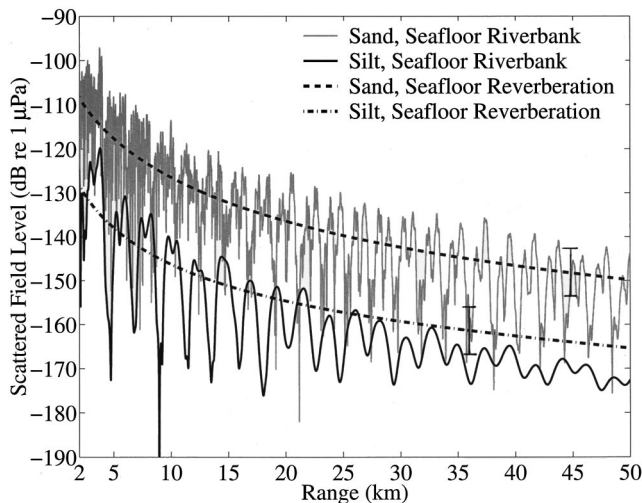


FIG. 7. The field at $f=300 \text{ Hz}$ scattered from a coherently scattering rectangular patch of area $100 \times 100 \text{ m}^2$ representing a seafloor riverbank for scenario shown in Fig. 6(a), constant sound speed water column over pure silt or sand half-spaces. Range increases along the x axis and depth along the z axis. The square riverbank surface has two edges parallel to the y axis, and is inclined 10° from the x axis. Constant sound speed in the water column is assumed for all examples with $c_{w1}=c_{w2}=1500 \text{ m/s}$. Lambert–Mackenzie reverberation within the range-dependent resolution footprint of the monostatic system is also shown separately for the water–sediment interface (seafloor). Source strength is $0 \text{ dB re } 1 \mu\text{Pa}$ @ 1 m . Diffuse reverberation modeled with $T=1/2 \text{ s}$ duration cw source signal at 300 Hz and receiving array resolution $\lambda/L=3.7$ degrees.

$=300 \text{ Hz}$ is used as a source waveform for all simulations of diffuse reverberation. Targets beyond L_A^2/λ are in the far field of the array, which begins at roughly 1.2 km . The beamformed field from an object that falls within the broadside beam of the array, in the absence of other sources or scatterers, equals the field received from that object by a single hydrophone at the array center when Eq. (36) is used with uniform taper $T(Y_r)=1/L_A$. If the same object is placed at the same range but within an off-broadside beam, a reduction in the beamformed output may occur due to modal dispersion, as is discussed in detail in Ref. 25. For simplicity, only objects and reverberation within the broadside beam are considered in the present article. Only monostatic scenarios are considered, where the source is located at the center of the receiving array. This leads to a range-dependent resolution footprint $A=\rho\Delta\rho\Delta\varphi$, where $d\rho=cT/2=375 \text{ m}$ and $d\varphi=\lambda/L_A\approx 3.7$ degrees for the given array, frequency, and cw pulse length.

A center frequency approximation, at $f=300 \text{ Hz}$, is made for all scattering calculations. For reverberation calculations this approximation differs from the full spectral integration by less than 0.1 dB for the examples shown. As may be expected in coherent scattering from targets where modal interference is significant, some range-dependent nulls and valleys in the sound pressure level of the received field found in the single frequency calculation may be partially filled when the full bandwidth is used for the narrow-band waveforms considered. Since this filling is window dependent, as shown in Appendix B, only center frequency calculations are presented in the main text. It is also shown in Appendix B that in some valleys of some single frequency calculations the target returns may fall below the expected reverberation level but will be above this level when the full bandwidth of a given narrow-band window function is employed.

Only the empirical Lambert–Mackenzie model is used in comparisons between seafloor reverberation and submerged-object returns since insufficient data on the requisite environmental parameters at low frequency are available to make a similar comparison with perturbation theory meaningful. Perturbation theory calculations are only used self-consistently to make inferences about the relative level of returns from different kinds of seafloor scatterers.

A. Submerged target echo versus diffuse reverberation level for varying source–receiver depth, target depth, water column, and bottom stratification

The geometry for active detection of a sphere submerged in an ocean waveguide is sketched in Fig. 2 for the illustrative examples of this section. The geometry is monostatic with co-located omni-directional point source and receiving array centers at 50-m depth. The sphere center is also at $D=50\text{-m}$ depth at array broadside with variable horizontal range. The field back scattered from a pressure release sphere of radius $a=10 \text{ m}$ at $f=300 \text{ Hz}$ is shown as a function of range in Figs. 3(a)–(c) in decibels, i.e., $20 \log|\Phi_s|$, for various bottom types under a water column with constant sound speed $c_w=1500 \text{ m/s}$, where $c_{w1}=c_{w2}=1500 \text{ m/s}$. The scattered field is computed by Eq. (1), with scatter function

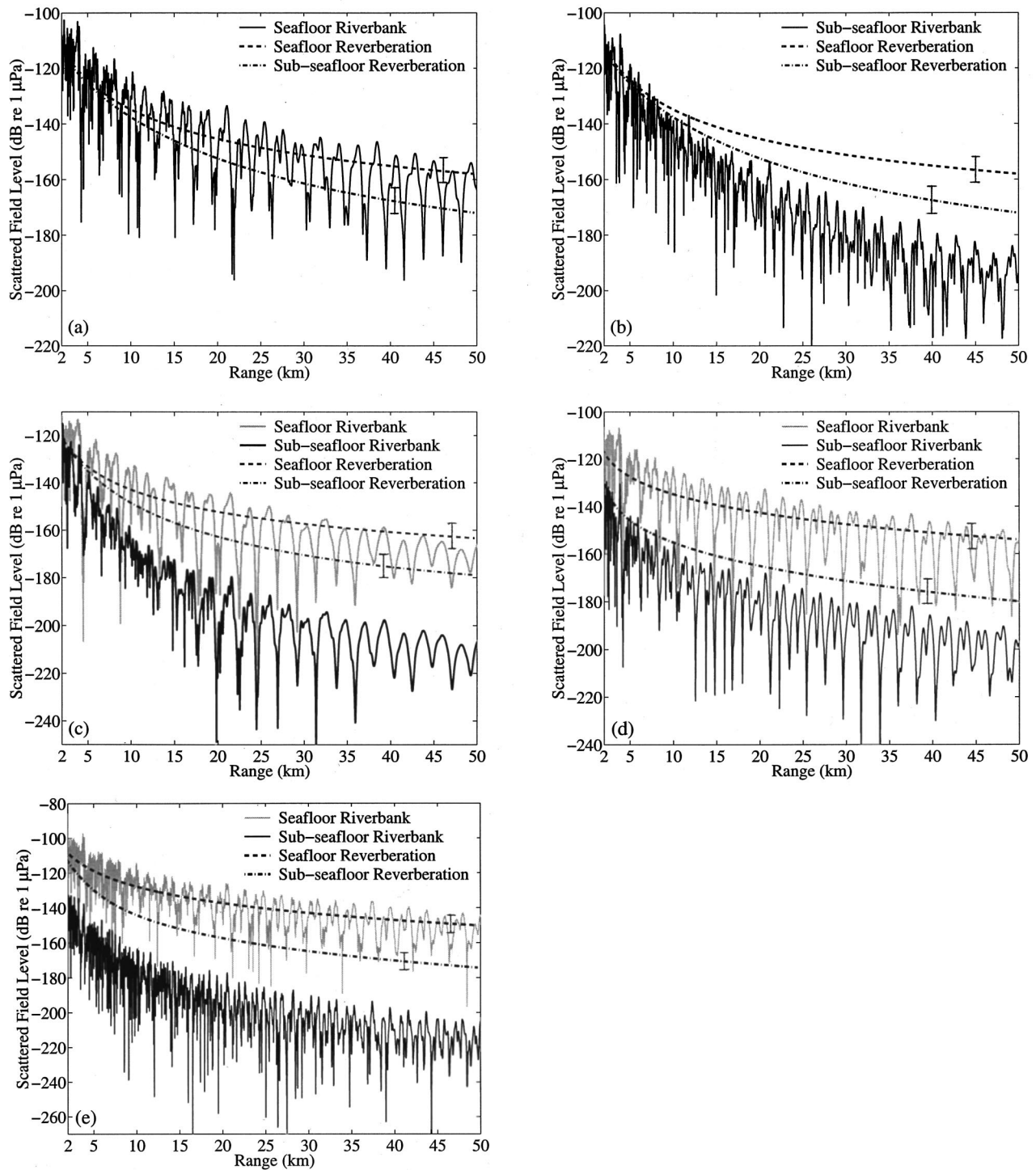


FIG. 8. Same as Fig. 7 except single layer bottom scenarios of Figs. 6(b) and (c) for coherent seafloor and subseafloor riverbank scattering are investigated. Lambert–Mackenzie reverb within the sonar resolution footprint is also shown for the sediment-layer to sediment half-space interface (subseafloor). (a) Seafloor riverbank with the upper sediment layer composed of silt with $h_1=2$ m and the lower sediment half-space composed of sand. Coherent riverbank scattering is from the double interface of water to silt to sand. (b) Subseafloor riverbank with the upper sediment layer composed of silt with $h_1=2$ m and the lower sediment half-space composed of sand. Coherent riverbank scattering is from the single silt to sand interface. (c) Seafloor and subseafloor riverbanks as in (a) and (b) but with the upper sediment layer now at $h_1=5$ m thickness. (d) Same as (c) but with the upper sediment layer composed of sand with $h_1=2$ m and the lower sediment half-space composed of silt. (e) Same as (d) except $h_1=5$ m.

given by Eqs. (8) and (9) of Ref. 11 with $f(n)$ replaced by $(-1)^n f(n)$ to convert from Ingenito’s definition to the standard one described in Sec. II A.³¹

The variance of the field scattered from the seafloor

within the range-dependent resolution footprint of the sonar system under the Lambert–Mackenzie assumption of Eq. (45) is also shown in Fig. 3 in decibels, i.e., $10 \log \bar{V}_B$. Modal interference is absent due to the modal decoupling

assumed in diffuse scattering from large seafloor patches. Ambiguous returns from both sides of the line array are included.

The scattered field from both the target sphere and seafloor is highly dependent on the geo-acoustic parameters of the bottom, as is evident in Fig. 3(a) where significant differences arise when the bottom type is changed from sand to silt. The differences arise primarily because the number of trapped modes is significantly larger for the sand half-space due to the higher critical angle of 28.1° for water to sand as compared with the 9.3° for water to silt. This leads to a correspondingly higher mean level, of roughly 20 dB, for both target and seafloor backscatter and a shorter modal interference length scale in the scattered field from the sphere.

In the Pekeris waveguide examples of Fig. 3(a), the target stands tens of decibels above the expected reverberation within the broadside beam regardless of whether the bottom is composed of sand or silt. This signal excess is well above the reverberation level standard deviation of 5.6 dB assuming the seafloor scattering obeys circular complex Gaussian statistics, in accord with the central limit theorem.²¹ If a single omni-directional hydrophone placed at the center of the receiving array replaces the full array, the reverberation levels are augmented by roughly $10 \log(2\pi/d\phi) \approx 20$ dB in Fig. 3. The target sphere then no longer consistently stands above the expected reverberation even at short ranges, for example, within a few kilometers. A directional array is then necessary to spatially filter the target from omni-directional reverberation so that detection can be practically achieved in the given scenarios.

The effect of bottom properties on both submerged target scattering and reverberation is again evident when layered bottoms are considered. For the silt-over-sand scenarios of Fig. 3(b), the characteristics of the field scattered from the target are a combination of those found for the silt and sand half-spaces. As the silt layer increases from roughly one-half to a full wavelength, the rate of modal interference decreases, as does the overall level of the scattered field from both the target and bottom. When the layer thickness reaches a full wavelength, the level of reverberation approaches that obtained for a pure silt bottom as range increases. The low critical angle between the water-silt interface enables greater bottom penetration than is possible with a water-sand interface. The high attenuation of the silt layer then leads to bottom loss that increases with the thickness of the layer.

For the sand-over-silt scenarios of Fig. 3(c), the field scattered from the target greatly resembles that obtained for the pure sand bottom of Fig. 3(a). The match becomes better as the sand layer increases in thickness from one-half to a full wavelength, in which case the reverberation increases from a few decibels below to roughly the level found for a pure sand bottom. In the latter case, the silt half-space is effectively insulated from the water column by evanescent decay of the trapped modes in the sand layer.

The absolute and relative levels of target and reverberation echo returns are highly dependent upon the water column sound speed structure as well as source, receiver, and target depth. To illustrate this, consider the typical shallow water downward refracting profile shown in Fig. 1, with

$c_{w1} = 1520$ m/s, $c_{w2} = 1500$ m/s, and a linear transition region in between, that is similar to what is found in continental shelf waters in late spring and summer months. Monostatic measurements of the field scattered from a 10-m-radius pressure-release sphere are again made with the same array and cw tone used in the previous examples. The target is at array broadside and both target returns and reverb within the broadside beam are plotted as a function of range, where the reverb is computed again for a $T = \frac{1}{2}$ s cw at 300 Hz center frequency. Three combinations of monostatic source-receiver and target depths are considered, as illustrated in Fig. 2.

First consider the case in Fig. 4(a), where the source, receiving array, and sphere center are at 50-m depth just as in the Pekeris waveguide examples. For the sand bottom, the levels are similar to those found in the corresponding example of Fig. 3(a), with the target standing out by tens of decibels. For the silt bottom, the target still stands tens of decibels above the reverberation but the absolute levels of the scattered fields decay more rapidly with range in the present scenario since the downward-refracting profile causes more acoustic energy to penetrate into the bottom.

Loss of energy to the bottom is augmented when the source and receiver array are placed in the mixed layer, at 10-m depth, while the target remains with center at 50-m depth, as shown in Fig. 4(b). The absolute levels of both the field scattered from the target sphere and the seafloor are reduced by tens of decibels beyond a few kilometers' range for the silt bottom. For the sand bottom, the reverberation level is not significantly changed by moving the source and receiver into the mixed layer. Returns from the target sphere, however, no longer stand prominently enough above the expected reverberation to insure detection, given a 5.6-dB standard deviation in reverberation level.

The situation for detection again changes when the target sphere is placed in the mixed layer, with sphere center at 15-m depth, along with the source and receiver at 10-m depth as shown in Fig. 4(c). This is especially so for the silt bottom, where the scattered field from the target sphere becomes so greatly reduced, when compared to the previous examples of this section, that its returns only stand above the expected reverberation level within roughly 16-km range. It is interesting that for the sand bottom, the placement of the target and source-receiver in the mixed layer leads to more favorable conditions for detection, which should be possible beyond 50-km range, than if only the source-receiver were placed in the mixed layer and the target was in the middle of the water column as in Fig. 4(b). This is because the higher-order modes stimulated by the shallow source, receiver, and target can be supported by the high-critical-angle sand bottom.

The exercise of changing the depths of the source-receiver and target is repeated in Fig. 5 for a constant sound speed water column. For the sand bottom, the level of the field scattered from the sphere is not affected significantly by moving the source-receiver and target depths. For the silt bottom, however, a significant decrease in the sphere's echo-return level is found for shallow source-receiver and target placements. Apparently, these shallow placements stimulate

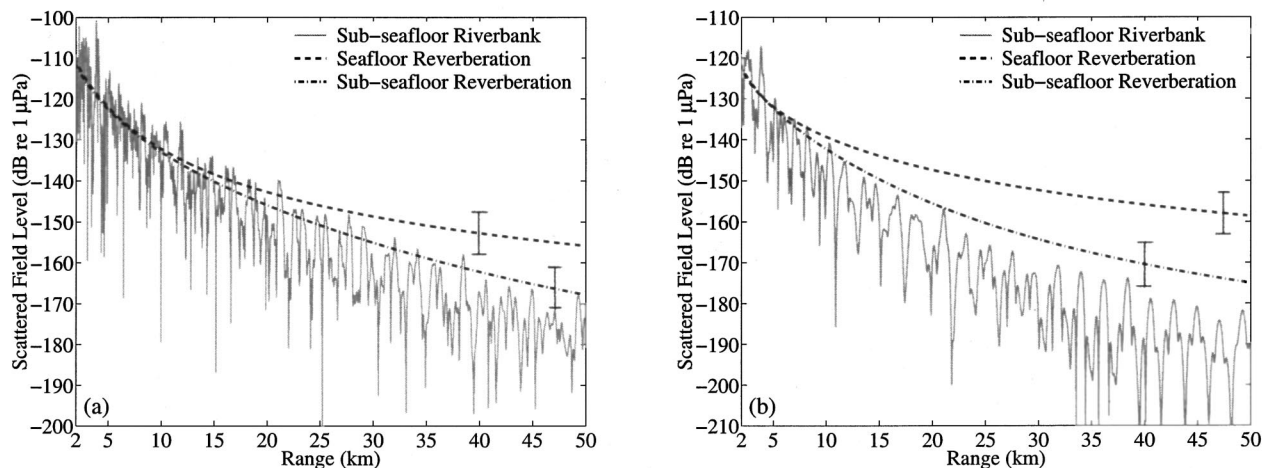


FIG. 9. Same as Fig. 8 except two-layer bottom scenario of Fig. 6(d) is investigated for coherent scattering from subseafloor riverbank. (a) Sediment is comprised of light silt layer of $h_1 = 1$ -m thickness over a silt layer of $h_2 = 1$ -m thickness over a sand half-space. Coherent riverbank scattering is from the double interface of light silt to silt to sand. (b) Sediment is comprised of light silt layer of $h_1 = 1$ -m thickness over a sand layer of $h_2 = 1$ -m thickness over a silt half-space. Coherent riverbank scattering is from the double interface of light silt to sand to silt.

higher-order modes that are not supported by the silt bottom. These results should be compared to those found in Fig. 3(a) for source–receiver and target depths in the middle of the waveguide at 50 m.

B. Geological clutter versus diffuse seafloor reverberation

Geomorphic features of the seafloor can return echoes that stand well above the diffuse reverberation background described in the previous section. Since these echoes appear as discrete events in time or range, they may be used to remotely image seafloor or subseafloor geomorphology in geophysical applications. They may, however, also be confused with returns from a submerged target in an active detection scenario.

Both coherent and incoherent scattering from the canonical seafloor and subseafloor features, shown in Fig. 6, are investigated. Both kinds of features are modeled as a flat 100×100 -m² surfaces at an inclination of 10 degrees. The dimensions and inclination are based on actual geophysical data characterizing seafloor and subseafloor riverbanks.³² Seafloor and subseafloor river channels are commonly found in continental shelf waters after a sea level rise. The latter requires an additional influx of sedimentation. In all cases to be considered here, the waveguide is modeled as an isovelocity water column overlying one or two sediment layers that cover a sediment half space.

For the coherent calculation, the riverbank is treated as a smooth but finite square surface with reflection coefficient appropriate to the given boundary conditions, including multiple reflection from various layers. The coherent scattered field from the riverbank in the layered waveguide follows when the scatter function for the smooth riverbank, given in Eq. (59), is inserted into Eq. (1). Coherent scattering from the riverbank is then completely determined by the boundary conditions at the riverbank and the riverbank geometry. For the incoherent calculation, the riverbank is modeled first as a

diffusely scattering Lambertian surface with the empirically derived Mackenzie albedo and riverbank tilt angle incorporated as indicated in Eq. (41). The diffuse calculations are also made using perturbation theory by substituting Eq. (58) into Eq. (17). In both cases, the assumption is that the seafloor feature falls within the resolution footprint of the sonar system.

Illustrative examples are given in Figs. 7–9, 13, 19, and 20. The geometry is again monostatic with colocated omnidirectional point source and receiving array centers at 50-m depth. The receiving array lies parallel to the y axis. The square riverbank surface has two edges parallel to the y axis, is centered at $y = 0$, and inclined 10 degrees about the x axis. All plots give the scattered field from the riverbank as a function of range from the monostatic sonar. For comparison, incoherent reverberation from the water–sediment interface within the resolution footprint of the sonar, based on the Lambert–Mackenzie model for an un-inclined surface, is also plotted as a function of range in Figs. 7–9 and 13 and based on perturbation theory in Figs. 19 and 20. This is referred to as diffuse seafloor reverberation. The range and cross-range resolution of the sonar system resolution footprint are the same as those stated in the introduction to Sec. IV. Similarly, incoherent reverberation from the sediment layer to sediment half-space interface, based upon the Lambert–Mackenzie model for an uninclined surface, is also plotted as a function of range in Figs. 7–9 and 13, and based on perturbation theory in Figs. 19 and 20. This is referred to as diffuse subseafloor reverberation. The far field of the coherent riverbank begins at roughly 2 km while the far field of the receiving array begins at roughly 1.2 km.

For the Pekeris waveguide scenario of Fig. 6(a), returns from the seafloor riverbank features stand well above diffuse seafloor reverberation from the silt bottom within ranges of roughly 20 km and from the sand bottom beyond ranges of 50 km when the riverbank is treated as a coherent scatterer, as shown in Fig. 7. The ordinate is in decibels, i.e., $20 \log |\Phi_s|$

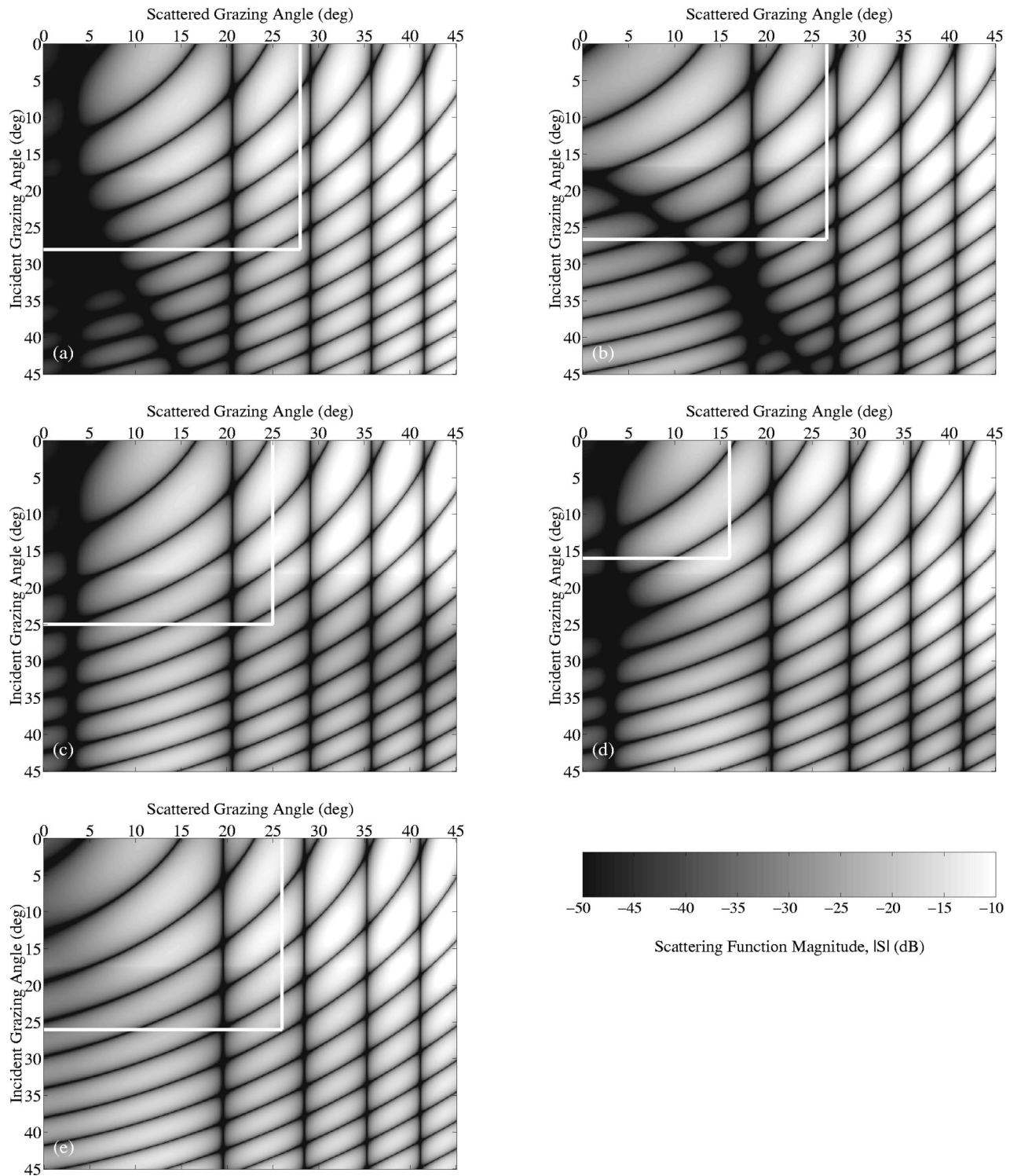


FIG. 10. Magnitudes of the coherent scattering functions $|S(\alpha, \beta = \pi, \alpha_i, \beta_i = 0)|$, i.e., $20 \log |S|$ dB, for the $100 \times 100\text{-m}^2$ seafloor and subsurface riverbank features at inclination $\chi = 10$ degrees of Fig. 6 over bistatic horizontal grazing angle $\pi/2 - \alpha_i$ for the incident and $\alpha - \pi/2$ for the scattered wave, as appropriate for backscatter in a waveguide. The boxes include all modes n where $0.5 \text{ rad/km} > \text{Im}\{\xi_n\}$. This includes all and only trapped modes for the Pekeris waveguide scenario of Fig. 6(a). (a) Reflection coefficient for water to sand is used for scenario of Fig. 6(a). (b) Reflection coefficient of silt to sand is used for scenario of Fig. 6(c). (c) Double reflection coefficient of water to 2-m silt layer over sand is used for scenario of Fig. 6(b). (d) Double reflection coefficient of water to 5-m silt layer over sand is used for scenario of Fig. 6(b). (e) Double reflection coefficient of light silt to 1-m silt layer over sand is used for scenario of Fig. 6(d).

for riverbank returns and $10 \log \bar{V}_B$ for diffuse reverberation.

For the single-layered bottom scenarios of Figs. 6(b) and (c), returns from both the seafloor riverbank and subsurface riverbank features can stand well above diffuse seafloor re-

verberation from the silt-over-sand bottom when the riverbank is treated as a coherent scatterer and the silt layer is 2 m or $\frac{2}{3}$ of a wavelength, as shown in Figs. 8(a) and (b). The subsurface riverbank and seafloor riverbank return echoes at

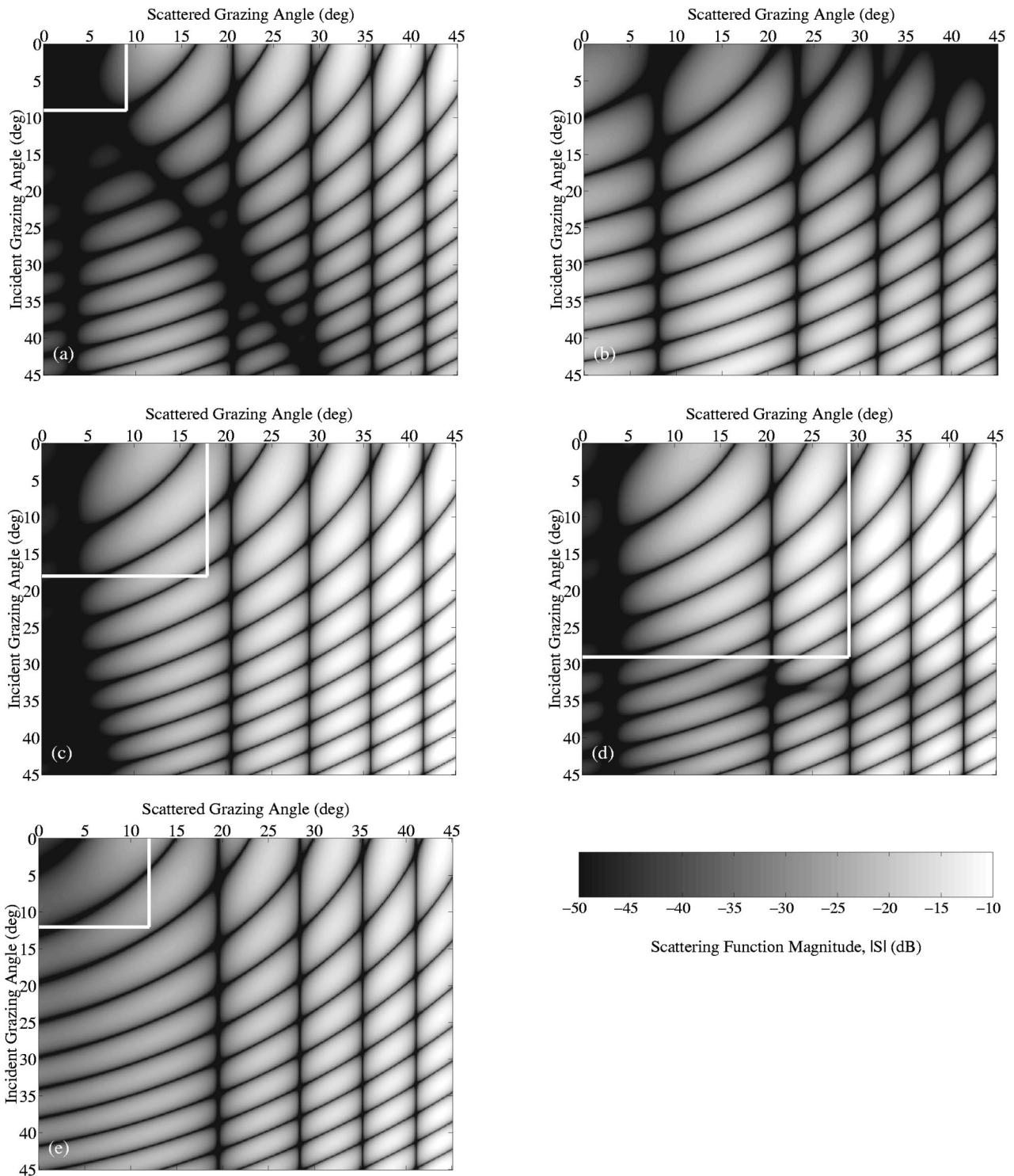


FIG. 11. Same as Fig. 10 except (a) reflection coefficient for water to silt is used for scenario of Fig. 6(a). (b) Reflection coefficient of sand to silt is used for scenario of Fig. 6(c). (c) Double reflection coefficient of water to 2-m sand layer over silt is used for scenario of Fig. 6(b). (d) Double reflection coefficient of water to 5-m sand layer over silt is used for scenario of Fig. 6(b). (e) Double reflection coefficient of light silt to 1-m sand layer over silt is used for scenario of Fig. 6(d).

similar levels within roughly 5 km, where both features typically stand above the diffuse seafloor reverberation by roughly 10 dB, which exceeds the 5.6-dB standard deviation. The prominence of the subseafloor riverbank returns follows from the greater impedance mismatch between the silt–sand interface than the water–silt interface incorporated in the riverbank scatter function. Beyond roughly 5 km, the subsea-

floor feature has returns that fall off more rapidly than those of the seafloor feature. This follows from the stripping of higher-order modes that propagate with high attenuation in the silt layer. Coherent returns from the riverbank arise because of its finite extent. Since the riverbank is modeled as a smooth flat surface, scattering is greatest in the specular direction and falls off in other directions in a manner similar to

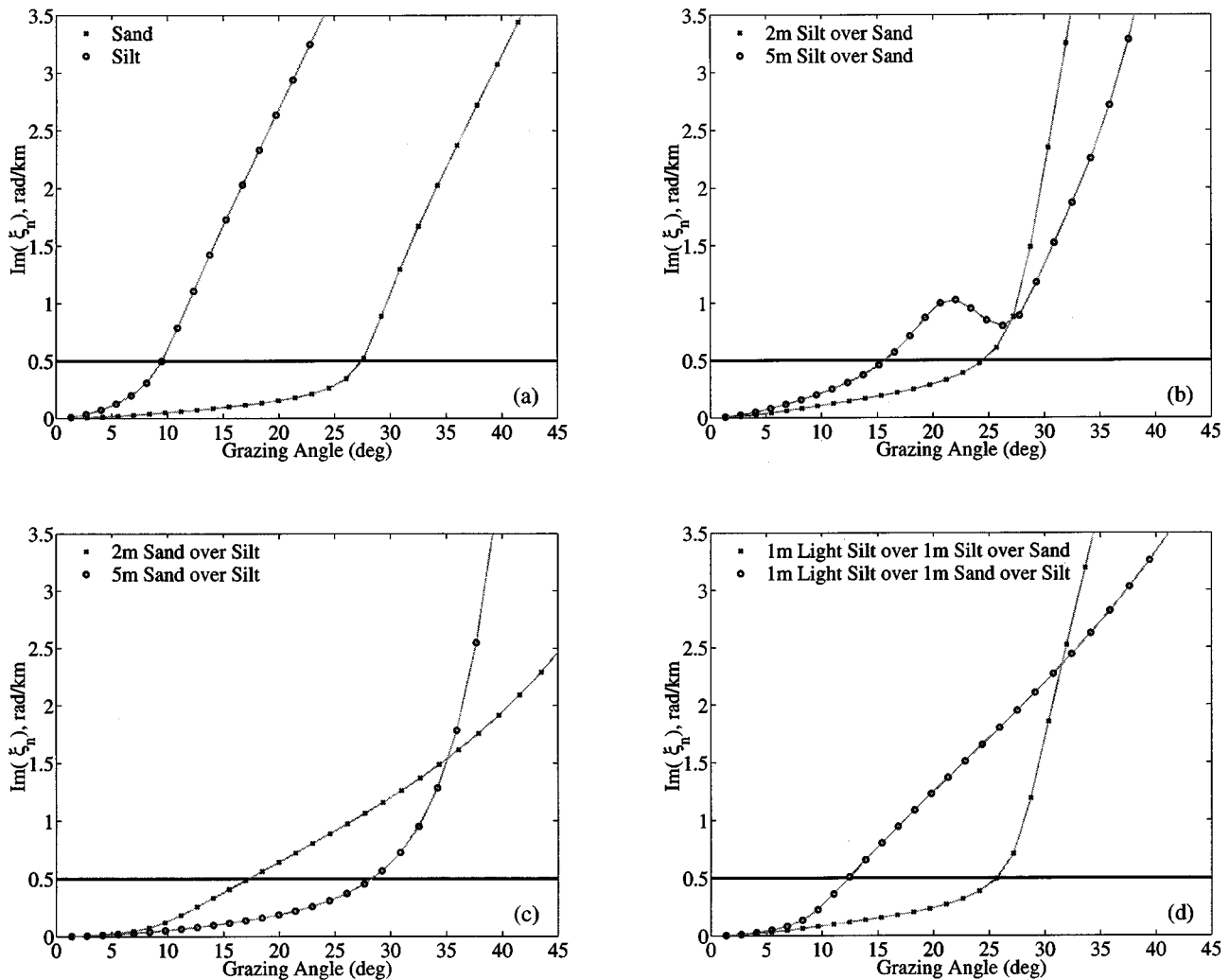


FIG. 12. The horizontal wave number's imaginary component $\text{Im}\{\xi_n\}$ is plotted as a function of horizontal grazing angle, $|\pi/2 - \alpha_i|$, for the various waveguides considered. Proper modes occur in Pekeris below the critical angle for $0.5 \text{ rad/km} > \text{Im}\{-\xi_n\}$. (a) Pekeris with sand bottom and Pekeris with silt bottom. (b) Constant water column sound speed of 1500 m/s over $h_1=2\text{-m}$ and $h_1=5\text{-m}$ silt layer over sand half-space. (c) Constant water column sound speed of 1500 m/s over $h_1=2\text{-m}$ and $h_1=5\text{-m}$ sand layer over silt half-space. (d) Constant water column sound speed of 1500 m/s over 1-m light silt layer over 1-m silt layer over sand half-space and constant water column sound speed of 1500 m/s over 1-m light silt layer over 1-m sand layer over silt half-space.

the sidelobes of a phased array's beampattern. In backscatter, for the given geometry, the riverbank returns increase in intensity with the square of its length, or cross-range extent. Longer riverbanks that fit within the sonar resolution footprint then yield significantly larger returns as a consequence of the coherent scattering assumption, and may stand well above diffuse seafloor reverberation beyond 10 km. Returns from such extended riverbanks, however, rapidly become more of a challenge to model since the near field moves out in range from the feature with the square of its length. As the range extent of the riverbank increases, the coherent area increases but the side lobe level decreases for the present geometry, rendering the effect on the backscattered field less apparent than in cross-range augmentation.

When the thickness of the silt layer is increased to 5 m, or one wavelength, returns from the subseafloor riverbank features are somewhat reduced, as shown in Fig. 8(c), and again only stand above diffuse seafloor reverberation within roughly 5 km. This follows from a related increase in the stripping of the higher-order modes that have propagating components in the sediment layer since the sediment layer

has much higher attenuation than the water column. The seafloor riverbank feature stands above diffuse seafloor reverberation beyond 20 km but rarely in excess of the Gaussian field standard deviation of 5.6 dB.

When the sediment layer is composed of sand and the half-space below is made of silt, the situation changes drastically, as shown in Figs. 8(d) and (e). Returns from the subseafloor riverbank no longer stand above diffuse seafloor reverberation beyond 2 km because in the sand layer, which is much faster than the water column and silt half-space, the trapped modes become evanescent. Seafloor riverbank returns stand well above diffuse seafloor reverberation, occasionally by 10 dB or more, even beyond 20 km for both the 2- and 5-m-thick sand layers, as expected given the large impedance contrast between water and sand. Older seafloor features, in fact, are more likely to be composed of consolidated material such as sand or limestone since such materials are better able to withstand erosion. Steeper seafloor features that are common in many continental shelves, such as glacier and iceberg scours, can yield even higher returns.

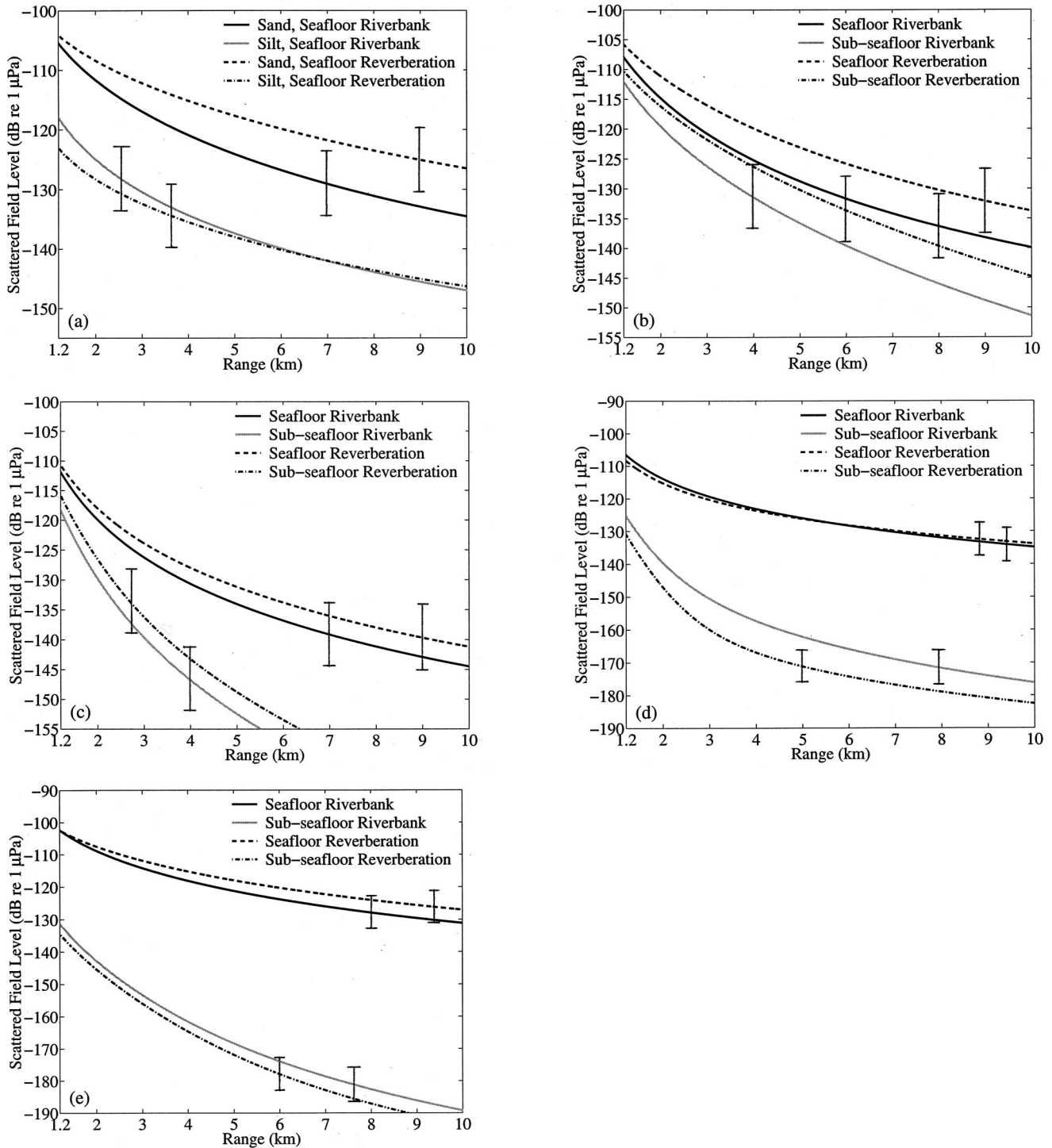


FIG. 13. Same as Figs. 7 and 8 except the Lambert–Mackenzie model is used to model scattering from inclined riverbank features. (a) Seafloor riverbank over sand and silt half-spaces. (b) Seafloor and subseafloor riverbank scattering with the upper sediment layer composed of silt with $h_1=2$ m and the lower sediment half-space composed of sand. (c) Same as (b) except $h_1=5$ m. (d) Seafloor and subseafloor riverbank scattering with the upper sediment layer composed of sand with $h_1=2$ m and the lower sediment half-space composed of silt. (e) Same as (d) except $h_1=5$ m.

For the two-layered bottom of Fig. 6(d), the subseafloor riverbank returns stand roughly 10 dB above diffuse seafloor reverberation out to roughly 10 km for a 1-m light-silt layer over a 1-m silt layer over a sand half-space, as shown in Fig. 9(a). The double layer reflection coefficient from the light-silt to silt to sand interfaces leads to the increased prominence of the subseafloor riverbank returns, compared with those obtained with the single-layer reflection coefficient of

Figs. 8(a)–(e). When the layering is altered to 1-m light-silt over sand over a silt half-space, returns from the subseafloor riverbank feature only stand above diffuse seafloor reverberation within roughly 5 km. This indicates that sediment stratification of the geomorphic feature can weigh in heavily in fixing its scattering amplitude.

The effect of bottom layering on the coherent scattering function of the inclined seafloor and subseafloor riverbank

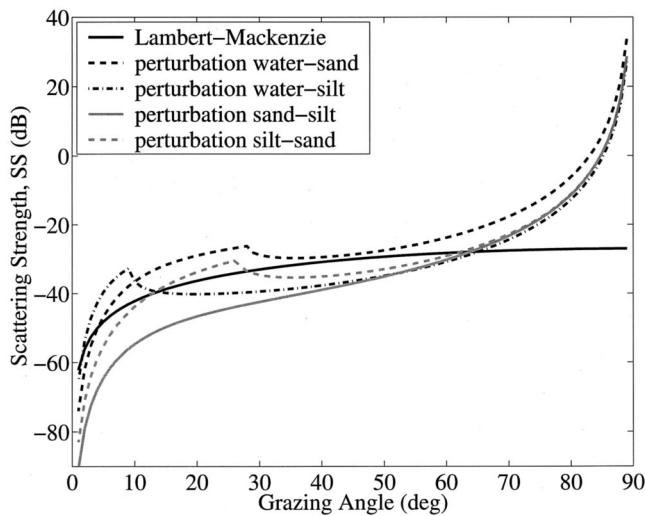


FIG. 14. Scattering strength $SS(\theta = \pi - \theta_i, \phi = 0; \theta_i, \phi_i = \pi)$ in free-space backscatter as a function of surface grazing angle $|\pi/2 - \theta_i|$ for a diffusely scattering surface obeying Lambert-Mackenzie and first-order perturbation theory scattering laws. The first-order perturbation theory curves are for cases where the plane wave is incident from an upper to a lower medium, where the upper and lower media can be water, sand, or silt.

features of Fig. 6 is illustrated in Figs. 10 and 11 as a function of horizontal grazing angle, $\pi/2 - \alpha_i$ for the incident and $\alpha - \pi/2$ for the scattered wave, at fixed incident and scattered azimuths, $\beta_i = 0, \beta = \pi$, as is appropriate to backscatter in a waveguide. The trapped modes for the Pekeris waveguide scenarios, Fig. 10(a) for a sand bottom and Fig. 11(a) for a silt bottom, have incident and scattered elevation angles that lie within the boxes shown, the dimensions of which correspond to the respective bottom critical angle. The boxes include all modes n where $0.5 \text{ rad/km} > \text{Im}\{\xi_n\}$. This includes all and only trapped modes for the Pekeris waveguide scenario of Fig. 6(a). The latter criterion is used to segment modes that dominate the incident propagation by similar boxes for the more complicated layered bottom cases illustrated in Figs. 10 and 11. The value $\text{Im}\{\xi_n\}$ is plotted as a function of equivalent modal angle α in Fig. 12 for the various waveguides considered. This makes it possible to see how the scattering functions of Figs. 10 and 11 are discretely sampled in the waveguide scattering theory defined by Eq. (1) and to estimate the attenuation of a given modal component as a function of range. Inspection of Figs. 10 and 11 reveals that seafloor and subseafloor riverbank features that backscatter most prominently in Figs. 7–9 have scatter functions with relatively large amplitudes at the equivalent angles of the propagating modes. While modes propagating at steeper angles suffer greater attenuation, as indicated in Fig. 12, these same modes are scattered much more efficiently by the slightly inclined riverbank features as indicated in Figs. 10–11, so that there is some balancing between the two effects that is unique to waveguide scattering. Higher-order modes, with elevation angles less than 45 degrees where 0 degrees points downward, however, contribute negligibly to the field scattered from the riverbank features for the ranges and features investigated in the present article.

When the riverbank is treated as an incoherent scatterer with the Lambert-Mackenzie model of Eq. (41), returns

from both the $100 \times 100\text{-m}^2$ seafloor and subseafloor riverbank features at 10 degrees inclination never stand above diffuse seafloor reverberation by more than a fraction of the expected 5.6-dB standard deviation, as shown in Fig. 13. Riverbank returns are again in decibels, i.e., 10 times the log of the covariance given in Eq. (41). This is still the case for the ranges shown in Fig. 13, except for the 2-m sand layer, even if the riverbank feature is extended laterally to fill the entire cross-range width of the system resolution footprint, as can be readily checked by noting that diffuse reverberation accrues in direct proportion to the area of the scattering patch. For the 2-m sand layer, the seafloor riverbank can have returns that exceed the diffuse reverberation background by more than 5.6 dB if it fills the entire resolution footprint in cross-range.

Diffuse subbottom reverberation, shown in Fig. 13, always returns at a lower level than diffuse seafloor reverberation if the same empirical Lambert-Mackenzie incoherent scattering law is used. This comparison highlights the differences in propagation to and from the seafloor and subbottom interfaces since the scattering function is held fixed. The comparison may be purely academic, however, because the Lambert-Mackenzie law serves as an empirical catch-all that describes the entire seabed scattering process and so already incorporates the effect of bottom layering and volume scattering in some average sense. There is, in other words, no reason to believe that scattering from the different interfaces can be modeled with exactly the same albedo and scattering law.

Perturbation theory offers a more fundamental approach to modeling rough surface scattering that can also be used to investigate potential mechanisms for geological clutter. While the impedance contrast at the scattering interface is fully accounted for in the perturbation theory formulation, additional parameters describing the roughness spectrum must be known. The perturbation theory formulation described in Sec. III D is used with the spectral strength and power law parameters $w_2 = 0.04/(2\pi)$ and $\gamma = 4.0$, yielding frequency-independent scattering, following Essen.³³ These values are not based on physical measurements, since none are presently available in the present frequency range, but rather have been chosen so that the scattering strength that perturbation theory yields is near that of the empirical Lambert-Mackenzie model for the various single and multiple reflection interfaces considered here, as shown in Fig. 14. In all curves where scattering arises from a wave incident from a slower medium, a discontinuity in slope is found at the critical angle. Beyond this a significant reduction in scattering occurs until roughly 45 degrees where shallow angle assumptions of first-order perturbation theory are no longer valid for the given surface roughness parameters, and the curves increase dramatically in an unphysical manner. Differences in the perturbation theory curves away from the critical angles arise principally from the impedance contrasts between the media considered. An exception occurs for fast sand over slow silt where no critical angle exists and transmission into the silt is significant even at very shallow angles, where low level scattering results.

The effect of scattering and reflection from multiple lay-

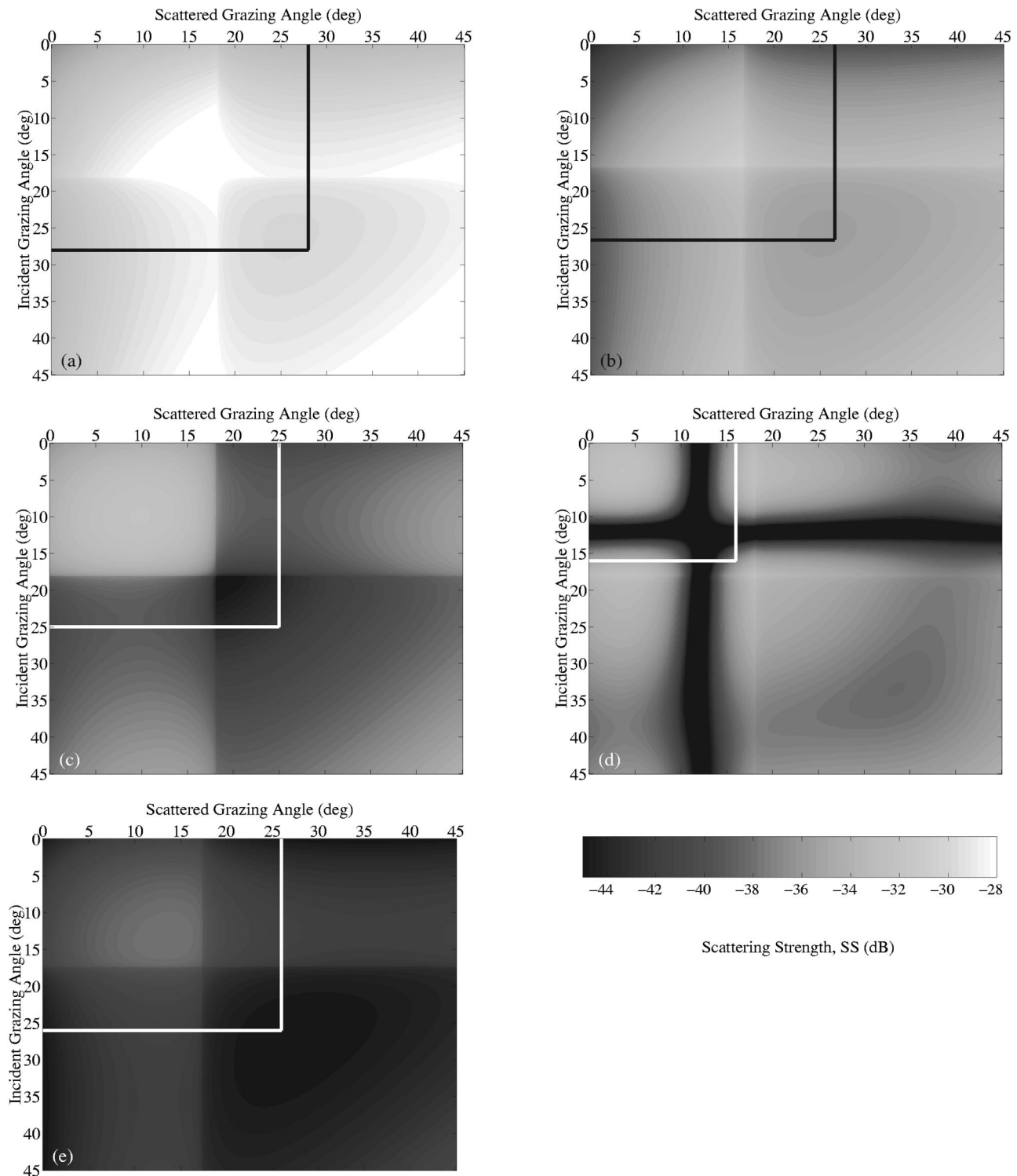


FIG. 15. Scattering strength $SS(\alpha, \beta = \pi, \alpha_i, \beta_i = 0)$, based on first-order perturbation theory for the seafloor and subseafloor riverbank features at inclination $\chi = 10$ degrees of Fig. 6 over bistatic horizontal grazing angle $\pi/2 - \alpha_i$ for incident waves and $\alpha - \pi/2$ for scattered waves, as appropriate to backscatter in a waveguide. The boxes include all modes n where $0.5 \text{ rad/km} > \text{Im}\{\xi_n\}$. This includes all and only trapped modes for the Pekeris waveguide scenario of Fig. 6(a). (a) Reflection coefficient for water to sand is used for scenario of Fig. 6(a). (b) Reflection coefficient of silt to sand is used for scenario of Fig. 6(c). (c) Double reflection coefficient of water to 2-m silt layer over sand is used for scenario of Fig. 6(b). (d) Double reflection coefficient of water to 5-m silt layer over sand is used for scenario of Fig. 6(b). (e) Double reflection coefficient of light slit to 1-m silt layer over sand is used for scenario of Fig. 6(d).

ers can be significant as shown in Figs. 15 and 16 for an inclined riverbank surface and Figs. 17 and 18 for general uninclined seafloor, where the perturbation theory scattering strength is presented for the bistatic scattering scenario rel-

evant to backscatter in a waveguide, as was done in Figs. 10 and 11 for the coherent scatter function.

Empirical values for the spectral strength and power law parameters of first-order perturbation theory have been ob-

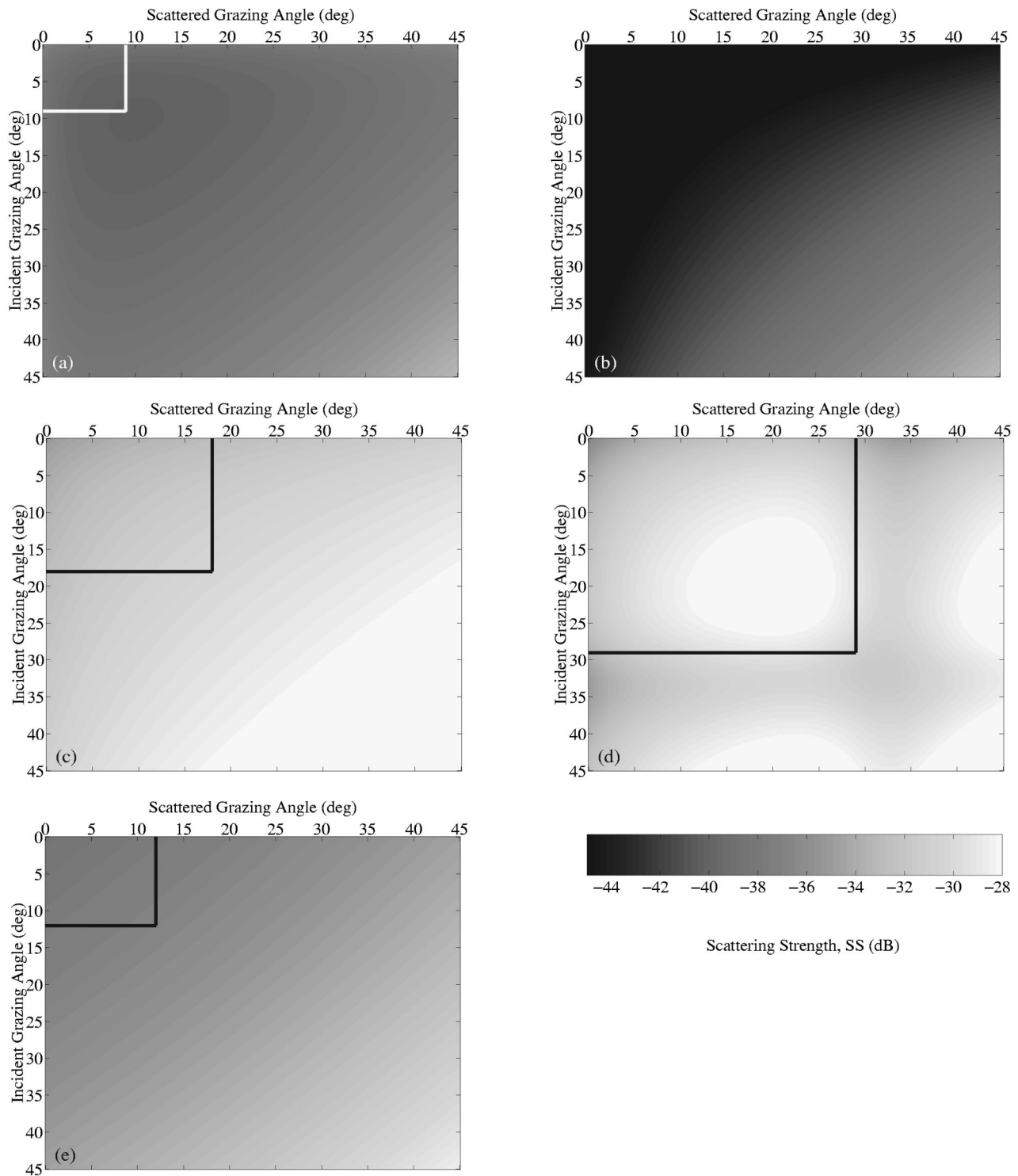


FIG. 16. Same as Fig. 15 except (a) reflection coefficient for water to silt is used for scenario of Fig. 6(a). (b) Reflection coefficient of sand to silt is used for scenario of Fig. 6(c). (c) Double reflection coefficient of water to 2-m sand layer over silt is used for scenario of Fig. 6(b). (d) Double reflection coefficient of water to 5-m sand layer over silt is used for scenario of Fig. 6(b). (e) Double reflection coefficient of light silt to 1-m sand layer over silt is used for scenario of Fig. 6(d).

tained for various seafloor types by Jackson³⁴ over the short spatial scales relevant to the analysis of high-frequency scattering in the ten kilohertz range and beyond, where this author has shown perturbation theory to match experimental data well. When these same values are used at low frequency, specifically $f = 300$ Hz, the resulting scattering law falls more than an order of magnitude below the empirical

Lambert–Mackenzie curve shown in Fig. 14. Unrealistically high roughness values for the spectral strength, as obtained for rough, rocky surfaces in the high-frequency analysis of Ref. 34, are necessary for first-order perturbation theory to match the empirical seafloor scattering strength curve of Mackenzie in the low-frequency regime of interest here. Since the Mackenzie curve summarizes the entire seafloor

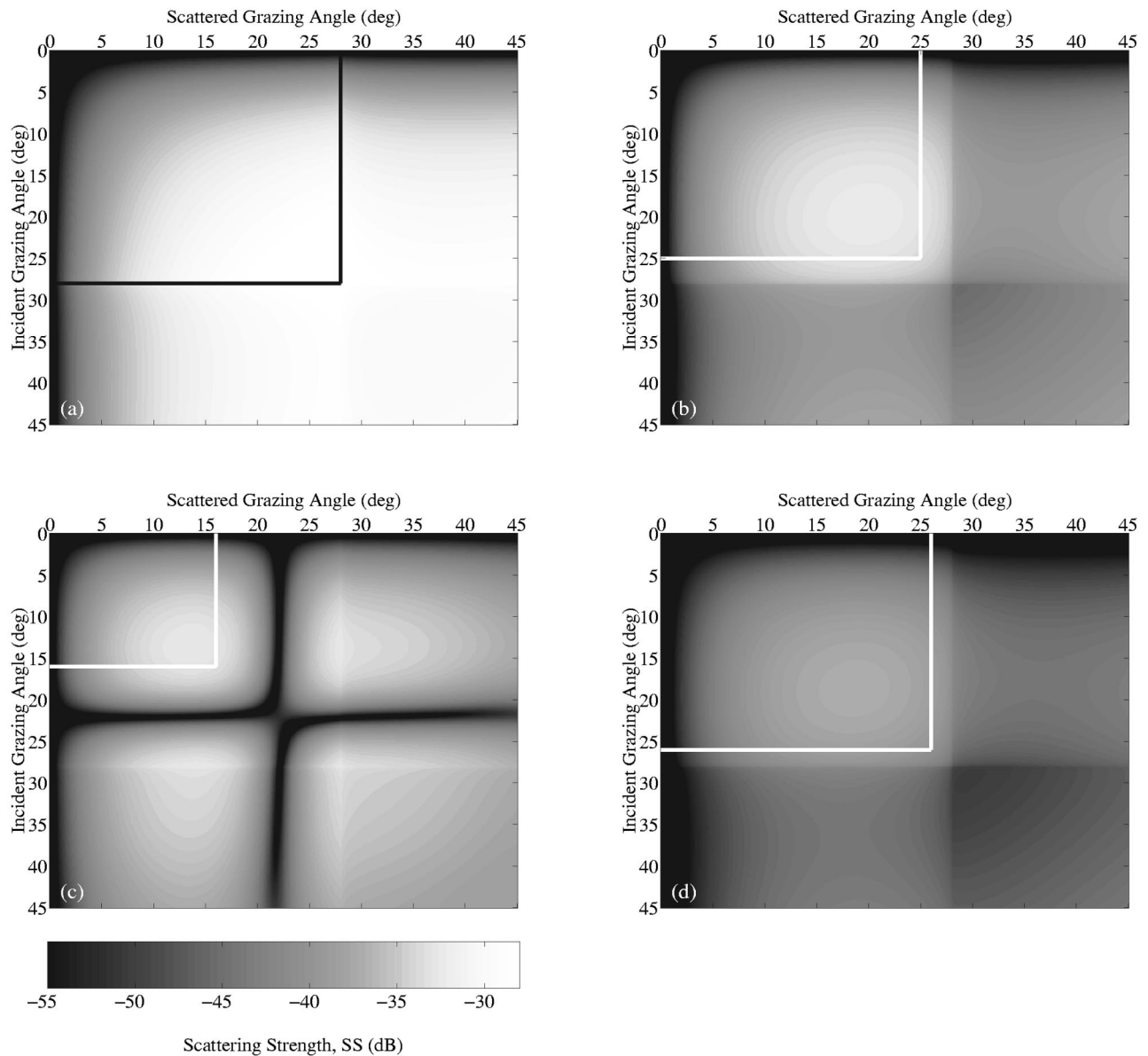


FIG. 17. Scattering strength $SS(\alpha, \beta=\pi, \alpha_i, \beta_i=0)$ based on first-order perturbation theory for level seafloor, $\chi=0$ degrees, over bistatic horizontal grazing angle $\pi/2 - \alpha_i$ for the incident wave and $\alpha - \pi/2$ for the scattered wave, as appropriate to backscatter in a waveguide. The boxes include all modes n where $0.5 > \text{Im}\{\xi_n\}$. This includes all and only trapped modes for the Pekeris waveguide scenario of Fig. 6(a). (a) Reflection coefficient for water over sand is used. (b) Double reflection coefficient of water over 2-m silt over sand is used. (c) Double reflection coefficient of water over 5-m silt layer over sand is used. (d) Triple reflection coefficient of water over 1-m light silt layer over 1-m silt layer over sand is used.

scattering process, and is not limited to interface scattering or the more restrictive type of interface scattering described by first-order perturbation theory, it is reasonable to conclude that either the assumptions of first-order perturbation theory are inadequate to properly model seafloor scattering at low frequency, a significantly different set of spectral strength and power law parameters must characterize seafloor interface scattering at low frequency, or a more sophisticated modeling of the seabed layering and sound speed gradients is necessary. It is also possible that scattering from volume heterogeneities may yield significant reverberation. This is most likely to be the case where a propagating, rather than evanescent, component of the modal spectrum exists in the layer where the volume heterogeneities are present.

When the riverbank feature is treated as an incoherent

scatterer using first-order perturbation theory, as in Figs. 19 and 20, only seafloor riverbank returns from a single sand layer can stand above diffuse seafloor reverberation by more than 5.6 dB, and this only occurs when the riverbank feature is extended laterally to fill the entire cross-range extent of the system resolution footprint. Returns from the subseafloor riverbank only stand above diffuse seafloor reverberation by more than 5.6 dB for the two-layered bottom in the light-silt over sand over silt scenario, and this only occurs if the feature is extended to fill the resolution footprint.

Comparison of Figs. 7 and 9 and Fig. 13 shows that coherent returns greatly outweigh incoherent returns from the riverbank feature. This finding is advantageous since only deterministic physical and geometrical parameters of the seafloor are necessary in the coherent model, whereas

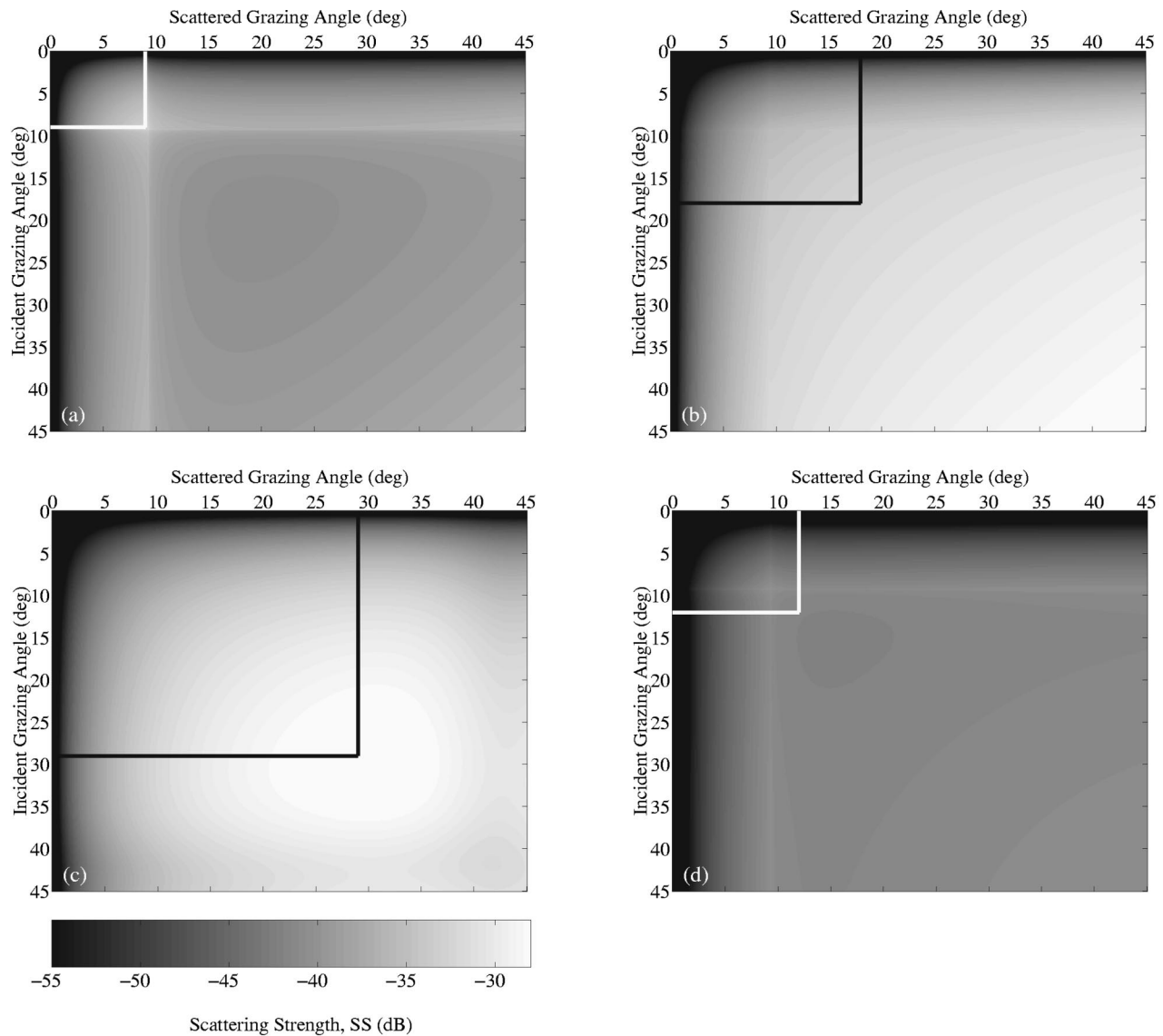


FIG. 18. Same as Fig. 17 except (a) reflection coefficient for water over silt is used. (b) Double reflection coefficient of water over 2-m sand over silt is used. (c) Double reflection coefficient of water over 5-m sand layer over silt is used. (d) Triple reflection coefficient of water over 1-m light silt layer over 1-m sand layer over silt is used.

either empirical data or a stochastic representation of the seafloor is necessary in the incoherent model. The environmental description necessary for the coherent model is then easier to obtain and rests on far fewer supporting assumptions than the incoherent one.

V. CONCLUSIONS

One of the greatest challenges to active sonar operations in shallow water arises when echo returns from the intended target become indistinguishable from reverberation returned by the waveguide boundaries and volume. To determine conditions in which a typical low-frequency active sonar system may operate effectively in a shallow water waveguide, a unified model for submerged object scattering and reverberation is developed. The approach is to use a waveguide scattering model that follows directly from Green's theorem but that takes advantage of simplifying single-scatter and far-field approximations that apply to a wide variety of problems where

the source and receiver are distant from the target. To treat reverberation from randomly rough boundaries and stochastic volume inhomogeneities, the waveguide scattering model is generalized to include stochastic targets. Analytic expressions for the spatial covariance of the field scattered from a stochastic target are then obtained in terms of the waveguide Green's function and the covariance of the target's plane wave scatter function. This makes the formulation amenable to a wide variety of approaches for computing a stochastic target's scatter function. For diffuse seafloor reverberation, two approaches are adopted, an empirical one of Lambert and Mackenzie and a fundamental one based on first-order perturbation theory. It is most convenient to describe the diffuse component of distant seafloor reverberation with a modal formulation since the modes comprise the statistical entities of the field that the scattering surface may decorrelate.

Since reverberation is measured in time but the waveguide scattering formulation is for harmonic field compo-

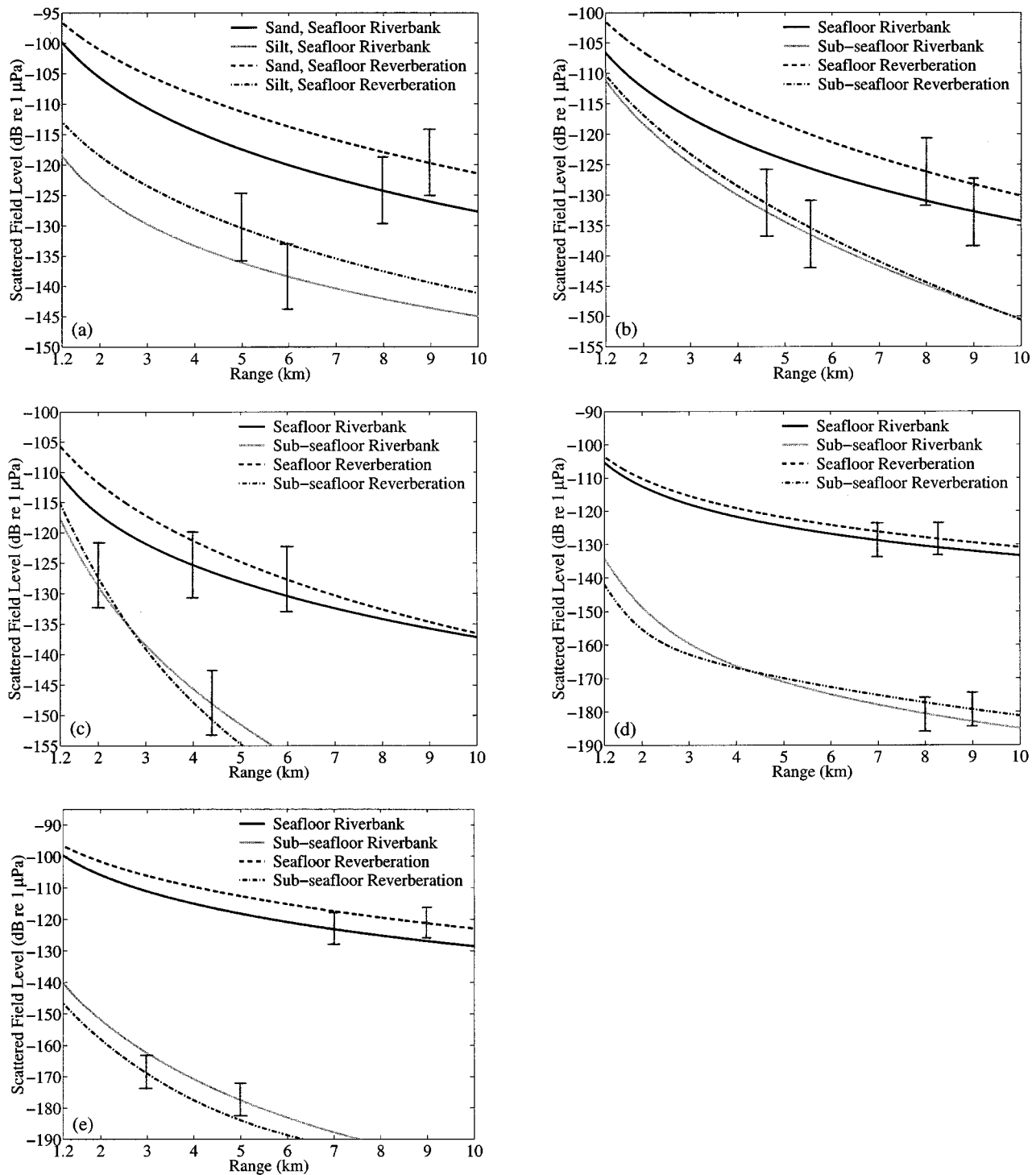


FIG. 19. Same as Figs. 7 and 8 except first-order perturbation theory is used to model scattering from the inclined riverbank features. (a) Seafloor riverbank over sand and silt half-spaces. (b) Seafloor and subseafloor riverbank scattering with the upper sediment layer composed of silt with $h_1=2$ m and the lower sediment half-space composed of sand. (c) Same as (b) except $h_1=5$ m. (d) Seafloor and subseafloor riverbank scattering with the upper sediment layer composed of sand with $h_1=2$ m and the lower sediment half-space composed of silt. (e) Same as (d) except $h_1=5$ m.

nents, the time dependence of the field scattered by a distant object from a source of arbitrary time dependence is derived analytically using the saddle point method. The resulting expression is given in terms of modal group velocities, the frequencies of which vary as a function of time and source, receiver, and target position. A simpler analytic approach involving Parseval's theorem can be applied when the integration time of the measurement system is sufficiently long

to include the dominant energy returned from the target or scattering patch. This approach is used in the illustrative examples. A viewer-oriented reference frame is then adopted, translating from the traditional target-oriented frame of waveguide scatter theory, to incorporate the continuous distribution of scatterers encountered in waveguide boundary and volume reverberation. This enables analytic expressions to be developed for the reverberant field returned bistatically

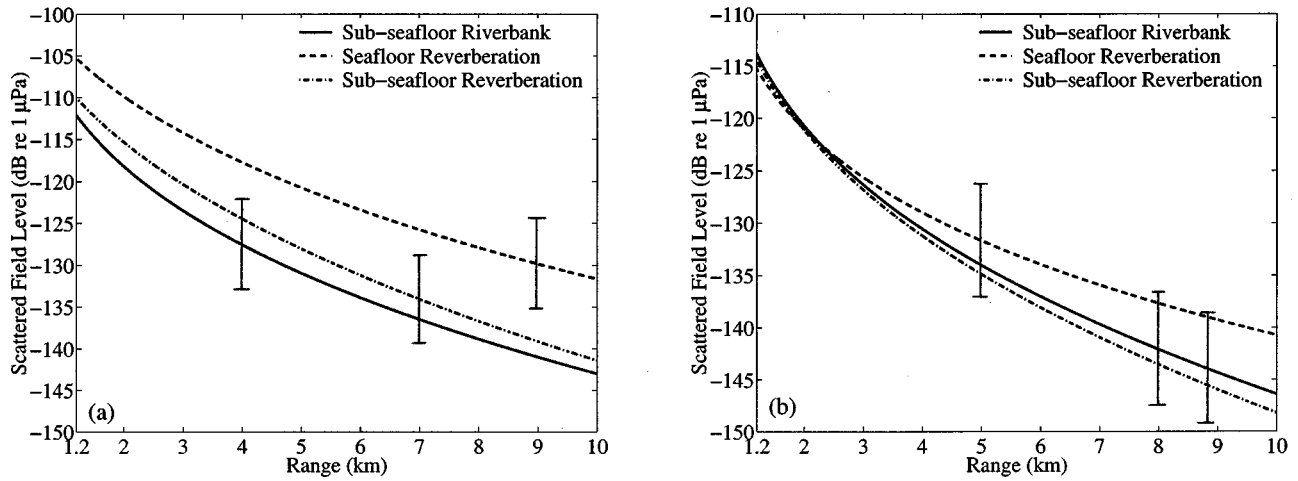


FIG. 20. Same as Fig. 9 except first-order perturbation theory is used to model scattering from the inclined subseafloor riverbank for the two-layer bottom scenario of Fig. 6(d). (a) Sediment is comprised of light silt layer of $h_1 = 1$ -m thickness over a silt layer of $h_1 = 1$ -m thickness over a sand half-space. Diffuse riverbank scattering is from the double interface of light silt to silt to sand. (b) Sediment is comprised of light silt layer of $h_1 = 1$ -m thickness over a sand layer of $h_2 = 1$ -m thickness over a silt half-space. Diffuse riverbank scattering is from the double interface of light silt to sand to silt.

from seafloor within the resolution footprint of a typical active sonar system after narrow-band beamforming with a horizontal array.

The unified model is used to investigate typical low-frequency active detection scenarios in shallow water. Sample calculations for finite-duration cw source signals indicate that the maximum range at which echo returns from a submerged target stand unambiguously above diffuse seafloor reverberation is highly dependent upon the water column and sediment stratification, as well as the receiving array aperture, source, receiver, and target location, and the scattering properties of the target and seafloor.

The model is also applied to determine conditions in which discrete morphological features of the seafloor and subseafloor return echoes that stand prominently above diffuse seafloor reverberation. Simulations for finite-duration cw source signals indicate that typical seafloor and subseafloor riverbank features, ubiquitously found throughout continental shelf waters, can return echoes that stand significantly above the diffuse component of seafloor reverberation in the operational ranges of typical low-frequency active sonar systems. This finding is significant since returns from these discrete features can be confused with returns from an intended submerged target. The relative prominence of this kind of geological clutter is highly dependent on the waveguide properties, measurement geometry, and scattering characteristics of the geological feature and surrounding seafloor. The finding that subseafloor features can cause significant clutter is particularly troubling for active sonar operations because it greatly increases the environmental characterization necessary to make accurate predictions of the expected clutter. The coherent component of the field scattered from the riverbank features examined, arising from the features' finite size, is found to far outweigh the diffuse component arising from random roughness of the features. The methods and findings of this article are presently being used to help design a number of field experiments to investigate the physical mechanisms that lead to geological clutter

in the output of active sonar systems operated in shallow water.

ACKNOWLEDGMENTS

The authors would like to thank the Office of Naval Research for financial support and encouragement as well as our colleagues in the Geological Clutter Program for many fruitful discussions.

APPENDIX A: THE PLANE WAVE SCATTER FUNCTION, TARGET STRENGTH, SURFACE SCATTERING STRENGTH, AND GREEN'S THEOREM

Standard parameters used to describe surface and target scattering in ocean acoustics can be traced back to Green's theorem by using some simple approximations involving the plane wave scatter function in free space. To do so, it must be recalled that the harmonic field $\Phi_s(\mathbf{r})$ scattered by an object can be expressed in terms of the medium Green function $G(\mathbf{r}|\mathbf{r}_t)$ and incident field $\Phi_i(\mathbf{r})$ by the Helmholtz-Kirckoff integral equation³⁵

$$\Phi_s(\mathbf{r}) = - \int_{A_t} \int [\Phi_i(\mathbf{r}_t) + \Phi_s(\mathbf{r}_t)] \frac{\partial G(\mathbf{r}|\mathbf{r}_t)}{\partial n_t} - G(\mathbf{r}|\mathbf{r}_t) \frac{\partial}{\partial n_t} [\Phi_i(\mathbf{r}_t) + \Phi_s(\mathbf{r}_t)] dA_t, \quad (A1)$$

a form of Green's theorem, where $G(\mathbf{r}|\mathbf{r}_t)$ and $\Phi_i(\mathbf{r})$ each satisfy the Helmholtz equation, driven by a source at angular frequency $\omega = 2\pi f$. The area integral encloses the scatterer and the surface normal points into the enclosed volume.

Consider, first, the problem of a plane wave

$$\Phi_i(\mathbf{r}_t) = e^{ikr_t \eta(\theta_i, \phi_i)}, \quad (A2)$$

incident on an object in free space traveling in the direction (θ_i, ϕ_i) where, for example,

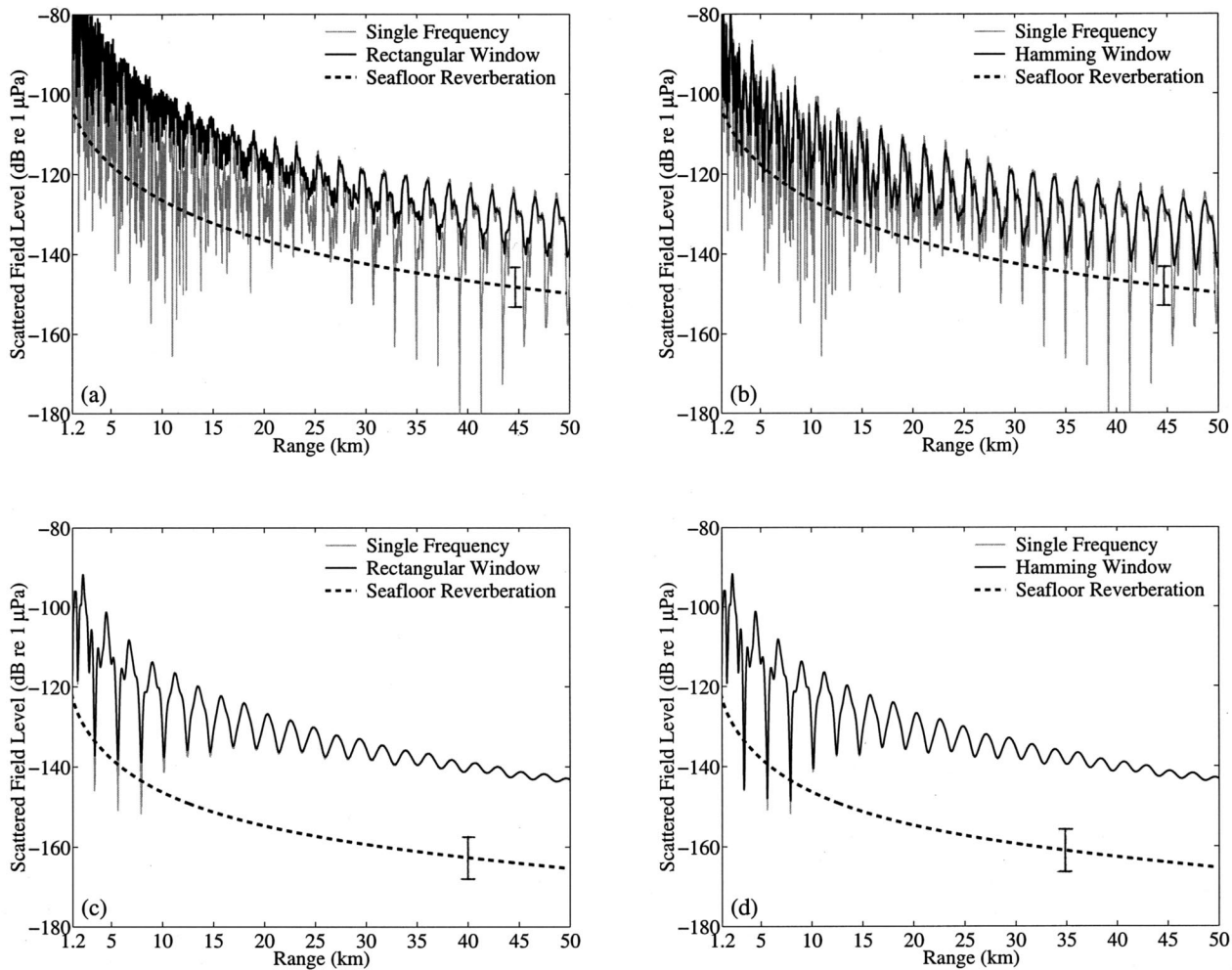


FIG. B1. A comparison of scattering using the single frequency approximation versus the full bandwidth of the given window function. Reverberation calculated using the single frequency approximation is indistinguishable from that calculated with the full bandwidth. (a) Same as Fig. 3(a) for sphere in waveguide with reverb except only the sand bottom case is shown. Single frequency approximation is compared to rectangular window. (b) Same as (a) except the Hamming window is used instead of the rectangular window. (c) Same as (a) except only the silt bottom case is shown. (d) Same as (c) except the Hamming window is used instead of the rectangular window.

$$\eta(\theta_i, \phi_i) = \cos \theta_i \cos \theta_t + \sin \theta_i \sin \theta_t \cos(\phi_i - \phi_t). \quad (\text{A3})$$

The Green function is

$$G(\mathbf{r}|\mathbf{r}_t) = \frac{1}{4\pi} \frac{e^{ik|\mathbf{r}-\mathbf{r}_t|}}{|\mathbf{r}-\mathbf{r}_t|} \approx \frac{1}{4\pi} \frac{e^{ik[r-r_t\eta(\theta, \phi)]}}{r}, \quad (\text{A4})$$

where the last approximation is for a receiver so far from the object that $r \gg r_t$. By application of Green's theorem, the scattered field at this distant receiver then can be written as

$$\begin{aligned} \Phi_s(\mathbf{r}) \approx & -\frac{e^{ikr}}{4\pi r} \iint_{A_t} [e^{ikr_t\eta(\theta_i, \phi_i)} + \Phi_s(\mathbf{r}_t)] \frac{\partial}{\partial n_t} e^{-ikr_t\eta(\theta, \phi)} \\ & - e^{-ikr_t\eta(\theta, \phi)} \frac{\partial}{\partial n_t} [e^{ikr_t\eta(\theta_i, \phi_i)} + \Phi_s(\mathbf{r}_t)] dA_t. \quad (\text{A5}) \end{aligned}$$

By the definition of the plane wave scatter function $S(\theta, \phi; \theta_i, \phi_i)$, however, it can also be written as

$$\Phi_s(\mathbf{r}) \approx S(\theta, \phi; \theta_i, \phi_i) \frac{e^{ikr}}{kr}, \quad (\text{A6})$$

in an object-centered coordinate system, which leads to the equality

$$\begin{aligned} S(\theta, \phi; \theta_i, \phi_i) & \\ & = -\frac{k}{4\pi} \iint_{A_t} [e^{ikr_t\eta(\theta_i, \phi_i)} + \Phi_s(\mathbf{r}_t)] \frac{\partial}{\partial n_t} e^{-ikr_t\eta(\theta, \phi)} \\ & - e^{-ikr_t\eta(\theta, \phi)} \frac{\partial}{\partial n_t} [e^{ikr_t\eta(\theta_i, \phi_i)} + \Phi_s(\mathbf{r}_t)] dA_t, \quad (\text{A7}) \end{aligned}$$

which relates Eq. (A5) directly to Green's theorem when $r \gg r_t$.

Equation (A5) can be recast as a sonar equation by taking $10 \log$ of the squared magnitude of both sides. In terms of the plane wave scatter function, the resulting target strength of the scatterer is then

$$T = 10 \log \left| \frac{S(\theta, \phi; \theta_i, \phi_i)}{k} \right|^2 \text{ dB re } 1 \text{ m}. \quad (\text{A8})$$

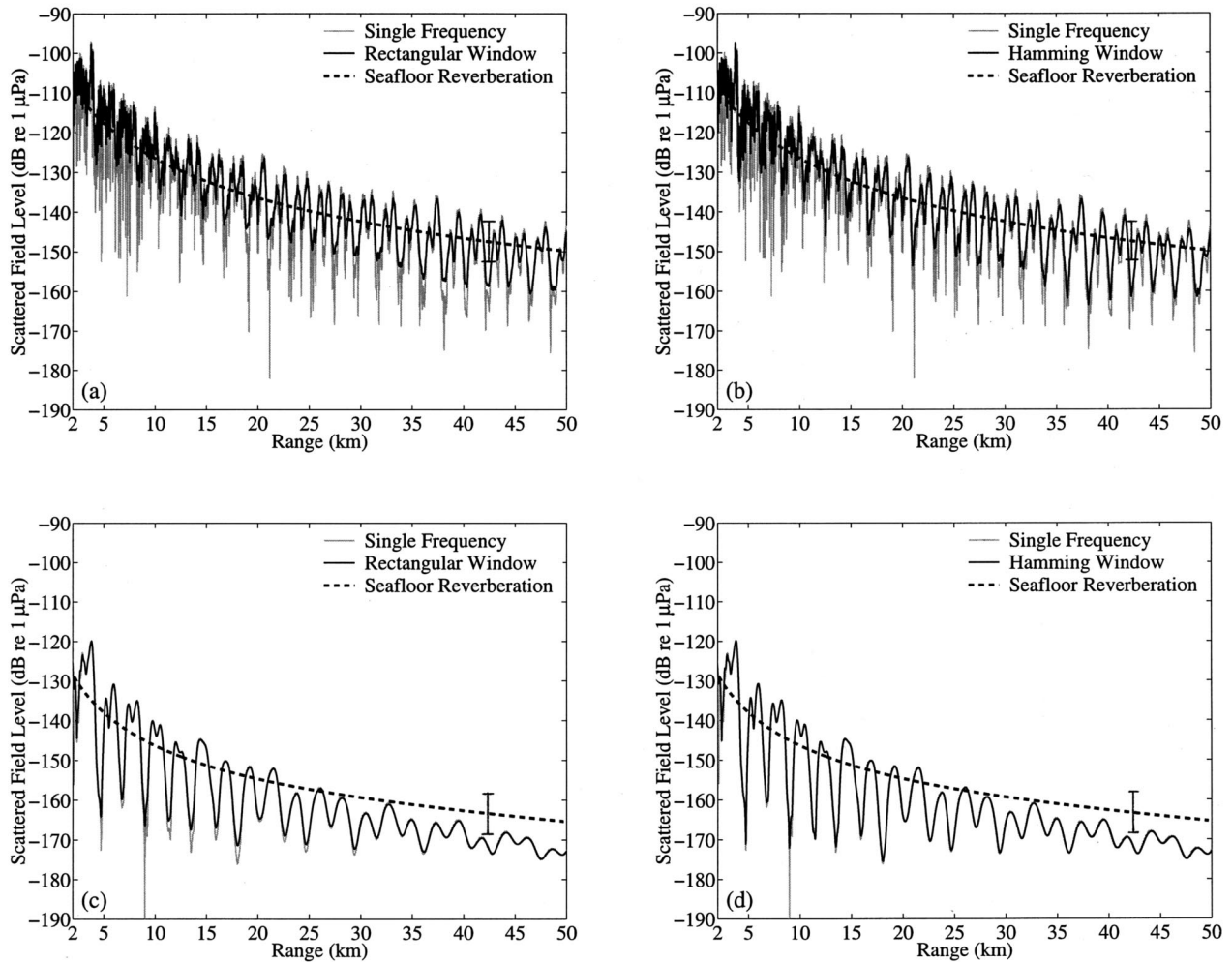


FIG. B2. A comparison of scattering using the single frequency approximation versus the full bandwidth of the given window function. Reverberation calculated using the single frequency approximation is indistinguishable from that calculated with the full bandwidth. (a) Same as Fig. 7(a) for seafloor riverbank with reverb except only the sand bottom case is shown. The single frequency approximation is compared to the rectangular window. (b) Same as (a) except the Hamming window is used instead of the rectangular window. (c) Same as (a) except only the silt bottom case is shown. (d) Same as (c) except the Hamming window is used instead of the rectangular window.

The differential scattering cross section of the target, defined as

$$\sigma = \lim_{r \rightarrow \infty} 4\pi r^2 \frac{|\Phi_s(\mathbf{r})|^2}{|\Phi_i(\mathbf{r})|^2}, \quad (\text{A9})$$

then becomes

$$\sigma(\theta, \phi; \theta_i, \phi_i) = 4\pi \left| \frac{S(\theta, \phi; \theta_i, \phi_i)}{k} \right|^2, \quad (\text{A10})$$

which in the high-frequency limit can be interpreted as the projected area of the target as seen with foreshortening from the combined perspectives of the source and receiver.

If the target is a random patch of rough surface rather than a finite object, Eqs. (A5) and (A6) can still be used so long as far-field conditions hold and $S(\theta, \phi; \theta_i, \phi_i)$ is interpreted as a stochastic parameter. The scattering coefficient of the surface is the expected scattering cross-section per solid angle $\langle \sigma/4\pi \rangle$. This can be written in terms of the bidirectional scattering (reflectance) distribution function²⁹

$f(\theta, \phi; \theta_i, \phi_i)$, a standard empirical descriptor of surface scattering properties in modern radiometry, via

$$\left\langle \frac{\sigma}{4\pi} \right\rangle = f(\theta, \phi; \theta_i, \phi_i) \cos \theta \cos \theta_i \Delta A, \quad (\text{A11})$$

where ΔA is the area of the surface patch. For diffuse scattering that is equal in all directions, the bidirectional scattering distribution function equals the constant ε/π , where ε is the albedo,²⁹ which is unity for a perfect Lambertian surface and roughly $\pi/10^{2.7}$ for a Lambert–Mackenzien surface.⁹ The conventional seafloor scattering strength of ocean acoustics²² is then

$$SS(\theta, \phi; \theta_i, \phi_i) = 10 \log \left\langle \left| \frac{S(\theta, \phi; \theta_i, \phi_i)}{k} \right|^2 \right\rangle - 10 \log \Delta A, \quad (\text{A12})$$

where the first term on the right-hand side can be interpreted as an equivalent target strength for the random scattering patch.

Many surfaces scatter with both a deterministic as well as a fluctuating component. It is conventional to assume that the fluctuating component scatters a zero-mean field. Diffuse scattering surfaces, as described by Lambert's law or first-order perturbation theory, scatter only zero-mean fluctuating fields.

The preceding analysis shows that the standard parameters used to describe surface and target scattering in free space can be traced back to Green's theorem through the plane wave scatter function.

APPENDIX B: SINGLE FREQUENCY APPROXIMATION VERSUS FULL BANDWIDTH IN NARROW-BAND SCATTERING CALCULATIONS

A single frequency approximation is used for all the narrow-band scattering calculations of Sec. IV. The time-averaged, expected mutual intensity of Eq. (35),

$$I(\mathbf{R}, \mathbf{R}_r, \mathbf{R}_0, t) = \frac{1}{T} \int_{-\infty}^{\infty} |Q(f)|^2 \langle |\Phi_s(\mathbf{R}_r - \mathbf{R} | \mathbf{R}_0 - \mathbf{R})|^2 \rangle df, \quad (\text{B1})$$

is approximated as

$$I(\mathbf{R}, \mathbf{R}_r, \mathbf{R}_0, t) \approx \langle |\Phi_s(\mathbf{R}_r - \mathbf{R} | \mathbf{R}_0 - \mathbf{R})|^2 \rangle \times \frac{1}{T} \int_{-\infty}^{\infty} |Q(f)|^2 df, \quad (\text{B2})$$

where $\langle |\Phi_s(\mathbf{R}_r - \mathbf{R} | \mathbf{R}_0 - \mathbf{R})|^2 \rangle$ is calculated at the center frequency f_c of the narrow-band waveform $q(t)$, where $f_c = 300$ Hz for the examples of Sec. IV. In practice, the narrow-band waveform or window function $q(t)$ has a spectrum $Q(f)$ with either a narrow main lobe such as the rectangular window, or a broader main lobe with lower side lobes such as the Bartlett, Hanning, and Hamming windows.³⁶ The window functions are normalized according to

$$\frac{1}{T} \int_{-\infty}^{\infty} |Q(f)|^2 df = 1, \quad (\text{B3})$$

so that the rectangular window, with a main lobe half-power bandwidth of $0.886/T$ and a first side lobe 13.4 dB down peak-to-peak from the main lobe, becomes

$$q(t) = \begin{cases} 1 & \text{for } -T/2 \leq t \leq T/2, \\ 0 & \text{otherwise,} \end{cases} \quad (\text{B4})$$

and the Hamming window, for example with main lobe half-power bandwidth of $1.30/T$ and a first side lobe 42.7 dB down peak-to-peak from the main lobe, becomes

$$q(t) = \begin{cases} \sqrt{1/0.3974} \{0.54 + 0.46 \cos(2\pi t/T)\} & \text{for } -T/2 \leq t \leq T/2, \\ 0 & \text{otherwise,} \end{cases} \quad (\text{B5})$$

where $T = 1/2$ s for the examples of Sec. IV.

For the reverberation calculations of Sec. IV, calculations show that this approximation differs from the full spectral integration by less than 0.1 dB.

As may be expected in the coherent scattering from targets where modal interference is significant, some range-

dependent nulls and valleys in the sound pressure level of the received field found in the single frequency calculation may be partially filled when the full bandwidth is used for the narrow-band waveforms considered. This is exhibited in Figs. B1 and B2 where the filling is shown to be window dependent and more negligible for bottoms that support fewer trapped modes. It is noteworthy that for narrow-band transmissions at the given center frequency and duration, the sphere target may have returns that fall below the expected reverberation level, but the quantity and location of these expected deep "fades" of the target are highly dependent on the window function used.

¹F. Ingenito, "Scattering from an object in a stratified medium," *J. Acoust. Soc. Am.* **82**, 2051–2059 (1987).

²N. C. Makris, F. Ingenito, and W. A. Kuperman, "Detection of a submerged object insonified by surface noise in an ocean waveguide," *J. Acoust. Soc. Am.* **96**, 1703–1724 (1994).

³D. D. Ellis, "A shallow water normal mode reverberation model," *J. Acoust. Soc. Am.* **97**, 2804–2814 (1995).

⁴H. P. Bucker and H. E. Morris, "Normal mode reverberation in channels or ducts," *J. Acoust. Soc. Am.* **44**, 827–828 (1968).

⁵R. H. Zhang and G. L. Jin, "Normal mode theory of the average reverberation intensity in shallow water," *J. Sound Vib.* **119**, 215–223 (1987).

⁶D. M. Fromm, B. J. Orchard, and S. N. Wolf, "Range-dependent normal mode reverberation model for bistatic geometries," in *Ocean Reverberation* (Kluwer, Dordrecht, The Netherlands, 1993), pp. 155–160.

⁷K. Lepage, "Bottom reverberation in shallow water: coherent properties as a function of bandwidth, waveguide characteristics, and scattering distributions," *J. Acoust. Soc. Am.* **106**, 3240–3254 (1999).

⁸H. Schmidt and J. Lee, "Physics of 3-D scattering from rippled seabeds and buried targets in shallow water," *J. Acoust. Soc. Am.* **105**, 1605–1617 (1999).

⁹K. V. Mackenzie, "Bottom reverberation for 530 and 1030 cps Sound I Deep Water," *J. Acoust. Soc. Am.* **33**, 1498–1504 (1961).

¹⁰T. C. Yang, "Scattering from boundary proturbances and reverberation imaging," *J. Acoust. Soc. Am.* **93**, 231–242 (1993).

¹¹N. C. Makris, "A spectral approach to 3-D object scattering in layered media applied to scattering from submerged spheres," *J. Acoust. Soc. Am.* **104**, 2105–2113 (1998); **106**, 518 (1999) (erratum).

¹²J. J. Bowman, T. B. A. Senior, and P. L. E. Uslenghi (Eds.), *Electromagnetic and Acoustic Scattering by Simple Shapes* (North-Holland, Amsterdam, 1969).

¹³F. B. Jensen, W. A. Kuperman, M. B. Porter, and H. Schmidt, *Computational Ocean Acoustics* (American Institute of Physics, New York, 1994).

¹⁴M. J. Lighthill, *An Introduction to Fourier Analysis and Generalized Functions* (Cambridge U. P., New York, 1980).

¹⁵N. C. Makris, "Active detection, classification and localization of fluctuating targets in shallow water," ASW Surveillance Programs FY99 Program Summaries (Office of Naval Research, 1999).

¹⁶P. Swerling, "Probability of detection for fluctuating targets," Rand Report RM-12-17 (1954); reissued in IRE Prof. Group Inf. Theory **IT-6**, 269–308 (1960).

¹⁷N. Levanon, *Radar Principles* (Wiley, New York, 1988).

¹⁸J. A. Ogilvy, *Theory of Wave Scattering from Random Rough Surfaces* (Hilger, New York, 1991).

¹⁹J. W. Goodman, *Statistical Optics* (Wiley, New York, 1985).

²⁰H. C. van de Hulst, *Light Scattering by Small Particles* (Dover, New York, 1981).

²¹N. C. Makris, "The effect of saturated transmission scintillation on ocean acoustic intensity measurements," *J. Acoust. Soc. Am.* **100**, 769–783 (1996).

²²R. J. Urick, *Principles of Sound in the Sea* (McGraw-Hill, New York, 1983).

²³D. H. Berman, "Reverberation in waveguides with rough surfaces," *J. Acoust. Soc. Am.* **105**, 672–686 (1999).

²⁴M. Sundvik and P. Cable, personal communication.

²⁵N. C. Makris, Y. Lai, and P. Ratilal, "Measuring signal bearing, delay and time-frequency characteristics in a dispersive shallow-water waveguide," to be submitted to *J. Acoust. Soc. Am.*

²⁶N. C. Makris, C. S. Chia, and L. T. Fialkowski, "The bi-azimuthal scat-

- tering distribution of an abyssal hill,” *J. Acoust. Soc. Am.* **106**, 2491–2512 (1999).
- ²⁷N. C. Makris, “Imaging ocean-basin reverberation via inversion,” *J. Acoust. Soc. Am.* **94**, 983–993 (1993).
- ²⁸N. C. Makris, L. Z. Avelino, and R. Menis, “Deterministic reverberation from ocean ridges,” *J. Acoust. Soc. Am.* **97**, 3547–3574 (1995). [Bathymetry in Fig. 5 of this reference should be labeled <3600 m not <3200 m as shown. Also, the bistatic reverb for lfm s478 should be labeled >87 dB *re* 1 μ Pa in Fig. 24, not >80 dB *re* 1 μ Pa as shown.]
- ²⁹B. K. P. Horn and R. W. Sjoberg, “Calculating the reflectance map,” *Appl. Opt.* **18**, 1770–1779 (1979).
- ³⁰J. Moe and D. R. Jackson, “First-order perturbation solution for rough surface scattering cross section including the effects of gradients,” *J. Acoust. Soc. Am.* **96**, 1748–1754 (1994).
- ³¹Note $P_n^m(-z) = (-1)^n P_n^m(z)$ where z is the cosine between the incident and scattered wave directions. This should be used to convert Eqs. (8) and (9) of Ref. 11 from Ingenito’s definition to the standard one. In the former the object scatter function is defined in terms of the direction the incident wave comes from and in the latter it is defined in terms of the direction the incident goes to. It should be noted that in Ref. 11 Ingenito’s definition is used implicitly for all equations except Eqs. (16) and (17), where the standard definition is used.
- ³²J. A. Austin, Jr., C. S. Fulthorpe, G. S. Mountain, D. L. Orange, and M. E. Field, “Continental-margin seismic stratigraphy: assessing the preservation potential of heterogeneous geological processes operating on continental shelves and slopes,” *Oceanography* **9**, 173–176 (1996).
- ³³H. H. Essen, “Scattering from a rough sediment seafloor containing shear and layering,” *J. Acoust. Soc. Am.* **95**, 1299–1310 (1994).
- ³⁴D. Jackson, *APL-UW High Frequency Ocean Environmental Acoustic Models Handbook*, Chap IV, Bottom, APL-UW Technical Report TR9407 (Applied Physics Laboratory, Univ. of Washington, 1994).
- ³⁵P. M. Morse and K. U. Ingard, *Theoretical Acoustics* (Princeton U. P., Princeton, NJ, 1986), pp. 418–436.
- ³⁶A. V. Oppenheim R. W. Schafer, and J. R. Buck, *Discrete Time Signal Processing* (Prentice Hall, Englewood Cliffs, NJ, 1999).

High-amplitude thermoacoustic effects in a single pore

G. Petculescu and L. A. Wilen^{a)}

Department of Physics and Astronomy, Ohio University, Athens, Ohio 45701-2979

(Received 21 March 2000; revised 21 September 2000; accepted 14 December 2000)

Nonlinear effects on thermoacoustic gain in a single pore are investigated experimentally. By creating a sharp temperature gradient in a uniform cross-section pore, the effect of high displacement amplitudes relative to the stack length is isolated from other high amplitude effects and also from effects due to geometrical discontinuities. The experiment probes displacement amplitudes which lie beyond the range of validity of the linear theory. The complex compressibility of nitrogen gas in the pore is measured for displacement amplitudes ranging from 2.5% to 60% of the stack length. No changes in the thermoacoustic response are observed over this range. Extending the upper limit to 175%, the power flow, as a function of the squared ratio of the displacement amplitude and the stack length, behaves linearly over the entire range. © 2001 Acoustical Society of America. [DOI: 10.1121/1.1348008]

PACS numbers: 43.35.Ud, 43.20.Mv, 43.20.Ye, 43.25.Cb [SGK]

I. INTRODUCTION

The goal of building powerful and efficient thermoacoustic devices has generated much interest in high-amplitude studies, from both an experimental and a theoretical point of view. Experimental investigations on devices driven at high amplitudes reveal the importance of understanding the effects of nonlinearities. For driving pressure amplitudes (the ratio of the acoustic pressure amplitude to the mean pressure of the gas) above approximately 0.5%,¹ disagreement arises between experimental data and the results of the linear theory. The source of the discrepancy is complex. It has been attributed to turbulence, streaming, gas displacement comparable to the stack or heat exchanger lengths, or other velocity-dependent effects. A number of workers have considered nonlinear thermoacoustic effects in various manifestations. Swift² made extensive measurements on a large prime mover and found significant deviations from the linear theory at high pressure amplitudes. Many, but not all, of the deviations could be explained by coupling to higher harmonics, turbulence, or a temperature defect caused by the steady-state heat flow from the heat exchangers to the gas. Poese and Garrett³ made similar measurements for a large thermoacoustic refrigerator which also displayed deviations from the linear theory at high amplitude. They discussed possible explanations, one likely candidate being turbulence resulting from geometric discontinuities. Atchley *et al.*¹ measured the temperature difference across a thermoacoustic couple as a function of position in a resonator for a wide range of pressure amplitudes. Again, deviations from the linear theory were observed and tentatively attributed to turbulence, acoustic streaming, or particle displacement comparable to the length of the couple. In another experiment,⁴ Atchley measured the build-up of oscillations in a thermoacoustic prime mover. He discussed some possible reasons for the saturation of the amplitude at a steady-state value due to linear and nonlinear effects. Yazaki *et al.*⁵

performed measurements on a simple thermoacoustic resonator and identified regimes of quasiperiodicity and even chaos occurring at large amplitude oscillations.

On the theoretical side, there have been a number of studies addressing nonlinearities and other effects, possibly linear, not accounted for in standard thermoacoustic theory. Watanabe *et al.* and Yuan *et al.* developed simplified one-dimensional nonlinear models which include convective terms up to second order in the velocity.⁶ These theories provide a framework for understanding the generation of higher harmonics in an unloaded prime mover which leads to a saturation in the amplitude caused by dissipation in these higher modes. Cao *et al.*⁷ performed a numerical calculation of the energy flux density in an isolated thermoacoustic couple having infinite thermal conductivity. This work was specifically aimed at understanding the effect of large amplitude displacements compared with the length of the stack or the heat exchangers. Surprisingly, they find that the energy flux density at the plate ends is not spread over a region on the order of the displacement amplitude, but rather is concentrated in a narrow region at the ends. The width of this region is nevertheless linearly proportional to the displacement amplitude. Mozurkewich⁸ developed an analytic approach to model heat flow along a thermoacoustic couple which agreed well with the numerical work by Cao *et al.* He extended his results⁹ to analyze a heat exchanger adjacent to a stack and found that temperature discontinuities develop between the two elements. Similar conclusions (which were also verified experimentally) were reached by Brewster *et al.*¹⁰ using physical arguments. As will be discussed later, the linear theory does not treat the effects of such temperature discontinuities. Models for turbulence in ducts and effects of minor losses have been incorporated into DeltaE, and give good results.¹¹

Although much progress has been made in understanding effects not described by the standard linear theory, a number of points remain poorly understood. Experimentally, the task is complicated by the number of factors which simultaneously contribute to the discrepancy between theory

^{a)}Electronic mail: wilens@helios.phy.ohiou.edu

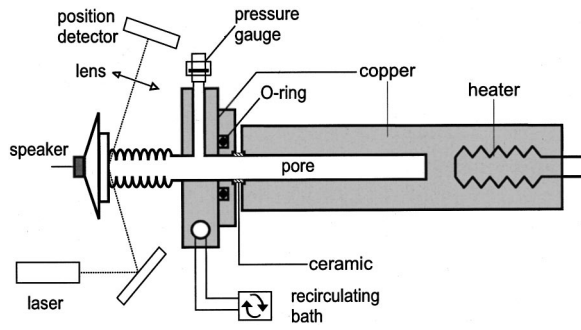


FIG. 1. Schematic diagram of the experimental setup.

and experiment. One approach to this problem was explored by Olson *et al.*¹² Employing the concept of similitude, they proposed to unravel nonlinear effects by varying single dimensionless parameters one at a time in an experiment. In the present experiment, a different approach was taken; we isolated the single effect of displacement amplitude comparable to stack length from all other nonlinear effects. We accomplished this by making measurements on a single pore (no discontinuities in cross section) at small acoustic Reynolds numbers ($R < 50$).¹³

II. EXPERIMENTAL TECHNIQUE

The experimental technique employed was very similar to the one used previously for determining thermoacoustic properties of single pores, such as the thermoacoustic function $F(\lambda_T)$ ¹⁴ or the complex compressibility $C(\omega)$.¹⁵ Consequently, only those aspects unique to this experiment will be described in detail. Figure 1 shows a schematic view of the setup. A sharp temperature gradient profile was achieved by sandwiching a short, thin, and poorly conducting ceramic material [$k = 1.6(W/m \cdot K)$ at $25^\circ C$] between two sections made out of copper [$k = 400(W/m \cdot K)$ at $25^\circ C$]. For simplicity, we will refer to the ceramic region as the “stack.”

The detailed geometry is shown in Fig. 2. The copper region to the left of the stack was in contact with a water bath controlled to a temperature of $24^\circ C$. The copper section to the right of the stack was heated and controlled to tem-

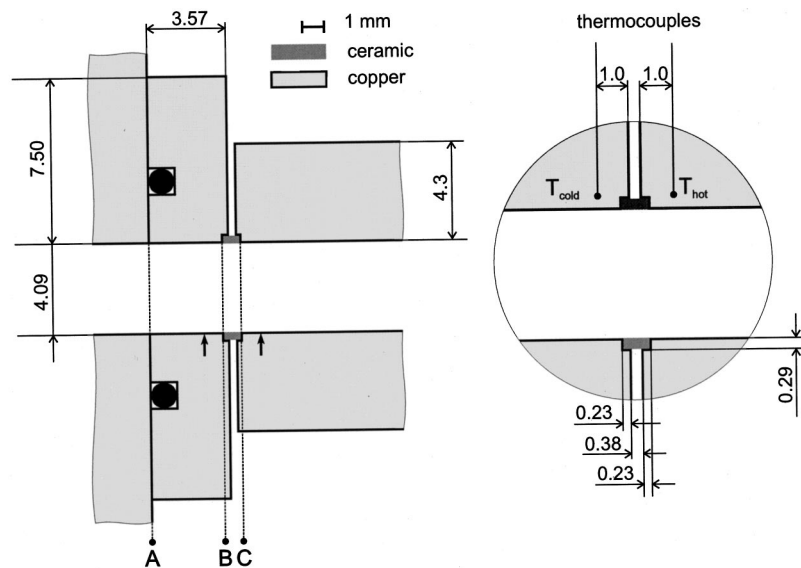


FIG. 2. Details of the pore in the sharp gradient zone. Dimensions are in millimeters. A, B, and C label positions along the pore referred to in the text. The two arrows indicate the range a gas parcel would span during a cycle at the highest amplitude measured.

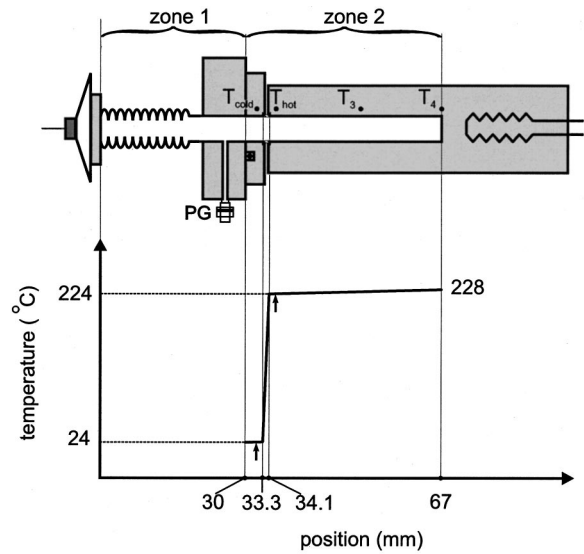


FIG. 3. Temperature profile along the pore; the solid line represents a piecewise linear approximation to the actual profile determined by solving the heat equation numerically. The two zones referred to in the text are shown.

peratures ranging from $24^\circ C$ to $224^\circ C$. When the temperature of the hot side was above $24^\circ C$, a temperature gradient was present in both the copper and ceramic sections of the cell. By measuring the temperature at several locations in the cell, we determined the average temperature gradient in the copper sections. The position at which these temperatures were measured is shown in Fig. 3. Type *K* thermocouples (wire size 0.3 mm) were used for all temperature measurements. The temperature measurements were accurate to about $2^\circ C$. The measurement positions were accurate to about 0.3 mm.

For the ceramic section and the copper region immediately adjacent, we calculated the detailed temperature profile along the inside wall of the pore using a finite-element relaxation calculation. The calculation assumed known values for the thermal conductivities of copper and the ceramic and used the measured temperature at two points in the copper as boundary conditions. As expected, the overall temperature

profile was closely approximated by a piecewise linear profile, with small temperature gradients in the copper and a temperature jump across the stack of roughly the difference in temperature between the hot and cold sides. Figure 3 shows the profile when the hot-side temperature (measured at the thermocouple just to the right of the stack) was 224 °C. Given that the length of the stack (0.84 mm) represents only 2% of the total pore length (67 mm) and 15% of the pore diameter (4.1 mm), the temperature gradient can be viewed as an extremely sharp one.

Because the experimental configuration here differs from the usual arrangement of a thermoacoustic stack and resonator, it is helpful to point out some of its basic features. The gas is driven back and forth (well below resonance) in the tube by the action of the bellows. As the gas is compressed it is displaced to the right and as it is expanded it is displaced to the left. The phasing is therefore principally that of a standing wave, just as in a typical standing wave thermoacoustic device. There is a small traveling wave component which is due to the dissipation or generation of power in the stack, also similar to what happens in a more conventional standing wave device. In the absence of a temperature gradient, the pore dissipates energy and the quantity we use to describe this process is a direct measure of the thermal function $F(\lambda_T)$.¹⁴ When a temperature gradient is applied, the effect of the thermoacoustic gain can be observed directly.¹⁵ As will be seen from the results, the gain term dominates the behavior of the system, even though the gradient region is a small fraction of the total pore length.

The experimentally measured quantities were: the amplitude and phase of the acoustic pressure $P_1(\omega)$ at the pressure gauge, the amplitude and phase of the speaker oscillatory motion $X_1(\omega)$, and the equilibrium pressure inside the pore P_0 . The volume oscillations V_1 are related to the speaker motion X_1 , by $V_1 = A_{\text{eff}} \cdot X_1$, where A_{eff} is the effective cross-sectional area of the bellows. The equilibrium volume V_0 was evaluated through a procedure which is described later in this section. The motion of the speaker was measured optically. Pressure measurements were made with a differential silicon pressure gauge, while the atmospheric pressure was measured with a capacitance manometer. All experiments were performed in a dry N_2 atmosphere.

For the frequency range used in the experiment (0.5 to 96 Hz), the total length of the pore (67 mm) is much shorter than the acoustic wavelength. This permits the assumption of a spatially uniform pressure along the pore. To first order, the pressure and the volume inside the pore have the form

$$P(t) = P_0 + P_1(\omega)e^{-i\omega t}, \quad V(t) = V_0 + V_1(\omega)e^{-i\omega t}, \quad (1)$$

where P_0 and V_0 are the equilibrium pressure and volume values, respectively, $P_1(\omega)$ is the acoustic pressure, and $V_1(\omega)$ is the volume oscillation. Measurements of the amplitude and phase of the gas pressure and volume, along with their equilibrium values, permit calculation of the complex compressibility $C(\omega)$, defined as

$$C(\omega) = -\frac{1}{V_0} \frac{V_1(\omega)}{P_1(\omega)}. \quad (2)$$

Generally, it is more convenient to work with the dimensionless compressibility $P_0 C(\omega)$

$$P_0 C(\omega) = -\frac{P_0}{V_0} \frac{V_1(\omega)}{P_1(\omega)}, \quad (3)$$

due to its simple physical interpretation in the low- and high-frequency limits.¹⁵

As can be inferred from Fig. 3, the measured compressibility included the cumulative effect of the end region including the bellows and the pressure gauge (zone 1) and the rest of the pore which includes the stack (zone 2). The compressibility of zone 1 was measured separately and subtracted from the total response by using a previously described method.^{14,15} For the remainder of the paper, when we refer to the compressibility or $P_0 C$, we mean the compressibility of zone 2 alone.

Two types of experimental runs were completed. In the first type (A), the frequency was swept from 0.5 to 96 Hz in 71 steps, while the loudspeaker displacement amplitude was held constant.¹⁶ For these frequencies, the thermal penetration depth varies from 3.7 to 0.3 mm, precisely the range for which thermoacoustic effects are most important for a pore of radius 2.05 mm. A total of eight sweeps was performed; four different speaker amplitudes, each with a temperature difference across the stack (ΔT_{stack}) of 0 °C (“no gradient runs”), and also of ≈ 200 °C (“gradient runs”). In the second run type (B), the frequency was held fixed at 5.74 Hz and the speaker displacement amplitude was varied over a wide range of values, again with and without a gradient across the stack.

As in previous work,¹⁵ we observed very small shifts in the sensitivity of the pressure and/or position gauges between (and to a much lesser extent, during) runs which translated into small errors in the volume of the cell. Therefore, the volume was adjusted for each A run so that the result for the measured compressibility agreed with the theory in the zero-frequency (dc) limit. In this limit, it is safe to assume that the gas in the cell is in local thermal equilibrium with the pore wall (for any amplitude), and the theoretical value for the dc compressibility can be determined analytically from the pore dimensions and the temperature profile. The maximum adjustment in volume required was less than 1%.

For the B runs, the measured values of P_1 and V_1 were used directly to calculate the power flow into zone 2, and no adjustment to the equilibrium volume was performed.

III. RESULTS

In Figs. 4(a) and (b), we plot $P_0 C(\omega)$ for four speaker amplitudes, with and without a gradient across the stack (A runs). The corresponding pressure amplitudes (P_1/P_0) are approximately 0.1%, 0.45%, 1.3%, and 2.5% of the equilibrium pressure. From the pressure amplitudes and the compressibility, we can also determine the gas displacement amplitudes at the left end of zone 2 (point A in Fig. 2). These displacement amplitudes are approximately 2.5%, 10%, 30%, and 60% of the stack length for the four runs. The displacement amplitudes at the position of the stack are very close to these values. (A discussion of how we determine the

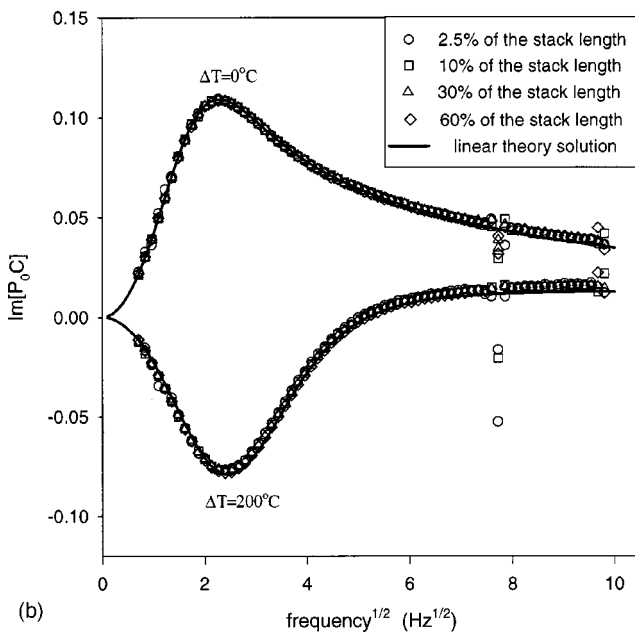
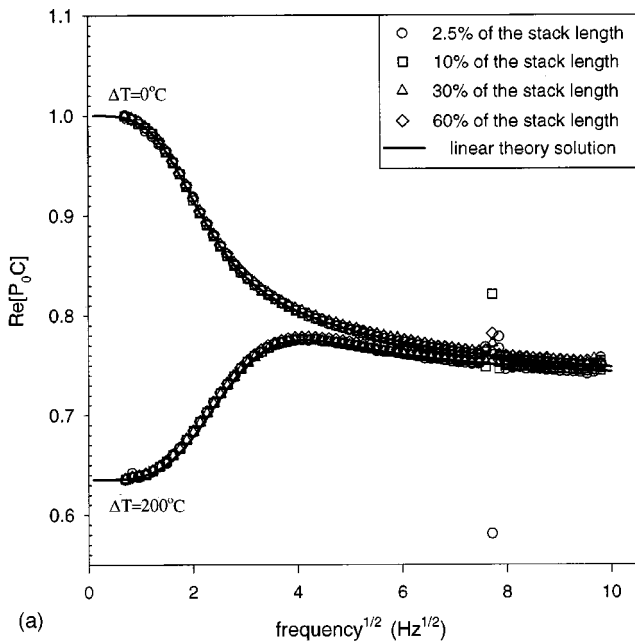
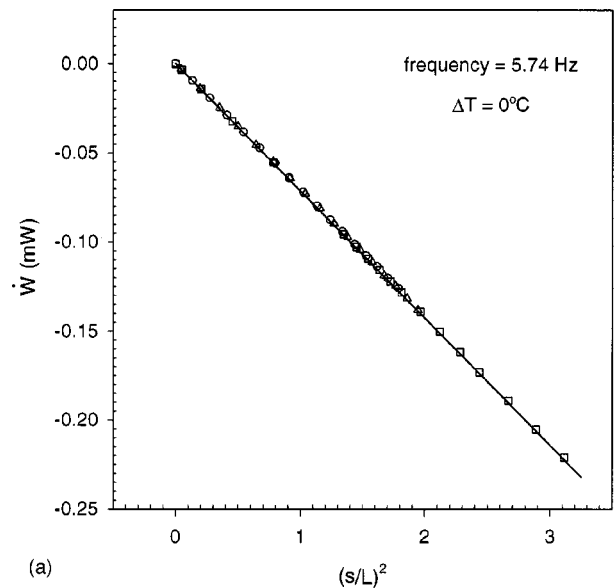


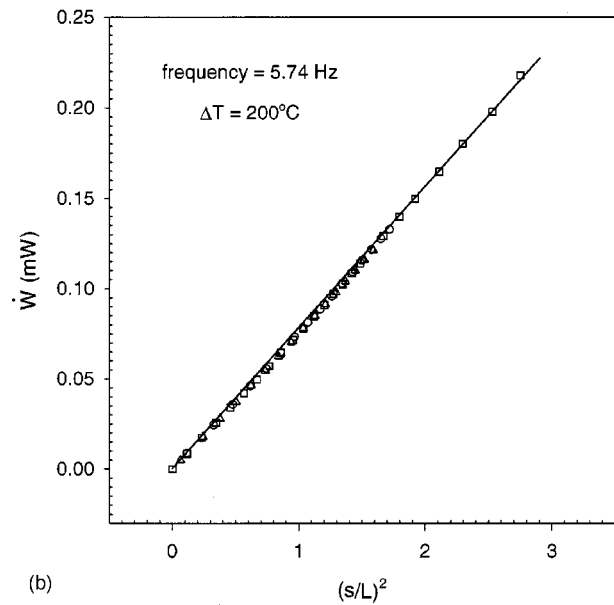
FIG. 4. P_0C real (a) and imaginary (b) parts, vs $f^{1/2}$ for 0°C temperature difference (upper) and for 200°C temperature difference (lower) across the stack; different symbols are used for the four displacement amplitudes. The solid lines are the theoretical results.

displacement amplitudes appears in the Appendix.) The glitch in the experimental curves is due to pickup at 60 Hz. The solid lines in the graphs represent the theoretical solutions of the linear thermoacoustic theory [Eq. (7) in Ref. 14] using the piecewise linear temperature profile shown in Fig. 3. We checked that the theoretical result was essentially independent of the details of the temperature profile in the stack. This is consistent with earlier work by Rott.¹⁷

Interestingly, no amplitude dependence is observed and the data for all amplitudes agree closely with the linear theory prediction. To illustrate this point in a different way, recall that the power flow \dot{W} into zone 2 is proportional to the imaginary part of the compressibility¹⁵



(a)



(b)

FIG. 5. Power as a function of the squared displacement amplitude s normalized to the stack length L at $f=5.74$ Hz for the no-gradient case (a) and gradient case (b). In both cases, the solid line is the linear theory prediction. At the highest displacement measured, the pressure amplitude (P_1/P_0) is $\approx 6\%$ and the acoustic Reynolds number is ≈ 35 .

$$\dot{W}(\omega) = -\frac{1}{2} \omega \frac{V_{\text{zone2}} |P_1|^2}{P_0} \text{Im}[P_0C(\omega)]. \quad (4)$$

Using the results of the B runs, we have plotted (Fig. 5) \dot{W} versus $(s/L)^2$, where s is the displacement amplitude (again, measured at point A) and L is the length of the ceramic. The measurements are taken at $f=5.74$ Hz, where the thermoacoustic gain in the gradient runs is largest (i.e., the imaginary part of the compressibility is minimum). The highest displacement amplitude in the stack is about 1.7 times larger than the length of the stack. In this case, a gas parcel situated in the center of the stack spans the two points marked by arrows in Figs. 2 and 3 during a cycle.

Nonlinear behavior would be indicated by deviation from a straight line. No nonlinearity is expected in the no-

gradient case [Fig. 5(a)], and the results confirm this. However, the lack of any nonlinear behavior in the gradient case [Fig. 5(b)] is a surprising result, as discussed in the next section.

Statistical errors in the experiment result in error bars roughly the size of the plotted points below 2 Hz, but decreasing to much smaller at higher frequencies. As noted earlier, large errors also occur for points very near 60 Hz. We also occasionally noted spurious results for points taken near 96 Hz, likely due to an overloading in one of the lock-in amplifiers.

Systematic errors can result from a number of factors. These include: (1) shifts in the equilibrium volume and pressure with speaker amplitude; (2) shifts in the equilibrium pressure/temperature during the course of a run; (3) shifts in the sensitivity of the pressure and position gauges with amplitude, due to nonlinearity in gauges, combined with dc shifts in the speaker position at higher drives; (4) shifts in sensitivity of the pressure and position detectors over time, possibly due to mechanical conditions, changes in room temperature and pressure, etc.; (5) errors in the absolute calibration of the pressure and position detectors.

All of these systematic errors can be estimated and in some cases have been measured and calibrated out. The combined effect of numbers (1)–(4) is judged to be of order 2%. Number (5) may be as large as 4%. For the A runs, number (5) has effectively been calibrated out. For the B runs, it would affect all measured data by a uniform multiplicative constant and therefore does not affect the linearity in the observed results.

IV. DISCUSSION

Rott examined oscillating flow over a nonisothermal surface^{17,18} and found that there are nonlinear terms introduced by the nonzero radial component of the velocity. These terms are of order

$$s \frac{d \log T(x)}{dx}, \quad (5)$$

where s is the gas displacement amplitude. Physically, they appear due to the variation of the boundary layer thickness with temperature. A linear solution to the equations can be carried out if the restriction

$$s \frac{d \log T(x)}{dx} \ll 1 \quad (6)$$

is enforced. This implies very small displacements s or, equivalently, very little temperature changes over the distance s . It is interesting to note that in Rott's¹⁷ numerical treatment of the linear problem with a temperature gradient, a "discontinuous model" is used as the limit of a case of practical importance. The temperature profile he considers is

$$T(x) = \begin{cases} T_1 & \text{for } 0 \leq x < l, \\ T_2 & \text{for } l < x \leq L, \end{cases} \quad (7)$$

which would be incompatible with the condition in Eq. (6). Therefore, he is careful to specify that the temperature jump at $x=l$ must be smoothed out over several diameters of the

tube. For small enough displacements, this ensures that the condition in Eq. (6) is fulfilled and the linearized equations hold. Rott¹⁹ states explicitly that the theory "does not cover the effect in which a real jump (over a fraction of a radius, say) of the tube wall temperature is maintained." Rott's theory was verified by Yazaki *et al.*²⁰ in a system with a sharp temperature gradient, but only for conditions of onset where the linear theory would be expected to hold.

The present experiment tests the behavior of a thermoacoustic system as the imposed limit for linearity [Eq. (6)] is exceeded. The range examined is

$$0.01 \leq s \frac{d \log T(x)}{dx} \leq 1.0. \quad (8)$$

In addition to the condition discussed above, it has been pointed out by Rott and others^{1,7,21} that the linear theory certainly should not hold when the gas displacement amplitude becomes comparable to the length of the stack and/or heat exchangers. The linear theory assumes a constant temperature gradient over the excursion distance of a gas parcel. This condition is satisfied when the displacement amplitude is small, except for parcels just at the ends of the stack whose contribution to the overall heat or work flow is negligible.²² In the present experiment, for the largest amplitude used, all of the gas in the stack is essentially within one displacement amplitude from the ends. In this case, an oscillating gas parcel does not see a constant gradient as is assumed by the theory. Conceptually, this also implies a breakdown of the usual bucket-brigade picture. For large displacement amplitudes the situation is closer to a single bucket shuttling heat directly from the hot to cold (or vice versa). Although we measure work flow rather than heat flow, the two are clearly related since the work depends on the phasing between the pressure and temperature in the gas.²³ Finally, it is worth pointing out that Swift,¹ and also Brewster *et al.*¹⁰ made the remarkable observation that no significant change in the thermoacoustic heat flow occurred when the displacement amplitude became comparable to the length of the heat exchangers. Comparing the outcome of two experiments having different-length heat exchangers, Swift found nothing to indicate that the engine performance was related to the ratio of displacement amplitude and heat exchanger length. It is interesting to speculate whether these observations are related to the results presented here. At this stage we have no explanation for the results of the experiment, but we believe they present an intriguing and well-defined challenge for theorists to explain.

V. CONCLUSIONS

An experimental investigation into the influence of high displacement amplitudes relative to the stack length has been performed. This effect was isolated from other high-amplitude effects with a special construction which imposed a sharp temperature gradient in a pore of uniform cross section. The results, including those for the highest amplitudes, are consistent with the prediction of the linear theory. We conclude that the limit imposed by the linear theory regarding high displacement amplitudes relative to stack length is

not critical. The practical aspect of this result is that other types of high-amplitude nonlinear effects must be responsible for some of the discrepancies commonly observed between experiment and theory.

ACKNOWLEDGMENTS

The authors gratefully acknowledge the support of the Office of Naval Research.

APPENDIX

In this Appendix, we explain how we determine the numbers quoted in Sec. III and Figs. 4 and 5 for the displacement amplitudes at point A and in the stack. We will denote the cross-sectional average of the gas displacement at the left end of zone 2 (point A in Fig. 2) by $|X_1(\omega)|_A$. This quantity can be calculated from the magnitude of the pressure oscillations of a given run, and the measured compressibility of zone 2 as follows:

$$|X_1(\omega)|_A = |P_1(\omega) \cdot P_0 C(\omega)| \frac{L_{\text{zone2}}}{P_0}, \quad (\text{A1})$$

where L_{zone2} is the length of zone 2. $|X_1(\omega)|_A$ depends on frequency for two reasons. First, the speaker amplitude itself is not perfectly constant as a function of frequency. We vary the voltage drive of the speaker to compensate for its mechanical and electrical impedance, but this compensation is not perfect, leaving a 7% variation. Second, were the speaker amplitude constant, $|X_1(\omega)|_A$ would still depend on frequency because the compressibility of the gas in zone 2 has a different frequency dependence from that of the gas in zone 1. Taking both of these effects into account, $|X_1(\omega)|_A$ varies with frequency by up to 35% over the course of a run. For any given pair of A runs (gradient and no-gradient at a particular speaker amplitude), we find the minimum value of $|X_1(\omega)|_A$ as a function of frequency. We denote this value by s , which is the number quoted in the results section. Thus, s is a lower limit to the actual amplitude at point A measured over the whole frequency range.

For the B runs, taken at a constant frequency of 5.74 Hz, we simply take s equal to the actual amplitude at point A: $s = |X_1(\omega = 2\pi \cdot 5.74 \text{ Hz})|_A$.

For both A and B runs, the displacement amplitude *in the stack* is not equal to $|X_1(\omega)|_A$ and, moreover, varies with position along the stack. For example, consider first a gradient run. Referring to Fig. 2, the displacement amplitude decreases slightly from point A to point B, but then increases from the cold to the hot side of the stack (point B to point C). The increase in amplitude along the stack is essentially a result of continuity; in the hotter region, the density is lower and so the displacement must be larger to compensate. In Fig. A1 we show how the displacement amplitude varies with position for three different frequencies. In Fig. A2, we plot the average displacement amplitude in the stack normalized by $|X_1(\omega)|_A$ vs frequency for a gradient and no-gradient run. These plots show the results of solving the linear thermoacoustic theory using the formalism described in Ref. 15.

From Fig. A2, we can see that for the B runs ($f = 5.74 \text{ Hz}$), $|X_1(\omega)|_A$ (and hence s) underestimates the dis-

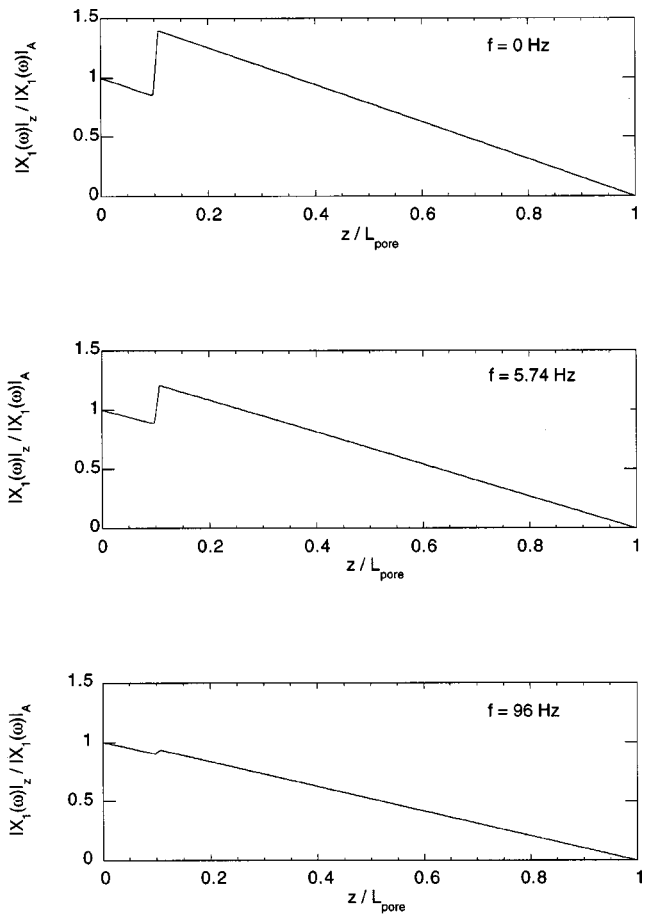


FIG. A1. Normalized displacement amplitude as a function of distance along pore. Curves are shown for gradient runs at three different frequencies.

placement in the stack by about 3% for the gradient runs and overestimates the displacement by 10% for the no-gradient runs.

For the gradient A runs, $|X_1(\omega)|_A$ varies from about 10% lower than to about 10% higher than the displacement in the stack. For the no-gradient A runs, $|X_1(\omega)|_A$ is 10% higher than the displacement in the stack at all frequencies.

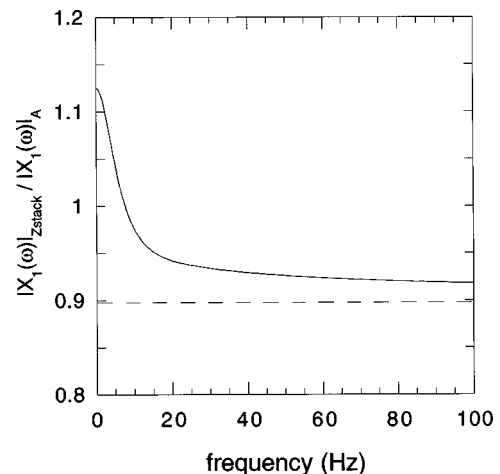


FIG. A2. Average displacement amplitude at the stack normalized by the displacement amplitude at point A vs frequency. Solid line is for the gradient run, dotted line for the no-gradient run.

However, our choice of s for the A runs, as described above, is such that it always underestimates the displacement in the stack (for gradient and no-gradient). In summary, s is less than the average displacement in the stack *in all cases* except the B no-gradient runs, where it is approximately 10% larger than the displacement in the stack.

It should also be emphasized that these are cross-sectional averages of the displacement. The local displacement in the center of the pore will be even higher because the gas is pinned at the pore wall due to viscosity.¹⁵

¹A. A. Atchley, T. J. Hofler, M. L. Muzzerall, and M. D. Kite, "Acoustically generated temperature gradients in short plates," *J. Acoust. Soc. Am.* **88**, 251–263 (1990).

²G. W. Swift, "Analysis and performance of a large thermoacoustic engine," *J. Acoust. Soc. Am.* **92**, 1551–1563 (1992).

³M. E. Poese and S. L. Garrett, "Performance measurements on a thermoacoustic refrigerator driven at high amplitudes," M.S. thesis, The Pennsylvania State University, 1998.

⁴A. A. Atchley, "Analysis of the initial buildup of oscillations in a thermoacoustic prime mover," *J. Acoust. Soc. Am.* **95**, 1661–1664 (1994).

⁵T. Yazaki, S. Takashima, and F. Mizutani, "Complex quasiperiodic and chaotic states observed in thermally induced oscillations of gas columns," *Phys. Rev. Lett.* **58**, 1108 (1987).

⁶M. Watanabe, A. Prosperetti, and H. Yuan, "A simplified model for linear and nonlinear processes in thermoacoustic prime movers. I. Model and linear theory," *J. Acoust. Soc. Am.* **102**, 3484–3496 (1997); H. Yuan, S. Karpov, and A. Prosperetti, "A simplified model for linear and nonlinear processes in thermoacoustic prime movers. II. Nonlinear oscillations," *ibid.* **102**, 3497–3506 (1997).

⁷N. Cao, J. R. Olson, G. W. Swift, and S. Chen, "Energy flux density in a

thermoacoustic couple," *J. Acoust. Soc. Am.* **99**, 3456–3464 (1996).

⁸G. Mozurkewich, "Time-average temperature distribution in a thermoacoustic stack," *J. Acoust. Soc. Am.* **103**, 380–388 (1998).

⁹G. Mozurkewich, "A model for transverse heat transfer in thermoacoustics," *J. Acoust. Soc. Am.* **103**, 3318–3326 (1998).

¹⁰J. R. Brewster, R. Raspet, and H. E. Bass, "Temperature discontinuities between elements of thermoacoustic devices," *J. Acoust. Soc. Am.* **102**, 3355–3360 (1997).

¹¹W. C. Ward (private communication), 1999.

¹²J. R. Olson and G. W. Swift, "Similitude in thermoacoustics," *J. Acoust. Soc. Am.* **95**, 1405–1412 (1994).

¹³P. Merkli and H. Thomann, "Transition to turbulence in oscillating pipe flow," *J. Fluid Mech.* **68**, 567 (1975).

¹⁴L. A. Wilen, "Measurements of thermoacoustic functions for single pores," *J. Acoust. Soc. Am.* **103**, 1406–1412 (1998).

¹⁵G. Petculescu and L. A. Wilen, "Thermoacoustics in a single pore with an applied temperature gradient," *J. Acoust. Soc. Am.* **106**, 688–694 (1999).

¹⁶The speaker amplitude varied by 7% over the course of a run. See the Appendix.

¹⁷N. Rott, "Thermoacoustics," *Adv. Appl. Mech.* **20**, 135–175 (1980).

¹⁸N. Rott, "Damped and thermally driven acoustic oscillations in wide and narrow tubes," *Z. Angew. Math. Phys.* **20**, 230–243 (1980).

¹⁹Reference 17, p. 153.

²⁰T. Yazaki, S. Tominaga, and Y. Narahara, "Experiments on thermally driven acoustic oscillations of gaseous helium," *J. Low Temp. Phys.* **41**, 45 (1980).

²¹A. A. Atchley, H. E. Bass, and T. J. Hofler, "Development of nonlinear waves in a thermoacoustic prime mover," in *Frontiers of Nonlinear Acoustics*, edited by M. F. Hamilton and D. T. Blackstock (Elsevier, New York, 1990), pp. 603–608.

²²Reference 17, p. 140.

²³G. W. Swift, "Thermoacoustic engines," *J. Acoust. Soc. Am.* **84**, 1145–1180 (1988).

Equivalent circuits and directivity patterns of air-coupled ultrasonic transducers

Lin Shuyu

Applied Acoustics Institute, Shaanxi Normal University, Xian, Shaanxi, 710062, People's Republic of China

(Received 8 October 1999; accepted for publication 28 November 2000)

Air-coupled transducers for producing ultrasonic radiation in gases are studied. The transducer consists of a circular thin plate in flexural vibration and a sandwich longitudinal electromechanical vibrator that is attached to the center of the plate. The lowest-order axially symmetric flexural vibrational mode of a circular thin plate is analyzed. The equivalent circuits of the circular plate in flexural vibration and the compound transducer are presented and the frequency equation is derived. The radiated ultrasonic field of the circular thin plate in flexural vibration is calculated and the directivity pattern is obtained theoretically. Some transducers of this type are designed according to the frequency equation, and their resonance frequencies are measured. The measured resonance frequencies are in good agreement with the theoretical results, and the calculated radiation ultrasonic field is also in good agreement with the measured results of a previous work. © 2001 Acoustical Society of America. [DOI: 10.1121/1.1342004]

PACS numbers: 43.38.Ar, 43.35.Yb [SLE]

I. INTRODUCTION

The use of sound in gases, such as in ultrasonic drying, defoaming, and aerosol particle precipitation,^{1,2} has increased during the past few years. However, as the specific acoustic impedances of gases are low compared with those of piezoelectric transducers, the application of ultrasound in gases is limited. In addition, the sensitivity and the radiating efficiency of the transducers are low because of the impedance mismatch.

In order to obtain an efficient transmission of ultrasonic energy in gases it is necessary to achieve a good impedance match between the transducer and the gases. The compound air-coupled transducer consisting of a sandwich longitudinal piezoelectric vibrator and a circular thin plate in flexural vibration has the advantages of large radiation surface and improved impedance matching and has been used in producing ultrasound of high directivity in air. It was found in the literature³⁻⁷ that an ultrasonic transducer of this type was developed which can improve the impedance match with the gas and can produce high directivity and intensity ultrasound in the medium. According to traditional design theory of this type of transducer, the transducer is divided into two parts. One part is the sandwich longitudinal electromechanical vibrator and the other is the circular plate in flexural vibration. They are designed according to their frequency equations. In this case, the transducer is considered as a combination of two resonators and they resonate at the same frequency. However, for the compound air-coupled transducer consisting of a longitudinal vibrator and a circular plate, its vibration modes are complex.

In this paper, the flexural vibration of a circular plate as an ultrasonic radiator is analyzed. The equivalent circuits of the flexural circular plate and the compound air-coupled transducer are derived. From this a total frequency equation for the compound transducer is obtained, rather than the two frequency equations for the circular plate and the longitudinal vibrator. Based on the total frequency equation and

equivalent circuit, the vibration characteristics of the compound transducer are discussed and compared with the experimentally measured resonance frequencies.

The radiated ultrasonic field is very important in practical applications. In this paper, the radiation ultrasonic field of the thin circular plate in flexural vibration is analyzed, the acoustic pressure in the far field is obtained, and the directivity function of the circular thin plate in flexural vibration is derived theoretically. The relationship between the directivity function and the vibrational mode of the flexural plate is analyzed. The calculated directivity pattern is compared with the measured results of a previous work,⁴ in which the angular distribution of the radiated acoustic field of the thin plate in flexural vibration was not analyzed theoretically because of the difficulty of the problem. It will be shown that the theoretically calculated angular distribution of the radiated acoustic field in our analysis is in good agreement with their measured result.

II. VIBRATION MODE ANALYSIS FOR A FLEXURAL CIRCULAR PLATE WITH A CLAMPED BOUNDARY CONDITION

Let the thickness and the radius of a circular thin plate be h and a . In the following analysis it is assumed that the thickness is far less than the radius, the flexural displacement amplitude is small, and the shearing strain and the rotary inertia of the plate are ignored.

A. Resonance frequency equation for the circular plate in flexural vibration

In the literature,^{8,9} the flexural vibrations of thin plates were studied, and complete solutions to the wave equation were obtained. However, in some practical cases, such as in ultrasonic drying and ultrasonic levitation, the axially symmetric flexural vibration of a circular thin plate that operates as an ultrasonic radiator in air is widely used. For the lowest-

order axially symmetric flexural vibrational mode of a circular plate, in the case of harmonic vibration, the transverse displacement can be expressed as

$$y(\rho, t) = [AJ_0(k\rho) + BI_0(k\rho)] \exp(j\omega t), \quad (1)$$

where $J_0(k\rho)$ is the Bessel function of the first kind of order zero, $I_0(k\rho)$ is the modified Bessel function, $k^4 = \rho_v h \omega^2 / D$, $D = Eh^3 / 12(1 - \sigma^2)$, which is the flexural rigidity of the plate, ρ_v is density, σ is Poisson's ratio, and ω is the angular frequency. To evaluate the constants A and B we must know the manner in which the plate is supported. In this paper, the plate is clamped all around its circumference at $\rho = a$. When the boundary of the plate is clamped, the displacement and its derivative at the edge disappear. From Eq. (1), we can obtain

$$-AJ_0(ka) = BI_0(ka), \quad (2)$$

$$AJ_1(ka) = BI_1(ka). \quad (3)$$

From Eqs. (2) to (3), the frequency equation for the circular plate in flexural vibration with clamped boundary can be obtained,

$$J_0(ka)I_1(ka) + I_0(ka)J_1(ka) = 0. \quad (4)$$

Let the root of Eq. (4) be $R(n)$, then we have

$$k_n a = R(n), \quad (5)$$

where n is a positive integer. Different values of n correspond to different vibrational orders of the plate. The first four values of $R(n)$ are 3.1962, 6.3064, 9.4395, and 12.5771. For different boundary conditions, such as free and simply supported, the value of $R(n)$ is different. However, the expression for the resonance frequency of a thin plate in flexural vibration is the same as for Eq. (6). From Eq. (5) the normal frequency f_n can be obtained,

$$f_n = \frac{R^2(n)h}{2\pi a^2} \sqrt{\frac{E}{12\rho_v(1-\sigma^2)}}, \quad n=1,2,3,\dots \quad (6)$$

For the normal mode of order n , its normal function can be expressed as

$$y_n(\rho, t) = [A_n J_0(k_n \rho) + B_n I_0(k_n \rho)] \exp(j\omega_n t). \quad (7)$$

Equation (7) is suitable for a solid circular thin plate. It can be seen that this is different from the flexural vibration of a circular membrane fixed at the rim. For the solution of the wave equation of a circular membrane, $B_n = 0$. The complete solution for the lowest-order axially symmetric flexural vibration of a circular plate with a clamped boundary condition is the sum of all the individual orders of vibration represented by Eq. (7),

$$y(\rho, t) = \sum_{n=1}^{\infty} [A_n J_0(k_n \rho) + B_n I_0(k_n \rho)] \exp(j\omega_n t). \quad (8)$$

B. Equivalent circuit of a circular plate in flexural vibration with a clamped boundary condition

For the analysis of the flexural vibrational characteristics of a circular thin plate, the concept of the lumped equivalent

parameter is useful. Based on Eq. (7), the kinetic energy of the normal mode of order n of the circular plate can be expressed as

$$E_n = -\pi \rho_v h \omega_n^2 \exp(2j\omega_n t) \int_0^a [A_n^2 J_0^2(k_n \rho) + B_n^2 I_0^2(k_n \rho) + 2A_n B_n J_0(k_n \rho) I_0(k_n \rho)] \rho d\rho. \quad (9)$$

Using the integral relations of the Bessel functions and Eqs. (2)–(4), the kinetic energy can be obtained from Eq. (9),

$$E_n = -\pi a^2 \rho_v h \omega_n^2 \exp(2j\omega_n t) A_n^2 J_0^2(k_n a). \quad (10)$$

In the above equations, the quantity $\exp(j2\omega_n t)$ is introduced when the kinetic energy of the plate is calculated by squaring of the velocity of the plate as described in Eq. (7). Since the stable flexural vibration of the plate is involved in this paper, the quantity $\exp(j2\omega_n t)$ has no effect on the final result of the kinetic energy. In fact, for stable vibration, only the amplitude is used, and the quantity $\exp(j2\omega_n t)$ can be dropped. From Eq. (7), the vibration velocity at the center of the circular plate can be obtained,

$$v_n = (A_n + B_n) j \omega_n \exp(j\omega_n t). \quad (11)$$

When the center of the circular plate is chosen as the reference point of the equivalent mass, the equivalent kinetic energy of the normal mode of order n can be written as

$$E_n' = -(1/2) M_n (A_n + B_n)^2 \omega_n^2 \exp(2j\omega_n t), \quad (12)$$

where M_n is the equivalent mass at the center of the plate in the normal mode of order n . In general cases, the usual way to define equivalent lumped parameters is to take the mean value of the displacement or velocity. However, in our case, the longitudinal sandwich piezoelectric vibrator is attached to the center of the plate. The plate in flexural vibration is excited at its center. Therefore, the center of the plate is chosen as the reference point. At this point, the forces and velocities of the sandwich vibrator and the plate are continuous. On the other hand, this is also beneficial to the analysis of the equivalent circuit of the compound system consisting of the longitudinal sandwich vibrator and the circular plate in flexural vibration. The reason is that one-dimensional theory is used in analyzing the equivalent circuit of the sandwich longitudinal piezoelectric transducer. In this case, the contacting position between the longitudinal vibrator and the plate is best suited for the reference point. Letting E_n' be equal to E_n , the equivalent mass can be obtained,

$$M_n = 2m \frac{J_0^2(k_n a) I_0^2(k_n a)}{[I_0(k_n a) - J_0(k_n a)]^2}, \quad (13)$$

where $m = \pi a^2 \rho_v h$, m being the mass of the plate. If the equivalent compliance of the normal mode of order n of the plate is C_n , we have

$$C_n = 1/\omega_n^2 M_n, \quad (14)$$

where $\omega_n = 2\pi f_n$, f_n is the normal frequency of the normal mode of order n and can be computed from Eq. (4). Based on the above-mentioned analyses, the equivalent mechanical impedance of the normal mode of order n of the plate can be expressed as

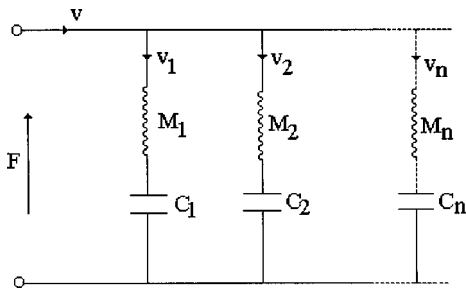


FIG. 1. Equivalent circuit of a circular plate in flexural vibration.

$$Z_n = jX_n = j(\omega_n M_n - 1/\omega_n C_n). \quad (15)$$

When a harmonic driving force $F = F_A \exp(j\omega t)$ acts at the center of the plate, the equivalent vibration velocity of the plate of the normal mode of order n can be obtained,

$$v_n = F_A \exp(j\omega t) / Z_n. \quad (16)$$

Using Eq. (8), the total equivalent vibration velocity of the plate is

$$v = \sum_{n=1}^{\infty} v_n = F_A \exp(j\omega t) \sum_{n=1}^{\infty} 1/Z_n. \quad (17)$$

Therefore, the equivalent circuit of the plate in flexural vibration can be obtained from Eq. (17) as shown in Fig. 1. From Fig. 1, we can get the equivalent mechanical impedance Z_i ,

$$Z_i = jX_i = 1/Y_i = 1 / \left(\sum_{n=1}^{\infty} Y_n \right), \quad (18)$$

where Y_i is the total equivalent input admittance and Y_n is the equivalent admittance of the normal mode of order n . When the angular frequency of the driving force approximates the normal angular frequency ω_n of the normal mode of order n of the plate, we have $Z_n \rightarrow 0, Y_n \rightarrow \infty$. In this case, for other normal modes of the plate, their equivalent impedances are large and the admittances are small. Therefore, Eq. (18) can be reduced to

$$Z_i = 1/Y_i = 1/Y_n = Z_n. \quad (19)$$

From Eq. (19), the equivalent circuit of the plate in the vicinity of the normal angular frequency ω_n can be represented by Fig. 2. In the above-given analysis, the loss in the plate is ignored. When the plate resonates, the mechanical

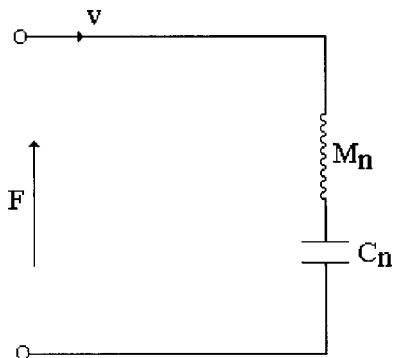


FIG. 2. Equivalent circuit of a plate in the n th flexural vibration.

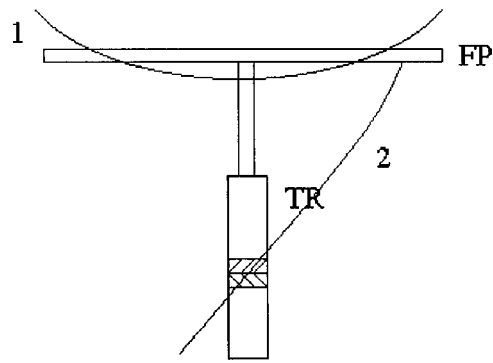


FIG. 3. Sketch of a compound air-coupled transducer consisting of a sandwich longitudinal piezoelectric vibrator and a circular thin plate in flexural vibration.

impedance is zero, and the vibration velocity becomes infinite. For the practical vibrator of the flexural circular plate, the loss is not zero, therefore, the vibration velocity is finite.

In practical cases, the transducer radiates ultrasonic waves into the surrounding medium. Thus, the load impedance is not zero. For the design and analysis of an air-coupled ultrasonic flexural transducer with load, the effect of the radiation impedance should be considered in deriving the resonance frequency equation of the transducer. However, the deduction of the radiation impedance is complicated. The analysis on the radiation impedance of a plane circular piston with uniformly distributed velocity can be found in elementary text on acoustics.⁹ Since the velocity distribution on the plate is complex, the radiation impedance of a thin plate in flexural vibration is different from that of a plane circular piston with uniformly distributed vibrational displacement. For additional knowledge of the radiation impedance of a circular thin plate in flexural vibration, readers can refer to the book by Pierce.¹⁰

III. RESONANCE FREQUENCY EQUATION AND EQUIVALENT CIRCUIT OF THE COMPOUND TRANSDUCER CONSISTING OF A LONGITUDINAL SANDWICH PIEZOELECTRIC TRANSDUCER AND A CIRCULAR PLATE

For traditional applications of high power ultrasound in gases, the compound transducer that is composed of a longitudinal sandwich piezoelectric transducer and a flexural circular plate is used because it can improve the impedance matching and increase the radiated ultrasonic power. The longitudinal piezoelectric transducer is attached to the center of the plate. In general cases, the sandwich longitudinal piezoelectric transducer is mainly composed of three parts, which are the back metal cylinder, the front metal horn, and the longitudinally polarized piezoelectric ceramic rings sandwiched between the back and front metals. In the compound transducer, the flexural plate can be regarded as a radiator of center-excitation as shown in Fig. 3. In the figure, FP is the circular thin plate in flexural vibration and TR is the sandwich longitudinal piezoelectric transducer. Curves 2 and 1 represent the longitudinal and flexural displacement distributions of the sandwich piezoelectric transducer and the circular plate. In this case, the longitudinal and the flexural dis-

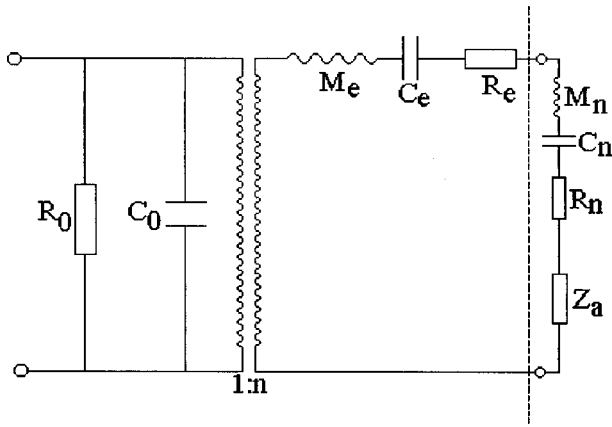


FIG. 4. Equivalent circuit of an air-coupled compound transducer.

placement amplitudes at the bonding point are large, i.e., the bonding point is a displacement antinode. Considering the above-mentioned analysis, the equivalent circuit of the compound transducer is shown in Fig. 4. In Fig. 4, the part before the dotted line denotes the half-wavelength sandwich longitudinal piezoelectric transducer and the part after the dotted line denotes the circular plate in flexural vibration. R_0 and C_0 are the dielectric loss resistance and the clamped capacitance of the sandwich longitudinal piezoelectric transducer; R_e , C_e , and M_e are the equivalent mechanical loss resistance, the equivalent elastic compliance constant, and the equivalent mass of the sandwich longitudinal transducer, respectively; M_n , C_n , and R_n are the equivalent mass, the equivalent compliance constant, and the mechanical loss resistance of the plate in the n th flexural vibration, respectively. Z_a is the radiation impedance of the flexural plate. It is different from that of a plane circular piston with uniformly distributed vibrational velocity. However, it can be expressed in a generalized form as

$$Z_a = R_a + jX_a. \quad (20)$$

Here R_a is the radiation resistance of the plate and X_a is the radiation reactance. It is well known that the radiation impedance is a complex quantity. It depends not only on the geometrical shape and dimensions, but also on the frequency and the distribution of vibration amplitude of the radiator. On the other hand, the radiation impedance also depends on the load medium of the transducer. From Fig. 4 the resonance frequency equation of the compound air-coupled transducer can be obtained as

$$X_a + \omega(M_e + M_n) - \frac{C_e + C_n}{\omega C_e C_n} = 0. \quad (21)$$

When the radiation impedance of the plate in flexural vibration is neglected, the resonance frequency equation can be rewritten as

$$\omega(M_e + M_n) - \frac{C_e + C_n}{\omega C_e C_n} = 0. \quad (22)$$

Substituting Eq. (14) into Eq. (22) yields

$$\omega^2 = \omega_n^2 \frac{1 + C_n/C_e}{1 + M_e/M_n}. \quad (23)$$

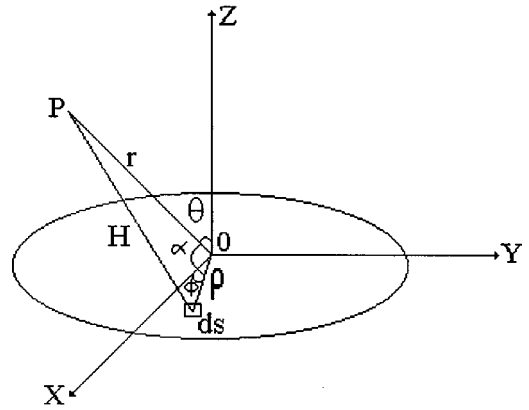


FIG. 5. Geometry used in deriving the radiated acoustic field characteristics of a flexural circular plate.

Here ω_n is the angular frequency of the n th flexural vibration of the plate. For the compound transducer to achieve optimum operating condition, the frequency of the compound transducer should be equal to that of the flexural circular plate. The optimum operating condition of the compound transducer means that when the sandwich longitudinal vibrator and the circular plate in flexural vibration are bonded together, their vibrational states remain unchanged, the resonance frequencies of the compound transducer, the half-wavelength longitudinal vibrator, and the flexural circular plate are all the same. In this case, Eq. (23) can be reduced to

$$C_n M_n = M_e C_e. \quad (24)$$

This means that in this case the resonance frequency of the half-wavelength sandwich longitudinal vibrator is equal to that of the flexural circular plate in the n th flexural vibration.

From the above-mentioned analysis, it can be concluded that for the compound air-coupled transducer, when the resonance frequency of the sandwich longitudinal transducer is equal to that of the flexural circular plate in the n th flexural vibration, the resonance frequency of the compound transducer is the same as that of the exciting transducer of the flexural plate. In this case, the natural vibrational states of the sandwich transducer and the circular plate in flexural vibration remain unchanged. The bonding point between the sandwich transducer and the circular plate is the displacement antinode of the two vibrations.

IV. RADIATION ULTRASONIC FIELD FROM A FLEXURAL CIRCULAR PLATE

Assume the flexural circular plate is mounted on a flat rigid baffle of infinite extent. The coordinates are sketched in Fig. 5. The acoustic pressure at the field point can be obtained by dividing the radiating surface of the flexural plate into infinitesimal elements, each of which acts like a baffled simple source of strength $dQ = u_A ds$. The pressure generated by one of these sources is given by

$$dp = j \frac{k_0 \rho_0 C_0}{2\pi H} u_A ds \exp[j(\omega t - k_0 H)], \quad (25)$$

where $k_0 = \omega/C_0$, C_0 is the sound speed in air, ρ_0 is the density of air, and H is the distance between the observation

point and the element. The total acoustic pressure is

$$p(r, \theta, t) = \int \int_s j \frac{k_0 \rho_0 C_0}{2\pi H} u_A \exp[j(\omega t - k_0 H)] ds, \quad (26)$$

where $s = \pi a^2$, $ds = \rho d\rho d\phi$, and u_A is the speed with which the flexural plate vibrates. It can be expressed as

$$u_A(\rho) = j\omega [AJ_0(k\rho) + BI_0(k\rho)]. \quad (27)$$

It is well known that for the symmetrical vibration of a flexural circular plate, the radiated acoustical field is also symmetrical. In Fig. 5, the Z axis is the symmetrical axis. Given the position $P(r, \theta)$ at which the acoustical pressure is desired, the X and Y axes are oriented so that the field point lies in the XZ plane. Since the far-field limit of the flexural plate radiation pattern is desired, the restriction $r \gg a$ is imposed. From Fig. 5, we have

$$H^2 = r^2 + \rho^2 - 2r\rho \cos(\alpha). \quad (28)$$

Here α is the spatial angle between the vector r and ρ . For $r \gg a$, H has the approximate form

$$H = r - \rho \cos(\alpha). \quad (29)$$

From Fig. 4, we have

$$\cos(\alpha) = \sin(\theta) \cos(\phi). \quad (30)$$

Thus, according to the far-field approximation, the far-field acoustic pressure can be obtained as

$$p(r, \theta, t) = j \frac{\omega \rho_0 \exp[j(\omega t - k_0 r)]}{2\pi r} \times \int_0^a u_A \rho d\rho \int_0^{2\pi} e^{jk_0 \rho \sin(\theta) \cos(\phi)} d\phi. \quad (31)$$

In terms of the integral formulas of the Bessel functions, Eq. (31) can be rewritten as

$$p(r, \theta, t) = j \frac{\omega \rho_0 \exp[j(\omega t - k_0 r)]}{r} \times \int_0^a u_A J_0(k_0 \rho \sin(\theta)) \rho d\rho. \quad (32)$$

Substituting Eq. (27) into Eq. (32) yields

$$p(r, \theta, t) = - \frac{\omega^2 \rho_0 \exp[j(\omega t - k_0 r)]}{r} \times \int_0^a [AJ_0(k\rho) + BI_0(k\rho)] J_0(k_0 \rho \sin(\theta)) \rho d\rho. \quad (33)$$

Equation (33) can be calculated in terms of the Bessel integral functions,

$$\int_0^x x J_0(\alpha x) J_0(\beta x) dx = \frac{x}{\alpha^2 - \beta^2} [-\beta J_0(\alpha x) J_1(\beta x) + \alpha J_0(\beta x) J_1(\alpha x)],$$

so that

$$\frac{p(r, \theta, t)}{A} = - \frac{\omega^2 \rho_0 a \exp[j(\omega t - k_0 r)]}{r} \left\{ \frac{1}{k^2 - k_0^2 \sin^2(\theta)} \{-k_0 \sin(\theta) J_0(ka) J_1[k_0 a \sin(\theta)] + k J_0[k_0 a \sin(\theta)] J_1(ka)\} + \frac{B}{A} \frac{1}{k^2 + k_0^2 \sin^2(\theta)} \{k_0 \sin(\theta) I_0(ka) J_1[k_0 a \sin(\theta)] + k J_0[k_0 a \sin(\theta)] I_1(ka)\} \right\}. \quad (34)$$

From Eq. (34), we can identify the directivity function $D(\theta)$ for the flexural circular plate as

$$D(\theta) = \frac{1}{k^2 - k_0^2 \sin^2(\theta)} \{-k_0 \sin(\theta) J_0(ka) J_1[k_0 a \sin(\theta)] + k J_0[k_0 a \sin(\theta)] J_1(ka)\} + \frac{B}{A} \frac{1}{k^2 + k_0^2 \sin^2(\theta)} \{k_0 \sin(\theta) I_0(ka) J_1[k_0 a \sin(\theta)] + k J_0[k_0 a \sin(\theta)] I_1(ka)\}. \quad (35)$$

It can be seen that the radiation pressure depends on the value of B/A that corresponds to different boundary conditions, such as clamped, free, and simply supported. Therefore, Eqs. (34) and (35) are the generalized expressions about the radiation acoustic pressure and the directivity pattern. Corresponding to different boundary conditions of the circular plate in flexural vibration, the concrete expressions of radiation acoustic pressure and directivity pattern are different. For a circular plate with a clamped boundary condition, substituting the expression of B/A from Eq. (2) or (3) into Eqs. (34) and (35) yields

$$\frac{p(r, \theta, t)}{A} = - \frac{\omega^2 \rho_0 a \exp[j(\omega t - k_0 r)]}{r} \left\{ \frac{1}{k^2 - k_0^2 \sin^2(\theta)} \{-k_0 \sin(\theta) J_0(ka) J_1[k_0 a \sin(\theta)] + k J_0[k_0 a \sin(\theta)] J_1(ka)\} + \frac{1}{k^2 + k_0^2 \sin^2(\theta)} \{-k_0 \sin(\theta) J_0(ka) J_1[k_0 a \sin(\theta)] + k J_0[k_0 a \sin(\theta)] J_1(ka)\} \right\}, \quad (36)$$

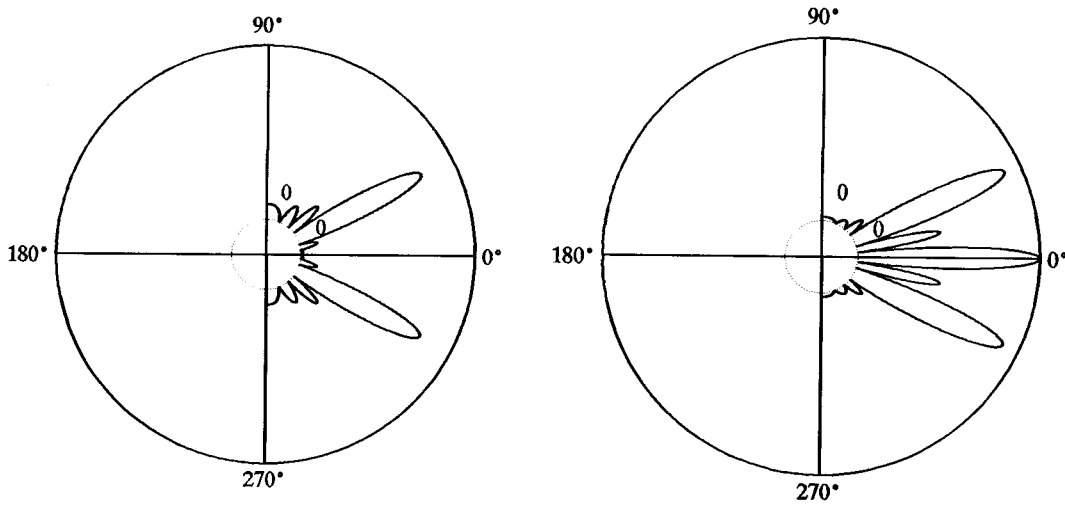


FIG. 6. (a) Calculated directional pattern of a flexural circular plate with a clamped boundary condition ($f=20$ kHz, $n=3$, $h=3$ mm, $a=56.6$ mm). (b) Calculated directional pattern of a flexural circular plate with a free boundary condition ($f=20$ kHz, $n=3$, $h=3$ mm, $a=56.1$ mm).

$$D(\theta) = \frac{1}{k^2 - k_0^2 \sin^2(\theta)} \{-k_0 \sin(\theta) J_0(ka) J_1[k_0 a \sin(\theta)] + k J_0[k_0 a \sin(\theta)] J_1(ka)\} + \frac{1}{k^2 + k_0^2 \sin^2(\theta)} \{-k_0 \sin(\theta) J_0(ka) J_1[k_0 a \sin(\theta)] + k J_0[k_0 a \sin(\theta)] J_1(ka)\}. \quad (37)$$

For a circular plate with a free boundary condition, i.e., the flexural moment and the lateral force at the edge of the plate disappear, the following expressions can be obtained:

$$A[kJ_0(ka) - J_1(ka)/a + \sigma J_1(ka)/a] - B[kI_0(ka) - I_1(ka)/a + \sigma I_1(ka)/a] = 0, \quad (38)$$

$$AJ_1(ka) + BI_1(ka) = 0. \quad (39)$$

Solving Eq. (39) for B/A and substituting the expression of B/A into Eqs. (34) and (35) yields the radiated acoustic pressure and the directivity function of a circular plate with a free boundary condition,

$$\frac{p(r, \theta, t)}{A} = -\frac{\omega^2 \rho_0 a \exp[j(\omega t - k_0 r)]}{r} \left\{ \frac{1}{k^2 - k_0^2 \sin^2(\theta)} \{-k_0 \sin(\theta) J_0(ka) J_1[k_0 a \sin(\theta)] + k J_0[k_0 a \sin(\theta)] J_1(ka)\} + \frac{1}{k^2 + k_0^2 \sin^2(\theta)} \{-k_0 \sin(\theta) J_1(ka) I_0(ka) J_1[k_0 a \sin(\theta)] / I_1(ka) - k J_0[k_0 a \sin(\theta)] J_1(ka)\} \right\}, \quad (40)$$

$$D(\theta) = \frac{1}{k^2 - k_0^2 \sin^2(\theta)} \{-k_0 \sin(\theta) J_0(ka) J_1[k_0 a \sin(\theta)] + k J_0[k_0 a \sin(\theta)] J_1(ka)\} + \frac{1}{k^2 + k_0^2 \sin^2(\theta)} \{-k_0 \sin(\theta) J_1(ka) I_0(ka) J_1[k_0 a \sin(\theta)] / I_1(ka) - k J_0[k_0 a \sin(\theta)] J_1(ka)\}. \quad (41)$$

Based on the vibrational theory of a circular plate in flexural vibration and the above-mentioned analysis, the resonance frequency equations of the flexural circular plate with different boundary conditions are different. Therefore, the roots $k_n a$ of the resonance frequency equations are different for different boundary conditions. Thus, the directional pattern is also different. Figures 6(a) and (b), 7(a) and (b) show the theoretically calculated directional patterns of the flexural plates with free and clamped conditions. The material used in the calculation is steel. The standard material parameters are as follows: $c=5000$ m/s, $\sigma=0.28$. It can be seen from the figures that when the vibrational order is

increased, the directional pattern becomes complicated. For the same vibrational order, the directional pattern of a circular plate with a clamped boundary condition is superior to that with a free boundary condition.

On the other hand, from the calculated acoustic field distribution of a circular plate in flexural vibration with free and clamped boundary conditions, it can be seen that for a circular plate in flexural vibration with free boundary, the acoustic pressure on the Z axis is zero. This means that the directivity of a flexural circular plate with a free boundary is worse. The reason is that the vibrational displacements on the plate have opposite phase.

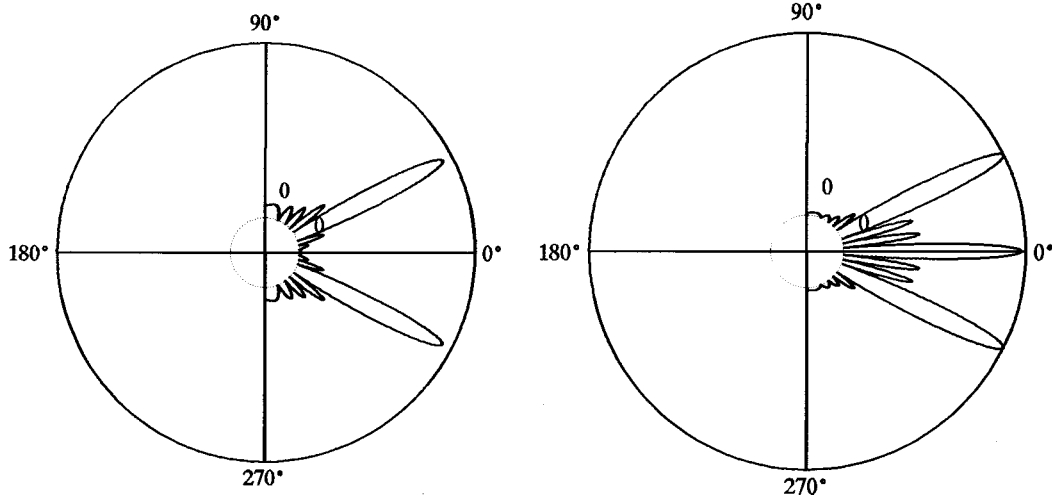


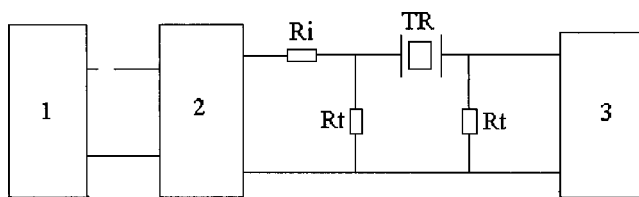
FIG. 7. (a) Calculated directional pattern of a flexural circular plate with a clamped boundary condition ($f=20$ kHz, $n=4$, $h=3$ mm, $a=75.3$ mm). (b) Calculated directional pattern of a flexural circular plate with a free boundary condition ($f=20$ kHz, $n=4$, $h=3$ mm, $a=75.0$ mm).

V. EXPERIMENTS

To verify the calculated results from our derived theory about the compound transducer and the flexural circular plate, some circular plates and longitudinal sandwich piezoelectric transducers were built and evaluated. The plate material was steel and the sandwich longitudinal transducer was a vibrator of half-wavelength. The sandwich longitudinal transducer was attached to the center of the flexural circular plate. In this section, two experiments are described.

A. Resonance frequency measurement

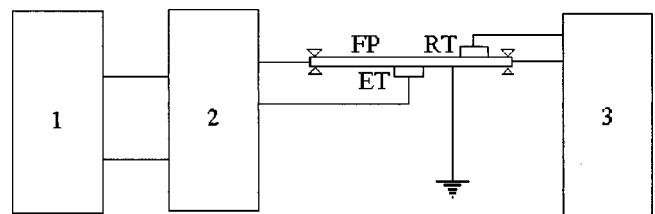
There are three kinds of resonance frequencies, which include the resonance frequency of the half-wavelength sandwich longitudinal piezoelectric transducer, the resonance frequency of the thin plate in flexural vibration, and the resonance frequency of the compound transducer. In the experiment, these resonance frequencies are measured under small input signal. The resonance frequencies of the sandwich longitudinal piezoelectric transducer and the compound air-coupled transducer were measured using the transmission line method as shown in Fig. 8. In the figure, TR is the transducer to be measured, R_i and R_t are two electric resistances, $R_i \gg R_t$. In the experiment, the frequency of the signal generator is changed until the output signal of the oscilloscope is a maximum. The frequency corresponding to this maximum output is the resonance frequency of the transducer being measured. The resonance frequencies of the flexural circular plate are measured using the emitting-



1:frequency meter; 2:signal generator; 3:oscilloscope

FIG. 8. Experimental setup for the measurement of the resonance frequency of the air-coupled transducer.

receiving method as shown in Fig. 9. Here FP is the circular plate in flexural vibration with a clamped boundary condition. ET and RT are the emitting and receiving transducers. In this case, the emitting and receiving transducers are rectangular piezoelectric ceramic elements in their thickness extensional vibration. Their lowest resonance frequencies are far larger than that of the circular plate in flexural vibration. In the experiment, the plate is clamped with bolts on its boundary. The frequency of the exciting signal is changed until the output of the oscilloscope is a maximum. This indicates that the plate is resonating at the frequency of the exciting signal and corresponds to the resonance frequency of the plate in the n th flexural vibration. The measured results are listed in Table I. In Table I, the designed resonance frequency of the half-wavelength longitudinal sandwich piezoelectric transducer and the thin plate in flexural vibration is 20 kHz. At this frequency, the half-wavelength longitudinal vibrator resonates at its fundamental vibrational mode. For the design of a thin plate in flexural vibration, it can be seen from Eq. (6) that the resonance frequency of the plate is determined by the vibrational order, the thickness, and the radius of the plate. Therefore, when the designed frequency (20 kHz) is determined, the vibrational order and the radius or thickness may be different. In this paper, the third and fourth vibrational orders of the plate are chosen, and two plates are designed and made. Their resonance frequencies and thickness are equal to each other, while their vibrational



1:frequency meter; 2:signal generator; 3:oscilloscope

FIG. 9. Experimental setup for the measurement of the resonance frequency of a plate in flexural vibration.

TABLE I. Measured resonance frequencies of the compound air-coupled transducer (h is the thickness of the thin plate, a is the radius of the plate, n is the order of the flexural vibrational mode of the plate, f is the designed frequency of the half-wavelength sandwich longitudinal transducer and the flexural circular plate, f_T , f_F , and f_C are the measured resonance frequencies of the sandwich transducer, the flexural circular plate, and the compound air-coupled transducer).

No.	n	h (mm)	a (mm)	f_T (Hz)	f_F (Hz)	f_C (Hz)	f (Hz)
1	3	3	56.6	19 976	19 435	19 631	20 000
2	4	3	75.3	19 976	19 378	19 528	20 000

order and radius are different in order to satisfy the resonance frequency equation (6). It can be seen that the measured resonance frequencies are in good agreement with the theoretical results.

As for frequency-measurement error, the following factors should be taken into account. First, the standard material parameters used in the calculation are different from the practical values of the material. Second, the boundary of the circular plate is not clamped completely. Third, the emitting and receiving transducers on the plate have finite geometrical dimension, their mass and contacting areas have effect on the free vibration of the plate. Finally, since the emitting and receiving transducers have finite geometrical dimensions, the conditions of point excitation and point receiving are not satisfied entirely.

B. Directional pattern measurement

From the above-mentioned analysis, it can be seen that the directivity pattern of the radiation acoustic field is determined by the plate in flexural vibration alone. In this section, we calculate the directional pattern of a circular plate in flexural vibration with a free boundary condition using a theory similar to that used in the above-given analysis. The dimensions, the resonance frequency, and the vibrational mode of the flexural circular plate are the same as those in a previous paper.⁴ The calculated results according to the above-given theory are shown in Fig. 10. It can be seen that the calculated directional pattern is in good agreement with the measured result of the previous work.⁴ In literature,^{4,5} because of the

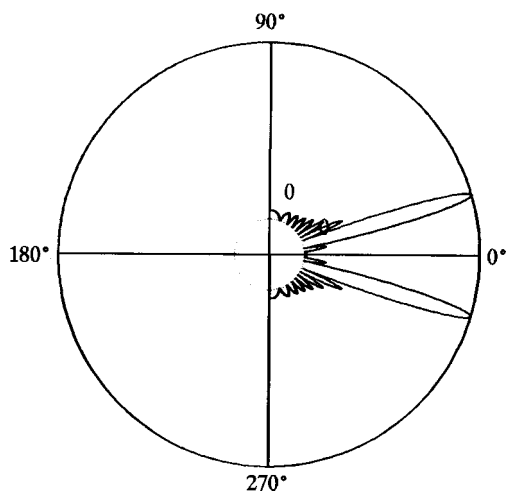


FIG. 10. Calculated directional pattern of a flexural circular plate with a free boundary condition ($f=39.4$ kHz, $n=3$, $a=45$ mm, $h=4$ mm, $R(n)=9.3573$, $\sigma=0.21$).

difficulty in calculating the radiation acoustic field, the theoretical directivity pattern of a thin plate in flexural vibration was not analyzed. Therefore, only the experimental results were given and compared with the calculated results according to the theory of a plane circular theoretical piston.

VI. CONCLUSION

In this paper, the compound air-coupled transducer consisting of a half-wavelength longitudinal sandwich piezoelectric vibrator and a flexural circular plate is described. The vibrational mode and the resonance frequency equation of a flexural circular plate are also analyzed. The equivalent circuits of the flexural circular plate and the compound transducer are given. From these, the resonance frequency equation of the compound air-coupled transducer is obtained. The radiation acoustic field of the flexural circular plate is calculated, and the directional function is obtained theoretically. The resonance frequencies of the compound transducer are measured and good agreement between the measured and calculated results is obtained. For the radiated acoustic field, the calculated result using the method in this paper is compared with the measured results of a previous work, and good agreement is obtained. This shows that the analysis and calculation in this paper are valid.

The method presented in this paper for the calculation of the radiated acoustic field of the flexural circular plate can be used in other cases, such as the flexural circular plate with free, clamped, and simply supported boundary conditions.

It can be seen that the radiated acoustic field of a circular flat plate in flexural vibration is complex. The directional pattern is worse. To improve the directional pattern, the stepped plate can be used. The calculation of the acoustic field of a stepped plate in flexural vibration is more complex. In this case, numerical methods can be used. On the other hand, the radiation impedance of a circular plate in flexural vibration is an important parameter in the design of the air-coupled transducer. Its analysis and calculation will be done in later work.

ACKNOWLEDGMENT

The author would like to thank the National Natural Science Foundation of China for the financial support of the subject.

¹G. Reethof, "Acoustic agglomeration of power plant fly ash environmental and hot gas clean-up," *ASME J. Vib., Acoust., Stress, Reliab. Des.* **100**, 552–555 (1988).

²T. L. Hoffmann, W. Chen, G. H. Koopmann, A. W. Scaroni, and L. Song,

- “Experimental and numerical analysis of bimodal acoustic agglomeration,” *ASME J. Vibr. Acoust.* **115**, 232–240 (1993).
- ³J. A. Gallego-Juarez, G. Rodriguez-Corral, and T. Gaete-Garretón, “An ultrasonic transducer for high power applications in gases,” *Ultrasonics* **16**, 267–271 (1978).
- ⁴A. Barone and J. A. Gallego-Juarez, “Flexural vibrating free-edge plates with stepped thickness for generating high directional ultrasonic radiation,” *J. Acoust. Soc. Am.* **51**, 953–959 (1972).
- ⁵A. Barone and J. A. Gallego-Juarez, “On a modification of vibrating flat plates in order to obtain phase-coherent radiation,” *Acustica* **22**, 187–188 (1969/1970).
- ⁶T. Otsuka, Y. Kamishima, and K. Seya, “Aerial ultrasound source by stepped circular vibrating plate,” *Jpn. J. Appl. Phys., Suppl.* **22-3**, 108–110 (1983).
- ⁷J. A. Gallego-Juarez, “Axisymmetric vibration of circular plates with stepped thickness,” *J. Sound Vib.* **26**, 411–416 (1973).
- ⁸P. M. Morse and K. U. Ingard, *Theoretical Acoustics* (McGraw-Hill, New York, 1968), pp. 214–216.
- ⁹L. E. Kinsler, A. R. Frey, A. B. Coppens, and J. V. Sanders, *Fundamentals of Acoustics* (Wiley, New York, 1982), pp. 92–95.
- ¹⁰A. D. Pierce, *Acoustics*, 2nd ed. (American Institute of Physics, New York, 1989), p. 129.

Robustness to head misalignment of virtual sound imaging systems

Takashi Takeuchi^{a)} and Philip A. Nelson

Institute of Sound and Vibration Research, University of Southampton, Highfield, Southampton SO17 1BJ, United Kingdom

Hareo Hamada

Department of Information and Communication Engineering, Tokyo Denki University, 2-2 Kanda-Nishikicho, Chiyoda-ku, Tokyo 101, Japan

(Received 22 November 2000; accepted for publication 26 December 2000)

When binaural sound signals are presented with two loudspeakers, the listener's ears are required to be in the relatively small region which is under control of the system. Misalignment of the head results in inaccurate synthesis of the binaural signals. Consequently, directional information associated with the acoustic signals is inaccurately reproduced. When the two loudspeakers are placed close together, the spatial rate of change of the generated sound field is much smaller than that generated by two loudspeakers spaced apart. Therefore, the performance of such a system is expected to be more robust to misalignment of the listener's head. Robustness of performance is investigated here with respect to head displacement in three translational and three rotational directions. A comparison is given between systems consisting of two loudspeakers either placed close together or spaced apart. The extent of effective control with head displacement and the resulting deterioration in directional information is investigated in the temporal and spectral domain by analyzing synthesized binaural signals. Subjective localization experiments are performed for cases in which notable differences in performance are expected from the previous analysis. It is shown that the system comprising two loudspeakers that are close together is very robust to misalignment of the listener's head. © 2001 Acoustical Society of America.

[DOI: 10.1121/1.1349539]

PACS numbers: 43.38.Md, 43.66.Qp, 43.60.Pt, 43.64.Bt [SLE]

I. INTRODUCTION

Binaural technology¹⁻³ is often used to present a virtual acoustic environment to a listener. The principle of this technology is to control the sound pressure at the listener's ears so that the reproduced sound pressure coincides with that which would be produced when he is in the desired real sound field. Producing the correct ear sound pressures should lead to almost the same sensation as the listener would experience in the real sound field for most realistic sound signals. The superiority of this binaural technique lies in its capability of providing a very accurate spatial impression to a listener. Appropriate control of directional information of direct and reflected sounds, as well as information regarding reflecting surfaces, distance which the sound has traveled, and information from the sound source itself, is essential to create a convincing virtual auditory space.

Unlike other types⁴⁻⁶ of attempts to give virtual directional information to a listener, binaural technology requires the control of sound at each of the two ears independently. One way of achieving this is to use a pair of headphones or similar types of transducers. An alternative to this is to use two loudspeakers at different positions in a listening space with the help of signal processing to ensure that appropriate binaural signals are obtained at the listener's ears.⁷⁻¹⁰

One disadvantage of such binaural sound reproduction over loudspeakers is that the listener's ears must be in the relatively small region in space at which the control is effective. Misalignment of the head position and orientation results in the inaccurate synthesis of the binaural signals at the ears. This results from the change in the transfer functions between the transducers and the listener's ears. Consequently, the performance of the system deteriorates, i.e., directional information associated with the sound is smeared as is other information.

It can also be shown that it is possible to achieve independent control of the sound signal at two ears with a monopole transducer and a dipole transducer at the same position.^{10,11} When two closely spaced monopole transducers are used, the sound field produced is a good approximation to that produced by a point monopole and a point dipole transducer up to a given frequency. We refer to such a system as "stereo dipole."¹² The sound field generated by such a system has a distinct character in that its rate of change over space is much smaller than that generated by two monopole transducers spaced apart.¹³ As a consequence, it is expected to be more robust to misalignment of the position and orientation of the listener's head.¹⁴ A certain amount of misalignment is inevitable in the practical use of such a system. Therefore, it is obviously advantageous if the system is more robust to misalignment. When, for example, the system is used to attempt to track head movement, it is essential to know the threshold at which the perception of the virtual

^{a)}Previously at the Kajima Technical Research Institute, 2-19-1 Tobitakyu, Chofu-shi, Tokyo 182-0036, Japan.

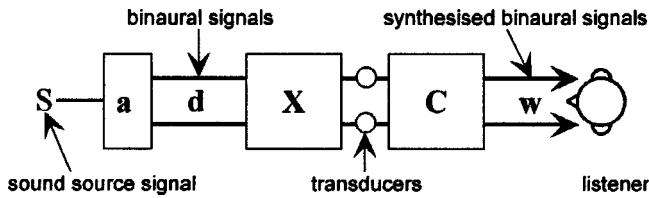


FIG. 1. The principle of binaural synthesis over loudspeakers.

acoustic environment collapses. The filter update would inevitably be discrete in time and hence the listener's movement would result in a certain amount of displacement from the intended position before the filters are updated for the new head position. In other words, the filters must be updated before the head moves a distance that is greater than the tolerances. Having larger tolerances will be advantageous in keeping track of head movement up to a higher velocity with a given update rate.

The objective of this study is to investigate the robustness of the performance of such a system when the listener's head is misaligned. Comparison between two different transducer arrangements is made; two transducers placed close together and two transducers spaced apart. The consequence of three translational and three rotational displacements of the head is examined. Much emphasis is put upon the preservation of directional information which depends mostly upon the head related transfer functions (HRTFs). First, the effectiveness of control is investigated by synthesis of a unit impulse at both ears in both the time and frequency domains. Presentation of an incident sound from various directions are then investigated as the very basic components of a virtual sound environment. The characteristics of the synthesised binaural signals are examined in several ways. In the temporal domain, the interaural time difference (ITD) of the synthesized binaural sound signals is investigated. The monaural spectral shape of the signals is also investigated since this will influence the spectral localization cue. Further consideration is also given to the binaural spectral difference, i.e., the interaural level difference (ILD) that is used to localise along the interaural direction and also the interaural difference of spectral shape that is used to localize around the interaural axis. Cues related to the dynamics of head movement are outside the scope of this study. Subjective localization experiments are performed for displacements for which notable differences in performance are expected from the previous analysis.

II. FACTORS IN THE SYNTHESIS OF A VIRTUAL ACOUSTIC ENVIRONMENT

The principle of the system under investigation is illustrated in Fig. 1. The following is described with a frequency domain representation of the acoustic paths (transfer functions) and sound signals. All the spatial information is in the transfer functions between sound source and both of the listener's ears. As the very basic components of a virtual sound environment, generation of a single incident sound wave is taken as an example here. A pair of binaural signals $\mathbf{d}(z)$ corresponding to a single incident sound wave are generated by filtering a sound source signal $S(z)$ through a vector of

filters $\mathbf{a}(z)$ which contains a pair of HRTFs for both ears corresponding to the desired direction of the incident sound. Thus,

$$\mathbf{d}(z) = \mathbf{a}(z)S(z). \quad (1)$$

When the signals at both ears of the listener are controlled by two transducers in the listening space, the 2×2 matrix $\mathbf{C}(z)$ of transfer functions can be defined between the transducers and the ears. In order to present the binaural signals at each ear, the signals $\mathbf{d}(z)$ are filtered through a 2×2 matrix $\mathbf{X}(z)$ of control filters which contains the pseudo-inverse of the transfer function matrix $\mathbf{C}(z)$. Then the synthesized binaural signals $\mathbf{w}(z)$ and the sound source signal $S(z)$ are related by

$$\mathbf{w}(z) = \mathbf{C}(z)\mathbf{X}(z)\mathbf{a}(z)S(z). \quad (2)$$

For convenience, the control performance matrix $\mathbf{R}(z)$ and vector of synthesized HRTFs $\mathbf{q}(z)$ are defined as follows:

$$\mathbf{R}(z) = \mathbf{C}(z)\mathbf{X}(z), \quad (3)$$

$$\mathbf{q}(z) = \mathbf{C}(z)\mathbf{X}(z)\mathbf{a}(z) = \mathbf{R}(z)\mathbf{a}(z). \quad (4)$$

A number of filter design methods have been presented.^{15,16} In short, with the use of a modeling delay Δ and a regularization parameter for causal stable inversion, $\mathbf{X}(z)$ is designed so that

$$\mathbf{R}(z) = \mathbf{C}(z)\mathbf{X}(z) \approx z^{-\Delta}\mathbf{I} \quad (5)$$

is satisfied, where \mathbf{I} is the identity matrix. This ensures the synthesised HRTFs $\mathbf{q}(z)$ are a good approximation to the original HRTFs $\mathbf{a}(z)$. Thus, from Eqs. (4) and (5),

$$\mathbf{q}(z) \approx z^{-\Delta}\mathbf{a}(z). \quad (6)$$

As the listener's head is displaced away from the exact position for which control filters $\mathbf{X}(z)$ are calculated, the transfer functions $\mathbf{C}(z)$ change gradually. Thus the pseudo-identity matrix $\mathbf{R}(z)$ and, as a consequence, the synthesized binaural HRTFs $\mathbf{q}(z)$ are degraded and may result in the wrong subjective perception.

III. ANALYSIS OF THE SYNTHESIZED BINAURAL SIGNALS

A. Model

The physical acoustic paths \mathbf{a} and \mathbf{C} are modeled with free field head related impulse responses (HRIRs: the time domain representation of HRTFs). A database comprising directionally discrete HRIRs on a virtual spherical surface 1.4 m from a KEMAR dummy head is obtained from the MIT Media Lab.¹⁷ Those between sampled directions are obtained by bilinear interpolation on the virtual spherical surface of magnitude and phase spectra in the frequency domain. Those at a different distance from a head are obtained by extrapolation with an appropriately chosen delay and spherical attenuation.¹⁸ The loudspeaker response is deconvolved from the data and thus each control transducer of the system is modeled as an ideal monopole source. The control filter matrix \mathbf{X} is determined by the frequency domain deconvolution method.¹⁶

The listener's head is displaced with respect to six orthogonal axes (three translational and three rotational) as in

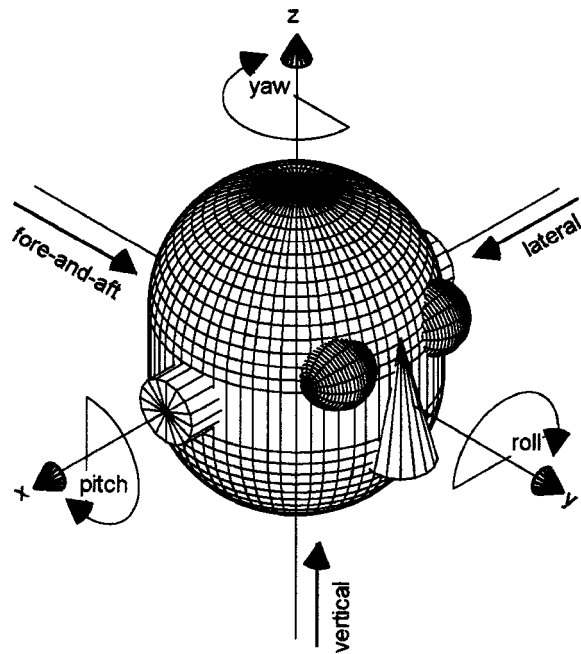


FIG. 2. The Cartesian coordinate system used to define head displacement relative to the optimal head position and orientation.

Fig. 2 and Table I. Since the robustness to relatively small displacement of the head position and orientation is of interest here, the robustness of the virtual sound image is evaluated relative to the listener's head, not relative to the listening space. In other words, when the listener's head is displaced, he should ideally perceive the same virtual sound image as in the optimal position and orientation, unlike those applications where the listener may want to move around in a virtual sound environment.

The spherical coordinate system used to define direction of sound and of transducers is shown in Fig. 3. The origin is at the intersection of the interaural axis and the median plane. The polar axis coincides with the interaural axis. The azimuth angle ranges from -90° to 90° as the direction changes from the pole at the left to the other pole at the right. A cone of constant azimuth is approximately the same as the cone of confusion where there are no ITDs. The elevation angle ranges from -180° on the horizontal plane behind the head to -90° below, 0° on the horizontal plane in front, 90° above the head to 180° again on the horizontal plane behind. Two different transducer arrangements are investigated for comparison. In both cases, two transducers are placed in front of the listener on the horizontal plane (0° elevation) and aligned symmetrically with respect to the median plane. The transducers positioned spanning 60° as seen by the listener

TABLE I. Terminology used to describe head displacement.

Description	Terminology
Translation along x -axis	lateral
Translation along y -axis	fore-and-aft
Translation along z -axis	vertical
Rotation about x -axis	pitch
Rotation about y -axis	roll
Rotation about z -axis	yaw

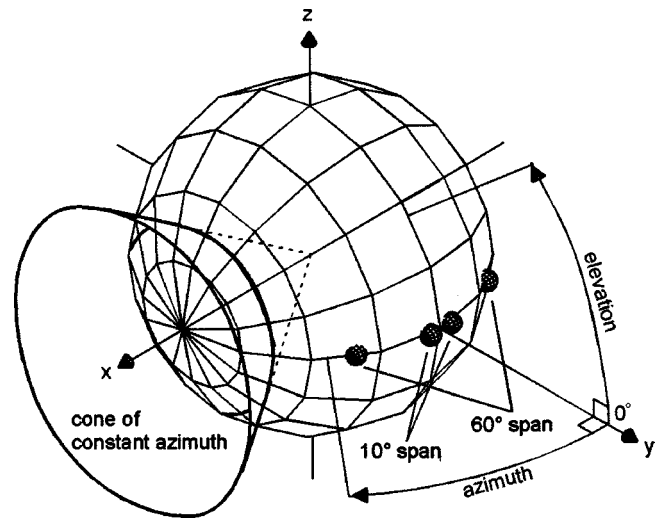


FIG. 3. The spherical coordinate system used to define the direction of sound sources relative to the listener's head position and orientation. An example of "cone of constant azimuth" is illustrated. The two different transducer arrangements investigated are also shown (relative to the optimal head position and orientation).

($\pm 30^\circ$ azimuth) are representative of a popular arrangement. The span of 10° ($\pm 5^\circ$ azimuth) represents close spacing.

B. Indices for analysis

In the temporal domain, the interaural cross-correlation function $\Psi_a(\tau)$ of HRIRs $\mathbf{a}(t)$ corresponding to the real source direction are examined and the time lag which gives the peak values of $\Psi_a(\tau)$ is used as an estimate of ITD of the acoustic signals at the two ears. The interaural cross-correlation function $\Psi_a(\tau)$ is expressed as follows in terms of the elements of $\mathbf{a}(t)$:

$$\Psi_a(\tau) = \lim_{T \rightarrow \infty} \frac{1}{2T} \int_{-T}^T a_1(t) a_2(t + \tau) dt. \quad (7)$$

There are other possible methods to estimate the ITD, for example, by detecting the leading-edge in the HRIRs, or by computing the phase spectrum or group delay of the binaural signals. However, the leading-edge method may misjudge the ITD by detecting the less potent onset ITD rather than the ongoing ITD to which neurones are sensitive.¹⁹⁻²¹ There is no indication that the nervous system could detect the high-frequency phase spectrum nor group delay. Anatomical and physiological studies strongly suggest that ITD information is extracted with the interaural cross-correlation of the auditory-nerve responses to the stimuli in the superior olivary complex then further processed at a higher level of auditory pathway.^{22,23} The envelope delay of high frequency signals as an ITD cue^{24,25} can be extracted by the cross-correlation method as well as the phase delay of low frequency signals. However, while this method extracts a single number ITD in binaural acoustic signals, it does not attempt to model the complex human auditory system which transduces acoustic signals at the ears into vibration of the auditory organs and then into nerve signals which are subsequently processed. Therefore, the absolute value of the ITD may not be completely significant although it can extract

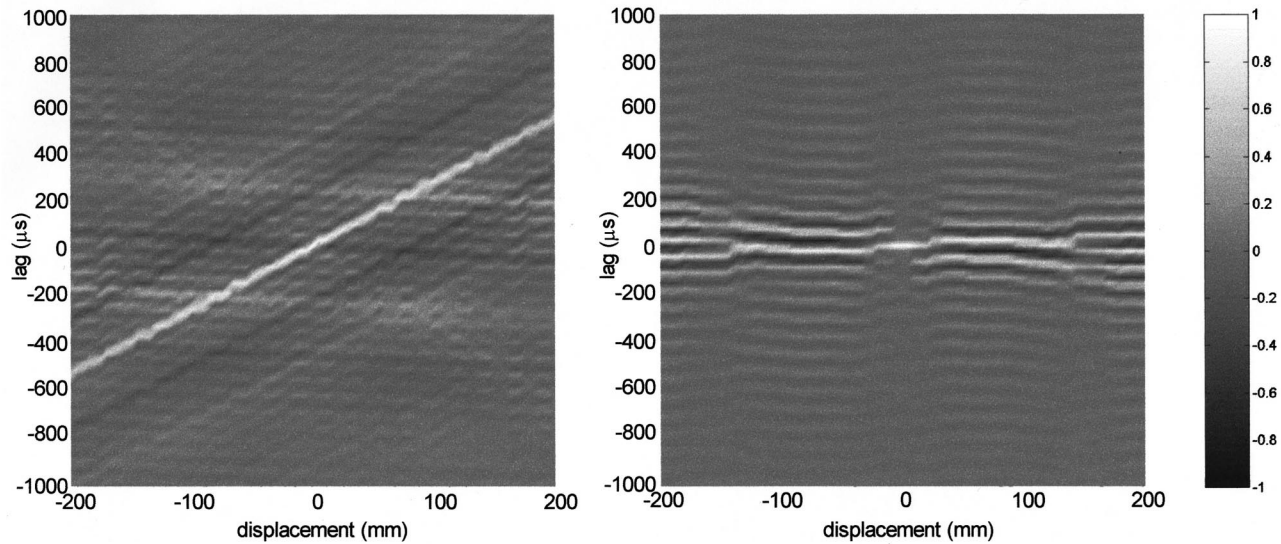


FIG. 4. The effect of lateral displacement on the interaural cross-correlation functions for the synthesis of simultaneous unit impulses. Left panel: 60° transducer span. Right panel: 10° transducer span.

tendencies and enables comparison between the two different conditions studied here.

In the spectral domain, a spectral analysis of synthesised HRTFs is performed over a logarithmic scale both in frequency and magnitude to account for the basic property of auditory filters. The monaural spectral shape is regarded as an important cue to identify one direction out of directions with no interaural differences. This cue utilizes the change of the spectral shape of the sound source signal due to the HRTF for each ear. The monaural spectral cues also have supplemental role in localization along the interaural direction.²⁶ Interaural difference of spectra could have two roles. The major role is to localize along the interaural direction (azimuth discrimination) with an interaural level difference (ILD). It could also be another cue to resolve confusion among directions with no interaural time difference (elevation discrimination) by utilizing the pattern of frequency dependent interaural spectral difference.²⁷ The advantage of this cue over the monaural spectral shape cue in practice would be that it does not depend on the spectrum of the sound source signal. Again it should be noted that this does not attempt a complete model of the human auditory system.

C. Robustness of temporal cues

First, the effectiveness of control as a function of head displacement is evaluated by analyzing the matrix of electroacoustic paths $\mathbf{R}(t)$ which is independent of the direction of the virtual source. Following this, the synthesised HRIRs $\mathbf{q}(t)$ with head displacement are analyzed in order to demonstrate what happens to temporal cues as a function of the relative direction of the virtual sound source.

1. Control performance (temporal)

When the inputs to $\mathbf{R}(t)$ is a pair of simultaneous delta functions $\delta(t)$ rather than binaural signals, the interaural cross-correlation function, $\Psi_{\mathbf{p}}(\tau)$, of the synthesised signals is expressed as

$$\Psi_{\mathbf{p}}(\tau) = \lim_{T \rightarrow \infty} \frac{1}{2T} \int_{-T}^T p_1(t)p_2(t+\tau)dt, \quad (8)$$

where

$$\mathbf{p}(t) = \begin{bmatrix} p_1(t) \\ p_2(t) \end{bmatrix} = \begin{bmatrix} R_{11}(t) + R_{12}(t) \\ R_{21}(t) + R_{22}(t) \end{bmatrix}. \quad (9)$$

When the listener's head is at the optimal position and orientation, the synthesized signals $\mathbf{p}(t)$ are approximately delta functions with an identical delay. Thus $\Psi_{\mathbf{p}}(\tau)$ is a delta function with ITD=0 (μ s). In this way, the directional dependence in $\mathbf{a}(t)$ can be excluded from the analysis of the interaural cross-correlation functions. As the head is displaced away from the optimal position and orientation, the synthesized signals $\mathbf{p}(t)$ are no longer delta functions. Thus $\Psi_{\mathbf{p}}(\tau)$ is also no longer a delta function. A degraded $\Psi_{\mathbf{p}}(\tau)$ indirectly suggests the degradation of the ITD cue of the synthesised HRIRs for all directions. A shift of the peak in $\Psi_{\mathbf{p}}(\tau)$ suggests a shift in the ITD of the synthesised HRIRs and multiple peaks in $\Psi_{\mathbf{p}}(\tau)$ may cause ambiguity or result in the wrong perception among multiple directions of sound.

Figure 4 shows the degradation of $\Psi_{\mathbf{p}}(\tau)$ (the interaural cross-correlation functions for the synthesised simultaneous unit impulses) with lateral displacement over the range of ± 200 mm. The maximum value of $\Psi_{\mathbf{p}}(\tau)$ '1' at 0 lag can be observed at 0 mm displacement (the optimal position) for both transducer arrangements. When the listener's head is displaced laterally, an ITD shift for the 60° transducer arrangement increases significantly as displacement increases, which is at the rate of approximately 2.7 μ s/mm. For example, 25 mm displacement results in about 65 μ s ITD shift which corresponds to about an 8° shift in azimuth direction. The threshold for the ITD discrimination is considered to be approximately 10 μ s (Ref. 28) and corresponds to about 4 mm displacement with the 60° arrangement. On the other hand, the rate of shift is much less for the 10° transducer arrangement (0.2 μ s/mm) and so 50 mm displacement would be just enough to produce the threshold value for the ITD

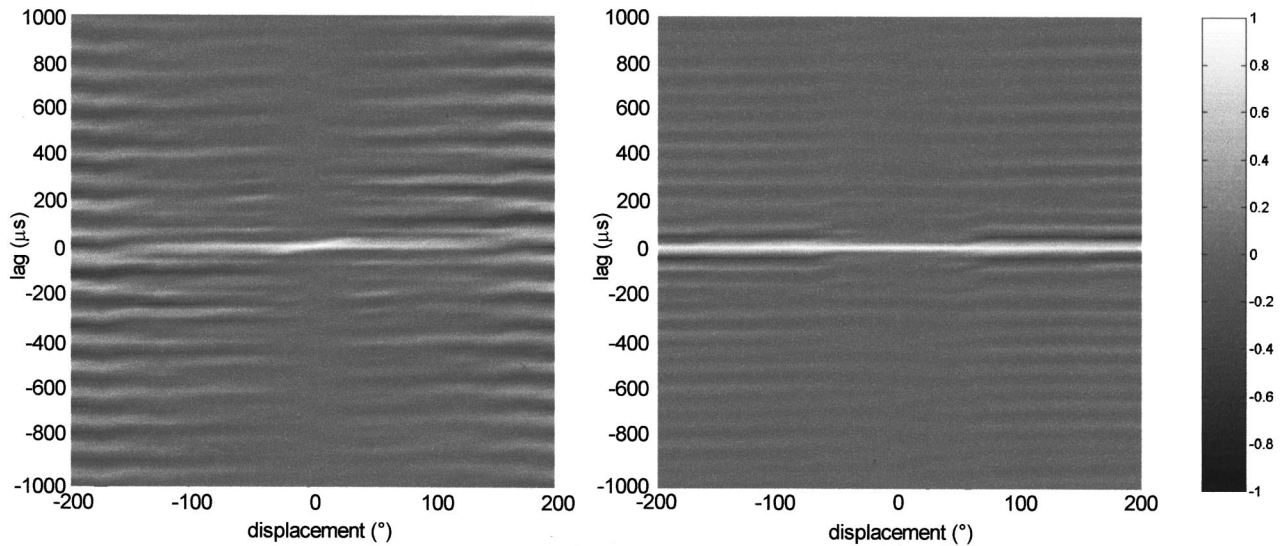


FIG. 5. The effect of roll displacement on the interaural cross-correlation functions for the synthesis of simultaneous unit impulses. Left panel: 60° transducer span. Right panel: 10° transducer span.

discrimination. When the listener's head is rolled, the ITD shift is again greater for the 60° arrangement though the difference between the two arrangements is much smaller (about 1.2 $\mu\text{s}/^\circ$ and 0.4 $\mu\text{s}/^\circ$) than the lateral displacement (Fig. 5). Yaw displacement showed the same ITD shift (about 8 $\mu\text{s}/^\circ$) which corresponds exactly to the yaw displacement angle for both of the two transducer arrangements (Fig. 6). However, better preservation (smaller amplitude of additional maxima) of the interaural cross correlation function can be observed for the 10° arrangement. Fore-and-aft, vertical and pitch displacement shows no shift of the original peak for both transducer arrangements, as expected from the symmetry, but slightly better preservation of the interaural cross correlation function can be observed for the 10° arrangement.¹⁸ The results for the six types of displacement are summarized in Table II.

Comparisons can be made between the six types of dis-

placement by normalizing the results by the amount of displacement of the ears produced by each of the six types of head displacement. The synthesized ITD cue is the most sensitive to yaw displacement followed by lateral and roll displacements. It is very robust to fore-and-aft, pitch, and vertical displacement. However, the difference in the robustness of the ITD cue between two different transducer arrangements is most significant for lateral displacement followed by roll displacements. There are no obvious differences other than additional maxima between two transducer arrangements for the other four displacements (yaw, fore-and-aft, vertical, pitch).

2. Accuracy of synthesis (temporal)

By analogy with $\Psi_a(\tau)$, the interaural cross-correlation functions of synthesised HRIRs, $\Psi_q(\tau)$, is expressed as follows in terms of the elements of $\mathbf{q}(t)$:

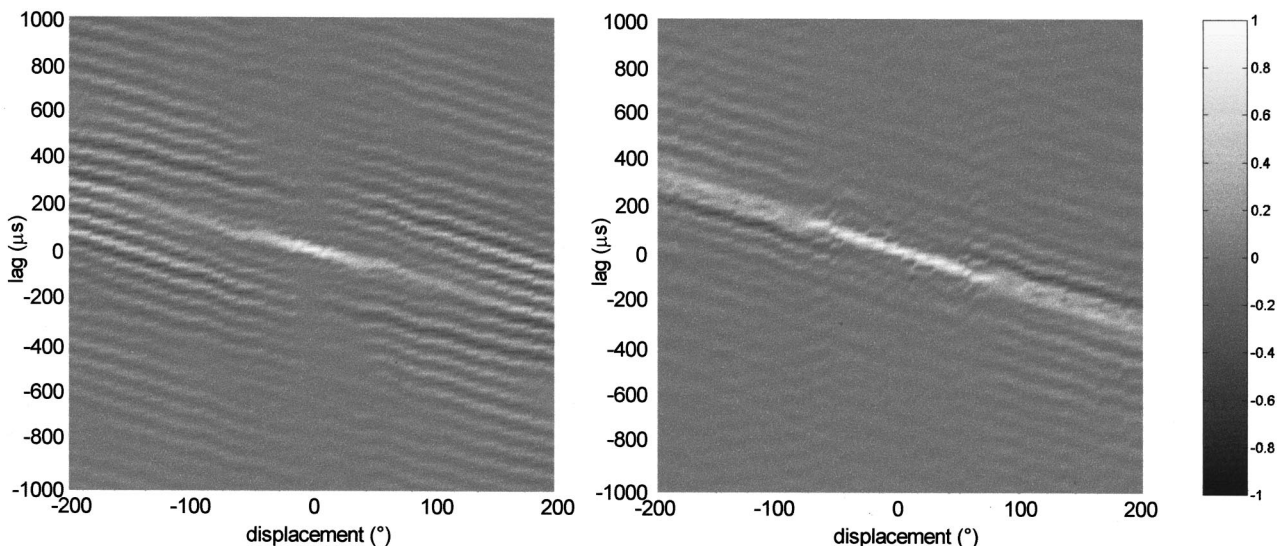


FIG. 6. The effect of yaw displacement on the interaural cross-correlation functions for the synthesis of simultaneous unit impulses. Left panel: 60° transducer span. Right panel: 10° transducer span.

TABLE II. Estimated rate of ITD shift and displacement which gives the threshold value of ITD discrimination ($10 \mu\text{s}$) for six types of displacement and two different transducer arrangements.

Type of displacement	Rate of ITD shift		Displacement at $10 \mu\text{s}$ ITD shift	
	60° span	10° span	60° span	10° span
lateral	$2.7 \mu\text{s}/\text{mm}$	$0.2 \mu\text{s}/\text{mm}$	4 mm	50 mm
fore-and-aft	$0 \mu\text{s}/\text{mm}$	$0 \mu\text{s}/\text{mm}$
vertical	$0 \mu\text{s}/\text{mm}$	$0 \mu\text{s}/\text{mm}$
pitch	$0 \mu\text{s}/^\circ$	$0 \mu\text{s}/^\circ$
roll	$1.2 \mu\text{s}/^\circ$	$0.4 \mu\text{s}/^\circ$	8°	24°
yaw	$-8 \mu\text{s}/^\circ$	$-8 \mu\text{s}/^\circ$	1.3°	1.3°

$$\Psi_q(\tau) = \lim_{T \rightarrow \infty} \frac{1}{2T} \int_{-T}^T q_1(t)q_2(t+\tau)dt. \quad (10)$$

As the ITD cue is regarded as the most salient cue that is used to determine the azimuth direction,²⁹ directions on the horizontal plane which contain two sets of all the azimuth directions are taken as examples to show the interaural cross-correlation functions of HRIRs (Fig. 7). That of the original HRIRs, $\Psi_a(\tau)$, is shown in Fig. 7(a) and that of synthesized HRIRs, $\Psi_q(\tau)$, when the listener's head is displaced 25 mm laterally are shown in Figs. 7(b) and (c). In Fig. 7(a), it can be observed that the ITD is increasing almost linearly with respect to azimuth angle over most of the range. (Note that the variation is not sinusoidal which would be the case if there were no head in the sound field.) $\Psi_q(\tau)$ is severely degraded with the 60° transducer arrangement [Fig. 7(b)]; a few large additional local maxima (especially around $\pm 250 \mu\text{s}$, corresponding to $\pm 30^\circ$ azimuth which are the control transducer directions) can be observed over wide range of virtual source directions as well as a shift (about $65 \mu\text{s}$, 8° azimuth) of the original peak. However, $\Psi_q(\tau)$ is better preserved with the 10° arrangement [Fig. 7(c)] except for very minor local maxima at virtual source directions around -90° azimuth, $0 \mu\text{s}$ lag (the largest around $-60 \mu\text{s}$ which again corresponds to the control transducer directions).

ITD estimated from the synthesized HRIRs without dis-

placement for both transducer arrangements are identical to the estimate from the original HRIRs for all the directions around the head. The estimated ITD from the synthesized HRIRs when the listener's head is displaced 25 mm laterally for most of the directions around the head is plotted in Fig. 8. There are no data points on the bottom part of the spherical plot. In general, it is observed that cones of constant ITD are shifted from the original value [Fig. 8(a)] for the 60° arrangement [Fig. 8(b)] but little shift is observed for the 10° arrangement [Fig. 8(c)], as observed in Fig. 4. The system with the 10° transducer arrangement preserved the synthesized ITD value for larger azimuth directions better than that of the 60° arrangement. A slightly worse performance is expected on the left-hand side of the head than the other side (right) for the 10° arrangement. Whereas the right-hand side shows worse performance than the left-hand side for the 60° arrangement. The loss of a large ITD value around large azimuth directions [e.g., $|\text{azimuth}| > \pm 30^\circ$ in Fig. 8(b), around -90° azimuth in Fig. 8(c)] is primarily because the additional peaks in the interaural cross-correlation function became larger than the original peak. When the head is displaced, large additional peaks which give ITD values corresponding to the direction of the control transducers appear. In cases when these additional peaks are larger than the original peaks, if the largest peak is taken to estimate ITD, the virtual sound source would vanish and the listener would localize the sound source in the direction of the control transducers. However, with existence of the other types of cue such as monaural spectral shape cues, the smaller magnitude of the original peak could be more plausible in estimating the ITD. If it is taken to estimate the ITD, it would result in a much better preserved ITD value and thus better preserve the direction of the virtual sound. This is down to the psychological function at higher levels of the nervous system. It is likely, inferring from the results from subjective experiment presented in a later section, that a smaller but more plausible original peak would result in the estimated ITD for head displacements below a certain value.

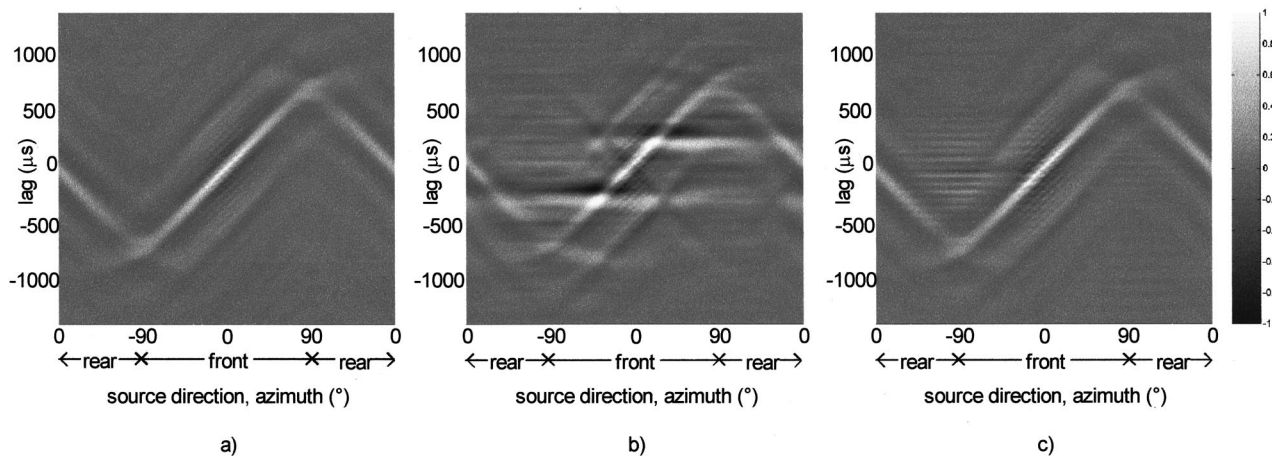


FIG. 7. Interaural cross-correlation functions of the original and synthesized HRIRs corresponding to source directions on the horizontal plane. (a) Calculated from the original HRIRs. (b) Calculated from the synthesized HRIRs with 60° transducer span when the listener's head is displaced 25 mm laterally. (c) Calculated from the synthesized HRIRs with 10° transducer span when the listener's head is displaced 25 mm laterally.

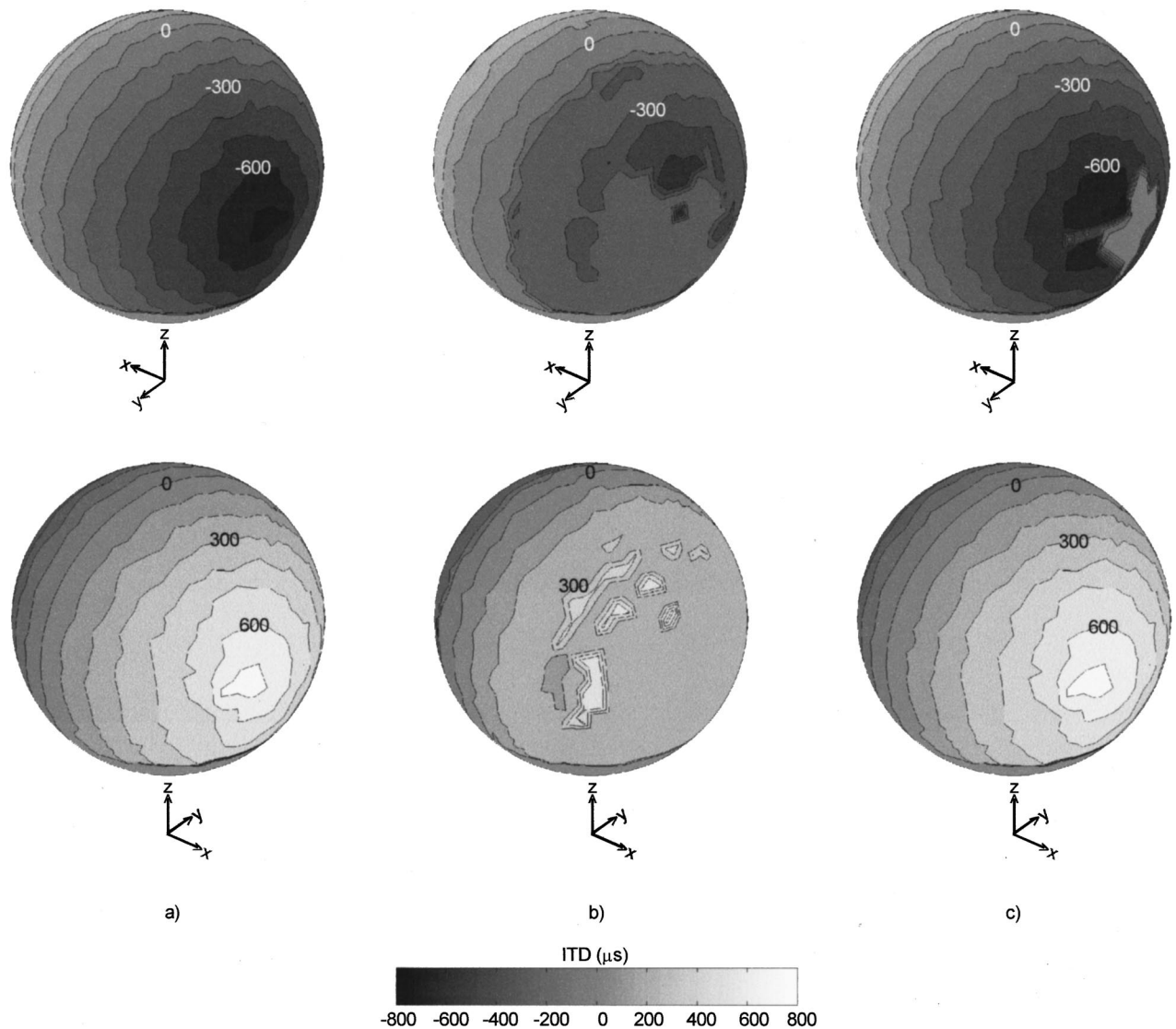


FIG. 8. Estimated ITD, plotted as a function of the intended direction of the virtual sound source. (a) Left column: estimated from the original HRIRs. (b) Middle column: estimated from synthesized HRIRs with 25 mm lateral displacement for the 60° transducer span. (c) Right column: estimated from synthesized HRIRs with 25 mm lateral displacement for the 10° transducer span. Upper row: view from the upper-front-left (azimuth = -45°, elevation = 30°). Lower row: view from the upper-rear-right (azimuth = 45°, elevation = 150°).

D. Robustness of spectral cues

As in the analysis of temporal cues, the effectiveness of control as a function of head displacement is evaluated first by analyzing the matrix of transfer functions $\mathbf{R}(z)$ which is independent of the virtual source direction. Then, synthesized HRTFs $\mathbf{q}(z)$ are analyzed in order to demonstrate what happens to spectral cues depending on the direction of the virtual sound source.

1. Control performance (spectral)

When the control system is required to synthesize particular spectra at two ears, head displacement results in leakage of some of the signal intended for one of the ears to the other ear. This is the so called “cross-talk” component of the signals, i.e., the component of the signal for right ear fed to the left ear and vice versa. This can be regarded as noise component in the intended signal. The components of the synthesised HRTFs $\mathbf{q}(z)$ are given by

$$\mathbf{q}(z) = \begin{bmatrix} Q_1(z) \\ Q_2(z) \end{bmatrix} = \begin{bmatrix} R_{11}(z)A_1(z) + R_{12}(z)A_2(z) \\ R_{21}(z)A_1(z) + R_{22}(z)A_2(z) \end{bmatrix}, \quad (11)$$

where $R_{11}(z)$ and $R_{22}(z)$ are the elements which contribute towards the correct synthesis of the HRTFs but $R_{12}(z)$ and $R_{21}(z)$ are noise elements which smear the synthesis. For the left ear, the signal (signal intended for the left ear) to noise (signal intended for the right ear) ratio of the control system is estimated from $|R_{11}(z)|/|R_{12}(z)|$. This is the case when the time histories of the inputs to $\mathbf{R}(z)$ are a pair of identical delta functions. This again excludes the effect of $\mathbf{a}(z)$, i.e., the direction dependence. Figure 9 shows the degradation of the signal to noise ratio (S/N) for the HRTF synthesis at the left ear with lateral displacement over the range of ± 250 mm. The S/N at the right ear, $|R_{22}(z)|/|R_{21}(z)|$, can be obtained by flipping over the left and right of the figure. Much larger displacements which maintain good S/N over wide frequency range (>500 Hz) are allowed for the 10° trans-

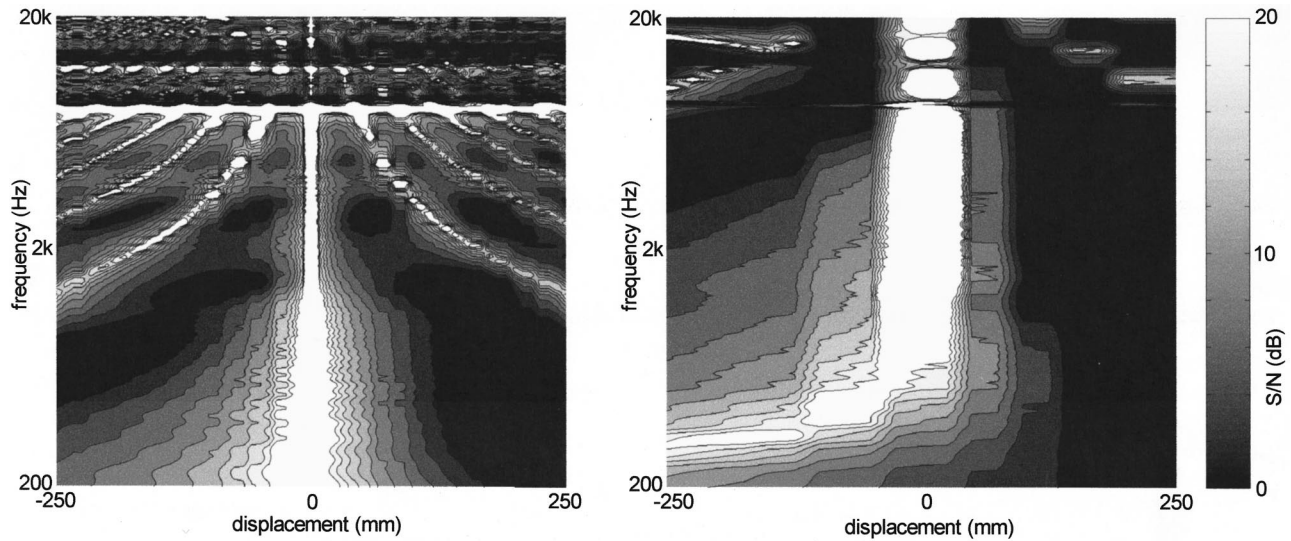


FIG. 9. Signal to noise ratio for the HRTF synthesis at the left ear as a function of lateral displacement. Left panel: 60° transducer span. Right panel: 10° transducer span.

ducer arrangement (roughly ± 40 mm for 20 dB S/N) compared to the 60° transducer arrangement (roughly ± 8 mm for 20 dB S/N). The dip in S/N around 9 kHz and 13 kHz even when the head is at the optimal position is due to low S/N of the measurement of the HRTFs. Good S/N with larger displacement for the 10° arrangement can also be observed for the fore-and-aft (roughly ± 410 mm compared to ± 120 mm for 20 dB S/N) and yaw (roughly $\pm 12^\circ$ compared to $\pm 6^\circ$ for 20 dB S/N) displacement as shown in Figs. 10 and 11. The 60° transducer arrangement has the advantage at frequencies below 500 Hz, however. This is where the ILD cues are less potent than the ITD cues. There are not large differences between the two arrangements for the other three displacements (roll, vertical, pitch).¹⁸ However, a slightly better S/N is preserved with the 60° arrangement for pitch and vertical displacement. With rotation about the interaural axis, transducers being at a large azimuth angle means less change of transducer direction than transducers being around

the median plane. The results for six types of displacements are summarized in Table III.

When compared in the same way as used in the temporal cue analysis, synthesized spectral cues are most sensitive to lateral and roll displacement followed by yaw, pitch, vertical, and fore-and-aft displacements. However, the difference in robustness of spectral cues between two different transducer arrangements is most significant for lateral displacement followed by fore-and-aft and yaw displacements. Note that the 20 dB S/N is roughly sufficient to synthesize the monaural spectra for the ipsi-lateral ear but much better S/N is required for the contra-lateral ear. This is because, if the level of two desired ear signals $\mathbf{d}(z)$ is compared, the level of the signal for the ipsi-lateral ear is smaller than that for the other ear over most of the frequency range and for most directions. As a result, at the contra-lateral ear, binaural synthesis is affected by a smaller input with a much larger noise input in

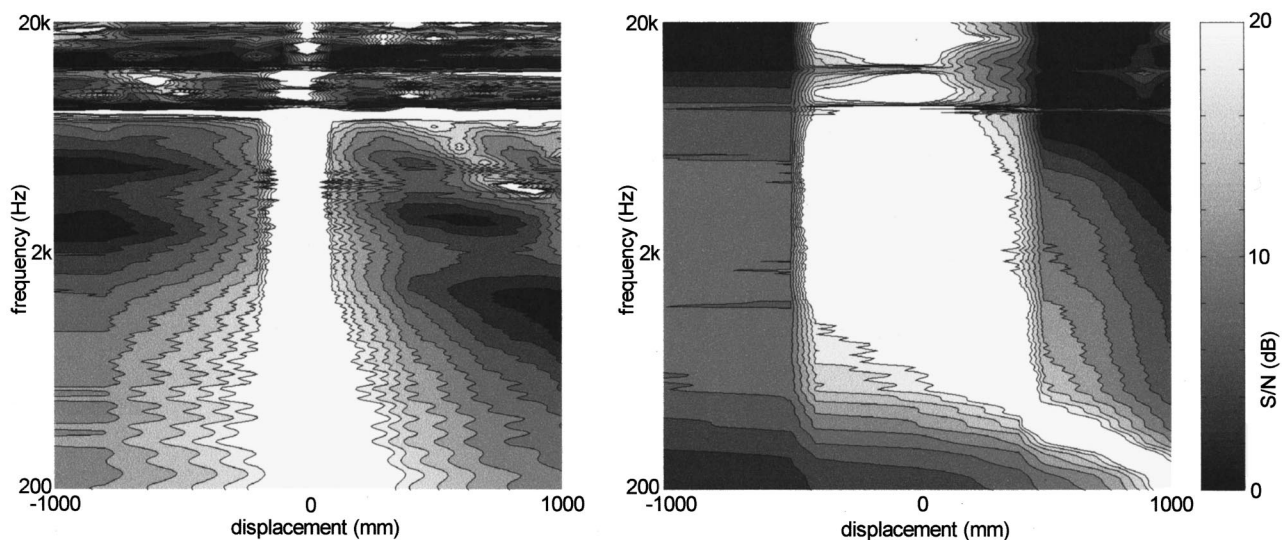


FIG. 10. Signal to noise ratio for the HRTF synthesis at the left ear as a function of fore-and-aft displacement. Left panel: 60° transducer span. Right panel: 10° transducer span.

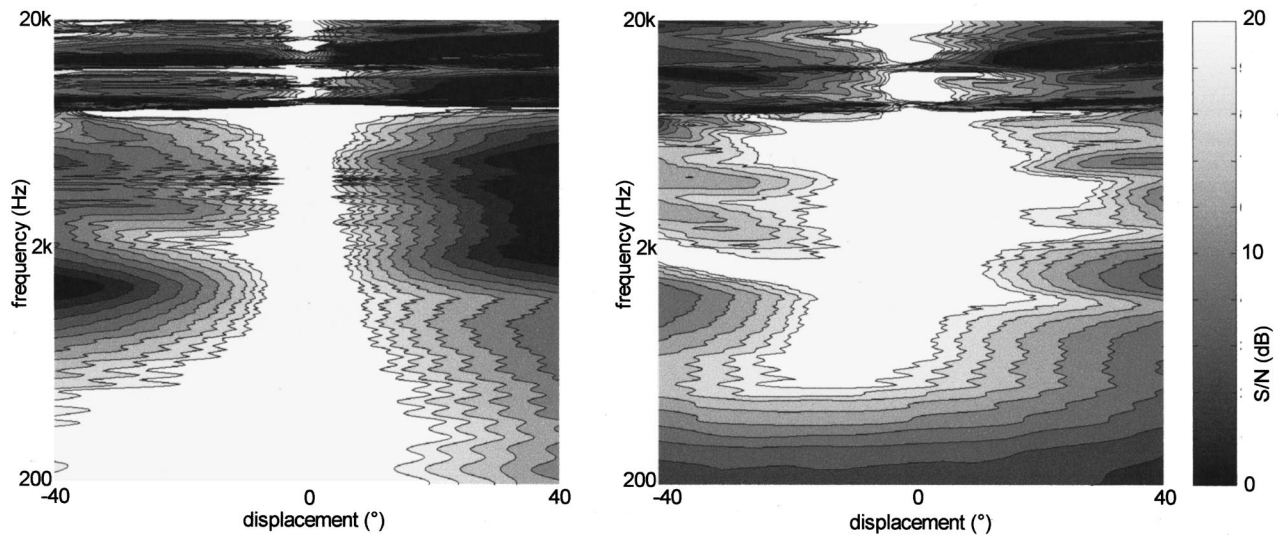


FIG. 11. Signal to noise ratio for the HRTF synthesis at the left ear as a function of yaw displacement. Left panel: 60° transducer span. Right panel: 10° transducer span.

addition to the response of the control performance of the system.

2. Accuracy of synthesis (spectral)

As the role of the monaural spectral shape cue is primarily to determine the elevation direction of sources located on the cone of confusion, directions along the cone of 50° azimuth are taken as examples to illustrate the monaural spectral shape cue in the HRTFs. Figure 12 shows examples of monaural spectral shape in HRTFs for the ipsi-lateral (right) ear at directions along the cone of constant azimuth (50°). Significant differences in spectrum pattern between the sources below (at negative elevation) and above (positive elevation) the horizontal plane can be observed easily in Fig. 12(a) for real sound sources (estimated from $|A_2(z)|$). There are less significant differences between sources in front (0 to $\pm 90^\circ$) and in the rear ($\pm 90^\circ$ to $\pm 180^\circ$) except on the horizontal plane where a significant dip in spectra around $\pm 180^\circ$ compared to those around $\pm 0^\circ$ can be seen in the mid-frequency range. The synthesized monaural spectral shape (estimated from $|Q_2(z)|$) when the listener's head is displaced 40 mm laterally are shown in Figs. 12(b) and (c). The elevation dependency is less clear for that of the 60° arrangement [Fig. 12(b)]. However, the synthesized monaural spectral shape for the 10° transducer arrangement [Fig. 12(c)] shows similar elevation dependent monaural spectra

TABLE III. Estimated displacement which gives 20 dB signal to noise ratio of the control system for six types of displacement and two different transducer arrangements.

Type of displacement	Displacement at 20 dB S/N	
	60° span	10° span
lateral	± 8 mm	± 40 mm
fore-and-aft	± 120 mm	± 410 mm
vertical	± 220 mm	± 190 mm
pitch	$\pm 18^\circ$	$\pm 14^\circ$
roll	$\pm 9^\circ$	$\pm 9^\circ$
yaw	$\pm 6^\circ$	$\pm 12^\circ$

to the original spectra [Fig. 12(a)]. The consequence of degraded monaural spectral shape would be an increased number of confusions among the directions on the constant azimuth cone. The degradation of this cue may also affect the azimuth localization since the monaural spectral cue has a supplemental role for azimuth discrimination, especially when the interaural cross-correlation function $\Psi_q(\tau)$ is degraded to present ambiguity in estimating the ITD due to a multiple choice of peaks.

When the listener's head is displaced 40 mm laterally, the monaural spectral shape cue for the synthesized contra-lateral (left ear) HRTF (estimated from $|Q_1(z)|$) is dominated by the noise, i.e., the cross-talk component, even for the 10° transducer arrangement due to the low S/N.¹⁸ The requirement for the preservation of monaural spectra for the contra-lateral ear is much more severe than that of the ipsi-lateral ear as pointed out in the previous section. For example, a lateral displacement of not more than 25 mm even for the 10° transducer arrangement and less than 5 mm for the 60° arrangement is required for the 50° azimuth directions. Obviously, the requirement varies as the direction of the virtual sound source varies. The variation of the azimuth direction (along the interaural axis) has more influence on it than the variation of the elevation direction (around the interaural axis).

Naturally, the same requirement as the contra-lateral monaural spectral shape cue, which is more severe than the ipsi-lateral ear, applies for both of the binaural spectral cues. In terms of analysis, these binaural spectral cues are essentially identical to the difference between the two monaural spectral shapes and estimated from $|Q_2(z)|/|Q_1(z)|$. Hence the interaural spectral shape difference is not shown here.¹⁸ Above all, these monaural and binaural spectral shape cues are well preserved by the 10° transducer arrangement, so less confusion along the cone of confusion is expected with this arrangement.

Examples of another type of binaural spectral cue, the interaural level difference (ILD), are shown in Fig. 13 for

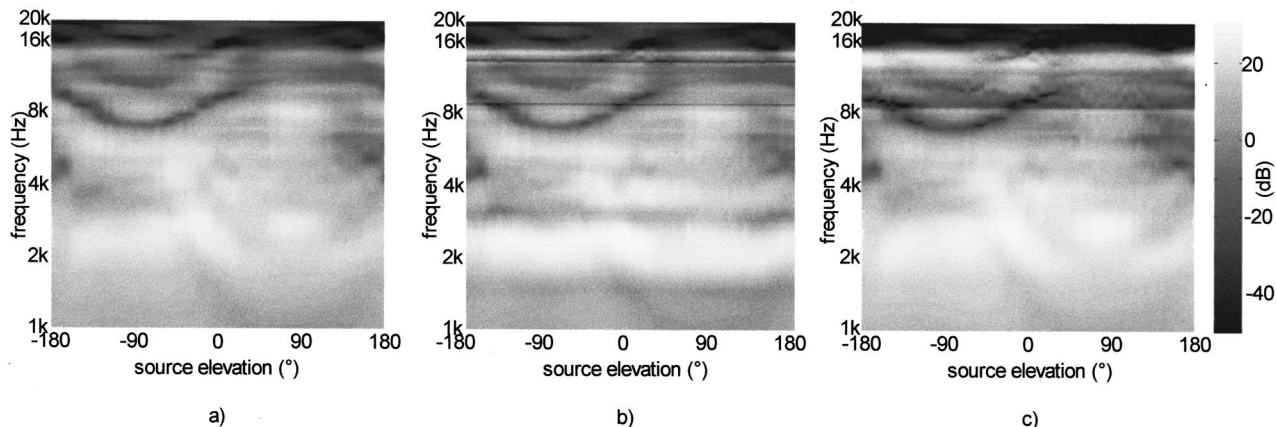


FIG. 12. Monaural spectral shape in HRTFs for the ipsi-lateral (right) ear. Sound source directions are along the cone of constant azimuth (50°). (a) Left panel: monaural spectral shape by real sound sources. (b) Middle panel: monaural spectral shape synthesized by the 60° transducer arrangement. The listener's head is displaced 40 mm laterally. (c) Right panel: monaural spectral shape synthesized by the 10° transducer arrangement. The listener's head is displaced 40 mm laterally.

sound source directions on the horizontal plane. As can be seen in Fig. 13(a), which shows the ILD with real sound sources, it is not a simple task to allocate one ILD value to a particular azimuth angle. Since complex interference at higher frequencies yields multiple (often more than 4) azimuth angles for one ILD value at each frequency. In addition, the ILD value for a particular azimuth direction varies depending on frequency. The ILD with synthesized HRTFs when the listener's head is displaced 25 mm laterally are shown in Figs. 13(b) and (c). The ILD with the 60° transducer arrangement is degraded severely but those with the 10° span preserved well. Generally speaking, the ILD value for larger azimuth angles cannot be achieved without a very good preservation of monaural spectra for the contra-lateral ear. For example, with the 60° transducer arrangement with 50 mm lateral head displacement, the ILD value (averaged over the mid-frequency range) for azimuth directions larger than $\pm 30^\circ$ cannot be achieved.¹⁴

IV. SUBJECTIVE EXPERIMENT

The virtual directional information synthesized with two different arrangements of monopole transducers were inves-

tigated by using subjective localization experiments. Experiments with real sound sources were also performed to establish the accuracy of the experimental procedure itself. Source directions on the horizontal plane were chosen to be examined since this covers the whole range of azimuth directions and two alternative elevation directions, i.e., 0° (front) and 180° (rear), in each cone of constant azimuth.

A. Procedure

A weighted noise signal (EAIJ RC-7603) was used as the source signal to minimize the consequence of the large high frequency discrepancy between the HRTFs of the subjects and the KEMAR HRTFs used in the filter design procedure. The signal has a flat spectrum between 200 Hz and 2 kHz and gradually rolls off towards lower and higher frequencies. The relative level is about -2 dB at 5 kHz, -5 dB at 10 kHz, -13 dB at 20 Hz and 20 kHz with respect to the level between 200 Hz and 2 kHz. Each stimulus consisted of a reference signal and a test signal. A reference signal was presented at 0° azimuth and 0° elevation, i.e., directly in front of the listener before each test signal. Both signals had the same sound source signal with a duration of 3 s for the

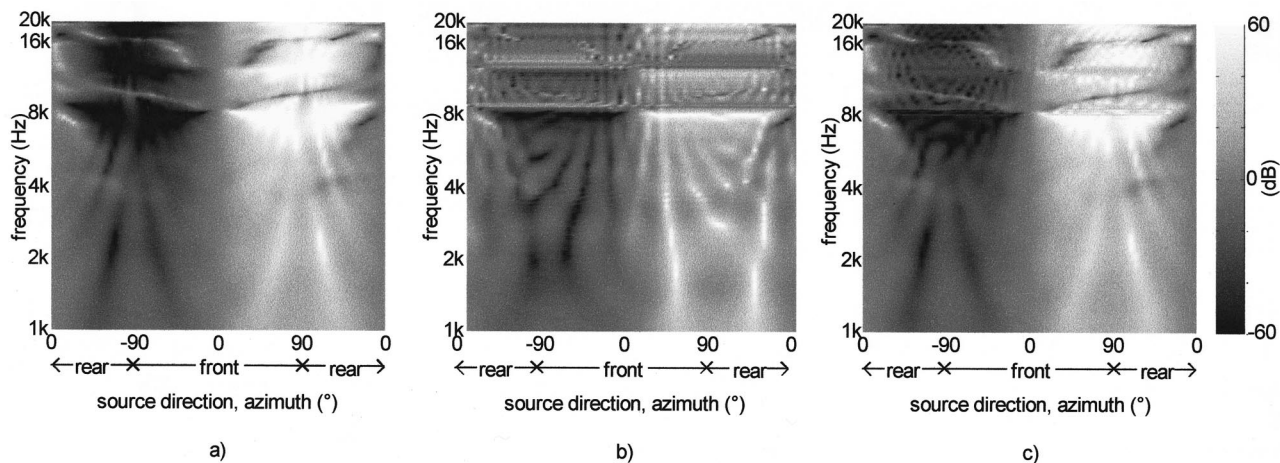


FIG. 13. Interaural level difference (ILD) for sound source directions on the horizontal plane. (a) Left panel: ILD produced by real sound sources. (b) Middle panel: ILD synthesized by the 60° transducer arrangement. The listener's head is displaced 25 mm laterally. (c) Right panel: ILD synthesized by the 10° transducer arrangement. The listener's head is displaced 25 mm laterally.

reference signal and 5 s for the test signal with a gap of 3 s in between. In order to avoid the effect of presentation order, the order of presentation from different directions was randomized. The reference stimulus not only cancelled the order effect, but also gave subjects prior knowledge of the sound source signal spectrum which is important for the monaural spectral cue. Stimuli, a set of reference and test signals, were repeated when subjects had difficulty in making a judgement.

Subjects were required to choose the closest marker to the perceived direction of sound. The markers were placed all around the head in the horizontal plane 1 m from the origin of the coordinate with 10° intervals. The subjects were allowed to choose more than one marker when they perceived two or more separate directions of sound. In order to avoid introducing dynamic cues which relate to head movement, the subject was instructed not to move the head or body while the stimuli were presented. However, the subject was allowed to turn his head to see markers after each test stimulus had stopped. The subject's head was not physically fixed but supported by a small head rest. The subject was surrounded by a thin black curtain placed between markers and loudspeakers in order to minimize the effect of visual information. Subjects were all European males with normal hearing.

The loudspeakers used had a fairly flat response between about 250 Hz and 5 kHz which gradually rolls off towards lower and higher frequencies. The relative level at 20 kHz is about 10 dB smaller with respect to the frequency which gives maximum response. The characteristics of the loudspeakers were well-matched (0.5 dB difference in amplitude and a few degrees difference in phase response). Difference in responses between two loudspeakers degrades the HRTF synthesis. When their responses are identical, their effects become independent of virtual source directions and can be regarded as degrading the sound source signal rather than synthesized HRTFs. The responses of the loudspeakers of course affect monaural cues and they also affect those associated with the real sound sources, but they do not affect the binaural cues. Therefore, for binaural synthesis, it is important to use a well-matched pair of loudspeakers. The loudspeaker pairs for different transducer arrangements were swapped for half of the subjects with the aim of minimizing bias errors which are induced by different responses between the loudspeakers.

In order to minimize other factors than head misalignment which affect synthesis, the experiments were carried out in an anechoic chamber. The same data for the acoustic paths \mathbf{a} and the control filter matrix \mathbf{X} as those used in the analysis were implemented by digital filters using a MTT Lory Accel digital signal processing system. The output of the digital filters were fed via an amplifier to two pairs of loudspeakers with the same geometrical arrangements as used in the analysis. The loudspeakers as control transducers and as real sound sources were placed 1.4 m from the origin of the spherical coordinate system. It is very important to bear in mind that there is a considerable amount of variability of the HRTFs among individuals. Inevitably, the matrix \mathbf{C} containing each subject's HRTFs in this experiment is different from that assumed when the matrix \mathbf{X} is designed.

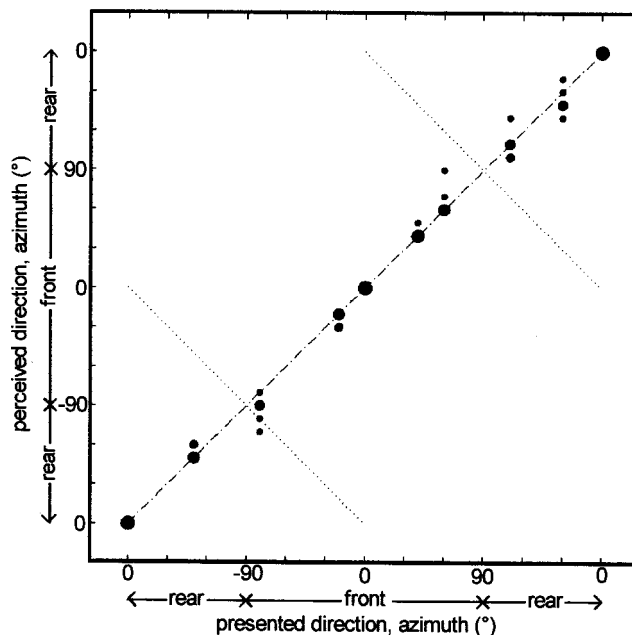


FIG. 14. Results of the subjective experiment for localizing real sound sources. Six subjects were tested.

This is the largest source of error when comparing the results with the analysis. The loudspeakers, rather than the listener's head, were displaced in both the lateral direction and in the fore-and-aft direction in order to achieve the displacement of the listener's head from the optimal position. The precision of the arrangement of the loudspeakers and listener's head was of the order of ± 10 mm.

The results from the subjective experiments are presented in the following format. The area of each circle in the figures is proportional to the number of subjects who perceived the source to be in the given direction. In cases where the subjects perceived sound sources in more than two directions, the area of the circle is distributed into those positions in accordance with the number of directions. The dashed-dotted line shows the position of the circles when the perceived direction is the same as the presented direction. The dotted line is in a symmetric position to the dashed-dotted line with respect to the interaural axis. Therefore, the subjective responses due to front-back confusion fall around these lines.

B. Real sound sources

Nine real sound sources were placed at 10° increments at different azimuthal angles except $\pm 20^\circ$ and $\pm 90^\circ$, and two sources were placed at azimuth 0° with different elevations of 0° and 180° (front and rear). Five of them were positioned in front (elevation 0°) and four of them were positioned in the rear (elevation 180°). Four of them were positioned to the left (negative azimuth) and five of them were positioned to the right (positive azimuth). The performance with real sound sources (Fig. 14) shows the localization performance of the subjects and the accuracy of the experimental procedure itself. This therefore implies the maximum precision achievable with the following experiments with synthesized virtual sound sources. More than 60% of the

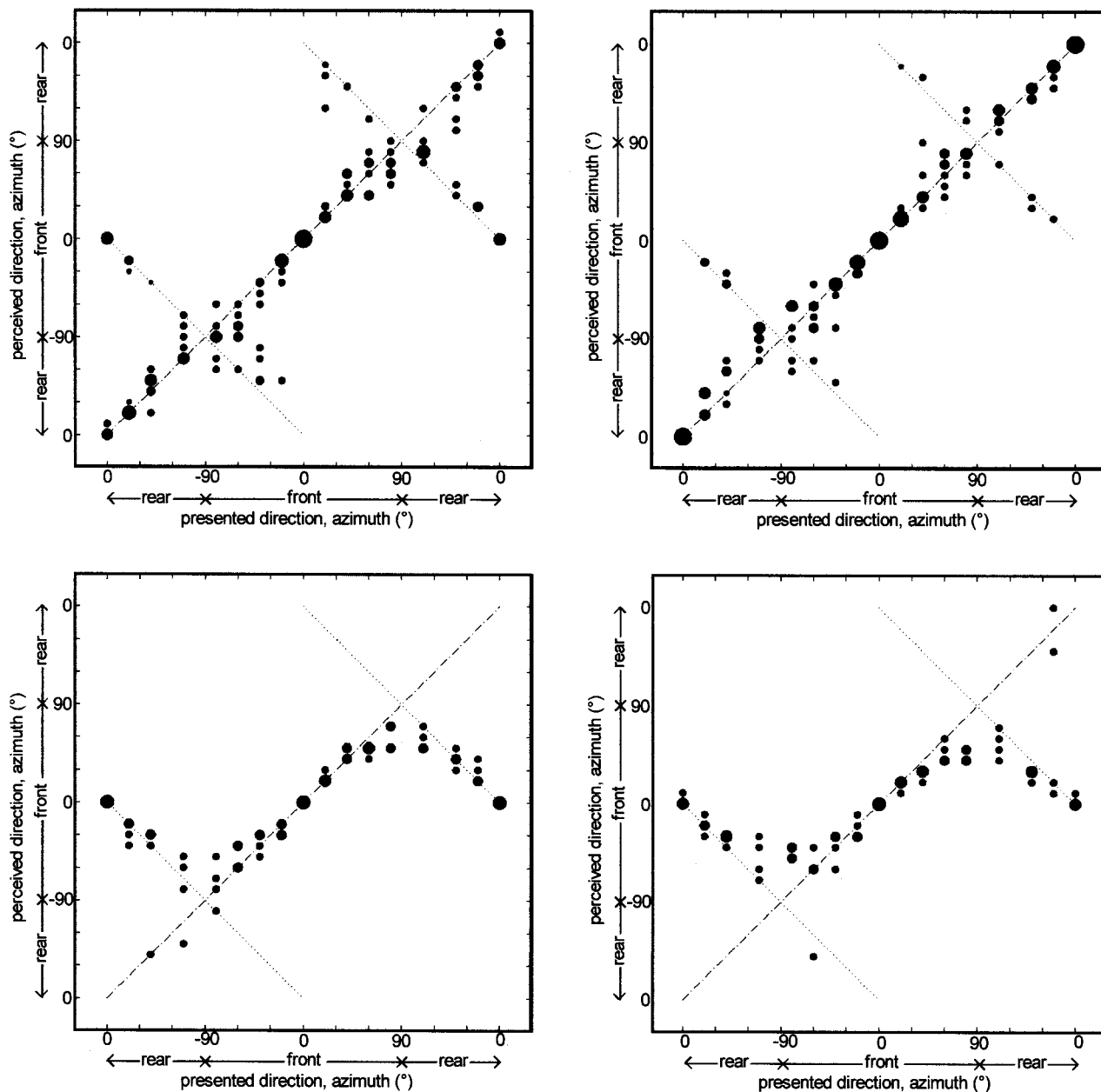


FIG. 15. Results of the localization experiment with binaural synthesis over loudspeakers. The listener's head is at the optimal position and orientation. 11 subjects were tested. Upper row: Responses by the subjects for whom the systems work well. Lower row: Responses by the subjects for whom the systems do not work well. Left column: 60° transducer span. Right column: 10° transducer span.

responses resulted in the correct marker and more than 90% of the responses resulted within the smallest ($\pm 10^\circ$) measurable error with the method. The judgements are more nearly accurate for smaller azimuth directions than for larger azimuth directions. The repeatability of the response is exceptionally good in that the responses associated with a particular direction for a particular subject almost always (more than 95%) resulted at the same marker (even for the wrong marker). The accuracy can be observed best at small azimuth directions (closer to the median plane) and deteriorates towards large azimuth directions (the side of the listener). There are no obvious signs of confusion along the cone of constant azimuth, i.e., front-and-back confusion. The subjects reported after the experiments that the task was very easy and did not have any ambiguity in deciding which marker to choose.

C. Virtual sound sources

Localization experiments with binaural synthesis over loudspeakers were first carried out with the listener's head at the optimal position. Sixteen virtual sound sources were placed at 0° , $\pm 20^\circ$, $\pm 40^\circ$, $\pm 60^\circ$, and $\pm 80^\circ$ azimuth with 0° elevation (front) and 0° , $\pm 20^\circ$, $\pm 40^\circ$, and $\pm 70^\circ$ azimuth with 180° elevation (rear). It was revealed that there was a population of subjects for whom the synthesis of virtual sound sources works reasonably well ("good" subjects) whereas it does not work so effectively for the rest of the subjects ("poor" subjects). Figure 15 shows the localization performance for 11 subjects when the head is at the optimal position. The localization in azimuth is again more accurate for smaller azimuth than larger azimuth. However, azimuth localization error in general is much larger than the localiza-

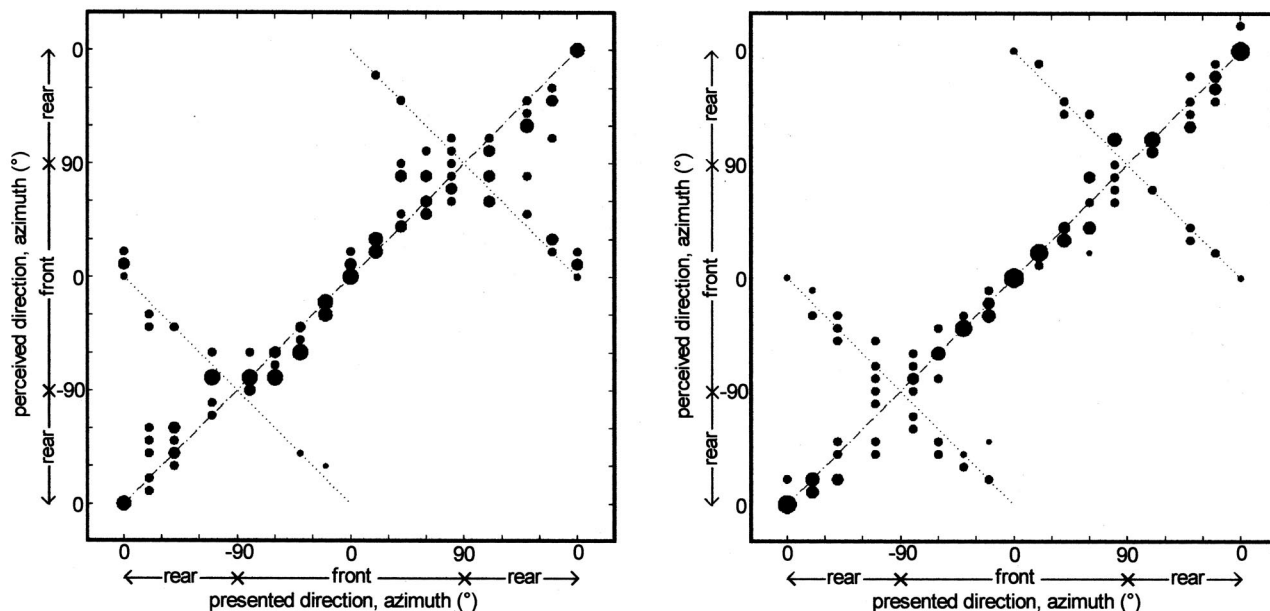


FIG. 16. Results of the localization experiment with binaural synthesis over loudspeakers when the listener's head is displaced 50 mm laterally (to the right). Seven subjects were tested. Left panel: 60° transducer span. Right panel: 10° transducer span.

tion of real sound sources. Only a few front–back confusions can be observed with the 7 “good” subjects. The 4 “poor” subjects did not localize the virtual sound sources in the rear half of the horizontal plane correctly, and instead, localized them around symmetric positions in the front half-plane. Moreover, virtual sound sources at large azimuth directions (around $\pm 90^\circ$ azimuth) were perceived at the offset position systematically towards the center (smaller azimuth angle). Clearly, the grouping of subjects has no relation to the different transducer span. It also has no relation to the ability of the subjects to localize real sound sources. Further investigation confirmed that a large disparity between each individual and KEMAR HRTFs resulted in inaccurate synthesis of binaural signals and resulted in systematic bias error for the “poor” subjects.³⁰

In principle, different transducer arrangements should not produce much difference in performance when the listener's head is at the optimal position and orientation. Nevertheless, the 10° transducer span showed slightly better performance, especially for “good” subjects around 0° azimuth where it showed no front–back confusion, contrary to the considerable amount of confusions with the 60° span. Although the listener's head was supposed to be at the optimal position and orientation in this experiment, some misalignment of the head is inevitable in practice. This may have caused the increase in front–back confusion with the 60° transducer span. The slight unintended displacement of the head would have probably exceeded the severe limit for the good synthesis of spectral cues for the 60° transducer arrangement (see Table III, Fig. 9), even though the same displacement may have been within the required limit for the 10° transducer arrangement. The 60° span transducer arrangement has a slight advantage in azimuth localization, which is in accord with the better control performance for the lower frequency region observed in Figs. 9–11.

D. Head displacement

Further experiments with head displacement were carried out only with the 7 “good” subjects. The results when the listener's head is displaced 50 mm to the right are shown in Fig. 16. The subjects reported after this experiment that the task was very difficult since sometimes they did not perceive a clear direction and sometimes they perceived the source to be at multiple directional locations. The multiple perception may be the consequence of multiple maxima in the interaural cross-correlation function. Discrepancy in different cues (e.g., ITD and ILD) could also be the cause. Virtual sound sources presented by the 60° transducer arrangement intended at 0° azimuth angle (both in front and rear) are often perceived at 10°–20° offset direction, whereas the virtual sources were mostly perceived in the intended direction by the 10° arrangement. These results agree with predicted direction by the ITD analysis where a 16° offset is expected from the 60° arrangement but a 0° offset is expected from the 10° arrangement. This systematic shift cannot be clearly seen at higher azimuth directions where the random localization error is much larger. Nevertheless considerable offset around $\pm 40^\circ$ to $\pm 60^\circ$ azimuth is also noticeable for the 60° arrangement. The azimuth localisation error is now more apparent with the 60° arrangement contrary to the previous case when the head is at the optimal position. More front–back confusions for the 60° arrangement than the 10° arrangement can still be observed. Degradation of spectral shape cues does not seem to affect the performance very much since little increase of front–back confusion can be observed, although some effect may have already been in the results at the optimal head position as discussed earlier. Another possibility is that the head displacement may not have degraded the spectral shape very much more than the disparity between each individual HRTFs and the KEMAR

HRTFs. A slightly better performance is observed on the side which the head is displaced to (right) for the 10° arrangement, whereas the other side (left) shows better performance for the 60° arrangement as predicted by ITD analysis. Contrary to the poor ILD values obtained, azimuth localization seems surprisingly accurate. Considering that the additional local maxima of the cross-correlation function start to become larger than the original maximum around 25 mm displacement for the 10° arrangement and much smaller displacement for the 60° arrangement, the performance of azimuth estimation is more likely to be determined by a more plausible local maximum than by the absolute maximum of the interaural cross-correlation function, as discussed in the analysis of temporal cues.

When the listener's head is displaced 200 mm and 400 mm to the rear, the 10° span transducer arrangement showed slightly better performance than the 60° arrangement for both azimuth localization and front-back discrimination. However, the difference in performance between the two transducer arrangements are much less significant compared to lateral displacement and has not been shown here.¹⁴

V. CONCLUSIONS

(1) In binaural synthesis over two loudspeakers, yaw, lateral, and roll displacement results in a shift of the ITD as well as the generation of additional local maxima in the interaural cross-correlation function. Fore-and-aft, vertical, and pitch displacement results only in the generation of additional local maxima. There is less degradation of temporal cues for lateral, roll, yaw, and fore-and-aft displacements when two loudspeakers are placed close together.

(2) Any displacement induces more "cross-talk" components in synthesized spectra. There is less degradation of the spectral cue for lateral, fore-and-aft, and yaw displacement when two loudspeakers are placed close together.

(3) The ITD cue is the most robust to head misalignment followed by the monaural spectral cue for the ipsi-lateral ear. The monaural spectral cue for the contra-lateral ear is the least robust together with binaural spectral cues (including ILD cues).

(4) Subjective experiments confirmed that two closely spaced loudspeakers have an advantage in performance with regard to the misalignment of the listener's head. The localization performance with subjective experiments were better than those predicted with any one individual localization cue. This suggests the importance of the combination of different localization cues.

ACKNOWLEDGMENTS

We would like to thank Dr. Ole Kirkeby for helpful discussions. This research was supported by Yamaha Corporation, Alpine Electronics, and Hitachi Ltd. T. Takeuchi is supported by Kajima Corporation.

¹J. Blauert, *Spatial Hearing: The Psychophysics of Human Sound Localization* (MIT Press, Cambridge, MA, 1997).

²H. Møller, "Fundamentals of binaural technology," *Appl. Acoust.* **36**, 171–218 (1992).

³D. R. Begault, *3D Sound for Virtual Reality and Multimedia* (AP Professional, Cambridge, MA, 1994).

⁴A. D. Blumlein, British Patent specification No. 394,324, 1958.

⁵M. A. Gerzon, "Ambisonics in multichannel broadcasting and video," *J. Audio Eng. Soc.* **33**, 859–871 (1985).

⁶A. J. Berkhout, D. de Vries, and P. Vogel, "Acoustic control by wave field synthesis," *J. Acoust. Soc. Am.* **93**, 2764–2778 (1993).

⁷M. R. Schroeder and B. S. Atal, "Computer simulation of sound transmission in rooms," *IEEE Intercon. Rec.* **7**, 150–155 (1963).

⁸P. Damaske, "Head-related two-channel stereophony with reproduction," *J. Acoust. Soc. Am.* **50**, 1109–1115 (1971).

⁹H. Hamada, N. Ikeshoji, Y. Ogura, and T. Miura, "Relation between physical characteristics of the orthostereophonic system and horizontal plane localization," *J. Acoust. Soc. Jpn. (E)* **6**, 143–154 (1985).

¹⁰J. L. Bauck and D. H. Cooper, "Generalized transaural stereo and applications," *J. Acoust. Soc. Am.* **44**, 683–705 (1996).

¹¹P. A. Nelson, O. Kirkeby, T. Takeuchi, and H. Hamada, "Sound fields for the production of virtual acoustic images," *J. Sound Vib.* **204**, 386–396 (1997).

¹²O. Kirkeby, P. A. Nelson, and H. Hamada, "Stereo dipole," U.K. Patent Application No. 9 603 236.2, 1996.

¹³O. Kirkeby, P. A. Nelson, and H. Hamada, "Local sound field reproduction using two closely spaced loudspeakers," *J. Acoust. Soc. Am.* **104**, 1973–1981 (1998).

¹⁴T. Takeuchi, P. A. Nelson, O. Kirkeby, and H. Hamada, "Robustness of the performance of the stereo dipole to misalignment of head position," 102nd AES Convention Preprint No. 4464(17), 1997.

¹⁵P. A. Nelson, F. Orduna-Bustamante, and H. Hamada, "Inverse filter design and equalization zones in multichannel sound reproduction," *IEEE Trans. Speech Audio Process.* **3**, 185–192 (1995).

¹⁶O. Kirkeby, P. A. Nelson, F. Orduna-Bustamante, and H. Hamada, "Local sound field reproduction using digital signal processing," *J. Acoust. Soc. Am.* **100**, 1584–1593 (1996).

¹⁷B. Gardner and K. Martin, "HRTF measurements of a KEMAR dummy-head microphone," MIT Media Lab Perceptual Computing-Technical Report No. 280, 1994.

¹⁸T. Takeuchi, and P. A. Nelson, "Robustness of the performance of the stereo dipole to head misalignment," ISVR Technical Report No. 285, University of Southampton, 1999.

¹⁹T. C. T. Yin and J. C. Chan, "Interaural time sensitivity in medial superior olive of cat," *J. Neurophysiol.* **64**, 465–488 (1990).

²⁰T. R. Stanford, S. Kuwada, and R. Batra, "A comparison of the interaural time sensitivity of neurons in the inferior colliculus and thalamus of the unanesthetized rabbit," *J. Neurophysiol.* **12**, 3200–3216 (1992).

²¹T. N. Buell, C. Trahiotis, and L. R. Bernstein, "Lateralization of low-frequency tones: Relative potency of gating and ongoing interaural delays," *J. Acoust. Soc. Am.* **90**, 3077–3085 (1991).

²²L. A. Jeffress, "A place theory of sound localization," *J. Comput. Physiol. Psychol.* **41**, 35–39 (1948).

²³H. S. Colburn, "Theory of binaural interaction based on auditory-nerve data. I. General strategy and preliminary results on interaural discrimination," *J. Acoust. Soc. Am.* **54**, 1458–1470 (1973).

²⁴G. B. Hanning, "Detectability of interaural delay in high-frequency complex waveforms," *J. Acoust. Soc. Am.* **55**, 84–90 (1974).

²⁵J. C. Middlebrooks and D. M. Green, "Directional dependence of interaural envelope delays," *J. Acoust. Soc. Am.* **87**, 2149–2162 (1990).

²⁶R. A. Butler and R. Flannery, "The spatial attributes of stimulus frequency and their role in monaural localization of sound in the horizontal plane," *Percept. Psychophys.* **28**, 449–457 (1980).

²⁷C. Lim and R. O. Duda, "Estimating the azimuth and elevation of a sound source from the output of a cochlea model," in *Proceedings of the Twenty-eighth Annual Asilomar Conference on Signals, Systems, and Computers* (IEEE, Asilomar, CA, 1994), pp. 399–403.

²⁸R. G. Klump and H. R. Eady, "Some measurements of interaural time difference thresholds," *J. Acoust. Soc. Am.* **28**, 859–860 (1956).

²⁹F. L. Wightman and D. J. Kistler, "The dominant role of low-frequency interaural time differences in sound localization," *J. Acoust. Soc. Am.* **91**, 1648–1661 (1992).

³⁰T. Takeuchi, P. A. Nelson, O. Kirkeby, and H. Hamada, "Influence of individual head related transfer function on the performance of virtual acoustic imaging systems," 104th AES Convention Preprint 4700 (1998), P4-3.

Implication of conservative and gyroscopic forces on vibration and stability of an elastically tailored rotating shaft modeled as a composite thin-walled beam

Ohseop Song and Nam-Heui Jeong

Mechanical Engineering Department, Chungnam National University, Taejon City 305-764, South Korea

Liviu Librescu

Department of Engineering Science and Mechanics, Virginia Polytechnic Institute and State University, Blacksburg, Virginia 24061

(Received 18 October 1999; accepted for publication 4 December 2000)

Problems related with the implications of conservative and gyroscopic forces on vibration and the stability of a circular cylindrical shaft modeled as a thin-walled composite beam and spinning with constant angular speed about its longitudinal axis are addressed. Taking into account the directionality property of fiber reinforced composite materials, it is shown that for a shaft featuring flapwise-chordwise-bending coupling, a dramatic enhancement of both the vibrational and stability behavior can be reached. In addition, the effects played in the same context by transverse shear, rotatory inertias as well as by the various boundary conditions are discussed and pertinent conclusions are outlined. © 2001 Acoustical Society of America. [DOI: 10.1121/1.1348301]

PACS numbers: 43.40.At [PJR]

I. INTRODUCTION

Shaft structural systems rotating about their longitudinal axis are employed for power transmission in aeropropulsion systems, in helicopter drive applications, industrial machines such as steam and gas turbines, turbogenerators, and production lines. In addition, the cutting tools used in boring and milling operations feature similarities in their structural modeling with the shaft systems.

In order to enhance the vibrational behavior, eliminate or even postpone the occurrence of any instability jeopardizing their normal operation, and reduce their weight, advanced structural models have to be devised. In this sense, the integration in their construction of composite materials systems is likely to solve, at least in good measure, the requirement of improved performance of these devices (see Ref. 1).

In addition to their superior strength/weight and stiffness/weight ratios, compared to their metallic counterparts, the directionality property featured by fiber composite material systems can be used to elastically tailor shaft stiffness properties. In such a way, new types of elastic couplings not featured by the standard metallic structures, having beneficial implications upon their response behavior, can be generated. Although belonging to the class of conservative systems, due to the presence of gyroscopic forces, the rotating shaft can behave like a nonconservative system, in the sense that, in some conditions, it can feature divergence and flutter instabilities.

One of the main goals of this study is to put into evidence the conditions under which such instabilities can occur, and the contribution brought about in this regard by the gyroscopic and conservative forces. Moreover, as will be shown, the directionality property of composite materials can be used as to delay the occurrence of both divergence and

flutter instabilities, and to enhance the vibrational behavior of the rotating shaft.

The governing equations used in this study incorporate a number of nonclassical features such as transverse shear, rotatory inertias, Coriolis acceleration, and the anisotropy of the spinning structure. Keeping that in mind, a circular cross section of the beam, proper to the shaft structure, is considered; in this case, as will be shown, both the primary and secondary warping functions become zero-valued quantities.

It should be mentioned that problems related with the spinning structures have been approached either in the framework of a solid beam theory (see, e.g., Refs. 2–9), of a circular cylindrical shell theory (see Refs. 10–15), and of the thin-walled beam theory of noncircular cross-section shape (Refs. 16 and 17). However, to the best of the authors' knowledge, with the exception of Refs. 16 and 17 whose results are used herein, no other paper has yet addressed the problems discussed within this work.

II. COORDINATE SYSTEMS AND BASIC ASSUMPTIONS

The case of a straight untwisted flexible beam of length L spinning along its longitudinal z -axis at a constant rate Ω and subjected to the longitudinal compressive dead force P is considered (see Fig. 1). Two coordinate systems, an inertial one, $OXYZ$, and a body attached rotating frame of reference $Oxyz$, with their common origin O at the geometric center (coinciding with the elastic center of the beam), are considered. It is supposed that the axes of the two coordinate systems coincide only when $t=0$ while, in the undeformed configuration, the body-fixed and inertial coordinates Oz and OZ coincide at any time t . Associated with the coordinate systems (x,y,z) and (X,Y,Z) , one defines the unit vectors $(\mathbf{i},\mathbf{j},\mathbf{k})$ and $(\mathbf{I},\mathbf{J},\mathbf{K})$, respectively (Fig. 2). In addition to the previously defined coordinate systems, a local (surface) one,

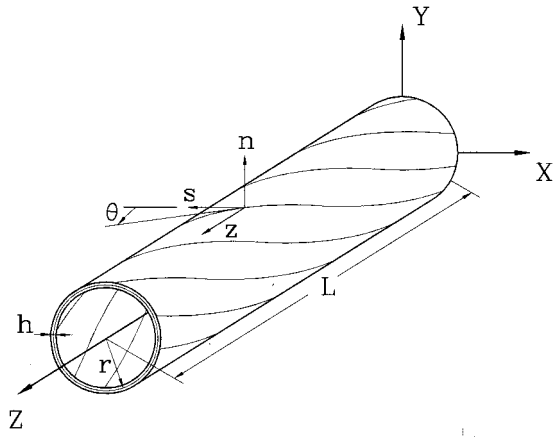


FIG. 1. Composite thin-walled beam of a circular cross section featuring CUS configuration.

(n, s, z) , associated with the thin-walled beam, is considered. In light of the stipulated assumptions one can represent the spin rate vector as $\mathbf{\Omega} = \Omega \mathbf{k} (\equiv \Omega \mathbf{K})$ with $\dot{\mathbf{\Omega}} = 0$.

The adopted structural model is that of a thin-walled beam. In this context, the case of a single-cell thin-walled beam of circular cross-sectional shape is considered. Toward its modeling the following assumptions are adopted: (i) the original cross section of the beam is preserved; (ii) transverse shear effects are incorporated; and (iii) the constituent material of the structure features anisotropic properties, and, in this context, a special lay-up inducing flapping-lagging coupling is implemented.

III. KINEMATICS

In light of the previously mentioned assumptions, and to reduce the 3D elasticity problem to an equivalent 1D one, the components of the displacement vector are represented as (see, e.g., Ref. 18)

$$u(x, y, z; t) = u_0(z; t) - y \phi(z; t), \quad (1a)$$

$$v(x, y, z; t) = v_0(z; t) + x \phi(z; t), \quad (1b)$$

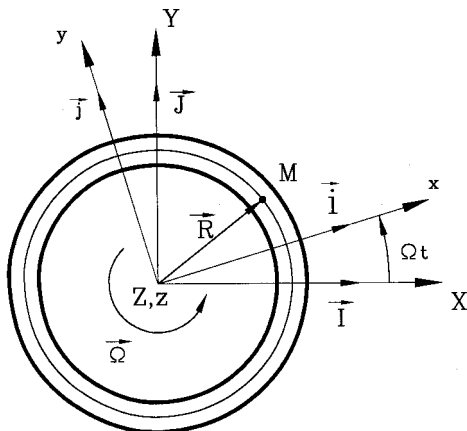


FIG. 2. Inertial (X, Y, Z) and body fixed (x, y, z) coordinate systems.

$$w(x, y, z; t) = w_0(z; t) + \theta_x(z; t) \left[y(s) - n \frac{dx}{ds} \right] + \theta_y(z; t) \left[x(s) + n \frac{dy}{ds} \right] - \phi'(z; t) [F_\omega(s) + na(s)]. \quad (1c)$$

In these equations $u_0(z; t)$, $v_0(z; t)$, $w_0(z; t)$ denote the rigid body translations along the x, y , and z -axes, while $\phi(z; t)$ and $\theta_x(z; t), \theta_y(z; t)$ denote the twist about the z -axis and rotations about the x - and y -axes, respectively. The expressions of θ_x and θ_y as well as of the geometric quantity $a(s)$ are

$$\theta_x(z; t) = \gamma_{yz}(z; t) - v_0'(z; t), \quad (2a)$$

$$\theta_y(z; t) = \gamma_{xz}(z; t) - u_0'(z; t), \quad (2b)$$

$$a(s) = -y(s) \frac{dy}{ds} - x(s) \frac{dx}{ds}. \quad (2c)$$

In Eqs. (1), $F_\omega(s)$ and $na(s)$ play the role of primary and secondary warping functions, respectively. For their definition see, e.g., Ref. 18. However, for thin-walled beams of circular cross sections, having in view that

$$x = -R \sin(s/R), \quad (2d)$$

$$y = R \cos(s/R), \quad (2e)$$

$$r_n(s) = R, \quad (2f)$$

where R is the beam radius of the mid-line cross section, it can readily be proven that both warping quantities exactly vanish, i.e.,

$$F_\omega(s) = 0, \quad (2g)$$

$$a(s) = 0. \quad (2h)$$

It is also seen that in the absence of transverse shear effects

$$\theta_x(z; t) = -v_0'(z; t); \quad \theta_y(z; t) = -u_0'(z; t). \quad (3)$$

In these equations, as well as in those that follow, primes denote differentiation with respect to the longitudinal z -coordinate. The position vector of a generic point $M(x, y, z)$ belonging to the deformed structure is

$$\mathbf{R}(x, y, z; t) = (x + u)\mathbf{i} + (y + v)\mathbf{j} + (z + w)\mathbf{k}, \quad (4)$$

where x, y , and z are the Cartesian coordinates of the points of the continuum in its undeformed state. Recalling that the spin rate was assumed to be constant, and using the expressions for the time derivatives of unit vectors, the velocity and acceleration of a generic point are:

$$\dot{\mathbf{R}} = [\dot{u} - \Omega(y + v)]\mathbf{i} + [\dot{v} + \Omega(x + u)]\mathbf{j} + \dot{w}\mathbf{k}, \quad (5a)$$

$$\ddot{\mathbf{R}} = [\ddot{u} - 2\Omega\dot{v} - (x + u)\Omega^2]\mathbf{i} + [\ddot{v} + 2\Omega\dot{u} - (y + v)\Omega^2]\mathbf{j} + \ddot{w}\mathbf{k}. \quad (5b)$$

In these equations the superposed dots denote derivatives with respect to time t .

IV. GOVERNING EQUATION SYSTEM

Toward the goal of deriving the equations of motion of spinning beams and the associated boundary conditions, Hamilton's variational principle is used. This variational principle may be stated as

$$\delta J = \int_{t_0}^{t_1} \left[\int_{\tau} \sigma_{ij} \delta \epsilon_{ij} d\tau - \delta K - \int_{\Omega_{\sigma}} \underline{s}_i \delta v_i d\Omega - \int_{\tau} \rho H_i \delta v_i d\tau \right] dt = 0, \quad (6)$$

where

$$U = \frac{1}{2} \int_{\tau} \sigma_{ij} \epsilon_{ij} d\tau, \quad (7a)$$

$$K = \frac{1}{2} \int_{\tau} \rho (\dot{\mathbf{R}} \cdot \dot{\mathbf{R}}) d\tau \quad (7b)$$

denote the strain energy and the kinetic energy functions, respectively.

In these equations, t_0 and t_1 denote two arbitrary instants of time; $d\tau (\equiv dn ds dz)$ denotes the differential volume element; $\underline{s}_i (\equiv \sigma_{ij} n_j)$ denotes the prescribed components of the stress vector on a surface element of the undeformed body characterized by the outward normal components n_i ; H_i denotes the components of the body forces; Ω_{σ} denotes the external area of the body over which the stresses are prescribed; ρ denotes the mass density; an underline sign identifies a prescribed quantity, while δ denotes the variation operator. In Eqs. (6) and (7) the Einstein summation convention applies to repeated indices where Latin indices range from 1 to 3. In the same equations, $(v_1, v_2, v_3) \equiv (u, v, w)$, $(x_1, x_2, x_3) \equiv (x, y, z)$.

In light of Eqs. (1), (4), (5), (7), and enforcing Hamilton's condition $\delta v_i = 0$ at t_0, t_1 , it can readily be shown that

$$\begin{aligned} \int_{t_0}^t \delta K dt & \left(\equiv - \int_{t_0}^{t_1} dt \int_{\tau} \rho \ddot{\mathbf{R}} \cdot \delta \mathbf{R} d\tau \right) = - \int_{t_0}^{t_1} dt \int_{\tau} \{ [\ddot{u} - 2\Omega \dot{v} - \Omega^2(x+u)] \delta u + [\ddot{v} + 2\Omega \dot{u} - (y+v)\Omega^2] \delta v + \ddot{w} \delta w \} \rho d\tau \\ & = - \int_{t_0}^{t_1} dt \int_{\tau} \left\{ [\ddot{u}_0 - y \ddot{\phi} - 2\Omega(\dot{v}_0 + x\dot{\phi}) - \Omega^2(x+u_0 - y\phi)] (\delta u_0 + y \delta \phi) \right. \\ & \quad + [\ddot{v}_0 + x \ddot{\phi} + 2\Omega(\dot{u}_0 - y\dot{\phi}) - (y+v_0 + x\phi)\Omega^2] (\delta v_0 + x \delta \phi) + \left. \left[\ddot{w}_0 + \left(y - n \frac{dx}{ds} \right) \ddot{\theta}_x \right. \right. \\ & \quad \left. \left. + \left(x + n \frac{dy}{ds} \right) \ddot{\theta}_y \right] \delta \left[w_0 + \theta_x \left(y - n \frac{dx}{ds} \right) + \theta_y \left(x + n \frac{dy}{ds} \right) - \phi' (F_{\omega} + na) \right] \right\} d\tau, \quad (8) \end{aligned}$$

where, in light of Eqs. (2g), (2b), the terms underscored by a solid line should be discarded.

To induce elastic coupling between flapwise bending and chordwise bending, a special ply angle distribution referred to as *circumferentially uniform stiffness* (CUS) configuration (see Refs. 18–20), achieved by skewing angle plies with respect to the longitudinal beam axis according to the law $\theta(y) = \theta(-y)$, and $\theta(x) = \theta(-x)$, is implemented. In this case, from the variational principle, Eq. (6), the equations of motion, and the boundary conditions involving this type of coupling are obtained. Employment of constitutive equations and strain-displacement relationships in these equations results in the following *governing equations* (see Ref. 16):

$$\begin{aligned} \delta u_0: \quad & a_{43} \theta_x'' + a_{44} (v_0'' + \theta_y') - P u_0'' \\ & = b_1 \ddot{u}_0 - \underline{\underline{2b_1 \Omega \dot{v}_0}} - b_1 u_0 \Omega^2, \quad (9a) \end{aligned}$$

$$\begin{aligned} \delta v_0: \quad & a_{52} \theta_y'' + a_{55} (v_0'' + \theta_x') - P v_0' \\ & = b_1 \ddot{v}_0 + \underline{\underline{2b_1 \Omega \dot{u}_0}} - b_1 v_0 \Omega^2, \quad (9b) \end{aligned}$$

$$\delta \theta_y: \quad a_{22} \theta_y'' + a_{25} (v_0'' + \theta_x') - a_{44} (v_0' + \theta_y) - a_{43} \theta_x'$$

$$= \underline{\underline{(b_5 + b_{15}) \ddot{\theta}_y}}, \quad (9c)$$

$$\begin{aligned} \delta \theta_x: \quad & a_{33} \theta_x'' + a_{34} (v_0'' + \theta_y') - a_{55} (v_0' + \theta_x) - a_{52} \theta_y' \\ & = \underline{\underline{(b_4 + b_{14}) \ddot{\theta}_x}}, \quad (9d) \end{aligned}$$

and the *boundary conditions* at $z=0, L$:

$$\delta u_0: \quad \underline{\underline{Q_x}} = \underline{\underline{Q_x}} \quad \text{or} \quad u_0 = \underline{\underline{u_0}}, \quad (10a)$$

$$\delta v_0: \quad \underline{\underline{Q_y}} = \underline{\underline{Q_y}} \quad \text{or} \quad v_0 = \underline{\underline{v_0}}, \quad (10b)$$

$$\delta \theta_y: \quad \underline{\underline{M_y}} = \underline{\underline{M_y}} \quad \text{or} \quad \theta_y = \underline{\underline{\theta_y}}, \quad (10c)$$

$$\delta \theta_x: \quad \underline{\underline{M_x}} = \underline{\underline{M_x}} \quad \text{or} \quad \theta_x = \underline{\underline{\theta_x}}. \quad (10d)$$

Herein $\underline{\underline{Q_x}}(z;t)$ and $\underline{\underline{Q_y}}(z;t)$ denote the shear forces in the x - and y -directions; $\underline{\underline{M_x}}(z;t)$ and $\underline{\underline{M_y}}(z;t)$ denote the moments about the x - and y -axis, respectively; P is the constant axial force, positive in compression, whereas the terms underscored by the dotted and solid lines are associated with Coriolis and rotatory inertia effects, respectively. Using the definitions of shear forces and moments, (see Refs. 16–18), the static version of homogeneous boundary conditions in terms of displacement quantities reads:

$$\delta u_0: a_{43}\theta'_x + a_{44}(u'_0 + \theta_y) - Pu'_0 = 0, \quad (11a)$$

$$\delta v_0: a_{52}\theta'_y + a_{55}(v'_0 + \theta_x) - Pv'_0 = 0, \quad (11b)$$

$$\delta \theta_y: a_{22}\theta'_y + a_{25}(v'_0 + \theta_x) = 0, \quad (11c)$$

$$\delta \theta_x: a_{33}\theta'_x + a_{34}(u'_0 + \theta_y) = 0. \quad (11d)$$

The coefficients $a_{ij} = a_{ji}$ and b_i appearing in these equations denote stiffness and reduced mass terms, respectively. Their expressions are displayed in the Appendix. Equations (9) and (11) reveal that in the context of ply angle configuration considered above, in addition to the elastic couplings already mentioned, the flapwise transverse shear is also coupled with chordwise bending, and chordwise transverse shear is coupled with flapwise bending. Moreover, the Coriolis acceleration terms induce a supplementary coupling between the flapwise and chordwise bendings.

Separate from the above-mentioned couplings, the extension-twist coupling is induced by the same ply angle configuration. This type of coupling is important and implemented as such, e.g., in helicopter blades and tilt rotor aircraft. However, the present study is confined to only the problem involving the flapwise-chordwise-bending coupling.

V. TWO REPRESENTATIONS OF GOVERNING EQUATIONS

Two complex representations of governing equations related to Case (i) and Case (ii) are carried out.

Within Case (i), the system of Eqs. (9) and boundary conditions Eqs. (11) associated with the shearable rotating shaft are used. Keeping in mind that for the circular cross-section beam:

$$a_{22} = a_{33} \equiv A, \quad (12a)$$

$$a_{44} = a_{55} \equiv B, \quad (12b)$$

$$a_{25} = -a_{34} \equiv S, \quad (12c)$$

$$b_4 + b_{14} = b_5 + b_{15} \equiv C, \quad (12d)$$

where A , B , C , and S are displayed in the Appendix, and defining the complex displacement variables

$$U = u_0 + iv_0; \quad (13a)$$

$$\Theta = \theta_y + i\theta_x, \quad (i = \sqrt{-1}) \quad (13b)$$

the governing equations can be cast in a complex form as:

$$BU'' + B\Theta' + iS\Theta'' - b_1\ddot{U} - 2ib_1\Omega\dot{U} + b_1U\Omega^2 = 0, \quad (14a)$$

$$A\Theta'' - BU' - B\Theta - iS(U'' + \Theta') - iS\Theta - C\dot{\Theta} = 0, \quad (14b)$$

while the homogeneous boundary conditions at $z=0, L$ read:

$$B(U' + \Theta) + iS\Theta = 0 \quad \text{or} \quad U = 0, \quad (15a)$$

$$A\Theta' - iS(U' + \Theta) = 0 \quad \text{or} \quad U' = 0. \quad (15b)$$

It is readily seen that the stiffness quantities B and S couple the two governing equations. Solutions of the eigenvalue problem based on this complex representation can be found, e.g., in Refs. 6, 7, and 8.

Case (ii) involves the nonshear deformable beam model. In this case, elimination from Eqs. (9) and (11) of the quantities $a_{44}(u''_0 + \theta'_y)$ and $a_{55}(v''_0 + \theta'_x)$, an operation followed by consideration of Eq. (3) stating the absence of transverse shear, results in the governing equations:

$$\delta u_0: a_{22}u''''_0 + Pu''_0 + b_1\ddot{u}_0 - \underline{(b_5 + b_{15})\dot{u}'_0} - 2b_1\Omega\dot{v}_0 - b_1u_0\Omega^2 = 0, \quad (16a)$$

$$\delta v_0: a_{33}v''''_0 + Pv''_0 + b_1\ddot{v}_0 - \underline{(b_4 + b_{14})\dot{v}'_0} + 2b_1\Omega\dot{u}_0 - b_1v_0\Omega^2 = 0, \quad (16b)$$

and of the boundary conditions. Their homogeneous counterpart is:

$$a_{22}u''''_0 + Pu''_0 - \underline{(b_5 + b_{15})\dot{u}'_0} = 0 \quad \text{or} \quad u_0 = 0, \quad (17a)$$

$$a_{33}v''''_0 + Pv''_0 - \underline{(b_4 + b_{14})\dot{v}'_0} = 0 \quad \text{or} \quad v_0 = 0, \quad (17b)$$

$$a_{22}u''_0 = 0 \quad \text{or} \quad u'_0 = 0, \quad (17c)$$

$$a_{33}v''_0 = 0 \quad \text{or} \quad v'_0 = 0. \quad (17d)$$

It should be remarked that the governing equations of shearable thin-walled beams Eqs. (9), and their nonshear deformable counterparts, Eqs. (16), exhibit the same order (eight), and as such, in both cases, four boundary conditions have to be prescribed at each end, $z=0, L$, of the beam. Equations (16) reveal that, in this special case, the coupling arises only via the Coriolis acceleration effect. In its absence both equations would be decoupled. However, when this effect is accounted for, upon defining the complex displacement variable $U (\equiv u_0 + iv_0)$, the governing equation system becomes

$$AU'''' + b_1\ddot{U} - C\dot{U}'' + PU'' - b_1\Omega^2U + \underline{2ib_1\Omega\dot{U}} = 0, \quad (18)$$

whereas the homogeneous boundary conditions reduce to

$$AU''' + PU' - C\dot{U}' = 0 \quad \text{or} \quad U = 0, \quad (19a)$$

$$AU'' = 0 \quad \text{or} \quad U' = 0. \quad (19b)$$

In this case, in order to study the associated eigenvalue problem, a modal analysis can be implemented.

VI. THE EIGENVALUE PROBLEM OF GYROSCOPIC SYSTEMS

For the cases described by Eqs. (9)–(11), the modal analysis fails to provide a solution to the associated eigenvalue problem. In contrast to this, in order to find an approximate solution to this problem, assuming synchronous motions, the generalized displacements are represented in the form

$$(u_0(z, t), v_0(z, t), \theta_x(z, t), \theta_y(z, t)) = (U(z), V(z), X(z), Y(z))e^{i\omega t}, \quad (20a)$$

where ω is the complex eigenfrequency, while the spatial parts are represented as

$$(U(z), V(z), X(z), Y(z)) = \sum_{j=1}^N (a_j u_j(z), b_j v_j(z), c_j x_j(z), d_j y_j(z)), \quad (20b)$$

where $u_j(z)$, $v_j(z)$, $x_j(z)$, and $y_j(z)$ are trial functions which have to fulfil all of the kinematic boundary conditions, whereas

$$\mathbf{B}^T = [a_1, a_2, \dots, a_N, b_1, b_2, \dots, b_N, c_1, c_2, \dots, c_N, d_1, d_2, \dots, d_N] \quad (20c)$$

is a constant vector.

Replacement of the representations in Eqs. (20) in the Hamilton's functional, Eq. (6), carrying out the indicated variations and the required integrations with respect to the spanwise z -coordinate and time t , and dividing through by $e^{i\omega t}$, the system of governing equations is cast in matrix form as

$$\delta \mathbf{B}^T [-\omega^2 \mathbf{M}_N + i\omega \mathbf{G}_N + \mathbf{K}_N] \mathbf{B} = 0. \quad (21)$$

Herein \mathbf{M}_N , \mathbf{G}_N , and \mathbf{K}_N are $(2N \times 2N)$ matrices, \mathbf{M}_N being symmetric positive definite, \mathbf{G}_N skew symmetric, and \mathbf{K}_N symmetric. Since contributions from the external compressive load and centrifugal forces are included in \mathbf{K}_N , its positive definiteness, positive, semidefiniteness, or negative definiteness cannot be posulated *ab initio*.

Equation (21) provides the following characteristic equation:

$$\Delta_N(\omega) = \det[-\omega^2 \mathbf{M}_N + i\omega \mathbf{G}_N + \mathbf{K}_N] = 0, \quad (22)$$

from which ω can be obtained. If \mathbf{K}_N is positive definite and $\mathbf{G}_N \neq 0$, the eigenvalues occur as $2N$ pure imaginary complex conjugate pairs $\lambda_r = \pm i\omega_r$ ($r = 1, 2N$), where ω_r is the *whirling* frequency (see Ref. 21).

For the fixed compressive load, the minimum spin rate at which the whirl frequency becomes zero valued corresponds to the critical spinning speed, denoted as Ω_{cr} . Conversely, for the fixed spin rate, the minimum compressive load for which one of the roots ω_j becomes zero corresponds to the critical compressive load P_{cr} . The instabilities described above are of the divergence type. In general, the condition of divergence is obtained by taking $\omega = 0$ in Eq. (22), which yields the equation

$$\Delta_N(P, \Omega^2) = 0. \quad (23)$$

This equation supplies the divergence instability boundary. On the other hand, combinations of compressive load and spin rate yielding two eigenfrequencies to coalesce constitute a flutter condition. Increasing either of these two parameters beyond the value of the load or spin rate corresponding to the flutter boundary results in complex conjugate eigenvalues, and correspondingly, to bending oscillations with exponentially increasing amplitudes. In the numerical simulations the occurrence of divergence and flutter instabilities will be analyzed for the following three cases of boundary conditions:

$$(a) \text{ Clamped at } z=0: \quad u_0 = v_0 = \theta_x = \theta_y = 0, \quad (24)$$

$$\text{Free at } z=L: \quad Q_x = Q_y = M_x = M_y = 0,$$

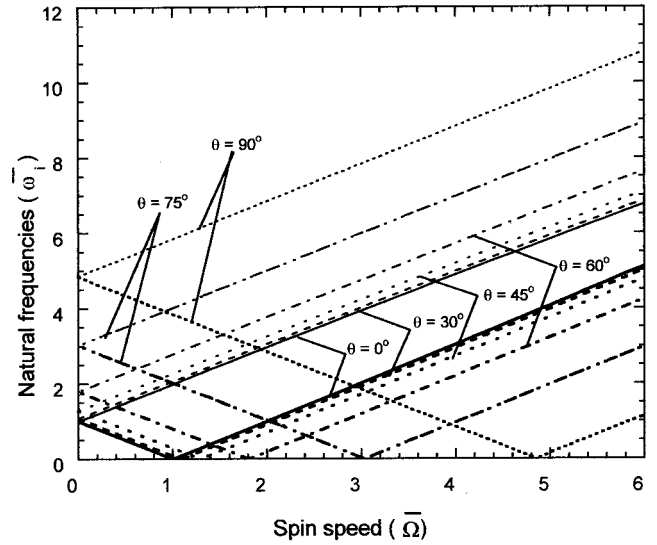


FIG. 3. Variation of upper and lower whirl frequencies with spin speed $\bar{\Omega}$ for selected values of the ply-angle [$\bar{P}=0$, boundary conditions (a)].

- (b) Simply supported at both $z=0, L$:
 $u_0 = v_0 = M_x = M_y = 0, \quad (25)$
 (c) Clamped at both $z=0, L$: $u_0 = v_0 = \theta_x = \theta_y = 0. \quad (26)$

VII. NUMERICAL SIMULATIONS

In Figs. 3–5, pictorial representations of the variation of natural frequencies $\bar{\omega}_i$ ($\equiv \omega_i / \hat{\omega}$) versus the spin speed $\bar{\Omega}$ ($\equiv \Omega / \hat{\omega}$) for selected ply angles and various boundary conditions, and for the case of the unloaded beam, are displayed. The normalizing factor $\hat{\omega} = 138.85$ rad/s is the fundamental frequency of the nonspinning beam counterpart, characterized by $\theta = 0^\circ$ and $P = 0$. The material of the beam is graphite-epoxy whose elastic characteristics are

$$E_1 = 30 \times 10^6 \text{ psi} (20.68 \times 10^{10} \text{ N/m}^2);$$

$$E_2 = E_3 = 0.75 \times 10^6 \text{ psi} (5.17 \times 10^9 \text{ N/m}^2),$$

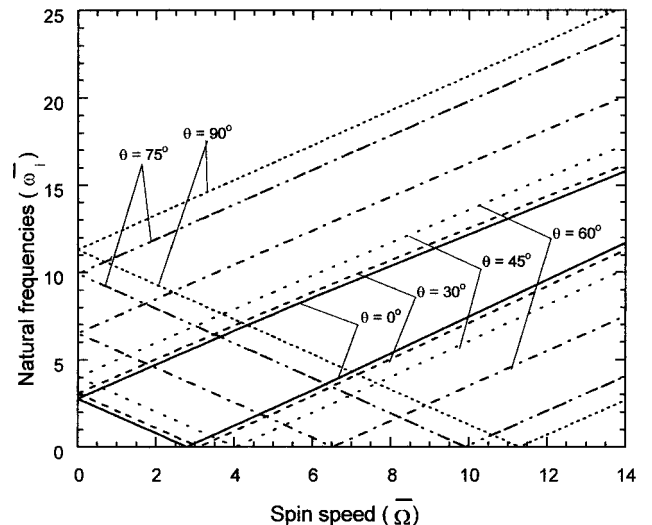


FIG. 4. Counterpart of Fig. 3 for the case of boundary conditions (b).

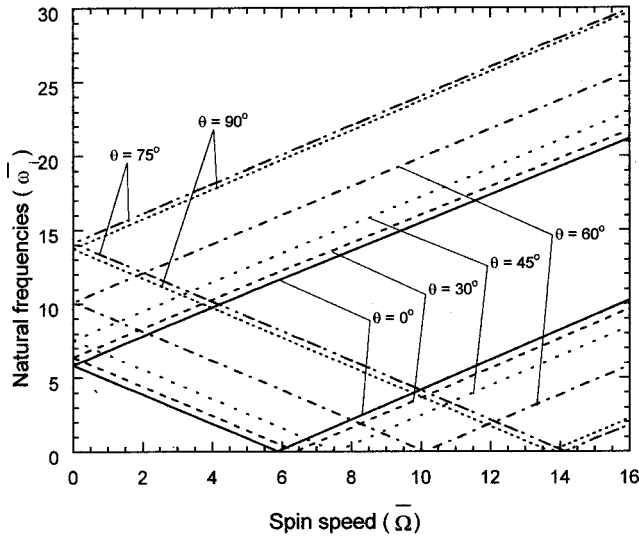


FIG. 5. Counterpart of Figs. 3 and 4 for the case of boundary conditions (c).

$$G_{12} = 0.45 \times 10^6 \text{ psi} (3.10 \times 10^9 \text{ N/m}^2);$$

$$G_{23} = G_{13} = 0.37 \times 10^6 \text{ psi} (2.55 \times 10^9 \text{ N/m}^2);$$

$$\nu_{21} = \nu_{31} = 0.00625; \quad \nu_{32} = 0.25;$$

$$\rho = 0.000143 \text{ lb s}^2/\text{in}^4 (1528.15 \text{ kg/m}^3).$$

Concerning the beam geometrical characteristics, these are: $r = 5 \text{ in.}$ (0.127 m), $L = 80 \text{ in.}$ (2.023 m), and $h = 0.4 \text{ in.}$ ($0.381 \times 10^{-3} \text{ m}$). For $\bar{\Omega} = 0$, i.e., in the case of the absence of gyroscopic effects, it is seen that the system is characterized, for each θ , by a single fundamental frequency. With the increase of the ply angle θ , an increase of nonrotating natural frequencies is obtained. This trend is attributed to the increase of bending stiffnesses $a_{22} = a_{33} (\equiv A)$ associated with the increase of θ (see, e.g., Ref. 22). As soon as the rotation starts, a fact which is accompanied by the generation of gyroscopic forces, a bifurcation of natural frequencies is experienced. This reverts to the conclusion that due the effect of the gyroscopic Coriolis force, two distinct frequency branches of free bending vibration are produced. The minimum spin rate at which the lowest rotating natural frequency becomes zero valued is called the critical spinning speed, denoted as $\bar{\Omega}_{cr}$, which corresponds to the divergence instability. Throughout these results it becomes apparent that at each ply angle there is a specific critical spinning speed and that the minimum and maximum ones occur for $\theta = 0^\circ$ and $\theta = 90^\circ$, respectively.

The results of these figures also reveal that, for boundary conditions labeled (a), both the critical spinning speed and the eigenfrequencies are, for the same ply angle, larger than those corresponding to boundary conditions (b) and (c), those corresponding to (c) being the least ones. Moreover, Fig. 3 reveals that, for boundary conditions (a), the increase of the ply angle yields a strong and continuous increase of both divergence spin speed $\bar{\Omega}_{cr}$ and of eigenfrequencies $\bar{\omega}_i$. However, for boundary conditions (b) and (c), the results

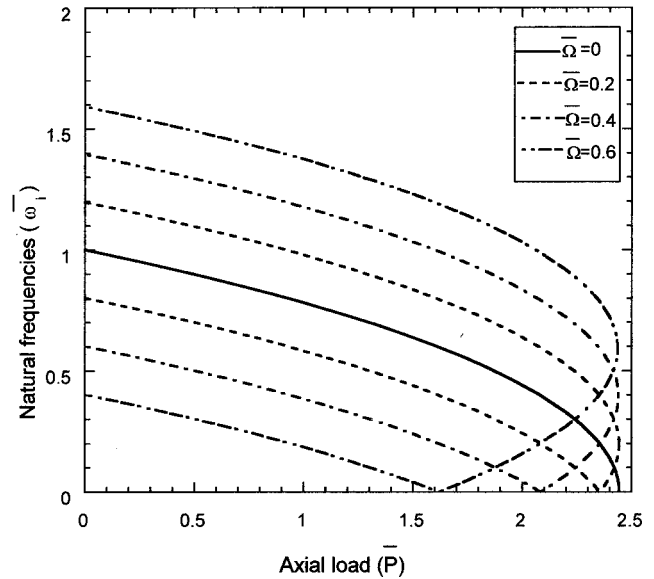


FIG. 6. Variation of upper and lower whirling frequencies with an increase of axial compressive load, for selected values of the spin speed [$\theta = 0^\circ$, boundary conditions (a)].

recorded in Figs. 4 and 5 reveal that, beyond the ply angle, $\theta \approx 75^\circ$, much smaller increases of the divergence rotating speed and eigenfrequencies are reached.

Figures 6–9 depict the variation of the upper and lower frequency branches for the boundary conditions (a), and for selected values of the spin rate $\bar{\Omega}$ versus the increase of the dimensionless axial load $\bar{P} (\equiv PL^2/\hat{a}_{22})$, where $\hat{a}_{22} = 1.1787 \times 10^8 \text{ lb in.}^2$ is the bending stiffness corresponding to the ply angle $\theta = 0$. For $\bar{\Omega} = 0$, the two frequency branches collapse into a single one. Each of these plots is depicted for a specific value of the ply angle. The results reveal that, for each value of $\bar{\Omega}$, as the axial compressive load increases, the associated eigenfrequency pairs decrease, and for a specific value of \bar{P} these approach the value of zero. The corresponding value of \bar{P} yielding the frequencies to vanish constitutes

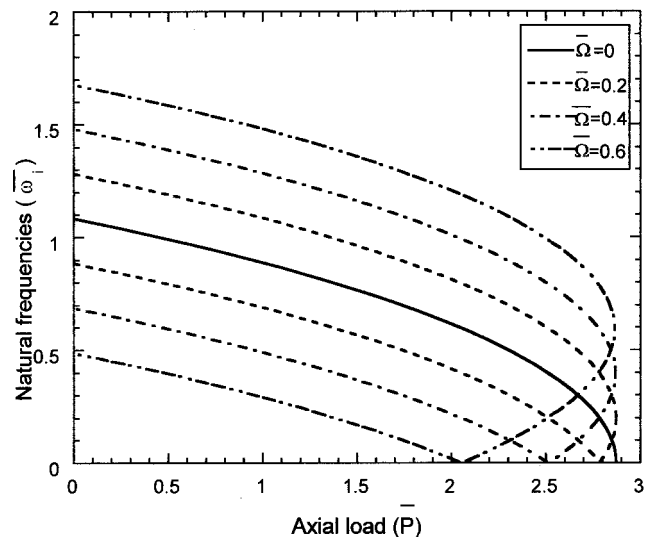


FIG. 7. Counterpart of Fig. 6 for $\theta = 30^\circ$.

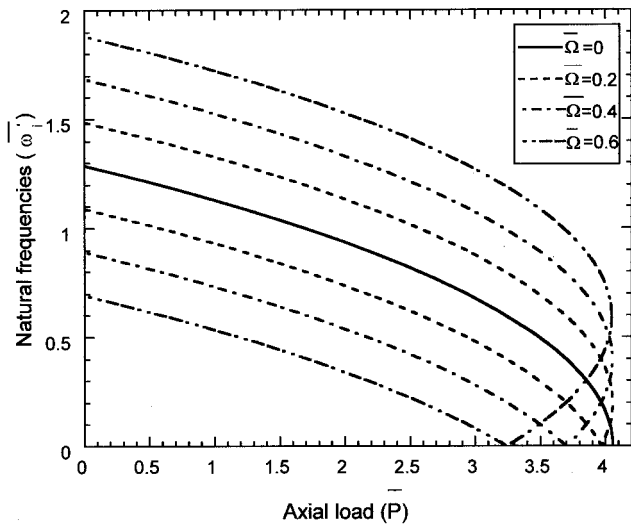


FIG. 8. Counterpart of Fig. 7 for $\theta=45^\circ$.

the critical axial compressive load (buckling load). This loss of stability is by divergence. The results of these plots reveal, that for a certain value of the ply angle, the critical axial load, \bar{P}_{cr} , corresponding to $\bar{\Omega}=0$ constitutes an upper bound, in the sense that for $\bar{\Omega}\neq 0$ the critical compressive loads diminish with increasing $\bar{\Omega}$.

However, a closer inspection of the region where the divergence occurs reveals that, for a slightly lower value of the compressive load and for $\bar{\Omega}>0$, the lower and upper lowest eigenfrequencies become complex conjugate. As a result, for $\bar{\Omega}>0$ and the compressive load slightly lower than that corresponding to the divergence instability, the instability by flutter is experienced. A similar trend was also reported in Ref. 23, where the study was accomplished via the finite element method.

The same plots also reveal that the increase of the ply angle results in a remarkable increase of the critical axial load. However, the same plots show that with the increase of the ply angle, the critical axial compressive load becomes

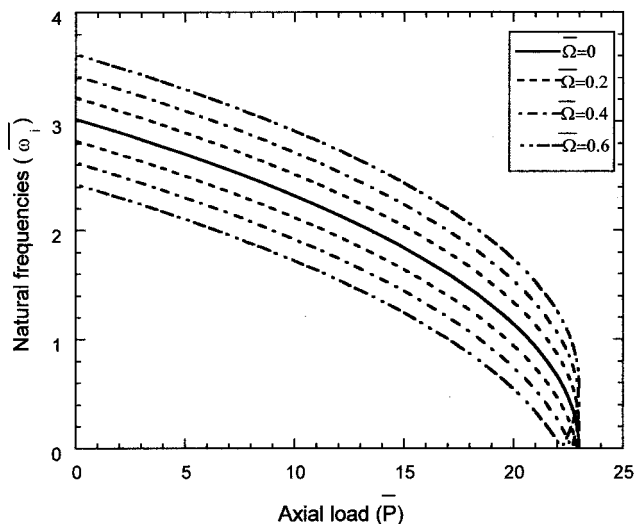


FIG. 9. Counterpart of Fig. 8 for $\theta=75^\circ$.

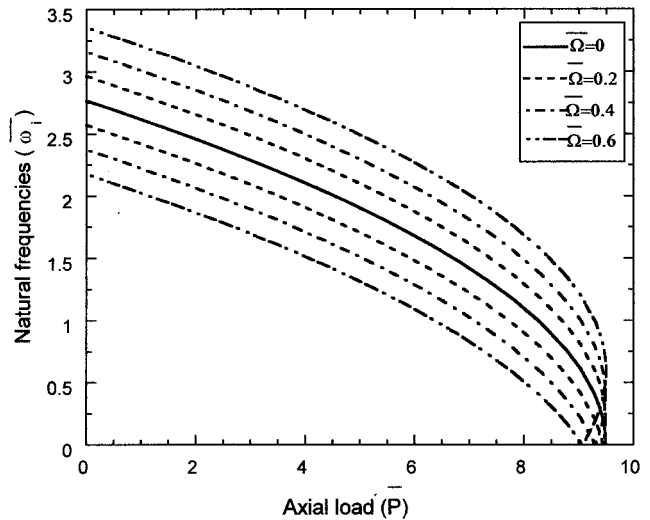


FIG. 10. Variation of upper and lower whirling frequencies with an increase of axial compressive load for selected values of the spin speed [$\theta=0^\circ$, boundary conditions (b)].

less and less sensitive to the increase of $\bar{\Omega}$. Figures 10–13 display the counterparts of Figs. 6–9, but generated for boundary conditions (b) and (c), respectively. For these cases, a reduction of the sensitivity of the variation of the buckling load with the spin rate is experienced. This trend becomes more and more prominent in the case of boundary conditions (b) and (c). It should be noticed that, in all of these cases, the tremendous beneficial influence played by the increase of the ply angle toward the increase of the buckling load is remarked.

In Figs. 14–16, stability plots of the spinning system in the $\bar{\Omega}-\bar{P}$ plane for the three cases of boundary conditions (a), (b), and (c) are displayed. In these plots S denotes the region of stability, D denotes the divergence boundary, while F that of the flutter instability. For $\bar{\Omega}$ and \bar{P} equal to zero, ω_i^2 are real and positive and the system is stable. With the increase of $\bar{\Omega}$ and/or \bar{P} , instabilities by divergence or flutter may occur. Due to the fact that the system is conservative,

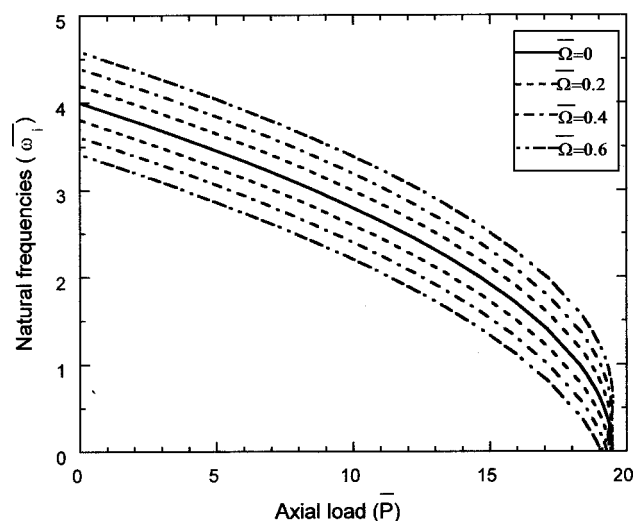


FIG. 11. Counterpart of Fig. 10 for $\theta=45^\circ$.

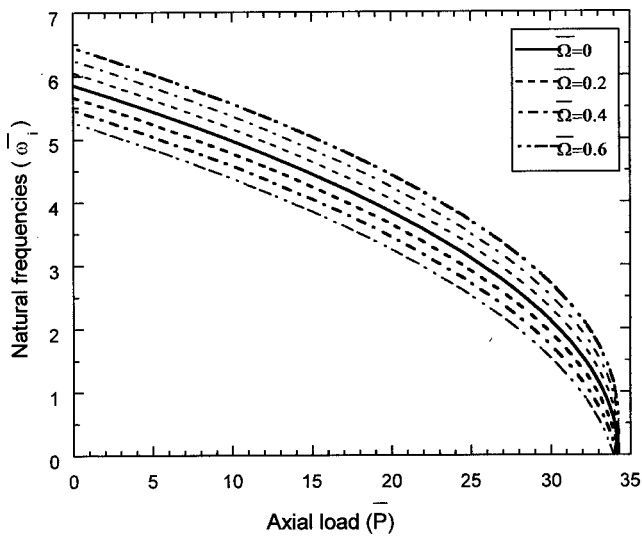


FIG. 12. Variation of upper and lower whirling frequencies with an increase of axial compressive load, for selected values of the spin speed [$\theta=0^\circ$, boundary conditions (c)].

initial instability will always be of a divergence type, characterized by $\omega_i^2=0$. The locus of such points in the plane $\bar{\Omega}-\bar{P}$ defines the divergence instability boundary. The plots reveal that in the plane $\bar{\Omega}-\bar{P}$ the instability boundary separates two stable regions, or in other words, divergence occurs only on this boundary, without the existence of regions of divergence instability. In all of these plots, the results reveal that the increase of the ply angle yields a considerable increase of the stability domains. Similar conclusions can be formulated in connection with the implications of boundary conditions, in the sense that as the boundary conditions change from type (a) to types (b) and (c), dramatic increases of the stability domains are experienced. The domain of stability adjacent to the divergence instability boundary and on the right-hand side reveals that the gyroscopic effects, increasing with $\bar{\Omega}$, contribute to the increase of the stability domain. On the same plots the flutter boundary correspond-

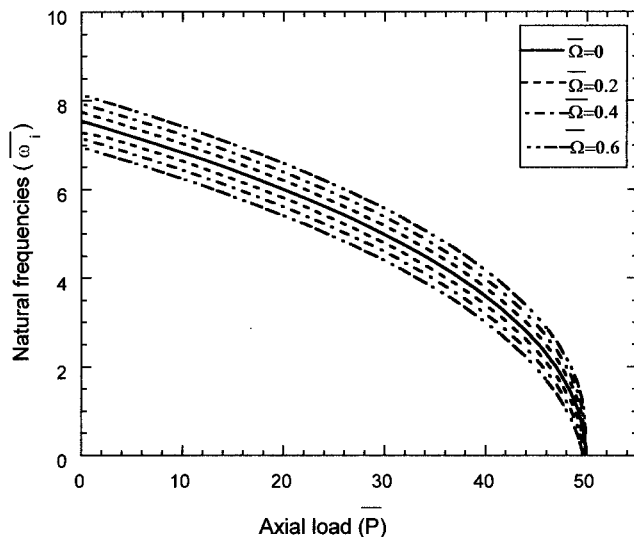


FIG. 13. Counterpart of Fig. 12 for $\theta=45^\circ$.

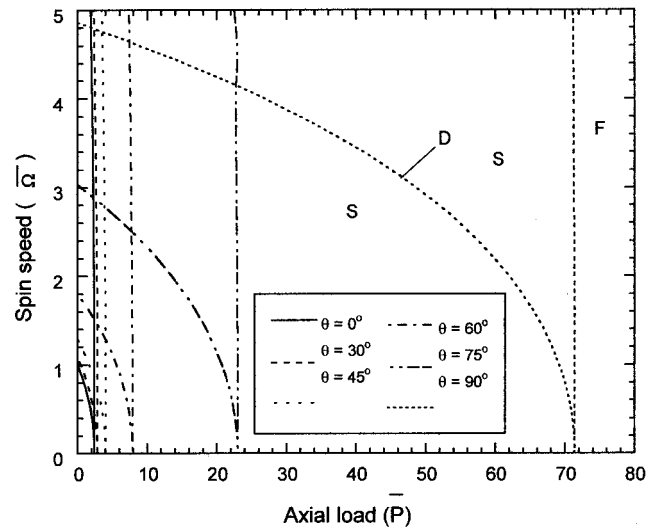


FIG. 14. Stability plot in the $\bar{\Omega}-\bar{P}$ plane displaying the domains of stability, divergence instability boundary, and flutter for selected values of the ply angle [boundary conditions (a)].

ing to conditions involving $\bar{\Omega}$ and \bar{P} yielding coalescence of two frequencies ω_j^2 is depicted. The results reveal that for specified ply angle and boundary conditions, the flutter boundary consists of slightly curved lines emerging at values of \bar{P} slightly lower than \bar{P}_{div} , and at spin rates $\bar{\Omega}>0$, where \bar{P}_{div} is the buckling load obtained at $\bar{\Omega}=0$. To have a better view of the flutter and divergence instabilities which appear in a very restrained region of the variation of $\bar{\Omega}$ and \bar{P} , Table I displays the trend of variation of the instability boundaries with that of θ and $\bar{\Omega}$, for boundary conditions (a). The flutter instability domain lies at the right of the curved line $\bar{P}=\bar{P}_{flutter}$ and for any $\bar{\Omega}>0$. This result coincides with that qualitatively obtained in Refs. 24, 25, with that reported in Ref. 16, and is consistent with that emerging from Figs. 6–13. However, when the rotatory inertia terms are ignored, in contrast to the abovementioned trend, the flutter boundary does not involve the dependence on $\bar{\Omega}$ and, as a result, in

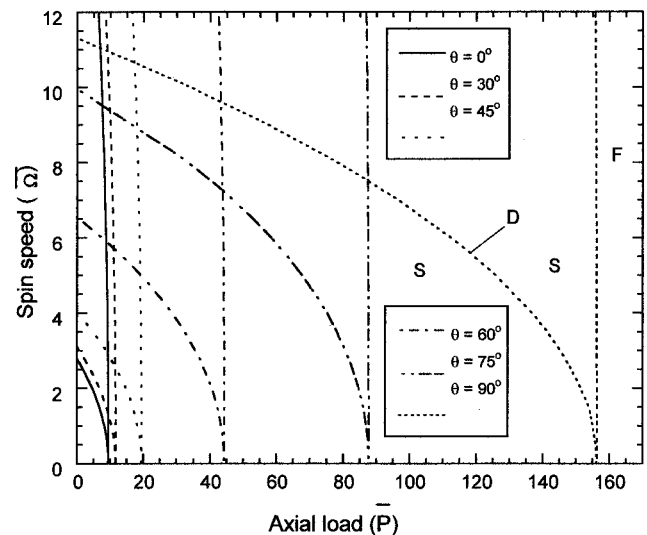


FIG. 15. Counterpart of Fig. 14 for boundary conditions (b).

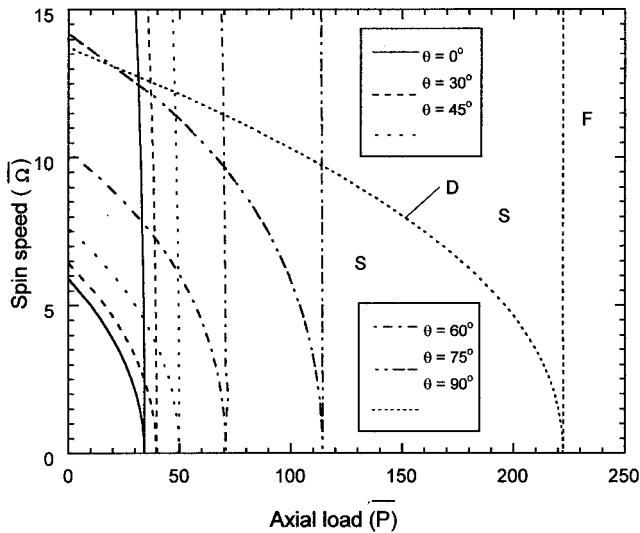


FIG. 16. Counterpart of Figs. 14 and 15 for boundary conditions (c).

that case the flutter boundary degenerates in a straight line $\bar{P} = \bar{P}_{div}$, parallel to the $\bar{\Omega}$ -axis. Such a trend was reported in Refs. 16 and 26.

Finally, in Fig. 17 the effects of transverse shear on the instability boundaries are highlighted. The results reveal that, in the absence of transverse shear effect, i.e., when the structure is unshearable, a significant increase of the stability domain is obtained as compared to the case when transverse shear effect is accounted for. As a result we can say that the classical (i.e., unshearable) structural model inadvertently overestimates the capacity of the rotating shaft to operate without the occurrence of the divergence and flutter instabilities.

VIII. CONCLUSIONS

A study devoted to the vibrational and stability behavior of spinning circular shafts modeled as thin-walled beams was presented, and the implications played by the conservative and gyroscopic forces on their instability behavior have been emphasized. As shown, in the conditions described in the paper, the rotating shaft can experience instabilities by flutter and divergence. Among others, the results reveal that structural tailoring can be successfully employed to enhance their behavior by increasing the spinning speed, and by shifting the domains of divergence and flutter instability toward larger spin rates. The implications of a number of effects,

TABLE I. Stability boundaries for selected values of the ply angle. Boundary conditions (a) and rotatory inertia effects included.

$\bar{\Omega}$	$\theta = 0^\circ$		$\theta = 45^\circ$		$\theta = 90^\circ$	
	\bar{P}_{div}	$\bar{P}_{flutter}$	\bar{P}_{div}	$\bar{P}_{flutter}$	\bar{P}_{div}	$\bar{P}_{flutter}$
0	2.444	-	4.056	-	71.44	-
1	-	2.421	1.713	4.033	69.19	71.43
2	-	2.353	-	3.965	62.02	71.39
3	-	2.238	-	3.852	48.61	71.33
4	-	2.078	-	3.692	26.90	71.24
5	-	1.872	-	3.488	-	71.13

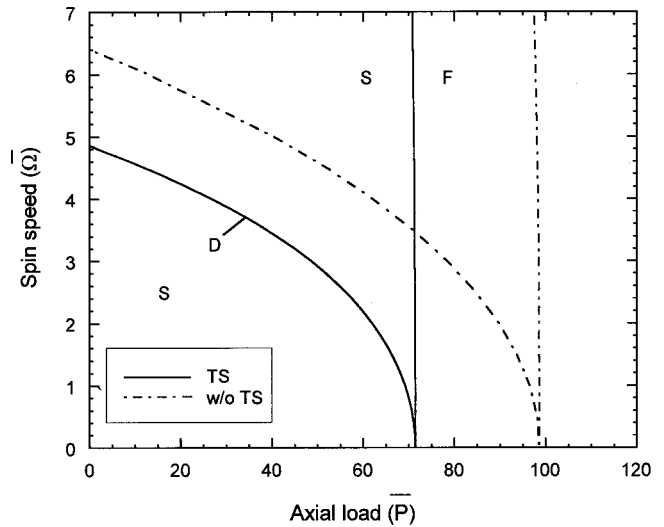


FIG. 17. Effect of transverse shear on the stability boundaries of the rotating shaft [boundary conditions (a); $\theta = 90^\circ$].

such as that of transverse shear upon the stability of the gyroscopic system, have been emphasized. In this context it was shown that discarding transverse shear effect results in an overestimation of the capacity of the system to operate safely, without the occurrence of flutter and divergence instabilities.

Finally, the effects of various boundary conditions on the variation of eigenfrequencies and stability of the system with the spin rate and axial load have been put into evidence.

APPENDIX

Expressions of stiffness quantities $a_{ij}(=a_{ji})$ and reduced mass terms for a cross-section circular shaft:

$$a_{22} = a_{33} = \pi R^2 \left[K_{11} + \frac{2}{R} K_{14} + K_{44} \right] \equiv A,$$

$$a_{44} = a_{55} = \pi [K_{22} + A_{44}] \equiv B,$$

$$a_{25} = -a_{34} = -\pi [RK_{12} - K_{24}] \equiv S,$$

$$b_4 + b_{14} = b_5 + b_{15} = \pi [m_0 R^2 + m_2] \equiv C.$$

Herein

$$K_{11} = A_{22} - A_{12}^2 / A_{11}; \quad K_{14} = B_{22} - (A_{12} B_{12} / A_{11}),$$

$$K_{12} = A_{26} - A_{12} A_{16} / A_{11} = K_{21},$$

$$K_{44} = D_{22} - B_{12}^2 / A_{11},$$

$$K_{22} = A_{66} - A_{16}^2 / A_{11},$$

$$K_{24} = B_{26} - A_{16} B_{12} / A_{11} = K_{42},$$

where A_{ij} , B_{ij} , and C_{ij} denote the local stretching, coupling, and bending stiffness components, respectively.

In addition, the mass terms m_0 and m_2 are expressed as

$$(m_0, m_2) = \sum_{k=1}^N \int_{h_{(k-1)}}^{h_{(k)}} \rho_{(k)} (1, n^2) dn.$$

- ¹O. Bauchau, "Design manufacturing and testing of high speed rotating graphite-epoxy shaft," Ph.D. Thesis, Massachusetts Institute of Technology, Department of Aeronautical and Astronautics, 1981.
- ²C. P. Filipich, M. J. Maurizi, and M. B. Rosales, "Free vibrations of a spinning uniform beam with ends elastically restrained against rotation," *J. Sound Vib.* **116**, 475–482 (1987).
- ³C. W. Lee, R. Katz, A. G. Ulsoy, and R. A. Scott, "Modal analysis of a distributed parameter rotating shaft," *J. Sound Vib.* **122**, 119–130 (1988).
- ⁴M. L. Chen and Y. S. Liao, "Vibrations of pretwisted spinning beams under axial compressive loads with elastic constraints," *J. Sound Vib.* **147**, 497–513 (1991).
- ⁵C. W. Bert and C. D. Kim, "Whirling of composite-material driveshafts including bending-twisting coupling and transverse shear deformation," *J. Vibr. Acoust.* **117**, 17–21 (1995).
- ⁶R. P. S. Han and J. W. Z. Zu, "Modal analysis of rotating shafts. A body fixed axis formulation approach," *J. Sound Vib.* **156**, 1–16 (1992).
- ⁷J. W.-Z. Zu and R. P. S. Han, "Natural frequencies and normal modes of a spinning Timoshenko beam with general boundary conditions," *J. Appl. Mech.* **59**, June, 197–204 (1992).
- ⁸C. L. Liao and Y. H. Dang, "Structural characteristics of spinning pretwisted orthotropic beams," *Comput. Struct.* **45**, 715–731 (1992).
- ⁹J. W. Zu and J. Melianon, "Natural frequencies and normal modes for damped spinning Timoshenko beam with general boundary conditions," *J. Appl. Mech.* **65**, 770–772 (1998).
- ¹⁰A. Zohar and J. Aboudi, "The free vibrations of a thin circular finite rotating cylinder," *Int. J. Mech. Sci.* **15**, 269–278 (1973).
- ¹¹S. C. Huang and W. Soedel, "On the forced vibration of simply supported rotating cylindrical shells," *J. Acoust. Soc. Am.* **84**, 275–285 (1988).
- ¹²O. Rand and Y. Stavsky, "Free vibrations of spinning composite cylindrical shells," *Int. J. Solids Struct.* **28**, 831–843 (1991).
- ¹³C. D. Kim and C. W. Bert, "Critical speed analysis of laminated composite hollow drive shaft," *Composites Eng.* **3**, 633–643 (1993).
- ¹⁴C. W. Bert and C. D. Kim, "Dynamic instability of composite-material drive shaft subject to fluctuating torque and/or rotational speed," *Dynamic and Stability of Systems* **10**, 125–147 (1995).
- ¹⁵L. Hua and K. Y. Lam, "Frequency characteristics of a thin rotating cylindrical shell using the generalized differential quadratic method," *Int. J. Mech. Sci.* **40**, 443–459 (1998).
- ¹⁶O. Song and L. Librescu, "Anisotropy and structural coupling on vibration and instability of spinning thin-walled beams," *J. Sound Vib.* **204**, 477–494 (1998).
- ¹⁷O. Song and L. Librescu, "Modelling and vibration of pretwisted spinning composite thin-walled beams," *Proceedings of the 38th AIAA/ASME/ASCE/AHS/ASC Structures, Structural Dynamics, Materials Conference and Exhibition and AIAA/ASME/AHS/Adaptive Structure Forum*, Paper AIAA 97-1091, Part 1, pp. 312–322, Kissimmee, Florida, April 7–10 (1997).
- ¹⁸O. Song and L. Librescu, "Free vibration of anisotropic composite thin-walled beams of closed cross-section contour," *J. Sound Vib.* **167**, 129–147 (1993).
- ¹⁹L. W. Rehfield and A. R. Atilgan, "Toward understanding the tailoring mechanisms for thin-walled composite tubular beams," *Proceedings of the First USSR-US Symposium on Mechanics of Composite Materials*, May, pp. 187–196 (1989).
- ²⁰E. C. Smith and I. Chopra, "Formulation and evaluation of an analytical model for composite box-beams," *J. Am. Helicopter Soc.* **36**(3), 23–25 (1991).
- ²¹L. Meirovitch, *Principles and Techniques of Vibration* (Prentice Hall, New York, 1997).
- ²²L. Librescu, L. Meirovitch, and O. Song, "Refined structural modeling for enhancing vibrational and aeroelastic characteristics of composite aircraft wings," *Rech. Aerosp.* **1**, 23–35 (1996).
- ²³D. M. Ku and L. W. Chen, "Stability and whirl speeds of rotating shaft under axial loads," *International Journal of Analytical and Experimental Modal Analysis*, **9**, 111–123 (1994).
- ²⁴K. Huseyin and R. H. Plaut, "Transverse vibrations and stability of systems with gyroscopic forces," *Journal of Structural Mechanics* **3**, 163–177 (1974–1975).
- ²⁵K. Huseyin and R. H. Plaut, "Divergence and flutter boundaries of systems under combined conservative and gyroscopic forces," 1975, *Dynamics of Rotors*, IUTAM Symposium, Lyngby, Denmark, August 12–16, pp. 182–205 (Springer-Verlag, Berlin, 1974).
- ²⁶R. C. Shieh, "Energy and variational principles for generalized (gyroscopic) conservative problems," *Int. J. Non-Linear Mech.* **5**, 495–509 (1971).

A new method for true and spurious eigensolutions of arbitrary cavities using the combined Helmholtz exterior integral equation formulation method

I. L. Chen

Department of Naval Architecture, National Kaohsiung Institute of Marine Technology, Kaohsiung, Taiwan

J. T. Chen,^{a)} S. R. Kuo, and M. T. Liang

Department of Harbor and River Engineering, National Taiwan Ocean University, P.O. Box 7-59, Keelung, Taiwan

(Received 22 November 1999; accepted for publication 4 December 2000)

Integral equation methods have been widely used to solve interior eigenproblems and exterior acoustic problems (radiation and scattering). It was recently found that the real-part boundary element method (BEM) for the interior problem results in spurious eigensolutions if the singular (UT) or the hypersingular (LM) equation is used alone. The real-part BEM results in spurious solutions for interior problems in a similar way that the singular integral equation (UT method) results in fictitious solutions for the exterior problem. To solve this problem, a Combined Helmholtz Exterior integral Equation Formulation method (CHEEF) is proposed. Based on the CHEEF method, the spurious solutions can be filtered out if additional constraints from the exterior points are chosen carefully. Finally, two examples for the eigensolutions of circular and rectangular cavities are considered. The optimum numbers and proper positions for selecting the points in the exterior domain are analytically studied. Also, numerical experiments were designed to verify the analytical results. It is worth pointing out that the nodal line of radiation mode of a circle can be rotated due to symmetry, while the nodal line of the rectangular is on a fixed position. © 2001 Acoustical Society of America. [DOI: 10.1121/1.1349187]

PACS numbers: 43.40.At [PJR]

I. INTRODUCTION

Acoustic problems are generally modeled using the wave equation, which is transient, or by the Helmholtz equation, which is time harmonic. While the solution to the original boundary value problem in the domain exterior to the boundary is perfectly unique for all wave numbers, this is not the case for the corresponding integral equation formulation, which breaks down at certain frequencies known as irregular frequencies or fictitious frequencies. This problem is completely nonphysical because there are no eigenvalues for the exterior problems. Schenck¹ proposed a Combined Helmholtz Interior integral Equation Formulation (CHIEF) method, which is easy to implement and is efficient but still has some drawbacks. A review article by Benthien and Schenck² is referenced. In the case of a fictitious frequency, the resulting coefficient matrix for the exterior acoustic problems becomes singular or ill-conditioned. This means that the boundary integral equations are not linearly independent and the matrix is rank deficient. In order to determine a unique solution, additional constraints for the system of equations are required. The missing constraints or equations can be found by applying the integral equation on a number of points located outside of the domain of interest. When these equations are added to the system of equations, we have an overdetermined system of equations which can be

solved in a least-squares sense. Schenck¹ introduced this method and proved that the resulting solution is unique. But, how can we decide where to place the interior points efficiently and how many numbers of extra equations are needed? When an interior point is placed on the node of the associated interior nodes in CHIEF, it will not add an effective constraint to the system of equations, i.e., the extra equation is not linearly independent. For a general geometry, these nodal lines are not known *a priori* and this has been one of the difficulties of this method. Particularly, the problem becomes worse for the high frequency range. Wu *et al.*³ introduced a method called CHIEF-block, in which the interior integral equation is satisfied in a weighted residual sense over a small region, called blocks, instead of discrete points. Since the interior eigensolutions cannot have a nodal block, this technique is effective. Juhl⁴ and Poulin⁵ proposed the CHIEF method in conjunction with the singular value decomposition (SVD) technique. This method is easy and efficient and produces a unique solution for the exterior problem.

For interior problems, eigensolutions are often encountered not only in vibration problems but also in acoustics. Since exact solutions are not always available, numerical methods are needed. Based on the complex-valued boundary element method (BEM),⁶ the eigenvalues and eigenmodes can be determined. Nevertheless, complex computation is time consuming and not simple. To avoid complex computation, Nowak and Neves⁷ proposed a multiple reciprocity method (MRM) in real-domain computation only. Tai and

^{a)} Author to whom correspondence should be addressed; electronic mail: jtchen@mail.ntou.edu.tw

Shaw⁸ employed only real-part kernels to solve the eigenproblem. A simplified method using only the real-part or imaginary-part kernel was also presented by De Mey.⁹ Although De Mey found that the zeros for a real-part determinant may be different from those for an imaginary-part determinant, the spurious solutions are not discovered if only a real-part formulation is employed. For a membrane vibration problem, Hutchinson¹⁰ also employed real-part kernels to solve the membrane vibration. He found the spurious modes and proposed a filtering-out technique by examining the modal shapes. However, this technique may fail in some cases discussed by Chen *et al.*^{11–13} This method using only the real-part BEM was later found to be equivalent to the multiple reciprocity method (MRM) if the zeroth-order fundamental solution in the MRM is properly chosen.¹³ Chen and Wong¹⁴ found that the MRM also results in spurious eigensolutions for one-dimensional examples. Numerical experiments using only the real-part kernels¹⁵ were performed for a two-dimensional case. The spurious solutions in MRM^{16–18} and real-part BEM¹⁹ were filtered out using the SVD technique. The relations among the conventional MRM, complete MRM, real-part BEM, and complex-valued BEM were discussed by Chen.¹³ It is obvious that one advantage of using only the real-part kernels is that real-valued computation is considered instead of complex-valued computation as used in the complex-valued BEM. Another benefit is that the lengthy derivation for the MRM can be avoided. However, two drawbacks of the real formulation have been found to be the occurrence of spurious eigenvalues as mentioned in Refs. 14–16 and 19, and the failure when it is applied to problems with a degenerate boundary. To deal with those two problems, the framework of a real-part dual BEM was constructed to filter out the spurious eigenvalues and to avoid the nonunique solution for problems with a degenerate boundary at the same time. As for the latter problem, the dual formulation²⁰ is a key step method to solve the problems with a degenerate boundary. As for the former problem, the reason why spurious eigenvalues occur in the MRM or the real-part BEM is the loss of the constraints in the imaginary part, which was investigated by Yieh *et al.*²¹ The smaller number of constraint equations makes the solution space larger. The spurious eigensolutions can be filtered out using many alternatives: e.g., the complex-valued formulation, the domain partition technique,²² and the dual formulation in conjunction with SVD.^{11,16–18} Using the dual MRM or the real-part dual BEM, spurious eigenvalues can be filtered out by checking the residue between the singular and hypersingular equations.^{14,23} Both the dual MRM method¹⁶ and the real-part dual BEM¹⁹ in conjunction with the SVD technique must calculate a $4N$ by $2N$ matrix, where $2N$ is the number of elements. In the series of work by Chen's group,^{16,19,24} the multiplicity for true eigenvalues was also determined. By employing the present CHEEF method, the missing constraints can be found again by applying the integral equations on a number of points located in the exterior domain. It is necessary to determine a matrix with only dimension $(2N+1)$ by $2N$ or $(2N+2)$ by $2N$ for CHEEF instead of $4N \times 2N$ in dual formulation.

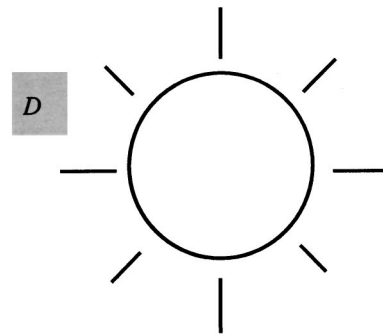


FIG. 1. The definitions of the exterior domain.

In this study, we employed the CHEEF BEM to filter out the spurious solutions for two-dimensional interior acoustic problems. The corresponding relationship between the CHIEF and CHEEF methods will be discussed. The optimum number and position for the interior points will be studied analytically and verified numerically. After assembling the CHEEF equations, an SVD technique is employed to determine the eigenvalues, multiplicity, and boundary modes. The boundary modes can be extracted easily from the right unitary matrix in SVD. Two examples for circular and rectangular domains with the Dirichlet boundary conditions are demonstrated to check the validity of the proposed method analytically and numerically.

II. REVIEW OF THE CHIEF METHOD FOR A TWO-DIMENSIONAL EXTERIOR ACOUSTIC PROBLEM USING THE SINGULAR INTEGRAL FORMULATION

Consider an acoustic problem which has the following governing equation:

$$\nabla^2 u(\mathbf{x}) + k^2 u(\mathbf{x}) = 0, \quad \mathbf{x} \in D, \quad (1)$$

where D is the domain of interest, as shown in Fig. 1, \mathbf{x} is the domain point, u is the acoustic pressure, and k is the wave number defined by the angular frequency divided by the sound speed. The boundary conditions are shown as follows:

$$u(\mathbf{x}) = \bar{u}, \quad \mathbf{x} \in B, \quad (2)$$

where B denotes the boundary enclosing D .

The acoustic field can be described using the following integral equation:²⁵

$$2\pi u(\mathbf{x}) = \int_B T(\mathbf{s}, \mathbf{x}) u(\mathbf{s}) dB(\mathbf{s}) - \int_B U(\mathbf{s}, \mathbf{x}) \frac{\partial u(\mathbf{s})}{\partial n_s} dB(\mathbf{s}), \quad \mathbf{x} \in D, \quad (3)$$

where $T(\mathbf{s}, \mathbf{x})$ is defined using

$$T(\mathbf{s}, \mathbf{x}) \equiv \frac{\partial U(\mathbf{s}, \mathbf{x})}{\partial n_s}, \quad (4)$$

in which n_s represents the outnormal direction at point \mathbf{s} on the boundary and $U(\mathbf{s}, \mathbf{x})$ is the fundamental solution which satisfies

$$\nabla^2 U(\mathbf{x}, \mathbf{s}) + k^2 U(\mathbf{x}, \mathbf{s}) = \delta(\mathbf{x} - \mathbf{s}), \quad \mathbf{x} \in D, \quad (5)$$

where $\delta(\mathbf{x}-\mathbf{s})$ is the Dirac delta function. By moving the field point x in Eq. (3) to the smooth boundary, the boundary integral equation for the boundary point can be obtained as follows:

$$\pi u(\mathbf{x}) = \text{C.P.V.} \int_B T(\mathbf{s}, \mathbf{x}) u(\mathbf{s}) dB(\mathbf{s}) - \text{R.P.V.} \int_B U(\mathbf{s}, \mathbf{x}) \frac{\partial u(\mathbf{s})}{\partial n_s} dB(\mathbf{s}), \quad \mathbf{x} \in B, \quad (6)$$

where C.P.V. is the Cauchy principal value and R.P.V. is the Riemann principal value. By moving the point x from the exterior domain (D^e) to the interior domain (D^i), the boundary integral equation for the interior point can be obtained as follows:

$$0 = \int_B T(\mathbf{s}, \mathbf{x}) u(\mathbf{s}) dB(\mathbf{s}) - \int_B U(\mathbf{s}, \mathbf{x}) \frac{\partial u(\mathbf{s})}{\partial n_s} dB(\mathbf{s}), \quad \mathbf{x} \in D^i. \quad (7)$$

After Eq. (7) is added to Eq. (6), we can produce an overdetermined system of equations.

By discretizing the boundary B into the boundary elements in Eq. (6), we have the algebraic system as follows:

$$\pi\{u\} = [T]\{u\} - [U]\{t\}, \quad (8)$$

where $t = \partial u(\mathbf{s})/\partial n_s$, and the $[U]$ and $[T]$ matrices are the corresponding influence coefficient matrices resulting from the U and T kernels, respectively. The detailed derivation can be found in Refs. 15 and 23. Equation (8) can be rewritten as

$$[\bar{T}]\{u\} = [U]\{t\}, \quad (9)$$

where $[\bar{T}] = [T] - \pi[I]$. For simplicity, the Dirichlet radiation problem, i.e., $\{u\} = \bar{u}$ is considered in Eq. (9). Therefore, we obtain the following equation:

$$[U]\{t\} = [\bar{T}]\{\bar{u}\}. \quad (10)$$

We can rewrite the singular equations as follows:

$$[U^B(k)]_{2N \times 2N} \{t\}_{2N \times 1} = \{q_1\}_{2N \times 1}, \quad (11)$$

where the superscript B denotes the boundary, and $\{q_1\} = [\bar{T}]\{\bar{u}\}$ and $2N$ is the number of boundary elements. Similarly, discretization of Eq. (7) can have

$$[U^I(k)]_{a \times 2N} \{t\}_{2N \times 1} = \{q_2\}_{a \times 1}, \quad (12)$$

where $\{q_2\} = [T]\{\bar{u}\}$, subscript a indicates the number of additional interior points and the number of selected points $a \geq 1$, and superscript I denotes the interior domain. We can merge the two matrices in Eqs. (11) and (12) together to obtain an overdetermined system

$$[C(k)]_{(2N+a) \times 2N} \{u\}_{2N \times 1} = \{q\}_{(2N+a) \times 1}, \quad (13)$$

where $\{q\}$ is assembled by $\{q_1\}$ and $\{q_2\}$, the $[C(k)]$ matrix is composed by the $[U^B]$ and $[U^I]$ matrices as shown below

$$[C(k)]_{(2N+a) \times 2N} = \begin{bmatrix} U^B(k) \\ U^I(k) \end{bmatrix} \quad (14)$$

for the Dirichlet problem. Therefore, an over-determined

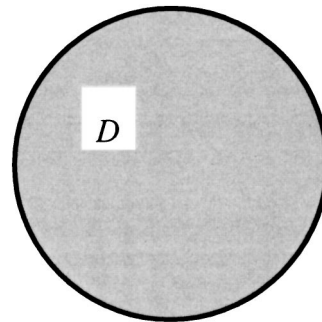


FIG. 2. The definitions of interior domain.

system is obtained to ensure a unique solution. Similarly, we can extend the Dirichlet problem to the Neumann problem.

III. REVIEW OF THE REAL-PART DUAL BEM FOR A TWO-DIMENSIONAL INTERIOR ACOUSTIC PROBLEM

According to the findings by Yeih *et al.*²¹ and Kamiya *et al.*,²⁶ the series forms of the kernels in the MRM are no more than the real parts of the closed-form kernels in the complex-valued BEM. The closed-form kernels for the real-part of BEM are shown below

$$U(\mathbf{s}, \mathbf{x}) = \frac{\pi Y_0(kr)}{2}, \quad (15)$$

$$T(\mathbf{s}, \mathbf{x}) = \frac{k\pi}{2} Y_1(kr) \frac{y_i n_i}{r}, \quad (16)$$

where $Y_n(kr)$ denotes the second-order kind Bessel function with order n , n_i denote the i th components of the normal vectors at \mathbf{s} , and $y_i = s_i - x_i$.

In order to filter out the spurious eigenvalues, Chen and Wong¹⁴ developed the dual method by taking the normal derivative of the first equation [Eq. (3)]. The second equation of the dual boundary integral equation for the domain point x can be derived as follows:

$$2\pi \frac{\partial u(\mathbf{x})}{\partial n_x} = \int_B M(\mathbf{s}, \mathbf{x}) u(\mathbf{s}) dB(\mathbf{s}) - \int_B L(\mathbf{s}, \mathbf{x}) \frac{\partial u(\mathbf{s})}{\partial n_s} dB(\mathbf{s}), \quad \mathbf{x} \in D, \quad (17)$$

where D is the domain of interest as shown in Fig. 2, and

$$L(\mathbf{s}, \mathbf{x}) \equiv \frac{\partial U(\mathbf{s}, \mathbf{x})}{\partial n_x}, \quad (18)$$

$$M(\mathbf{s}, \mathbf{x}) \equiv \frac{\partial^2 U(\mathbf{s}, \mathbf{x})}{\partial n_x \partial n_s}, \quad (19)$$

in which n_x represents the outnormal direction at point \mathbf{x} . For the real-part BEM, the closed forms for the L and M kernels are shown below

$$L(\mathbf{s}, \mathbf{x}) = \frac{-k\pi}{2} Y_1(kr) \frac{y_i \bar{n}_i}{r}, \quad (20)$$

$$M(\mathbf{s}, \mathbf{x}) = \frac{k\pi}{2} \left\{ -k \frac{Y_2(kr)}{r^2} y_i y_j n_i \bar{n}_j + \frac{Y_1(kr)}{r} n_i \bar{n}_i \right\}. \quad (21)$$

By moving the field point x in Eq. (17) to the smooth boundary, the boundary integral equations for the boundary point can be obtained as follows:

$$\pi \frac{\partial u(\mathbf{x})}{\partial n_{\mathbf{x}}} = \text{H.P.V.} \int_B M(\mathbf{s}, \mathbf{x}) u(s) dB(\mathbf{s}) - \text{C.P.V.} \int_B L(\mathbf{s}, \mathbf{x}) \frac{\partial u(\mathbf{s})}{\partial n_{\mathbf{s}}} dB(\mathbf{s}), \quad \mathbf{x} \in B, \quad (22)$$

where H.P.V. is the Hadamard (Mangler) principal value. By moving the interior point x to the exterior domain, the boundary integral equations for the exterior point can be obtained as follows:

$$0 = \int_B M(\mathbf{s}, \mathbf{x}) u(s) dB(\mathbf{s}) - \int_B L(\mathbf{s}, \mathbf{x}) \frac{\partial u(\mathbf{s})}{\partial n_{\mathbf{s}}} dB(\mathbf{s}), \quad \mathbf{x} \in D^e. \quad (23)$$

By discretizing the boundary B into boundary elements in Eq. (6) and Eq. (22), we have the dual algebraic system as follows:

$$\pi \{u\} = [T] \{u\} - [U] \{t\}, \quad (24)$$

$$\pi \{t\} = [M] \{u\} - [L] \{t\}, \quad (25)$$

where the $[U]$, $[T]$, $[L]$, and $[M]$ matrices are the corresponding influence coefficient matrices resulting from the U , T , L , and M kernels, respectively. Equation (24) and Eq. (25) can be rewritten as

$$[\bar{T}] \{u\} = [U] \{t\}, \quad (26)$$

$$[\bar{L}] \{t\} = [M] \{u\}, \quad (27)$$

where $[\bar{T}] = [T] - \pi[I]$ and $[\bar{L}] = [L] + \pi[I]$. For the Neumann problem, the eigenequation obtained from the UT and LM equations in Eqs. (26) and (27) can be rewritten as

$$[\bar{T}(k)]_{2N \times 2N} \{u\}_{2N \times 1} = \{0\}, \quad (28)$$

$$[M(k)]_{2N \times 2N} \{u\}_{2N \times 1} = \{0\}. \quad (29)$$

By employing the real-part dual BEM, we merge the two matrices in Eqs. (28) and (29) together to obtain an overdetermined system

$$[A(k)]_{4N \times 2N} \{u\}_{2N \times 1} = \{0\}, \quad (30)$$

where the $[A(k)]$ matrix is assembled by the $[\bar{T}]$ and $[M]$ matrices as shown below:

$$[A(k)]_{4N \times 2N} = \begin{bmatrix} \bar{T}(k) \\ M(k) \end{bmatrix} \quad (31)$$

for the Neumann problem. Also, an overdetermined system is obtained. Similarly, we can extend the Neumann problem to the Dirichlet problem. To distinguish spurious eigenvalues, we can use the SVD technique.¹⁶⁻¹⁹ Using the real-part dual BEM, spurious eigenvalues can be filtered out. The main advantage of this method is that it can solve problems

in the real domain. However, the dimension of $[A]$ is $4N$ by $2N$. To reduce the dimension, the CHEEF method is proposed in the following section.

IV. THE CHEEF METHOD FOR AN INTERIOR TWO-DIMENSIONAL ACOUSTIC PROBLEM IN CONJUNCTION WITH SVD TECHNIQUE

Based on the concept of the CHIEF method, we extend the CHIEF for exterior problems to the CHEEF method for interior problems. Since only the real-part formulation (MRM or real-part BEM) is of concern, one approach to obtaining enough constraints for the eigenequation instead of obtaining the imaginary part of the complex-valued formulation is to derive additional equations on exterior points. This method is similar to the CHIEF method. For simplicity, we will deal with the Dirichlet problem. Therefore, we can obtain the following equation:

$$[U(k)] \{t\} = \{0\}. \quad (32)$$

Now, we present a more efficient way to filter out spurious eigenvalues which can avoid determining the spurious boundary mode in advance. We can rewrite the singular equation and additional equations by collocating on the exterior points, as follows:

$$[U^B(k)]_{2N \times 2N} \{t\}_{2N \times 1} = \{0\}, \quad (33)$$

$$[U^E(k)]_{a \times 2N} \{t\}_{2N \times 1} = \{0\}, \quad (34)$$

where the number of selected points $a \geq 1$ and E denote the exterior domain, respectively. To filter out spurious eigenvalues using the SVD technique, we can merge the two matrices in Eqs. (33) and (34) together to obtain an overdetermined system

$$[G(k)]_{(2N+a) \times 2N} \{t\}_{2N \times 1} = \{0\}, \quad (35)$$

where the $[G(k)]$ matrix with dimension $(2N+a)$ by $2N$ instead of $4N$ by $2N$ in Eq. (30), is derived from the $[U^B]$ an additional $[U^E]$ matrix as shown below

$$[G(k)]_{(2N+a) \times 2N} = \begin{bmatrix} U^B(k) \\ U^E(k) \end{bmatrix}_{(2N+a) \times 2N} \quad (36)$$

for the Dirichlet problem.

Even though the $[G(k)]$ matrix has dependent rows resulting from the degenerate boundary, the SVD technique can still be employed to find all the true eigenvalues since enough constraints are imbedded in the overdetermined matrix, $[G(k)]$. As for the true eigenvalues, the rank of the $[G(k)]$ matrix with dimension $(2N+a)$ by $2N$ must be at most $2N-1$ to have a nontrivial solution. As for the spurious eigenvalues, the rank must be $2N$ to obtain a trivial solution. Based on this criterion, the SVD technique can be employed to detect the true eigenvalues by checking whether or not the first minimum singular value, σ_1 , is zero. Since discretization creates errors, very small values for σ_1 , but not exactly zeros, will be obtained when k is near the critical wave number. In order to avoid determining the threshold for the zero numerically, a value of σ_1 closer to zero must be obtained using a smaller increment near the critical wave

number, k . Such a value is confirmed to be a true eigenvalue. For the true eigenvalues with multiplicity of 2, we can consider the eigenvalues which make $\sigma_2=0$ and $\sigma_1=0$ at the same k value.

Since Eq. (36) is overdetermined, we will consider a linear algebra problem with more equations than unknowns

$$[\mathbf{A}]_{m \times n} \{\mathbf{x}\}_{n \times 1} = \{\mathbf{b}\}_{m \times 1}, \quad m > n, \quad (37)$$

where m is the number of equations, n is the number of unknowns, and $[\mathbf{A}]$ is the leading matrix, which can be decomposed into

$$[\mathbf{A}]_{m \times n} = [\mathbf{U}]_{m \times m} [\mathbf{\Sigma}]_{m \times n} [\mathbf{V}]_{n \times n}^*, \quad (38)$$

where $[\mathbf{U}]$ is a left unitary matrix constructed by the left singular vectors ($\mathbf{u}_1, \mathbf{u}_2, \mathbf{u}_3, \dots, \mathbf{u}_m$), $[\mathbf{\Sigma}]$ is a diagonal matrix which has singular values $\sigma_1, \sigma_2, \dots$, and σ_n allocated in a diagonal line as

$$[\mathbf{\Sigma}] = \begin{bmatrix} \sigma_n & \cdots & 0 \\ \vdots & \ddots & \vdots \\ 0 & \cdots & \sigma_1 \\ 0 & \cdots & 0 \\ 0 & \cdots & 0 \end{bmatrix}, \quad m > n, \quad (39)$$

in which $\sigma_n \geq \sigma_{n-1} \geq \dots \geq \sigma_1$ and $[\mathbf{V}]^*$ is the complex conjugate transpose of a right unitary matrix constructed by the right singular vectors ($\mathbf{v}_1, \mathbf{v}_2, \mathbf{v}_3, \dots, \mathbf{v}_m$). As we can see in Eq. (39), there exist at most n nonzero singular values. This means that we can find at most n linear independent equations in the system of equations. If we have p zero singular values ($0 \leq p \leq n$), this means that the rank of the system of equations is equal to $n - p$. However, the singular value may be very close to zero numerically, resulting in rank deficiency. For a general eigenproblem as shown in this paper, the $[G(k)]$ matrix with dimension $(2N + a)$ by $2N$ will have a rank of $2N - 1$ for the true eigenvalue with multiplicity 1 and $\sigma_1 = 0$, theoretically. For the true eigenvalues with multiplicity Q , the rank of $[G(k)]$ will be reduced to $2N - Q$ in which $\sigma_1, \sigma_2, \dots$, and σ_Q are zeros, theoretically. In other words, the matrix has a nullity of Q . In the case of spurious eigenvalues, the rank for the $[G(k)]$ matrix is $2N$, and the minimum singular value is not zero. Determining the eigenvalues of the system of equations has now been transformed into finding the values of k which make the rank of the leading coefficient matrix smaller than $2N$. This means that when $m = 2N + a, n = 2N$ and $\mathbf{b}_{(2N+a) \times 1} = \mathbf{0}$, the eigenvalues will make $p \geq 1$, such that the minimum singular values must be zero or very close to zero. Since we have employed the SVD technique to filter out the spurious eigenvalues, we can obtain the boundary mode by extracting the right unitary vector in SVD.

According to the definition of SVD, we have

$$[\mathbf{A}] \mathbf{v}_p = \sigma_p \mathbf{u}_p, \quad p = 1, 2, 3, \dots, n, \quad (40)$$

where \mathbf{u} and \mathbf{v} are the left and right unitary vectors, respectively. By choosing the q th zero singular value, σ_q , and substituting the q th right eigenvector, \mathbf{v}_q , into Eq. (40), we have

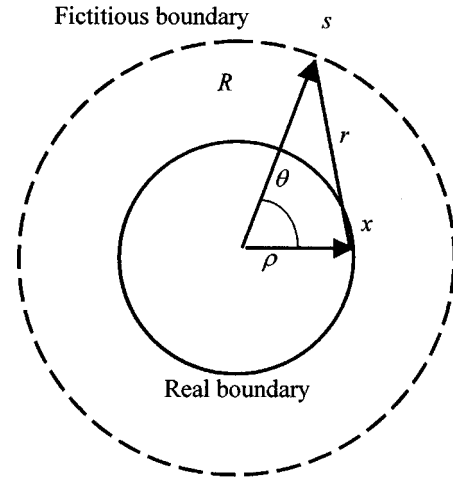


FIG. 3. The definitions of ρ , θ , R , and r .

$$[\mathbf{A}] \mathbf{v}_q = 0 \mathbf{u}_q = \mathbf{0}, \quad q = 1, 2, 3, \dots, Q. \quad (41)$$

According to Eq. (41), the nontrivial boundary mode is found to be the column vector of \mathbf{v}_q in the right unitary matrix.

When we take all of the $2N + a$ equations into account, these apparently cause the rank of the leading coefficient matrix to be equal to $2N - 1$ for the true eigenvalue with multiplicity 1. The boundary modes can be obtained from the $[\mathbf{V}]$ matrix in Eq. (38) using SVD. Another advantage for using SVD is that it can determine the multiplicities for the true eigenvalues by finding the number of successive zeros in the singular values.

V. ANALYTICAL STUDY OF THE FAILURE POINTS IN THE CHEEF METHOD

In Refs. 27–29, the real-part U kernel can be expanded into

$$U(\mathbf{s}, \mathbf{x}) = \frac{\pi}{2} Y_0(kr) = \frac{\pi}{2} Y_0(k \sqrt{R^2 + \rho^2 - 2R\rho \cos \theta}), \quad (42)$$

where $\mathbf{x} = (\rho, \phi)$ and $\mathbf{s} = (R, \theta)$, ρ , r , R , and θ are shown in Fig. 3. Since \mathbf{x} and \mathbf{s} are on the boundaries of radius ρ and R , respectively, $U(\mathbf{s}, \mathbf{x})$ can be expanded into degenerate form as follows:

$$U(\mathbf{s}, \mathbf{x}) = \begin{cases} U(\theta, 0) = \sum_{n=-\infty}^{n=\infty} \frac{\pi}{2} Y_n(kR) J_n(k\rho) \cos(n\theta), & R > \rho, \\ U(\theta, 0) = \sum_{n=-\infty}^{n=\infty} \frac{\pi}{2} Y_n(k\rho) J_n(kR) \cos(n\theta), & R < \rho, \end{cases} \quad (43)$$

where the source point \mathbf{s} and field point $\mathbf{x} (\phi = 0)$ in the two-point function is separated and $J_n(k\rho)$ is the n th order Bessel function of the first kind. Equation (43) can also be obtained through the addition theorem for the Hankel function. By superimposing $2N$ constant source distribution $\{\bar{t}\}$ along the fictitious boundary with radius R and collocating the $2N$ points on the boundary with radius ρ , we have

$$[U]\{\bar{t}\} = \begin{bmatrix} a_0 & a_1 & a_2 & \cdots & a_{2N-2} & a_{2N-1} \\ a_{2N-1} & a_0 & a_1 & \cdots & a_{2N-3} & a_{2N-2} \\ a_{2N-2} & a_{2N-1} & a_0 & \cdots & a_{2N-4} & a_{2N-3} \\ \vdots & \vdots & \vdots & \ddots & \vdots & \vdots \\ a_1 & a_2 & a_3 & \cdots & a_{2N-1} & a_0 \end{bmatrix} \times \begin{bmatrix} \bar{t}_0 \\ \bar{t}_1 \\ \bar{t}_2 \\ \vdots \\ \bar{t}_{2N-1} \end{bmatrix} = \{0\} \quad (44)$$

for the Dirichlet problem, where \bar{t}_j is the fictitious density of single layer potential distributed on the boundary with radius R , and $[U]$ is the influence matrix with the elements shown below

$$a_m = \int_{(m-1/2)\Delta\theta}^{(m+1/2)\Delta\theta} U(\theta,0)R d\theta \approx U(\theta_m,0)R\Delta\theta, \quad m=0,1,2, \dots, 2N-1, \quad (45)$$

where $\Delta\theta = 2\pi/2N$ and $\theta_m = m\Delta\theta$.

The matrix $[U]$ in Eq. (44) is found to be a circulant since rotation the symmetry for the influence coefficients is considered. By introducing the following bases for the circulants $I, C_{2N}^1, C_{2N}^2, \dots, C_{2N}^{2N-1}$, we can expand $[U]$ into

$$[U] = a_0 I + a_1 C_{2N}^1 + a_2 C_{2N}^2 + \cdots + a_{2N-1} C_{2N}^{2N-1}, \quad (46)$$

where I is a unit matrix and

$$C_{2N} = \begin{bmatrix} 0 & 1 & 0 & \cdots & 0 & 0 \\ 0 & 0 & 1 & \cdots & 0 & 0 \\ \vdots & \vdots & \vdots & \ddots & \vdots & \vdots \\ 0 & 0 & 0 & \cdots & 0 & 1 \\ 1 & 0 & 0 & \cdots & 0 & 0 \end{bmatrix}_{2N \times 2N}. \quad (47)$$

Based on the theory of circulants,³⁰ the spectral properties for the influence matrices, U , can be easily found as follows:

$$\lambda_l = a_0 + a_1 \alpha_l + a_2 \alpha_l^2 + \cdots + a_{2N-1} \alpha_l^{2N-1}, \quad l=0, \pm 1, \pm 2, \dots, \pm(N-1), N, \quad (48)$$

where λ_l and α_l are the eigenvalues for $[U]$ and $[C_{2N}]$, respectively. It is easily found that the eigenvalues for the circulants $[C_{2N}]$ are the roots for $z^{2N} = 1$ as shown below

$$\alpha_n = e^{i(2\pi n/2N)}, \quad n=0, \pm 1, \pm 2, \dots, \pm(N-1), N \quad \text{or } n=0, 1, 2, \dots, 2N-1, \quad (49)$$

and the eigenvectors are

$$\{\phi_n\} = \begin{Bmatrix} 1 \\ \alpha_n \\ \alpha_n^2 \\ \alpha_n^3 \\ \vdots \\ \alpha_n^{2N-1} \end{Bmatrix}. \quad (50)$$

Substituting Eq. (49) into Eq. (48), we have

$$\lambda_l = \sum_{m=0}^{2N-1} a_m \alpha_l^m = \sum_{m=0}^{2N-1} a_m e^{i(2\pi/2N)ml} \quad l=0, \pm 1, \pm 2, \dots, \pm(N-1), N. \quad (51)$$

According to the definition for a_m in Eq. (45), we have

$$a_m = a_{2N-m}, \quad m=0, 1, 2, \dots, 2N-1. \quad (52)$$

Substituting Eq. (52) into Eq. (51), we have

$$\lambda_l = a_0 + (-1)^l a_N + \sum_{m=1}^{N-1} (\alpha_l^m + \alpha_l^{2N-m}) a_m = \sum_{m=0}^{2N-1} \cos(ml\Delta\theta) a_m. \quad (53)$$

Substituting Eq. (45) into Eq. (53), we have

$$\lambda_l \approx \sum_{m=0}^{2N-1} \cos(ml\Delta\theta) U(m\Delta\theta, 0) R \Delta\theta = \int_0^{2\pi} \cos(l\theta) U(\theta, 0) R d\theta, \quad (54)$$

as N approaches infinity. Equation (54) reduces to

$$\lambda_l = \int_0^{2\pi} \cos(l\theta) \sum_{m=-\infty}^{\infty} \frac{\pi}{2} Y_m(kR) J_m(k\rho) \cos m\theta R d\theta = \pi^2 R Y_l(kR) J_l(k\rho). \quad (55)$$

Since the wave number k is imbedded in each element of the $[U]$ matrix, the eigenvalues for $[U]$ are also functions of k . Finding the eigenvalues for the Helmholtz equation or finding the zeros for the determinant of $[U]$ is equal to finding the zeros for the multiplication of all of the eigenvalues of $[U]$. Based on the following equation:

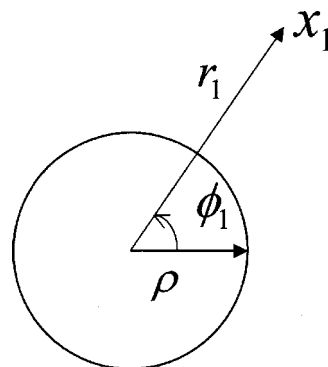


FIG. 4. One sample point.

TABLE I. Zeros of Bessel function for $J_n(k)$ and $Y_n(k)$.

	1	2	3	4	5
$J_0(k)=0$	2.404 8	5.520 1	8.653 7	11.791 5	14.930 9
$J_1(k)=0$	3.831 71	7.015 59	10.173 46	13.323 7	16.4706
$J_2(k)=0$	5.135 6	8.417 2	11.619 8	14.796 0	17.959 8
$J_3(k)=0$	6.380 16	9.760 12	13.015 2	16.223 46	19.409 41
$J_4(k)=0$	7.588 34	11.064 7	14.372 5	17.616 0	20.826 9
$J_5(k)=0$	8.771 48	12.338 6	15.700 2	18.980 1	22.217 8
$Y_0(k)=0$	0.893 58	3.957 68	7.086 05	10.222 34	13.361 10
$Y_1(k)=0$	2.197 14	5.429 68	8.596 01	11.749 15	14.897 44
$Y_2(k)=0$	3.384 24	6.793 81	10.023 48	13.209 99	16.378 97
$Y_3(k)=0$	4.527 02	8.097 75	11.396 47	14.623 07	17.818 45
$Y_4(k)=0$	5.645 15	9.361 62	12.730 1	15.999 6	19.224 4
$Y_5(k)=0$	6.747 18	10.597 2	14.033 8	17.347 1	20.602 9

$$\det[U] = \lambda_0 \lambda_N (\lambda_1 \lambda_2 \cdots \lambda_{N-1}) (\lambda_{-1} \lambda_{-2} \cdots \lambda_{-(N-1)}), \quad (56)$$

the possible eigenvalues (true or spurious) occur at

$$Y_l(kR)J_l(k\rho) = 0, \quad l = 0, \pm 1, \pm 2, \dots, \pm(N-1), N. \quad (57)$$

The k values satisfying Eq. (57) may be spurious eigenvalue or true eigenvalue. Here, we adopted the CHIEF method concept to filter out the spurious eigenvalues.

If we adopt one exterior point (r_1, ϕ_1) , where $r_1 > \rho$ as shown in Fig. 4, we have

$$0 = \int_B U(s, x) t(s) dB(s) = [w_1^T] \{t\}, \quad (58)$$

where $[w_1^T] = (w_1^1, w_1^2, w_1^3, \dots, w_1^{2N})$ is the row vector of the influence matrix by collocating the exterior point x_1 . Combining Eq. (44) and Eq. (58), we obtain an overdetermined system

$$\begin{bmatrix} U(k) \\ w_1^T(k) \end{bmatrix} \{t\} = \{0\}, \quad (59)$$

where $\{t\} = \{1, e^{in\Delta\theta}, e^{in2\Delta\theta}, \dots, e^{in(2N-1)\Delta\theta}\}^T$.

The additional constraint $[w_1^T] \{t\} = 0$ provide the discriminant, Δ , to be

$$\Delta = [w_1^T] \{t\} = \pi^2 r_1 Y_n(kr_1) J_n(k\rho) e^{in\phi_1} = 0. \quad (60)$$

For the single spurious eigenvalues $k_{0,m}^s$, we have $Y_0(k_{0,m}^s) = 0$, where the superscript s denotes the spurious eigenvalues and $k_{0,m}$ denotes the m th zeros for the Y_0 function [zeros of the Bessel function for $J_n(k)$ and $Y_n(k)$ are shown in Table I]. If the selected exterior point (r_1, ϕ_1) , satisfies

$$k_{0,m}^s r_1 = k_{0,p} \quad (m < p), \quad (61)$$

where $k_{0,p}$ denotes the p th zeros for the Y_0 function, then the spurious eigenvalues $k_{0,m}^s$ cannot be filtered out. For the double spurious eigenvalues $k_{n,m}^s$, we have $Y_n(k_{n,m}^s) = 0, n > 0$. If the selected exterior point (r_1, ϕ_1) , satisfies

$$k_{n,m}^s r_1 = k_{n,p} \quad (m < p), \quad (62)$$

then the spurious eigenvalues $k_{n,m}^s$, cannot be filtered out. The possible failure positions for r_1 are shown in Table II. When the spurious eigenvalues are double roots, rank reduces by 2. One point provides at most one constraint. One point cannot filter out the double spurious roots, so an additional independent equation is required by adding one more point.

If we adopt another exterior point (r_2, ϕ_2) with a radial distance $r_2 > \rho$ as shown in Fig. 5, and combine with Eq. (59), we have

$$\begin{bmatrix} U(k) \\ w_1^T(k) \\ w_2^T(k) \end{bmatrix} \{t\} = \{0\}, \quad (63)$$

where $[w_2^T] = (w_2^1, w_2^2, w_2^3, \dots, w_2^{2N})$ is the row vector of the influence matrix by collocating the exterior point x_2 . When the spurious eigenvalues are double roots, we have

$$\begin{bmatrix} w_1^T(k) \\ w_2^T(k) \end{bmatrix} \{t\} = \begin{bmatrix} w_1^T \\ w_2^T \end{bmatrix} \{\alpha t_1 + \beta t_2\} = \begin{bmatrix} w_1^T t_1 & w_1^T t_2 \\ w_2^T t_1 & w_2^T t_2 \end{bmatrix} \begin{Bmatrix} \alpha \\ \beta \end{Bmatrix}, \quad (64)$$

where $\{t_1\} = \{1, e^{in\Delta\theta}, e^{in2\Delta\theta}, \dots, e^{in(2N-1)\Delta\theta}\}^T$ and $\{t_2\} = \{1, e^{-in\Delta\theta}, e^{-in2\Delta\theta}, \dots, e^{-in(2N-1)\Delta\theta}\}^T$ are two independent boundary modes, α and β are two constants, and

$$\begin{aligned} w_1^T t_1^T &= \pi^2 r_1 Y_n(kr_1) J_n(k\rho) e^{in\phi_1}, \\ w_1^T t_2^T &= \pi^2 r_1 Y_n(kr_1) J_n(k\rho) e^{-in\phi_1}, \\ w_2^T t_1^T &= \pi^2 r_2 Y_n(kr_2) J_n(k\rho) e^{in\phi_2}, \\ w_2^T t_2^T &= \pi^2 r_2 Y_n(kr_2) J_n(k\rho) e^{-in\phi_2}. \end{aligned}$$

Since the spurious double roots make the rank less than 2, the additional two points must provide independent constraints, as follows:

$$\begin{bmatrix} \pi^2 r_1 Y_n(kr_1) J_n(k\rho) e^{in\phi_1} & \pi^2 r_1 Y_n(kr_1) J_n(k\rho) e^{-in\phi_1} \\ \pi^2 r_2 Y_n(kr_2) J_n(k\rho) e^{in\phi_2} & \pi^2 r_2 Y_n(kr_2) J_n(k\rho) e^{-in\phi_2} \end{bmatrix} \begin{bmatrix} \alpha \\ \beta \end{bmatrix} = 0. \quad (65)$$

TABLE II. The failure points with difference radial circular.

Failure point				
$Y_{0,1}$	3.96/0.89=4.429	7.09/0.89=7.97	10.22/0.89=11.48	13.36/0.89=15.01
$Y_{0,2}$	7.09/3.96=1.79	10.22/3.96=2.58	13.36/3.96=3.37	
$Y_{0,3}$	10.22/7.09=1.44	13.36/7.09=1.88		
$Y_{1,1}$	5.43/2.2=2.47	8.6/2.2=3.91	11.75/2.2=5.34	14.9/2.2=6.77
$Y_{1,2}$	8.6/5.43=1.58	11.75/5.43=2.16	14.9/5.43=2.74	
$Y_{1,3}$	11.75/8.6=1.37	14.9/8.6=1.73		
$Y_{2,1}$	6.79/3.38=2.007	10.02/3.38=2.96	13.21/3.38=3.91	16.38/3.38=4.85
$Y_{2,2}$	10.02/6.79=1.48	13.21/6.79=1.94	16.38/6.79=2.41	
$Y_{2,3}$	13.21/10.02=1.32	16.38/10.02=1.63		
$Y_{3,1}$	8.1/4.53=1.79	11.4/4.53=2.52	14.62/4.53=3.23	17.82/4.53=3.93
$Y_{3,2}$	11.4/8.1=1.41	14.62/8.1=1.80	17.82/8.1=2.2	
$Y_{3,3}$	14.62/11.4=1.28	17.82/11.4=1.56		
$Y_{4,1}$	9.36/5.64=1.66	12.73/5.64=2.26	16/5.64=2.84	19.22/5.64=3.41
$Y_{4,2}$	12.73/9.36=1.36	16.0/9.36=1.71	19.22/9.36=2.05	
$Y_{4,3}$	16.0/12.73=1.26	19.22/12.73=1.51		
$Y_{5,1}$	10.6/6.75=1.57	14.03/6.75=2.08	17.35/6.75=2.57	20.6/6.75=3.05
$Y_{5,2}$	14.03/10.6=1.32	17.35/10.6=1.64	20.6/10.6=1.94	
$Y_{5,3}$	17.35/14.03=1.24	20.6/14.03=1.47		

If they are dependent, we have

$$\Delta = \det \begin{vmatrix} \pi^2 r_1 Y_n(kr_1) J_n(k\rho) e^{in\phi_1} & \pi^2 r_1 Y_n(kr_1) J_n(k\rho) e^{-in\phi_1} \\ \pi^2 r_2 Y_n(kr_2) J_n(k\rho) e^{in\phi_2} & \pi^2 r_2 Y_n(kr_2) J_n(k\rho) e^{-in\phi_2} \end{vmatrix}$$

$$= r_1 r_2 Y_n(kr_1) Y_n(kr_2) J_n(k\rho) J_n(k\rho) (e^{in(\phi_1 - \phi_2)} - e^{-in(\phi_1 - \phi_2)}) = i 2 r_1 r_2 Y_n(kr_1) Y_n(kr_2) J_n(k\rho) J_n(k\rho) \sin(n\phi) = 0, \tag{66}$$

where $\phi = \phi_1 - \phi_2$ indicates the intersecting angle between the two exterior points. The discriminant Δ indicates

- (1) If the two points with the intersection angle ϕ produce $\sin(n\phi) = \sin(\pi) = 0$, i.e., $\phi = \pi/n$, we will fail to filter out the double spurious roots for Y_n , $n \geq 1$.
- (2) If the two points produce $Y_n(kr_1) = 0$ or $Y_n(kr_2) = 0$, $n = 1, 2, 3, \dots$, then we will fail to filter out the double spurious root of Y_n .
- (3) No more than two points are needed if the points are properly chosen.

For the Neumann problem

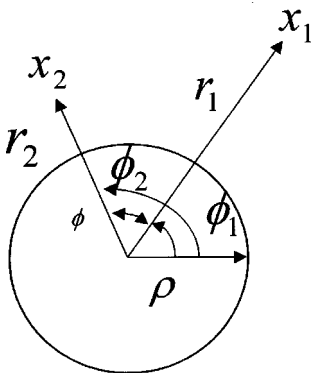


FIG. 5. Two sample points.

$$[T]\{\bar{u}\} = \begin{bmatrix} b_0 & b_1 & b_2 & \cdots & b_{2N-2} & b_{2N-1} \\ b_{2N-1} & b_0 & b_1 & \cdots & b_{2N-3} & b_{2N-2} \\ b_{2N-2} & b_{2N-1} & b_0 & \cdots & b_{2N-4} & b_{2N-3} \\ \vdots & \vdots & \vdots & \ddots & \vdots & \vdots \\ b_1 & b_2 & b_3 & \cdots & b_{2N-1} & b_0 \end{bmatrix} \times \begin{bmatrix} \bar{u}_0 \\ \bar{u}_1 \\ \bar{u}_2 \\ \vdots \\ \bar{u}_{2N-1} \end{bmatrix} = 0, \tag{67}$$

where \bar{u}_j is the fictitious density of single layer potential distributed on the boundary with radius R , and the boundary mode for $\{\bar{u}\}$ is

$$\{\bar{u}\} = \{1, e^{in\Delta\theta}, e^{i2n\Delta\theta}, \dots, e^{i(2N-1)\Delta\theta}\}^T \tag{68}$$

where n denotes the n th boundary mode. The matrix $[T]$ is the influence matrix with the elements shown below

$$b_m = \int_{(m-1/2)\Delta\theta}^{(m+1/2)\Delta\theta} T(\theta, 0) R d\theta \approx T(\theta_m, 0) R \Delta\theta, \tag{69}$$

$$m = 0, 1, 2, \dots, 2N-1,$$

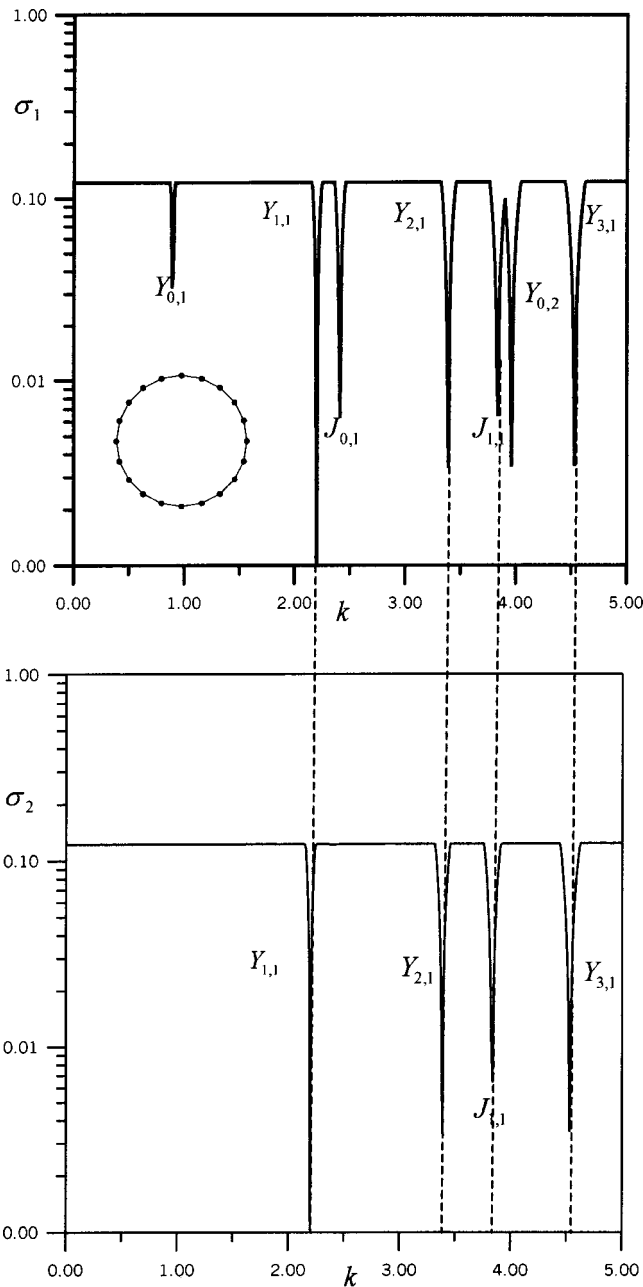


FIG. 6. The first and second minimum singular values σ_1 and σ_2 vs k of a circular subject to Dirichlet boundary conditions and boundary mesh.

where $\Delta\theta = 2\pi/2N$ and $\theta_m = m\Delta\theta$, $T(\mathbf{s}, \mathbf{x})$ can be expanded into

$$T(\mathbf{s}, \mathbf{x}) = T(\theta, 0) = \sum_{n=-\infty}^{\infty} \frac{\pi}{2} Y_n(kR) J'_n(k\rho) \cos(n\theta), \quad R > \rho. \quad (70)$$

The matrix $[T]$ in Eq. (67) is a circulant since rotation symmetry for the influence coefficients are considered. We can expand $[T]$ into

$$[T] = b_0 I + b_1 C_{2N}^1 + b_2 C_{2N}^2 + \dots + b_{2N-1} C_{2N}^{2N-1}. \quad (71)$$

Based on the theory of circulants, the spectral properties for the influence matrix, $[T]$, can be found as follows:

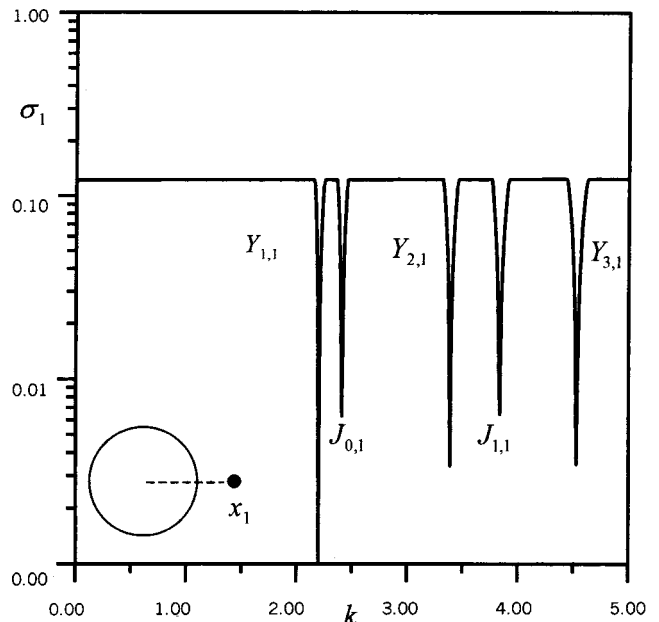


FIG. 7. One sample point $x_1(1.5, 0)$, σ_1 vs k using the real-part UT equation.

$$\mu_l = b_0 + b_1 \alpha_l + b_2 \alpha_l^2 + \dots + b_{2N-1} \alpha_l^{2N-1}, \quad l = 0, \pm 1, \pm 2, \dots, \pm(N-1), N, \quad (72)$$

where μ_l and α_l are the eigenvalues for $[T]$ and $[C_{2N}]$, respectively.

We have

$$\begin{aligned} \mu_l &= \sum_{m=0}^{2N-1} b_m \alpha_l^m \\ &= \sum_{m=0}^{2N-1} b_m e^{i(2\pi/2N)ml}, \\ & \quad l = 0, \pm 1, \pm 2, \dots, \pm(N-1), N. \end{aligned} \quad (73)$$

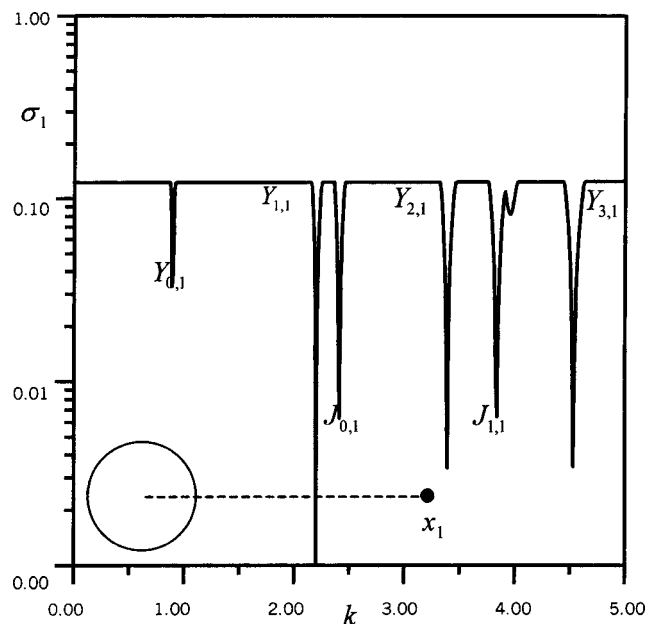


FIG. 8. One sample point $x_1(4.429, 0)$, σ_1 vs k using the real-part UT equation.

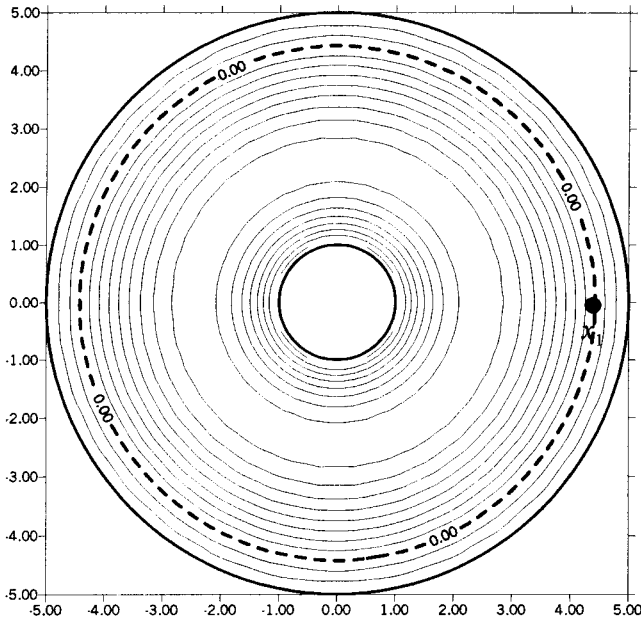


FIG. 9. The spurious eigenvalue radiation mode of a circular cavity for the Dirichlet problem with $k_s=0.894$.

According to the definition for b_m in Eq. (69), we have

$$b_m = b_{2N-m}, \quad m=0,1,2, \dots, 2N-1. \quad (74)$$

Substituting Eq. (74) into Eq. (73), we have

$$\begin{aligned} \mu_l &= b_0 + (-1)^l b_N + \sum_{m=1}^{N-1} (\alpha_l^m + \alpha_l^{2N-m}) b_m \\ &= \sum_{m=0}^{2N-1} \cos(ml\Delta\theta) b_m. \end{aligned} \quad (75)$$

Substituting Eq. (69) into Eq. (75), we have

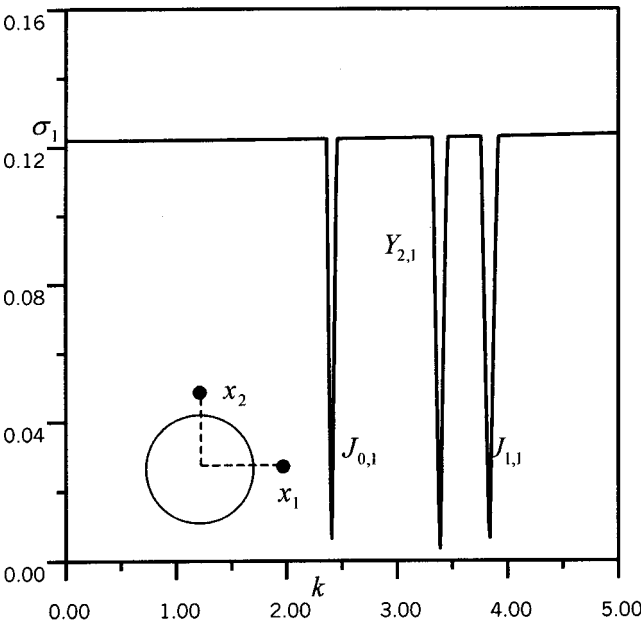


FIG. 10. Two sample points $x_1(1.5,0)$ and $x_2(1.5,\pi/2)$, σ_1 vs k using the real-part UT equation.

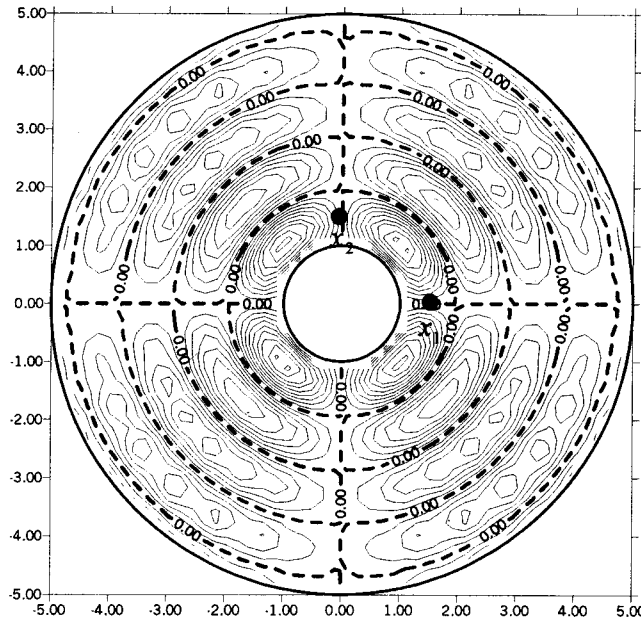


FIG. 11. The spurious eigenvalue radiation mode of a circular cavity for the Dirichlet problem with $k_s=3.384$.

$$\begin{aligned} \mu_l &\approx \sum_{m=0}^{2N-1} \cos(ml\Delta\theta) T(m\Delta\theta,0) R \Delta\theta \\ &= \int_0^{2\pi} \cos(l\theta) T(\theta,0) R d\theta, \end{aligned} \quad (76)$$

as N approaches infinity. Equation (76) reduces to

$$\begin{aligned} \mu_l &= \int_0^{2\pi} \cos(l\theta) \sum_{m=-\infty}^{\infty} \frac{\pi}{2} Y_m(kR) J'_m(k\rho) \cos m\theta R d\theta \\ &= \pi^2 R Y_l(kR) J'_l(k\rho). \end{aligned} \quad (77)$$

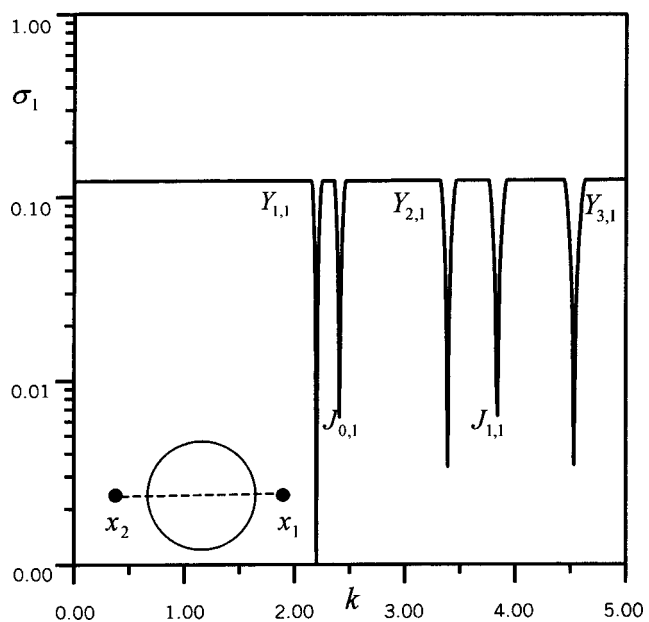


FIG. 12. Two sample points $x_1(1.5,0)$ and $x_2(1.5,\pi)$, σ_1 vs k using the real-part UT equation.

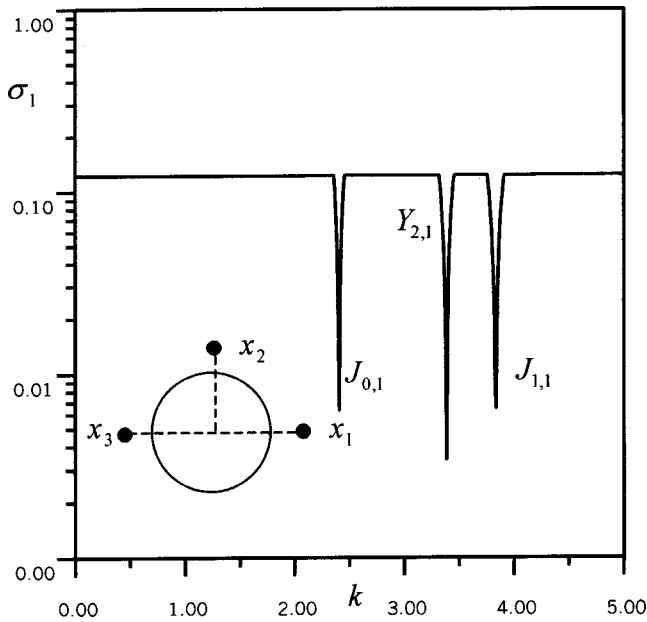


FIG. 13. Three sample points $x_1(1.5,0)$, $x_2(1.5,\pi/2)$, and $x_3(1.5,\pi)$, σ_1 vs k using the real-part UT equation.

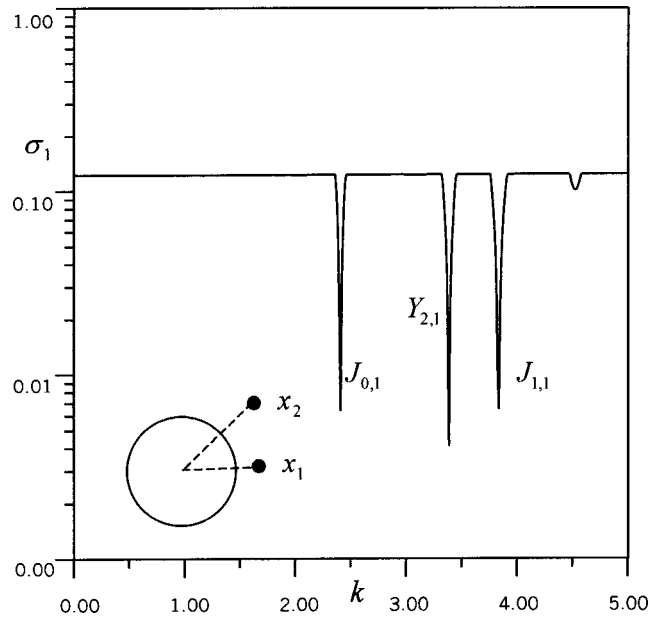


FIG. 15. Two sample points $x_1(2.007,\pi/4)$ and $x_2(1.4,0)$, σ_1 vs k using the real-part UT equation.

Since the wave number k is imbedded in each element of the $[T]$ matrix, the eigenvalues for $[T]$ are also a function of k . Finding the eigenvalues for the Helmholtz equation or finding the zeros for the determinant of $[T]$ is equal to finding the zeros for multiplication of all the eigenvalues of $[T]$. Based on the following equation:

$$\det[T] = \mu_0 \mu_N (\mu_1 \mu_2 \cdots \mu_{N-1}) (\mu_{-1} \mu_{-2} \cdots \mu_{-(N-1)}), \quad (78)$$

the possible eigenvalues (true or spurious) occur at

$$Y_l(kR)J'_l(k\rho) = 0, \quad l = 0, \pm 1, \pm 2, \dots, \pm(N-1), N. \quad (79)$$

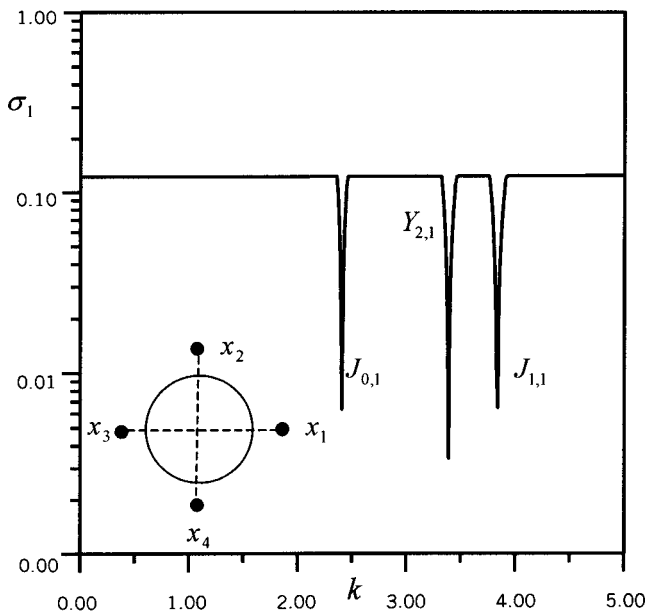


FIG. 14. Four sample points $x_1(1.5,0)$, $x_2(1.5,\pi/2)$, $x_3(1.5,\pi)$, and $x_4(1.5,3\pi/2)$, vs k using the real-part UT equation.

The values satisfying Eq. (79) may be spurious eigenvalues or true eigenvalues. Similarly, we adopted the same method to filter out the spurious eigenvalues.

If we adopt one exterior point (r_1, ϕ_1) , where $r_1 > \rho$ as shown in Fig. 4, for exterior point

$$0 = \int_B T(s, x) t(s) dB(s) = [v_1^T] \{u\}, \quad (80)$$

where $[v_1^T] = (v_1^1, v_1^2, v_1^3, \dots, v_1^{2N})$ is the row vector of the influence matrix by collocating the exterior point x_1 . Com-

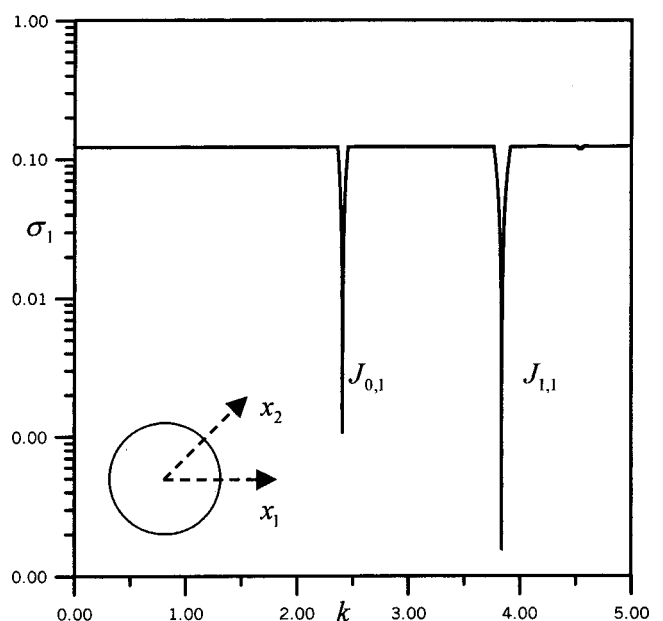


FIG. 16. Two sample points $x_1(1.5,0)$ and $x_2(1.5,\pi/4)$, σ_1 vs k using the real-part.

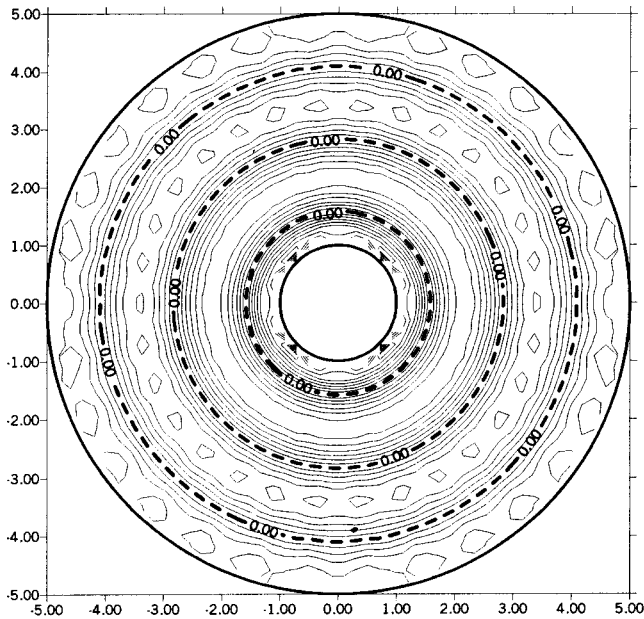


FIG. 17. The true eigenvalue radiation mode of a circular cavity for the Dirichlet problem with $k_T=2.405$.

binning Eq. (67) and Eq. (80), we obtain an overdeterminate system

$$\begin{bmatrix} T(k) \\ v_1^T(k) \end{bmatrix} \{u\} = \{0\}, \quad (81)$$

where $\{u\} = \{1, e^{in\Delta\theta}, e^{in2\Delta\theta}, \dots, e^{in(2N-1)\Delta\theta}\}^T$.

The additional constraint $[v_1^T]\{u\} = 0$ provides the discriminant, Δ , to be

$$\Delta = [v_1^T]\{u\} = \pi^2 r_1 Y_n(kr_1) J_n'(k\rho) e^{in\phi_1} = 0. \quad (82)$$

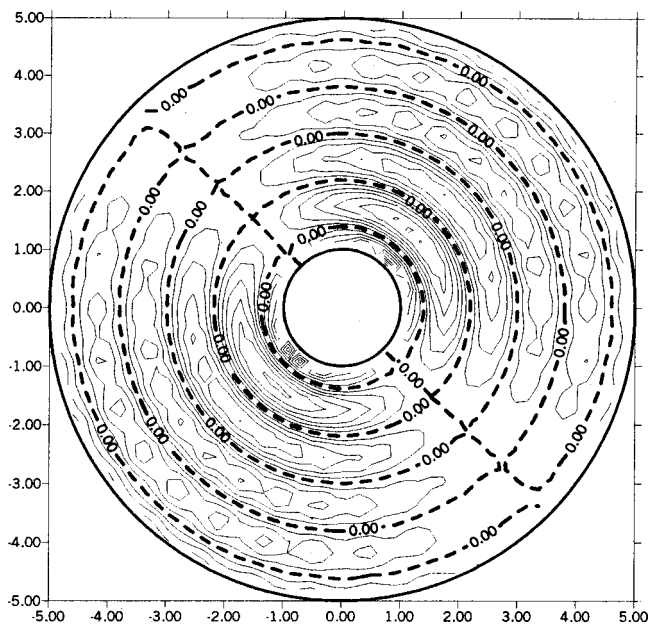


FIG. 18. The true eigenvalue radiation mode of a circular cavity for the Dirichlet problem with $k_T=3.832$.

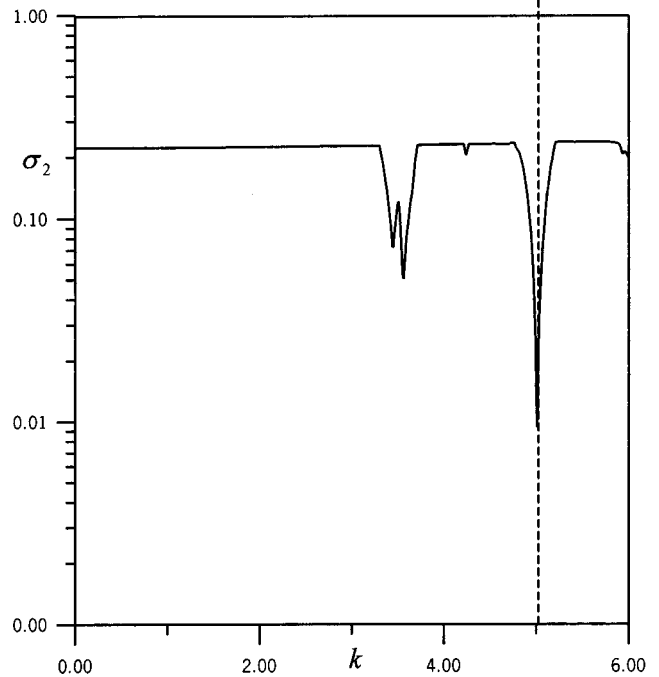
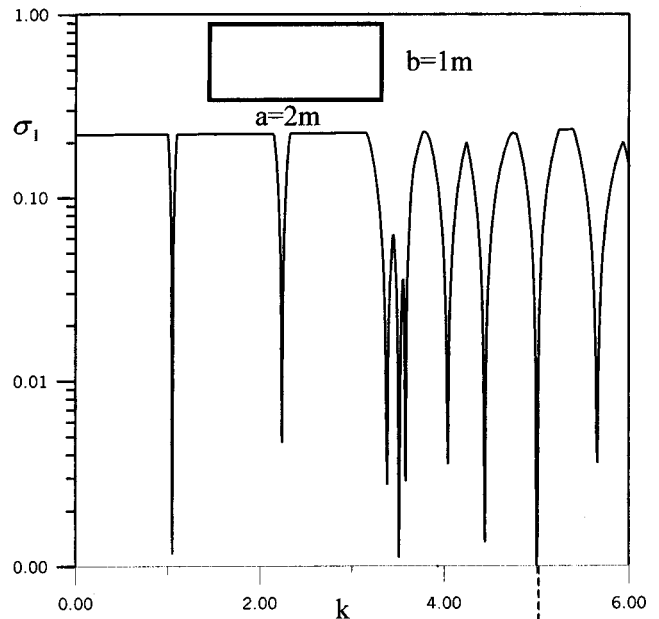


FIG. 19. The first and second minimum singular values σ_1 and σ_2 vs k of a rectangle using the real-part UT equation subject to Dirichlet boundary conditions with size $2\text{m} \times 1\text{m}$.

It is similar to Eq. (60), it can filter out a single root only.

If we adopt another exterior point (r_2, ϕ_2) with a radial distance $r_2 > \rho$ as shown in Fig. 5, and combine with Eq. (81), we have

$$\begin{bmatrix} T(k) \\ v_1^T(k) \\ v_2^T(k) \end{bmatrix} \{u\} = \{0\}, \quad (83)$$

where $[v_2^T] = (v_2^1, v_2^2, v_2^3, \dots, v_2^{2N})$ is the row vector of the influence matrix by collocating the exterior point x_2 . When the spurious eigenvalues are double roots, we have

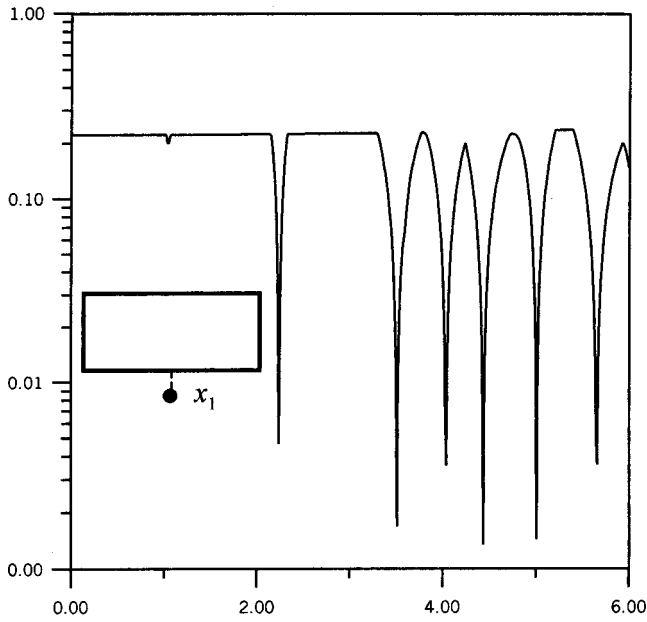


FIG. 20. One sample point $x_1(1.0, -0.25)$, σ_1 vs k using the real-part UT equation.

$$\begin{bmatrix} v_1^T(k) \\ v_2^T(k) \end{bmatrix} \{u\} = \begin{bmatrix} v_1^T \\ v_2^T \end{bmatrix} \{\alpha u_1 + \beta u_2\} = \begin{bmatrix} v_1^T u_1 & v_1^T u_2 \\ v_2^T u_1 & v_2^T u_2 \end{bmatrix} \begin{Bmatrix} \alpha \\ \beta \end{Bmatrix}, \quad (84)$$

where $\{u_1\} = \{1, e^{in\Delta\theta}, e^{i2n\Delta\theta}, \dots, e^{i(2N-1)\Delta\theta}\}^T$ and $\{u_2\} = \{1, e^{-in\Delta\theta}, e^{-i2n\Delta\theta}, \dots, e^{-i(2N-1)\Delta\theta}\}^T$ are two independent boundary modes, α and β are constants, and

$$\begin{aligned} v_1^T u_1^T &= \pi^2 r_1 Y_n(kr_1) J'_n(k\rho) e^{in\phi_1}, \\ v_1^T u_2^T &= \pi^2 r_1 Y_n(kr_1) J'_n(k\rho) e^{-in\phi_1}, \\ v_2^T u_1^T &= \pi^2 r_2 Y_n(kr_2) J'_n(k\rho) e^{in\phi_2}, \end{aligned}$$

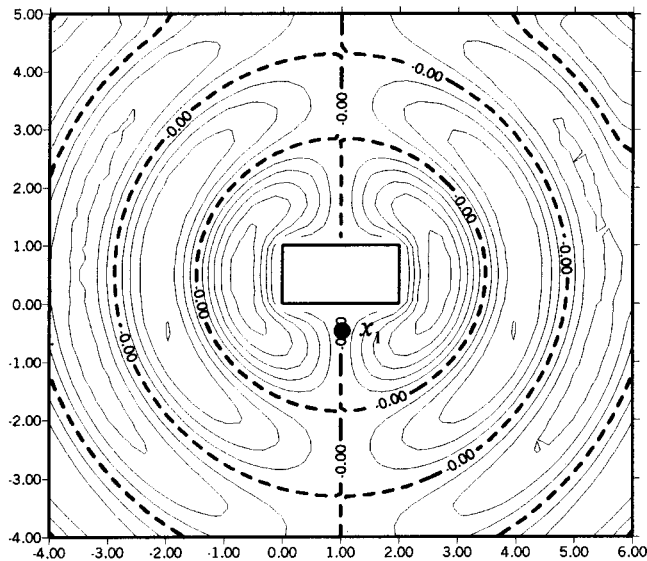


FIG. 21. The spurious eigenvalue radiation mode of a rectangle for the Dirichlet problem with $k_s = 2.23$.

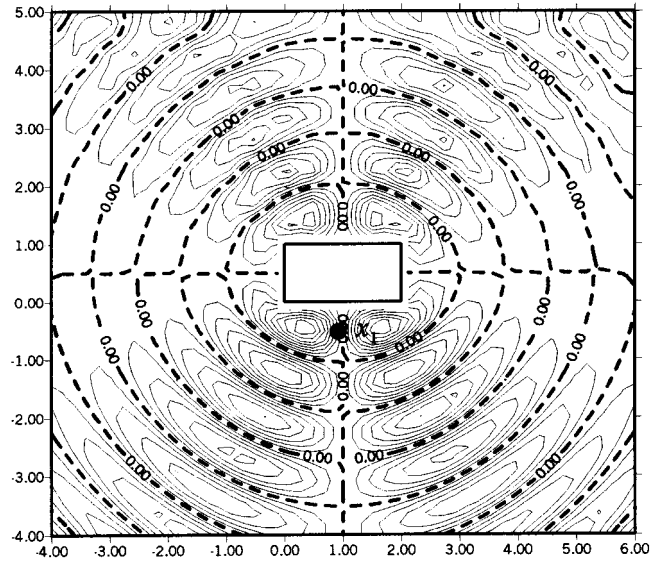


FIG. 22. The spurious eigenvalue radiation mode of a rectangle for the Dirichlet problem with $k_s = 4.02$.

$$v_2^T u_2^T = \pi^2 r_2 Y_n(kr_2) J'_n(k\rho) e^{-in\phi_2}.$$

Since the spurious double roots make the rank less than 2, the additional two points must provide independent constraints, as follows

$$\begin{bmatrix} \pi^2 r_1 Y_n(kr_1) J'_n(k\rho) e^{in\phi_1} & \pi^2 r_1 Y_n(kr_1) J'_n(k\rho) e^{-in\phi_1} \\ \pi^2 r_2 Y_n(kr_2) J'_n(k\rho) e^{in\phi_2} & \pi^2 r_2 Y_n(kr_2) J'_n(k\rho) e^{-in\phi_2} \end{bmatrix} \times \begin{Bmatrix} \alpha \\ \beta \end{Bmatrix} = 0. \quad (85)$$

If they are dependent, we have

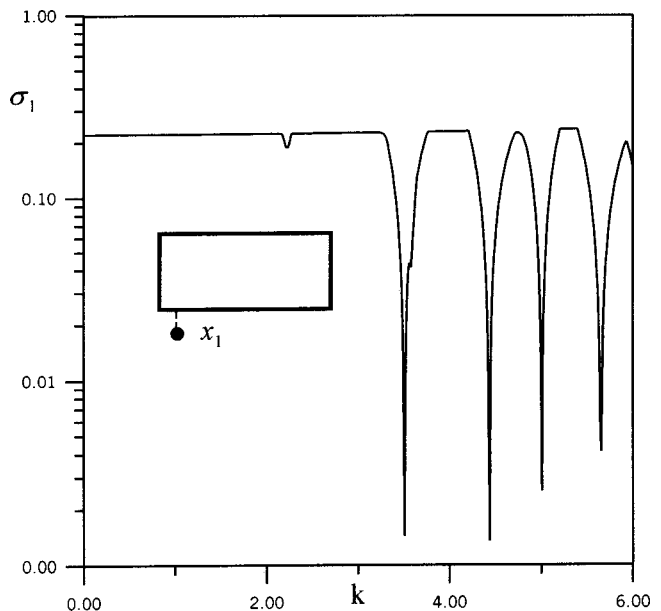


FIG. 23. One sample point $x_1(0.25, -0.25)$, σ_1 vs k using the real-part UT equation.

$$\Delta = \det \begin{vmatrix} \pi^2 r_1 Y_n(kr_1) J'_n(k\rho) e^{in\phi_1} & \pi^2 r_1 Y_n(kr_1) J'_n(k\rho) e^{-in\phi_1} \\ \pi^2 r_2 Y_n(kr_2) J'_n(k\rho) e^{in\phi_2} & \pi^2 r_2 Y_n(kr_2) J'_n(k\rho) e^{-in\phi_2} \end{vmatrix}$$

$$= r_1 r_2 Y_n(kr_1) Y_n(kr_2) J'_n(k\rho) J'_n(k\rho) (e^{in(\phi_1 - \phi_2)} - e^{-in(\phi_1 - \phi_2)}) = r_1 r_2 Y_n(kr_1) Y_n(kr_2) J'_n(k\rho) J'_n(k\rho) 2i \sin(n\phi) = 0, \quad (86)$$

where $\phi = \phi_1 - \phi_2$ indicates the intersecting angle between the two exterior points. Similarly, the discriminant Δ can justify whether the selected point is effective or not. It can filter out a double root. It was found that the spurious eigenvalues of an interior problem are dependent on the chosen method, i.e., singular integral equation results in the spurious eigenvalues at $Y_n(k\rho) = 0$, and independent of boundary condition (Dirichlet or Neumann).

VI. NUMERICAL EXAMPLES

For the numerical experiment, we considered a circular cavity with radius 1 m subjected to the Dirichlet boundary condition to check the validity of the CHEEF method. Furthermore, in order to extend to the general geometry problem using the CHEEF method, we used a rectangular cavity subjected to the Dirichlet boundary condition to demonstrate the generality.

Sixty elements were adopted in the boundary element mesh for a circular domain. Figure 6 shows the first minimum singular value, σ_1 , vs k where the true and spurious eigenvalues are obtained if only real-part UT is used. In the range of $0 < k < 5$, we have two true eigenvalues [$J_{0,1}(2.405)$ and $J_{1,1}(3.832)$] and five spurious eigenvalues [$Y_{0,1}(0.894)$, $Y_{1,1}(2.197)$, $Y_{2,1}(3.384)$, $Y_{0,2}(3.958)$, and $Y_{3,1}(4.527)$].¹¹ Figure 6 also indicates the second minimum singular value, σ_2 , vs k where the true and spurious double roots can be

obtained, when σ_1 and σ_2 are both zeros at the same k value. Figure 7 shows σ_1 vs k by additionally considering Eq. (58) for collocating one exterior point, \mathbf{x}_1 , with radius $r_1 = 1.5$ m, $\phi_1 = 0$. This treatment can filter out the spurious roots of $Y_{0,1}$ and $Y_{0,2}$ as expected in the analytical derivation. If the collocating exterior point is located at the circular boundary with radius $r_1 = k_{0,2}/k_{0,1} = 3.590/0.894 = 4.429$ as described in Eq. (61), which is on the nodal line of the radiation mode of $Y_{0,1}$, then the spurious eigenvalue of $Y_{0,1}$ cannot be filtered out as shown in Fig. 8. The spurious radiation mode of $Y_{0,1}$ is shown in Fig. 9.

If the additional two points $\mathbf{x}_1(r_1 = 1.5, \phi_1 = 0)$ and $\mathbf{x}_2(r_2 = 1.5, \phi_2 = \pi/2)$ with intersecting angle of $\phi = \pi/2$ are selected, then the spurious root of $Y_{2,1}$ cannot be filtered out as shown in Fig. 10, since $\sin 2\phi = 0$. The spurious radiation mode of $Y_{2,1}$ is shown in Fig. 11. Similarly, in both positions \mathbf{x}_1 and \mathbf{x}_2 with intersecting angle π , only the spurious eigenvalue $Y_{0,1}$ and $Y_{0,2}$ can be filtered out as shown in Fig. 12. Figure 13 and Fig. 14 are the results by adopting three [$\mathbf{x}_1(r_1 = 1.5, \phi_1 = 0)$, $\mathbf{x}_2(r_2 = 1.5, \phi_2 = \pi/2)$, $\mathbf{x}_3(r_3 = 1.5, \phi_3 = \pi)$] and four [$\mathbf{x}_1(r_1 = 1.5, \phi_1 = 0)$, $\mathbf{x}_2(r_2 = 1.5, \phi_2 = \pi/2)$, $\mathbf{x}_3(r_3 = 1.5, \phi_3 = \pi)$, $\mathbf{x}_4(r_4 = 1.5, \phi_4 = 3\pi/2)$] exterior points with different intersecting angles, respectively. It is very obvious that the results of Figs. 13 and 14 are the same as those of Fig. 10. This represents that the additional exterior points with intersecting angle π provide dependent equations. At the same time, if the additional exterior points,

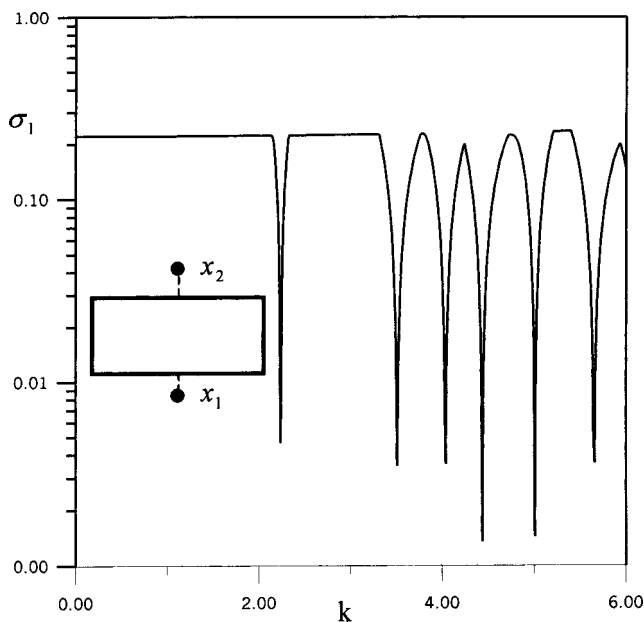


FIG. 24. Two sample points $x_1(1.0, -0.25)$ and $x_2(1.0, 1.25)$, σ_1 vs k using the real-part UT equation.

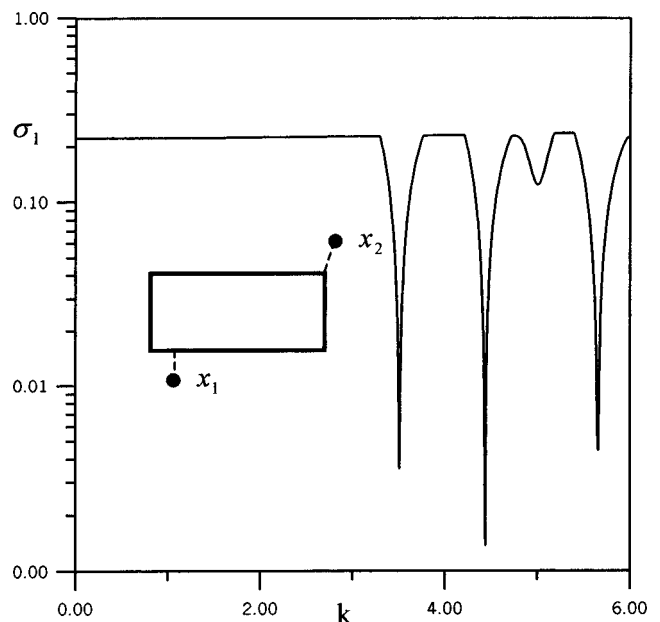
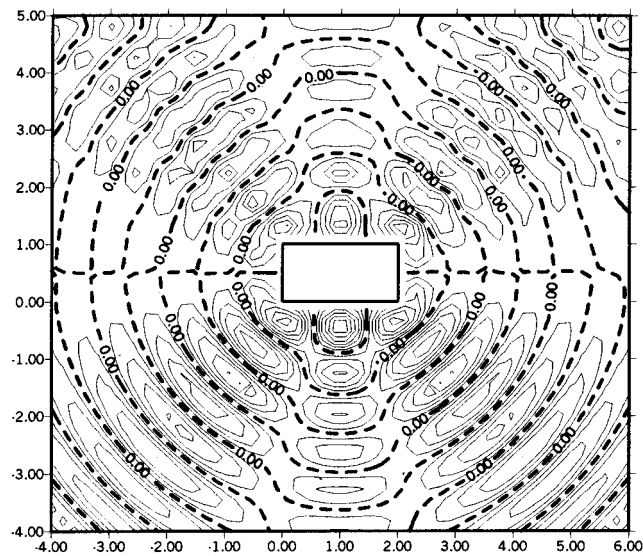
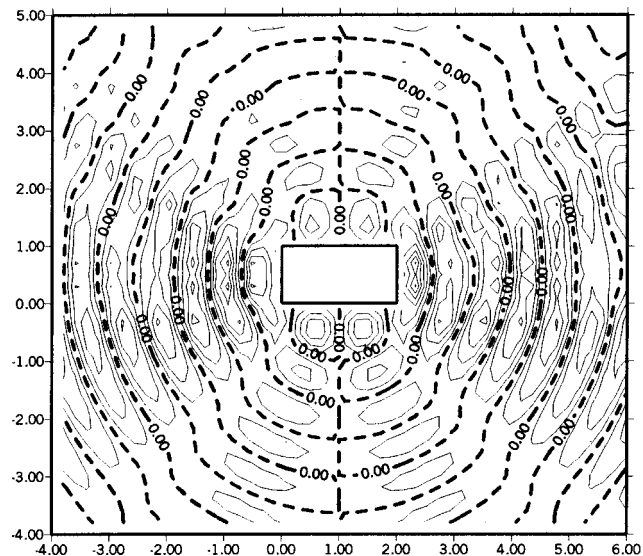


FIG. 25. Two sample points $x_1(0.3, -0.3)$ and $x_2(2.1, 1.3)$, σ_1 vs k using the real-part UT equation.



(a)



(b)

FIG. 26. (a) The spurious double root of the first radiation mode of a rectangle for the Dirichlet problem with $k_s=4.98$. (b) The spurious double root of the second radiation mode of a rectangle for the Dirichlet problem with $k_s=4.98$.

one point \mathbf{x}_1 with $r_1=k_{2,2}/k_{2,1}=6.794/3.384=2.007$ as described in Eq. (62) and $\phi_1=\pi/4$ and another point \mathbf{x}_2 with $r_2=1.4$ and $\phi_2=0$, are both chosen, then the spurious roots can be filtered out, except $Y_{2,1}$ as illustrated in Fig. 15. Figure 16 indicates that if the additional two exterior points $\mathbf{x}_1(r_1=1.5, \phi_1=0)$ and $\mathbf{x}_2(r_2=1.5, \phi_2=\pi/4)$ are carefully chosen, then all the spurious eigenvalues can be filtered out. It is interesting to find that the potential distribution is not trivial for the spurious eigenvalues; however, the potential distribution in the exterior domain for a true case is trivial, as shown in Fig. 17 [$J_{0,1}(2.405)$] and Fig. 18 [$J_{1,1}(3.832)$]. The dotted lines in the radiation modes represent the nodal lines. The radius of these nodal lines match the data in Table II. Table II also shows that most of spurious eigenvalues with low frequencies can be filtered out efficiently by select-

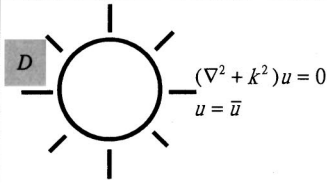
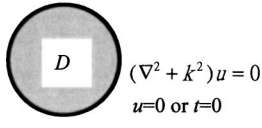
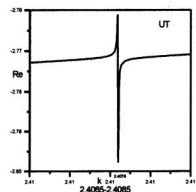
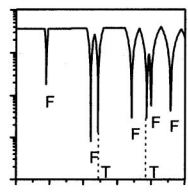
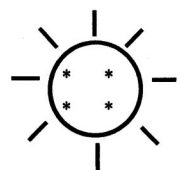
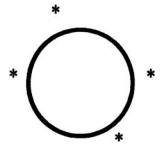
ing the points in the region of $1 < r < 1.24$, since the density of nodal lines in that area is low.

A rectangular cavity with length $a=2$ m and width $b=1$ m subjected to the Dirichlet boundary condition is demonstrated to see the validity for a problem with general geometry. Sixty elements in the BEM mesh were adopted. Figure 19 indicates the first and second minimum singular values, σ_1 and σ_2 vs k , where the true and spurious, single and double eigenvalues can be obtained. In the range of $0 < k < 6$, we have three true eigenvalues (3.51, 4.44, and 5.66) and six spurious eigenvalues [1.05, 2.23, 3.37, 3.57, 4.02, and 4.98 (double root)]. If the additional exterior point $\mathbf{x}_1(x_1=1.0, y_1=-0.25)$ is chosen, then the spurious roots can be filtered out except for the double spurious eigenvalue (4.98) and some single spurious eigenvalues (2.23, 4.02), where the selected points are on the nodal line as illustrated in Fig. 20. The spurious radiation modes of $k=2.23$ and $k=4.02$ are shown in Fig. 21 and Fig. 22. Figure 23 shows that if one additional exterior point $\mathbf{x}_1(x_1=0.25, y_1=-0.25)$ is chosen, then the spurious eigenvalues can be filtered out except for the double spurious eigenvalue $k=4.98$. Figure 24 shows that if the additional two exterior points $\mathbf{x}_1(x_1=1.0, y_1=-0.25)$ and $\mathbf{x}_2(x_2=1.0, y_2=1.25)$ are both chosen, then some spurious eigenvalues (2.23, 4.02, and 4.98) cannot be filtered out, since the additional exterior points are on the nodal line of the spurious radiation modes. If the additional two exterior points $\mathbf{x}_1(x_1=0.3, y_1=-0.3)$, $\mathbf{x}_2(x_2=0.21, y_2=1.3)$ are chosen, then all the spurious eigenvalues can be filtered out as illustrated in Fig. 25. At the same time, we know that the spurious eigenvalue of $k=4.98$ is a spurious eigenvalue with multiplicity 2, because one additional exterior point cannot work well. The two radiation modes of the spurious eigenvalue 4.98 are shown in Figs. 26(a) and (b). From these radiation mode figures, it is shown that if the additional exterior points are close to the boundary and are not located on a special position, such as on the nodal lines of $x=a/n$ or $y=b/n$ ($n \in N$), then the spurious eigenvalues can be filtered out efficiently. It is worthy to point out that the nodal lines of radiation mode for a circle can be rotated, since a circle has the property of rotation symmetry. However, the nodal lines of radiation modes for a rectangle cannot be rotated.

VII. CONCLUSIONS

The CHEEF method in conjunction with the SVD technique was applied to determine the true and spurious eigenvalues of circular and rectangle cavities subjected to the Dirichlet boundary conditions. The relationship between the CHIEF and CHEEF methods was summarized in Table III. The failure cases in selecting the exterior points for circular and rectangle cavities were studied analytically and demonstrated numerically. If the additional points are properly chosen, there are no more than two points required. The true eigenvalues obtained by the CHEEF method match very well with the exact solutions. It is very worthy to point out that the nodal line of radiation mode for a circle can be rotated due to its symmetry, whereas the nodal line of radiation

TABLE III. Comparison between the CHIEF and CHEEF methods.

Method	CHIEF Combined Helmholtz Interior integral Equation Formulation	CHEEF Combined Helmholtz Exterior integral Equation Formulation
Description		
Problem statement	 <p>Radiation or scattering problem</p>	 <p>eigenproblem</p>
Method of solution	complex-valued BEM (UT or LM)	BEM (real-part or imaginary-part)
Numerical trouble	 <p>fictitious wave number</p>	 <p>spurious eigenvalue</p>
Additional constrain		
Risk	nodal lines for interior modes	nodal lines for radiation modes
Treatment	dual formulation	complex-valued formulation

mode of rectangle is on a fixed position. The multiplicity was also examined. The CHEEF method can reduce memory storage and computation time in comparison with the real-part dual BEM.

¹H. A. Schenck, "Improved integral formulation for acoustic radiation problems," *J. Acoust. Soc. Am.* **44**(1), 41–58 (1968).
²G. W. Benthien and H. A. Schenck, "Nonexistence and nonuniqueness problems associated with integral equation method in acoustic," *Comput. Struct.* **65**, 295–305 (1997).
³T. W. Wu and D. W. Lobitz, "SuperCHIEF: A modified CHIEF method," SANDIA Labs Report SAND-90-1266 (1991).
⁴P. Juhl, "A numerical study of the coefficient matrix of the boundary element method near characteristic frequencies," *J. Sound Vib.* **175**(1), 39–50 (1994).
⁵S. Poulin, "A boundary element model for diffraction of water waves on varying water depth," Ph.D. dissertation of Department of Hydrodynamics and Water Resources, Technical University of Denmark, ISVA Series Paper No 64, ISSN 0107-1092, Lyngby (1997).
⁶G. De Mey, "Calculation of eigenvalues of the Helmholtz equation by an integral equation," *Int. J. Numer. Methods Eng.* **10**, 59–66 (1976).
⁷A. J. Nowak and A. C. Neves, editors, *The Multiple Reciprocity Boundary Element Method* (Comp. Mech., Southampton, 1994).
⁸G. R. G. Tai and R. P. Shaw, "Helmholtz equation eigenvalues and eigen-

modes for arbitrary domains," *J. Acoust. Soc. Am.* **56**, 796–804 (1974).
⁹G. De Mey, "A simplified integral equation method for the calculation of the eigenvalues of Helmholtz equation," *Int. J. Numer. Methods Eng.* **11**, 1340–1342 (1977).
¹⁰J. R. Hutchinson, "Determination of membrane vibrational characteristic by the boundary-integral equation method," in *Recent Advances in Boundary Element Method*, edited by C. A. Brebbia (Pentech, London, 1978), pp. 301–316.
¹¹J. T. Chen, S. R. Kuo, and C. X. Huang, "Analytical study and numerical experiments for true and spurious eigensolutions of a circular cavity using the real-part dual BEM," *IUTAM/IACM/IABEM Symposium on BEM*, Cracow, Poland, pp. 18–19 (1999).
¹²J. T. Chen, S. R. Kuo, and K. H. Chen, "A nonsingular integral integral formulation for the Helmholtz eigenproblems of a circular domain," *J. Chin. Inst. Chem. Eng.* **22**(6), 729–739 (1999).
¹³J. T. Chen, "Recent development of dual BEM in acoustic problems," *Comput. Methods Appl. Mech. Eng.* **188**(3–4), 1–15 (2000).
¹⁴J. T. Chen and F. C. Wong, "Analytical derivations for one-dimensional eigenproblems using dual BEM and MRM," *Eng. Anal. Boundary Elem.* **20**(1), 25–33 (1997).
¹⁵D. Y. Liou, J. T. Chen, and K. H. Chen, "A new method for determining the acoustic modes of a two-dimensional sound field," *J. Chin. Inst. Civ. Hydr. Eng.* **11**(2), 89–100 (1999) (in Chinese).
¹⁶J. T. Chen, C. X. Huang, and F. C. Wong, "Determination of spurious eigenvalues and multiplicities of true eigenvalues in the dual multiple

- reciprocity method using the singular value decomposition technique," *J. Sound Vib.* **230**(2), 203–219 (2000).
- ¹⁷W. Yieh, J. R. Chang, C. M. Chang, and J. T. Chen, "Applications of dual BEM for determining the natural frequencies and natural modes of a rod using the singular value decomposition method," *Adv. Eng. Softw.* **30**(7), 459–468 (1999).
- ¹⁸W. Yieh, J. T. Chen, and C. M. Chang, "Applications of dual MRM for determining the natural frequencies and natural modes of a Euler-Bernoulli beam using the singular value decomposition method," *Eng. Anal. Boundary Elem.* **23**(4), 339–360 (1999).
- ¹⁹J. T. Chen, C. X. Huang, and K. H. Chen, "Determination of spurious eigenvalues and multiplicities of true eigenvalues using the real-part dual BEM," *Comput. Mech.* **24**(1), 41–51 (1999).
- ²⁰J. T. Chen and H-K. Hong, "Review of dual boundary element methods with emphasis on hypersingular integrals and divergent series," *Appl. Mech. Rev.* **52**(1), 17–33 (1999).
- ²¹W. Yieh, J. T. Chen, K. H. Chen, and F. C. Wong, "A study on the multiple reciprocity method and complex-valued formulation for the Helmholtz equation," *Adv. Eng. Softw.* **29**(1), 1–6 (1997).
- ²²J. R. Chang, W. Yieh, and J. T. Chen, "Determination of natural frequencies and natural mode of a rod using the dual BEM in conjunction with the domain partition technique," *Comput. Mech.* **24**(1), 29–40 (1999).
- ²³J. T. Chen and F. C. Wong, "Dual formulation of multiple reciprocity method for the acoustic mode of a cavity with a thin partition," *J. Sound Vib.* **217**(1), 75–95 (1998).
- ²⁴J. T. Chen, K. H. Chen, and S. W. Chyuan, "Numerical experiments for acoustic modes of a square cavity using the dual BEM," *Appl. Acoust.* **57**(4), 293–325 (1999).
- ²⁵J. T. Chen and H-K. Hong, *Boundary Element Method*, 2nd ed. (New World, Taipei, 1992) (in Chinese).
- ²⁶N. Kamiya, E. Andoh, and K. Nogae, "A new complex-valued formulation and eigenvalue analysis of the Helmholtz equation by boundary element method," *Adv. Eng. Softw.* **26**, 219–227 (1996).
- ²⁷J. D. Jackson, *Classical Electrodynamics* (Wiley, New York, 1975).
- ²⁸J. T. Chen, "On fictitious frequencies using dual series representation," *Mech. Res. Commun.* **25**(5), 529–534 (1998).
- ²⁹J. T. Chen and S. R. Kuo, "On fictitious frequencies using circulants for radiation problems of a cylinder," *Mech. Res. Commun.* **27**(1), 49–58 (2000).
- ³⁰J. L. Goldberg, *Matrix Theory with Applications* (McGraw-Hill, New York, 1991).

Modeling vibrational energy transmission at bolted junctions between a plate and a stiffening rib

Ivan Bosmans and Trevor R. T. Nightingale

National Research Council Canada, Institute for Research in Construction, Acoustics, 1500 Montreal Road, Ottawa, Ontario K1A 0R6, Canada

(Received 11 July 2000; revised 13 November 2000; accepted 28 November 2000)

An analytical model is presented for structure-borne sound transmission at a bolted junction in a rib-stiffened plate structure. The model is based on the wave approach for junctions of semi-infinite plates and calculates coupling loss factors required by statistical energy analysis. The stiffening rib is modeled as a plate strip and the junction is represented by an elastic interlayer with a spatially dependent stiffness. Experimental verification is carried out on a series of Plexiglas plate structures with varying rib depth and bolt spacing. A well-defined connection length at the junction was created by inserting thin spacers between the plate and the rib at each bolt. Comparison between numerical and experimental data for this case showed good agreement. Measured results for the bolted junction without spacers suggested that structure-borne sound transmission could be modeled as a series of connections characterized by a finite connection length. This concept is explored further by determining an equivalent connection length which gives the best agreement between numerical and experimental data. © 2001 Acoustical Society of America.

[DOI: 10.1121/1.1344162]

PACS numbers: 43.40.Dx, 43.40.At, 43.55.Ti [CBB]

I. INTRODUCTION

The application of statistical energy analysis¹ (SEA) for predicting the vibro-acoustic response of complex structures requires accurate models for structure-borne sound transmission at junctions between plates and beams. In SEA, coupling loss factors quantify the energy flow between coupled plates and are usually calculated by modeling the interaction of plane waves at a junction of corresponding semi-infinite plates. This wave approach has been developed primarily for line connections between semi-infinite plates and infinite beams. In automotive, aerospace and lightweight building structures, many plate junctions are created using rivets, spot weldings, bolts, screws, or nails. These junctions generally behave as line connections as long as the wavelengths in the plate are large compared to the fastener spacing. At high frequencies, the plate and rib surfaces between the fastening points do not move in phase, and the junction acts as an array of local connections rather than as a line connection.

This paper investigates structure-borne sound transmission at a bolted junction between a plate and a rib. This type of junction is commonly applied in walls and floors in lightweight building structures, and a thorough understanding of the dynamic behavior of these junctions is necessary for studying the effects of flanking transmission. The main objective of this paper is to investigate whether a bolted junction should be modeled by considering an equivalent connection length between the connected elements in the vicinity of each fastener. For this purpose, an analytical prediction model must provide an accurate and unified mathematical description of the boundary conditions applicable to the complete frequency range of interest.

An overview of existing methods to predict structure-borne sound transmission is now given. Calculation models predicting structure-borne sound transmission between plates

have been published by several authors and the complexity of the modeled junctions has increased considerably over the last two decades. Structure-borne sound transmission at a variety of plate and beam junctions has been studied by Cremer *et al.*² for the cases of normal and random incidence. Low frequency approximations were derived for the normal incidence bending wave transmission loss at corner, tee, and cross junctions. The more complicated case including conversion between bending and in-plane waves has been treated for a corner junction. Apart from rigid connections, Cremer's work included junctions with elastic interlayers as well as plate/beam junctions.

Kihlman³ derived closed form expressions for bending and in-plane wave transmission at symmetric cross-junctions. The symmetry of the junctions simplified the analysis significantly, since in-plane waves are generated only in the plates perpendicular to the excited plate. More general cases of corner, tee, and cross junctions including bending, quasi-longitudinal, and transverse waves were solved several years later. Wöhle *et al.*^{4,5} modeled a junction of semi-infinite plates rigidly attached to a massless beam. Craven *et al.*⁶ and Gibbs *et al.*⁷ developed a similar calculation model but their approach used a different formulation of the boundary conditions and included the internal loss of the plate material.

Junctions of elastically connected plates are traditionally modeled by introducing a spring element between the connected plates.^{2,4,5} This approach has been applied by Craik and Osipov⁸ when modeling structure-borne sound transmission involving elastically supported walls in buildings and is satisfactory when interlayer thickness is small with respect to the wavelengths in the interlayer. Mees and Vermeir⁹ improved applicability by treating the elastic layer as a wave supporting medium.

With respect to the properties of the connected plates, most of the authors adopted thin plate theory to describe the bending response and considered junctions of isotropic plates. McCollum *et al.*¹⁰ used thick plate theory to model bending and in-plane wave transmission at a corner junction. Bosmans *et al.*¹¹ developed a model for junctions of thin orthotropic plates and discussed its application in the context of an SEA calculation scheme.

Bending wave transmission between plates connected by a common beam has been investigated by Cremer *et al.*² Steel¹² applied a more extensive theory to predict flanking transmission in framed buildings. The analysis included all wave types and the description of the dynamic behavior of the beam allowed for a springlike deformation of the beam cross-section. Langley *et al.*¹³ adopted a “wave dynamic stiffness” approach for modeling vibration transmission at plate/beam junctions. The latter approach is applicable to beams with solid cross-sections and to thin walled beam elements with closed or open cross-sections. Later, Heron¹⁴ treated a thin walled beam as an assembly of individual plate strips and modeled their interconnection using a wave line impedance method. A similar plate strip formulation was used by Bosmans *et al.*¹⁵ for predicting structure-borne sound transmission across a line connected stiffening rib in an orthotropic plate. Craik *et al.*¹⁶ applied a plate strip model to predict vibration transmission between the leafs of light-weight walls.

Most of the models published in literature were developed for plates connected along a line. Structure-borne sound transmission between point connected plates has traditionally been modeled using the modal approach in SEA.¹ Craik *et al.*¹⁶ used this to model point connections between a beam and two parallel plates. In this approach, coupling loss factors are expressed in terms of point mobility functions. Since this simplified model ignores the phase relationship between each point connection (because it is assumed all points are acting independently), these models cannot accurately represent the typical transition from line to point connection that occurs with increasing frequency.

Traditionally, point connected plate junctions have been modeled as line connections at low frequencies and as independently acting point connections at high frequencies. The transition between both regimes is rather arbitrarily chosen as the frequency at which one-half bending wavelength is equal to the point spacing.¹⁶ Although this assumption is correct for bending wave transmission at co-planar junctions, the transition from line to point connection for more complicated cases like corner junctions occurs over a finite frequency range¹⁷ and can not be represented accurately by the traditional approach.

Bosmans and Vermeir¹⁷ presented a more complete theory where a point connected plate junction is modeled using an interlayer with a spatially dependent stiffness. The spatial variation is assumed to be periodic and the plate response is described by a scattered wave field. This scattered wave field actually corresponds to a Fourier series expansion of the space dependent boundary conditions at the junction. As a result, no simplifying assumptions concerning the interaction between the various connections were introduced and

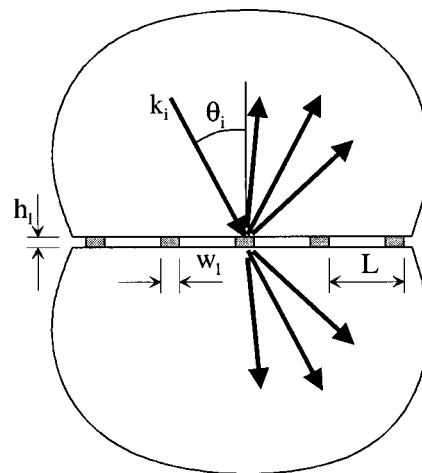


FIG. 1. An incident plane wave, with wave number k_i and angle of incidence θ_i , causes scattered wave fields on the periodically connected plates. The junction is modeled using a periodic elastic interlayer characterized by a thickness h_i , connection width w_i , and spatial period L .

the model is applicable to practically any ratio of the structural wave length to the point spacing.

Heron¹⁸ discusses a similar technique to formulate the plate response at a junction of point connected plates. The cross transfer matrix description of each connection incorporates all six degrees-of-freedom, but assumes an infinitely small connection length. The latter assumption may not be appropriate when the size of the connection is comparable to the wavelengths in the plate.

To create a model that has a unified description of the boundary conditions, which is necessary to study structure-borne sound transmission across a stiffening rib bolted to a plate at all frequencies the plate strip approach and the point connection theory of Refs. 15 and 17 are combined. The accuracy of this model is demonstrated by experimental verification for the case where spacers are inserted at each point connection to create a well-defined connection length. Experimental results for the case without spacers is compared to numerical data obtained for a variable width of the connections. By comparing these data, it is shown that the transmission across a bolted stiffening rib can be modeled using an equivalent connection length.

II. CALCULATION MODEL

The calculation model is based on the wave approach for periodic junctions of semi-infinite plates as discussed in Ref. 17. The basic principles of this approach are illustrated in Fig. 1. Consider an incident plane wave, with wave number k_i and angle of incidence θ_i , traveling toward the junction on one of the plates. The periodic boundary condition at the junction, characterized by a spatial period L , causes diffuse reflection and transmission of structure-borne sound waves on the source and receiving plates.¹⁷ The forces and displacements at the edges of the coupled plates are expressed in terms of the unknown amplitudes of the waves in the resulting scattered wave fields. The wave amplitudes are calculated as the solution of a system of equations consisting of equilibrium and continuity conditions at the junction. Structure-borne sound transmission is evaluated by the angle

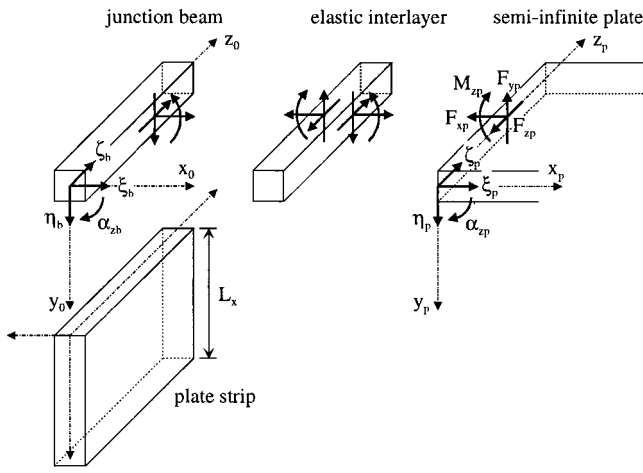


FIG. 2. Conventions for forces and displacements at the junction. An arbitrary junction is modeled using a combination of four basic elements: a junction beam, a semi-finite plate, or infinite plate strip and an elastic layer.

dependent transmission coefficient, which is obtained as the ratio of the intensities carried by the incident and transmitted waves. By integrating the transmission coefficient over all angles of incidence, an angle-averaged result is obtained which may be used to calculate SEA coupling loss factors.^{1,2}

The theory presented in the following paragraphs is developed for plates consisting of a linear elastic, homogeneous, and isotropic material. Damping is not included in the calculation model, since it is introduced in the final SEA calculations. Classical thin plate theory is applied to describe the bending wave response and the analysis includes quasi-longitudinal and in-plane transverse waves.

Since the calculation model basically represents an extension to the theory of Ref. 17, only the essential modifications are discussed in this paper. The major difference from the existing model is the introduction of a plate strip at the junction. The model also uses a more complete formulation of the junction eccentricity. These modifications affect the forces and displacements at the junction, as well as the formulation of the boundary conditions. Both aspects are discussed in the following paragraphs.

A. Junction geometry

Figure 2 shows that the junction is composed of four basic elements: junction beam, semi-infinite plate, plate strip, and elastic interlayer. All plate structures are connected to the junction beam. For the junctions considered in this paper, the junction beam does not have any physical properties within the model and can be considered as a common node (similar to the use of nodes in finite elements). The junction beam simply facilitates the formulation of the boundary conditions at the junction. A global coordinate system (x_0, y_0, z_0) is located at the center of the junction beam. The displacement of the junction beam is described by three translations (ξ_b, η_b, ζ_b) and a rotation around the z_0 -axis (α_{zb}) . The response of semi-infinite plates and plate strips are expressed in local coordinate systems (x_p, y_p, z_p) . Figure 2 further shows the conventions for the forces (F_{xp}, F_{yp}, F_{zp}) and moment (M_{zp}) per unit width acting on the plate edge, as well as for the plate edge displacements

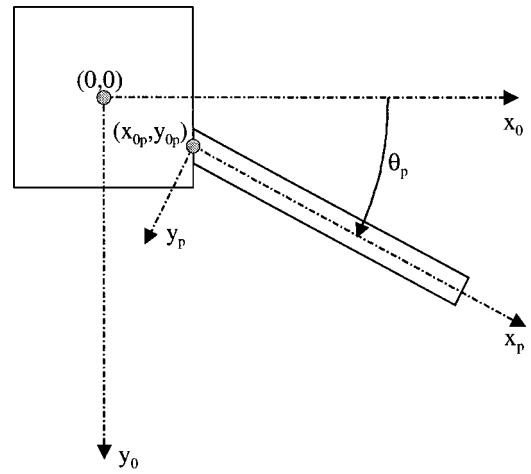


FIG. 3. The plate orientation and position in the global coordinate system (x_0, y_0, z_0) is determined by the coupling angle θ_p , and the fixation point coordinates (x_{0p}, y_{0p}) .

$(\xi_p, \eta_p, \zeta_p, \alpha_{zp})$. As opposed to a semi-infinite plate, a plate strip has an additional boundary parallel to the junction, and is infinitely extended only in the z_p -direction. Both plate elements can be coupled directly to the junction beam, or indirectly using an elastic interlayer. The interlayer is modeled as a spring, and its influence is taken into account by transforming forces and displacements at the plate edge to the corresponding parameters at the edge of the interlayer. Treating the interlayer as a spring is justified as long as the wavelengths in the interlayer material are considerably larger than the interlayer thickness. The spring stiffness for each of the four degrees-of-freedom are calculated as in Ref. 17. In this paper, the bolted connection is modeled by a stepwise variation of the spring stiffness, leading to a periodic boundary condition.

Each plate element can be coupled to the junction at any arbitrary coupling angle θ_p , which represents the angle between the (x_0, z_0) -plane and the (x_p, z_p) -plane (see Fig. 3). The fixation point coordinates (x_{0p}, y_{0p}) locate the point in the global coordinate system where the plate is assumed to be attached to the junction. These coordinates determine the eccentricity by which a plate is mounted at the junction.

B. Plate strip response at a periodic junction

The harmonic unit amplitude plane wave traveling toward the junction on the source plate is described by (the time dependence $e^{j\omega t}$ is omitted in the following equations):

$$e^{jk_x x} e^{-jk_z z}, \quad (1)$$

where x and z refer to the local coordinate system. To satisfy the periodic boundary conditions imposed by a periodic interlayer with spatial period L , the response of the plates is given by a superposition of plane waves traveling away from the junction:¹⁷

$$\sum_{n=-N}^{+N} A_n e^{-jk_x x} e^{-j[k_z \sin \theta_i + (2\pi n/L)]z}, \quad (2)$$

where A_n denotes the wave amplitude. The maximum number of wave components N is determined based on conver-

gence criteria. An expression for the wave number k_x can be derived by substituting Eq. (2) into the appropriate equations of motion. Substitution of Eq. (2) into the thin plate bending wave equation yields four wave numbers per wave component n .

In case of a semi-infinite plate, valid wave numbers are either real and positive, or imaginary and negative. The first set of wave numbers correspond to waves traveling away from the junction, and the second set to exponentially decaying near fields. As a result, the general solution for the bending wave response is given as¹⁷

$$\begin{aligned} \eta_p(x, z) &= \sum_{n=-N}^{+N} \eta_{pn}(x) e^{-j(k_i \sin \theta_i + \frac{2\pi n}{L})z} \\ &= \sum_{n=-N}^{+N} (A_n e^{-jk_{Bxn1}x} + B_n e^{-jk_{Bxn2}x}) \\ &\quad \times e^{-j[k_i \sin \theta_i + (2\pi n/L)z]}, \end{aligned} \quad (3)$$

where the wave numbers k_{Bxn1} and k_{Bxn2} are given in Ref. 17. Since the remaining bending wave parameters ($\alpha_{zp}, F_{yp}, M_{zp}$) can be expressed in terms of the transverse displacement η_p , they can be written in a form very similar to Eq. (3). As a result, the x -dependent part corresponding to wave component n for all bending wave parameters can be written as a function of the unknown bending wave amplitudes A_n and B_n :

$$\begin{bmatrix} \eta_{pn}(x) \\ \alpha_{zpn}(x) \\ F_{ypn}(x) \\ M_{zpn}(x) \end{bmatrix} = \begin{bmatrix} C_{n11} & C_{n12} & C_{n13} & C_{n14} \\ C_{n21} & C_{n22} & C_{n23} & C_{n24} \\ C_{n31} & C_{n32} & C_{n33} & C_{n34} \\ C_{n41} & C_{n42} & C_{n43} & C_{n44} \end{bmatrix} \begin{bmatrix} e^{-jk_{Bxn1}x} & 0 & 0 & 0 \\ 0 & e^{-jk_{Bxn2}x} & 0 & 0 \\ 0 & 0 & e^{+jk_{Bxn1}x} & 0 \\ 0 & 0 & 0 & e^{+jk_{Bxn2}x} \end{bmatrix} \begin{bmatrix} A_n^+ \\ B_n^+ \\ A_n^- \\ B_n^- \end{bmatrix}, \quad (7)$$

or

$$\mathbf{B}_{Bn}^{4 \times 1}(x) = \mathbf{C}_{Bn}^{4 \times 4} \mathbf{E}_{Bn}^{4 \times 4}(x) \mathbf{A}_{Bn}^{4 \times 1}. \quad (8)$$

The superscripts + and - in Eq. (7) refer to the amplitudes of right and left running waves, respectively. In order to reduce the number of unknowns, it is desirable to eliminate the left running wave amplitudes based on the free boundary condition at $x=L_x$. At this edge, F_{yp} and M_{zp} are equal to zero, which implies that $F_{ypn}(L_x) = M_{zpn}(L_x) = 0$ for every wave component n . By rearranging Eq. (7) for $x=L_x$, it is possible to express A_n^- and B_n^- , as a function of A_n^+ and B_n^+ :

$$\begin{bmatrix} A_n^- \\ B_n^- \end{bmatrix} = \begin{bmatrix} T_{n11} & T_{n12} \\ T_{n21} & T_{n22} \end{bmatrix} \begin{bmatrix} A_n^+ \\ B_n^+ \end{bmatrix}. \quad (9)$$

Using this equation, it is now possible to eliminate the left running wave amplitudes by transforming the coefficient matrix $\mathbf{C}_{Bn}^{4 \times 4}$ as follows:

$$\begin{bmatrix} \eta_{pn}(x) \\ \alpha_{zpn}(x) \\ F_{ypn}(x) \\ M_{zpn}(x) \end{bmatrix} = \begin{bmatrix} C_{n11} & C_{n12} \\ C_{n21} & C_{n22} \\ C_{n31} & C_{n32} \\ C_{n41} & C_{n42} \end{bmatrix} \begin{bmatrix} e^{-jk_{Bxn1}x} & 0 \\ 0 & e^{-jk_{Bxn2}x} \end{bmatrix} \times \begin{bmatrix} A_n \\ B_n \end{bmatrix}, \quad (4)$$

or

$$\mathbf{B}_{Bn}^{4 \times 1}(x) = \mathbf{C}_{Bn}^{4 \times 2} \mathbf{E}_{Bn}^{2 \times 2}(x) \mathbf{A}_{Bn}^{2 \times 1}. \quad (5)$$

The coefficient matrix $\mathbf{C}_{Bn}^{4 \times 2}$ is obtained by substitution of Eq. (3) into the formulas of mechanics.¹⁹ At the plate junction $x=0$, $\mathbf{E}_{Bn}^{2 \times 2}(x)$ becomes a unit matrix and Eq. (5) reduces to

$$\mathbf{B}_{Bn}^{4 \times 1}(0) = \mathbf{C}_{Bn}^{4 \times 2} \mathbf{A}_{Bn}^{2 \times 1}. \quad (6)$$

In case of a plate strip, a free plate edge is introduced parallel to the junction, at a distance L_x from the coupled plate edge (see Fig. 2). Reflections from the free edge must be taken into account and the bending wave response of the strip is determined by waves traveling in the positive as well as in the negative x -direction. Consequently, Eq. (4) should be rewritten as

$$\bar{\mathbf{C}}_{Bn}^{4 \times 2} = \mathbf{C}_{Bn}^{4 \times 4} \mathbf{T}_{Bn}^{4 \times 2}, \quad (10)$$

where the transformation matrix $\mathbf{T}_{Bn}^{4 \times 2}$ is given as

$$\mathbf{T}_{Bn}^{4 \times 2} = \begin{bmatrix} 1 & 0 & T_{n11} & T_{n21} \\ 0 & 1 & T_{n12} & T_{n22} \end{bmatrix}^T. \quad (11)$$

The forces and displacements at $x=0$ of a plate strip can be evaluated by substituting $\bar{\mathbf{C}}_{Bn}^{4 \times 2}$ in Eq. (6). As a result, the boundary conditions of plate strips and semi-infinite plates are described in exactly the same form. Consequently, the elimination of unknowns has improved the computational efficiency, without significantly increasing the complexity of the model. Although the previous analysis was restricted to bending waves, the same procedure can be applied to in-plane waves.

C. Boundary conditions

The boundary conditions at the junction consist of equilibrium conditions of the junction beam and of continuity

conditions between the displacements of the plate edge and the corresponding displacements of the junction beam. The equilibrium conditions are expressed in the global coordinate system, whereas the continuity conditions are formulated in the local coordinate system.

Equilibrium of the junction beam in the x_0 -direction is described by

$$\sum_p \left(F_{xp}(0,z) \cos \theta_p - F_{yp}(0,z) \sin \theta_p + x_{0p} \frac{\partial F_{zp}(0,z)}{\partial z} \right) = 0, \quad (12)$$

where the summation is taken over all plates. The third term in Eq. (12) accounts for the additional bending moment applied to the junction beam by the in-plane shear force F_{zp} . Since bending of the junction beam is caused by forces acting normal to the beam axis, the influence of the in-plane shear force is taken into account by an equivalent force in the x_0 -direction. The equilibrium condition for the remaining degrees-of-freedom are written as

$$\sum_p \left(F_{xp}(0,z) \sin \theta_p + F_{yp}(0,z) \cos \theta_p + y_{0p} \frac{\partial F_{zp}(0,z)}{\partial z} \right) = 0, \quad (13)$$

$$\sum_p F_{zp}(0,z) = 0, \quad (14)$$

$$-\sum_p M_{zp}(0,z) - \sum_p y_{0p}(F_{xp}(0,z) \cos \theta_p - F_{yp}(0,z) \sin \theta_p) + \sum_p x_{0p}(F_{xp}(0,z) \sin \theta_p + F_{yp}(0,z) \cos \theta_p) = 0. \quad (15)$$

As outlined in Ref. 17, the equilibrium conditions are multiplied by $e^{+j(m\pi/L)z}$ and integrated over the spatial period L . By repeating this procedure for m ranging from $-N$ to $+N$, each equilibrium condition is expressed by $2N+1$ equations. Applying this procedure to Eq. (12) yields

$$\sum_p \left(F_{xpm}(0) \cos \theta_p - F_{ypm}(0) \sin \theta_p - jx_{0p} \left(k_i \sin \theta_i + \frac{2\pi m}{L} \right) F_{zpm}(0) \right) = 0 \quad \forall m = -N \dots +N. \quad (16)$$

Similar expressions can be obtained for Eqs. (13)–(15).

The continuity conditions of a plate coupled to a periodic elastic interlayer are given by

$$K_x(z) (\xi_p(0,z) - \xi_b \cos \theta_p - \eta_b \sin \theta_p - \alpha_{zb}(x_{0p} \sin \theta_p - y_{0p} \cos \theta_p)) - F_{xp}(0,z) = 0, \quad (17)$$

$$K_y(z) (\eta_p(0,z) + \xi_b \sin \theta_p - \eta_b \cos \theta_p - \alpha_{zb}(x_{0p} \cos \theta_p + y_{0p} \sin \theta_p)) - F_{yp}(0,z) = 0, \quad (18)$$

$$K_z(z) \left(\zeta_p(0,z) - \zeta_b + x_{0p} \frac{\partial \xi_b}{\partial z} + y_{0p} \frac{\partial \eta_b}{\partial z} \right) - F_{zp}(0,z) = 0, \quad (19)$$

$$K_{rz}(z) (\alpha_{zp}(0,z) - \alpha_{zb}) + M_{zp}(0,z) = 0. \quad (20)$$

In these equations, $K_x(z)$, $K_y(z)$, $K_z(z)$, and $K_{rz}(z)$ represent the space dependent, periodically varying spring stiffness of the elastic interlayer.¹⁷ For local connections with a finite width, the spring stiffness is constant over the width of each connection, and zero elsewhere. For idealized point connections, the spring stiffness is expressed in terms of a dirac function. The two partial derivatives in Eq. (19) correspond to the rotation of the junction beam cross-section around the x_0 - and y_0 -axes. By applying the same procedure as the one used to derive Eq. (16), each continuity condition is expressed by $2N+1$ equations.¹⁷ Application of this procedure to Eq. (17) leads to the following expression:

$$\sum_{n=-N}^{+N} K_{xmn} (\xi_{pn}(0) - \xi_{bn} \cos \theta_p - \eta_{bn} \sin \theta_p - \alpha_{zbn}(x_{0p} \sin \theta_p - y_{0p} \cos \theta_p)) - LF_{xpm}(0) = 0 \quad \forall m = -N \dots +N. \quad (21)$$

An expression for the stiffness coefficient K_{xmn} is given in Ref. 17. Similar expressions are obtained for Eqs. (18)–(20). The equilibrium and continuity conditions derived from Eqs. (12)–(15) and (17)–(20) are combined with Eq. (6) to create a set of equations in the unknown wave amplitudes. The solution of this set of equations is then used to calculate the intensity carried by the waves transmitted at the junction.

III. EXPERIMENTAL VERIFICATION ON BOLTED JUNCTIONS WITH SPACERS

In this section, the calculation model is validated on a bolted junction between a plate and a stiffening rib (Fig. 4), where thin metal spacers were inserted between both elements to create a well-defined connection length at each fastener. A Plexiglas sheet ($2.46 \times 1.24 \times 0.0119$ m) was suspended from the laboratory ceiling using two soft springs. Three different stiffening ribs were attached to the plate using equally spaced bolts. The ribs were mounted in the middle of the sheet and effectively divided the sheet in two identical plates. All ribs had a thickness of 0.0187 m, but were characterized by three different depths L_x : 0.05 m, 0.10 m, and 0.235 m. Based on measured resonance frequencies of small beam samples, the elastic properties of Plexiglas were determined as Young's modulus $E = 4.8 \times 10^9$ Pa and Poisson's ratio $\nu = 0.4$, with a density of 1183 kg/m³.

For each depth of the rib, three bolt spacings were considered, as listed in Table I. The bolted junction is illustrated in Fig. 5. At each fastener, a square metal spacer ($0.0187 \times 0.0187 \times 0.0006$ m) was inserted between the plate and the rib. The interlayer stiffness corresponding to the metal spacers was calculated using the following literature data: $E = 7.1 \times 10^{10}$ Pa and $\nu = 0.3$. The bolts were driven in the rib manually using a torque wrench. It was found that increasing the torque above 4.2 Nm did not noticeably affect the measured results. The additional mass introduced at the junction by the bolts, washers and spacers (5.6 g per connection) was not taken into account in the model.

Velocity level difference (VLD) measurements were carried out using a two channel technique as reported by Craik.²⁰ Using this method, the transverse velocity level is

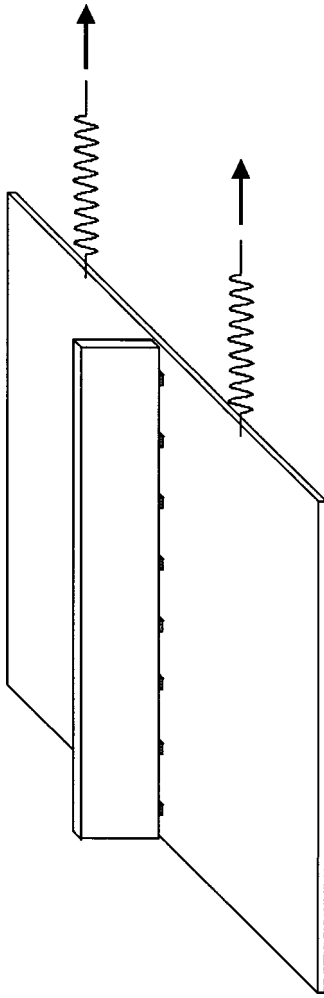


FIG. 4. Experiments were carried out on a Plexiglas sheet suspended from the laboratory ceiling using two soft springs. The stiffening ribs were attached using equally spaced bolts. Thin metal spacers were inserted between the plate and the rib at each bolt.

measured in one randomly positioned measurement point on each plate while the source plate is excited randomly using a light impact device. The average VLD between the source and the receiving plate is estimated by repeating this procedure for several pairs of measurement points until the average converges to a stable value.

For the calculations, the Plexiglas sheet was modeled as two semi-infinite plates with coupling angles $\theta_p = 0^\circ$ and 180° . For both plates, the fixation point coordinates (x_{0p}, y_{0p}) were assumed to coincide with the origin of the global coordinate system. The stiffening rib was modeled as a plate strip with coupling angle $\theta_p = 90^\circ$ and fixation point coordinates $(0, h_p/2)$, where h_p denotes the thickness of the Plexiglas sheet. The spacers are modeled by a periodic elas-

TABLE I. Bolt spacing and location of first bolt, for the junctions with 16, 8, and 4 equally spaced fasteners.

Number of bolts	Bolt spacing L [m]	Distance of first bolt from rib end at $z=0$ [m]
16	0.078	0.039
8	0.156	0.117
4	0.312	0.195

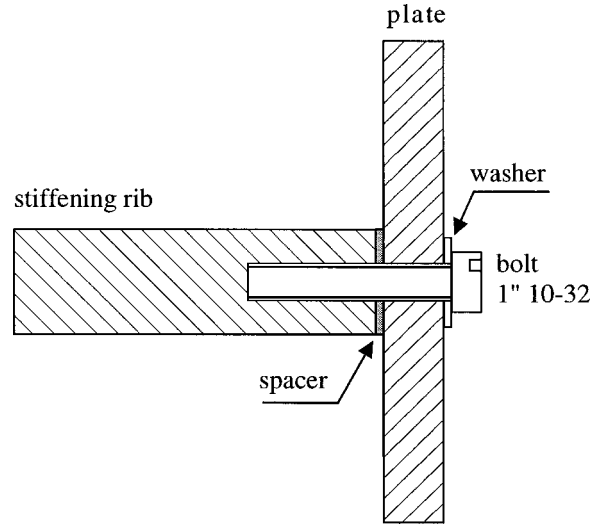


FIG. 5. Detail of the bolted junction between the plate and the rib.

tic interlayer connecting the plate strip to the junction beam. The coupling loss factor corresponding to bending wave transmission between both plates was calculated in frequency steps of $1/27$ of an octave, and then averaged to obtain one-third octave band results from 100 to 5000 Hz. The VLD between both plates was estimated using a simple SEA model which consisted of two subsystems corresponding to bending waves on both plates. The rib was not included in the SEA model, since its influence was taken into account when calculating the coupling loss factors.¹⁵ Further, in-plane wave subsystems were not considered since their influence is only important for complex structures involving many junctions and long transmission paths.²¹ The total loss factors used in the SEA formulation were simply the sum of the internal loss factor, radiation losses (which were both incorporated in the loss factor measured on the entire plate without the rib as shown in Fig. 6) and the computed CLF for the junction.

There are factors that might hinder comparison of the measured and predicted VLDs using the SEA formulation. In the low frequencies, strong coupling effects, which might bias SEA predictions for two nominally identical rectangular plates, are not expected to be important above 160 Hz since the modal overlap factors of both bending wave subsystems

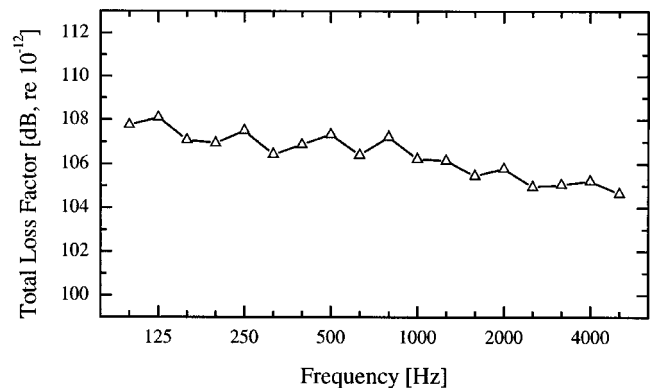


FIG. 6. Measured total loss factor of the Plexiglas sheet without ribs as a function of frequency.

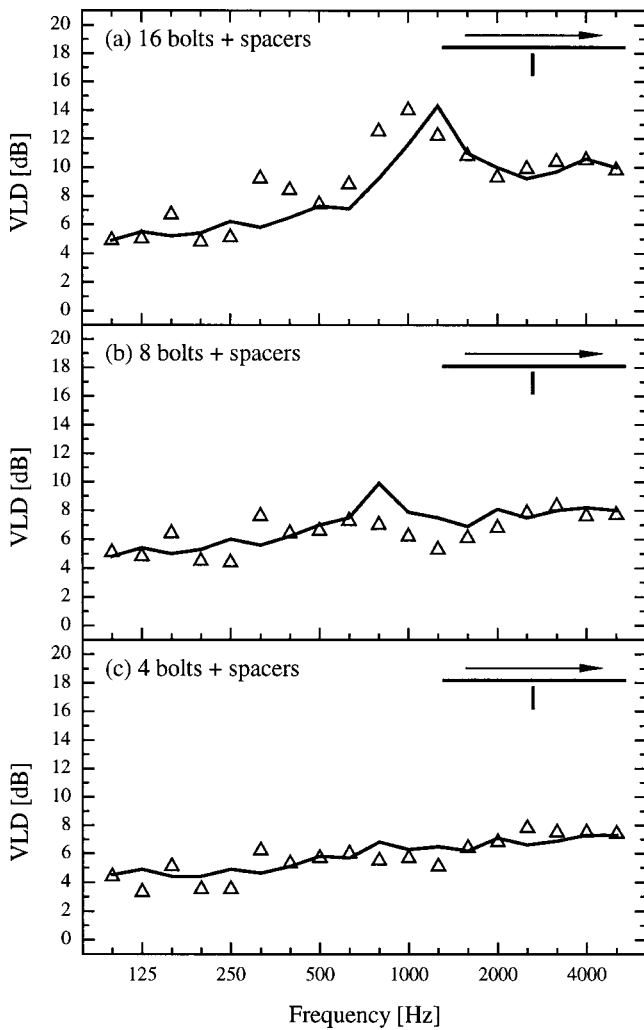


FIG. 7. Comparison between measured and predicted VLD for the 5 cm deep rib with spacers for three different numbers of bolts. Measurement (Δ), prediction (—).

exceed unity at this frequency. A high frequency limit will occur when the rib can support a significant number of modes and the assumption that the rib does not dissipate energy is no longer valid. A further high frequency limit will occur when the shear and rotary inertia of the plates can no longer be neglected and thin plate theory breaks down. This is estimated to be well above the frequency range considered here.

Measured and predicted data for the junction with a 5 cm rib are compared in Fig. 7 for the three cases of point spacing. The measured VLD for the case with 16 connections displays a pronounced peak at 1 kHz. At this frequency, an anti-resonance of the stiffening rib significantly reduces the rotation of the junction, leading to a reduction in bending wave transmission.¹⁵ The predicted data also show a maximum in the VLD, but its location is shifted to a higher frequency. The measured results also show a less pronounced maximum at 315 Hz, which is not predicted by the model. A detailed vibration mapping of the plates and ribs was not conducted so that it can only be speculated that these discrepancies might be due to uncertainties in the measured material properties, inaccuracies in the modeled boundary conditions of the plate strip or the fact that the inertia due to

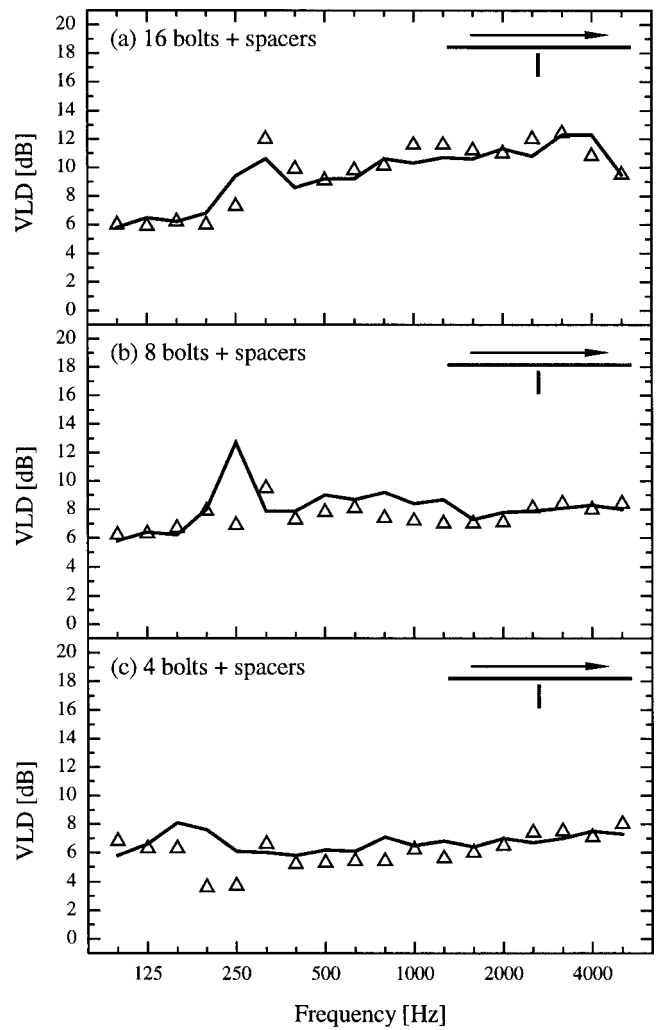


FIG. 8. Comparison between measured and predicted VLD for the 10 cm deep rib with spacers for three different numbers of bolts. Measurement (Δ), prediction (—).

the fasteners was neglected in the model. Overall, the agreement between theoretical data and measured results is fair since both curves show a similar trend. Good agreement is achieved for the case with eight connections in Fig. 7(b), although the peak predicted at 800 Hz seems to be missing in the measured data. The four connection case in Fig. 7(c) clearly shows the best agreement between measurement and prediction.

Figure 8 shows the experimental and numerical data for the 10 cm deep rib. The agreement between measurement and calculation is excellent for the case with 16 connections in Fig. 8(a). A relatively large prediction error of 6.9 dB can be observed in Fig. 8(b) at 250 Hz, where the predicted maximum in the VLD does not coincide with the measured maximum at 315 Hz. Also, the calculation model slightly overestimates the VLD in the mid-frequency range. For the case with four connections in Fig. 8(c), the largest discrepancy amounts to 4 dB at 200 Hz, but the agreement above 200 Hz is good.

Finally, the result for the 23.5 cm deep stiffening rib are plotted in Fig. 9. For all cases of point spacing, the model consistently overestimates the VLD below 315 Hz. Above

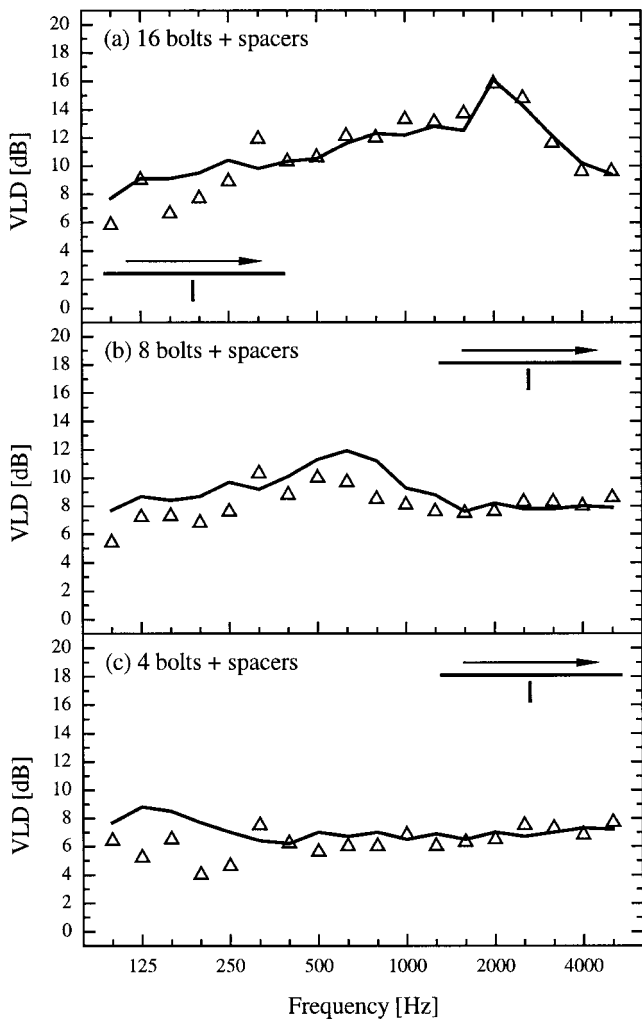


FIG. 9. Comparison between measured and predicted VLD for the 23.5 cm deep rib with spacers for three different numbers of bolts. Measurement (Δ), prediction (—).

this frequency, the agreement between measurement and calculation is very good for the cases with 16 and 4 bolts [Figs. 9(a) and (c)]. The predictions for the case with eight bolts in Fig. 9(b) are very accurate above 1 kHz, but the VLD is slightly overestimated at low and mid frequencies.

Overall, the agreement between measurement and calculation for the three stiffening ribs in Figs. 7–9 is good. The influence of the rib depth and the number of connections is reliably predicted. The calculation model has a tendency to slightly overestimate the VLD, which indicates that the coupling strength between the rib and the plate is overestimated. Nevertheless, the model has proven to be suitable to predict structure-borne sound transmission at a periodic junction between a plate and a stiffening rib.

IV. EQUIVALENT CONNECTION LENGTH AT BOLTED JUNCTIONS WITHOUT SPACERS

In many realistic junctions using rivets or bolts, the two connected elements are coupled without spacers. Consequently, there will be contact between both elements over the entire length of the junction, even though the actual contact may be discontinuous over time at some locations. However,

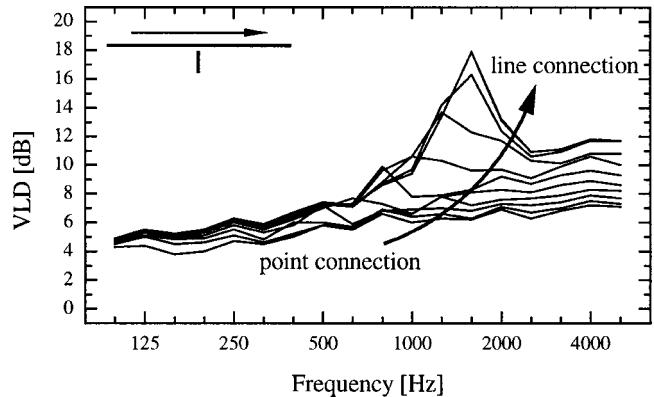


FIG. 10. Calculated VLDs for the 5 cm deep beam with four connections with variable width. The arrow indicates the trend of the results when increasing the width of the connections.

for an arbitrary plate/beam system where one or both are warped, there may not be contact. Modeling structure-borne sound transmission at these junctions is not as straightforward compared to the case with spacers. In this section, it is shown that junctions without spacers can be treated as an array of local connections characterized by an equivalent connection length. For this purpose, an additional series of experiments was carried out on the Plexiglas structure without spacers for all nine combinations of rib depth and bolt spacing. To ensure contact between the surfaces without spacers, both surfaces were machined flat. The equivalent connection length is determined for each junction by fitting numerical data to the measured results.

To understand the behavior of a bolted junction, it is instructive to review some aspects of bending wave transmission between point connected plates. Co-planar junctions of point connected plates are characterized by a “cutoff” frequency which marks the transition from line connection to point connection.¹⁷ The transition frequency depends on the point spacing and the bending wavelength in the plates. It must be stressed that unless the point connected model explicitly allows for the phase response of the connection points, like the model used in this paper, then this behavior will not be predicted. When the plate junction involves local connections with a finite coupling length, the width of each connection also has an influence on the bending wave transmission. This is illustrated by the parametric calculation shown in Fig. 10 for the 5 cm deep rib with four bolts. By increasing the width of the connections from one that is infinitely small to one that is equal to the bolt spacing, the junction gradually changes from an idealized point connection to a line connection. Figure 10 shows that the vibration attenuation increases with increasing connection width. In addition, the transition frequency below which the junction can be considered as a line connection also increases with increasing coupling length.

The experimental data in Fig. 11(a) for the 5 cm deep rib illustrate that a junction without spacers shows some distinct features of a point connected plate junction. Structure-borne sound transmission clearly depends on the spacing between the fasteners, even though the rib is nominally in direct contact with the plate. The results for the junctions with 4 and 8

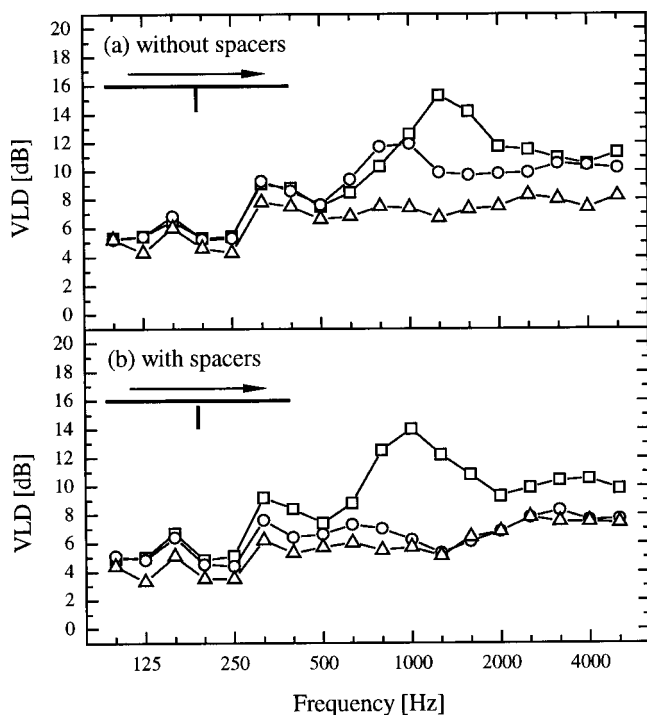


FIG. 11. Measured VLD for the 5 cm deep rib without (a) and with (b) spacers for different numbers of bolts: 16 (□), 8 (○), and 4 (△) bolts.

bolts in Fig 11(a) start to deviate significantly from the result for the 16 bolt case at 500 and 1000 Hz, respectively. In the frequency range where the point spacing does not have a profound influence, the junctions may be considered as line connections. Consequently, 500 Hz and 1000 Hz mark the frequencies above which a transition occurs from line to local connection for the junctions with four and eight bolts. The reduction of the transition frequency with increasing point spacing is typical of point connected plate junctions. When comparing the measured results for the case without spacers [Fig. 11(a)] to the case with spacers [Fig. 11(b)], it can be observed that the VLD tends to decrease when spacers are inserted at the junction. Also, the maximum in the VLD for the case with 16 bolts is shifted from 1250 Hz to 1000 Hz as a result of the spacers. Consequently, the spacers have weakened the connection between the plate and the rib.

These observations suggest that a junction without spacers neither behaves as an idealized point connection nor as a line connection, but as something in between. More specifically, the plates appear to be connected by equally spaced connections with (unknown) finite width, and the spacing between the connections is equal to the bolt spacing. Based on the experimental data in Fig. 11, the equivalent connection width seems to be greater than the width of the spacers. In the following paragraphs, it is shown that structure-borne sound transmission at a bolted junction can be described by assigning an equivalent connection length to each fastener.

The application of the calculation model presented in the Introduction to the junction without spacers requires two assumptions. The first assumption concerns the linearity of the problem. In between fasteners, the surfaces of the plate and the rib, which are nominally in contact with each other, move apart and together during one cycle of vibration. The

discontinuous contact between both elements essentially causes the motion in between two fasteners to be nonlinear. Consequently, the application of the theory of the Introduction requires the assumption that the nonlinearity can be ignored and that the transmission at the bolted junction can be described using a linear model.

The second assumption is that the additional damping caused by air pumping can be neglected and that the junction can be treated as a conservative junction. Fortunately, Plexiglas has a relatively high internal damping, and the additional damping due to air pumping, as estimated using the procedure given by Ungar *et al.*,²² generally represents only a small fraction of the internal loss factor. In fact, these small differences would be rather difficult to measure, since the uncertainty of the decay time measurement for the Plexiglas sheet is of the order of 10%. Consequently, the numerical results presented below are based on the same damping data as those used in Sec. I.

To evaluate the concept of an equivalent connection length, a parametric calculation is carried out with varying width w_l of the connections (see Fig. 1). In the absence of the spacers, the periodic interlayer was rather arbitrarily chosen as a 1 mm thick layer of Plexiglas. For a particular combination of rib depth and bolt spacing, the equivalent connection length, w_e , is the same for all frequencies, and is determined as the connection width which minimizes the rms prediction error averaged over all one-third octave bands. The measured data for the junctions without spacers, together with the results calculated using the equivalent connection lengths, are shown in Figs. 12–14. The equivalent connection lengths w_e are listed in Table II for all combinations of rib depth and bolt spacing. Also shown in Figs. 12–14 are the results for the extreme cases considered in the parametric calculations: idealized point connection (infinitely small connection length at each bolt) and continuous line connection. The point connection and the line connection correspond to the weakest and the strongest coupling, respectively, between the rib and the plate, and the difference between both cases increases with increasing bolt spacing.

The experimental data and the numerical results corresponding to the equivalent connection length for the 5 cm deep rib are given in Fig. 12. In all three cases, the best agreement between measurement and calculation is obtained when using the equivalent connection length, because the rms prediction error was minimized while maintaining the correct trends in the data. The measured data for the junction with 16 bolts approaches the results for a line connection, the main difference being a shift in the peak of the VLD. The junction with eight bolts clearly represents an intermediate case between a line and a point connection. Figure 12(c) demonstrates that the junction with four bolts can be modeled in first approximation by a point connection, although the latter approach leads to a systematic underestimation of the VLD.

Good agreement is also achieved when using the equivalent connection length for the 10 cm deep stiffening rib, as illustrated in Fig. 13. When excluding the large discrepancy around 315 Hz in Fig. 13(a), the rms prediction error is less than 1.5 dB for all cases of bolt spacing. The predictions

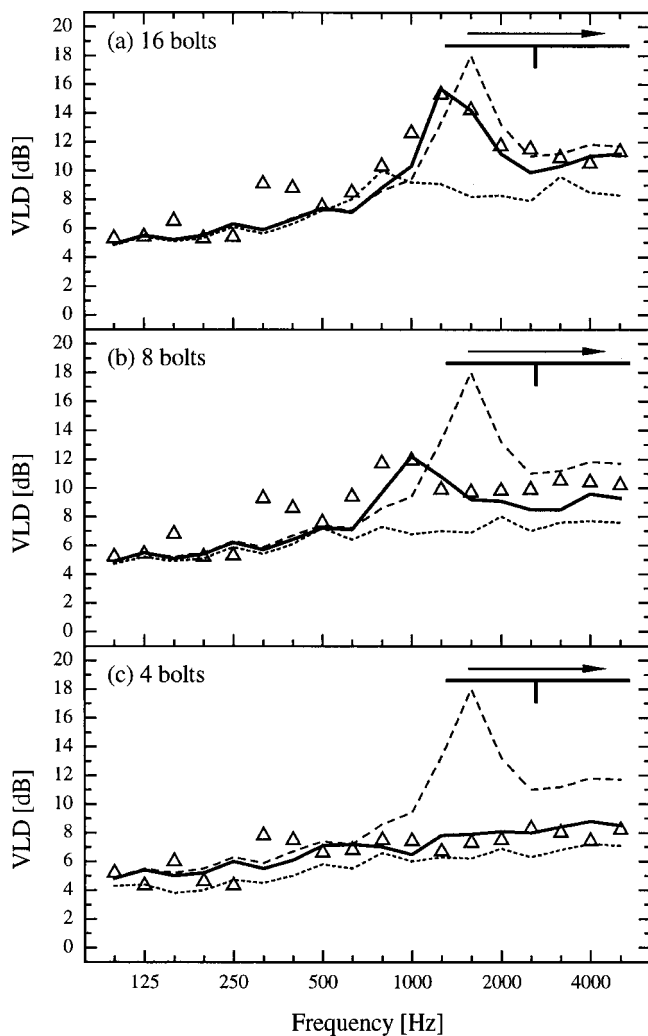


FIG. 12. Comparison between measured and predicted VLD for the 5 cm deep rib without spacers for three different numbers of bolts. Measurement (Δ), calculation: equivalent connection length (—), line connection (---), point connection (.....).

using a line connection are very accurate for the junction with 16 bolts, and work equally well for the case with 8 bolts below 4 kHz. The junction with 4 bolts represents an intermediate case, as the measured VLD lies between those of the line and point connections. The calculations using the idealized point connections consistently underestimate the VLD above 250 Hz for all cases of bolt spacing.

The comparison between measured and calculated data for the 23.5 cm rib in Fig. 14, reveals an overestimation of the VLD when using the equivalent connection length at low frequencies. A similar overestimation was observed for the junction with spacers in Fig. 9. Further, the measured VLD at high frequencies for the junction with 16 bolts in Fig. 14(a) is higher than predicted using a line connection. As a result, good agreement could only be achieved below 2 kHz. Above 250 Hz, the concept of an equivalent connection length seems to work well for the remaining cases in Figs. 14(b) and (c). The predictions using a line connection are reasonably accurate for the cases with 16 and 8 bolts. The point connection model underestimates the VLD above 500 Hz for all cases of bolt spacing.

The poor agreement above 2000 Hz for the case with the

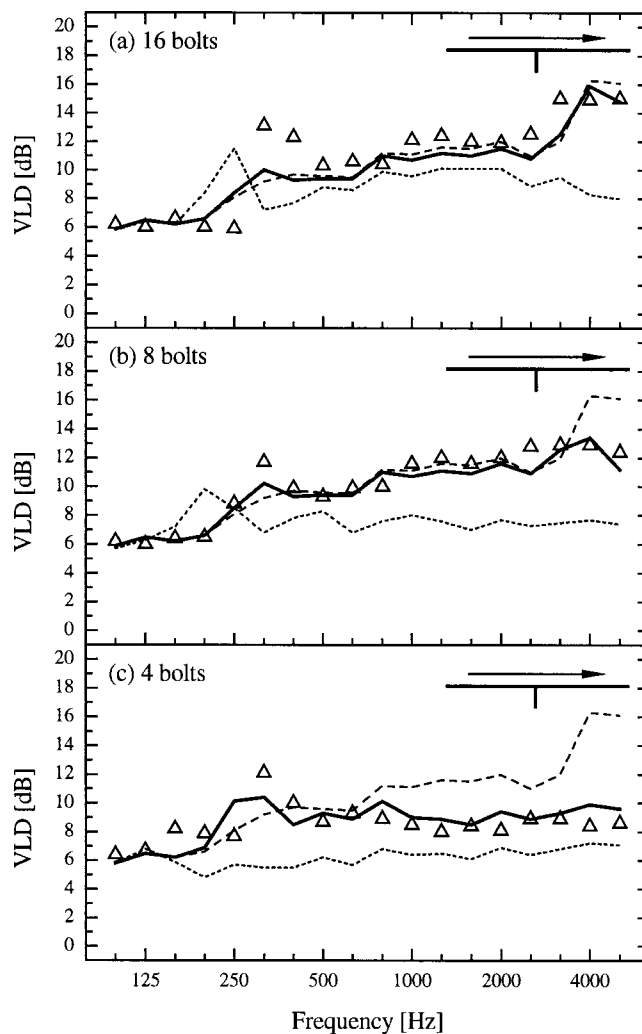


FIG. 13. Comparison between measured and predicted VLD for the 10 cm deep rib without spacers for three different numbers of bolts. Measurement (Δ), calculation: equivalent connection length (—), line connection (---), point connection (.....).

23.5 cm deep rib is due to the assumption in the plate strip formulation that the rib does not dissipate energy. (Apparently, the other rib sizes were not large enough to act as a significant energy loss mechanism.) Included in Fig. 14(a) is the prediction for a T-junction where the 23.5 cm rib is modeled as a line connected plate which supports modes and the internal loss factor of the rib was taken to be the same as the plate without any ribs. The agreement is greatly improved above 2000 Hz. Thus, at high frequencies, it may be necessary to consider the rib as a subsystem,¹⁵ depending on its dimensions.

Table II presents the equivalent connection lengths for the nine cases. The data indicate that the equivalent connection length increases with increasing bolt spacing. However, the table also shows that an increase in w_e does not necessarily correspond to an increase in the ratio w_e/L . In most cases, this ratio actually decreases with increasing bolt spacing. Unfortunately, the sensitivity of the equivalent connection length to the rib depth does not show a clear trend. This may be caused by the fact that the calculation model has a limited accuracy and is based on a number of simplifying assumptions. The effect of prediction uncertainty may be

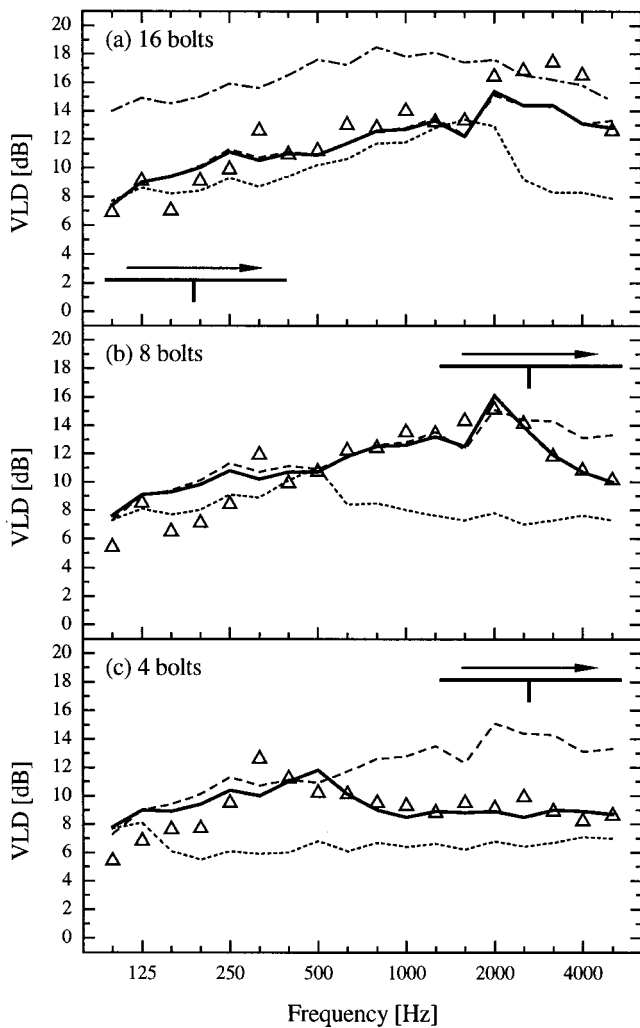


FIG. 14. Comparison between measured and predicted VLD for the 23.5 cm deep rib without spacers for three different numbers of bolts. Measurement (Δ), calculation: equivalent connection length (—), line connection (---), point connection (.....).

compounded by a weak dependence on the ratio w_e/L so that clear trends cannot be identified in this limited set of data. A detailed study is suggested, but is outside the scope of this paper.

Overall, the results in Figs. 12–14 illustrate that an appropriate choice of the connection width yields calculated data which agree well with measured results. Although the equivalent connection length was assumed to be frequency independent, the calculated data matched the measured results in most of the frequency range. Consequently, it was demonstrated that a bolted plate/rib junction can be modeled

TABLE II. Equivalent connection length w_e , and the ratio of the connection length to the bolt spacing w_e/L as a function of the rib depth and number of bolts.

Rib depth L_x [m]	Equivalent connection length w_e [m] (w_e/L)		
	16 bolts	8 bolts	4 bolts
0.05	0.0390 (0.50)	0.0562 (0.36)	0.1186 (0.38)
0.10	0.0421 (0.54)	0.0967 (0.62)	0.1560 (0.50)
0.235	0.0546 (0.70)	0.0905 (0.58)	0.1310 (0.42)

by assigning an equivalent connection length to each fastener. It should be stressed that the equivalent connection length does not represent a physical parameter, since the detailed behavior of the junction in reality is much more complex. The results of this paper merely show that a structure-borne sound transmission model, which incorporates the periodic boundary condition of a bolted junction, can be improved if a finite connection length is assigned to the fasteners.

V. CONCLUSIONS

Structure-borne sound transmission at a bolted junction between a plate and a stiffening rib is investigated theoretically and experimentally. A calculation model was presented where the rib was modeled as an infinite plate strip and the bolted connection was treated as an elastic interlayer with periodically varying elastic properties. The model was verified experimentally on a Plexiglas structure where thin metal spacers were inserted between the plate and the rib. Several combinations of the rib depth and bolt spacing were considered and good agreement was achieved between measured and calculated data. Experimental results on a similar structure without spacers demonstrated that the bolted junction behaves as a series of local connections. By comparing measured data to the results of a parametric calculation, an equivalent connection length was determined for each bolt. Measured and calculated results showed good agreement, which confirmed that a bolted junction between a plate and a rib can be modeled using an equivalent connection length. Unfortunately, a clear relationship between the equivalent connection length and the physical properties of the junction could not be identified. This is suggested for future work.

- ¹R. H. Lyon and R. G. DeJong, *Theory and Application of Statistical Energy Analysis*, 2nd ed. (Butterworth-Heinemann, Boston, 1995).
- ²L. Cremer, M. Heckl, and E. E. Ungar, *Structure-Borne Sound* (Springer-Verlag, Berlin, 1988).
- ³T. Kihlman, *Transmission of Structure-Borne Sound Through Buildings* (Report 9, National Swedish Institute for Building Research, Stockholm, 1967).
- ⁴W. Wöhle, Th. Beckmann, and H. Schreckenbach, "Coupling loss factors for statistical energy analysis of sound transmission at rectangular structural slab joints, part I," *J. Sound Vib.* **77**, 323–334 (1981).
- ⁵W. Wöhle, Th. Beckman, and H. Schreckenbach, "Coupling loss factors for statistical energy analysis of sound transmission at rectangular structural slab joints, part II," *J. Sound Vib.* **77**, 335–344 (1981).
- ⁶P. G. Craven and B. M. Gibbs, "Sound transmission and mode coupling at junctions of thin plates, part I: Representation of the problem" *J. Sound Vib.* **77**, 417–427 (1981).
- ⁷B. M. Gibbs and P. G. Craven, "Sound transmission and mode coupling at junctions of thin plates, part II: Parametric survey," *J. Sound Vib.* **77**, 429–435 (1981).
- ⁸R. J. M. Craik and A. Osipov, "Structural isolation of walls using elastic interlayers," *Appl. Acoust.* **46**, 233–249 (1995).
- ⁹P. Mees and G. Vermeir, "Structure-borne sound transmission at elastically connected plates," *J. Sound Vib.* **166**, 55–76 (1993).
- ¹⁰M. D. McCollum and J. M. Cuschieri, "Bending and in-plane wave transmission in thick connected plates using statistical energy analysis," *J. Acoust. Soc. Am.* **88**, 1480–1485 (1990).
- ¹¹I. Bosmans, P. Mees, and G. Vermeir, "Structure-borne sound transmission between thin orthotropic plates: Analytical solutions," *J. Sound Vib.* **191**, 75–90 (1996).
- ¹²J. A. Steel, "Sound transmission between plates in framed structures," *J. Sound Vib.* **178**, 379–394 (1994).

- ¹³R. S. Langley and K. H. Heron, "Elastic wave transmission through plate/beam junctions," *J. Sound Vib.* **143**, 241–253 (1990).
- ¹⁴K. H. Heron, "Predictive SEA using line wave impedances," In *IUTAM Symposium on Statistical Energy Analysis*, edited by F. J. Fahy and W. G. Price (Kluwer, Dordrecht, 1999), pp. 107–119.
- ¹⁵I. Bosmans and T. R. T. Nightingale, "Structure-borne sound transmission in rib-stiffened plate structures typical of wood frame buildings," *J. Build. Acoust.* **6**, 289–308 (1999).
- ¹⁶R. J. M. Craik and R. S. Smith, "Sound transmission through lightweight parallel plates. Part II: Structure-borne sound," *Appl. Acoust.* **61**, 247–269 (2000).
- ¹⁷I. Bosmans and G. Vermeir, "Diffuse transmission of structure-borne sound at periodic junctions of semi-infinite plates," *J. Acoust. Soc. Am.* **101**, 3443–3456 (1997).
- ¹⁸K. H. Heron, "The wave approach to predictive Statistical Energy Analysis and equally spaced point connections with isolators," *Proceedings NOISE-CON 98*, 579–584 (1998).
- ¹⁹W. Weaver, S. P. Timoshenko, and D. H. Young, *Vibration Problems in Engineering*, 5th ed. (Wiley, New York, 1990).
- ²⁰R. J. M. Craik, "The measurement of structure-borne sound transmission using impulsive sources," *Appl. Acoust.* **15**, 355–361 (1982).
- ²¹R. Lyon, "In-plane contribution to structural noise transmission," *Noise Control Eng. J.* **26**, 22–27 (1986).
- ²²E. E. Ungar and J. R. Carbonell, "On panel vibration damping due to structural joints," *J. Acoust. Soc. Am.* **4**, 1385–1390 (1966).

Prediction models for sound leakage through noise barriers

Hon Yiu Wong and Kai Ming Li^{a)}

Department of Mechanical Engineering, The Hong Kong Polytechnic University, Kowloon, Hong Kong

(Received 22 August 2000; accepted for publication 1 December 2000)

Two numerical models are presented for the prediction of sound leakage through openings in thin hard barriers. The first numerical method is based on a simple procedure of numerical integration that can be implemented straightforwardly. This model is a more general approach, suitable for barriers with arbitrary gaps. The second model is a new method that permits prediction of sound leakage due to the presence of horizontal gaps in a long barrier. In the new method, effective barriers of appropriate heights represent the edges of the horizontal gaps. The sound diffracted by each effective barrier is calculated by a closed-form analytic expression. The total sound-pressure level is determined from a sum of these diffracted fields. Hence, the new method is fast, simple, and intuitive, allowing the leakage to be assessed accurately. The validity of these two numerical models is confirmed by precise experimental measurements. © 2001 Acoustical Society of America.

[DOI: 10.1121/1.1345698]

PACS numbers: 43.50.Gf, 43.28.Fp, 43.20.Fn [MRS]

I. INTRODUCTION

Noise reduction by barriers is a popular measure for environmental protection in built-up areas. In particular, transportation noise from highways, railways, and airports can be shielded by a barrier, which intercepts the line of sight from the source to the receiver. When the transmission of sound through the barrier is negligible, the acoustic field in the shadow region is mainly dominated by the sound diffracted around the barrier. However, in some cases, leakage will occur due to shrinkage, splitting, and warping of the panels, and weathering of the acoustic seals. The problems of shrinkage and splitting are particularly acute for noise barriers made of timber. In addition, gaps are sometimes unavoidable, as spaces are required, for example, for the installation of lampposts in urban districts.

Research on diffraction and noise reduction by barriers has been extensive, leading to many publications in the past few decades. For instance, Maekawa¹ has developed a semi-empirical model for the prediction of sound fields behind a barrier, Hothersall *et al.*² and Terai and Kawai^{3,4} have used the integral equation methods to predict sound fields around barriers, and Hadden and Pierce^{5,6} have derived asymptotic formulas for sound diffraction around screens and wedges. Although considerable effort has been made to predict the diffracted sound field around noise barriers, the study of sound leakage in barriers has received relatively little attention. However, in a recent study, Watts⁷ investigated the resulting degradation of screening performance due to the leakage effect. A two-dimensional numerical model based on the boundary element method (BEM) is used in his study to predict the sound fields behind barriers of various heights with different gap widths and distributions.

We remark that the use of a two-dimensional model has inevitably restricted consideration to the presence of horizontal gaps in barriers only. Moreover, BEM is an elaborate numerical scheme that demands significant computational re-

sources. This is particularly the case at high frequencies and when the separation between source and receiver is longer than a few wavelengths.

The purpose of this paper is to develop a simple model for the accurate prediction of the insertion loss degradation due to the presence of gaps in thin rigid barriers. The numerical scheme is based on the theory developed by Thomasson⁸ and Rasmussen.⁹ To validate the proposed scheme, numerical predictions are compared with accurate experimental measurements. An interesting outcome of the numerical scheme is that it leads to a new formulation of a simple ray-method solution. The ray method is based on Pierce's formulation for the sound diffracted by wedges, and is used to predict the sound leakage due to horizontal gaps in a long barrier.

The contents of the present paper are as follows. The development of the numerical models for calculating sound leakage through a barrier is presented in Sec. II. We start from the physical optics solution⁸ and suggest a more compact numerical procedure for the evaluation of sound fields around the barriers with arbitrary gaps. A two-dimensional model is considered next. By linking solutions according to the physical optics and Pierce, we can derive a simple asymptotic expression for the computation of sound fields around a barrier with horizontal gaps. In Sec. III, validations of numerical models are shown. Finally, in Sec. IV, experimental results are compared with theoretical predictions for sound fields behind a barrier with either a horizontal or vertical gap.

II. THEORY

A. Formulation of the problem

The problem considered here consists of a two-dimensional, flat, locally reacting surface of infinite extent, $z=0$. A thin rigid screen of arbitrary shape, Γ_B , is situated at the plane of $x=0$. A point source with the harmonic time factor $e^{-i\omega t}$ is located above the impedance surface at $\mathbf{r}_S \equiv (x_S, 0, z_S)$ where $x_S < 0$. We wish to investigate the sound

^{a)}Electronic mail: mmkml@polyu.edu.hk

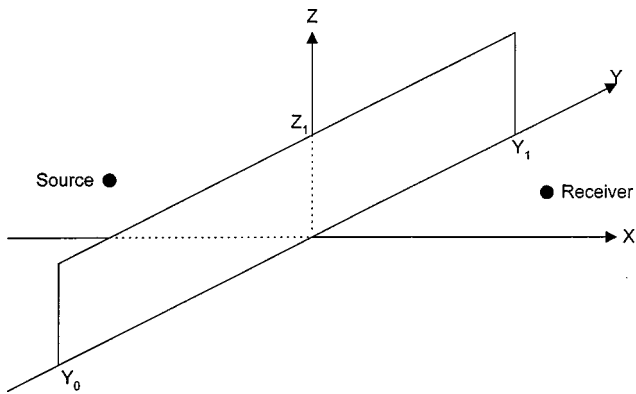


FIG. 1. The geometry of a source, receiver, and noise screen. The screen is placed at the plane $x=0$, $-\infty \leq y \leq +\infty$ and $-\infty \leq z \leq z_1$. The plane $z=0$ is an impedance boundary.

field behind the rigid screen where the receiver is located at $\mathbf{r}_R \equiv (x_R, 0, z_R)$ and $x_R, z_R > 0$ (see Fig. 1). Based on the Helmholtz integral formulation, Thomasson derived an approximate scheme (the so-called Rayleigh or physical optics solution¹⁰) for the prediction of sound fields behind an infinitely long barrier. The solution for a thin rigid screen is given by

$$\phi(\mathbf{r}_R, \mathbf{r}_S) = \phi_L(\mathbf{r}_R | \mathbf{r}_S) - 2 \int \int_{\Gamma_B} \phi_L(\mathbf{r}_0 | \mathbf{r}_S) \frac{\partial \phi_L(\mathbf{r}_R | \mathbf{r}_0)}{\partial x_R} dS, \quad (1)$$

where dS is the differential element of the barrier surface, \mathbf{r}_S , \mathbf{r}_R , and \mathbf{r}_0 are, respectively, the position of source, receiver, and barrier surface. The symbol $\phi_L(\mathfrak{R} | \mathfrak{J})$ signifies the sound field at receiver points \mathfrak{R} (which can either be \mathbf{r}_R or \mathbf{r}_0) due to the source located at \mathfrak{J} (which can either be \mathbf{r}_S or \mathbf{r}_0). Thomasson has suggested that $\phi_L(\mathbf{r}_R | \mathbf{r}_S)$ can be determined by noting the sound field vanishes when the rigid screen, Γ_∞ say, occupies the infinite plane of $y=0$. Then

$$\phi_L(\mathbf{r}_R | \mathbf{r}_S) = 2 \int \int_{\Gamma_\infty} \phi_L(\mathbf{r}_0 | \mathbf{r}_S) \frac{\partial \phi_L(\mathbf{r}_R | \mathbf{r}_0)}{\partial x_R} dS, \quad (2a)$$

or

$$\phi_L(\mathbf{r}_R | \mathbf{r}_S) = 2 \int_0^\infty \int_{-\infty}^\infty \phi_L(\mathbf{r}_0 | \mathbf{r}_S) \frac{\partial \phi_L(\mathbf{r}_R | \mathbf{r}_0)}{\partial x_R} dy dz. \quad (2b)$$

The sound field behind a rigid screen can be computed by substituting Eq. (2a) into Eq. (1) to yield

$$\phi(\mathbf{r}_R, \mathbf{r}_S) = 2 \int \int_{\Gamma_\infty - \Gamma_B} \phi_L(\mathbf{r}_0 | \mathbf{r}_S) \frac{\partial \phi_L(\mathbf{r}_R | \mathbf{r}_0)}{\partial x_R} dS. \quad (3)$$

The double integral of Eq. (3) can be computed readily by means of direct numerical integration. Indeed, Thomasson used this approach to calculate the diffraction of sound by a rigid screen above an impedance boundary. However, we note that the computation of $\phi_L(\mathfrak{R} | \mathfrak{J})$ is straightforward, as the Weyl-van der Pol formula can be used

$$\phi_L(\mathfrak{R} | \mathfrak{J}) = \frac{e^{ikR_1}}{4\pi R_1} + Q \frac{e^{ikR_2}}{4\pi R_2}, \quad (4)$$

where Q is the spherical wave reflection coefficient,¹¹ R_1 is the direct ray path, and R_2 is the specularly reflected ray path. The use of Eq. (1) in conjunction with Eq. (4) is preferable because the area required for numerical integration is generally smaller than that indicated in Eq. (3). Hence, fewer computational resources are required for the evaluation of sound fields behind a thin barrier.

B. Barriers with vertical gaps—An integral approach

Equation (1) is the most general formula for the computation of a sound field behind a thin barrier. It can be generalized to any arbitrary gaps in the barrier. In other words, if there are any gaps in the barrier, then their areas should not be included in the computation of the integral in Eq. (1). For instance, suppose there is a vertical gap of width $2d$ in an otherwise infinitely long barrier of height H . Without loss of generality, we assume the gap extends from $y=-d$ to $y=d$. The sound field behind such a barrier can be computed by

$$\begin{aligned} \phi(\mathbf{r}_R, \mathbf{r}_S) &= \phi_L(\mathbf{r}_R | \mathbf{r}_S) \\ &- 2 \int_0^H \int_{-\infty}^{-d} \phi_L(\mathbf{r}_0 | \mathbf{r}_S) \frac{\partial \phi_L(\mathbf{r}_R | \mathbf{r}_0)}{\partial x_R} dy dz \\ &- 2 \int_0^H \int_d^\infty \phi_L(\mathbf{r}_0 | \mathbf{r}_S) \frac{\partial \phi_L(\mathbf{r}_R | \mathbf{r}_0)}{\partial x_R} dy dz. \end{aligned} \quad (5)$$

It is worth noting that the term $\partial \phi_L(\mathbf{r}_R | \mathbf{r}_0) / \partial x_R$ can be regarded as the contribution due to horizontal dipoles on the surface of the barrier. The asymptotic solution for a horizontal dipole above an impedance plane can be found elsewhere¹⁰ and will not be repeated here.

C. Semi-infinite barriers with horizontal gaps—An integral approach

In many practical situations, the thin barrier may be assumed to be infinitely long and has a constant cross section along the y direction. In view of Eq. (1), the sound field can therefore be expressed as

$$\begin{aligned} \phi(\mathbf{r}_R, \mathbf{r}_S) &= \phi_L(\mathbf{r}_R | \mathbf{r}_S) \\ &- 2 \int_{l_B} \int_{-\infty}^\infty \phi_L(\mathbf{r}_0 | \mathbf{r}_S) \frac{\partial \phi_L(\mathbf{r}_R | \mathbf{r}_0)}{\partial x_R} dy dz, \end{aligned} \quad (6)$$

where l_B is the barrier ‘height’ which l_B indicates the extent of the barrier surface in the z direction and is constant along the y direction.

A close examination of the right-hand side of Eq. (6) reveals that the y integral of the second term can be evaluated asymptotically to yield a closed-form analytical expression. The evaluation of the integral is fairly straightforward, involving tedious algebraic manipulations that will not be shown here for brevity. Nevertheless, the sound field can be simplified to⁹

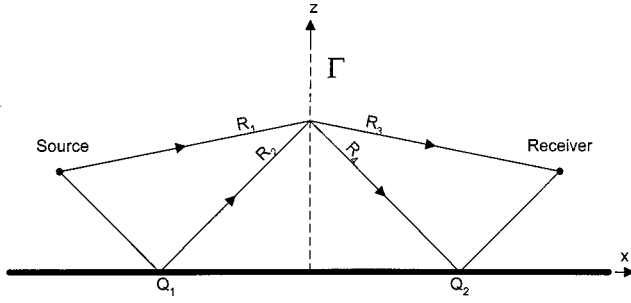


FIG. 2. Schematic diagram to show the direct and reflected waves used in the approximate integral solution. The plane used in the integration for the numerical model contains the source and receiver.

$$\begin{aligned} \phi(r_R, r_S) &= \phi_L(r_R|r_S) \\ &- X_R \sqrt{(8\pi k)} \frac{e^{-i\pi/4}}{16\pi^2} \int_{l_B} \left[\frac{e^{ik(R_1+R_3)}}{\sqrt{R_3^3 R_1 (R_1+R_3)}} \right. \\ &+ \frac{Q_2 e^{ik(R_1+R_4)}}{\sqrt{R_4^3 R_1 (R_1+R_4)}} + \frac{Q_1 e^{ik(R_2+R_3)}}{\sqrt{R_3^3 R_2 (R_2+R_3)}} \\ &\left. + \frac{Q_1 Q_2 e^{ik(R_2+R_4)}}{\sqrt{R_4^3 R_2 (R_2+R_4)}} \right] dz, \end{aligned} \quad (7)$$

where R_1 , R_2 , R_3 , and R_4 are defined in Fig. 2 and X_R is the shortest distance measured from the receiver to the barrier plane. The spherical wave reflection coefficients Q_1 and Q_2 are calculated on the basis of ground impedance on the source side and receiver side, respectively. In our case, the ground impedance is the same for both sides but, as demonstrated by Rasmussen,⁹ they can be different.

Again, if the barrier is extended to infinity, then the sound field $\phi(\mathbf{r}_R, \mathbf{r}_S)$ is zero. Hence, $\phi_L(\mathbf{r}_R|\mathbf{r}_S)$ can be rewritten in an integral form, cf. Eq. (2b), as

$$\begin{aligned} \phi_L(\mathbf{r}_R|\mathbf{r}_S) &= X_R \sqrt{(8\pi k)} \frac{e^{-i\pi/4}}{16\pi^2} \int_0^\infty \left[\frac{e^{ik(R_1+R_3)}}{\sqrt{R_3^3 R_1 (R_1+R_3)}} \right. \\ &+ \frac{Q_2 e^{ik(R_1+R_4)}}{\sqrt{R_4^3 R_1 (R_1+R_4)}} + \frac{Q_1 e^{ik(R_2+R_3)}}{\sqrt{R_3^3 R_2 (R_2+R_3)}} \\ &\left. + \frac{Q_1 Q_2 e^{ik(R_2+R_4)}}{\sqrt{R_4^3 R_2 (R_2+R_4)}} \right] dz. \end{aligned} \quad (8)$$

Normally, as mentioned in Sec. II A, the Weyl–van der Pol formula [Eq. (4)] will be used to compute $\phi_L(r_R|r_S)$ instead. Nevertheless, the computation serves to benchmark the accuracy of the numerical model developed in this paper. These comparisons will be shown in Sec. III.

Use of Eq. (7) greatly reduces the computational time in calculating the diffraction of sound behind the thin barrier as the double integral is reduced to a onefold integral. We point out that the integral limits of Eq. (7) specify the height of the thin barrier. If there are horizontal gaps in the barrier, the height of the barrier can be adjusted accordingly. Take the following case as an example. A barrier of height H has a horizontal gap with size $(h_2 - h_1)$ as shown in Fig. 3. The

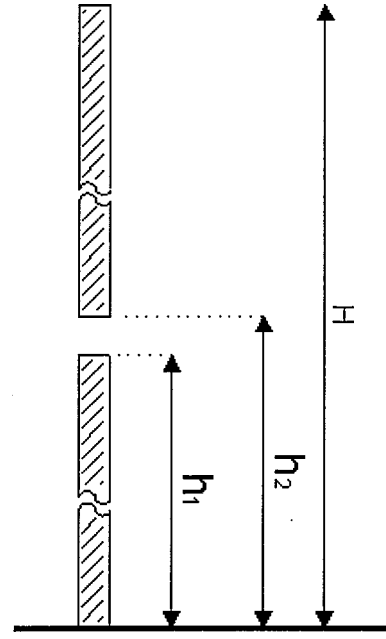


FIG. 3. The general configuration for a horizontal gap started and ended at respective heights of h_1 and h_2 on a barrier with overall height z_1 .

integral term in Eq. (5) is broken down into two parts where the integral limits for l_B range from $z=0$ to $z=h_1$ and from $z=h_2$ to $z=H$ as follows:

$$\begin{aligned} \phi(r_R, r_S) &= \phi_L(r_R|r_S) - X_R \sqrt{(8\pi k)} \frac{e^{-i\pi/4}}{16\pi^2} \left\{ \int_0^{h_1} + \int_{h_2}^H \right\} \\ &\times \left[\frac{e^{ik(R_1+R_3)}}{\sqrt{R_3^3 R_1 (R_1+R_3)}} + \frac{Q_2 e^{ik(R_1+R_4)}}{\sqrt{R_4^3 R_1 (R_1+R_4)}} \right. \\ &\left. + \frac{Q_1 e^{ik(R_2+R_3)}}{\sqrt{R_3^3 R_2 (R_2+R_3)}} + \frac{Q_1 Q_2 e^{ik(R_2+R_4)}}{\sqrt{R_4^3 R_2 (R_2+R_4)}} \right] dz. \end{aligned} \quad (9)$$

It is straightforward to generalize the formulation that allows for multiple slits on the barrier by splitting the integral into appropriate smaller intervals representing the barrier surface. The details are not shown here.

D. Ray model for barriers with horizontal gaps

The sound field behind a barrier with horizontal gaps can also be calculated by means of a simple ray method, which eliminates the need for the time-consuming numerical integration procedure described in Sec. II C. Based on the classical diffraction theory, Hadden and Pierce have derived a high-frequency asymptotic solution for the diffraction of sound by a semi-infinite wedge. Their analytic solution considers cases where the source and receiver are located at many wavelengths (large distances) from the wedge. The following symbols are found useful in writing the analytic expression: d_S and d_R are, respectively, the radial distance from the source and receiver to the edge of the wedge; θ_S and θ_R are, respectively, the angular position between the source and receiver measured from the plane $\theta=0$. We note that the diffraction of sound due to a semi-infinite thin screen

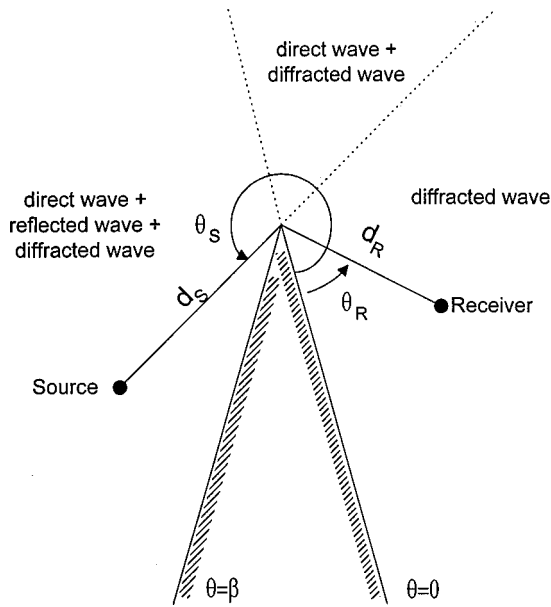


FIG. 4. The geometrical configuration used in the computation of sound fields in the presence of a barrier according to the ray method.

is a special case when the angle β is equal to 2π , see Fig. 4. For a point monopole source, the diffracted sound field can be expressed as

$$P = [A_D(X_+) + A_D(X_-)] \left(\frac{e^{i\pi/4}}{\sqrt{2}} \right) \left(\frac{e^{i \cdot k \cdot (d_S + d_R)}}{4\pi \cdot (d_S + d_R)} \right), \quad (10)$$

where

$$X_+ = X(\theta + \theta_0), \quad X_- = X(\theta - \theta_0),$$

$$X(\theta) = \sqrt{\frac{2 \cdot d_S \cdot d_R}{\lambda \cdot (d_S + d_R)}} \left[-2 \cos\left(\frac{\theta}{2}\right) \right],$$

$$A_D(X) = \text{sgn}(X) [f(|X|) - i \cdot g(|X|)],$$

$$\text{sgn}(X) = \begin{cases} 1 & \text{if } X \geq 0, \\ -1 & \text{if } X < 0. \end{cases}$$

The functions f and g are the auxiliary Fresnel functions¹² and $A_D(X)$ is known as the diffraction integral. The total diffracted sound field by a thin rigid barrier above a hard ground can be calculated by summing the four different diffracted rays as shown in Fig. 5. The total sound field depends, among other parameters, on the height of the barrier, H , and is given by

$$P_T(H) = P_1 + P_2 + P_3 + P_4, \quad (11)$$

where the P_1 , P_2 , P_3 , and P_4 indicate the sound field diffracted through path 1–3, 2–3, 1–4, and 2–4, respectively as shown in Fig. 5. They can be computed according to Eq. (10). It is important to recognize that $P_T(H)$ may be regarded as the asymptotic solution for the right side of Eq. (7). Hence, putting $Q=1$ for a hard ground and combining the two terms of Eq. (7), we can state the integral as

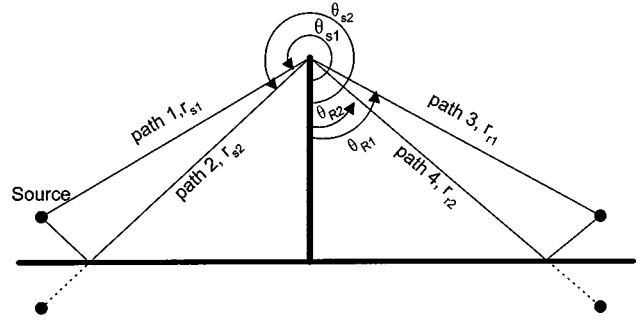


FIG. 5. Diffracted path of using the ray method for a thin barrier.

$$\int_H^\infty \left[\frac{e^{ik(R_1+R_3)}}{\sqrt{R_3^3 R_1 (R_1+R_3)}} + \frac{e^{ik(R_1+R_4)}}{\sqrt{R_4^3 R_1 (R_1+R_4)}} \right. \\ \left. + \frac{e^{ik(R_2+R_3)}}{\sqrt{R_3^3 R_2 (R_2+R_3)}} + \frac{e^{ik(R_2+R_4)}}{\sqrt{R_4^3 R_2 (R_2+R_4)}} \right] dz \\ = \frac{16\pi^2 e^{i\pi/4}}{X_R \sqrt{8\pi k}} P_T(H). \quad (12)$$

In the case of a barrier of height H with a horizontal gap starting from $z=h_1$ extending to $z=h_2$ (see Fig. 3), the sound field can be calculated by using Eq. (9) to yield

$$\phi(r_R, r_S) = X_R \sqrt{8\pi k} \frac{e^{-i\pi/4}}{16\pi^2} \left\{ \int_H^\infty + \int_{h_1}^\infty \right. \\ \left. - \int_{h_2}^\infty \left[\frac{e^{ik(R_1+R_3)}}{\sqrt{R_3^3 R_1 (R_1+R_3)}} + \frac{e^{ik(R_1+R_4)}}{\sqrt{R_4^3 R_1 (R_1+R_4)}} \right. \right. \\ \left. \left. + \frac{e^{ik(R_2+R_3)}}{\sqrt{R_3^3 R_2 (R_2+R_3)}} + \frac{e^{ik(R_2+R_4)}}{\sqrt{R_4^3 R_2 (R_2+R_4)}} \right] dz \right\}. \quad (13)$$

With the use of Eq. (13), we can compute the sound field behind a barrier that has a horizontal gap as follows:

$$\phi_T(\mathbf{r}_R, \mathbf{r}_S) = P_T(H) + P_T(h_1) - P_T(h_2). \quad (14)$$

The first term of Eq. (14) corresponds to the sound field diffracted by a thin rigid barrier without any gaps. Grouping the second and third terms of Eq. (9), we can interpret it as the sound field due to the leakage through the barrier gap. That is to say, the ‘‘leakage’’ of sound through a single gap can be represented by the difference of two barriers with different heights, h_1 and h_2

$$\phi_{\text{gap}}(\mathbf{r}_R, \mathbf{r}_S) = P_T(h_1) - P_T(h_2). \quad (15)$$

The total sound field behind a barrier with n horizontal gaps can be generalized to give

$$\phi_T(\mathbf{r}_R, \mathbf{r}_S) = \phi(\mathbf{r}_R, \mathbf{r}_S) + \sum_{i=1}^n \phi_{\text{gap}}(\mathbf{r}_R, \mathbf{r}_S), \quad (16)$$

where $\phi(\mathbf{r}_R, \mathbf{r}_S)$ is the sound field behind the thin barrier (with no gaps) and $\sum_{i=1}^n \phi_{\text{gap}}(\mathbf{r}_R, \mathbf{r}_S)$ is the leakage of sound through gaps. The leakage of sound at each gap can be cal-

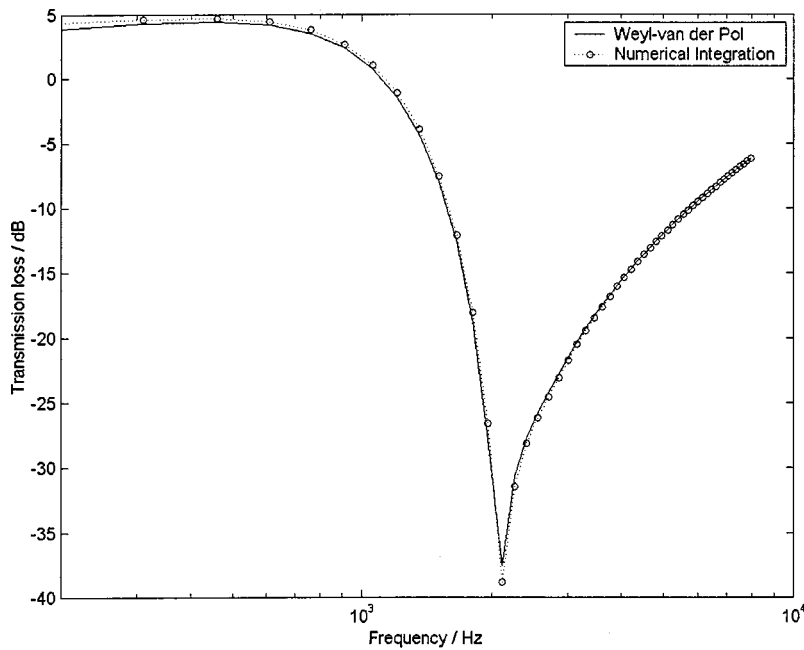


FIG. 6. Comparisons of two numerical schemes in computing sound fields. Source height=0.06 m, receiver height=0.06 m, and range=1.3 m. The impedance parameters: $\sigma_e = 10 \text{ kPa s m}^{-2}$ and $\alpha_e = 100 \text{ m}^{-1}$.

culated by using Eq. (15) with the appropriate barrier heights.

III. COMPARISON OF NUMERICAL MODELS

It is apparent that the sound field due to a point source above a flat impedance ground may be computed by evaluating the integral given in Eq. (8). However, the Weyl-van der Pol formula [Eq. (4)] is normally used in most practical situations. To confirm the validity of the computational scheme, it is useful to compare Eqs. (4) and (8) numerically. Figure 6 displays the numerical results of the sound fields predicted by these two computational schemes. The transmission loss, which is defined as the total sound field at the receiver with reference to the free-field measurements at 1 m, is plotted against frequency. Further, a two-parameter model¹³ is used to calculate the impedance of the ground in this figure and subsequent plots. The impedance, Z , is given by

$$Z = 0.436(1 + i) \sqrt{\frac{\sigma_e}{f} + 19.74i \frac{\alpha_e}{f}}, \quad (17)$$

where σ_e is the effective flow resistivity and α_e is the effective rate of change of porosity with depth. In the plot, σ_e of 10 kPa s m^{-2} and α_e of 100 m^{-1} are used. Although these parameters represent a relatively soft ground, they are the parameter values for the ground model we used in our experimental study in this paper, see Sec. IV B below.

In the numerical computations, the plane (parallel to the x - y plane) equidistant from the source and receiver is chosen for use in Eq. (8) although, in principle, any parallel plane a few wavelengths from the source and receiver may also be used. In addition, there is no general method of setting the required upper limit for z in the integral of Eq. (8). A practical way is to increase the upper limit until the numerical results converge. In our experience, the choice of the upper limit of about 70 wavelengths will normally give converged results in most cases. As shown in Fig. 6, the

agreements of these numerical results are remarkably good, and also hold for other parameter values of more realistic outdoor ground surfaces. This gives us the confidence to use the current numerical scheme, Eq. (5), in the computation of the leakage effect due to vertical gaps in a barrier. The prediction of the barrier leakage, together with the experimental results of a scale model, will be shown in the next section.

We wish to compare the integral approach, Eqs. (7) and (9), with the ray method, Eqs. (11) and (14), for the assessment of barrier leakage due to horizontal gaps over a hard ground. Numerical predictions are carried out for barriers with different geometrical configurations. A barrier of 3-m height with no gap is used. The source and receiver heights are 0.5 and 1.5 m, respectively. The distances from the source and receiver to the barrier are 7.5 and 22.5 m, respectively. This is a situation where a direct line of sight between the source and receiver cannot be established. Figure 7 shows the predicted transmission loss by using the integral approach and the ray method. Both predictions agree reasonably well with each other.

In Fig. 8, we show the transmission loss for a barrier with a shorter height of 0.7 m, such that the source can “see” the receiver. The source and receiver heights are 0.5 and 1.5 m, respectively. The source and receiver are located, respectively, at 7.5 and 22.5 m from the thin barrier. In terms of the ray method, the total sound field at the receiver consists of a direct field, a reflected sound by the ground surface, and a diffracted sound by the top edge of the barrier. Again, the numerical predictions by the integral approach and by the ray method are in accord with each other.

Next, comparisons of the predicted sound field behind a barrier with a horizontal gap are shown in Figs. 9 and 10. Equations (9) and (16) are used to predict the transmission loss of the barrier with a horizontal gap. In these two examples, the height of the barrier is 3 m and the horizontal gap starts from the hard ground, i.e., with $h_1 = 0$. The heights of the source and receiver and their relative positions from

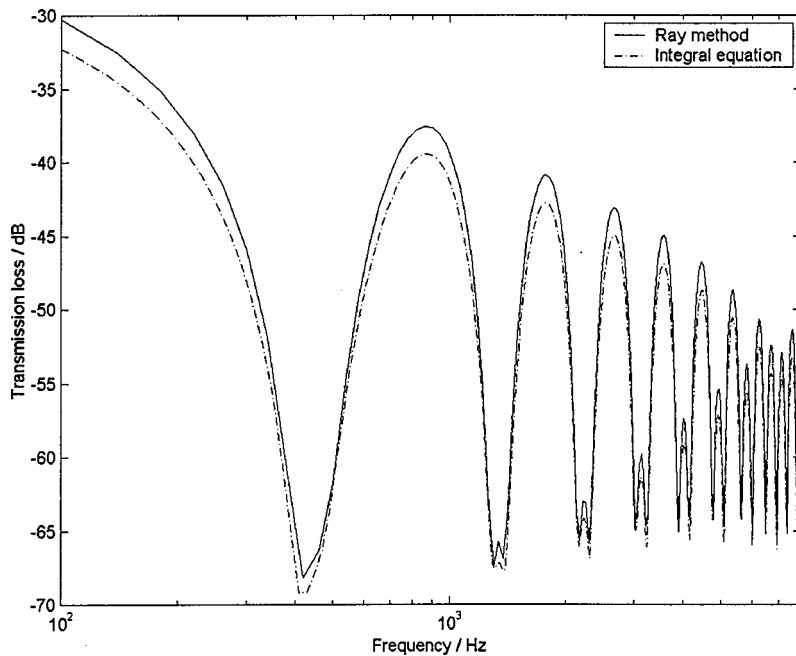


FIG. 7. Comparison of the transmission loss calculated according to the ray method (solid line) and the approximate integral equation method (chain line) for source height of 0.5 m, receiver height of 1.5 m, and barrier height of 3 m. The distances of source and receiver from the barrier are 7.5 and 22.5 m, respectively.

the barrier are the same as in the previous cases shown in Figs. 7 and 8. Horizontal gaps of 0.7 and 0.07 m, respectively, are chosen in Figs. 9 and 10 for the purpose of illustration. It can be seen from Figs. 9 and 10 that the predictions using both prediction methods match well, especially at higher frequencies.

It is shown in Figs. 7–10 that the integral approach and the ray method provide different ways of predicting the sound field behind a barrier with horizontal gaps. These two computational schemes give comparable numerical results. However, the ray method is preferable because it provides a physically interpretable solution and a more computationally efficient scheme to predict the sound field behind a barrier with horizontal gaps.

Next, we wish to investigate the accuracy of the ray model for smaller gaps where dimensions are much smaller

than the wavelength of interest. This is of considerable practical importance because many gaps in timber barriers are of the order of millimeter dimensions. In these cases, spreading from a slot would be cylindrical with effective source position centered on the gap. To establish the validity of the ray model, we compare its result with that computed by the integral approach. In the numerical simulations, the maximum gap size is set at one-third of the barrier height because any large gap sizes would be unrealistic in a practical situation. Again, the ground is assumed to be a hard, reflecting surface. The transmission loss predicted by both models for different gap sizes is shown in Fig. 11. We can see that the numerical results agree well for these two prediction schemes, although there is a slight mismatch for the case of 1 kHz. With these comparisons, we are confident that the ray method is equally applicable to wide gaps as well as smaller gaps.

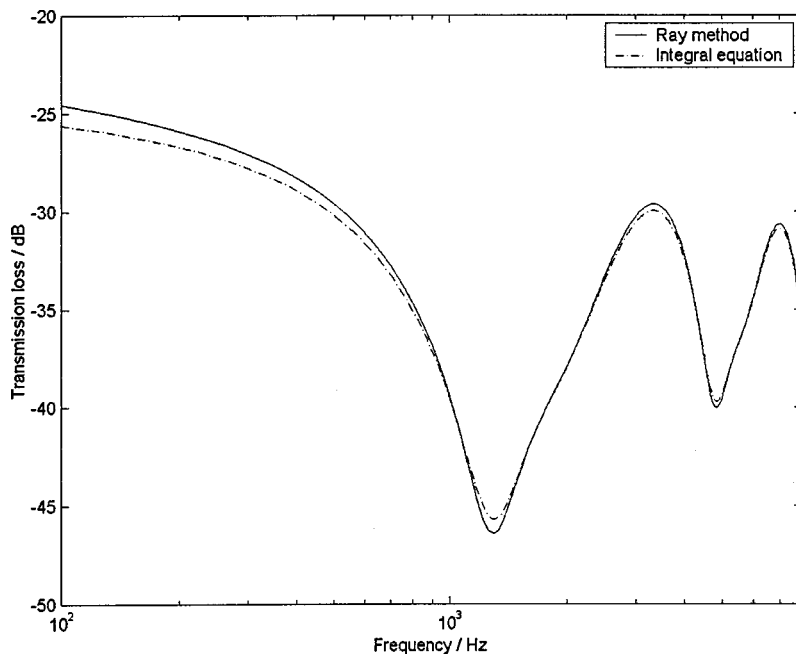


FIG. 8. Same as Fig. 7 except barrier height of 0.7 m only.

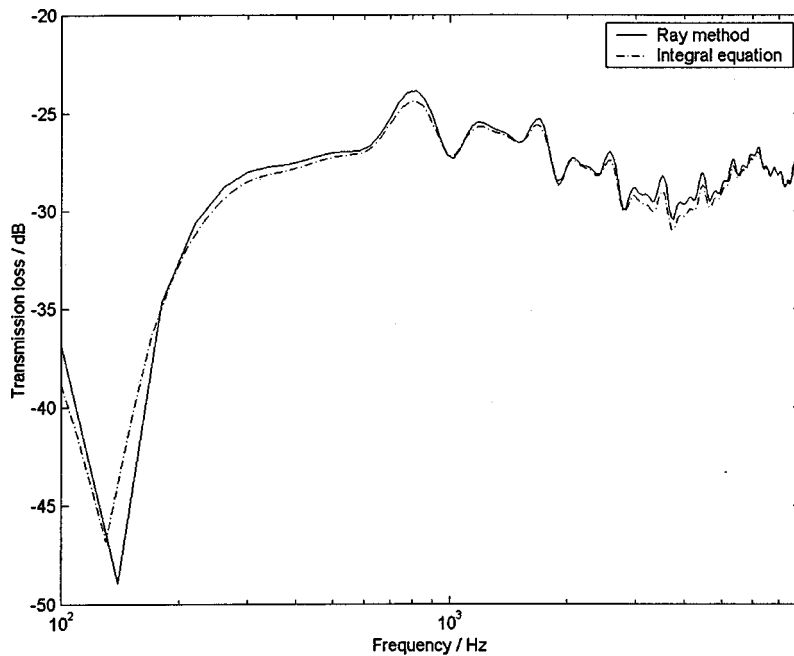


FIG. 9. Predicted transmission loss of a barrier with leakage. Source height=0.5 m, receiver height=1.5 m, source distance=7.5 m, receiver distance=22.5 m, and barrier height of 3 m with a horizontal gap of 0.7 m starting from the ground.

IV. EXPERIMENTS

A. Equipment used in indoor measurements

Indoor experiments were carried out in an anechoic chamber with an effective size of $6 \times 6 \times 4$ (high) m. The attenuation of the barrier was measured by a maximum length sequence system analyzer (MLSSA). A low-end PC with 32 MB RAM memory installed with an MLSSA card was used. A 30-W Tannoy loudspeaker was used as a point source. It was connected to an MLSSA card through an amplifier (B&K 2713). A BSWA TECH MK224 microphone, together with a BSWA TECH MA201 preamplifier, was used as a receiver. The microphone was connected to the MLSSA card through a BSWA TECH amplifier MC102. Two sets of measurements were conducted to study the ef-

fects of a vertical gap and a horizontal gap in a model barrier with different configurations described in the following sections.

B. Experimental results for a vertical gap in a barrier

In this experiment, the barrier was made of two identical hardwood boards, 0.26 m high and 2.44 m long. These two hardwood boards were placed adjacent to each other and a gap of 3 cm was left between them. The overall length of the barrier was approximately 4.91 m. The plane containing the source and receiver was perpendicular to the barrier plane. That plane was placed either in the middle barrier gap or offset from the middle of barrier gap. The barrier was placed on an absorbing ground which was simulated by laying a

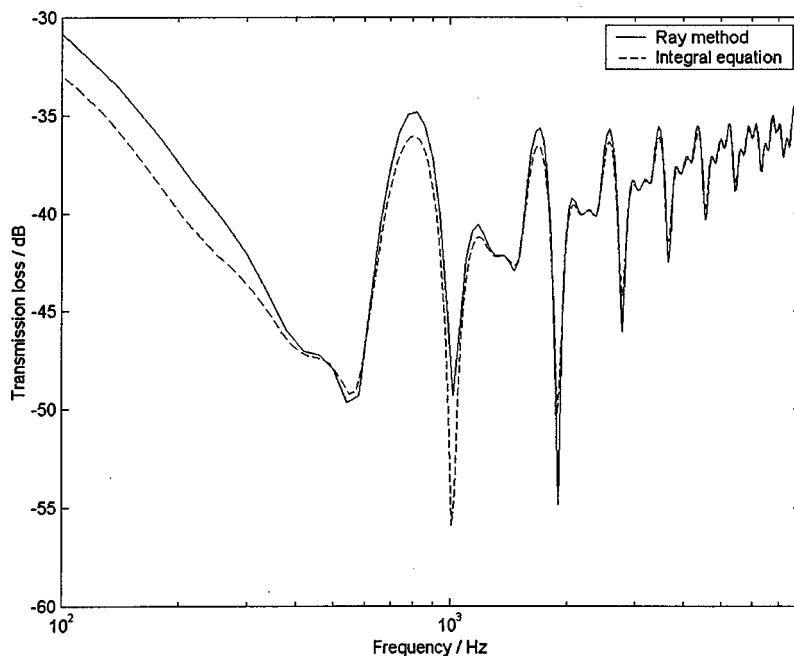


FIG. 10. Same as Fig. 9 except that the horizontal gap is 0.07 m wide starting from the ground.

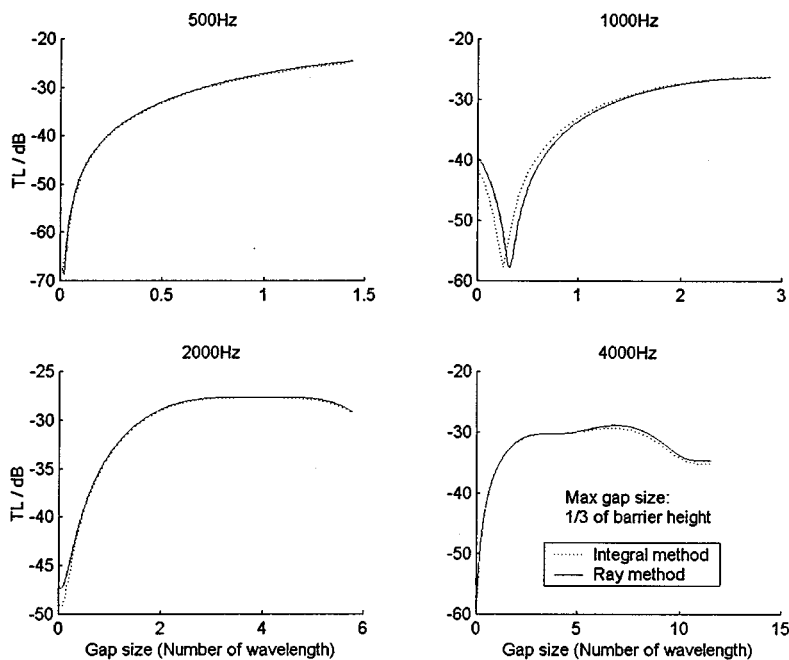


FIG. 11. Predicted transmission loss of a barrier with different gap sizes. Source height=0.5 m, receiver height=1.5 m, source distance=7.5 m, receiver distance=22.5 m, and barrier height of 3 m (a) Frequency=500 Hz; (b) Frequency=1000 Hz; (c) Frequency=2000 Hz; and (d) Frequency=4000 Hz.

thick layer of carpet on a hardwood board. Preliminary measurements were conducted to characterize the impedance of the ground surface. The two-parameter model was used to compute the impedance of the ground. Best-fit parameters for σ_e and α_e are 10 kPa s m^{-2} and 100 m^{-1} , respectively. Figure 12 shows typical measured and theoretical results by Eq. (4) for impedance characterization of the carpet.

The predictions by the integral method, cf. Eq. (5), and experimental measurements for a barrier with a vertical gap are shown in Figs. 13 and 14. The width of the vertical gap, the source and receiver heights, the distance from the source to the barrier, and the distance from the barrier to the receiver are 0.03, 0.045, 0.045, 0.3, and 0.6 m, respectively. As shown in the figures, the numerical predictions agree reasonably well with the experimental measurements. The experi-

ments were arranged such that the line of sight can be established from source to receiver. Under this stringent condition, other simple numerical models^{4,5} cannot be used, but the proposed integral approach [see Eq. (5)] may be used instead to predict the sound field with reasonable accuracy.

C. Experimental results for a horizontal gap in a barrier

The barrier used in the experiments was made of a thin hardwood board, 0.26 m high and 2.44 m long. The barrier was raised up 0.018 m above the ground so that the effective height of the barrier was 0.278 m with a gap of 0.018 m. The total area of the gap was approximately 6.5% of the total area of the barrier. The barrier was laid on a hardwood board,

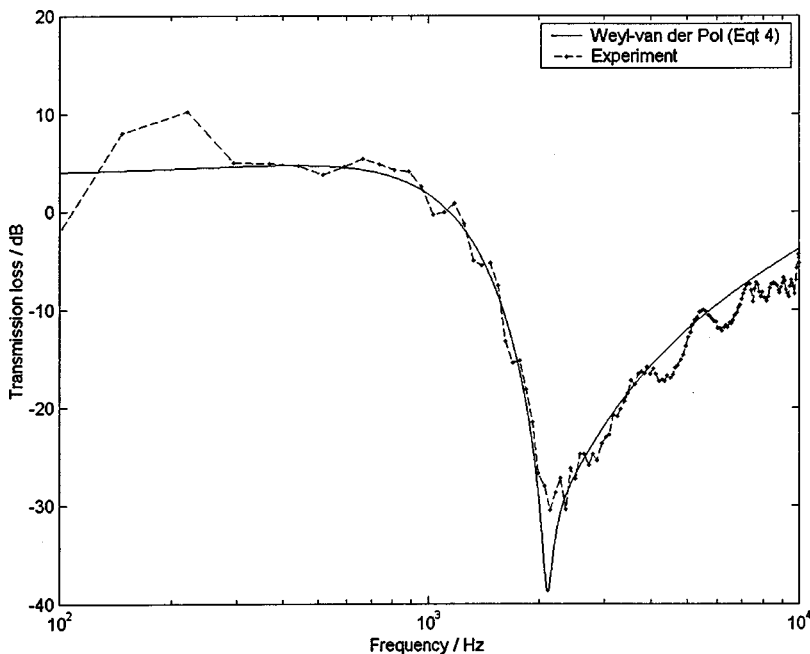


FIG. 12. Predicted and experimental results of a point source above a carpet. Source height=0.06 m, receiver height=0.06 m, and range=1.3 m. The best-fit parameters are found to be $\sigma_e=10 \text{ kPa s m}^{-2}$ and $\alpha_e=100 \text{ m}^{-1}$.

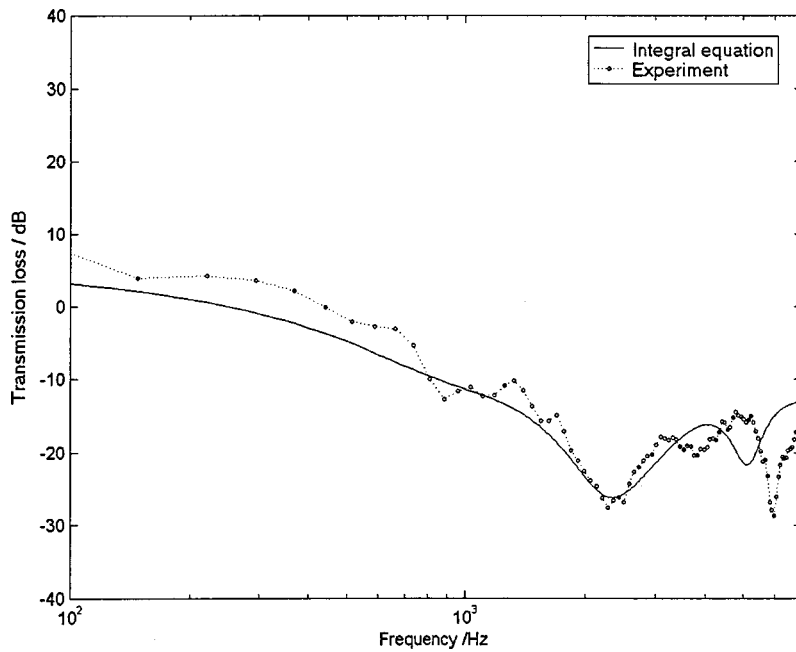


FIG. 13. Predicted and measured transmission loss spectra of a barrier with height 0.26 m and a vertical gap of width 0.03 m. The source and receiver are aligned in the same plane perpendicular to the barrier, i.e., no offset. In the measurements, the source and receiver are located at 0.045 m above an impedance ground surface. The distances of source and receiver from the barrier are 0.3 and 0.6 m, respectively. This configuration contained line of sight between source and receiver.

which was varnished to ensure an acoustically hard surface. The source and receiver were placed in the middle of the barrier, and the height of the gap was measured from the hard ground.

The numerical prediction using Eq. (9) and experimental data for a model barrier with a horizontal gap are shown in Figs. 15(a)–(d). The source height and receiver heights are 0.065 and 0.105 m, respectively. The distance of the source from the barrier is 0.5 m. Transmission loss is plotted against the distance of the receiver from the barrier. The distance ranges from 0.4 to 0.8 m. It can be seen that the numerical results agree reasonably well with the experimental data in the spatial domain. We have also compared the measured and predicted transmission loss spectra for different source and receiver configurations. The results are not shown for

brevity but the agreements between theory and experiments are generally good.

D. Outdoor experiments

Outdoor field measurements were conducted to validate the numerical schemes for the assessment of leakage due to the presence of a horizontal gap in a barrier. A roadside barrier with dimensions 75 m long and 1.87 m high was under investigation. The roadside barrier was designed for the noise abatement of a nearby community that was about 20 m from the nearside of an existing road. The barrier was still under construction during the measurement periods. We visited the site twice, in November and in March of the following year. In all measurements, Plexiglas[®] transparent

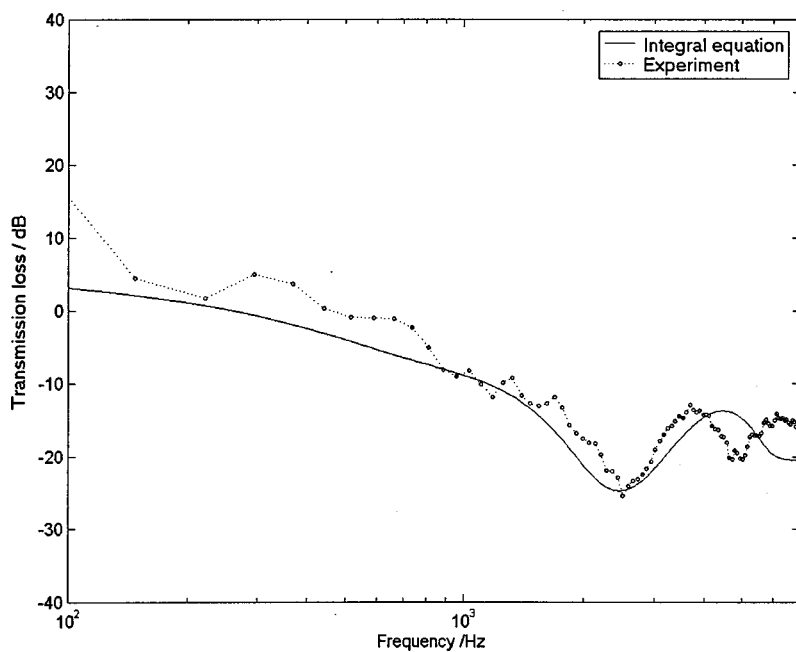


FIG. 14. Same as Fig. 13 but the source and receiver are located at an offset of 0.1 m. This configuration contained no line of sight between source and receiver.

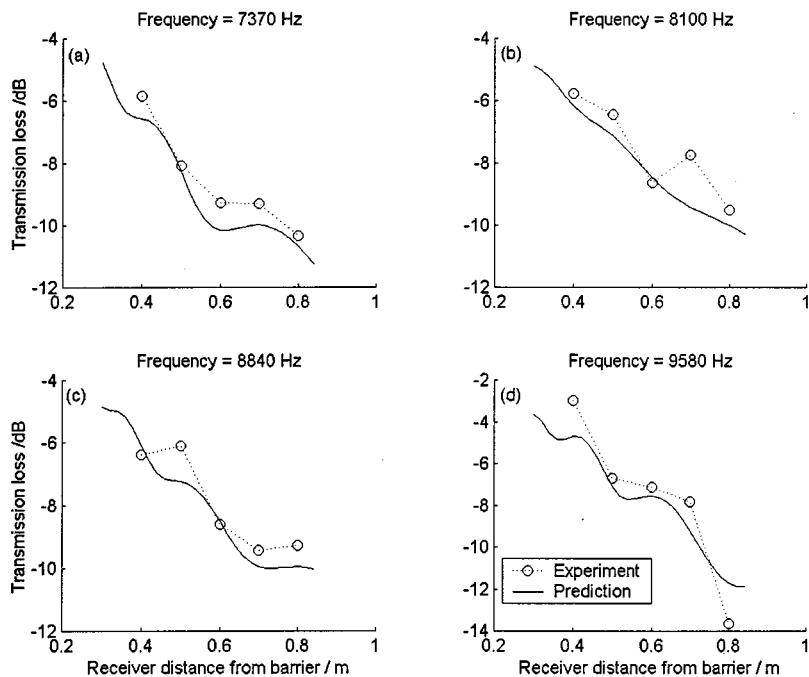


FIG. 15. Predicted and measured transmission loss of barrier with a horizontal gap at different frequencies for different distances from the receiver to the barrier. Source height = 0.065 m, receiver height = 0.105 m, and the distance from the source to the barrier is 0.5 m. (a) Frequency = 7370 Hz; (b) Frequency = 8100 Hz; (c) Frequency = 8840 Hz; and (d) Frequency = 9580 Hz.

panels were installed above a hard ground. However, during our first visit, a horizontal gap with 4.2% of the total barrier height (size 0.08 m and located at 0.99 m above the ground) was present in the barrier. By our second visit, the construction of the barrier was near completion, such that the gap was sealed.

Noise emissions from passing vehicles were used as the noise source. The roadside barrier was erected at the roadside of a two-lane road with vehicles running in opposite directions in each traffic lane. Due to the construction of the barrier, the traffic was reduced to a single lane. A traffic light was used to control the traffic flow in a single direction at any time. The distance of the effective source was estimated to be 5.8 m from the barrier. The ground on either side of the barrier was at different levels and was treated simply as acoustically hard. The geometrical details of the outdoor experiments with dimensions are shown in Fig. 16.

As a result of two site visits, we were able to record experimental data “before” and “after” the gap was sealed. The experimental data for the two field measurements were

collected essentially at the same receiver locations. This allowed us to assess the barrier leakage by comparing two sets of field data. Two RION NA-27 sound-level meters were used to record the sound field. In each set of measurements, a fixed sound-level meter was placed 1.28 m above the top edge of the barrier as a reference position. The reference position was chosen so that the effect of the barrier could be minimized. Hence, the measured results at the reference position may be used to quantify the noise level generated by the traffic. In addition, simultaneous measurements were conducted at the reference position and a target receiver position. Five-minute A-weighted equivalent sound levels ($L_{Aeq,5 \text{ min}}$) were taken and three sets of measurements were taken in each position. Five receiver positions, namely m1, m2, m3, m4, and m5, as shown in Fig. 16, were chosen for our measurements. Traffic flow on the lane was also counted for reference purposes. It was shown that the predicted noise levels based on the traffic flow count¹⁴ were consistent with the measured results.

The attenuation, which was defined as the sound levels

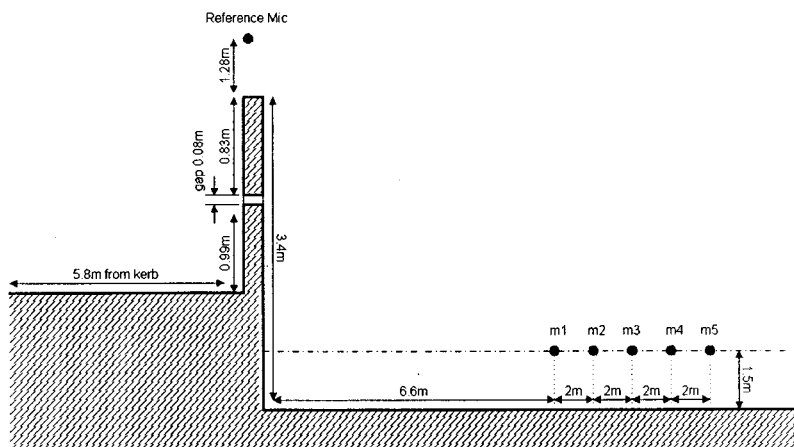


FIG. 16. A schematic diagram for outdoor measurements.

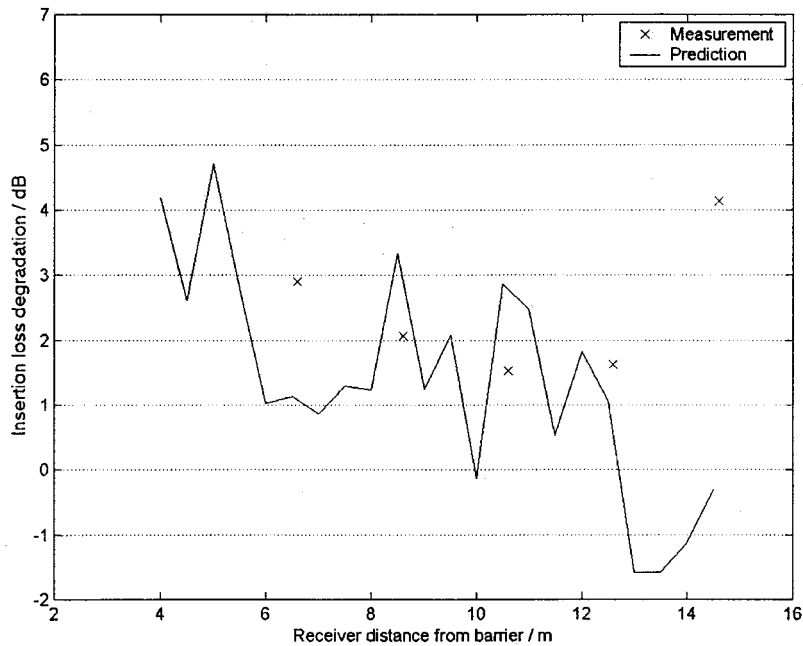


FIG. 17. Predicted and measured insertion loss degradation in A-weighting of a barrier due to the presence of a horizontal gap at different receiver locations.

between the reference and receiver positions, was calculated by subtracting their corresponding equivalent sound levels, $L_{Aeq,5 \text{ min}}$. To assess the effect of the horizontal gap on the acoustic performance of the barrier, we define the insertion loss degradation of the barrier as the difference of the attenuation between the before and after measurements. This also allows us to validate our numerical scheme developed in Sec. III.

Outdoor experiments to illustrate the effect of a horizontal gap in barriers are shown in Fig. 17. We remark that it is advantageous to use the insertion loss degradation in our comparisons because it is insensitive to the change of the source spectrum. In fact, a white-noise source spectrum is assumed in our numerical predictions. The octave sound fields are initially computed and subsequently weighted to obtain the A-weighted noise levels. The change in A-weighted noise levels with or without a horizontal gap can then be calculated which gives the required insertion loss degradation.

The insertion loss degradation is plotted against five different receiver positions. From outdoor measurements, it is found that the 4.2%-gap has led to the degradation of the insertion loss by an average of about 2dB(A) at different receiver positions. Numerical predictions of the insertion loss using Eq. (9) are shown in the same figure. It can be seen that the discrepancy between the numerical models and the experimental data is less than 2dB(A), except at the receiver's position m5. This position was closest to the neighborhood community adjacent to the roadside barrier. The large error of m5 was due to the "unwanted" disturbances generated by local residents as a result of various community activities.

V. CONCLUSIONS

The leakage of sound through barriers has been investigated by using two different numerical methods. Numerical comparisons of these two methods have suggested that both

schemes yield good accuracy as compared with experimental data. The first method, which is based on an approximation of the Helmholtz integral equation, reduces the problem to a simple numerical integration procedure. This allows a more straightforward implementation of a numerical scheme that does not require the solution of a large set of simultaneous equations. When the previous work was published,⁸ accurate asymptotic formulas were not widely used to predict the sound field above an impedance ground. We have demonstrated that a more efficient calculation procedure can be achieved through the use of the Weyl-van der Pol formula in Eq. (1).

The second method is a ray approach based on Pierce's solution for the diffraction of sound around wedges. The ray approach can be generalized to compute the sound fields around a thin rigid barrier with horizontal gaps. It is advantageous to use Eq. (16) to compute the noise levels around barriers because the need for a numerical integration is not required.

ACKNOWLEDGMENTS

The authors are grateful to the Research Committee of the Hong Kong Polytechnic University (PolyU) for financial support. H.Y.W. is supported by a PolyU research studentship. The project is supported in part by the Research Grants Committee of the Hong Kong Special Administrative Region. The provisions of an outdoor experimental test site and partial financial support by Active Way Ltd. are gratefully acknowledged.

¹Z. Maekawa, "Noise reduction by screens," *Appl. Acoust.* **1**, 157-173 (1968).

²D. C. Hothersall, S. N. Chandler-Wilde, and M. N. Hajmirzae, "Efficiency of single noise barriers," *J. Sound Vib.* **146**(2), 303-322 (1991).

³T. Terai, "On calculation of sound fields around three-dimensional objects by integral equation method," *J. Sound Vib.* **69**(1), 71-100 (1980).

⁴Y. Kawai and T. Terai, "The application of integral equation methods to

- the calculation of sound attenuation by barriers," *Appl. Acoust.* **31**, 101–117 (1990).
- ⁵A. D. Pierce, "Diffraction of sound around corners and over wide barriers," *J. Acoust. Soc. Am.* **55**, 941–955 (1991).
- ⁶W. J. Hadden and A. D. Pierce, "Diffraction of sound around corners and over wide barriers," *J. Acoust. Soc. Am.* **69**, 1266–1276 (1981).
- ⁷G. R. Watts, "Effects of sound leakage through noise barriers on screening performance," 6th International Congress on Sound and Vibration, Copenhagen, Denmark, pp. 2501–2508 (1999).
- ⁸S. I. Thomasson, "Diffraction by a screen above an impedance boundary," *J. Acoust. Soc. Am.* **63**, 1768–1781 (1978).
- ⁹K. B. Rasmussen, "A note on the calculation of sound propagation over impedance jumps and screens," *J. Sound Vib.* **84**(4), 598–602 (1982).
- ¹⁰J. J. Bowman, T. B. A. Senior, and P. L. E. Uslenghi, *Electromagnetic and Acoustic Scattering by Simple Shapes* (North-Holland, Amsterdam, 1969), p. 29.
- ¹¹C. F. Chien and W. W. Soroka, "Sound propagation along an impedance plane," *J. Sound Vib.* **43**, 9–20 (1975).
- ¹²M. Abramowitz and A. Stegun, *Handbook of Mathematical Functions with Formulas, Graphs, and Mathematical Tables* (Dover, New York, 1970), Chap. 7, p. 300.
- ¹³K. Attenborough, "Ground parameter information for propagation modeling," *J. Acoust. Soc. Am.* **92**, 418–427 (1992).
- ¹⁴Department of Transport, UK, *Calculation of Road Traffic Noise* (Her Majesty's Stationery Office, London, 1988).

Community noise exposure and stress in children

Gary W. Evans^{a)}

*Design and Environmental Analysis, Human Developments, Cornell University,
Ithaca, New York 14853-4401*

Peter Lercher^{b)}

Institute of Social Medicine, University of Innsbruck, Sonnenburgstrasse 16, A-6020 Innsbruck, Austria

Markus Meis

*Institute for Research into Man-Environment-Relations, Department of Psychology,
University of Oldenburg, D-26111 Oldenburg, Germany*

Hartmut Ising

Federal Environmental Agency, Institute for Water, Soil, and Air Hygiene, Germany

Walter W. Kofler

*Institute of Hygiene and Social Medicine, Section Social Medicine and School of Public Health,
University of Innsbruck, Sonnenburgstrasse 16, A-6020 Innsbruck, Austria*

(Received 19 June 2000; accepted for publication 23 November 2000)

Although accumulating evidence over the past two decades points towards noise as an ambient stressor for children, all of the data emanate from studies in high-intensity, noise impact zones around airports or major roads. Extremely little is known about the nonauditory consequences of typical, day-to-day noise exposure among young children. The present study examined multimethodological indices of stress among children living under 50 dB or above 60 dB (A-weighted, day-night average sound levels) in small towns and villages in Austria. The major noise sources were local road and rail traffic. The two samples were comparable in parental education, housing characteristics, family size, marital status, and body mass index, and index of body fat. All of the children were prescreened for normal hearing acuity. Children in the noisier areas had elevated resting systolic blood pressure and 8-h, overnight urinary cortisol. The children from noisier neighborhoods also evidenced elevated heart rate reactivity to a discrete stressor (reading test) in the laboratory and rated themselves higher in perceived stress symptoms on a standardized index. Furthermore girls, but not boys, evidenced diminished motivation in a standardized behavioral protocol. All data except for the overnight urinary neuroendocrine indices were collected in the laboratory. The results are discussed in the context of prior airport noise and nonauditory health studies. More behavioral and health research is needed on children with typical, day-to-day noise exposure. © 2001 Acoustical Society of America. [DOI: 10.1121/1.1340642]

PACS numbers: 43.50.Qp, 43.50.Lj [MRS]

I. INTRODUCTION

Although the predominant health concern of chronic noise exposure is auditory damage, increasing attention is being paid to the nonauditory health effects of noise. The nonauditory effects of noise have been conceptualized in terms of stress, suggesting that chronic noise exposure leads to an overload of stimulation that is experienced as an irritating, annoying stimulus that interferes with relaxation as well as the ability to concentrate (Broadbent, 1971; Evans and Cohen, 1987; Lercher, 1998). The uncontrollability of chronic noise exposure also appears to be a salient aspect of its stressful properties (Cohen *et al.*, 1986; Glass and Singer, 1972). Evidence that noise can function as a stressor includes elevated psychophysiological activation, greater psychosomatic symptoms of anxiety and nervousness, and deficits in motivation indicative of helplessness (Cohen *et al.*, 1986;

Evans, 2001; Ising, Babisch, and Kruppa, 1999; Ising and Braun, 2000; Kryter, 1994; Lercher, 1996; Medical Research Council, 1997). It is important to recognize that most of the evidence for these findings comes from individuals with no discernible hearing deficits. Nonauditory effects of noise appear to occur at levels far below those required to damage hearing.

The present study fills a gap in the noise and health effects literature by examining stress outcomes of typical, everyday community noise exposure among children. Prior work on the stress effects of noise has focused on high-intensity noise, predominantly occupational and airport noise sources, which typically exceed day-night sound levels (L_{dn}) of 70 dBA (Kryter, 1994; World Health Organization, 1995). We currently know very little about the nonauditory health effects of chronic, lower intensity, everyday noise exposure. A typical urban neighborhood residential area in the United States ranges from 55 to 70 dBA L_{dn} (Kryter, 1994). In the European Union about 20% of the population lives in areas with daytime $Leq > 65$ dBA (Gottlob, 1995).

^{a)}Electronic mail: gwel@cornell.edu

^{b)}Electronic mail: peter.lercher@uibk.ac.at

Psychophysiological activation, particularly blood pressure, has been inconsistently related to occupational noise (Babisch, 1998; Medical Research Council, 1997; Thompson, 1993) but is correlated with airport noise exposure among children (Cohen *et al.*, 1986; Evans, Hygge, and Bullinger, 1995; Evans, Bullinger, and Hygge, 1998a; Ising *et al.*, 1990; Regecova and Kelleroval, 1995). Herein, we examine both cardiovascular and neuroendocrine sequelae of low-intensity noise exposure among young children. Furthermore, only one prior developmental study has examined psychosomatic symptoms of high-intensity noise, revealing a positive correlation between aircraft noise and high stress symptoms among 11-year-olds (Evans *et al.*, 1995). Thus, we need to determine whether more typical community noise exposure has analogous impacts.

Beginning with the pioneering work of Glass and Singer (1972), many studies have demonstrated, both in the laboratory and in the field, that exposure to high-intensity, uncontrollable noise can cause motivational deficits (Cohen, 1980). Work with children has shown that chronic aircraft noise exposure is associated with similar deficits (Bullinger *et al.*, 1999; Cohen *et al.*, 1986; Evans *et al.*, 1995).

All prior nonauditory noise research with children with one exception (Evans *et al.*, 1998a) is cross sectional, and thus subject to concerns about the comparability of noise and quiet community samples. Although most of these studies have employed statistical controls for social class, none has examined a wide range of other potentially important variables including biological (e.g., gender), social (e.g., family size), or other environmental conditions (e.g., housing). Thus in addition to examining the potential nonauditory health concomitants of regular, everyday community noise exposure, we investigate other biological, social, and environmental variables that might covary with community noise exposure and nonauditory health.

II. METHOD

A. Sample

The sample consists of 115 children in grade 4 who were selected from a large, representative sample of children living in the lower Inn Valley of Tyrol Austria. This area consists of small towns and villages with a mix of industrial and agricultural activities in rural areas outside of Innsbruck. The purpose of the larger study is to investigate alpine environmental conditions in Austria and monitor over time how changes in environmental quality are related to children's physical and mental health. The selected subsample was chosen for the purpose of more in-depth investigation of children exposed to either relatively low or relatively high, typical community noise levels. The primary noise sources are road and rail traffic. One half of the sample reside in neighborhoods below 50 dBA (day-night average sound level) ($M = 46 L_{dn}$) and one half live in areas above 60 dBA ($M = 62 L_{dn}$). The interquartile range of sound levels in the low exposure sample was 34–50 dBA, L_{dn} with 1% peak levels 57 dBA. For the high exposure group the interquartile range was 52–71 dBA, L_{dn} , with an $L_1 = 74$). Overall median night rail sound levels were 3 dBA higher than daytime lev-

TABLE I. Sample background information.

	Low noise sample	High noise sample	Statistic
Age	9.90	10.25	$t(113) < 1.0^a$
Gender (% male)	54	60	$X^2(1) < 1.0$
Mother's education (1 = <high school–5 = graduate school)	2.50	2.44	$t(112) < 1.0$
% Single parent	7	5	$X^2(1) < 1.0$
Family size	4.33	4.41	$t(113) < 1.0$
Density (people/room)	0.80	0.84	$t(112) < 1.0$
Housing type			
% multiple dwelling	22	27	$X^2(2) = 2.47, ns$
% row house	26	14	
% single family detached	52	59	
Body mass index (kg/m ²)	17.31	17.77	$t(107) < 1.0$

^aDegrees of freedom vary because of missing data.

els and road traffic levels during the day exceeded night-time levels by 7 dBA. Noise measurement was based on sound exposure modeling data (Soundplan) according to Austrian guidelines (OAL Nr. 28+30, ONORM 8 5011). Afterwards, calibration was conducted and corrections were applied to the modeled data based on day and night recordings from 31 measuring points. Based on both data sources, approximate day–night levels (L_{dn} in dBA) were calculated and linked via GIS to each home address.

Table I depicts basic background information for the two samples. Note that the samples do not differ on any of these variables. The sociodemographic homogeneity of the selected subsamples also closely matches the overall representative sample and is consistent with Austrian national census data for rural, alpine regions.

B. Procedure

The children were tested individually in a mobile laboratory that was climate controlled and sound attenuated ($Leq < 35$ dBA). The experimenter was blind to the child's ambient noise condition. Data collection from the children took approximately 1 h and consisted of three general topics: noise annoyance, cognitive processing, and stress. All children were given the same protocol in the exact same order. Given the focus of the present article on stress, only these measures are detailed.

School children were tested in the trailer for normal hearing with a calibrated screening audiometer (EFEU type A 120). The audiometer and training of the testers were provided by the Environmental Protection Agency in Berlin and its exclusion criteria applied (30 dB at 250 or 500 Hz or 4 kHz).

1. Psychophysiological stress

Overnight (8-h) urine was collected with the assistance of the child's mother. The total volume was measured and four small subsamples were randomly extracted. For two of these the pH was adjusted with HCl to reduce catecholamine oxidation. The four subsamples were immediately frozen and stored at -70 °C until assayed. The catecholamines, epi-

nephrine and norepinephrine, were assayed with high-performance liquid chromatography (HPLC) with electrochemical detection (Riggin and Kissinger, 1977) and free cortisol (Schoneshofer *et al.*, 1985) and 20a-dihydrocortisol, a cortisol metabolite (Eisenschmid *et al.*, 1987; Schoneshofer *et al.*, 1986) with HPLC. Recent biochemical research indicates that 20a-dihydrocortisol may be a more sensitive index of chronically elevated corticosteroids. Urinary cortisol, epinephrine, and norepinephrine are valid indices of chronic stress (Baum and Grunberg, 1995). Resting blood pressure was evaluated while the child was seated quietly. After acclimating the child to the apparatus and an initial practice reading, two blood-pressure readings were taken with a calibrated sphygmomanometer (Bosch, Sysdion model) over a 6-min period. These two readings were then averaged. Resting heart rate was monitored continuously (Polar Accurex Plus) over the 6-min rest period and during the experimental protocol. Heart rate reactivity was calculated by subtracting the mean resting heart rate from the average heart rate during the most stressful part of the protocol (a difficult reading test that lasted approximately 5 min).

2. Motivation

An adaptation for children of the Glass and Singer (1972) stress-aftereffects test was given to measure motivational deficits (Evans *et al.*, 1995). Children were given geometric puzzles consisting of common objects (e.g., animals) interconnected by lines. The child's task was to trace over the lines between all of the objects without going over any line twice or lifting their pencil. Multiple copies of the same puzzle were stacked in a pile, and the children instructed to work on each puzzle until solved or to take another copy when they wished to try it again. The children were informed that they could work on the first pile of puzzles until solved or they felt unable to complete the puzzle. At that point they could move on to a second set of puzzles. The children were also informed that once they moved on to the second pile of puzzles, they could not return to the first pile. Unbeknownst to the child, the first pile of puzzles was unsolvable. The number of puzzles attempted on the first pile of puzzles is the index of motivation. The second set of puzzles was solvable to insure that all children completed the procedure with a success experience. All children were assured that they did very well and that most children find the initial puzzle very difficult. Many studies of both acute and chronic stressors have shown the sensitivity of performance on this task to exposure to uncontrollable stressors including noise, crowding, and electric shock (Cohen, 1980; Evans, 2001; Glass and Singer, 1972). The child-adapted version of this procedure has also proven reliable in measuring exposure to both crowding and noise (Evans, 2001). The measure is believed to reflect motivational deficits indicative of learned helplessness because of its sensitivity to experimental or naturalistic variability in controllability of adverse stimuli. This measure is also sensitive to individual differences in control-related beliefs (e.g., locus of control) (Cohen, 1980; Evans, 2001; Glass and Singer, 1972).

TABLE II. Psychophysiological results.

	Low noise sample	High noise sample
Diastolic blood pressure	73.00 mmHg	72.75 mmHg
Systolic blood pressure	115.32 mmHg	117.29 mmHg ^c
Heart rate	89.99 bpm ^a	90.43 bpm
Heart rate reactivity	3.87 bpm	5.81 bpm ^c
Epinephrine	697.96 ng/8 h ^b	690.48 ng/8 h
Norepinephrine	8920.38 ng/8 h	9900.86 ng/8 h
20A-dihydrocortisol	7.75 ug/8 h	9.80 ug/8 h ^c
Cortisol	3.86 ug/8 h	4.87 ug/8 h ^c

^abpm=beats per minute.

^bh=hours.

^cStatistically significant difference (see the text for details).

3. Stress symptoms

A symptoms subscale of a standardized German instrument for the assessment of stress in children, StreBerleben und Streßbewältigung im Kindesalter (SSK) (Lohaus *et al.*, 1996) was administered to each child. The SSK subscale for stress symptoms consists of eight, 3-point ratings (never, sometimes, often) of symptoms for the previous week. Sample items include "felt tired," "didn't have a good appetite." The eight items formed a coherent scale ($\alpha = 0.62$). As a partial check on ambient noise exposure, each child was also asked to indicate how noisy he/she felt their neighborhood was on a three-item, 4-point rating scale ($\alpha = 0.72$).

III. RESULTS

As a partial check on the ambient noise comparisons, children from noisier areas rated their neighborhoods as significantly more noisy ($M = 2.57$, $s.d. = 0.86$) than those from relatively quiet areas ($M = 2.21$, $s.d. = 0.75$), $t(113) = 2.35$, $p < 0.01$ (all significance levels are one tailed, unless otherwise noted). Except where noted there were no interactions between gender and noise exposure, and thus the results are collapsed across gender. As expected, given the homogeneity of the two samples (Table I), statistical controls for background factors had no impact on the results.

As shown in Table II, children exposed to higher levels of ambient noise had marginally elevated resting systolic blood pressure in comparison to their low-noise counterparts, $t(107) = 1.34$, $p < 0.09$. Degrees of freedom vary throughout because of missing data. Both resting diastolic blood pressure and heart rate were equivalent between the two groups (see Table II). However, the noise group had higher reactivity to the acute stressor (difficult reading test) than the quiet group, $t(106) = 1.74$, $p < 0.04$. Addition of a statistical control for body fat (body mass index) had no effect on the results and thus was omitted from the analyses of cardiovascular functioning. Overnight resting epinephrine levels were equivalent for the quiet and noisy groups, $U = 1388$, $p < 0.23$. Similar results were found for urinary norepinephrine, $U = 1617$, $p < 0.97$. Total free cortisol was elevated in the noise group relative to the quiet group, $U = 1273$, $p < 0.05$, as was the 20a-hydroisomers, $U = 1184$, $p < 0.02$. Because the neuroendocrine data were highly skewed, non-parametric tests (Mann-Whitney U) were employed.

TABLE III. Motivation results (number of puzzle attempts).

Sex	Noise	
	Low	High
Male	4.91	5.54
Female	5.50	4.26

Children from the noisier neighborhoods reported greater stress symptoms over the previous week ($M=1.55$, $s.d.=0.38$) in comparison to those from quiet areas ($M=1.39$, $s.d.=0.34$), $t(113)=2.41$, $p<0.005$.

Table III depicts the motivation results. For the number of attempts on the unsolvable puzzle, there was a significant gender by noise interaction $F(1,111)=4.61$, $p<0.03$ (two tailed). Inspection of the simple slopes revealed that noise had no effect on motivation for the boys [$b=0.93$, $t(111)=1.41$ ns]; whereas for girls, increases in noise were related to decreased task performance [$b=-1.24$, $t(111)=1.62$, $p<0.05$]. There were no main effects for noise or gender on motivation.¹ Given prior research showing similar patterns of motivational deficits and residential density, the above analysis was repeated with an additional control for density (people per room). The statistical interaction remained significant with this additional control.

IV. DISCUSSION

To our knowledge the present results represent the only published data on the nonauditory health effects of typical, ambient community noise levels. Utilizing a cross-sectional sample of fourth-grade children from towns and villages in alpine areas in Austria, we provide evidence that differences among low-intensity, common everyday noise exposures may have health consequences for children. Children residing in noisier areas of communities have marginally higher resting systolic blood pressure, greater heart rate reactivity to an acute stressor (a test), and higher overnight cortisol levels indicative of modestly elevated physiological stress. Recall also that these physiological measures were taken at rest, and in the case of the cardiovascular measures, under well-controlled, quiet conditions. Since the overnight neuroendocrine measures were taken at home overnight, noise exposure during the assessments were different for the two samples. However, the overnight data represent the long-term, habitual noise environment, which typically remains stable over time. The combination of elevated cardiovascular and neuroendocrine measures provides support for the stress model of chronic noise exposure (Baum and Grunberg, 1995; Evans and Cohen, 1987). These elevations are similar but smaller than those found in prior studies of high-intensity aircraft noise exposure among children (Evans, 2001; Medical Research Council, 1997). Although the degree of physiological activation is modest and well below levels indicative of pathology, it does suggest that children living in noisier areas of residential communities are subject to stress. This interpretation is bolstered by the findings that these same children also report higher levels of stress symptoms on a standardized scale. The latter data also replicate and

extend the one prior finding on chronic, high-intensity airport noise exposure and psychological distress in children (Evans *et al.*, 1995).

When people are continuously confronted with aversive stimuli that they cannot control, negative motivational consequences ensue (Peterson, Maier, and Seligman, 1993). Learned helplessness describes a syndrome in which the organism learns that the outcomes of its efforts to control or escape from an uncontrollable stimulus are futile (Seligman, 1975). Several studies have shown that both acute and chronic high-intensity noise are capable of inducing helplessness (Cohen, 1980; Evans, 1998; Glass and Singer, 1972). The present motivational results replicate three prior airport noise studies (Bullinger *et al.*, 1999; Cohen *et al.*, 1986; Evans *et al.*, 1995), but demonstrate the noise–helplessness relation only among girls. There is evidence in the general learned-helplessness literature of greater vulnerability to helplessness among females (Dweck and Elliot, 1983). Furthermore, a recent residential crowding study found the same gender interaction pattern (Evans *et al.*, 1998b).

Although the two groups of children in the present study reside in sociodemographically homogeneous communities and are very similar on a host of background variables (see Table I), the results are based on a cross-sectional design. We have demonstrated that typical, relatively low-intensity community noise is associated with modest, nonauditory health effects. The data need replication, preferably in a prospective, longitudinal study. Our intention is to monitor these same children over time with expected changes in noise levels coincident with Austrian compliance with European Union-mandated improvements in transportation infrastructure.

Since the geographic location of the present study is in small towns and villages in an alpine region, it would also be good to extend the findings to urban residential areas. It would also be valuable to evaluate children's nonauditory health responses to acute noise under laboratory conditions. We currently have a much more developed knowledge base on the nonauditory health effects of atypical, high-intensity noise exposure among children. We need to learn more about the potential consequences of typical ambient noise conditions for children's nonauditory health and well being.

ACKNOWLEDGMENTS

We are grateful to the families and teachers who cooperated with this study. We also acknowledge Annette Roner and Elke Roitner-Grabher for their assistance in conducting this study. This research was partially supported by the Austrian Ministry of Science and Transportation, the Austrian-US Fulbright Commission, the National Institute of Child Health and Human Development, No. 1F33 HD08473-01, and the College of Human Ecology, Cornell University. The order of authorship for the first two authors is arbitrary.

¹Use of the more conventional t tests to compare individual group means yielded the same pattern of results; for boys there was no noise effect, $t(64)=1.31$, whereas for girls there was an effect, $t(47)=1.83$, $p<0.04$. Tests for the simple slope are preferable, however, because they enable use of the overall error term in the analysis (see Aiken and West, 1991).

- Aiken, L., and West, T. (1991). *Multiple Regression: Testing and Interpreting Interactions* (Sage, Los Angeles).
- Babisch, W. (1998). "Epidemiological studies of cardiovascular effects of traffic noise," in *Proceedings of the Seventh International Congress on Noise as a Public Health Problem*, edited by N. L. Carter and R. F. S. Job (Noise Effects 98, Sydney), Vol. 1, pp. 221–229.
- Baum, A., and Grunberg, N. (1995). "Measurement of stress hormones," in *Measuring Stress*, edited by S. Cohen, R. C. Kessler, and L. Gordon (Oxford, New York), pp. 175–192.
- Broadbent, D. E. (1971). *Decision and Stress* (Academic, New York).
- Bullinger, M., Hygge, S., Evans, G. W., Meis, M., and van Mackensen, S. (1999). "The psychological cost of aircraft noise for children," *Zentralblatt für Hygiene und Umweltmedizin* **202**, 127–138.
- Cohen, S. (1980). "Aftereffects of stress on human performance and social behavior: A review of research and theory," *Psychol. Bull.* **88**, 82–108.
- Cohen, S., Evans, G. W., Stokols, D., and Krantz, D. S. (1986). *Behavior, Health, and Environmental Stress* (Plenum, New York).
- Dweck, C., and Elliott, E. (1983). "Achievement motivation," in *Handbook of Child Psychology*, 3rd ed., edited by P. Mussen (Wiley, New York), pp. 643–691.
- Eienschmid, B., Heilmann, P., Oelkers, W., Rejaibi, R., and Schonesshofer, M. (1987). "20-Dihydroisomers of cortisol and cortisone in human urine: Excretion rates under different physiological conditions," *J. Clin. Chem. Clin. Biochem.* **25**, 345–349.
- Evans, G. W. (2001). "Environmental stress and health," in *Handbook of Health Psychology*, edited by A. Baum, T. Revenson, and J. E. Singer (Erlbaum, Mahwah, NJ), pp. 365–385.
- Evans, G. W. (1998). "The motivational consequences of exposure to noise," in *Proceedings of the Seventh International Congress on Noise as a Public Health Problem*, edited by N. Carter and R. F. S. Job (Noise Effects of Ltd., Sydney, Australia), Vol. 1, pp. 311–320.
- Evans, G. W., Bullinger, M., and Hygge, S. (1998a). "Chronic noise and physiological response: A prospective, longitudinal study," *Psychol. Sci.* **9**, 75–77.
- Evans, G. W., and Cohen, S. (1987). "Environmental stress," in *Handbook of Environmental Psychology*, edited by D. Stokols and I. Altman (Wiley, New York), pp. 571–610.
- Evans, G. W., Hygge, S., and Bullinger, M. (1995). "Chronic noise and psychological stress," *Psychol. Sci.* **6**, 333–338.
- Evans, G. W., Lepore, S. J., Shejwal, B. R., and Palsane, M. N. (1998b). "Chronic residential crowding and children's well being: An ecological perspective," *Child Dev.* **69**, 1514–1523.
- Glass, D. C., and Singer, J. E. (1972). *Urban Stress* (Academic, New York).
- Gottlob, D. (1995). *Regulations for Community Noise* (Noise/New International), pp. 223–236.
- Ising, H., Babisch, W., and Kruppa, B. (1999). "Acute and chronic noise stress as cardiovascular risk factors," *Noise Hlth* **4**, 37–48.
- Ising, H., and Braun, C. (2000). "Acute and chronic endocrine effects of noise," *Noise Hlth* **7**, 7–24.
- Ising, H., Rebentisch, R., Babisch, W., Curio, I., Sharp, D., and Baumgartner, H. (1990). "Medically relevant effects of noise from military low altitude flights: Results of an interdisciplinary pilot study," *Environ. Int.* **16**, 411–423.
- Kryter, K. (1994). *The Handbook of Hearing and the Effects of Noise* (Academic, New York).
- Lercher, P. (1996). "Environmental noise and health: An integrated research perspective" *Environ. Int.* **22**, 117–128.
- Lercher, P. (1998). "Context and coping as moderators of potential health effects in noise-exposed persons," in *Biological Effects of Noise*, edited by D. Prasher and L. Luxor (Whurr, London), pp. 328–335.
- Lohaus, A., Fleeer, B., Freytag, P., and Klein-Hessling, J. (1996). *Fragebogen zur Erhebung von Stresserleben und Stressbewältigung im Kindesalter (SSK)* (Hogrefe, Göttingen).
- Medical Research Council. (1997). *The Nonauditory Effects of Noise*, Report R10, Institute for Environment and Health (Leicester, UK., University of Leicester).
- Peterson, C., Maier, S., and Seligman, M. E. P. (1993). *Learned Helplessness* (Oxford, New York).
- Regecova, V., and Kllerova, E. (1995). "Effects of urban noise pollution on blood pressure and heart rate in preschool children," *J. Hypertens.* **3**, 405–412.
- Riggin, R., and Kissinger, P. (1977). "Determination of catecholamines in urine by reverse phase chromatography with electrochemical detection," *Analyt. Chem.* **49**, 2109–2111.
- Schonesshofer, M., Kage, A., Weber, B., Lenz, I., and Kottgen, E. (1985). "Determination of urinary free cortisol by on-line liquid chromatography," *Clin. Chem.* **31**, 564–568.
- Schonesshofer, M., Weber, B., Oelkers, W., Nahoul, K., and Mantero, F. (1986). "Measurement of urinary free 20a-dihydrocortisol in biochemical diagnosis of chronic hypercorticism," *Clin. Chem.* **32**, 808–810.
- Seligman, M. E. P. (1975). *Helplessness* (Freeman, San Francisco)
- Thompson, S. J. (1993). "Extraaural health effects of chronic noise exposure in humans," in *Lärm und Krankheit*, edited by H. Ising and B. Kruppa (Springer, Berlin), pp. 107–117.
- World Health Organization (1995). "Community noise," edited by B. Berglund and T. Lindvall, in *Archives of the Center for Sensory Research*, **2**, 1–195 (University of Stockholm, Stockholm).

Relation of acoustical parameters with and without audiences in concert halls and a simple method for simulating the occupied state^{a)}

Takayuki Hidaka and Noriko Nishihara

Takenaka Research & Development Institute, 1-5-1, Otsuka, Inzai, Chiba 270-1395, Japan

Leo L. Beranek

975 Memorial Drive, #804, Cambridge, Massachusetts 02138

(Received 1 October 1998; revised 20 November 2000; accepted 22 November 2000)

Five acoustical parameters—reverberation time RT, early decay time EDT, clarity C_{80} , strength G , and interaural cross-correlation coefficient IACC—were measured using identical procedures with and without audiences in six concert and opera halls. Reverberation times without audiences were measured in 15 additional halls using the same measuring techniques as for the six halls above, but for full occupancy the data were taken from musical stop chords at symphonic concerts. This paper shows that in all halls (1) the occupied RT can be predicted from the unoccupied RT using a linear regression equation, $y = a - b \exp(x)$, within acceptable limits, at low- and mid-frequencies. It is also shown for the six halls that (2) occupied C_{80} 's are predicted accurately from unoccupied values by the newly proposed equation; (3) G 's with and without audiences are highly correlated by a first degree linear regression equation; and (4) IACCs have nearly the same value in both occupied and unoccupied halls. As a separate subject, the successful use of a cloth covering for seats in a concert or opera hall to simulate the occupied condition has been developed. © 2001 Acoustical Society of America. [DOI: 10.1121/1.1340649]

PACS numbers: 43.55.Br, 43.55.Fw, 43.55.Gx, 43.55.Mc [JDQ]

I. INTRODUCTION

Room acoustical parameters have evolved in the literature for the purpose of evaluating the acoustical quality of concert and opera halls. It is important that the values of these parameters be available for the occupied state of a hall if an evaluation is to be meaningful. However, in existing halls, arranging for exact measurements at many seats with 100% audience is almost impossible. Hence, occupied values in halls are usually derived from unoccupied data employing some empirical and/or physical assumptions. Existing methods for accomplishing this transformation are known to be inaccurate and the extent of their inaccuracies is not known (Barron and Lee, 1988; Bradley, 1991; Fukuchi and Fujiwara, 1985; Jordan, 1980; Meyer, 1978; Nagata, 1991; Schultz, 1980). References to earlier works appear in pertinent places later.

Based on exact measurements of five common acoustical parameters, with and without audiences, the purposes of this research are: ① to find more accurate formulas for conversion of unoccupied to occupied values; and ② to demonstrate a practical method for obtaining occupied data in a hall without employing a live audience.

II. BASIC ACOUSTICAL DATA

A. Exact measurements

Five acoustical parameters—reverberation time, RT, early decay time, EDT, clarity, C_{80} , strength, G , and interaural cross-correlation coefficient IACC—were measured

precisely in the six halls of Table I in octave bands employing the procedures of ISO 3382 (1997) and definitions in Beranek (1996) and Hidaka *et al.* (2000). The sound source for the measurements was a dodecahedral loudspeaker (diameter of each diaphragm=120 mm) that was accurately calibrated in an anechoic room (ISO 3745, 1977) and a reverberation chamber (ISO 3741, 1988). The acoustic signals that it produced in the hall were recorded at various positions both monaurally and binaurally. For the monaural measurements omnidirectional microphones were employed. For the binaural measurements either (a) dummy heads with imbedded microphones at eardrum positions, along with artificial torsos, or (b) persons with tiny microphones taped at the entrances to their ear canals, were employed. The radiated acoustic signal was a time-stretched impulse (Appendix A) generated ten times in succession so that when analyzed the S/N ratio would be improved by synchronous summation. The time required for one measurement (i.e., all seats simultaneously or for any one seat in a sequence) was about 1 min.

The recorded monaural and binaural impulse responses were convolved with the impulse responses of an octave-band filter set with mid-frequencies from 125 to 4000 Hz. From those results each of the acoustical parameters was calculated. The early decay time EDT was determined from the best regression line for the initial 10 dB of the decay curve.

During a measurement, the positions of the sound source and the receivers are shown in Fig. 1. The source was placed on the center line of the hall, 3 m from the front edge of the stage, at a height of 1.5 m (designated by S_0). The receivers were distributed uniformly at 8 to 21 positions, throughout

^{a)}Presented at the ASA/ICA meeting in Seattle, Washington, 25 June 1998.

TABLE I. The six halls in this study for which the measured unoccupied and occupied data were measured accurately. V is room volume; S_{Total} is the total surface area, including (a) S_A the area over which the audience sits, with edge effect included (Beranek, 1996) and (b) S_0 the area over which the orchestra sits; and N is the number of seats. The degree of upholstering of the seats is shown. Also listed are the reverberation times (averages at 500 and 1000 Hz) for the halls, occupied and unoccupied, and the number of receivers (microphones and dummy heads) used for the measurements. The numbers in parentheses are standard deviations.

Hall	V m^3	S_{Total} m^2	S_A m^2	N –	Seat –	$RT_{M,occ}$ s	$RT_{M,unocc}$ s	Num. of receivers
Kanagawa Auditorium	3576	1723	418	482	Heavy	1.25 (0.05)	1.23 (0.02)	8
Hamarikyu Asahi Hall	5800	2570	395	552	Medium	1.81 (0.06)	1.99 (0.06)	13
Mitaka Concert Hall	5500	2315	413	625	Very Light	1.92 (0.07)	2.49 (0.03)	13
New National Theater, Medium Theater	7200	2786	614	1038	Very Light	1.05 (0.04)	1.31 (0.04)	12
New National Theater, Opera House	14 500	5666	1153	1810	Very Light	1.49 (0.07)	1.80 (0.05)	21
Tokyo Opera City Concert Hall	15 300	5843	1052	1632	Very Light	2.16 (0.09)	2.92 (0.03)	17

the audience areas. The number was determined by the symmetry, the size, and the number of balconies. For example, on the main floor the measurement positions would be spaced five or six rows apart, more than 1 m off the centerline of the hall, and more than 2 m from the side and rear walls.

Short descriptions of the halls studied are shown in Table I. The range in volumes is from 3576 to 15 300 m^3 and the upholstering of the seats ranged from very light to heavy. Briefly, the principal architectural features are as follows: The Kanagawa Auditorium is fan-shaped with no balcony. The Hamarikyu and Mitaka halls are shoebox-shaped with one balcony. The NNT Medium Theater is wide fan-shaped, with one balcony, a proscenium stage, and a low reverberation time. The NNT Opera House is mildly fan-shaped and has three balconies. The TOC Concert Hall has two balconies and is rectangular below the ceiling line, but the “ceiling” is a high distorted pyramid. Further information about some of the halls are documented in references: NNT Opera House (Beranek *et al.*, 2000); NNT Medium Theater (Be-

ranek *et al.*, 1998); TOC (Hidaka *et al.*, 2000) and Hamarikyu (Beranek, 1996).

For the measurements in the NNT Opera House and Medium Theater, the prosceniums were open (no curtain), the orchestra pits were lowered to their normal position (2.2 m below the stage level), and the fly towers were made equivalent in sound absorption to those at opera performances by hanging and installing complete sets of curtains and stage equipment. At the Kanagawa Auditorium, the stage enclosure designed for chamber music recitals was in place. The TOC, Mitaka, and Hamarikyu Concert halls have neither fly towers nor stage enclosures, although TOC has a canopy over the stage.

Throughout the measurements, all architectural conditions inside the hall with and without audiences were exactly the same. In the TOC hall measurements were conducted both before and after installation of the pipe organ (designated TOC-no-organ or -organ in this paper). There were no players on stage or in the orchestra pit at the time of the exact measurements. For the three chamber-music halls,

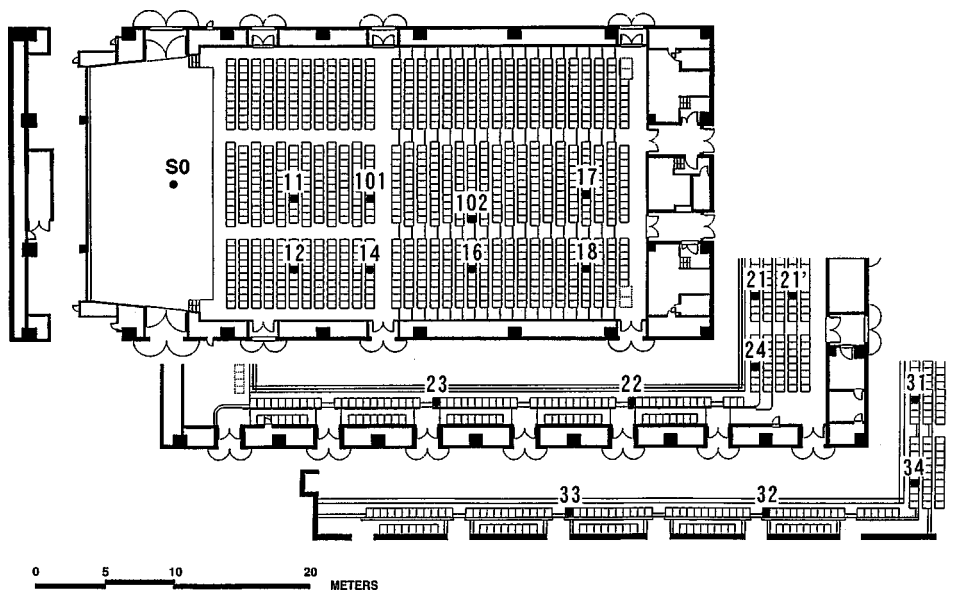


FIG. 1. Definition of receiver locations and source position in the TOC Concert Hall (Hidaka *et al.*, 2000). These locations and position were used typically in all halls studied.

TABLE II. List of RTs measured for the 6 1/1 octave bands in 22 halls; all of the unoccupied values and the occupied values of upper seven halls were measured by the exact method in accordance with ISO 3382. RTs of NNT Opera, NNT Medium, and TOC are compensated by adding absorption power of the orchestra. The occupied values of lower 15 halls were obtained from music stop chord with Schroeder Integration Method (SIM), where the numerical numbers are shown only when 8 or more stop chords were available for the analysis.

Hall	Unoccupied								Occupied							
	125	250	500	1000	2000	4000	<i>L</i>	<i>M</i>	125	250	500	1000	2000	4000	<i>L</i>	<i>M</i>
Hamarikyu Asahi	1.64	1.74	1.93	2.05	1.97	1.73	1.69	1.99	1.60	1.63	1.73	1.89	1.79	1.60	1.62	1.78
Mitaka Concert	2.02	2.22	2.38	2.60	2.41	2.03	2.12	2.49	1.90	1.95	1.95	1.88	1.74	1.44	1.95	1.90
NNT Opera	1.67	1.64	1.73	1.84	1.71	1.41	1.65	1.79	1.60	1.57	1.46	1.44	1.35	1.26	1.59	1.45
NNT Medium	1.33	1.27	1.29	1.34	1.44	1.31	1.30	1.31	1.24	1.13	1.06	1.02	1.01	0.93	1.18	1.04
TOC no-organ	2.25	2.65	2.86	2.98	3.12	2.92	2.45	2.92	2.16	2.08	2.13	2.02	1.88	1.65	2.12	2.08
TOC organ	2.11	2.56	2.74	2.85	2.92	2.67	2.33	2.80	1.99	1.97	1.91	1.87	1.77	1.58	1.98	1.89
Kanagawa Auditorium	1.07	1.14	1.23	1.28	1.25	1.15	1.11	1.25	1.09	1.12	1.22	1.28	1.17	1.10	1.11	1.22
Boston Symphony	2.14	2.16	2.31	2.69	2.79	2.45	2.15	2.50	1.82	1.86	1.87	1.84	1.65	1.36	1.84	1.86
Vienna Gross. Musik	2.94	2.93	3.01	2.97	2.66	2.19	2.94	2.99	2.11	2.13	1.94	1.84	1.65	1.48	2.12	1.89
Munich Gasteig	2.39	2.17	2.24	2.27	2.29	2.05	2.28	2.26	2.15	1.99	1.95	1.97	2.01	1.90	2.07	1.96
Berlin Konzerthaus	2.84	2.78	2.51	2.44	2.24	1.90	2.81	2.48	2.53	2.34	2.05	1.87	1.74	1.59	2.44	1.96
Vienna Staatsoper	1.84	1.61	1.55	1.54	1.44	1.28	1.73	1.55	1.65	1.51	1.37	1.23	1.14	1.03	1.58	1.30
Suntory Hall	2.15	2.31	2.44	2.57	2.59	2.30	2.23	2.51	2.14	2.08	1.95	2.03	2.00	1.77	2.11	1.99
Tokyo Met. Art	2.84	2.54	2.45	2.43	2.36	2.14	2.69	2.44	2.50	2.23	2.11	2.15	2.06	1.91	2.37	2.13
Orchard Hall	2.29	2.25	2.22	2.27	2.28	2.04	2.27	2.25	2.05	1.95	1.83	1.77	1.64	1.42	2.00	1.80
Katsushika Symphony	2.10	1.90	2.00	1.85	1.65	1.40	2.00	1.93	2.02	1.89	1.74	1.64	1.58	1.52	1.96	1.69
Kanagawa Kenmin	1.69	1.56	1.72	2.09	2.15	1.90	1.63	1.91	...	1.47	1.43	1.43	1.39	1.25	...	1.43
Sumida Triphony	2.18	2.02	2.25	2.28	2.21	1.94	2.10	2.27	...	2.04	1.91	1.85	1.74	1.48	...	1.88
NHK Hall	2.40	1.95	1.90	2.05	2.00	1.65	2.18	1.98	1.63	1.72	1.75	1.68
Orange County	2.28	2.14	2.14	2.27	2.10	1.83	2.21	2.21	...	1.85	1.61	1.53	1.38	1.08	...	1.57
Munich Herkules	2.29	2.06	2.18	2.28	2.19	1.90	2.18	2.23	...	2.01	1.88	1.63	1.76	1.76
Sapporo Symphony	2.31	2.03	2.08	2.17	2.13	1.89	2.17	2.13	1.93

Hamarikyu, Mitaka, and Kanagawa, the absorption powers of a few players on stage were negligible compared to the total absorptions. Previous studies yielded the absorption powers (in m^2) of two sizes of orchestras in a concert hall and in an opera house (see Table AI). For the TOC concert hall, the NNT opera house and the NNT medium theater, knowing V and RT , the total absorption powers (without orchestra) were determined from the denominator of Eq. (2) of Sec. II A. The absorption power of 92 orchestra players was added to the value just determined for the TOC hall; that of 80 players for the NNT opera; and that of 40 players for the NNT theater. The RTs were then recalculated and are shown in the first rows of Table II, and are used in the figures and tables that follow. The numerical values in this paper are a little different from those in other published documents because those reported here were obtained before the final tuning took place.

B. RT measurements from musical stop chords

In addition to the RT_{occ} and RT_{unocc} data obtained as discussed above, measurements were carried out in 15 other halls (see Table II). In each, the unoccupied data were taken as in Sec. IA above, but the occupied data were obtained from decay curves associated with stop chords recorded during concerts with full audience. Only one or two measurement positions in the audience were possible during a concert. In the Orange County Hall the music was recorded by an air-monitor microphone. In the Katsushika Hall, the microphone was hung above the stage as for a professional recording.

Since there are various factors that can affect the values of RT_{occ} measured from music stop chords, data from other researchers are not used in this paper. Analysis procedures and measurement precautions for RTs determined from stop chords are presented in Appendix B.

The standard deviations of the data for any one hall that were obtained from a succession of stop chords recorded during concerts at one or two audience positions is large owing to combinations of (a) the small number of decay curves, (b) the limited spectral components in each chord, and (c) the number and arrangement of the musicians on stage. Obviously, the impulse method with measuring stations at 8 to 21 positions is much more accurate. Finally, all decay times recorded from stop chords were made during full symphonic concerts, i.e., music from chamber groups was not judged suitable.

III. PREDICTION OF OCCUPIED ACOUSTICAL PARAMETERS FROM UNOCCUPIED VALUES

A. Reverberation time, RT

1. Prediction of occupied RT from unoccupied RT when chair characteristics are unknown

Plotted in Fig. 2 are the exact measurements for the six halls of Table I (solid dots, whose numbers are given in Table II) and the stop chord data for the lower 15 halls of Table II (\times 's). The vertical bars give the variation range of the RTs for the 9 to 15 stop chords. The dotted lines mean ± 0.1 s relative to the solid lines. To obtain the solid lines on the graphs of Fig. 2, the best linear regression model was used that minimizes the Akaike's Information Criterion

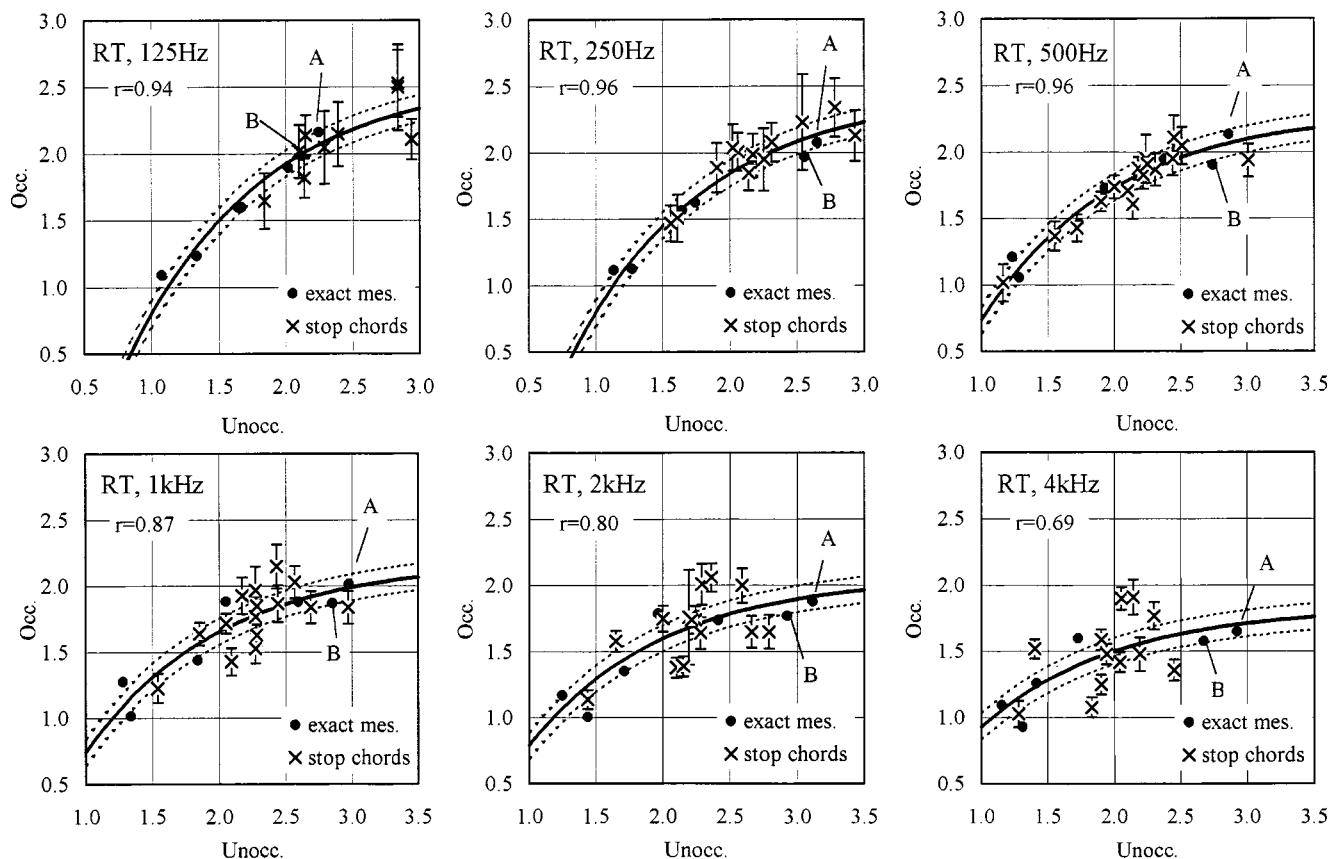


FIG. 2. Plot of occupied RTs versus unoccupied RTs for the octave bands with mid-frequencies from 125 to 4 kHz, where the RTs for the 6 halls of Table I are shown by the solid dots and the “×’s” are for stop chords taken in 15 other halls in Table II (usually at very few audience positions at very few concerts). The vertical bars give the variation range of the RTs for the eight or more stop chords used in each case. The solid line is calculated from the best regression values of Eq. (1) and the dotted line means ± 0.1 relative to the solid line. The TOC-no-organ, symbolized by (A), and TOC-organ (B) points are measurements made before and after the installation of a pipe organ. Also, we know from successive measurements made in the TOC Hall that audiences absorb sound slightly differently at different times, even though the exact absorption power of the pipe organ, based on independent measurements, was taken into account.

(Akaike, 1973),¹ AIC, defined as $[-2(\text{maximum log-likelihood of statistical model}) + 2(\text{number of parameters in the model})]$, which comes out to be

$$RT_{\text{occ}} = a - b \times \exp(-RT_{\text{unocc}}). \quad (1)$$

When the hall is occupied we designate the RT as RT_{occ} and unoccupied as RT_{unocc} . The coefficients of this best regression equation are tabulated in Table III, and the suffix “L,” “M,” and “3bands” means the average over 125 and 250 Hz, 500 and 1000 Hz, and 500, 1000, and 2000 Hz, respectively, in the following. At mid-frequencies, it is seen that the regression lines tend to level off near 2.0 to 2.2 s (occupied values). This was shown by Beranek (1996, p. 437) to be true of all concert halls, presumably because higher reverberation times are not desirable for today’s symphonic repertoires (see Fig. 3). The other coefficients (a^* , b^*) in Table III are for Eq. (1) corresponding to the exact RT measurement values without orchestra in the six halls, and are listed here for use later.

The spread for the RTs obtained from stop chords in the bottom four bands is reasonable because in any given hall only one seat was often available for the measurement, and any one stop chord may have had less than full instrumental participation. For the two higher bands, the spread is greater due, in part, to relative humidity and temperature differences,

in part to the fact that the audiences may have had different clothing and in part to such unknown factors as the state of sound diffusion. For example, if the RT is calculated for TOC-no-organ using one of the customary temperature/humidity conditions found in European halls, 20 °C and 30%, the RTs at 2000 and 4000 Hz are lower by 0.05 and 0.26 s, respectively, from values measured in Tokyo, 23 °C and 63%. Similarly for other halls, with $RT \approx 2$ s and assuming 20 °C, reductions in the RTs at 4000 Hz equal to 0.3 s would occur if the relative humidities were to drop from

TABLE III. Regression coefficients, a and b , obtained by the least square method for the reverberation time determined in each of the six octave bands with mid-frequencies from 125 to 4000 Hz. The equation, $RT_{\text{occ}} = a - b \exp(-RT_{\text{unocc}})$, was chosen as the proper form because it minimizes the Akaike’s Information Criteria (AIC). The coefficients, a^* and b^* , are those without orchestra obtained from the exact measurement at six halls in Table I.

Frequency (Hz)	125	250	500	1000	2000	4000	L	M
a	2.58	2.46	2.31	2.19	2.07	1.84	2.52	2.26
b	4.83	4.50	4.26	3.91	3.48	2.45	4.69	4.15
a^*	2.49	2.37	2.33	2.24	2.15	1.93	2.42	2.28
b^*	4.37	4.13	4.24	3.96	3.83	2.82	4.24	4.10

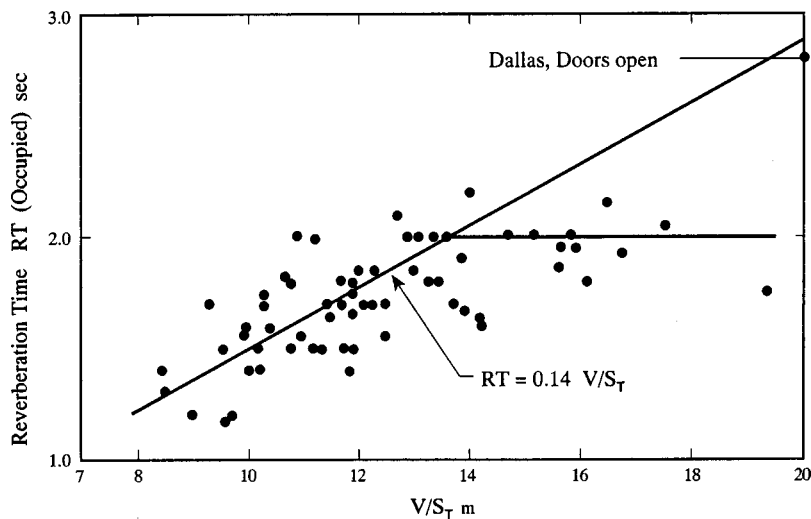


FIG. 3. Plot of RT_{Mocc} vs V/S_{Total} after Beranek (1996), which shows that RTs in existing 76 halls and opera houses converges to their upper optimum value.

50% to 30%. It is obvious that whenever possible the relative humidity and ambient temperature should be measured at the time a test is being performed. Another influencing factor, namely, the effect of an orchestra's absorption on reverberation times obtained from measurements of stop chords, is discussed in Appendix B. The orchestra absorption variable is not as significant as the variations in air absorption.

Shown in Figs. 4 and 5 are comparisons of occupied reverberation times obtained by using Eq. (1) (dashed lines) with those measured from stop chords (solid lines), where

the unoccupied RTs were determined from exact measurements in all cases.

2. Prediction of occupied RT from unoccupied RT when chair characteristics are known

The Sabine equation is

$$RT = 0.161V / (S_T \alpha_T + S_R \alpha_R + 4mV), \quad (2)$$

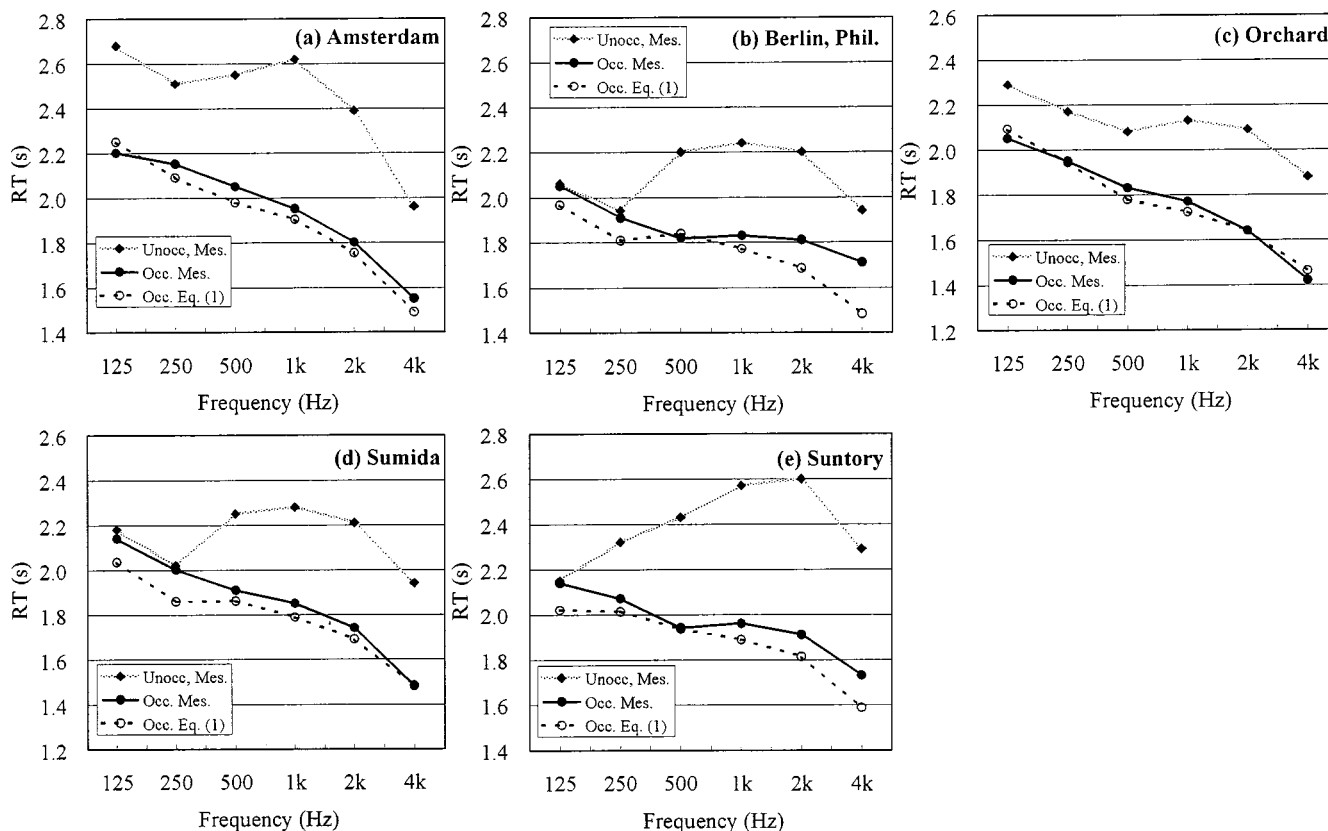


FIG. 4. Comparison of RT_{occ} from music stop chords and that by Eq. (1) at five concert halls: (a) Amsterdam, Concertgebouw; (b) Berlin, Philharmonie Hall; (c) Tokyo, Orchard Hall; (d) Tokyo, Sumida Triphony Hall; and (e) Tokyo Suntory Hall. The measured RT_{occ} 's of (a) and (b) are from Beranek (1996), and other three are given in Table II.

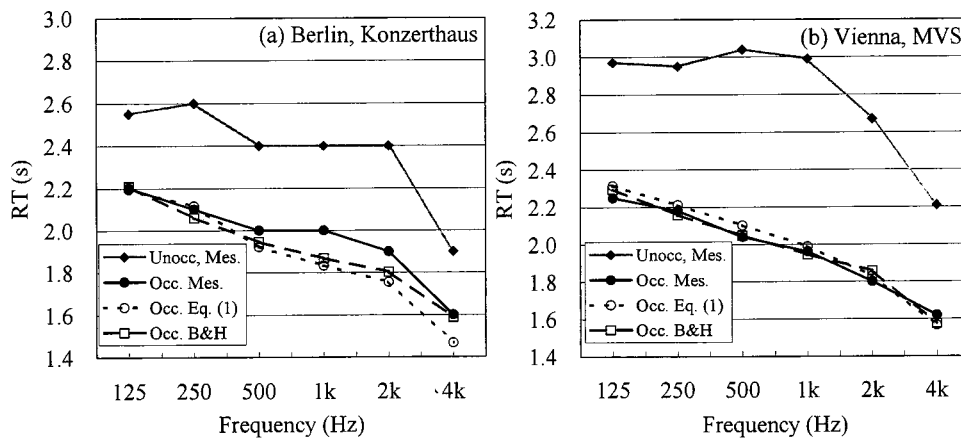


FIG. 5. Comparison of measured RT_{occ} with those by Eq. (1) and by Beranek-Hidaka's scheme (1998) by Eq. (2) at two concert halls; (a) Berlin, Konzerthaus GroÙersaal; and (b) Vienna, GroÙer Musikvereinssaal. RT_{occ} and RT_{unocc} of (a) are those by Falsold's exact measurement (1988) with and without audiences, and RT_{occ} of (b) is from Table II.

where S_T is the ‘‘acoustical’’ area (composed of blocks of areas in a hall) over which the audience chairs sit (plus 0.5 m on edges of blocks of seating except where blocks are adjacent to walls or balcony fronts) and including the stage area when the orchestra is present; S_R is the actual area of the other surfaces in the room (including the stage area when the orchestra is not present); and α_T and α_R are the absorption coefficients for the corresponding areas.

Beranek and Hidaka (1998) published sound absorption coefficients for unoccupied and occupied chairs with different degrees of upholstery (heavy, medium, light, and very light) and for the surfaces of a room not occupied by an audience. These values, with a few changes, are given in Table IV. Because, in general, the term $S_T\alpha_T$ is 4 or so times larger than the residual absorption, we can assume an average residual absorption coefficient for the nonaudience surfaces in a concert hall as typical for all halls, within the accuracy of the measurement of reverberation times. Then,

from the Sabine formula, we can calculate the RT_{occ} and RT_{unocc} values for halls with different audience sizes and cubic volumes of rooms. Let us now designate a Vienna Musikvereinssaal type of hall, i.e., rectangular with one balcony as Example A and a Boston Symphony Hall, rectangular with two balconies as Example B (see Table IV). The resulting calculations are plotted in Fig. 6.

The four solid lines at each frequency correspond to any number of halls that meet the Examples A and B criteria of Table IV,

$$RT_{occ} = c \cdot RT_{unocc} - d. \quad (3)$$

It was found that the points for the two different types of halls fell on their respective lines, i.e., interleaved, perfectly ($r > 0.99$). The coefficients c and d are tabulated in Table V.

Because the Sabine formula is applicable to any room without regard to shape, and, as we have assumed, small

TABLE IV. Absorption coefficients and air absorption for the determination of RT_{occ} from RT_{unocc} using examples from Beranek and Hidaka (1998). Seating Group No. 1 to 4, respectively, corresponds to heavily, medium, lightly, and very lightly upholstery.

		Frequency (Hz)					
		125	250	500	1000	2000	4000
Residual absorption coefficient		0.14	0.12	0.10	0.09	0.08	0.07
4 m (20 °C; 50%)		0	0	0.0024	0.0042	0.0089	0.0262
Chair coefficients (Unoccupied)	a. Group 1	0.70	0.76	0.81	0.84	0.84	0.81
	b. Group 2	0.54	0.62	0.68	0.70	0.68	0.66
	c. Group 3	0.36	0.47	0.57	0.62	0.62	0.60
	d. Group 4	0.35	0.40	0.41	0.38	0.33	0.27
Audience absorp. coefficient (Occupied)	a. Group 1	0.72	0.80	0.86	0.89	0.90	0.90
	b. Group 2	0.62	0.72	0.80	0.86	0.89 ^a	0.89 ^a
	c. Group 3	0.54 ^a	0.65 ^a	0.78 ^a	0.85 ^a	0.88 ^a	0.89 ^a
	d. Group 4 ^a	0.47	0.59	0.67	0.70	0.72	0.76

Example A. Shoebox Hall, One Balcony

Number of seats=1500; Total absorptive area, $S(T)=1059 \text{ m}^2$

Volumes investigated, 11 000 to 19 000 m^3 ; Residual areas, 2700 to 3976 m^2

Example B. Shoebox Hall, Two Balconies

Number of seats=2320; Total absorptive area, $S(T)=1600 \text{ m}^2$

Volumes investigated, 18 000 to 30 000 m^3 ; Residual areas, 4123 to 5027 m^2

^aThese coefficients are different from those in B&H paper. Group 4 was measured in Mitaka and TOC halls.

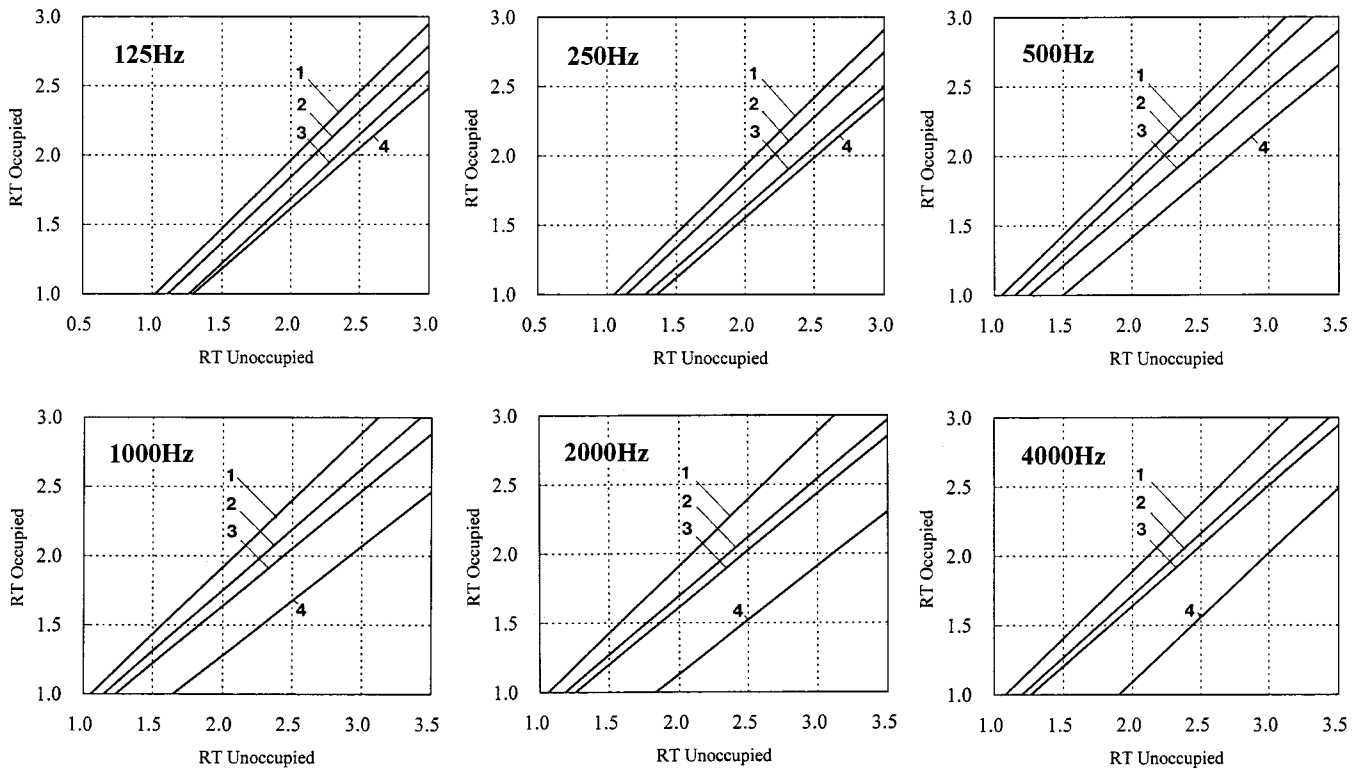


FIG. 6. Calculated curves to estimate RT_{occ} from RT_{unocc} in concert hall for the octave band with mid-frequencies from 125 to 4 kHz, based on the Beranek–Hidaka’s method (1998). Four solid lines correspond to the seat upholstering group number defined in Table IV. Two typical shoebox halls with one balcony and with two balconies (each seating number is 1500 and 2200) are used to draw the lines, when the length and width were constant in each but the ceiling height, i.e., room volume and residual area were varied.

variations in the residual absorption term are not significant, this set of curves serves as a means to estimate RT_{occ} if RT_{unocc} and the type of upholstering on the seats are known. Two examples of its accuracy are shown in Fig. 5.

B. Clarity, C_{80}

There is some indication that clarity does not change much when an audience enters a hall. This may mean that the general structure of the early reflections is almost the same regardless of whether the hall is occupied or not. To support this view, it has been shown that $IACC_{E3}$ does not change its value under various occupancy and curtain condi-

tions in concert and opera halls (Beranek *et al.*, 2000). Tachibana and his group (Watanabe *et al.*, 1985) reported that the sound quality of a hall can be judged approximately by “listening” to the impulse response itself in an unoccupied hall. Accordingly, one may assume, at least approximately, that the early energy in the definition of C_{80} substantially does not change for both occupied and unoccupied conditions and that the late energy in C_{80} is described by an exponential decay function. The latter approximation is seemingly proper since the reverberant decay curves in many halls are almost straight unless long path echo or coupling effects occur. When these assumptions hold, the occupied C_{80} is written as

$$C_{80,occ} = 10 \log \frac{\int_0^{0.08} p_{occ}^2(t) dt}{\int_{0.08}^{\infty} p_{occ}^2(t) dt} \cong 10 \log \frac{\int_0^{0.08} p_{unocc}^2(t) dt}{\int_{0.08}^{\infty} A \cdot 10^{-6t/RT_{occ}} dt}, \quad (4)$$

then $C_{80,occ}$ is given by $C_{80,unocc}$ and RT as

$$C_{80,occ} = C_{80,unocc} + 10 \log \left[\frac{RT_{unocc}}{RT_{occ}} \cdot 10^{0.48(1/RT_{occ} - 1/RT_{unocc})} \right]. \quad (5)$$

Here, RT_{occ} is calculated by Eq. (1), and A is an unknown constant that cancels out in Eq. (5).

TABLE V. Regression coefficients, c and d [see Eq. (3)], obtained by the least square method for four kind of chairs in each of the six octave bands with mid-frequencies from 125 to 4000 Hz.

		Frequency (Hz)					
		125	250	500	1000	2000	4000
Group 1	c	0.99	0.98	0.96	0.97	0.97	0.97
	d	0.01	0.03	0.01	0.02	0.03	0.05
Group 2	c	0.95	0.94	0.92	0.88	0.85	0.90
	d	0.05	0.07	0.06	0.01	0.00	0.07
Group 3	c	0.93	0.87	0.84	0.83	0.83	0.87
	d	0.17	0.11	0.05	0.02	0.04	0.10
Group 4	c	0.87	0.87	0.82	0.79	0.78	0.93
	d	0.12	0.18	0.23	0.29	0.43	0.77

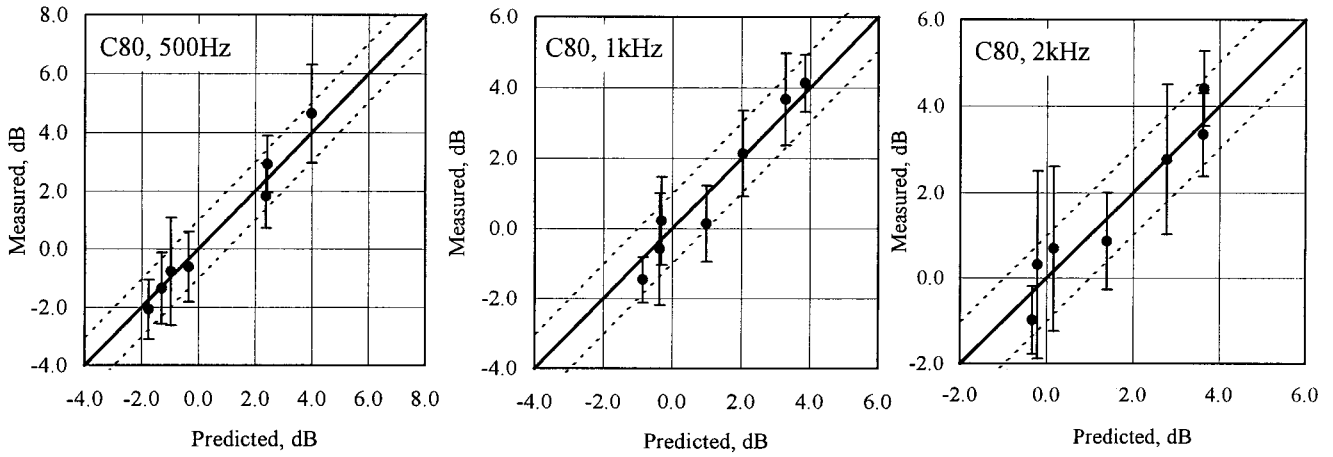


FIG. 7. Plot of occupied C_{80} 's by exact measurement without orchestra versus those in the six halls with their best regression (solid) curve by Eq. (5) for three octave bands with mid-frequencies of 500, 1000, and 2000 Hz. The solid lines mean Predicted=Measured and the broken lines mean ± 1 dB to those. The vertical bars mean the average plus/minus the standard deviation of the C_{80} 's in each hall.

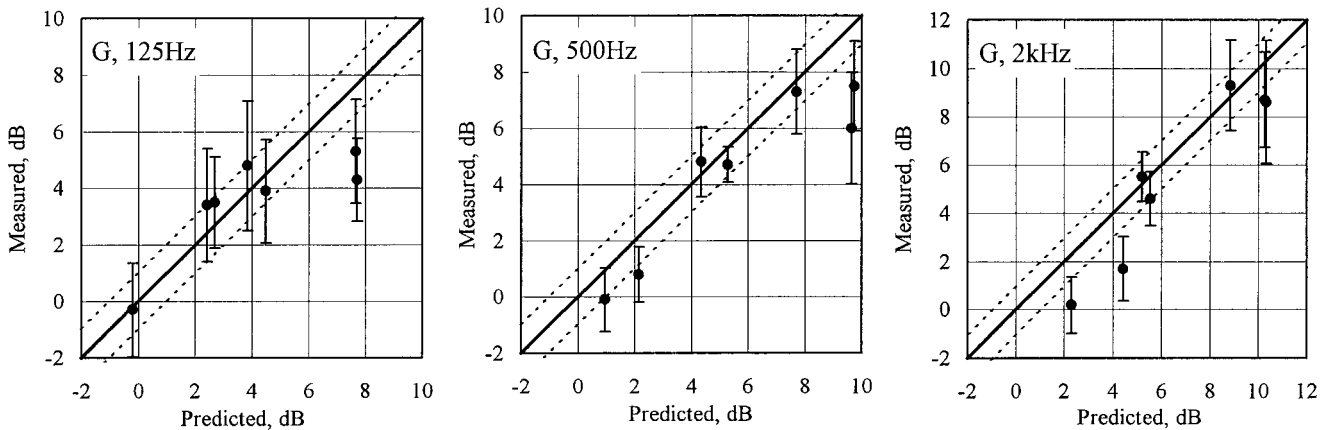


FIG. 8. Key as in Fig. 7, but for G and by Eq. (7).

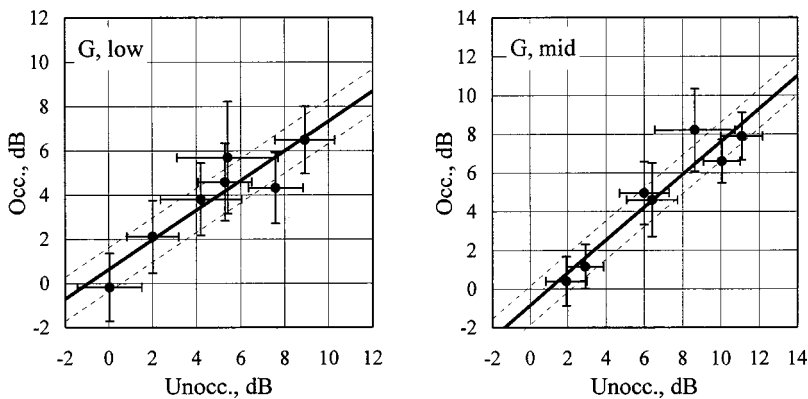


FIG. 9. Comparison of occupied G 's with unoccupied G 's measured in the six halls. "Low" and "Mid" mean the average over 125 and 250 Hz, and 500 and 1000 Hz, respectively. The solid lines mean their first order regression line of Eq. (8) and the broken lines mean ± 1 dB to those. The vertical and horizontal bars mean the average plus/minus the standard deviation of the G 's in each hall.

TABLE VI. Regression coefficients, e and f [see Eq. (8)], obtained by the least square method for three parameters determined in each of the six octave bands with mid-frequencies from 125 to 4000 Hz. The occupied value for each parameter equals (e times the unoccupied value) plus f .

		Frequency (Hz)							
		125	250	500	1000	2000	4000	M	Three bands
EDT	e	0.82	0.74	0.59	0.54	0.46	0.37	0.57	
	f	0.19	0.25	0.36	0.45	0.53	0.61	0.41	
C_{80}	e	1.09	0.75	0.92	0.83	0.73	0.57	0.88	0.84
	f	-0.07	0.71	1.20	1.39	1.79	2.01	1.29	1.45
G	e	0.52	0.80	0.79	0.91	1.08	0.99	0.85	
	f	1.31	-0.12	-0.59	-1.19	-2.67	-1.89	-0.85	

Using Eq. (5), predicted and measured values of $C_{80,occ}$ are compared in Fig. 7. It is noted that this is a comparison with no orchestra because the exact $C_{80,occ}$'s were measured under the condition without orchestra. For this figure, RT_{occ} in Eq. (5) was obtained by substituting the coefficients (a^*, b^*) in Table III into Eq. (1). It is seen that 15 out of 21 plots are predicted within the error of ± 0.5 dB for the three (500 to 2000 Hz) octave bands. The hall-averaged $C_{80,3-band}$ for all the seven halls are predicted within ± 0.5 dB. These errors are acceptable in comparison with the tolerable variation range of C_{80} for concert hall, such as (0 ± 1.6) dB for Mozart symphony and (-3.3 ± 1.8) dB for Wagner's moderate music studied by Reichardt *et al.* (1975). The numerical calculation indicates that $C_{80,occ}$ at 500/1000 Hz is higher by about 1 to 2 dB than $C_{80,unocc}$ when the RT_{unocc} takes the value from 2 to 3 s.

One may estimate the change in $C_{80,occ}$ with and without the orchestra by using (a, b) in Table III into RT_{occ} of Eq. (5). Then it is found that $C_{80,occ}$ (3 bands) with the orchestra will rise about 0.1 to 0.15 dB, when RT_{unocc} is longer than 1.2 sec.

It is also known that the beginning time of the statistical feature of a sound field, such as the "beginning time of the reverberation" (Cremer and Müller, 1982), depends on the size of a hall. To test this effect, a similar comparison of measurement and predicted value of occupied $C(t)$ for $t=40$ and 160 ms was made, and it was found that the assumption of Eq. (5) still holds within the same accuracy.

Additionally, there are several methods reported to predict $C_{80,occ}$'s from unoccupied values (Jordan, 1980; Barron

and Lee, 1988; Bradley, 1991). Those methods have been tried, and found unsatisfactory by comparison with Eq. (5).

Further comment

C_{80} and EDT are substantially governed by the structure of the sequence of early reflections, which vary seat-to-seat with rather large deviations. In particular, for the measurement of C_{80} , it is worthwhile to note two serious problems: (1) local reflections from individual audience members near the microphones may cause changes of the early reflection patterns at high frequencies resulting in different numerical values of C_{80} for successive measurements; and (2) early reflections are bounded at the precise cutoff of 80 ms in accordance with the definition, which means that an extreme discrepancy will take place when a major isolated reflection arrives on either side of the 80-ms figure. In that case, the reflection belongs either to early or to late energy depending on a trivial shift in its time position, and a jump in C_{80} value results. Similar concern about the use of a sudden cutoff has been indicated by several authors (Cremer and Müller, 1982; Barron, 1993; Kuttruff, 1991).

In order to confirm the problem, the early to late energy ratio, $C(t) = 10 \log[E(0,t)/E(t,\infty)]$ was plotted with and without audiences sitting in front of the receivers in the TOC Hall, where $E(t_1, t_2)$ is the sound energy of the impulse response between t_1 and t_2 . There, it was found that there exists more than ca. 1-dB difference between the two measurements for $t < 100$ ms in the octave bands above 500 Hz, which is significant considering the difference limen of C_{80} (Cox *et al.*, 1993).

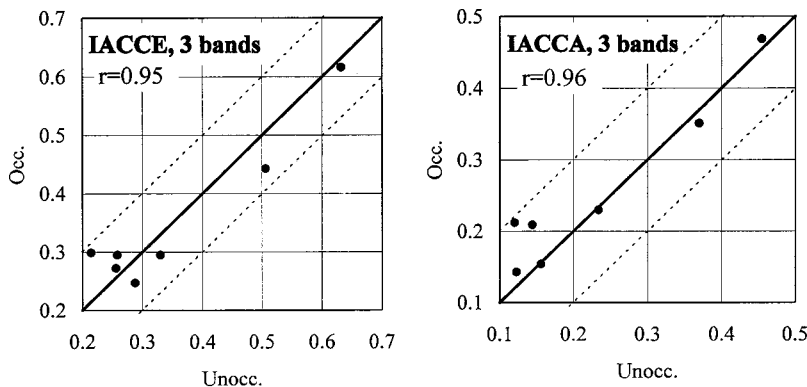


FIG. 10. Plot of unoccupied IACCs versus occupied IACCs in the six halls, where three bands mean the average over 500-, 1000-, and 2000-Hz bands; E means integration over the first 80 ms and A means integration over 3.5 s. The left graph is for the "early" part of the impulse response and the right for "all" of it. The solid lines mean Occ versus Unocc and the broken lines mean ± 0.1 to those.

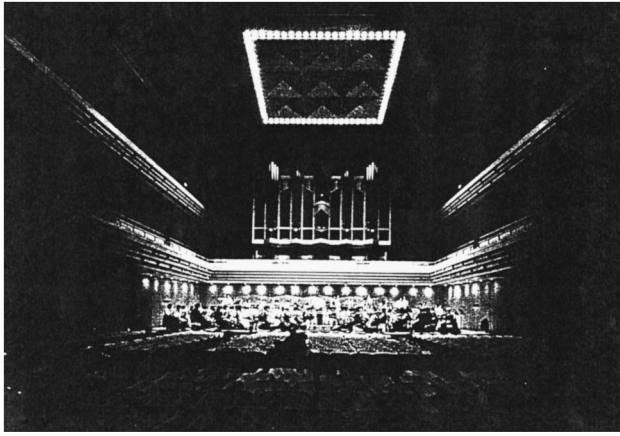


FIG. 11. The cloth used to simulate an audience is shown spread over the seats in the TOC Concert Hall.

C. Strength, G

By introducing an approximation similar to that for C_{80} above, G is expressed by the following equation:

$$\begin{aligned}
 &G_{\text{unocc}} - G_{\text{occ}} \\
 &= 10 \log \frac{\int_0^{0.08} p_{\text{unocc}}^2(t) dt + \int_{0.08}^{\infty} p_{\text{unocc}}^2(t) dt}{\int_0^{0.08} p_{\text{occ}}^2(t) dt + \int_{0.08}^{\infty} p_{\text{occ}}^2(t) dt} \\
 &\cong 10 \log \frac{\int_0^{0.08} p_{\text{unocc}}^2(t) dt + \int_{0.08}^{\infty} A \cdot 10^{-6t/RT_{\text{unocc}}} dt}{\int_0^{0.08} p_{\text{unocc}}^2(t) dt + \int_{0.08}^{\infty} A \cdot 10^{-6t/RT_{\text{occ}}} dt}, \quad (6)
 \end{aligned}$$

which yields the equation for calculating G_{occ} from G_{unocc} :

$$\begin{aligned}
 &G_{\text{unocc}} - G_{\text{occ}} \\
 &= 10 \log \left[\frac{10^{(C_{80,\text{unocc}})/10} + 1}{10^{(C_{80,\text{unocc}})/10} + \left(\frac{RT_{\text{occ}}}{RT_{\text{unocc}}} \right) \cdot 10^{0.48(1/RT_{\text{unocc}} - 1/RT_{\text{occ}})}} \right], \quad (7)
 \end{aligned}$$

where RT_{occ} and $C_{80,\text{occ}}$ are calculated values by Eqs. (1) and (5), respectively.

Figure 8 is a comparison between measurement and calculation by Eq. (7). It is also noted that this is the comparison without the orchestra as in Fig. 7. It is seen that the accuracy of Eq. (7) is not as good as that for C_{80} and, on average, G_{occ} is predicted to be about 1-dB smaller than the exact G_{occ} . Probably, this result is explained by the following reasons: (A) G is an absolute value while C_{80} is a relative one, so an error in calibration of the sound source may cause a small numerical shift in G ; and (B) some unknown factor that can be canceled out by a dividing operation [like term A in Eq. (4)] does not canceled for the case of G .

On the other hand, using a straight-line formula, one can find fairly good correlation between G_{unocc} and G_{occ} both measured in the six halls in Table I (Fig. 9), where the correlation coefficients r for the six octave bands from 125 to 4000 Hz are 0.83, 0.95, 0.95, 0.95, 0.96, 0.94, respectively. Therefore, the simple regression equation,

$$G_{\text{occ}} = e \cdot G_{\text{unocc}} + f, \quad (8)$$

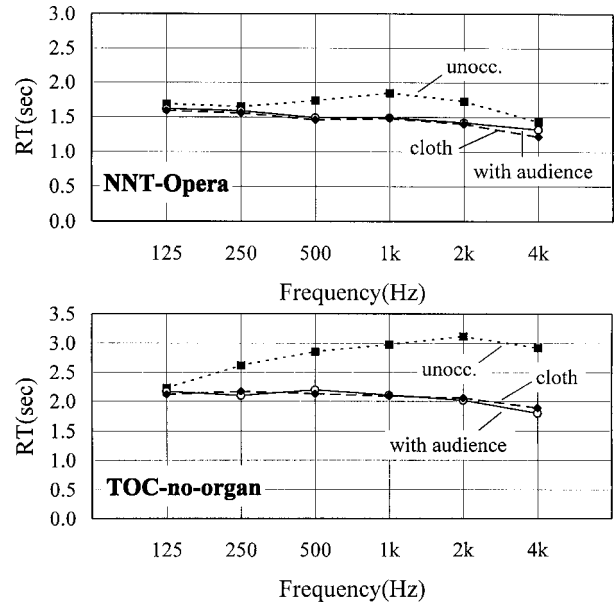


FIG. 12. Comparison of RTs with cloth covering and by real audiences measured in NNT Opera House and TOC Concert Hall.

may be most reliable for practical purposes. The coefficients, e and f , are tabulated in Table VI. Also, as before, we examined the relation between occupied and unoccupied G by investigating existing equations that predict G_{occ} from its unoccupied value assuming perfect diffusion (Meyer, 1978; Bradley, 1991). Those results were also unsatisfactory.

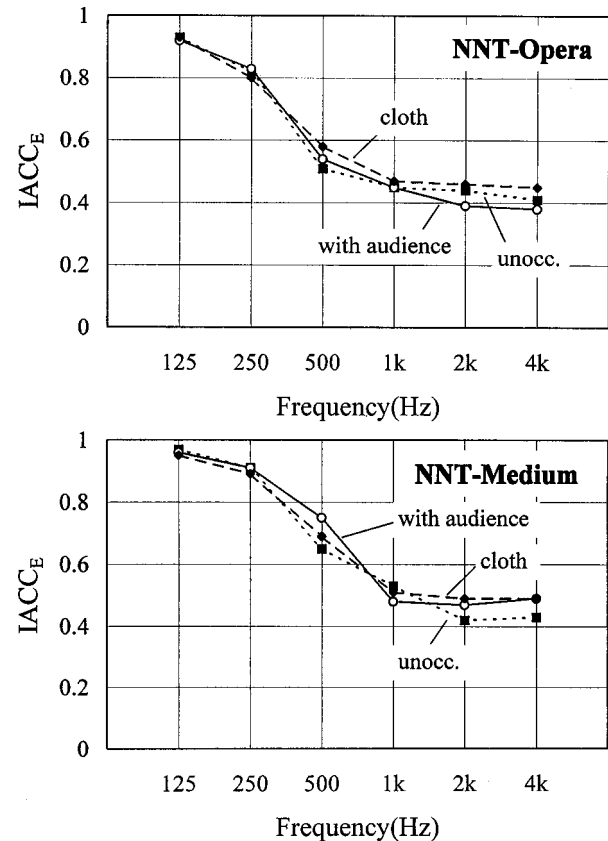


FIG. 13. Comparison of $IACC_E$'s with cloth covering and by real audiences measured in NNT Opera House and NNT Medium Theater.

TABLE VII. Range of absolute difference of the four parameters between cloth covering and exact occupied condition determined in each of the six frequency bands with mid-frequencies from 125 to 4000 Hz.

	Frequency (Hz)					
	125	250	500	1000	2000	4000
RT(s)	-0.1-0	0-+0.1	-0.1-+0.1	-0.1-+0.1	0-+0.1	-0.1-+0.1
EDT(s)	-0.1-+0.2	-0.1-+0.1	-0.1-+0.1	-0.1-+0.1	-0.1-+0.2	-0.2-+0.2
C_{80} (dB)	-2.1-+0.8	-0.3-+0.6	-0.1-+0.5	-0.4-+0.2	-1.0-+0.6	-1.3-+1.2
G (dB)	-0.5-+1.1	-1.1-+0.9	-0.6-+0.3	-0.4-+0.7	-1.3-+0.8	-1.2-+0.3

D. EDT

RT and EDT correlate highly with each other for the halls in Table I, so EDT is not an independent variable. The regression coefficients between EDT_{unocc} and EDT_{occ} (without orchestra) assuming the similar first order regression equation of Eq. (8) are given in Table VI as a reference.

E. IACC

The formula for IACC yields high correlations. Most striking is that $IACC_{unocc}$ is approximately equal to $IACC_{occ}$ for both $IACC_E$ and $IACC_A$ (Fig. 10). The suffixes “E” and “A” stand for “early” and “all” part of the impulse response, respectively, i.e., within the first 80 ms after the direct sound arrival and within 3.5 s after that, respectively. Thus $IACC_{E,unocc}$ appears to be a very satisfactory parameter to use in estimating the overall acoustical quality of a concert hall (Hidaka and Beranek, 1995; Beranek, 1996).

IV. SIMULATION OF THE OCCUPIED STATE IN A HALL USING A CLOTH COVERING OVER SEATS

It is impossible to ask real audiences again and again to a hall to sit while tests are made of various acoustical conditions, but we can execute such experiments at any time by making use of a simple means to simulate the occupied state. The method is to lay a suitable cloth over the entire seating area. The flow resistance of the cloth should lie between 630 and 870 Pa s/m, the surface-area mass should be about 0.26 kg/m², and the thickness about 0.5 mm. The cloth used here is made for interior curtains and is 100%-polyester (Type

KA 0149-0172, Kawashima Orimono Corp., Japan). Figure 11 shows this cloth spread over the seats in the TOC Concert Hall.

The validity of this method of simulation is shown in Figs. 12 and 13 and in Table VII, where RT was measured in five halls (Hamarikyu, NNT Opera, NNT Medium, TOC-organ and TOC-no-organ) and the other three parameters were measured in four halls (NNT Opera, NNT Medium, TOC-organ and TOC-no-organ). It is seen that the cloth simulates RT fairly well. All the RT data coincided with the exact values within 0.1 s, and for 75% they are within 0.05 s. It was also found that 88% of the G data are within 1 dB of the exact values. EDT and C_{80} with cloth have less accuracy, but 67% of EDT and 75% of C_{80} values are within 0.1 s and 0.7 dB, respectively. The latter figure is the average difference limen reported by Cox *et al.* (1993). Thus it appears that the cloth method is capable of simulating all of the parameters with small errors over the frequency range covered by the 250-Hz to 2000-Hz bands. A larger error is observed for 125-Hz and 4000-Hz bands, which may be mainly explained by interference effects at the lower frequencies and ambiguity in air absorption in the whole space at higher frequencies. Beyond this, there could be another explanation, namely, that the reflection from an audience area during the initial 80 ms has little meaning both objectively and subjectively, because of the seat dip effect. The $IACC_{E3}$ has unchanged values in spite of the occupancy, so that the result in Fig. 13 is not surprising.

Because the occupied sound field can be simulated satisfactorily between the 250-Hz and 2000-Hz bands with the cloth covering, listeners should be able to judge fairly well the acoustical quality of a hall prior to its opening, especially if the orchestral music chosen has a typical frequency spectrum (Okano *et al.*, 1998).

Figure 14 shows a comparison of the incremental absorption coefficients $\Delta\alpha$ measured in a standard reverberation chamber both with the cloth covering and with real people in Mitaka’s seats. Also plotted are the values of $\Delta\alpha$

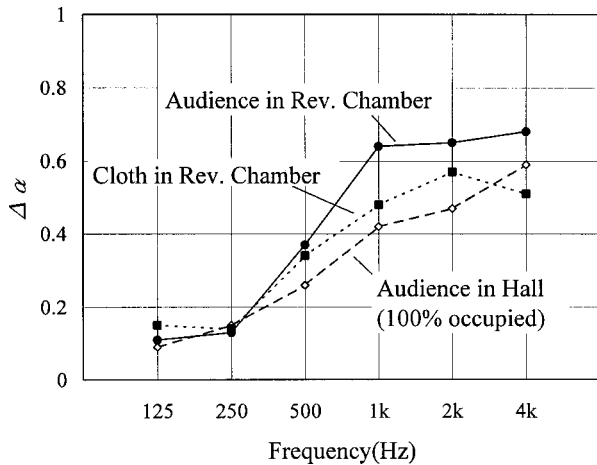


FIG. 14. The incremental absorption coefficient $\Delta\alpha$ equal to the difference between the absorption coefficients measured with the cloth covering and with real audience in the reverberation chamber and in the Mitaka Hall.

TABLE VIII. Comparison of ST1 and ST2 measured with and without the cloth covering in a shoebox shaped concert hall with a volume of 18 000 cubic meters.

		Frequency (Hz)					
		125	250	500	1000	2000	4000
ST1	Unoccupied	-9.8	-12.0	-14.0	-13.5	-13.8	-12.1
	Cloth	-9.6	-12.0	-14.1	-13.5	-14.1	-12.4
ST2	Unoccupied	-8.6	-10.3	-12.1	-11.8	-12.2	-10.3
	Cloth	-8.4	-10.4	-12.2	-11.9	-12.4	-10.6

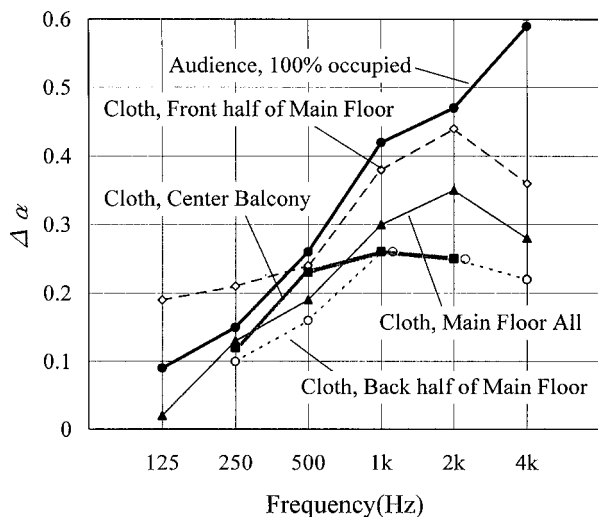


FIG. 15. Comparisons of the $\Delta\alpha$ for three cases of cloth covering in the Mitaka Hall. The coverings were, respectively, in the front and back half of the main floor and in the center balcony.

measured in the Mitaka hall with real audiences. In the reverberation chamber, the cloth covering over the seats absorbs less sound than when the seats are occupied by a real audience. The cause of this difference appears to be differences in the diffusion of the sound field in the two cases. A finding on the uniformity of sound diffusion in a hall is given in Sec. II B.

A. Some observations made in a hall using the cloth to simulate an audience

1. Stage acoustics as affected by an audience

An experiment to see how orchestral stage acoustics are affected by entry of an audience was performed in a shoebox shaped concert hall with a volume of 18 000 m³. Two well-known stage parameters, ST_1 , ST_2 (Gade, 1989),² were measured with and without the cloth covering. The results are shown in Table VIII. Both ST_1 and ST_2 were found to be independent of audience conditions. Based on this limited evidence, we assume that these stage parameters are mainly determined by the acoustical conditions in the stage enclosure, whether or not the audience is in the hall. In this hall, RT_{occ} at 500 Hz measured from music stop cords both with audiences and with the cloth covering, were 1.96 and 1.91 s, respectively. This slight time difference may be caused by other factors as discussed previously.

2. Evidence of variations in the diffusivity of the sound field in a hall

In the Mitaka Hall, the cloth described above was used to cover separately three parts of the audience area: (a) front half of the main floor; (b) back half; and (c) first balcony. The increment of the absorption coefficient $\Delta\alpha$, i.e., the change in α for the entire seating area owing to the addition of the cloth covering, for each of the coverings is plotted in Fig. 15. It should be noted that Mitaka Hall is shoebox-shaped with sufficient amount of fine- and large-scale diffusive elements on every side wall and on the ceiling. No ad-

ditional sound absorbing materials were used anywhere ($RT_{M,unocc}=2.49$ s), so that the sound diffusion conditions in the hall should be fairly good.

It would appear that when near the sound source, an acoustic material is more absorptive; that is to say, the absorption by an audience in a hall may be a function of its distance from the sound source. This result may have some influence on the RT predictions by the formulas in this paper, particularly when they are used for comparisons in both large and small halls. Also, the difference between the absorption coefficients measured in a real hall and those in a reverberation chamber may also be explained in part by this phenomenon. Further research is indicated.

V. CONCLUSION

Simple linear equations are presented for predicting the hall-averaged occupied values of RT, G , C_{80} , and $IACC_{E3}$, given measured unoccupied values. These equations are more accurate than conversion schemes that now appear in the literature, at least for the halls studied here. The important features of the present study (that led to the greater accuracy of these predictions) were that in each hall, both when unoccupied and *occupied with real audiences*, the same dummy heads and their positions were used for the measurement of $IACC_{E3}$, and the same omnidirectional microphones and positions were used for the measurement of the other parameters. There were 8 to 21 receiver positions in each hall. We are only confident that the proposed equations are applicable to halls that do not have peculiar shapes or unusual frequency characteristics. In addition, it was found that a simple cloth covering over the seats in four of the halls studied resulted in acoustical conditions that simulated closely those that exist with real audiences. It is suggested that these studies be extended to a wider range of halls, using similar experimental conditions.

APPENDIX A: REVISED MEASUREMENT METHOD OF IMPULSE RESPONSE BY STRETCHED IMPULSE

The stretched impulse signal used in this study, $s(t)$, is defined in the frequency domain, as the inverse Fourier transform of $Z(m)$, which is given by the following equation:

$$Z(m) = X(m) + iY(m) = A(m)\exp[B(m)],$$

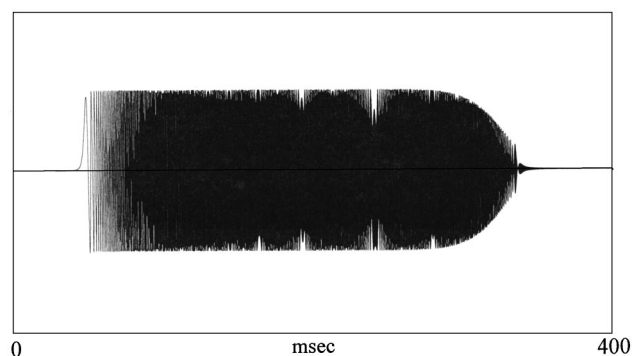


FIG. A1. Waveform of the stretched impulse signal, $s(t)$.

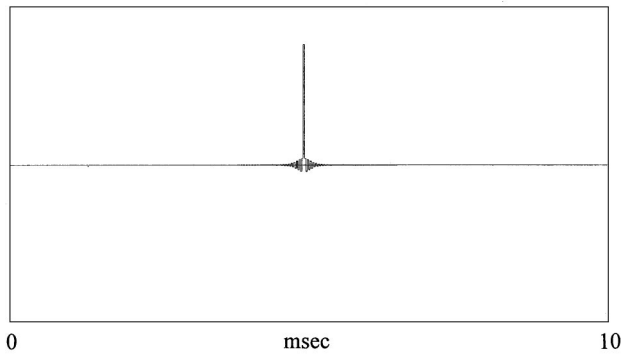


FIG. A2. Waveform of the exact impulse, $FT^{-1}[\exp[-B] \cdot FT[s(t)]]$, compressed by the phase shift filter.

$$m = 1 \text{ to } 2^{14} \quad (\text{A1})$$

where

$$X(m) = \begin{cases} \exp\left[-\left(\frac{m-3000}{5000}\right)^{12}\right] \cos\left(\frac{3m^2}{10000}\right) & \text{for } m = 1 \text{ to } 2^{13} \\ 0 & \text{for } m = 2^{13} + 1 \\ X(2^{14} + 2 - m) & \text{for } m = 2^{13} + 2 \text{ to } 2^{14} \end{cases} \quad (\text{A2})$$

and

$$Y(m) = \begin{cases} -\exp\left[-\left(\frac{m-3000}{5000}\right)^{12}\right] \cos\left(\frac{3m^2}{10000}\right) & \text{for } m = 1 \text{ to } 2^{13} \\ 0 & \text{for } m = 2^{13} + 1 \\ -Y(2^{14} + 2 - m) & \text{for } m = 2^{13} + 2 \text{ to } 2^{14} \end{cases} \quad (\text{A3})$$

The envelop function in Eqs. (A2) and (A3) is improved from Aoshima's (1981) shape so as to cover a wider frequency range, i.e., up to 20 000 Hz, with the sampling frequency 44 100 Hz. Sequences of $s(t) = FT^{-1}[Z(m)]$ are generated and radiated from a loudspeaker in the field. Using a synchronous summation technique, ten sequences will usually improve S/N by 10 dB. The observed signal is written by

$$u(t) = s(t) \otimes h(t), \quad (\text{A4})$$

where $h(t)$ means the impulse response between source and receiver in the hall and " \otimes " means a convolution operator. Taking the Fourier transform for both sides,

$$FT[u] = FT[s]FT[h] = A \exp[B]FT[h] \quad (\text{A5})$$

TABLE AI. Absorption power (m^2) of the orchestra derived from the exact measurements after Beranek and Hidaka (1998).

		Frequency (Hz)					
		125	250	500	1000	2000	4000
Concert Hall	44 players	12	21	24	46	74	100
	92 players	22	37	44	64	102	132
Opera House	40 players(in pit)	10	13	17	41	50	57
	80 players(in pit)	12	17	23	56	67	71

and multiplying the inverse phase filter, $\exp[-B]$, at both sides, one obtains

$$h(t) = FT^{-1}[\exp[-B]FT[u]/A]. \quad (\text{A6})$$

The computation program to execute above operations consists of 2^N points FFT algorithm ($N \geq 17$), provided the impulse response with a duration time of less than 3 s is calculable for $N = 17$. The waveform of the stretched impulse signal $s(t)$ and the exact impulse compressed by the phase shift filter are shown in Figs. A1 and A2.

When one wishes to improve the S/N at low frequencies because of the background noise, the following equations instead of Eqs. (A2), (A3) is useful, for example, where energy of the pulse signal is limited within octave band with mid-frequency of 125 Hz:

$$X(m) = \begin{cases} \exp\left[-\left(\frac{m-104}{42}\right)^{12}\right] \cos\left(\frac{96m^2}{10000}\right) & \text{for } m = 1 \text{ to } 2^{14} \\ 0 & \text{for } m = 2^{14} + 1 \\ X(2^{15} + 2 - m) & \text{for } m = 2^{14} + 2 \text{ to } 2^{15} \end{cases} \quad (\text{A7})$$

and

$$Y(m) = \begin{cases} -\exp\left[-\left(\frac{m-104}{42}\right)^{12}\right] \cos\left(\frac{96m^2}{10000}\right) & \text{for } m = 1 \text{ to } 2^{14} \\ 0 & \text{for } m = 2^{14} + 1 \\ X(2^{15} + 2 - m) & \text{for } m = 2^{14} + 2 \text{ to } 2^{15} \end{cases} \quad (\text{A8})$$

APPENDIX B: REVERBERATION TIME MEASUREMENT FROM STOP CHORDS

It is well known that smooth decay curves are hardly obtainable from stop chords, since most music signals do not have an ideal spectrum for acoustical measurements (Schultz, 1963). Also irregular decay curves which are not suitable for RT measurement are often observed with the traditional level recorder method at low frequencies, even if pink noise is employed as a source signal. Based on numerous similar analyses, it was found that applying *Schroeder's Integration Method* (SIM) to the stop chords is useful not merely to obtain smoothed decay curves, but also to detect unusable ones.

Figure B1 gives comparisons of decay curves by the two methods for four stop chords from Beethoven's *ninth symphony* recorded in a concert hall with 2000 seats, fully occupied. It is seen that very smooth curves are obtained by the SIM as compared to those from a graphic level recorder. Observation of SIM curves enables one to judge, for example, that (1) curve A has an ideal decay shape and the reverberation time (1.92 s) obtained by the two-point method in a computer program is satisfactory, that is, a best regression line fits well between the two points -5 and -30 dB on the SIM curve; (2) curve B is fairly smooth, but because of the obvious bulge at its beginning a much shorter RT value is derived, (3) neither curve C nor D is suitable for the two-

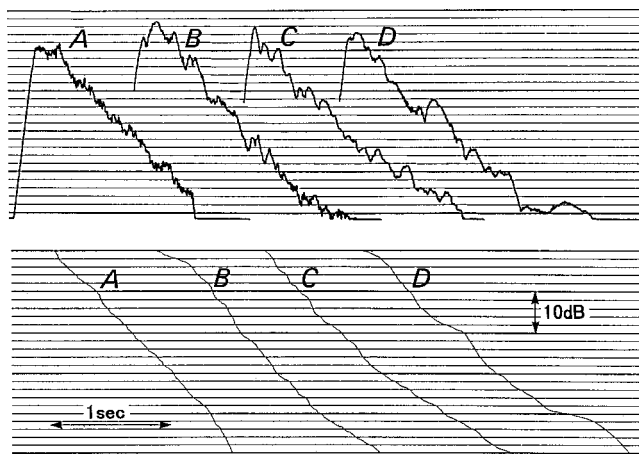


FIG. B1. Decay curves obtained by traditional level recorder method (upper) and the Schroeder's Integration Method (lower) at octave band with mid-frequency 500 Hz for four stop chords from Beethoven's ninth symphony: curve A is from fourth movement bar-215; curve B from fourth movement bar-594; curve C from second movement bar-559; and curve D from first movement bar-547. The reverberation time calculated from the best regression line between -5 dB and -30 dB of the lower curves A to D are 1.92, 1.66, 1.98, 2.27 s, respectively. As discussed in the text, from visual inspection curves B, C, and D should be judged unsuitable for use with the two-point SIM method.

point method because of the serious irregularity or bending. If one finds that the music signal is a surrogate of broadband noise based on an examination of the corresponding music score, the SIM is a very efficient way to measure occupied RT from stop chords.

It should be emphasized that a decay curve should be plotted for each pulse or stop chord so that one is sure that the RTs obtained by the two-point SIM are correct. The typical problems are the irregularity and bending at low frequencies as shown in Fig. B1, C and D. Such curves should be excluded from the analysis. If we could apply the SIM to Schultz's data and sort out in addition to his careful examination on the stop chords, his equations might have changed.

Finally, the median values of the standard deviation of RT by the exact method and the stop chord method are compared in Table BI, when the latter data is based on the measurement at the halls in Table II. It is found that the stop chord method has about twofold spreads to the exact method except 4000-Hz band based on the various reasons discussed before. This means that very careful examination is necessary when the musical signal is utilized to obtain the RT of a hall. Further research is needed to clarify the ambiguities between RT values obtained by ideal impulses and by stop chords.

TABLE BI. Average of standard deviations of RT for the exact measurement and from music stop chord with Schroeder Integration Method (SIM) at each hall in Table II.

	Frequency (Hz)					
	125	250	500	1000	2000	4000
Exact meas.	0.09	0.09	0.06	0.05	0.05	0.06
Stop chord	0.20	0.15	0.11	0.11	0.11	0.08

¹One can evaluate the "distance" between the true statistical distribution that expresses experimental data and the estimated statistical distribution obtained by the maximum likelihood method by utilizing the AIC, if the former distribution is unknown. More practically, when there are several multiple regression equations combined with various parameters, AIC is an objective measure to investigate which equation is statistically best.

²The support factor is defined as the level difference between two measurements of sound pressure on a stage. By using the omnidirectional sound source, the impulse response is measured by a microphone at 1 m from the center of the sound source. The first measurement is of the energy in the time interval from 0 to 10 ms. The second one is that from 20 to 100 ms for ST1 and from 20 to 200 ms for ST2, respectively.

Akaike, H. (1973). *Information Theory and an Extension of the Maximum Likelihood Principle* (Akademiai Kiado, Budapest).

Aoshima, N. (1981). "Computer-generated pulse signal applied for sound measurement," *J. Acoust. Soc. Am.* **69**, 1484–1488.

Barron, M. (1993). *Auditorium Acoustics and Architectural Design* (E and FN Spon and Chapman & Hall, London).

Barron, M., and Lee, L.-J. (1988). "Energy relation in concert auditoria. I," *J. Acoust. Soc. Am.* **84**, 618–628.

Beranek, L. L. (1996). *Concert and Opera Halls* (Acoustical Society of America).

Beranek, L. L., and Hidaka, T. (1998). "Sound absorption in concert halls by seats, occupied and unoccupied, and by the hall's interior surfaces," *J. Acoust. Soc. Am.* **104**, 3169–3177.

Beranek, L. L., Hidaka, T., and Masuda, S. (1998). "Acoustical design of the Drama and experimental Theaters of the New National Theater, Tokyo, Japan," *Proc. ICA* **98**, 1793–1794.

Beranek, L. L., Hidaka, T., and Masuda, S. (2000). "Acoustical design of the Opera House of the New National Theater, Tokyo, Japan," *J. Acoust. Soc. Am.* **107**, 355–367.

Bradley, J. S. (1991). "A comparison of three classical concert halls," *J. Acoust. Soc. Am.* **89**, 1176–1192.

Cox, T. J., Davies, W. J., and Lam, Y. W. (1993). "The sensitivity of listeners to early sound field changes in auditoria," *Acustica* **79**, 27–41.

Cremer, L., and Müller, H. A. (1982). *Principles and Applications of Room Acoustics* (Applied Science).

Fasold, W., Tennhardt, H., and Winkler, H. (1988). "Ergänzende raumakustische Maßnahmen im Großen Konzertsaal des Schauspielhauses Berlin," *Bauakademie der DDR*.

Fukuchi, T., and Fujiwara, K. (1985). "Sound absorption area per seat of upholstered chairs in a hall," *J. Acoust. Soc. Jpn. (E)* **6**, 271–279.

Gade, A. C. (1989). "Investigation of musicians' room acoustic conditions in concert halls. II: Field experiments and synthesis of results," *Acustica* **69**, 249–262.

Hidaka, T., Beranek, L. L., and Okano, T. (1995). "Interaural cross-correlation, lateral fraction, and low- and high-frequency sound level as measures of acoustical quality in concert halls," *J. Acoust. Soc. Am.* **98**, 988–1007.

Hidaka, T., Beranek, L. L., Masuda, S., Nishihara, N., and Okano, T. (2000). "Acoustical design of the Tokyo Opera City (TOC) Concert Hall, Japan," *J. Acoust. Soc. Am.* **107**, 340–354.

ISO 3745 (1977). "Acoustics—Determination of sound power levels of noise sources using pressure—Precision methods for anechoic and semi-anechoic rooms."

ISO 3741 (1988). "Acoustics—Determination of sound power levels of noise sources using pressure—Precision methods for reverberation rooms."

ISO 3382 (1997). "Acoustics—Measurement of the reverberation time of rooms with reference to other acoustical parameters."

Jordan, V. L. (1980). *Acoustical Design of Concert Halls and Theaters* (Applied Science), p. 217.

Kuttruff, H. (1991). *Room Acoustics* (Elsevier Applied Science, New York).

Meyer, J. (1978). *Acoustics and the Performance of Music* (Verlag Das Musikinstrument, Frankfurt/Main).

Nagata, M. (1991). *Acoustic Design of Architecture* (Ohmu-Sya, Tokyo), p. 215 (in Japanese).

Okano, T., Beranek, L. L., and Hidaka, T. (1998). "Relations among interaural cross-correlation coefficient ($IACC_E$), lateral fraction (LF_E), and apparent source width (ASW) in concert halls," *J. Acoust. Soc. Am.* **104**, 255–265.

- Reichardt, W., Abdel, Alim, O., and Schmidt, W. (1975). "Definition und Messgrundlage eines objektiven Masses zur Ermittlung der Grenze zwischen brauchbarer und unbrauchbarer Durchsichtigkeit bei Musikdarbietung," *Acustica* **32**, 126–137.
- Schultz, T. J. (1963). "Problems in the measurement of reverberation time," *J. Audio Eng. Soc.* **11**, 307–317.
- Schultz, T. J. (1980). "Concert Hall Tour of North America," BBN Tech. Inf. Rep. No. 98.
- Watanabe, K., Yoshihisa, K., and Tachibana, H. (1985). "Subjective evaluation of room acoustics by using impulsive sound source," *Proceedings of the Autumn Meeting of the Acoustical Society of Japan*, pp. 479–480 (in Japanese).

Simulation of jet-noise excitation in an acoustic progressive wave tube facility

Alexander Steinwolf^{a)}

Department of Mechanical Engineering, University of Sheffield, South Yorkshire S1 3JD, United Kingdom

Robert G. White

Department of Aeronautics and Astronautics, University of Southampton, Hampshire SO17 1BJ, United Kingdom

Howard F. Wolfe

Air Force Research Laboratory, AFRL/VASS Building 24C, Wright-Patterson AFB, Ohio 45433

(Received 18 December 1999; accepted for publication 2 December 2000)

Acoustic excitation produced by jet-engine effluxes was simulated in a progressive wave tube (APWT) facility with a computer-based control system. The APWT siren is driven by a signal generated numerically in a PC and then converted into analog form. Characteristics of the acoustic pressure measured by a microphone are analyzed in digital form and compared with those prescribed for simulation. Divergence is compensated by immediate modification of the driving signal and this action is repeated in the form of iterative process until the test specification is attained. Typical power spectral density (PSD) shapes with maxima at low and high frequencies were simulated. A "tailoring" approach has been also achieved when a test specification was determined directly from field measurements for the particular aircraft under consideration. Since acoustic pressure signals of high level differ from the Gaussian random process model, particularly in terms of asymmetric probability density function, a method has been developed to make the driving signal also non-Gaussian by simulating skewness and kurtosis parameters of the APWT acoustic excitation simultaneously with PSD control. Experimental results with Gaussian and non-Gaussian characteristics obtained for various PSD specifications including sharp and narrow peaks are presented in the paper. © 2001 Acoustical Society of America.

[DOI: 10.1121/1.1344159]

PACS numbers: 43.58.Jq, 43.28.We, 43.38.Ar, 43.58.Ta [SLE]

I. INTRODUCTION

In the aircraft and spacecraft industry there has been considerable interest in experimental simulation of acoustic pressures due to jet-engine effluxes. Such an excitation is a high-frequency random process and the sound-pressure level is so high that acoustic fatigue damage happens often for structural components behind the jet engine. This is an ever-present problem for aircraft and it is not possible to overcome it without relevant experimental studies. Since full-scale jet-noise testing in field conditions is a very expensive and time-consuming process, the present policy is to use acoustic progressive wave tube (APWT) facilities of the siren type for experimental simulation of jet-noise excitations in the laboratory.^{1,2} Such facilities are in use at the US Air Force,³ Lockheed Martin Company,⁴ NASA Langley,⁵ Boeing St. Louis, and, for research purposes, at the University of Southampton, UK.⁶

The facility (Fig. 1) consists of a large horn, which is exponential in shape about one axis and tapered along the other, coupled to a parallel wall duct. The horn dimensions vary depending on the necessary sound-pressure levels (SPL) and reach several meters of length and height. The APWT is driven by an electro-pneumatic exciter (siren) located at the

narrower end. At the other end there is a sound-absorbing termination. Test specimens can be mounted inside the tube having a rectangular cross section or, if this is a skin panel, can be clamped in steel frames, in the wall of the horn. Sound-pressure signals are measured by a microphone mounted in the test section of the tunnel.

APWT facilities are capable of simulating wideband random excitation with frequencies up to thousands of Hz and sound-pressure levels comparable with those produced by modern aircraft engines. However, the equivalence of APWT and field tests may still be debated because the test specifications imposed on APWT simulation are routinely simplified to prescribing just overall SPL and a simple flattened shape of power spectral density (PSD). This approach describes basic knowledge about jet noise. However, it is clear that the particular service conditions under consideration may vary and be rather different from the above averaged specification. Further difficulties depend on how control of the system is realized.

When the APWT siren is driven by an analog signal generator via set of manually adjusted 1/3-octave filters,⁶ the system ability for PSD shaping, i.e., frequency-domain control, is critically limited by the filter bandwidths. At higher frequencies, the 1/3-octave filters are too wide to control considerable gradients and sharp peaks which may exist in the PSD prescribed for simulation. Moreover, one must be

^{a)}Electronic mail: A.Steinwolf@sheffield.ac.uk

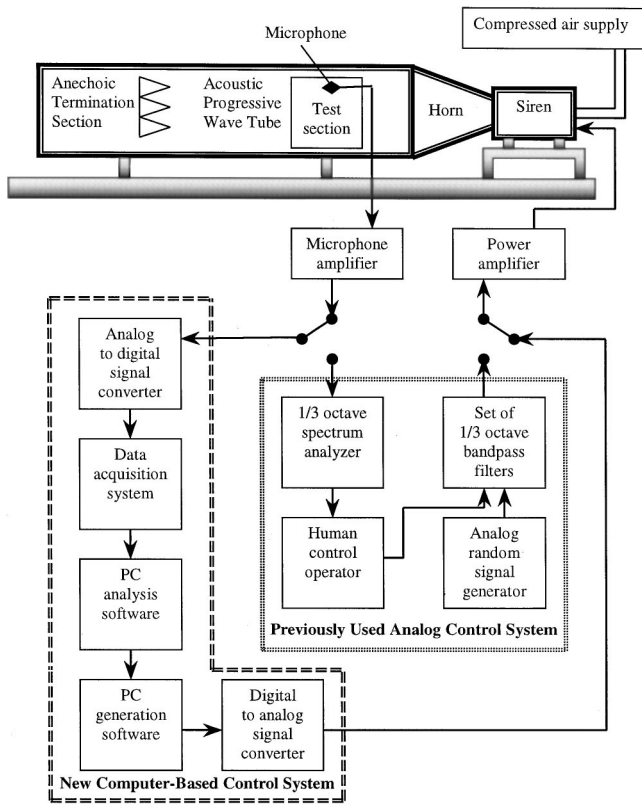


FIG. 1. Acoustic progressive wave tube facility setup.

aware of unavoidable fluctuations in the PSD curves because of the use of 1/3-octave analog filters. The plot presented in Fig. 2 is a PSD of the acoustic pressure signal measured by a microphone in the test section of the APWT when the driving signal was supposed to be of a uniform PSD. The filter bounds are introduced into the plot by circles. Their comparison with the PSD shape suggests that there is a problem of unwanted notches in the output PSD caused by the same behavior of the input PSD strictly at the bounds between 1/3-octave intervals (100, 125, 160, 200, 250, 316, 400, 500 Hz). Thus, if 1/3-octave filter devices are used for driving the APWT, it is impossible to avoid distortions in the PSD shape at the above frequencies. No less important is that the control procedure is manual and, hence, subjective as an operator

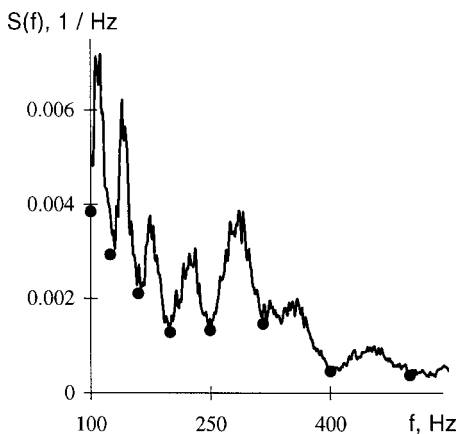


FIG. 2. PSD of APWT acoustic excitation compared to the bounding frequencies (circles) of 1/3-octave filters of the analog driving system.

inspects the obtained PSD of the acoustic excitation and then adjusts amplification for each of the bandpass filters at the system input.

All earlier discussion relates to the frequency domain as the PSD of acoustic excitation is controlled more or less accurately. However, the probability density function (PDF), i.e., amplitude distribution domain, remains absolutely out of control, whereas the PDF may vary and become different from the conventional Gaussian model due to asymmetry in acoustic wave propagation and nonlinear effects in the APWT system itself. The latter appears to be a general restriction which, the authors believe, is inherent in all previous acoustic testing carried out using APWTs. Control of the PDF of the APWT acoustic excitation has not been previously reported. Even if the PDF were checked, there was no way to adjust the driving signal in the amplitude distribution domain with use of an analog driving system because analog generators only produce Gaussian random signals.

The aforementioned difficulties can be overcome and precision of jet acoustic pressure simulation in APWT can be increased if the siren coil is driven via a digital-analog converter by a computer-based control system which is able to analyze signals from the microphone at the APWT output, to compare their characteristics with those prescribed for simulation, and to compensate for the difference by immediate correction of the driving signal generated in the computer. In so doing, one would have much more flexibility in changing the characteristics of the driving signal both in frequency and amplitude distribution domains. This would make it possible to reproduce both the PSD and the PDF inherent in jet-noise excitations. The PDF control via skewness and kurtosis adjustments is advantageous to the main purpose of APWT experiments, which is acoustic fatigue testing, because an influence of the excitation kurtosis and skewness on time to fatigue failure has been reported in the literature.⁷⁻⁹

The computer-based control system would facilitate use of the up-to-date testing methodology known as ‘‘tailoring’’ of in-service environment¹⁰ when the excitation to be simulated on a test rig is determined directly from field measurements. To implement this approach, which is well developed for shaker testing,¹¹ a preliminary stage of processing flight data records of jet noise is required. The results of that, as discussed below, can be used as a source material to simulate these particular flight conditions by APWT in laboratory experiments.

II. THEORETICAL BACKGROUND FOR BI-DOMAIN SIMULATION IN TERMS OF PSD AND PDF

To generate digitally a driving signal for the APWT siren, the method of pseudorandom time history simulation¹² was used and further developed, which is based on the Fourier expansion with a large number N of harmonics

$$x(t) = \sum_{k=1}^N A_k \cos(2\pi k \Delta f t + \varphi_k). \quad (1)$$

According to this approach, amplitudes A_k are determined by the required PSD values $S(f)$ at the corresponding frequencies

$$A_k = \sqrt{2\Delta f S(k\Delta f)}, \quad k = \overline{1, N}. \quad (2)$$

In so doing, any prescribed PSD shape can be provided for the APWT driving signal. As explained above, this PSD shape is estimated by comparing results of processing sound-pressure measurements in the field test and those made in the APWT facility by the reference microphone. The procedure of PSD simulation takes the form of an iteration process. If the APWT was driven by a signal with a PSD equal to $S_i^d(f)$ and this action produced an acoustic excitation with power spectrum $S_i^a(f)$, which is somewhat different from the required shape $S_*(f)$ prescribed for simulation, the PSD of the driving signal $S_{i+1}^d(f)$ for the next $(i+1)$ th iteration should be given by correction of the previous driving spectrum $S_i^d(f)$ according to the relationship

$$S_{i+1}^d(k\Delta f) = S_i^d(k\Delta f) \frac{S_*(k\Delta f)}{S_i^a(k\Delta f)}, \quad k = \overline{1, N}. \quad (3)$$

When a new shape of the driving PSD is found, the result obtained from Eq. (3) is substituted into Eq. (2) to define a new set of harmonic amplitudes A_k^{i+1} which should be used to generate by Eq. (1) a new driving signal time history for the next $(i+1)$ th iteration. This control process is finished on some n th iteration when a satisfactory closeness between PSDs of field $S_*(f)$ and APWT $S_n^a(f)$ acoustic excitations is attained. The last set of amplitudes A_k^n of the polyharmonic driving signal (1) is then kept constant while testing structural components in APWT under this properly simulated acoustic excitation.

Thus, the amplitudes of the driving signal (1) are deterministic values, which are uniquely defined by the necessary PSD shape $S_*(f)$ of the acoustic excitation. In order to endow the polyharmonic process (1) with a random nature, as is the case for field acoustic excitation, a traditional technique is to prescribe all harmonic phase angles φ_k to be random numbers uniformly distributed in the $[0, 2\pi]$ interval. However, in this case the PDF of the APWT driving signal cannot be varied and is always close to the Gaussian law. This restriction is an essential drawback for two reasons. The first is that real acoustic pressure signals produced by jet engines are somewhat different from the model of a Gaussian random process (examples are presented below). It is desirable to retain these non-Gaussian features in the acoustic excitation produced by the APWT. Another reason is that even if the required acoustic excitation does not possess non-Gaussian features and, hence, the driving signal can be a Gaussian process, the high sound-pressure levels in the narrow section of the APWT horn cause nonlinear acoustic propagation effects which distort the pressure waveform and introduce non-Gaussian properties. To compensate for these distortions it may be necessary to control the PDF of the driving signal together with its PSD. This objective could be met if the aforementioned iteration procedure is updated with additional control of skewness λ and kurtosis γ parameters describing non-Gaussian features of the PDF function $P(u)$. A relationship between $P(u)$ and λ, γ is established by equations

$$\lambda = \frac{M_3}{(M_2)^{1.5}}, \quad \gamma = \frac{M_4}{(M_2)^2},$$

$$M_L = \int_{-\infty}^{\infty} (u-m)^L P(u) du, \quad (4)$$

$$L = 2, 3, 4; \quad m = \int_{-\infty}^{\infty} u P(u) du.$$

A solution to the problem can be found¹³ by operating in Eq. (1) with phase angles φ_k and prescribing some of them not randomly but in a special deterministic way which makes use of their influence on skewness and kurtosis parameters. Since the PSD is not phase dependent, it will not change by any manipulations of phases φ_k . The necessary frequency content of the driving signal is still provided by appropriate choice of the harmonic amplitudes according to Eq. (2). Thus, both basic characteristics (PSD and PDF) can be controlled simultaneously and independently when the variables in the driving signal are arranged in such a way: amplitudes are responsible for the PSD and the phase angles for the PDF.

To develop a mathematical model for proper phase adjustment, a relationship of the skewness and kurtosis parameters to amplitudes and phase angles of the pseudorandom polyharmonic process (1) has been established. For this purpose, the PDF central moments M_L in Eqs. (4) were determined by time averaging the function (1). Then, the complex form of the Fourier series was used and, finally, the following expression for skewness has been obtained:

$$\lambda = \frac{3}{4} \sum_{n=2k} A_n A_k^2 \cos(\varphi_n - 2\varphi_k) + \frac{3}{2} \sum_{\substack{n=j+k \\ j < k}} A_n A_j A_k \cos(\varphi_n - \varphi_j - \varphi_k). \quad (5)$$

In this formula, summation should be carried out only for those combinations of indices j, k, n (ranging from 1 to N) which satisfy equalities written in Eq. (5) under both summation signs. A similar expression, although more complicated in nature, has been obtained for kurtosis.¹³

If the phase angles φ_k of the harmonics are chosen in a random manner, as is the case in the classical method with PSD fitting only, the cosine functions in Eq. (5) also produce random values distributed uniformly in the region from -1 to 1 . Hence, different terms of the sums compensate each other, bringing the result of summation to zero as the number of harmonics N is large in the polyharmonic process (1). To tend skewness to positive values, some of the cosine arguments in Eq. (5) should be prescribed equal to zero, changing the corresponding term of the sum from some random value to a certain positive deterministic value defined by amplitudes, for instance $A_n A_k^2$ for the first summation in Eq. (5). Thus, two equations are used in the choice of phase angles increasing the skewness value (5): the first equation $\varphi_n - 2\varphi_k = 0$ is for two frequencies, one of which $f_n = n\Delta f$ doubles another $f_k = k\Delta f$, and the second $\varphi_n - \varphi_j - \varphi_k = 0$ is for three frequencies satisfying the equality $f_n = f_j + f_k$.

On the basis of the above concepts and a similar analysis made for the kurtosis parameter, a technique for simulation of time history data with the prescribed PSD shape $S(f)$ and controlled skewness and kurtosis values has been developed. First, as with simulation of the Gaussian process, the amplitudes A_k are determined according to Eqs. (2) and (3), while the phase angles φ_k are chosen randomly. Then, keeping all amplitudes and most of the phases fixed, a few phase angles are rearranged from random values to a deterministic group that maximizes or minimizes one of the summations in the expression for skewness or kurtosis. This action leads to some increase or decrease of these parameters. A similar operation can be performed for another sum and corresponding group of phases which will be also eliminated from the initial random phase set. In so doing, the skewness and kurtosis of the APWT driving signal can be gradually increased or decreased from starting values, when all phases were random, to the desired magnitudes λ_* and γ_* different from those of the Gaussian process.

A computer algorithm executing the above numerical simulation procedure has been developed. Before implementing it for generation of driving signals for progressive wave tube experiments, the tailoring approach, as stated in the introductory section, was used to set up test specifications for the acoustic pressure signal to be simulated by the APWT. This problem was treated in terms of PSD describing frequency-domain characteristics and in terms of skewness and kurtosis parameters describing amplitude distribution properties.

III. RESULTS OF ANALYSIS OF ACOUSTIC EXCITATION MEASUREMENTS MADE IN FLIGHT TESTS

Recordings of noise produced by jet engines were measured in flight by microphones mounted on the outside surface of the aft equipment bay of a military aircraft. The time histories of the acoustic excitation signals were analyzed on a PC with help of well-established algorithms¹⁴ for determination of PSD and PDF characteristics. Probability distribution analysis and, especially, consideration of non-Gaussian features requires much longer time history samples than ordinary PSD processing. In this study the whole amount of flight data was about 320 000 points with the time discretization step of 0.000 15 s.

As a result of flight data analysis in the frequency domain, it appeared that the main part of the acoustic energy concentrated between 100 and 300 Hz with a gradual decrease of level at higher frequencies. However, the latter was affected by a sharp narrow peak at 370 Hz, which is even larger than the level of the main frequency components around 200 Hz. The PSD graph is shown below (dotted curve in Fig. 5) when being simulated in the APWT. Thus, the flat PSD of sound pressure, which is the common model, would not be appropriate in this case. To achieve tailoring of the measured environmental acoustic excitation, the sharp peak at high frequencies must be included in the APWT test specification. The results of PDF analysis are presented in Fig. 3. The experimental distribution shown by solid curves is compared with the Gaussian law dotted curve. Deviations

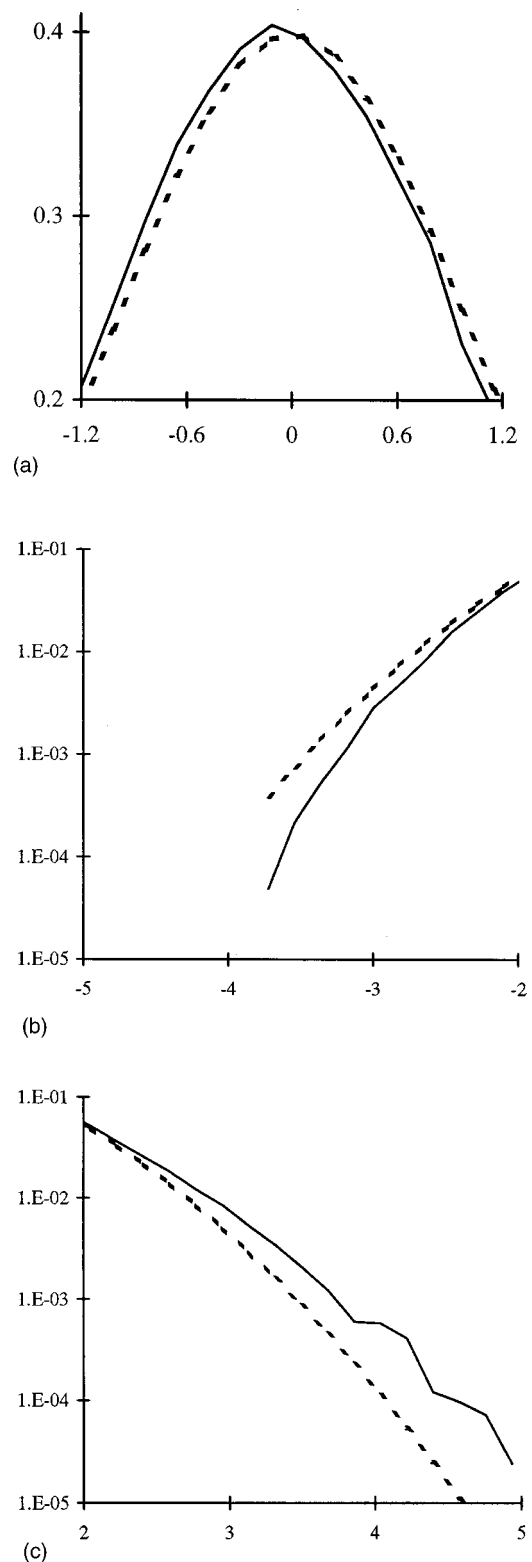


FIG. 3. Probability density function (kurtosis=3.1, skewness=0.2) of acoustic excitation in flight tests (solid curves) compared with the Gaussian law (dotted curve). (a) Central part; (b) Left tail; (c) Right tail.

from the Gaussian model may occur not only in the central part of the PDF [Fig. 3(a)] but also at the tails. Therefore, besides the conventional view as in Fig. 3(a), the PDF was also presented on a logarithmic scale [Figs. 3(b), (c)]. Such a presentation displays low probabilities at high argument values in the experimental and theoretical distributions. The

PDFs presented here and below in the paper are in nondimensional form. The horizontal axis represents the ratio between actual values and the rms value σ of the acoustic excitation.

The probability distributions under consideration appeared to be asymmetrical with a skewness parameter of about 0.2. This skewness value is very stable and varies no more than the rms value σ . Asymmetry is visible in the central region of the PDF [see Fig. 3(a)]. The vertex of the experimental curve is shifted to the left and slightly upwards compared with the Gaussian curve. As a result, for negative arguments in the interval $[-1.5\sigma, 0]$ the experimental PDF exceeds the theoretical curve and for positive arguments $[0, 1.5\sigma]$ the opposite situation occurred. Distribution asymmetry has been also observed at the tails for arguments exceeding a value of $|2\sigma|$. At the left tail [Fig. 3(b)] the experimental PDF lies under the Gaussian curve whereas at the right tail [Fig. 3(c)] the situation is reversed. It is also important to note that there is a considerable difference between left and right edges of the PDF, i.e., between minimum and maximum values in the time histories. The left tail tends to cut off at -3.7σ and the right is much longer up to 5σ . Apart from skewness there is some increase of kurtosis value (it was about 3.1) compared to that of the Gaussian random process which is equal to 3. Thus, the acoustic excitation caused by jet-engine effluxes can be a non-Gaussian process.

IV. RESULTS OF SIMULATING ACOUSTIC EXCITATIONS BY ACOUSTIC PROGRESSIVE WAVE TUBE

Experimental studies were conducted at the University of Southampton, UK in the APWT facility of $7.0 \times 3.0 \times 0.6$ -m dimensions which is equipped with a Wyle WAS

3000 siren and has the configuration described in Fig. 1. The previously used analog control system was disconnected and a new computer-based control system was set up. The APWT siren was driven by a PC via an analog–digital–analog conversion (ADC) electronic board PCI-20428W. The VISUAL DESIGNER software supplied with the ADC board was used for data acquisition, translation, and presentation, as well as for monitoring the experiment. Precautions have been taken when concatenating successive segments of the driving signal as discontinuities exist at the segment boundaries. To overcome this difficulty and to generate a continuous time history, the beginning of each subsequent segment was scanned point by point until the appropriate time moment was found where the signal itself and its derivative were close to those which occurred at the last point of the previous segment. The past section of the new signal segment was cut out and the successive segments were smoothly joined. Instead of the above, one may prefer to implement a windowing and overlapping procedure used in shaker digital controllers. To do so a specific correction of the input kurtosis and skewness values should be added as discussed in Ref. 15.

Two types of PSD test specifications were considered. The first is a triangular shape in the interval from 100 to 600 Hz with one broad maximum that is a conventional representation of jet noise PSD according to Ref. 2. The second test specification resulted from tailoring the flight test measurements described in Sec. III. Before initiating simulation experiments with the bi-domain (PSD plus PDF) digital control procedure developed, attention was focused on the achievable advantages over the analog system in the frequency domain only, which were discussed in the Introduction. Power spectrum control was performed by iterations when each

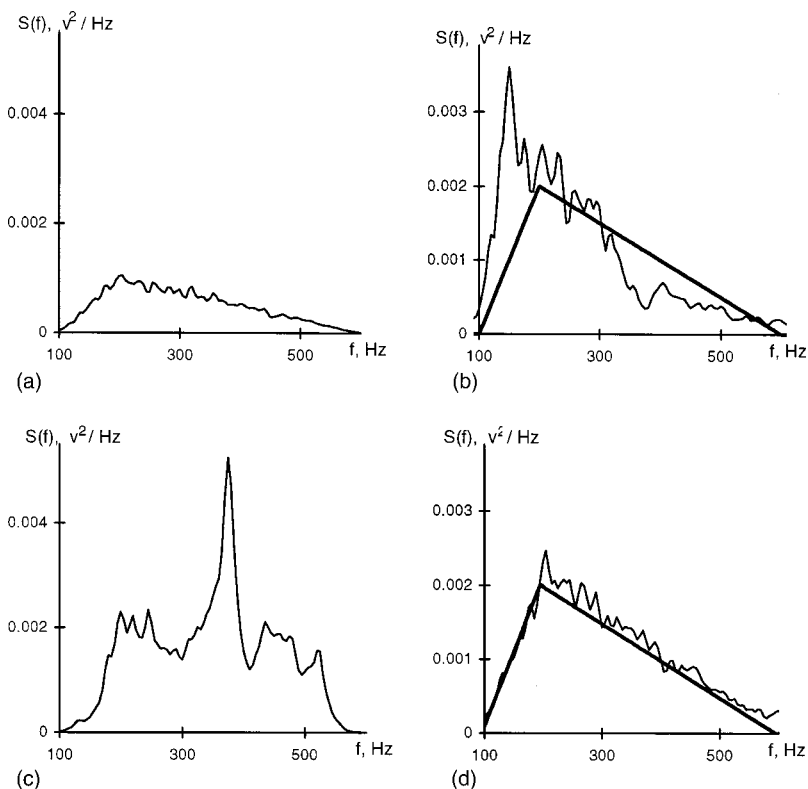


FIG. 4. Results of experiments for digital control of APWT to simulate a triangular PSD (thick curve) with a maximum at 200 Hz. (a) PSD of driving signal on the first iteration; (b) PSD of acoustic signal in APWT (first iteration); (c) PSD of driving signal on the sixth iteration; (d) PSD of acoustic signal in APWT (sixth iteration).

subsequent PSD of the driving signal was corrected according to formula (3). Figure 4 shows results obtained for the triangular PSD with a maximum at 200 Hz, i.e., with most of the acoustic pressure energy concentrated at lower frequencies. The left-hand plots [Figs. 4(a), (c)] display PSDs of driving signals generated in the computer. On the corresponding right-hand plots [Figs. 4(b), (d)] one can see PSDs of the response, which is the spectrum of the acoustic pressure signal measured by the reference microphone in the APWT test section. The experimental response PSD obtained (thin curve) can be compared with the test specification (thick triangular line) prescribed. In all of these figures and similar PSD plots below, v indicates the voltage of the driving signal at the system input or the signal coming from the microphone amplifier at the output.

Since the APWT is a complicated dynamic system with its own resonances and nonlinear features, the necessary PSD shape introduced to the driving signal for the first experimental run [Fig. 4(a)] was distorted during passage through the APWT: the response PSD exceeded the prescribed shape (thick triangular curve) at low frequencies [Fig. 4(b)]. When, at the second iteration, the driving PSD was decreased to compensate for the above effect, the response PSD appeared to be closer to that required. The response shape improved in further iterations and, as a result, the prescribed PSD was achieved [see Fig. 4(d)] by a driving signal with a rather specific PSD [Fig. 4(c)]. Similar results were obtained for another PSD with a maximum shifted to higher frequencies (from 200 to 400 Hz). In this case, the number of required iterations was three.

A more complicated problem was then considered to reproduce the acoustic PSD shape obtained by tailoring of flight test measurements [thick dotted curve in Fig. 5(a)]. A principal difference and complication compared with the previous experiments was in simulation of a sharp peak at high frequency. This became possible only with digital control of the APWT. On the first iteration the PSD peak under consideration was completely absent in the APWT response [thin solid curve in Fig. 5(a)] even though it existed in the driving signal. It appeared to be necessary to increase excitation level considerably at this specific frequency (about 370 Hz). That was done in the second and, then, third iterations when satisfactory simulation of this PSD peak was achieved in the APWT response [Fig. 5(b)].

Power spectrum graphs for intermediate iterations omitted in Figs. 4 and 5 and for the case of triangular PSD with a maximum at 400 Hz can be found in Ref. 16. Once PSD simulation had been comprehensively tested, attention was turned to the amplitude distribution (PDF) domain. When there was no relevant control the PDF changed significantly, taking various non-Gaussian forms (see Figs. 6 and 7). For example, for the PSD with the 400-Hz maximum, kurtosis tended to values less than 3 (particularly, 2.57 in this experiment), i.e., PDF tails were narrower [solid curve in Figs. 6(b), (c)] than those of the Gaussian model (dotted curve). For the PSD specification obtained by simulating field environmental conditions, there was an opposite tendency and kurtosis increased up to 3.85, making the PDF tails essentially wider [Figs. 7(b), (c)]. At the same time, the distribu-

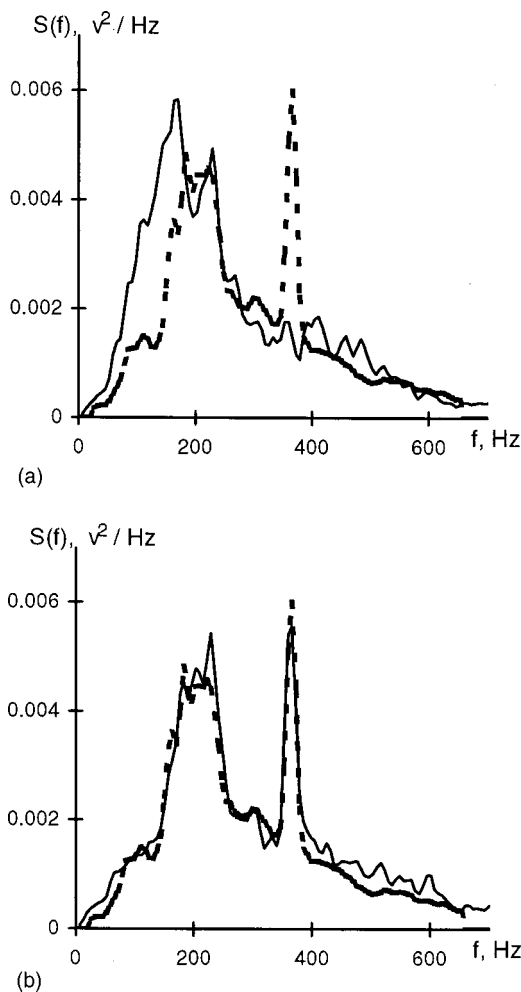
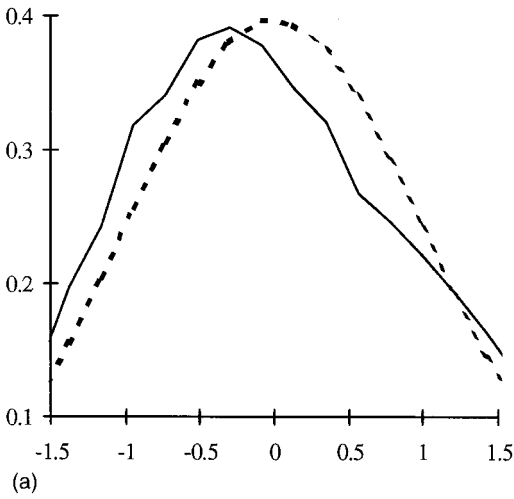


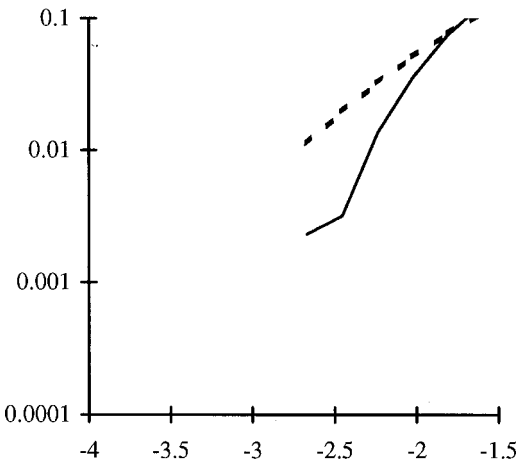
FIG. 5. Results of APWT experiments (thin solid curve) for the PSD obtained by tailoring of flight test measurements (thick dotted curve). (a) PSD of acoustic signal in APWT (first iteration); (b) PSD of acoustic signal in APWT (third iteration).

tion vertex was sharper than for the Gaussian law [Fig. 7(a)]. In both cases the PDF was asymmetric with positive skewness. Because of that the PDF tails were different: the right tail was longer and had higher values than the left one for the same arguments [see Figs. 6(b), (c) and 7(b), (c)]. The distribution vertex point was shifted to the left [Figs. 6(a) and 7(a)].

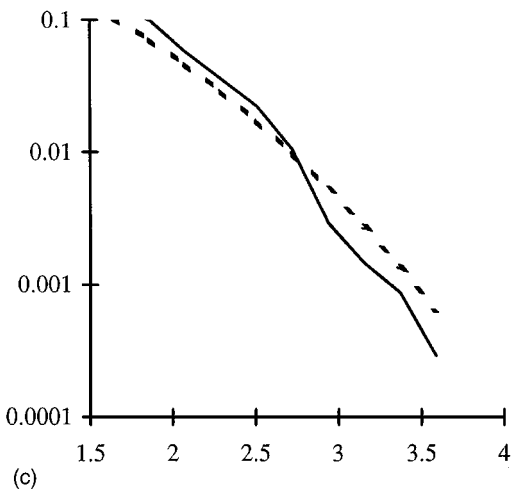
Taking into account the above non-Gaussian behavior, the APWT control procedure changed in further experiments and deterministic adjustment of some phase angles in the polyharmonic pseudorandom model was implemented as described in Sec. II. The procedure was first applied to the case of a triangular PSD with a maximum at 400 Hz. The objective was to increase the above-mentioned kurtosis value 2.57 obtained before PDF control and to reach the value of 3.1 observed in flight test measurements. Since a Gaussian driving signal with kurtosis about 3.0 produced APWT system response with lower kurtosis (2.57), then, to have the latter increased, a non-Gaussian driving signal with kurtosis higher than 3.0 was necessary and a figure of 6.0 was tried on the first iteration. However, this value appeared to be too high and the response kurtosis of 4.5 on the first iteration was larger than necessary. Similarly to the above experiments,



(a)



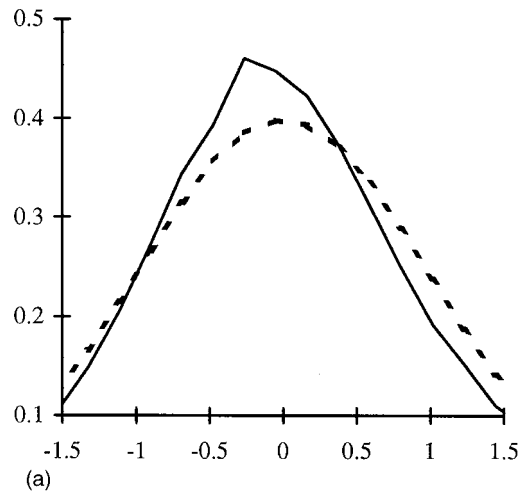
(b)



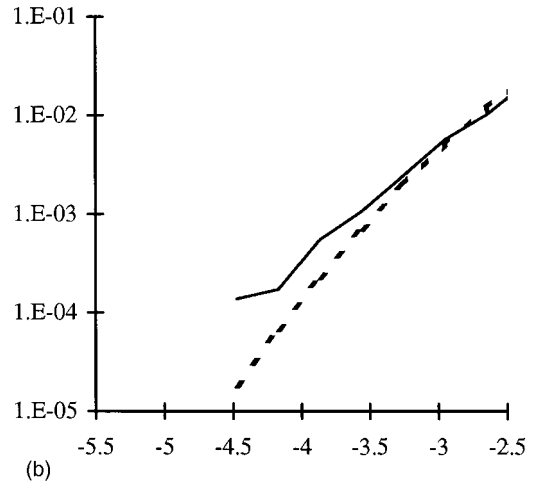
(c)

FIG. 6. Probability density function (solid curve) of the APWT acoustic signal (kurtosis=2.57, skewness=0.28) with a PSD maximum at 400 Hz (dotted curve is the Gaussian law). (a) Central part; (b) Left tail; (c) Right tail.

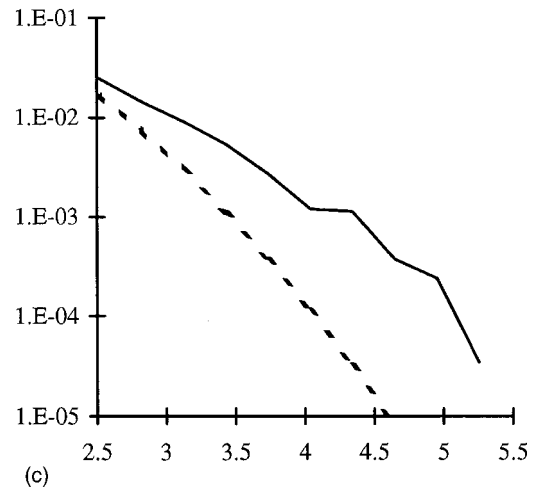
the response PSD on the first iteration was very different from the required triangular form [Fig. 8(a)]. A kurtosis value of 5.5 was prescribed for the driving signal on the second iteration. As a result, the response kurtosis which was 3.3 became much closer to the required value. The response PSD on the second iteration [Fig. 8(b)] gained the necessary



(a)



(b)



(c)

FIG. 7. Probability density function (solid curve) of the APWT acoustic signal (kurtosis=3.85, skewness=0.31) obtained by tailoring environmental conditions (dotted curve is the Gaussian law). (a) Central part; (b) Left tail; (c) Right tail.

triangular form, although it was still different from the prescribed shape (thick line). The next two iterations were made with the same kurtosis value (5.5) of the driving signal to overcome fluctuations in the response PSD and to check stability of the response kurtosis, which was 3.15 and 3.25 on the third and fourth iterations, respectively. With these val-

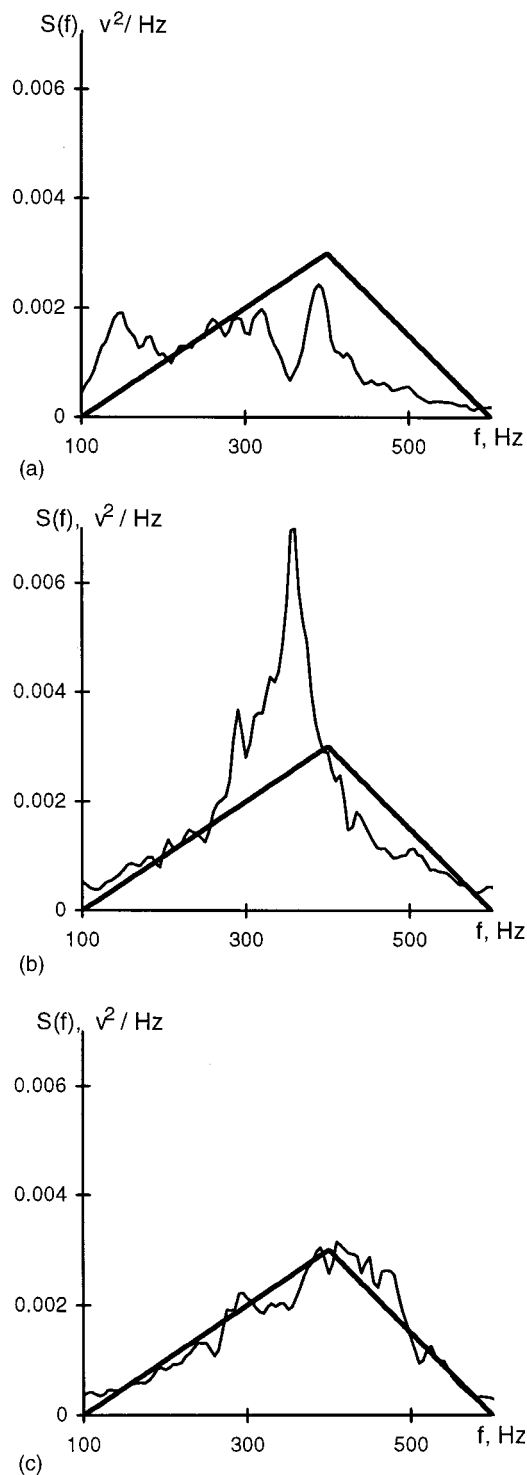


FIG. 8. PSD of acoustic pressure signals in experiments for digital control of APWT to concurrently simulate kurtosis and PSD. (a) First iteration: input kurtosis=6.0, output kurtosis=4.5; (b) Second iteration: input kurtosis=5.5, output kurtosis=3.3; (c) Fifth iteration: input kurtosis=5.4, output kurtosis=3.08.

ues in mind, which slightly exceeded, on average, the prescribed kurtosis of 3.1, the fifth and last iteration was driven by a signal with a kurtosis value of 5.4 and both characteristics of the APWT response, PSD and kurtosis, were fitted [Fig. 8(c)]. Thus, simulation of the non-Gaussian kurtosis parameter was made simultaneously with PSD correction and this did not require additional experimental runs. Plots

with PSDs of driving signals were presented in Ref. 16.

Correction of the APWT acoustic pressure skewness value appeared to be necessary for the third PSD obtained by tailoring flight test measurements. At the end of PSD corrections made without control of non-Gaussian features of the response [see Fig. 5(b) for PSD and Fig. 7 for PDF], the skewness of the acoustic signal generated by the APWT was 0.31. In flight tests, the lower value of 0.2 has been observed. Thus, if a driving signal with zero skewness produced response with a too-positive skewness value, it was necessary to reduce the response skewness by generating a driving signal with some negative skewness. This was done for the next iteration and the skewness value was -0.2 . The result of this action led to a trend in the required direction: the response skewness was reduced, and a value about zero appeared. It meant that the necessary skewness value 0.2 had been overstepped (initial value 0.31 changed to 0). Therefore, the next driving signal with skewness value of -0.11 , lower than -0.2 for the previous iteration, was input to the APWT and, as a result, the response skewness turned back to positive values, although it was smaller (0.07) than required. Thus, negative skewness of the driving signal needed to be further reduced and a new driving signal with -0.07 skewness was generated. This was accepted as the last iteration because the response skewness (0.22) obtained was different from the required value of 0.2 by no more than the scatter of the experiment.

To evaluate performance of the technique developed for control of the APWT-generated acoustic excitation in the amplitude distribution domain, one should compare Figs. 3(a) and 9(a) where the central parts of the PDFs in the flight test and in the APWT simulation are shown. The behavior of distribution tails is presented in Figs. 3(b) and (c) and 9(b) and (c). It is clear from these plots that deviations of the PDF from Gaussian distribution (dotted curve) are similar in both cases (for field data and for acoustic excitation, generated in APWT). Thus, the simulation method presented in Sec. II can provide PDF fitting in addition to conventional PSD modeling.

V. CONCLUSIONS AND RECOMMENDATIONS

A computer-based control system was used for running the acoustic progressive wave tube test rig. The methodology, which is of considerable significance in relation to acoustic fatigue testing of aircraft structures, is based on digital generation of the driving signal sent to the APWT siren input. The acoustic pressure signal measured at the test section of the tube is acquired by the same computer and then, the PSD and PDF characteristics obtained are compared with those prescribed for simulation. The divergence is compensated by immediate modification of the driving signal and this process is repeated until the test specification has been attained with a reasonable precision.

An up-to-date testing technique known as ‘‘tailoring’’ of in-service environment has been achieved in APWT experiments: characteristics of the acoustic excitation to be simulated in the APWT were determined directly from flight test measurements for the particular aircraft. The test specification setup included two features that could not be realized

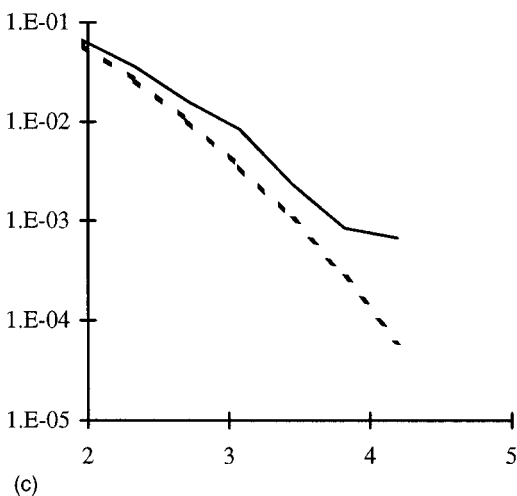
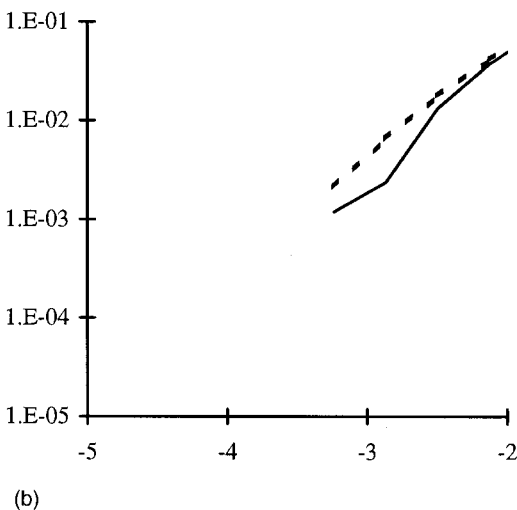
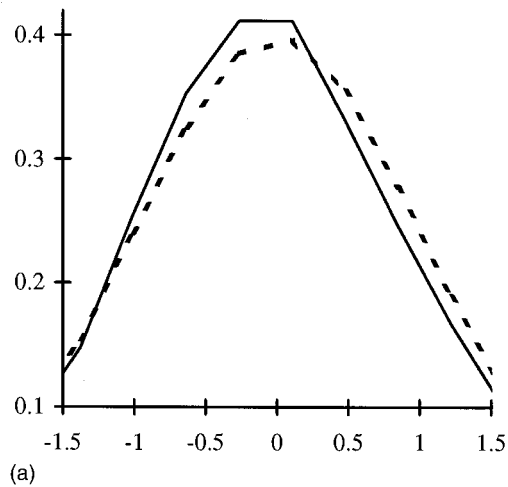


FIG. 9. Probability density function of APWT acoustic excitation (solid curve) obtained by simultaneous control of skewness and PSD (dotted curve is the Gaussian law). (a) Central part; (b) Left tail; (c) Right tail.

with analog driving systems. The first feature is the presence of sharp PSD peaks which are too narrow to be simulated by the analog 1/3-octave filters. Digital simulation in the form of Fourier expansion enabled implementation of any small frequency discretization step and, hence, large gradients in the PSD shape were allowed. Another difficulty which

emerged with the tailoring approach was that the acoustic excitation measured in flight appeared to be a non-Gaussian random process. The APWT system itself also introduces distortions from the Gaussian model because of nonlinear behavior. To reflect the environmental non-Gaussian effects or to compensate for those caused by the APWT, a novel method for adjustment of harmonic phase angles has been developed to make the driving signal non-Gaussian with the prescribed skewness and kurtosis parameters.

A comprehensive experimental program has been carried out and iterative control procedure was used within the bounds of the Gaussian model and for non-Gaussian simulation when kurtosis and skewness parameters were under control together with PSD. In the latter case, the conclusion is that the necessary PDF parameters of acoustic excitation can be achieved in the APWT after a few iterations of driving signal correction and the number of iterations for simultaneous kurtosis or skewness and PSD control has not exceeded the number required for single PSD correction as in the traditional simulation technique.

ACKNOWLEDGMENTS

This study has been carried out with a grant from the Leverhulme Trust. The authors are also grateful to the US Air Force EOARD office for the support of WOS exchange visits, where discussions on the matter of this research took place. Section II of the paper is partially based on the studies of the first author when he had a sponsorship from the A. von Humboldt Foundation.

¹C. Mei and H. F. Wolfe, "On large deflection analysis in acoustic fatigue design," in *Random Vibration—Status and Recent Developments* (Elsevier, Amsterdam, 1986), pp. 279–301.

²B. L. Clarkson, "Acoustic fatigue test facilities," in *Noise and Acoustic Fatigue in Aeronautics*, edited by E. J. Richards and D. J. Mead (Wiley, New York, 1968).

³J. Pearson, "High-temperature acoustic test facilities and methods," in *AGARD Proceedings #549*, Lillehammer, Norway, 1994 (Advisory Group for Aerospace Research and Development under the NATO Military Committee, Paris), pp. 7.1–7.9.

⁴J. Soovere, "Sonic fatigue testing of an advanced composite aileron," *J. Aircr.* **19**, 304–310 (1982).

⁵S. A. Rizzi, and T. L. Turner, "Enhanced capabilities of the NASA Langley Thermal Acoustic Fatigue Apparatus," in *Proceedings of the 6th International Conference on Recent Advances in Structural Dynamics*, Southampton, 1997 (Institute of Sound and Vibration Reserch, University of Southampton, UK), Vol. 2, pp. 919–933.

⁶R. G. White, "Developments in the acoustic fatigue design process for composite aircraft structures," *Compos. Struct.* **16**, 171–192 (1990).

⁷J. M. Hu, "Life prediction and damage acceleration based on the power spectral density of random vibration," *J. Inst. Environ. Sci.* **38**(1), 34–40 (1995).

⁸L. D. Lutes, M. Corazo, S. J. Hu, and J. Zimmerman, "Stochastic fatigue damage accumulation," *ASCE J. Struct. Eng.* **102**(11), 2585–2601 (1984).

⁹A. Steinwolf and R. G. White, "Analysis of non-Gaussian random responses of aircraft CFRP panels under acoustic excitation in a progressive wave tunnel," in *Proceedings of Int. Forum on Aeroelasticity and Structural Dynamics*, Manchester, 1995 (Royal Aeronautical Society, London, UK), pp. 69.1–69.14.

¹⁰MIL-STD-810F. Department of Defense test method standard for environmental engineering considerations and laboratory tests, 1 January 2000.

¹¹J. Leuridan, H. Grzeskowiak, and P. Bouchard, "Eureka Project 420 EN-VIB. Using tailoring for environmental vibration testing," in *Proceedings of the 37th IES Annual Technical Meeting*, San Diego, CA, 1991 (Institute of Environmental Sciences and Technologies, USA), pp. 78–84.

- ¹²M. Shinozuka and C.-M. Jan, "Digital simulation of random processes and its applications," *J. Sound Vib.* **25**, 111–128 (1972).
- ¹³A. Steinwolf, "Approximation and simulation of probability distributions with a variable kurtosis value," *Comput. Stat. Data Anal.* **21**, 163–180 (1996).
- ¹⁴J. S. Bendat and A. G. Piersol, *Random Data. Analysis and Measurement Procedures* (Wiley, New York, 1986).
- ¹⁵A. Steinwolf, "True-random mode simulation of non-Gaussian vibrations with high kurtosis value," in *Proceedings of the 46th IEST Annual Technical Meeting*, Providence, RI, 2000 (Institute of Environmental Sciences and Technology, USA), pp. 148–155.
- ¹⁶A. Steinwolf and R. G. White, *Implementation of Computer Control of a Progressive Wave Tube Facility for Acoustic Testing of Aircraft Panel Components* (Leverhulme Visiting Project Report, Department of Aeronautics and Astronautics, University of Southampton, UK, 1998).

Underwater source detection using a spatial stationarity test

A. Ephraty

Department of Electrical Engineering—Systems, Tel-Aviv University, Tel-Aviv 69978, Israel

J. Tabrikian

Department of Electrical and Computational Engineering, Ben-Gurion University of the Negev, Beer-Sheva 84105, Israel

H. Messer

Department of Electrical Engineering—Systems, Tel-Aviv University, Tel-Aviv 69978, Israel

(Received 21 January 1999; accepted for publication 19 December 2000)

The problem of detecting a source in shallow water is addressed. The complexity of such a propagation channel makes precise modeling practically impossible. This lack of accuracy causes a deterioration in the performance of the optimal detector and motivates the search for suboptimal detectors which are insensitive to uncertainties in the propagation model. A novel, robust detector which measures the degree of spatial stationarity of a received field is presented. It exploits the fact that a signal propagating in a bounded channel induces spatial nonstationarity to a higher degree than mere background noise. The performance of the proposed detector is evaluated using both simulated data and experimental data collected in the Mediterranean Sea. This performance is compared to those of three other detectors, employing different extents of prior information. It is shown that when the propagation channel is not completely known, as is the case of the experimental data, the novel detector outperforms the others in terms of threshold signal-to-noise ratio (SNR). In the presence of environmental mismatch, the threshold SNR of the novel detector for the experimental data appears 2–5 dB lower than the other detectors. That is, this detector couples good performance with robustness to propagation uncertainties. © 2001 Acoustical Society of America. [DOI: 10.1121/1.1349536]

PACS numbers: 43.60.Cg, 43.60.Bf [JCB]

I. INTRODUCTION

Source detection in noise is a classic problem with applications in many fields (e.g., sonar, radar, communication, etc.). The optimal procedure, i.e., the likelihood ratio test, can only be applied when the joint probability density function (pdf) of the received signal and noise are known. This, in turn, requires perfect knowledge of the propagation channel. Shallow water, however, is an example for a channel that is, in practice, too complex to be fully characterized. It is therefore necessary to revert to suboptimal methods relying on lesser degrees of prior knowledge of the propagation channel. In this work, we compare the performance of four detectors that employ different extents of such information. These detectors range from the optimal, maximum-likelihood detector to the simple and robust energy detector. In particular, a novel detector first suggested in Ref. 1 is studied.

This detector is based on a test for spatial stationarity which exploits stationary-specific spectral characteristics. To understand how this test is applied to the detection problem, one must consider the sufficient and necessary conditions for spatial stationarity. For a measured field (generated by uncorrelated sources whose signals are propagating) to be spatially stationary, the following, proven in Appendix A, must hold:

- (1) The sources are located in the far-field zone relative to the site of measurement.
- (2) The measured signals are uncorrelated.

- (3) The sources are temporally stationary.
- (4) The additive noise is spatially stationary.

Thus, if condition 4 is met, but at least one of conditions 1–3 is not met, then measurements of the levels of spatial stationarity can differentiate between noise-only and signal+noise scenarios. When a signal propagates in a bounded channel, such as an underwater one, condition 2 is obviously violated because of the induced echoes (multipath). These echoes are expected to increase the level of nonstationarity of mere underwater background noise. This forms the motivation for using the level of spatial stationarity a measure for the existence of a source in shallow water: even when the background noise is not purely spatially stationary (condition 4), it suffices that the degree of spatial nonstationarity induced by the multipath is greater than that of the noise. Thus, it is apparent that for such a detector, the only prior information assumed is:

- (1) the propagation channel is bounded; and
- (2) the additive noise is of a low degree of spatial nonstationarity.

Most importantly, the exact nature of the propagation channel is of no direct importance.

In order to compare the performance of the stationarity-based detector to that of the other detectors, both simulated data and experimental data are used. The simulations were carried out on one of the benchmarks (“genlmis”) used in

the May 1993 NRL Workshop on Acoustic Models in Signal Processing.² Experimental results were obtained by processing data collected in the Mediterranean Sea by the NATO SACLANT Center.³

We proceed next with a formulation of the detection problem. A digression is then made to discuss in detail the proposed principle for testing for spatial stationarity. The principle behind the test is presented together with various issues related to its implementation. These include effects of finite array aperture, a spectrum estimator, and its statistics. After these preliminaries, the proposed detector is presented, followed by three alternative detectors. Finally, simulation and experimental results are shown, followed by a discussion.

II. PROBLEM FORMULATION AND DEFINITIONS

Consider a stochastic field, $y(t; \mathbf{X})$, where t denotes the time coordinate and \mathbf{X} is a vector representing a point in a spatial coordinate system. Assume this field to be temporally ergodic, temporally stationary, zero-mean, and with a spatial-covariance function defined as

$$\text{Cov}_y(0; \mathbf{X}_1, \mathbf{X}_2) \equiv E\{y(t; \mathbf{X}_1)y^*(t; \mathbf{X}_2)\}, \quad (1)$$

where $E\{\cdot\}$ is the expectation operator. Cov_y is not a function of t due to the temporal stationarity of $y(t; \mathbf{X})$.

The field, existing in a horizontally bounded channel, is sampled in space and time. The spatial samples are obtained using a vertical array of P sensors located at known depths $\{\mathbf{X}_p\}_{p=0}^{P-1}$. Temporal sampling takes place at L time instants, $\{t_l\}_{l=0}^{L-1}$. Assume the temporal samples at different t_l 's are uncorrelated—while this is certainly not a requirement, it certainly simplifies the expressions and analyses presented below. Denote for brevity: $y(l, p) = y(t_l, \mathbf{X}_p)$ and $\mathbf{y}(l) \equiv [y(l, 0), \dots, y(l, P-1)]^T$.

The source detection problem is formulated as a decision problem: given the $L \cdot P$ temporal and spatial samples, accept the null hypothesis H_0 , or reject it in favor of the alternative H_1

$$\begin{aligned} H_0: \mathbf{y}(l) &= \mathbf{n}(l), \\ H_1: \mathbf{y}(l) &= \sigma_s \mathbf{g}(r_s, z_s, \boldsymbol{\theta}) s(l) + \mathbf{n}(l). \end{aligned} \quad (2)$$

The signal, s , and noise, \mathbf{n} , are considered temporally stationary, zero-mean, independent processes.

The spatial transfer function from the source to the array is denoted $\mathbf{g}(\cdot)$, and is normalized so that σ_s^2 is the unknown average signal power for a single sensor in the array (the signal power varies from sensor to sensor, depending on the absolute values of the different elements of $\mathbf{g}(\cdot)$; σ_s^2 is defined such, that $P \cdot \sigma_s^2$ is the total energy received by the array). The transfer function, $\mathbf{g}(\cdot)$, depends on the following parameters: r_s , the distance of the source from the array; z_s , the depth of the source; and $\boldsymbol{\theta}$, other parameters characterizing the propagation channel.

In practice, $\mathbf{g}(\cdot)$, r_s , z_s , and $\boldsymbol{\theta}$ are often completely unknown, partially known (model uncertainties), or incorrectly characterized (mismatches between model and reality). Such incomplete knowledge of the channel limits the perfor-

mance of standard detectors. We propose to circumvent this difficulty by employing a test for spatial stationarity which is described next.

III. TESTING FOR SPATIAL STATIONARITY

Spatial stationarity is defined in an analogous fashion to the well-known temporal stationarity. That is, in a wide sense spatially stationary field the correlation between the data received at two sensors located at any points, \mathbf{X}_{p_1} and \mathbf{X}_{p_2} , is only a function of the distance between them, $\|\mathbf{X}_{p_1} - \mathbf{X}_{p_2}\|$. A test for spatial stationarity is particularly appealing for source detection in shallow water because a signal propagating in a bounded channel induces spatial nonstationarity. Thus, detection is possible without the need for complete knowledge of the propagation channel.

Unfortunately, the literature does not offer an abundance of test procedures for spatial stationarity. A noteworthy exception is Ref. 4, whose authors check for spatial stationarity using a covariance structure. This test is sensitive to the property of centrosymmetry which is exhibited by the sample covariance matrix of a spatially stationary field sampled by a uniform, linear array. We propose another test which relies on spectral structure (rather than covariance structure), and is applicable to an arbitrary geometry of sensors. The principle and implementation of this test are now described.

A. Principle

The proposed test, first suggested in Ref. 1, exploits a relationship between the second-order spatial cumulant spectrum and the second-order spatial spectrum of a spatially stationary field. Differentiating between the cumulant spectrum and the spectrum, the terminology given in Ref. 5 is used. Note that the literature is not consistent in definitions. Compare, for example, Refs. 5 and 6.

The spatial cumulant spectrum (we refer throughout to second-order spectra) is defined as a two-dimensional Fourier transform

$$\begin{aligned} \text{SCS}_y(\boldsymbol{\kappa}_1, \boldsymbol{\kappa}_2) &\equiv \int_{\mathbf{X}_1} \int_{\mathbf{X}_2} \text{Cov}_y(0; \mathbf{X}_1, \mathbf{X}_2) \\ &\times e^{-j(\boldsymbol{\kappa}_1^T \mathbf{X}_1 + \boldsymbol{\kappa}_2^T \mathbf{X}_2)} d\mathbf{X}_1 d\mathbf{X}_2. \end{aligned} \quad (3)$$

Cov_y is defined in (1), and $\boldsymbol{\kappa}$ is the angular spatial frequency vector (of the same dimension as the vector \mathbf{X}) containing the directional wave numbers.

The spatial cumulant spectrum is well defined for any field. However, for a (spatially) stationary field, $\text{Cov}_y(0; \mathbf{X}_1, \mathbf{X}_2)$ is constant for all $\|\mathbf{X}_1 - \mathbf{X}_2\| = \mathbf{X}$, and is denoted $\text{Cov}_y(0; \mathbf{X})$. In this case the spatial-poly-spectrum (or simply spatial spectrum), can be defined as a one-dimensional Fourier transform

$$\text{SS}_y(\boldsymbol{\kappa}) \equiv \int_{\mathbf{X}} \text{Cov}_y(0; \mathbf{X}) e^{-j\boldsymbol{\kappa}^T \mathbf{X}} d\mathbf{X}. \quad (4)$$

Furthermore, under spatial stationarity⁵

$$SCS_y(\boldsymbol{\kappa}_1, \boldsymbol{\kappa}_2) = SS_y(\boldsymbol{\kappa}_1) \delta(\boldsymbol{\kappa}_1 + \boldsymbol{\kappa}_2), \quad (5)$$

where $\delta(\cdot)$ is Dirac's delta function. That is, $SCS_y(\boldsymbol{\kappa}_1, \boldsymbol{\kappa}_2)$ vanishes identically outside the plane defined by $\boldsymbol{\kappa}_1 + \boldsymbol{\kappa}_2 = 0$. It is this property upon which the test for spatial stationarity is based.

B. Implementation

In order to implement the test for spatial stationarity [Eq. (5)], an estimate of the spatial cumulant spectrum, based on the available temporal-spatial samples of the field, is required. Spectrum estimation has been thoroughly studied and a variety of estimators exists in the literature. In this context, we want to highlight a few points of spectral estimation which are relevant to the application at hand. To simplify the presentation, we assume from this point on that the available samples are collected from a linear array whose sensors are equally spaced (LES array). For nonuniform spatial sampling (array of arbitrary geometry), appropriate spectrum estimation algorithms can be found in the literature.^{7,8} In particular, an indirect spatial cumulant-spectrum estimator and its statistics are described below. First, however, we comment on the effects of a finite array length on the identity (5).

1. Effects of finite array aperture

Given P spatial samples, obtained from a uniform, linear array of sensors, define the $P \times P$ spatial-covariance matrix as

$$[\mathbf{C}_y]_{p_1, p_2} = C_y(p_1, p_2) = \text{Cov}_y(0; p_1, p_2) \quad (6)$$

$$p_1, p_2 = 0, \dots, P-1,$$

where p_1 and p_2 now represent one-dimensional coordinates of the arrays. Thus, the covariance matrix can be viewed as a grid sample of the covariance function defined in (1).

The two-dimensional discrete Fourier transform of this matrix yields the spatial cumulant-spectrum matrix

$$[\mathbf{S}_y]_{k_1, k_2} = S_y(k_1, k_2) \quad (7)$$

$$= \sum_{p_1=0}^{P-1} \sum_{p_2=0}^{P-1} C_y(p_1, p_2) e^{-j(2\pi/P)(p_1 k_1 + p_2 k_2)},$$

where k_1, k_2 are discrete spatial frequency indices.

One might expect (5) to hold for the finite-aperture spatial cumulant-spectrum matrix (7) so that its "off-diagonal" ($k_1 + k_2 = 0 \pmod{P}$) elements should be zero under stationarity. However, the finite number of sensors, manifested in the finite summation of (7), create a "spatial-windowing" effect. Hence, \mathbf{S}_y is not, in general, a grid sample of the spatial cumulant spectrum, $SCS_y(\boldsymbol{\kappa}_1, \boldsymbol{\kappa}_2)$. Therefore, Eq. (5) does not precisely hold for the matrix \mathbf{S}_y , even under stationarity. In fact, the off-diagonal elements ($k_1 + k_2 \neq 0 \pmod{P}$) are related to the actual spatial spectrum as

$$S_y(k_1, k_2) = \frac{2j \text{Im}\{S_y(k_1) - S_y(P - k_2)\}}{1 - e^{-j(2\pi/P)(k_1 + k_2)}}, \quad (8)$$

where $S_y(k)$, $k = 1, \dots, P$ is the discrete spatial spectrum defined in the stationary case

$$S_y(k) = \sum_{p=0}^{P-1} \text{Cov}_y(0; p) e^{-j(2\pi/p)kp}. \quad (9)$$

For proof, see Appendix B. It is evident that in general [unless $S_y(k)$ is constant or real] (8) is not zero. This leakage from the diagonal to the off-diagonal elements should be taken into account in devising the test for spatial stationarity based on (5).

2. Spectrum estimation

We turn now to estimate the spatial cumulant-spectrum matrix according to the indirect method. The first step is to estimate the spatial-covariance matrix, (6). Exploiting the temporal ergodicity of the measured field, the expectation operator in (1) is approximated by temporal averaging

$$\widehat{\mathbf{C}}_y = \frac{1}{L} \sum_{l=0}^{L-1} \mathbf{y}(l) \mathbf{y}^H(l). \quad (10)$$

It is well known that this is a consistent estimator of \mathbf{C}_y . Moreover, for a Gaussian field, it is also the maximum-likelihood estimator. Next, the finite aperture spatial cumulant-spectrum matrix, \mathbf{S}_y of (7), is estimated as

$$[\widehat{\mathbf{S}}_y]_{k_1, k_2} = \widehat{S}_y(k_1, k_2) \quad (11)$$

$$= \sum_{p_1=0}^{P-1} \sum_{p_2=0}^{P-1} \widehat{\mathbf{C}}_y(p_1, p_2) e^{-j(2\pi/P)(p_1 k_1 + p_2 k_2)}.$$

An interesting fact about (11) is that it is a consistent estimator of (7). In particular, in Ref. 9 it is shown that asymptotically, under general conditions

$$\text{Var}\{\widehat{S}_y(k_1, k_2)\} \propto \frac{1}{L}. \quad (12)$$

In practice, if there are no stringent limitations on the number of temporal snapshots, L , the variance of (11) can be arbitrarily reduced. Note, however, that although (11) is unbiased with respect to (7), it is biased with respect to (3) due to the spectral leakage. As discussed in the previous subsection, this bias is a result of the finite number of sensors, and is reduced when the array aperture is increased.

3. Statistics of the spectrum estimator

The asymptotic statistics of the spatial cumulant-spectrum matrix estimator, (11), is now derived for the special case where the field has a complex Gaussian distribution. Assume $\mathbf{y}(l) \sim N^C(\mathbf{0}, \mathbf{C}_y)$, and the $\mathbf{y}(l)$'s are uncorrelated as assumed in Sec. II. Then, (10) has the complex Wishart distribution,⁶ with the following mean and covariance:

$$E\{\widehat{\mathbf{C}}_y(p_1, p_2)\} = C_y(p_1, p_2), \quad (13)$$

$$\text{Cov}\{\widehat{\mathbf{C}}_y(p_1, p_2), \widehat{\mathbf{C}}_y(p_3, p_4)\} = \frac{1}{L} C_y(p_1, p_3) C_y^*(p_2, p_4). \quad (14)$$

Asymptotically, applying the multivariate central limit theorem,¹⁰ the elements of $\widehat{\mathbf{C}}_y$ are jointly Gaussian. The elements of $\widehat{\mathbf{S}}_y$ are each a linear transformation, and are therefore also asymptotically jointly complex Gaussian. Their mean and covariance can be computed directly

$$E\{\widehat{S}_y(k_1, k_2)\} = S_y(k_1, k_2), \quad (15)$$

$$\begin{aligned} \text{Cov}\{\widehat{S}_y(k_1, k_2), \widehat{S}_y(k_3, k_4)\} \\ = \frac{1}{L} S_y(k_1, -k_3 \bmod P) S_y^*(k_2, -k_4 \bmod P). \end{aligned} \quad (16)$$

It is convenient, for future reference, to arrange the elements of the covariance and spectrum matrices in vectors. Let $\widehat{\mathbf{c}}_1$ contain the P diagonal elements of $\widehat{\mathbf{C}}_y$, and $\widehat{\mathbf{c}}_2$ the $P(P-1)/2$ elements of the upper (or lower) triangle. Similarly, arrange the P diagonal elements $\widehat{S}_y(k, -k \bmod P)$ into the P -length vector $\widehat{\mathbf{s}}_1$, and the $P(P-1)/2$ elements of the upper (or lower) triangle into $\widehat{\mathbf{s}}_2$. We can now write:

$$\widehat{\mathbf{c}} = \begin{bmatrix} \widehat{\mathbf{c}}_1 \\ \widehat{\mathbf{c}}_2 \end{bmatrix} \stackrel{L \rightarrow \infty}{\sim} N^C \left(\widehat{\boldsymbol{\mu}}^c = \begin{bmatrix} \widehat{\boldsymbol{\mu}}_1^c \\ \widehat{\boldsymbol{\mu}}_2^c \end{bmatrix}, \widehat{\boldsymbol{\Lambda}}^c = \begin{bmatrix} \widehat{\boldsymbol{\Lambda}}_{11}^c & \widehat{\boldsymbol{\Lambda}}_{12}^c \\ \widehat{\boldsymbol{\Lambda}}_{21}^c & \widehat{\boldsymbol{\Lambda}}_{22}^c \end{bmatrix} \right) \quad (17)$$

$$\widehat{\mathbf{s}} = \begin{bmatrix} \widehat{\mathbf{s}}_1 \\ \widehat{\mathbf{s}}_2 \end{bmatrix} \stackrel{L \rightarrow \infty}{\sim} N^C \left(\widehat{\boldsymbol{\mu}}^s = \begin{bmatrix} \widehat{\boldsymbol{\mu}}_1^s \\ \widehat{\boldsymbol{\mu}}_2^s \end{bmatrix}, \widehat{\boldsymbol{\Lambda}}^s = \begin{bmatrix} \widehat{\boldsymbol{\Lambda}}_{11}^s & \widehat{\boldsymbol{\Lambda}}_{12}^s \\ \widehat{\boldsymbol{\Lambda}}_{21}^s & \widehat{\boldsymbol{\Lambda}}_{22}^s \end{bmatrix} \right), \quad (18)$$

where the elements of the mean subvectors, $\boldsymbol{\mu}$, and covariance submatrices, $\boldsymbol{\Lambda}$, are given by (13)–(16).

IV. THE PROPOSED DETECTOR

We now apply the test for spatial stationarity, as described in the previous section, to the detection problem. To do so, the decision problem (2) is rephrased in a much more general form:

H_0 : The field is spatially stationary to a low (or, to a known arbitrary) degree.

H_1 : The field is spatially nonstationary to a high degree.

According to (5), under H_0 , the off-diagonal elements of the spatial cumulant-spectrum matrix are expected to be close to zero. However, (8) predicts a leakage to the off-diagonal elements. Furthermore, this leakage is a function of the actual spatial spectrum of the received field. In devising a robust detector for a highly unknown channel, such as shallow water, we have the following objectives in mind. First, the dependence of the detector on the actual spectrum should be diminished. Second, the detector should work well even if the field, under H_0 , is not completely spatially stationary. Rather, it is required to detect a difference in the degree of spatial stationarity when there is only noise and when there is a source. Last, low computational complexity is preferred.

To meet these objectives, the nonstationary energy is found to be a good criterion. That is, we propose to sum the magnitude square of all the off-diagonal elements in the spatial cumulant-spectrum matrix. The following portrays the algorithm for this detector:

- (1) Estimate the second-order spatial-cumulant-spectrum matrix, $\widehat{\mathbf{S}}$, according to (11) and (10), (alternatively, use any suitable estimator).
- (2) Form the test statistic as the sum of the magnitude square of the off-diagonal elements of (11), and perform the test

$$\zeta = \widehat{\mathbf{s}}_2^H \widehat{\mathbf{s}}_2 = \frac{1}{2} \sum_{\substack{k_1=0 \\ k_1+k_2 \neq 0 \bmod P}}^{P-1} \sum_{k_2=0}^{P-1} |\widehat{S}_y(k_1, k_2)|^2 \underset{H_0}{\overset{H_1}{>}} \gamma, \quad (19)$$

where the threshold γ determines the probability of ‘‘false alarm,’’ P_{fa} .

As stated, the test procedure does not require any information in addition to that which is described in Sec. II. Thus, it is not necessary to know the channel characteristics (apart from it being bounded), nor the distribution of signal and noise. However, to fix γ , the distribution of the field under H_0 is required. Below is an example derivation of the statistics of ζ under additional assumptions.

Assume that $H_0: \mathbf{y}(l) = \mathbf{n}(l)$, where the noise, $\mathbf{n}(l)$, is Gaussian, and spatially white. That is, $\mathbf{n}(l) \sim N^C(\mathbf{0}, \mathbf{C}_n)$, where $\mathbf{C}_n = \sigma_n^2 \mathbf{I}$. Using (7) one obtains

$$S_y(k_1, k_2) = \begin{cases} P \sigma_n^2, & k_1 + k_2 = 0 \bmod P, \\ 0, & \text{otherwise,} \end{cases} \quad (20)$$

and using (15)–(16), and the vector notation in (18),

$$\widehat{\mathbf{s}}_2 \stackrel{L \rightarrow \infty}{\sim} N^C \left(\mathbf{0}, \frac{P^2}{L} \sigma_n^4 \mathbf{I} \right). \quad (21)$$

Hence, $\zeta \equiv \widehat{\mathbf{s}}_2^H \widehat{\mathbf{s}}_2$ is asymptotically distributed (e.g., Ref. 6)

$$\zeta \stackrel{L \rightarrow \infty}{\sim} \frac{P^2 \sigma_n^4}{2L} \chi_{(P^2-P)}^2, \quad (22)$$

where $\chi_{(n)}^2$ is the standard chi-square distribution with n degrees of freedom. Thus, for any given false alarm, $P_{fa} = \text{Pr}\{\zeta | H_0 > \gamma\}$, the threshold γ can be set.

V. ALTERNATIVE DETECTORS

It is instructive to compare the proposed novel detector to others that combine different degrees of computational complexity, *a priori* assumptions, and performance. In particular, an energy detector (ED), a variation on the stationarity test (LRT1), and a generalized likelihood ratio test (GLRT2) are selected.

A. Energy detector

The energy detector (ED) uses a simple comparison of the measured energy of the received signal to a threshold

$$\zeta_0 \equiv \mathbf{1}^T \widehat{\mathbf{c}}_1 = \text{trace} \widehat{\mathbf{C}}_y \underset{H_0}{\overset{H_1}{>}} \gamma_0, \quad (23)$$

where $\mathbf{1}$ is an all-ones vector, $\widehat{\mathbf{C}}_y$ is defined in (10), and $\widehat{\mathbf{c}}_1$ follows the notation (17). The test statistic is thus ignorant of

any prior information. However, as in the case of the novel detector, setting the threshold, γ_0 , requires knowledge of the distribution of the noise (H_0).

For the special case discussed in the preceding section, i.e., $\mathbf{n}(l) \sim N^C(\mathbf{0}, \sigma_n^2 \mathbf{I})$, each element of $\hat{\mathbf{c}}_1$ is distributed as $(\sigma_n^2/2L)\chi_{(2L)}^2$.⁶ As defined, ζ_0 is a P sum of such variates; therefore

$$\zeta_0 \sim \frac{\sigma_n^2}{2L} \chi_{(2LP)}^2. \quad (24)$$

B. Likelihood ratio stationarity test

Both the proposed stationarity test and the ED assume no prior knowledge on the distribution of the field. The following test, LRT1, is carried out with a known distribution of the noise. That is, H_0 is fully characterized. In this case, a more powerful variation to the stationarity test can be posed. Instead of using the ‘‘energy’’ criterion (19), we can set up a likelihood ratio test.

Assuming that under H_0 the additive noise is Gaussian with a known mean, $\boldsymbol{\mu}^s$, and covariance, $\boldsymbol{\Lambda}^s$, whereas under H_1 the distribution is also Gaussian but with unknown parameters, the generalized likelihood ratio test is

$$\frac{\max_{\boldsymbol{\mu}, \boldsymbol{\Lambda}} f(\hat{\mathbf{s}}|H_1; \boldsymbol{\mu}, \boldsymbol{\Lambda})}{f(\hat{\mathbf{s}}|H_0; \boldsymbol{\mu}^s, \boldsymbol{\Lambda}^s)} \propto \zeta_1 = \frac{H_1}{H_0} [\hat{\mathbf{s}} - \boldsymbol{\mu}^s]^H [\boldsymbol{\Lambda}^s]^{-1} [\hat{\mathbf{s}} - \boldsymbol{\mu}^s] > \gamma_1, \quad (25)$$

where the vector notation is defined in (18). If, for example, the covariance matrix of the noise is given as $\mathbf{C}_n = \sigma_n^2 \mathbf{I}$, and its mean is zero, ζ_1 can further be simplified using (20), (15), and (16)

$$\zeta_1 = \frac{L}{P^2 \sigma_n^4} (\hat{\mathbf{s}}_2^H \hat{\mathbf{s}}_2 + [\hat{\mathbf{s}}_1 - 1P\sigma_n^2]^H [\hat{\mathbf{s}}_1 - 1P\sigma_n^2]). \quad (26)$$

In a manner similar to that of (22), the distribution of ζ_1 is

$$\zeta_1 \underset{L \rightarrow \infty}{\sim} \frac{P^2 \sigma_n^4}{2L} \chi_{(P^2+P)}^2, \quad (27)$$

and γ_1 can be set.

C. Generalized likelihood test

The last test considered, GLRT2, is a two-sided generalized likelihood ratio test for the original hypotheses problem (2). It exploits even more prior information than do the other tests presented above. Specifically, this test is formulated in the matched-field processing (MFP) framework. In MFP one tries to incorporate *a priori* knowledge of the propagation channel into estimators and detectors. It has been shown that MFP indeed exhibits a considerable improvement over other schemes.¹¹ Moreover, techniques based on MFP usually do more than just detection: they provide estimates of the source location, as well as model parameters. However, such techniques are not always applicable. First, the propagation channel may be too complex to model correctly. Then, even when acceptable models do ex-

ist, these methods are very sensitive to parameter mismatches in the propagation channel. Last, dealing with model uncertainties usually involves an intense computational complexity. As shown below, a MFP procedure attempting to detect just one source involves a multidimensional extremum problem. In this manuscript we are concerned with robust detectors, i.e., detectors that perform well despite the fact that they are applied in the presence of model mismatches. We include this likelihood-ratio test to get an idea of what might be accomplished (i.e., some kind of a performance bound), rather than as a practical, robust, detector alternative.

Assume as known the distribution of the field under H_0 . Under H_1 , assume knowledge of the channel transfer function, $\mathbf{g}(\cdot)$, but not of its parameters, r_s , z_s , and $\boldsymbol{\theta}$. For a complex Gaussian noise and signal, the likelihood ratio is

$$\frac{\max_{r_s, z_s, \boldsymbol{\theta}} \prod_{l=0}^{L-1} f(\mathbf{y}(l)|H_1; r_s, z_s, \boldsymbol{\theta}, \sigma_s)}{\prod_{l=0}^{L-1} f(\mathbf{y}(l)|H_0)}. \quad (28)$$

When $\mathbf{C}_n = \sigma_n^2 \mathbf{I}$, the test statistics may be simplified as (see Appendix C)

$$\zeta_2 \equiv \begin{cases} \min_{r_s, z_s, \boldsymbol{\theta}} [\ln \phi(\mathbf{y}, r_s, z_s, \boldsymbol{\theta}) - \phi(\mathbf{y}, r_s, z_s, \boldsymbol{\theta})] & \text{when } \widehat{snr}_{ML} > 0, \\ -1 & \text{when } \widehat{snr}_{ML} \leq 0, \end{cases} \quad (29)$$

where $\phi(\mathbf{y}, r_s, z_s, \boldsymbol{\theta}) \equiv (\mathbf{g}^H \widehat{\mathbf{C}}_y \mathbf{g} / \sigma_n^2 \mathbf{g}^H \mathbf{g})$, $\widehat{snr}_{ML} \equiv [\phi(\mathbf{y}, r_s, z_s, \boldsymbol{\theta}) - 1] / \mathbf{g}^H \mathbf{g}$, and $\widehat{\mathbf{C}}_y$ is defined in (10). The test procedure then becomes

$$\zeta_2 \underset{H_0}{>} \underset{H_1}{\gamma_2}. \quad (30)$$

For a given P_{fa} , the threshold for this detector, γ_2 , is analytically difficult to obtain even for this simple case.

VI. SIMULATION RESULTS

The four detectors were tested using simulated data. The propagation model used for the underwater channel is one of the benchmarks (‘‘genlmis’’) defined in the May 1993 NRL Workshop on Acoustic Models in Signal Processing.² This model is presented in Fig. 1. It consists of a single source which is located at a depth z_s , and at a distance r_s from a vertical array of sensors. The propagation channel has two layers and is characterized by seven parameters. First, the water layer, has a depth of D . The sound-speed profile is linear, beginning with C_0 at sea level and ending with C_D^- at depth D . Next is the sediment layer with a density ρ and attenuation α . The sound-speed profile in the sediment layer starts at C_D^+ at depth D , is linear till a depth of 200 m where it is C_{bot} , and remains constant at lower depths. The benchmark also specifies nominal values for these seven channel parameters together with allowed uncertainties. These are presented in Table I.

The field in this channel was simulated, using a normal mode propagation program, KRAKEN,¹² for a narrow-band

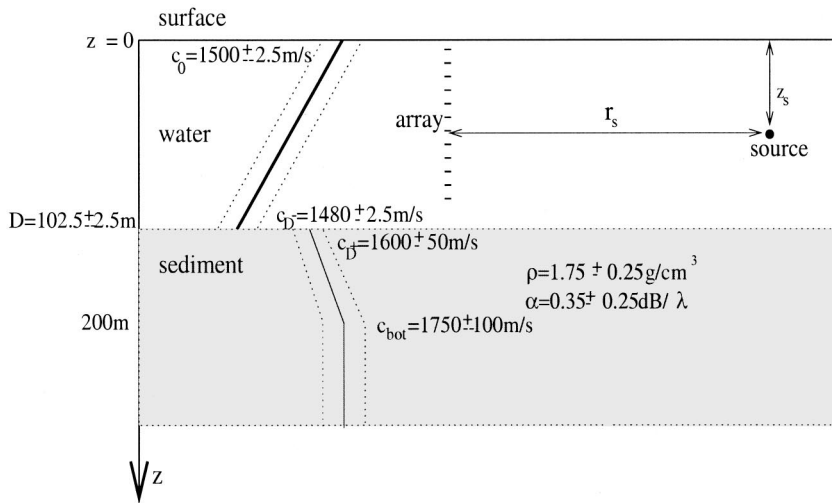


FIG. 1. The “genlmis” benchmark propagation model.

point source located at $r_s=7000$ m, $z_s=50$ m and centered around 100 Hz. Temporally and spatially white Gaussian noise was added to the signal. As for the channel parameters, two simulations were performed. In the first, the nominal values were used (Table I), whereas in the second, mismatches (within the allowed tolerances of the benchmark) were introduced (see below). The simulated field was sampled in space using a uniform, vertical array of 13 sensors whose aperture is the depth of the water layer.

In each simulation (with and without parameter mismatches), each detector processed 1000 time “frames,” (each composed of 100 temporal snapshots). The detectors were implemented as described in (19), (23), (26), and (29). In applying GLRT2, (29), the minimization over all nine parameters ($r_s, z_s, \theta = [D, C_0, C_D^-, C_D^+, C_{\text{bot}}, \rho, \alpha]$) were not carried out. Rather, θ was assumed to equal the nominal parameters as shown in Table I, and the minimization was done over r_s, z_s only. That is, in the simulation with no mismatches, the same nominal parameters were used for creating both the field and for GLRT2. However, in the simulation involving mismatches, a different set of channel parameters, θ , was used for creating the field (see Table I), but the nominal values were still used by the test. This deliberate, erroneous choice of parameters served our intention of testing GLRT2 under model mismatches, as discussed in Sec. V C. Figures 2 and 3 (corresponding to the no-mismatch and the mismatch simulations, respectively) depict the prob-

ability of detection (P_D) for each detector for different signal-to-noise ratios. The indicated SNRs are per snapshot per sensor. For each detector the threshold was fixed to correspond to $P_{fa} = 10^{-3}$.

VII. EXPERIMENTAL RESULTS

In addition to the simulations, we applied experimental data to the four detectors. The data were collected by the SACLANT Center in a shallow-water area off the Italian coast in October 1993. A detailed description of the experimental setup and data may be found in Ref. 3. We were particularly interested in the data collected on 27 October, where a support ship towed a source away from an array of 48 hydrophones (with hydrophone interspacing of approximately 2 m), located in a shallow-water environment with a depth of 200 m. The source transmitted in the 160–180-Hz frequency band only 30 s out of every 60 s. These data were filtered and decimated to extract the 160–180-Hz band, and then grouped into frames; each frame was composed of 100 complex snapshots (the length of each frame corresponding to 6 s approximately, i.e., the source location was almost constant during each frame/trial). To give an idea of the effect of motion on the experiment, we note from Ref. 3 that the tow ship was cruising at 3.5 kn, so the source progressed

TABLE I. Values for parameters of “genlmis” benchmark propagation model.

Channel parameter	Nominal value & uncertainty	Simulation values	
		No-mismatch	Mismatch
D —depth of water layer [m]	102.5 ± 2.5	102.5	100.0
C_0 —sound speed at surface [m/s]	1500.0 ± 2.5	1500.0	1502.5
C_D^- —sound speed at bottom of water layer [m/s]	1480.0 ± 2.5	1480.0	1477.5
C_D^+ —sound speed at top of sediment layer [m/s]	1600 ± 50	1600	1550
C_{bot} —sound speed at lower half of sediment layer [m/s]	1750 ± 100	1750	1850
α —sediment attenuation [dB/ λ]	0.35 ± 0.25	0.35	0.60
ρ —sediment density [g/cm ³]	1.75 ± 0.25	1.75	2.00

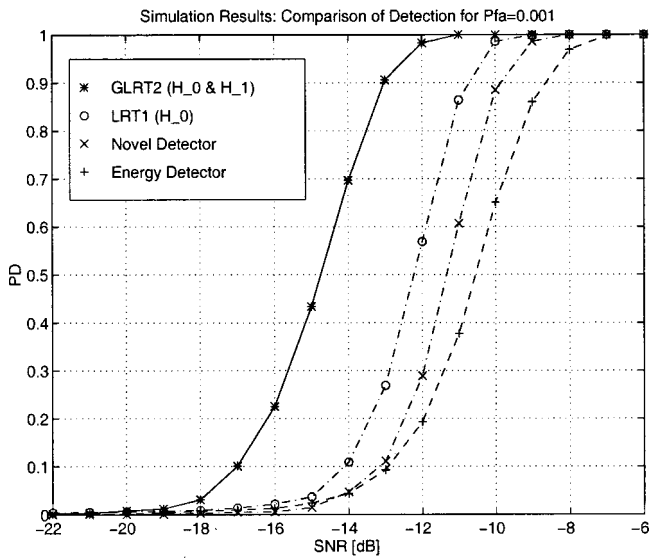


FIG. 2. Simulation results (no mismatch): Probability of detection as a function of SNR.

approximately 10 m in 6 s. Furthermore, Fig. 1 in Ref. 3 implies that during the experiment, the source was in the 5–15-km range from the array.

From the available data we were able to obtain only 50 frames of noise only (n_k), and 50 frames of signal+noise(s_k). The limited amount of data introduced some difficulties which we discuss below:

- (1) The limited number of test frames cannot constitute a proper performance analysis. However, we trust that it suffices to demonstrate what can be achieved in a practical situation, where one knows little about the received signal and noise, and even less about the channel.
- (2) The LRT1 and GLRT2 detectors assume that C_n is known. It was therefore necessary to estimate the noise covariance matrix so that the data could be prewhitened for these two detectors. This was done using five of the noise-only frames. Note that both the energy detector

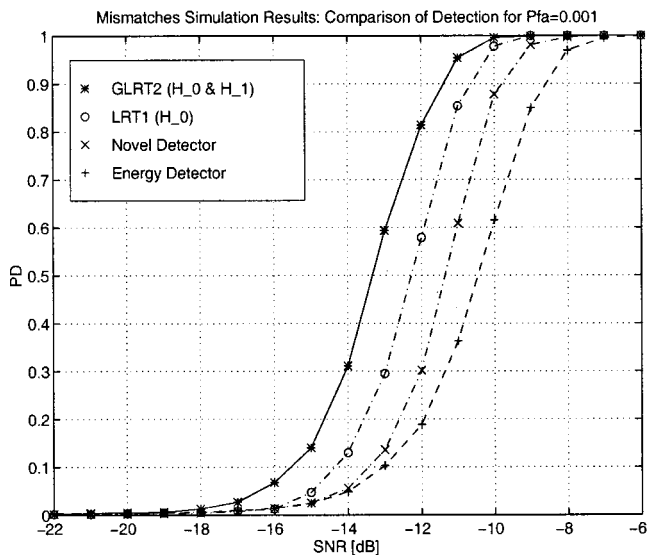


FIG. 3. Simulation results with mismatches: Probability of detection as a function of SNR.

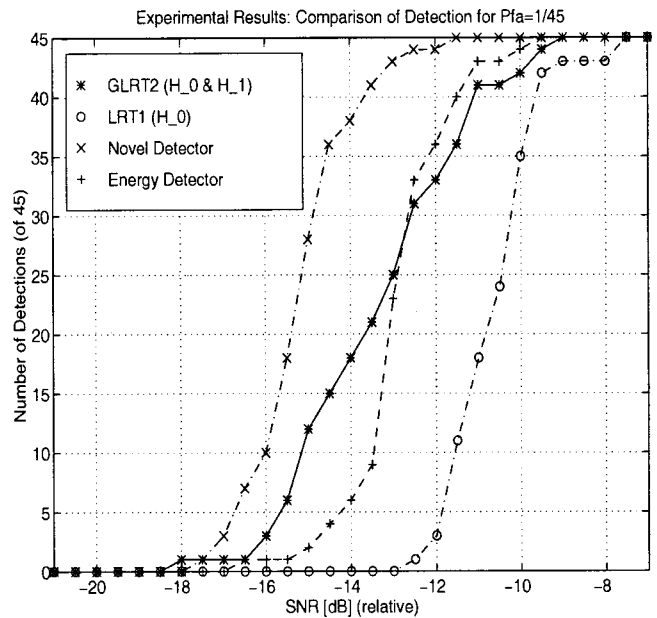


FIG. 4. Experimental results: Probability of detection as a function of relative SNR.

and the proposed one do not require the noise to be white, and indeed processed the original, unwhitened data.

- (3) Comparing the performances of the detectors at varying signal-to-noise ratios (SNR) was not directly possible because the s_k frames are of a fixed and unknown SNR (denote this SNR as β). We therefore constructed compound frames, y_k , of varying relative SNRs (relative to β) by adding together the remaining 45 signal+noise and noise-only frames $y_k = s_k + (\alpha - 1)n_k$, $k = 1, \dots, 45$. That is, α controls the SNR (relative to β) of the compound frames y_k . In other words, the true SNR of y_k constructed with a given α is approximately β/α^2 . Thus, for large values of α , as α is increased, the SNR of y_k is decreased by approximately $20 \log(\alpha)$ in dB.
- (4) As the distribution of the ocean noise could not be properly estimated for lack of data, the detectors' thresholds were empirically obtained by processing the noise-only frames, $\{n_k\}_{k=1}^{45}$ and selecting values matching a false-alarm probability of 1/45.

The 45 compound frames were processed using the four described detectors. As with the simulated data, we did not attempt to perform the multidimensional minimization in (29). As discussed, we are interested in evaluating the performance of GLRT2 in the presence of mismatches. Thus, instead of searching over all unknown parameters, we searched only over the source's depth and range, confining the search to the approximate locations given in Ref. 3. The rest of the parameters, however, were taken from Ref. 3: some (depth, sound-speed profile) were measured on the day of the experiment; others were taken from measurements done on previous occasions in the nearby area. Figure 4 shows the total number of detections (of 45 frames) for different relative signal-to-noise ratios.

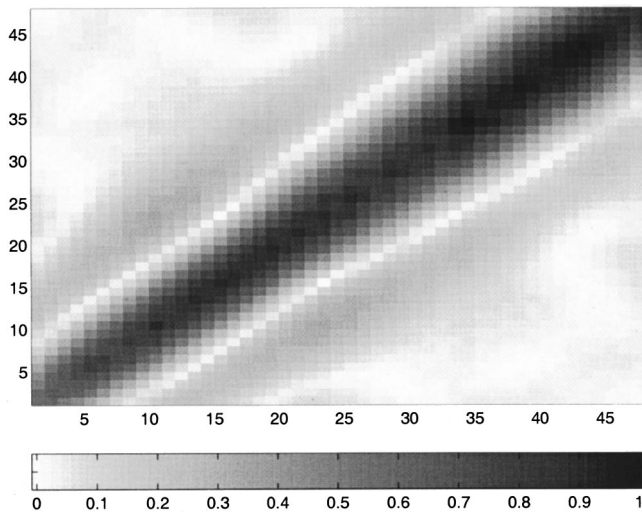


FIG. 5. Experimental results: Normalized estimated noise-only spatial-covariance matrix (absolute values).

As mentioned above, accurate estimation of the distribution of the received signal and noise was not possible. Nevertheless, it is interesting to observe, at least qualitatively, the spatial nature of the experimental measurements. To this end, five noise-only and five signal+noise data frames were used to respectively estimate their spatial covariance matrices. To highlight the differences, both matrices were normalized so that the maximum of the absolute value of the elements of each matrix is unity. The absolute values of these matrices are shown in Figs. 5 and 6. Next, the respective spatial cumulant-spectrum matrices based on the normalized covariance matrices were computed. The absolute values of these are shown (in a logarithmic scale) in Figs. 7 and 8.

VIII. DISCUSSION

It is instructive to study the simulation results together with the experimental results. As statistically valid conclusions cannot be drawn from the experimental results (only 45

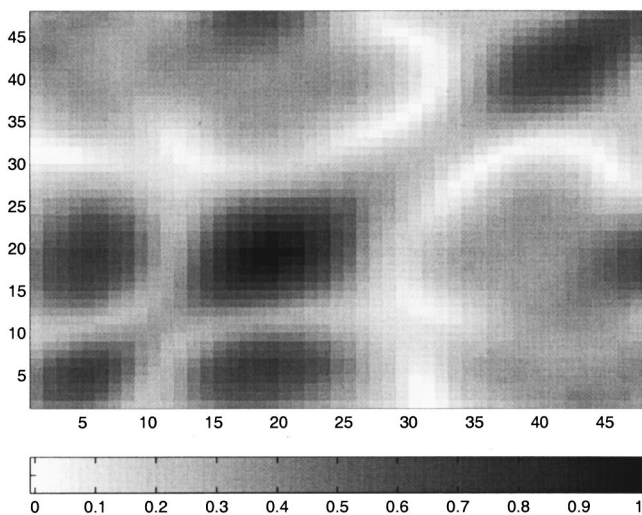


FIG. 6. Experimental results: Normalized estimated signal+noise spatial-covariance matrix (absolute values).

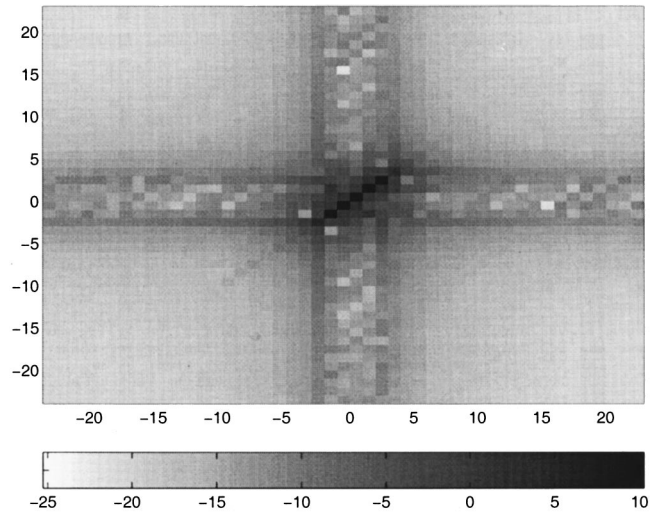


FIG. 7. Experimental results: Normalized estimated noise-only spatial-cumulant-spectrum matrix (absolute values in dB).

test frames were used), these results serve only to demonstrate what happens in the practical case, as well as to support the simulation results.

GLRT2, employing information on both H_0 and H_1 , is clearly the best detector in the simulations in which the channel closely resembles its model. The sensitivity of this detector to channel mismatches is demonstrated in Figs. 2 and 3: the performance dropped by ~ 2 dB when small mismatches were introduced into the model. This effect is greatly amplified in practice, where the propagation model is only a gross approximation (based on measurements and historic data) of the real channel. Indeed, in the experimental results (where considerable mismatches are very likely) GLRT2 is seen in Fig. 4 to have an erratic behavior and its performance is drastically degraded. In fact, the simple energy detector is comparable in performance. It is important to clarify that GLRT2 was tested in the presence of mismatches. One may justifiably argue that if we had employed means of reducing model uncertainties [such as carrying out the multidimensional search, referred to in (29), or some other clever opti-

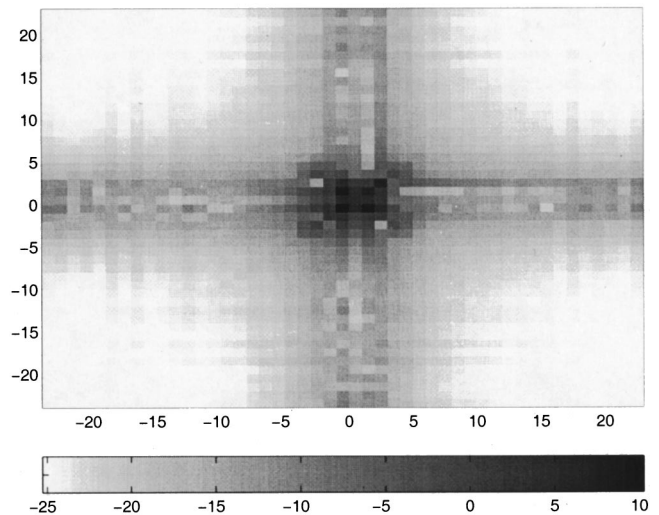


FIG. 8. Experimental results: Normalized estimated signal+noise spatial-cumulant-spectrum (absolute values in dB).

mization algorithm, e.g., simulated annealing, genetic algorithm, etc.], the performance of GLRT2 would have probably improved. While this may be so, the objective is to demonstrate the performance of a robust, simple detector that is not burdened by the limitations of GLRT2 (such as channel modeling, parametrization, and computational complexity).

Ranking next in performance in the simulations results in LRT1. This detector assumes knowledge of the noise spatial covariance matrix under H_0 . In the simulations, this information is indeed accurate. Note in Figs. 2 and 3 that the detector is not sensitive to channel mismatches as this information is not used. On the other hand, the performance does depend on accurate statistical modeling of the noise: In the experimental data, the noise spatial-covariance matrix was not known and was only inaccurately estimated in order to prewhiten the data before applying LRT1. However, this procedure is shown in Fig. 4 to be inefficient. Indeed, LRT1 performs the worst.

On the other hand, the energy detector that performed the worst in the simulations (Figs. 2 and 3) is not a bad option in the practical case. This detector assumes no prior information at all; hence, its poor performance in the simulations. However, this also makes the ED robust in cases where the *a priori* information is inaccurate. This is illustrated in Fig. 4, where the ED exhibits a performance corresponding to that of GLRT2.

The proposed novel detector, which is based on spatial stationarity, is seen in Figs. 2 and 3 to have a comparable performance to those of the energy detector and LRT1. But, in the practical case of the experimental data, it performs the best (Fig. 4). Indeed, it is robust, by definition, to channel and signal mismatches and to colored ocean noise (Fig. 5 clearly demonstrates that the measured noise is not white). However, this detector also appears to tolerate some degree of spatial nonstationarity, even in the noise. The ocean noise is definitely not spatially stationary, as shown in Fig. 5 (the spatial covariance matrix is not exactly Toeplitz) and in Fig. 7 (the spatial cumulant matrix is not completely diagonal). However, Fig. 8 indicates (note the dark square in the middle) that the measured signal is spatially nonstationary to a higher degree. That is, the mere qualitative nature of the assumptions in the novel detector, i.e., the difference in degree of spatial stationarity, appears sufficient to grant it both performance and robustness. Last, note that the novel detector is, in fact, a weighted-energy detector. That is, the nonstationary energy is emphasized. Furthermore, in both simulation and experimental results, the novel detector outperforms the regular ED. We thus deduce that the energy of the nonspatially stationary part of the field is a better indicator for a source in a bounded channel than is the field's total energy.

IX. SUMMARY

In selecting a detector one searches for good performance, robustness, and a low computational complexity. In this paper, a novel detector that exploits the different degrees of spatial stationarity for signal and noise is proposed. To get an idea of the performance of this detector, it was compared to three others, using both simulated and experimental data.

In the presence of environmental mismatch, the threshold SNR of the novel detector for the experimental data appears 2–5 dB lower than the other detectors. The proposed detector was shown to have good, robust performance, while requiring a modest computational complexity.

ACKNOWLEDGMENT

The authors would like to thank Dr. D. F. Gingras of ONR for making the SACLANT data available.

APPENDIX A

Proof of necessary conditions for spatial stationarity:

Assume Q sources located at spatial (three-dimensional) coordinates $\mathbf{V}_1, \mathbf{V}_2, \dots, \mathbf{V}_Q$. Each source radiates a signal $s(t, \mathbf{V}_q)$, where t is the time index, and \mathbf{V}_q is the spatial coordinate of the q th source. The sensor array is located near the axes origin. The p th sensor, located at coordinate \mathbf{X}_p , measures the signal $y(t, \mathbf{X}_p)$.

When the propagation is without dispersion, the signal received at coordinate \mathbf{X}_p is

$$y(t, \mathbf{X}_p) = \sum_{q=1}^Q \alpha_{p,q} s(t - \tau(\mathbf{V}_q, \mathbf{X}_p), \mathbf{V}_q), \quad (\text{A1})$$

where $\alpha_{p,q}$ is the attenuation coefficient from the q th source to the p th sensor, and $\tau(\mathbf{V}_q - \mathbf{X}_p)$ is the propagation delay. This delay is a function of the distance and c , the speed of propagation

$$\tau(\mathbf{V}_q, \mathbf{X}_p) = \frac{\|\mathbf{V}_q - \mathbf{X}_p\|}{c}, \quad (\text{A2})$$

where $\|\cdot\|$ denotes two-norm (Euclidean, ‘‘vector’’ distance).

We now compute the correlation between the received signals at two sensors. Take for example the sensors located at \mathbf{X}_1 and \mathbf{X}_2

$$\begin{aligned} \rho_y &\equiv E\{y(t + \Delta t, \mathbf{X}_1)y^*(t, \mathbf{X}_2)\} \\ &= \sum_{q=1}^Q \sum_{r=1}^Q \alpha_{1,q} \alpha_{2,r} E\{s(t + \Delta t - \tau(\mathbf{V}_q, \mathbf{X}_1), \mathbf{V}_q) \\ &\quad \cdot s^*(t - \tau(\mathbf{V}_r, \mathbf{X}_2), \mathbf{V}_r)\}. \end{aligned} \quad (\text{A3})$$

For spatial stationarity to hold, ρ_y should be a function of $(\mathbf{X}_1 - \mathbf{X}_2)$ only. We now specify the necessary conditions for this.

a. Condition 1: The sources must be temporally stationary.

Only then is it possible for the two $\tau(\cdot)$ terms to be related by an addition operator

$$\begin{aligned} \rho_y &= \sum_{q=1}^Q \sum_{r=1}^Q \alpha_{1,q} \alpha_{2,r} \rho_s[\Delta t + \tau(\mathbf{V}_r, \mathbf{X}_2) \\ &\quad - \tau(\mathbf{V}_q, \mathbf{X}_1), \mathbf{V}_q, \mathbf{V}_r], \end{aligned} \quad (\text{A4})$$

where ρ_s is the correlation between two source signals

$$\rho_s(\Delta t, \mathbf{V}_q, \mathbf{V}_r) \equiv E\{s(t + \Delta t, \mathbf{V}_q)s^*(t, \mathbf{V}_r)\}. \quad (\text{A5})$$

Next, $\tau(\mathbf{V}, \mathbf{X})$ is required to be linear in \mathbf{X}

$$\tau(\mathbf{V}, \mathbf{X}) = \frac{\|\mathbf{V} - \mathbf{X}\|}{c} = \frac{(\mathbf{V} - \mathbf{X})^T (\mathbf{V} - \mathbf{X})}{c \cdot \|\mathbf{V} - \mathbf{X}\|} \approx \frac{(\mathbf{V} - 2\mathbf{X})^T \mathbf{V}}{c \cdot \|\mathbf{V}\|}, \quad (\text{A6})$$

where the last approximation holds only when $\|\mathbf{V}\| \gg \|\mathbf{X}\|$; that is.

b. Condition 2: The sources are far away from the array (relative to the size of the array); that is, the sources are located in the far field.

When this condition holds, (A4) turns to

$$\rho_y = \sum_{q=1}^Q \sum_{r=1}^Q \alpha_{1,q} \alpha_{2,r} \rho_s \left(\Delta t + \frac{(\mathbf{V}_r - 2\mathbf{X}_2)^T \mathbf{V}_r}{c \cdot \|\mathbf{V}_r\|} - \frac{(\mathbf{V}_q - 2\mathbf{X}_1)^T \mathbf{V}_q}{c \cdot \|\mathbf{V}_q\|} \right). \quad (\text{A7})$$

Finally, for (A7) to be a function of $(\mathbf{X}_1 - \mathbf{X}_2)$, there are two possibilities: First, for all q and r , $\mathbf{V}_r \approx \mathbf{V}_q$. This implies that all the sources are located in the same direction, or that there is really only one source. This possibility is therefore not interesting. The only other possibility follows:

c. Condition 3: The signals are uncorrelated.

This means that $\rho_s(\Delta t, \mathbf{V}_q, \mathbf{V}_r) \neq 0$ only when $\mathbf{V}_q = \mathbf{V}_r$. Applying this condition to (A7),

$$\rho_y = \sum_{q=1}^Q \alpha_{1,q}^2 \rho_s \left(\Delta t + \frac{(\mathbf{V}_q - 2\mathbf{X}_2)^T \mathbf{V}_q}{c \cdot \|\mathbf{V}_q\|} - \frac{(\mathbf{V}_q - 2\mathbf{X}_1)^T \mathbf{V}_q}{c \cdot \|\mathbf{V}_q\|} \right), \quad (\text{A8})$$

and ρ_y is a function of $(\mathbf{X}_1 - \mathbf{X}_2)$ as required.

We have shown that three conditions are necessary for the general expression (A3) to become dependent only on the vector difference $(\mathbf{X}_1 - \mathbf{X}_2)$. When these conditions are applied, (A3) can be written as (A8). Finally, by superposition, if the added noise is also spatially stationary (condition 4), then the measured field is also spatially stationary. This completes the proof.

APPENDIX B

Proof of (8) for $k_1 + k_2 \neq 0 \pmod{P}$:

In addition to (9), which defines $S(k)$, the discrete spatial spectrum for the stationary case, define for convenience

$$S_y^*(k) \equiv \sum_{p=0}^{P-1} C_y^*(p) e^{+j(2\pi/P)pk}, \quad (\text{B1})$$

$$S_y(-k) \equiv \sum_{p=0}^{P-1} C_y(p) e^{+j(2\pi/P)pk}, \quad (\text{B2})$$

$$S_y(-k) = S_y(P - k \pmod{P}),$$

$$S_y^*(-k) \equiv \sum_{p=0}^{P-1} C_y^*(p) e^{-j(2\pi/P)pk}, \quad (\text{B3})$$

$$S_y^*(-k) = S_y^*(P - k \pmod{P}).$$

Break the double sum in (7) into three subsums

$$S_y(k_1, k_2) = \sum_{p_1=0}^{P-1} \sum_{p_2=0}^{P-1} C_y(p_1, p_2) e^{-j(2\pi/P)(p_1 k_1 + p_2 k_2)} \\ = I_1 + I_2 - I_3. \quad (\text{B4})$$

The first subsum, I_1 , is carried over the upper triangle of \mathbf{C}_y , including the diagonal

$$I_1 = \sum_{p_1=0}^{P-1} \sum_{p_2=0}^{P-1-p_1} C_y(p_1, p_2) e^{-j(2\pi/P)(p_1 k_1 + p_2 k_2)} \\ = \sum_{p=0}^{P-1} \sum_{p_2=0}^{P-1-p} C_y(p) e^{-j(2\pi/P)(p+p_2)k_1} e^{-j(2\pi/P)p_2 k_2},$$

where in the last equation we used the fact that \mathbf{C}_y is Toeplitz; hence, $C_y(p_1, p_2) = C_y(p_1 - p_2) = C_y(p)$. Computing the sums in the last equation

$$I_1 = \sum_{p=0}^{P-1} C_y(p) e^{-j(2\pi/P)p k_1} \frac{1 - e^{-j(2\pi/P)(k_1 + k_2)(P-p)}}{1 - e^{-j(2\pi/P)(k_1 + k_2)}} \\ = \frac{S(k_1) - S_y(-k_2)}{1 - e^{-j(2\pi/P)(k_1 + k_2)}}. \quad (\text{B5})$$

Similar derivation for I_2 , the lower triangle of \mathbf{C}_y , including the diagonal, yields

$$I_2 = \sum_{p=0}^{P-1} \sum_{p_1=0}^{P-1-p} C_y^*(p) e^{-j(2\pi/P)p_1 k_1} e^{-j(2\pi/P)(p_1 + p)k_2} \\ = \frac{S_y^*(-k_2) - S_y^*(k_1)}{1 - e^{-j(2\pi/P)(k_1 + k_2)}}. \quad (\text{B6})$$

Finally, the contribution of the diagonal elements of \mathbf{C}_y , counted both in I_1 and in I_2 , must be deducted:

$$I_3 = \sum_{p_1=0}^{P-1} C_y(p_1, p_1) e^{-j(2\pi/P)p_1(k_1 + k_2)} \\ = C_y(0) \sum_{p_1=0}^{P-1} e^{-j(2\pi/P)p_1(k_1 + k_2)} = 0. \quad (\text{B7})$$

Combining (B5)–(B7) into (B4) yields

$$S_y(k_1, k_2) = \frac{[S_y(k_1) - S_y^*(k_1)] - [S_y(-k_2) - S_y^*(-k_2)]}{1 - e^{-j(2\pi/P)(k_1 + k_2)}} \\ = \frac{2j \operatorname{Im}\{S_y(k_1) - S_y(-k_2)\}}{1 - e^{-j(2\pi/P)(k_1 + k_2)}},$$

which is the desired result.

APPENDIX C

Proof of the simplified expression (29) for GLRT2:

For uncorrelated samples, $\mathbf{y}(l)$, of a complex Gaussian field, the generalized likelihood ratio test for the decision problem (2) is given in (28), where the average signal power at each sensor, σ_s^2 , is unknown, and the known spatial transfer function $\mathbf{g}(\cdot)$ is a function of the unknown parameters $r_s, z_s, \boldsymbol{\theta}$. Assume in addition

Under H_0 :

$$E\{\mathbf{y}(l)\} = \mathbf{0},$$

$$E\{\mathbf{y}(l)\mathbf{y}^H(l)\} = \sigma_n^2 \mathbf{I} \equiv \mathbf{C}_n.$$

Under H_1 :

$$E\{\mathbf{y}(l)\} = \mathbf{0},$$

$$E\{\mathbf{y}(l)\mathbf{y}^H(l)\} = \sigma_s^2 \mathbf{g}\mathbf{g}^H + \mathbf{C}_n \equiv \mathbf{C}_s + \mathbf{C}_n,$$

where the dependence of \mathbf{g} on its parameters is made implicit. Under these assumptions, taking the logarithm of (28)

$$\begin{aligned} \zeta_2 \propto \max_{\sigma_s^2, r_s, z_s, \theta} & \left\{ L \ln \det(\mathbf{C}_n) - L \ln \det(\mathbf{C}_s + \mathbf{C}_n) \right. \\ & \left. + \sum_{l=0}^{L-1} \mathbf{y}^H(l) [\mathbf{C}_n^{-1} - (\mathbf{C}_s + \mathbf{C}_n)^{-1}] \mathbf{y}(l) \right\}. \end{aligned} \quad (\text{C1})$$

Consider each term in the equation above. The first is not a function of the measurements or the parameters and can be discarded. The second term can be simplified

$$\begin{aligned} L \ln \det(\mathbf{C}_s + \mathbf{C}_n) &= L \ln \det(\sigma_s^2 \mathbf{g}\mathbf{g}^H + \sigma_n^2 \mathbf{I}) \\ &= L \ln \det \frac{1}{\sigma_n^2} (snr \mathbf{g}\mathbf{g}^H + \mathbf{I}) \\ &= PL \ln \frac{1}{\sigma_n^2} + L \ln(1 + snr \mathbf{g}^H \mathbf{g}), \end{aligned} \quad (\text{C2})$$

where snr is defined as σ_s^2 / σ_n^2 . As for the third term in (C1)

$$\begin{aligned} & \sum_{l=0}^{L-1} \mathbf{y}^H(l) [\mathbf{C}_n^{-1} - (\mathbf{C}_s + \mathbf{C}_n)^{-1}] \mathbf{y}(l) \\ &= \sum_{l=0}^{L-1} \text{trace}([\mathbf{C}_n^{-1} - (\mathbf{C}_s + \mathbf{C}_n)^{-1}] \mathbf{y}(l) \mathbf{y}^H(l)) \\ &= L \text{trace} \left([\mathbf{C}_n^{-1} - (\sigma_s^2 \mathbf{g}\mathbf{g}^H + \mathbf{C}_n)^{-1}] \frac{1}{L} \sum_{l=0}^{L-1} \mathbf{y}(l) \mathbf{y}^H(l) \right) \\ &= L \text{trace} \left(\left[\mathbf{C}_n^{-1} - \left(\mathbf{C}_n^{-1} - \frac{\sigma_s^2}{1 + \sigma_s^2 \mathbf{g}^H \mathbf{C}_n^{-1} \mathbf{g}} \right. \right. \right. \\ & \quad \left. \left. \left. \times \mathbf{C}_n^{-1} \mathbf{g}\mathbf{g}^H \mathbf{C}_n^{-1} \right) \right] \widehat{\mathbf{C}}_y \right) \\ &= \frac{L}{\sigma_n^2} \text{trace} \left(\frac{snr}{1 + snr \mathbf{g}^H \mathbf{g}} \mathbf{g}\mathbf{g}^H \widehat{\mathbf{C}}_y \right) = \frac{L}{\sigma_n^2} \frac{snr}{1 + snr \mathbf{g}^H \mathbf{g}} \mathbf{g}^H \widehat{\mathbf{C}}_y \mathbf{g}, \end{aligned} \quad (\text{C3})$$

where $\widehat{\mathbf{C}}_y$ is defined as in (10). Plugging (C2)–(C3) into (C1) and discarding the constant term in (C2)

$$\begin{aligned} \zeta_2 \propto \min_{snr, r_s, z_s, \theta} & \left\{ L \ln(1 + snr \mathbf{g}^H \mathbf{g}) \right. \\ & \left. - \frac{L}{\sigma_n^2} \frac{snr}{1 + snr \mathbf{g}^H \mathbf{g}} \mathbf{g}^H \widehat{\mathbf{C}}_y \mathbf{g} \right\}. \end{aligned} \quad (\text{C4})$$

The minimization over snr can be analytically performed (by differentiation) to obtain its maximum likelihood estimator, \widehat{snr}_{ML} :

$$\widehat{snr}_{ML} = \frac{1}{\mathbf{g}^H \mathbf{g}} \left(\frac{\mathbf{g}^H \widehat{\mathbf{C}}_y \mathbf{g}}{\sigma_n^2 \mathbf{g}^H \mathbf{g}} - 1 \right). \quad (\text{C5})$$

Finally, using (C5) in (C4) one obtains the desired expression (29).

- ¹A. Ephraty, J. Tabrikian, and H. Messer, "A Test for Spatial Stationarity and Applications," Proceedings of the 8th IEEE Signal Processing Workshop on SSAP, 412–415 (1996).
- ²M. B. Porter and A. Tolstoy, "The Matched-Field Processing Benchmark Problem," J. Comput. Acoust. 2, 161–185 (1994).
- ³D. F. Gingras and P. Gerstoft, "Inversion for Geometric and Geoacoustic Parameters in Shallow Water: Experimental Results," J. Acoust. Soc. Am. 97, 3589–3598 (1995).
- ⁴S. Bose and A. O. Steinhardt, "Invariant Tests for Spatial Stationarity Using Covariance Structure," IEEE Trans. Signal Process. 44(6), 1523–1533 (1996).
- ⁵M. J. Hinich, "Higher Order Cumulants and Cumulant Spectra," Circuits Syst. Signal Process. 13(4), 391–402 (1994).
- ⁶D. R. Brillinger, *Time Series: Data Analysis and Theory* (Holden-Day, San Francisco, 1981).
- ⁷D. H. Johnson and D. E. Dudgeon, *Array Signal Processing: Concepts and Techniques* (Prentice-Hall, Englewood Cliffs, NJ, 1993).
- ⁸F. A. Marvasti, *A Unified Approach to Zero-Crossings and Nonuniform Sampling of Single Multidimensional Signals and Systems* (Department of Electrical Engineering, Illinois Institute of Technology, Chicago, IL, 1987).
- ⁹A. Ephraty, J. Tabrikian, and H. Messer, "On The Consistency of Non-Parametric Estimation of the Spatial Spectrum," Proceedings of the 19th Convention of Electrical and Electronics Engineers in Israel, pp. 247–250 (1996).
- ¹⁰T. W. Anderson, *An Introduction to Multivariate Statistical Analysis*, 2nd ed. (Wiley, New York, 1984).
- ¹¹V. Premus, D. Alexandrou, and L. W. Nolte, "Full-Field Optimum Detection in an Uncertain, Anisotropic Random Wave Scattering Environment," J. Acoust. Soc. Am. 98, 1097–1110 (1995).
- ¹²M. B. Porter and E. L. Reiss, "A Numerical Method for Ocean Acoustic Normal Modes," J. Acoust. Soc. Am. 76, 244–252 (1984).

Feature dependence in the automatic identification of musical woodwind instruments

Judith C. Brown^{a)}

*Physics Department, Wellesley College, Wellesley, Massachusetts 02181
and Media Lab, Massachusetts Institute of Technology, Cambridge, Massachusetts 02139*

Olivier Houix and Stephen McAdams

*Institut de Recherche et de Coordination Acoustique/Musique (Ircam-CNRS), 1 place Igor Stravinsky,
F-75004 Paris, France*

(Received 18 May 1999; revised 16 November 2000; accepted 22 November 2000)

The automatic identification of musical instruments is a relatively unexplored and potentially very important field for its promise to free humans from time-consuming searches on the Internet and indexing of audio material. Speaker identification techniques have been used in this paper to determine the properties (features) which are most effective in identifying a statistically significant number of sounds representing four classes of musical instruments (oboe, sax, clarinet, flute) excerpted from actual performances. Features examined include cepstral coefficients, constant-Q coefficients, spectral centroid, autocorrelation coefficients, and moments of the time wave. The number of these coefficients was varied, and in the case of cepstral coefficients, ten coefficients were sufficient for identification. Correct identifications of 79%–84% were obtained with cepstral coefficients, bin-to-bin differences of the constant-Q coefficients, and autocorrelation coefficients; the latter have not been used previously in either speaker or instrument identification work. These results depended on the training sounds chosen and the number of clusters used in the calculation. Comparison to a human perception experiment with sounds produced by the same instruments indicates that, under these conditions, computers do as well as humans in identifying woodwind instruments. © 2001 Acoustical Society of America. [DOI: 10.1121/1.1342075]

PACS numbers: 43.60.Gk, 43.75.Cd, 43.75.Ef [JCB]

I. INTRODUCTION AND BACKGROUND

Despite the massive research which has been carried out on automatic speaker identification, there has been little work done on the identification of musical instruments by computer. See Brown (1999) for a summary. Applications of automatic instrument identification include audio indexing (Wilcox *et al.*, 1994), automatic transcription (Moorer, 1975), and Internet search and classification of musical material.

One technique used widely in speaker identification studies is pattern recognition. Here, the most important step is the choice of a set of features which will successfully differentiate members of a database. Brown (1997, 1998a, 1999) applied this technique to the identification of the oboe and the saxophone using a Gaussian mixture model with cepstral coefficients as features. Included in this reference is an introduction to pattern recognition and to the method of clusters. Definitions which will be useful for this paper can be found in the Appendix.

Two later reports on computer identification of musical instruments also use cepstral coefficients as features for pattern recognition. Dubnov and Rodet (1998) used a vector quantizer as a front end and trained on 18 short excerpts from 18 instruments, but reported no quantitative classification results. Marques (1999) examined eight instruments trained on excerpts from one CD with the test set excerpted

from other CDs (one per instrument class) and reported a 67% success rate. In a study which will be examined further in this paper, Dubnov *et al.* (1997) explored the effectiveness of higher-order statistics using the calculation of moments for musical instrument identification. They concluded that these features were effective in distinguishing families of musical instruments, but not the instruments within families. As with earlier work, none of these studies includes enough samples for statistically valid conclusions.

In marked contrast to the relatively few articles on automatic recognition of musical instruments, there has been a great deal of interest in human timbre perception. For comparison with this study, we focus on experiments involving the woodwind family. These instruments are difficult to distinguish from each other since they have similar attacks and decays, overlapping frequency ranges, and similar modes of excitation. The literature on these experiments is summarized in Table I. For a short, general summary of human perception experiments, see Brown (1999). For more complete reviews, see McAdams (1993), Handel (1995), and Hajda *et al.* (1997).

Although the vast majority of the experiments of Table I has been on single notes or note segments, Saldanha and Corso (1964) pointed out that the transitional effects from note to note could provide one of the major determiners of musical quality. In the earliest study including note-to-note transitions, Campbell and Heller (1978) found more accurate identifications using transitions than with isolated tones. They called the transition region the legato transient. In an-

^{a)}Electronic mail: brown@media.mit.edu

TABLE I. Summary of percent correct for previous human perception experiments on wind instruments. Results for the oboe, sax, clarinet, and flute are given when possible. The final column is the total number of instruments included in the experiment.

	Date	Oboe	Sax	Clar	Flute	Overall	Number of instruments
Eagleson/Eagleson	1947		59	45	20	56	9
Saldanha/Corso	1964	75		84	61	41	10
Berger	1964					59	10
Clark/Milner	1964					90	3 (flute, clar, oboe)
Strong/Clark	1967a					85	8
Campbell/Heller	1978					72	6 (2-note legato)
Kendall	1986					84	3 (trumpet, clar, violin)
Brown	1999	85	92			89	2 (oboe, sax)
Martin	1999					46	27 (isolated tone)
						67	27 (10-s excerpt)
Houix/McAdams/Brown		87	87	71	93	85	4 (oboe, sax, clar, flute)

other study using musical phrases, Kendall (1986) emphasized the importance of context and demonstrated that results on musical phrases were significantly higher than on single notes.

More recently, Brown (1997, 1998a, 1998b, 1999) has found excellent results using multinote segments from actual musical performances. Martin (1999) has explored both types of experiments and found more accurate results with multinote segments than with isolated single notes. The results of Houix, McAdams, and Brown (unpublished) on multinote human perception will be compared to our calculations in a later section.

In this paper we have used a large database of sounds excerpted from actual performances with the oboe, saxophone, clarinet, and flute. We present calculations to show:

- (i) The accuracy with which computers can be used to identify these very similar instruments;
- (ii) The best signal processing features for this task; and
- (iii) The accuracy compared with experiments on human perception.

II. SOUND DATABASE

A. Source and processing

Sounds were excerpted as short segments of solo passages from compact disks, audio cassettes, and records from the Wellesley College Music Library. This method of sample collection ensured a selection of typical sounds produced by each instrument, such as might be encountered on Internet sites or stored audio tapes. At least 25 sounds for each instrument were used to provide statistical reliability for the results. Features were calculated for 32-ms frames overlapping by 50% and having rms averages greater than 425 (for 16-bit samples).

B. Training and test sets

Sounds of longer duration (1 min or more) representing each instrument were chosen as training sounds and are given in Table II. These training sounds were varied in the calculations with one sound representing each instrument in all possible combinations to determine the optimum combi-

nation for identification. From Table II, with two, four, three, and four sounds for each of the four instruments, there were 96 combinations.

The constant-Q transforms of the most effective training sounds are shown in Fig. 1. Both the oboe and flute examples have strong peaks at a little over 1000 Hz. The oboe has an additional bump at 1200 Hz, giving rise to its nasal quality. The saxophone has a low-frequency spectral-energy distribution with a peak around 400 Hz, while the clarinet has less prominent peaks at around 400 and 900 Hz.

Properties of the test set are given in Table III. The training sounds were included in the identification calculations but were not included in the calculation of the average durations reported here. Two longer flute sounds with durations on the order of 40 s were also omitted as their durations were not representative of the flute data as a whole and skewed the average.

TABLE II. Training sounds identified by performer and piece of music performed. The third column is the length of the sound in seconds which was excerpted for the calculation.

Performer	Music	Length (s)
Peter Christ	Persichetti's Parable for Solo Oboe	60.7
Joseph Robinson	Rochberg's Concerto for Oboe and Orchestra	82.2
Frederick Tillis	"Motherless Child"	77.7
Johnny Griffin	"Light Blue"	99.3
Coleman Hawkins	"Picasso"	63.0
Sonny Rollins	"Body and Soul"	88.8
Benny Goodman	Copland's Concerto for Clarinet and String Orch	74.05
Heinrich Matzener	Eisler's Moment Musical pour clarinette Solo	70.1
David Shifrin	Copland's Concerto for Clarinet and String Orch	63.2
Samuel Baron	Martino's Quodlibets for Flute	74.1
Sue Ann Kahn	Luening's Third Short Sonata for Flute and Piano	69.0
Susan Milan	Martino's Sonata for Flute and Piano	54.3
Fenwick Smith	Koechlin's Sonata for 2 Flutes Op 75	106.0

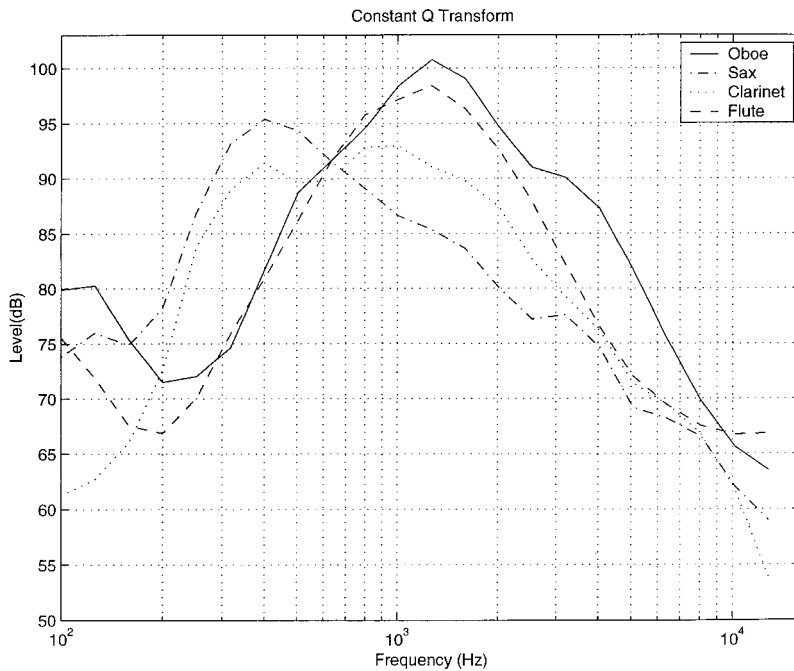


FIG. 1. Comparison of the constant-Q spectra for examples of successful training sounds for each of the four instrument classes. These were the sounds performed by Christ, Griffin, Matzener, and Baron. See Table II for details.

III. CALCULATIONS

A. Probability calculation

The details of the calculations described in Brown (1999) will be summarized here. For each training sound, cepstral coefficients or other features were calculated for each frame; and from these values, a k -means algorithm was used to calculate clusters. A Gaussian mixture model (Reynolds and Rose, 1995), i.e., a sum of weighted Gaussians, was then calculated based on the mean μ_k , standard deviation σ_k , and population given by the cluster calculation for this sound; this model was used to give the probability density function representing the data calculated for the training sounds. For a single cluster k belonging to class Ω , the probability density of measuring the feature vector \mathbf{x}^i is

$$p(\mathbf{x}^i|\Omega_k) = \frac{1}{\sqrt{2\pi}\sigma_{\Omega_k}^2} \exp\left(-\frac{(\mathbf{x}^i - \mu_{\Omega_k})^2}{2\sigma_{\Omega_k}^2}\right). \quad (1)$$

Summing over all K clusters, the total probability density that feature vector \mathbf{x}^i is measured if unknown sound \mathbf{U} belongs to class Ω is

$$p(\mathbf{x}^i|\Omega) = \sum_{k=1}^K p_k p(\mathbf{x}^i|\Omega_k), \quad (2)$$

TABLE III. Data on sounds in the test set by instrument class. The number of sounds is given in column two with the average length and standard deviation in the last two columns.

Instrument	Number of sounds	Average length (s)	Standard deviation (s)
Oboe	28	2.5	2.1
Sax (Gp I)	31	2.0	0.8
Sax (Gp II)	21	7.8	2.4
Clarinet	33	6.1	2.1
Flute	31	7.8	4.1

where p_k is the probability of occurrence of the k th cluster. It is equal to the number of vectors in the training set assigned to this cluster divided by the total number of vectors in the training set. If we define $\mathbf{X} = \{\mathbf{x}^1, \dots, \mathbf{x}^N\}$ as the set of all feature vectors measured for \mathbf{U} , then the total probability density that all of the N feature vectors measured for unknown \mathbf{U} belong to class Ω is given by the product of the individual probability densities

$$p(\mathbf{X}|\Omega) = p(\mathbf{x}^1, \dots, \mathbf{x}^N|\Omega) = \prod_{i=1}^N p(\mathbf{x}^i|\Omega). \quad (3)$$

This assumes statistical independence of the feature vectors. While this simplifying assumption is not strictly valid here, it is a widely accepted technique in the speech community and has been experimentally shown to be effective in calculations (Rabiner and Huang, 1993). As the sounds used in the study had many rapid note changes, it proves a better assumption here than for speech. Equation (3) is the probability density of measuring the set of feature vectors \mathbf{X} for unknown \mathbf{U} if \mathbf{U} belongs to class Ω , whereas the quantity of interest for a Bayes decision rule is the *a posteriori* probability

$$\hat{\Omega} = \arg \max \Pr(\Omega^{(m)}|\mathbf{X}) \quad (4)$$

that a measurement of \mathbf{X} means it is more probable that \mathbf{U} is a member of a particular class $\Omega^{(m)}$ than another class. Here, $\Omega^{(m)}$ represents the m th class, $\hat{\Omega}$ is the class which maximizes this probability, and $m = 1, 2, \dots, M$.

Using the argument that the four classes are equally probable and dropping terms which do not vary with class, it can be shown for the present case (Brown, 1999) that $\hat{\Omega}$ in Eq. (4) above can be expressed as

$$\hat{\Omega} = \arg \max p(\mathbf{X}|\Omega^{(m)}). \quad (5)$$

This equation states the results in terms of the probability density of Eq. (3), which is the quantity calculated in our

experiment. Here, $m=1,2,3,4$, and each sound in the test set is assigned to the class which maximizes the probability in this equation.

The values for the features from each frame of a particular sound from the test set were used to calculate the probability density of Eq. (3) for each of the four instrument classes. That sound was then assigned to the class for which this function was a maximum. After this was done for each of the sounds, a four-by-four confusion matrix was computed showing what percent of each of the test sounds in each of the classes was assigned to each of the four possibilities. An overall percent correct (equal to the total number of correct decisions divided by the total number of members of the test set) for this particular set of training sounds was also computed.

The training sounds (listed in Table II) and total number of clusters were then varied. Pairwise comparisons were also made with calculations identical to those described in Brown (1997, 1998a, 1998b, 1999).

B. Features

Features from both the frequency and time domains were examined; in some cases approximations to the frequency and time derivatives were calculated as well.

1. Frequency domain

Cepstral coefficients provide information about formants for speech/speaker identification in humans which translates into resonance information about musical instruments. They were calculated (O'Shaughnessy, 1987) from 22 constant- Q coefficients with frequency ratio 1.26 and frequencies ranging from 100–12 796 Hz. Channel effects were explored, where the long-term average is subtracted from each coefficient to eliminate the effects of different recording environments (Reynolds and Rose, 1995). Cepstral time derivatives (approximated by subtracting coefficients separated by four time frames) were calculated, again to eliminate effects of the recording environment. Other features derived from the spectrum were the constant- Q coefficients and their bin-to-bin differences as a measure of spectral smoothness (McAdams, Beauchamp, and Meneguzzi, 1999). Spectral centroid (the Fourier amplitude-weighted frequency average) and average energy (Beauchamp, 1982) were calculated from the Fourier transform.

2. Time domain

In addition to autocorrelation coefficients, the Dubnov *et al.* (1997) method of calculating moments of the residual of the LPC (linear prediction coefficients) filtered signal was examined along with the straightforward calculation of the third (skew), fourth (kurtosis), and fifth moments of the raw signal. Finally, the second through fifth moments of the envelope of the signal were examined by taking the Hilbert transform (Hartmann, 1998) of the signal and low-pass filtering its magnitude.

IV. RESULTS AND DISCUSSION

A. Four instruments

1. Feature dependence

Results with different sets of features are summarized in Fig. 2. The optimum choice of training sounds and clusters is indicated by "Opt." The mean is the average over all training sounds and numbers of clusters, and is the accuracy obtainable with an arbitrary set of training sounds. The standard deviation is a measure of the confidence interval of the results. Note that all features except moments of the time wave gave much better identification than chance.

Feature sets and number of coefficients are indicated on the graph. The most successful feature set was the frequency derivative of the constant- Q coefficients measuring spectral smoothness (also called spectral irregularity in the human perception literature) with 84% correct. Next most successful were bin-to-bin differences (frequency derivative) of the cepstral coefficients with 80%, even though, considering the roughly 7% standard deviation, this does not mark a significant difference from cepstral coefficients. An explanation for this slight advantage is that taking differences removes the effect of frequency-independent interference, and this gives a constant additive term for all cepstral coefficients.

Other successful features were cepstral coefficients and autocorrelation coefficients with over 75% correct. From the point of view of computational efficiency, the best choice is cepstral coefficients, since only ten were required. The cepstral transform acts as an information compaction transform with most of the variance (and hence information) in the lower coefficients.

Spectral centroid alone, i.e., a one-dimensional feature or single number per frame, was sufficient to classify the sounds with close to 50% accuracy. There is an optimum range for the number of features (10–22 for cepstra and 25–49 for autocorrelation) as has been discussed for pattern recognition calculations (Schmid, 1977; Kanal, 1974).

Unlike improvements obtained in calculations for speaker identification with the inclusion of channel effects and frame-to-frame differences in cepstral coefficients, we found no such improvement in our results. This indicates that for music, in contrast to speech, significant information is contained in the long-term average value.

That autocorrelation coefficients were successful as features is surprising since they have not been used for speaker or vowel identification, and there is no *a priori* reason to anticipate this success. Also of note is the fact that changing the sample rate from 11 to 32 kHz has little effect on the autocorrelation results, since the time range examined varies by a factor of about 3. This indicates the importance of high-frequency or formant information present in both representations.

Cepstral coefficients were combined with spectral centroid to determine whether combining features would lead to better identifications. The result was slightly poorer than that with cepstral coefficients alone, although not outside the standard deviation.

Finally, consistent with the findings of Dubnov *et al.* (1997), the average moment calculations gave results no bet-

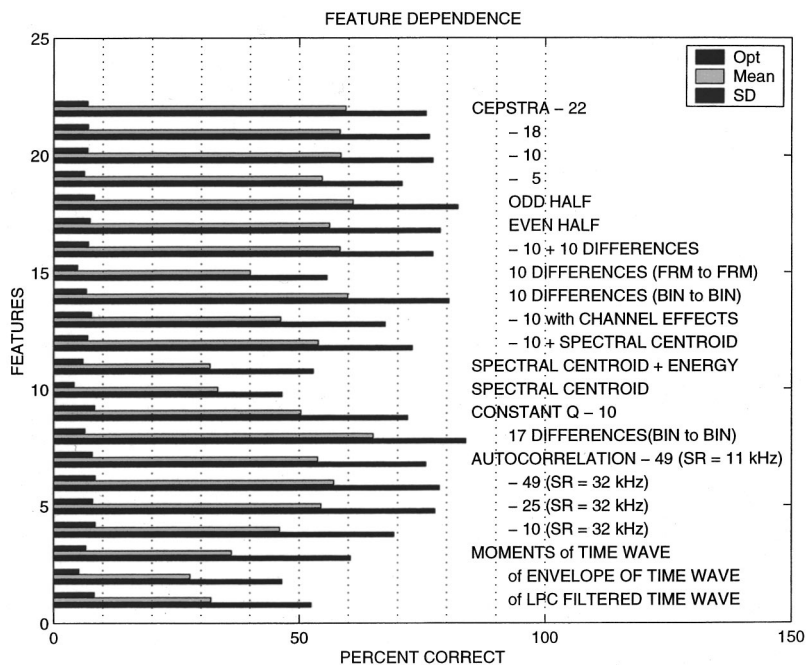


FIG. 2. Accuracy as a function of features. ‘‘Opt’’ gives the percentage correct with the optimum choice of training sounds and number of clusters for the four instruments. The mean and standard deviation were obtained by varying the training sounds and clusters.

ter than random, indicating that instruments cannot be distinguished within an instrumental family with these features.

The most successful feature sets (cepstra, constant- Q differences, and autocorrelation coefficients) can all be derived from the Fourier transform and in that sense can be considered as transformations of spectral information. The advantage of taking the transforms is that they decorrelate the components of the feature vector, as tacitly assumed in Eq. (1). In contrast, components of the Fourier transform are highly correlated since they are proportional to the amplitude of the original sound wave. Decorrelation occurs in taking the log for the transformation to cepstral coefficients; the amplitude information is all contained in the dc component, which is usually dropped. Similarly, with the constant- Q differences, the overall amplitude term is a constant additive term for each coefficient (expressed in dB) and drops out when taking the differences (Macho *et al.*, 1999).

2. Number of clusters

The maximum number of clusters was varied, with the results given in Fig. 3. They show no significant change in going from seven to ten clusters, and only 4 percent from two to ten clusters, so calculations can be carried out using seven clusters with confidence that there will be no loss of accuracy.

3. Training sounds

The results shown in Fig. 2 indicate that the choice of training sound combinations is significant in obtaining optimum results. Information on the best training sounds and corresponding number of clusters for the most successful features is collected in Table IV. The features are identified in column one, followed by the number of combinations of training sounds which gave identical results. Column three indicates the number of combinations from column two in which only the number of clusters varied, i.e., the sounds

were identical. Finally, in columns four to seven, the training sounds referred to in column three are identified along with the range of cluster values of each in parentheses.

The sounds by Christ (oboe), Griffin (sax), Matzener (clarinet), and Baron (flute) were the most effective for the majority of these feature sets, indicating that a single set of training sounds is optimum for different feature sets. Analysis of these sounds shows that it is important to have many notes (rapid passages) over a wide frequency range with a reasonably smooth spectrum.

As a further test of generality of training sounds, the sounds in the test set were split arbitrarily (odd and even sample numbers) into two halves and run independently. As shown in Fig. 2, the results were similar (82% vs 79%), indicating no disparity in the two sets of data. The calculation was then carried out using the optimum training sounds for the second half on the first half and vice versa. The results on the first half changed from 82% correct with its optimum training sounds to 73% correct with the sounds from Table IV optimized for the second half. The corresponding change for the second half of the sounds was from 79% to 67%. The effect is greater than the 7% significance level, but the results are still quite good and indicate that this method is generalizable.

4. Confusion matrices

Confusion matrices were calculated for each of the feature sets and can be obtained from the author. Figure 4 is a summary of the diagonal elements (percent correct for each instrument) of the confusion matrices for the best feature sets.

For ten cepstral coefficients, the clarinet identification is poor with only 50% correct. It was confused with the sax 27% of the time, with all other confusions 12% or less. With 18 cepstral coefficients, the results on the clarinet are much better than with ten coefficients, although more confusions of

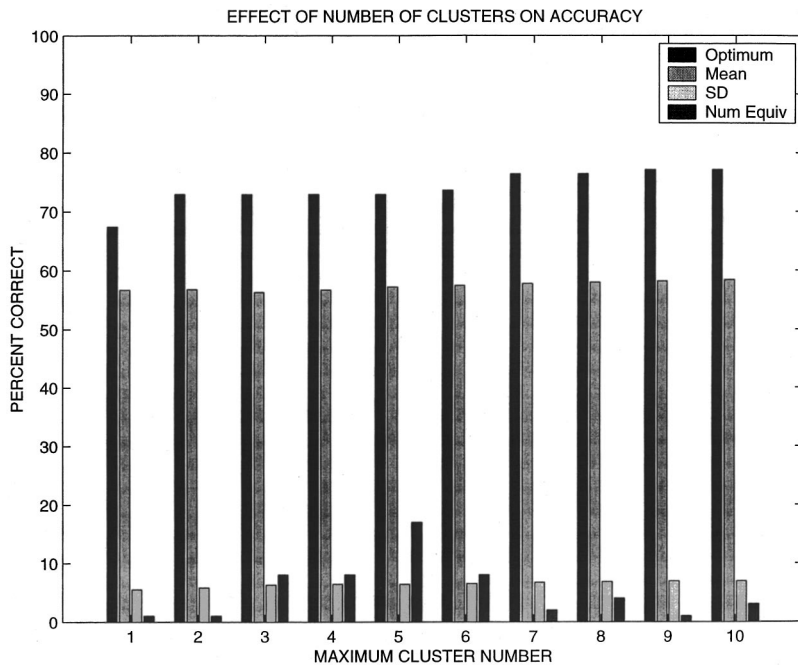


FIG. 3. Effect of varying the maximum number of clusters with ten cepstral coefficients as features. “Optimum” gives the percent correct for the optimum choice of training sounds and number of clusters. The mean and standard deviation are taken over all combinations of training sounds and cluster numbers up to the maximum. “Num equiv” is the number of combinations which gave identical optimum results.

other instruments identified as clarinet occur. Results on the oboe and flute are somewhat poorer. For better overall identifications, 18 coefficients would be preferable to ten. The largest confusions were of the flute as clarinet (26%) and the oboe as clarinet (19%). Strong and Clark (1967b) also found oboe–clarinet confusions.

Results with 25 autocorrelation coefficients were quite good overall with all identifications of instruments 70% or above. The major confusions were sax–clarinet confusions of 19% and 24%. Better overall correct identifications were found for 49 autocorrelation coefficients as seen in Fig. 4. Here, all diagonal elements are over 75%. Confusions in the range 10%–16% were found for sax as oboe, clarinet as sax, clarinet as flute, and flute as clarinet.

The results for the bin-to-bin frequency differences were of particular interest since they are directly related to the spectral smoothness studied by McAdams, Beauchamp, and Meneguzzi (1999). These are the best overall results, and unlike the others, clarinet identifications are the best. This is

due to the missing even harmonics at the lower end of the spectrum, which make bin-to-bin differences distinctive, and is consistent with the results of Saldanha and Corso (1964). The oboe was identified as a flute almost 30% of the time. Other confusions were all less than 10%.

For all other feature sets, oboe and sax identifications are best overall.

B. Pairs of instruments

The sounds from the four instruments were also compared in pairs, as was done for the oboe and sax in Brown (1999). Results are given in Fig. 5, which plots percent error for each of the six pairs along with an overall percent error. As with the four-way calculations, the poorest results were obtained with spectral centroid, a single number. Again, the best results occurred with bin-to-bin differences of constant- Q coefficients as features. There, the error was only 7% overall. Confusions of the flute with each of the three

TABLE IV. Optimum choice of training sounds for different features for four instrument identification. Column one indicates the features. Column two (NW=number of winners) gives the number of combinations of training sounds and clusters which gave optimum results. Column three gives the number of identical (NI) sounds from column two in which only the number of clusters is different. The last four columns give the optimum training sound for each instrument with the range of cluster values in parentheses or simply the number if there was a single cluster value.

Features	NW	NI	Oboe	Sax	Clarinet	Flute
10 Cepstral coefficients	3	3	Christ2	Griffin(2–3)	Matzener(9–10)	Baron2
18 Cepstral coefficients	24	24	Christ(6–10)	Griffin(9–10)	Goodman10	Baron(7–9)
22 Cepstral coefficients	8	8	Christ(8–10)	Griffin(9–10)	Goodman10	Baron(5–6)
10 Cepstra—half of sounds	12	12	Christ2	Griffin(2–3)	Matzener(9–10)	Baron(2–6)
10 Cepstra—other half of sounds	4	4	Christ4	Griffin(6–7)	Goodman9	Baron(4–6)
17 Cepstral diffs (bin-to-bin)	6	6	Robinson6	Griffin(6–9)	Matzener10	Baron(4–10)
17 Constant- Q diffs (bin-to-bin)	1	1	Christ(9)	Griffin(5)	Matzener(9)	Luening(10)
49 Autoc coeffs (SR=11 kHz)	14	12	Christ(7–10)	Griffin(5,10)	Matzener(4–6)	Luening(7–10)
49 Autoc coeffs (SR=32 kHz)	2	2	Christ9	Griffin10	Matzener9	Baron9
25 Autoc coeffs	12	12	Christ(9–10)	Griffin(8–9)	Matzener(9–10)	Baron(7–8)
10 Autoc coeffs	6	3	Christ(9–10)	Griffin(7–8)	Matzener(7,10)	Baron(7–8)

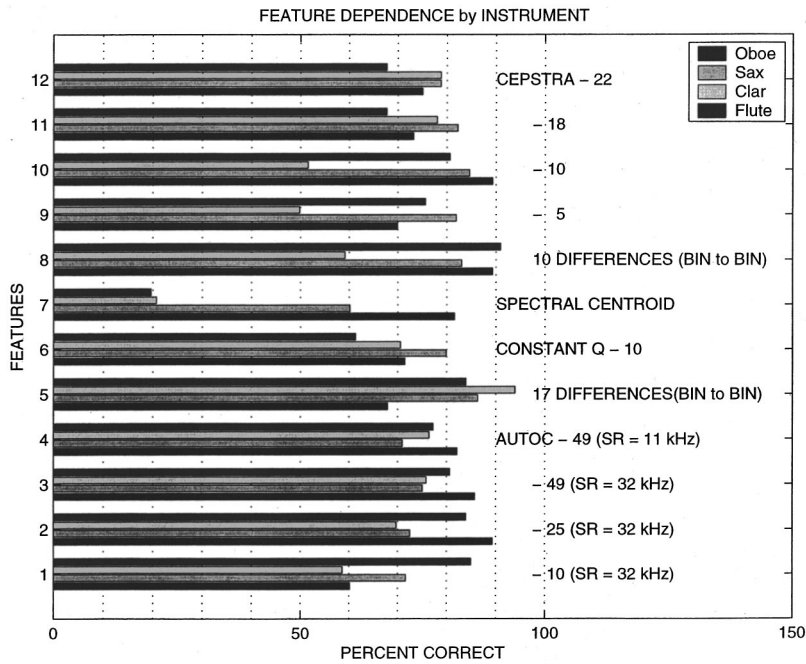


FIG. 4. Summary of correct identifications of each instrument class taken from diagonal elements of confusion matrices for feature sets indicated. Note that data are in inverse order from captions.

other instruments were highest, consistent with Berger's finding of maximum confusions for the flute as oboe and flute as sax. The clarinet was most easily identified, in agreement with Saldanha and Corso's (1964) finding.

C. Human perception experiment

None of the published human perception studies was carried out with exactly the same instruments as were used in these calculations; for the most part, they were carried out on single notes. For purposes of comparison, therefore, we conducted a free classification experiment on short solo segments of music played by the oboe, sax, clarinet, and flute. In many cases these were the same segments used for the calculations.

Fifteen musicians were asked to classify 60 sound samples into as many categories as they wished, but to make no distinction regarding the register of instrument, e.g., soprano or alto. They organized the sounds into five major groups. If four of these groups are named for the instrument with the most sounds present (one group was a mixture of several instruments), then the percent correct is given in the last row of Table I. More details on this experiment will be given in a subsequent paper (Houix, McAdams and Brown, unpublished).

Confusions were on average small, with no overall pattern. The overall percent correct for all classifications is 85%, which is close to the results for the computer calculations.

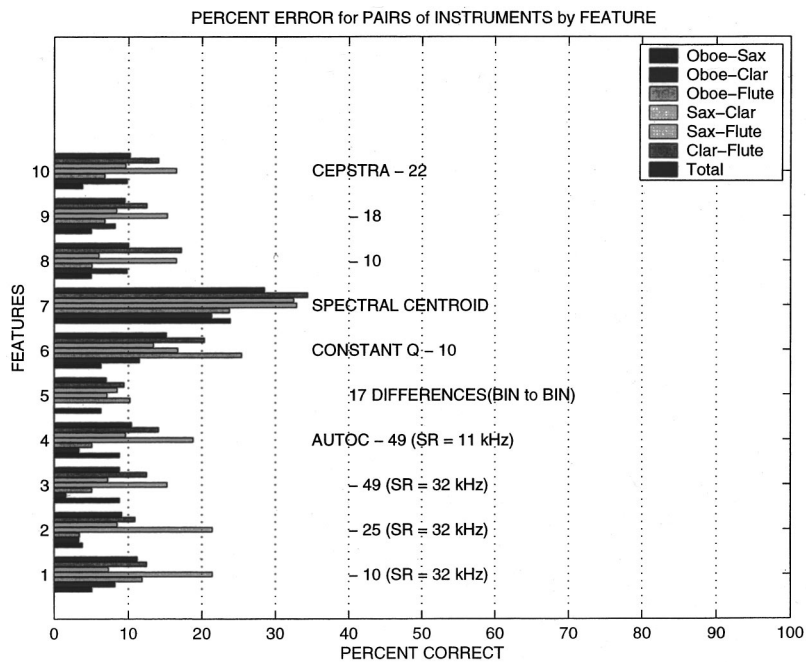


FIG. 5. Errors in identification of pairs of instruments. Instruments are given in the legend. The total represents the total number of errors divided by the total number of decisions for all pairs for a given feature set. Note that data are in inverse order from captions.

V. CONCLUSIONS

The success of cepstral coefficients (77% correct) for identification indicates that these woodwind instruments have distinct formant structures and can be categorized with the same techniques used for speaker/speech studies. Spectral smoothness (bin-to-bin differences of the constant- Q spectrum) was also effective (over 80% correct) and indicates a characteristic shape of the spectrum for sounds produced by these instruments. The success of these features is due to the property that individual components of their feature vectors are uncorrelated.

The actual numerical percentage correct for these sounds is dependent on the particular training set and number of clusters chosen. The choice of training sounds is generalizable for a randomly chosen set of test sounds with about a 10% drop in accuracy.

Most important, several sets of features can be used for computer identification of the oboe, sax, clarinet, and flute with 75%–85% accuracy. Because a much larger test set was used than in previous studies, the feature sets and methods used are applicable to arbitrary examples of these instruments. These results are as good or better than results on human perception and indicate that the computer can do as well as humans on woodwind instrument identification under the present conditions.

ACKNOWLEDGMENTS

J.C.B. is very grateful to the Marilyn Brachman Hoffman Committee of Wellesley College for a fellowship supporting this study. Part of this work was carried out during a sabbatical leave by J.C.B. tenured in the Music Perception and Cognition group at IRCAM and was made possible by Wellesley College's generous sabbatical leave policy. Finally, thanks go to Peter Cariani for suggesting the use of autocorrelation coefficients as features, and to Dan Ellis and Douglas Reynolds for valuable e-mail discussions.

APPENDIX: TERMS USED IN PATTERN RECOGNITION AND THE METHOD OF CLUSTERS

Pattern recognition—A method in which a set of unknown patterns called the *test set* is grouped into two or more *classes* by comparison to a *training set* consisting of patterns known to belong to each class.

Features—also called *feature vectors*—Properties (the patterns) calculated for the test set which are compared to the same properties of the training set for classification. In general, a feature has N associated values and can be considered an N -dimensional vector, e.g., for autocorrelation coefficients, each lag time gives one component of the vector.

Clustering—a means of summarizing the calculations on members of the training set to simplify comparison to the test set. In the calculation described in this paper, a feature vector is calculated every 16 ms for each training sound, each time contributing a point in an N -dimensional feature space. These data are summarized by grouping nearby points into *clusters* each with a mean μ , standard deviation σ , and probability p given by the number of points in that cluster divided by the total number of points for the sound.

Gaussian mixture model—A probability density function is formed as a sum of Gaussian functions obtained from the means, standard deviations, and probabilities for each cluster of a given member of the training set. This is described in more mathematical detail in Sec. III.

- Beauchamp, J. W. (1982). "Synthesis by spectral amplitude and brightness matching of analyzed musical instrument tones," *J. Audio Eng. Soc.* **30**, 396–406.
- Berger, K. W. (1964). "Some factors in the recognition of timbre," *J. Acoust. Soc. Am.* **36**, 1888–1891.
- Brown, J. C. (1997). "Cluster-based probability model for musical instrument identification," *J. Acoust. Soc. Am.* **101**, 3167.
- Brown, J. C. (1998a). "Computer identification of wind instruments using cepstral coefficients," *J. Acoust. Soc. Am.* **103**, 1889–1890(A).
- Brown, J. C. (1998b). "Musical instrument identification using autocorrelation coefficients," Proceedings of the International Symposium on Musical Acoustics 1998, Leavenworth, Washington, pp. 291–295.
- Brown, J. C. (1999). "Computer identification of musical instruments using pattern recognition with cepstral coefficients as features," *J. Acoust. Soc. Am.* **105**, 1933–1941.
- Campbell, W. C., and Heller, J. J. (1978). "The contribution of the legato transient to instrument identification," in Proceedings of the Research Symposium on the Psychology and Acoustics of Music, edited by E. P. Asmus, Jr. (University of Kansas, Lawrence, KS), pp. 30–44.
- Clark, M., and Milner, P. (1964). "Dependence of timbre on the tonal loudness produced by musical instruments," *J. Audio Eng. Soc.* **12**, 28–31.
- Dubnov, S., and Rodet, X. (1998). "Timbre recognition with combined stationary and temporal features," Proceedings of the International Computer Music Conference, Los Angeles.
- Dubnov, S., Tishby, N., and Cohen, D. (1997). "Polyspectra as measures of sound texture and timbre," *J. New Music Res.* **26**, 277–314.
- Eagleson, H. V., and Eagleson, O. W. (1947). "Identification of musical instruments when heard directly and over a public-address system," *J. Acoust. Soc. Am.* **19**, 338–342.
- Hajda, J. M., Kendall, R. A., Carterette, E. C., and Harshberger, M. L. (1997). "Methodological issues in timbre research" in *Perception and Cognition of Music*, edited by Irene Deliege and John Sloboda (Psychology, East Essex, UK), pp. 253–307.
- Handel, S. (1995). "Timbre perception and auditory object identification," in *Hearing*, edited by B. C. J. Moore (Academic, New York).
- Hartmann, W. M. (1998). *Signals, Sound, and Sensations* (Springer, New York, Secaucus, NJ).
- Houix, O., McAdams, S., and Brown, J. C. (unpublished).
- Kanal, L. (1974). "Patterns in pattern recognition 1968–1974," *IEEE Trans. Inf. Theory* **IT-206**, 697–722.
- Kendall, R. A. (1986). "The role of acoustic signal partitions in listener categorization of musical phrases," *Music Percept.* **4**, 185–214.
- Macho, D., Nadeu, C., Janovic, P., Rozinaj, G., and Hernando, J. (1999). "Comparison on time and frequency filtering and cepstral-time matrix approaches in ASR," Proceedings of Eurospeech '99, Vol. 1, pp. 77–80.
- Marques, J. (1999). "An automatic annotation system for audio data containing music," Master's thesis, MIT, Cambridge, MA.
- Martin, K. D. (1999). "Sound-source recognition: A theory and computational model," Ph.D. thesis, Massachusetts Institute of Technology, Cambridge, MA.
- McAdams, S. (1993). "Recognition of Auditory Sound Sources and Events," in *Thinking in Sound: The Cognitive Psychology of Human Audition*, edited by S. McAdams and E. Bigand (Oxford University Press, Oxford).
- McAdams, S., Beauchamp, J. W., and Meneguzzi, S. (1999). "Discrimination of musical instrument sounds resynthesized with simplified spectrotemporal parameters," *J. Acoust. Soc. Am.* **105**, 882–897.
- Moorer, J. A. (1975). "On the segmentation and analysis of continuous musical sound by digital computer," Ph.D. dissertation, Stanford Department of Music Report No. STAN-M3.
- O'Shaughnessy, D. (1987). *Speech Communication: Human and Machine* (Addison-Wesley, Reading, MA).
- Rabiner, L. R., and Huang, B.-H. (1993). *Fundamentals of Speech Recognition* (Prentice Hall, Englewood Cliffs, NJ).

- Reynolds, D. A., and Rose, R. C. (1995). "Robust text-independent speaker identification using Gaussian mixture speaker models," *IEEE Trans. Speech Audio Process.* **3**, 72–83.
- Saldanha, E. L., and Corso, J. F. (1964). "Timbre cues and the identification of musical instruments," *J. Acoust. Soc. Am.* **36**, 2021–2026.
- Schmid, C. E. (1977). "Acoustic Pattern Recognition of Musical Instruments," Ph.D. thesis, University of Washington.
- Strong, W., and Clark, M. (1967a). "Perturbations of synthetic orchestral wind-instrument tones," *J. Acoust. Soc. Am.* **41**, 277–285.
- Strong, W., and Clark, M. (1967b). "Synthesis of wind-instrument tones," *J. Acoust. Soc. Am.* **41**, 39–52.
- Wilcox, L., Kimber, D., and Chen, F. (1994). "Audio indexing using speaker identification," ISTL Technical Report No. ISTL-QCA-1994-05-04.

The feasibility of maximum length sequences to reduce acquisition time of the middle latency response

S. L. Bell,^{a)} R. Allen, and M. E. Lutman

Institute of Sound and Vibration Research, University of Southampton, Highfield, SO17 1BJ Southampton, United Kingdom

(Received 28 February 2000; revised 25 May 2000; accepted 21 November 2000)

Maximum length sequences (MLS) have been used to improve the signal-to-noise ratio (SNR) of otoacoustic emissions [Thornton, *J. Acoust. Soc. Am.* **94**, 132–136 (1993)] and the auditory brainstem response [Thornton and Slaven, *Br. J. Audiol.* **27**, 205–210 (1993)]. By implication, a shorter recording time would be required to give equal signal-to-noise ratio (SNR). This study aimed to establish whether it is also possible to improve the SNR of the auditory-evoked potential termed the middle latency response (MLR) using maximum length sequences (MLS). Recordings of 180 s each were made using a conventional recording rate and MLS rates of 42, 89, and 185 clicks/s. Three different stimulus intensities were used in the range 30 to 70 dB nHL. The rate of 89 clicks/s was found to produce most improvement in SNR for both the N_a-P_a region of the MLR and the N_a-P_b region. This improvement in SNR using MLS implies that an MLS rate of 89 clicks/s would produce a fourfold reduction in recording time for equal SNR over conventional recording for the P_a-N_b region of the MLR at a stimulus intensity of 70 dB nHL. The latency of the N_b wave was found to reduce significantly using MLS. An MLR could not be recorded from every subject in this study, but more subjects had an identifiable response for MLS than for conventional recordings. Use of MLS to record the MLR appears to offer the potential for reduction in test time and better wave identification. © 2001 Acoustical Society of America. [DOI: 10.1121/1.1340645]

PACS numbers: 43.64.Ri, 43.64.Yp [LHC]

I. INTRODUCTION

Reducing the recording time of auditory-evoked potentials is almost always desirable, either because there is limited time available to make a recording on a subject or because a large number of recordings have to be made. The middle latency response (MLR) is an auditory-evoked potential which is usually elicited using click stimuli and which occurs approximately 20 to 70 ms after the stimulus. It varies in amplitude from tenths of a microvolt to a few microvolts and is embedded in the spontaneous EEG waveform which has an amplitude typically of 10 to 30 μV (Elkfafi *et al.*, 1997). Thus, the signal-to-noise ratio (SNR) is less than 1:10 (–20 dB). The MLR waveform has a characteristic pattern with six features. These are three negative waves (N_a , N_b , and N_c) and three positive peaks (P_a , P_b , and P_c).

The traditional method for improving the SNR of auditory-evoked potentials is to use a synchronized average of many successive responses, where the onset of the stimulus triggers the synchronization process. Theoretically, for n averages, the SNR increases by a factor \sqrt{n} . The maximum length sequence technique (MLS; Eysholdt and Schreiner, 1982) allows a higher stimulation rate to be used than for conventional MLR by overlapping successive recording epochs. A particular deconvolution technique is then used to extract the responses which overlap in time. A maximum length sequence is a pseudorandom binary sequence (PRBS). An MLS sequence of order b (where b is an integer) is of length $2^b - 1$ (stimulus opportunities) and contains $2^{(b-1)}$

stimuli. MLS order 1 is the redundant case of a conventional stimulation pattern. Table I shows the MLS sequences used for orders 3, 4, and 5.

In conventional MLR recording, successive responses do not overlap. As the MLR occurs up to 70 ms after the auditory stimulus, the highest stimulation rate that can be used with the conventional technique is 14 clicks/s. If, instead, responses are allowed to overlap using MLS, higher stimulus rates can be achieved. MLS has been used to improve the recording time of transient-evoked otoacoustic emissions (Thornton, 1993) and it has been demonstrated that MLS can be used to record auditory-evoked potentials such as the auditory brainstem response (ABR) (Burkard, Shi, and Hecox, 1990; Burkard, 1991; Lina-Granada, 1994; Jiang, 1999) and the MLR (Picton, Champagne and Kellett, 1992; Musiek and Lee, 1997). Thornton and Slaven (1993) have suggested that it might be possible to reduce the recording time of the ABR using MLS; however, no studies have assessed the possible reduction in the recording time of the MLR by using MLS. An important application of the MLR may be for measuring depth of anesthesia of patients undergoing surgery. A number of recent studies have demonstrated auditory-evoked potentials (AEPs) to be a more reliable indicator of unconsciousness than the EEG (Doi *et al.*, 1997; Thornton, 1991). For example, Gajraj *et al.* (1998) compared three indices derived from the EEG and one index derived from the MLR in their ability to distinguish the state of consciousness of patients as they passed repeatedly from consciousness to unconsciousness while undergoing orthopaedic surgery. The AEP index that they used represents the configuration of the MLR (Mantzariadis and Kenny, 1997).

^{a)}Electronic mail: slb@isvr.soton.ac.uk

TABLE I. The MLS sequences used in the study.

Order	Length	Stimulation sequence (1 corresponds to a click, 0 to a silence)
3	7	1101100
4	15	100110101111000
5	31	1001011001111100011011101010000

They found that only the AEP index demonstrated a significant difference on all mean values 1 minute before recovery of consciousness and all mean values 1 min after recovery of consciousness. Furthermore, the AEP index demonstrated the highest sensitivity of all the measures for detecting unconsciousness.

Although the exact relationship between MLR components and awareness is still controversial (Jessop and Jones, 1992), Thornton and Newton (1989) have demonstrated that the latencies and amplitudes of the midlatency waves change to both inhaled and intravenous agents. With increased anesthetic dose, latency increases and amplitude decreases. Furthermore, N_b latencies shorter than about 45 ms appear to correspond to awareness, as demonstrated with the isolated forearm technique. Also, the configuration of the waveform changes so that at light stages of anesthesia all three peaks are seen, at a moderate depth of anesthesia only P_a and P_b are seen, and at a deeper level of anesthesia than is desirable, none of the peaks is seen (Elkfafi *et al.*, 1997).

Typically, to obtain an MLR trace when monitoring depth of anesthesia in surgery, a rolling average of 1000 clicks is used which is regularly updated (say, every 50 clicks). The responsiveness of the change in this moving average estimator to a change in anesthesia is crucial. At 5.95 clicks per s, averaging 1000 clicks to fully update the average takes 168 s. This is too slow to monitor potentially rapid changes in depth of anesthesia. The MLR has therefore been criticized for this purpose due to recording times of 3 to 5 min (Heier and Steen, 1996).

An alternative to improve acquisition time of the MLR has been developed by Elkfafi *et al.* (1997) and uses signal estimation. If the average of fewer responses is taken to obtain the MLR (e.g., 192 sweeps), the signal obtained will be noisier, but it will be obtained faster (31 s). Using an algorithm based upon an autoregressive model with exogenous input (ARX), an estimate of the true waveform can be obtained from the noisy trace (Cerutti *et al.*, 1987). This trace can then be fed into a fuzzy logic control system for the purpose of control of anesthesia. However, the drawback of such an approach is that it uses an estimate of the signal for control, rather than the true signal, which could only be obtained by averaging more responses. The estimate of the signal obtained from the model may therefore differ from the true signal and may make the control system less reliable. (The ARX modeling reduces degrees of freedom and hence increases the confidence interval surrounding the signal estimate.)

It is more desirable to derive the true signal using a large number of responses, thus preserving the degrees of freedom, but in a shorter time. This may be possible with MLS. However, when a higher MLS stimulation rate is used, the neural

response to the stimulus adapts and reduces in size. There is therefore a trade-off between the improvement in SNR with high MLS stimulation rates as more stimuli are recorded and averaged in a given time period and the reduction in SNR due to neural adaptation. The question arises when MLS is applied to the MLR as to whether the improvement in SNR with rate exceeds the deterioration due to adaptation. The main aim of this study was therefore to test the hypothesis that the MLS technique can be used to increase SNR, or by implication, reduce the time required to record the MLR for a given SNR.

II. METHOD

A study of subjects with normal hearing was performed in which the MLR was recorded at different click stimulus levels for equal time periods using both a conventional rate (5.95 clicks per s) and higher MLS stimulation rates (up to 185 clicks per s). The principle was that peak amplitudes of the traces obtained were used to calculate relative SNRs of recordings. These were used to infer whether an MLS recording of equal SNR to the conventional recording could have been obtained in a shorter time.

A. Determination of signal-to-noise ratio

With conventional averaging, if a signal of amplitude S embedded in random noise amplitude N is averaged over n sweeps, the signal-to-noise ratio is given by $S\sqrt{n}/N$. When using high stimulation rates, the response S will be reduced by a factor k due to adaptation, so the SNR is also reduced by a factor of k . Furthermore, each sequence of MLS contains noise from $2^b - 1$ stimulus opportunities but only $2^{(b-1)}$ stimuli, so the SNR of an MLS sequence is further reduced by a factor $c = 2^{(b-1)}/2^b - 1$. If averaged over m stimulus opportunities, the SNR using MLS is given by $ck\sqrt{mS}/N$.

If the conventional recording rate is r_o , the MLS rate is r , and the recording time used is t , then $n = r_o t$ and $m = r t$ (Note that here the MLS rate used is the peak stimulation rate or stimulus opportunity rate, i.e., the inverse of the minimum interval between clicks in the sequence. In an MLS sequence, not all stimulus opportunities are filled with stimuli, and the stimuli are presented quasirandomly, so in some studies of MLS, the average stimulation rate is quoted instead of the peak stimulation rate.)

Then, the relative SNR (MLS to conventional) is given by

$$\frac{\text{SNR}_{\text{MLS}}}{\text{SNR}_{\text{CONV}}} = ck \sqrt{\frac{r}{r_o}} \quad (1)$$

(Thornton, 1993).

By measuring k (the ratio of the MLS amplitude to that of the conventional amplitude), the SNR of the conventional and MLS recordings can be compared. In the present study, two measures of amplitude were used to estimate relative SNR between MLS and conventional recordings: the $P_a - N_a$ and the $N_a - P_b$ amplitudes (peak-to-peak amplitudes). For each recording condition, the amount of neural adaptation, k ,

was determined by dividing the MLS amplitude by the conventional amplitude (amplitudes were averaged across the two recording sessions).

An alternative to using relative wave amplitudes to estimate relative SNR might be to estimate actual SNR in each based on the \pm difference method (Wong and Bickford, 1980). This compares two recordings made in the same conditions to estimate SNR. However, in the present study recordings were repeated on each subject on different days as it was deemed desirable to assess the test–retest reliability of MLR recordings across different recording sessions. It is unlikely that either signal or noise conditions were identical for the two recordings sessions, so use of the \pm difference is of limited validity.

B. Subjects

To determine the number of subjects required for the study, an estimate was made of the likely variation in peak amplitude that would be detectable. For a pooled standard deviation of $0.10 \mu\text{V}$, a sample size of 18 would allow a difference of means as small as $0.06 \mu\text{V}$ to be detected with a power of 0.80 and a significance of 0.05. In fact, 20 subjects were included. These were taken from a student population at the University of Southampton. There were ten male and ten female subjects. The mean age was 24.3 years. To minimize effects of age and hearing impairment, subjects included in the study were otologically normal. They were aged between 18 and 30 years with hearing threshold levels better than 20 dB throughout the range 500–4000 Hz in each ear and all had normal tympanograms. No subjects had a history of ear disease or undue noise exposure.

C. Stimuli

Three click stimulation levels nominally at 30, 50, and 70 dB nHL were used.¹ Here, “dB nHL” refers to the level of the click above the mean threshold level of subjects, as determined by a preliminary experiment (see below). The order of stimulation level was rotated between subjects. At each stimulation level, recordings were made at a conventional stimulation rate of 5.95 clicks/s. Three MLS stimulation sequences of order 3, 4, and 5 were used which have corresponding peak stimulation rates of 42, 89, and 185 clicks/s, respectively (these correspond to average stimulation rates of 24, 47, and 95 clicks/s). To prevent stimulation order effects, the order of stimulation at each level given to each subject (in terms of MLS order) was varied using five different consecutive Latin squares.

The study was carried out in a soundproof booth. Auditory click stimuli were delivered to subjects’ right ears through an insert earphone (Etymotic ER-3A) via a Kamplex KC50 audiometer. To prevent cross hearing, the left ear received a broadband masking noise at 40 dB below the click stimulation level through a similar insert earphone. Relaxing subjects reduces electrophysiological noise and hence subjects were seated in a comfortable chair with a headrest. Room temperature was maintained as near to 26 °C as possible (which minimizes the metabolic activity needed by a subject to maintain body temperature) and ranged from 24 to

28 °C. To reduce electrical interference, screened cables were used and the biological amplifier (see below) was placed near the subject.

With an audiometer dial setting of 90 dB, click stimuli had a mean level of 80.1 dB peak-equivalent SPL. It was also desirable to know the click level in dB nHL. For this to be calculated a preliminary study was performed to find the average threshold of normal subjects to the clicks presented at the conventional rate of 5.95 Hz. From this study, the mean click threshold dial setting was 39.3 dB and the mean pure-tone threshold averaged between 2 and 4 kHz was 3.3 dB HL. This is a difference of 36.0 and indicated that an audiometer dial setting of 90 dB corresponds to 54 dB nHL.

D. Equipment

Maximum length sequences were generated and recorded using a computer-controlled CEDmicro1401 laboratory interface containing analog-to-digital and digital-to-analog converters and CED1902 biological amplifiers. When recording MLS, the sequences need to be generated contiguously, with no gaps between sequences. For each experimental condition, an appropriate sequence was loaded into an output buffer in the CEDmicro1401 and this was then repeated cyclically at a sample rate of 10 kHz. The output sequence could consist of either a single click for conventional recording, or a maximum length sequence of order 3, 4, or 5 which contains several clicks. A click consisted of a 0.1-ms (one sample) 5-V square wave output from the CEDmicro1401. An output sequence of 168 ms therefore corresponded to 1680 possible click opportunities. Note that this is a lowest common multiple of the lengths of MLS order 2, 3, and 4 (3, 7, and 15), but not of order 5. The buffer length therefore had to be changed to 1674 for MLS order 5 (length 31) so that an exact number of sequences could fit into the output buffer.

The CEDmicro1401 sampled the outputs of the biological amplifiers at a rate of 10 kHz. Samples were placed into buffers of length 168 ms which were the same length as the continuously repeating stimulus output buffer (corresponding to a repeat rate of 5.95 Hz—the conventional stimulation rate.) Two buffers were used cyclically and their contents were alternately transferred to the computer for checking and averaging. Hence, while one buffer was acquiring data, the other was being transferred and analyzed. This process was effected by software specifically written for this purpose.

Analog filters were set to 1 Hz (high pass) and 100 Hz (low pass). Hall (1992) suggested that a high-pass filter setting of 15 Hz is optimal for the MLR, so the averaged data were also digitally high-pass filtered off-line at 15 Hz.

E. Recording the MLR

Auditory-evoked responses to the clicks were picked up by three silver–silver chloride electrodes placed on the skin: active electrode on the vertex of the head, ground electrode on the forehead, and reference electrode on the mastoid of the right ear after skin preparation. Recordings were made with impedances of less than 5 kohms between all pairs of the electrode array.

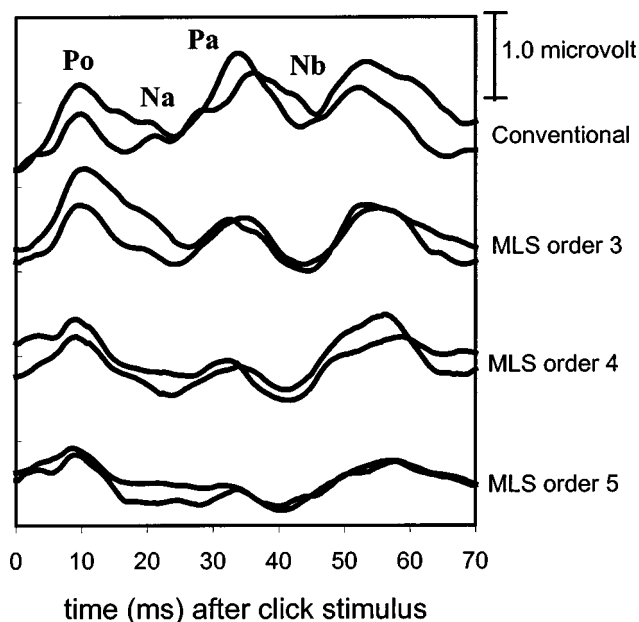


FIG. 1. Waveform morphology for a typical subject.

The same 12 recording conditions were used for each subject on two separate occasions (a total of 24 recordings). The mean time between recordings was 10.25 days. Subjects were tested at approximately the same time of day on each occasion. The same duration was used for each measurement and was sufficient for 1000 click responses to be recorded at the conventional recording rate of 5.95 clicks/s (168 s).

During recording, artifact rejection was utilized so that noisy responses were not included in the average. The amplitude criterion for artifact rejection was varied between subjects and conditions. It was chosen by the experimenter such that approximately 95% of sweeps were accepted on average (so that recording time was not unduly extended). There were no significant differences in the amount of artifact rejection between the orders of MLS used (see below). The overall percentage of sweeps accepted was 93.3%. This meant that the recording time of the MLR was extended from 168 to 180.2 s (3 min) on average once artifact rejection time was added.

III. RESULTS

A. Waveform morphology

Figure 1 displays typical MLRs recorded from one subject at a click intensity of 70 dB nHL for each order of MLS used. The two recordings, made on separate occasions, are overlaid. Some variation is seen between the recordings from the different occasions (which occurred to varying degrees for all subjects).

Wave P_o due to the ABR occurs approximately 10 ms after the stimulus, N_a , at around 25 ms, P_a at around 33 ms, and N_b at around 42 ms. For this subject, a P_b wave at around 55 ms can also be seen.

B. Wave detection rates

The rating of the presence and measurement of amplitudes and latencies of the N_a , P_a , and N_b waves of the

TABLE II. Wave detection rates.

Click intensity	MLS order	MLR wave			Overall
		N_a	P_a	N_b	
29 dB nHL	1	93%	83%	75%	83%
	3	95%	93%	78%	88%
	4	93%	90%	88%	90%
	5	88%	78%	88%	84%
	Means	92%	86%	82%	86%
49 dB nHL	1	90%	88%	78%	85%
	3	95%	93%	83%	90%
	4	88%	93%	90%	90%
	5	85%	78%	88%	83%
	Means	89%	88%	84%	87%
69 dB nHL	1	95%	85%	80%	87%
	3	95%	95%	93%	94%
	4	93%	95%	90%	93%
	5	93%	90%	88%	90%
	Means	93%	91%	88%	91%

MLR waveforms were carried out by the first author.² For each of the three waves of the MLR (N_a , P_a , and N_b), the percentage of responses with an identifiable wave present was calculated for each order of MLS and each click intensity used. For each condition a total of 40 recordings was made (two for each subject).

Table II shows the wave detection rates for each of the MLR waves and for the three waves combined. It can be seen that at each click intensity, MLS orders 3 and 4 produced higher overall wave detection rates than conventional recording. The greatest number of peaks was identified at the highest click stimulation level (70 dB nHL). A total of 87.5% of N_b waves was identified. Not all subjects had an identifiable N_b wave. One subject had no identifiable MLR waves. Recordings from this subject appeared to have interference from a large postauricular muscle response and attempts to relax the subject did not result in a repeatable MLR.

C. Test-retest reliability

For each subject, MLR recordings were made on two separate occasions for each of the 12 recordings conditions used. This meant that the test-retest reliability of wave amplitudes and wave latencies of recordings could be characterized using Pearson correlation coefficients.

The overall correlation between wave amplitudes (N_a , P_a , and N_b waves) was 0.76 ($P < 0.0001$) and for wave latencies was 0.70 ($P < 0.0001$). The mean amplitude was 0.28 μV (s.d. 0.17) and the mean difference in amplitude between recordings was 0.022 μV (s.d. 0.15). Hence, the amplitude replication s.d. was 0.11 μV ($0.15/\sqrt{2}$). The mean latency was 31.80 ms (s.d. 9.63) and the mean difference in latency between recordings was 0.22 ms (s.d. 3.41). Hence, the latency replication s.d. was 2.41 ms ($3.41/\sqrt{2}$).

Test-retest correlations for each order of MLS used were also calculated. Correlations for all orders were highly significant. As wave latency and amplitude were each highly correlated between recording sessions, averages across the

TABLE III. Mean raw wave amplitudes in μV (averaged across subjects and recording sessions). Standard deviations are shown in parentheses.

Stimulation intensity	MLR wave	MLS order			
		1	3	4	5
30 dB nHL	N_a-P_a	0.74 (0.23)	0.50 (0.16)	0.46 (0.15)	0.26 (0.08)
	P_a-N_b	0.59 (0.24)	0.48 (0.15)	0.44 (0.17)	0.30 (0.12)
50 dB nHL	N_a-P_a	0.88 (0.31)	0.64 (0.22)	0.53 (0.15)	0.28 (0.10)
	P_a-N_b	0.64 (0.28)	0.54 (0.23)	0.54 (0.22)	0.31 (0.12)
70 dB nHL	N_a-P_a	0.97 (0.32)	0.68 (0.22)	0.71 (0.28)	0.34 (0.13)
	P_a-N_b	0.72 (0.26)	0.56 (0.25)	0.63 (0.24)	0.37 (0.15)

two sessions were taken when calculating SNRs from wave amplitudes and for statistics on wave latencies.

D. Comparison of signal-to-noise ratio

It is desirable to compare the SNRs of MLS and conventional recordings. The amplitude of an MLS recording can be multiplied by a correction factor (“adjusted”) so that when the adjusted MLS amplitude equals that of the conventional recording, the SNRs of the two recordings are equal. From Eq. (1) for the comparison of MLS and conventional SNR above, and putting $r=(2^b-1)r_o$ and $c=2^{(b-1)}/2^b-1$, then for MLS and conventional recording to have equal SNR

$$\text{amp}_{\text{MLS}} \frac{2^{b-1}}{\sqrt{2^b-1}} = \text{amp}_{\text{CONV}},$$

where $2^{b-1}/\sqrt{2^b-1}$ equals 1.51 (MLS order 3), 2.07 (MLS order 4), and 2.87 (MLS order 5). If amp_{MLS} is significantly greater than this, the MLS recording will have a greater SNR than the conventional recording. Therefore, for the purposes of statistical analysis, the MLS peak-to-peak amplitudes were multiplied by the appropriate correction factors shown above according to the order of MLS used. Repeated measures analysis of variance and *post hoc* paired *t* tests were then used to test whether the adjusted MLS peak-to-peak amplitudes were significantly different from the conventional peak-to-peak amplitudes for the N_a-P_a difference and the P_a-N_b difference, at each click intensity.

The variation of MLR wave amplitudes with stimulus intensity and MLS order are shown in Table III along with standard deviations. One-sample Kolmogorov–Smirnov tests showed that the distribution of the transformed data did not differ significantly from a normal distribution and hence parametric statistics were applied. Repeated measures analysis of variance was used to test for an effect of rate on the adjusted amplitudes (amplitude being the dependent-variable, rate the within-subject factor). For the N_a-P_a and P_a-N_b waves at all stimulus intensities, a significant within-subject effect of rate on adjusted amplitude was seen ($p < 0.05$). *Post hoc t* tests were then used to evaluate which orders of MLS produced most increase in adjusted amplitude.

For the N_a-P_a amplitude, MLS order 4 had a significantly higher ($p < 0.005$) adjusted amplitude than the conventional recordings at all stimulus intensities. This corresponds to an improved SNR. There was no significant

difference between the conventional recording amplitude and the adjusted amplitudes for MLS orders 3 and 5.

For the P_a-N_b amplitudes, all orders of MLS showed significantly larger adjusted amplitudes than the conventional recordings ($p < 0.05$) at all stimulus intensities, with the exception of order 3 at 30 dB nHL, which did not have a significantly different adjusted amplitude from the conventional recording. Almost all the MLS recordings showed an improved SNR over conventional recordings for this part of the MLR.

From Eq. (1), the inferred relative test speed between MLS and a conventional recording, when run to equal SNR, is given by

$$\text{Relative speed} = c^2 k^2 \frac{r}{r_o}.$$

Relative test speeds based on the N_a-P_a and P_a-N_b amplitudes are shown in Figs. 2 and 3. Outlier analysis was performed and data lying outside the interquartile range by an amount equal to three times the interquartile range were excluded. The mean relative test speed across subjects has been used.³ For both the N_a-P_a waves and the P_a-N_b waves there is a test speed advantage and this is greater for 50- and 70- dB nHL stimulus intensity than for 30 dB nHL. The improvement in test speed is greater for the P_a-N_b waves. For the P_a-N_b waves, the maximum calculated speed im-

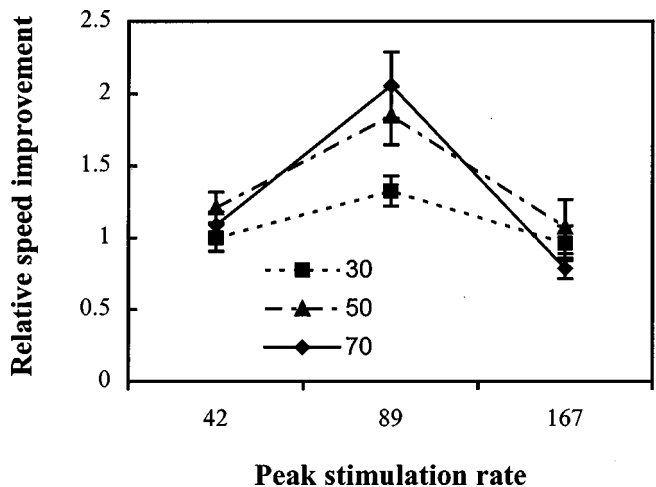


FIG. 2. Relative test speed of MLS recordings to conventional recordings as a function of stimulus intensity and rate calculated from raw N_a-P_a amplitudes. Error bars represent one standard error of the mean.

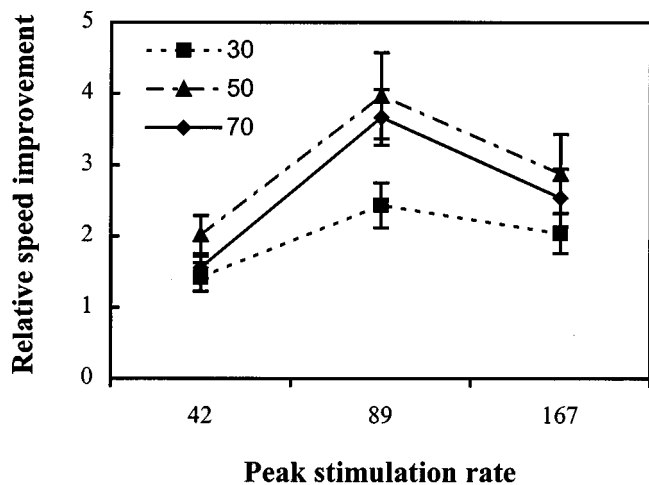


FIG. 3. Relative test speed of MLS recordings to conventional recordings as a function of stimulus intensity and rate calculated from raw P_a-N_b amplitudes. Error bars represent one standard error of the mean.

provement is 3.7 times for MLS order 4 at 50 dB nHL. This would represent a test time reduction from 180 to 49 s.

E. Latency variation with increasing stimulus rate

The present study investigated whether MLS recording of the MLR results in a change in wave latency. Figure 4 shows variation in latency of the N_a , P_a , and N_b waves with peak stimulation rate. It appears that wave latency reduces with increasing click rate. Repeated measures analysis of variance showed a significant within-subject effect of rate ($p < 0.05$) for all waves and stimulus intensities apart from the N_b wave at 30 dB nHL.

IV. DISCUSSION

A. Test speed improvement using MLS

From the present study, MLS order 4 was shown to produce the best inferred improvement in test speed for the MLR. Figures 2 and 3 show the assumed improvement in test speed for different MLS peak stimulation rates and different stimulus intensities calculated using a derivation of test time based on the N_a-P_a and P_a-N_b amplitudes, respectively. It can be seen that MLS order 4 (89.25 opportunities/s) shows an improvement in test time for all stimulus intensities. MLS order 4 represents the best balance between increase in recording time with stimulation rate and decrease in response size with stimulus rate due to neural adaptation.

Of course, simply increasing the conventional recording rate may result in a reduction in test time. Van Veen and Lasky (1994) have demonstrated that for the ABR, MLS cannot reduce recording time more than can be achieved by using the optimal conventional recording rate. Unfortunately, we did not explore this parameter space and so it is unclear whether the time advantage found in this study is only true when referenced to 5.95 Hz. However, for a MLR of up to 70 ms, the maximum conventional click rate obtainable is 14 clicks/s which would represent a 2.3 times reduction in test

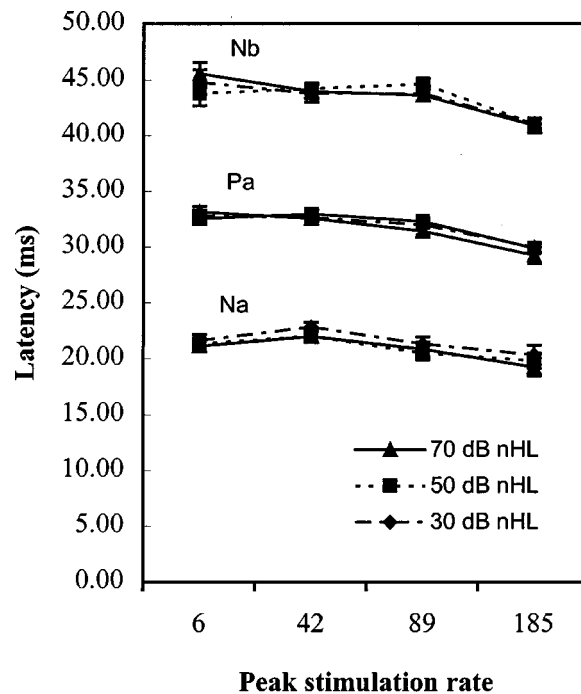


FIG. 4. Latency variation with peak stimulation rate. Error bars represent one standard error of the mean.

time assuming no adaptation of the response amplitude with rate. This is not as great as the 3.7 times reduction in test time using MLS found in this study.

Improvement in relative test speed also increases with stimulus intensity. This increase with stimulus intensity is consistent with the findings of Leung (1996), who also found an improvement with stimulus intensity when recording the ABR at different MLS rates.

The maximum speed improvement found in the present study was 3.7 times, using MLS order 4 at a click intensity of 50 dB nHL. This might represent a reduction in test time from 180 to 49 s, which would represent a significant improvement if the MLR is used as an indicator of depth of anesthesia. The MLR has been criticized as a possible indicator due to recording times of 3 to 5 minutes (Heier and Steen, 1996). Although there is no defined criterion as to what is an acceptable recording time, a recording time of under a minute appears to have reasonable face validity and would allow a more rapid assessment of changes in the depth of anesthesia of a patient. Of course, simply increasing the conventional recording rate from 6 clicks/s may reduce recording time, although this was not assessed in this study.

An interesting finding from the present study is that MLS appears to produce greater improvement in recording speed for the P_a-N_b segment of the MLR than for the N_a-P_a segment. The maximum improvement for the N_a-P_a segment was 2.1 times, and for P_a-N_b was 3.7 times using MLS. A possible explanation might be that different regions of the auditory pathway are responsible for producing the N_a-P_a and P_a-N_b segments of the MLR.

The improvement in MLR recording speed of 3.7 times found in this study is not quite as great as that obtained by some signal processing methods. For example, the method of Elkfafi *et al.* (1997) [autoregressive model with exogenous

input (ARX)] reduced the MLR recording time to 32 s. However, such models are based on an assumption regarding the morphology of the underlying MLR. If change in the morphology of the MLR is to be used as an indicator of anesthetic depth, then it is important not to introduce distortions in the morphology by making assumptions regarding that morphology and fitting data around the assumptions. MLS has the advantage that no assumptions are made regarding the morphology of the underlying MLR and so it records a “true” morphology. Although it may be slightly slower than ARX modeling in recording the MLR, there is no risk of the model distorting the latencies of the MLR waves. This is particularly critical if N_b wave latency is to be used as the basis of a control system for administration of an anesthetic agent.

B. The usefulness of the MLR in assessing anaesthetic depth

This study has addressed some of the issues concerning whether the MLR is a viable measure to be used as an indicator of anesthetic depth. In particular, the number of subjects possessing an MLR was measured, as was the test–retest reliability of the MLR measurement.

If N_b wave latency is to be used as an indicator of anesthetic depth, it is necessary for subjects to have a recordable N_b wave. Table II shows the detectability of the N_a , P_a , and N_b waves of the MLR for different recording conditions. An important finding is that the detectability of N_b waves is not 100%. Indeed, for conventional recordings at 70 dB nHL stimulus intensity, the N_b wave only had 87% detectability. This would imply that use of the MLR as an indicator of depth of anesthesia is not possible for all subjects. There was one subject in this study from whom no clear MLR could be recorded. Recordings from this subject appeared to have interference from muscle activity. While muscle artifact interference is a negative indicator for using the MLR to measure depth of anesthesia in surgery, muscle activity reduces when a patient is relaxed under anesthesia, so the MLR may become more detectable and in operations in which a muscle relaxant is given to a patient, such muscle activity is almost abolished. Furthermore, it may not be possible to record an MLR from subjects who do not have normal hearing, or from young children in whom the MLR response is not fully developed (Hall, 1992).

It should be noted that the detectability of MLR waves is dependent on equipment filter settings and length of recording time. The quality of recordings may be improved by optimizing the filter settings for each patient. However, if an MLR recording system is to be used in an operating theater, it is unlikely that a large amount of time would be available to optimize the MLR recording settings for each patient. Nonetheless, it might be possible to combine MLS with signal processing techniques such as ARX or adaptive filtering to further reduce the acquisition time of the MLR.

It can also be seen from Table II that wave detectability is better for the MLS than the conventional recording conditions. MLS order 4 has a N_b wave detectability of around 90% for the three stimulus intensities used. This is consistent with the findings of Musiek and Lee (1997), who found the

detectability of the MLR waves was improved by using MLS. This improved wave detectability implies that MLS recording of the MLR would be better than conventional recording in theater as it would increase the likelihood of recording a clear N_b wave for assessment of depth of anesthesia.

The test–retest reliability of MLR recordings was assessed in the present study. An important finding was that the latency replication standard deviation for the N_b wave is small (2.08 ms using MLS order 4 at 70 dB nHL) compared to the variation in N_b wave latency expected to be caused by increasing anesthetic depth (20 ms, according to Beer *et al.*, 1996). This means that the uncertainty in N_b wave latency estimation would not mask the variation in N_b latency caused by changes in anesthetic depth, a necessary condition if N_b latency is to be used to assess anesthetic depth. The latency replication standard deviation is better for MLS recordings than conventional recordings, with MLS order 4 showing the smallest replication standard deviation. This implies that MLS recordings would be better than conventional recordings in assessing depth of anesthesia as less variation in N_b latency would be introduced by test–retest variability.

The wave amplitude increases with stimulus intensity, so SNR increases. Due to concern that the postauricular muscle response would interfere with recordings, 70 dB nHL was the highest stimulus intensity used in the study. However, postauricular muscle interference was not generally found to be a problem at this intensity, probably because subjects were reclined with their necks supported when recordings were made. If MLR recordings are to be made when patients are under general anesthetic and are given a muscle relaxant then the postauricular muscle response will not occur. This means that even higher stimulus intensities than 70 dB nHL could be used and a greater improvement in SNR with MLS than that found in this study might be obtained.

C. Wave latency variation with MLS

Figure 4 shows the effect of recording rate on N_b wave latency. It is clear that wave latency decreases at higher MLS recording rates. This was found to be a significant effect using repeated measures analysis of variance for all waves and stimulus intensities, apart from the N_b wave at 30 dB nHL. This effect of decreasing MLR wave latency with MLS rate is in opposition to the effect of MLS on the ABR, where wave latency has been shown to increase with MLS rate. For example Picton *et al.* (1992) and Lasky *et al.* (1993) have demonstrated a significant increase in wave V latency of the ABR at high MLS rates. However, there is no evidence of a decrease in wave latency for the MLR: Musiek and Lee (1997) found no significant change in MLR wave latency using high MLS rates and Picton *et al.* (1992) describe a significant decrease in the MLR N_b wave latency with high MLS rates, which is consistent with our findings. The values of N_b wave latency found in our study are similar to those found by Picton *et al.* (1991). The discrepancy between the change in ABR and MLR wave latencies with increasing MLS rate may arise due to differences in the properties of the neural generating sites of the responses.

This implies that if MLS MLR recordings are to be used to assess depth of anesthesia, then the normative values of N_b latency obtained with conventional recordings at different depths of anesthesia would have to be reviewed so that the reduction in N_b latency caused by a high MLS recording rate is included. This would involve carrying out a normative study of N_b latency variation with anesthetic depth for MLS recordings. Variation in MLS N_b latency for different age groups should also be assessed and normative data for different age groups should be collected. Such normative data are essential if an automated system is to be developed that could control infusion rate of an intravenous anesthetic using N_b latency recorded with MLS. Furthermore, if N_b latency is to be used as a measure of depth of anesthesia in operations which involve cooling the body, such as cardiac surgery, normative data of the effect of cooling on MLS N_b latency will need to be collected.

Although this study has found an improvement in recording time of the P_a-N_b portion of the MLR using MLS, the study was carried out on otologically normal subjects in a sound-treated room. It is important to verify that such an improvement in MLR recording time is shown when recordings are made in the noisy conditions typical in an operating theater. It would also be useful to assess whether binaural MLS MLR recording is significantly faster than monaural recording, as this may further reduce the time taken to obtain a measure of anesthetic depth.

V. SUMMARY AND CONCLUSIONS

MLR recordings can be made reliably using maximum length sequences. Wave presence is greatest for MLS order 4, which shows a higher wave presence than recordings made at a conventional recording rate of 5.95 clicks/s.

Test-retest reliability in terms of replication of wave amplitudes and latencies is better for MLS than conventional recordings. MLS order 4 had the lowest test-retest latency variation and MLS order 5 had the lowest test-retest amplitude variation (although this may be a consequence of MLS order 5 having the smallest wave amplitudes). However, using a fast MLS stimulation rate produces a significant reduction in wave latency. If MLS MLR wave latencies are to be used to assess depth of anesthesia, then the effect of using MLS on the normative wave latencies at different stages of anesthesia must be assessed.

Using a fast MLS stimulation rate reduces the amplitude of the MLR waves. However, this effect is more pronounced for the N_a-P_a segment of the MLR than the P_a-N_b segment. This may be because there are different neural generation sites for the different waves of the MLR and these sites may be affected differently when using MLS.

Wave amplitudes can be used to calculate the relative SNR between conventional and MLS recordings made in the same time period (Thornton and Slaven, 1993). Greater improvement in SNR is obtained for the P_a-N_b segment of the MLR than for the N_a-P_a segment. MLS order 4 produces a better SNR than orders 3 or 5. For both the N_a-P_a segment and the P_a-N_b segment of the MLR, the SNR of MLS order 4 is significantly greater than that of a conventional recording, or of recordings made with MLS order 3 or 5. MLS

order 4 therefore represents the best balance between improvement in SNR due to increased stimulation rate and reduction in SNR with rate due to neural adaptation.

The improvement in SNR using MLS corresponds to a reduction in test time of 3.7 times. This corresponds to a reduction in test time from 180 to 49 s if 1000 averages are taken. This would represent a valuable reduction in test time if N_b latency is to be used to assess depth of anesthesia in an operating theater and it does not require assumptions to be made regarding the morphology of the MLR that it measures.

¹In fact, the levels used turned out to correspond to 29, 49, and 69 dB nHL but they are referred to here by their nominal levels.

²To verify that the rating of waveforms was not subject to rater bias and not dependent on experience of waveforms, a second person who was not expert also rated the first quarter of all the waveforms. Pearson correlation coefficients were calculated for the latency and amplitude ratings of the two observers. The correlation between raters for amplitudes was 0.92 ($P < 0.0001$) and for latencies was 0.98 ($P < 0.0001$). The amount of missing data was estimated as 6.1% by rater 1 and 4.2% by rater 2. It did not appear that the rating of wave amplitudes and latencies was subject to rater bias.

³This is not the same as the test speed calculated from the mean adjusted amplitudes shown in Table III. To calculate the relative test speeds, the mean relative test speed across subjects has been used. This is not the same as the test speed calculated from the mean adjusted amplitudes. Either approach may be valid; however, we felt that averaging across subjects was the most representative way to express relative test speed. If test speed is instead calculated using the mean adjusted amplitudes, the values obtained for test time improvement for MLS order 4 over conventional recordings are 2.3 for the N_a-P_a wave at 70 dB nHL and 3.2 for the P_a-N_b wave at 50 dB nHL. However, we have chosen to use the mean relative test speed which results in the values of 2.1 and 3.7, respectively, and these are the values which we quote in the text.

- Beer, N. A. M., Van Hooff, J. V., Brunia, C. H. M., Cluitmans, P. J. M., Korsten, H. H. M., and Beneken, J. E. W. (1996). "Midlatency auditory evoked potentials as indicators of perceptual processing during general anaesthesia," *Br. J. Anaesthesia* **77**, 617-624.
- Burkard, R. (1991). "Human brain-stem auditory evoked responses obtained by cross correlation to trains of clicks, noise bursts, and tone bursts," *J. Acoust. Soc. Am.* **90**, 1398-1404.
- Burkard, R., Shi, Y., and Hecox, K. E. (1990). "Brain-stem auditory-evoked responses elicited by maximum length sequences: Effects of simultaneous masking noise," *J. Acoust. Soc. Am.* **87**, 1665-1672.
- Cerutti, S., Bersani, V., Carrar, A., and Liberati, D. (1987). "Analysis of visual evoked potentials through Wiener filtering applied to a small number of sweeps," *J. Biomed. Eng.* **9**, 3-12.
- Doi, M., Gajraj, R. J., Mantzaris, H., and Kenny, G. N. C. (1997). "Effects of cardiopulmonary bypass and hypothermia on electroencephalographic variables," *Anaesthesia* **52**, 1048-1055.
- Elkfafi, M., Shieh, J. S., Linkens, D. A., and Peacock, J. E. (1997). "Intelligent signal processing of evoked potentials for anaesthesia monitoring and control," *IEE Proc-Control Theory Appl.* **4**, 354-360.
- Eysholdt, U., and Schreiner, C. (1982). "Maximum length sequences—a fast method for measuring brainstem evoked responses," *Audiology* **21**, 242-250.
- Gajraj, R. J., Doi, M., Mantzaris, H., and Kenny, G. N. C. (1998). "Analysis of the EEG bispectrum, auditory evoked potentials and the EEG power spectrum during repeated transitions from consciousness to unconsciousness," *Br. J. Anaesthesia* **80**, 46-52.
- Hall J. W., (1992). *Handbook of Auditory Evoked Responses* (Allyn and Bacon, Boston).
- Heier, T., and Steen, P. A. (1996). "Assessment of anaesthesia depth," *Acta Anaesthesiol. Scand.* **40**, 1087-1100.
- Jessop, J., and Jones, J. G. (1992). "Evaluation of the actions of general anaesthetics in the human brain," *Gen. Pharmacol.* **23**(6), 927-935.
- Jiang, Z. D., Brosi, D. M., and Wilkinson, A. R. (1999). "Brainstem audi-

- tory evoked response recording using maximum length sequences in term neonates," *Biol. Neonate* **76**(4), 193–199.
- Jones, J. G., editor (1989). "Depth of Anaesthesia," in *Clinical Anaesthesiology* (Bailliere Tindall, London).
- Lasky, R. E., Shi, Y., and Hecox, K. E. (1993). "Binaural maximum length sequence auditory-evoked brain-stem responses in human adults," *J. Acoust. Soc. Am.* **93**, 2077–2087.
- Leung, S. M. (1996). "Maximum length sequence technique in auditory brainstem evoked response testing: A normative study," MSC Dissertation. ISVR, Faculty of Engineering, University of Southampton.
- Lina-Granada, G., Collet, L., and Morgon, A. (1994). "Auditory-evoked brainstem responses elicited by maximum-length sequences in normal and sensorineural ears," *Audiology* **33**(4), 218–236.
- Mantzaridis, H., and Kenny, G. N. C. (1997). "Auditory evoked potential index: A quantitative measure of changes in auditory evoked potentials during general anesthesia," *Anaesthesia* **52**, 1030–1036.
- Musiek, F. E., and Lee, W. W. (1997). "Conventional and maximum length sequences middle latency response in patients with central nervous system lesions," *J. Am. Acad. Audiol.* **8**, 173–180.
- Picton, T. W., Champagne, S. C., and Kellett, A. J. C. (1992). "Human auditory potentials recorded using maximum length sequences," *Electroencephalogr. Clin. Neurophysiol.* **84**, 90–100.
- Thornton, A. R. D., and Slaven, A. (1993). "Auditory brainstem responses recorded at fast stimulation rates using maximum length sentences," *Br. J. Audiol.* **27**, 205–210.
- Thornton, A. R. D. (1993). "High rate otoacoustic emissions," *J. Acoust. Soc. Am.* **94**, 132–136.
- Thornton, C., and Newton, D. E. F. (1989). "The auditory evoked response: A measure of depth of anaesthesia," in *Balliere's Clinical Anaesthesiology: Depth of Anaesthesia*, edited by J. G. Jones (Bailliere-Tindall, London), pp. 559–585.
- Thornton, C. (1991). "Evoked potentials in anaesthesia," *Eur. J. Anaesthesiology* **8**, 89–107.
- Van Veen, B. D., and Lasky, R. E. (1994). "A framework for assessing the relative efficiency of stimulus sequences in evoked response measurements," *J. Acoust. Soc. Am.* **96**, 2235–2243.
- Wong, P. K. H., and Bickford, R. G. (1980). "Brain stem auditory evoked potentials: The use of noise estimate," *Electroencephalogr. Clin. Neurophysiol.* **50**, 25–34.

Searching for the time constant of neural pitch extraction

Lutz Wiegrebe^{a)}

Zoologisches Institut der Universität München, Luisenstrasse 14, 80333 München, Germany

(Received 23 August 2000; revised 30 October 2000; accepted 4 December 2000)

Multichannel, auditory models have been repeatedly used to explain many aspects of human pitch perception. Among the most successful ones are models where pitch is estimated based on an analysis of periodicity in the simulated auditory-nerve firing. This periodicity analysis is typically implemented as a running autocorrelation, i.e., the autocorrelation is calculated within a temporal window which is shifted along the time axis. The window was suggested to have an exponential decay with time-constant estimates between 1.5 and 100 ms. The window length determines the minimal integration time of pitch extraction. The present experiments are designed to quantify the temporal window of pitch extraction using regular-interval noises (RINs). RINs were generated by concatenating equal-duration noise samples which produce a pitch corresponding to the reciprocal of the sample duration when the samples are identical (periodic noise). When the samples are independent, the stimulus is Gaussian noise and produces no pitch. Using RIN stimuli where periodic portions interchange with aperiodic portions, it is shown that the temporal window of pitch extraction cannot be modeled using a single time constant but that the size of the temporal window depends on the pitch itself. © 2001 Acoustical Society of America. [DOI: 10.1121/1.1348005]

PACS numbers: 43.66.Ba, 43.66.Hg, 43.66.Jh, 43.66.Mk [SPB]

I. INTRODUCTION

Multichannel computer simulations of the human auditory periphery have become a valuable tool as a front end for models of sound perception. The perception of the pitch of harmonic complex sounds has been modeled with different approaches featuring either a spectral or a temporal processing of the output of a peripheral preprocessing module which typically consists of a broadband filter simulating the outer- and middle-ear transfer functions and a filterbank simulating cochlear frequency selectivity. The temporal integration quantified by the impulse response of the narrow-band filters plays an important role for both temporal and spectral models of pitch extraction. The duration of the impulse response determines the filter bandwidth and thus the limit of spectral resolution of individual harmonics in spectral models of pitch. Also, in temporal models of pitch the temporal integration of the cochlear filters has been shown to have a critical impact on the perception of pitch (Wiegrebe *et al.*, 2000). Following cochlear preprocessing, temporal models of pitch typically recruit an autocorrelation of the firing activity of simulated auditory-nerve fibers as a functional tool to analyze the firing pattern in terms of periodicity. As with any periodicity analysis, autocorrelation cannot be instantaneous but it works in a finite-duration, temporal window and this window shifts along the time axis. Licklider (1951) was the first to introduce the autocorrelation function into human pitch perception and he suggested that the temporal window of the autocorrelation function would have an exponential decay with a time constant of 2.5 ms. This time constant determines the minimal degree of temporal integration of periodicity information in autocorrelation models and the time constant should thus resemble the size of a pitch-extraction window in a presumed auditory neural periodicity

analysis. In later studies where autocorrelation models were used to model many aspects of pitch perception, estimates of the time constant varied considerably between 2.5 ms (Meddis and Hewitt, 1991a,b) and 10 ms (Meddis and O'Mard, 1997) and an integration time that was limited only by the signal duration (e.g., Yost *et al.*, 1996). However, the time constant was mostly regarded as a free parameter and up to now, no experiments have been explicitly designed to quantify this time constant. Here, an attempt is made to quantify the time constant of neural periodicity analysis using regular-interval noises (RINs). These stimuli have been repeatedly used to investigate pitch perception and, due to their high degree of variability, RINs can be manipulated to provide critical tests for pitch models. One subclass of RINs is repeated-period noise (RPN). RPNs are generated by concatenating equal-duration noise samples which are either identical or independent. A nomenclature $RPN(d,n,x)$ is used to indicate the duration of each noise sample, d , the number of consecutive, identical samples, n , and the number of independent noise samples between the periodic sequences, x . Using a notation where noise samples are represented by letters, a stimulus of the form $AABBCC, \dots$, is an $RPN(d,2,0)$ and a stimulus of the form $AAABCCCD, \dots$, is an $RPN(d,3,1)$. When n is equal to or higher than 2, RPN stimuli have harmonically structured long-term spectra and their pitch always corresponds to $1/d$. Two examples of RPN, their spectra, and the oscillation of the stimulus periodicity over time, measured as the height of the first peak in the running normalized autocorrelation of the stimulus over time, $Rh1(t)$, are shown in Fig. 1. As shown in Fig. 1, $Rh1(t)$ oscillates periodically in RPN stimuli. This is the case because periodic sections in the stimulus (e.g., AAA) are interleaved with aperiodic sections (e.g., ABC). Perceptually,

^{a)}Electronic mail: wiegrebe@zi.biologie.uni-muenchen.de

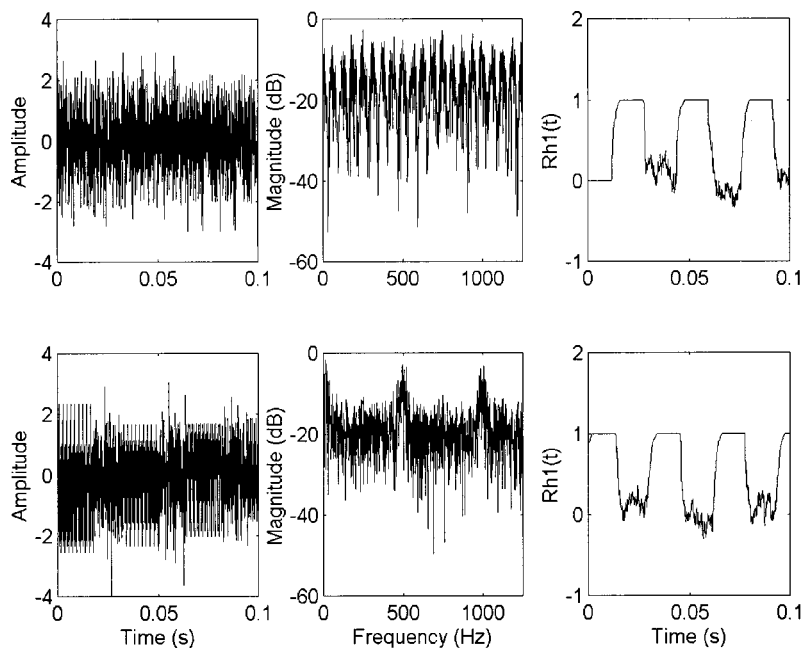


FIG. 1. Waveforms (left column), long-term spectra (middle column), and $Rh1(t)$ (right column) of RPN(16,2,0) (top) and RPN(2,9,7) (bottom). The stimuli have pitches corresponding to about 62.5 and 500 Hz, respectively. $Rh1(t)$, the height of the first peak in the running, normalized autocorrelation function of the stimulus was calculated with a time constant of 1.5 ms.

an $Rh1(t)$ oscillation would correspond to an oscillation in pitch strength because the height of $h1$ is a measure of pitch strength (Yost, 1996b).

Previous studies on the temporal dynamics of pitch strength using a single type of RPN stimulus (Wiegrefe *et al.*, 1998, 2000) have shown that RPN($d,2,0$) stimuli have a stronger pitch than rippled noise stimuli with the same d , although their long-term spectra are identical. Moreover, it was shown that the pitch-strength differences depend on the spectral listening region in that the differences were only perceived in the frequency region where the spectral ripple of rippled noise and RPN($d,2,0$) is unresolved. In Wiegrefe *et al.* (1998) it was shown that for RPN($d,2,0$), the $Rh1(t)$ oscillations were inaudible. Based on these data, it was concluded that the time constant of pitch integration must be long enough to smooth the $Rh1(t)$ oscillations. The following experiments were designed to quantify this time constant using an extended set of RPN stimuli. The stimuli are characterized with respect to pitch strength and the audibility of oscillations corresponding to the $Rh1(t)$ oscillations. The results show that (a) an autocorrelation model can account for changes in pitch strength in RPN(d,n,x) with increasing n , but (b) a running autocorrelation model with a fixed integration time constant cannot account for the changes of the perception of the $Rh1(t)$ oscillations with increasing n . It is concluded that the temporal window of neural pitch extraction is not constant but depends on the pitch itself.

II. EXPERIMENT 1: MATCHING THE PERCEPTION OF RPN TEST STIMULI

A. Method

In an adjustment experiment, listeners were asked to match the sensation of the RPN test stimuli in terms of pitch strength and pitch-strength oscillations. For reasons given below, matching stimuli consisted of a compound of iterated rippled noise (IRN) and square-wave modulated noise.

1. Stimuli

RPN test stimuli were produced exactly as described in the Introduction. The combinations of d and n used are given in Table I; x was always set to $n-2$. This set of RPN test stimuli was used because, along the diagonal lines in Table I, the RPN test stimuli have the same $Rh1(t)$ oscillation period. When x equals $n-2$, the oscillation period is

$$\text{oscillation period} = d * (2 * n - 2). \quad (1)$$

Thus, an RPN (16,2,0) has the same $Rh1(t)$ oscillation period as an RPN(2,9,7). Their pitches, however, differ because the pitch is determined solely by d .

Matching stimuli consisted of a square-wave modulated noise added to IRN. IRN was generated by an iterated process where a noise waveform is delayed and added back to itself (add-same configuration; Yost, 1996a,b). The delay, d , was set equal to the noise-sample duration in the RPN test stimuli, i.e., test and matching stimulus had the same pitch. By multiplying the delayed waveform with a gain factor between zero and one, the pitch strength of IRN can be continuously varied between no pitch (Gaussian noise) and the maximum pitch strength given by the number of iterations. Thus, to match the RPN test stimuli in terms of pitch strength, listeners varied the gain factor in the IRN matching

TABLE I. Combinations of the noise-sample duration, d (in ms) and the number of successive periodic noise samples, n , for the generation of the test stimuli. The number of independent noise samples between the periodic sequences (x) is always $n-2$. The oscillation period of $Rh1(t)$ equals $d * (2 * n - 2)$. It is constant along diagonal lines in this table.

d/n	2	3	5	9	17
1	+	+	+	+	+
2	+	+	+	+	
4	+	+	+		
8	+	+			
16	+				

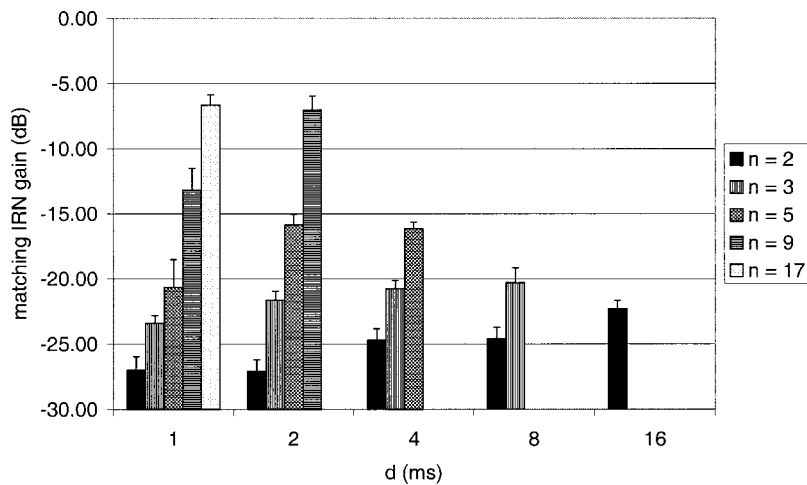


FIG. 2. Pitch-strength matching of the RPN test stimuli with IRN matching stimuli for test stimuli with different values of d (different pitches, abscissa) and different values of n expressed by different bar styles. An increase in IRN matching gain corresponds to an increase in pitch strength for a specific d . For a specific d , matches show that there is a strong increase in pitch strength when n is increased. The increase in matching gain with increasing d for n equals 2 (black bars) is consistent with the results of Wiegrebe *et al.* (1998).

stimuli. As in Yost (1996a,b), a nomenclature $IRN(d, g, n)$ is used to indicate the delay, d , the gain factor, g , and the number of iterations, n .

In IRN stimuli, $Rh1(t)$ does not oscillate over time and the IRN pitch strength is time invariant. To produce a matching stimulus which allowed to match a percept of an oscillating pitch strength, a square-wave modulated noise was added to the IRN. The modulation period equaled the $Rh1(t)$ oscillation period and in informal listening experiments, it was found that a duty cycle of 10% was suitable to match pitch-strength oscillations in RPN test stimuli. Listeners could adjust the level of the square-wave modulated noise added to the IRN to allow a match to the percept of $Rh1(t)$ oscillations. The addition of modulated noise to IRN stimuli at a significant level relative to the IRN level leads to a periodic breakdown of $Rh1(t)$ in the matching stimulus, as is the case for the RPN test stimuli. The stronger the relative level of the square-wave modulated noise, the stronger the breakdown. Thus, the compound of IRN with a variable gain and a square-wave modulated noise with a variable level serves well to match the sensation of RPN test stimuli in terms of pitch strength and pitch-strength oscillation, respectively.

The stimulus duration was 1 s, and the presentation level of the test stimuli was 65 dB SPL as calibrated with a B&K 4153 artificial ear. Stimuli were digitally generated on a personal computer and played back using a Soundblaster PCI 128 soundcard into AKG K270 Studio headphones. The sampling rate was 44.1 kHz. Sounds were presented diotically. Listeners were individually tested in a quiet room.

2. Procedure

Listeners made the adjustments on an animated computer screen. By mouse clicks, they could listen to either the test or the matching stimulus. By moving sliders with the mouse, listeners could adjust the IRN gain and the modulated-noise level. Listeners were asked to proceed by first adjusting the IRN gain so that the test and matching stimuli had equal pitch strength. In cases where listeners heard an oscillation in the test stimulus which equaled the $Rh1(t)$ oscillation, they were asked to match the level of the square-wave modulated noise so that the matching stimulus

appeared to have the same oscillation strength as the test stimulus. Finally, listeners were asked to adjust the pitch strength again in case the addition of the modulated noise had affected pitch strength. Three adjustments were obtained for each listener and test stimulus. The mean of these three adjustments was used for further analysis.

To obtain the sensation level of the square-wave modulated noise adjusted by the listeners, the adjusted level has to be reduced by the threshold level with the specific IRN masker for a specific listener and test stimulus. This was done in a separate experiment (see experiment 2).

3. Listeners

Six listeners aged between 23 and 34 years took part in all experiments; one of them was the author. All but one of the listeners had absolute thresholds at all audiometric frequencies within 10 dB of the 1969 ANSI standard. One listener had a unilateral hearing loss of about 30 dB for test frequencies above 2 kHz. Listeners had very little difficulty with the matching paradigm, so training was confined to a 2-h period prior to data collection.

B. Results

Adjustment results for the matching IRN gain were pooled across listeners; error bars represent across-listeners' standard errors. Results are shown in Fig. 2. The pitch-strength matches for RPN stimuli increase monotonically with increasing n for all values of d . For constant values of n , higher matching gains were obtained with increasing d . This confirms the results of Wiegrebe *et al.* (1998,2000). The sensation level of the square-wave modulated noise, as adjusted by the listeners, is a measure of the extent to which the $Rh1(t)$ oscillations are audible in RPN stimuli. To obtain the sensation level, the modulated-noise levels adjusted by the listeners have to be reduced by the threshold of the modulated noise masked by an IRN with the parameters as adjusted for a specific test stimulus in experiment 1. In experiment 2, masked thresholds for the square-wave modulated noise were measured in a two-alternative, forced-choice paradigm.

Square-Wave Modulated Noise Thresholds

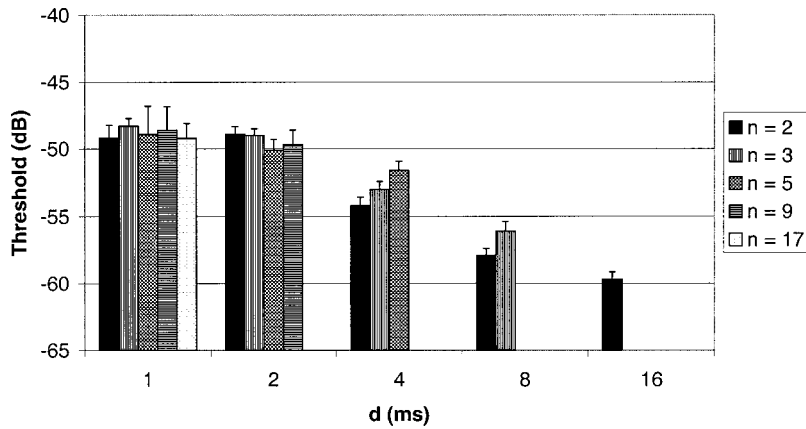


FIG. 3. Averaged detection thresholds for a square-wave modulated noise signal masked by an IRN masker with the parameters as set by the listeners in experiment 1. Error bars represent across-listeners' standard errors. No systematic changes in detection thresholds are present when d is held constant. With increasing d , detection thresholds improve slightly.

III. EXPERIMENT 2: MASKED THRESHOLDS FOR THE SQUARE-WAVE MODULATED NOISE WITH VARIOUS IRN MASKERS

A. Method

1. Stimuli

Stimulus duration and presentation level were the same as in experiment 1. The signal was a square-wave modulated noise with a 10% duty cycle and a modulation frequency equal to the $Rh1(t)$ oscillation frequency of the corresponding test stimulus in experiment 1. The masker was an IRN stimulus with the same d as the corresponding RPN test stimulus, a gain as adjusted in experiment 1 for the specific test stimulus and listener and the same number of iterations. Stimulus generation and presentation were identical to those in experiment 1.

2. Procedure

Thresholds were measured in an adaptive two-alternative, forced-choice paradigm with visual feedback. The level of the modulated-noise signal was decreased after three consecutive correct responses and increased after each incorrect response, estimating the 79.4%-correct point on the psychometric function. The step size of the level changes was initially set to 10 dB and it was reduced to 3 dB after the third reversal and to 2 dB after the fifth reversal. Eleven reversals (transitions from decreasing to increasing modulated-noise level or vice versa) were obtained in one

experimental run and threshold was taken as the averages of reversals 6 to 11. As these thresholds are compared to the adjustment results of experiment 1, which have limited accuracy due to the adjustment paradigm, only a single run was obtained for each listener and each condition. Listeners were the same as in experiment 1.

B. Results

The detection thresholds for a square-wave modulated noise signal masked by an IRN with the parameters as set individually in experiment 1 is plotted in Fig. 3. Note that masked thresholds are rather invariant for different values of n when d is constant. Masked thresholds decrease slightly with increasing d . As pointed out above, the sensation level of the square-wave modulated noise is a measure of the extent to which the $Rh1(t)$ oscillations are audible. The sensation levels of the square-wave modulated noise, calculated by subtracting the individual, masked thresholds of experiment 2 from the individual noise-level adjustments of experiment 1, are plotted in Fig. 4. Again, data are pooled across listeners; error bars represent standard errors. When n equals 2, modulated-noise sensation levels are near 0 dB independent of d . With increasing n , the sensation level increased monotonically for all values of d . The modulated-noise sensation level is a measure of the audibility of the $Rh1(t)$ oscillations, because its modulation frequency is the same as that of $Rh1(t)$. The absolute oscillation period of $Rh1(t)$ is

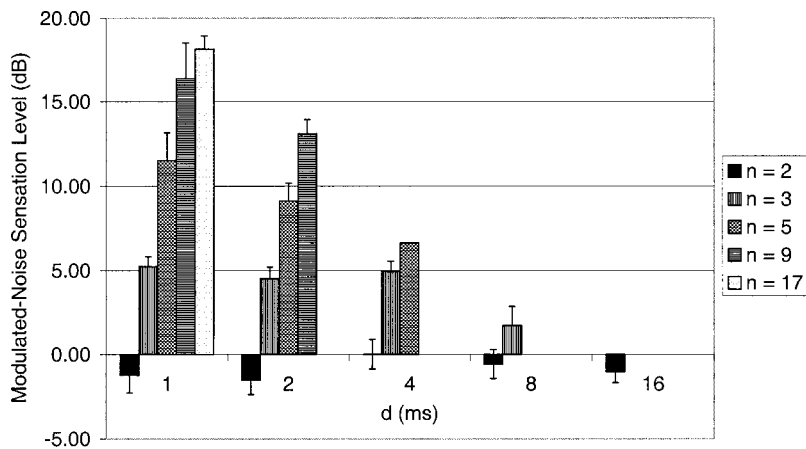


FIG. 4. Sensation level of the square-wave modulated noise added to the IRN matching stimuli to match the $Rh1(t)$ oscillation strength of the RPN test stimuli. When n equals 2, the sensation level is around zero, i.e., the oscillation in the test stimulus is inaudible. With increasing n , however, the oscillation strength becomes audible for all values of d .

Pitch-Strength Simulation using Height of first SACG Peak

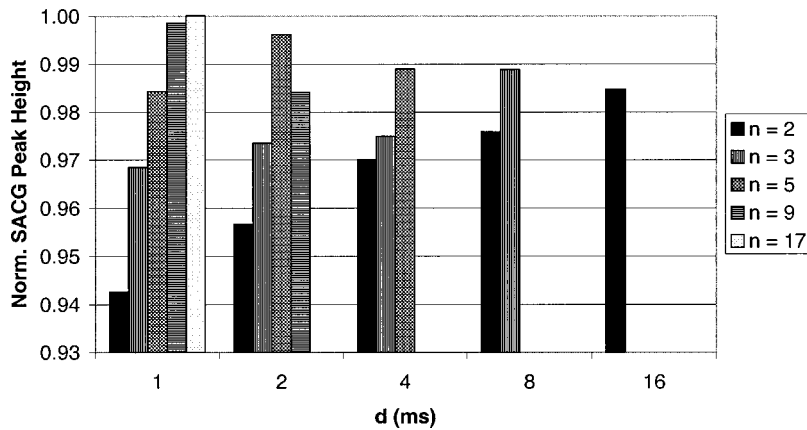


FIG. 5. Simulations of the RPN pitch-strength changes with increasing n using the auditory model of Wiegrebe *et al.* (2000) and a pitch-strength measure based on the height of the first peak in the summary autocorrelogram. Although the model captures the pitch-strength increases for d equals 1 ms, it fails to predict the highly significant increases for higher values of d .

determined by d , n , and x . In the current conditions, x always equals $n - 2$. The current results show that whether the $Rh1(t)$ oscillation is audible or not does not depend on the absolute oscillation period of $Rh1(t)$ but on the relation between d and the oscillation period. If the oscillation period equals 2 times d (n equals 2), the $Rh1(t)$ oscillation is inaudible independent of d and thus independent of the absolute oscillation period. If the oscillation period is longer than 2 times d (for $n > 2$) the $Rh1(t)$ oscillation becomes audible and its perception becomes more pronounced with increasing n .

IV. SIMULATIONS

A. Effects of pitch strength

When n equals 2 (solid black bars), the test stimuli are identical to the *AABB* stimuli in experiment 2 of Wiegrebe *et al.* (1998). The finding of Wiegrebe *et al.* (1998) that the matching IRN gain for *AABB* test stimuli increases with increasing d is confirmed in experiment 1. Wiegrebe *et al.* (2000) showed that this increase can be modeled with an autocorrelation model based on the height of the first peak in the summary autocorrelogram (SACG). Here, the auditory model used in Wiegrebe *et al.* (2000) is tested with the RPN stimuli with $n > 2$. In short, the model of Wiegrebe *et al.* (2000) consists of a broad bandpass filter simulating the transfer function of the outer and middle ear. This filter is followed by a gammatone filterbank and half-wave rectification of the filter output. Each rectified output is subjected to a long-term autocorrelation and the height of the first peak in the summary autocorrelogram (autocorrelation functions are summed up over all filter outputs) is taken as a measure for the pitch strength of the stimulus. It was already pointed out in Wiegrebe *et al.* (2000) that the model could not handle changes of pitch strength when d was changed. Thus, the judgments of the model predictions are restricted to the effect of changing n (and with it x) in the current RPN stimuli. SACG peak heights are shown in the same format as the experimental results (Fig. 2) in Fig. 5.

For RPN ($1, n, x$), the simulation results capture the general trend in that SACG peak height increases with increasing n as does the matching IRN gain in experiment 1. For RPN ($2, n, x$), this increase is not found in the simulation re-

sults although the experimental data show a highly significant increase in matching gain with increasing n .

The qualitatively correct simulations of pitch-strength changes for d equals 1 are surprising at first sight because the stimuli were designed so that the first peak in the waveform autocorrelation ($h1$) is the same independent of n . How does an auditory model based on the height of the first peak in the summary autocorrelogram capture the pitch-strength changes? The basis for the model performance lies in the interaction between cochlear filtering and the subsequent nonlinearity associated with inner hair cell transduction. When, with constant d and increasing n , the $Rh1(t)$ oscillations become slower, they are better preserved at the output of the filterbank. The occurrence of the oscillations at the filterbank output leads to an increase in SACG peak height due to the subsequent nonlinearity. [See Wiegrebe *et al.* (2000) for a more detailed explanation of the interaction between the filterbank and half-wave rectification.] With increasing d , the $Rh1(t)$ oscillation period increases further and the pitch-strength effect associated with this cochlear interaction saturates. This is the reason why a systematic increase in pitch strength is not predicted for higher values of d with a model based on the height of the first SACG peak. Taken together, the failure of the model to predict changes in pitch strength with increasing n for all d 's results from the fact that the model only takes the first peak in the SACG as a measure of pitch strength. With increasing n , however, additional autocorrelation peaks appear at integer multiples of d in the stimulus autocorrelation as well as in the SACG. But, these higher-order peaks are not taken into account in a model of pitch strength based only on the first peak in the SACG. It has been shown by Yost (1999) that higher-order autocorrelation peaks contribute to pitch strength. The occurrence of these higher-order peaks means that periodicity in the stimulus extends more than just two adjacent periods.

Why this leads to a stronger pitch is more easily understood in spectral terms: In low-frequency auditory filters, where the integration time of the filter is much longer than d , the filter can integrate over multiple periods which leads to a more pronounced interference between the carrier frequency of the filter and the periodicity in the stimulus. Across an

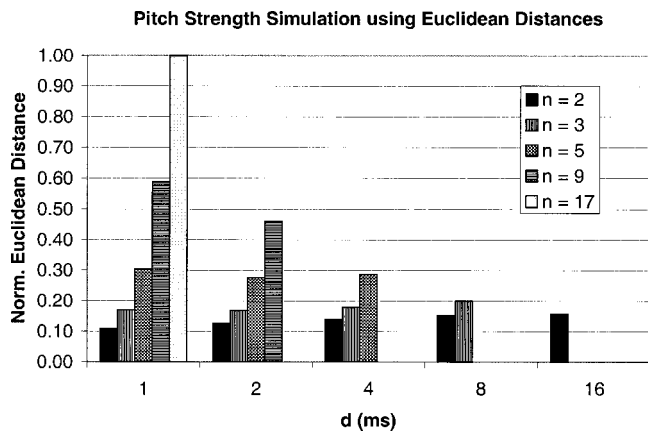


FIG. 6. Simulations of the RPN pitch-strength changes with increasing n using the auditory model of Wiegrebe *et al.* (2000) and a pitch-strength measure based on Euclidean distances in the summary autocorrelogram. With this measure, the model predicts changes in pitch strength with increasing n reasonably well.

auditory filterbank, this leads to a more pronounced spectral ripple in the low-frequency filters. The advantage of integrating over multiple periods is lost in an autocorrelation model where pitch estimates are based only on the first peak in the SACG. Interestingly, Meddis and O'Mard (1997) did not exclusively use the first peak in the SACG but compared Euclidean distances of SACGs derived from different stimuli, i.e., model performance is based on the whole shape of the SACG, not only on the height and position of the first peak. This approach is used here by calculating the Euclidean distances between each of the SACGs of the different RPN stimuli and the SACG of a Gaussian noise. Euclidean distances are plotted in Fig. 6 in the same format as the pitch-strength matching results in Fig. 2. Euclidean distances are in good qualitative agreement with the experimental results. For each value of d , the SACG Euclidean distance increases monotonically with increasing n . Thus, it appears that a simulation statistic based on the Euclidean distances provides a reasonable qualitative explanation for the changes of pitch strength with n in RPN stimuli.

It is also possible to try a quantitative simulation of the observed n -dependent pitch-strength changes. To this end, SACGs were not only calculated for the RPN test stimuli but also for a series of IRN matching stimuli with the same d , gain values varying from -30 to 0 dB in 2-dB steps and 16 iterations. Figure 7 shows simulated pitch-strength matches obtained with matching stimuli with those IRN gains where the SACGs reveal the smallest Euclidean distances to the SACGs of the corresponding test stimuli. Although the simulation captures the general pitch-strength effects, the simulated matching gains do not fit the experimental data very well. The reason for this discrepancy may lie in the differences of the SACG structure. Although both the test and the matching stimuli have higher-order SACG peaks, the distribution of peak heights is different. This is illustrated in Fig. 8, where SACGs are plotted for an RPN(1,5,3) test stimulus and the IRN matching stimulus with the best-fitting gain of -20 dB. Currently, there is no evidence relating to what kind of relative weighting higher-order SACG peaks contrib-

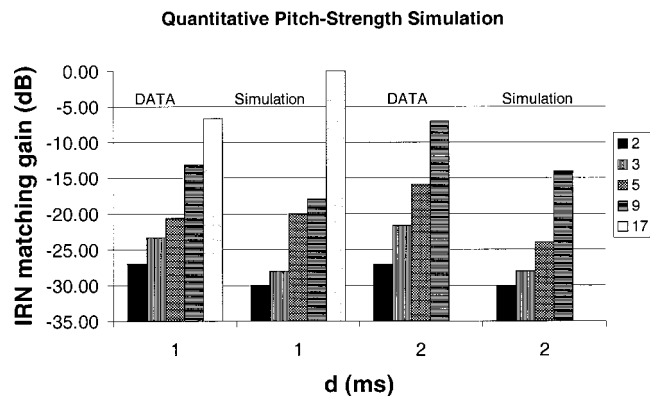


FIG. 7. Quantitative simulation of pitch-strength matches between RPN test stimuli with a d of either 1 or 2 ms and various numbers of repetitions (n) and IRN matching stimuli generated with the same d and 16 iterations. Simulated matches are based on the minimal Euclidean distances between the SACG of the test stimuli and the SACGs of IRN matching stimuli with gain values ranging from -30 to 0 dB in 2-dB steps.

ute to pitch strength. A future SACG model will clearly need refinement in this domain.

B. Effects of $Rh1(t)$ oscillations

The simulations in the previous section were based on a long-term autocorrelation of the spike-probability patterns at the output of an auditory filterbank. With this approach, periodicity information is integrated over the whole stimulus duration. This is clearly not what the auditory system does. As mentioned in the Introduction, periodicity analysis has been implemented as a running autocorrelation to account for the fact that pitch is an ongoing perception and not a *post hoc* analysis after a sound has finished. Potentially, RPN stimuli can help to characterize time constants of pitch extraction because, as shown in Fig. 1, a running autocorrelation of the stimuli reveals that their pitch strength is supposed to oscillate between that of Gaussian noise and that of

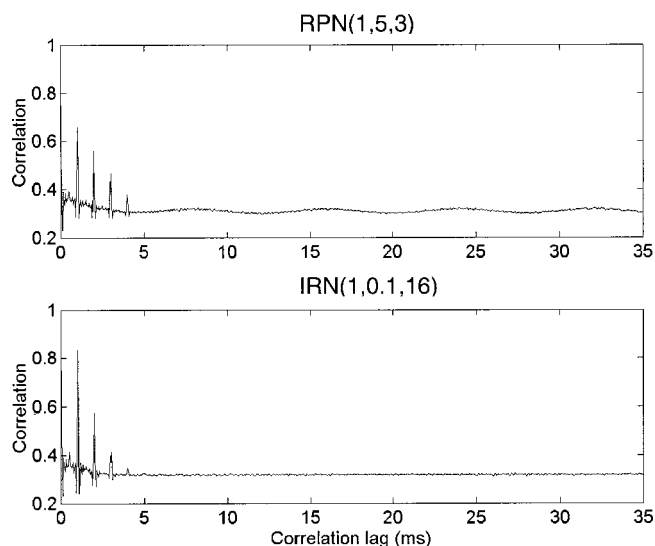


FIG. 8. SACGs for an RPN(1,5,3) (upper panel) and an IRN(1, g ,16) with a gain value, g , of -20 dB (lower panel) which produces the minimal Euclidean distance between the SACGs. This approach to simulate pitch-strength matches between an RPN test stimulus and an IRN matching stimulus is limited by the differences in the distribution of higher-order SACG peaks.

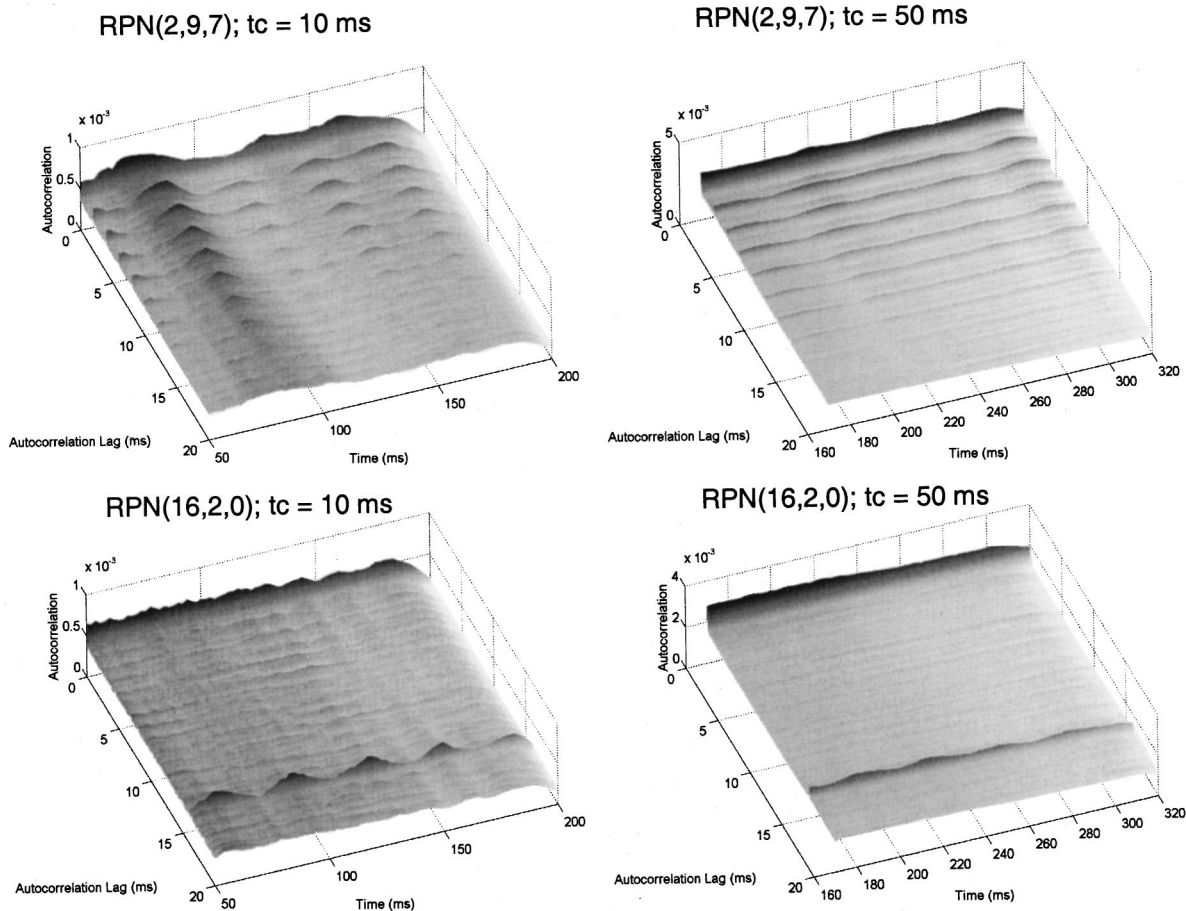


FIG. 9. Running summary autocorrelograms as a function of time for RPN(2,9,7) (upper row) and RPN(16,2,0) (lower row) for time constants of the running autocorrelation of 10 ms (left column) and 50 ms (right column). A fixed time constant smooths the running summary autocorrelogram independent of the correlation lag. This leads to a smoothing of either none of the RPN oscillations in the running SACG (left column) or of both the RPN(16,2,0) and the RPN(2,9,7) oscillations. Thus, simulations with both time constants are inconsistent with the experimental results.

a random-phase harmonic complex with a fundamental frequency equal to $1/d$. The current experiments show to which extent these pitch-strength oscillations are audible. Is it possible to set the time constant of the running autocorrelation long enough so that the SACG does not oscillate over time whenever no oscillation is heard and short enough so that the SACG oscillates whenever an oscillation is heard? Based on the experimental results, the answer must be no for the following reason. The sensation level of the $Rh1(t)$ oscillation for RPN(16,2,0) is 0 dB, whereas it is 13 dB for RPN(2,9,7). However, the two stimuli have the same $Rh1(t)$ oscillation period of 32 ms. It is not possible to design a running-autocorrelation analysis with a single time constant that preserves the $Rh1(t)$ oscillations of RPN(2,9,7) but does not preserve the oscillations of RPN(16,2,0). SACGs from a running autocorrelation with a time constant of either 10 or 50 ms are plotted as a function of time in the left and right column of Fig. 9, respectively.

The effect of the time constant is the smoothing of the running SACGs along the time axis. However, this smoothing is independent of the correlation lag and thus either the $Rh1(t)$ oscillations of both RPNs are preserved (left column) or the oscillations of none of them (right column). These simulation results are in clear disagreement with the experimental data, where a 32-ms $Rh1(t)$ oscillation period

is audible in RPN(2,9,7) but inaudible in RPN(16,2,0). To reconcile an autocorrelation model with the current experiments, one could imagine a time constant which is not fixed but which increases with increasing autocorrelation lag. For the following simulations, the time constant of the running autocorrelation was 2.5 ms for correlation lags smaller than 1.25 ms and double the correlation lag for lags equal to or higher than 1.25 ms. Simulation results are shown for RPN(2,9,7) and RPN(16,2,0) in the left and right panel of Fig. 10, respectively. With this modification, the running SACGs match the sensation of the RPN stimuli in that the SACG peak at a correlation lag of 2 ms oscillates with its 32-ms period for RPN(2,9,7), but the SACG peak at the 16-ms correlation lag for RPN(16,2,0) is averaged over oscillation periods resulting in a time-invariant peak height.

V. DISCUSSION

The current experiments were designed to quantify time constants of pitch processing. The results show that the temporal window of pitch extraction cannot be described by a single time constant as it is implemented in current models of pitch perception, independent of whether they are based on a spectral or temporal analysis of the cochlear output. The current data strongly suggest that the temporal window of

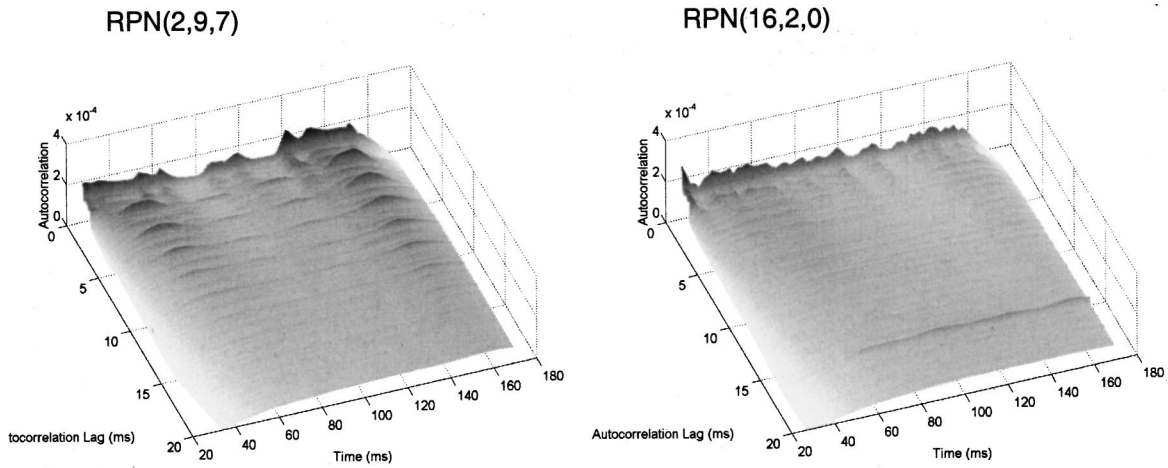


FIG. 10. Running summary autocorrelograms as a function of time for RPN(2,9,7) (left) and RPN(16,2,0) (right) calculated with a time constant that was fixed at 2.5 ms for correlation lags equal to or smaller than 1.25 ms. For longer correlation lags, the time constant is always 2 times the correlation lag. With these lag-dependent integration time constants, oscillations in the running SACG are in agreement with the experimental results.

pitch extraction depends on the pitch itself, i.e., the minimal integration time is longer for lower pitches. A computer model of pitch perception based on a channel-wise autocorrelation of the cochlear output can be modified to accommodate the pitch-dependent integration time by making the time constant of the running autocorrelation a function of the correlation lag. Qualitatively useful results were obtained with the time constant being fixed at 2.5 ms for correlation lags smaller than or equal to 1.25 ms, and the time constant being 2 times the correlation lag for correlation lags larger than 1.25 ms.

The temporal window which is characterized by these time constants represents the minimal integration, i.e., it should be interpreted as a measure for the temporal resolution of the pitch extraction mechanism. The time constants of pitch extraction addressed in the current study are not suitable to describe long-term integration of pitch information as it occurs for example in a fundamental-frequency (f_0) discrimination task. Thus, it is important to try and separate experiments designed to investigate temporal integration of pitch information from those designed to address the temporal resolution of the pitch extraction mechanism.

A. Relationship to other investigations of the pitch of complex tones

Plack and Carlyon (1995) showed that temporal integration of pitch is longer for spectrally unresolved harmonic complex sounds than for resolved complexes. When trying to relate these findings one has to note first that the paradigm of Plack and Carlyon (1995) addresses long-term pitch integration, not the resolution of the pitch extraction mechanism. Second, their results appear to be difficult to compare to the present findings with RPN stimuli because in Plack and Carlyon (1995), stimuli were bandpass filtered, whereas the current RPN experiments employed broadband stimulation. Previous experiments with RPN stimuli indicate that perception of broadband RPN(16,2,0) is dominated by the spectrally unresolved frequency region, whereas perception of RPN(2,9,7) is dominated by resolved peaks. This can be concluded because pitch-strength differences between RPN

($d,2,0$) and rippled noise with the same d arise only when the perception is dominated by unresolved spectral peaks (Wiegrebe *et al.*, 2000) and pitch-strength differences are high when d equals 16 but very small when d equals 2 (Wiegrebe *et al.*, 1998). The current data show that integration of pitch is long for RPN(16,2,0), which is a complex dominated by unresolved spectral peaks, but short for RPN(2,9,7), which is dominated by resolved spectral peaks. Thus, the current data are in line with those of Plack and Carlyon (1995).

White and Plack (1998) investigated the sensitivity to changes in f_0 of complex tones as a function of the tone duration and as a function of the length of a temporal gap between two short complex tones. When using complex tones which included spectrally resolved harmonics, White and Plack (1998) found that integration of pitch information depended on f_0 : In an f_0 discrimination task, listeners needed longer stimulus durations to achieve asymptotic performance for a reference f_0 of 62.5 Hz than for a reference f_0 of 250 Hz. Although these data are not directly comparable to the current data as they address long-term integration, not temporal resolution, they follow the same trends in that there are longer processing times involved for low pitches than for high pitches.

The concept of a flexible third integration stage is supported by results of Plack and White (2000a), who suggest that there is no fixed long pitch integration time but that integration is reset dynamically when a discontinuity is perceived in an ongoing stimulus. This resetting mechanism is likely to be implemented in higher-order processing stages of the auditory system.

Plack and White (2000b) investigated the critical features of a discontinuity so that it resets pitch integration. While the integration mechanism is reset by a temporal gap in an unresolved harmonic complex, impairment is much less when the gap is filled with noise of the same spectrum level and shape as the complex. This stimulation with two bursts of harmonic complexes separated by noise is very similar to the structure of RPN stimuli. RPN stimuli can be viewed as

periodically switching between a random-phase harmonic complex and white noise. However, due to the fact that a different sample of Gaussian noise defines each of the random-phase complex portions, there is a phase discontinuity associated with each disruption of the complex. Plack and White (2000b) pointed out that the auditory system remains sensitive to phase discontinuity even across a temporal gap if this gap is filled with noise. Based on these data, it can be hypothesized that pitch strength of RPN stimuli is supposed to increase when, with the same values of d , n , and x , each sequence of periodic noise is generated from the same sample, i.e., an RPN of the structure *AAABCAADEAAA*,..., should produce a stronger pitch than *AAABCDDDEFGGG*, This hypothesis remains to be tested.

Carlyon (1996) and Micheyl and Carlyon (1998) designed an f_0 discrimination paradigm which contains elements of both temporal resolution and integration of pitch information. They asked listeners to detect an f_0 difference between two harmonic complexes (“target complexes”) when both the complexes are bracketed by additional harmonic complexes (“temporal fringes”) which had the same f_0 in both observation intervals. When the f_0 of the fringes were similar to the nominal target f_0 , listeners’ f_0 discrimination thresholds were impaired by the presentation of the fringes when the stimuli were filtered to contain resolved harmonics. In the spectrally unresolved range, f_0 discrimination was impaired independent of the relation between target- and fringe f_0 . Presumably the best processing strategy to solve this task would be accurate temporal resolution to dissociate target complexes from the fringes and long-term integration during the perception of the targets to improve the f_0 estimate. As both long-term integration (Plack and White, 1998) and temporal resolution (current study) of the pitch extraction mechanism depend on f_0 , one would expect to see an effect of f_0 . The prediction would be that when the f_0 s of target complexes and fringes are low (88 Hz), fringes would impair f_0 discrimination of the target complexes more than when the f_0 s of the target complexes and fringes are high (250 Hz). However, the experimental data of Micheyl and Carlyon (1998) show strong impairment for both low and high nominal f_0 s. An interesting test of the f_0 dependence of pitch integration and resolution would be to vary the temporal separation between targets and fringes and to investigate if there is a systematic effect of nominal f_0 on the degree of impairment as a function of temporal separation. But this experiment remains to be done.

Carlyon *et al.* (2000) investigated the sensitivity to frequency modulation as a function of modulation rate for harmonic complexes with different f_0 s and filtered into different frequency regions. This experimental task probes the temporal resolution of the pitch extraction mechanism, and long-term pitch integration is not beneficial. When the complexes were filtered to contain resolved harmonics, threshold frequency-modulation depth increased with increasing modulation rate. This increase represents a low-pass characteristic in our ability to follow dynamic changes in f_0 . Based on the mean data of Carlyon *et al.* (2000), the low-pass characteristic appears to have a lower cutoff for a carrier f_0 of 88 Hz than for a carrier f_0 of 250 Hz. This is consistent with

the current findings. However, this carrier f_0 -dependent difference was not observed when the complexes contained unresolved harmonics only.

B. Implications for the modeling of pitch perception

In Plack and White (2000a,b), listeners were asked to discriminate f_0 s between two short, unresolved harmonic complexes where one of them (the test stimulus) included a phase discontinuity and/or a temporal gap. This work shows that although listeners perceive the stimulus as being discontinuous, they are nevertheless able to integrate pitch information across this discontinuity. When trying to produce an auditory representation of these stimuli in a computer model, one is faced with the paradox to set the integration time short enough so that the discontinuity is not smoothed out (because it is audible) but long enough to work across the discontinuity if the temporal gap is filled with noise (because pitch is integrated across this noise gap). The current simulations of the RPN sensation reveal the same problem. On one hand, a long-term average over the stimuli provides a good estimate for the pitch-strength differences across different RPNs. The audibility of pitch-strength oscillations, on the other hand, implies generally shorter and pitch-variant integration times.

Based on the current results, those of Wiegrebe *et al.* (1998,2000) and considering the extensive work of Plack and White (2000a,b) and White and Plack (1998), the following can be hypothesized: The pitch-processing properties of our auditory system appear to be consistent with a model including several integration stages where the first two integration stages are hard wired and represent limits in terms of the temporal resolution of the pitch extraction mechanism and the third integration stage is flexible and determines long-term pitch integration. The first stage is the frequency-dependent integration of the cochlear filters; the second stage is the pitch-dependent integration in the temporal window of a periodicity extractor. The third integration stage is a central neural integrator which determines long-term pitch integration. The nature of this third stage appears to be very different from that of the first two integration stages because the third stage is not hard wired, it can be reset (Plack and White, 2000a,b), and it is recruited only in an experimental or environmental context where its influence is beneficial.

ACKNOWLEDGMENTS

I would like to thank Ian Winter, Daniel Pressnitzer, Katrin Krumbholz, and Roy Patterson for very fruitful discussions on the physiology and psychophysics of RIN stimuli. Also, many thanks to Laurent Demany for his continued interest and important comments on this work. I would also like to thank Chris Plack and an unknown reviewer for very constructive comments on a previous version of this paper.

Carlyon, R. P. (1996). “Encoding the fundamental frequency of a complex tone in the presence of a spectrally overlapping masker.” *J. Acoust. Soc. Am.* **99**, 517–524.

- Carlyon, R. P., Moore, B. C. J., and Micheyl, C. (2000). "The effect of modulation rate on the detection of frequency modulation and mistuning of complex tones," *J. Acoust. Soc. Am.* **108**, 304–315.
- Licklider, J. C. R. (1951). "A duplex theory of pitch perception," *Experientia* **7**, 128–133.
- Meddis, R., and Hewitt, J. (1991a). "Virtual pitch and phase sensitivity of a computer model of the auditory periphery. I. Pitch Identification," *J. Acoust. Soc. Am.* **89**, 2688–2882.
- Meddis, R., and Hewitt, J. (1991b). "Virtual pitch and phase sensitivity of a computer model of the auditory periphery. II. Phase sensitivity," *J. Acoust. Soc. Am.* **89**, 2883–2894.
- Meddis, R., and O'Mard, L. (1997). "A unitary model of pitch perception," *J. Acoust. Soc. Am.* **102**, 1811–1820.
- Micheyl, C., and Carlyon, R. P. (1998). "Effects of temporal fringes on fundamental-frequency discrimination," *J. Acoust. Soc. Am.* **104**, 3006–3018.
- Plack, C. J., and Carlyon, R. P. (1995). "Differences in frequency modulation detection and fundamental frequency discrimination between complex tones consisting of resolved and unresolved harmonics," *J. Acoust. Soc. Am.* **98**, 1355–1364.
- Plack, C. J., and White, L. (2000a). "Pitch matches between unresolved complex tones differing by a single interpulse interval," *J. Acoust. Soc. Am.* (in press).
- Plack, C. J., and White, L. (2000b). "Perceived continuity and pitch perception," *J. Acoust. Soc. Am.* (in press).
- White, L., and Plack, C. J. (1998). "Temporal processing of the pitch of complex tones," *J. Acoust. Soc. Am.* **103**, 2051–2063.
- Wiegerebe, L., Patterson, R. D., Demany, L., and Carlyon, R. P. (1998). "Temporal dynamics of pitch strength in regular interval noises," *J. Acoust. Soc. Am.* **104**, 2307–2313.
- Wiegerebe, L., Hirsch, H. S., Patterson, R. D., and Fastl, H. (2000). "Temporal dynamics of pitch strength in regular interval noises: Effect of listening region and an auditory model," *J. Acoust. Soc. Am.* (in press).
- Yost, W. A. (1996a). "Pitch of iterated rippled noise," *J. Acoust. Soc. Am.* **100**, 511–518.
- Yost, W. A. (1996b). "Pitch strength of iterated rippled noise," *J. Acoust. Soc. Am.* **100**, 3329–3335.
- Yost, W. A., Patterson, R. D., and Sheft, S. (1996). "A time domain description for the pitch strength of iterated rippled noise," *J. Acoust. Soc. Am.* **99**, 1066–1078.
- Yost, W. A. (1999). "Pitch-strength discrimination involving regular-interval stimuli," ARO abstract #232.

Auditory backward recognition masking in children with a specific language impairment and children with a specific reading disability

G. M. McArthur^{a)}

Department of Experimental Psychology, University of Oxford, South Parks Road, Oxford OX1 3UD, United Kingdom

J. H. Hogben

Department of Psychology, The University of Western Australia, Nedlands 6907, Western Australia, Australia

(Received 21 April 2000; revised 17 August 2000; accepted 10 November 2000)

The auditory backward recognition masking (ABRM) and intensity discrimination (ID) thresholds of children with a specific language impairment and poor reading (SLI-poor readers), children with an SLI and average reading (SLI-average readers), children with a specific reading disability and average spoken language skills (SRD-average language), and children with normal spoken and written language (controls) were estimated with “child-friendly” psychophysical tasks. The pattern of ABRM and ID scores suggests that a subset of children with concomitant oral language and reading impairments has poor ABRM thresholds, and that a subgroup of children with an SLI or SRD has poorer ID thresholds than controls. The latter result warns against using rapid auditory processing tasks that do not actively control for auditory discrimination ability. Further, some unusually poor ABRM scores and ID scores question the validity of extreme scores produced by children on psychophysical tasks. Finally, the poor oral language scores of many of the children who had impaired reading highlight the need to test the oral language skills of SRD samples to ascertain how homogeneous and specifically disabled they really are. © 2001 Acoustical Society of America. [DOI: 10.1121/1.1338559]

PACS numbers: 43.66.Dc, 43.66.Fe, 43.66.Mk [DWG]

I. INTRODUCTION

Specific language impairment (SLI) is a failure in normal oral language development despite at least average intelligence, no known hearing, physical, or emotional problems, and an adequate learning environment (Bishop, 1992). Specific reading disability (SRD) is a failure in normal reading development despite at least average intelligence, intact peripheral perceptual abilities, no known neurological, physical, emotional, or social problems, and an adequate opportunity to learn to read (Vellutino, 1979). Although there is growing recognition that many children have deficits in both oral language and reading (Anderson *et al.*, 1993; Catts, 1993; McArthur *et al.*, 2000a), these conditions have traditionally been regarded as discrete disorders. This being the case, it is intriguing that both conditions have been postulated to stem from exactly the same deficit: an impaired ability to process rapidly presented sounds.

What evidence exists for this claim? The rapid auditory processing abilities of children with an SLI have been tested with a number of psychophysical tasks that present rapid nonverbal auditory information. These include tasks that require listeners to identify the order of pairs of high- and low-frequency tones presented in rapid succession (the rapid perception test; Ludlow *et al.*, 1983; Tallal, 1976; Tallal and Piercy, 1973a, 1973b; Tallal *et al.*, 1981); judge whether two rapidly presented tones are the same pitch (the same-

different discrimination task; Tallal and Piercy, 1973a); respond as quickly as possible to target tones presented among rapidly presented standard tones (an auditory choice reaction time task; Neville *et al.*, 1993); track the location of rapidly presented clicks through space (an auditory tracking task; Visto *et al.*, 1996); detect the presence of a tone followed by a backward mask (an auditory backward detection masking task;¹ Wright *et al.*, 1997); and detect a brief gap in a sound burst (a gap detection task; Ludlow *et al.*, 1983). In each case, the mean performance of the SLI group was found to be significantly lower than that of a group of control children.

The rapid auditory processing abilities of children with an SRD have been tested on a similar variety of nonverbal auditory psychophysical tasks. Again, these include the rapid perception test (Farmer and Klein, 1993; Heath *et al.*, 1999; Ludlow *et al.*, 1983; Reed, 1989; Tallal, 1980; Tallal and Stark, 1982), the same-different discrimination test (Tallal, 1980), an auditory choice reaction time task (Fawcett *et al.*, 1993; Nicolson and Fawcett, 1994), and gap detection tasks (Farmer and Klein, 1993; McCroskey and Kidder, 1980). And again, each of these experiments reports that children with an SRD perform poorly relative to control children.

Almost all these experiments tend to present only group statistics, creating the impression that all children with an SLI or SRD have impaired rapid auditory processing. The exceptions are Tallal (1980) and Heath *et al.* (1999) who report that only a subgroup of their SRD participants per-

^{a)}Electronic mail: genevieve.mcarthur@psy.ox.ac.uk

formed poorly on the rapid perception test; and Neville *et al.* (1993) and Ludlow *et al.* (1983), who note that only a subgroup of their children with an SLI performed poorly on an auditory choice reaction time task and gap detection task, respectively. Further, some experiments have failed to find a significant difference between the auditory processing skills of control and SLI or SRD groups (Bishop *et al.*, 1999; Rosen, 1999; Helzer *et al.*, 1996). These findings suggest that not all children with an SLI or SRD have impaired rapid auditory processing, and prompted the first question asked by this research: Do all children with an SLI or SRD have a rapid auditory processing deficit?

The second question concerns auditory discrimination ability, defined here as the ability to detect the difference between sounds that differ along a single dimension such as frequency, intensity, or duration. Specifically, are children with an SLI or SRD as able to discriminate between unmasked tones that differ in intensity as control children? This question merits attention because poor performance on rapid auditory processing tasks may stem from poor auditory discrimination abilities rather than an inability to process rapidly presented sounds (Heath *et al.*, 1999; Reed, 1989; Studdert-Kennedy and Mody, 1995). This has serious implications for many previous studies that have tested children with an SLI or SRD on rapid auditory processing tasks that do not control for differences between participants in auditory discrimination: It is not clear whether the poor scores of these children stem from impaired rapid auditory processing, poor auditory discrimination, or a combination of the two. This may be a real concern as adults with an SRD have been found to have poor auditory discrimination for frequency relative to adults with normal reading (McAnally and Stein, 1996), although it should be noted that the results of Hill *et al.* (1999) do not support this finding.

A promising means to answering both of these questions is a “child-friendly” version of an auditory backward recognition masking (ABRM) task developed by Massaro and Burke (1991). This task assesses rate of auditory perceptual processing in the context of Massaro’s auditory processing model (Massaro, 1970a, 1970b, 1972, 1973, 1977, 1984; Kallman and Massaro, 1983). This model postulates that auditory information is processed through a number of stages. The first is a preperceptual auditory store that holds unprocessed nonverbal and verbal sounds. Rate of auditory perceptual processing can be defined as the rate at which the basic features of these sounds are read out, or perceptually processed, from the preperceptual auditory store (Massaro, 1972; Kallman and Massaro, 1983).

ABRM tasks are typically composed of a test tone, a variable silent interstimulus interval (ISI), and a masking sound that is the same intensity as the test tone (Massaro, 1972). The listener’s task is to ignore the masking sound and report a feature of the test tone, such as its pitch (high or low) or loudness (loud or soft). Numerous experiments (e.g., Kallman and Massaro, 1983; March *et al.*, 1999; Massaro and Burke, 1991; Newman and Spitzer, 1983) have established that the recognition of the test tone’s features improves with increases in ISI up to 250 ms, where performance reaches asymptote (Massaro, 1972, 1975; March

et al., 1999). Impaired test-tone recognition at ISIs less than 250 ms is thought to occur because the masking sound interrupts the processing of the test tone by replacing its features in the preperceptual auditory store (Kallman and Massaro, 1979, 1983; Massaro and Burke, 1991). Thus, the longer the ISI, the more perceptual processing carried out on the test tone before the arrival of the mask, and the better test-tone recognition. Further, the faster the rate of auditory perceptual processing, the shorter the ISI needed to read out enough features of the test tone to recognize it. For this reason, performance on ABRM tasks can be taken to reflect rate of auditory perceptual processing.

Massaro and Burke’s (1991) ABRM task is appealing for two reasons. First, unlike many tasks that have been used to assess rapid auditory processing in children with an SLI or SRD, it actively controls for auditory discrimination ability by ensuring that each listener can discriminate between the test tones equally well when they are not masked. This involves administering a simple intensity discrimination (ID) task that adjusts the intensity of a test tone to the point where a listener can detect the difference between it and a standard tone 100 percent of the time; and then an ABRM task that adds a backward-masking sound to the same standard and test tones. Second, Massaro and Burke’s (1991) procedure produces an intensity discrimination score for each participant. These scores can be used to address the question of whether children with an SLI or SRD are as able as control children at discriminating between unmasked tones that differ in intensity.

To summarize, this experiment was designed to answer two questions. First, do all children with an SLI or SRD have poor ABRM thresholds? And second, are children with an SLI or SRD as able to discriminate between unmasked tones that differ in intensity as control children? These questions were addressed by testing SLI-poor readers, SLI-average readers, children with an SRD and average spoken language, and control children on a child-friendly version of Massaro and Burke’s (1991) procedure. To anticipate the results, a subgroup of children with both a language impairment and a reading disability had poor ABRM thresholds, and subgroups of children with an SLI and children with an SRD had poorer intensity discrimination for unmasked tones than control children.

II. METHOD

A. Listeners

Four groups of children were recruited for the experiment: SLI-poor readers, SLI-average readers, children with an SRD with average spoken language skills (SRD-average language group), and control children. The characteristics of these groups are presented in Table I.

All children had (1) a performance IQ of at least 85 on the Wechsler Intelligence Scale for Children—Third Edition (WISC-III; The Psychological Corporation, 1991); (2) no reported peripheral sensory, neurological, physical, social, or emotional problems; (3) absolute thresholds (50 percent) below 11 dB HL for a 1000-Hz tone in both ears; and (4) had

TABLE I. SLI-poor readers, SLI-average readers, SRD-average language, and control groups.

Variable	Statistics	SLI-poor readers	SLI-average readers	SRD-average language	Control children	Group comparisons
Age	<i>N</i>	28	14	6	15	
	Range (years;months)	7;0–9;10	7;3–8;9	8;4–9;6	7;7–8;9	$H(3) = 6.97$
	Mdn	8;6	8;0	8;2	8;3	$p = 0.07^a$
	Mean	8;6	7;11	8;4	8;3	
Performance IQ	s.d. (months)	9.54	5.42	8.68	3.73	
	Range	87–126	87–130	89–116	90–123	$H(3) = 3.77$
	Mdn	99.50	102.00	106.50	113.00	$p = 0.29^a$
	Mean	103.14	105.43	104.67	109.93	
Receptive Language	s.d.	10.49	14.00	9.93	10.94	
	Range	65–91	67–103	87–107	89–122	$U = 3.00$
	Mdn	76.00	71.00	98.00	99.00	$p < 0.001^b$
	Mean	77.19	76.07	98.33	100.2	$U = 10.50$
Expressive Language	s.d.	8.14	10.23	7.23	8.60	$p < 0.001^c$
	Range	50–80	54–76	80–101	82–115	$U = 0.00$
	Mdn	67.00	64.00	86.00	101.00	$p < 0.001^b$
	Mean	67.63	64.57	87.17	97.67	$U = 0.00$
Total Language	s.d.	9.37	6.06	7.49	10.62	$p < 0.001^c$
	Range	55–83	61–84	86–100	86–114	$U = 0.00$
	Mdn	66.69	66.00	91.50	101.00	$p < 0.001^b$
	Mean	70.63	68.64	92.33	98.67	$U = 0.00$
Reading Z Score	s.d.	8.14	7.03	5.54	8.91	$p < 0.001^c$
	Range	–1.75–0.64	–0.44–0.61	–1.23–0.88	0.18–1.89	$U = 0.00$
	Mdn	–1.28	0.00	–1.02	0.88	$p < 0.001^b$
	Mean	–1.28	0.09	–1.03	1.02	$U = 0.00$
	s.d.	0.32	0.35	0.12	0.62	$p < 0.001^d$

^aFour groups compared.

^bSLI-poor readers compared to controls.

^cSLI-average readers compared to controls.

^dSRD-average language group compared to controls.

adequate opportunity to acquire spoken and written language skills.

The SLI-poor readers and SLI-average readers were recruited from government language development centers and mainstream schools in the Perth (Western Australia) metropolitan area, and had total language standard scores less than 85 on the Clinical Evaluation of Language Fundamentals—Revised (CELF-R; Semmel *et al.*, 1987). The SLI-poor readers had standardized reading accuracy subtest (form 1) scores on the Neale Analysis of Reading Ability—Revised (NARA-R; Neale, 1988) worse than -0.63 . The SLI-average readers had standardized reading scores better than -0.47 .

The SRD-average language and control groups were recruited from mainstream primary schools. The SRD-average language children had standardized reading accuracy scores worse than -0.88 . Control children were reading at a level close to that expected for their age. Both groups had total language standard scores of at least 85 on the CELF-R.

B. Materials

Receptive and expressive language were assessed with subtests from the CELF-R. The CELF-R has norms for American children aged from 5 years 0 months to 16 years 11 months. This test produces standardized receptive language, expressive language, and total language scores. Reading was assessed with the accuracy subtest of the NARA-R, which is a standardized reading test composed of three subtests (accuracy, comprehension, rate) with norms for Australian children aged between 6 years 0 months and 11 years 11

months. The accuracy subtest (form 1) measures how accurately a child identifies words in story passages. Performance IQ was assessed with the performance IQ subscales of the WISC-III. These scales have norms for Australian children aged from 6 years 0 months to 16 years 11 months.

A background questionnaire was used to obtain information about pregnancy, the birth, and infancy of the child; the child's medical background (illnesses, operations, medical conditions, vision, audition, language); the child's preschool and school years (schools attended, reading ability, spelling ability, mathematical ability, behavior, psychological assessment); and the child's family background.

C. Stimuli and procedures

Children were screened for their receptive language, expressive language, reading, and performance IQ in a quiet room at their school during school hours. If the child fulfilled the appropriate criteria, a background questionnaire was sent to their parents or guardians. If responses indicated that the child continued to meet criteria, the child was invited to the university to complete the auditory assessment.

The auditory assessment was modeled on the procedure developed by Massaro and Burke (1991), and comprised two tasks. The auditory intensity discrimination (ID) task presented brief standard and test tones, and adjusted the intensity of the test tone to the point where the participant could detect an intensity difference between it and the standard tone 75 percent of the time. The ABRM task presented the same standard and test tones (with the exception that the

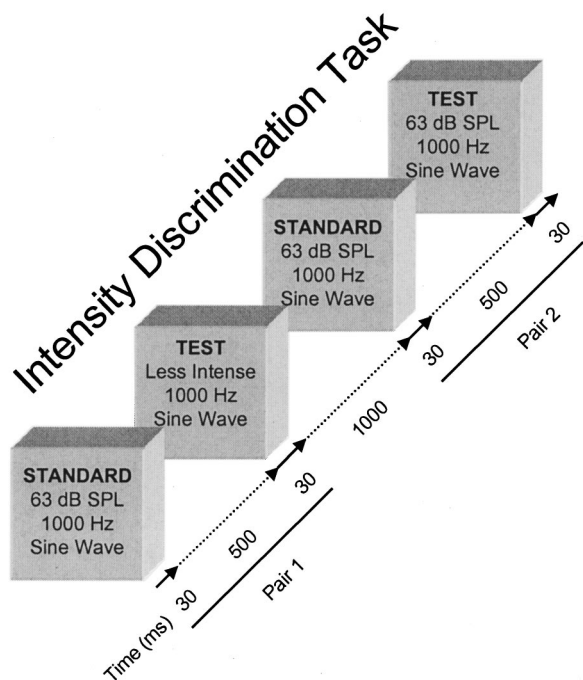


FIG. 1. Parameters of the ID task. The correct response (i.e., the tone pair that contained the softer test tone) for this example of a trial is pair 1.

latter was set 3 dB SPL below the ID threshold score) plus a backward-masking sound that followed the test tone after a variable silent ISI. The length of the silent ISI was adjusted to the point where the subject could identify the group with the less intense test tone 75 percent of the time. The length of the ISI at threshold was taken to reflect the amount of time needed to read sufficient tonal information out of the preperceptual store: The higher the ISI threshold needed to identify the correct test tone, the slower the rate of auditory perceptual processing.

1. The intensity discrimination task

The 20 practice and 100 experimental trials of the ID task were composed of two pairs of sequential tones (pair 1 and pair 2). These two pairs were separated by a 1000-ms silent interval. Each pair contained a standard tone and a test tone separated by 500 ms. All tones had a frequency of 1000 Hz, 5-ms onset and offset linear ramps, and a duration of 30 ms (including the 5-ms onset and offset ramps; see Fig. 1).

The intensity of the standard tones in both pairs, and the test tone in one pair, was 63 dB SPL. The intensity of the remaining test tone was lower than the standard tones, and was adjusted between trials. After each trial, the listener used one of two marked keys on a keyboard to indicate, in their own time, which pair (1 or 2) contained the less intense test tone. Listeners received feedback after each response: If they were correct, the word “right” was presented on the screen and the listener heard an “explosion;” if they were incorrect, the word “wrong” was presented on the screen and the listener heard a low-pitched frog “riddup.”

The 20 ID practice trials were presented through speakers. The intensity of the less intense test tone increased from 42 to 47 to 54 to 60 dB SPL for five successive trials, respectively. The progression from easy to difficult trials (i.e.,

from a large intensity difference between the standard and test tone to a small difference) made the task easier to explain and to learn. The listeners were trained on the practice trials until they responded correctly on at least 80 percent of “easy” (42- and 47-dB SPL) trials.

The 100 ID experimental trials were presented diotically through headphones, divided into four blocks of 25 trials. The listener was given a short break between each block, during which they were given feedback about their performance and were encouraged to concentrate. Over the 100 trials, a parameter estimation by sequential tracking (PEST) procedure (Taylor and Creelman, 1967) used a target level of 0.75 and Wald deviation limit of 1.0 to adjust the intensity of the test tone to the level where the listener identified the correct pair 75 percent of the time. The threshold value was the mean intensity of the less intense test tone after the fourth reversal in response adjustment. After the final trial, a graph of the listener’s performance over the 100 ID task trials was presented on the computer monitor. Stable performance after the fourth reversal in response adjustment was taken to indicate the listener understood the task and had concentrated consistently over the 100 trials.

2. The ABRM task

The ABRM task comprised 20 practice and 100 experimental trials. All ABRM trials were composed of two groups of tones, each including three tones: the standard and test tones used in the ID task, followed by a masking sound after a silent variable ISI. The mask was an approximation² of a 200-ms, 1000-Hz sawtooth wave with a sharp (0 ms) onset. The intensity of the standard and masking tones in both groups was 63 dB SPL. The intensity of one of the test tones was also 63 dB SPL. The intensity of the remaining test tone was fixed 3 dB SPL below the observer’s ID threshold score. The length of the silent ISI between the test tone and the masking sound in each group was varied between trials, with a floor value of 10 ms to eliminate cues present at very brief ISIs (see Fig. 2).

The 20 practice ABRM trials were presented through speakers. The first five trials used an ISI between the test and masking tone of 500 ms, the next 250 ms, the next 125 ms, and the last 50 ms. Listeners were instructed to ignore the third sound (mask) and indicate which group (1 or 2) contained the less intense test tone. Listeners responded with the same response keys as the ID task and received the same type of feedback. Again, listeners were trained on the practice trials until the listener responded correctly on 80 percent of easy (500- and 250-ms) trials.

The 100 experimental ABRM trials were presented diotically through headphones. Again, listeners were given a rest after each block of 25 trials to maximize their concentration. The PEST procedure was used to adjust the length of the silent ISI between the test tone and masking sound to the point where the listener was able to identify the group with the less intense test tone 75 percent of the time. A graph of the listener’s performance over the 100 trials was presented on the computer monitor after the last trial. Again, stable performance after the fourth reversal in response adjustment

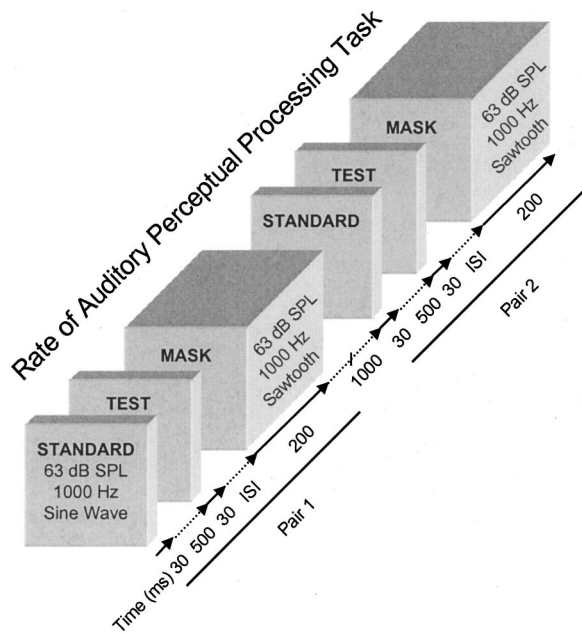


FIG. 2. Parameters of the ABRM task. The correct response (i.e., the tone pair that contained the softer test tone) for this example of a trial is group 1.

was taken to indicate that the listener understood the task and had concentrated consistently over the 100 trials.

III. RESULTS

A. Auditory backward recognition masking scores

ABRM scores were the mean length of the ISI separating the test tone from the masking sound after the first four reversals in response adjustment. An alpha level of 0.05 was used for all tests of statistical significance. The ABRM scores of the SLI-poor readers, SLI-average readers, SRD-average language group, and control group are illustrated in Fig. 3.

The ABRM scores of two SLI-poor readers, one SLI-average reader, and one SRD-average language child were not included because they were produced by unstable performance over the 100 ABRM trials. The scores of nine SLI-poor readers (621.0, 641.6, 681.0, 779.0, 805.4, 823.0, 1265.5, 1449.8, and 1527.0 ms), two SLI-average readers (1529.9 and 2246.0 ms), one SRD-average language child (836.9 ms), and two control children (832.9 and 1015.2 ms) were removed because they were too high (i.e., were greater than 600 ms) to be valid ABRM scores. Specifically, these scores suggest that the mask continued to interrupt the perceptual processing of the test tones from the preperceptual auditory store 620 to 2250 ms after the test tones' offset. However, the features of the test tones would no longer be available in this store after this period of time. Granted, the exact length of the preperceptual auditory store has yet to be established, and estimates vary between psychophysical tasks (Cowan, 1984; Raab, 1963), but even the most generous estimates (500 ms in some integration tasks; Cowan, 1984) fall short of the scores (620 to 2250 ms) produced by some of the children in this experiment. Further, Massaro and Burke's (1991) finding that the performance of young children, tested with the same tones as the present experi-

ABRM scores
Leaf Unit = 1.0 ms

SLI-poor readers	SLI-average readers	SRD-average language	Control
0	0 43 46	0	0
0 90 93	(0) 51 55 75 76	0	0 91 99
1 14 27 39	1 19	1 17	1 13 47 48
1 83 92	1 50	(1) 64 82	(1) 55 60 75 76 80 97
2 10 16 18	2 26 31	2	2
2	2 60	2	2 50
(3) 17 32	3	3 14	3
3 80	3	3	3
4 36	4	4	4
4 87	4	4	4
5 21 33	5	5	5
<i>N</i> = 17	<i>N</i> = 11	<i>N</i> = 4	<i>N</i> = 12
<i>Mdn</i> = 216.06	<i>Mdn</i> = 76.20	<i>Mdn</i> = 172.55	<i>Mdn</i> = 157.55
<i>M</i> = 270.00	<i>M</i> = 120.98	<i>M</i> = 194.00	<i>M</i> = 157.64
<i>SD</i> = 152.80	<i>SD</i> = 82.61	<i>SD</i> = 116.19	<i>SD</i> = 44.06

FIG. 3. Stem-and-leaf plots of ABRM scores (rounded to the nearest 1 ms) produced by SLI-poor readers, SLI-average readers, SRD-average language, and control groups. Numbers in the left-hand columns are the "stems." These are paired with each number to the right (the "leaves") to represent a single score. For example, the stem 3 is paired with the leaf 17 to represent 317 ms (see Tukey [1977] for a more detailed explanation of stem-and-leaf plots). Brackets indicate the stem category that contains the group median.

ment, reached asymptote at 580 ms, paired with Newman and Spitzer's (1983) finding that elderly listeners with a slow rate of auditory perceptual processing reached asymptote on a similar task at ISIs between 360 and 440 ms, suggest that a valid ABRM score for even the slowest perceptual processor should not exceed approximately 600 ms.

The mean and median valid ABRM scores of the SLI-poor readers (see Fig. 3) were considerably higher than those of the control group (note that the valid ABRM score [521 ms] of one control child was removed as an outlier as it fell more than 3 standard deviations above the mean valid ABRM score of the control group). A Mann-Whitney test indicated that the difference between the median ABRM scores of the two groups was statistically significant [$U = 57$, $n(\text{small}) = 12$, $n(\text{big}) = 17$, $p = 0.04$]. The stem-and-leaf plots indicated that this was the product of a subgroup of seven SLI-poor readers (41.18 percent) who had poor ABRM scores relative to the remaining 10 SLI-poor readers, whose ABRM scores were similar to control children. The ABRM scores of the SLI-poor readers were not significantly correlated with any of the other measures in the test battery.

The stem-and-leaf plots also showed that the SLI-average readers had ABRM scores similar to the control children, and a Mann-Whitney test indicated that the difference between the median ABRM scores of the two groups was not statistically significant [$U = 42$, $n(\text{small}) = 11$, $n(\text{big}) = 12$, $p = 0.15$].

The four children in the SRD-average language group with valid ABRM thresholds had similar scores to the control children. The mean and median ABRM scores of the SRD-average language group were slightly higher than the control group. However, a Mann-Whitney test indicated that the difference between the median ABRM scores of the SRD-average language and control groups was not statisti-

ID Scores Leaf Unit = 0.1 dB SPL			
SLI-poor readers	SLI-average readers	SRD-average language	Control
44	44 6 7	44	44
45	45	45	45
46	46	46	46
47 3	47 2	47	47
48	48	48	48
49	49	49	49
50 8	50	50	50
51 8	51	51	51
52 7	52 1	52	52
53 6 8	53	53 9	53
54 2	54	54 0	54
55 9	55	55	55
56 3 8	56	56	56
(57)0 1 3 7 8	57 1	57	57 7
58 3 4	(58)8 2 4	(58)6	58 9
59 0 1 2 4 6 7	59 4	59 3 5 9	59 5 8
60 2 4 5 6	60 1 3 4 5 5	60	(60)0 1 5 5 7 8 8 9 9
61 6	61	61	61 0 3
<i>N</i> = 28	<i>N</i> = 14	<i>N</i> = 6	<i>N</i> = 15
<i>Mdn</i> = 57.75	<i>Mdn</i> = 58.60	<i>Mdn</i> = 58.96	<i>Mdn</i> = 60.50
<i>M</i> = 57.00	<i>M</i> = 55.87	<i>M</i> = 57.54	<i>M</i> = 60.24
<i>SD</i> = 3.42	<i>SD</i> = 6.05	<i>SD</i> = 2.80	<i>SD</i> = 0.96

FIG. 4. Stem-and-leaf plots of ID scores, rounded to the nearest 0.1 dB SPL, produced by SLI-poor readers, SLI-average readers, SRD-average language group, and control children. Numbers in the left-hand columns are the stems. These are paired with each number to the right (the leaves) to represent a single score. For example, the stem 47 is paired with the leaf 3 to represent 47.3 dB SPL (see Tukey [1977] for a more detailed explanation of stem-and-leaf plots). Brackets indicate the stem category that contains the group median.

cally significant [$U=16$, $n(\text{small})=4$, $n(\text{big})=12$, $p=0.38$].

B. Intensity discrimination scores

ID scores were the mean intensity of the softer test tone after the first four reversals in response adjustment. The ID scores of the four groups of children are illustrated in Fig. 4. A Kruskal-Wallis test was used to compare the median ID scores of the four groups.

The difference between the median ID scores of the four groups was statistically significant [$H(3)=16.86$, $p<0.001$]. *Post hoc* Mann-Whitney tests showed that there was no statistical difference between the median ID scores of the SLI-poor readers, SLI-average readers, and SRD-average language group. However, the median ID score of each of these groups differed significantly from that of the control group [SLI-poor readers: $U=60$, $n(\text{small})=15$, $n(\text{big})=28$, $p<0.001$; SLI-average readers: $U=36.5$, $n(\text{small})=14$, $n(\text{big})=15$, $p<0.00$; SRD-average language group: $U=10$, $n(\text{small})=6$, $n(\text{big})=15$, $p<0.01$]. The stem-and-leaf plots indicated that these significant group differences were the product of only a subgroup of children in each group: 13 SLI-poor readers (46.43 percent), five SLI-average readers (35.71 percent), and two children from the SRD-average language group (33.33 percent) had poorer ID scores than the poorest ID score in the control group. The remaining children had ID scores similar to control children.

It should be noted that some SLI children had particularly low ID scores despite their normal hearing. These scores may be a concern for two reasons: (1) they could be

taken to suggest poor attention or poor task understanding, and (2) they could confound ABRM scores by making the ABRM task artificially easy because the intensity difference used in the task was above true threshold. In fact, these concerns are allayed somewhat by three observations. Regarding (1), the stable performance of the listeners in the ID task after the first four reversals in response adjustment suggested that each child had a consistent level of attention and understanding throughout the task. Further, these task-related factors should produce poor scores on both the ID and ABRM tasks. However, the correlation coefficient between these two sets of scores was very small ($r=-0.10$, $p=0.49$ for all children combined; $r=-0.22$, $p=0.13$ when invalid extreme ABRM scores were included in the analysis). Regarding (2), the small correlation coefficient indicates that poor ID scores were not necessarily associated with good ABRM scores. Thus, children with poor ID scores did not necessarily demonstrate an ABRM advantage. Thus, the poor ID scores produced by a subgroup of the children were puzzling, but there was no objective reason to remove them or their corresponding ABRM scores from the analysis. In fact, removing the ABRM scores of the listeners who had worse ID thresholds than the children in Massaro and Burke's study (i.e., lower than 51 dB SPL) made very little difference to the results: There was still a large proportion of SLI-poor readers (38 per cent) with poor ABRM thresholds relative to the remaining 10 SLI-poor readers and control children. And, there was still no statistically significant difference between the ABRM thresholds of the control group and the SLI-average readers [$U=42$, $n(\text{small})=10$, $n(\text{big})=12$, $p=0.25$] and SRD-average language groups (no change in statistics).

IV. DISCUSSION

The first question asked by this research was whether all children with an SLI or SRD have poor ABRM thresholds. The results of this experiment suggest not. Only a subgroup of children with both an oral language impairment *and* a reading disability (41.18 percent) exhibited poorer ABRM threshold scores. It is unclear what differentiated this subgroup from the SLI-poor readers who had normal ABRM scores. At this point, it should suffice to conclude that children with poor valid ABRM thresholds have concomitant oral language and reading impairments. However, not all children with concomitant oral language and reading impairments have poor ABRM thresholds.

This finding is inconsistent with previous experiments whose group data suggest that all children with an SLI or SRD have elevated thresholds. However, it is consistent with Tallal (1980), Heath *et al.* (1999), Ludlow *et al.* (1983), and Neville *et al.* (1993) who found that only a subgroup of their children with an SLI or SRD performed poorly on a rapid auditory processing task. Further, finding that this subgroup was characterized by poor oral language *and* poor reading is consistent with Heath *et al.* (1999), who found that only children with an SRD with poorer oral language ability performed poorly on a modified version of the rapid perception test. It is also consistent with Tallal and Piercy (1973a, 1973b) and Tallal (1976) who found poor scores in a group

of children with an SLI, the majority of whom were reading at least 1 year below the level expected for their age; and with Ludlow *et al.* (1983) and Neville *et al.* (1993), whose subgroups of children with an SLI with impaired performance had poor reading skills. The results of these studies and the present experiment highlight the importance of reporting the data of individuals rather than group summary statistics.

This finding also offers an explanation for why children with an SLI and children with an SRD have demonstrated poor psychophysical scores in previous experiments. Because the SLI experiments did not consider the reading abilities of their children, and the SRD experiments did not screen for oral language (with the exception of Heath *et al.*, 1999), both sets of experiments may have inadvertently recruited children with concomitant oral language and reading problems, a subgroup of whom had a slow rate of auditory perceptual processing. It is possible that these experiments recruited enough children from this subgroup to find a statistical difference between the average scores of a control and SLI or SRD group. It follows that there may be experiments that did not recruit enough children from this subgroup to find a statistical difference between a control and SLI or SRD group, and consequently have not been published (the file-drawer problem).

This finding may also explain why a variety of deficits, both nonverbal and verbal, has been found in children with an SLI. It is now widely recognized that SLI is a heterogeneous disorder (Enderby and Philipp, 1986; Montgomery *et al.*, 1991; Sloan, 1992) that is composed of different subtypes of children (Rapin and Wilson, 1978). This raises the possibility that different subtypes of SLI stem from different underlying deficits (Bishop, 1997). For example, the results of this experiment could be taken to suggest that the poor oral language and poor reading abilities of some children stem from a slow rate of auditory perceptual processing. The chain of events leading from a slow rate of auditory processing to concomitant language and reading has yet to be established. However, it is feasible that a slow rate of processing impairs speech perception (Tallal, 1980; Merzenich *et al.*, 1996), which may affect the processing of phonological information. This may simultaneously impair (1) the encoding or retrieval of phonological information from memory (for example) giving rise to an oral language deficit (Leonard *et al.*, 1983; Kamhi and Catts, 1986) and (2) phonological awareness and phonological decoding, giving rise to disabled reading (Heath *et al.*, 1999).

However, this series of events will not explain the language and reading deficits of all children. A deficit in phonological short-term memory may account for the difficulties of some children (Gathercole and Baddeley, 1990), and a specific deficit in processing speech may explain the problems of others (Mody *et al.*, 1997). Regarding the latter, Mody *et al.* (1997) have argued that nonverbal auditory deficits in reading-disabled children are a more variable finding, which may be an epiphenomenon rather than causally related to poor phonological discrimination. In future studies, it will be of interest to use methods such as those adopted here to

consider how far deficits in rate of auditory processing relate to phonological discrimination.

The second question asked by this experiment was whether children with an SLI or SRD are as able as control children at discriminating between unmasked tones that differ in intensity. The results of this experiment suggest that this is not always the case: One-third to one-half of the participants in the SLI-poor readers group, the SLI-average readers group, and the SRD-average language group had poorer ID scores than the control group. This finding is congruent with Cacace *et al.* (2000), who found that children with poor reading had larger just-noticeable differences for intensity than children with normal reading ability. These findings require replication as they raise questions about the results of previous studies that used rapid auditory processing tasks. Do the poor scores of the children in these studies reflect impaired rapid auditory processing or impaired auditory discrimination ability? Or did some children have problems with one and not the other? This ambiguity flags the need for future studies to control for auditory discrimination ability while measuring rapid auditory processing in SLI and SRD samples.

An unexpected finding of this experiment was the extremely high invalid ABRM threshold scores produced by nine SLI-poor readers, two SLI-average readers, one child in the SRD-average language group, and two control children. What do these very high threshold scores reflect? It is interesting that two other experiments have found similar ISI thresholds in their SRD and control data. Specifically, Heath *et al.* (1999) found that one child with an SRD and two control children needed silent ISIs of 1554, 1153, and 1346 ms, respectively, between pairs of high and low tones to identify their order 75 percent of the time. Similarly, Pammer and McGregor (2000) found that ten children with an SRD needed silent ISIs of at least 1000 ms between high and low tones to identify their correct order 71 percent of the time. Like the present research, these experiments used a PEST procedure to adjust the length of the silent ISI between the tones. Perhaps the PEST procedure is not appropriate for all stimulus parameters for all listeners. For example, if the PEST procedure is used to adjust the difference between the frequency or intensity of two tones, incorrect responses prompt an increase in this difference, which decreases task difficulty. However, if the PEST is used to adjust the ISI between stimuli, the increase in ISI due to incorrect responses may not decrease task difficulty for all listeners. Longer ISIs increase the memory load of the task. Thus, listeners with weaker memory skills may be relatively disadvantaged at longer ISIs, forcing them to adopt alternative response strategies that lead to unusual thresholds. This possibility reinforces our reluctance to interpret the extremely high ABRM threshold scores as valid representations of rate of auditory perceptual processing. Further, it highlights the need for future studies to consider the validity of extreme scores produced by children on psychophysical tasks. And, it supports claims that the poor performance of some children on psychophysical tasks may stem from their inability to cope with psychophysical task demands, such as memory or attention, rather than impaired perception (Bishop *et al.*,

1999; Elfenbein *et al.*, 1993; Gomes *et al.*, 1999; Wightman *et al.*, 1989).

A second unexpected finding of this research was the number of children with a reading disability who also had impaired language (i.e., the SLI-poor readers): 82 percent of children with poor reading had a total language more than 1 standard deviation below the level expected for their age. This questions how “specifically” reading-disabled (i.e., problems with reading alone) and homogeneous children with an SRD recruited by previous experiments using typical SRD criteria such as Vellutino’s (1979) really are. This in turn highlights the need for future experiments to index the oral language abilities of SRD recruits (see McArthur *et al.*, 2000b, for a more detailed discussion).

In summary, the present research addressed two questions. The first asked whether all children with an SLI or SRD have poor ABRM thresholds. The answer is clearly no. The results indicate that a subgroup of children with concomitant oral language and reading impairments have elevated ABRM thresholds compared to control children. The second question asked whether children with an SLI or SRD are as able as control children at discriminating between unmasked tones that differ in intensity. The results suggest that at least a third of children with an SLI or SRD have poorer discrimination for intensity than children with normal oral language and reading. This warns against using rapid auditory processing tasks that do not actively control for auditory discrimination abilities. Further, some unusually poor ABRM scores and ID scores question the acceptance of extreme auditory perceptual scores without considering the parameters of the task. They also highlight the possibility that children’s poor performance on rapid auditory processing tasks may stem from an inability to cope with task demands rather than an impaired ability to process rapidly presented sounds. And finally, the poor total language scores of the majority of children who had a reading disability indicate that future SRD studies need to index the oral language abilities of their samples to determine how homogeneous and specifically disabled they really are.

ACKNOWLEDGMENTS

We would like to thank all the children, parents, and staff associated with the Western Australian primary schools and language development centers who participated in this experiment. Further, we are grateful to Professor Dorothy Bishop for her comments on this manuscript, and for her continuous support and encouragement. This research was supported by an Australian Postgraduate Award (G. M. McArthur) and by the Australian Research Council (J. H. Hogben).

¹This task differs from Massaro and Burke’s (1991) ABRM task in that it fixes the ISI between a test and masking sound and then adjusts the intensity of the test tone to determine whether a listener can detect its presence (hence auditory backward *detection* masking), rather than fixing the intensity of the test tone and then adjusting the length of the ISI between the test and masking sounds to determine whether a listener can recognize its loudness (auditory backward *recognition* masking).

²The “approximate” sawtooth wave was produced by emitting 1000-, 2000-, and 3000-Hz sine waves simultaneously, with the intensities of the

second and third harmonics set at one-half and one-third of the 1000-Hz sine wave, respectively, and the phase of all harmonics starting at 0 deg. A “true” sawtooth wave is composed of an infinite number of harmonically related sine waves (rather than just three), each with an amplitude that is 1/harmonic number of the amplitude of the first harmonic.

- Anderson, K. C., Brown, C. P., and Tallal, P. (1993). “Developmental language disorders: Evidence for a basic processing deficit,” *Curr. Opin. Neurol. Neurosurg.* **6**, 98–106.
- Bishop, D. V. M. (1992). “The underlying nature of specific language impairment,” *J. Child. Psychol. Psychiatry.* **33**, 3–66.
- Bishop, D. V. M. (1997). *Uncommon Understanding* (Psychology, Hove, UK).
- Bishop, D. V. M., Carlyon, R. P., Deeks, J. M., and Bishop, S. J. (1999). “Auditory temporal processing impairment: Neither necessary nor sufficient for causing language impairment in children,” *J. Speech. Lang. Hear. Res.* **42**, 1295–1310.
- Cacace, A. T., McFarland, D. J., Ouimet, J. R., Schrieber, E. J., and Marro, P. (2000). “Temporal processing deficits in remediation-resistant reading-impaired children,” *Audiol. Neuro-Otol.* **5**, 83–97.
- Catts, H. W. (1993). “The relationship between speech-language impairments and reading disabilities,” *J. Speech. Lang. Hear. Res.* **36**, 948–958.
- Cowan, N. (1984). “On short and long auditory stores,” *Psychol. Bull.* **96**, 341–370.
- De Weirtd, W. (1988). “Speech perception and frequency discrimination in good and poor readers,” *Appl. Psycholinguist.* **9**, 163–183.
- Elfenbein, J. L., Small, A. M., and Davis, J. M. (1993). “Developmental patterns of duration discrimination,” *J. Speech. Lang. Hear. Res.* **36**, 842–849.
- Enderby, P., and Philipp, R. (1986). “Speech and language handicap: Towards knowing the size of the problem,” *Br. J. Disord. Commun.* **21**, 151–165.
- Farmer, M. E., and Klein, R. (1993). “Auditory and visual temporal processing in dyslexic and normal readers,” in *Temporal Information Processing in the Nervous System: Special Reference to Dyslexia and Dysphasia*, edited by P. Tallal, A. M. Galaburda, R. R. Llinas, and G. von Euler (The New York Academy of Sciences, New York), pp. 339–341.
- Fawcett, A. J., Chattopadhyay, A. K., Kandler, R. H., Jarrat, J. A., Nicolson, R. I., and Proctor, M. (1993). “Event-related potentials and dyslexia,” in *Temporal Information Processing in the Nervous System: Special Reference to Dyslexia and Dysphasia*, edited by P. Tallal, A. M. Galaburda, R. R. Llinas, and G. von Euler (The New York Academy of Sciences, New York), pp. 342–345.
- Gathercole, S. E., and Baddeley, A. D. (1990). “Phonological memory deficits in language disordered children: Is there a causal connection?,” *J. Mem. Lang.* **29**, 336–360.
- Gomes, H., Sussman, E., Ritter, W., Kurtzberg, D., Cowan, N., and Vaughan, Jr., H. G. (1999). “Electrophysiological evidence of developmental changes in the duration of auditory sensory memory,” *Dev. Psychol.* **35**, 294–302.
- Heath, S. M., Hogben, J. H., and Clark, C. D. (1999). “Auditory temporal processing in disabled readers with and without oral language delay,” *J. Child. Psychol. Psychiatry.* **40**, 637–647.
- Helzer, J. R., Champlin, C. A., and Gillam, R. B. (1996). “Auditory temporal resolution in specifically language-impaired and age-matched children,” *Percept. Mot. Skills* **3**, 1171–1181.
- Hill, N. L., Bailey, P. J., Griffiths, Y. M., and Snowling, M. J. (1999). “Frequency acuity and binaural masking release in dyslexic listeners,” *J. Acoust. Soc. Am.* **106**, L53–L57.
- Kallman, H. J., and Massaro, D. W. (1979). “Similarity effects in backward recognition masking,” *J. Exp. Psychol. Hum. Percept. Perform.* **5**, 110–128.
- Kallman, H. J., and Massaro, D. W. (1983). “Backward masking, the suffix effect, and preperceptual storage,” *J. Exp. Psychol. Learn. Mem. Cog.* **9**, 312–327.
- Kamhi, A. G., and Catts, H. W. (1986). “Toward an understanding of developmental language and reading disorders,” *J. Speech. Hear. Disord.* **51**, 337–347.
- Leonard, L. B., Nippold, M. A., Kail, R., and Hale, C. A. (1983). “Picture naming in language-impaired children,” *J. Speech Hear. Res.* **26**, 609–615.
- Ludlow, C. L., Cudahy, E. A., Bassich, C., and Brown, G. L. (1983). “Auditory processing skills of hyperactive, language-impaired, and reading-

- disabled boys," in *Central Auditory Processing Disorders: Problems of Speech, Language, and Learning*, edited by E. Z. Lasky and J. Katz (University Park, Baltimore), pp. 163–184.
- March, L., Cienfuegos, A., Goldbloom, L., Ritter, W., Cowan, N., and Javitt, D. C. (1999). "Normal time course of auditory recognition in schizophrenia, despite impaired precision of the auditory sensory ("echoic") memory code," *J. Abnormal Psychol.* **108**, 69–75.
- Massaro, D. W. (1970a). "Preperceptual auditory images," *J. Exp. Psychol. Hum. Percept. Perform.* **85**, 411–417.
- Massaro, D. W. (1970b). "Perceptual processes and forgetting in memory tasks," *Psychol. Rev.* **77**, 557–567.
- Massaro, D. W. (1972). "Preperceptual images, processing time, and perceptual units in auditory perception," *Psychol. Rev.* **79**, 124–145.
- Massaro, D. W. (1973). "A comparison of forward versus backward recognition masking," *J. Exp. Psychol. Hum. Percept. Perform.* **100**, 434–436.
- Massaro, D. W. (1975). "Backward recognition masking," *J. Acoust. Soc. Am.* **58**, 1059–1065.
- Massaro, D. W. (1977). "Capacity limitations in auditory information processing," in *Proceedings of the Sixth International Symposium on Attention and Performance*, edited by S. Dornic (Erlbaum, Hillsdale, NJ), pp. 213–229.
- Massaro, D. W. (1984). "Time's role for information, processing, and normalization," *Ann. N.Y. Acad. Sci.* **423**, 372–384.
- Massaro, D. W., and Burke, D. (1991). "Perceptual development and auditory backward recognition masking," *Dev. Psychol.* **27**, 85–96.
- McAnally, K. I., and Stein, J. F. (1996). "Auditory temporal coding in dyslexia," *Proc. R. Soc. London, Ser. B.* **263**, 961–965.
- McArthur, G. M., Bishop, D. V. M., and Nobre, A. C. (unpublished).
- McArthur, G. M., Hogben, J. H., Edwards, V. T., Heath, S. M., and Mengler, E. D. (2000b). "On the 'specifics' of specific reading disability and specific language impairment," *J. Child. Psychol. Psychiatry.* **41**, 869–874.
- McCroskey, R. L., and Kidder, H. C. (1980). "Auditory fusion among learning disabled, reading disabled, and normal children," *J. Learn. Disabil.* **13**, 69–76.
- Merzenich, M. M., Jenkins, W. M., Johnston, P., Schreiner, C., Miller, S. L., and Tallal, P. (1996). "Temporal processing deficits of language-learning impaired children ameliorated by training," *Science* **271**, 77–81.
- Mody, M., Studdert-Kennedy, M., and Brady, S. (1997). "Speech perception deficits in poor readers: Auditory processing or phonological coding?," *J. Exp. Child Psychol.* **64**, 199–231.
- Montgomery, J. W., Windsor, J., and Stark, R. E. (1991). "Specific speech and language disorders," in *Neuropsychological Foundations of Learning Disabilities: A Handbook of Issues, Methods and Practice*, edited by J. Obrzut and G. W. Hynd (Academic, California), pp. 573–601.
- Neale, M. D. (1988). *Neale Analysis of Reading Ability Revised: Manual* (Australian Council for Educational Research, Hawthorn, Australia).
- Neville, H. J., Coffey, S. A., Holcomb, P. J., and Tallal, P. (1993). "The neurobiology of sensory and language processing in language-impaired children," *J. Cognit. Neurosci.* **5**, 235–253.
- Newman, C. W., and Spitzer, J. B. (1983). "Prolonged auditory processing time in the elderly: Evidence from a backward recognition-masking paradigm," *Audiology* **22**, 241–252.
- Nicolson, R. I., and Fawcett, A. J. (1994). "Reaction times and dyslexia," *Quarterly J. Exp. Psychol.* **47A**, 29–48.
- Pammer, K., and McGregor, R. (unpublished).
- Raab, D. H. (1963). "Backward masking," *Psychol. Bull.* **60**, 118–129.
- Rapin, I., and Wilson, B. C. (1978). "Children with developmental language disability: Neurological aspects and assessment," in *Developmental Dysphasia*, edited by M. A. Wyke (Academic, London), pp. 13–41.
- Reed, M. A. (1989). "Speech perception and the discrimination of brief auditory cues in reading disabled children," *J. Exp. Child Psychol.* **48**, 270–292.
- Rosen, S. (1999). "Language disorders: A problem with auditory processing?," *Curr. Biol.* **9**, R698–R700.
- Semmel, E., Wiig, E. H., and Secord, W. (1987). *Clinical Evaluation of Language Fundamentals—Revised* (The Psychological Association, San Antonio, TX).
- Sloan, C. (1992). "Language, language learning, and language disorder: Implications for central auditory processing," in *Central Auditory Processing: A Transdisciplinary View*, edited by J. Katz, N. A. Slesker, and D. Henderson (Mosby Year Book, St. Louis, MO), pp. 179–186.
- Studdert-Kennedy, M., and Mody, M. (1995). "Auditory temporal perception deficits in the reading-impaired: A critical review of the evidence," *Psychon. Bull. Rev.* **2**, 508–514.
- Tallal, P. (1976). "Rapid auditory processing in normal and disordered language development," *J. Speech. Hear.* **3**, 561–571.
- Tallal, P. (1980). "Auditory temporal perception, phonics, and reading disabilities in children," *Brain Language* **9**, 182–198.
- Tallal, P., and Piercy, M. (1973a). "Defects of non-verbal auditory perception in children with developmental aphasia," *Nature (London)* **241**, 468–469.
- Tallal, P., and Piercy, M. (1973b). "Developmental aphasia: Impaired rate of non-verbal processing as a function of sensory modality," *Neuropsychologia* **11**, 389–398.
- Tallal, P., and Stark, R. E. (1982). "Perceptual/motor profiles of reading impaired children with or without concomitant oral language deficits," *Ann. Dyslexia* **32**, 163–176.
- Tallal, P., Stark, R., Kallman, C., and Mellits, D. (1981). "A reexamination of some nonverbal perceptual abilities of language-impaired and normal children as a function of age and sensory modality," *J. Speech Hear. Res.* **24**, 351–357.
- Taylor, M. M., and Creelman, C. D. (1967). "PEST: Efficient estimates on probability functions," *J. Acoust. Soc. Am.* **41**, 782–787.
- The Psychological Corporation (1991). *Wechsler's Intelligence Scale for Children*, 3rd ed. (The Psychological Corporation, New York).
- Tukey, J. W. (1977). *Exploratory Data Analysis* (Addison-Wesley, Reading, MA).
- Vellutino, F. R. (1979). *Dyslexia: Theory and Research* (The MIT Press, Cambridge, MA).
- Visto, J. C., Cranford, J. L., and Scudder, R. (1996). "Dynamic temporal processing of nonspeech acoustic information by children with specific language impairment," *J. Speech Hear. Res.* **39**, 510–517.
- Wightman, F., Allen, P., Dolan, T., Kistler, D., and Jamieson, D. (1989). "Temporal resolution in children," *Child Dev.* **60**, 611–624.
- Wright, B. A., Lombardino, L. D., King, W. M., Puranik, C. S., Leonard, C. M., and Merzenich, M. M. (1997). "Deficits in auditory temporal and spectral resolution in language-impaired children," *Nature (London)* **387**, 176–178.

Informational and energetic masking effects in the perception of two simultaneous talkers

Douglas S. Brungart^{a)}

Air Force Research Laboratory, Human Effectiveness Directorate, Wright-Patterson AFB, Ohio 45433

(Received 5 June 2000; revised 25 October 2000; accepted 12 December 2000)

Although most recent multitalker research has emphasized the importance of binaural cues, monaural cues can play an equally important role in the perception of multiple simultaneous speech signals. In this experiment, the intelligibility of a target phrase masked by a single competing masker phrase was measured as a function of signal-to-noise ratio (SNR) with same-talker, same-sex, and different-sex target and masker voices. The results indicate that informational masking, rather than energetic masking, dominated performance in this experiment. The amount of masking was highly dependent on the similarity of the target and masker voices: performance was best when different-sex talkers were used and worst when the same talker was used for target and masker. Performance did not, however, improve monotonically with increasing SNR. Intelligibility generally plateaued at SNRs below 0 dB and, in some cases, intensity differences between the target and masking voices produced substantial improvements in performance with decreasing SNR. The results indicate that informational and energetic masking play substantially different roles in the perception of competing speech messages. [DOI: 10.1121/1.1345696]

PACS numbers: 43.66.Pn, 43.66.Rq, 43.71.Gv [DWG]

I. INTRODUCTION

When a speech signal is obscured by a second simultaneous competing speech signal, overall performance is determined by the cumulative effects of two different types of masking (Freyman *et al.*, 1999; Kidd *et al.*, 1998). Traditional “energetic” masking occurs when both utterances contain energy in the same critical bands at the same time and portions of one or both of the speech signals are rendered inaudible at the periphery. Higher-level “informational masking” occurs when the signal and masker are both audible but the listener is unable to disentangle the elements of the target signal from a similar-sounding distracter (Doll and Hanna, 1997; Kidd *et al.*, 1994; Kidd, Mason, and Rohtla, 1995; Neff, 1995; Watson, Kelly, and Wroton, 1976). It is difficult to isolate the informational and energetic elements of speech-on-speech masking, so no previous studies have directly examined their relative contributions to multitalker speech perception. However, the results of previous experiments do provide some insights about each type of masking.

The effects of purely energetic noise masking on speech intelligibility are well documented. The Articulation Index (AI) (French and Steinberg, 1947; Fletcher and Galt, 1950), which is based on a comprehensive series of experiments with non-speech-masking signals conducted in the early days of the telephone industry, is capable of predicting speech intelligibility directly from the long-term rms spectra of the speech and masker signals. Articulation theory has shown that energetic speech masking depends almost exclusively on the spectral overlap between the speech signal and the

masker, and that performance decreases monotonically with decreasing signal-to-noise ratio (SNR).

The effects of informational masking on speech intelligibility can only be determined from multitalker experiments. Only a handful of early experiments has examined the effects of SNR in monaural speech-on-speech masking (Miller, 1947; Egan, Carterette, and Thwing, 1954; Dirks and Bower, 1969).¹ The two later studies found that performance generally increased with increasing SNR but was independent of SNR in the region from -10 to 0 dB. Although one would expect the similarity of the target and masker voices to be an important component in informational masking, very few studies have systematically examined the roles of voice characteristics such as talker and masker sex in speech-on-speech masking. The studies that have examined same-sex and different-sex talkers have shown that performance is substantially better in the different-sex condition (Festen and Plomp, 1990). This is consistent with informational masking, which is based on the listener’s ability to segregate perceptually similar sounds, and should increase when the target and masking voices resemble one another.

The majority of recent multitalker research has focused primarily on the binaural effects of spatially separating the target and masking signals (Drullman and Bronkhorst, 2000; Duquesnoy, 1983; Freyman *et al.*, 1999; Hawley, Litovsky, and Colburn, 1999; Festen and Plomp, 1986; Peissig and Kollmeier, 1997; Plomp, 1976; Yost, Dye, and Sheft, 1996). These “cocktail party” studies provide valuable information about the spatial unmasking of speech, but they do not provide many insights into the types of cues listeners use to segregate monaurally or diotically presented competing speech signals. The results of recent experiments do, however, suggest that the informational component of speech-on-speech masking may play a critical role in the “binaural

^{a)}Electronic mail: douglas.brungart@he.wpafb.af.mil

advantage'' of spatially separating the talkers. Kidd and colleagues (1998) have shown that an exceptionally large release from masking can occur when a purely informational masker is moved to a different spatial location than the signal. More recent results have also shown that spatial separation or perceived spatial separation can produce a much larger release from speech-on-speech masking than from speech-on-noise masking (Hawley, Litovsky, and Culling, 2000; Freyman *et al.*, 1999). These results suggest that the informational component of speech-on-speech masking is particularly sensitive to differences in the perceived locations of the target and masker, and may account for a large portion of the spatial unmasking found in cocktail party experiments.

In this experiment, the intelligibility of a target phrase masked by a single competing talker was examined as a function of SNR, target sex, and masker sex under diotic listening conditions. The responses were used to determine the relative contributions of energetic and informational masking to overall performance. The results are discussed in terms of their potential implications in multitalker listening environments.

II. METHODS

A. Stimuli

The stimuli were derived from a publicly available speech corpus for multitalker communications research (Bolia *et al.*, 2000). This corpus, which is based on the coordinate response measure (CRM) first developed by Moore (1981), consists of phrases of the form ''Ready (call sign) go to (color) (number) now'' spoken with all possible combinations of eight call signs (''arrow,'' ''baron,'' ''charlie,'' ''eagle,'' ''hopper,'' ''laker,'' ''ringo,'' ''tiger''), four colors (''blue,'' ''green,'' ''red,'' ''white''), and eight numbers (1–8). Thus, a typical utterance in the corpus would be ''Ready baron go to blue five now.'' Eight talkers (four male, four female) were used to record each of the 256 possible phrases, so a total of 2048 phrases is available in the corpus.

In the speech-masker condition of this experiment, the stimuli consisted of two simultaneous phrases from the CRM corpus: a target phrase with the call sign baron and a masker phrase with a randomly selected call sign other than baron. In each trial, the target and masker phrases were selected randomly from the speech corpus with the restriction that different colors and different numbers were used in the two phrases. First, the overall level (rms power) of the masker phrase was set to a comfortable listening level (approximately 60–70 dB SPL). Then, the overall level (rms power) of the target phrase was adjusted relative to the level of the masker phrase to produce one of ten different SNRs ranging from –12 to 15 dB in 3-dB steps. The target and masker signals were then added together, and the combined signal was randomly roved over a 6-dB range (in 1-dB steps) before being presented to the listener over headphones. Within each block of 240 trials, each talker in the corpus was used as the speaker of the target phrase in exactly 30 trials. All other variables, including the masking talker, the masking call sign, the numbers and colors of the target and masker

phrases, and the SNR, were chosen randomly with replacement on each trial.

Performance was also measured for two types of noise maskers. The first noise masker consisted of Gaussian noise that was spectrally shaped with a finite impulse response (FIR) filter matching the average long-term rms spectrum of the 2048 sentences in the CRM corpus and rectangularly gated to the same length as the target phrase. SNRs were varied from –18 to +15 dB in 3-dB steps in this condition, which is described in more detail elsewhere (Brungart, 2001). The second noise masker consisted of speech-shaped noise that was modulated with the envelope of a randomly selected competing speech phrase selected from the CRM corpus in the same way as in the speech-masker condition. The envelope was calculated by convolving the absolute value of the competing speech waveform with a 7.2-ms rectangular window. SNRs were varied from –21 to 0 dB in 3-dB steps in this modulated noise condition. As in the speech-masker conditions, the SNRs in the noise-masker conditions were calculated from the overall rms powers of the noise and speech waveforms. The noise-masker conditions were otherwise similar to the speech-masking conditions.

B. Listeners

Nine paid listeners, five male and four female, participated in the experiment. All had normal hearing (15 dB HL from 500 Hz to 6 kHz) and their ages ranged from 21–55. Each had participated in previous auditory experiments, and all but two had previous experience in experiments using the CRM speech materials.

C. Procedure

The listening task was performed while seated at a control computer. In each trial, the speech stimulus was generated by a sound card in the control computer (Soundblaster AWE-64) and presented to the listener over headphones (Sennheiser HD-520). Then an eight-column, four-row array of colored digits corresponding to the response set of the CRM was displayed on the CRT, and the listener used the mouse to select the colored digit corresponding to the color and number used in the target phrase containing the call sign baron. The trials were divided into blocks of 240 trials, with one or two blocks collected on each day of the experiment. A total of 2000 trials for each of the nine listeners was collected in the speech-masker condition of this experiment.² The speech-masker condition was followed by 960 trials per subject in the continuous-noise-masker condition, and then by 240 trials per subject in the speech-envelope modulated noise-masker condition.

III. RESULTS AND DISCUSSION

A. The dominance of informational masking

The results in Fig. 1 show substantial differences between the speech-shaped noise masker and the three speech maskers used in the experiment. These differences reflect the different mechanisms involved in the two masking condi-

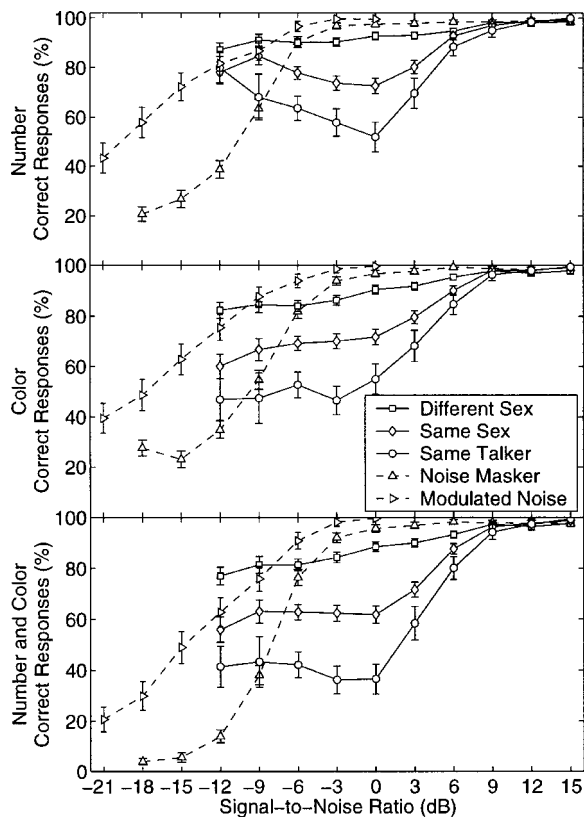


FIG. 1. Percentage of correct identifications as a function of SNR. The top panel shows the percentage of trials where the listener correctly identified one of eight different numbers. The middle panel shows the percentage of correct identifications of one of four colors. The bottom panel shows the percentage of trials in which the listener correctly identified both the number and color. The data are shown separately for trials where the competing talkers were of different sexes, where the talkers were different but were both male or female, and for trials where the same talker was used for both the target and masker sentences. Results are also shown for a speech-shaped noise masker and an envelope-modulated speech-shaped noise masker. In each case, the data at each SNR value were averaged across the nine listeners used in the experiment. Note that each data point represents approximately 900 trials for the different-sex condition, 675 trials for the same-sex condition, 225 trials for the same-talker condition, 720 data points for the noise-masker condition, and 270 trials for the modulated noise-masker condition. The error bars represent the 95%-confidence intervals for each point. Note that the SNR ratios were calculated from the overall rms power of each signal.

tions: with the speech-shaped noise masker, the masking is primarily energetic and results from acoustic degradation of the speech signal; with the competing speech maskers, energetic masking occurs when the two fluctuating speech signals overlap in time and frequency, and higher-level informational masking occurs when the listener tries to segregate the two similar-sounding talkers into distinct utterances. While there is no question that some energetic masking occurs in the simultaneous speech conditions, there is substantial evidence that informational masking effects dominated performance in the two-talker conditions.

An upper bound on the influence of energetic masking in the two-talker conditions is provided by the percentages of correct responses at the lowest SNR tested, -12 dB. At this level, the listeners were still able to correctly identify 80% of the target numbers and 50% of the target colors, even when the same talker was used for the target and masker phrases.

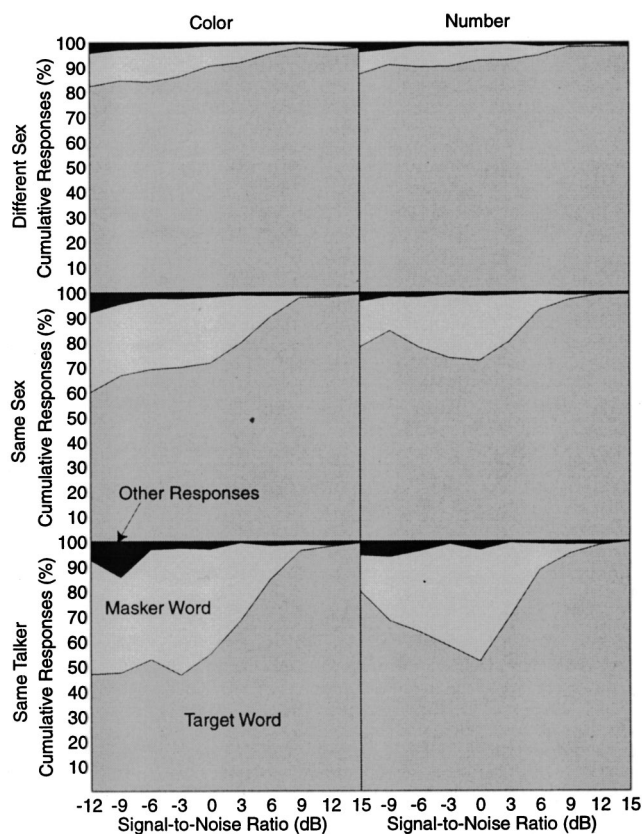


FIG. 2. These area graphs show the distribution of the listeners' responses among the correct word spoken by the target talker, the incorrect word spoken by the masking talker, and all other possible incorrect responses. In all conditions, the masking word occurred in the overwhelming majority of the incorrect responses.

The effects of energetic masking decrease monotonically with increasing SNR, so these performance levels reflect the greatest possible influence of energetic masking in this experiment. Any reduction in performance below these levels, such as the significant reductions in correct number identifications that occur when the SNR is near 0 dB in the same-sex and same-talker conditions, can only be attributable to informational masking effects.

The distributions of incorrect responses in the experiment provide additional evidence that informational masking dominates the perception of two-talker speech. When energetic masking interferes with the perception of a speech stimulus, the utterance is rendered inaudible by the noise and the listener must randomly choose the response from among all words in the vocabulary. Thus, energetic masking should produce roughly random distributions of incorrect responses. There is, however, no evidence of this type of error distribution in the two-talker conditions of this experiment. An analysis of the errors in the experiment (Fig. 2) shows that the listeners who failed to correctly identify the words in the target phrase were much more likely to respond to the words heard in the masker phrase than to the other possible words in the response set. At negative SNRs, where the target phrase was difficult to comprehend, it is not surprising that the listeners tended to respond to the coordinates in the easily understood masker phrase. At large positive SNRs, however, it is much harder to explain the masker-word responses

in the context of energetic masking. In the same-talker condition at 9 dB SNR, where substantial energetic masking of the masker phrase by the target phrase should have occurred, approximately 66% of the incorrect color responses and 75% of the incorrect number responses were assigned to the masker word (compared to the 33% and 14% expected for randomly distributed errors). This suggests that the listeners were usually able to detect the color–number coordinates, even when they were energetically masked by a 9-dB more intense voice. At 0 dB SNR, where energetic masking should have been roughly equivalent for the two talkers, the target or masker coordinates appear in virtually all the responses. It is interesting to note that the percentages of nonmasker, non-target responses were not much higher at -6 dB than they were at 15 dB, where the target phrase should have been clearly audible and the incorrect responses were probably the result of extraneous factors such as subject inattention. These extraneous errors should be evenly distributed across all the SNR levels in the experiment, so there is little evidence that energetic masking is causing any of the incorrect responses at SNRs above -6 dB.

The results of the modulated noise condition provide a final indication that energetic masking plays a relatively small role in the speech-masker conditions. With the modulated noise masker, the energy in the masking signal is located in roughly the same spectral region as in the speech maskers, and the level of the noise signal fluctuates in the same way as the level of the speech maskers. Thus, the temporal distribution of energy in the modulated noise should be very similar to the temporal distribution of energy in the speech.³ In the same-sex condition, performance does seem to be bounded by the modulated noise condition. At -9 dB SNR, there is a local maximum in the percentage of correct number identifications where the same-sex performance curve intersects with the modulated noise masker. Elsewhere, however, performance was substantially better in the modulated noise condition than in any of the two-talker conditions. Again, this suggests that energetic masking had relatively little impact on the intelligibility of the color and number coordinates in the two-talker conditions, and that the color–number coordinates of both masker phrases were audible across most of the range of SNRs tested.

A final comment should be made about the relationship between energetic masking and the type of speech intelligibility test used. From articulation theory, it is known that the relationship between speech intelligibility and noise level is highly dependent on the type of test used to measure intelligibility. Previous work relating the CRM task to the AI (Brungart, 2001) has shown that the CRM test is relatively insensitive to energetic masking by noise: 50% performance with the CRM requires an AI of only 0.08, compared to 0.17 with the well-known Modified Rhyme Test (MRT). Indeed, the insensitivity of the CRM to noise is readily apparent from the performance curves in Fig. 1: substantial noise masking does not occur until the noise is at least 6 dB more intense than the speech. It is likely that the amount of energetic masking that occurs in multiple-talker speech is directly related to the noise sensitivity of the speech utterances tested. Thus, one would expect to see larger energetic-

masking effects in a multitalker experiment based on a more sensitive speech test such as the MRT than were found in this CRM-based experiment. The relative absence of energetic effects with the CRM speech corpus makes it a relatively good choice for experiments focusing on the effects of informational masking in speech.

B. Talker and masker voice characteristics

The informational masking in this experiment is related to the listener's inability to segregate similar-sounding speech signals, so one would expect the effects of informational masking to increase when the target and masking voices have similar characteristics. This is clearly seen in the results of this experiment (Fig. 1). At negative SNRs, correct identifications were 15%–20% lower in the same-sex condition than in the different-sex condition, and 15%–20% lower in the same-talker condition than in the same-sex condition. These large differences in performance with the talker and masker voice characteristics are consistent with the concept of informational masking. A listener's ability to segregate two simultaneous voice signals is dependent on the distinctive characteristics of the two voices. Male and female voices are so different that the listener has little difficulty discriminating between the target and masker phrases. The voices of two different talkers of the same sex are much more difficult to segregate, but still provide the listener with substantial acoustic cues about the identity of the two talkers. Two voices from the same talker provide only minor acoustic discrimination cues and make the multitalker listening task extremely difficult. Clearly, in experiments focusing on informational masking, same-talker voices are preferred and different-sex voices should be avoided.

Of course, energetic masking should also increase with the similarity of the target and masker voices because the energy is concentrated in the same frequency ranges when same-sex and same-talker voices are used. However, the informational masking component appears to dominate this increase in energetic masking. Festen and Plomp (1990) used noise maskers that matched the long-term rms spectra of male and female voices and found much larger differences in performance between speech-on-speech masking with same-sex and different-sex talkers than they found between noise-on-speech masking with same-sex and different-sex speech-shaped noise maskers.

The relationship between the sexes of the target and masking talkers had a much larger impact on overall performance than did the particular sex of the target talker (Fig. 3). In each masking condition, performance was similar for male and female target talkers. However, there were some differences in performance across the eight individual talkers used in the CRM speech corpus. One male talker consistently produced more accurate responses than the others did (Fig. 4). When Talker 3 was used for the target phrase, the listeners correctly identified the number and color in 11% more trials than the average of the other seven talkers. When Talker 3 was used for the masker, the listeners correctly identified the color and number in 9% more trials than the average of the other talkers. This result implies that distinctive individual voice characteristics can improve the intelligibility of a par-

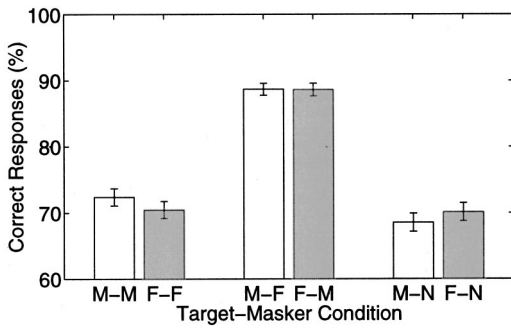


FIG. 3. Overall percentages of correct identifications of both color and number for each talker-masker combination. The conditions are shown as A-B where A is the target and B is the masker. M=male speech; F=female speech; N=speech-shaped noise. The error bars represent the 95%-confidence intervals of each point. The noise-masker data have been averaged over a wider range of SNR values than the speech-masker data (-18 to $+15$ dB for the noise versus -12 to $+15$ dB for the speech), so these results should not be used to compare overall performance in the noise-masking and speech-masking conditions.

ticular voice in multichannel communications, both when the voice serves as the target and when the voice serves as the masker.

C. Signal-to-noise ratio

From direct comparison of the speech masker results to those with the speech-shaped noise masker, it is immediately apparent that SNR does not have the same effect in informational masking as it does in energetic masking. In this experiment, the continuous speech-shaped noise serves as a classical energetic masker (Fig. 1). Intelligibility is essentially unaffected by the noise until the noise becomes loud enough to mask the energy in the speech signal (at about -3 dB). Once this masking starts to occur, performance degrades very rapidly. In just a 9-dB drop in SNR (from -3 to -12 dB), the speech signal is swamped by the masker and the number of correct responses falls by 90%. As the SNR continues to decrease, the target phrase becomes inaudible and the listener responses approach random guessing (this occurs for the color response at SNRs less than -15 dB). The speech-shaped noise masker is spectrally similar to the speech, so energetic masking causes a very rapid drop-off in performance with decreasing SNR in this experiment. When the noise has a different frequency distribution than the speech, or its level varies with time, different spectral and temporal regions of the speech are masked at different SNR levels and the onset of energetic masking is more gradual. This is exactly the case with the speech-modulated noise masker shown in Fig. 1. The listener is able to hear the speech during the quiet portions of the modulated masker, and performs substantially better than with the continuous noise despite the higher peak levels that must occur in the modulated noise to maintain the same overall SNR. As SNR decreases, the less intense regions of the modulated masker gradually become loud enough to mask the target phrase and overall performance slowly decreases. However, energetic masking always causes monotonic decreases in performance with decreasing SNR: increasing the noise level can only decrease the amount of information in the stimulus and, as

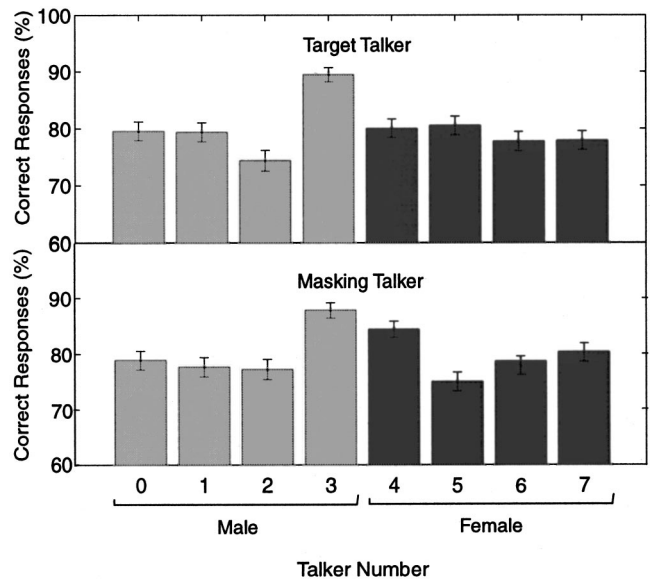


FIG. 4. Percentage of correct overall responses as a function of the talker used in the target phrase (top panel) and the masker phrase (bottom panel). Error bars show the 95%-confidence intervals for each data point.

long as there is some masker energy in all the frequency bands and temporal regions of the signal, energetic masking will eventually reduce the signal to inaudibility.

The role of SNR in informational masking is quite different. At high SNR values (above $+9$ dB), the target phrase is so loud relative to the masker signal that near-perfect performance occurred regardless of the masker signal used. At lower SNR values, however, there are substantial differences among the three speech-masking conditions. Performance in the different-sex condition was largely independent of the SNR—performance dropped by approximately 1%/dB at SNRs less than 9 dB, and correct overall identifications occurred in approximately 80% of the trials even at the lowest SNR value tested (-12 dB). In the same-sex and same-talker conditions, overall correct identifications decreased sharply as SNR fell from 9 to 0 dB, then plateaued well above chance level as SNRs decreased from 0 to -12 dB. Correct number identifications actually *increased* substantially (as much as 25% in the same-talker condition) as SNR decreased from 0 to -12 dB. Clearly, SNR has a much different impact on speech intelligibility in the information-masking dominated same-sex and same-talker conditions than it does in the energetic-masking dominated speech-shaped noise condition.

These results are consistent with previous studies that have examined the effect of SNR on the intelligibility of speech masked by a single competing talker. Egan, Carterette, and Thwing (1954) and Dirks and Bower (1969) examined a wide range of SNRs and found performance curves very similar to the ones found in this experiment: performance fell rapidly as SNR dropped from 10 to 0 dB, plateaued or increased slightly as SNR dropped from 0 to -10 dB, and fell rapidly again at SNRs lower than -10 dB. Stubbs and Summerfield (1990) examined only positive SNRs and found a rapid increase in performance from 0 to 9 dB and near-perfect performance above 9 dB. Freyman *et al.*

(1999) examined only negative SNRs and found that performance decreased much less rapidly when the speech was masked by colocated speech from the same talker (decreasing approximately 2.5%/dB) than when the speech was masked by a colocated speech-shaped noise masker (decreasing 6.7%/dB).

Taken together, the data from this experiment and the results of these previous studies tell a consistent story about speech intelligibility in the presence of a single competing talker: (1) Speech intelligibility is unimpeded by a competing talker when the target phrase is at least 10 dB more intense than the masker; (2) Speech intelligibility drops substantially as the SNR drops from 10 to 0 dB; (3) Speech intelligibility is roughly independent of SNR at SNRs from 0 to -10 dB.

The somewhat paradoxical third result can be explained in the context of informational masking. In order to understand multiple simultaneous talkers, the listener needs some way to differentiate the target voice from the masking voice. In the case where both talkers have the same voice and speak at the same level, the cues available for this discrimination are minimal (Egan *et al.*, 1954). This is exactly the case in the same-talker condition at 0 dB, where both the target and masker phrases were spoken by the same voice at the same level (Fig. 1). Correct number and color identifications occurred in only about half of the trials in that condition, and nearly all of the incorrect responses included the colors and numbers used in the masker phrase (Fig. 2). From an informational masking standpoint, this is effectively chance performance: the listeners were able to hear both the target and masker phrases, but were unable to determine which color-number pair was addressed to the call sign baron.

When the listener is faced with two similar or identical voices, any differences in the characteristics of the two talkers can help improve performance. When the intensity of the target is lowered relative to the masker, the intensity difference provides a means to discriminate the target and masking talkers, and the advantages of this level difference outweigh the increase in energetic masking caused by decreasing the SNR. In other words, the listeners were able to recognize that the baron call sign was spoken by the less-intense talker and could selectively tune their attention to the quieter voice. This explains why number identifications in the same-sex conditions of this experiment were least accurate at an SNR of 0 dB (Fig. 1) and increased substantially (by as much as 25%) when the intensity of the target voice was reduced relative to the masker.⁴

Note that the gains in performance afforded by level differences between the target and masking voices were not symmetric: positive SNRs always produced a larger performance benefit than negative SNRs of the same magnitude. Not surprisingly, it was always easier to attend to the louder of two simultaneous talkers than to the quieter one.

D. Statistical dependence of color and number errors

Within each trial in the CRM, the listener is required to respond independently to the color and number used in the target phrase. It is therefore informative to know whether the errors in the color and number responses are evenly distrib-

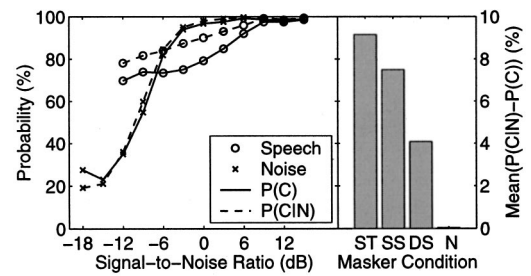


FIG. 5. Statistical dependence of correct responses for the color and number in the target phrase. The left panel shows the overall probability of a correct color response [$P(C)$] and the probability of a correct color response when the listener correctly identified the number in the target phrase [$P(C|N)$] averaged across all the target and masking talkers used in the experiment. The right panel shows the average value of $P(C|N) - P(C)$ across all SNRs for the same-talker (ST), same-sex (SS), different-sex (DS), and noise-masker (N) conditions.

uted across all trials or grouped into the same trials. This can be determined by checking the responses for statistical independence (Fig. 5). If the errors are statistically independent, the probability of correctly identifying the color across all trials at a given SNR [$P(C)$] should be the same as the probability of correctly identifying the color in trials where the number was also correctly identified [$P(C|N)$]. As seen in the figure, this is true for the energetic noise masker. Thus, the ability to correctly identify the number in a given noise-masker trial was independent of the ability to correctly identify the color. With the informational speech maskers, however, the listeners were substantially more likely to correctly identify the color when they were also able to correctly identify the number. Thus, with the speech maskers, the color and number errors tended to be grouped into the same trials. As shown in the right panel of Fig. 5, this effect was strongest in the same-talker condition and weakest (but still substantial) in the different-sex condition. The tendency to group color and number trials together in the speech-masker conditions relates directly to the listeners' attempts to segregate the target and masker phrases. Because the colors and numbers occur sequentially in the CRM phrases, there are strong prosodic cues that link together the color-number pairs spoken by the same talkers. Also, when there are differences in speaking rates across the talkers, the color-number pairs will occur at different times in the target and masker phrases. These temporal and prosodic cues influence the listeners to respond to the color-number pair spoken by one of the two talkers (thus getting both coordinates correct or missing both) rather than responding to the color spoken by one talker and the number spoken by the other (and getting only one of the two coordinates correct).

E. Color and number effects

The specific colors and numbers used in the target and masker phrases had relatively little impact on performance in the experiment (Fig. 6). The percentages of correct responses varied by less than 8% across the eight numbers and four colors used in the experiment. Note, however, that there was a strong negative correlation between performance when the

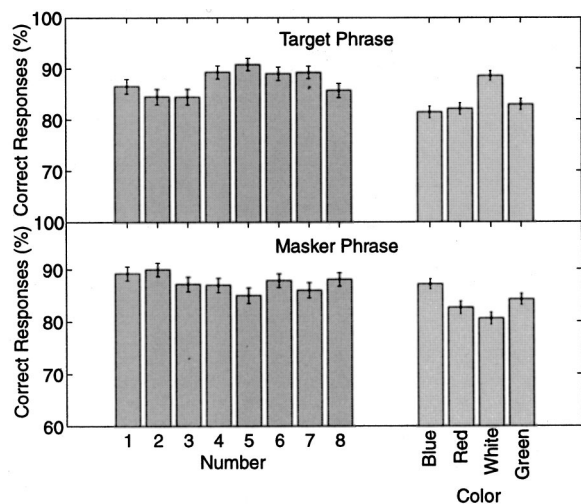


FIG. 6. Correct identifications for the different color and number words used in the CRM corpus. The data on the left show the percentages of correct number identifications as a function of the number coordinate used in the target phrase (top panel) and in the masker phrase (bottom panel). The data on the right show the percentages of correct color identifications as a function of the color coordinate used in the target phrase (top panel) and in the masker phrase (bottom panel). The error bars represent 95%-confidence intervals.

individual words appeared in the target and masker phrases. The color “white,” for example, produced the best overall performance when it appeared in the target phrase and the worst overall performance when it appeared in the masker phrase. The correlation coefficient between the percentage of correct responses when each word appeared in the target phrase and the percentage of correct responses when each word appeared in the masker phrase was -0.74 for the number coordinates and -0.80 for the color coordinates. This negative correlation indicates that the words that were easy to identify in the target phrase were especially effective maskers when they appeared in the masker phrase. Note that this is in direct contrast to the effects of the individual talker voices on performance. Talker 3 produced better performance than any other talker, both as a target talker and as a masking talker (Fig. 4), and the correlation coefficient between overall performance when each talker was used for the target phrase or the masking phrase was $+0.74$. These results suggest that the intelligibility of the individual coordinate words is based primarily on their ability to overpower the coordinates in the competing phrase, while the intelligibility of the individual talkers is based primarily on the acoustic similarities between the target and masking voices.

F. Intersubject differences

In general, the differences across the listeners were small relative to the large effects of SNR and the sexes of the target and masker. The pattern of responses (with respect to the SNR, as shown in Fig. 1) was roughly similar for each listener, and the percentage of correct overall identifications ranged from 72% to 86% across the nine listeners used in the experiment.

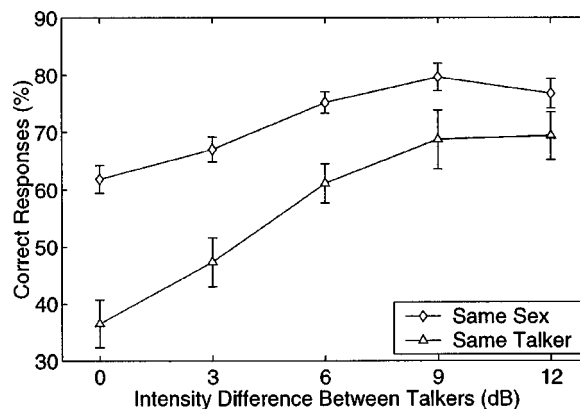


FIG. 7. Percentage-correct identifications of both color and number for two competing phrases spoken by different same-sex talkers and by the same talker when the target sentence is equally likely to come from either of the two voices. The results are shown as a function of the difference in intensity between the two talkers. The error bars in the top panel represent 95%-confidence intervals.

IV. THE IMPACT OF SNR ON THE OVERALL INTELLIGIBILITY OF TWO-TALKER SPEECH

The plateauing in performance that occurs in the same-sex conditions at SNRs less than 0 dB has important implications in monaural or diotic multitalker listening situations. Consider, for example, a listener who is monaurally monitoring two radio channels for information that is equally likely to originate from either channel. If the listener is able to control the levels of the two channels independently, how should the radio be configured for optimal performance in this task? Because both channels are equally important, intuition would suggest that both should be set at the same level. However, the results of this experiment suggest not only that setting the channels to the same level is less than optimal, but that it is among the worst possible strategies. The explanation for this apparent paradox lies in the performance curves shown in Fig. 1. Assume that two different talkers are used on the two channels and that both are males or both are females. If both channels are set to the same level, overall correct identifications should occur in approximately 60% of all trials. Now, if one channel is set to a 3-dB-higher SNR than the other channel, a substantial (10%) improvement in intelligibility occurs when the target phrase occurs in the more intense channel, while performance is effectively unchanged when the target phrase occurs in the less intense channel. The number of correct overall identifications in this scenario will be the average of performance in the two channels, or 65%. Thus, by setting the overall levels of the two channels 3 dB apart, a 5% gain in overall intelligibility has been achieved. As the level difference between the two channels is increased (Fig. 7), overall performance continues to improve until reaching its peak value when the channel separation is 9 dB. At separations greater than 9 dB, intelligibility approaches 100% in the more intense channel and begins degrading due to energetic masking in the less-intense channel. Consequently, no further performance gains can be achieved by separating the channels by more than 9 dB. Note that this improvement is driven more by the rapid intelligibility increase at positive SNRs than by the increase in per-

formance that occurs in number identifications at negative SNRs: performance is maximized for both the color and number coordinates when the channel separation is 9 dB.

The improvements in performance obtained by varying the levels of the talkers are substantial. When the intensities of two different same-sex talkers differ by 9 dB, the percentage of overall correct identifications is more than 20% higher than when the talkers are at the same level. The improvement is even larger when both competing messages are spoken by the same talker. These improvements are roughly equivalent to increasing the SNR by 5 dB in both channels.

V. CONCLUSIONS

This experiment has examined the factors that influence a listener's ability to selectively attend to one of two competing speech messages in the coordinate response measure paradigm. There is substantial evidence that informational masking, rather than energetic masking, dominated performance in this experiment. Thus, it is possible to draw some general conclusions about the differences between informational and energetic masking in a two-competing-talker task:

- (i) The voice characteristics of the target and masking talkers have a profound effect on the intelligibility of competing speech messages. Performance was substantially better when the talkers were of different sexes than when they were the same sex, and substantially better with different talkers of the same sex than when the same talker was used for both the target and masker phrase.
- (ii) The SNR generally has a much smaller influence on speech intelligibility with a speech masker than with a noise masker. When an energetic noise masker is used, performance decreases monotonically with the SNR, and falls off rapidly to chance level when the masker begins to overpower the target speech signal. When a speech masker is used, performance decreases when the SNR is reduced from 9 to 0 dB, but plateaus at well above chance level and, in some cases, increases when the SNR is reduced from 0 to -9 dB.
- (iii) In some cases, the intelligibility of two competing talkers can be substantially improved by introducing a level difference in the two voices. With the CRM phrases, overall intelligibility could be improved from about 60% to about 80% by introducing a 9 dB level difference between two same-sex talkers.

The results also suggest that the phrases in the CRM speech corpus are ideally suited for speech intelligibility experiments that focus on the informational component of speech on speech masking. When the CRM phrases are used at SNRs near 0 dB, there is strong evidence that both the target and masker voices are clearly audible and that the vast majority of incorrect responses were due to the listeners' inability to correctly determine which color and number coordinates were directly addressed to their assigned call sign. Thus, it appears that the CRM phrases would be an excellent choice for researchers who want to isolate the informational

masking component of speech in future two-talker cocktail party experiments.

ACKNOWLEDGMENTS

The author would like to thank Brian Simpson, Mark Ericson, Todd Nelson, and Bob Bolia both for the use of their CRM corpus and for their helpful comments during the preparation of this manuscript. This work was supported in part by AFOSR Grants F49620-98-1-0108 and 01-HE-01-COR.

¹See Bronkhorst (2000) for a recent review of studies examining monaural or diotic multitalker speech perception.

²Due to a technical error, some trials were collected with the same number or color in the target and masker phrases. These trials were discarded, and the first 2000 valid trials for each subject were used in the analyses.

³Note that the spectral distribution of energy is fixed in the modulated noise masker but time variant in speech.

⁴It is not clear why the advantage of negative SNRs was limited to the number response. It may be related to the placement of the number after the color in the carrier phrase, where variations in the speaking rates of the talkers are more likely to reduce the temporal overlap of the numeric coordinates in the target and masking phrases. It may also be related to the greater sensitivity of the color coordinate to energetic masking (Brungart, 2000). The fact that color identification performance did not decrease at negative SNRs may imply that the decrease in informational masking caused by the difference in the target and masker levels was offset by a corresponding increase in energetic masking in these conditions.

Bolia, R., Nelson, W., Ericson, M., and Simpson, B. (2000). "A speech corpus for multitalker communications research," *J. Acoust. Soc. Am.* **107**, 1065–1066.

Bronkhorst, A. (2000). "The cocktail party phenomenon: A review of research on speech intelligibility in multiple-talker conditions," *Acustica* **86**, 117–128.

Brungart, D. (2001). "Evaluation of speech intelligibility with the coordinate response measure," *J. Acoust. Soc. Am.* (to be published).

Dirks, D., and Bower, D. (1969). "Masking effects of speech competing messages," *J. Speech Hear. Res.* **12**, 229–245.

Doll, T., and Hanna, T. (1997). "Directional cueing effects in auditory recognition," in *Binaural and Spatial Hearing in Real and Virtual Environments*, edited by R. H. Gilkey and T. R. Anderson (Erlbaum, Hillsdale, NJ).

Drullman, R., and Bronkhorst, A. (2000). "Multichannel speech intelligibility and talker recognition using monaural, binaural, and three-dimensional auditory presentation," *J. Acoust. Soc. Am.* **107**, 2224–2235.

Duquesnoy, A. (1983). "Effect of a single interfering noise or speech source on the binaural sentence intelligibility of aged persons," *J. Acoust. Soc. Am.* **74**, 739–943.

Egan, J., Carterette, E., and Thwing, E. (1954). "Factors affecting multi-channel listening," *J. Acoust. Soc. Am.* **26**, 774–782.

Festen, J., and Plomp, R. (1986). "Speech reception threshold in noise with one and two hearing aids," *J. Acoust. Soc. Am.* **79**, 465–471.

Festen, J., and Plomp, R. (1990). "Effects of fluctuating noise and interfering speech on the speech reception threshold for impaired and normal hearing," *J. Acoust. Soc. Am.* **88**, 1725–1736.

Fletcher, H., and Galt, R. (1950). "The perception of speech and its relation to telephony," *J. Acoust. Soc. Am.* **22**, 89–151.

French, N., and Steinberg, J. (1947). "Factors governing the intelligibility of speech sounds," *J. Acoust. Soc. Am.* **19**, 90–119.

Freyman, R., Helfer, K., McCall, D., and Clifton, R. (1999). "The role of perceived spatial separation in the unmasking of speech," *J. Acoust. Soc. Am.* **106**, 3578–3587.

Hawley, M., Litovsky, R., and Culling, J. (2000). "The 'cocktail party' effect with four kinds of maskers: Speech, time-reversed speech, speech-shaped noise, or modulated speech-shaped noise," in *Proceedings of the Midwinter Meeting of the Association for Research in Otolaryngology*, 31.

Hawley, M., Litovsky, R., and Colburn, H. (1999). "Speech intelligibility and localization in a multisource environment," *J. Acoust. Soc. Am.* **105**, 3436–3448.

- Kidd, G. J., Mason, C., Deliwala, P., Woods, W., and Colburn, H. (1994). "Reducing informational masking by sound segregation," *J. Acoust. Soc. Am.* **95**, 3475–3480.
- Kidd, G. J., Mason, C., and Rohtla, T. (1995). "Binaural advantage for sound pattern identification," *J. Acoust. Soc. Am.* **98**, 1977–1986.
- Kidd, G. J., Mason, C., Rohtla, T., and Deliwala, P. (1998). "Release from informational masking due to the spatial separation of sources in the identification of nonspeech auditory patterns," *J. Acoust. Soc. Am.* **104**, 422–431.
- Miller, G. (1947). "The masking of speech," *Psychol. Bull.* **44**, 105–129.
- Moore, T. (1981). "Voice communication jamming research," in AGARD Conference Proceedings 331: Aural Communication in Aviation, pp. 2:1–2:6, Neuilly-Sur-Seine, France.
- Neff, D. (1995). "Signal properties that reduce masking by simultaneous random-frequency maskers," *J. Acoust. Soc. Am.* **96**, 1909–1921.
- Peissig, J., and Kollmeier, B. (1997). "Directivity of binaural noise reduction in spatial multiple noise-source arrangements for normal and impaired listeners," *J. Acoust. Soc. Am.* **35**, 1660–1670.
- Plomp, R. (1976). "Binaural and monaural speech intelligibility of connected discourse in reverberation as a function of the azimuth of a single competing sound source (speech or noise)," *Acustica* **34**, 325–328.
- Stubbs, R., and Sommerfield, Q. (1990). "Algorithms for separating the speech of interfering talkers: Evaluations with voiced sentences, and normal-hearing and hearing-impaired listeners," *J. Acoust. Soc. Am.* **87**, 359–372.
- Watson, C., Kelly, W., and Wroton, H. (1976). "Factors in the discrimination of tonal patterns. II. Selective attention and learning under various levels of stimulus uncertainty," *J. Acoust. Soc. Am.* **60**, 1176–1185.
- Yost, W., Dye, R., and Sheft, S. (1996). "A simulated 'cocktail party' with up to three sources," *Percept. Psychophys.* **58**, 1026–1036.

Elevation localization and head-related transfer function analysis at low frequencies

V. Ralph Algazi

CIPIC, Center for Image Processing and Integrated Computing, University of California, Davis, California 95616

Carlos Avendano

Creative Advanced Technology Center, 1600 Green Hills Road, Scotts Valley, California 95067

Richard O. Duda

Department of Electrical Engineering, San Jose State University, San Jose, California 95192

(Received 22 May 2000; revised 9 August 2000; accepted 20 December 2000)

Monaural spectral features due to pinna diffraction are the primary cues for elevation. Because these features appear above 3 kHz where the wavelength becomes comparable to pinna size, it is generally believed that accurate elevation estimation requires wideband sources. However, psychoacoustic tests show that subjects can estimate elevation for low-frequency sources. In the experiments reported, random noise bursts low-pass filtered to 3 kHz were processed with individualized head-related transfer functions (HRTFs), and six subjects were asked to report the elevation angle around four cones of confusion. The accuracy in estimating elevation was degraded when compared to a baseline test with wideband stimuli. The reduction in performance was a function of azimuth and was highest in the median plane. However, when the source was located away from the median plane, subjects were able to estimate elevation, often with surprisingly good accuracy. Analysis of the HRTFs reveals the existence of elevation-dependent features at low frequencies. The physical origin of the low-frequency features is attributed primarily to head diffraction and torso reflections. It is shown that simple geometrical approximations and models of the head and torso explain these low-frequency features and the corresponding elevations cues. © 2001 Acoustical Society of America. [DOI: 10.1121/1.1349185]

PACS numbers: 43.66.Qp, 43.66.Pn [DWG]

I. INTRODUCTION

It is well established that the interaural time difference (ITD) and the interaural level difference (ILD) provide the primary cues for the horizontal localization of a sound source, whereas the monaural spectral modifications introduced by the pinna provide the primary cues for vertical localization (Middlebrooks and Green, 1991; Carlile, 1996; Blauert, 1997; Wightman and Kistler, 1997). Pinna effects start to appear at frequencies around 3 kHz, where the wavelength becomes comparable to the pinna size, with the so-called “pinna notch” appearing within the octave from 6 to 12 kHz (Shaw, 1997). This supports the general belief that the source must have substantial high-frequency energy over a fairly wide band for accurate judgment of elevation (Rofler and Butler, 1967; Gardner and Gardner, 1973; Butler, 1986; Asano, Suzuki, and Sone, 1990).

The role of the torso in localization is less well understood. The fact that the torso disturbs incident sound waves at low frequencies has been recognized for a long time (Hanson, 1944; Kuhn and Guernsey, 1983). However, the effects of the torso are relatively weak, and experiments to establish the perceptual importance of low-frequency cues have produced mixed results. For example, Theile and Spikofski (1982) concluded from their experiments that the torso does not provide significant cues for front/back discrimination. However, while agreeing that high-frequency spectral cues are needed for front/back discrimination, Asano *et al.* (1990)

observed that front/back discrimination is significantly improved when the subjects are provided with the correct low-frequency spectrum.

The effect of the torso on vertical localization in the median plane was first systematically investigated by Gardner (1973), who observed that—although the subjective sense of source location was greatly diminished when high frequencies were removed—it was possible for some subjects to localize sounds from loudspeakers located in the anterior median plane, despite the fact that the source had no spectral energy above 4 kHz. Gardner also measured the head-related transfer function (HRTF) of a mannequin, both with and without pinna occlusion and with and without a torso. By comparing the change in the response at $+18^\circ$ elevation to that at -18° elevation, he concluded that the pinna had no influence below 3.5 kHz, but that the torso introduced important “clues of a secondary nature” between 0.7 and 3.5 kHz. However, he cautioned that the mere presence of elevation-dependent low-frequency spectral features does not mean that they can be exploited by the auditory system. Searle *et al.* (1976) identified six localization cues in their statistical model of human sound localization, and used Gardner’s data to estimate the variance due to the torso reflection or “shoulder bounce.” They concluded that the shoulder bounce provided by far the weakest elevation cue.

Kuhn (1987) used a KEMAR mannequin with and without pinnae and torso in a study of the behavior of the HRTF

for all elevations in the median plane. He showed that median plane directivity is governed by specular reflection from the torso at frequencies below 2 kHz and by complex pinna phenomena for frequencies above 4 kHz. However, the question of whether or not the low-frequency features provided effective elevation cues was not addressed.¹

Going outside the median plane, Genuit and Platte (1981) showed that the torso introduced both direction- and distance-dependent effects on the HRTF that are limited to the spectral range below 3 kHz, and Genuit (1984) subsequently included separate torso and shoulder submodels in his structural HRTF model. Brown and Duda (1998) observed torso reflections in head-related impulse response (HRIR) data, and also included a “shoulder echo” in their structural HRTF model. However, that component was omitted during their formal tests of the model because informal listening experiments had indicated that the simulated torso reflections did not have a significant effect on perceived elevation in the median plane.

This paper reports on psychoacoustic experiments with individualized HRTFs that show that there are significant elevation cues for sources having little high-frequency energy, but the source must be away from the median plane. Some of the experiments used measured HRTFs, and others used a simplified low-frequency HRTF model. The methods used for the psychoacoustic experiments are described in Sec. II. The experimental results obtained with measured HRTFs are reported, analyzed, and discussed in Sec. III. Section IV presents an analysis of the low-frequency characteristics of HRTF that demonstrates that the pinnae do not contribute to the HRTF at frequencies below 3 kHz. Simple geometric models of the head and torso of each subject are then developed and analyzed to establish that the head and torso are the determinant contributors to the HRTFs at low frequencies. Finally in Sec. V, the results of psychoacoustic experiments with synthetic approximations and simple models of the head and torso are reported that confirm the contributions of head and torso to the perceived elevation.

II. METHODS

A. HRTF measurements

The HRTFs employed in this study were measured using the blocked-ear-canal technique (Møller, 1992; Algazi, Avendano, and Thompson, 1999). The probe tubes of two Etymotic Research ER-7C microphones were attached to plastic ear plugs, which were then inserted into the subject’s ear canals. The subjects were seated and, to minimize head movements, were asked to control their head position by viewing their reflection in a mirror; however, they were not otherwise physically constrained. The impulse responses were obtained using Golay codes (Crystal River Engineering Snapshot™ system), played through Bose Acoustimass™ Cube speakers. The speakers were mounted on a 1-m-radius hoop that was rotated about the subject’s interaural axis. The sampling rate for the measurements was 44.1 kHz. To remove most room reflections, the resulting impulse responses

were windowed and truncated to a duration of 4.5 ms, and were equalized to compensate for the loudspeaker and microphone transfer functions.

The geometry of the HRTF measurement apparatus leads naturally to use of the interaural–polar spherical coordinate system shown in Fig. 1. The origin of this spherical coordinate system is at the interaural midpoint, which is usually somewhat below and behind the center of the head. The azimuth angle θ is measured between the median plane and a ray from the origin to the source. An azimuth angle of $+90^\circ$ corresponds to the right side of the subject, and -90° to the left, with $\theta=0^\circ$ defining the median plane. The elevation angle ϕ is the polar rotation angle, with $\phi=0^\circ$ defining the anterior horizontal half-plane. The elevation sequence -90° , 0° , 90° , 180° , and 270° corresponds, respectively, to locations below, in front of, above, in back of, and below the subject.²

The HRTFs were measured at 1250 locations in space, with elevation increments of $\Delta\phi=5.625^\circ$ for a range $-45^\circ\leq\phi\leq 231^\circ$ and at 25 different azimuth angles with a 5° spacing in the front, increasing towards the interaural poles (Algazi *et al.*, 1999).

To a first degree of approximation, in this coordinate system the ITD depends on azimuth alone (Searle *et al.*, 1976; Wightman and Kistler, 1997). A surface of constant interaural–polar azimuth is often called a “cone of confusion.” Thus, in principle, knowledge of the ITD would allow one to estimate the azimuth, and hence to constrain the location of the source to a particular cone of confusion. For a constant range, the source moves around a “circle of confusion” which corresponds to the trajectory described by one of the loudspeakers as the hoop rotates.

B. Subjects

Six subjects were tested, four males and two females ranging in age from 20 to 42 years. None of the subjects was related to the research and all had normal hearing. All subjects were students or staff members at UC Davis, and had no previous experience with listening tests.

C. Experiments

The experiments involved listening to simulated or virtual auditory sources through headphones. The headphone stimuli were produced by convolving a test signal with the left and right impulse responses for each position tested, and the subjects were asked to report the perceived elevation.

Localization accuracy was measured on the left side of the subject in 16 different situations, one for each of the possible combinations of the following three factors:

- Azimuth angle θ : 0° , -25° , -45° , -65° ;
- Source location: front, back;
- Source bandwidth: 22 kHz, 3 kHz.

The aim of the experiments was to compare the accuracy of the elevations reported by the subjects for full-bandwidth sound sources with that for low-pass-filtered, limited-bandwidth sources. In an “absolute-judgment” approach, the subject listened to a presentation of a test signal and used

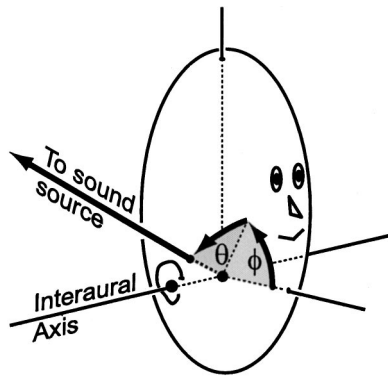


FIG. 1. The interaural–polar coordinate system. A surface of constant interaural azimuth θ is a cone of confusion, while a surface of constant interaural elevation ϕ is a half-plane through the interaural axis.

a graphical interface to select any point on a circle that best corresponded to the perceived elevation. To familiarize subjects with the procedure, test sessions were preceded by a brief description of the coordinate system and a presentation of a subset of the stimuli. Subjects were asked to think of the circle as a projection of the circle of confusion onto a plane. To visualize this mapping, circles of confusion were constructed on the surface of a three-dimensional image of a sphere, and subjects could immediately relate the circles to the trajectories of the loudspeakers at the time when their HRTFs were measured. To provide familiarization with the procedure, each subject was allowed a brief time period in which she or he could follow a marker on the circle and hear the corresponding stimulus. Front and back locations were tested separately and the subject always knew which condition prevailed.³

Each of the 16 situations was tested separately. For example, a particular test might be for a low-pass-filtered source at -45° azimuth located in the front. For each test, one of 12 elevation angles was randomly selected, subject to the constraint that each angle would eventually be repeated 10 times. This gave a total of $n=120$ responses per test

situation. When the source was in the front, the elevation angles ranged from -45° to 78.75° in 11.25° steps. Subjects were allowed to respond with an elevation anywhere between -90° and 90° . The mirror image locations were used when the source was in back: 225° to 101.25° in -11.25° steps, and subjects could respond anywhere between 90° and 270° . Each test situation required approximately 15 min to complete, with all 16 situations tested in about 4 h. To reduce fatigue, experiments were split into sessions of 2 h each, performed on different days.

D. Stimuli

The 22-kHz test signal was a sequence of two Gaussian noise bursts, sampled at 44.1 kHz and independently generated on each presentation. Each noise burst had a duration of 500 ms, with a 250-ms silent period between bursts. In addition, to increase the effective number of localization “looks” (Buell and Hafter, 1988), each noise burst was 100% amplitude modulated with a 40-Hz sinusoid, phased to begin and end with zero slope. Thus, each noise burst was essentially 20 bursts of 25-ms duration each. The 3-kHz test signal was obtained by filtering the wideband signal with a 40th-order Butterworth low-pass filter having a 3-kHz cutoff frequency. The convolution of the test signals with the HRTFs was done numerically in MATLAB. In addition, the resulting signals were filtered by a headphone compensation filter designed following Møller’s procedure (Møller, 1992). The resulting sound files were played back through AKG 240-DF headphones using a PC equipped with a Turtle-Beach Tahiti sound board. Although the energy in the test signal was constant, the variation of the HRTF with elevation produced a corresponding small variation in loudness, with an average SPL of 73 dB. Finally, the electrical signals driving the headphones were analyzed with a spectrum analyzer to verify that nonlinearities or noise in the processing and the hardware were not introducing spurious high-frequency signals.

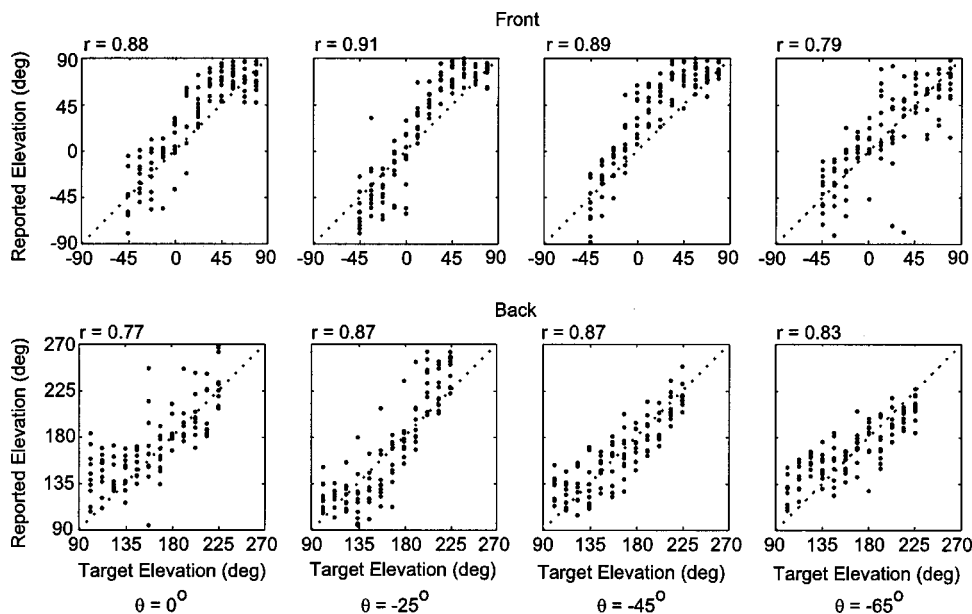


FIG. 2. Scatterplots for judged source elevation versus actual elevation for Subject S6 for a 22-kHz-bandwidth source at four different azimuths. In the top row the sound source was in the front hemisphere, while in the bottom row it was in back. Each plot shows data for 10 judgments at each of 12 different elevations, together with the sample correlation coefficient. The performance is comparable for all azimuths and hemispheres.

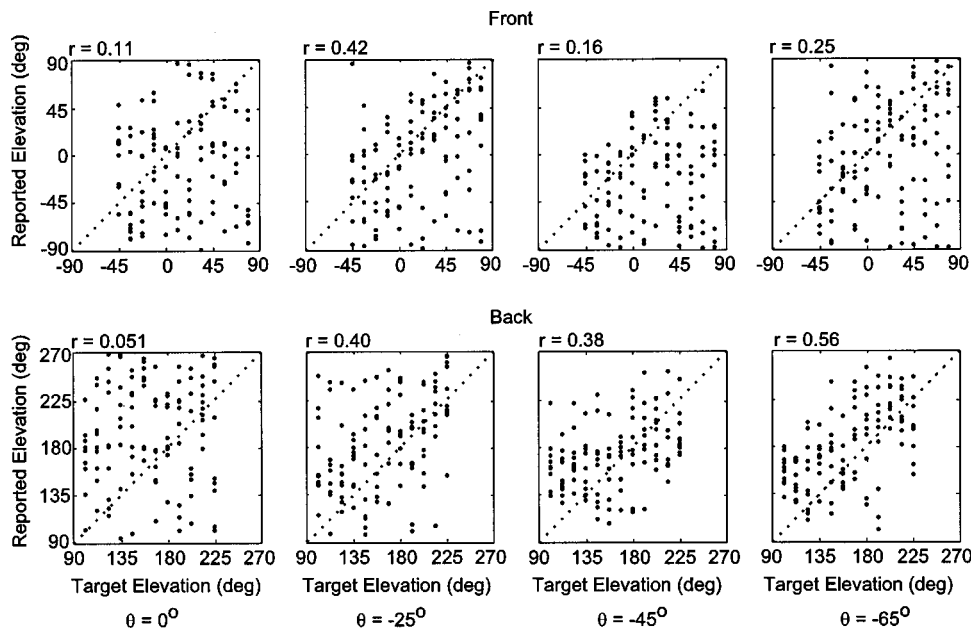


FIG. 3. Scatterplots as in Fig. 2, but with the signal low-pass filtered to remove frequency components above 3 kHz. Performance in the median plane ($\theta=0^\circ$) is severely degraded. As the magnitude of the azimuth increases, the performance improves, particularly for sources in the back hemisphere.

III. EXPERIMENTS WITH MEASURED HRTFS

Scatterplots of experimental results for a typical subject (S6) using full-bandwidth and 3-kHz low-pass stimuli are shown in Figs. 2 and 3. The eight situations shown in Fig. 2 are for the 22-kHz-bandwidth source at the four different azimuths. All eight cases are quite comparable, showing that the accuracy of judging elevation was not particularly sensitive to whether the source was in the median plane or on any of the cones of confusion, or whether the source was in front or in back. By contrast, Fig. 3 shows that when the maximum signal frequency was reduced to 3 kHz, performance was very poor in the median plane, but improved at other azimuths. Figure 4 shows similar 3-kHz bandwidth results for another subject (S1). Once again, the subject performed very poorly in the median plane, and was more accurate in the back than in front away from the median plane. While

wideband results confirm that high frequencies are the major contributors to elevation perception, it is surprising that, away from the median plane, one can still judge elevation with a low-bandwidth source.

The effect of reducing the bandwidth can be measured by the change in the sample correlation coefficient. For Subject S6 we observe that the degradation in the median plane was about 90% in both hemispheres. The performance was better for azimuths away from the median plane and was better in back than in front. Figure 5 shows that this general trend was exhibited by the majority of the subjects tested. This figure compares side-by-side the sample correlation coefficients for full-bandwidth stimuli and for 3-kHz low-pass stimuli for all subjects and all azimuths. The average correlation coefficient r for all subjects is summarized in Table I for both wideband and low-pass tests.

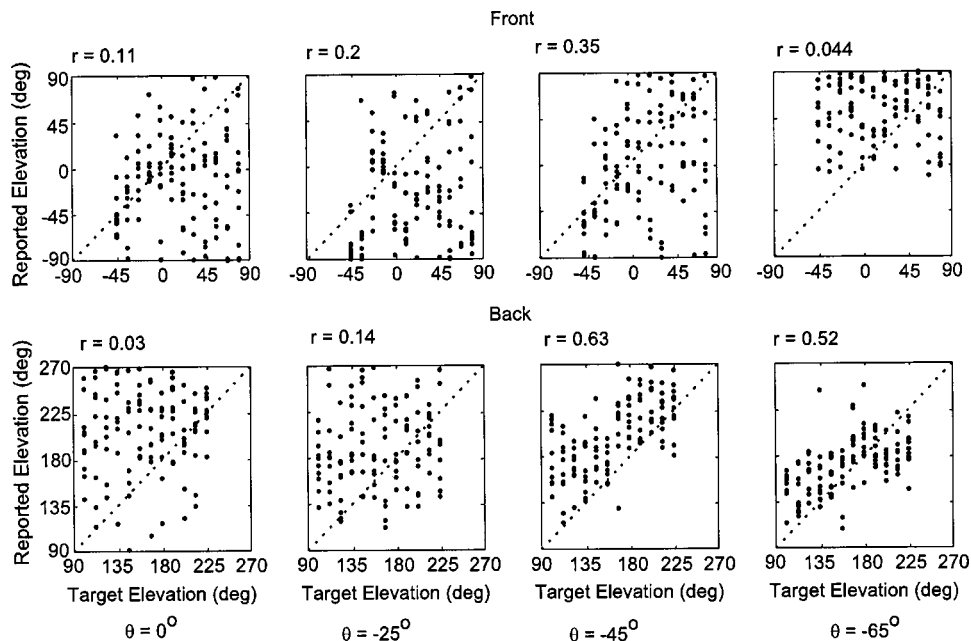


FIG. 4. Scatterplots as in Fig. 3, but for Subject S1. The performance is generally similar. In both cases, performance in the median plane is severely degraded, but a good correlation appears for sources away from the median plane and in back.

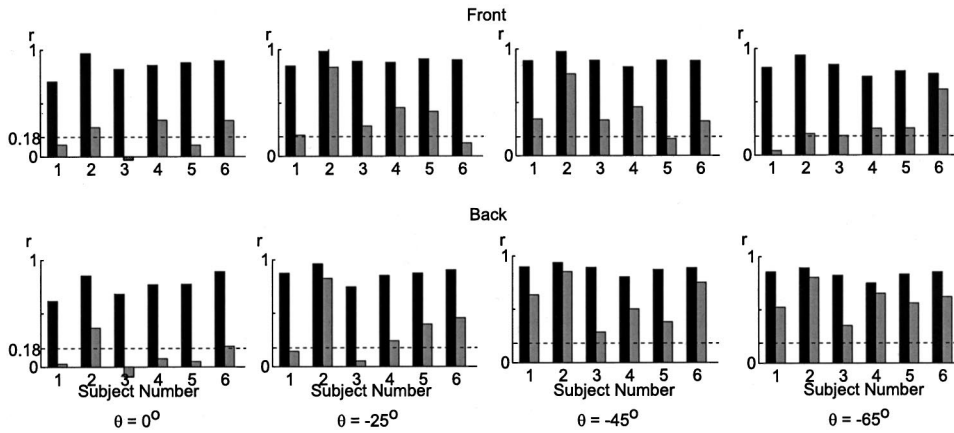


FIG. 5. Comparison of low-pass and full-bandwidth correlation coefficients for all subjects. Black: full bandwidth; gray: 3-kHz low pass. Values of $|r|$ above 0.18 are statistically significant at the 95% level.

A standard significance test for the sample correlation coefficient r is the Fisher z statistic, $z = 0.5 \ln(1+r)/(1-r)$; if the true correlation coefficient is ρ and if the sample size n is greater than 10, this statistic is approximately normally distributed with mean $0.5 \ln(1+\rho)/(1-\rho)$ and variance $1/(n-3)$ (Cramer, 1946). For our data, where $n = 120$, any correlation whose magnitude is less than 0.18 is not statistically significant at the 95% confidence level.

Analysis of the performance of individual subjects shows that the correlation was always statistically significant for the full-bandwidth source for all subjects. When the signal was low-pass filtered and the source was in the median plane, the correlation was not significant for most subjects and the degradation in performance was highest. When the source was away from the median plane, the performance improved, as shown in Fig. 5 and Table I, and was best in the back.

Inspection of the scatterplots in Figs. 3 and 4 reveals a significant amount of bias in the subjects' estimates. To be more specific, most of the time the subjects estimated the virtual source location to be lower than it actually was. As a measure of accuracy, the correlation coefficient is invariant to bias, but the rms error includes it.⁴ Table II shows both the bias and the rms error (in degrees), averaged over all six subjects for each experimental condition. The rms error for random guessing between -90° and $+90^\circ$ is 51.96° , and the rms values for low-pass stimuli in front or in the median plane indicate performance at the chance level. However, lower rms errors are achieved when the source is away from the median plane and in back. Because bias contributed significantly to the rms error, we believe that the correlation coefficient is a better indicator that low-frequency information is providing an elevation cue.

Finally, we observe that the results were subject dependent. At the extremes, one subject performed poorly in both the wideband and low-pass tests, while another subject had a surprisingly good performance in all the low-pass tests, and at -45° and -65° in the back had an increase in rms error

from 20° to 23° (less than 20%) when the bandwidth was reduced from 22 to 3 kHz.

IV. LOW-FREQUENCY HRTF ANALYSIS

The perceptual experiments in the previous section confirmed the existence of low-frequency elevation cues. The physical sources of these cues are reflected in features present in the HRTFs. Given the frequency range in which these features appear, it is natural to assume that they are caused by larger body structures such as the torso and head, whose dimensions are comparable to the wavelengths in question. Although Gardner (1973) and Kuhn (1987) showed that the effects of the pinnae on the spectrum become noticeable above 3.5 kHz, it was important to establish that they were negligible below 3 kHz.

The hypothesis that the low-frequency elevation cues were not due to the pinnae was tested in three ways:

- (1) By analyzing and identifying features of measured HRTFs obtained by including or removing different body parts (pinnae or torso);
- (2) By synthesizing HRTFs based on simple torso and head models and comparing such synthetic HRTFs to measurements; and
- (3) By psychoacoustic tests of perceived elevation for customized approximations to the HRTFs that are based solely on the geometry of the torso and of the head.

Several sets of HRTFs obtained by including or removing the pinnae and torso of a KEMAR mannequin were analyzed. The goal was to separate the effects of the different anatomical structures and to isolate their partial contributions to the low-frequency portion of the HRTFs. Strictly speaking, these contributions cannot be isolated this way, because the combination of structures does not imply the superposition of their acoustic fields. However, the effects of the torso, head, and pinnae are sufficiently separated in time, frequency, and spatial location that they can be observed by

TABLE I. Average correlation coefficient r for four different azimuths. F=front and B=back.

Condition	F, 0°	B, 0°	F, -25°	B, -25°	F, -45°	B, -45°	F, -65°	B, -65°
Wideband HRTF	0.86	0.75	0.90	0.87	0.89	0.88	0.82	0.83
Low-pass HRTF	0.19	0.10	0.39	0.35	0.40	0.57	0.24	0.58

TABLE II. The average rms error and bias. W=wideband, L=3-kHz low pass.

Condition	F, 0°	B, 0°	F, -25°	B, -25°	F, -45°	B, -45°	F, -65°	B, -65°
W rms	25.8	27.9	25.7	22.0	27.7	21.9	28.3	22.3
W bias	5.8	5.5	7.2	5.4	9.8	5.5	6.6	3.7
L rms	55.9	57.5	51.8	47.3	50.0	40.0	53.3	37.1
L bias	18.4	21.8	20.3	18.0	18.3	15.5	19.4	13.2

selecting the domain in which their individual influences dominate.

A. HRTF data

Three sets of HRTFs of a KEMAR mannequin were obtained by including or removing different anatomical structures. The data sets were collected according to the combinations shown in Table III.

The HRTFs of two human subjects were also measured. For each subject, two HRTFs were measured, a standard HRTF and a “pinna-less” HRTF, obtained by suppressing the effects of the subjects’ pinnae. This was achieved by the use of a rubber swimming cap that covered the outer ears. Adhesive tape was placed on the pinna regions to further smooth the surface. Microphone probe tubes were placed on the outside surface of the tape at positions corresponding to the ear canals. All measurements were made at the same spatial locations and with the techniques described in Sec. II.

B. Contribution of the pinnae

The contribution of the pinnae to the HRTFs at low frequencies can readily be evaluated on a KEMAR mannequin with removable pinnae. Figure 6 illustrates the elevation dependence of the KEMAR HRTF with and without pinnae. The measurements were made for the ipsilateral ear on a cone of confusion at $\theta = -45^\circ$. The squared magnitudes of the HRTFs were smoothed with simple auditory filters ($Q = 8$) and the results were displayed as images. In these image displays, the HRTF data at a particular elevation are displayed along a vertical line, where the gray scale indicates power in decibels. Because 90° elevation is in the center, front/back differences are revealed as lack of bilateral symmetry in the images.

Clearly, the pinnae have a major effect on the spectrum above 3 kHz, but relatively little effect below 3 kHz. Below 3 kHz, the average difference between the spectra with and without pinnae is 0.86 dB. Thus, the pinnae do not appear to contribute significant monaural cues below 3 kHz. However, in both cases, one can see elevation-dependent, arch-shaped notches in the spectrum that extend as low as 700 Hz. These are potential sources of elevation information that are clearly not due to the pinnae.

The contribution of the pinnae to binaural ILD cues at low frequencies was also evaluated. The ILD was computed as the difference between the right and the left dB values of the smoothed HRTF spectra. For frequencies below 3 kHz, a comparison of the ILDs of data set 1 (both pinnae and torso present) and data set 2 (pinnae removed) in the cone of confusion at $\theta = -45^\circ$ is shown in Figs. 7(a) and (b). The magnitude of the ILD is shown in a gray scale as a function of

elevation and frequency. We also evaluated the ILD for two human subjects. In Figs. 7(c) and (d) we show the ILDs for the one of these subjects. For the KEMAR mannequin and for both of the two human subjects, the contribution of the pinnae to the low-frequency ILD was insignificant.

The essential identity of the pinnae/no-pinnae ILDs pairs for frequencies below 3 kHz was observed for all azimuths and for all subjects. This is in agreement with the observation of Kuhn (see Fig. 14 in Kuhn, 1977), who attributed the ILD variations he observed in this frequency range to the torso.

C. Contribution of the torso

Now that it has been established that the effect of pinnae is negligible below 3 kHz, what remains to be clarified is the nature of the separate head and torso contributions to the low-frequency cues. To this end we make use of the measurements in data set 2 (pinnae removed). The removal of the pinnae reduces the complexity of the HRIRs, particularly on the contralateral side, and simplifies identification of the head and torso contributions.

Figure 8 shows both the HRIR and the HRTF of KEMAR for an azimuth angle of -45° with torso but no pinnae (data set 2). Both ipsilateral and contralateral responses are displayed as functions of elevation and of time or frequency. The ipsilateral HRTF image is clearly brighter than the contralateral image, which is a consequence of the ILD at -45° azimuth. Notice that the ipsilateral HRTF data (the lower-left panel) are actually the same as in the right panel in Fig. 6; the difference in visual appearance is due to a combination of (a) a linear instead of a logarithmic frequency scale, and (b) a gray scale that encompasses both the high-amplitude ipsilateral data and the low-amplitude contralateral data.

The HRIR images shown in Fig. 8(a) expose features of the HRTF that are hard to see in the frequency domain, and they deserve a more detailed description. In either image, an impulse response at a particular elevation is displayed along vertical line. To reduce the effect of the ILD on “washing out” the contralateral image, the impulse responses were scaled so that the maximum magnitude was unity for both the ipsilateral and the contralateral ear. As the color bar on the right indicates, bright values are positive and dark values are negative. The gray band at the very top of either image

TABLE III. KEMAR HRTF data sets.

Set	Pinnae	Torso
1	Yes	Yes
2	No	Yes
3	No	No

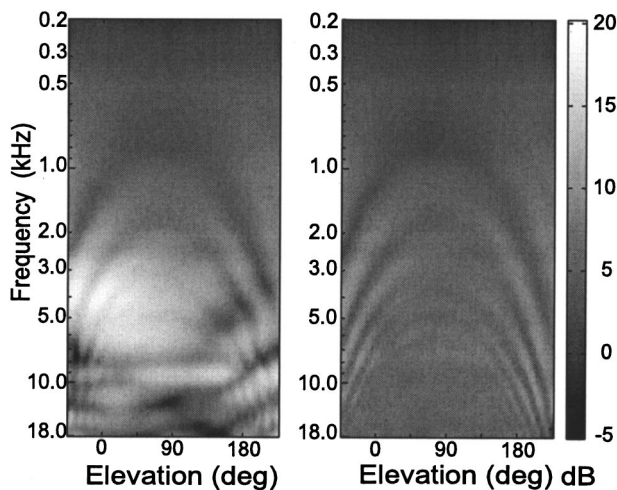


FIG. 6. Comparison of HRTF spectra. The left panel shows the spectrum with the pinnae attached, and the right panel shows the effect of removing the pinnae. The data are for the left ear at $\theta = -45^\circ$, so that these are ipsilateral data. The measurements were smoothed by a constant-Q auditory filter ($Q=8$). The gray scale indicates the magnitude of the smoothed spectra in decibels. The elevation-dependent arch-shaped patterns that are present in both cases are due to head and torso effects. Notice that they extend down to fairly low frequencies (below 3 kHz).

corresponds to the zero value before the impulse response starts. The strong white band or ridge near the top corresponds to the initial peak of the response. This peak was actually “clipped” to allow the weaker parts of the impulse to be visible. This initial ridge is horizontal in the ipsilateral image because the time of arrival was the same for all elevations. The initial ridge occurs about 0.4 ms later in the contralateral image than in the ipsilateral image, corresponding to the ITD at -45° azimuth. Note that the ITD is actually not constant, but varies by about ± 0.1 ms; this phenomenon is discussed further in Sec. IV E.

The initial pulse is followed by a series of subsequent pulses. We focus on the response of the ipsilateral ear (upper-left panel of Fig. 8) because it is simpler than the response of the contralateral ear. Probably the most prominent feature is the pair of V-shaped ridges, one that is stronger in the front and one that is stronger in the back. From the way that these delays increase and then decrease with elevation, we infer that the reflections come from below the ears. The delays are maximum for sound source locations above the subject (at about $\phi = 90^\circ$). The maximum delay of about 1 ms corresponds to a distance of 33 cm, which is roughly twice the distance from the ear canal to the shoulder. Thus, the pattern of delays suggests that the reflections are indeed due to a specular reflection from the torso. This was further verified using data set 3, where removal of the torso resulted in a loss of these reflections (compare the upper-right panel of Fig. 8 and the upper-middle panel of Fig. 9).

In the frequency domain the torso reflections act as a comb filter, introducing roughly bilaterally symmetric, arch-shaped periodic notches in the spectrum that are particularly clear for the ipsilateral ear [see Fig. 8(b)]. The frequencies at which the notches occur are inversely related to the delays, and thus produce a pattern that varies with elevation. The lowest notch frequency corresponds to the longest delay. De-

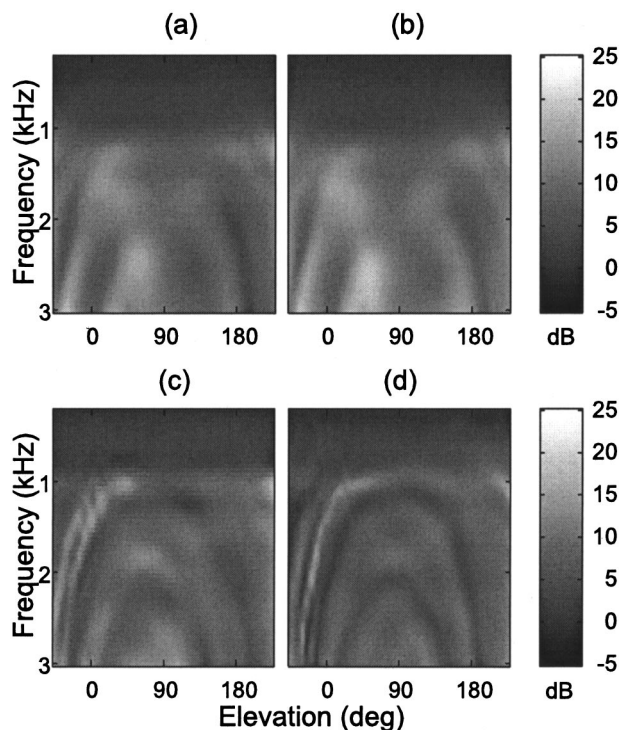


FIG. 7. Comparison of ILDs with and without pinnae. (a) KEMAR with pinnae; (b) KEMAR without pinnae; (c) Subject SA1; (d) Subject SA1 with pinnae “removed.” Data shown for $\theta = -45^\circ$ and frequencies below 3 kHz.

lays longer than a sixth of a millisecond will produce one or more notches below 3 kHz and will contribute to the low-frequency ILD of Fig. 7. Although the complexity of response of the contralateral ear makes it somewhat difficult to see, analysis of data set 3 in the frequency domain confirmed that removing the torso indeed eliminated the large arch-

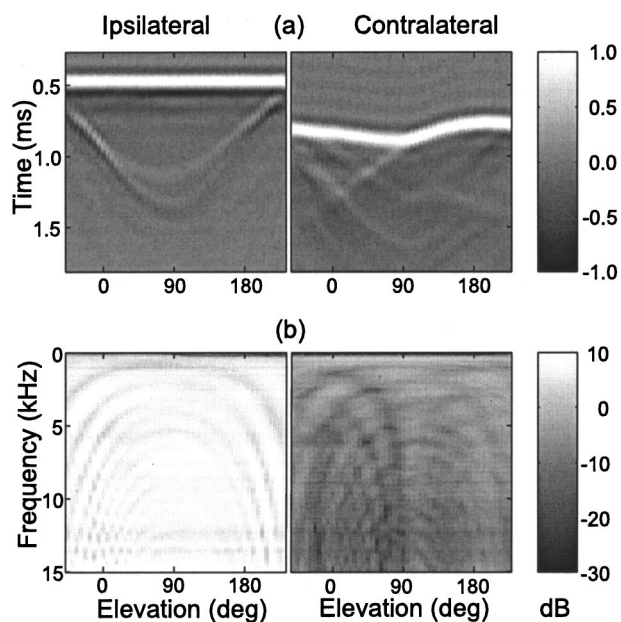


FIG. 8. (a) HRIRs and (b) magnitude HRTFs for KEMAR with no pinnae. The responses are shown for the cone of confusion at $\theta = -45^\circ$ and frequencies up to 15 kHz. In the time-domain plots the amplitude of the HRIRs has been scaled to enhance the gray-scale image.

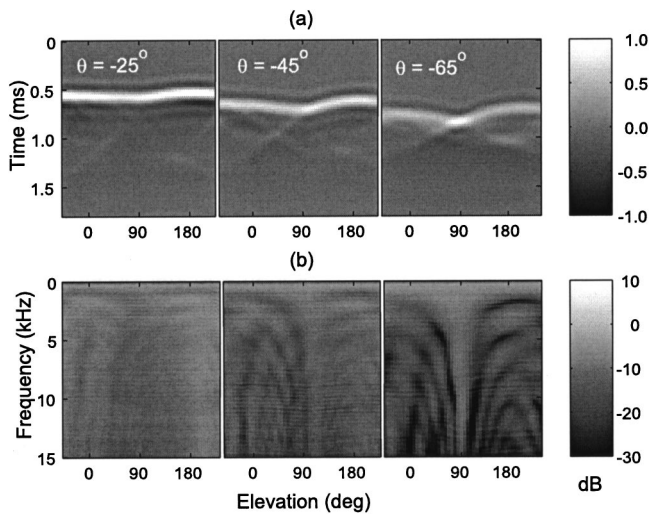


FIG. 9. (a) Right HRIR data for the KEMAR head with no pinnae and no torso. (b) Magnitude of the HRTF. Three azimuths on the contralateral side are shown.

shaped notches [compare the lower-right panel of Fig. 8(b) and the lower-middle panel of Fig. 9(b)].

The contralateral impulse response in the right panel of Fig. 8(a) exhibits similar but weaker torso reflections, with their corresponding notches in frequency domain. The contralateral response displays other features, not explained by torso reflections, that become visible because of the relative weakness of the direct sound and torso reflections. These features are considered further in Sec. IV E.

Next, we develop a simple geometrical model for the torso that accounts for the delayed reflections.

D. Geometric model of the torso

Although the human torso does not have a regular shape, it can be approximated by a simple ellipsoid, illustrated in Fig. A1 in the Appendix. The choice of an ellipsoid is based on analytical simplicity and its small number of parameters, which can be related to and estimated from anthropometry (height, width, depth). An algorithm for computing the delay $D(\theta, \phi)$ of the torso reflection relative to the initial pulse as a function of azimuth, elevation, and the geometrical parameters is outlined in the Appendix.

This algorithm was used to compute the delays using anthropometric measurements for three subjects (KEMAR and two humans). Considering the simplicity of the model, the resulting delays were remarkably close to the measured data. Figure 10 compares the delays produced by the model against the delays measured from the corresponding HRIR data (data set 2—with torso but without pinnae). The three subjects exhibited different torso reflection patterns that depended on body dimensions, and the anthropometry-based geometric model was able to account for these differences. Figure 10 shows that the behavior of the model follows the measured data closely.

E. Contribution of the head

Given its size, the head is the other anatomical structure that may contribute elevation-dependent features at low fre-

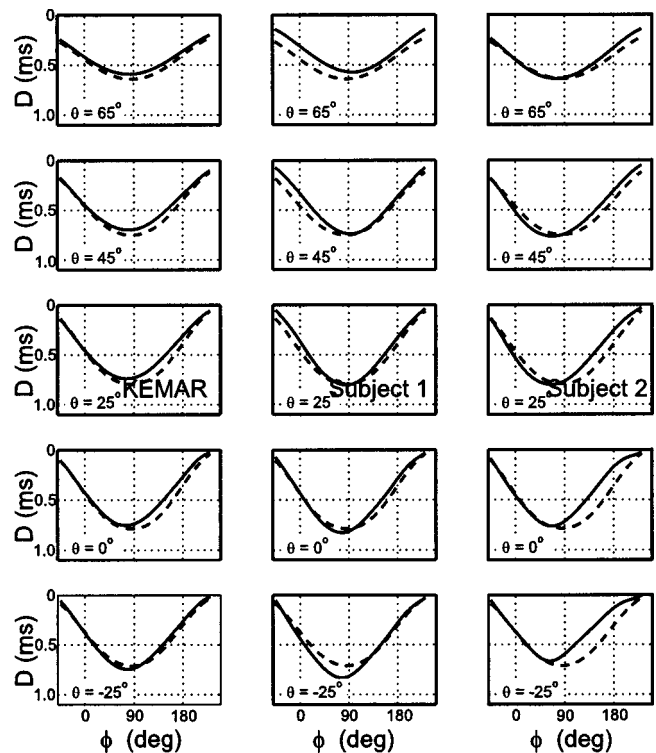


FIG. 10. Comparison of the delay D from the model (dashed) and the measured subject data (solid): (a) KEMAR; (b) Subject 1; and (c) Subject 2. The delays are shown as functions of elevation for five azimuths in each case.

quencies. To isolate the effect of the head, we use measurements with both the pinnae and torso removed. The resulting ipsilateral response is rather featureless, because the energy of the direct sound is large relative to the energy of the secondary waves that are diffracted around the head (Avendano, Duda, and Algazi, 1999). Thus, here we focus on the contralateral response.

Figure 9 displays contralateral HRTF data in data set 3 (both pinnae and torso removed) for three different azimuths (-25° , -45° , and -65°). The impulse response exhibits a prominent X-shaped pattern, particularly away from the median plane [see Fig. 9(a)]. A simplified explanation is that the incident sound wave travels to the contralateral ear by two paths, one around the front of the head and the other around the back (Duda and Martens, 1998); the upper or primary part of the X-shaped pattern arises from the shorter path, and the lower or secondary part from the longer path.

As we noted earlier, the onset of the primary wave varies slightly as a function of elevation, indicating some elevation asymmetry. This asymmetry has been discussed in Duda, Avendano, and Algazi (1999), where it was observed that the ITD on a cone of confusion is actually not constant, but can vary by as much as 0.12 ms as a function of elevation. For a spherical head, the HRTF can be computed exactly from the head radius and the angle of incidence, the angle between the source and the position of the ear canal (Duda and Martens, 1998). If the ear canals are diametrically opposed, the primary and secondary waves would each have the same delay for all elevations on a cone of confusion, and no X-shaped pattern would be seen. However, an X-shaped

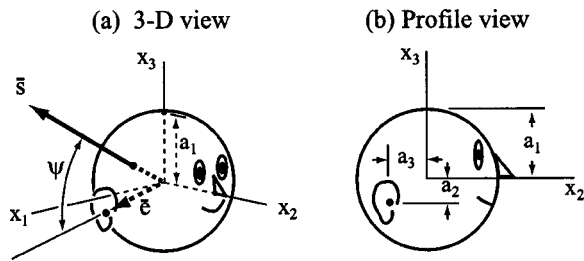


FIG. 11. Geometry for the head model. Here, \vec{s} is a vector from the center of the head to the sound source, \vec{e} is a vector from the center of the head through the entrance of the ear canal, and ψ is the angle between them. The anthropometric parameters are the head radius a_1 , the downward offset of the ear a_2 , and the backward offset of the ear a_3 .

pattern appears if the ears are displaced. Several researchers have noted that human ears typically lie behind and below the horizontal axis (Genuit, 1984; Blauert, 1997). Because the interaural axis defines the axis of rotation, this displacement causes the angle of incidence to change as the source moves around the cone of confusion, with larger changes occurring towards the contralateral hemisphere. Although other factors, such as the nonspherical shape of the head, also affect the time delay (Duda *et al.*, 1999), the ear location is particularly important.

F. Geometric model of the head

A simple spherical-head-with-offset-ears model is now used to account for the features observed in Fig. 9. With this model, both the ILD and the ITD vary on a cone of confusion. The HRTF for the sphere is obtained from Rayleigh's infinite series solution to the equations for the diffraction of sound by a sphere (Duda and Martens, 1998). To compute the transfer function from the source to the ear, three quantities are needed: the distance r to the source, the angle of incidence ψ , and the head radius a_1 [see Fig. 11(a)]. The distance to the source was 1 m for our experimental data. The angle of incidence ψ is the angle between the vector \vec{s} to the source and the vector \vec{e} to the ear: $\psi = \cos^{-1}[(\vec{s}^T \vec{e}) / \|\vec{s}\| \|\vec{e}\|]$, where \vec{s}^T is the transpose of \vec{s} and $r = \|\vec{s}\|$ is the length of \vec{s} (see Fig. 11). The only anthropometric data needed are the head radius a_1 and the vector \vec{e} , which is determined by the offsets of the ear down a_2 , and back a_3 .

A comparison between the spherical head model with size and offset parameters extracted from KEMAR ($a_1 = 8.5$ cm, $a_2 = 3$ cm, and $a_3 = 0.5$ cm) and the data in data set 3 (both pinnae and torso removed) reveals that the spherical-head-with-offset-ears model provides a good approximation to the elevation-dependent patterns in both the frequency and the time domain (cf. Figs. 9 and 12). Notice that the X-shaped pattern due to the elevation-dependent onset and secondary waves is introduced by the ear offset. As expected, some discrepancies remain, because neither a human head nor KEMAR's head is really spherical, and effects of the neck have not been modeled. However, the basic elevation-dependent features introduced by the head appear to be captured.

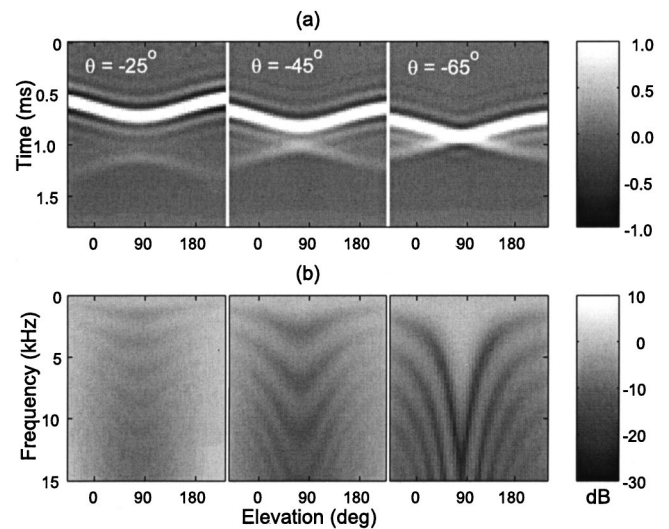


FIG. 12. (a) The HRIR and (b) the magnitude of the HRTF for the head model at three different azimuths on the contralateral side. A comparison with Fig. 9 shows a good general correspondence with the measured data.

V. EXPERIMENTS WITH A HEAD-AND-TORSO APPROXIMATION

In Sec. IV, we demonstrated that a simple geometrical head-and-torso (HAT) model accounts for the behavior of the low-frequency experimental HRTFs. In this section, we report on psychophysical experiments employing a classical spherical-head model and an empirical torso-delay model. Although this HAT approximation does not capture all the details of the experimental HRTFs at low frequencies, it incorporates the principal subject-dependent effects of the head, shoulders, and torso. Thus, the purpose of these new experiments is to assess the elevation cues that are conveyed by simple geometrical features, individualized for each subject.

The spherical-head model was computed from the infinite-series solution to the problem of the scattering of acoustic waves from a point source by a rigid sphere (Duda and Martens, 1998). The resulting HRTF $H_s(i\omega, r, \psi, a_1)$ depends on the angular frequency ω , the distance r from the center of the head to the source, the incidence angle ψ between the ear and the source, and the radius a_1 of the sphere. The HAT model approximates the complete HRTF by assuming that the wave incident on the head is the sum of a direct wave and a weaker torso reflection that arrives after a delay $D(\theta, \phi)$ that depends on azimuth θ and elevation ϕ . For simplicity, it was assumed that the direct wave and the torso reflection arrive from the same direction, so that the HAT HRTF can be written as

$$H_{\text{HAT}}(i\omega) = \alpha [1 + \rho e^{i\omega D(\theta, \phi)}] H_s(i\omega, r, \psi, a_1),$$

where ρ is the torso reflection coefficient, and $\alpha = 1/(1 + \rho)$ is a scale factor that guarantees that $H_{\text{HAT}}(0) = 1$.⁵

The resulting H_{HAT} was individualized for each of the six subjects by making separate estimates for the various parameters. For all subjects, we used $r = 1$ m, because that was the range for the measured data, and for simplicity we assumed that $\rho = 1/3$, independent of direction or frequency.⁶ The head radius a_1 and the ear locations (which are needed

TABLE IV. Average correlation coefficient r for four different azimuths. F=front and B=back.

Condition	F, 0°	B, 0°	F, -25°	B, -25°	F, -45°	B, -45°	F, -65°	B, -65°
Wideband HRTF	0.86	0.75	0.90	0.87	0.89	0.88	0.82	0.83
Low-pass HRTF	0.19	0.10	0.39	0.35	0.40	0.57	0.24	0.58
Low-pass HAT model	0.11	0.16	0.25	0.47	0.42	0.66	0.05	0.47

to calculate the incidence angle ψ) were individualized for each subject by optimizing a least-squares fit to experimentally measured ITD data estimated from individual HRIR images like those shown in Fig. 8. We could have used the ellipsoidal torso model to compute the delay $D(\theta, \phi)$ of the torso reflection, but, as Fig. 10 illustrates, that would have introduced some additional error into the HAT approximation. Instead, we chose to determine the torso delays from measurements taken from individual HRIR images.

The experiments conducted with the HAT approximation used the signals and methods described in Sec. II. As before, a 3-kHz stimulus was produced by filtering the wideband, amplitude-modulated noise signal with a 40th-order Butterworth filter having a 3-kHz cutoff frequency. That low-pass signal was then convolved with the location-dependent HAT HRTF approximation. Localization accuracy was measured in eight different situations, for azimuth angles θ of 0°, -25°, -45°, -65°, using a source location either in front or in back. The results for the HAT approximation could therefore be compared directly to the results obtained for each subject's measured HRTF with the same 3-kHz low-pass stimulus.

As a whole, the results of these experiments with the HAT approximation complement and confirm the results obtained with measured HRTFs. The results are summarized in Table IV, which adds to Table I the correlation coefficient for all eight conditions for the HAT approximation, averaged over the six subjects used in the study. We note that the HAT approximation and the measured HRTF gave quite similar results. Performance in the median plane was very poor, and

the larger correlations occurred away from the median plane and in the back.

However, examination of the details of individual results reveals some interesting differences. For all subjects, the HAT approximation provided a more consistent elevation cue than the measured HRTFs. However, for some subjects the correspondence between intended and perceived elevations was poorer when the HAT approximation was used. These observations are exemplified by the experimental data of Subject S6 (Figs. 3 and 13) and Subject S1 (Figs. 4 and 14). These figures show that the HAT approximation led to substantially less scatter of reported elevations for each target elevation than when the measured HRTF was used. However, with the HAT model, target elevations between 90° and 140° were not well discriminated, with the mean being around 160° regardless of target elevation, while target elevations greater than 140° were more consistently and correctly reported. Thus, the linear correspondence between target and reported elevations that the correlation coefficient measures is only a partial characterization of the differences between the results for the measured HRTF and for the HAT approximation.

VI. DISCUSSION AND CONCLUSIONS

The experimental results reported have clearly established the existence of low-frequency cues for elevation that are significant away from the median plane. The analysis of the HRTFs has shown that the HRTF features below 3 kHz are primarily due to the torso reflection and head diffraction,

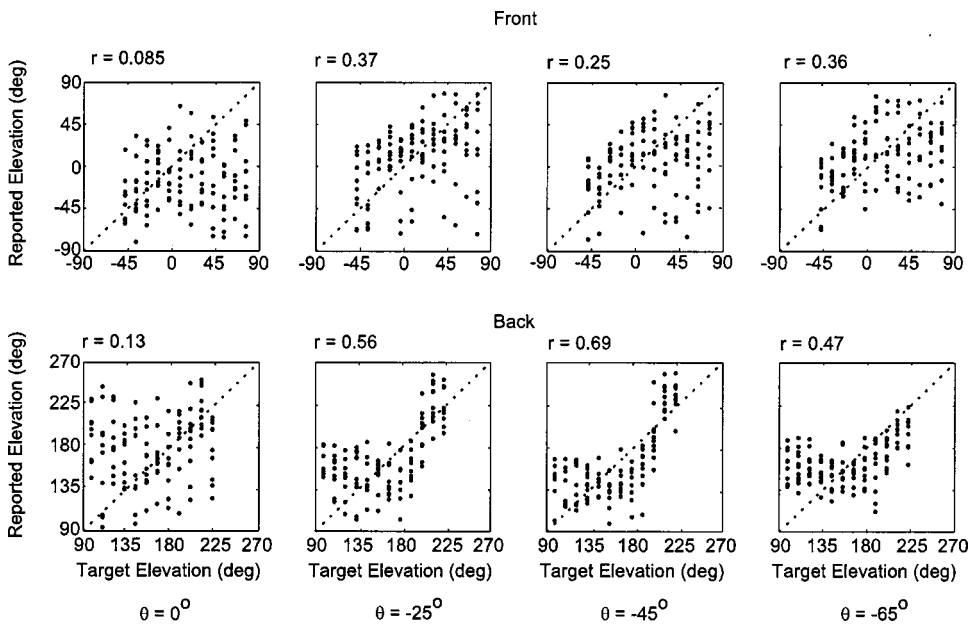


FIG. 13. Scatterplots for the HAT model, 3-kHz bandwidth, Subject S6. A comparison with Fig. 3 where the measured HRTF was used shows very similar results. The ability to localize in back actually appears to be better than the performance with the measured HRTF. However, at azimuths of -25° and -45°, the HAT model seems to lead to more of a bimodal (low/high) response.

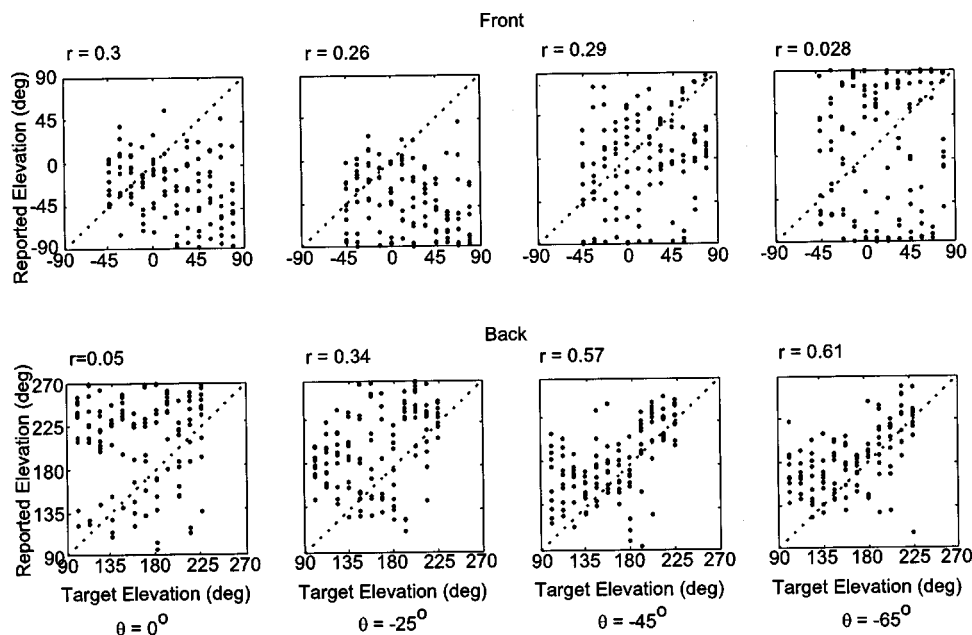


FIG. 14. Scatterplots for the HAT model, 3-kHz bandwidth, Subject S1. A comparison with Fig. 4 where the measured HRTF was used shows very similar results. The greatest difference occurs at large azimuth in front, where very few low elevations were reported with the measured HRTF. However, elsewhere the results are quite comparable.

while the pinnae do not contribute significantly at these low frequencies. The torso reflection effects are stronger on the ipsilateral side, while the head diffraction effects are stronger on the contralateral side where the direct sound is attenuated by the head. Further, it was shown that simple geometric models for the head and the torso provide strong corroboration of the physical basis for low-frequency elevation cues. The parameters of these models can be estimated from anthropometry to account for individual differences. A simple head-and-torso (HAT) geometric model was used to synthesize approximate HRTFs. Below 3 kHz, the synthetic HRTF was basically similar to the measured HRTF. Psychoacoustic experiments were conducted with an individualized HAT approximation of low-frequency HRTF data. It was observed that the approximate HRTFs provided low-frequency elevation cues that were just as effective as those provided by the measured HRTFs.

This study did not systematically examine other possible sources of low-frequency elevation cues. We now discuss these briefly and speculate on their importance on the basis of the results of this work. First, the changes of the ITD with elevation that were discussed in Sec. IV E could provide elevation cues. However, these ITD deviations are significant in only a fairly small range of spatial locations, and could not by themselves explain the full range of low-frequency effects observed. Second, timbre and loudness are monaural spectral properties that vary with elevation. Based on the results reported for the median plane in this and previous studies, these physical variations are clearly ineffective as low-frequency elevation cues. Finally, there are other larger anatomical structures (such as the legs) that effect the HRTF at low frequencies. Although not included in this paper, other HRIR measurements with seated subjects reveal knee reflections at low elevations and in the front, but they vanished at about -35° and occurred only in the front where low-frequency elevation cues are weak. Thus, we believe that knee reflections can at best provide very limited elevation cues. An interesting unanswered question is the general ef-

fect of posture or of head rotation on low-frequency elevation cues.

The existence of low-frequency cues has implications for the binaural simulation of virtual sources. Spherical head models are commonly used to estimate the low-frequency behavior of the HRTF; this work suggests that the torso provides additional cues that also should be taken into account. Finally, recognition of the presence of low-frequency cues provides a possible opportunity for enhancing elevation cues for listeners with hearing loss at higher frequencies.

ACKNOWLEDGMENTS

The authors would like to thank Dennis Thompson for his help with much of the experimental work, and the Editor and anonymous reviewers for their very thorough, thoughtful, and helpful suggestions. Support of the research was provided by the University of California DiMI University-Industry collaborative program, by the Creative Advanced Technology Center, by Aureal, by the Interval Research Corporation and by the Hewlett-Packard Research Laboratories. Support was also provided by the National Science Foundation under Grants No. NSF IRI-96-19339 and NSF ITR-00-86075. Any opinions, findings, and conclusions or recommendations expressed in this material are those of the authors and do not necessarily reflect the view of the National Science Foundation.

APPENDIX: THE ELLIPSOIDAL TORSO MODEL

This Appendix explains the algorithm used to compute the time delay $D(\theta, \phi)$ for the torso reflection as a function of the azimuth θ and elevation ϕ of the sound source. The geometry for the ellipsoidal torso model is shown in Fig. A1, which identifies the following anthropometric parameters:

- a_1 —head radius;
- a_2 —ear-canal offset down;
- a_3 —ear-canal offset back;

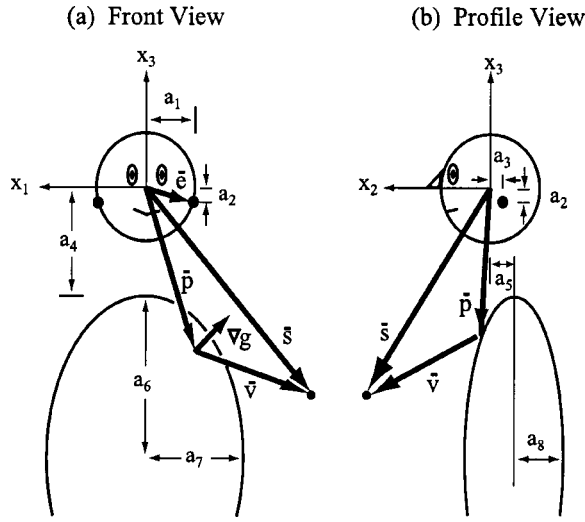


FIG. A1. Anthropometry for the torso model and related geometry.

- a_4 —distance from the center of the head to the top of the torso;
- a_5 —displacement of the head in front of the torso;
- a_6 —torso half-height;
- a_7 —torso half-width;
- a_8 —torso half-depth.

In contrast to the spherical-head model, we do not attempt to solve the wave equation for the ellipsoid, for which there is no simple analytical solution. Instead, we assume that the ellipsoid is a rigid surface and a specular reflector for sound with suitably short wavelengths. This approach is justified by the data, which exhibit a strong isolated reflection due to the torso. Thus, a ray-tracing algorithm is used to compute the time delay $D(\theta, \phi)$ of the torso reflection.

The algorithm can be outlined as follows. Given a sound source at the point \bar{s} , the problem is to compute the point \bar{p} on the surface of the ellipsoid where the reflection will occur, and use \bar{p} to calculate the difference in path lengths to the ears \bar{e} for the direct and the reflected sound waves. The calculation makes use of the vector $\bar{v} = \bar{s} - \bar{p}$ from the reflection point \bar{p} to the source \bar{s} . Once \bar{p} is determined, the torso reflection delay is obtained by first computing the difference between the path length for the direct and the reflected sound from the source to the center of the head, $d = \|\bar{p}\| + \|\bar{v}\| - \|\bar{s}\|$, where $\|\bar{p}\|$ is the length of \bar{p} . A correction based on Woodworth's formula (Blauert, 1997) is then applied to account for the additional distance of each component to the ear position \bar{e} . The total delay is obtained as $D(\theta, \phi) = (d + d_r + d_s)/c$ where c is the speed of sound in air (340 m/s) and d_r and d_s are the corrections for the diffraction around the head for the reflection and the source, respectively. For example, the correction for the direct sound can be computed as $d_s = a_1 \sin(\psi_s - \pi/2)$, where ψ_s is the angle between the source vector \bar{s} and the ear vector \bar{e} . This formula gives positive values for angles of incidence greater than 90° , and negative otherwise. The same formula is applied to correct the path length of the reflection.

The main problem is to compute the reflection point \bar{p} on the surface of the ellipsoid for a given source location \bar{s} .

Our approach is to work backwards, stepping systematically across the surface of the ellipsoid at points \bar{p}_i to find the source direction \bar{s}_i that would cause a reflection at that point. For a given $\bar{p} = \bar{p}_i$ we apply Snell's law to determine the direction \bar{u} of the incident sound vector $\bar{v} = \alpha \bar{u}$. To obtain \bar{u} we first compute the normal to the ellipsoid surface ∇g at point \bar{p} , where the equation for the ellipsoid is written as

$$g(x_1, x_2, x_3) = \left(\frac{x_1}{a_7}\right)^2 + \left(\frac{x_2 + a_5}{a_8}\right)^2 + \left(\frac{x_3 + a_4 + a_6}{a_6}\right)^2 = 1,$$

and thus the normal vector is

$$\nabla g = 2 \left[\frac{x_1}{a_7^2} \quad \frac{x_2 + a_5}{a_8^2} \quad \frac{x_3 + a_4 + a_6}{a_6} \right]^T,$$

where T is the transposition operator. We use ∇g to resolve \bar{p} into its normal and tangential components. The mirror source about the tangential plane will have the same tangential component as \bar{p} , while its normal component will be opposite in direction. Thus

$$\bar{u} = \bar{p} - 2 \frac{\bar{p}^T \nabla g}{\|\nabla g\|^2} \nabla g.$$

Once the direction vector \bar{u} is found, the source location can be obtained by noting that $\bar{s} = \bar{p} + \alpha \bar{u}$. To compute α we use the constraint that the range of the source is known. In this case we assume that all source locations are on the surface of a sphere with radius $r = 1$ m (which is the case in our measurements). Thus, the constraint can be written as $\|\bar{p} + \bar{v}\| = \|\bar{p} + \alpha \bar{u}\| = 1$, and the value of α is computed as the positive root of

$$\alpha = \frac{-\bar{p}^T \bar{u} \pm \sqrt{(\bar{p}^T \bar{u})^2 - \|\bar{u}\|^2 (\|\bar{p}\|^2 - 1)}}{\|\bar{u}\|^2}.$$

With values of vectors \bar{p} , \bar{v} , and \bar{s} , we can now compute the torso delay $D(\theta, \phi)$.

This procedure yields the values of the torso delay for source locations which do not lie on a regular spatial grid and that usually do not coincide with our measurement points. We solve this final problem by applying an interpolation procedure based on a spherical harmonic expansion.

¹Only static localization cues are considered in this paper. Low-frequency dynamic cues are also important. Perrett and Noble (1997) verified Wallach's hypothesis that horizontal head rotation can be used to resolve front/back confusion as well as to determine the magnitude of the elevation angle. Moreover, they showed that this dynamic cue requires the presence of acoustic energy below 2 kHz. They observed in passing that, although horizontal head rotation cannot resolve an up/down ambiguity in elevation, their subjects were nonetheless able to tell if the source was above or below the horizontal plane; they speculated that spectral cues created by the shoulders and torso were responsible.

²Note that these angles are different from the angles in a conventional vertical-polar coordinate system. In particular, a surface of constant interaural-polar azimuth is a horizontal cone, while a surface of constant vertical-polar azimuth is a vertical plane. The advantages of interaural-polar coordinates were pointed out by Searle *et al.* (1976), and they have also been used by Morimoto and Aokata (1984) and by Middlebrooks (1999). However, these authors have named the angles differently. Morimoto and Aokata call $90^\circ - \theta$ the "lateral angle" and ϕ the "rising angle," while Middlebrooks calls θ the "lateral angle" and ϕ the "polar angle." At the risk of some confusion, we have chosen to retain conventional terminology.

³As expected, front/back confusion was greater for low-pass stimuli than for

full-bandwidth stimuli (see Carlile and Pralong, 1994). For some subjects, the location of the low-pass-filtered sound always appeared to be in the back.

⁴Some caution must be exercised in computing statistics for directional data because of the 360° ambiguity (Mardia, 1972) and the possibility of up/down as well as front/back confusion (Wenzel *et al.*, 1993). However, because we separated front and back stimuli, and because the reported data were confined to a semicircle, we computed the bias and rms error using the target and reported angles as if they were rectangular coordinates. In particular, the bias was computed as the average signed error, and the rms error as the square root of the average of the squared error. The probable presence of up/down confusion makes the resulting values a bit more pessimistic than necessary, but does not change the conclusion that the angular errors are large.

⁵Mathematically, the HRTF is defined as the ratio of two transfer functions, one from the source to the ear with the subject present, and the other from the source to the location of the center of the head under free-field conditions. For an infinitely distant source, these transfer functions become identical at very low frequencies, and the HRTF approaches 1 (unity DC gain). However, at close ranges, the inverse square law results in a higher DC gain for the ipsilateral ear and a lower DC gain for the contralateral ear (Duda and Martens, 1998). In our HAT model, these small differences are ignored.

⁶Avendano, Algazi, and Duda (1999) describe a more elaborate torso model in which the reflection coefficient varied with azimuth, elevation, and frequency. The torso model used in this paper seems to produce similar elevation perceptions, and was chosen for its simplicity.

Algazi, V. R., Avendano, C., and Thompson, D. (1999). "Dependence of subject and measurement position in binaural signal acquisition," *J. Audio Eng. Soc.* **47**(11), 937–947.

Asano, F., Suzuki, Y., and Sone, T. (1990). "Role of spectral cues in median plane localization," *J. Acoust. Soc. Am.* **88**, 159–168.

Avendano, C., Algazi, V. R., and Duda, R. O. (1999). "A head-and-torso model for low-frequency binaural elevation effects," in Proceedings of the 1999 IEEE Workshop on Applications of Signal Processing to Audio and Acoustics, New Paltz, NY, pp. 179–182.

Avendano, C., Duda, R. O., and Algazi, V. R. (1999). "Modeling the contralateral HRTF," in *Proceedings of the AES 16th Conference on Spatial Sound Reproduction* (Rovaniemi, Finland), pp. 313–318.

Blauert, J. P. (1997). *Spatial Hearing* (revised edition) (MIT Press, Cambridge, MA).

Brown, C. P., and Duda, R. O. (1998). "A structural model for binaural sound synthesis," *IEEE Trans. Speech Audio Process.* **6**(5), 476–488.

Buell, T. N., and Hafter, E. R. (1988). "Discrimination of interaural differences of time in the envelopes of high-frequency signals: Integration times," *J. Acoust. Soc. Am.* **84**, 2063–2066.

Butler, R. A. (1986). "The bandwidth effect on monaural and binaural localization," *Hear. Res.* **21**, 67–73.

Carlile, S., and Pralong, D. (1994). "The location-dependent nature of perceptually salient features of the human head-related transfer functions," *J. Acoust. Soc. Am.* **95**, 3445–3459.

Carlile, S., editor (1996). *Virtual Auditory Space: Generation and Applications* (R. G. Landes, Austin, TX).

Cramer, H. (1946). *Mathematical Methods of Statistics* (Princeton University Press, Princeton, NJ), pp. 397–400.

Duda, R. O., and Martens, W. L. (1998). "Range dependence of the response of a spherical head model," *J. Acoust. Soc. Am.* **104**, 3048–3058.

Duda, R. O., Avendano, C., and Algazi, V. R. (1999). "An adaptable ellip-

soidal head model for the interaural time difference," in Proceedings of the IEEE International Conference on Acoustics Speech and Signal Processing ICASSP'99, II-965–968.

Gardner, M. B., and Gardner, R. S. (1973). "Problem of localization in the median plane: Effect of pinna cavity occlusion," *J. Acoust. Soc. Am.* **53**, 400–408.

Gardner, M. B. (1973). "Some monaural and binaural facets of median plane localization," *J. Acoust. Soc. Am.* **54**, 1489–1495.

Genuit, K., and Platte, H. J. (1981). "Untersuchungen zur Realisation einer richtungsgetreuen Übertragung mit elektroakustischen Mitteln (Investigations on the implementation of directionally faithful transmission by electroacoustical means)," *Fortschritte der Akustik, FASE/DAGA '81*, Berlin (VDE-Verlag, Berlin), pp. 629–632.

Genuit, K. (1984). "Ein Modell zur Beschreibung von Außenohrübertragungseigenschaften (A model for the description of the outer-ear transfer function)," Doctoral dissertation, Dept. of Elec. Engr., Rheinisch-Westfälischen Technischen Hochschule Aachen, Aachen, Germany.

Hanson, W. W. (1944). "The baffle effect of the human body on the response of a hearing aid," *J. Acoust. Soc. Am.* **16**, 60–62.

Kuhn, G. F. (1977). "Model for the interaural time differences in the azimuthal plane," *J. Acoust. Soc. Am.* **62**, 157–167.

Kuhn, G. F., and Guernsey, R. M. (1983). "Sound pressure distribution about the human head and torso," *J. Acoust. Soc. Am.* **73**, 95–105.

Kuhn, G. F. (1987). "Physical acoustics and measurements pertaining to directional hearing," in *Directional Hearing*, edited by W. A. Yost and G. Gourevitch (Springer, New York), pp. 3–25.

Mardia, K. V. (1972). *Statistics of Directional Data* (Academic, London).

Middlebrooks, J. C., and Green, D. M. (1991). "Sound localization by human listeners," *Annu. Rev. Psychol.* **42**, 135–159.

Middlebrooks, J. C. (1999). "Virtual localization improved by scaling non-individualized external-ear transfer functions in frequency," *J. Acoust. Soc. Am.* **106**, 1493–1510.

Møller, H. (1992). "Fundamentals of binaural technology," *Appl. Acoust.* **36**(5), 171–218.

Morimoto, M., and Aokata, H. (1984). "Localization cues of sound sources in the upper hemisphere," *J. Acoust. Soc. Jpn. (E)* **5**(3), 165–173.

Perrett, S., and Noble, W. (1997). "The effect of head rotations on vertical plane sound localization," *J. Acoust. Soc. Am.* **102**, 2325–2332.

Roffler, S. K., and Butler, R. A. (1967). "Factors that influence the localization of sound in the vertical plane," *J. Acoust. Soc. Am.* **43**, 1255–1259.

Searle, C. L., Braid, L. D., Davis, M. F., and Colburn, H. S. (1976). "Model for auditory localization," *J. Acoust. Soc. Am.* **60**, 1164–1175.

Shaw, E. A. G. (1997). "Acoustical features of the human external ear," in *Binaural and Spatial Hearing in Real and Virtual Environments*, edited by R. H. Gilkey and T. R. Anderson (Erlbaum, Mahwah, NJ), pp. 25–47.

Theile, G., and Spikofski, G. (1982). "Die Bedeutung des menschlichen Rumpfes für die Lokalisation in der Medianebene (The importance of the human torso for localization in the median plane)," *Fortschritte der Akustik, FASE/DAGA '82*, Göttingen (DPG-Verlag, Bad Honnef), pp. 1181–1186.

Wenzel, E. M., Arruda, M., Kistler, D. J., and Wightman, F. L. (1993). "Localization using nonindividualized head-related transfer functions," *J. Acoust. Soc. Am.* **94**, 111–123.

Wightman, F. L., and Kistler, D. L. (1997). "Factors effecting the relative salience of sound localization cues," in *Binaural and Spatial Hearing in Real and Virtual Environments*, edited by R. H. Gilkey and T. R. Anderson (Erlbaum, Mahwah, NJ), pp. 1–23.

Performance of an adaptive beamforming noise reduction scheme for hearing aid applications. I. Prediction of the signal-to-noise-ratio improvement

Martin Kompis^{a)}

University Clinic of ENT, Head and Neck Surgery, Inselspital, 3010 Bern, Switzerland

Norbert Dillier

ENT-Department, University Hospital of Zurich, 8091 Zurich, Switzerland

(Received 5 November 1999; revised 24 April 2000; revised 25 September 2000; accepted 14 November 2000)

Adaptive beamformers have been proposed as noise reduction schemes for conventional hearing aids and cochlear implants. A method to predict the amount of noise reduction that can be achieved by a two-microphone adaptive beamformer is presented. The prediction is based on a model of the acoustic environment in which the presence of one acoustic target-signal source and one acoustic noise source in a reverberant enclosure is assumed. The acoustic field is sampled using two omnidirectional microphones mounted close to the ears of a user. The model takes eleven different parameters into account, including reverberation time and size of the room, directionality of the acoustic sources, and design parameters of the beamformer itself, including length of the adaptive filter and delay in the target signal path. An approximation to predict the achievable signal-to-noise improvement based on the model is presented. Potential applications as well as limitations of the proposed prediction method are discussed and a FORTRAN subroutine to predict the achievable signal-to-noise improvement is provided. Experimental verification of the predictions is provided in a companion paper [J. Acoust. Soc. Am. **109**, 1134 (2001)]. © 2001 Acoustical Society of America. [DOI: 10.1121/1.1338557]

PACS numbers: 43.66.Ts, 43.60.Lq, 43.60.Gk [RVS]

LIST OF SYMBOLS

A, B, C, D	models of impulse responses between acoustic sources and input of adaptive filter (cf. Fig. 2)	$g_{nR,i}$	i th coefficient of filter G_{nR}
a_i	i th coefficient of filter A	$g_{nL,i}$	i th coefficient of filter G_{nL}
b_i	i th coefficient of filter B	h	noise reduction of the adaptive filter, defined as $E\{d^2\} - E\{\epsilon^2\}$
c	sound speed, m/s	k	sample index
d	sum of both microphone signals, delayed by Δ samples	l_n	distance between noise source and center of listener's head, m
d'	sum of both microphone signals	l_s	distance between target signal source and center of listener's head, m
$E\{\}$	expected value	n	signal emitted by the noise source
F_d	coefficient to scale the direct portion of the impulse responses A and B	N	number of coefficients in the adaptive filter
F_σ	coefficient to scale the reverberant portion of the impulse responses A and B	W	cross-correlation vector
F_{sample}	sampling rate = $1/T_{\text{sample}}$, Hz	N_1, N_2, N_B, N_S	variances of noise signal at microphone 1, microphone 2, sum of microphone signals, and output of beamformer, respectively
G_0	magnitude of the first coefficient of the impulse responses A and B	P	cross-correlation vector
G_1	magnitude of the second coefficient of the impulse responses A and B	P_i	i th element of the cross-correlation vector P
G_{nR}	impulse response between noise source and output signal of right microphone	$P_{d/r}$	direct-to-reverberant ratio of the noise signal at location of the listener
G_{nL}	impulse response between noise source and output signal of left microphone	$Q_{d/r}$	direct-to-reverberant ratio of the target signal at location of the listener
G_{sR}	impulse response between target signal source and output signal of right microphone	r_c	critical distance, m
G_{sL}	impulse response between target signal source and output signal of left microphone	R	autocorrelation matrix
		s	signal emitted by the target source
		$S(\vartheta)$	ratio between rms value of a white noise signal in free field and on the surface of a rigid sphere
		S_1, S_2, S_B, S_S	variances of target signal at microphone 1, microphone 2, sum of microphone signals, and output of beamformer, respectively

^{a)}Electronic mail: martin.kompis@insel.ch

T	time constant for exponential decay of the filter coefficients modeling reverberation in impulse responses A and B , in multiples of the sampling period T_{sample}
T_r	reverberation time of room, s
T_{sample}	sampling period = $1/F_{\text{sample}} \cdot s$
V	volume of room or enclosure, m^3
W	vector representing coefficients of the adaptive filter
W^0	vector representing coefficients of the adaptive filter in the adapted state
x	reference signal (difference of microphone signals)
X	vector of last N values of signal x
y	output of the adaptive filter

Greek

α_n	azimuth of noise source
α_s	azimuth of target signal source
Δ	delay in target signal path between d' and d , in samples
ϵ	output signal of the adaptive beamformer
σ_i^2	variance of the i th coefficient in filters A and B
ϑ	angle between point on surface of a rigid sphere and direction of incidence of plane wave
γ_n	index of directionality of the noise source
γ_s	index of directionality of the target signal source

Note: All parameters are dimensionless, unless otherwise noted

I. INTRODUCTION

Many users of cochlear implants and conventional hearing aids complain about insufficient intelligibility of speech in noisy situations, even if the performance of their aid is satisfactory in quiet environments (Kochkin, 1993). As many hearing impaired listeners need significantly higher signal-to-noise ratios (SNR) for satisfactory communication than normal hearing listeners (Lurquin and Rafhay, 1996; Valente, 1998), numerous noise reduction methods for hearing aids and cochlear implants have been proposed (Lim and Oppenheim, 1979; Graupe *et al.*, 1987; Soede *et al.*, 1993; Bächler and Vonlanthen, 1995; Whitmal *et al.*, 1996; Vanden Berghe and Wouters, 1998). Some of the most promising noise reduction schemes assume that target signals are emitted in front of the listener, while signals arriving from other directions are considered to be noise (Peterson *et al.*, 1987; Soede *et al.*, 1993; Bächler and Vonlanthen, 1995). Directional noise reduction methods have been shown to improve SNR and to be of practical use for the hard-of-hearing (Peterson *et al.*, 1987; Greenberg and Zurek, 1992; Kompis and Dillier, 1994; Valente *et al.*, 1995; Kochkin, 1996; Cochlear Inc., 1997; Gravel *et al.*, 1999; Wouters *et al.*, 1999). Several methods are known to achieve spatial directionality. Besides the use of directional microphones, the output signals of several (omnidirectional or directional) microphones can be postprocessed using either fixed or adaptive postprocessing (Soede *et al.*, 1993; Kompis, 1998). In fixed postprocessing, all transfer functions between the microphone signals and the output are time independent. In adaptive postprocessing, the coefficients of at least one filter are continuously adjusted to optimize noise reduction in the given environment. In general, adaptive beamformers achieve higher noise reductions at the expense of higher computational loads and greater system complexity (DeBrunner and McKinney, 1995; Kates and Weiss, 1996; Kompis *et al.*, 1999; Kompis *et al.*, 2000).

While fixed beamformers have been theoretically analyzed and the achievable noise reduction can be predicted based on these theoretical considerations (Cox *et al.*, 1986; Stadler and Rabinowitz, 1993), predictions of the performance of adaptive systems are rare (Widrow *et al.*, 1975;

DeBrunner and McKinney, 1995). To date, they do not take into account the length of the adaptive filter and reverberation time of the environment, two factors which have been found to be of major importance (Peterson *et al.*, 1987; Peterson *et al.*, 1990; Kompis and Dillier, 1991; Greenberg and Zurek, 1992; Dillier *et al.*, 1993). Most reports on adaptive beamformer applications provide experimental data using either speech recognition tests with normal hearing or hearing impaired listeners (Peterson *et al.*, 1987; Kompis and Dillier, 1994; van Hoesel and Clark, 1995; Hamacher *et al.*, 1996; Welker *et al.*, 1997) or different measures related to signal-to-noise ratio improvement (Greenberg and Zurek, 1992; Greenberg *et al.*, 1993; Dillier *et al.*, 1993; Welker *et al.*, 1997; Kates, 1997). It is difficult to compare the results of these reports because of the numerous differences in the experimental setting, such as reverberation time, directionality of sound sources or filter adaptation. The effect of each difference is hard to estimate because of the lack of a theoretical background or sufficient experimental data. In this report, the noise reduction that can be achieved by a two-microphone adaptive beamformer (Griffiths and Jim, 1982; Peterson *et al.*, 1987) is analyzed. An approximate method to predict its noise reduction as a function of the design parameters of the beamformer and the acoustic parameters of the acoustic environment including the sound sources is derived. In Sec. II, the investigated adaptive beamformer is defined. In Sec. III, the assumptions for the theoretical analysis are discussed. Models of the impulse responses between the acoustic noise sources and the beamformer are presented in Sec. IV, and in Secs. V and VI, an approximation to predict the achievable improvement in signal-to-noise ratio is derived. Potential applications and limitations of the presented method to predict SNR improvements are discussed in Sec. VII. A short FORTRAN subroutine which performs the calculation to predict SNR improvement is included in the Appendix. Experimental verification of the predictions is provided in a companion paper (Kompis and Dillier, 2001).

II. THE ADAPTIVE BEAMFORMER

Figure 1 shows a schematic diagram of the two-microphone adaptive beamformer (Griffiths and Jim, 1982;

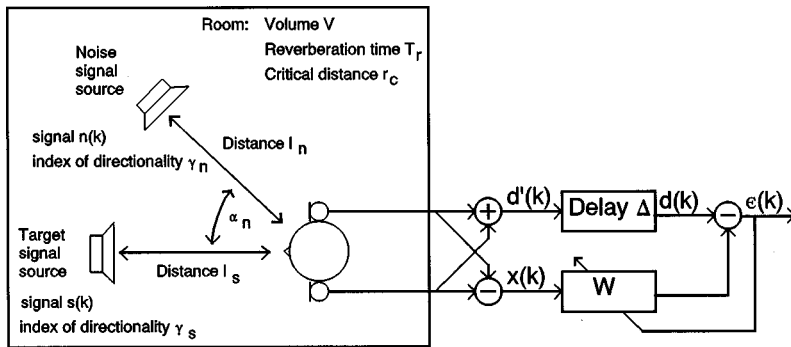


FIG. 1. Schematic diagram of the adaptive beamformer in the acoustic environment used to predict SNR improvements.

Peterson *et al.*, 1987) considered in this research. Note that some researchers prefer the term *Griffiths–Jim beamformer* to describe the same system.

Two omnidirectional microphones are mounted close to the ears of a user. The sum and the difference of the two microphone signals is calculated first. As the target signal source is assumed to lie in front of the listener, the sum d' will contain predominantly target signal, while the difference signal x will contain mainly noise, as noise is assumed to arrive from other directions. A finite-impulse response structured adaptive filter W transforms x in such a way that it can serve as a model of the remaining noise in d . The resulting signal y can then be directly subtracted from d , yielding the output ϵ . The coefficients of the adaptive filter are updated by a least-mean-squares (LMS) algorithm (Widrow *et al.*, 1975) which minimizes the total variance of the output signal. The LMS algorithm relies on the assumption that target and noise signals are uncorrelated. The delay in the target signal path between d' and d can be adjusted to optimize noise reduction. Typically, the length of the adaptive filter is chosen in the range of 10–50 ms, and delay is set to 25%–50% of the filter length (Peterson *et al.*, 1987; Kompis and Dillier, 1991; Greenberg and Zurek, 1992; Dillier *et al.*, 1993; Kompis and Dillier, 1994).

The adaptive beamformer minimizes the variance of any signal of which a—possibly linearly transformed—copy is present in the reference signal x . Due to reverberation and misalignment of the target signal source with respect to the microphones, in most practical situations a part of the target signal will be present in the reference signal x . To prevent target signal cancellation, several algorithms, which stop filter adaptation when a target signal is detected, have been proposed (Van Compernelle, 1990; Greenberg and Zurek, 1992; Kompis and Dillier, 1994; van Hoesel and Clark, 1995; Kompis *et al.*, 1997). Using one of these algorithms, filter adaptation is limited to time segments in which no target signal is present, e.g., the numerous short pauses that occur in the running speech of a target speaker.

III. MODEL ASSUMPTIONS

To predict the SNR improvement that can be achieved by the adaptive beamformer, a simplified model of the acoustic setting is assumed as follows (cf. the left-hand side of Fig. 1 for a graphic representation). A listener in a reverberant room faces a single target signal source. A second acoustic source, emitting the noise signal, is placed at an

azimuth α_n from the listener, where α_n is large enough to give rise to a difference in the time of arrival of the noise signal between the two microphones of at least one sampling period T_{sample} . No movement of either the listener or the sound sources is allowed. The directionality of the acoustic sources is described by the index of directionality γ_n for the noise source and γ_s for the target signal source, defined as the ratio between the signal intensity emitted in the direction of the listener to the intensity of a hypothetical omnidirectional source with the same total acoustic output power (DeBrunner and McKinney, 1995). The head of the listener is modeled as a rigid sphere of 9.3 cm in radius, as proposed by Kuhn (1977) and used in an earlier study (Kompis and Dillier, 1993). Two omnidirectional microphones are mounted on the surface of the rigid sphere opposite each other, serving as inputs to the adaptive beamformer. The acoustic properties of the room are defined by any two of the three parameters volume V , reverberation time T_r , and critical distance r_c . Reverberation time is defined as the time required for the reverberant signal to decay by 60 dB. The critical distance is defined as the distance from an omnidirectional acoustic source at which the direct-to-reverberant ratio is 1. The relationship between these parameters can be approximated by

$$r_c \approx \sqrt{\frac{6 \ln 10}{4 \pi c} \frac{V}{T_r}}, \quad (1)$$

where c is the sound speed (Zwicker and Zollner, 1984). For the calculations in the Appendix, a sound speed of $c = 340$ m/s is assumed. Both the noise and the target signal source are assumed to emit white noise, with the signals of the two sources being uncorrelated. The adaptive beamformer processing the two microphone signals is configured as shown in Fig. 1 and defined by its sampling rate F_{sample} , the number of coefficients N of the adaptive filter, and the number of samples Δ of delay in the target signal path between d' and d . A perfectly adapted filter is assumed, i.e., it is assumed that filter adaptation took place in the absence of the target signal and the coefficients of the adaptive filter have converged to their optimal state. The state of the adaptive filter is assumed to be frozen at the end of adaptation, so that only the noise signal, but not the target signal, has had an influence on the filter coefficients.

In principle, no restrictions are imposed by the model on the variances of either the noise or the target signal. However, in order to simplify calculations and without loss of

generality, it is assumed that the variance of the noise signal $n(k)$ equals 1, and room transfer functions are scaled in such a way as to let the variances of the noise signal equal 1 in both the sum signal $d(k)$ and the difference signal $x(k)$. Similarly, i.e., in order to simplify calculations and without loss of generality, the variance of the reverberant portion of the target signal at either microphone is assumed to be 1. Clearly, some of the above-mentioned assumptions are more limiting than others. The assumptions on the variances of the target and noise signals exclude situations without any reverberation. To generate a difference of at least one sampling period, at a sampling rate of, e.g., $F_{\text{sample}} = 10 \text{ kHz}$, the minimum azimuth of the noise source must be roughly 10° , which does not seriously limit general applicability. The model requires that the signals of both acoustic sources are white noise. Furthermore, effects of the frequency dependence of the acoustic diffraction by the head of the listener of the directionality of the sound sources are not taken into account. While this is clearly unrealistic in light of the predominantly low-frequency speech and noise sounds, which are to be expected as input signals in a hearing aid application, this assumption becomes more acceptable when considering that the most frequently used adaptation algorithm, the LMS algorithm (Widrow *et al.*, 1975), minimizes total signal variance, i.e., the spectral components of a noise signal are reduced according to their relative power. Therefore, in numerous realizations of the adaptive beamformer, microphone signals are prewhitened by usually 6 dB per octave to account for the importance of the spectral components with respect to speech intelligibility (Peterson *et al.*, 1987; Dillier *et al.*, 1993; Kompis and Dillier, 1994; Welker *et al.*, 1997). Usually, changes introduced by these pre-emphasis filters are compensated by a de-emphasizing filter in the output path of the adaptive beamformer (Kompis, 1998). With these provisions, the spectra of the practically important speech signals actually being processed by the beamforming algorithm approach the white spectra of the model. Although it can be shown that broadband SNR improvement corresponds closely to an intelligibility-weighted measure of speech-to-interference ratio gain (Greenberg *et al.*, 1993) in numerous realistic experimental settings (Kompis and Dillier, 2001), the noninclusion of frequency dependence remains a limitation of the model. In the model of the listener, no pinnae or shoulders are accounted for. This simple model has been verified earlier and seems to be sufficient for a number of hearing aid applications (Kompis and Dillier, 1993). As there are several ways to mount hearing aid microphones with respect to the pinnae, and as the presented model does not generally take into account frequency dependence, the inclusion of pinnae or shoulder effects into the model does not seem to be justified. Again, however, the noninclusion of the alterations in the frequency spectra due to the head of the listener may be a limiting factor for a number of applications.

Although the two assumptions that (a) the filter has been adapted in the absence of the target signal and is (b) perfectly adapted cannot be expected to be met perfectly in real situations, these assumptions are reasonably realistic for many practical applications. Several target-signal detection/

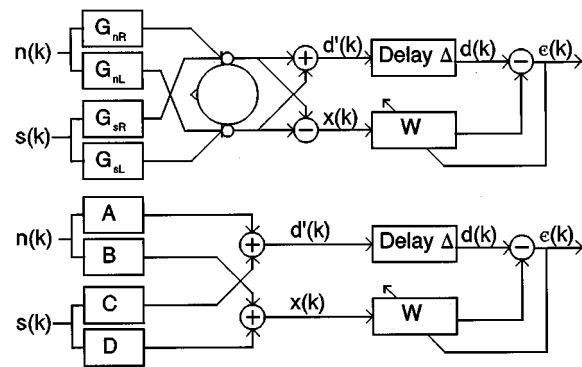


FIG. 2. Relationship between the transfer functions G_{nR} , G_{nL} , G_{sR} , and G_{sL} and A , B , C , and D .

adaptation-inhibition algorithms have been proposed and used in experiments (Van Compernelle, 1990; Greenberg and Zurek, 1992; Kompis and Dillier, 1994; van Hoeseel and Clark, 1995; Kompis *et al.*, 1997). Using one of these algorithms, it can be assumed that the target signal does not significantly influence filter adaptation and filter adaptation takes place in the presence of the noise signal only (Kompis *et al.*, 1997). At filter lengths of 10–50 ms, which are usually used for adaptive beamformers, short adaptation time constants on the order of magnitude of 0.1 s (Dillier *et al.*, 1993; Kompis and Dillier, 1994) can be combined with small convergence errors. Therefore, the coefficients of the adaptive filter can be reasonably expected to have converged, e.g., during the short pauses between the first words of an utterance of a target speaker.

IV. MODELING OF THE IMPULSE RESPONSES BETWEEN THE ACOUSTIC SOURCES AND THE MICROPHONES

The transfer functions between the two acoustic sources and the two microphones can be modeled as impulse responses G_{nR} , G_{nL} , G_{sR} , and G_{sL} , respectively. The first subscript (n or s) marks the source (noise or target signal), the second subscript (L or R) marks the left or right microphone. These impulse responses account for all effects of source directionality, room reverberation, and sound diffraction by the listener's head. For the analysis in Sec. V, it is convenient to convert these impulse responses into four slightly different impulse responses A , B , C , and D as follows:

$$\begin{aligned}
 A &= G_{nR} + G_{nL} = (a_0, a_1, a_2, \dots), \\
 B &= G_{nR} - G_{nL} = (b_0, b_1, b_2, \dots), \\
 C &= G_{sR} + G_{sL}, \\
 D &= G_{sR} - G_{sL}.
 \end{aligned}
 \tag{2}$$

Using this definition, the calculation of the sum and difference of the microphone signals at the first stage of the adaptive beamformer is already included in A , B , C , and D , as shown schematically in Fig. 2.

While the impulse responses between the *target* sound source and the microphones do not influence filter adaptation and can therefore be handled in a simplified manner in Sec.

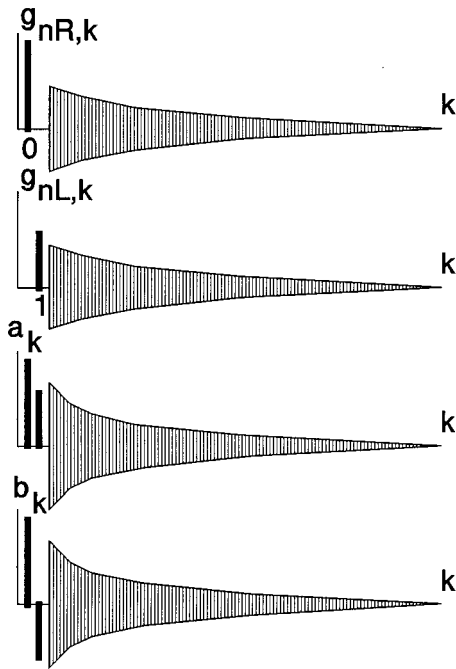


FIG. 3. Schematic representation of the model-transfer functions G_{nR} , G_{nL} , A , and B between noise source and the adaptive beamformer. The solid lines represent the directly incident portions of the noise signal, hatched areas represent the reverberant response.

VI, a more detailed model of the impulse responses between the noise source and the beamformer (i.e., G_{nR} , G_{nL} , A , and B) is required. These impulse responses are modeled by adding the direct response of the microphone which is closer to the noise source in coefficient 0, the direct response to the microphone farther away from it in coefficient 1, and the reverberation in coefficients 2 through ∞ , as depicted in Fig. 3. In general, the difference in the time of arrival between the two microphones will not be exactly one sampling period T_{sample} as modeled, but usually larger, e.g., four samples at a sampling rate of $F_{\text{sample}} = 10 \text{ kHz}$ and an azimuth of $\alpha_n = 45^\circ$ (differences smaller than T_{sample} are excluded by the model definitions in Sec. III). It was found that larger differences are negligible as long as the adaptive filter is much longer than the difference in the time of arrival. In most practical applications, filters are 10–100 times longer than the time-of-arrival difference of the noise sound and this prerequisite is met.

The size of the first two coefficients is a function of the angle of incidence of the direct, nonreverberated portion of the noise signal. The total rms value of a white noise signal at a point on the surface of a rigid sphere at an angle ϑ with respect to the angle of incidence and relative to the root-mean-square value of the same white noise in free field can be calculated from the formulas provided, e.g., by Schwarz (1943) or Morse (1983). Figure 4 shows the resulting function $S(\vartheta)$ for a rigid sphere with a radius of 9.3 cm for three different frequency bands of 0–2.5, 0–5, and 0–10 kHz, corresponding to sampling rates of 5, 10, and 20 kHz, if ideal nonaliasing filters are assumed. The differences between the three curves arise because of the more pronounced diffraction of the high frequency components of the signals.

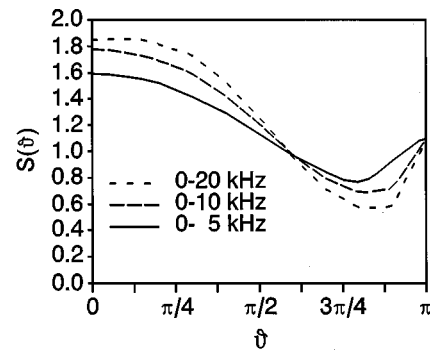


FIG. 4. Sound pressure at the surface of a head-sized ($r=9.3 \text{ cm}$) rigid sphere as a function of the angle of sound incidence ϑ . $S(\vartheta)$ represents rms values relative to free field, for white noise processed by three different low-pass filters.

Using $S(\vartheta)$, the first two coefficients of A and B can be written as

$$\begin{aligned} a_0 &= b_0 = G_0 = S(\pi/2 - \alpha_n) F_d, \\ a_1 &= -b_1 = G_1 = S(\pi/2 + \alpha_n) / F_d, \end{aligned} \quad (3)$$

where F_d is a constant, the value of which will be determined shortly to account for the direct-to-reverberant ratio $P_{d/r}$ of the noise signal. All other coefficients, i.e., $a_i, b_i, i \geq 2$, representing the reverberant part of the room filter are modeled as a series of independent, normally distributed random variables, where

$$\begin{aligned} E\{a_i a_j\} &= E\{b_i b_j\} = \begin{cases} 0, & i \neq j \\ \sigma_i^2, & i = j \end{cases} \\ E\{a_i b_j\} &= 0 \end{aligned} \quad (4)$$

holds for all i and j . Note that for any given acoustic setting, A and B are linear impulse responses with fixed, well-defined and time-independent values a_i and b_i for all i . However, as the exact values of every a_i and b_i for the reverberant part ($i \geq 2$) are neither known nor required for the following computation, only some relevant statistical properties of the coefficients are used. Nevertheless, the underlying impulse responses are time invariant and linear. The variance σ_i^2 decreases exponentially with the index i as the reverberant portion of the signal decays exponentially:

$$\sigma_i^2 = F_\sigma e^{-i/T}, \quad (5)$$

where F_σ is another newly introduced coefficient to account for the correct direct-to-reverberant ratio and T is a time constant (dimensionless, in multiples of the sampling period T_{sample}).

To complete the model of the impulse responses A and B , the three newly introduced variables T , F_d , and F_σ must be calculated first. To derive the value of the dimensionless time constant T from the reverberation time T_r and the sampling period T_{sample} , the definition of the reverberation time (i.e., time required for the reverberant signal to decay by 60 dB) can be used:

$$e^{-T_r/T T_{\text{sample}}} = 10^{-60/10} \quad (6)$$

from which T can be calculated as

$$T = \frac{T_r F_{\text{sample}}}{6 \ln(10)}. \quad (7)$$

The direct-to-reverberant ratio $P_{d/r}$ of the noise signal at the location of the listener can be estimated as

$$P_{d/r} = \left(\frac{r_c}{l_n} \right)^2 \gamma_n. \quad (8)$$

Using the two coefficients F_d and F_σ , it is possible to adjust the direct-to-reverberant ratio $P_{d/r}$ correctly,

$$\frac{G_0^2 + G_1^2}{\sum_{i=2}^{\infty} \sigma_i^2} = P_{d/r}, \quad (9)$$

and at the same time guarantee that

$$\sum_{i=0}^{\infty} a_i^2 = \sum_{i=0}^{\infty} b_i^2 = G_0^2 + G_1^2 + \sum_{i=2}^{\infty} \sigma_i^2 = 1 \quad (10)$$

as stated in Sec. III in order to keep calculations in the following sections as simple as possible. Using the identity

$$\sum_{i=M}^N e^{-i/T} = \frac{e^{-M/T} - e^{-(N+1)/T}}{1 - e^{-1/T}} \quad (11)$$

it can be found that

$$F_d = \sqrt{\frac{P_{d/r}}{(1 + P_{d/r})(S^2(\pi/2 - \alpha_n) + S^2(\pi/2 + \alpha_n))}}, \quad (12)$$

$$F_\sigma = \frac{1 - e^{-1/T}}{(1 + P_{d/r})e^{-2/T}}. \quad (13)$$

V. APPROXIMATE SOLUTION FOR THE AMOUNT OF NOISE SUPPRESSION BY THE ADAPTIVE FILTER

In this section, an approximate solution for the amount of noise reduction h provided by the adaptive filter, defined as

$$h = E\{d^2\} - E\{\epsilon^2\}, \quad (14)$$

is derived. The noise reduction h for an ideally adapted filter can be calculated analytically if the delayed sum signal $d(k)$ and the reference signal $x(k)$ are known. The derivation of the corresponding equations can be found in standard textbooks (e.g., Widrow and Stearns, 1985) on adaptive filters and is not repeated here. To calculate the *approximate* noise reduction for the problem of the adaptive beamformer in a reverberant room, the following definitions are needed. Let X be a vector of the last N samples in the reference signal x , where N is the number of coefficients in the adaptive filter. Then an autocorrelation matrix R can be defined as

$$R = E\{X \cdot X^T\}, \quad (15)$$

where the superscript T stands for transposition and $E\{\}$ denotes the expected value over time. Similarly, let the cross-correlation vector P be

$$P = E\{X \cdot d\} = \begin{bmatrix} P_0 \\ P_1 \\ \vdots \\ P_{N-1} \end{bmatrix}. \quad (16)$$

Using these definitions, the vector W^0 containing the N filter coefficients of the ideally adapted filter for which the variance of the output signal $E\{\epsilon^2(k)\}$ becomes minimal can be written as

$$W^0 = R^{-1}P. \quad (17)$$

The noise reduction h can then be expressed as

$$h = E\{d^2\} - E\{\epsilon^2\} = W^{0T}P = P^T R^{-1}P. \quad (18)$$

For the investigated problem, signals x and d are not known. However, as the source signal n is known to be white noise signal with variance 1, the samples of n are known to be statistically independent. Using the coefficients a_i and b_i of the impulse responses A and B , the elements of the cross-correlation vector P can then be written as

$$P_i = \sum_{k=\max(0, \Delta-i)}^{\infty} a_k \cdot b_{k-i+\Delta}. \quad (19)$$

As long as the samples of the noise signal remain statistically independent in the reference signal $x(k)$, i.e., *after* modification by the impulse response B , the autocorrelation matrix R can be approximated by the identity matrix I ,

$$R \approx I. \quad (20)$$

However, this approximation is reasonably accurate only for low direct-to-reverberant ratios $P_{d/r}$ of the noise signal, where the statistically independent coefficients of the reverberant response dominate the impulse response B . At high direct-to-reverberant ratios of the noise signal, B and therefore $x(k)$ are dominated by the directly incident noise portions and the assumption of statistically independent samples $x(k)$ is violated. It can be shown (Kompis and Dillier, 2001) that the given approximation is reasonably accurate for direct-to-reverberant ratios of the noise signal $P_{d/r} < +3$ dB. Using this approximation and Eqs. (18)+(19), the noise reduction h could be calculated if all model coefficients a_i and b_i were explicitly known. Except for a_0 , a_1 , b_0 , and b_1 however, only the expected value, which is zero, and the expected variance, which is σ_i^2 , are known. Therefore h cannot be calculated, but its expected value $E\{h\}$ can be approximated by

$$E\{h\} = E\{P^T R^{-1}P\} \approx \sum_{i=0}^{N-1} E\{P_i^2\}. \quad (21)$$

There is a meaningful interpretation of this equation. To simplify the discussion, let the delay in the target signal path Δ equal zero for this paragraph only. Equation (21) shows that in order to calculate the expected value of the noise reduction h , N positive values $E\{P_i^2\}$ are summed, thus increasing the noise reduction h with the length of the adaptive filter [P_i can never equal zero because of Eq. (19)]. Using the program in the Appendix it can even be shown that $E\{h\}$ approaches 1 (i.e., perfect noise cancellation) for any reverberation time with increasing filter lengths N , as long as the

directly incident portion of the sound remains negligible. From the schematic representation of the impulse responses A and B and the definition of P_i in Eq. (19) it can be seen that in environments with short reverberation times T_r , only the first few coefficients a_i and b_i will contribute significantly to P_i^2 , and P_i^2 will therefore only contribute significantly to $E\{h\}$ for small values of the index i . Calculating the contribution of the terms with large values of the index i is equivalent to shifting the impulse responses A and B significantly with respect to each other before multiplying and summing the corresponding coefficients in Eq. (19). Therefore, in situations with short reverberation times, after the first few terms in Eq. (21), $E\{h\}$ will increase only very slowly with N , meaning that already short adaptive filters can significantly reduce noise. For long reverberation times, the reverberant tails in Fig. 3 become long as well, but the first few coefficients a_i and b_i are smaller than for short reverberation times because of Eq. (10). This means that the contribution of the first few of the N filter coefficients of the adaptive beamformer are smaller than at short reverberation times, but the increase in noise reduction of the $N+1$ st coefficient of the adaptive filter is larger for large N and longer filters will be needed to reach the same amount of noise reduction. At high direct-to-reverberant ratios $P_{d/r}$ of the noise source, the first two coefficients in A and B (a_0 , a_1 , b_0 , and b_1) representing the direct response are large, and the effect is similar to that of shortening reverberation time. Because of the approximation [Eq. (20)] used, Eq. (21) is only valid if the $P_{d/r}$ is small, i.e., less than approximately +3 dB (Kompis and Dillier, 2001). This is a new assumption which was not discussed in Sec. III and which limits the range of applicability of the given analysis. As a consequence, achievable gains in signal-noise ratio will be underestimated for situations with high direct-to-reverberant ratios of the noise source. Consequences will be discussed in Sec. VII.

To estimate $E\{h\}$, each of the N terms of the sum in Eq. (23) must be calculated first. Each term is itself a sum, which can be conveniently split into three terms as follows:

$$\begin{aligned}
 E\{P_i^2\} &= E\left\{\left(\sum_{k=\max(0,\Delta-i)}^{\infty} a_k \cdot b_{k-i+\Delta}\right)^2\right\} \\
 &= E\left\{\left(\sum_{k=\max(0,\Delta-i)}^{\infty} a_k \cdot b_{k-i+\Delta} \Bigg|_{\substack{k < 2\wedge \\ k-i+\Delta < 2}}\right)^2\right\} \\
 &\quad + E\left\{\left(\sum_{k=\max(0,\Delta-i)}^{\infty} a_k \cdot b_{k-i+\Delta} \Bigg|_{\substack{k < 2\oplus \\ k-i+\Delta < 2}}\right)^2\right\} \\
 &\quad + E\left\{\left(\sum_{k=\max(0,\Delta-i)}^{\infty} a_k \cdot b_{k-i+\Delta} \Bigg|_{\substack{k \geq 2\wedge \\ k-i+\Delta \geq 2}}\right)^2\right\} \\
 &= \varphi_{dd}(i) + \varphi_{dr}(i) + \varphi_{rr}(i). \tag{22}
 \end{aligned}$$

The three portions cover the terms concerning the directly incident portion of the noise only (φ_{dd}), the terms concerning the reverberant terms only (φ_{rr}), and the mixed

terms (φ_{dr}). As a_0 , a_1 , b_0 , and b_1 are explicitly known from Eq. (4), φ_{dd} can be directly calculated as follows:

$$\varphi_{dd}(i) = \begin{cases} (G_0^2 - G_1^2)^2, & |i - \Delta| = 0 \\ (G_0 \cdot G_1)^2, & |i - \Delta| = 1 \\ 0, & |i - \Delta| \geq 2. \end{cases} \tag{23}$$

For the mixed term φ_{dr} the properties

$$\begin{aligned}
 E\{(\xi_1 + \xi_2)^2\} &= E\{\xi_1^2\} + E\{\xi_2^2\}, \\
 E\{(\xi_1 \cdot \xi_2)^2\} &= E\{\xi_1^2\} \cdot E\{\xi_2^2\}, \tag{24}
 \end{aligned}$$

of any two independent random variables ξ_1 and ξ_2 can be used, as all a_i and b_i are independent of each other for $i \geq 2$ and independent from G_0 and G_1 . The result yields

$$\begin{aligned}
 \varphi_{dr}(i) &= \sum_{k=\max(0,\Delta-i)}^{\infty} E\{a_k^2\} \cdot E\{b_{k-i+\Delta}^2\} \Bigg|_{\substack{k < 2\oplus \\ k-i+\Delta < 2}} \\
 &= \begin{cases} 0, & |i - \Delta| = 0 \\ G_1^2 \cdot \sigma_{|i-\Delta|+1}^2, & |i - \Delta| = 1 \\ G_0^2 \cdot \sigma_{|i-\Delta|}^2 + G_1^2 \cdot \sigma_{|i-\Delta|+1}^2, & |i - \Delta| \geq 2. \end{cases} \tag{25}
 \end{aligned}$$

Similarly, using Eq. (11), the reverberant term φ_{rr} can be calculated as

$$\begin{aligned}
 \varphi_{rr}(i) &= \sum_{k=\max(0,\Delta-i)}^{\infty} E\{a_k^2\} \cdot E\{b_{k-i+\Delta}^2\} \Bigg|_{\substack{k \geq 2\wedge \\ k-i+\Delta \geq 2}} \\
 &= \sum_{k=2}^{\infty} \sigma_k^2 \cdot \sigma_{k+|\Delta-i|}^2 \\
 &= \frac{F_\sigma^2 \exp\left(-\frac{4+|\Delta-i|}{T}\right)}{1 - e^{-2/T}}. \tag{26}
 \end{aligned}$$

By substituting Eqs. (23), (25), and (26) into Eq. (22), using Eq. (21) an approximation for $E\{h\}$ can now be calculated.

VI. IMPROVEMENT OF THE SIGNAL-TO-NOISE RATIO

To estimate SNR improvement, the level of the target signal and of the noise signal will be compared at the following four different points of the signal processing chain (cf. Fig. 1) of the adaptive beamformer: (i) at the microphone with the less favorable SNR lying closer to the noise source (index 1), (ii) at the microphone with the more favorable SNR lying farther away from the noise source (index 2), (iii) after summation of both microphone signals, i.e., signal d' in Fig. 1 (index S), and (iv) at the output of the adaptive beamformer, i.e., signal ϵ in Fig. 1 (index B). By calculating the SNRs in those four signals, the SNR improvement of the adaptive beamformer can be related to either microphone signal or to the SNR gain of a simple fixed two-microphone beamformer (Kompis and Diller, 1994), in which both microphone signals are summed.

To calculate the level of the target signal in these four signals, the direct-to-reverberant ratio of the target signal $Q_{d/r}$ at the location of the listener can be estimated—in analogy to Eq. (8)—as

$$Q_{d/r} = \left(\frac{r_c}{l_s}\right)^2 \cdot \gamma_s. \quad (27)$$

As discussed in Sec. V, reverberation must be present for the approximation (20) to be valid. Without loss of generality, the variance of the reverberant portion of the target signal can therefore be set to 1, and the total variance (i.e., including the direct *and* reverberant portions) of the target signal in the two microphones becomes

$$S_1 = S_2 = 1 + Q_{d/r}. \quad (28)$$

By adding both microphone signals, which corresponds to the signal processing of a part of the front end of the adaptive beamformer, the *variance* of the (uncorrelated) reverberant portion is doubled, while, assuming perfect alignment of the target source, the *amplitude* of the direct portion of the sound is doubled, and therefore its variance is multiplied by a factor of 4. However, this is only true for perfect alignment of the target signal source with respect to the microphones. In a realistic setting, e.g., for head-sized spacing between the microphones and for a sampling rate of, e.g., $F_{\text{sample}} = 10$ kHz, this is valid for azimuths of the target signal source $\alpha_s = -3^\circ \dots +3^\circ$. If the misalignment gives rise to a time difference of more than approximately T_{sample} , which in the above-mentioned example occurs at $\alpha_s > 10^\circ$, uncorrelated samples of the white noise signal will add up and the variance of the direct portion of the signal is only doubled. To account for this effect, an alignment factor A is introduced, which can be assessed experimentally in anechoic environments and will, for white noise, yield values in the range of 4 (perfect alignment) down to approximately 2 (no alignment). The variance of the target signal portion in the sum d' can thereby be written as

$$S_S = 2 + A \cdot Q_{d/r}. \quad (29)$$

Similarly, the variance of the target signal in the reference path x becomes

$$S_D = 2 + (4 - A) \cdot Q_{d/r}. \quad (30)$$

As, according to the model assumptions, noise and target signal are uncorrelated and as the filter W was adapted in the absence of the target signal, the variance of the target signal portion in the reference signal x will increase by the factor of $W^{0T}W^0$ at the output of the adaptive filter (signal y). Using Eq. (17) and approximations (20) and (21), this factor can be shown to be equal to $E\{h\}$. The variance of the target signal at the output ϵ of the adaptive beamformer can now be written as the sum of the variances of the filtered reference signal y and the delayed sum signal d ,

$$S_B = S_S + E\{h\} \cdot S_D. \quad (31)$$

So much for the target signal. As to the signal of the noise source, its variance in the sum signal d' can be set to 1 without loss of generality:

$$N_S = 1. \quad (32)$$

The variance of the noise signal at the output of the beamformer can then be written as

$$N_B = 1 - E\{h\}. \quad (33)$$

The variance of the reverberant portion of the noise in the microphone signals is on average $\frac{1}{2}$ of that of the sum signal, the direct portion of the noise is not changed, thus

$$N_1 = \frac{1}{2} \cdot \frac{1}{P_{d/r} + 1} + G_0^2, \quad N_2 = \frac{1}{2} \cdot \frac{1}{P_{d/r} + 1} + G_1^2. \quad (34)$$

Now the improvement in SNR at the output of the adaptive beamformer, when compared to the SNR the microphone with the less favorable SNR (V_1), to the microphone with the more favorable SNR (V_2), or when compared to the two microphone fixed beamformer (V_S) can be calculated as follows:

$$\begin{aligned} V_1 &= 10 \log_{10} \frac{S_B \cdot N_1}{N_B \cdot S_1}, \\ V_2 &= 10 \log_{10} \frac{S_B \cdot N_2}{N_B \cdot S_2}, \\ V_S &= 10 \log_{10} \frac{S_B \cdot N_S}{N_B \cdot S_S}. \end{aligned} \quad (35)$$

The FORTRAN subroutine provided in the Appendix performs all computations necessary to determine all three SNR improvements in Eq. (35).

VII. DISCUSSION

The presented procedure used to estimate the SNR improvement of an adaptive beamformer in the given model setting is based on a number of assumptions and approximations. Its applications are therefore limited. A set of underlying assumptions have been listed and discussed in Sec. III. One additional limitation concerning the range of validity of the predictions is not listed in Sec. III, as it is not a consequence of the underlying model but rather of the approximation used in Eq. (20). For this approximation to be applicable, the direct-to-reverberant ratio $P_{d/r}$ of the noise source must be small, as stated in Sec. V. This limits the predictions to situations with at least a small level of reverberation. It can be shown experimentally (Kompis and Dillier, 2001) that, for realistic sets of parameter values, it is sufficient for $P_{d/r}$ to be below approximately +3 dB for reasonably accurate predictions. For higher $P_{d/r}$, SNR improvement will be systematically underestimated. However, for many applications, this is not a serious limitation. As the model is limited to low direct-to-reverberant ratios of the *noise* source only, predictions for high direct-to-reverberant ratios of the *target* signal source are not affected by this limitation. Although as a side effect of the precedence effect it may not always be easy to appreciate the amount of reverberation subjectively, in many acoustic settings in rooms with realistic amounts of reverberation direct-to-reverberant ratios are below +3 dB even at distances well below 1 m (Kompis and Dillier, 2001), and users of the system will probably tend to keep away from disturbing noise sources, thus further decreasing direct-to-reverberant ratio. Mainly in anechoic environments,

however, where the adaptive beamformer is known for its excellent performance (Peterson *et al.*, 1987), the presented method does not adequately predict SNR improvement.

For hearing aid applications, the primary goal is improved speech intelligibility and not improved SNR, as predicted by the presented method. Because some frequency bands contribute more to speech intelligibility than others, SNR improvement may correlate poorly with improvement in speech recognition, if substantial differences between SNR improvements in different frequency bands exist. However, it can be shown that in the present context, SNR and intelligibility-weighted gain (Greenberg *et al.*, 1993) agree reasonably for a wide range of relevant experimental conditions (Kompis and Dillier, 2001).

The validation of the predicted SNR improvements is of major importance. Validation of the prediction procedure by comparisons to published experimental data is complicated by several factors. Comparisons are limited to experiments which meet or at least approach the model assumptions listed in Sec. III. Comparisons are not possible if different numbers or arrangements of microphones or several noise sources are used (e.g., Peterson *et al.*, 1990; Greenberg and Zurek, 1992). As the proposed prediction method is limited to reverberant conditions, comparisons with experiments in anechoic environments (Peterson *et al.*, 1987; Peterson *et al.*, 1990; Greenberg and Zurek, 1992) are not meaningful. Some of the results reported in the literature list the improvement in terms of speech recognition scores rather than SNR improvement, and in some instances it is not possible to extract the latter information from these data (Kompis and Dillier, 1994; van Hoesel and Clark, 1995). In some reports (van Hoesel and Clark, 1995; Hamacher *et al.*, 1996), no data on the directionality of the sound sources are given. Directionality of the sound sources are required input parameters to calculate the predicted SNR improvement using the presented method. For these reasons, a series of 92 experiments using the adaptive beamformer was performed and experimental results were compared to the predicted SNR improvements. These data are reported separately (Kompis and Dillier, 2001).

Despite some limitations, the presented prediction method offers several advantages over actual experiments in real or simulated environments. Results for a wide range of acoustic settings can be obtained in a fraction of the time required for actual experiments. Results are substantially less prone to errors and problems in the experimental setting such as programming errors, inadvertently wrong entry of simulation data, wiring or microphone problems, etc. Furthermore, predictions are not influenced by technical limitations of experimental settings such as limited resolution of analog-to-digital converters, nonideal adaptation of the adaptive filter, effects of electrical or acoustic noise, etc. Therefore, the predictions offer a unique method to differentiate between implementational and/or experimental limitations and limitations of the adaptive beamforming method per se. Even if the prediction method is not used, it may be helpful for experiments by providing a list of parameters which have to be controlled in every experiment.

The presented prediction method cannot be expected to

replace experiments completely, but experiments and predictions can complement each other favorably. One potential application of the presented algorithm is to enable a validation of experimental data, e.g., if experimental results are either unexpectedly favorable or unexpectedly poor. If the predictions are sufficiently verified experimentally, many time-consuming experiments can be even omitted completely in the early stages of the development of a practical adaptive beamforming noise reduction system.

Probably the most interesting application is the study of the complex behavior of the adaptive beamformer in a wide variety of acoustic situations within a reasonable time span. A first effort in this direction is presented in a companion paper (Kompis and Dillier, 2001).

Because of the numerous underlying assumptions and the approximation used, there is considerable room for improvement for the presented prediction algorithm. Extension to situations with higher P_{dir} , to frequency-dependent predictions of the SNR improvement, or extensions to cases using other numbers or arrangements of microphones (Peterson *et al.*, 1990; Greenberg and Zurek, 1992; Kates and Weiss, 1996) or directional microphones (Kompis and Dillier, 1994; DeBrunner and McKinney, 1995) might prove to be very useful.

To perform the relatively complex calculations to predict SNR improvements, a FORTRAN subroutine is provided in the Appendix. FORTRAN was chosen as it is still one of the most widely used programming languages among scientists and engineers (Kornbluh, 1999) and its code can be easily translated to other programming languages.

Despite the above-discussed drawbacks and limitations, the presented method to predict the SNR improvement of adaptive beamformer may be a useful tool in the design and further development of adaptive multimicrophone noise reduction systems for conventional hearing aids and cochlear implants. With its unique possibility to preliminarily evaluate different adaptive beamformers in a wide range of acoustic settings, it may help to point to new directions in research by showing where inherent limitations of the current adaptive beamformer design need to be overcome by innovative concepts.

VIII. SUMMARY

A method to predict the SNR improvement of a two-microphone adaptive beamformer in a reverberant environment has been presented. Predictions are limited to static situations with one noise and one target signal source and perfect adaptation of the adaptive filter is assumed. A FORTRAN subroutine to perform the necessary calculations has been provided. A systematic validation study of the predictions is provided in a separate text (Kompis and Dillier, 2001).

ACKNOWLEDGMENTS

This work was supported by the Swiss National Research Foundation, Grant Nos. 4018-10864 and 3238-56352.99, and Ascom Tech Ltd.

APPENDIX: FORTRAN SUBROUTINE

```

SUBROUTINE BEAMF(V, Tr, Fls, GammaS, A, Fln,
1      GammaN, AlphaN, Fsampl, N, ID, V1, V2, Vs)
C Input:
C V Volume of room (m3)
C Tr Reverberation time Tr (s)
C Fls Distance listener - target signal
C source (m)
C GammaS Index of directionality of target
C signal source
C A Alignment factor for target signal
C source (range 2 to 4)
C Fln Distance listener-noise source (m)
C GammaN Index of directionality of target
C signal source
C AlphaN Azimuth of noise source (degrees)
C Fsampl Sampling rate (Hz)
C N Number of coefficients in the
C adaptive filter
C ID Delay in target signal path (in
C multiples of 1/Fsampl)
C Output:
C V1 SNR-improvement vs.
C signal of microphone 1 (dB)
C V2 SNR-improvement vs.
C signal of microphone 2 (dB)
C Vs SNR-improvement vs.
C sum of microphone signals (dB)
C Array for function S(theta) for 3 sampling
C rates Fsampl=5,10, and 20kHz
      DIMENSION S(3,11)
      DATA(S(1,I), I=1,4)/1.59,1.57,1.52,1.42/
      DATA(S(1,I), I=5,8)/1.29,1.13,0.97,0.84/
      DATA(S(1,I), I=9,11)/0.76,0.93,1.10/
      DATA(S(2,I), I=1,4)/1.78,1.75,1.69,1.59/
      DATA(S(2,I), I=5,8)/1.42,1.21,0.98,0.79/
      DATA(S(2,I), I=9,11)/0.68,0.72,1.09/
      DATA(S(3,I), I=1,4)/1.85,1.86,1.81,1.73/
      DATA(S(3,I), I=5,8)/1.53,1.26,0.96,0.71/
      DATA(S(3,I), I=9,11)/0.57,0.58,1.06/
      rc=0.057*SQRT(V/Tr) ! critical distance
      Pdr=SQR(rc/Fln)*GammaN
      Qdr=SQR(rc/Fls)*GammaS
      T=Tr*Fsampl/13.815 ! 13.815=6*ln 10
      IFS=2
      IF(Fsampl.LT. 7500.) IFS=1
      IF(Fsampl.GT.15000.) IFS=3
C limit AlphaN to values of 0...90 degrees
C because of symmetry
      AlphaN=ABS(AlphaN)
      IF(AlphaN.GT.90.) AlphaN=180.-AlphaN
C S(theta) for position of each microphone
C (ST0,ST1) by interpolation
      RINDEX=(90.-AlphaN)/18.+1.
      INDEX=INT(RINDEX)
      RINDEX=RINDEX-INDEX
      ST0=S(IFS,INDEX)*(1.-RINDEX)+
1 S(IFS,INDEX+1)*RINDEX
      RINDEX=AlphaN/18.+6.
      INDEX=INT(RINDEX)
      RINDEX=RINDEX-INDEX
      ST1=S(IFS,INDEX)*
1 (1.-RINDEX)+S(IFS,INDEX+1)*RINDEX
      Fd=SQRT(Pdr/((1.+Pdr)*
1 (SQR(ST0)+SQR(ST1))))
      Fsigma=(1.-EXP(-1./T))/
1 ((1+Pdr)*EXP(-2./T))
      G0=Fd*ST0
      G1=Fd*ST1
      h=0.
      DO 100 I=0,N-1
      PHIdd=0.
      IF(IABS(I-ID).EQ.1) PHIdd=SQR(G0*G1)
      IF(I.EQ.ID) PHIdd=SQR(G0*G0-G1*G1)
      PHIdr=0.
      IF(IABS(I-ID).EQ.1) PHIdr=G1*G1*
1 SIGMA2(IABS(I-ID)+1,Fsigma,T)
      IF(IABS(I-ID).GE.2) PHIdr =
1 G0*G0*SIGMA2(IABS(I-ID) ,Fsigma,T)+
1 G1*G1*SIGMA2(IABS(I-ID)+1,Fsigma,T)
      PHIr=SQR(Fsigma)*
1 EXP((-4-IABS(I-ID))/T)/(1.-EXP(-2./T))
      P2=PHIdd+PHIdr+PHIr
      h=h+P2
100 CONTINUE
      S1=1.+Qdr
      S2=S1
      Ss=2.+A*Qdr
      SD=2.+(4.-A)*Qdr
      SB=Ss+h*SD
      FNs=1.
      FNB=1.-h
      FN1=0.5/(1.+Pdr)+G0*G0
      FN2=0.5/(1.+Pdr)+G1*G1
      V1=10.*ALOG10((SB*FN1)/(FNB*S1))
      V2=10.*ALOG10((SB*FN2)/(FNB*S2))
      Vs=10.*ALOG10((SB*FNs)/(FNB*Ss))
      RETURN
      END
      FUNCTION SIGMA2(I,Fsigma,T)
      SIGMA2=Fsigma*EXP(-I/T)
      RETURN
      END
      FUNCTION SQR(X)
      SQR=X*X
      RETURN
      END

```

Bächler, H., and Vonlanthen, A. (1995). "Audio-Zoom Signalverarbeitung zur besseren Kommunikation im Störschall," *Phonak Focus* **18**, 1–20.

Cochlear, Inc. (1997). "Introducing the Audallion BEAMformer Digital Noise Reduction System," *Cochlear Clinical Bulletin*, April, 1–5.

Cox, H., Zeskind, R. M., and Kooij, T. (1986). "Practical supergain," *IEEE Trans. Acoust., Speech, Signal Process.* **ASSP-34**, 393–398.

DeBrunner, V. E., and McKinney, E. D. (1995). "Directional adaptive least mean square acoustic array for hearing aid enhancement," *J. Acoust. Soc. Am.* **98**, 437–444.

Dillier, N., Fröhlich, T., Kompis, M., Bögli, H., and Lai, W. L. (1993). "Digital signal processing (DSP) applications for multiband loudness correction digital hearing aids and cochlear implants," *J. Rehabil. Res. Dev.* **24**, 95–109.

Graupe, D., Grosspietsch, J. K., and Basseas, S. P. (1987). "A single-microphone-based self-adaptive filter of noise from speech and its performance evaluation," *J. Rehabil. Res. Dev.* **24**, 119–126.

Gravel, J. S., Fausel, N., Liskow, C., and Chobot, J. (1999). "Children's speech recognition in noise using omni-directional and dual-microphone hearing aid technology," *Ear Hear.* **20**, 1–11.

Greenberg, J. E., Peterson, P. M., and Zurek, P. M. (1993). "Intelligibility-

weighted measures of speech-to-interference ratio and speech system performance," *J. Acoust. Soc. Am.* **94**, 3009–3010.

Greenberg, J. E., and Zurek, P. M. (1992). "Evaluation of an adaptive beamforming method for hearing aids," *J. Acoust. Soc. Am.* **91**, 1662–1676.

Griffiths, L. J., and Jim, C. W. (1982). "An alternative approach to linearly constrained adaptive beamforming," *IEEE Trans. Antennas Propag.* **30**, 27–34.

Hamacher, V., Mauer, G., and Döring, W. H. (1996). "Untersuchung eines adaptiven beamforming-systems zur Störunterdrückung für Hörgeschädigte," *Proceedings of the 22nd Deutsche Jahrestagung für Akustik (DAGA)*, Bonn, Germany (unpublished).

Kates, J. M. (1997). "Relating change in signal-to-noise ratio to array gain for microphone arrays used in rooms," *J. Acoust. Soc. Am.* **101**, 2388–2390.

Kates, J. M., and Weiss, M. R. (1996). "A comparison of hearing-aid array-processing techniques," *J. Acoust. Soc. Am.* **99**, 3138–3148.

Kochkin, S. (1993). "Consumer satisfaction with hearing instruments in the United States," *The Marketing Edge*, Special issue June 1993, pp. 1–4.

- Kochkin, S. (1996). "Customer satisfaction and subjective benefit with high performance hearing aids," *Hearing Rev.* **3**, 16–26.
- Kompis, M. (1998). "Improving speech intelligibility with multi-microphone noise reduction systems for hearing aids," *Curr. Top. Acoust. Res.* **2**, 1–16.
- Kompis, M., and Dillier, N. (1991). "Noise reduction for hearing aids: Evaluation of the adaptive beamformer approach," *Proc. Annu. Int. Conf. IEEE Eng. Med. Biol. Soc.* **13**, 1887–1888.
- Kompis, M., and Dillier, N. (1993). "Simulating transfer functions in a reverberant room including source directivity and head shadow effects," *J. Acoust. Soc. Am.* **93**, 2779–2787.
- Kompis, M., and Dillier, N. (1994). "Noise reduction for hearing aids: Combining directional microphones with an adaptive beamformer," *J. Acoust. Soc. Am.* **96**, 1910–1913.
- Kompis, M., and Dillier, N. (2001). "Performance of a two-microphone adaptive beamforming noise reduction scheme for hearing aids. II. Experimental verification of the predictions," *J. Acoust. Soc. Am.* **109**, 1134–1143.
- Kompis, M., Dillier, N., Francois, J., Tinembart, J., and Häusler, R. (1997). "New target-signal-detection schemes for multi-microphone noise-reduction systems for hearing aids," *Proc. Annu. Int. Conf. IEEE Eng. Biol. Soc.* **19**, 1990–1993.
- Kompis, M., Feuz, P., François, J., and Tinembart, J. (1999). "Multi-microphone digital-signal-processing system for research into noise reduction for hearing aids," *Innovation Technol. Biol. Medicine* **20**, 201–206.
- Kompis, M., Oberli, M., and Brugger, U. (2000). "A novel real-time noise reduction system for the assessment of evoked otoacoustic emissions," *Comput. Biol. Med.* **30**, 341–354.
- Kornbluh, K. (1999). "Math and science software," *IEEE Spectr.* January, 88–91.
- Kuhn, G. F. (1977). "Model for the interaural time difference for the azimuthal plane," *J. Acoust. Soc. Am.* **62**, 157–167.
- Lim, J. S., and Oppenheim, A. V. (1979). "Enhancement and bandwidth compression of noisy speech," *Proc. IEEE* **67**, 1586–1604.
- Lurquin, P., and Rafhay, S. (1996). "Intelligibility in noise using multi-microphone hearing aids," *Acta Oto-Laryngol. Belg.* **50**, 103–109.
- Morse, P. M. (1983). *Vibration and Sound* (American Institute of Physics, New York), 2nd (Paperback) printing, Chap. 27, pp. 311–326.
- Peterson, P. M., Durlach, N. I., Rabinowitz, W. M., and Zurek, P. M. (1987). "Multimicrophone adaptive beamforming for interference reduction in hearing aids," *J. Rehabil. Res. Dev.* **24**, 103–110.
- Peterson, P. M., Wie, S. M., Rabinowitz, W. M., and Zurek, P. M. (1990). "Robustness of an adaptive beamforming method for hearing aids," *Acta Oto-Laryngol., Suppl.* **469**, 85–90.
- Schwarz, L. (1943). "Zur theorie der Beugung einer ebenen Schallwelle an der Kugel," *Akust. Z.* **8**, 91–117.
- Soede, W., Berkhout, A. J., and Bilsen, F. A. (1993). "Development of a new hearing instrument based on array technology," *J. Acoust. Soc. Am.* **94**, 785–798.
- Stadler, R. W., and Rabinowitz, W. M. (1993). "On the potential of fixed arrays for hearing aids," *J. Acoust. Soc. Am.* **94**, 1332–1342.
- Valente, M. (1998). "The bright promise of microphone technology," *Hear. J.* **51**, 10–15.
- Valente, M., Fabry, D. A., and Potts, L. G. (1995). "Recognition of speech in noise with hearing aids using dual microphones," *J. Am. Acad. Audiol.* **6**, 440–449.
- Van Compernelle, D. (1990). "Hearing aids using binaural processing principles," *Acta Oto-Laryngol., Suppl.* **469**, 76–84.
- Vanden Berghe, J., and Wouters, J. (1998). "An adaptive noise canceller for hearing aids using two nearby microphones," *J. Acoust. Soc. Am.* **103**, 3621–3626.
- van Hoesel, R. J. M., and Clark, G. M. (1995). "Evaluation of a portable two-microphone adaptive beamforming speech processor with cochlear implant patients," *J. Acoust. Soc. Am.* **97**, 2498–2503.
- Welker, D. P., Greenberg, J. E., Desloge, J. G., and Zurek, P. M. (1997). "Microphone-array hearing aids with binaural output. II. A two-microphone adaptive system," *IEEE Trans. Speech Audio Process.* **5**, 543–551.
- Whitmal, N. A., Rutledge, J. C., and Cohen, J. (1996). "Reducing correlated noise in digital hearing aids," *IEEE Eng. Med. Biol. Mag.* **15**, 88–96.
- Widrow, B., Glover, J. R., McColl, J. M., Kaunitz, J. M., Williams, C. S., Hearn, R. H., Zeidler, J. R., Dong, J. R., and Goodlin, R. C. (1975). "Adaptive noise cancelling: Principles and applications," *Proc. IEEE* **63**, 1692–1716.
- Widrow, B., and Stearns, S. D. (1985). *Adaptive Signal Processing* (Prentice-Hall, Englewood Cliffs, NJ).
- Wouters, J., Litière, L., and van Wieringen, A. (1999). "Speech intelligibility in noisy environments with one- and two-microphone hearing aids," *Audiology* **38**, 91–98.
- Zwicker, E., and Zollner, M. (1984). *Elektroakustik* (Springer, Heidelberg).

Performance of an adaptive beamforming noise reduction scheme for hearing aid applications. II. Experimental verification of the predictions

Martin Kompis^{a)}

University Clinic of ENT, Head and Neck Surgery, Inselspital, 3010 Bern, Switzerland

Norbert Dillier

ENT-Department, University Hospital of Zurich, 8091 Zurich, Switzerland

(Received 5 November 1999; revised 24 April 2000; revised 25 September 2000; accepted 14 November 2000)

A method to predict the amount of noise reduction which can be achieved using a two-microphone adaptive beamforming noise reduction system for hearing aids [J. Acoust. Soc. Am. **109**, 1123 (2001)] is verified experimentally. 34 experiments are performed in real environments and 58 in simulated environments and the results are compared to the predictions. In all experiments, one noise source and one target signal source are present. Starting from a setting in a moderately reverberant room (reverberation time 0.42 s, volume 34 m³, distance between listener and either sound source 1 m, length of the adaptive filter 25 ms), eight different parameters of the acoustical environment and three different design parameters of the adaptive beamformer were systematically varied. For those experiments, in which the direct-to-reverberant ratios of the noise signal is +3 dB or less, the difference between the predicted and the measured improvement in signal-to-noise ratio (SNR) is -0.21 ± 0.59 dB for real environments and -0.25 ± 0.51 dB for simulated environments (average \pm standard deviation). At higher direct-to-reverberant ratios, SNR improvement is systematically underestimated by up to 5.34 dB. The parameters with the greatest influence on the performance of the adaptive beamformer have been found to be the direct-to-reverberant ratio of the noise source, the reverberation time of the acoustic environment, and the length of the adaptive filter. © 2001 Acoustical Society of America. [DOI: 10.1121/1.1338558]

PACS numbers: 43.66.Ts, 43.60.Lq, 43.60.Gk [RVS]

I. INTRODUCTION

Poor speech recognition in noisy environments is a major source of dissatisfaction for numerous users of cochlear implants and conventional hearing aids (Kochkin, 1993; Kiefer *et al.*, 1996). One promising approach to solve this problem is the two-microphone Griffiths–Jim beamformer or adaptive beamformer (Griffiths and Jim, 1982; Peterson *et al.*, 1987), where the signals of two microphones mounted close to the user's ears are postprocessed by an adaptive noise reduction scheme (Widrow *et al.*, 1975). A schematic representation is shown in the lower part of Fig. 1. A detailed description of the adaptive beamformer can be found elsewhere (Peterson *et al.*, 1987; Greenberg and Zurek, 1992; Kompis and Dillier, 2001) and is not repeated here. Numerous experiments have already been performed with this method, showing a wide range of signal-to-noise-ratio (SNR) improvements of 0 to 30 dB (Peterson *et al.*, 1987; Peterson *et al.*, 1990; Greenberg and Zurek, 1992; Dillier *et al.*, 1993; van Hoesel and Clark, 1995; Hamacher *et al.*, 1996). Comparison of these data is difficult because of the different experimental settings and a lack of theoretical background to estimate the contribution of each of these differences on the results. In the companion paper (Kompis and Dillier, 2001), a theoretical framework has been presented, which allows the prediction of the noise reduction that can be expected

from an adaptive beamforming noise reduction system in different acoustic settings. However, this framework by itself is of limited value only for two reasons. First, the predictions have not been validated by comparisons to experimental results. Second, as the prediction is a complex function of 11 input parameters, it is still relatively difficult to gain a concept of the complex behavior of the beamformer without systematic variations of all parameters. It is the aim of this investigation to start to close both of these gaps.

II. METHODS

The computer program presented in the companion paper estimates the SNR improvement which can be expected to be reached by an adaptive beamformer as a function of 11 acoustic and design parameters. It is not possible to test all parameter combinations with a reasonable number of different values for each of the 11 parameters. Instead, a different approach was chosen, in which a realistic experimental setting was defined first, from which each parameter is varied separately toward both greater and smaller values. In this way, the number of experiments was reduced to a manageable 92. Throughout this text, the experimental setting from which all parameters are varied will be called central setting.

A. Central setting

The definition of the central setting includes the room, the noise, and the signal source, and a set of design parameters of the adaptive beamformer. Figure 1 shows a sche-

^{a)}Electronic mail: martin.kompis@insel.ch

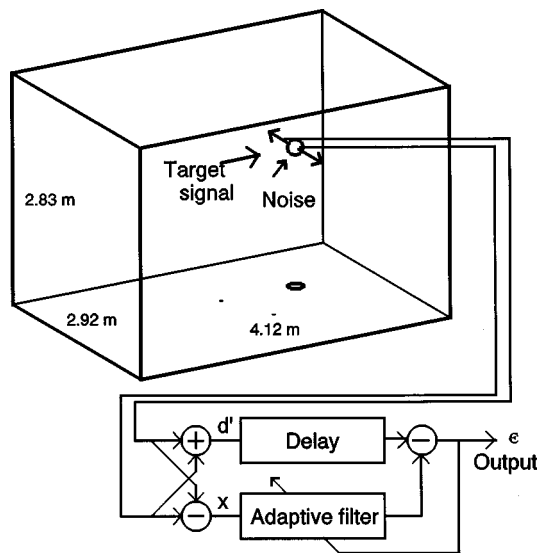


FIG. 1. Schematic drawing of the experimental setup at the central setting (top) and the adaptive beamformer (bottom). The starting points of the arrows in the upper portion of the diagram denote the locations of the loudspeakers and microphones.

matic representation. The parameters of the central setting have been chosen to represent a realistic situation, in which variations of all relevant parameters toward both higher and lower values appear to be reasonable. To define the properties of a suitable room, the dimensions and reverberation times of 18 different rooms (4 offices, 11 living or bedrooms, 1 bath, 2 kitchens) were measured. In this limited sample, the average volume was 34.1 m^3 and the average reverberation time (measured in octave bands with center frequencies of 125–4000 Hz) was 0.41 s and almost frequency independent. These average values may differ, e.g., in a different cultural context. One of these 18 rooms, a shoebox-shaped room with a volume of 34.0 m^3 and an almost frequency independent reverberation time of 0.42 s, was available for experiments for a limited time and was used for the central setting.

Two loudspeakers (Phillips 22AHS86/16R) were placed at a distance of 1 m from a dummy head equipped with a stereo microphone, both from a Sennheiser MKE 2002 set. The azimuth of the loudspeaker emitting the target signal was 0° (i.e., in front of the dummy head), the noise source was 45° to its right. The index of directionality of the loudspeakers was estimated to be 3.4 for band-limited noise 125 and 5000 Hz in an earlier work (Kompis and Dillier, 1993). As to the adaptive beamformer, a sampling rate of 10 240 Hz, a filter length of 25 ms (256 filter coefficients), and a delay of 50% of the filter length (12.5 ms) in the target signal path (marked d' in Fig. 1) was chosen.

B. Experiments in real and simulated rooms

As far as possible, experiments were performed in the real room described. Some of the experimental parameters, most notably the volume of the room and the reverberation time, cannot be readily varied independently using real rooms. Furthermore, the room which was used for the central setting was available only for a limited time for recordings. For these reasons, 58 of the 92 experiments were performed

TABLE I. Synopsis of the input parameters used to predict the performance for the central setting.

Parameter	Value
Room size V	34 m^3
Reverberation time T_r	0.42 s
Distance listener to target signal source l_s	1 m
Index of directionality of target signal source γ_s	3.4
Alignment factor of target signal source A	4
Distance listener to noise source l_n	1 m
Index of directionality of noise source γ_n	3.4
Azimuth of noise source α_n	45°
Sampling rate F_s	10 240 Hz
Number of coefficients in adaptive filter N	256
Delay in target signal path Δ	128 samples

in simulated rooms, using a simulation method presented earlier (Kompis and Dillier, 1993). This simulation procedure is based on an image method introduced by Allen and Berkley (1979). It simulates the impulse responses between acoustic sources and microphones in shoebox-shaped rooms, taking into account the effects of directional sound sources and the acoustic head-shadow of the listener. The head is modeled as a rigid sphere. For the simulations, a value of 18.6 cm was chosen for the diameter of this sphere, as proposed by Kuhn (1977) and used in an earlier study (Kompis and Dillier, 1993). The index of directionality of 3.4 for the two sound sources was approximated by an opening angle of $\pm 65^\circ$. Within this opening angle, the signal is emitted equally into all directions, and no signal is emitted outside this angle. For the simulated version of the central setting, all other simulation parameters (i.e., reverberation time, room dimensions, relative positions of the sound sources and the listener) were the same as the corresponding parameters of the real room. The suitability of the simulation method for the purpose at hand was validated in the first experiment (Sec. III A). For the prediction of the performance of the adaptive beamformer, the same set of input parameters was used for both the real and the simulated central setting. Table I shows a synopsis of these input parameters.

As the signals from the real and simulated central setting were used for several experiments with different values of the design parameters of the adaptive beamformer, only 14 different sets of recordings in real environments and 37 different sets of simulated signals were used. Table II shows a synopsis of the experiments and environments used.

C. Signal acquisition and signal processing

Target and noise signals were recorded (or for the experiments in simulated rooms: simulated) separately. According to the paradigm used for the prediction of the improvement of the signal-to-noise ratio (SNR) described previously (Kompis and Dillier, 2001), the signals of both the noise and the target signal source were white noise. White noise was generated on a computer and played back via a digital audio tape (DAT) recorder driving only one of the two loudspeakers at a time. Uncorrelated noise sequences of 3 s duration were used for the target and the noise signals, respectively. Recordings of the microphone signals at the dummy head were digitized at a sampling rate of 10 240 Hz

TABLE II. Synopsis of the number of experiments in real and simulated environments.

Parameter varied	Experiments in real environments	Experiments in simulated environments	Sets of recorded signals	Sets of simulated signals
None (central setting)	1	1	1	1
Azimuth of noise signal source (Fig. 3)	5 ^a	...	5 ^b	...
Distance to noise source (Fig. 4)	2 ^a	4	2	4
Index of directionality of noise source (Fig. 5)	1 ^a	6	1	6
Alignment factor (Fig. 6)	1 ^a	3	1	3
Distance to target signal source (Fig. 7)	2 ^a	4	2	4
Index of directionality of target signal source (Fig. 8)	1 ^a	6	1	6
Reverberation time (Fig. 9)	1 ^a	7 ^c	1	7
Room size (Fig. 10)	...	6	...	6
Filter length (Fig. 11)	4 ^a	...	0 ^b	...
Delay in target signal path (Fig. 12)	16 ^{a,d}	17 ^c	0 ^b	0 ^b
Sampling rate (Fig. 13)	...	4 ^c	...	0 ^b
Total	34	58	14	37

^aIn addition, results from the real central setting are shown in the corresponding figure.

^bRecorded or simulated input signals used are identical to those at central setting.

^cIn addition, results from the simulated central setting are shown in the corresponding figure.

^dIn addition, results of one experiment already shown in Fig. 11 (filter length 512, delay 50%) is shown in Fig. 12.

into a computer using a custom-built 12 bit stereo analog-to-digital converter and appropriate antialiasing filters. The spectra of the recorded signals were found to rise slightly toward higher frequencies. Although the effect of this spectral feature on the SNR improvement was found to be small, a two-coefficient finite impulse-response filter (coefficients 0.5 and 0.65) was used to equalize the spectra to within 2 dB in the frequency range of 125–4900 Hz. For experiments in simulated environments, white noise was directly filtered by the impulse responses generated by the room simulation program. The spectra of the microphone signals in the simulations were found to be flat to within 2 dB without further conditioning.

To measure the gain in signal-to-noise ratio, first the recording of the noise signal alone was processed by an adaptive beamforming algorithm. The adaptation of the filter was performed using a normalized least-mean squares algorithm (Bellanger, 1987), where the adaptation time constant was chosen to be 0.2 s. After 2 s the filter was assumed to be in an adapted state and the signal variance in the following second was used as a measure of the variance of the noise signal at the output of the beamformer. The adapted filter was temporarily stored and used in a second run, where the recorded or simulated target signal was processed alone, with the adaptation disabled, i.e., maintaining the adapted coefficients from the first run. Again, the variance of the output signal during 1 s was used as a measure of the variance of the target signal at the output of the adaptive beamformer. Using this procedure, a perfect target-signal detection scheme, which prevents any filter adaptation while a target signal is present, is mimicked. Several such schemes have been proposed (Van Compernelle, 1990; Greenberg and Zurek, 1992; Dillier *et al.*, 1993; Kompis *et al.*, 1997) and used in experiments, and the theoretical analysis and prediction of SNR improvement (Kompis and Dillier, 2001) is based on the assumption that one of these schemes is employed. For all experiments involving longer filters (>25

ms), filter adaptation was allowed for 4 s instead of only 2 s to compensate for the proportionally longer adaptation time constant.

D. SNR improvement and intelligibility-weighted gain

As the investigated prediction method predicts SNR improvement, this measure is used to represent the experimental results. However, for hearing aid applications, the primary goal is improved speech intelligibility and not improved SNR. Because some frequency bands contribute more to speech intelligibility than others, SNR improvement may correlate poorly with improvement in speech recognition, if substantial differences between SNR improvements in different frequency bands do exist. To estimate this effect on the presented data, all experimental results which were compared to the theoretical predictions were also examined by an intelligibility-weighted measure proposed by Greeberg *et al.* (1993). To calculate this intelligibility-weighted gain, signal-to-noise ratios were calculated in 15 one-third-octave bands with center frequencies between 200 and 5000 Hz and weighted according to their contribution to the articulation index (ANSI, 1969).

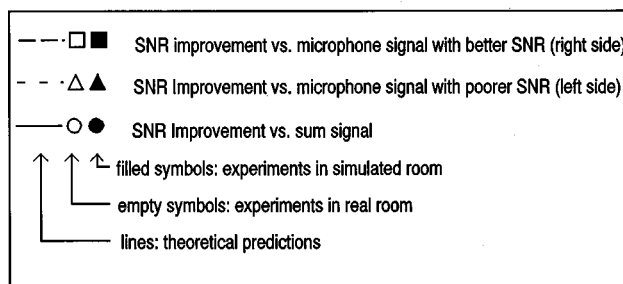


FIG. 2. Legend for the symbols and lines used in Figs. 3–14.

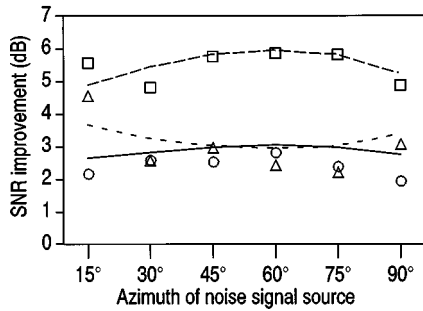


FIG. 3. Influence of the azimuth of the noise signal source. See Fig. 2 for a legend of the symbols used.

E. Representation of the results

The computer program (Kompis and Dillier, 2001) implementing the prediction of the SNR improvement of the adaptive beamformer calculates three different numbers: the SNR improvement versus the microphone signal with the more favorable SNR, the SNR improvement versus the microphone signal with the poorer SNR, and the improvement versus the sum of both microphone signals. The latter corresponds to a simple two-microphone beamformer with fixed postprocessing.

To allow direct comparison, the results of the experiments are similarly calculated as improvements versus each microphone signal and the sum of both microphone signals. Therefore, six sets of data are shown in the figures of Sec. III. All predicted improvements are connected by different lines, and all results from experiments are shown as individual symbols. Results from experiments in real environments are shown using open symbols; results from experiments in simulated environments are shown using closed symbols. Figure 2 shows a legend for all lines and symbols

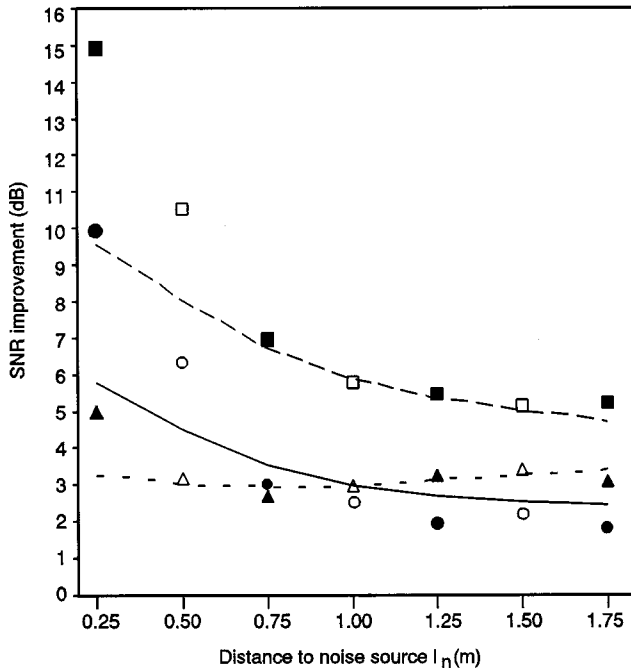


FIG. 4. Influence of the distance between noise source and listener. See Fig. 2 for a legend of the symbols used.

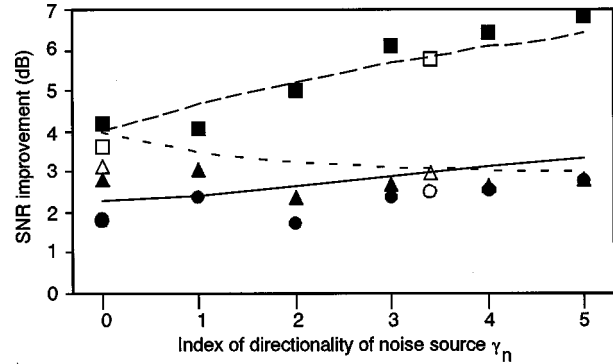


FIG. 5. Influence of the directionality of the noise source. See Fig. 2 for a legend of the symbols used.

used in Figs. 3–14. SNR improvements at the output of the adaptive beamformer, compared to the SNR at the left microphone (opposite from the noise source and therefore more favorable SNR; triangles in figures) will be lower than SNR improvement versus the right microphone facing the noise source (poorer SNR; squares in figures).

III. RESULTS

A. Results at central setting

At central setting, the predicted SNR improvement was compared to the results from both the experiments in the real room and in the simulated environment. Table III shows the results. All three sets of SNR improvements, i.e., the prediction and the two sets of experimental results, are within 0.5 dB within each other with absolute values ranging from 2.50 to 5.97 dB. None of the data sets exhibit systematically higher or lower values for all SNR improvements when compared to the other two sets.

B. Effect of the acoustic parameters of the noise signal source

The three parameters characterizing the noise signal source are its azimuth α_n (with $\alpha_n = 0$ defined as the forward direction of the listener), the distance between noise source

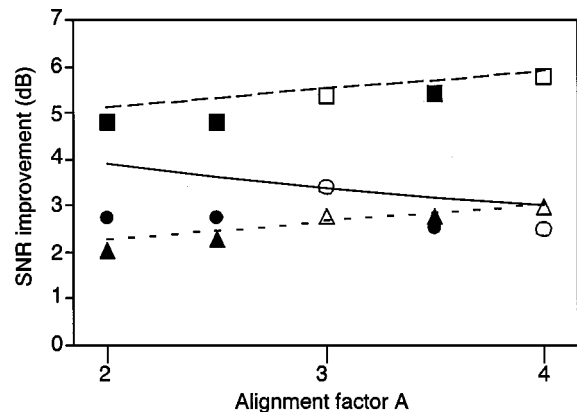


FIG. 6. Influence of the alignment of the target signal source. See the text for the definition of the alignment factor A. See Fig. 2 for a legend of the symbols used.

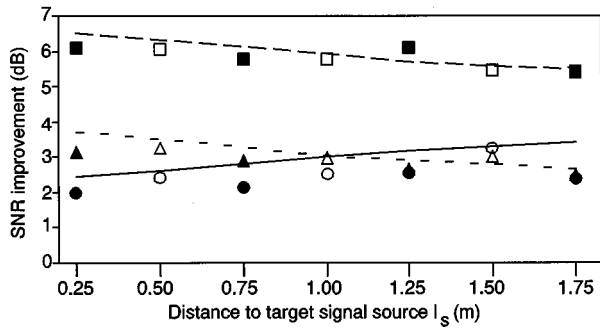


FIG. 7. Influence of the distance between target signal source and listener. See Fig. 2 for a legend of the symbols used.

and listener l_n , and the index of directionality γ_n of the noise source. The last two factors influence the direct-to-reverberant P_{dr} ratio of the noise signal. The index of directionality is defined as the ratio between the signal intensity emitted in the direction of the listener to the intensity of a hypothetical omnidirectional source with the same total acoustic output power (DeBrunner and McKinney, 1995).

Figure 3 shows the results of the experiments at 6 different angles of incidence between 15° and 90° . Because of the symmetry of the setting, results can be extrapolated for all angles in the horizontal plane, except for the front (0°) and the rear (180°), where the adaptive beamformer assumes the position of a target- and not of a noise-signal source. The largest difference between prediction and experimental results is 0.89 dB, with more than half of the experimental results lying within 0.5 dB of the predictions.

Figure 4 shows the SNR improvement as a function of the distance between listener and noise source. For distances of 0.75 m ($P_{dr}=2.0$ dB) and more, predictions and experimental results are reasonably in accordance. At distances of 0.5 m ($P_{dr}=5.5$ dB) and less, however, predictions considerably underestimate the SNR improvement which can actually be achieved using the adaptive beamformer. At $l_n = 0.25$ m, the difference is as large as 5.34 dB.

Figure 5 shows the SNR improvement as a function of the index of directionality γ_n of the noise source. For the experiments in the real acoustic environment, $\gamma_n=3.4$ corresponds to the loudspeaker facing the dummy head (central

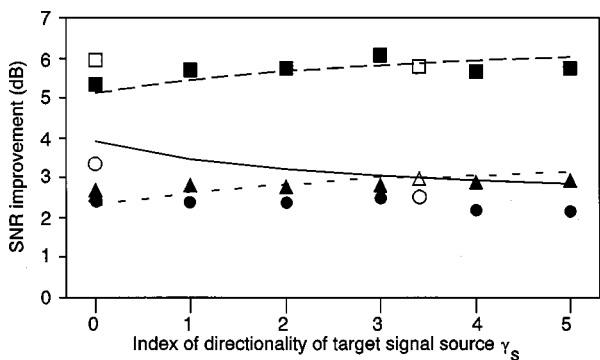


FIG. 8. Influence of the directionality of the target signal source. See Fig. 2 for a legend of the symbols used.

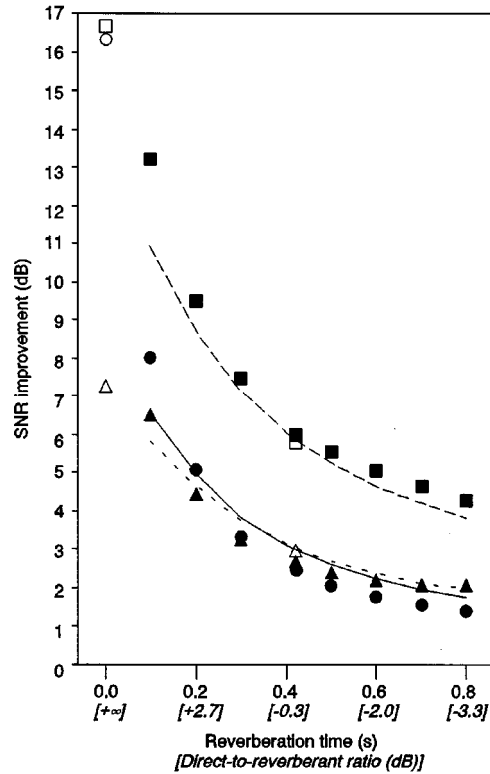


FIG. 9. Influence of the reverberation time. See Fig. 2 for a legend of the symbols used.

setting), whereas $\gamma_n=0$ was approximated by turning the loudspeaker away from the dummy head. For the simulations, $\gamma_n = 1, 2, 3, 4,$ and 5 was approximated similar to the central setting with opening angles of $\pm 180^\circ, \pm 90^\circ, \pm 70^\circ, \pm 60^\circ, \pm 53^\circ$, respectively. For $\gamma_n=0$, an opening angle of $\pm 90^\circ$ facing away from the dummy head was used.

There is a reasonable agreement between the predicted SNR improvement and the results of the actual measurements, with an average error of 0.51 dB (range 0.02–1.14 dB). SNR improvement increases with γ_n when compared to the sum signal and to the microphone signal with the less favorable SNR, but decreases slightly when compared to the microphone signal with the higher SNR, presumably due to the increased direct-to-reverberant ratio of the noise signal.

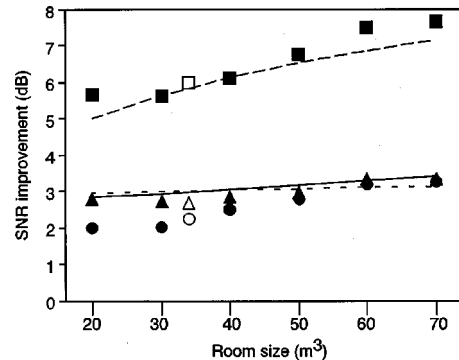


FIG. 10. Influence of the room size. See Fig. 2 for a legend of the symbols used.

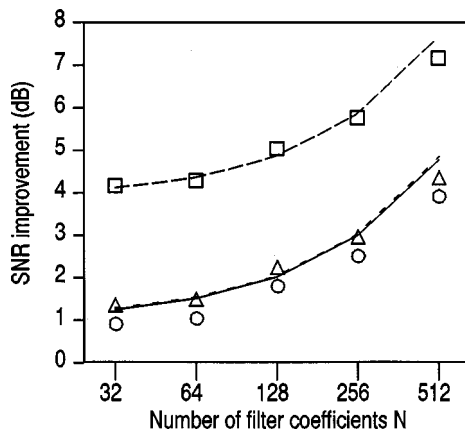


FIG. 11. Influence of the length of the adaptive filter. See Fig. 2 for a legend of the symbols used.

C. Effect of the acoustic parameters of the target signal source

The three parameters describing the target signal source are the alignment factor A , the distance between dummy head and target signal source l_s , and the index of directionality of the target signal source γ_s .

The alignment factor A is defined as the ratio between the variance of the nonreverberant portion of a white noise signal after summation of the microphone signals (signal d' in Fig. 1) and the sum of the variances of the two individual microphone signals [cf. Kompis and Dillier (2001) for a detailed discussion]. For perfect alignment, i.e., if there is no delay between the nonreverberant part of the target at the two microphones, A is 4. For a head-sized spacing between microphones and a sampling rate of 10 240 Hz, A drops to 2 (no alignment) for azimuths of approximately 8° and more. The alignment factor can be directly measured in anechoic (real

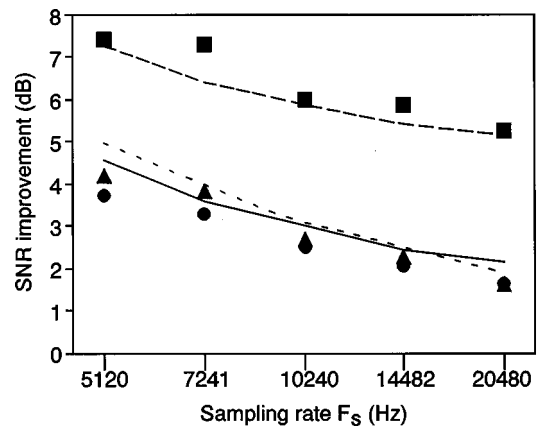


FIG. 13. Influence of the sampling rate. See Fig. 2 for a legend of the symbols used.

or simulated) environments. For the given setting, the alignment factor was found to be 4 at an azimuth α_s of 0° , 3.5 at $\alpha_s = 3^\circ$, 3 at $\alpha_s = 5^\circ$, 2.5 at $\alpha_s = 6^\circ$, and 2 at $\alpha_s = 8^\circ$.

Figure 6 shows the comparison between predictions and experimental results. The values are in reasonable agreement, i.e., within 0.5 dB when taking either one microphone signal as a reference. For $A = 2$ and $A = 2.5$, the agreement between predicted and measured SNR improvement versus the sum signal differ by 0.88 and 1.15 dB, respectively. The reason for this difference is not completely clear, but most probably a result of the relatively simple model of the direct and reverberant signal parts used to predict the SNR improvement (Kompis and Dillier, 2001).

Figure 7 shows the dependence of the SNR improvement as a function of the distance l_s between listener and the target sound source. Again, the majority of all measured values lie within 0.5 dB of the predictions and display the same tendencies (i.e., SNR improvements decreasing with the distance when taking the microphone signals as a reference, but

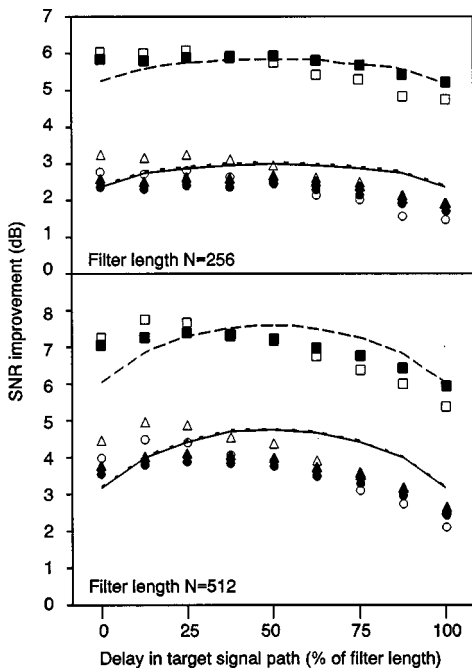


FIG. 12. Influence of the delay in the target signal path. See Fig. 2 for a legend of the symbols used.

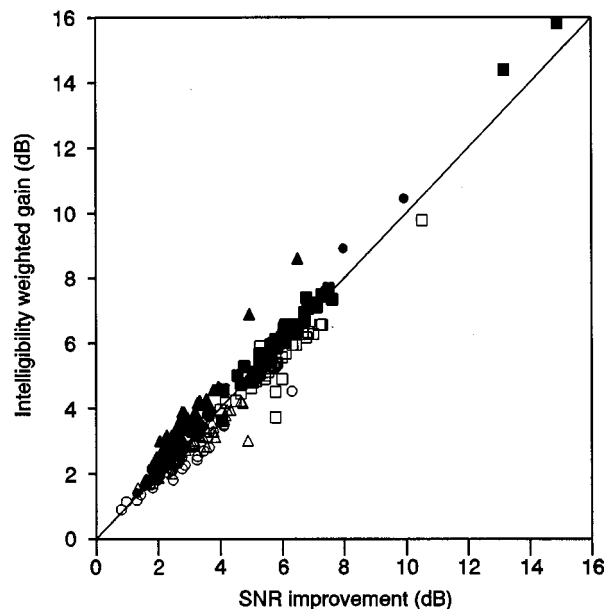


FIG. 14. SNR improvement vs Intelligibility-weighted gain for the experiments in real and simulated environments. See Fig. 2 for a legend of the symbols used.

TABLE III. SNR Improvement at central setting.

	Improvement vs microphone with better SNR (dB)	Improvement vs microphone with poorer SNR (dB)	Improvement vs sum of microphone signals (dB)
Model prediction	3.03	5.85	2.99
Experiment in real room	2.97	5.77	2.52
Experiment in simulated room	2.69	5.97	2.50

increasing when taking the sum signal as a reference). For the given range of distances between 0.25 and 1.75 m, SNR improvements change on the order of magnitude of 1 dB.

Figure 8 shows the dependence of the SNR improvement as a function of the index of directionality of the target signal source γ_s . To obtain the different values for γ_s between 0 and 5, exactly the same procedures were used as for the noise source in Sec. III C. Again, there is a reasonable agreement between prediction and measurement for most data points, with the greatest differences lying toward small γ_s and SNR improvements versus the sum of the microphone signals. For the given range of values $\gamma_s=0-5$, SNR improvements change on the order of magnitude of 1 dB.

D. Room size and reverberation time

The two acoustical parameters of the room considered in the theoretical analysis of the performance of the adaptive beamformer are volume V of the room and reverberation time T_r . Reverberation time is the time required for a reverberant signal to decay by 60 dB. To vary these two parameters independently, experiments were performed predominantly in simulated rooms. Apart from the central setting, only one experiment was performed in a real, anechoic environment.

Figure 9 shows the dependence of the SNR improvement as a function of reverberation time. SNR improvement increases rapidly at short reverberation times. Theoretical predictions and results from the experiments are in reasonable agreement for reverberation times of approximately 0.2 s and above. For shorter reverberation times, the predictions systematically underestimate SNR improvements by up to 2.28 dB at $T_r=0.1$ s. At $T_r=0$ s (anechoic environment) the prediction cannot be calculated, as one of the underlying assumptions, the existence of a reverberant signal portion, is violated. The direct-to-reverberant ratio of the noise source is approximately 5.7 dB at $T_r=0.1$ s, 2.7 dB at $T_r=0.2$ s, and 1.0 dB at $T_r=0.3$ s.

Figure 10 shows SNR improvement by the adaptive beamformer as a function of room size. For these experiments, rooms with volumes of 20–70 m³, in steps of 10 m³ were simulated. The reverberation time T_r of all these rooms was 0.42 s. To keep T_r constant, the absorption coefficients of the simulated rooms were higher for the larger rooms. Note that for the same absorption coefficients for all rooms, reverberation time would have increased with room size, as everyday experience suggests. As the direct-to-reverberant ratio increases with room size (−2.8 dB at $V=20$ m³, +2.7

dB at $V=70$ m³), SNR improvement, especially when compared to the microphone signal with the lower signal-to-noise ratio, increases by approximately 2 dB.

E. Design parameters of the adaptive beamformer

In the theoretical analysis (Kompis and Dillier, 2001), the influence of three design parameters of the adaptive beamformer is considered: the number of filter coefficients in the adaptive filter N , the delay in the sum signal path, and the sampling rate F_s of the system. In practical situations, there will be additional design parameters which influence the performance of a given beamformer, such as the adaptation time constant, the resolution of the analog-to-digital converters, and the performance of any target-signal-detection/adaptation inhibition scheme to prevent filter adaptation in the presence of target signal and therefore target signal cancellation. However, in the theoretical analysis and as a consequence in this study, these additional factors are assumed to be ideal, i.e., filter adaptation is perfect and occurred in the presence of the noise signal only, and all implementation issues are considered to be negligible.

Figure 11 shows SNR improvement as a function of the number N of coefficients in the adaptive filter. In the literature in similar noise reduction algorithms filter lengths of up to 40 ms (Peterson *et al.*, 1987) have been reported. At a sampling rate of 10 240 Hz, this corresponds to a range of $N=410$ coefficients. In this study, filter lengths between $N=32$ (3.125 ms) and $N=512$ (50 ms) have been studied. It can be seen that the amount of SNR improvement increases substantially with filter length, especially for values of N of 128 and more. With short filters, e.g., $N=32$ or $N=64$, the adaptive beamformer practically routes the microphone signal with the more favorable SNR to the output, but provides only relatively little (approximately 1 dB) SNR improvement above that. In Fig. 11 this is shown by the SNR improvement versus the microphone with the lower SNR improving by more than 4 dB, but only by just above 1 dB when compared to the other microphone signal. For long filters ($N=512$), the SNR is improved by more than 4 dB, even when compared to the microphone signal with the *more* favorable SNR. The agreement between experimental results and the predictions is reasonable for the entire range of $N=32-512$, and is poorest for the longest filter.

The theoretical analysis predicts that influence of the delay in the target signal path d' on the amount of noise reduction depends on the length of the adaptive filter N . For this reason, experiments with delays between 0% and 100% of the filter lengths and two different filter lengths ($N=256$ and $N=512$ coefficients) were performed for both the real and the simulated central setting. Figure 12 shows the results. It can be seen that for the shorter filter, a variation of only 0.6 dB in SNR improvement is predicted for the entire range of delays between 0 and 100% of the filter length. For the longer filter, this effect is predicted to be larger (1.59 dB). In both cases, the maximal noise reduction is predicted at a delay of 50% of the filter length. The experimental results show an amount of noise reduction and—to a certain degree—a shape of the curves which are similar to the pre-

dicted ones. However, there is one major difference: The maximal noise reduction is reached at delays between 12.5% and 25% of the filter length and not at 50%, as predicted. This holds for both the real and the simulated environment and for both filter lengths. For the shorter filter, there is a second, only slightly smaller maximum at a delay of 0% in both environments. In this respect, the theoretical prediction clearly fails. The reasons for and implications of this failure will be discussed in Sec. IV E.

The last design parameter to be considered is the sampling rate F_s in Fig. 13. In real applications, the range of possible values is small, as sampling rates below approximately 7000 Hz will reduce speech recognition unacceptably, and the computational load rises rapidly with higher sampling rates. For the range of $F_s = 5120$ – $20\,480$ Hz, the SNR improvement drops on the order of magnitude of 2 dB. This effect can be explained by the effectively shorter filter (12.5 ms at $F_s = 20\,480$ Hz, compared to 50 ms at $F_s = 5120$ Hz) for the same number of coefficients $N = 256$, which was kept constant.

F. SNR improvement and intelligibility-weighted gain

Figure 14 shows the comparison between SNR improvement (as shown in Figs. 3–13) and intelligibility-weighted gain G_i (Greenberg *et al.*, 1993) for all experimental results which were compared to the theoretical predictions. Although differences up to 2.11 dB do exist, for the majority of all data points SNR improvement and intelligibility-weighted gain G_i are within 0.5 dB. On the average, SNRs are slightly higher than G_i for experiments in real environment (average difference +0.37 dB), while SNRs are slightly lower for the experiments in simulated environments (average difference –0.34 dB).

IV. DISCUSSION

A. Agreement between predictions and measurements

Agreement between experimental results and predictions appear to be reasonable for low direct-to-reverberant ratios of the noise signal $P_{d/r}$, but considerably poorer for high direct-to-reverberant ratios (cf. Figs. 4 and 9). When the experimental results are compared for all 88 experiments with a $P_{d/r} < +3$ dB, an average difference of –0.23 dB and a standard deviation of 0.54 dB can be observed. For the 32 experiments in real rooms, the mean difference is –0.21 dB (std. dev. 0.59 dB) and for the 56 experiments in simulated rooms it is –0.25 dB (std. dev. 0.51 dB). As to the 4 experiments with a $P_{d/r}$ above +3 dB, one comparison with the predicted values is not possible, as the predictions fail at infinite $P_{d/r}$ (anechoic environment, Fig. 9), and for the other 3 cases differences up to 5.34 dB (Fig. 4) can be observed. From the assumptions of the underlying theoretical analysis (Kompis and Dillier, 2001), it can be expected that agreement between experimental results and predictions is reasonable for low direct-to-reverberant ratios of the noise signal $P_{d/r}$, but poor for high direct-to-reverberant ratios. From the results shown in Figs. 4 and 9 it can be concluded that the prediction is reasonable for situations with direct-to-reverberant ratios of the noise source of up to approximately

+3 dB, while noise suppression is underestimated for higher $P_{d/r}$. In contrast, the influence of direct-to-reverberant ratio of the *target* signal source appears to be small.

If $P_{d/r}$ is less than +3 dB, predictions give, on average, a slightly (0.23 dB) higher noise suppression than the experimental results. As the delay in the target-signal path (between d' and d in Fig. 1) is kept at a suboptimal 50% of the filter length (cf. Fig. 12) for the majority of the experiments, it can be expected that experimental results are slightly poorer than the predictions. The standard deviation of the differences between predicted and measured values of approximately 0.5 dB is comparable to the small variations in results, if, e.g., the entire experimental apparatus is shifted by a few centimeters in any direction, as verified by informal tests (Kompis and Dillier, 1993). As seen in Table III, and confirmed by the data presented in Figs. 3–13, results of the experiments in real and simulated rooms are in reasonable agreement, thus supporting the assumption that the chosen room-simulation algorithm (Kompis and Dillier, 1993) is suitable for these experiments involving the adaptive beamformer. One difference between the results of the experiments in real and simulated environments is the tendency to overestimate intelligibility-weighted gain G_i by using SNR improvements for real rooms, and underestimate G_i for simulated environments. This relatively small difference can be attributed to the small differences in the spectra of the simulated and recorded signals.

B. Influence of the noise signal source

From the three parameters defining the noise source, the azimuth has the smallest effect on the amount of noise reduction of the adaptive beamformer. Experimental results and predictions are in reasonable agreement.

Noise reduction is greatly increased with smaller distances between noise source and listener (Fig. 4). The agreement between experimental results and predicted noise reduction is reasonable for distances of 0.75 m or more, but poor for smaller distances. From the assumptions used to derive the predictions (Kompis and Dillier, 2001) it is known that the direct-to-reverberant ratio of the noise signal may not become too large for the predictions to remain valid. The estimated direct-to-reverberant ratio is 2.0 dB at 75 cm and 5.5 dB at 50 cm. According to the presented data, the transition between reasonable prediction and substantial underestimation of the SNR improvement takes place in this range. Although this does limit the usefulness of the prediction method in environments with no or very little reverberation, it is not a serious limitation for most normal rooms with realistic amounts of reverberation. To reach a direct-to-reverberant ratio of +3 dB or more in the room used for the central setting, an omnidirectional noise source must be less than 36 cm away from the listener.

For the investigated range of the index of directionality of the noise source ($\gamma_n = 1$ – 5), noise reduction changes only moderately (order of magnitude 1–2 dB), depending on the reference signal (left microphone, right microphone, or sum of microphone signals) to which SNR improvement is compared.

C. Influence of the target signal source

The influence of the target signal source on the performance of the adaptive beamformer is small. For the entire range of the alignment factor $A=2$ to $A=4$, the measured and predicted SNR improvement changes by less than 1 dB. SNR improvements differ by the same order of magnitude for the range of values considered for the distance to the signal sound source ($l_s=0.25-1.75$ m) as well as the index of directionality ($\gamma_s=0$ to 5).

D. Influence of room size and reverberation

While room size has only a limited effect on the performance of the adaptive beamformer at a fixed reverberation time (Fig. 10), noise reduction drops rapidly with increasing reverberation times T_r (Fig. 9). This phenomenon has been reported previously by several researchers (Peterson *et al.*, 1987; Greenberg and Zurek, 1992; Dillier *et al.*, 1993; van Hoesel and Clark, 1995).

Experimental results and predictions are in reasonable agreement for the range of room sizes considered in this study and for reverberation times of 0.2 s and more, i.e., corresponding to direct-to-reverberant ratios $P_{d/r}$ of the noise source of +2.7 dB or less. As noted earlier, predictions systematically underestimate the noise reduction for lower T_r and—consequently—higher $P_{d/r}$.

E. Influence of the design parameters of the adaptive beamformer

From the three design parameters considered, the sampling rate (Fig. 13) has the smallest range of reasonable values and at the same time a relatively small impact on the performance. The length of the adaptive filter significantly influences the SNR improvement of the adaptive beamformer, as has been noted by several researchers (Peterson *et al.*, 1987; Peterson *et al.*, 1990; Greenberg and Zurek, 1992; Dillier *et al.*, 1993). From our data, we conclude that short filters (e.g., $N=32$) improve SNR to only little above the SNR of the microphone with the more favorable SNR. Only a longer filter in the range of 128–512 coefficients provides substantial additional gains in SNR of 2–4 dB.

The influence of the amount of delay (Fig. 12) is clearly not predicted correctly. For both filter lengths and in both the real and the simulated environment, optimal performance of the beamformer is reached at considerably shorter delays than the predicted 50% of the length of the adaptive filter. This may also explain why in Fig. 11 the agreement between prediction and experimental result is poorest for the longest filter, where the influence of the delay is largest. The reason for the shorter optimal delay is not completely understood. Preliminary results from a small separate investigation suggest a loose relationship between the direct-to-reverberant ratio $P_{d/r}$ of the noise signal and the optimal delay: for small $P_{d/r}$, the optimum seems to be close to the predicted 50%, whereas for greater $P_{d/r}$, e.g., above 0 dB, the optimum tends to be often between 12.5% and 25%.

F. Applicability of the results for hearing aid applications

The presented experiments involve several simplifications, which are not necessarily met in real-life situations encountered by potential future users of an adaptive beamformer. These simplifications, which were made necessary by the assumptions on which the theoretical predictions are based, include: (1) a completely adapted filter, (2) filter adaptation in the absence of the target signal, (3) white noise emitted by both the noise and the target signal source, (4) no movement of either listener or either sound source, and (5) the presence of a single noise source only. Because of the usually fast adaptation time constants [order of magnitude: below 0.1 s (Dillier *et al.*, 1993)] and the availability of several target-signal-detection/adaptation-inhibition schemes (Van Compernelle, 1990; Greenberg and Zurek, 1992; van Hoesel and Clark, 1995; Kompis *et al.*, 1997) assumptions (1) and (2) are likely to be reasonably approached in real-life situations. Acoustic signals in relevant everyday situations will probably be composed of predominately low frequency signals such as speech and traffic noise rather than white noise, as assumed here. However, many implementations of adaptive beamformers use pre-emphasis filters just after the microphones, which prewhiten the spectra of these signals. Therefore, the spectra of probable real-life acoustic signals will at least approach that of white noise to a certain degree. SNR improvements appear to be reasonable estimates for the expected improvement in intelligibility in a number of situations as shown by the data in Fig. 14 and confirmed by tests using a portable real-time realization of the adaptive beamformer (Kompis *et al.*, 1999).

In every-day situations, a certain amount of relative movement between the listener and sound sources must be expected. It is difficult to estimate the influence of such movements. However, due to the usually short adaptation time constants this influence may be small. As to the presence of multiple noise sources, a limited number of experiments have already been reported (Peterson *et al.*, 1990). A substantial drop in performance can be expected if the spectra and levels of the sound sources are similar (Greenberg and Zurek, 1992).

V. SUMMARY AND CONCLUSIONS

A method to predict the amount of noise reduction which can be achieved using a two-microphone adaptive beamforming noise reduction system for hearing aids (Kompis and Dillier, 2001) was verified experimentally. 92 experiments were performed in real and simulated environments and the results were compared with the predictions. It was shown that predictions and experimental results agree reasonably, if the direct-to-reverberant ratio $P_{d/r}$ of the noise source is smaller than approximately +3 dB. For higher $P_{d/r}$, the predictions systematically underestimate the performance of the adaptive beamformer. The parameters with the greatest influence on the performance of the adaptive beamformer were found to be the direct-to-reverberant ratio of the noise source, the reverberation time of the acoustic environment, and the length of the adaptive filter.

ACKNOWLEDGMENTS

This work was supported by the Swiss National Research Foundation, Grant Nos. 4018-10864 and 3238-56352.99, and Ascom Tech Ltd.

- Allen J. B., and Beakley, D. A. (1979). "Image method for efficiently simulating small-room acoustics," *J. Acoust. Soc. Am.* **65**, 943–950.
- ANSI (1969). ANSI S3.5-1969, "American National Standard Methods for the Calculation of the Articulation Index" (American National Standards Institute, New York).
- Bellanger, M. G. (1987). *Adaptive Digital Filters and Signal Analysis* (Marcel Dekker, New York).
- DeBrunner, V. E., and McKinney, E. D. (1995). "Directional adaptive least mean square acoustic array for hearing aid enhancement," *J. Acoust. Soc. Am.* **98**, 437–444.
- Dillier, N., Fröhlich, T., Kompis, M., Bögli, H., and Lai, W. L. (1993). "Digital signal processing (DSP) applications for multiband loudness correction digital hearing aids and cochlear implants," *J. Rehabil. Res. Dev.* **24**, 95–109.
- Greenberg, J. E., and Zurek, P. M. (1992). "Evaluation of an adaptive beamforming method for hearing aids," *J. Acoust. Soc. Am.* **91**, 1662–1676.
- Greenberg, J. E., Peterson, P. M., and Zurek, P. M. (1993). "Intelligibility-weighted measures of speech-to-interference ratio and speech system performance," *J. Acoust. Soc. Am.* **94**, 3009–3010.
- Griffiths, L. J., and Jim, C. W. (1982). "An alternative approach to linearly constrained adaptive beamforming," *IEEE Trans. Antennas Propag.* **30**, 27–34.
- Hamacher, V., Mauer, G., and Döring, W. H. (1996). "Untersuchung eines adaptiven Beamforming-Systems zur Störunterdrückung für Hörgeschädigte," Proceedings of the 22nd Deutsche Jahrestagung für Akustik (DAGA), Bonn, Germany (unpublished).
- Kiefer, J. *et al.* (1996). "Speech understanding in quiet and in noise with the CIS speech coding strategy (MED-EL Combi-40) compared to the multipeak and spectral peak strategies (Nucleus)," *ORL* **58**, 127–135.
- Kochkin, S. (1993). "Consumer satisfaction with hearing instruments in the United States," *The Marketing Edge*, Special issue June 1993, 1–4.
- Kompis, M., and Dillier, N. (1993). "Simulating transfer functions in a reverberant room including source directivity and head shadow effects," *J. Acoust. Soc. Am.* **93**, 2779–2787.
- Kompis, M., and Dillier, N. (2001). "Performance of a two-microphone adaptive beamforming noise reduction scheme for hearing aids. II. Experimental verification of the predictions," *J. Acoust. Soc. Am.* **109**, 1123–1133.
- Kompis, M., Dillier, N., Francois, J., Tinembart, J., and Häusler, R. (1997). "New target-signal-detection schemes for multi-microphone noise-reduction systems for hearing aids," *Proc. Annu. Int. Conf. IEEE Eng. Biol. Soc.* **19**, 1990–1993.
- Kompis, M., Feuz, P., François, J., and Tinembart, J. (1999). "Multi-microphone digital-signal-processing system for research into noise reduction for hearing aids," *Innovation Technol. Biol. Med.* **20**, 201–206.
- Kuhn, G. F. (1977). "Model for the interaural time difference for the azimuthal plane," *J. Acoust. Soc. Am.* **62**, 157–167.
- Peterson, P. M., Durlach, N. I., Rabinowitz, W. M., and Zurek, P. M. (1987). "Multimicrophone adaptive beamforming for interference reduction in hearing aids," *J. Rehabil. Res. Dev.* **24**, 103–110.
- Peterson, P. M., Wie, S. M., Rabinowitz, W. M., and Zurek, P. M. (1990). "Robustness of an adaptive beamforming method for hearing aids," *Acta Oto-Laryngol., Suppl.* **469**, 85–90.
- Van Compernelle, D. (1990). "Hearing aids using binaural processing principles," *Acta Oto-Laryngol., Suppl.* **469**, 76–84.
- van Hoesel, R. J. M., and Clark, G. M. (1995). "Evaluation of a portable two-microphone adaptive beamforming speech processor with cochlear implant patients," *J. Acoust. Soc. Am.* **97**, 2498–2503.
- Widrow, B., Glover, J. R., McColl, J. M., Kaunitz, J., Williams, C. S., Hearn, R. H., Zeidler, J. R., Dong, J. R., and Goodlin, R. C. (1975). "Adaptive noise cancelling: Principles and applications," *Proc. IEEE* **63**, 1692–1716.

The role of the mora in the timing of spontaneous Japanese speech

Natasha Warner^{a)}

Max Planck Institute for Psycholinguistics, Wundtlaan 1, PB 310, NL-6500 AH Nijmegen,
The Netherlands and Department of Linguistics, University of Arizona, PO Box 210028, Tucson,
Arizona 85721-0028

Takayuki Arai

Department of Electrical and Electronics Engineering, Sophia University, 7-1 Kioi-cho, Chiyoda-ku,
Tokyo 102-8554, Japan

(Received 15 August 1999; accepted for publication 28 November 2000)

This study investigates whether the mora is used in controlling timing in Japanese speech, or is instead a structural unit in the language not involved in timing. Unlike most previous studies of mora-timing in Japanese, this article investigates timing in spontaneous speech. Predictability of word duration from number of moras is found to be much weaker than in careful speech. Furthermore, the number of moras predicts word duration only slightly better than number of segments. Syllable structure also has a significant effect on word duration. Finally, comparison of the predictability of whole words and arbitrarily truncated words shows better predictability for truncated words, which would not be possible if the truncated portion were compensating for remaining moras. The results support an accumulative model of variance with a final lengthening effect, and do not indicate the presence of any compensation related to mora-timing. It is suggested that the rhythm of Japanese derives from several factors about the structure of the language, not from durational compensation. © 2001 Acoustical Society of America.

[DOI: 10.1121/1.1344156]

PACS numbers: 43.70.Fq, 43.70.Bk [AL]

I. INTRODUCTION

Japanese is often called mora-timed, in opposition to stress-timed languages like English and syllable-timed languages like French. This division is usually taken to mean that moras are approximately regularly timed in Japanese, such that each mora is of similar duration. (In the same way, stresses are said to be nearly regular in English, and syllables in French.) One commonly argued position has been that if variability in durations of different segments interferes with this regularity, speakers compensate to make the durations of the relevant unit more regular than they would otherwise be. However, another possibility is that factors in the phonology of the language cause the relevant unit to be more regularly timed than other units, but that there is no control mechanism to create regular timing of that unit. In this article, we present new analyses of Japanese speech timing which support the latter hypothesis. We also extend the investigation to spontaneous speech, which has rarely been used in past studies.

There are at least two types of variation which would have to be compensated for to make mora durations equal in Japanese. First, there are inherent differences in segmental durations: high vowels are shorter than low vowels, [r] is very short while [s] is relatively long, etc. Second, several types of moras in Japanese do not consist of a consonant-vowel string. Long vowels have two moras, so that /tookyo/ “Tokyo” has the same number of moras as /tokonoma/ “alcove.” Geminate obstruents and the mora nasal (/N/) con-

tribute a mora: /katta/ “bought,” /kaNda/ (place name), and /karita/ “borrowed” each have three moras. High vowels in a voiceless environment can be devoiced or deleted in Japanese, but their mora remains, so that /kita/ [k̟ita] “North” has two moras. A word with any of these special mora types is unlikely to have the same duration as a word with only CV moras.

A. Mora-timing as durational compensation

Early experimental work on Japanese duration claimed that speakers adjust the duration of the segments within a mora to make mora durations more similar to each other than they would be based on inherent variability. We will call this the “tendency toward isochrony” version of the mora-timing hypothesis. Under this theory, if one segment of a CV mora is shorter than average (e.g., [r]), or longer than average (e.g., [s]), the other segment of that mora will be lengthened, or shortened, in order to maintain near-constant mora duration. This compensation might not be complete. This theory also predicts that non-CV moras such as the mora nasal or the beginning of a geminate obstruent will have duration similar to a CV mora. Some form of this position is supported by Han (1962), Homma (1981), Sagisaka and Tohkura (1984), and Sagisaka (1992, 1999), while Beckman (1982) and Hoequist (1983a, b) find contradictory evidence. For a full review of the literature on Japanese mora-timing, please see Warner and Arai (2001).

Based on the finding (Port *et al.*, 1980; Sagisaka and Tohkura, 1984) of negative correlations across mora boundaries (in VC strings) as well as within moras (CV strings),

^{a)}Electronic mail: Natasha.Warner@mpi.nl

Port *et al.* (1987) propose an important revision to the concept of mora-timing. They suggest that compensation takes place not only within the mora, but also across several moras, and that compensation serves not to normalize the duration of individual moras, but rather to make the duration of larger units (perhaps the word) predictable from the number of moras in them. This leads to different predictions: under the tendency toward isochrony theory, all moras are expected to have nearly equal duration. However, Port *et al.* (1987) propose that if a segment, for example the consonant of a word-medial CV mora, is shorter than average, nearby segments both in the same and other moras will be lengthened to compensate for it. Thus if one mora is shorter than average, nearby moras would be longer than average to compensate for it, making mora durations less similar to each other, not more similar. Port *et al.* (1987) refer to this relationship as “anti-compensation.”

This modification to the theory focuses attention on the duration of larger units, such as words. However, this theory does not claim that all moras within a word compensate for each other, or that the domain of compensation is exactly the word. Evidence adduced for this version of mora-timing emphasizes the relationship between duration of entire words (as a convenient unit larger than the mora) and the number of moras in them. Several studies demonstrate strong positive correlations between word duration and the number of moras in a word in Japanese (Port *et al.*, 1987; Bradlow *et al.*, 1995; Sato, 1995; Kondo, 1999), although Otake (1989) shows similar effects for Spanish (syllable-timed) and English (stress-timed). One difficulty is that it is not clear how strong these correlations must be in order to demonstrate mora-timing. Since all moras have segmental content, it is not surprising that this correlation is strong. A strong correlation between word duration and number of moras does not, of itself, demonstrate compensation. [See Warner and Arai (2001) for further details.]

B. The mora as a nontemporal unit and accumulation of variability

Alternatively, the mora could play a structural role in Japanese as an abstract unit which does not control timing. Factors in the phonology of Japanese could result in the mora being more regularly timed than the syllable or the foot in Japanese speech, without any compensation to bring moras closer to regular timing than they inherently would be. Factors which would have this effect include the lack of an effect of pitch accent on duration, the lack of reduction of unaccented vowels, the prevalence of CV syllables, and the lack of nondurational cues to the geminate/singleton consonant and long/short vowel distinctions. In all of these points, Japanese differs strongly from stress-timed English. It is clear that the mora exists as a phonological and psycholinguistic unit in Japanese (see Warner and Arai, 2001), but its role need not involve temporal compensation, even if the relatively regular timing of the mora brought about by phonological factors gives Japanese a distinctive rhythm.

Dauer (1983, 1987) offers several phonological correlates of stress- and syllable-timing, and proposes that these factors combine to create a rhythm in which stresses or syl-

lables seem to be the prominent feature of timing in a language, without any temporal compensation. She does not discuss mora-timing, but Otake (1990) and Beckman (1992) extend her proposals to Japanese. They emphasize the role of statistical predominance of CV syllables and of the pitch accent system, respectively, in creating mora-rhythm. For example, Dauer points out that stress-timed languages allow fewer syllables within a stress-foot than syllable-timed languages do. Beckman (1992) points out that Japanese even allows entire phrases with no pitch accent at all, thus going further than the syllable-timed languages in this respect. She also points out the importance of the lack of an effect of pitch accent on duration. Work by Ramus *et al.* (1999) is also relevant in pointing out acoustic correlates of rhythm class other than regular timing.

The phonological length distinctions may also contribute to the impression of regularly timed moras in Japanese. Duration is effectively the only difference between Japanese long and short vowels (e.g., /kooki/ “school flag” versus /koki/ “exhalation”), unlike English (e.g., “beet” versus “bit”). Thus, this duration difference is very large in Japanese. The same applies to geminate and singleton obstruents in Japanese (e.g., /katta/ “bought” versus /kata/ “form”), where closure duration is nearly the only difference. The large durational difference between such phonologically short and long segments does not indicate any compensation, but it makes moras more regular than in a language with smaller durational differences, such as English.

If “mora-timing” reflects phonological facts about the language, and speakers do not employ temporal compensation to regularize the timing of moras, then the inherent variation in segment durations, and thus mora durations, would remain. Without compensation, each mora in a larger unit (such as a word) would contribute its variability to the variability of the whole. That is, the hypothesis that the mora is a structural unit which only indirectly affects timing (without compensation) predicts that the variance of individual smaller units, in this case moras, accumulates in larger units, instead of canceling out. One prediction of this hypothesis is that the duration of words containing many moras will be more variable than the duration of words containing fewer moras, since longer words contain more sources of variability (Ohala, 1975). This prediction is the basis of several analyses we present later to test for compensation versus only a structural role for the mora.

C. Goals of the current study

Nearly all of the past work on Japanese mora-timing has used very careful speech. [Exceptions are work by Sagisaka and his colleagues (Sagisaka, 1992, 1999; Sagisaka and Tohkura, 1984), as well as by Campbell (1992) and Arai and Greenberg (1997), of which the last two do not support mora-timing.] While it is desirable to study timing under controlled conditions, it is also desirable to confirm findings from controlled speech under natural conditions if this can be done in a reliable way. Because so much work has been done on timing in controlled Japanese speech, extension to natural materials should now be possible.

Even if compensatory mora-timing exists in careful speech, speakers may not be able to maintain it in the face of the many other effects on duration present in connected speech, such as final lengthening, focus (on words other than the target item), etc. These factors might have a legitimate influence on any mora-timing, rather than simply adding noise. Since target words in the focus position of predictable frame sentences are not what speakers normally produce or listeners normally perceive, it is important to determine whether patterns which exist in that environment are also present in speech which is more typical of daily life. This is particularly important for mora-timing because Japanese listeners use the mora to help locate word boundaries (Otake *et al.*, 1993, 1996; Cutler and Otake, 1994), which must be done for connected speech. It is important to know whether it is the temporal role of the mora or something else that leads to its usefulness for segmentation. If mora-timing compensation does not exist in connected speech, then mora-timing could not be the source of the mora's usefulness for segmentation.

Of course, in studying connected speech, one must control for effects which might mask the effect under investigation, such as overall speech rate variation. We control for interspeaker rate variation by making only within-subjects comparisons. Our analyses also control for intraspeaker overall rate variation within the monologue, since nearly all of our analyses¹ compare different measurements from the same words. This also controls for any factors which affect the duration of a specific word, such as syntactic position in the sentence, length of the sentence, part of speech, focus, or slowing at a high level prosodic boundary. As for factors which affect units smaller than the word, we test for word-final lengthening, and other effects on sub-word-level units (such as the mora) are precisely the subject of investigation. We also exercised considerable caution in the selection of the words to test (as described later) to avoid including words which might disrupt compensation effects for known reasons. Finally, because any data on natural speech is expected to be more noisy than similar data on careful speech, null effects in natural speech would not argue strongly for any conclusion, but significant effects should not be discounted.

One goal of this study is to test past findings from careful speech in natural speech. A second goal of the study is to present new tests, particularly the analyses of truncated words, for which the compensation hypothesis makes clearer predictions than a strong correlation, since it is not clear how strong a correlation is necessary to demonstrate compensation. Some type of compensatory mora-timing has been widely accepted in the recent literature (Han, 1994; Bradlow *et al.*, 1995; Sato, 1995; Itô and Mester, 1995, p. 834; Tsujimura, 1996, p. 66; Kubozono, 1999; Kondo, 1999; Minagawa-Kawai, 1999), so these new tests are warranted. Furthermore, previous evidence for a structural, nontemporal role for the mora has been limited to the inconsistency of evidence for compensation (Beckman, 1992) or to the finding of supposed mora-timing effects in non-mora-timed languages (Otake, 1989). The truncation analyses presented in this article, however, make clear and contradictory predic-

tions for structural versus temporal, compensatory, function of the mora, and thus avoid the limitations of past evidence for both hypotheses.

Specific predictions will be discussed for each test below. In general, we predict that timing relationships will be more variable in spontaneous speech than in the careful speech of previous studies. We also predict that analyses of duration will show evidence of each mora contributing variance to the variance of the whole, rather than of compensation among moras, supporting the structural rather than temporal role of the mora.

II. GENERAL METHODS

A. The corpus

The materials for this study consist of 50 s of spontaneous speech, collected over the telephone, from each of 11 volunteer native speakers of Japanese [a subset of the larger corpus described by Muthusamy *et al.* (1992) and Arai and Greenberg (1997)]. Most speakers were living in the United States when the data was recorded. A recorded voice (in Japanese) asked speakers to talk on any subject they wished for approximately a minute. Speakers who read a text aloud instead of speaking spontaneously were excluded. For the current study, five native speakers of Japanese (three with phonetics training, including the second author) evaluated the corpus used by Arai and Greenberg (1997) for foreign accents. (Although the speakers stated that Japanese was their native language, some had been living in the United States for many years.) Only speakers who all five evaluators judged as having no foreign accent were included. Speakers of nonstandard dialects were not excluded, since mora-timing is not claimed to differ in most nonstandard dialects. One evaluator, an expert in phonetics and Japanese dialectology, found that only 3 of the remaining 11 speakers spoke nonstandard dialects (speakers A, E, and J).²

The corpus was labeled at the mora level by the second author, using standard criteria for the boundaries of segments, and based on spectrograms, waveforms, and listening. Filled and unfilled pauses and nonspeech noises were also labeled. In the case of word-initial voiceless stops, if the voiceless stop was immediately preceded by the final segment of the preceding word, with no pause, the intervening silence was included as the closure of the voiceless stop. However, if an initial voiceless stop followed a pause, the silence was included in the pause and the duration of the stop was counted from the burst. For vowels followed by a voiceless segment, the end of voicing was counted as the end of the vowel. Periods of creaky voicing, such as at the beginning of a word-initial vowel or end of a final one, were included in the vowel. For a vowel followed by a voiced obstruent, the boundary was placed at the sudden drop in amplitude and cessation of formants. For vowel-nasal or nasal-vowel transitions, the sudden change in formant frequencies and amplitudes was identified as the boundary. The onset of /r/ (the only liquid in Japanese, realized usually as [r], but sometimes as [l] or [d]) was identified as the beginning of low amplitude voicing with a gap in the formant structure. In vowel-glide sequences, the beginning of a re-

TABLE I. Examples of included types of items, with the environment in which they were produced. The exemplified word is shown in bold. Transcriptions are phonemic.

1a. atasi-wa daigaku saNneN pause de pause I-topic college 3rd. year nihoN-no minami-no pause Japan-gen. South-gen. gakoo-made-wa nizikaN kakari pause school-to-topic 2.hours take	“I’m a third year college (student)” “of the South of Japan” “It takes 2 hours to get to school”
1b. kazaNbai-ga hurimasu pause volcanic.ash-subj. fall-polite-non-past toku-ni zyanru-wa toimaseN especially genre-topic care-polite-non-past-negative tookyoo-kara kimasita Tokyo-from come-polite-past	“volcanic ash falls” “I don’t really care about the genre” “I came from Tokyo”
1c. pause maa tomokaku pause well anyway sorekara pause tikaku-ni and.then nearby	“well, anyway” “and then...nearby”
1d. tookyoo-ni umarete tookyoo-ni sodatte Tokyo-in born-and Tokyo-in grow.up-and amerikaziN bakari-kana-to omottara Americans only-wonder-quot. think-and	“(was) born and raised in Tokyo and” “I thought it was just Americans, and”
1e. daitokai pause no seekatu-ni nareteru big.city gen. lifestyle-to used.to	“(I’m) used to big city life”

gion of reduced amplitude (or in the absence of such, the beginning of change in the formant frequencies) was identified as the beginning of the glide. For vowel–vowel sequences, the point of most rapid change in the formant frequencies or F_0 was chosen as the boundary. Listening, in combination with spectrographic cues, played a greater role in the identification of vowel–vowel boundaries than for other transitions. The speech was labeled at a phonetic level, reflecting the phenomena typical of fast, spontaneous speech.

In order to confirm the accuracy of this procedure, the first author independently relabeled all boundaries used in any analysis below for a subset of the data, namely all words with three moras (including particle, if any was produced with the word). This resulted in a total of 364 boundaries from 108 words. The time points of the boundaries placed by the two authors were subtracted, and the absolute values of these differences analyzed. The average error in boundary placement over these 364 measurements was 7.58 ms. The error for most boundaries was quite small: the median error was 4 ms, and 30.5% of boundaries had errors of less than 3.0 ms. These errors are very small relative to the average duration of a mora (136.36 ms for the words which were relabeled). Since most results in this article are based on the correlation of the duration of some larger string with the number of moras in it, these measurement errors are unlikely to affect the strength of the correlations much. Furthermore, there is no significant difference in the size of the measurement errors at the various points which were labeled in the words (beginning and end of the word, beginning of the particle, if any, and end of the first and second moras) [$F(4,359) = 1.35, p > 0.05$]. Therefore, measurement error is not likely to have any systematic effect on the results.

B. Word boundaries

Determining what constitutes a word in Japanese is not trivial. Japanese orthography does not mark word boundaries, and there are many tightly bound syntactic constructions which may often form a single prosodic unit. Japanese also has many grammatical particles, which usually form a prosodic word with the preceding lexical item. It is important to identify word boundaries correctly in order to maximize the chance of detecting any compensation effect. If compensation takes place across mora boundaries but stops at the word boundary³ then identifying too small a string as a word might obscure the compensation effect. We included only words for which the boundaries are clear, exemplified in Table I. We included nouns followed by zero, one, or two particles (1a), verbs ending in the polite or nonpolite past or nonpast suffixes or the negative suffix (1b), and adverbs or conjunctions in isolation (1c). We also included verbs ending in the /-te/ suffix (continuative) if not followed by an auxiliary verb, as well as other continuative forms (1d), and particles isolated from the preceding utterance by a pause (1e).

Examples of excluded items appear in Table II. We excluded special constructions which may be grammaticalized (e.g., those with /tame, wake, no hoo, -to yuu/, 2a), nominalized verbs (both /no/ and /koto/ nominalizers, 2b), verbs derived from nouns (2c), anything followed by the copula (2d), and verbs ending in the /-te/ suffix followed by auxiliary verbs (2e). In the case of the copula, for example, there is no way to be sure whether a noun and the copula after it are two different words, or whether the copula is equivalent to an inflection. For all of these constructions, the number of lexical words may not equal the number of prosodic words. We also excluded any form followed by three or more particles or by a very long conjunction (2f), because long strings of

TABLE II. Examples of excluded items. The excluded word and the environment which necessitates its exclusion are shown in bold. Transcriptions are phonemic unless bracketed.

2a. umi-ni tikai tame-ni sea-to near since seekatu-ni nareteru wake desu-ga lifestyle-to used.to reason copula-but inaka-no hoo kara kita country-gen. direction from came boku-no suNderu ryoo-tte yuu-no-wa I-subj living dorm-quot. called-nom.-topic	“since it’s near the sea” “it’s that I’m used to the lifestyle, but” “came from the country” “as for the dorm I’m living in”
2b. syumi-wa piano-o hiku-koto desu hobby-topic piano-obj. play-nom. copula koNsaato-ni iku-no-ga suki desu concert-to go-nom.-subj. like copula	“(my) hobby is playing the piano” “(I) like going to concerts”
2c. saNka suru yoo-ni narimasita participation do case-into became	“it became the case that I participated”
2d. yuume datta -node popular copula-past-because	“because (it) was popular”
2e. rai-to yuu mati-ni suNde imasu Rye-quot called town-in live-TE be	“I’m living in a town called Rye.”
2f. tigai-nado-ni-mo yoru difference-etc.-on-also depend maeoki-o simasita-keredomo introduction-obj. did-but	“it depends on differences and such too” “I did an introduction, but”
2g. nineNkaN imasu-kedo maa 2.year.period be-but well	“I’ve been (here) two years, but, well”
2h. ippuN kudasatte arigat[o] gozaimasu 1.minute give-and thank you	“Thank you for giving me one minute”
2i. umare pause u pause [m]mareta-no-wa born (interrupted twice) born-nom.-topic	“As for where (I) was born”
2j. hoka-no kata-wa mina amekaziN -na-node other-gen. person-topic all American-be-because	“Since everyone else is American” (amekaziN for /amerikaziN/)
2k. pause [ato:] pause yuuhaN-ga owatte-kara after dinner-subj. finish-after	“after...after dinner was over”

particles may form a separate prosodic word. Interjections (2g) and set phrases (2h) were excluded because they may have abnormal durations for pragmatic reasons. Speech errors with self-repairs were excluded (2i), as were fast speech deletions which result in a form with a different number of moras than it would have in careful speech (2j). Furthermore, utterances in which a segment (usually the final vowel) was held unnaturally long, forming a type of filled pause, were excluded (2k).

All cases which could be considered as compounds (e.g., /tenisu-kurabu/ “tennis club”) were treated as single words. This provides a fairer test of the compensation hypothesis, since compensation is more likely to cross a compound boundary than a word boundary. All words with more than seven moras (without particles) were excluded from all analyses. Port *et al.* (1987) tested words with one to seven moras, so this facilitates comparison of results, and also minimizes the possibility of the few words with many moras (e.g., /wasiNtoNdiisii-koogai/ “Washington D.C.-suburb,” 13 moras) unduly influencing the statistical correlations. These exclusions left 28 to 49 words from each of the 11

speakers, and a total of 416 words. All analyses are based on these words or a subset of them.

III. ANALYSES

A. Correlation of word duration with number of moras

One of the main claims of the across-mora compensation proposal is that the duration of some larger unit such as a word is (nearly) predictable from the number of moras in it, and Port *et al.* (1987, experiment 2) showed very strong correlations ($r \geq 0.998$) between the duration of whole words and the number of moras in the word. However, if the mora is not used for temporal compensation, one would still expect a strong correlation between word duration and number of moras, since moras do contribute segmental material.

We calculated this correlation for each speaker in our corpus separately. Port *et al.* (1987) excluded particles from word duration, so we initially also excluded particles [e.g., in /minami-no/ “South-genitive,” the duration of /minami/ (three moras) was used]. The correlations between whole

TABLE III. (a) Correlation coefficients (r) between whole word duration and number of units in the word for each speaker, with moras, syllables, and segments (long vowels as one or two segments) as the unit. Number of words in parentheses. (b) Average word durations by number of each unit. Number of words in parentheses.

(a) Speaker	Moras	Syllables	Segments (VV=1)	Segments (VV=2)
A (34)	0.832	0.595	0.724	0.738
B (42)	0.795	0.598	0.795	0.769
C (31)	0.701	0.596	0.713	0.716
D (39)	0.759	0.567	0.708	0.699
E (49)	0.884	0.729	0.799	0.885
F (46)	0.818	0.669	0.783	0.806
G (31)	0.931	0.746	0.847	0.884
H (32)	0.800	0.812	0.823	0.831
I (28)	0.798	0.554	0.645	0.754
J (48)	0.874	0.819	0.907	0.915
K (36)	0.845	0.651	0.807	0.799

Average word duration (ms)				
(b) No.	Moras	Syllables	Segments (VV=1)	Segments (VV=2)
1	195.85 (10)	206.89 (24)	151.27 (5)	154.89 (1)
2	252.71 (106)	334.35 (199)	214.72 (15)	185.01 (13)
3	369.93 (133)	449.33 (126)	253.62 (35)	246.07 (35)
4	484.41 (120)	518.60 (52)	294.64 (95)	273.60 (79)
5	596.53 (30)	719.63 (11)	389.07 (76)	366.01 (72)
6	649.89 (12)	783.08 (4)	429.73 (91)	425.02 (96)
7	872.13 (5)		522.10 (39)	480.45 (50)
8			545.84 (36)	549.79 (40)
9			657.92 (10)	623.05 (13)
10			657.13 (8)	646.78 (9)
11			773.14 (1)	754.69 (3)
12			741.29 (3)	682.53 (2)
13			883.63 (2)	875.35 (3)

word duration and number of moras in the word, as well as average word durations, are shown in Table III (along with results from Sec. III B). The correlation coefficients vary from $r=0.701$ to $r=0.931$. These correlations are far weaker than those of Port *et al.* (1987). (In that study, word durations were averaged across speakers for each of the 28 utterances before calculating the correlations, minimizing variability. Because ours is a corpus study, one cannot average across speakers' productions of the same utterances, so a direct comparison is not possible.) Although this analysis cannot establish compensation, it does show that predictability of word durations from number of moras is much weaker in spontaneous speech than in careful speech, and that the strength of the relationship between number of moras and word duration varies greatly across speakers.

B. Correlation of word duration with other units

Port *et al.* (1987) point out that the correlation of word duration with number of syllables for their data would be far worse than the correlation with number of moras, and claim this as evidence for mora-timing. We calculated the correlation of word duration with both the number of syllables and the number of segments in the word (without particles), and compared these results to the correlations with number of moras. The compensation hypothesis claims that moras are used to determine word duration, so it predicts a stronger correlation of word duration with number of moras than with any other unit. However, the hypothesis that the mora only

seems to be regularly timed because of phonological, structural factors predicts that the correlations of word duration with number of moras and number of segments will be about equally strong. This is because there is very little variability in how many segments occur within a mora. This hypothesis also predicts that the correlation with number of syllables will be weaker, because of the large durational difference between one- and two-mora syllables discussed earlier.

For this analysis, the palatalized noncoronal consonants /py, by, ky, gy, hy/ were counted as two segments, while the palatalized coronal segments /sy/ [ʃ], /ty/ [tʃ], /zy/ [dʒ] (which undergo assimilation and are phonetically a single segment) were counted as single segments.⁴ Since there is no consensus as to whether long vowels are one or two segments, we calculated the correlations in two ways, with long vowels (e.g., /oo/ in /gakkoo/ "school") counted as one and as two segments. In both cases, sequences of nonidentical vowels (e.g., /ai/ in /ikkai/ "once") and geminate obstruents⁵ were counted as two segments. For the syllable count, /(C)ai/ and /(C)oi/ (e.g., /ai/ in /ikkai/ "once," /oi/ in /sugoi/ "great"), as well as syllables containing a long vowel, the mora nasal, or the beginning of a geminate obstruent, were counted as single syllables. /(C)au/ did not occur, and other nonidentical vowel sequences (e.g., /ia/ in /azia/ "Asia," /oa/ in /huroa/ "floor") were counted as two syllables (Vance, 1987).

The results of these analyses appear in Table III. Correlation with number of syllables is significantly weaker than

with number of moras [$F(1,10)=43.46, p<0.0001$]. The correlation with number of segments is significantly weaker than that with number of moras if long vowels are counted as a single segment [$F(1,10)=6.10, p<0.04$], but the difference is not significant if long vowels are counted as two segments [$F(1,10)=3.08, p>0.10$]. Even if long vowels are counted as single segments, the correlation with number of segments is only weaker than that with number of moras for 7 of the 11 speakers.

This shows that a strong correlation between word duration and the number of some unit is not sufficient evidence for that being a unit of timing normalization for the language. It has never been claimed that Japanese (or any other language we know of) is “segment-timed,” and yet segments are, by one count, statistically equivalent to moras in the strength of their relationship to word duration. If one were to calculate, in some arbitrary language, the correlation of word duration with the number of each potential sub-word-level unit (segments, moras, syllables, feet), one of these would be the best predictor of word duration. Which that is may reflect syllable structure constraints, and does not mean that speakers normalize the duration of words to adjust for variability according to this unit.

C. Particles and the domain of compensation

One important issue for Japanese word duration is grammatical particles, which clearly form part of a prosodic word with the preceding lexical item. Thus, although the genitive particle /no/ in /nihoN-no/ “Japan’s” is not part of the lexical item /nihoN/ “Japan,” it is part of the word for prosodic purposes. If there is compensation, the correlation of duration of some larger unit with number of moras should be strongest if the larger unit is exactly the domain within which compensation occurs. For example, if compensation takes place within the prosodic word /nihoN-no/, but the duration of only the lexical word /nihoN/ is measured, compensation between the final moras of /nihoN/ and the particle /no/ will be disturbed.

Since the proposed across-mora compensation effect is a prosodic process, its domain is more likely to be the prosodic than the lexical word. [Itô and Mester (1995) assume this.] Port *et al.* (1987) do not test the domain of across-mora compensation, but if compensation stops at the boundary of the prosodic word, their theory would predict that the correlation between word duration and number of moras would be stronger when particles are included in the word. (That is, in the string /nihoN-no minami/ “South of Japan,” if there is compensation within /nihoN-no/ and within /minami/ but not between /no/ and /mi/, correlations would be stronger if the duration of /nihoN-no/ is measured than if that of /nihoN/ alone is.) If the domain of compensation is the lexical word (i.e., compensation within /nihoN/ but not between /nihoN/ and /no/), their theory would predict a stronger correlation of number of moras with lexical word duration (particles excluded) than with prosodic word duration (particles included). If there is compensation even across word boundaries (i.e., compensation between /no/ and /mi/ as well as within /nihoN-no/ and /minami/), their theory would predict equally strong correlations whether particles are included in

TABLE IV. (a) Correlations (r) between word duration and number of moras, with particles included and excluded. Only words which were produced with a following particle are included in the analysis. Number of words in parentheses. (b) Average durations for these words, by number of moras. Number of words in parentheses. (Since particles can have more than one mora, number of words in the two columns does not match.)

(a) Speaker (n)	Particles excluded	Particles included
A (21)	0.916	0.785
B (28)	0.818	0.748
C (14)	0.736	0.782
D (23)	0.795	0.618
E (27)	0.924	0.740
F (19)	0.872	0.710
G (16)	0.973	0.936
H (16)	0.872	0.752
I (14)	0.800	0.790
J (30)	0.902	0.853
K (17)	0.901	0.860

(b) No. of moras	Average duration without particles (ms)	Average duration with particles (ms)
1	171.68 (4)	not applicable
2	246.08 (61)	351.69 (3)
3	339.83 (79)	404.12 (54)
4	430.28 (55)	497.79 (72)
5	607.23 (17)	588.79 (57)
6	583.08 (7)	771.88 (22)
7	857.40 (2)	740.96 (11)
8	not applicable	985.13 (4)
9	not applicable	1233.72 (2)

word duration or not, since neither the prosodic nor the lexical word would be the domain of compensation.

However, the hypothesis that there is no mora-based compensation (that each mora simply contributes its variability to the variability of the larger unit, the word) predicts that the correlation between number of moras and whole word duration will be stronger without particles than with them. This is because the particles, as additional moras, contribute additional variability to the variability of whole word duration. Thus, a stronger correlation when particles are excluded than when they are included would favor either the hypothesis that the mora is a nontemporal unit (i.e., no compensation) or the hypothesis that the lexical word is the domain of compensation. Any other outcome would favor the hypothesis that there is compensation within some domain larger than the lexical word.

We calculated the correlation between whole word duration and number of moras in the word, with particles included, for each speaker. Thus, the entire duration of /minami-no/ “South-genitive” (four moras) was used. For this analysis, only words which were produced with a particle were included. (Words such as /daigaku/, /hurimasu/, and /tomokaku/ (1a–c), which were produced with no following particle, were excluded.) We also calculated the correlation between whole word duration and number of moras with particles excluded for these same words. Results appear in Table IV. Of the 11 speakers, 10 (all but speaker C) show a stronger relationship when particles are excluded, and the difference in strength of correlation coefficients is significant [$F(1,10)=14.17, p<0.004$]. Thus, word duration is more

TABLE V. Types of syllable structures into which words were classified, number of words of each type in the corpus, and average mora duration (average duration of moras of each word, then averaged across words of that syllable type). No word is counted in more than one category.

Type	No. of words	Average mora duration (ms)
Geminate obstruent	29	130.30
Mora nasal	51	123.85
Long vowel	52	108.31
Devoiced vowel (word containing a voiceless or deleted vowel in a devoicing environment)	34	130.49
Fast speech deletion (word with an underlying segment elided in a non-devoicing environment)	27	112.05
Multiple (word containing more than one of the above)	47	110.86
Other (word containing only CV or V moras, where no CVV is CV ₁ V ₁)	176	132.88

predictable if particles are excluded (leaving duration of the lexical word) than if they are included. For the compensation hypothesis, this is an unlikely result, since it suggests that the domain of compensation is the lexical word rather than the prosodic word or some other unit. However, it is in accord with accumulation of variance: there are simply more moras to contribute variability if particles are included.

D. Effects of syllable structure—Special types of moras

The compensation hypothesis predicts that if a syllable containing the mora nasal, a long vowel, or the beginning of a geminate obstruent is not as long as two CV moras, compensation will normalize for such durational differences, keeping the total duration of the word (nearly) predictable from its number of moras regardless of the structures of its syllables. The hypothesis that the mora is a structural, non-temporal unit, however, predicts that non-CV syllables will affect total word duration. This hypothesis claims that the mora-rhythm of Japanese stems not from compensation for non-CV moras, but rather from (among other things) the statistical predominance of CV moras. Port *et al.* (1987, pp. 1577–1578, experiment 2) find little or no effect of syllable type on word duration, but they do not statistically test the apparent low durations of words in their data with geminate obstruents and a devoiced vowel. In another experiment (Port *et al.*, 1987, pp. 1582–1583, experiment 4), they find that CVVCV and CVCCV words are significantly shorter than CVCVCV words, although they are certainly longer than CVCV words. [Han (1994) shows similar results.]

To test the effect of non-CV syllables, we classified all words in the corpus by syllable type. The categories and number of words in them are shown in Table V (along with results described below). This classification is somewhat abstract: fast speech deletions were counted as a separate category, even if the deletion produced one of the other special syllable types phonetically. For example, [bok^wa] or [bokya] for /boku-wa/ ‘‘I-topic’’ was counted as a fast speech deletion rather than as a devoiced (or deleted) vowel, because the environment for phonological devoicing is not present, and

these forms cannot occur in careful speech. [maintʃi] for /mainiti/ ‘‘every day’’ was classified as a fast speech deletion rather than as a mora nasal. Words containing more than one special mora type were treated as a separate category.

Words of the special syllable types are not equally distributed across the range of number of moras in the word. For example, geminate obstruents can only occur in a word with at least three moras, since they can be neither word-initial nor word-final. Furthermore, individual speakers did not produce words of each special syllable type for each possible number of moras (e.g., eight speakers produced three-mora long-vowel words, but only three produced five-mora long-vowel words). The effect of special mora type on duration thus cannot be investigated for each speaker separately.

We therefore tested the effect of syllable type on the average duration of a mora within each word, using a within subjects analysis of variance. If non-CV syllables affect word duration, this will be reflected as an effect on average mora duration (Table V). The effect of syllable type is significant [$F(6,58)=5.260$, $p<0.0003$]. Words with long vowels, fast speech deletions, or multiple non-CV syllable types are relatively short. While it is somewhat surprising that words with devoiced vowels are hardly shorter than words with no special moras, the fact that there are significant differences among the syllable types argues against compensatory mora-timing. There could be limited compensation which is not strong enough to equalize all differences, but it is clear that special mora types affect duration in significantly different ways.

E. Truncating words by removing arbitrary portions

1. Final truncation

As discussed in Sec. III C, Port *et al.* (1987) do not establish whether the word is the domain of compensation, but do claim that compensation functions to make the duration of some unit such as the word predictable from its number of moras. If the domain of the across-mora compensation effect is the word (so that there is no compensation across word boundaries), then when one removes some arbitrary part of the word, the relationship between the duration of the remaining part of the word and the number of moras in it should be weaker than the relationship between duration and number of moras for the entire word. This is because one has removed some of the segments which are compensating for variation in the remaining segments, or removed some of the segments for which the remaining segments are compensating.

For example, if the final mora of a word contains a segment which is inherently shorter than average, such as /r/, under Port *et al.*’s prediction, segments both in that mora and in others lengthen in compensation. If one removed the duration of the final mora, the duration of the remainder of the word would be longer than predicted by the number of moras it contains, because the compensatory adjustments would remain, without the segment /r/ that caused them. The reverse would apply if a segment of the final mora were longer than usual. If a segment in the penultimate, rather than final, mora

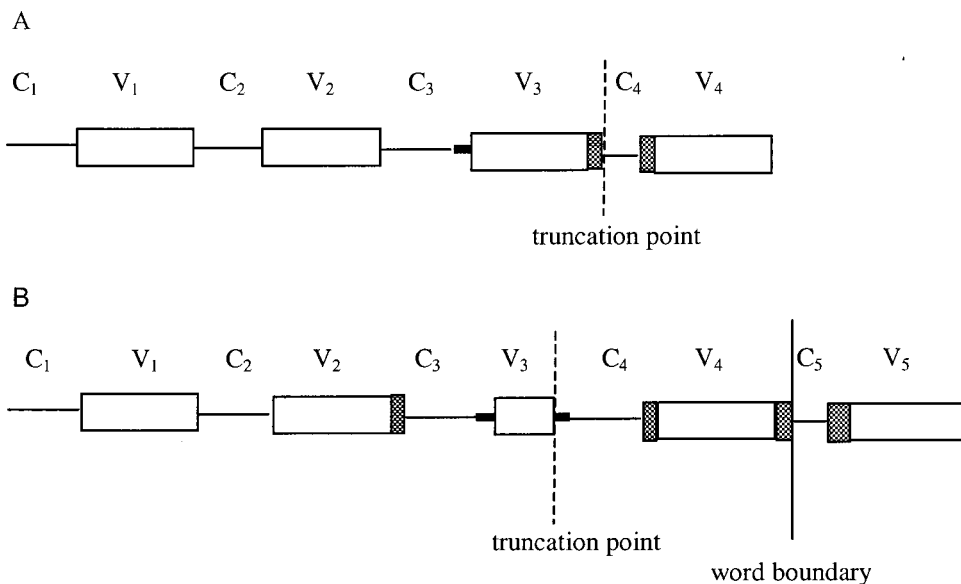


FIG. 1. (a) Durations of consonants (lines) and vowels (boxes) in a hypothetical four-mora word, where the fourth consonant is shorter than average, assuming compensation across moras within the word. Gray portions of boxes and the thick portion of the line for C_3 represent compensatory lengthening to adjust for the short C_4 . The noncompensatory portions of all vowels (white boxes) are of equal length, as are the noncompensatory part of C_1 , C_2 , and C_3 (thin lines). (b) The same, for a hypothetical four-mora word and the first mora of the following word (C_5V_5), where V_3 and C_5 are shorter than average, assuming compensation both within the word and across word boundaries. Lengths of the thin lines (except C_5) and the white boxes (except V_3) are equal.

were longer or shorter than normal, the final mora (among others) would compensate for it, so removing the final mora would leave uncompensated variation. Thus, removing any arbitrary portion of the word would leave undercompensated or overcompensated variability, so that the duration of the remaining portion of the word would not be predicted as well by the number of moras in it as the duration of the entire word is.

This is demonstrated schematically in Fig. 1(a), which shows a hypothetical four-mora word in which the fourth consonant is shorter than average (perhaps /r/). The preceding and following vowels, as well as the consonant before that, are lengthened to compensate (shown as the gray boxes and thick line). If the final mora is removed, the compensatory lengthening of the penultimate consonant and vowel will remain, making the remaining portion of the word longer than would be expected based on its mora count. Such disturbances of the compensation relationship would lower the predictability of the duration of the remaining portion. However, the hypothesis that moras simply contribute variability to the variability of larger units, without compensation, predicts that the duration of an arbitrarily truncated part of a word will be more predictable from the number of moras in it than the duration of the whole word is. This is because a truncated word has fewer moras—truncation removes sources of variability by removing moras.

Port *et al.* (1987) do not rule out the possibility that compensation applies within some unit larger than the word, resulting in compensation even across word boundaries (e.g., between /no/ and /mi/ in /nihoN-no minami/ “South of Japan”). If there were substantial compensation across word boundaries, they could not have found the strong correlation between word duration and number of moras that they did. However, even if there is compensation within some unit larger than the word, so that moras spanning a word boundary also compensate for each other, the compensation hypothesis would still predict that truncation would lower the predictability of duration, as long as there is more compensation among the moras within the word than across the

word boundary. Figure 1(b) shows a hypothetical four-mora word followed by another mora (which is in a different word), with the third vowel and the fifth consonant shorter than average. The durations of the second and fourth vowels and the third and fourth consonants are lengthened to compensate for the short third vowel, and the fourth and fifth vowels are lengthened to compensate for the short fifth consonant. Unless there is at least as much compensation across the word boundary as between the third and fourth moras, removing the last mora of the word (the fourth mora) will still reduce the predictability of the duration of the first three moras. In our corpus, it is unlikely that there is on the average more compensation across word boundaries than within words, since some words precede a pause.

We tested this prediction of the across-mora compensation hypothesis by measuring the durations of words without their final two moras (e.g., the duration of /kagosi/ in the word /kagosimasi/ “Kagoshima City”). The correlation of these truncated durations with the number of moras in the remaining part of the word was then calculated. Particles were excluded before truncation. The final two moras do not form any prosodic unit, and constitute an arbitrary portion of the word. Removing only one mora might not be enough to demonstrate a clear effect (either of increased or decreased predictability), while removing more than two moras would make many words too short to examine. Words with only one or two moras were, of course, excluded from this analysis. Words in which the boundary between penultimate and antepenultimate moras falls during a geminate obstruent (e.g., /ikkai/ “one time”) or long vowel (e.g., /nyuuyooku/ “New York”) were also excluded, as it is difficult to place an accurate mora boundary within these segments. To allow accurate comparison of truncated and nontruncated words, we also calculated the usual whole word correlation for exactly those words which could be used for the truncation analysis.

As shown in Table VI, the correlations between number of moras and duration are significantly stronger for the truncated words than for the corresponding whole words

TABLE VI. (a) Correlation coefficients (r) of final-truncated duration and whole word duration with number of moras in the truncated or whole word string. Number of words in parentheses. (b) Average durations for the same words. Number of words in parentheses.

(a) Speaker	Truncated	Entire word
A (26)	0.947	0.790
B (25)	0.915	0.749
C (20)	0.934	0.702
D (26)	0.846	0.745
E (34)	0.952	0.870
F (30)	0.930	0.745
G (21)	0.936	0.904
H (18)	0.910	0.577
I (21)	0.922	0.707
J (25)	0.862	0.781
K (21)	0.879	0.766

(b) No. of moras	Truncated (ms)	Whole word (ms)
1	118.81 (125)	not applicable
2	224.16 (103)	not applicable
3	356.14 (23)	374.68 (125)
4	416.99 (12)	484.51 (103)
5	590.22 (5)	616.22 (23)
6	not applicable	649.89 (12)
7	not applicable	872.13 (5)

[$F(1,10) = 36.03, p < 0.0002$]. This result contradicts the hypothesis of across-mora compensation, and supports the hypothesis of accumulation of variance. Rather than disturbing the compensation relationships within the word and making the duration of the remainder less predictable, removal of a portion of the word makes the duration of the remainder significantly more predictable by removing sources of variability.

The compensation hypothesis proposed by Port *et al.* (1987) could only account for this result if many words had compensation across the word boundary, but less or none across the truncation point. This is unlikely, since there is no reason for durations to be particularly stable at the arbitrary truncation point, but compensation might well stop at the word boundary, and words which were followed by a pause cannot possibly have compensation across the word boundary. However, a modified version of the earlier hypothesis that there is compensation only within the mora might be able to account for this result with the addition of a final-lengthening effect. If compensation made each mora more similar in duration to other moras, but an additional final-lengthening effect, independent of mora-timing, made the last few moras of a word longer, then the last few moras of a word would be the most divergent from the average duration of a mora because they would be the only ones subject to any effect other than normalization. Thus, their exclusion would improve the predictability of the duration of the remaining string.

2. Initial truncation

The question of whether the final truncation results indicate traditional mora-timing (within-mora compensation) plus final lengthening or simply the lack of compensation (accumulative variance) can be addressed by removing the

TABLE VII. Same as Table VI, for initial truncation.

(a) Speaker	Truncated	Entire word
A (23)	0.810	0.796
B (23)	0.844	0.758
C (20)	0.827	0.702
D (26)	0.885	0.712
E (33)	0.937	0.902
F (32)	0.815	0.806
G (19)	0.884	0.902
H (16)	0.568	0.534
I (21)	0.775	0.717
J (22)	0.874	0.776
K (19)	0.846	0.453

(b) No. of moras	Truncated (ms)	Whole word (ms)
1	130.16 (110)	not applicable
2	261.41 (102)	not applicable
3	364.92 (28)	371.56 (110)
4	433.51 (11)	485.74 (102)
5	571.70 (3)	595.15 (28)
6	not applicable	638.34 (11)
7	not applicable	863.54 (3)

initial two moras of the word instead of the final two. If the stronger correlations under final truncation mean that moras tend toward the same duration with the exception of the lengthened final few, then removing the initial two moras should lead to weaker correlations, because one would be removing two of the least divergent moras. The across-mora compensation hypothesis of Port *et al.* makes the same prediction as with final truncation: weaker correlations when any arbitrary portion of the word is removed. The accumulation of variance hypothesis (lack of compensation) also makes the same prediction as for final truncation: correlations should be stronger when moras are removed, whichever moras those are.

For this analysis, the procedures were identical to those of the final truncation analysis, but correlations were calculated with the initial two moras removed instead of the final two (i.e., the duration of /simasi/ in /kagosimasi/ “Kagoshima City” was measured). Words in which the boundary between the second and third moras falls during a geminate obstruent or long vowel, such as /tyotto/ “a little” and /izyoo/ “above,” were excluded. These are not always the same words as must be excluded for final truncation. The correlation of (untruncated) whole word duration with number of moras was also calculated for exactly those words which could be used for the initial truncation analysis.

The choice to exclude the initial two moras is motivated by the same factors as the truncation of the final two moras, but the initial two moras of a word do usually constitute a foot in Japanese, and thus could form a prosodic unit. However, mora-timing has not to our knowledge been proposed to depend on foot structure. There is relatively little evidence of foot structure influencing duration in Japanese, and this evidence regards highly rhythmic speech (Tajima, 1998). Since the speech in our corpus is relatively fast, foot structure is unlikely to influence the predictions of the various theories regarding initial truncation.

Table VII shows the correlations of duration of initial-

truncated words with number of remaining moras, as well as correlations for the same words intact. All speakers except speaker G have a stronger relationship between duration and number of moras for initial-truncated words than whole words, and this difference in the correlation coefficients is significant [$F(1,10) = 7.03, p < 0.03$].⁶ This result contradicts the across-mora compensation hypothesis, and also rules out the possibility that the final-truncation result was due to within-mora compensation (tendency toward isochrony) plus final lengthening, but supports the hypothesis that moras simply contribute variability to the variability of the whole. It is not simply that the final two moras are the most variable. Rather, removing either the final or the initial two moras decreases variability in the remainder of the word. One could extend this test by removing other arbitrary portions of words, but it appears thus far that no matter what portion of the word is removed, the duration of the remainder of the word is more predictable than duration of the whole word.

For most speakers, final truncation improves the predictability of duration by more than initial truncation does. This may indicate a final lengthening effect without any tendency toward isochrony. We tested for the presence of final lengthening in this corpus in several ways. We found that the average duration of moras located in the final two moras of the word (exclusive of particle), 128.71 ms, was significantly longer than the average duration of moras earlier in the word, 115.40 ms [$F(1,267) = 18.33, p < 0.001$, excluding the same words as in the final truncation analysis]. The average duration of a mora within the first two moras of the word, 116.16 ms, is significantly shorter than the average duration of later moras, 128.31 ms [$F(1,253) = 11.43, p < 0.002$]. The average duration of moras in particles, which are always final (151.50 ms), is significantly longer than the average duration of moras in the word stem (115.77 ms) [$F(1,224) = 62.03, p < 0.001$]. Finally, words produced without any particle have significantly higher average mora duration, 134.76 ms, than the stems of words produced with particles (115.77 ms) [$F(1,10) = 16.68, p < 0.003$], indicating that when particles are present, final lengthening affects them rather than the stem.

These tests indicate that there is final lengthening in this data. We do not investigate the domain of final lengthening, and have no reason to doubt Kaiki, Sagisaka, and colleagues' finding that it is the last mora of the "breath group" that is lengthened in Japanese (Takeda *et al.*, 1989; Kaiki *et al.*, 1992a, b; Sagisaka, 1992; Kaiki and Sagisaka, 1992, 1993). Our results mean simply that the boundaries of the units to which final lengthening applies often enough coincide with word boundaries to show a significant lengthening effect at word boundaries. This clarifies the difference between the final- and initial-truncation results. Because of final lengthening, the final two moras of a word diverge from the typical duration of a mora by more than other moras in the word do. Final lengthening indicates that there is at least one form of speaker control or planning of duration: it is one way in which mora durations systematically diverge from random variance. However, final lengthening does not require any relationship to the mora, and is orthogonal to the issue of mora-timing.

IV. DISCUSSION

These results contradict the mora-timing hypothesis based on across-mora compensation as put forth by Port *et al.* (1987). They support the hypothesis that moras simply contribute variability to the variability of the word, without compensation. This is therefore evidence that the importance of the mora in Japanese rhythm stems from structural factors in the phonology of the language rather than durational normalization. We have shown that the relationship between word duration and number of moras is far weaker in spontaneous speech than in the careful speech of the previous literature, and that the mora is only a slightly better predictor of word duration than the segment, a nonprosodic unit (Secs. III A and B). We have also shown that word duration is more predictable within the lexical than the prosodic word, which would be an unexpected result for a prosodic compensation effect but is predicted by the hypothesis that variance accumulates (Sec. III C). There is also a significant effect of non-CV syllable structures on word duration (Sec. III D).

Finally, our analyses of word duration predictability in truncated and whole words (Sec. III E) provide very strong evidence against compensatory mora-timing, particularly against the hypothesis that compensation serves to normalize the duration of some higher unit such as the word. As discussed earlier, the only way, under this hypothesis, that truncating words could increase the predictability of their durations would be if there were compensation across word boundaries, but little or none within the word at the truncation point, which is unlikely. However, both types of truncation show an increase in predictability of duration under truncation.

All of the results are consistent, however, with the hypothesis that the mora is not used for normalizing duration, and that its importance in Japanese rhythm rather derives from phonological factors. If there is no compensation, then the simplest assumption is that each mora (or other subword unit) contributes variability to the variability of the larger unit, the word. That is, variance accumulates (Ohalo, 1975). The variance of a word with many moras is greater than the variance of a word with few moras, because there are more sources of variability. By showing that the duration of whole words is less predictable than the duration of truncated words, we have shown that the truncated moras also contribute variability to the duration of the whole. They do not reduce the variability of the whole, as they would if there were a compensation relationship between the truncated portion and the remaining portion. The comparison of correlations with and without particles also supports this finding, since removing particles is a type of truncation as well. The only systematic effect on word duration for which we find evidence is final lengthening, which is not related to mora-timing.

Our results do show that for most speakers, the mora is the unit which best predicts word duration in Japanese (among the units tested). If mora-timing were re-defined to mean only that the mora is for most speakers the best predictor of word duration in the language (a definition without compensation or isochronous moras), then one could state that Japanese is mora-timed. However, this is not one of the

definitions of mora-timing which appears in the literature.

Since the mora is clearly relevant in the segmentation, and generally the psycholinguistic processing, of Japanese, the evidence against compensatory mora-timing brings up the question of what makes the mora psycholinguistically important, if it is not a tendency toward regular timing. We conclude that the mora is *relatively* regularly timed in Japanese (in that it is more regularly timed than other prosodic units), and is a relatively good predictor of word duration, not because of compensation but because of phonological, structural factors. These include the lack of an effect of pitch accent on duration, the lack of reduction of unaccented vowels, the lack of an opposition or alternation between accented and unaccented vowels, the statistical predominance of CV syllables in Japanese, and the lack of perceptual cues other than duration difference to the phonemic length distinctions. We propose that these factors, without any durational compensation, create the mora-rhythm of Japanese, which is what listeners make use of in parsing. Thus, we do not conclude that the mora is a historical relic maintained only by orthography (as in Beckman, 1982). The mora is important in Japanese, but it is factors in the structure of the language, not durational compensation, which create its mora rhythm.

ACKNOWLEDGMENTS

We thank Anne Cutler, Steven Greenberg, Setsuko Imatomi, Hajime Inozuka, Masahiko Komatsu, Terry Nearey, John Ohala, Toni Rietveld, and Roel Smits for discussions of this material. We are also grateful to the four volunteer Japanese speakers who judged the recordings, and to Pieter Meima and Bram de Kruijff for help with the data. Any errors are, of course, our own. Some of these results were presented at the ICPHS 1999 in San Francisco, and a preliminary version of part of this research appeared in the proceedings of that conference.

¹The only analyses which do not use the same words in all conditions are the syllable structure analysis (Sec. III D) and one test for final lengthening [comparing words produced with and without particles (Sec. III E 2)].

²One speaker, A, came from Kagoshima, the dialect of which is said to have syllable-timing rather than mora-timing. This speaker's results are included here nonetheless, because they do not seem to differ from other speakers' results. In particular, speaker A shows a very weak effect of number of syllables on duration, just as other speakers do (Table III). The speaker may have used a variety of Japanese which is rhythmically similar to the standard dialect during the recording because he was not addressing members of his own dialect community. There is some evidence from pitch accent that the speaker was attempting to speak Standard Japanese in the recording. The other speakers of nonstandard dialects were not from Kagoshima.

³Port *et al.* (1987) do not rule out the possibility of compensation across word boundaries, but since the recent literature on mora-timing focuses on predictability of word duration, we chose a careful definition of the word.

⁴Even noncoronal palatalized segments are sometimes analyzed as single segments on phonological grounds, thus /kʲ/ instead of /ky/. We also performed this analysis with all palatalized segments counted as single segments, with similar results.

⁵Geminate obstruents are best analyzed as two segments: they make up the coda of one syllable and the onset of the next. The fact that they cannot occur word-initially or word-finally supports this analysis. There are reasons based on the pitch accent system to count long vowels as two segments, as well (Vance, 1987), but the situation is less clear than for geminate obstruents.

⁶Since the closure portion of a post-pausal word-initial voiceless stop cannot be measured, the closure duration of word-initial voiceless stops was in-

cluded in the total word duration only if the stop followed some other speech sound rather than a pause. This unavoidable difference in measurements could increase the variability of the word-initial mora. Therefore, we also performed the initial truncation analysis excluding any voiceless stop-initial words which follow a pause (those for which closure duration could not be measured). This leaves rather few words (as few as 11 for one speaker), so the correlations are less reliable. Still, 9 of the 11 speakers have a stronger correlation for initial truncated words than for the same words intact, although the difference is not quite significant [$F(1,10) = 4.45, p = 0.061$].

- Arai, T., and Greenberg, S. (1997). "The Temporal Properties of Japanese are Similar to those of English," in Proceedings of the 5th European Conference on Speech Communication and Technology, Vol. 2, pp. 1011–1014.
- Beckman, M. (1982). "Segment Duration and the 'Mora' in Japanese," *Phonetica* 39, 113–135.
- Beckman, M. (1992). "Evidence for Speech Rhythms across Languages," in *Speech Perception, Production, and Linguistic Structure*, edited by Y. Tohkura, E. Vatikiotis-Bateson, and Y. Sagisaka (Ohmsha, Tokyo), pp. 458–463.
- Bradlow, A., Port, R. F., and Tajima, K. (1995). "The Combined Effects of Prosodic Variation on Japanese Mora Timing," in Proceedings of the International Congress of Phonetic Sciences, Vol. 4, pp. 344–347.
- Campbell, N. (1992). "Segmental Elasticity and Timing in Japanese Speech," in *Speech Perception, Production, and Linguistic Structure*, edited by Y. Tohkura, E. Vatikiotis-Bateson, and Y. Sagisaka (Ohmsha, Tokyo), pp. 403–418.
- Cutler, A., and Otake, T. (1994). "Mora or Phoneme? Further Evidence for Language-specific Listening," *J. Memory Lang.* 33, 824–844.
- Dauer, R. M. (1983). "Stress-timing and Syllable-timing Reanalyzed," *J. Phonetics* 11, 51–62.
- Dauer, R. M. (1987). "Phonetic and Phonological Components of Language Rhythm," in Proceedings of the Eleventh International Congress of Phonetic Sciences, Vol. 5, pp. 447–450.
- Han, M. S. (1962). "The Feature of Duration in Japanese," *Onsei no Kenkyu* 10, 65–80.
- Han, M. S. (1994). "Acoustic manifestations of mora timing in Japanese," *J. Acoust. Soc. Am.* 96, 73–82.
- Hoequist, Jr., C. (1983a). "Durational Correlates of Linguistic Rhythm Categories," *Phonetica* 40, 19–31.
- Hoequist, Jr., C. (1983b). "Syllable Duration in Stress-, Syllable-, and Mora-timed Languages," *Phonetica* 40, 203–237.
- Homma, Y. (1981). "Durational Relationship Between Japanese Stops and Vowels," *J. Phonetics* 9, 273–281.
- Itô, J., and Mester, R. A. (1995). "Japanese Phonology," in *A Handbook of Phonological Theory*, edited by J. A. Goldsmith (Blackwell, Cambridge), pp. 817–838.
- Kaiki, N., and Sagisaka, Y. (1992). "The Control of Segmental Duration in Speech Synthesis Using Statistical Methods," in *Speech Perception, Production, and Linguistic Structure*, edited by Y. Tohkura, E. Vatikiotis-Bateson, and Y. Sagisaka (Ohmsha, Tokyo), pp. 391–402.
- Kaiki, N., and Sagisaka, Y. (1993). "Prosodic Characteristics of Japanese Conversational Speech," *IEICE Trans. Fundamentals* E76-A, 1927–1933.
- Kaiki, N., Takeda, K., and Sagisaka, Y. (1992a). "Gengojoohoo o Riyoo shita Boin Keizoku Jikanchoo no Seigyo [Vowel duration control using linguistic information]," *IEICE Trans.* J75-A, 467–473.
- Kaiki, N., Takeda, K., and Sagisaka, Y. (1992b). "Linguistic Properties in the Control of Segmental Duration for Speech Synthesis," in *Talking Machines: Theories, Models, and Designs*, edited by G. Bailly, C. Benoit, and T. R. Sawallis (Elsevier Science, Amsterdam), pp. 255–263.
- Kondo, M. (1999). "Manifestation of Lexical Accent and Timing Strategy in English Speakers' Japanese," in Proceedings of the Fourteenth International Congress of Phonetic Sciences, pp. 1467–1470.
- Kubozono, H. (1999). "Mora and Syllable," in *The Handbook of Japanese Linguistics*, edited by N. Tsujimura (Blackwell, Malden, MA), pp. 31–61.
- Minagawa-Kawai, Y. (1999). "Preciseness of Temporal Compensation in Japanese Mora Timing," in Proceedings of the Fourteenth International Congress of Phonetic Sciences, pp. 365–368.
- Muthusamy, Y. K., Cole, R. A., and Oshika, B. T. (1992). "The OGI Multi-language Telephone Speech Corpus," in Proceedings of the Third International Conference on Spoken Language Processing, pp. 895–898.

- Ohala, J. J. (1975). "The Temporal Regulation of Speech," in *Auditory Analysis and Perception of Speech*, edited by G. Fant and M. A. A. Tatham (Academic, London), pp. 431–453.
- Otake, T. (1989). "Counter Evidence for Mora Timing," in Proceedings of the 16th Lacus Forum, pp. 313–322.
- Otake, T. (1990). "Gengo no Rizumu to Onsetsu Koozoo" [Rhythmic Structure of Japanese and Syllable Structure], IEICE Technical Report 89, pp. 55–61.
- Otake, T., Hatano, G., and Yoneyama, K. (1996). "Speech Segmentation by Japanese Listeners," in *Phonological Structure and Language Processing*, edited by T. Otake and A. Cutler (Mouton de Gruyter, Berlin), pp. 183–201.
- Otake, T., Hatano, G., Cutler, A., and Mehler, J. (1993). "Mora or Syllable? Speech Segmentation in Japanese," *J. Memory Lang.* **32**, 258–278.
- Port, R. F., Al-Ani, S., and Maeda, S. (1980). "Temporal Compensation and Universal Phonetics," *Phonetica* **37**, 235–252.
- Port, R. F., Dalby, J., and O'Dell, M. (1987). "Evidence for Mora Timing in Japanese," *J. Acoust. Soc. Am.* **81**, 1574–1585.
- Ramus, F., Nespors, M., and Mehler, J. (1999). "Correlates of linguistic rhythm in the speech signal," *Cognition* **73**, 265–292.
- Sagisaka, Y. (1992). "On the Modeling of Segmental Duration Control," in *Speech Perception, Production, and Linguistic Structure*, edited by Y. Tohkura, E. Vatikiotis-Bateson, and Y. Sagisaka (Ohmsha, Tokyo), pp. 451–455.
- Sagisaka, Y. (1999). "Koopasu Beesu Onsei Goosei: Onsei Kagaku Chishiki ni Motozuku Goosei Shisutemu Koochiku Gijutsu no Shin Paradimu" (Corpus-based speech synthesis—A new paradigm for synthesis system building based on the knowledge in speech science), in Proceedings of the Meeting of the Acoustical Society of Japan, September–October, pp. 197–200.
- Sagisaka, Y., and Tohkura, Y. (1984). "Phoneme Duration Control for Speech Synthesis by Rule," *IEICE Trans.* **J67-A:7**, 629–636.
- Sato, Y. (1995). "The Mora Timing in Japanese: A Positive Linear Correlation between the Syllable Count and Word Duration," *Onsei Gakkai Kaihoo* **209**, 40–53.
- Tajima, K. (1998). "Speech Rhythm in English and Japanese," unpublished dissertation, Indiana University, Bloomington.
- Takeda, K., Sagisaka, Y., and Kuwabara, H. (1989). "On sentence-level factors governing segmental duration in Japanese," *J. Acoust. Soc. Am.* **86**, 2081–2087.
- Tsujimura, N. (1996). *An Introduction to Japanese Linguistics* (Blackwell, Malden, MA).
- Vance, T. J. (1987). *An Introduction to Japanese Phonology* (State Univ. of New York, Albany, NY).
- Warner, N., and Arai, T. (2001). "Japanese Mora-timing: A Review," *Phonetica* **58**, 1–25.

Acoustic and linguistic factors in the perception of bandpass-filtered speech^{a)}

Ginger S. Stickney and Peter F. Assmann^{b)}

School of Human Development, The University of Texas at Dallas, Box 830688, Richardson, Texas 75083-0688

(Received 15 February 2000; accepted for publication 14 November 2000)

Speech can remain intelligible for listeners with normal hearing when processed by narrow bandpass filters that transmit only a small fraction of the audible spectrum. Two experiments investigated the basis for the high intelligibility of narrowband speech. Experiment 1 confirmed reports that everyday English sentences can be recognized accurately (82%–98% words correct) when filtered at center frequencies of 1500, 2100, and 3000 Hz. However, narrowband low predictability (LP) sentences were less accurately recognized than high predictability (HP) sentences (20% lower scores), and excised narrowband words were even less intelligible than LP sentences (a further 23% drop). While experiment 1 revealed similar levels of performance for narrowband and broadband sentences at conversational speech levels, experiment 2 showed that speech reception thresholds were substantially (>30 dB) poorer for narrowband sentences. One explanation for this increased disparity between narrowband and broadband speech at threshold (compared to conversational speech levels) is that spectral components in the sloping transition bands of the filters provide important cues for the recognition of narrowband speech, but these components become inaudible as the signal level is reduced. Experiment 2 also showed that performance was degraded by the introduction of a speech masker (a single competing talker). The elevation in threshold was similar for narrowband and broadband speech (11 dB, on average), but because the narrowband sentences required considerably higher sound levels to reach their thresholds in quiet compared to broadband sentences, their target-to-masker ratios were very different (+23 dB for narrowband sentences and -12 dB for broadband sentences). As in experiment 1, performance was better for HP than LP sentences. The LP-HP difference was larger for narrowband than broadband sentences, suggesting that context provides greater benefits when speech is distorted by narrow bandpass filtering. © 2001 Acoustical Society of America.

[DOI: 10.1121/1.1340643]

PACS numbers: 43.71.Es, 43.71.Gv [CWT]

I. INTRODUCTION

Speech communication is a remarkably robust process for listeners with normal hearing. Evidence for this comes from studies of speech perception in adverse listening conditions. These include listening environments with complex forms of interfering noise (e.g., competing voices: Cherry, 1953) and reverberation (e.g., Helfer, 1994), as well as distortions which disrupt the temporal structure by replacing segments of speech with silence (e.g., Miller and Licklider, 1950; Huggins, 1975) or restrict the frequency range of the signal by filtering (Lippmann, 1996; Warren *et al.*, 1995).

An example of extreme resilience to spectrally impoverished speech was provided by Warren *et al.* (1995). They showed that listeners were able to correctly identify more than 95% of the key words in a set of everyday English sentences, which had been passed through one-third octave bandpass filters with center frequencies of 1100, 1500, and

2100 Hz. Filters with lower center frequencies (530 and 750 Hz) and higher frequencies (3000 and 4200 Hz) produced somewhat lower scores, though still generally above 50%, while the two most extreme filters (370 and 6000 Hz) resulted in recognition scores lower than 25%. The pattern of identification accuracy across frequency bands approximates the importance function of the Articulation Index (Fletcher, 1953) which reaches a maximum between 1500 and 2000 Hz (Bell, Dirks, and Trine, 1992; Pavlovic, 1994).

The high intelligibility of narrowband sentences is noteworthy, given that the one-third octave bandwidths and 96 dB/octave skirts of the elliptical filters used by Warren *et al.* eliminated a substantial proportion of the frequency spectrum. This is illustrated in Fig. 1, which shows broadband and narrowband versions of the phrase “the watchdog.” The right panel shows that only fragments of the formant pattern remain visible in the spectrogram of the narrowband version, centered at 1500 Hz. The narrowband speech lacks several features that may contribute to the identification of vowels and consonants. For example, the spectral peak associated with the first formant is completely removed by filtering. Only a small segment of the rising second-formant transition of the /w/ in “watchdog” remains visible, and the

^{a)}Portions of the results were reported at the 134th Meeting of the Acoustical Society of America [Stickney and Assmann, *J. Acoust. Soc. Am.* **100**, 2680(A) (1997)] and at the 21st Midwinter Meeting of the Association for Research in Otolaryngology [Stickney and Assmann, Abstracts of the 21st midwinter meeting of the Association for Research in Otolaryngology, p. 43 (1998)].

^{b)}Electronic mail: assmann@utdallas.edu

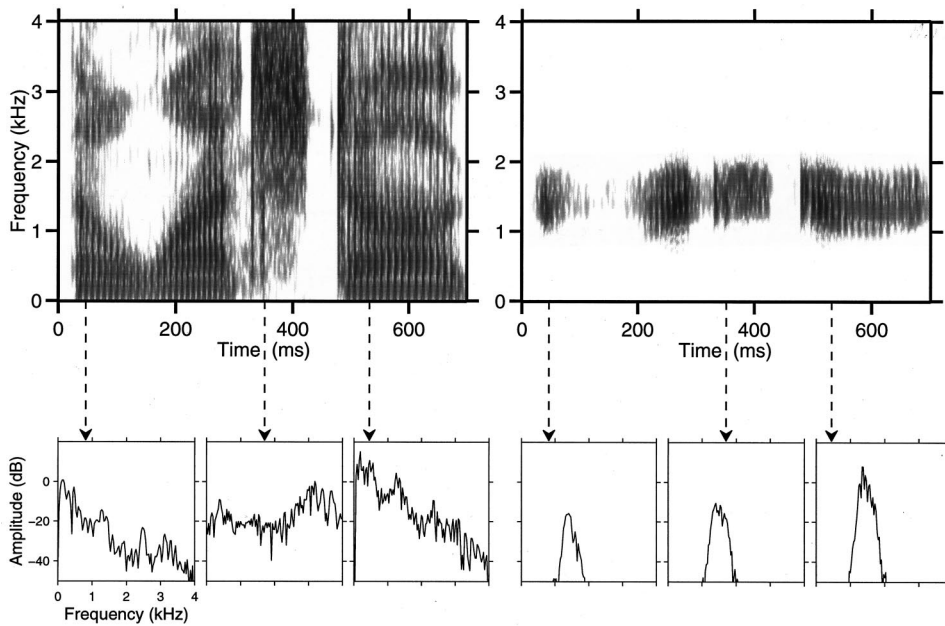


FIG. 1. Spectrograms and amplitude spectra for the phrase "The watchdog." The broadband version is shown in the left panel and the narrowband version in the right panel. The narrowband version is the output of an elliptical bandpass filter centered at 1.5 kHz with a one-third-octave bandwidth, similar to the filter used by Warren *et al.* (1995).

frication noise associated with the affricate /č/ appears at a lower frequency.

How do listeners recognize speech under such extreme forms of distortion? Part of the answer lies in the temporal modulation structure of speech (Steeneken and Houtgast, 1980; Drullman, Festen and Houtgast, 1996). The amplitude modulations in narrowband speech preserve some information about time-varying changes in the frequencies of the formants. Variation in overall amplitude provides cues for manner of articulation for consonants (Faulkner and Rosen, 1999) and prosodic information about the stress pattern of the sentence and the timing of vowel and consonant alternation (Grant and Walden, 1996). Periodicity in the narrowband waveform makes it possible to estimate the fundamental frequency and contributes cues for voicing, even though speech filtered through a one-third-octave band centered at 1500 Hz or higher does not convey a strong sensation of voice pitch.

A second factor contributing to the high intelligibility of narrowband speech is linguistic context (Miller, Heise, and Lichten, 1951). Context restricts the number of plausible lexical candidates and activates the matching mechanisms of the lexicon. The stimuli used by Warren *et al.* were meaningful sentences from the CID test battery (Silverman and Hirsh, 1955) which contain a high degree of semantic context. It is reasonable to expect that lower intelligibility would have resulted had they used sentences with reduced linguistic redundancy. Further declines would be expected with word lists or nonsense syllables which, in addition to loss of semantic context, eliminate the syntactic and prosodic cues provided by the sentence.

A third factor is that not only the passbands, but also the transition bands of narrowband speech contribute to its intelligibility. Warren *et al.* (1995) amplified their narrowband sentences to match the level of the broadband sentences. In a subsequent study, Warren and Bashford (1999) showed that both the passband and the transition bands contribute to intelligibility when narrowband speech is amplified to levels

near the high end of the conversational speech range (around 75 dB), with the greater contribution coming from the transition bands. Narrowband speech may be more intelligible when amplified to the level of conversational speech than at lower levels, because at lower levels some frequency components in the sloping transition bands of the filters would fall below the detection threshold.

The high intelligibility of narrowband speech raises the question of the ecological significance of the wide bandwidth of natural speech. Greenberg (1996) suggested that the wide bandwidth and complex temporal modulation structure of natural speech serves to shield the signal from masking and distortion. Although Warren *et al.* showed that narrowband speech is identified as well as broadband speech in quiet, narrowband speech may prove to be less robust in the presence of interfering sounds. Reducing the signal bandwidth decreases the spectral redundancy of the signal and possibly its resilience to masking.

The present study had three aims: first, to investigate the contribution of linguistic context to the perception of narrowband speech, as a function of filter center frequency; second, to examine the effects of reducing the signal level by comparing the intelligibility of narrowband speech at conversational and threshold levels; and third, to study the robustness of narrowband speech in the presence of competing speech maskers.

In experiment 1, the contribution of linguistic factors to the intelligibility of narrowband speech was examined by comparing high predictability (HP) and low predictability (LP) sentences from the Speech Perception in Noise (SPIN) test (Kalikow, Stevens, and Elliott, 1977), as well as their final words in isolation. The contribution of semantic predictability was based on a comparison of identification accuracy for the final keywords in HP and LP sentences. The LP sentences eliminated the semantic context, but retained the syntactic word-class distribution along with the acoustic and prosodic structure of natural English sentences. Hence, the separate contribution of syntactic and prosodic factors could

be assessed by comparing performance on the final words in LP sentences and in isolation.

In experiment 2, the effects of competing speech on sentence intelligibility were measured using the speech-reception threshold (SRT), defined as the signal-to-noise ratio required for 50% intelligibility (Plomp and Mimpen, 1979; Duquesnoy, 1983). SRTs were used to test the prediction that larger differences between narrowband and broadband speech would emerge at lower sound levels. If the transition bands provide a major contribution to the high intelligibility of narrowband speech at conversational levels, then differences between these two conditions would be expected to emerge at lower levels, since a greater proportion of each transition band would lie below the threshold of audibility. Experiment 2 also compared performance in quiet and with a competing voice to ascertain whether narrowband speech would be more susceptible to masking than broadband speech.

II. EXPERIMENT 1

A. Method

1. Listeners

One hundred twenty young native English listeners from the University of Texas at Dallas undergraduate psychology program were recruited for this experiment. None of the listeners reported hearing loss. Course credit was offered for their participation.

2. Stimuli

The experimental stimuli consisted of either sentences or their final words (lists 1 and 2) taken from the SPIN test of Kalikow *et al.* (1977). SPIN sentences are phonetically balanced, have a length of five to eight words, and end with a monosyllabic noun. Each sentence is labeled as either an HP or LP sentence. HP sentences contain keywords (usually two to three) that provide semantic links to the final word (e.g., "The boat sailed across the bay"). In contrast, the final word in a low predictability sentence cannot be anticipated from the preceding context (e.g., "John was talking about the bay"). Each final word appearing in a high predictability sentence also occurs as a final word in a low predictability sentence. The keywords, selected from the Thorndike-Lorge list, consist of words that are neither frequently used nor uncommon in English.

The list of 100 sentences was recorded by a male speaker from the north-central Texas region. Speech recordings were made in an IAC sound booth using a Shure SM94 microphone, Symmetrix SX202 preamplifier, and AIWA HD-X300 digital audiotape recorder. The digital recordings (48-kHz sample rate, 16-bit resolution) were transferred directly to computer disk via a DAT-Link interface.

Narrowband sentences were constructed by processing each broadband sentence with a gammatone bandpass filter (Patterson *et al.*, 1992; Slaney, 1993). Gammatone filters were chosen because they provide a reasonable characterization of auditory frequency selectivity measured psychophysically and physiologically at low sound levels. The bandwidths of the filters increased with center frequency in

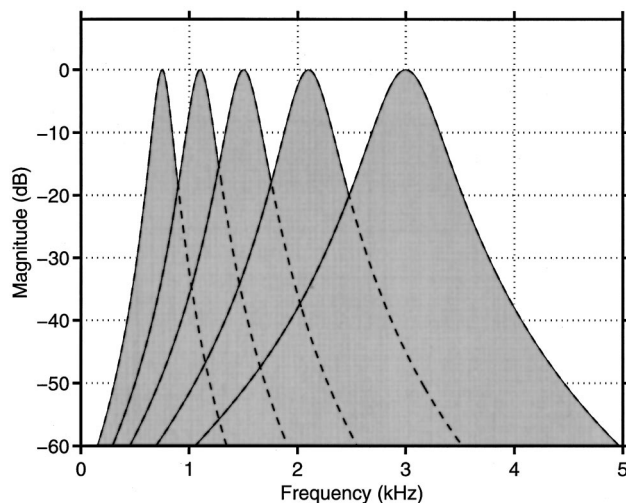


FIG. 2. Transfer functions of the gammatone filters used to generate the narrowband speech stimuli used in experiment 1. The filter center frequencies were 750, 1100, 1500, 2100, and 3000 Hz, and their equivalent rectangular bandwidths were 106, 143, 187, 251, and 349 Hz, respectively.

accordance with the equivalent rectangular bandwidth (ERB) function described by Glasberg and Moore (1990). Figure 2 displays the transfer functions of five gammatone filters with center frequencies of 750, 1100, 1500, 2100, and 3000 Hz.

The final keywords were excised from the broadband sentences using a waveform editing program prior to filtering. The onset and offset of the final word were determined by a combination of visual and auditory criteria. In most of the sentences, the final word started with a stop consonant or a fricative, and the cursor was placed at the nearest zero crossing prior to the burst or onset of frication. In about 10% of the sentences, the final word started with a vowel or an approximant (/w/, /l/, /j/, or /r/) and the preceding word ended in a vowel, and hence there was no clear demarcation between the final and penultimate words. In these cases the cursor was placed at a zero crossing in the transition region and was adjusted so that the initial consonant of the final word was clearly audible, but no portion of the preceding word could be heard.

3. Procedure

Separate groups of 60 listeners heard either complete sentences or just their final words. Within each of these two main groups, ten listeners were assigned to each of five filter conditions or the broadband speech condition. Listeners were tested individually in a sound-treated chamber with stimuli presented diotically through headphones. The sound-pressure levels of the broadband sentences ranged from 68 to 73 dB (Bruel & Kjaer artificial ear type 4152, microphone type 4134, sound-level meter type 2235, A-weighting, slow time averaging). The narrowband sentences were scaled to the same rms level as their broadband versions, and were presented at an average level of 70 dB. Sentences were approximately 4.5 dB higher than the excised final words, because the final word was not always the most intense word in the sentence. However, since scoring was based on the final word only, the excised final words were presented at the same levels they had in the original sentences.

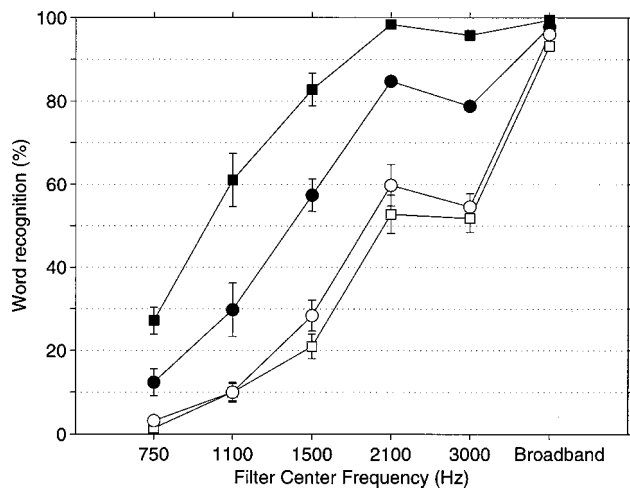


FIG. 3. Results of experiment 1: Word recognition accuracy for narrowband and broadband speech. Square symbols: HP condition; circles: LP condition. Filled symbols: final words in sentence context; unfilled symbols: excised final words. Error bars show ± 1 standard error across the ten listeners in each condition.

Prior to the experiment, listeners completed a practice set with ten sentences (the first ten sentences from the SPIN test, list #3). These sentences, or their final words (depending on the experimental group) were presented twice—once as unfiltered, broadband speech, and subsequently as either narrowband speech or broadband speech (again, depending on the experimental group). Listeners responded by typing the word or sentence they heard using the computer keyboard. After each trial, the correct response was displayed on the screen. Listeners were required to identify at least 89% of all keywords correctly in the broadband speech condition to participate in the experiment. Only one listener scored below 89%, and those data were not included in the analyses reported below. The practice sessions lasted approximately 15 min.

During the experimental session which followed, each group of listeners heard 50 HP and 50 LP sentences or their final words, using a randomized presentation order for each listener. The response procedure was the same as that for the practice session, except that feedback was not provided. Intelligibility for sentences was measured by scoring the number of correctly identified final words. The experimental session lasted approximately 30 min.

B. Results and discussion

1. Effects of filter center frequency

Figure 3 shows the recognition scores for the final words in HP and LP sentences (filled symbols) and for the final words presented alone (unfilled symbols). It is evident that speech processed through narrow bandpass filters can remain highly intelligible in some conditions. This result is consistent with findings reported by Warren *et al.* (1995). Word recognition scores varied as a function of center frequency [$F_{(5,108)} = 237.22$; $p < 0.01$]. The 2100- and 3000-Hz filter bands produced the highest identification scores, averaging

better than 95% for HP sentences. Scores were higher for the 2100-Hz band than for the 3000-Hz band, although this difference was not statistically significant.

Compared to the elliptical filters used by Warren *et al.* (1995), gammatone filters have shallower skirts and narrower tips, and hence may transmit a greater proportion of the speech spectrum outside their nominal filter passband. During time intervals when the speech signal contains little energy in the passband region, the transition bands can indicate the location of a formant peak in the frequency region above or below the passband. This property is more pronounced in the high-frequency filters (cf. Fig. 2) and may explain why the 2100- and 3000-Hz bands were more intelligible than the 1500-Hz band in the current study, while Warren *et al.* obtained the reverse pattern. Intelligibility was substantially reduced for the lower bands (750 and 1100 Hz), consistent with Warren *et al.* Overall, the 1500–3000-Hz range was the most resilient to the effects of filtering.

2. Effects of semantic predictability

Figure 3 shows that the final words in HP sentences (squares) were more intelligible than the final words in LP sentences (circles) [$F_{(1,108)} = 154.11$; $p < 0.01$]. For the 2100- and 3000-Hz bands, the semantic context provided by the HP sentences boosted identification accuracy to levels found with broadband speech. In fact, planned comparisons showed that the HP sentences filtered at 2100 Hz were identified as well as the broadband sentences ($> 98\%$). In contrast, performance on the LP narrowband sentences dropped to 84.8% when semantic predictability was removed.

There was a significant interaction of filter \times semantic predictability [$F_{(5,108)} = 16.52$; $p < 0.01$]. Figure 3 shows that the importance of semantic predictability, as measured by the difference in intelligibility between HP to LP sentences, was greater for filter bands with lower center frequencies, with the exception of the lowest band (750 Hz). However, the interaction must be interpreted with caution since floor and ceiling effects might have contributed to the pattern.¹ To circumvent this difficulty, experiment 2 used threshold measures instead of percent correct scores.

3. Effects of sentence context

Listeners identified the final words in sentences more accurately than the final words in isolation [$F_{(1,108)} = 288.21$; $p < 0.01$]. The difference between excised words and sentences was large (34%) for narrowband speech, but diminished in the broadband condition (4%) where performance was again close to ceiling, contributing to the significant filter \times context interaction [$F_{(1,108)} = 13.28$; $p < 0.01$], and a significant three-way interaction of filter \times context \times predictability [$F_{(5,108)} = 14.92$; $p < 0.01$]. For narrowband speech, the pattern of identification accuracy as a function of center frequency was similar for sentences and excised words. This result was expected since performance in each case was based on the identification of the acoustically identical final word.

Since there were no acoustic differences between the final words in isolation and in sentence context, the perfor-

mance drop can be attributed to contextual information provided by the preceding sentence fragment. In the case of LP sentences, even the semantic context had been removed, and yet intelligibility was 23% higher for narrowband LP sentences than for excised words. This result emphasizes the important contribution of sentence context to the high intelligibility of narrowband speech.

For the excised final words, performance was expected to be similar for LP and HP conditions since the sentence context had been removed. Figure 3 shows that the excised final words were identified more accurately when they came from LP sentences rather than HP sentences for the 1500- and 2100-Hz bands. Although the same words appeared in HP and LP sentences, they were derived from acoustically different productions. Therefore, HP-LP differences in final word identification might be the result of variations in speaking style or vocal effort, or differences in word context. The final words in LP sentences were always preceded by the article "the," providing a more consistent word context (and more stable patterns of coarticulation) than in the corresponding HP sentences. Given that the acoustic cues provided by the penultimate word in a carrier phrase can contribute to the identification of the final word (Lynn and Brotman, 1981; Revoile *et al.*, 1995), it is possible that the disruption of the pattern of coarticulation caused by excising the final word resulted in poorer identification. The more uniform context provided by the LP condition would be less disruptive, leading to higher identification scores.²

III. EXPERIMENT 2

Experiment 1 showed that HP sentences filtered at center frequencies of 2100 and 3000 Hz were just as intelligible as broadband sentences. However, the elimination of linguistic context greatly reduced the intelligibility of the narrowband sentences. It is also important to recognize that the narrowband and broadband sentences in experiment 1 were presented at conversational speech levels and in quiet. Warren and Bashford (1999) showed that the high intelligibility of narrowband speech at conversational speech levels depends, in part, on the sloping transition bands of the band-pass filters. At lower signal levels, the spectral components that occupy the transition bands are more likely to fall below the audibility threshold. In comparison, the intelligibility of broadband speech does not decline materially over a range of about 100 dB or more (Pollack and Pickett, 1958). Experiment 2 tested the hypothesis that thresholds would be poorer for narrowband than broadband sentences because of the reduced audibility of spectral components in the transition bands at lower signal levels.

Experiment 2 also tested the prediction that the narrow bandwidth of filtered speech would make it more vulnerable to masking by interfering sounds. Broadband speech maskers were used because they overlap in spectral and temporal structure with the target sounds, and represent a common form of interference in everyday life. Therefore, to determine the generality of the results and to eliminate floor and ceiling effects, experiment 2 compared the intelligibility of narrowband and broadband speech using SRTs (Plomp and

Mimpen, 1979), both in quiet and in the presence of speech maskers.

A. Method

1. Listeners

A separate group of 24 young native English speakers was recruited from the undergraduate psychology program at the University of Texas at Dallas. The listeners recruited for experiment 2 had no previous experience with these tasks. All had normal hearing (absolute thresholds better than 20 dB HL at octave frequencies between 500 and 4000 Hz in the right ear). Course credit was offered for their participation.

2. Stimuli

The target sentences were the narrowband and broadband sentences from experiment 1. Only three of the five filter conditions (1500, 2100, and 3000 Hz) were included. Excised final words were not presented in this experiment.

The 100 masker sentences were recorded by an adult female talker from the north-central Texas region. Recordings were made as described in experiment 1, except that the sentences were obtained from lists 7 and 8 of the SPIN test. The masker sentences were presented at a mean level of 50 dB(A), while the target speech varied in level according to an adaptive procedure. The target and masker sentences were aligned at their offsets so that the final word in each target sentence terminated at the same time as the final word in the masker sentence. The masker sentences were chosen to be similar to (but never shorter than) the target sentences in duration.

3. Procedure

Listeners were assigned to one of three filter conditions, with eight subjects per condition. In addition to narrowband speech, each listener completed trials with broadband target sentences. At the beginning of each session, pure-tone thresholds were obtained, followed by two practice sessions with broadband and narrowband sentences. The first practice session was the same as in experiment 1; the second session provided experience with the adaptive procedure, and included six of the eight test conditions:

- (1) HP narrowband sentences in quiet;
- (2) LP narrowband sentences in quiet;
- (3) HP broadband sentences with speech maskers;
- (4) LP broadband sentences with speech maskers;
- (5) HP narrowband sentences with speech maskers; and
- (6) LP narrowband sentences with speech maskers.

Two examples from each condition were presented during the practice session for a total of 12 sentences. Two additional test conditions were omitted from the practice session:

- (7) HP broadband sentences in quiet; and
- (8) LP broadband sentences in quiet.

For the test session, listeners were presented with 96 sentences, 12 for each condition. The order of the sentences within each condition remained constant, but the presenta-

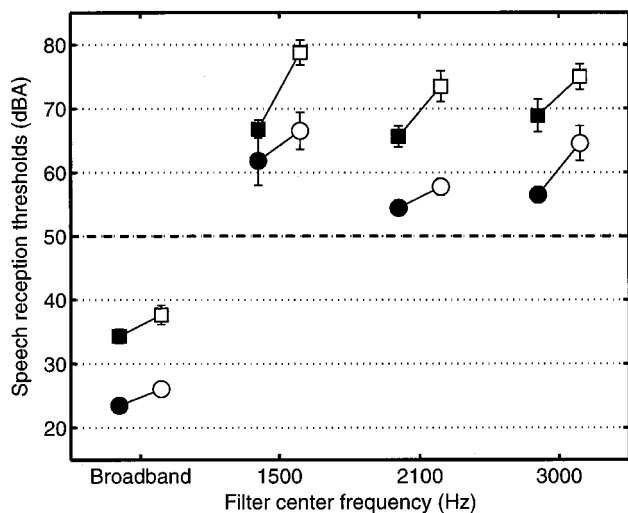


FIG. 4. Results of experiment 2: SRTs in quiet (circles) and masked by 50 dB broadband speech (squares) for HP sentences (filled symbols) and LP sentences (unfilled symbols). Error bars show standard errors across the 8 listeners.

tion order of the conditions was varied using a digram-balanced Latin square design.

SRTs were calculated for the eight conditions using the following procedure. The first test sentence started below threshold and was presented repeatedly, each time with an increase of 4 dB, until the listener correctly identified the final keyword. Although listeners identified all words in the sentence, only the final keyword was used to adaptively adjust the presentation level of the target sentence. Subsequent sentences were presented only once and level adjustments were made depending on whether or not the final word in the sentence was correctly identified. An incorrect response resulted in a 2-dB increase in the presentation level of the following sentence and a correct response produced a 2-dB decrease. The SRT was determined as the average SPL for sentences 4–12. As in experiment 1, listeners were seated in a double-walled sound booth, listened to the stimuli monaurally (right ear) over headphones, and responded by computer keyboard as described earlier.

B. Results and discussion

SRTs were expressed as sound levels in dB(A). Figure 4 shows the means and standard errors across the eight listeners. Lower numbers reflect better performance.

1. Effects of filtering

Although experiment 1 revealed similar intelligibility for broadband and narrowband sentences at a fixed level of 70 dB, experiment 2 showed substantially higher thresholds for narrowband than broadband sentences (>30 dB in quiet). The appearance of such large threshold differences for stimuli that are equally intelligible at conversational speech levels is striking. One explanation is that listeners depend on the acoustic cues provided by the transition bands in narrowband speech to sustain intelligibility. For the 2100- and 3000-Hz bands, the SRTs for the narrowband HP sentences in quiet are between 55 and 58 dB, only 12–15 dB lower than the 70-dB presentation level used in experiment 1.

Since the SRT provides an estimate of threshold required to achieve a 50% level of intelligibility, this suggests a drop in performance from 98% to 50% when the presentation level was reduced by as little as 12–15 dB. This outcome is consistent with the hypothesis that a significant contribution to intelligibility comes from spectral components within the transition bands of the filters. Some of these components are likely to fall below the audibility threshold when the signal is attenuated. The effect of filter center frequency approached significance [$F_{(2,21)}=2.77$; $p=0.08$] with higher thresholds for 1500 and 3000 Hz, relative to the 2100-Hz filter, consistent with the pattern of intelligibility in experiment 1.

2. Effects of semantic predictability

Thresholds were on average 3.4 dB lower for HP than LP sentences in the broadband speech condition [$F_{(1,21)}=38.74$; $p<0.01$]. Narrowband speech also showed lower thresholds for HP than LP sentences, [$F_{(1,21)}=78.33$; $p<0.01$], and the difference increased to 6.9 dB. The effects of predictability did not vary as a function of filter center frequency [$F_{(1,21)}=1.45$; $p=0.26$]. Threshold differences between narrowband and broadband speech revealed a significant effect of predictability [$F_{(1,21)}=16.90$; $p<0.01$], suggesting that semantic predictability makes a greater contribution to the intelligibility of narrowband than broadband speech. In other words, the LP narrowband/broadband difference was greater than the HP narrowband/broadband difference, confirming the pattern found in experiment 1.

3. Effects of a competing voice masker

The introduction of competing speech maskers elevated thresholds by 11.0 dB for the broadband sentences [$F_{(1,21)}=352.97$; $p<0.01$], consistent with earlier findings (Peters *et al.*, 1998). Surprisingly, speech maskers elevated thresholds by a similar amount (11.7 dB, on average) for the narrowband sentences [$F_{(1,21)}=130.48$; $p<0.01$]. This result was unexpected, since it was anticipated that bandlimited speech would be more susceptible to masking by interfering sounds. None of the interaction terms in the analysis of variance (ANOVA) was significant.

Although the introduction of a speech masker results in a similar increase in threshold for narrowband and broadband sentences, the target-to-masker ratios are very different: –12 dB for broadband LP sentences compared to +23 dB for narrowband sentences. Figure 4 shows that in quiet, the thresholds for narrowband sentences were about 30 dB higher than the corresponding broadband sentences. As a result, the target-to-masker ratios were appreciably higher for narrowband than broadband speech when speech maskers were introduced. Figure 5 compares the long-term average spectra of the narrowband (2100-Hz center frequency) LP sentences and broadband LP sentences at their respective thresholds in quiet (left panel) and in the presence of 50-dB speech maskers (right panel). The right panel shows that the spectrum levels of the target sentences were at least 10 dB below the masker across the entire frequency range, while the narrowband sentences were more than 30 dB higher in the region of the filter passband. Thus, at the

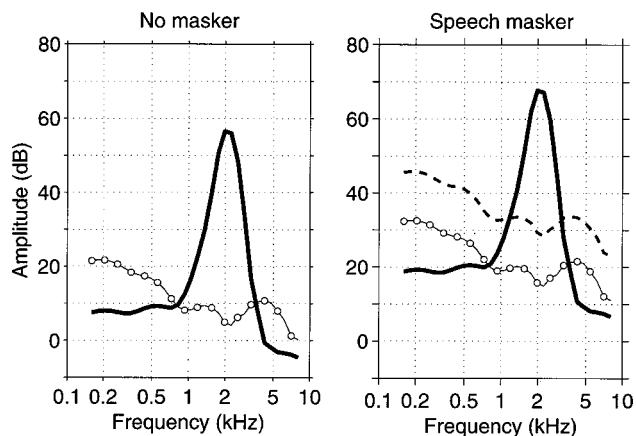


FIG. 5. Long-term average spectra of the LP sentences in experiment 2, obtained from a 32-channel one-third octave filter bank analysis. The left panel shows the spectra of the broadband sentences (thin lines with unfilled circles) and narrowband sentences (2100 Hz, thick solid lines) at their thresholds in quiet. The right panel shows the spectra of the broadband and narrowband target sentences at threshold in the presence of a 50-dB speech masker (dashed line).

higher sound levels needed to reach their identification thresholds in quiet, the susceptibility of narrowband speech to 50-dB speech maskers was no greater than broadband speech.

IV. GENERAL DISCUSSION

Two experiments have confirmed that narrowband speech can be highly intelligible (Warren *et al.*, 1995) and have identified several acoustic and linguistic factors that contribute to this effect. Fragments of the temporal or spectral composition preserved in narrowband speech are responsible for sustaining its high intelligibility: these may include amplitude envelope cues, fundamental frequency, and partial formant information. The filter bands in the midfrequency range (1.5–3.0 kHz) were more intelligible than lower frequency bands (<1.0 kHz), replicating earlier findings by Warren *et al.* This region encompasses the center frequencies of the second and third formants, which are important for the identification of both vowels and consonants (Stevens, 1997).

Two aspects of linguistic structure were found to contribute significantly to the intelligibility of narrowband speech. First, *semantic predictability* helps listeners restrict the set of lexical candidates evoked by a target word on the basis of plausibility. Experiment 1 showed that narrowband sentences with high semantic predictability could be as intelligible as broadband sentences (consistent with Warren *et al.*, 1995), but sentences with low predictability were 20% less intelligible. Consistent with this finding, experiment 2 showed that SRTs were more than 3 dB lower for HP than LP sentences. Moreover, the HP-LP difference was greater for narrowband than broadband sentences, suggesting that listeners increase their reliance on semantic predictability when listening to distorted speech.

Second, *sentence context without semantics* helps by establishing links between the target word and earlier words in the sentence based on syntax or prosody. An important result

of experiment 1 was that the final words in narrowband sentences were substantially more intelligible (by 34%) than those same words in isolation. This remained true even for LP sentences, from which semantic predictability was removed (23% difference). In comparison, broadband final words were recognized with near-perfect accuracy, both in sentence context and in isolation. The difference between narrowband LP sentences and excised words may arise because syntactic and prosodic links across words in the sentence help to restrict the number of competing lexical candidates. The results are consistent with recent findings by Grant and Seitz (2000), who compared the identification of words in isolation with words in sentence context, and found larger effects of context in conditions where bandpass filtering produced lower intelligibility.

While syntactic and prosodic links provide a basis for uncertainty reduction, nonlinguistic factors may also contribute to the difference between narrowband LP sentences and excised words. One such mechanism was proposed by Watkins and Makin (1996), who demonstrated that the perception of a test vowel preceded by a narrowband precursor phrase is altered by central processes that compensate for distortions of the communication channel, such as filtering. They proposed that listeners extract contrast-invariant features of the narrowband precursor in order to apply a form of “inverse filtering” to correct the distortion of the entire spectral envelope. If this account is correct, then the benefits of sentence context should emerge even when the syntactic links are removed from the sentence and the prosody is disrupted.

Although similar performance was found for narrowband and broadband sentences in some conditions at conversational levels (experiment 1), large differences emerged at threshold (experiment 2). SRTs for narrowband sentences were consistently elevated by as much as 30 dB compared to broadband speech. This difference in SRTs between narrowband and broadband speech is a combined function of the reduced presentation level and the sloping skirts of the filters. Warren and Bashford (1999) showed that the intelligibility of narrowband speech (1500-Hz center frequency) benefits from the residual acoustic information within the 1/3-octave passband, but receives a greater contribution from cues provided by the transition bands. They found that narrowband sentences were considerably less intelligible (24% compared to 92% keywords correct) when the filter skirts were increased from 96 dB/oct to near-vertical (approximately 1000 dB/oct). They presented their sentences at a mean level of 75 dB(A), which is at the high end of conversational speech. However, at reduced presentation levels, the low-amplitude regions of the transition bands fall below the detection threshold. The reduced audibility of spectral components in the transition bands may be responsible, at least in part, for the increased effects of filtering obtained with threshold measures.

An unexpected finding was that broadband speech maskers led to similar increases in threshold for narrowband and broadband speech. Contrary to the prediction that the reduction in bandwidth would increase the susceptibility of narrowband speech to masking, SRTs were raised by com-

parable amounts for narrowband and broadband speech (11 dB) in the presence of a 50-dB speech masker. However, this comparison may be misleading, since a 30-dB increase in overall level was required to bring the narrowband sentences up to the same (threshold) level as the corresponding broadband sentences in quiet. Comparison of the long-term average spectra of the narrowband and broadband speech revealed even greater differences in the region of the filter passband. Thus, at the levels required to make the narrowband sentences intelligible in quiet, they were relatively impervious to the effects of the 50-dB speech maskers.

V. SUMMARY AND CONCLUSIONS

(1) English sentences processed through narrow (1-ERB-bandwidth) bandpass filters with center frequencies between 1.5 and 3.0 kHz were well recognized (82%–98% correct), provided that the narrowband sentences were presented at conversational speech levels and retained a high level of linguistic redundancy.

(2) Low predictability (LP) sentences were less accurately recognized than high predictability (HP) sentences (20% lower scores), indicating the importance of semantic context. Consistent with this result, speech reception thresholds (SRTs) were at least 3 dB higher for LP than HP sentences. Predictability played a greater role as the speech signal was further degraded in conditions with maskers, suggesting that semantic predictability can be useful for “filling in the gaps” when portions of the acoustic signal are missing.

(3) Excised narrowband words were even less intelligible (by 23%) than those same words in LP sentences, indicating that nonsemantic links across words in sentences (possibly derived from syntax or prosody) provide a further contribution.

(4) Narrowband speech was as intelligible as broadband speech in several conditions when presented at conversational levels (experiment 1). However, SRTs were about 30 dB higher for narrowband compared to broadband sentences. This discrepancy reflects the contribution of spectral components in the transition bands of the filters that become less audible at the lower presentation levels used in threshold experiments.

(5) Performance was degraded by the introduction of a speech masker (a single competing talker), but surprisingly, the masker had similar effects for narrowband and broadband speech. Comparisons of the long-term spectra of narrowband and broadband target sentences and maskers revealed substantial differences in target-to-masker ratio, especially near the filter passband.

ACKNOWLEDGMENTS

The authors would like to thank Chris Turner and two anonymous reviewers for their helpful comments on the manuscript, Elaine Teoh and Tracy Current for their assistance in data collection, and Matthew Sommers and Tracey Robinson for donating their time for stimulus recording. This work was supported in part by a doctoral student fellowship from Alcatel Corporation to the senior author.

¹To stabilize the variances, percentage scores were transformed to root-arcsin proportions (Winer, 1971) and the statistical analyses in experiment 1 were repeated. The same pattern of results emerged from these analyses.

²We are grateful to an anonymous reviewer for drawing our attention to the contextual differences between the LP and HP sentences and their potential contribution to the intelligibility of the final words.

- Bell, T. S., Dirks, D. D., and Trine, T. D. (1992). “Frequency-importance functions for words in high- and low-context sentences,” *J. Speech Hear. Res.* **35**, 950–959.
- Cherry, C. (1953). “Some experiments on the recognition of speech, with one and two ears,” *J. Acoust. Soc. Am.* **25**, 975–979.
- Drullman, R., Festen, J. M., and Houtgast, T. (1996). “Effect of temporal modulation reduction on spectral contrasts in speech,” *J. Acoust. Soc. Am.* **99**, 2358–2364.
- Duquesnoy, A. J. (1983). “Effect of a single interfering noise or speech source upon the binaural sentence intelligibility of aged persons,” *J. Acoust. Soc. Am.* **74**, 739–743.
- Faulkner, A., and Rosen, S. (1999). “Contributions of temporal encodings of voicing, voicelessness, fundamental frequency, and amplitude variation to audio-visual and auditory speech perception,” *J. Acoust. Soc. Am.* **106**, 2063–2073.
- Fletcher, H. (1953). “Speech and hearing in communication,” in *The ASA Edition of Speech and Hearing in Communication*, edited by J. B. Allen (Acoustical Society of America, New York).
- Glasberg, B. R., and Moore, B. J. C. (1990). “Derivation of auditory filter shapes from notched-noise data,” *Hear. Res.* **47**, 103–138.
- Grant, K. W., and Seitz, P. F. (2000). “The recognition of isolated words and words in sentences: Individual variability in the use of sentence context,” *J. Acoust. Soc. Am.* **107**, 1000–1011.
- Grant, K. W., and Walden, B. E. (1996). “Spectral distribution of prosodic information,” *J. Speech Hear. Res.* **39**, 228–238.
- Greenberg, S. (1996). “Understanding speech understanding: Towards a unified theory of speech perception,” in *Proceedings of the ESCA Workshop on the Auditory Basis of Speech Perception*, edited by S. Greenberg and W. A. Ainsworth, pp. 1–8.
- Helfer, K. S. (1994). “Binaural cues and consonant perception in reverberation and noise,” *J. Speech Hear. Res.* **37**, 429–438.
- Huggins, A. W. F. (1975). “Temporally segmented speech,” *Percept. Psychophys.* **18**, 149–157.
- Kalikow, D. N., Stevens, K. N., and Elliott, L. L. (1977). “Development of a test of speech intelligibility in noise using sentence materials with controlled word predictability,” *J. Acoust. Soc. Am.* **61**, 1337–1351.
- Lippmann, R. P. (1996). “Accurate consonant perception without mid-frequency speech energy,” *IEEE Trans. Speech Audio Process.* **4**, 66–69.
- Lynn, J. M., and Brotman, S. R. (1981). “Perceptual significance of the CID W-22 carrier phrase,” *Ear Hear.* **2**, 95–99.
- Miller, G. A., and Licklider, J. C. R. (1950). “The intelligibility of interrupted speech,” *J. Acoust. Soc. Am.* **22**, 167–173.
- Miller, G. A., Heise, G. A., and Lichten, W. (1951). “The intelligibility of speech as a function of the context of the test materials,” *J. Exp. Psychol.* **41**, 329–335.
- Patterson, R. D., Robinson, K., Holdsworth, J., McKeown, D., Zhang, C., and Allerhand, M. H. (1992). “Complex sounds and auditory images,” in *Auditory Physiology and Perception*, edited by Y. Cazals, L. Demany, and K. Horner (Pergamon, Oxford), pp. 429–446.
- Pavlovic, C. V. (1994). “Band importance functions for audiological applications,” *Ear Hear.* **15**, 100–104.
- Peters, R. W., Moore, B. C., and Baer, T. (1998). “Speech reception thresholds in noise with and without spectral and temporal dips for hearing-impaired and normally hearing people,” *J. Acoust. Soc. Am.* **103**, 577–587.
- Plomp, R., and Mimpen, A. M. (1979). “Improving the reliability of testing the speech reception threshold for sentences,” *Audiology* **8**, 43–52.
- Pollack, I., and Pickett, J. M. (1958). “Masking of speech by noise at high sound levels,” *J. Acoust. Soc. Am.* **30**, 127–130.
- Revoile, S., Kozma-Spytek, L., Holden-Pitt, L., Pickett, J., Droge, J. (1995). “Acoustic-phonetic context considerations for speech recognition testing of hearing-impaired listeners,” *Ear Hear.* **16**, 254–262.
- Silverman, S. R., and Hirsch, I. J. (1955). “Problems related to the use of speech in clinical audiometry,” *Ann. Otol. Rhinol. Laryngol.* **64**, 1234–1244.

- Slaney, M. (1993). "An efficient implementation of the Patterson-Holdsworth Auditory Filter Bank," Apple Technical Report # 35, Apple Computer, Inc.
- Steeneken, H. J., and Houtgast, T. (1980). "A physical method for measuring speech-transmission quality," *J. Acoust. Soc. Am.* **67**, 318–326.
- Stevens, K. N. (1997). "Articulatory–Acoustic–Auditory Relationships," in *The Handbook of Phonetic Sciences*, edited by W. J. Hardcastle and J. Laver (Blackwell, Oxford).
- Stickney, G. S., and Assmann, P. F. (1997). "Intelligibility of bandpass-filtered speech," *J. Acoust. Soc. Am.* **100**, 2680 (A).
- Stickney, G. S., and Assmann, P. F. (1998). "Masking of filtered speech by a single competing voice," Abstracts of the 21st Midwinter Meeting of the Association for Research in Otolaryngology, p. 43.
- Warren, R. M., and Bashford, Jr., J. A. (1999). "Intelligibility of 1/3-octave speech: Greater contribution of frequencies outside than inside the nominal passband," *J. Acoust. Soc. Am.* **106**, L47–52.
- Warren, R. M., Riener, K. R., Bashford, Jr., J. A., and Brubaker, B. S. (1995). "Spectral redundancy: Intelligibility of sentences heard through narrow spectral slits," *Percept. Psychophys.* **57**, 175–182.
- Watkins, A. J., and Makin, S. J. (1996). "Effects of spectral contrast on perceptual compensation for spectral-envelope distortion," *J. Acoust. Soc. Am.* **99**, 3749–3757.
- Winer (1971). *Statistical Principles in Experimental Design* (McGraw-Hill, New York).

Recognition of spectrally asynchronous speech by normal-hearing listeners and Nucleus-22 cochlear implant users

Qian-Jie Fu^{a)} and John J. Galvin III

Department of Auditory Implants and Perception, House Ear Institute, 2100 West Third Street, Los Angeles, California 90057

(Received 9 June 2000; accepted for publication 28 November 2000)

This experiment examined the effects of spectral resolution and fine spectral structure on recognition of spectrally asynchronous sentences by normal-hearing and cochlear implant listeners. Sentence recognition was measured in six normal-hearing subjects listening to either full-spectrum or noise-band processors and five Nucleus-22 cochlear implant listeners fitted with 4-channel continuous interleaved sampling (CIS) processors. For the full-spectrum processor, the speech signals were divided into either 4 or 16 channels. For the noise-band processor, after band-pass filtering into 4 or 16 channels, the envelope of each channel was extracted and used to modulate noise of the same bandwidth as the analysis band, thus eliminating the fine spectral structure available in the full-spectrum processor. For the 4-channel CIS processor, the amplitude envelopes extracted from four bands were transformed to electric currents by a power function and the resulting electric currents were used to modulate pulse trains delivered to four electrode pairs. For all processors, the output of each channel was time-shifted relative to other channels, varying the channel delay across channels from 0 to 240 ms (in 40-ms steps). Within each delay condition, all channels were desynchronized such that the cross-channel delays between adjacent channels were maximized, thereby avoiding local pockets of channel synchrony. Results show no significant difference between the 4- and 16-channel full-spectrum speech processor for normal-hearing listeners. Recognition scores dropped significantly only when the maximum delay reached 200 ms for the 4-channel processor and 240 ms for the 16-channel processor. When fine spectral structures were removed in the noise-band processor, sentence recognition dropped significantly when the maximum delay was 160 ms for the 16-channel noise-band processor and 40 ms for the 4-channel noise-band processor. There was no significant difference between implant listeners using the 4-channel CIS processor and normal-hearing listeners using the 4-channel noise-band processor. The results imply that when fine spectral structures are not available, as in the implant listener's case, increased spectral resolution is important for overcoming cross-channel asynchrony in speech signals. © 2001 Acoustical Society of America. [DOI: 10.1121/1.1344158]

PACS numbers: 43.71.Es, 43.71.Ky, 43.66.Ts [CWT]

I. INTRODUCTION

It has been widely assumed that the spectro-temporal details of the short-term acoustic spectrum are essential for understanding spoken language. However, reduced auditory (spectral and temporal) resolution, competing speech and noise, cross-channel spectral desynchronization (due to reverberant listening environments) can all impact listeners' ability to perform such detailed acoustic analyses. The highly redundant information available in speech allows for various forms and degrees of signal degradation before speech perception is adversely affected. Indeed, results from several perceptual experiments with normal-hearing adults indicate that a detailed spectro-temporal analysis of speech may be less important than traditionally thought.

An earlier study by Remez *et al.* (1983) showed that phonetic information could be conveyed by sine wave representations of speech signals. In their study, the tonal patterns were made from three sinusoids whose frequency and amplitude were equal to the respective peaks of the first three

formants of natural-speech utterances. Unlike natural and most synthetic speech, the spectrum of sinewave speech contains neither harmonics nor broadband formants, and could be described as sounding grossly unnatural in terms of vocal timbre. Despite the marked alteration of the short-term speech spectrum, listeners were able to perceive the phonetic content. The investigators argued that phonetic perception might then depend on properties of coherent spectrum variation (a second-order property of the acoustic signal) rather than any particular set of acoustic elements present in speech signals.

Warren *et al.* (1995) measured the intelligibility of the Central Institute of the Deaf (CID) sentences when heard through narrow spectral slits. They found that very little spectral information was required to identify the key words in the "everyday speech" sentences. Near-perfect intelligibility was obtained for single $\frac{1}{3}$ -oct bands whose center frequencies were in the vicinity of 1500 Hz. Greenberg *et al.* (1998) also measured sentence recognition by normal-hearing subjects listening to narrow-band speech. In their study, each sentence was spectrally partitioned into 14 $\frac{1}{3}$ -oct-wide channels and the stimulus for any single presentation

^{a)}Electronic mail: qfu@hei.org

consisted of between 1 and 4 channels presented concurrently. They found that nearly 90% of sentences could be accurately identified with only 4 of the 14 spectral channels presented synchronously, despite the fact that more than 70% of the spectrum was missing.

Shannon *et al.* (1995) measured speech performance as a function of spectral resolution. In their approach, speech was divided into several frequency bands. The temporal envelope was extracted by half-wave rectification and low-pass filtering and used to modulate noise that was spectrally shaped by the same filters as those used in the analysis bands. The spectral resolution was systematically changed by manipulating the number of bands. Their results showed near-perfect sentence recognition when only four frequency bands were available, suggesting that the acoustic spectrum of speech is redundant enough to overcome reduced spectral resolution. Similar results have been reported by other studies (Fu *et al.*, 1998; Dorman *et al.*, 1998).

The necessity of detailed spectro-temporal information of the short-term acoustic spectrum has also been challenged by studies involving spectrally asynchronous speech. Spectrally asynchronous speech is somewhat analogous to the delayed channel synchronization and resultant spectral smearing found in reverberant listening environments. Arai and Greenberg (1998) measured speech intelligibility in the presence of cross-channel spectral desynchronization. In their study, the spectrum of speech signals was partitioned into $\frac{1}{4}$ -oct bands and the onset of each band was randomly shifted in time relative to the others so as to desynchronize spectral information across frequency. In this type of signal processing, although a large amount of spectral resolution is preserved, the significant alteration of cross-channel spectral cues can disrupt the speech decoding process and thereby degrade intelligibility. They found that normal-hearing listeners were highly tolerant of cross-channel spectral desynchronization. Speech intelligibility remained relatively unaffected until the average asynchrony spanned three or more phonetic segments. The investigators also found that such perceptual robustness was significantly correlated with the magnitude of the low-frequency (3–6 Hz) modulation spectrum, thus illustrating the importance of syllabic segmentation and analysis for speech perception.

These results indicate that the spectro-temporal details of the short-term acoustic spectrum may not be required for speech perception because of the spectral and temporal redundancy contained in speech signals. Unfortunately, such high degrees of the spectral and temporal redundancy may not be available for some listeners, such as cochlear implant users.

The cochlear implant is an electronic device that transforms acoustic sounds into electrical signals that directly stimulate remaining auditory nerve fibers, and can thereby partially restore the hearing sensation to profoundly deaf listeners. Modern multi-channel cochlear implant devices divide speech sounds into several frequency bands, extract the temporal envelope information from each band, convert the acoustic amplitudes into electric currents, and deliver the electric currents to electrodes located in the different places within the cochlea. To recreate the tonotopic distribution of

activity within the normal cochlea, the envelope cues from low-frequency bands are delivered to electrodes located near the apex and the envelope cues from high-frequency bands are delivered to basal electrodes. Although this approach can preserve the temporal envelope within each frequency band or the approximate spectral envelope across frequency bands, the detailed fine structure inherent in each band is lost.

Many cochlear implant users are able to achieve high levels of speech recognition in quiet despite the loss of fine spectral information; similar results were reported in normal-hearing subjects listening to spectrally degraded speech via noise-band speech processors (Shannon *et al.*, 1995; Fu *et al.*, 1998; Dorman *et al.*, 1998). However, speech performance of cochlear implant users is highly susceptible to adverse listening conditions such as noise or reverberant environments. While there has been a fair amount of research involving implant listeners' performance in noise, little is known about the effect of cross-channel spectral desynchronization on speech intelligibility when the spectral resolution of speech signals is severely limited and/or the fine spectral structures are not available. The purpose of the present study was to investigate the effect of fine spectral structure and spectral resolution on recognition of spectrally asynchronous speech by normal-hearing listeners and cochlear implant users. Several hypotheses concerning spectral resolution, fine spectral structure, and spectrally asynchronous speech perception were explored.

The first hypothesis was that a loss of fine spectral information would cause listeners to perform more poorly when speech signals were spectrally desynchronized. A noise-band channel vocoder (Shannon *et al.*, 1995) was used to eliminate the fine spectral structure available in the speech signals. Sentence recognition was measured in normal-hearing listeners using either full-spectrum processors (with fine spectral information) or noise-band processors (without fine spectral information) as a function of the amount of cross-channel asynchrony. The contribution of fine spectral information to the recognition of spectrally asynchronous speech was assessed by comparing normal-hearing listeners' performance between the full-spectrum processor and noise-band processor.

The second hypothesis was that a reduction of spectral resolution would reduce listeners' ability to recognize spectrally asynchronous speech. Performance with a noise-band channel vocoder was used to quantify the effect of reduced spectral resolution on spectrally asynchronous speech recognition. Sentence recognition was measured in normal-hearing listeners using either 16-channel noise-band processors (fine spectral resolution) or 4-channel noise-band processors (coarse spectral resolution) as a function of the amount of cross-channel asynchrony. The effect of spectral resolution was determined by comparing normal-hearing listeners' performance between the 16- and 4-channel noise-band processors.

The third hypothesis was that cochlear implant listeners could perform as well as normal-hearing listeners listening to corresponding spectral conditions. The continuous interleaved sampling (CIS) strategy is a multi-channel vocoder-like speech processor that has been used successfully in sev-

TABLE I. Subject information for the Nucleus-22 cochlear implant listeners who participated in the present study.

Subject	Age	Gender	Cause of deafness	Duration of use (years)	Insertion depth (no. of rings out)
N3	55	M	Trauma	6	3
N4	39	M	Trauma	4	4
N7	54	M	Unknown	4	0
N9	55	F	Hereditary	7	4
N19	68	M	Noise-induced	3	6

eral implant systems (Wilson *et al.*, 1991). Sentence recognition was measured in cochlear implant listeners fitted with experimental 4-channel CIS speech processors as a function of the amount of cross-channel asynchrony. The sentence recognition performance of cochlear implant listeners was compared to that of normal-hearing subjects listening to the 4-channel noise-band processor.

II. METHODS

A. Subjects

Six normal-hearing (NH) listeners aged 25 to 35 and five Nucleus-22 cochlear implant (CI) users aged 40 to 60 participated in the present experiment. All NH subjects had thresholds better than 15 dB HL at audiometric test frequencies from 250 to 8000 Hz and all were native speakers of American English. All implant subjects had at least five years experience utilizing the SPEAK speech processing strategy (Nucleus-22 device) and all were native speakers of American English. The Nucleus-22 speech processor with the SPEAK strategy divides the acoustic signal into 20 frequency bands, extracts the amplitude envelope from each band, and stimulates the electrodes that correspond to the six to ten bands with the highest amplitudes (Seligman and McDermott, 1995). All implant subjects had 20 active electrodes available for use. Table I contains relevant information about the five CI subjects. All subjects were paid for their efforts and gave informed consent before proceeding with the experiment.

B. Stimuli

Speech materials consisted of words in sentences taken from the Hearing in Noise Test (HINT) sentence set (Nilsson *et al.*, 1994). This set consists of 260 phonetically balanced high-context sentences. The sentences are organized into 26 lists with ten sentences per list. The intelligibility of HINT sentence recognition was controlled by experimental speech processors. Two kinds of speech processors (full-spectrum and noise-band) were created for normal-hearing listeners in this experiment. For the full-spectrum processor, the speech signal was band-pass filtered into either 4 or 16 frequency bands using eighth-order Butterworth filters. The corner frequencies of the bands were 300, 713, 1509, 3043, and 6000 Hz for the 4-channel processor and 300, 379, 473, 583, 713, 866, 1046, 1259, 1509, 1804, 2152, 2561, 3043, 3612, 4281, 5070, and 6000 Hz for the 16-channel processor. The output

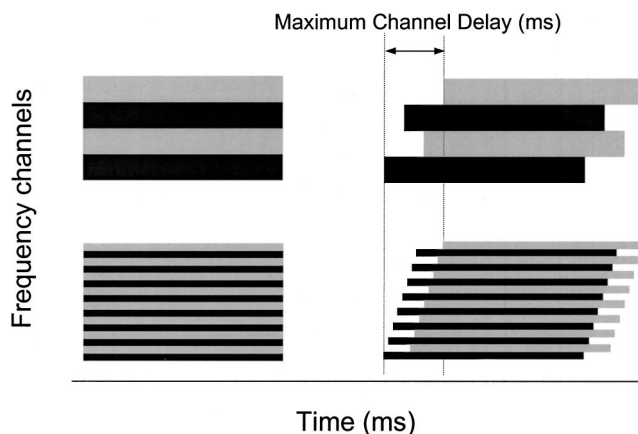


FIG. 1. Schematic diagram of the delay patterns across channels in both 4-channel processor (top) and 16-channel processor (bottom).

of each channel was then time-shifted, varying the maximum channel delay from 0 to 240 ms (in 40-ms steps). The delay sequences used to desynchronize channels of spectral information were generated as follows. For odd-numbered channels, the amount of delay for a particular channel can be represented as

$$D_i = \frac{i-1}{N-1} \times \frac{D_{\max}}{2}, \quad i = 1, 3, 5, \dots, N-1, \quad (1)$$

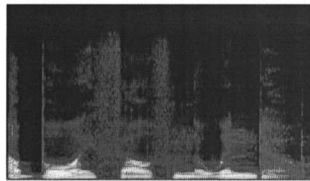
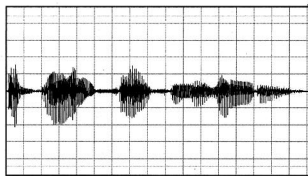
where D_i is the amount of delay in i th channel, D_{\max} is the maximum channel delay, and N is the number of channels (either 4 or 16). Similarly, for even-numbered channels, the amount of delay for a particular channel can be represented as

$$D_i = \frac{N+i-2}{N-1} \times \frac{D_{\max}}{2}, \quad i = 2, 4, 6, \dots, N. \quad (2)$$

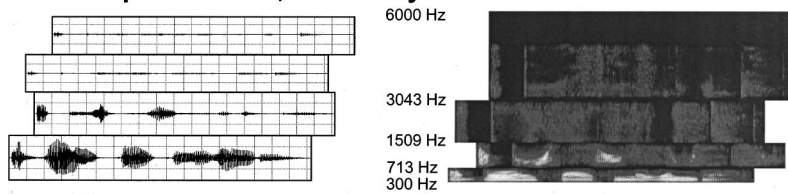
Based on this fixed delay sequence, the maximum channel delay (D_{\max}) will always occur between channel 1 and channel N . For example, for a 4-channel processor with a maximum delay of 240 ms, the channel delays were 0, 160, 80, 240 for channel 1, 2, 3, 4, respectively. In this way, a minimum of 80-ms delay was placed between adjacent channels, with 160 ms between channels 1 and 2 and between channels 3 and 4. Figure 1 shows the delay patterns across channels in both the 4-channel (top) and 16-channel processors (bottom). Figure 2 shows the waveform and spectrograph representation of the 4-channel full-spectrum processor and the 4-channel noise-band processor for the 240-ms maximum delay condition.

For the noise-band processor, after band-pass filtering into 4 or 16 channels, the envelope of each channel was extracted by half-wave rectification and low-pass filtering at 160 Hz using eighth-order Butterworth filters. The envelope was then used to modulate noise of the same bandwidth as the analysis band, thus eliminating the fine spectral structures available in the full-spectrum processor. Channel delay sequences were generated using the same method as in the full-spectrum processor. To examine frequency-specific effects of spectral asynchrony, one additional delay sequence

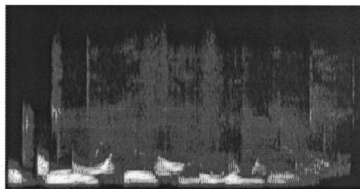
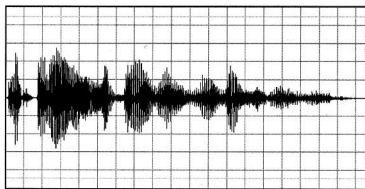
A: Original speech



B: Band-pass filtered, then delayed



C: 4-channel full-spectrum speech with maximum delay (240ms)



D: 4-channel noise-band speech with maximum delay (240ms)

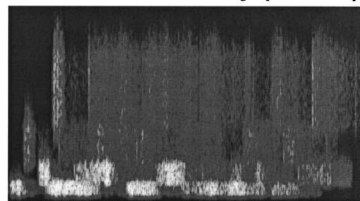
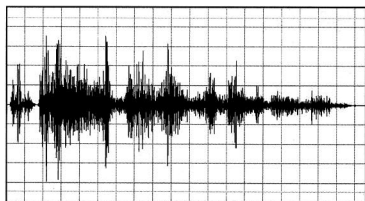


FIG. 2. Waveform and spectrogram representations of the 4-channel full-spectrum processor and 4-channel noise-band processor at the 240-ms maximum delay condition. (a) original speech; (b) the band-pass filtered and delayed; (c) 4-channel full-spectrum speech with the maximum delay at 240 ms; and (d) 4-channel noise-band speech with the maximum delay at 240 ms.

was created for the 4-channel noise-band processor. In this condition, each of the four channels was delayed 120 ms in separate trials.

For CI users, experimental speech processors were fitted with the continuous interleaved sampling (CIS) speech processing strategy (Wilson *et al.*, 1991). The experimental CIS processors provided better comparison to the noise-band processors used for NH listeners than would the clinical SPEAK processors subjects used regularly. Due to the limitation of overall pulse rate for the Nucleus-22 device, only 4-channel experimental CIS speech processors were created for CI users. The 4-channel CIS processor was implemented through a custom research interface (Shannon *et al.*, 1990), thereby bypassing subjects' Spectra-22 speech processors. The signal was band-pass filtered into four broad frequency bands using eighth-order Butterworth filters. The corner frequencies of the bands were 300, 713, 1509, 3043, and 6000 Hz. The envelope of the signal in each band was extracted by half-wave rectification and low-pass filtering at 160 Hz. The acoustic amplitude (40-dB range) was transformed into electric amplitude by a power-law function with an exponent of 0.2 ($E = A^{0.2}$; Fu and Shannon, 1998) between each subject's threshold (T-level) and upper level of loudness (C-level). This transformed amplitude was then used to modulate the amplitude of a 500-Hz biphasic pulse train with a 100- μ s/phase pulse duration, and delivered to four electrode pairs interleaved in time: (18,22), (13,17), (8,12), and (3,7). Note

that a relatively broad stimulation mode (BP+3) was used in the present study because several subjects were unable to reach an upper level of loudness (C-level) on the apical electrode pairs with BP+1 stimulation mode. Channel delay sequences were generated using the same method as in the full-spectrum and noise-band processors. The additional delay sequence was also used to examine any frequency-specific effects of spectral asynchrony.

C. Procedures

For HINT sentence recognition, a list was chosen randomly from among 26 lists, and sentences were chosen randomly, without replacement, from the ten sentences within that list. The subjects gave their responses verbally and the number of correct key words was scored online by the experimenter. For NH listeners, the speech materials were presented at 70 dBA in free field via a loudspeaker (Tannoy Reveal) in a sound-treated booth (IAC double-walled). Six out of the 26 lists were presented twice because of the insufficient number of lists per condition (32 conditions versus 26 lists). However, the conditions with repeated sentence lists were conducted in different time periods (either several hours or several days apart) and different lists were repeated for each subject. The final score for each condition was the average of one list (about 50 key words per list). For CI listeners, the sentences were presented at comfortably loud

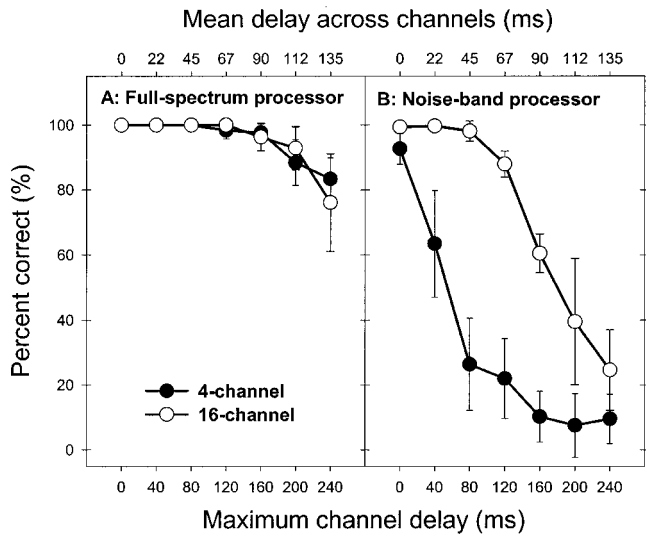


FIG. 3. Sentence recognition as a function of maximum channel delay. (a) Full-spectrum processor and (b) noise-band processor. The filled circles show the mean scores for 4-channel processor and the open circles show the mean scores for 16-channel processor. The error bars represent one standard deviation.

levels via a custom research interface (Shannon *et al.*, 1990). Each of the 26 sentence lists was presented only once; no list was repeated for any condition. The final score for each condition was the average of two to four lists. The order of conditions was randomized and counterbalanced across subjects for both NH and CI users. Note that some NH listeners had been previously exposed to the HINT sentences in other experiments; all CI listeners had previously been tested with the HINT materials in other experiments.

III. RESULTS

Figure 3 shows the percent of words in sentences correctly identified as a function of the maximum channel delay by NH listeners. Panel (a) shows the recognition scores for the full-spectrum processors. For the 16-channel full-spectrum processor, there was no significant drop in performance until the maximum channel delay was 240 ms; even at this extreme delay, average performance only dropped about 20 percentage points. For the 4-channel full-spectrum processor, there was no significant drop in performance until the maximum channel delay was 200 ms. Again, even at this extreme delay, average performance remained high at around 80% correct.

Figure 3(b) shows the recognition scores for the noise-band processors. For the 16-channel noise-band processor, performance dropped significantly for a maximum channel delay of 160 ms. Average performance continued to decline to 24% correct at the 240-ms maximum channel delay. For the 4-channel noise-band processor, there was a significant drop in performance, even with a maximum channel delay of only 40 ms. Average performance continued to drop as the amount of asynchrony increased, nearing chance level at 160 ms.

Statistical analyses were performed to determine what, if any, differential effects of spectral resolution on spectrally asynchronous speech perception. A two-way ANOVA re-

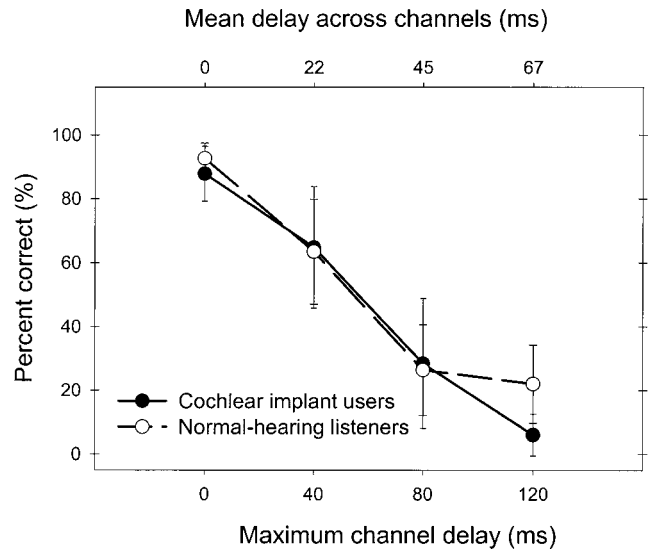


FIG. 4. Sentence recognition as a function of maximum channel delay for both normal-hearing listeners using the 4-channel noise-band processor and cochlear implant listeners using the 4-channel CIS processor. The filled circles show the mean scores from five cochlear implant listeners and the open circles show the mean scores from six normal-hearing listeners. The error bars represent one standard deviation.

vealed no significant interaction between the 4- and 16-channel full-spectrum processors [$F(6,70)=1.35$, $p=0.247$]; the high performance for both spectral conditions was most likely due to the available spectro-temporal details. However, recognition scores between the 16-channel full-spectrum processor and 16-channel noise-band processor began to significantly differ when the maximum channel delay was 120 ms. The difference is even more evident when comparing the 4-channel full-spectrum processor and 4-channel noise-band processor. The best performance with the 4-channel noise-band processor was at 0-ms maximum channel delay where average performance was only seven percentage points lower than that obtained with the 4-channel full-spectrum processor. While the 4-channel full-spectrum processor performance remained high even at a maximum channel delay of 240 ms, the 4-channel noise-band processor performance was degraded at only 40 ms. A two-way ANOVA revealed a significant interaction between the 16-channel full-spectrum processor and 16-channel noise-band processor [$F(6,70)=27.57$, $p<0.001$] as well as between the 4-channel full-spectrum and 4-channel noise-band processors [$F(6,70)=37.01$, $p<0.001$]; here the effects of spectral asynchrony were more pronounced for spectrally coarse speech. A significant interaction was also observed between 4- and 16-channel noise-band processors [$F(6,70)=17.28$, $p<0.001$]; the absence of spectro-temporal details was compensated by a greater number of channels.

Figure 4 shows the percent of words in sentences correctly identified by CI listeners using the experimental 4-channel CIS processors and NH listeners using the 4-channel noise-band processors, as a function of the maximum channel delay. The solid line represents the mean recognition score from five CI listeners and the dashed line represents the mean recognition score from six NH listeners. Implant and normal-hearing performance was very compa-

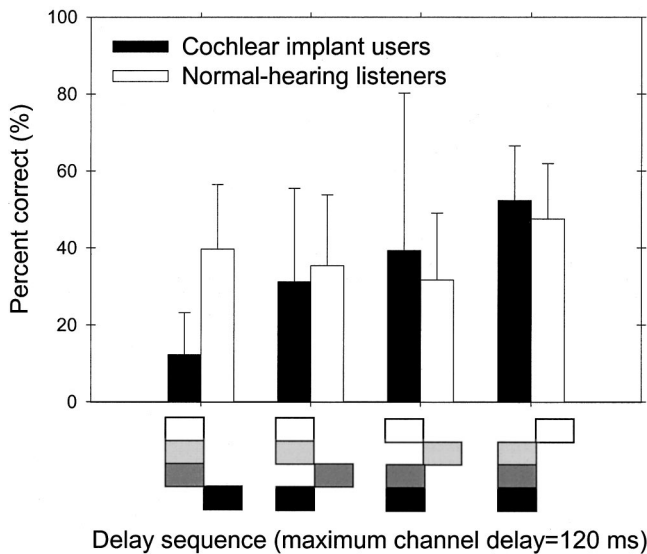


FIG. 5. Sentence recognition as a function of channel delay sequence for both normal-hearing listeners using the 4-channel noise-band processor and cochlear implant listeners using the 4-channel CIS processor. The filled bars show the mean scores from five cochlear implant users and the open bars show the mean scores from six normal-hearing listeners. The error bars represent one standard deviation.

able for these delay conditions. A one-way ANOVA revealed a significant effect of spectral asynchrony on sentence recognition for CI listeners [$F(3,16) = 29.82, p < 0.001$]. A two-way ANOVA also revealed no significant interaction between CI users with the 4-channel CIS processor and NH listeners with the 4-channel noise-band processor [$F(3,16) = 1.01, p = 0.402$].

Figure 5 shows the results for the frequency-specific asynchrony conditions conducted with NH listeners using the 4-channel noise-band processor and CI listeners using the 4-channel CIS processor. The pictures under the ordinate show the delay sequence; the lowest bar represents the lowest frequency band. On average, delaying the highest frequency channel (3–6 kHz) had the least effect, although performance did drop about 40 percentage points as compared to the 4-channel noise-band processor with no delay. While there is significant intersubject variability in this data set, the overall pattern was consistent across subjects. A one-way ANOVA showed no significant effect of delay sequence both for CI listeners [$F(3,20) = 2.66, p = 0.084$] and NH listeners [$F(3,20) = 0.984, p = 0.42$] as well as no significant interaction between CI users and NH listeners [$F(3,36) = 1.76, p = 0.172$]. However, a Student *t*-test revealed a slightly significant difference between NH listeners and CI users when delaying the lowest frequency channel ($p = 0.038$).

IV. DISCUSSION

The present results clearly demonstrate that the intelligibility of full-spectrum speech is highly tolerant of cross-channel spectral asynchrony, indicating that a detailed spectro-temporal analysis of the speech signal is not required to understand spoken language. The present results are in general agreement with the results of Arai and Greenberg (1998). There are, however, slight differences between the

present study's results and those of the previous studies. In the present study, average recognition scores were about 80% correct, even when the maximum channel delay reached 240 ms. However, in the previously cited study, recognition scores were only about 75% correct for 140 ms of maximum channel delay; intelligibility was further reduced to 50% correct when the cross-channel asynchrony exceeded 200 ms of maximum channel delay. One explanation for this difference may be the different speech materials used in the two studies. In the present study, recognition of words in sentences was measured using the Hearing in Noise Test (HINT) sentences (Nilsson *et al.*, 1994); in the studies by Greenberg and his colleagues (Greenberg *et al.*, 1998; Arai and Greenberg, 1998), the DARPA TIMIT acoustic-phonetic continuous speech corpus was used. The sentences are of easy-to-moderate difficulty for HINT and of moderate-to-hard difficulty for TIMIT. Besides a difference in sentence difficulty, the mean sentence duration for these two speech corpora also differs significantly. The average duration per phoneme is about 100 ms for the HINT sentences, while the mean duration per phoneme for the TIMIT sentences is about 72 ms.

When the spectro-temporal details were available to listeners (full-spectrum processors), spectral desynchronization only had a minor effect on speech intelligibility. However, the loss of spectro-temporal details had a dramatic effect on speech recognition in the presence of cross-channel spectral asynchrony; when the cross-channel spectral cues were synchronized (0 ms maximum channel delay), the loss of these spectro-temporal details (noise-band processors) had only a minor effect. As shown in Fig. 3, speech performance between the 16-channel full-spectrum and noise-band processors began to significantly differ at 120 ms of maximum channel delay, indicating that the spectro-temporal fine structure contributed greatly in overcoming spectral asynchrony in speech. This contribution is even more evident when comparing the 4-channel full-spectrum and noise-band processors. While performance with the 4-channel full-spectrum processor remained high even at 240 ms of maximum channel delay, performance with the 4-channel noise-band processor was severely degraded at only 40 ms. The difference in performance between the full-spectrum and noise-band processors indicates that the fine spectral structures provide the redundant spectro-temporal information necessary for speech recognition under adverse listening environments, such as noisy or reverberant rooms.

When the spectro-temporal details are not available, as in implant users' case, spectral resolution becomes very important for overcoming adverse listening situations. The contribution of increased spectral resolution is most apparent when comparing performance between the 4- and 16-channel noise-band processors. Again, the 4-channel noise-band processor showed a significant decline in performance at only 40 ms of maximum channel delay. However, performance with the 16-channel noise-band processor began to drop significantly at the much longer 160-ms condition; at the extreme delay of 240 ms, average performance was about 30% correct, well above the chance level performance exhibited for this delay with the 4-channel noise-band processor. The

importance of spectral resolution when fine spectral structures are not available has also been observed for other adverse listening conditions, such as noisy backgrounds (Fu *et al.*, 1998; Dorman *et al.*, 1998).

There are significant similarities between CI and NH listeners' ability to perceive spectrally asynchronous speech. When the same coarse spectral resolution was available (4-channel processors), CI users performed as well as NH listeners in most conditions. This suggests a potential commonality between acoustic hearing and electric hearing for speech perception in the presence of cross-channel asynchrony. This result also indicates that the CI users are likely to be highly susceptible to cross-channel asynchrony due to the loss of fine spectral structures. These CI subjects' performance in the tests may have been much better had they been listening via a processor with more spectral channels, e.g., the clinical SPEAK processor. Some interesting differences were also observed between NH listeners and CI users. One difference was observed at 120-ms maximal channel delay, where average CI users' performance was only 6% correct while NH listeners scored about 22% correct. Another difference was observed for the frequency-specific delay conditions. For NH listeners, a delay of 120 ms in any one frequency band had an equally detrimental effect on speech intelligibility. However, the delay of the lowest frequency band showed a much more detrimental effect on speech intelligibility for CI listeners than any of the other frequency channels. It remains unclear why the CI listeners were more sensitive to the delay of the lowest frequency bands. One possible explanation is that CI users rely on the spectral cues from the low-frequency channel more than those from the high-frequency channels.

V. SUMMARY AND CONCLUSION

A detailed auditory analysis of the short-term spectrum is not required to understand spoken language. A spectral representation that lacks fine spectro-temporal details may be sufficient for high levels of sentence recognition, at least under ideal listening conditions. However, the loss of fine spectral information has a marked detrimental effect on speech intelligibility in the presence of cross-channel spectral asynchrony. The results indicate that the redundant information in speech signals may be contained in the fine spectro-temporal cues and this redundancy within speech signals is important in overcoming adverse listening environments. The recognition pattern is remarkably similar between normal-hearing listeners using the 4-channel noise-band processor and cochlear implant listeners using the

4-channel CIS processor. The results imply that when fine spectral structures are not available, as in the implant listener's case, increased spectral resolution is very important in overcoming spectral distortions such as cross-channel asynchrony in speech signals.

ACKNOWLEDGMENTS

We appreciate the efforts of all subjects, especially the cochlear implant users. We are grateful to Dr. Chris Turner, Dr. Ken Grant, Dr. Bob Shannon, Dr. Monita Chatterjee, and an anonymous reviewer for useful suggestions on an earlier draft of this article. This research was supported by Grant No. R03-DC-03861 and Contract No. N01-DC-92100 from National Institute of Deaf and Communication Disorders (NIDCD).

- Arai, T., and Greenberg, S. (1998). "Speech intelligibility in the presence of cross-channel spectral asynchrony," in IEEE International Conference on Acoustics, Speech and Signal Processing, Seattle, pp. 933–936.
- Dorman, M. F., Loizou, P. C., Fitzke, J., and Tu, Z. (1998). "The recognition of sentences in noise by normal-hearing listeners using simulations of cochlear-implant signal processors with 6–20 channels," *J. Acoust. Soc. Am.* **104**, 3583–3585.
- Fu, Q.-J., and Shannon, R. V. (1998). "Effects of amplitude nonlinearity on phoneme recognition by cochlear implant users and normal-hearing listeners," *J. Acoust. Soc. Am.* **104**, 2570–2577.
- Fu, Q.-J., Shannon, R. V., and Wang, X. (1998). "Effects of noise and number of channels on vowel and consonant recognition: Acoustic and electric hearing," *J. Acoust. Soc. Am.* **104**, 3586–3596.
- Greenberg, S., Arai, T., and Silipo, R. (1998). "Speech intelligibility derived from exceedingly sparse spectral information," in Proceedings of the International Conference of Spoken Language Processing, Sydney, 1–4 December.
- Nilsson, M., Soli, S. D., and Sullivan, J. A. (1994). "Development of the Hearing in Noise Test for the measurement of speech reception thresholds in quiet and in noise," *J. Acoust. Soc. Am.* **95**, 1085–1099.
- Remez, R. E., Rubin, P. E., and Pisoni, D. B. (1983). "Coding of the speech spectrum in three time-varying sinusoids," *Ann. N.Y. Acad. Sci.* **405**, 485–489.
- Seligman, P. M., and McDermott, H. J. (1995). "Architecture of the Spectra-22 speech processor," *Ann. Otol. Rhinol. Laryngol.* **104**, Suppl. 166, 139–141.
- Shannon, R. V., Adams, D. D., Ferrel, R. L., Palumbo, R. L., and Grantgenett, M. (1990). "A computer interface for psychophysical and speech research with the Nucleus cochlear implant," *J. Acoust. Soc. Am.* **87**, 905–907.
- Shannon, R. V., Zeng, F.-G., Kamath, V., Wygonski, J., and Ekelid, M. (1995). "Speech recognition with primarily temporal cues," *Science* **270**, 303–304.
- Warren, R. M., Riener, K. R., Bashford, Jr., J. A., and Brubaker, B. S. (1995). "Spectral redundancy: Intelligibility of sentences heard through narrow spectral slits," *Percept. Psychophys.* **57**, 175–182.
- Wilson, B. S., Finley, C. C., Lawson, D. T., Wolford, R. D., Eddington, D. K., and Rabinowitz, W. M. (1991). "New levels of speech recognition with cochlear implants," *Nature (London)* **352**, 236–238.

Vowel perception by adults and children with normal language and specific language impairment: Based on steady states or transitions?

Joan E. Sussman^{a)}

Department of Communicative Disorders and Sciences, University at Buffalo, 105 Cary Hall,
3435 Main Street, Buffalo, New York 14214

(Received 12 October 1999; accepted for publication 19 December 2000)

The current investigation studied whether adults, children with normally developing language aged 4–5 years, and children with specific language impairment, aged 5–6 years identified vowels on the basis of steady-state or transitional formant frequencies. Four types of synthetic tokens, created with a female voice, served as stimuli: (1) steady-state centers for the vowels [i] and [æ]; (2) vowelless tokens with transitions appropriate for [bib] and [bæb]; (3) “congruent” tokens that combined the first two types of stimuli into [bib] and [bæb]; and (4) “conflicting” tokens that combined the transitions from [bib] with the vowel from [bæb] and vice versa. Results showed that children with language impairment identified the [i] vowel more poorly than other subjects for both the vowelless and congruent tokens. Overall, children identified vowels most accurately in steady-state centers and congruent stimuli (ranging between 94%–96%). They identified the vowels on the basis of transitions only from “vowelless” tokens with 89% and 83.5% accuracy for the normally developing and language impaired groups, respectively. Children with normally developing language used steady-state cues to identify vowels in 87% of the conflicting stimuli, whereas children with language impairment did so for 79% of the stimuli. Adults were equally accurate for vowelless, steady-state, and congruent tokens (ranging between 99% to 100% accuracy) and used both steady-state and transition cues for vowel identification. Results suggest that most listeners prefer the steady state for vowel identification but are capable of using the onglide/offglide transitions for vowel identification. Results were discussed with regard to Nittrouer’s developmental weighting shift hypothesis and Strange and Jenkin’s dynamic specification theory. © 2001 Acoustical Society of America. [DOI: 10.1121/1.1349428]

PACS numbers: 43.71.Es, 43.71.Ft [CWT]

I. INTRODUCTION

There is general agreement that speech perception abilities in children are not completely adult-like even by 11 years of age (e.g., Parnell and Amerman, 1978; Elliott *et al.*, 1981; Ohde and Haley, 1997; Sussman and Carney, 1989). However, there is no agreement regarding why children’s perception is not adult-like. According to one set of data, sensory differences are responsible for auditory and speech perception differences of children and adults. This sensory hypothesis has attempted to locate the site of maturation in the auditory system. The cochlea is developed at birth (Schneider and Trehub, 1992), which suggests that the peripheral auditory system should not be responsible for speech perception differences between children and adults.

In line with the sensory explanation, the speech perception differences of children have been related to why children also demonstrate poorer detection of pure tones in quiet and in noise (e.g., Elliott and Katz, 1980; Trehub *et al.*, 1988). Elliott and Katz (1980) reported that normally developing 6-year-olds had significantly poorer thresholds in quiet for 500-Hz tones compared with 10-year-olds and adults. Children with “learning problems” performed even more poorly than age-matched peers. Trehub *et al.* (1988) similarly found that for stimuli with center frequencies of 400

and 1000 Hz, maximal sensitivity was not found until 10 years of age. They noted that children’s sensitivity, particularly for lower frequencies, continued to develop into late childhood and that 5-year-olds in a prior study (Schneider *et al.*, 1986) had poorer sensitivity to most frequencies than adults. Schneider and Trehub (1992) further stated that for children over 3 years of age, differences in their sensitivity were believed to be linked to “changes in the signal-to-noise ratio required for their detection” (p. 43). More recently, Berg and Boswell (2000) showed that very young children did not demonstrate adult-like discrimination of intensity increments at low intensities until sometime after 3 years of age. They believed that immaturities in sensory mechanisms were responsible for the differences. Continued development of the neural pathways in the “central auditory system” by young children has been another explanation offered by Schneider and Trehub (1992) based on work of Eggermont (1985). Eisenberg *et al.* (2000) cite the work of Moore *et al.* (1997) showing continued maturation of the auditory cortex. Thus, regardless of the exact anatomical location for the differences, some researchers have linked younger children’s auditory and speech perception differences to their need for greater amounts of the acoustic cue of interest such that they require either louder or longer duration speech cues (e.g., Elliott *et al.*, 1981; Ohde and Haley, 1997) or greater amounts of spectral information (Dorman *et al.*, 1998; Eisenberg *et al.*, 2000). Eisenberg *et al.* suggested that, because

^{a)}Electronic mail: jsussman@acsu.buffalo.edu

children's auditory perceptual abilities are still developing during the first 10–12 years, degraded or limited sensory information cannot be used as efficiently by young children.

In contrast, a different group of researchers has suggested that children's sensitivity to the acoustic cues is not important for their speech perception differences so that neither duration nor the amount of spectral information is critical. Rather, young children use the acoustic cues of speech differently than adults, a perceptual strategy difference. Morrongiello *et al.* (1984) and Nittrouer and colleagues (Nittrouer and Studdert-Kenney, 1987; Nittrouer and Miller, 1997) suggest that children use the dynamic frequency cues of speech such as formant frequency transitions more than adults do in identification tasks. Nittrouer and colleagues, in several studies, have found a preference only by younger children for formant transitions rather than steady-state noise cues for identification of fricatives [s] and [ʃ]. As children get older, it has been suggested that children learn to use the steady-state cues also for speech perception. Nittrouer has termed this pattern of learning the developmental weighting shift hypothesis.

Evidence for the sensory explanation of children's speech perception differences comes from studies by Ohde and colleagues. In contrast to findings by Morrongiello *et al.* (1984) and Nittrouer and colleagues (1987, 1997), Ohde *et al.* (1995) found that children 5–11 years of age did not rely more heavily on the formant transitions than did adults for identification of stop consonants. Younger children (3–4-year-olds) did so only for the velar place of articulation (Ohde and Haley, 1997). For short vowels with bursts and transitions, Ohde, Haley, and McMahon (1996) found for children aged 5–11 years that movement of formant transitions did not significantly improve their perception of the brief vowels. In addition, longer-duration vowel portions significantly improved the identification of the vowels by children but not by adults. In their follow-up study, Ohde and Haley (1997) used synthetic stimuli composed of either one or five glottal pulses from the initial portion of consonant–vowel syllables to investigate both vowel and consonant identification. They found that children aged 3–11 showed improved identification of the vowels [i], [u], and [a] with either straight or moving formant transitions as the duration of the vowel component increased. They also showed that for 3–4-year-olds that the most important cues for vowel perception were the steady-state formants or their target frequencies. Ohde and Haley (1997) concluded that developmental differences in auditory sensitivity and discrimination of temporal and frequency differences appeared linked to the differences noted in children's speech perception, particularly for vowel perception. Although the length of the vowel steady-state frequencies influenced children's accuracy of vowel identification, suggesting that vowel target frequencies were most important in perception, the Ohde and Haley (1997) study did not directly compare children's identification of vowels that contained only transitions (and no vowel) or only steady-state portions. Thus, Ohde and Haley (1997) could not definitively determine which type of cue is most important, as might a study that looked at the perception of each separately and when transitions and steady states did

not identify the same vowel. From a theoretical standpoint it would be of interest to learn whether children prefer to use transitional elements in perception of vowels rather than the longer, more powerful steady-state formant frequencies as work of Elliott and Katz (1980) and Ohde and Haley (1997) might suggest.

A study by Murphy, Shea, and Aslin (1989) began looking at vowel perception in 3-year-olds using transitional and full vowel stimuli. They showed that 3-year-olds identified good exemplars of three-formant synthetic stimuli [æ] and [ʌ] at above-chance levels in a b–d context even when up to 90% of the vowel was removed. However, performance was significantly poorer than that of adults. Adults identified the full vowels with 100% in all conditions, whereas the 3-year-olds identified the full vowels with approximately 88% accuracy. For the 90% vowelless condition, the 3-year-olds identified the missing vowels with approximately 66% accuracy. Thus, results confirm Eisenberg *et al.*'s (2000) suggestion that young children require more complete stimuli for most adult-like perception. Further study regarding the relative importance of transitions compared with that for steady-state formants in children older than 3 years would thus be of interest.

Finally, children with language impairment have been found by some investigators (e.g., Sussman, 1993; Tallal and Piercy, 1974, 1975; Tallal *et al.*, 1996) to have poorer speech perception performance for tokens differing by their formant transition cues in stop consonants. The reasons for perception difficulties with short-transition speech tokens are again unknown. Leonard (1998) has suggested that children with specific language impairment may misidentify certain speech elements because of their inherent “low phonetic substance;” that is, short-duration, low-intensity acoustics. Furthermore, Wright *et al.* (1997) have suggested that backward masking by longer, more powerful vowels may contribute to the poorer perception of preceding stops in consonant–vowel utterances. Thus, longer and stronger acoustic cues as present in vowel formant frequencies, rather than in formant transitions, might be predicted to be preferred for children with language impairment who appear at risk for identification of the short-duration elements in speech. Apparently, having a long-enough signal may enable listeners to process the signals best, perhaps through temporal summation, the addition of energy that can last up to a 200-ms window of time. Or, perhaps the longer, stronger signal may enable listeners to sample the signal more efficiently (Schneider and Trehub, 1992). Thus, the current study also investigated the vowel identification abilities of children with language impairment to learn whether they more accurately used the steady-state formants containing longer duration and louder frequencies or whether they preferred the formant transitions that are of shorter duration and contain less overall energy.

Although research has shown that formant transitions may be important cues for vowel perception in adults (e.g., Strange, Jenkins, and Johnson, 1983), and that young children are able to use these same cues to identify vowels in syllables with reduced duration vowel steady states (e.g., Murphy *et al.*, 1989), it is not yet known definitively whether the steady-state formant frequencies or the formant fre-

quency transitions when 100% of the vowel steady states are absent are most important for vowel perception. Thus, in the current study children and adults identified full syllables, steady-state formant frequencies, and “vowelless” syllables. In addition, the current investigation used methods similar to those of Walley and Carrell (1983) by including a “conflicting” condition in which transitions and steady states specified different vowels. Furthermore, other studies to date have used synthetic male voices in their stimuli, whereas the current investigation used a synthetic female voice, one thought to be more like that heard most frequently by young children since the primary caregivers of young children continue to be adult females. The purpose of the study was to learn whether adults and young children, both with normal and impaired language, identified vowels primarily on the basis of the formant transitions leading into and out of the vowel or because of the steady-state formant frequencies. The study set about to ask three main questions.

- (1) What is the primary acoustic cue (transitions or steady states) used by listeners to identify vowels in nonsense syllables composed of consonant–vowel–consonant sounds?
- (2) Do children prefer to use the transitions for vowel identification as might be predicted by the developmental weighting shift hypothesis or by the dynamic specification theory (e.g., Strange, 1989)?
- (3) Do children with language impairment prefer to use the longer-duration vowel steady-state cues because of a difficulty with formant transitions?

Results from these three questions may help to determine whether children’s speech perception differences are related to perceptual strategy differences or to the need for a longer duration and complete acoustic signal due to sensory immaturities as suggested by Eisenberg *et al.* (2000).

II. METHOD

A. Participants

Fifteen adults (mean age: 21 years, 6 months), 11 children with normally developing language (mean age: 4 years, 11 months), and 11 children with specific language impairment (mean age: 6 years, 2 months) participated in the current project. All adults had normal speech, language, and hearing abilities. They were college students who passed a hearing screening, administered bilaterally for the octave frequencies 250–8000 Hz at 20-dB HL (ANSI, 1989). In addition to the hearing screening, all children were given standardized tests (The Token Test for Children, DiSimoni, 1978; screening portion of the CELF-P, Wiig *et al.*, 1992; Goldman–Fristoe test of articulation, Goldman and Fristoe, 1986) for estimation of speech and language abilities. The children with normal language were required to pass all tests within their age/grade limits. The children with specific language impairment were required to be in the second standard deviation range below the mean for their age on at least one of the standardized language tests. The average performance of the group with language impairments was in the negative second standard deviation range for the Token Test and the

linguistics concepts subtest of the CELF-P. Articulation performance was noted in each group and was fairly similar across group. All testing results are listed in Table I. As noted in the table, the children with normal language abilities were approximately 1 year younger than the children with language impairments. However, the language abilities of the children with normal language (as approximated from performance on the Token Test for Children) were approximately 1 year above the abilities of the children with language impairment. Thus, it was possible to observe whether chronological age vs language age might be a more important component related to speech perception abilities, as was done in Sussman (1993). In addition, the method of subject selection used reduces the disparity in language age that might otherwise exist if the children were the same chronological ages. The speech and language testing was completed in a separate, initial session for all child participants. The speech perception sessions were completed within 1 week of the initial speech–language evaluation. Children were free from colds and infections during testing days.

B. Stimuli and apparatus

All stimuli were synthetic, created with the SENSIMETRICS (1992) software package that used the Klatt and Klatt (1990) parameters on a 386 computer. An adult female voice was created with the SENSIMETRICS program to produce: (1) [bib] and [bæb] “congruent” tokens, the complete syllables; (2) 220-ms steady-state [i] and [æ] centers taken from the #1 tokens; (3) vowelless tokens that used the transitions into and out of the [bib] and [bæb] syllables but contained no periods of the vowel; and (4) “conflicting” syllables that were composed of the transitions from one nonsense token (e.g., [bib]) with the steady-state formant frequencies from the other (e.g., [bæb]). To create the vowelless, steady-state, and conflicting tokens, the steady-state centers and transitions were excised from the complete synthetic tokens at zero-crossing points using a waveform editing program (WAVEDIT, Miller, 1989) and procedures identical to those used by Murphy *et al.* (1989). Then, for the conflicting stimuli, the separate parts were recombined at zero points so that no transients were present in the stimuli. Spectrograms of the stimuli are shown in Figs. 1 and 2.

The formant frequency onsets and steady states of the synthetic stimuli are listed in Table II. The syllables were all created with a 10-kHz sampling rate. The $F1$ began at 10 ms and reached steady state by 40 ms, creating a 30-ms $F1$ transition. The $F2$ and $F3$ transitions were both 40 ms. $F4$ and $F5$ did not have transitions but were steady state from onset. The steady-state target frequencies were maintained through 320 ms, then a linear decline to the offset frequencies occurred. The fundamental frequency of the stimuli started at 220 Hz and declined linearly throughout the tokens to 180 Hz by the end of the full stimuli. The amplitude of voicing began at 20 dB at 0 ms, reached 60 dB by 20 ms, maintained that value until 340 ms, and declined to 50 dB by the stimulus end. The somewhat-elevated ending amplitude was maintained so that listeners could perceive the final [b] since there were no bursts in the stimuli. The spectral tilt of

TABLE I. Speech and language test results for the children with normal language (C) and those with language impairments (LIC).

Subject	C.A. ^a	GFTA ^b		CELF-P ^c		TOKEN ^d		Age
		Tot #	%	Std score	s.d.	Std score	s.d.	
C1	3;8	0	99	14;11	+2,+1	503	+1	4.0
C2	4;8	3	79	16;12	+2,+1	509	+2	6;6
C3	4;4	13	31	16;14	+2,+2	506	+2	6.0
C4	5;9	0	99	12;11	+1,+1	503	+1	7.0
C5	4;4	0	99	17;17	+3,+3	504	+1	5.0
C6	5;3	3	65	15;10	+2,0	505	+1	8;6
C7	4;6	6	55	11;7	+1,-1	499	-1	4;6
C8	4;10	4	64	10;10	0,0	502	+1	4;9
C9	5;6	15	19	14;9	+2,-1	501	+1	6.0
C10	5;10	0	99	11;13	+1,+1	503	+1	7.0
C11	5;5	0	99	15;15	+2,+2	500	0	5.0
Mean	4.92	4.0	73.5	13.7;11.7	1.6,0.27	503	0.91	5.84
s.d.	8.25	5.4	29.3	2.4;2.9	0.81,2.6	2.8	0.83	1.34
LIC1	5;8	3	68	9;6	-1,-2	488	-3	3;11
LIC2	6;5	0	99	9;6	-1,-2	489	-3	4.0
LIC3	6;9	1	84	3;3	-3,-3	491	-2	5.0
LIC4	5;6	10	32	6;4	-3,-3	494	-2	4.11
LIC5	5;7	9	25	4;7	-2,-1	490	-2	4.0
LIC6	6;11	0	99	6;8	-2,-1	495	-1	5.6
LIC7	6;7	1	84	6;13	-2,+1	490	-2	5.0
LIC8	6;3	1	84	7;9	-1,-1	492	-2	4;8
LIC9	5;9	6	47	3;8	-3,-1	493	-2	4.11
LIC10	6;5	22	7	5;6	-2,-2	487	-3	4.0
LIC11	6;6	0	99	5;6	-2,-2	483	-3	4.0
Mean	6.21	4.8	66.2	5.7;6.9	-2,-1.5	490	-2.3	4.54
s.d.	6.00	6.8	33.0	2.1;2.7	0.77,1.1	3.4	0.65	0.57

^aC.A.—chronological age in years;months.

^bGFTA=Goldman-Fristoe test of articulation (sounds in word subtest)—total number of sounds in error with percentile (%) score.

^cCELF-P=Clinical Evaluation of Language Fundamentals—Preschool—standard score and number of standard deviations above/below the mean for the Linguistic Concepts and Recalling Sentences subtests.

^dTOKEN=Token Test for Children—standard score and number of standard deviations above/below mean, age equivalency in years;months.

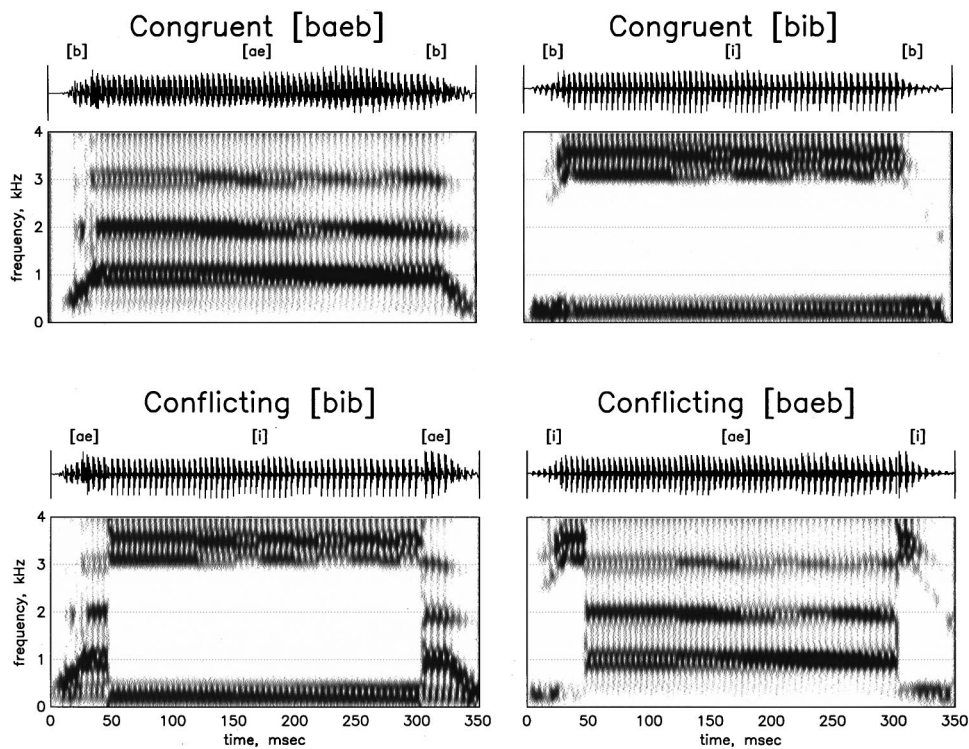


FIG. 1. Waveform and three-dimensional (3D) spectrograms of “congruent” [baeb] and [bib] and “conflicting” [bib] and [baeb].

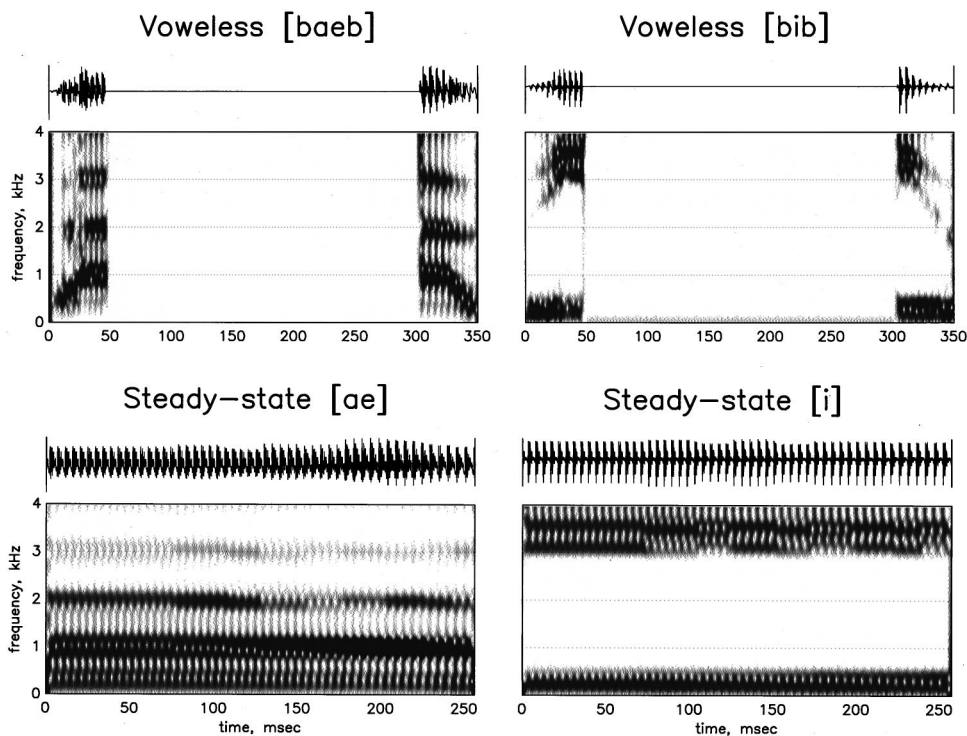


FIG. 2. Waveform and 3D spectrograms of “vowelless” [bæb] and [bib] and “steady-state” [æ] and [i].

the syllables was set to 16 and no flutter was used.

The gender and phonetic identity of the complete syllables were verified by having a separate group of 12 adults who were graduate students in communicative disorders and sciences listen to the stimuli as well as to other variations of the stimuli that differed slightly by formant frequencies or fundamental frequency. The listeners’ task was to identify whether the tokens could have been produced by adult female, male, or adolescent speakers and also rate the stimuli according to “best” to “poorest” “beeb” and “bæb” tokens on a 4-point scale. All listeners heard the stimuli as produced by an adult female and each believed that the syllables used in the current experiment were the best “beeb” and “bæb” tokens.

Natural tokens were used in training. These were digitized productions (at a sampling rate of 10 kHz) of an adult female talker’s voice for the same [i,æ,bub,baeb] stimuli used in the experimental trials. The WAVEDIT program (Miller, 1989) was used to capture and digitize the productions. The synthetic syllables had also been based on the same talker’s productions; thus, the natural stimuli had durations, formant, and fundamental frequencies similar to the synthetic experimental stimuli.

TABLE II. Onset, offset, and target frequencies of the five formants (in Hz) of [bib] and [bæb].

	Onset frequency for both [bib] and [bæb]	Target frequency [i] [æ]	Offset frequency for both
F1	275	311 1000	275
F2	1800	3100 1950	1800
F3	2800	3500 3000	2800
F4	4352	4352 4352	4352
F5	4600	4600 4600	4600

C. Procedures

Each listener participated in one (adults) to two (children) test sessions during which the four stimulus sets, preceded by training, were administered. The tokens were outputted through a Data Translations (model 2821) digital-to-analog converter at a sampling rate of 10 kHz and low-pass filtered at 4200 Hz. Four of the children with language impairment heard the stimuli from a high-quality tape recorder (Sony, WMDC6) that used type IV metal tape and type C Dolby noise reduction, using the same headphones (Sony, MDR-CD6) used by the other listeners. Subjects heard the stimuli in the right ear at a comfortable listening level (77 dB SPL, A weighting) confirmed with a B&K sound-level meter (model 2215). All subjects except the four using the tape recorder heard the tokens in a sound-treated, double-walled booth. The other four children heard the stimuli in a small, very quiet room located in their school.

1. Training

In the first part of training, children were presented with a fictional story read by the investigator or a trained assistant about a sister and brother who had contrasting shapes and colors for bodies named “Beeb” and “Baeb,” respectively. The children were trained to point to the appropriate fictional character that matched [bib] or [bæb] or to their “nicknames” [i] or [æ]. During training and throughout the experimental trials the children, particularly the ones with language impairment, were encouraged to say out loud each single stimulus token heard after each stimulus was presented as either “beeb” or “bæb” or “ee” or “æ.” Before the experimental trials were presented, ten items were administered in a “natural token” practice. Another ten natural token practice trials were available if children did not reach criterion in the first ten trials. No child required the extra

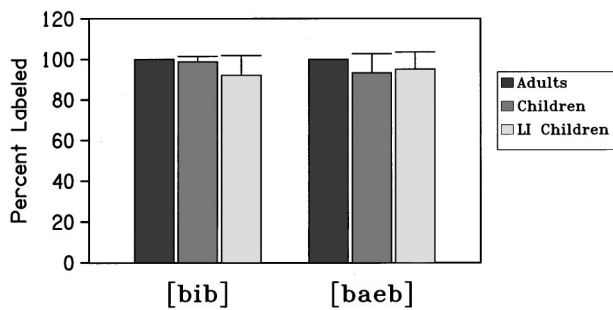


FIG. 3. Percent labeled [bib] or [baeb] (with standard deviations) of “congruent” [bib] and [baeb] tokens by adults and children with normally developing language and children with language impairment.

practice. Initial training concluded with children required to point to/label the pictures for 9/10 naturally produced tokens of [bib] and [baeb]. Following the natural token practice, there were 16 practice trials with the synthetic tokens for familiarization.

2. Experimental trials

Forty experimental trials from one of the four sets of synthetic stimuli followed the synthetic token practice. Thirty of the experimental trials were the actual synthetic stimuli of interest, with 15 being [i] vowels, and 15 tokens being [æ] vowels. Ten of the experimental trials were natural tokens used for validity checks on performance. Five of those were natural [i] vowels; five were natural [æ] vowels. The same number of trials, with the same order of natural, followed by synthetic trials was followed for all four sets of stimuli: congruent, steady-state, voweless, conflicting, each with [i] and [æ] responses. For the child subjects, the investigator or a trained assistant pushed the buttons attached to the computer that also administered the stimuli. Feedback regarding “correctness” was only provided for the naturally produced tokens. The children’s responses would not have been used if responses to natural tokens presented during the course of testing with synthetic tokens was not maintained at 80% or higher in all test conditions. However, all children met the 80% criterion and there was no difference in the results of the four children who heard the stimuli via tape recording compared to the other child listeners. The experimental trials were administered in one of two orders: (1) steady state; (2) voweless; (3) conflicting; (4) congruent, or (1) voweless; (2) steady state; (3) congruent; (4) conflicting.

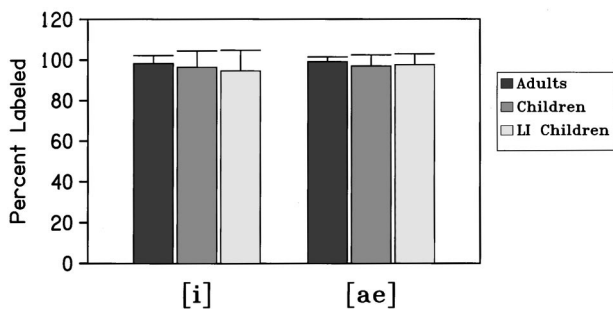


FIG. 4. Percent labeled [i] or [æ] (with standard deviations) of “steady-state” centers from [bib] and [baeb] by adults and children with normally developing language and children with language impairment.

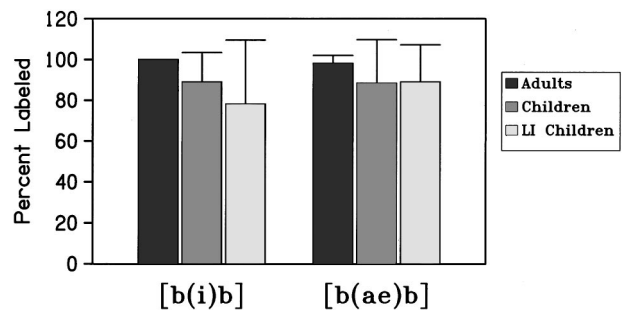


FIG. 5. Percent labeled [i] or [æ] (with standard deviations) of voweless tokens of [bib] and [baeb] by adults and children with normally developing language and children with language impairment.

III. RESULTS

Figures 3–6 show the results from each stimulus set. The Y axis of each figure shows the percent labeling for each vowel target shown along the X axis. In Fig. 6 with the conflicting tokens, the ordinate indicates percent labeled by the steady-state target. Adults labeled the vowels correctly with the highest percentages in all cases of the voweless, steady-state, and congruent tokens. With two exceptions, the children with normally developing language had higher correct labeling percentages than the children with language impairment. The two stimulus sets that had slightly higher percent-correct labeling for the children with language impairment were: congruent–æ (95% vs 93%) and steady-state–æ (98% vs 97%). However, children’s labeling of the voweless tokens, although at a generally high level, was not as good as adults’. Moreover, for the “conflicting” tokens, children with normally developing language primarily labeled the tokens by the steady states (on average in 87% of all cases), whereas children with language impairments did so at a lower level (on average in 79% of all cases). Adults used steady states to label the conflicting tokens in 84% of all cases but more unevenly than for the child groups (see Fig. 6). When the steady states were [æ], the adults used them to determine the conflicting tokens in 94% of all cases. But, when the steady states were [i], adults used the steady states in only 74% of all cases.

A two-way multivariate analysis of variance (MANOVA) (subject group: adults, children, and children with language impairment by vowel stimulus: voweless [i],

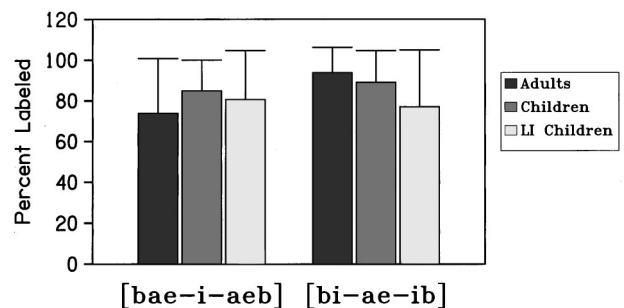


FIG. 6. Percent labeled by steady-state [i] or [æ] (with standard deviations) of “conflicting” tokens by adults, children with normally developing language, and children with language impairment. The phonetic symbols on the X axis denote the identity of the initial transitions, followed by the steady-state center, followed by the final transitions.

vowelless [æ], steady state [i], steady state [æ], congruent [i], congruent [æ], conflicting [bi-æ-ib], conflicting [bæ-i-æb]) was used to analyze the data to avoid potential problems due to sphericity (Max and Onghena, 1999). The MANOVA showed significant effects due to vowel stimulus (Wilk's lambda $F=3.590$, $p<0.007$) and a vowel stimulus \times subject group interaction (Wilk's lambda $F=2.337$, $p<0.013$). *Post hoc* tests done with Tukey HSD comparisons showed that children with language impairment identified the vowelless [bib] stimuli with significantly lower accuracy levels than adults ($p<0.016$). In addition, children with language impairment identified the congruent [i] tokens with significantly lower accuracy levels than the children with normally developing language ($p<0.02$) and adults ($p<0.003$). Thus, children with language impairment in the current study did not perform as well as other listeners when the stimuli contained either the transitions or the steady states of the [i] vowel.

IV. DISCUSSION

Children and adults are able to identify vowels by transitions with generally over 80% accuracy, as shown in Fig. 5, supporting the dynamic specification theory of vowel perception (e.g., Strange *et al.*, 1983). However, young children were not quite as good as adults in correctly identifying the vowel when no glottal pulses from the original vowel were present in the signal. Thus, current results are similar to results by Murphy *et al.* (1989) for 3-year-olds when 90% of the vowel was removed. Children with language impairment performed the poorest of all groups for the vowelless stimuli, particularly for the vowelless [bib] tokens. Thus, younger children appear to benefit from longer, more complete tokens for vowel identification but significantly so only for the children with language impairment for the [i] vowel. The advantage in processing for the longer duration cue was clear from the results with conflicting tokens that combined transitions and steady states from differing vowels. That is, all groups primarily used the longer, more powerful steady-state formants to identify vowels in 80 percent or more cases. Children with normally developing language skills more consistently used this strategy of preference for the steady-state formants than the adults, as shown in Fig. 4. Thus, the current results suggest that children rely more on the longer, louder, or more acoustically salient cue, the formant steady states, than on the dynamic formant transitions, for vowel identification in difficult listening conditions. Adults were better able to use the dynamic, but shorter transitions for vowel identification. Therefore, the current results do not support predictions of the developmental weighting shift hypothesis (e.g., Nittrouer and Miller, 1997), which theorized that children rely more heavily on the transitional elements of speech for perception than adults. That theory was based primarily on data from perception of fricatives from either the transition or the steady-state noise elements and had not been tested for perception of vowels. It is conceivable that children may use different strategies for perception of consonants than vowels, although results from Ohde and Haley (1997) would suggest otherwise.

Interestingly, the children with language impairment used the transitions for vowel identification more often in the conflicting stimuli than did the children with normally developing language. This strategy or choice appeared unwise given that the children with language impairment were the poorest at identifying vowels from just the transition elements, as can be observed in Fig. 5. Thus, the children with language impairment had lower accuracy levels for the vowelless tokens than other groups, but used those transitions for vowel identification in the conflicting syllables to a higher degree than did children with normally developing language. Such a strategy may explain in part why children with language impairment are less successful in some speech perception tasks. Training on use of the longer-duration elements of the speech token may result in improved performance. However, the children with language impairment may be at a disadvantage for identification tasks because of a weaker, more poorly defined underlying phonetic category structure (e.g., Sussman, 1993; Leonard, 1998).

Finally, it was observed that children with language impairment performed more poorly on the tokens containing either the transitions or steady states of the [bib] token. Their poorer perception of the [i] vowel was interesting in light of prior findings by Ohde *et al.* (1996) showing that [i] was identified best by their children aged 5–11 years. In the current study, there did not appear to be any explanation based on the particular acoustic characteristics of the stimulus or its parts. Adults identified the congruent [i] and [æ] tokens with identical 100% accuracy and labeled the vowelless [bib] tokens with 100% accuracy and the vowelless [æ] tokens with 98% accuracy. They labeled the [i] steady state with 98% accuracy and the steady-state [æ] token with 99% accuracy. Even the children with normally developing language performed as well or better with the [i] tokens than with the [æ] tokens. Thus, the "control" listeners behaved superiorly with all tokens, particularly [i] stimuli, suggesting that none of the physical attributes of the stimuli could explain the poorer performance by the children with language impairment for [i] tokens. As Ohde *et al.* (1996) and Ohde and Haley (1997) suggest, perception of vowel stimuli in particular may depend more on the listeners' auditory sensitivity as listeners are better able to take advantage of short-term auditory store and compare the acoustic attributes of the tokens (Pisoni, 1973). The low first formant ($F1$) of [i] compared with the high $F1$ of [æ] may have contributed to difficulty with perception of [i], possibly related to poorer perception of low frequencies (e.g., Elliott and Katz, 1980; Schneider *et al.*, 1986) or patterns of the low-frequency components (e.g., Syrdal and Gopal, 1986). The relative importance of the low $F1$ cue versus the higher frequency components for children's perception is not known, however. Further study with stimuli that could directly compare the contribution of particular frequency components might better address this question.

ACKNOWLEDGMENTS

The current project was supported by a Research Development Fund award from the Research Foundation and by a seed grant from the Center for Hearing and Deafness at the

University of Buffalo. The author appreciates the contributions of former students Jason Steinberg and Julie Fenwick for their help with stimulus construction and for some of the data collection. Much appreciation is extended to all the parents and child participants, especially to Ms. Chris Myszka, speech–language pathologist for the Council Rock Elementary School in Brighton, N.Y., for quick and accurate identification of the last four children with language impairment.

- ANSI (1989). "Specifications for Audiometers," ANSI S 3.6-1989 (American National Standards Institute, New York).
- Berg, K. M., and Boswell, A. E. (2000). "Noise increment detection in children 1 to 3 years of age," *Percept. Psychophys.* **62**(4), 868–873.
- DiSimoni, F. (1978). *The Token Test for Children* (DLM Teaching Resources, Allen, TX).
- Dorman, M. F., Loizou, P. C., Kirk, K. I., and Svirsky, M. (1998). "Channels, children and the Multisyllabic Lexical Neighborhood Test (MLNT)," NIH Neural Prosthesis Workshop, Bethesda, MD, October 1998.
- Eggermont, J. (1985). "Physiology of the developing auditory system." *Auditory Development in Infancy*, edited by S. E. Trehub and B. A. Schneider (Plenum, New York), pp. 21–46.
- Eisenberg, L. S., Shannon, R. V., Martinez, A. S., Wygonski, J., and Boothroyd, A. (2000). "Speech recognition with reduced spectral cues as a function of age," *J. Acoust. Soc. Am.* **107**, 2704–2710.
- Elliott, L. L., and Katz, D. (1980). "Children's pure-tone detection," *J. Acoust. Soc. Am.* **67**, 343–344.
- Elliott, L. L., Longinotti, C., Meyer, D., Raz, I., and Zucker, K. (1981). "Developmental differences in identifying and discrimination of CV syllables," *J. Acoust. Soc. Am.* **70**, 669–677.
- Goldman, R., and Fristoe, M. (1986). *Goldman–Fristoe Test of Articulation* (American Guidance Service, Circle Pines, MN).
- Klatt, D. H., and Klatt, L. (1990). "Analysis, synthesis, and perception of voice quality variations among female and male talkers," *J. Acoust. Soc. Am.* **87**, 820–857.
- Leonard, L. (1998). *Children with Specific Language Impairment* (MIT Press, Cambridge, MA).
- Max, L., and Onghena, P. (1999). "Some issues in the statistical analysis of completely randomized and repeated measures designs for speech, language, and hearing research," *J. Speech, Lang., Hear. Res.* **42**, 261–270.
- Miller, C. (1989). WAVEDIT. Dept. of Speech, Theatre, and Communication Disorders, Louisiana State University, Baton Rouge, LA.
- Moore, J. K., Guan, Y.-L., and Wu, B. J. (1997). "Maturation of human auditory cortex: Laminar cytoarchitecture and axonal ingrowth," 20th ARO Midwinter Meeting, 28 (abstract), St. Petersburg, FL (Association for Research in Otolaryngology, Des Moines), p. 28.
- Morroneglio, B. A., Robson, R. C., Best, C. T., and Clifton, R. K. (1984). "Trading relations in the perception of speech by 5-year-old children," *J. Exp. Child Psych.* **37**, 231–250.
- Murphy, W. D., Shea, S. L., and Aslin, R. N. (1989). "Identification of vowels in vowelless syllables by 3-year-olds," *Percept. Psychophys.* **46**, 375–383.
- Nittrouer, S., and Miller, M. (1997). "Developmental weighting shifts for noise components of fricative-vowel syllables," *J. Acoust. Soc. Am.* **102**, 572–580.
- Nittrouer, S., and Studdert-Kennedy, M. (1987). "The role of coarticulatory effects in the perception of fricatives by children and adults," *J. Speech Hear. Res.* **32**, 120–132.
- Ohde, R. N., and Haley, K. L. (1997). "Stop-consonant and vowel perception in 3- and 4-year-old children," *J. Acoust. Soc. Am.* **102**, 3711–3722.
- Ohde, R. N., Haley, K. L., and McMahon, C. W. (1996). "A developmental study of vowel perception from brief synthetic consonant–vowel syllables," *J. Acoust. Soc. Am.* **100**, 3813–3824.
- Ohde, R. N., Haley, K. L., Vorperian, H. K., and McMahon, C. W. (1995). "A developmental study of the perception of onset spectra for stop consonants in different vowel environments," *J. Acoust. Soc. Am.* **97**, 3800–3812.
- Parnell, M. M., and Amerman, J. D. (1978). "Maturational influences on perception of coarticulatory effects," *J. Speech Hear. Res.* **21**, 682–701.
- Pisoni, D. B. (1973). "Auditory and phonetic memory codes in the discrimination of consonants and vowels," *Percept. Psychophys.* **13**, 253–260.
- Schneider, B., Trehub, S., Morroneglio, B., and Thorpe, L. (1986). "Auditory sensitivity in preschool children," *J. Acoust. Soc. Am.* **79**, 447–452.
- Schneider, B., and Trehub, S. (1992). "Sources of Developmental Change in Auditory Sensitivity," in *Developmental Psychoacoustics*, edited by Lynne Werner and Edwin Rubel (American Psych. Assoc., Washington, D.C.).
- Sensimetrics Corporation (1992). SENSYN: Klatt synthesis software (Cambridge, MA).
- Strange, V. (1989) "Evolving theories of vowel perception," *J. Acoust. Soc. Am.* **85**, 2081–2085.
- Strange, W., Jenkins, J. J., and Johnson, T. L. (1983). "Dynamic specification of coarticulated vowels," *J. Acoust. Soc. Am.* **74**, 695–705.
- Sussman, J. E. (1993). "Perception of formant transition cues to place of articulation in children with language impairments," *J. Speech Hear. Res.* **36**, 1286–1299.
- Sussman, J. E., and Carney, A. E. (1989). "Effects of transition length on the perception of stop consonants by children and adults," *J. Speech Hear. Res.* **32**, 151–160.
- Syrdal, A. K., and Gopal, H. S. (1986). "A perceptual model of vowel recognition based on the auditory representation of American English vowels," *J. Acoust. Soc. Am.* **79**, 1086–1100.
- Tallal, P., Miller, S., Bedi, G., Wang, X., Nagarajan, S., Schreiner, C., Jenkins, W., and Merzenrich, M. (1996). "Language comprehension in language-learning impaired children improved with acoustically modified speech," *Science* **271**, 81–84.
- Tallal, P., and Piercy, M. (1974). "Developmental aphasia: Rate of auditory processing and selective impairment of consonant perception," *Neuropsychologia* **12**, 83–93.
- Tallal, P., and Piercy, M. (1975). "Developmental aphasia: The perception of brief vowels and extended stop consonants," *Neuropsychologia* **13**, 69–74.
- Trehub, S., Schneider, B., Morroneglio, B., and Thorpe, L. (1988). "Auditory sensitivity in school-age children," *J. Exp. Child Psych.* **46**, 273–285.
- Walley, A. C., and Carrell, T. D. (1983). "Onset spectra and formant transitions in the adult's and child's perception of place of articulation in stop consonants," *J. Acoust. Soc. Am.* **73**, 1011–1022.
- Wiig, E. H., Secord, W., and Semel, E. (1992). *Clinical Evaluation of Language Fundamentals—Preschool* (The Psychological Corporation, Harcourt Brace Jovanovich, San Antonio, TX).
- Wright, B. A., Lombardino, L. J., King, W. M., Puranik, C. S., Leonard, C. M., and Merzenich, M. (1997). "Deficits in auditory temporal and spectral resolution in language-impaired children," *Nature (London)* **387**, 176–178.

The perceptual consequences of within-talker variability in fricative production

Rochelle S. Newman,^{a)} Sheryl A. Clouse, and Jessica L. Burnham
Department of Psychology, University of Iowa, E11 Seashore Hall, Iowa City, Iowa 52242

(Received 14 February 2000; accepted for publication 7 December 2000)

The effect of talker and token variability on speech perception has engendered a great deal of research. However, most of this research has compared listener performance in multiple-talker (or variable) situations to performance in single-talker conditions. It remains unclear to what extent listeners are affected by the *degree* of variability within a talker, rather than simply the existence of variability (being in a multitalker environment). The present study has two goals: First, the degree of variability among speakers in their /s/ and /ʃ/ productions was measured. Even among a relatively small pool of talkers, there was a range of speech variability: some talkers had /s/ and /ʃ/ categories that were quite distinct from one another in terms of frication centroid and skewness, while other speakers had categories that actually overlapped one another. The second goal was to examine whether this degree of variability within a talker influenced perception. Listeners were presented with natural /s/ and /ʃ/ tokens for identification, under ideal listening conditions, and slower response times were found for speakers whose productions were more variable than for speakers with more internal consistency in their speech. This suggests that the degree of variability, not just the existence of it, may be the more critical factor in perception. © 2001 Acoustical Society of America. [DOI: 10.1121/1.1348009]

PACS numbers: 43.71.Es, 43.71.Gv, 43.71.Bp [CWT]

I. INTRODUCTION

One of the primary issues in the field of speech perception has been the apparent “lack of invariance” between the acoustic information in a signal and the listener’s phonemic perception. This variability can be caused by a variety of factors, including dialect (Byrd, 1992), social group (Johnson and Beckman, 1996), speaking rate (Miller and Liberman, 1979), emotional state (Shankweiler, Strange, and Verbrugge, 1977), gender (Byrd, 1992), vocal tract length (Fant, 1973; Peterson and Barney, 1952), articulatory habits (Johnson and Beckman, 1996; Klatt, 1986), and phonetic context (Liberman *et al.*, 1967). Regardless of the cause, the effect is that the same intended phoneme can be produced with a wide range of acoustic values, and that two different intended phonemes can occasionally have similar or identical acoustic values. Although the existence of this variability in production is not in question, the degree to which listeners have to account for it in everyday listening situations is unclear. There have been few studies that have examined the *extent* of this variability, even for individual phonemes in a laboratory setting. While different phonemes may occasionally overlap on some acoustic values, it is not at all clear how common an event this is. Without this information, it is difficult to determine the degree to which individuals need to adjust perception for the individual talker or utterance.

Furthermore, few studies have examined closely the ways in which production variability can influence speech perception. Recent research has demonstrated that perception of and memory for speech is more accurate in single-talker situations than in multiple-talker situations (Cole, Coltheart,

and Allard, 1974; Craik and Kirsner, 1974; Creelman, 1957; Goldinger, 1996; Martin *et al.*, 1989; Mullennix, Pisoni, and Martin, 1989; Nusbaum and Morin, 1992; Palmeri, Goldinger, and Pisoni, 1993; Ryalls and Pisoni, 1997; Verbrugge *et al.*, 1976). For example, Mullennix, Pisoni, and Martin (1989) presented listeners with a naming task, and found poorer performance on blocks in which the voice of the talker changed from trial to trial as compared to blocks on which the voice remained constant. Craik and Kirsner (1974; see also Palmeri *et al.*, 1993) found that listeners were more likely to recognize words when they had been presented previously in the same voice as compared to a different voice. But, these studies all focused on the number of talkers, or on whether an item was presented in the same voice versus a different voice. They did not examine whether the degree to which those talkers differed from one another might matter, or whether the degree to which individual tokens within a talker varied might have an influence. Furthermore, some of these studies suggested that the only significant differences for perception were between single-talker situations and multiple-speaker situations; the number of talkers beyond two had little effect. This might suggest that while there is a degradation in performance caused by the existence of variability, the amount of such variability is not a critical factor. (In contrast, see Goldinger, 1996, who reported that listeners were affected by similarity between voices.)

Uchanski *et al.* (1992) suggest that variability within a talker has perceptual effects similar to variability across talkers. They presented participants with ten different vowels for identification. All were spoken by the same talker, but some listeners heard only one token of each vowel, and others heard up to 16 tokens of each vowel. Those who heard the single-token set had higher identification scores than those

^{a)}Electronic mail: rochelle-newman@uiowa.edu

who listened to more tokens of each vowel. Reed *et al.* (1991) likewise found poorer performance for multiple-token sets of low-pass filtered speech. Similarly, variability across speaking rates within a talker also influences perception, both during on-line processing and during later recall (Nygaard, Sommers, and Pisoni, 1995; Sommers, Nygaard, and Pisoni, 1994). These results suggest that utterance-to-utterance variability within a talker can have substantial effects on perception, similar to that of talker-to-talker variability.

These token-variability studies compared performance in multiple-token situations to performance for single tokens, in much the same way that research on talker variability compared multiple-talker situations to single-talker situations. But, even within multiple-token situations, some speakers are likely to have more variability in their productions than do others, and this degree of variability may also have an effect on perception. Listeners might have greater difficulty when listening to a talker with more variable productions than when listening to a talker whose productions are more consistent. It remains to be shown whether this degree of variability, and not just the existence of it, influences perceptual processing.

There have been a few studies suggesting that this may be the case. Nusbaum and Morin (1992) found that talker variability effects were less strong when the speakers were more similar in their productions. This suggests that the degree to which listeners are affected by talker variability outside the laboratory will depend critically on the extent to which individuals are dissimilar in their productions. In fact, Wannemacher (1995) suggests that the distinction between talker variability and token variability may be unnecessary, as productions from different, similar talkers can potentially be as alike as different tokens from the same talker. If so, the degree of variability (whether within a talker or across talkers) may be more important than the mere presence of variability.

The present research investigates these issues in greater depth. In order to examine the influence of variability, it is first necessary to characterize the amount of this variability that exists in a range of talkers. There have been a number of recent calls for this type of research (Byrd, 1992; Klatt, 1986; Shadle, Badin, and Moulinier, 1991; Stevens, 1996; Syrdal, 1996; Uchanski *et al.*, 1992), and although research has examined variability for some speech sounds (Crystal and House, 1988; Fischer-Jørgensen, 1954; Lisker and Abramson, 1964; Syrdal, 1996), it has not been investigated systematically. The present research focuses on the /s/-/ʃ/ distinction, for which studies of production variability do not currently exist. Thus, experiment 1 measures the production variability for these phonemes across a set of talkers.

We then selected speakers with varying degrees of internal consistency in their productions. These talkers formed the basis of perceptual studies in experiments 2 through 4. If the degree of talker variability influences perception, listeners should find it easier to identify the speech of talkers who are more consistent in their productions. Rather than present speech tokens in noise, as did Uchanski *et al.* (1992), we presented items under ideal listening conditions, and looked

for differences in identification reaction times. If a speaker is more variable in his or her productions, listeners may require additional processing in order to accurately identify that individual's speech. This will lead to slowed reaction times to speakers with less internal consistency (more variability) among their productions.

II. EXPERIMENT 1

In order to examine the influence of variability on perception, it is necessary to determine the degree of variability that naturally occurs, and to select speakers that represent the range of this variability. In our first experiment, we performed acoustic measurements on productions of the sibilant fricatives /s/ and /ʃ/ across a set of speakers.

A number of studies have examined the possible acoustic correlates of the /s/-/ʃ/ distinction. Harris (1958; see also Behrens and Blumstein, 1988; Heinz and Stevens, 1961; Hughes and Halle, 1956; Jassem, 1965; May, 1976) found that the noise center frequency information (roughly the frequency mean) is the primary cue for distinguishing these particular phonemes.¹ Stevens (1960) reported that the friction range for /s/ was shifted higher than that for /ʃ/, which would likewise imply that the mean frequency for /s/ would be higher (although he measured only the range of frequencies at which energy occurred, and did not actually calculate average values). Others have examined spectral peaks, which are more akin to a statistical mode than a mean (Seitz, Bladon, and Watson, 1987), or have examined the lower edge of friction information (Bladon and Seitz, 1986; Seitz *et al.*, 1987). In contrast to results focusing on a single acoustic measure, Forrest and colleagues (1988) examined three spectral moments (centroid, skewness, and kurtosis), and found that skewness of friction was the primary feature distinguishing these phonemes, although centroids might also aid in their discriminability. Thus, there is wide agreement that the friction noise is the primary acoustic cue for distinguishing /s/ and /ʃ/, although there is less agreement on the appropriate way of measuring this cue. However, most of this disagreement is historical, and recent work has focused on frequency means and skewness, or on spectral moments more generally (for example, see Baum and McNutt, 1990; Faber, 1991; Jongman and Sereno, 1995; Shadle and Mair, 1996; Tomiak, 1991).

We decided to examine the spectral moments, as these include the cues the literature appears to be converging upon (skewness and centroid). There are no reports in the literature on the range of variability for these measures in sibilant production. While there have been some reports on variability in other phonemic distinctions (for example, voice onset time; see Crystal and House, 1988; Fischer-Jørgensen, 1954; Lisker and Abramson, 1964; Syrdal, 1996), there are few studies that have attempted to measure this variability for fricatives. This is important information for determining the cues listeners might regularly use in perception: even if the average centroid for /s/ is higher than that for /ʃ/, centroids will only be particularly useful cues for distinguishing these phonemes to the extent that their distributions do not overlap. High variability in a particular cue is likely to reduce the degree to which listeners make use of that cue in normal

listening, all other things being equal.² Thus, knowing a cue's variability may be as important as knowing its average value in determining whether that cue is likely to be used by listeners.

Participants were asked to produce tokens of /s/ and /ʃ/ in CV syllables, in a variety of vowel contexts. The range of vowels should provide some degree of variability in production, even among fairly consistent speakers. However, we also asked speakers to produce multiple tokens of each CV syllable. Those speakers who are more consistent will likely produce the same syllable in similar ways, whereas those speakers with more variable speech production will tend to have high variability within a vowel context, as well as across vowel contexts. Thus, these speakers should show a wider range of values for frication centroids and skewness than do the more consistent talkers, and might also have categories that are less clear-cut. We examined only syllable-initial tokens, as it is not yet clear whether syllable-initial and syllable-final fricatives are treated as members of the same phonetic category. [Some researchers have suggested that speech perception works on the basis of position-specific phonemes, rather than more abstract phonemes; see Gagnon, Palmer, and Sawusch (unpublished).]

Rather than ask participants to read aloud a written representation of the syllables, they instead listened to a model of the syllable and were asked to repeat it back. This method of recording has previously been used by Forrest *et al.* (1988). The advantage of presenting an auditory exemplar, rather than a typewritten representation of the syllable, is that it encourages listeners to maintain a fairly even speaking rate. Since previous research has indicated that speaking rate variability has an influence on perception, and we were most interested in measuring the perceptual consequences of variability beyond that induced by rate changes, it was important to have talkers produce these items at a roughly constant speaking rate. Pilot work suggested that written lists tended to encourage talkers to speak progressively more quickly as the recording continued, whereas this method of repeating syllables led to a more constant speaking rate.³

The present experiment was designed to investigate the variability of spectral moments for productions of /s/ and /ʃ/, produced in isolation at a normal speaking rate. A female speaker (RSN) recorded four tokens of each of the syllables consisting of the English consonants /s/ and /ʃ/ and the vowels /i/, /e/, /æ/, /u/, /o/, /ʌ/, and /a/ (the vowels that occur in "see," "say," "sat," "Sue," "sew," "sun," and "sod"). These vowels were chosen because they represent the range of monothongal vowels that occurs in English, and because all of them could occur in an open syllable (that is, in a CV environment). The decision to record four tokens of each syllable was based on work by Uchanski *et al.* (1992), who suggested that this provides a reasonable sample of variability. Participants heard these syllables one at a time over a loudspeaker, and were asked to repeat back each syllable in the way that they would normally produce it (that is, they were to produce the utterances naturally, not mimic the speaker). They heard each of the possible items twice during the course of the experiment, and their recordings were stored for later acoustic measurement.

A. Method

1. Subjects

The productions came from 20 volunteers (7 male, 13 female) whose speech was recorded as part of a separate experiment (see Newman, 1998). All were native speakers of English with no reported history of a speech or hearing disorder, and received a cash payment for their participation. Although age information was not specifically gathered, all of the participants were members of the University at Buffalo student community, and ranged from young adults to adults.

2. Stimuli

A female native talker of English (RSN) recorded four tokens of each CV syllable beginning with either /s/ or /ʃ/ and followed by the seven vowels /i, e, æ, u, o, ʌ, a/. All of the tokens were amplified, low-pass filtered at 9.5 kHz, digitized via a 16-bit, analog-to-digital converter at a 20-kHz sampling rate, and stored on computer disk.

3. Procedure

Listeners were run individually as part of a longer experiment, and were recorded at the beginning of their first session. Participants were seated in front of a Digital Equipment Corporation VAX station 4000 computer, which controlled stimulus presentation and response collection. The subjects held an Electro-Voice D054 Dynamic Omni microphone, and listened to the stimuli over a Realistic loudspeaker in a sound-treated room. Although the talkers were asked to maintain a roughly constant distance between their mouth and the microphone, this distance was not controlled. As the purpose of this study is to examine the role of variability on speech perception, and distance between talkers and listeners typically varies, we were not particularly concerned with this variation.

The stimuli, which were stored on disk, were converted to analog form by a 16-bit, digital-to-analog converter at a 20-kHz sampling rate, and low-pass filtered at 9.5 kHz. The syllables were presented in random order at a comfortable listening level. Listeners were asked to repeat each syllable into the microphone in the manner they would normally produce that syllable. The computer waited 4 s for a response. If the listener did not respond within that time frame, the computer presented an error message and presented that trial again. If the listener's response was too loud (peak clipped), the computer would similarly repeat the trial. Otherwise, the computer gave the listener the opportunity to decide whether to accept that trial or not. Participants were instructed to respond "no" if they were unsure of what they were supposed to have said, or if some other noise interfered with the recording (such as a cough). If the subject responded "no," the trial was repeated. Otherwise, the program proceeded to the next trial. There were a total of 56 trials in this block (4 tokens \times 2 consonants \times 7 vowel environments). The program was then run a second time, so that each subject recorded eight tokens of each CV syllable. A few productions

were lost due to computer recording error; these made up less than 1% of the total recordings, and no more than 7% of the recordings for any one speaker.

Each production was analyzed using an attribute extraction program, which computed a sequence of spectra. Each spectrum was computed over a 15-ms window, with the initial analysis window centered on the onset of frication. Each subsequent spectra was computed over a window centered 5 ms further into the signal, resulting in a series of measurements containing 2/3 overlap. The number of analysis windows was set at 20; thus, analysis occurred over a total of 110 ms. This duration was suggested by Tomiak (1991) to provide a valid estimate of the fricative, based on results from a masking study. Although other researchers have made different choices in this regard, these methodological differences are unlikely to result in substantial disparity. Behrens and Blumstein (1988) examined three separate 15-ms windows, one at the onset of frication, one at the end of frication, and one in the middle of the frication, and found that peak measures were relatively constant across time. To the extent that frication remains fairly steady state, the duration over which these measures are calculated should not unduly influence the results.

A Fourier spectrum was computed for each analysis interval using a linear scale with a pre-emphasis of 0.94. These measures were then treated as random probability distributions. The first four moments of the distribution (the mean, standard deviation, skewness, and kurtosis) were then calculated for each spectrum, and the values averaged across the 20 frames. These measures have been shown by Forrest *et al.* (1988) to be successful at classification of both voiceless stops and sibilants. Measures of $d_{(a)}$ (a measure of sensitivity in the theory of signal detection) were calculated both within each subject, and across all subjects, for all four spectral moments. This is roughly a measure of the degree of difference between the two categories.⁴ Although we are using a measure from signal detection theory, we do not mean to imply that we are wedded to the assumptions of that theory (specifically, assumptions as to how this difference between categories will influence perception).

B. Results and discussion

Figure 1 plots the histograms for the frequency mean (or centroid) and skewness across all subjects; Table I gives a summary of these measurements. The sensitivity, or $d_{(a)}$, measures for these cues are 2.56 and 3.02 respectively, supporting the idea that these two cues are particularly useful for distinguishing these phonemes. These two cues are strongly correlated across subjects ($r=0.94$, $z=7.033$, $p<0.0001$, based on $d_{(a)}$ scores⁵), suggesting that individual differences in production may alter both cues simultaneously. It does not appear to be the case that listeners “trade off” these two potential cues to fricative place of articulation.

Across subjects, we found average values for /s/ and /ʃ/ of 5198 and 5652 Hz, respectively, for frication centroids, and of -0.030 and -0.303 for skewness. Productions in the context of back vowels tended to be lower in average frequency than those in front vowel contexts [$F(1,19)=9.55$, $p<0.01$], as would be predicted on the basis of prior

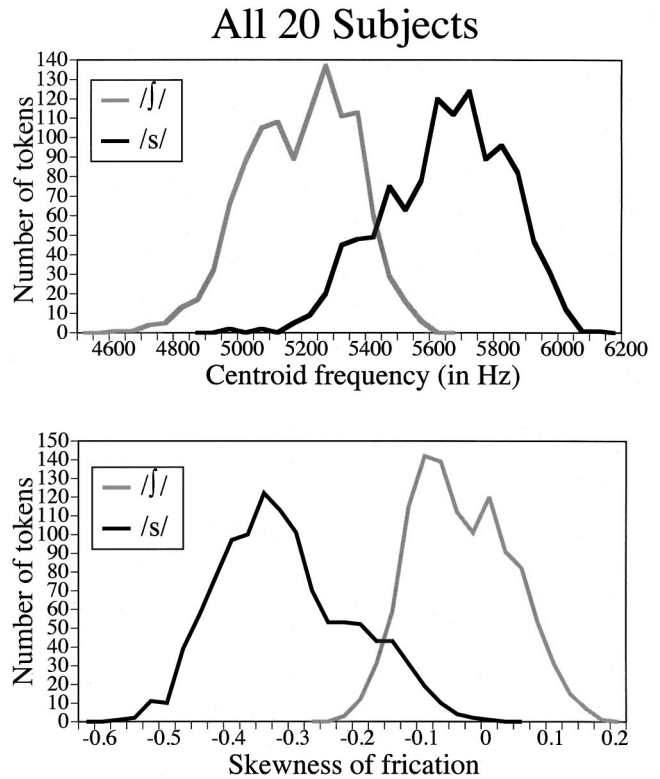


FIG. 1. Histograms of frication centroids and skewness for productions of /s/ and /ʃ/ syllables, across all 20 subjects.

research (Mann and Repp, 1980; Soli, 1981). Although these average values are quite distinct, there is overlap across individual subjects’ productions, as can be seen in Fig. 1: Some speakers’ productions of /s/ were quite similar to other speakers’ productions of /ʃ/. For example, individual subjects’ average centroids tended to be higher for /s/ than for /ʃ/, but average values for /s/ were as low as 5325 Hz, while they were as high as 5424 Hz for /ʃ/. Similar overlap occurs in the skewness measures, suggesting that there is no single value which could be used to distinguish these phonemes across all talkers. Although part of this overlap may have been due to gender (see Flipsen *et al.*, 1999; Johnson, 1991; Mann and Repp, 1980; May, 1976; Schwartz, 1967; Strand and Johnson, 1996; Whiteside, 1998), there was substantial variability in production within each gender as well. (For /s/ means, standard deviation overall was 189; for the 7 males alone it was 153 and for the 13 females alone it was 147. For /ʃ/ means, the standard deviations were 164 overall, and 138 and 152 for males and females, respectively.)

In general then, frication centroids and skewness measures serve to distinguish /s/ and /ʃ/ to a high degree. However, some overlap in the distributions exists, suggesting that these cues alone may not be sufficient. That is, there is no criterion point for either cue that would allow all items to be properly categorized, even within a particular gender.

This overlap is at least partially due to averaging across speakers. If listeners were able to adjust their perception for a particular speaker (that is, to normalize their perception on the basis of that talker), much of this category overlap would disappear. As an example, Fig. 2 presents the frication centroids for two talkers, ACY and IAF.⁶ Neither speaker has

TABLE I. Means and standard deviations of frication measurements for each talker (all measurements in Hz).

Initials	Gender	/j/		/s/	
		Centroid	Skewness	Centroid	Skewness
ACY	F	4980 (896)	-0.223 (.037)	5840 (939)	-0.400 (.065)
BAM	F	4926 (1022)	-0.034 (.046)	5690 (761)	-0.323 (.052)
CAB	F	5261 (688)	-0.076 (.039)	5594 (1263)	-0.316 (.068)
CER	F	5141 (1434)	+0.015 (.062)	5784 (772)	-0.338 (.048)
CLK	F	5323 (493)	-0.069 (.026)	5844 (912)	-0.397 (.044)
DDY	M	5320 (582)	-0.078 (.021)	5710 (730)	-0.324 (.038)
GGG	M	5167 (654)	+0.002 (.029)	5325 (781)	-0.112 (.038)
HEM	M	4997 (1186)	+0.041 (.048)	5570 (939)	-0.278 (.056)
IAF	M	5004 (684)	+0.091 (.026)	5414 (982)	-0.157 (.057)
IC	M	5116 (914)	-0.016 (.034)	5419 (1225)	-0.209 (.053)
JEM	M	5087 (556)	+0.031 (.027)	5440 (745)	-0.156 (.036)
JG	F	5196 (1167)	-0.062 (.053)	5648 (1392)	-0.324 (.082)
KFB	F	5014 (1117)	+0.029 (.042)	5578 (1321)	-0.277 (.055)
KJP	F	5351 (920)	-0.120 (.043)	5784 (886)	-0.372 (.050)
KSK	F	5424 (836)	-0.106 (.042)	5859 (822)	-0.403 (.050)
LCG	F	5080 (996)	+0.033 (.038)	5911 (908)	-0.447 (.048)
MLT	M	5011 (1222)	+0.075 (.058)	5566 (1182)	-0.221 (.051)
NV	F	5297 (1020)	-0.055 (.040)	5620 (840)	-0.297 (.046)
TLG	F	5241 (1197)	-0.069 (.050)	5648 (1114)	-0.355 (.056)
VJL	F	5338 (868)	-0.102 (.031)	5770 (931)	-0.345 (.048)

any category overlap among his or her own productions; however, the /s/ productions for IAF almost entirely overlap with the intended /j/ productions for speaker ACY. Averaging across these two speakers, then, leads to a much greater categorical overlap than is found in either speaker alone.

Some form of talker normalization could provide a means of avoiding perceptual difficulties arising from much of the category overlap across talkers.

However, this normalization would not be sufficient to deal with all of the category overlap among these talkers. The top panel of Fig. 3 shows the centroids and skewness measures for talker GGG. This talker has a considerable amount of category overlap within his productions. Normalizing on the basis of talker identity would not serve to adequately discriminate this talker's /s/ and /j/ productions. Some items would remain ambiguous, even knowing the talker.

Having collected these speech productions, it is now possible to examine the influence of talker variability on listeners' perception. There are (at least) three ways in which variability might influence identification:

- (1) If a talker is more variable in his or her production of a given phoneme, listeners may find it more difficult (or be slower) to identify that particular phoneme;
- (2) If a talker has sufficient variability in his or her productions to produce overlap between two of his or her speech categories, listeners may find it more difficult to identify these tokens; and
- (3) If a talker has a smaller distance between two speech categories, even when there is no category overlap, listeners may find it more difficult to identify these tokens.

The first of these possibilities is an absolute measure, inherent in that particular phoneme's production, while the second and third possibilities are relative measures, focusing on the relationship between different phoneme categories. The more absolute possibility suggests that listeners should be slower to identify items from those phonetic categories that have higher degrees of variability. This also implies that some phonetic categories may naturally be more difficult

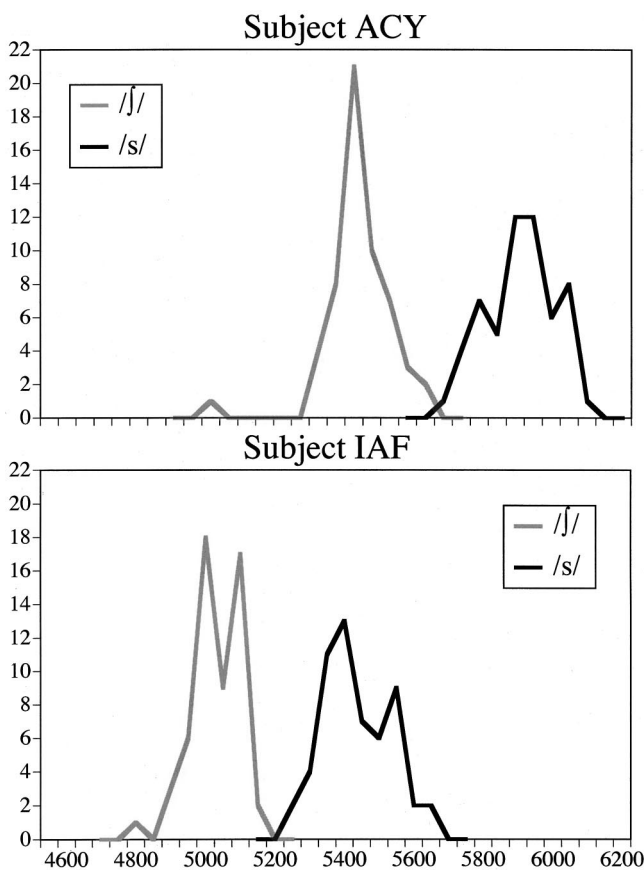


FIG. 2. Histogram of frication centroids for productions of /s/ and /j/ syllables for talkers ACY and IAF.

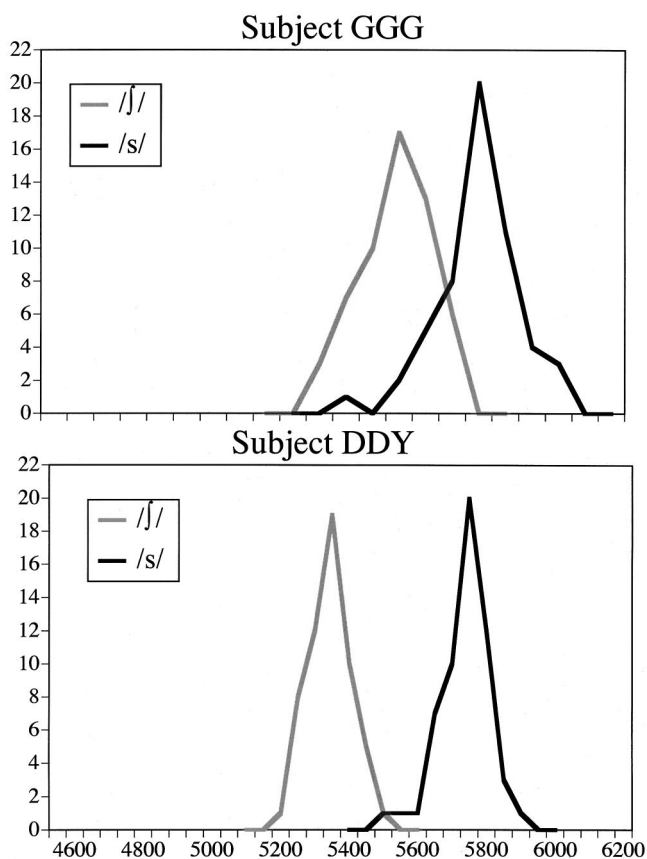


FIG. 3. Histograms of frication centroids for productions of /s/ and /ʃ/ syllables for talkers GGG and DDY.

than others; in particular, categories that are more free to vary in their productions (and thus can be produced with more variation) may be naturally more difficult for listeners than are those speech categories that are more constrained.

Although the absolute measure has not been addressed in the literature, both of the relational forms of variability have been assumed to have an influence on perception. Possibility (3), category separability, has received strong support in other domains. Reaction time studies frequently find that listeners are faster to classify items belonging to more separable categories (Melara and Mounts, 1994), and this presumably would influence speech perception as well. Indeed, reaction time measures have been taken as being a direct measure of this category separability (Moyer and Bayer, 1976). This suggests that reaction time measures should be sensitive to this form of variability, although accuracy scores may be less affected: A signal-detection analysis would imply that once two categories are completely separable, identification accuracy should be perfect, and greater discriminability beyond that point should have no effect. Thus, there is greater reason to suspect that this form of variability would influence reaction times rather than accuracy. However, even the reaction time result may be somewhat in question. Speech perception is a particularly overlearned skill, and speech categories are generally identified quite effortlessly in normal conversation. This overlearning may allow listeners to classify items purely in terms of phonological category, without direct reference to the acoustic dimensions underlying that identification. If so, the degree of difference

between categories may not be particularly relevant to identification. In addition, work on auditory psychophysics has demonstrated that reaction times only vary with discriminability to a particular point; beyond a certain level, they are not free to decrease further (Stebbins, 1966). Given the large amount of practice listeners have at discriminating speech categories, latency may not be affected by these subtle differences in variability. Furthermore, it is not always clear what cues listeners use as a basis of perception. Although the /s/-/ʃ/ distinction is clearly cued by frication frequency, listeners' perception of that dimension may not be purely linear. Indeed, work on categorical perception (Cutting and Rosner, 1974; Eimas, 1975) explicitly claims that listeners do not perceive acoustic differences in a linear manner, suggesting that linear acoustic separability may not be an accurate measure of discriminability for listeners. The only work examining these types of differences in speech stimuli focused on same/different responding, rather than categorization, and the former task may focus listeners' attention on acoustic properties in a manner different than identification (Pisoni and Tash, 1974). And, while recent work investigating how infant-directed speech results in more extreme examples of phonetic categories (Andruski and Kuhl, 1996; Andruski, Kuhl, and Hayashi, 1999) makes the implicit assumption that young listeners would find it easier to separate these more extreme (i.e., separable) productions, this has not actually been demonstrated. Thus, whether this type of talker variability would have measurable effects on either listeners' reaction times or listeners' accuracy remains an open question. Experiment 3 examines whether this type of production difference has any real consequences for perception, using $d_{(a)}$ as a measure of category distance.

Overlap among categories [possibility (2), above] can also be an indication of talker variability. Presumably, a talker who had more consistent productions would be less likely to have overlaps between phonetic categories, all other things being equal. This has also been assumed to lead to a perceptual decrement for listeners. Yet, while a number of researchers have argued that centroids and skewness serve as the primary cues to distinguish /s/ and /ʃ/ (see the discussion prior to experiment 1), these are not the only such cues. One of the most ubiquitous facts about speech is its redundancy—researchers have yet to find any single cue which is necessary for proper identification. Listeners always have multiple cues at their disposal, and may be able to switch among these cues with ease (however, see Christensen and Humes, 1996, 1997 for evidence that adults tend to focus on only a single cue even when multiple cues are available). Indeed, many researchers have claimed that the spectral moments are only two of a set of cues used to identify fricatives (Hedrick, 1997; Shadle and Mair, 1996; Tomiak, 1991; see also Whalen, 1981). If no cue is absolutely necessary, then listeners faced with a cue that does not distinguish between categories are likely to switch to using a more distinctive cue. While they may be slowed initially, they should soon realize the source of the difficulty, and should then be unaffected by the overlap between categories.

We decided to begin our examination of talker variability by examining whether this category overlap actually

leads to a perceptual decrement for listeners. Experiment 2 compares listeners' perception of tokens spoken by GGG with those spoken by a second male talker, DDY. DDY showed no category overlap on either measure (see the bottom portion of Fig. 3) and the $d_{(a)}$ measures for his productions are much higher than those for GGG (DDY: 5.915 and 8.082 for centroids and skewness respectively; GGG: 2.197 and 3.344 respectively). As both talkers are male, gender differences (such as those shown by Bradlow, Torretta, and Pisoni, 1996) are not a factor. Any differences in ease of perception for these two talkers are likely to be due to the difference in degree of category overlap.

There are three possible sets of results that might be obtained in this experiment. First, we may find that listeners have little or no difficulty perceiving the utterances of talker GGG. Such results would clearly indicate that listeners are able to adjust for idiosyncrasies in speech production by switching to alternative cues. As long as a talker does not produce category overlap in all of the potential cues to a given distinction, this form of variability within a talker would be thus unlikely to have substantial influence on perception.

A second possible set of results would be that listeners are slower at recognizing GGG's utterances, but are not less accurate. If listeners have a variety of acoustic cues available to them, their recognition accuracy need not be affected by category overlap on spectral moments. However, the conflict between different acoustic cues, or the act of switching to alternative cues, might require additional processing resources, slowing perception. This might be particularly the case early in the experiment; as listeners learn the cues necessary for distinguishing among these productions, they may be less affected perceptually.

Finally, listeners may actually be less accurate at perceiving GGG's tokens. If spectral moments are the primary (or only) acoustic cue used by listeners, we would expect such a performance decrement for talker GGG. This would further suggest that one form of variability, namely category overlap, can strongly affect perception.

Although this experiment was designed to investigate the effect of category overlap, these particular talkers also allow us to examine variability within a phonetic category. Both talkers demonstrate higher degrees of variability in their /s/ productions than in their /ʃ/ productions by both acoustic measures. More specifically, the standard deviations for talker DDY's /s/ productions are 72.98 for centroids, and 0.038 for skewness; his /ʃ/ productions have standard deviations of 58.22 according to centroid measures, and 0.021 for skewness. Talker GGG's /s/ productions have a standard deviation of 78.08 for centroids, and 0.038 for skewness; his /ʃ/ productions have standard deviations of 65.38 by centroid measures, and 0.029 for skewness. If this within-category variability has an effect on perception, we would expect to find a significant effect of phoneme, over and above any effects of talker. In particular, listeners should be slower, and perhaps less accurate, at identifying /s/ tokens than at identifying /ʃ/ tokens within each talker.

We have no particular expectations with regards to an interaction between talker and phoneme. Talker DDY has a

greater degree of difference between the variability in his /s/ and /ʃ/ productions, which might imply that the effect of phoneme would be stronger in his voice than in GGG's; however, these two effects (that of within-category variability and of category overlap) may not be strictly independent. If these two potential sources of confusion are additive in some manner, we would expect a greater effect of phoneme in talker GGG than in DDY. Because of these conflicting expectations, we are unable to make strong predictions as to the existence or direction of any interaction.

III. EXPERIMENT 2

This experiment was designed to examine the influences of categorical overlap and phoneme variability on perceptual identification. Listeners were presented with the natural /s/ and /ʃ/ utterances of two talkers, GGG and DDY, and asked to identify each item as beginning with an "s" or an "sh." Talker GGG has a fair degree of categorical overlap in his productions, whereas talker DDY does not. Both talkers have more variability among their /s/ productions than among their /ʃ/ productions. These two types of variability are both predicted to influence listeners' perception, resulting in poorer identification for talker GGG than for DDY and for the phoneme /s/ than for /ʃ/. Listeners' accuracy and response times were both measured, in order to separate out effects of misperception with more subtle effects of slowed processing.

A. Method

1. Subjects

Twenty undergraduate students (13 female, 7 male) took part in this experiment in exchange for course credit. All participants were right-handed native speakers of English, with no reported history of speech or hearing impairment.

2. Stimuli

All of the CV recordings for both talker DDY and talker GGG were used as stimuli in this experiment. This led to a total of 222 stimulus items.⁷ Fourteen items from a third male speaker (half /s/, half /ʃ/) were presented as a practice block.

3. Procedure

Listeners were tested individually and heard the tokens from both talkers in an intermixed fashion. Stimulus presentation and response collection were controlled by an Apple Macintosh 7100 A/V computer. The stimuli were presented binaurally through AudioTechnica ATH-M40fs headphones. Syllables were played in random order, and listeners were asked to identify each item as either an "s" or an "sh" as quickly and accurately as possible by pressing the appropriate button on a computer-controlled response box; both accuracy and speed were emphasized. The mapping of response to hand was counterbalanced across listeners. Presentation rate depended upon the listeners' response speed. The next trial began 1.0 s after the listener had responded, or after an interval of 3.0 s from stimulus onset had elapsed, whichever came first. Responses from the block of practice trials were not included in the analysis. Listeners

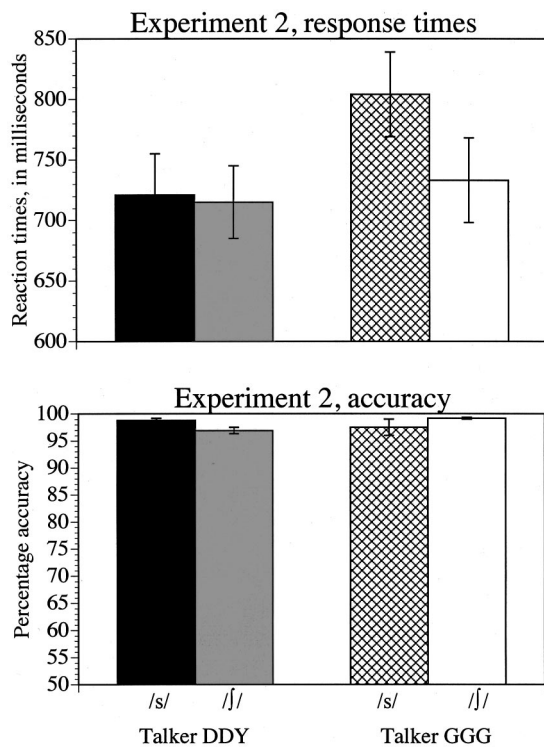


FIG. 4. Listener reaction times and accuracy scores for /s/ and /ʃ/ productions for talkers DDY and GGG.

heard all 222 stimulus items in a single block, and heard two such blocks. This led to a total of 224 responses for talker DDY (half /s/, half /ʃ/) and 220 responses for GGG (108 for /s/, 112 for /ʃ/) from each listener.

B. Results and discussion

Performance accuracy and response times were calculated for each consonant and each talker. Response times were measured from stimulus onset, rather than stimulus offset; as listeners frequently responded prior to the end of the syllable, measuring response times from stimulus offset would serve to eliminate many of their responses. Any item whose response time was greater than 2 standard deviations outside the average response time for that listener on that block, or for which the listener gave no response, was not included in the data. In addition, all trials with response times greater than 1500 ms were likewise eliminated. Combined, less than 10% of the total trials were excluded from analysis. These dropped trials were spread across types, but not evenly so: Out of 108 or 112 trials per type, data from an average of 6 items per listener were dropped from DDY /s/ items, 8 from DDY /ʃ/ items, 13 from GGG /s/ items, and 6 from GGG /ʃ/ items.

Listeners were highly accurate at identifying the intended productions, with average accuracies above 97% for each talker (97.85% for DDY; 98.38% for GGG; see Fig. 4). A repeated-measures analysis of variance (ANOVA) comparing accuracy performance on /s/ and /ʃ/ items for both talkers showed no effect of talker or fricative (both $F < 1$), and only a marginal interaction [$F(1,19) = 4.22$, $p < 0.10$]. If anything, listeners were slightly more accurate overall at classifying talker GGG's productions than talker DDY's, al-

though this depended on the particular fricative (listeners were 1.3% more accurate for talker DDY on /s/ items, and 2.3% more accurate for talker GGG for /ʃ/ items).

The high level of accuracy suggests that listeners were able to compensate for category overlap on a given cue and successfully identify the intended speech. However, this required additional processing resources, as demonstrated by the slowed reaction times to talker GGG's speech, as compared to that of talker DDY. A repeated-measures ANOVA comparing reaction times to the /s/ and /ʃ/ items in both talkers showed a substantial effect of talker [$F(1,19) = 131.32$, $p < 0.0001$; mean response time to talker DDY = 718 ms and to talker GGG = 768 ms]. There was also an effect of fricative, with listeners slower to identify the /s/ tokens than the /ʃ/ tokens [$F(1,19) = 29.37$, $p < 0.0001$; average response time to /s/ = 763 ms and to /ʃ/ = 724 ms], and a significant interaction [$F(1,19) = 53.36$, $p < 0.0001$]. Follow-up t tests showed that response times were slower to talker GGG than talker DDY for both /s/ and /ʃ/ productions [for /s/, $t(19) = 15.823$, $p < 0.0001$; for /ʃ/, $t(19) = 2.676$, $p < 0.05$], although the difference between talkers was smaller on /ʃ/ items. The reason for this asymmetry is less clear, but it may be that when multiple sources of variability are present in a signal, the effects are multiplicative rather than additive. That is, the /s/ items for talker GGG suffer from two forms of variability: the greater variability caused by category overlap, and the greater variability in the /s/ phoneme across the two talkers. Together, these two forms of variability may slow processing more than a simple additive model might predict. However, since the effect of talker is nonetheless present in both the /s/ and /ʃ/ phonemes, this asymmetry in effect size does not negate the primary point that category overlap results in slowed reaction times.

These reaction time findings have a number of implications. First, the measurements of frication centroid and skewness do seem to catch some of the information listeners use when making phonetic categorization; were this not the case, there would be no reason to predict that performance would be slower to talker GGG than to talker DDY. Although it is possible that the category overlap in these two measures is simply a coincidence (and that listeners are relying on other cues that happen to produce the same effect), it seems more likely that the measurements taken in experiment 1 have some bearing on listeners' perception of the items. Listeners appear to be attempting to use these cues, and are being slowed by the fact that these cues do not provide sufficient discriminatory information. Second, although prior research has suggested that these cues are the primary ones used in sibilant discrimination (Forrest *et al.*, 1988; Harris, 1958), they are clearly not the only cues available to listeners. If they were, listeners would likely have difficulty discriminating the /s/ and /ʃ/ productions that fell into the overlapping region of talker GGG's production space. The high accuracy scores in the present experiment demonstrate that this was not the case. Third, both category overlap and within-category variability have demonstrable effects on perception. Even though listeners had alternative cues at their disposal, they were slower at identifying targets spoken by GGG, and were slower at identifying /s/ tokens than /ʃ/ tokens. The

increase in response time to talker GGG may be due to the need to switch to alternative measures, or may be caused by the conflict between different acoustic cues. It may also simply be due to the variability in production in this talker's voice, or to uncertainty among the listeners (see Haley and Ohde, 1996 for a discussion on the role of uncertainty in speech experiments). Regardless, the results clearly show that the degree of speaker variability does result in subtle influences on perception, which can be measured using an appropriate task.

Given that category overlap results in poorer comprehension, why did talker GGG not adjust his speech in order to avoid such overlap? One possibility is that familiarity with a talker's voice might alleviate some of these perceptual difficulties. Participants in our perceptual experiments did not know the speakers to whom they were listening. Yet, most real-life conversations likely take place between individuals who have had the opportunity to become familiar with each other's speech production idiosyncrasies. Familiarity with a voice might allow listeners to learn which acoustic cues are most appropriate for recognizing that individual's speech. Although the present study was not designed to examine this issue, one way of addressing it is to compare listeners' performance on the first block with their performance on block two. If familiarity with a voice allows listeners to adjust for a talker's category overlap, then the performance difference between tokens from GGG and DDY should be reduced in block 2. We examined reaction time performance on the two blocks in a $2(\text{block}) \times 2(\text{talker}) \times 2(\text{fricative})$ ANOVA. There was an overall effect of block [$F(1,19) = 5.52, p < 0.05$] such that listeners responded more quickly overall on the second block. There was also a marginal interaction between block and talker in the correct direction [$F(1,19) = 4.23, p < 0.06$]: in block 1, the reaction time difference between talkers was 59 ms, whereas it was only 43 ms in block 2. Listeners suffered less decrement with talker GGG's voice as they became more familiar with it. However, even after hearing more than 100 tokens from this talker, the participants in this experiment remained unable to respond to tokens in his voice as quickly as they could to tokens in talker DDY's voice, suggesting that relatively modest degrees of familiarity with a talker are not sufficient to alleviate these perceptual difficulties.

The similarity between GGG's /s/ and /ʃ/ productions resulted in slowed processing on the part of listeners. Yet, it is not clear whether this slowed processing was due to the poorer discriminability of talker GGG's productions, or was caused specifically by the category overlap. That is, was it the fact that the /s/ and /ʃ/ distributions *overlapped* in this talker that caused problems, or were problems caused by the fact that the distance between the categories was smaller (that is, that $d_{(a)}$ for GGG was reduced relative to that from talker DDY)? These possibilities cannot be distinguished in the current experiment. One way to address this issue would be to compare performance on two talkers who do not show category overlap, but who have similar discriminability differences as do talkers GGG and DDY. For example, Fig. 5 shows frequency centroids for talkers KSK and LCG, neither of whom have category overlap on either acoustic measure.

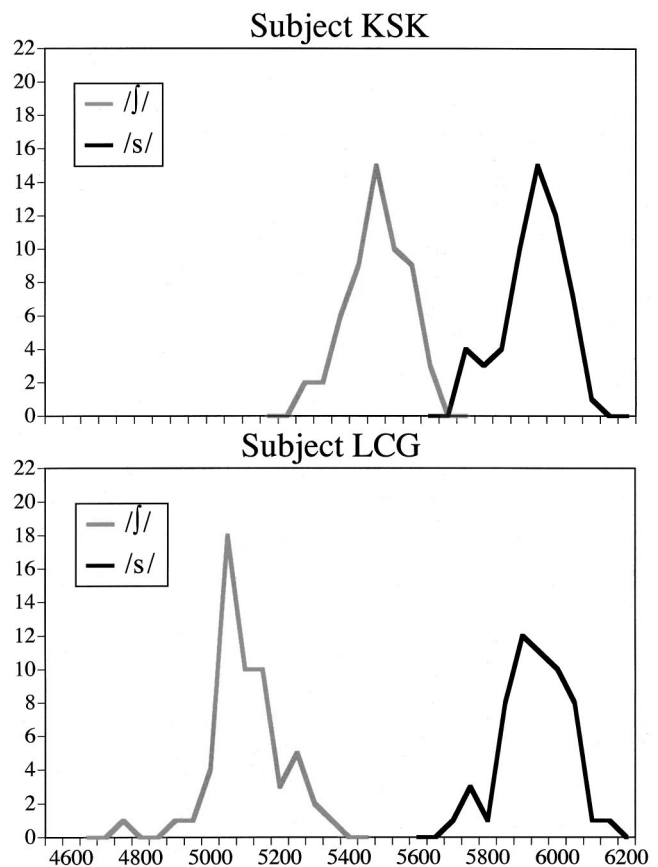


FIG. 5. Histograms of frication centroids for productions of /s/ and /ʃ/ syllables for talkers KSK and LCG.

These talkers do differ in the distance between their categories (for talker KSK, $d_{(a)} = 5.249$ for centroids, $d_{(a)} = 6.469$ for skewness; for talker LCG, $d_{(a)} = 9.231$ for centroids, $d_{(a)} = 11.128$ for skewness). In fact, the difference in discriminability between these two talkers is quite comparable to the difference in discriminability between talkers GGG and DDY (for centroids, $d_{(a)DDY} - d_{(a)GGG} = 3.718$, $d_{(a)LCG} - d_{(a)KSK} = 3.982$; for skewness, $d_{(a)DDY} - d_{(a)GGG} = 4.738$, $d_{(a)LCG} - d_{(a)KSK} = 4.659$). Comparing perception of these two talkers allows us to separate out influences of category overlap with influences of category distance *per se*, and determine which type of talker variability is most detrimental to listeners.

IV. EXPERIMENT 3

This experiment compares listeners' categorization performance for two talkers who differ in their sibilant discriminability (see Fig. 5). Although all items are perfectly discriminable in both voices (that is, there is no category overlap in either speaker), the two categories lie further apart in perceptual space for talker LCG than talker KSK.

The degree of category separability between the talkers in the present experiment is quite comparable to the difference between talkers GGG and DDY from experiment 2. If category overlap were the primary factor in the slowed response times to GGG, then performance on talkers KSK and LCG should be quite comparable (as neither talker has any category overlap). However, if listeners respond more

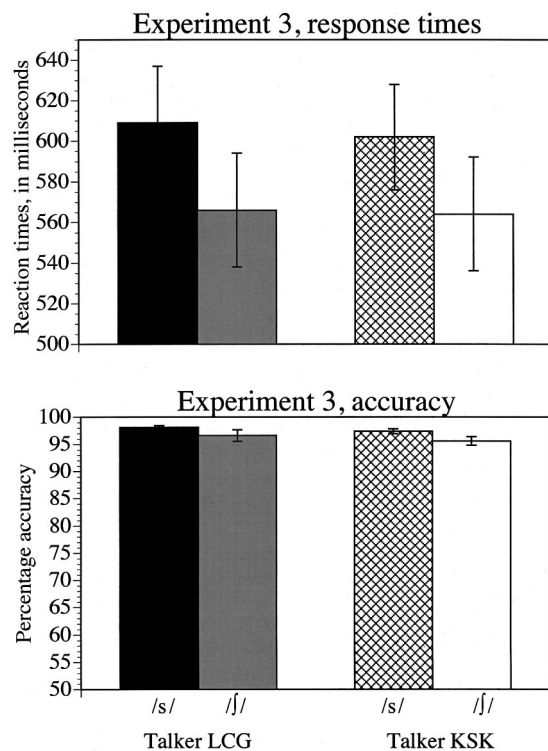


FIG. 6. Listener reaction times and accuracy scores for /s/ and /ʃ/ productions for talkers KSK and LCG.

quickly to talkers with more discriminable categories, then listeners in the present experiment should have faster reaction times to talker LCG than talker KSK, and the amount of this difference should be comparable to that for the difference between the talkers in experiment 1.

Neither of these talkers shows the degree of difference between the variability of their /s/ and /ʃ/ productions that talkers GGG and DDY showed. For example, the standard deviations for centroids differed by nearly 14 for both GGG and DDY; they differ by only 9 for LCG and by less than 2 for KSK. Furthermore, while both female talkers are slightly more variable in their /ʃ/ productions by measurements of centroids, they are also slightly more variable in their /s/ productions by skewness measures. Listeners may vary in terms of which of these two cues they focus their attention on, and if so, some may hear the /s/ items as more variable and others the /ʃ/ items, causing these effects to balance out (Christensen and Humes, 1996, 1997). Thus, we do not predict any effect of phoneme in the current study.

A. Method

1. Subjects

Twenty-two undergraduate students (19 female, 3 male) took part in this experiment in exchange for course credit. All participants were right-handed native speakers of English, with no reported history of speech or hearing impairment. The data from two additional listeners were dropped for experimenter error.

2. Stimuli

All of the CV recordings for two female talkers (LCG and KSK) were used as stimuli in this experiment. This led to a total of 223 items.⁸ Fourteen items from a third female speaker (half /s/, half /ʃ/) were presented as a practice block.

3. Procedure

All aspects of the procedure were identical to those in experiment 2. Syllables were played in random order, and listeners were asked to identify each item as either an ‘s’ or an ‘sh’ as quickly and accurately as possible by pressing the appropriate button on a computer-controlled response box. The mapping of response to hand was counterbalanced across listeners. Listeners heard all items in an intermixed fashion, and heard a total of two blocks of trials.

B. Results and discussion

Performance accuracy and response times were calculated for each consonant and each talker, as in experiment 2. Any item that was more than 2 standard deviations outside the average response time for that listener, or for which the listener gave no response, was not included in the data. In addition, all trials with response times greater than 1500 ms were likewise eliminated. Data from less than 6% of trials were eliminated for these reasons. (These dropped trials were spread across types, but were slightly larger for /s/ items than for /ʃ/ items: Out of 110 or 112 trials per type, data from an average of 6 items per listener were dropped from KSK /s/ items, 7 from LCG /s/ items, and 5 each from KSK and LCG /ʃ/ items.)

Overall accuracy was again quite high, at 96.6% for talker KSK, and 97.4% for talker LCG (see Fig. 6). This slight difference in accuracy was marginally significant [$F(1,21)=4.14$, $p<0.10$], suggesting a tendency towards better identification of talker LCG. However, listeners’ response times also showed a marginal effect of talker, with listeners responding slightly faster for talker KSK [$F(1,21)=2.97$, $p=0.10$]. There was a significant effect of phoneme in both measures, with more accurate identification for /s/ than /ʃ/ [$F(1,21)=5.01$, $p<0.05$], but with /s/ being slower [$F(1,21)=40.96$, $p<0.0001$]. There was no interaction between phoneme and talker on either measure ($F<1$).

The trend toward an effect of talker in this experiment seems to be caused by speed-accuracy trade-offs: Listeners were marginally more accurate at identifying tokens from LCG, but also marginally slower. Since neither tendency even reached significance, there appears to be no strong evidence for an effect of talker in this study. It is possible that the tendency towards a speed-accuracy trade-off masked an effect of talker, but such an effect would likely not be of the magnitude of difference seen between talkers GGG and DDY. Furthermore, any effect in the reaction times in the present experiment is in the opposite direction of that predicted. Apparently, the difference between perception for talkers GGG and DDY in experiment 2 was due more to the category overlap among talker GGG’s productions than to the reduced discriminability of his categories.

There was an effect of phoneme in both measures, with /s/ being both more accurate and slower. Part of the reaction time difference may also be due to a speed–accuracy trade-off, but not necessarily the entire effect. As discussed earlier, we had no predictions for a phoneme effect in this study, since the two measures (centroids and skewness) predicted effects in different directions. The greater effect in reaction times suggests the possibility that listeners’ response times were based more on skewness than on centroids (since skewness measures were more variable for /s/ than /ʃ/). However, further research will be needed to test this more explicitly.

The speed–accuracy trade-offs make the interpretations of the talker effects unclear. Furthermore, listeners responded much more quickly to the items in this experiment than to those in the prior experiment, raising the possibility that they were at ceiling performance. That is, they may have been responding so quickly that differences in processing speed could not be seen. A comparison of the two blocks argues against this, however: Listeners were approximately 26 ms faster overall in block 2 than in block 1 [$F(1,21) = 5.99, p < 0.05$], yet the pattern of results is consistent across the two blocks.

The results for phonemes may also be due to speed–accuracy trade-offs, but here the results are more murky. Responses to the /s/ tokens were both significantly more accurate than the /ʃ/ items, and significantly slower. The fact that the effects go in opposite directions limits our ability to make any substantive claims about directionality of the effect of phoneme in these talkers.

Another possible concern is that the results in these experiments were caused by some aspect of the signal other than that of the initial fricative; perhaps the stimuli differed in their average length, or in some aspect of the vowel, and those differences influenced perception. This is especially worrisome given the speed–accuracy trade-offs; it appears likely that some aspect of the signal served to cause listeners to use a different strategy for responding to /s/ items than /ʃ/ items. To address these concerns, experiment 4 reexamines the items from all four talkers, while controlling for other possible differences in the syllables. All but the initial 100 ms of each syllable was removed, leaving only the first portion of the frication for each item. This equates the syllables for length, and removes all information other than the friction from the items. If the same pattern of results occurs, it could not be caused by factors such as vowel quality or syllable duration.

V. EXPERIMENT 4

This experiment was designed to examine whether the pattern of results found in the prior experiments might be due to other differences in the stimuli. Listeners were again presented with the natural /s/ and /ʃ/ utterances of two talkers (either GGG and DDY or KSK and LCG), but in this experiment they heard only the first 100 ms of the frication itself. Thus, there was no additional information in the vowel or transitions that could help to distinguish the phonemes, and there were no differences in other factors (such as duration or fundamental frequency) that might be the cause of any differences in response times. Any effect of talker in the present

experiment could not be due to factors other than those in the frication itself. Similarly, any effect of phoneme in the present experiment would necessarily be caused by differences in the frication, rather than differences in the transitions or the remainder of the syllable.

We proposed in experiment 2 that listeners were switching to alternative cues for talker GGG. Some of these alternative cues may have been in the transitions between the fricative and vowel (Whalen, 1991). Since the transitions are not present in the current experiment, we may be more likely in the present experiment to see effects in both accuracy and reaction times, rather than in reaction times alone. This is especially the case for the male voices, where the frication cues are not sufficient for discriminating all items; we would not expect such accuracy results in the female voices, where the frication does provide sufficient cues to identification.

A. Method

1. Subjects

Forty undergraduate students (31 female, 9 male) took part in this experiment in exchange for course credit or for a small monetary compensation. All participants were right-handed native speakers of English, with no reported history of speech or hearing impairment. Half of the listeners heard the two male voices from experiment 2, whereas the others heard the female voices from experiment 3. Data from an additional five participants were dropped from analysis, three for experimenter error, one for equipment failure, and a fifth for being a nonnative speaker.

2. Stimuli

All of the CV recordings from the prior two experiments were used as stimuli in this experiment. These items were edited, leaving only the initial 100 ms of each item (all of the items had natural frications longer than 100 ms, such that the cut point remained within the fricative itself). This controls for differences in duration among items. In addition, by removing the vowel portion of all syllables, we are ensuring that any effects of talker are actually caused by differences in the frication, rather than differences in other portions of the syllables. Fourteen items from a third speaker (half /s/, half /ʃ/) were presented as a practice block.

3. Procedure

Listeners were tested individually in the same manner as in the prior experiments, with one exception. The vocalic portions of the syllables in the prior experiments allowed the listeners to easily distinguish between the two talkers. Without those portions, it was often difficult to determine which talker was actually producing each syllable. As we wanted to ensure that listeners were judging each talker’s utterances on the basis of the cues appropriate for that talker, we felt it important for listeners to be able to distinguish the talkers easily. We therefore decided to block the items by talker, rather than intermix them. Listeners thus heard two blocks of items from a single talker, and then two blocks from the second talker of the same gender. Which talker was heard first was counterbalanced across participants.

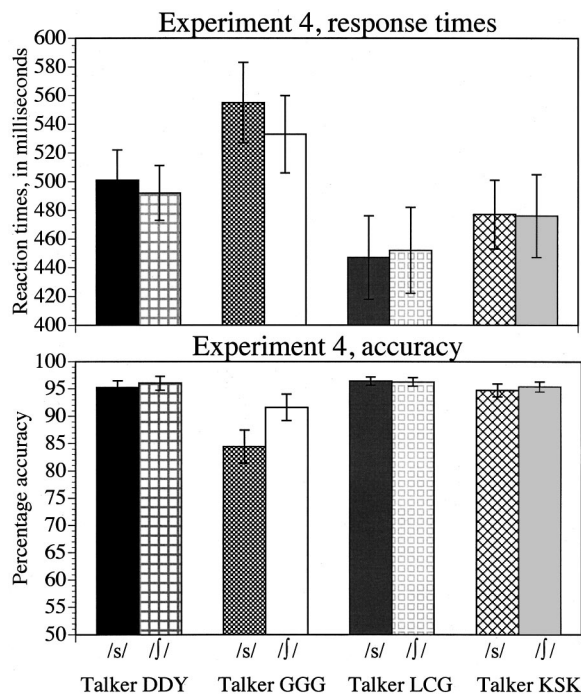


FIG. 7. Listener reaction times and accuracy scores for identifying the first 100 ms of frication for all four talkers.

B. Results and discussion

Performance accuracy and response times were calculated for each consonant and each talker, as in experiments 2 and 3. Any item that was more than 2 standard deviations outside the average response time for that listener, or for which the listener gave no response, was not included in the data. In addition, all trials with response times greater than 1500 ms were likewise eliminated. The dropped trials were not spread evenly among conditions, although they were still a minority of items, ranging from 5 to 12 trials per condition (where conditions consisted of 108–112 trials). For the male voices, talker DDY lost an average of 7 trials per listener for the /s/ items, and 6 for the /ʃ/ items; talker GGG lost an average of 12 for the /s/ items and 8 for the /ʃ/ items. For the female voices, talker KSK lost an average of 7 trials per listener each on the /s/ and /ʃ/ items, and talker LCG lost an average of 6 trials for the /s/ items and 5 for the /ʃ/ trials.

We began by comparing the results for the 20 listeners hearing the two male talkers. Although listeners were fairly accurate at identifying the intended productions, their overall accuracies were not as great as in the prior experiments, suggesting that this task was substantially more difficult (see Fig. 7). In addition, a repeated-measures ANOVA comparing accuracy performance on /s/ and /ʃ/ items for both talkers showed significant effects of both talker and fricative, as well as a significant interaction [effect of talker, $F(1,19) = 23.68$, $p < 0.0001$; effect of phoneme, $F(1,19) = 8.33$, $p < 0.01$; interaction, $F(1,19) = 10.06$, $p < 0.005$]. Listeners showed a 96% accuracy for talker DDY, but only an 88% accuracy for talker GGG, demonstrating the effect of talker overlap on listeners' perception. In addition, the listeners were 4% more accurate at identifying the /ʃ/ tokens than the /s/ tokens, again demonstrating an effect of variability within

phoneme category. The interaction was caused by a larger difference between the two talkers among the /s/ productions than in the /ʃ/ productions. Follow-up tests showed the effect of talker to be significant in both phonemes: Listeners were 11% more accurate to talker DDY in the /s/ items, and 4% more accurate to talker DDY in the /ʃ/ items [for the /s/ items, $t(19) = 4.79$, $p < 0.0001$; for /ʃ/, $t(19) = 3.25$, $p < 0.005$].

The reaction time results showed a similar pattern. Listeners were 47 ms faster on average to identify those fricatives spoken by talker DDY than those spoken by talker GGG [$F(1,19) = 11.90$, $p < 0.005$]. There was also a significant effect of phoneme, with listeners 16 ms faster to identify the /ʃ/ tokens than the /s/ tokens [$F(1,19) = 5.06$, $p < 0.05$]. The interaction between talker and phoneme was marginal [$F(1,19) = 3.12$, $p < 0.10$]. Again, follow-up tests showed the effect of talker to be significant in both phonemes [for the /s/ items, $t(19) = 3.96$, $p < 0.001$; for /ʃ/, $t(19) = 2.73$, $p < 0.02$].

Looking at the two blocks separately showed the same pattern of results. Neither the effect of block nor any interaction involving block was significant [in accuracy, effect of block $F < 1$; interaction of block and talker, $F(1,19) = 1.79$, $p > 0.10$; interaction of block with phoneme, $F(1,19) = 3.37$, $p < 0.10$; three-way interaction, $F(1,19) = 1.25$, $p > 0.10$; in reaction times, $F(1,19) = 3.54$, $p < 0.10$; all interactions $F < 1$].

Unlike the results from Experiment 2, the current results cannot be due to other aspects of the signal, such as duration or vowel quality. Thus, these results support the idea that both category overlap among fricative productions and variability within a category have significant effects on listeners' perceptions. Listeners are capable of switching to alternative cues (such as those in the transitions into the vowel) when these cues are available, as was the case in experiment 2. When they are unavailable, listeners' accuracy at identifying the items decreases in addition to their speed.

This also suggests a distinction between direct and indirect effects of variability. In the present experiment, the effect of variability appears to directly affect reaction times and accuracy. In the prior experiments, however, the variability seemed to encourage listeners to switch to alternative cues. This switching (or the reliance on cues not typically used) then slowed processing speed—but the slowed response times may have been only indirectly caused by the variability in the signal. The direct effect of variability was the switching to other cues.

We next compared the results for the 20 listeners hearing the two female talkers. The speed–accuracy trade-offs did not reoccur, suggesting that they may have been caused by other aspects of the syllable. Furthermore, once this variability was no longer present, a trend towards an effect of talker became apparent. The accuracy results were not significant, with listeners slightly more accurate to tokens from LCG [by 1.4%; $F(1,19) = 2.40$, $p > 0.10$]. However, listeners responded marginally faster to talker LCG [by nearly 28 ms; $F(1,19) = 4.12$, $p < 0.06$], suggesting that separability of categories also has an effect on listeners' perception. Follow-up t tests showed the results to be significant for the /s/ items [$t(19) = 2.11$, $p < 0.05$] but only marginal for the /ʃ/ items

[$t(19) = 1.76, p < 0.10$]. As originally predicted, there was no effect of phoneme for these two talkers, and no interaction between talker and phoneme in either analysis (all $F < 1$).

Looking at the two blocks separately showed a somewhat different pattern of results. The effect of talker on reaction times was only significant in block 1 [$F(1,19) = 4.64, p < 0.05$], not in block 2 [$F(1,19) = 1.08, p > 0.10$], although the block by talker interaction did not reach significance [$F(1,19) = 1.73, p > 0.20$]. The effect of talker was not significant in accuracy in either block [for block 1, $F(1,19) = 1.52, p > 0.10$; for block 2, $F(1,19) = 1.89, p > 0.10$]. The latter is not surprising, as the listeners had no need to switch to alternative cues for these talkers (unlike with the male talkers). However, the difference across blocks in reaction times is more surprising. It suggests that while listeners were initially slowed by the decreased category separability between these talkers' voices, this effect began to disappear with further practice. Looking at the means, it appears that performance with talker LCG remained quite stable across blocks (average reaction times of 449 ms for block 1 and 450 ms for block 2). Listeners' performance improved with talker KSK as they became more practiced with her voice, with an average reaction time of 489 ms during block 1 but only 465 ms for block 2.

Why were the effects for the female talkers so different here than in experiment 3? One possibility is that the participants in experiment 3 may have been responding at ceiling performance. However, comparing across the two experiments suggests that listeners were actually responding significantly faster in the current experiment than in the prior experiment [by over 120 ms; $F(1,40) = 10.12, p < 0.005$]. A more likely possibility is that the tendency towards a speed-accuracy trade-off masked the slight effects of talker in that experiment. As this speed-accuracy trade-off did not occur with only the first 100 ms of the frication being presented, it seems likely that other aspects of the signal (such as vowel quality or syllable duration) may have been the primary cause for those results. It is less clear why the effect of phoneme, which seemed fairly strong in experiment 3, did not reappear here. One possibility is that, with less information present, listeners were relying both on skewness and centroids here, but were relying more heavily on skewness in the prior experiment. Or, perhaps the reaction time effects in that experiment were due to syllable durations, or other cues not found in the present experiment. Regardless, there does not appear to be any consistent phoneme effect for these talkers.

It appears that category discriminability may have a slight effect on listener perception. However, this effect of talker for the female voices was clearly weaker than that for the male voices, as it only approached significance with the female voices. Furthermore, a comparison across the male and female voices showed a highly significant interaction in accuracy scores between talker (easy versus hard) and gender (male vs female), with the poorest performance for the difficult male talker [$F(1,38) = 12.732, p < 0.001$ for accuracy; $F(1,38) = 1.095, p > 0.10$ for reaction times]. This suggests that category overlap may have effects above and beyond those of category discriminability. That is, the effect of cat-

egory overlap was not simply caused by a linear measure of discriminability; overlap between categories is substantially more difficult for listeners than are categories that are simply close together.

This cross-experiment analysis shows a phoneme by gender interaction as well [$F(1,38) = 5.91, p < 0.05$ by accuracy; $F(1,38) = 3.34, p < 0.10$ by reaction time], with the /s/ items for the male voice having a lower accuracy and higher reaction time than all other items. This supports the idea that the decreased performance for /s/ items was limited to the male voices (where the /s/ items had higher variability than the /ʃ/ items).

VI. GENERAL DISCUSSION

The results from this study are a step towards the goal of examining the role of production variability on perception. These results demonstrate that a number of forms of talker variability have perceptual consequences for listeners. To begin with, greater consistency of production within a phonetic category appears to make items in that category easier to classify. When a speaker had a substantially greater amount of variability in production for one phonetic category than for the other, listeners were slower to identify the tokens from the more variable category. Listeners were also less accurate at identifying those items when there were no other cues available on which they could rely.

Clearly, variability within a category influences listeners' ability to identify tokens from that category. In some cases, this effect of within-phoneme variability may be primarily due to idiosyncrasies in an individual's speech production. This is likely to be the case in the present experiment. However, some phoneme categories may naturally be more prone to variability than are others, and may therefore be consistently harder to identify. For example, among stop consonants, voiced items are bounded in their VOT measures, while voiceless items are not.⁹ This leaves voiceless items more free to vary, and suggests that they may be naturally harder to identify than voiced items, at least when categories are equally separable. Future research will be needed to explore this more fully.

In addition to this absolute measure of variability, there are also relational effects of variability that can influence perception. Both the discriminability of phonetic categories, and their discreteness (or degree of overlap) can influence a listener's ability to identify particular tokens. As with the variability within a category, these effects are primarily seen in reaction times when listeners have the opportunity to switch to alternative cues for identification. In these cases, either the need to switch to alternative cues, or the conflict between cues, slowed perceptual processing. When such alternative cues are unavailable, however, listeners are also less accurate at identifying tokens from talkers with category overlap in production, although they do not appear to be less accurate at identifying items from categories that are non-overlapping but less separable. Although few talkers show actual overlap on most cues, experiment 1 shows that talkers do vary substantially in the degree to which their phonetic categories differ from one another. This is therefore likely to

be one factor in what makes individual talkers more or less intelligible.

Although the discriminability of categories did have a marginal effect on listeners' reaction times in experiment 4, this effect was relatively weak. The effect was primarily due to the first block of trials, and appears to have dissipated by the second block. This may seem surprising, given the substantial literature suggesting that reaction times are a fairly consistent measure of discriminability (Melara and Mounts, 1994). However, speech perception is a particularly well-learned skill, and reaction time differences tend to asymptote once a particular level of discriminability has been reached (Stebbins, 1966). It may be that these subtle forms of talker variability have only minor effects on perception which may not even be measurable in many situations.

In addition to suggesting that talker overlap is a not uncommon situation, experiment 1 also has implications for theories of talker normalization or adjustment. Given the degree of overlap across some pairs of talkers (such as ACY and IAF in Fig. 2), a process of talker normalization is likely to be needed in order to correctly perceive the intended utterance. This is the case even for talkers whose productions are individually quite consistent. When a listener hears a talker's voice for the first time, he or she will not know that individual's ranges of frication production, and needs some method of discovering what intended phoneme a single token is most likely to represent. For example, a token with a centroid value of 5400 Hz could be a typical /s/ from talker IC, or a typical /ʃ/ from talker KJP. Without familiarization with the specific talker, some type of normalization process is likely to be required in order to interpret the speech production accurately. This process may involve tracking the fundamental frequency, the higher formants (such as F_4), higher-order moments, or some form of auditory transformation. This normalization process is not yet understood, and further research along this line is also necessary.

However, normalization for the talker is clearly not sufficient to account for all forms of production variability, as shown by the present experiments. Even after substantial experience with a talker (hearing over 100 tokens of a particular phonetic category within a short span of time), listeners continue to have difficulty with more variable talkers. This is particularly well demonstrated by the fact that effects of variability generally did not disappear by the second block of trials in the present experiments; the one exception to this is that of category separability, where the effect of talker no longer remained significant by the second block of trials (although the cross-block comparison was not significant, making interpretation of this result tentative). Future work investigating such effects in very well-known voices (such as that of close family members) may be able to determine whether these effects of talker variability ever disappear entirely (see Magnuson, Yamada, and Nusbaum, 1995 for similar work demonstrating that effects of variability across talkers do not disappear even with highly familiar voices).

The types of production variability described here might have an even greater effect on perception by hearing-impaired listeners. As these listeners may have access to fewer supplementary cues (see Zeng and Turner, 1990),

overlap between acoustic categories may cause more severe difficulties in speech recognition. Thus, one direction for future research would be to examine whether the identification difference between talkers such as GGG and DDY is greater for listeners with hearing impairments than it is for normal listeners.

The present methodology may also provide a manner of examining the appropriateness of different measurement strategies. The current study examined spectral moments, but there are other possible acoustic cues that could be examined. Presumably, listeners' performance will be poorer whenever there is greater variability on an acoustic cue to which listeners are sensitive. If a cue is not used by listeners, there should be little decrement caused by inconsistency on that cue. This may provide a new means of comparing different acoustic measures.

In conclusion, talkers appear to differ in the ease with which their speech can be understood. Talkers with more consistent productions (that is, talkers whose speech categories are both very distinct from one another and highly internally consistent) appear to be more intelligible to listeners. Despite this, speakers do not seem to avoid producing speech with even the most extreme type of variability, category overlap: Out of 20 talkers, we found at least one talker with overlap on each of the acoustic measures examined. If this proportion generalizes to the population as a whole, even this form of variability within a talker is likely to be one that listeners must deal with on a regular basis.

ACKNOWLEDGMENTS

Experiment 1 was performed at the State University of New York at Buffalo as part of a doctoral thesis, under the direction of James R. Sawusch. The authors would like to thank Jim Sawusch, Paul Luce, Donald Dorfman, Peter Juszczyk, Gail Mauner, Gregg Oden, Ken Stevens, Chris Turner, and an anonymous reviewer for helpful commentary and suggestions, and Jim Sawusch for design of the test program and spectral analysis program used for these experiments. We also thank Ben Schnoor, Rachael Dolezal, Isma Hussain, Erica Stewart, Sarah Stilwill, Phillippe Taborga, Susan Timm, and Andrea Tuttle for assistance in running subjects for experiment 4. This research was supported in part by NIH Grant No. DC00219 to SUNY at Buffalo, and by a University of Iowa Old Gold Summer Fellowship to the first author. Some of these data were previously presented at the 133rd meeting of the Acoustical Society of America, State College, PA, June, 1997 and at the 138th meeting of the Acoustical Society, Columbus, OH, November, 1999. Comments may be sent to the first author at the Department of Psychology, E11 Seashore Hall, University of Iowa, Iowa City, IA 52242.

¹A study by Datschewit (1990) suggests that F_2 onset frequencies also are used in the perception of voiceless fricatives, but that while these influence goodness ratings, they do not serve to differentiate /s/ and /ʃ/. Zeng and Turner (1990) also suggest that these transition cues are secondary.

²We do not mean to imply that this is the only factor that will influence listeners' use of a particular cue. Sensitivity to the cue, availability of the cue, and other such factors will also play a role. However, the variability of

the cue in normal listening will be one of the factors that will influence its usefulness.

³A potential problem is that the listeners may have been mimicking the talker they heard, even though they were explicitly instructed to produce the items normally. If this were the case, it would serve to reduce the amount of variability that exists across talkers (as all of the talkers' speech would regress towards that of the original speaker). In addition, as the participants repeated each exemplar more than once, mimicking should lead to reduced variability within a speaker as well: those productions following the same token should be more similar than would be expected ordinarily. Thus, to the extent that mimicking does take place, our task is an underestimate of the true variability that occurs both within and across talkers. It is difficult to determine whether such mimicking might be taking place; however, variability among the female speakers was actually higher than among the male speakers, which tends to argue against this notion.

⁴Since the standard deviations of the two phoneme categories were not identical, we used $d_{(a)}$ rather than d' . $D_{(a)}$ equals the difference in the means of the two categories times the square root of 2, divided by the square root of the sum of the variances. When the variances are equal, this reduces to the well-known d' (see Swets and Pickett, 1982, p. 32).

⁵The raw values of skewness and centroid are also highly correlated. For /s/ productions, $r = 0.96$, $p < 0.0001$; for /ʃ/ productions, $r = 0.95$, $p < 0.0001$.

⁶These two talkers are of different genders, which may explain part of their overlap. However, they are fairly representative of the remainder of the talkers, and high degrees of overlap could also be found among talkers of the same gender.

⁷Ideally, each talker recorded 112 syllables (2 repetitions of each of 4 productions of each fricative, in 7 different vowel environments). However, due to a computer recording error, two of the /s/ productions of talker GGG were lost. As this was a very slight proportion of the total number of stimuli, we assume that it will not affect the perceptual results.

⁸One of talker LCG's original /ʃ/ recordings was lost to an equipment error.

⁹This assumes that prevoicing is a separate cue from VOT, which may be a matter of some contention. However, for the sake of the present argument, voiced items have both a minimum VOT (0 ms) and a maximum VOT (the voiced/voiceless category boundary), while voiceless items are bounded only at the low end, leaving them more free to vary. Clearly, there is still a limit on voiceless items, in that extreme items (beyond those that typically occur in natural productions) may not consistently be heard as good members of the category (Miller and Volaitis, 1989). However, the lack of an upper boundary results in a much larger range of acceptable category members for the voiceless items than for the voiced items (Miller and Volaitis, 1989; Newman, 1998).

Andruski, J. E., and Kuhl, P. K. (1996). "The acoustic structure of vowels in mothers' speech to infants and adults," 4th International Conference on Spoken Language Processing (ICSLP), Philadelphia.

Andruski, J. E., Kuhl, P. K., and Hayashi, A. (1999). "Point vowels in Japanese mothers' speech to infants and adults," 137th Meeting of the Acoustical Society of America, Berlin, Germany.

Baum, S. R., and McNutt, J. C. (1990). "An acoustic analysis of frontal misarticulation of /s/ in children," J. Phonetics 18, 51–63.

Behrens, S. J., and Blumstein, S. E. (1988). "Acoustic characteristics of English voiceless fricatives: A descriptive analysis," J. Phonetics 16, 295–298.

Bladon, A., and Seitz, F. (1986). "Spectral edge orientation as a discriminator of fricatives," J. Acoust. Soc. Am. Suppl. 1 80, S18–S19.

Bradlow, A. R., Torretta, G. M., and Pisoni, D. B. (1996). "Intelligibility of normal speech. I. Global and fine-grained acoustic-phonetic talker characteristics," Speech Commun. 20, 255–272.

Byrd, D. (1992). "Preliminary results on speaker-dependent variation in the TIMIT database," J. Acoust. Soc. Am. Suppl. 1 92, 593–596.

Christensen, L. A., and Humes, L. E. (1996). "Identification of multidimensional complex sounds having parallel dimension structure," J. Acoust. Soc. Am. 99, 2307–2315.

Christensen, L. A., and Humes, L. E. (1997). "Identification of multidimensional stimuli containing speech cues and the effects of training," J. Acoust. Soc. Am. 102, 2297–2310.

Cole, R. A., Coltheart, M., and Allard, F. (1974). "Memory of a speaker's voice: Reaction time to same- or different-voiced letters," Q. J. Exp. Psychol. 26, 1–7.

Craik, F. I. M., and Kirsner, K. (1974). "The effect of speaker's voice on word recognition," Q. J. Exp. Psychol. 26, 274–284.

Creelman, C. D. (1957). "Case of the unknown talker," J. Acoust. Soc. Am. 29, 655.

Crystal, T. H., and House, A. S. (1988). "The duration of American-English stop consonants: An overview," J. Phonetics 16, 285–294.

Cutting, J. E., and Rosner, B. S. (1974). "Categories and boundaries in speech and music," Percept. Psychophys. 16, 564–570.

Datschewit, W. (1990). "Frication noise and formant-onset frequency as independent cues for the perception of /f/, /s/ and /ʃ/ in vowel-fricative-vowel stimuli," Paper presented at the ICSLP 90, Kobe, Japan, 18–22 November 1990.

Eimas, P. D. (1975). "Auditory and phonetic coding of the cues for speech: Discrimination of the [r-l] distinction by young infants," Percept. Psychophys. 18, 341–347.

Faber, A. (1991). "Inter-speaker variability in sibilant production and sound change involving sibilants," Paper presented at the 12th International Congress on Phonetic Sciences, Aix-en-Provence, France, 19–24 August 1991.

Fant, G. (1973). *Speech Sounds and Features* (MIT Press, Cambridge, MA). Fischer-Jørgensen (1954). "Acoustic analysis of stop consonants," *Miscellanea Phonetica*, II, 42–59.

Flipsen, P., Jr., Shriberg, L., Weismer, G., Karlsson, H., and McSweeney, J. (1999). "Acoustic characteristics of /s/ in adolescents," J. Speech Lang. Hear. Res. 42, 663–677.

Forrest, K., Weismer, G., Milenkovic, P., and Dougall, R. N. (1988). "Statistical analysis of word-initial voiceless obstruents: Preliminary data," J. Acoust. Soc. Am. 84, 115–123.

Gagnon, D. A., Palmer, N. J., and Sawusch, J. R. (unpublished). The segmental representation of spoken words.

Goldinger, S. D. (1996). "Words and voices: Episodic traces in spoken word identification and recognition memory," J. Exp. Psychol.: Learning, Memory Cognition 22(5), 1166–1183.

Haley, K. L., and Ohde, R. N. (1996). "Stimulus uncertainty and speaker normalization processes in the perception of nasal consonants," *Phonetica* 53, 185–199.

Harris, K. S. (1958). "Cues for the discrimination of American English fricatives in spoken syllables," *Language Speech* 1(1), 1–7.

Hedrick, M. (1997). "Effect of acoustic cues on labeling fricatives and affricates," J. Speech, Lang. Hear. Res. 40, 925–938.

Heinz, J. M., and Stevens, K. N. (1961). "On the properties of voiceless fricative consonants," J. Acoust. Soc. Am. 33, 589–596.

Hughes, G. W., and Halle, M. (1956). "Spectral properties of fricative consonants," J. Acoust. Soc. Am. 28, 303–310.

Jassem, W. (1965). "The formants of fricative consonants," *Lang. Speech* 8, 1–16.

Johnson, K. (1991). "Differential effects of speaker and vowel variability on fricative perception," *Lang. Speech* 34(3), 265–279.

Johnson, K., and Beckman, M. E. (1996). "Production and perception of individual speaking styles," J. Acoust. Soc. Am. 100, 2599(A).

Jongman, A., and Sereno, J. A. (1995). "Acoustic properties of non-sibilant fricatives," Paper presented at the XIIIth International Congress on Phonetic Sciences (ICPhS), Stockholm, Sweden, 13–19 August 1995.

Klatt, D. H. (1986). "The problem of variability in speech recognition and in models of speech perception," in *Invariance and Variability in Speech Processes*, edited by J. S. Perkell and D. H. Klatt (Erlbaum, Hillsdale, NJ), pp. 300–324.

Liberman, A. M., Cooper, F. S., Shankweiler, D. P., and Studdert-Kennedy, M. (1967). "Perception of the speech code," *Psychol. Rev.* 74(6), 431–461.

Lisker, L., and Abramson, A. S. (1964). "A cross-language study of voicing in initial stops: Acoustical measurements," *Word* 20(3), 384–422.

Magnuson, J. S., Yamada, R. A., and Nusbaum, H. C. (1995). "The effects of familiarity with a voice on speech perception," Paper presented at the Spring Meeting of the Acoustical Society of Japan (Paper 3-9-17).

Mann, V. A., and Repp, B. H. (1980). "Influence of vocalic context on perception of the [j]–[s] distinction," *Percept. Psychophys.* 28(3), 213–228.

Martin, C. S., Mullennix, J. W., Pisoni, D. B., and Summers, W. V. (1989). "Effects of talker variability on recall of spoken word lists," J. Exp. Psychol.: Learning, Memory Cognition 15(4), 676–684.

May, J. (1976). "Vocal tract normalization for /s/ and /ʃ/," *Haskins Laboratories: Status Report on Speech Research*, SR-48, pp. 67–73.

Melara, R. D., and Mouts, J. R. W. (1994). "Contextual influences on interactive processing: Effects of discriminability, quantity, and uncertainty," *Percept. Psychophys.* 56(1), 73–90.

- Miller, J. L., and Liberman, A. M. (1979). "Some effects of later-occurring information on the perception of stop consonant and semivowel," *Percept. Psychophys.* **25**, 457–465.
- Miller, J. L., and Volaitis, L. E. (1989). "Effect of speaking rate on the perceptual structure of a phonetic category," *Percept. Psychophys.* **46**, 505–512.
- Moyer, R. S., and Bayer, R. H. (1976). "Mental comparison and the symbolic distance effect," *Cogn. Psychol.* **8**, 228–246.
- Mullenix, J. W., Pisoni, D. B., and Martin, C. S. (1989). "Some effects of talker variability on spoken word recognition," *J. Acoust. Soc. Am.* **85**, 365–378.
- Newman, R. S. (1998). "Individual differences and the link between speech perception and speech production," *Dissertation Abstracts International: Section B: the Sciences & Engineering*, 58(8-B), p. 4484.
- Nusbaum, H. C., and Morin, T. M. (1992). "Paying attention to differences among talkers," in *Speech Perception, Production and Linguistic Structure*, edited by Y. Tohkura, E. Vatikiotis-Bateson, and Y. Sagisaka (Ohmsha, Tokyo), pp. 113–134.
- Nygaard, L. C., Sommers, M. S., and Pisoni, D. B. (1995). "Effects of stimulus variability on perception and representation of spoken words in memory," *Percept. Psychophys.* **57**(7), 989–1001.
- Palmeri, T. J., Goldinger, S. D., and Pisoni, D. B. (1993). "Episodic encoding of voice attribution and recognition memory for spoken words," *J. Exp. Psychol.: Learning, Memory Cognition* **19**, 309–328.
- Peterson, G. E., and Barney, H. I. (1952). "Control methods used in a study of vowels," *J. Acoust. Soc. Am.* **24**, 175–189.
- Pisoni, D. B., and Tash, J. (1974). "Reaction times to comparisons within and across phonetic categories," *Percept. Psychophys.* **15**, 285–290.
- Reed, C. M., Power, M. H., Durlach, N. I., Braid, L. D., Foss, K. K., Reid, J. A., and Dubois, S. R. (1991). "Development and testing of artificial low-frequency speech codes," *J. Rehabil. Res. Dev.* **28**(3), 67–82.
- Ryalls, B. O., and Pisoni, D. B. (1997). "The effect of talker variability on word recognition in preschool children," *Dev. Psychol.* **33**(3), 441–452.
- Schwartz, M. F. (1967). "Identification of speaker sex from isolated, voiceless fricatives," *J. Acoust. Soc. Am.* **43**, 1178–1179.
- Seitz, P. F. D., Bladon, R. A. W., and Watson, I. M. C. (1987). "Across-speaker and within-speaker variability of British English sibilant spectral characteristics," *J. Acoust. Soc. Am. Suppl.* **1** **82**, S37.
- Shadle, C. H., Badin, P., and Moulinier, A. (1991). "Towards the spectral characteristics of fricative consonants," *Proceedings of the XIIth International Congress on Phonetic Sciences*, Aix-en-Provence, France, 19–24 August 1991, Vol. 3, pp. 42–45.
- Shadle, C. H., and Mair, S. J. (1996). "Quantifying spectral characteristics of fricatives," 4th International Conference on Spoken Language Processing (ICSLP).
- Shankweiler, D., Strange, W., and Verbrugge, R. (1977). "Speech and the problem of perceptual constancy," in *Perceiving, Acting and Knowing: Toward an Ecological Psychology*, edited by R. Shaw and J. Bransford (Erlbaum, Hillsdale, NJ), pp. 315–345.
- Soli, S. D. (1981). "Second formants in fricatives: Acoustic consequences of fricative–vowel coarticulation," *J. Acoust. Soc. Am.* **70**, 976–984.
- Sommers, M. S., Nygaard, L. C., and Pisoni, D. B. (1994). "Stimulus variability and spoken word recognition. I. Effects of variability in speaking rate and overall amplitude," *J. Acoust. Soc. Am.* **96**, 1314–1324.
- Stebbins, W. C. (1966). "Auditory reaction time and the derivation of equal loudness contours for the monkey," *J. Exp. Anal. Behav.* **9**, 135–142.
- Stevens, K. N. (1996). "Understanding variability in speech: A requisite for advances in speech synthesis and recognition," *J. Acoust. Soc. Am.* **100**, 2634(A).
- Strand, E. A., and Johnson, K. (1996). "Gradient and visual speaker normalization in the perception of fricatives," in *Natural Language Processing and Speech Technology: Results of the 3rd KONVENS Conference, Bielefeld, October, 1996*, edited by D. Gibbon (Mouton de Gruyter, Berlin), pp. 14–26.
- Stevens, P. (1960). "Spectra of fricative noise in human speech," *Lang. Speech* **3**, 32–49.
- Swets, J. A., and Pickett, R. M. (1982). *Evaluation of Diagnostic Systems: Methods from Signal Detection Theory* (Academic, New York).
- Syrdal, A. K. (1996). "Acoustic variability in spontaneous conversational speech of American English talkers," 4th International Conference on Spoken Language Processing (ICSLP), Philadelphia.
- Tomiak, G. R. (1991). "An acoustic and perceptual analysis of the spectral moments invariant with voiceless fricative obstruents," *Dissertation Abstracts International*, 51(8-B), pp. 4082–4083.
- Uchanski, R. M., Miller, K. M., Reed, C. M., and Braid, L. D. (1992). "Effects of token variability on vowel identification," in *The Auditory Processing of Speech: From Sounds to Words*, edited by M. E. H. Schouten (Mouton de Gruyter, Berlin).
- Verbrugge, R. R., Strange, W., Shankweiler, D. P., and Edman, T. R. (1976). "What information enables a listener to map a talker's vowel space?" *J. Acoust. Soc. Am.* **60**, 198–212.
- Wannemacher, C. A. (1995). "The relationship between processing of talker voice and phonetic information in speech perception," *Dissertation Abstracts International Section A: Humanities & Social Sciences* **56**(4-A), 2488.
- Whalen, D. H. (1981). "Effects of vocalic formant transitions and vowel quality on the English [s]–[ʃ] boundary," *J. Acoust. Soc. Am.* **69**, 275–282.
- Whalen, D. H. (1991). "Perception of the English /s/–/ʃ/ distinction relies on fricative noises and transitions, not on brief spectral slices," *J. Acoust. Soc. Am.* **90**, 1776–1785.
- Whiteside, S. P. (1998). "Identification of a speaker's sex: A fricative study," *Percept. Mot. Skills* **86**, 587–591.
- Zeng, F.-G., and Turner, C. W. (1990). "Recognition of voiceless fricatives by normal and hearing-impaired subjects," *J. Speech Hear. Res.* **33**(3), 440–449.

Relations between intelligibility of narrow-band speech and auditory functions, both in the 1-kHz frequency region^{a)}

Ingrid M. Noordhoek,^{b)} Tammo Houtgast, and Joost M. Festen

Department of Otolaryngology, University Hospital VU, P.O. Box 7057,
1007 MB Amsterdam, The Netherlands

(Received 29 September 1999; revised 12 December 2000; accepted 18 December 2000)

Relations between perception of suprathreshold speech and auditory functions were examined in 24 hearing-impaired listeners and 12 normal-hearing listeners. The speech intelligibility index (SII) was used to account for audibility. The auditory functions included detection efficiency, temporal and spectral resolution, temporal and spectral integration, and discrimination of intensity, frequency, rhythm, and spectro-temporal shape. All auditory functions were measured at 1 kHz. Speech intelligibility was assessed with the speech-reception threshold (SRT) in quiet and in noise, and with the speech-reception *bandwidth* threshold (SRBT), previously developed for investigating speech perception in a limited frequency region around 1 kHz. The results showed that the elevated SRT in quiet could be explained on the basis of audibility. Audibility could only partly account for the elevated SRT values in noise and the deviant SRBT values, suggesting that suprathreshold deficits affected intelligibility in these conditions. SII predictions for the SRBT improved significantly by including the individually measured upward spread of masking in the SII model. Reduced spectral resolution, reduced temporal resolution, and reduced frequency discrimination appeared to be related to speech perception deficits. Loss of peripheral compression appeared to have the smallest effect on the intelligibility of suprathreshold speech. © 2001 Acoustical Society of America.

[DOI: 10.1121/1.1349429]

PACS numbers: 43.71.Ky, 43.66.Sr, 43.66.Dc, 43.66.Fe [DOS]

I. INTRODUCTION

Sensorineural hearing loss often interferes with understanding speech in a noisy environment, even when the speech is presented well above the hearing threshold. Therefore, reduced speech intelligibility cannot be just a result of the elevated hearing threshold per se. There also has to be a deterioration in suprathreshold sound processing. Various researchers studied correlations between speech perception and specific auditory functions (Tyler *et al.*, 1982; Festen and Plomp, 1983; Dreschler and Plomp, 1985; Glasberg and Moore, 1989; van Rooij and Plomp, 1990; Smoorenburg, 1992; Divenyi and Haupt, 1997a, 1997b). However, finding the specific deficits that are responsible for reduced intelligibility of suprathreshold speech has proved to be difficult. The main reason for this may be that correlations between a listener's ability to understand *wideband* speech and auditory functions in a *limited* frequency region were studied. Furthermore, auditory functions and hearing loss are usually not independent. Therefore, when examining correlations between these two factors, it is difficult to determine whether the underlying cause for reduced intelligibility lies in the deterioration of a specific auditory function, or whether it is due to part of the speech spectrum falling below the absolute threshold.

In the present study, the relation between speech percep-

tion and auditory functions was investigated while avoiding the above-mentioned difficulties. The auditory functions were all measured at 1 kHz. Speech intelligibility was measured for a restricted frequency range with a center frequency of 1 kHz. For this purpose, the speech-reception *bandwidth* threshold (SRBT) test has been developed, as described in a previous study (Noordhoek *et al.*, 1999). Thus, the auditory functions and speech perception refer to the same frequency region, which may well increase the chance to find clear correlations. The influence of audibility on speech intelligibility was evaluated with the speech intelligibility index, or SII (ANSI, 1997). After accounting for audibility, correlations between speech perception and auditory functions were examined. In this way, the effects of suprathreshold deficits were separated from the effects of audibility.

Ching *et al.* (1997) used a similar approach. They calculated the deviations of measured intelligibility scores for filtered speech from the intelligibility scores predicted by the SII model, and found that these deviations were moderately correlated with the measured spectral and temporal resolution in the same frequency region, and with the hearing threshold. Because audibility was accounted for, they concluded that the correlations with the hearing threshold may be related to suprathreshold deficits that covary with hearing loss.

In the present study, suprathreshold speech perception will not only be related to spectral and temporal resolution, but also to the results of a set of other detection and discrimination tests. The detection tests assessed spectral and temporal resolution, and spectral and temporal integration. In the discrimination tests, just-noticeable differences were mea-

^{a)}Part of the data were presented at the Joint ASA/EAA/DEGA Meeting "Berlin 99" [Collected papers from the joint meeting "Berlin 99," Deutsche Gesellschaft für Akustik, Oldenburg].

^{b)}Current address: TNO TPD, P.O. Box 155, 2600 AD Delft, The Netherlands, electronic mail: ingridn@dss.nl

sured in intensity, frequency, rhythm, and spectro-temporal shape. Many auditory functions are known to change with sound pressure level. For example, intensity discrimination improves with level, whereas spectral resolution deteriorates with level. So, differences in results for hearing-impaired and normal-hearing listeners can be caused by level effects. Such level effects can be the result of differences in either the absolute level or in the sensation level of the stimuli. The level dependence of auditory functions was accounted for in our investigations by measuring the thresholds of the normal-hearing listeners at three presentation levels.

Speech intelligibility was assessed for narrow-band speech with the novel SRBT. For broadband speech, various speech-reception thresholds (SRTs) were determined, namely the SRT in quiet, the SRT in noise, and the spectrally adapted SRT in noise (in which stimuli are adjusted to fit in the individual's dynamic range). In a previous study (Noordhoek *et al.*, 2000) the same intelligibility tests were measured using 34 hearing-impaired listeners. For most listeners, elevated SRT values in quiet and in noise could be explained on the basis of audibility. However, for the spectrally adapted SRT in noise, and especially for the SRBT, the data of most listeners could not be explained from audibility, suggesting that effects of suprathreshold deficits influenced intelligibility in these conditions. In the present study, an attempt is made to determine which specific suprathreshold deficits reduce intelligibility for hearing-impaired listeners.

II. METHOD

A. Stimuli

The speech material consisted of eight lists of 13 meaningful Dutch sentences, uttered by a female speaker (Plomp and Mimpen, 1979). For masking, a Gaussian noise that was spectrally shaped according to the long-term average spectrum of the sentences was used. Both the speech and the noise signals were digitized at a sampling frequency of 15 625 Hz. Noise bands of $\frac{1}{3}$ octave were used for determination of the absolute thresholds and the levels of uncomfortable loudness.

In the measurements of the auditory functions, three types of signals were used: a tone, a click, and a Gaussian-windowed tone pulse. The tone was a sinusoid with a frequency of 1 kHz, which was gated with a 20-ms cosine squared ramp, and had a half-amplitude duration of 100 ms. The click was a filtered step-function of two octaves wide (500–2000 Hz). The Gaussian-windowed tone pulse was defined by

$$s(t) = A \sqrt{\alpha f_0} \sin\left(2\pi f_0 t + \frac{\pi}{4}\right) \exp(-\pi(\alpha f_0 t)^2). \quad (1)$$

The carrier frequency f_0 of the Gaussian pulse was 1 kHz and the shape factor α was 0.25. This shape factor was chosen because it defines a signal with the spectral width of a critical band (equivalent rectangular bandwidth: $\frac{1}{4}$ octave) combined with a short duration (equivalent rectangular duration: 2.8 ms). For low-level stimuli with this particular spectro-temporal shape, listeners are not able to combine stimulus information across multiple frequency channels or

across “multiple looks” in time (van Schijndel *et al.*, 1999). The energy of the Gaussian pulse only depends on the amplitude factor A . In its generation, the Gaussian pulse was cut off at 60 dB below the top. For masking, a noise with Gaussian-amplitude distribution was used with a bandwidth of four octaves (250–4000 Hz). The noise masker was gated with a 20-ms cosine-squared ramp, and had a half-amplitude duration of 400 ms.

B. Apparatus

Stimuli were generated with a personal computer using TDT (Tucker-Davis Technologies) System II add-on hardware. In the intelligibility tests, stimuli were upsampled by a factor of 2 and delivered at a 31 250-Hz sampling frequency. In the auditory-function tests, stimuli were delivered at a sampling frequency of 40 kHz. Stimuli were converted to analog using a 16-bit D/A converter (TDT DD1) and they were low-pass filtered at 16 kHz (TDT FT5). Signals and noise were attenuated separately (TDT PA4), and subsequently summed (TDT SM3). For frequency shaping in the intelligibility tests and in the determination of the broadband uncomfortable loudness level (see Sec. IID), the total signal was passed through a programmable filter (TDT PF1). Listeners were seated in a soundproof room. Stimuli were presented monaurally through headphones (Sony MDR-CD999). Sound-pressure levels of the stimuli were measured with the headphone placed on a Brüel & Kjær type 4152 artificial ear with a flat-plate adapter.

C. Listeners

Twenty-four sensorineurally hearing-impaired persons were selected from the files of the University Hospital VU and served as subjects. Information about individual listeners is given in Table I. Their ages ranged from 39 to 67 years. Their native language was Dutch. Only listeners who could reach an intelligibility score for monosyllabic words in quiet of at least 75% were selected. They were tested at their better ear. Pure-tone air-conduction thresholds in the ear under test, averaged over 500, 1000, and 2000 Hz, ranged from 5 to 62 dB HL. The thresholds were at least 20 dB HL at one or more octave frequencies between 500 and 2000 Hz and at least 40 dB HL at one or more octave frequencies between 250 and 4000 Hz. Twelve normal-hearing listeners, ranging in ages from 19 to 63 years, participated in the experiment as a control group. The pure-tone air-conduction thresholds did not exceed 15 dB HL at octave frequencies from 250 to 4000 Hz for their tested ears.

D. Procedure

The hearing-impaired listeners were tested in two sessions of 4 h on two separate days. Session 1 consisted of six test blocks (blocks 1–6 described in the following) and session 2 of five test blocks (blocks 2–6 in retest) of about 20 min. The blocks were presented in a fixed order to avoid possible differences among listeners due to sequence effects. After each test block, the listeners had a break of the same duration. In the first test block, the listeners' thresholds and uncomfortable loudness levels (UCLs) were determined. The

TABLE I. Hearing threshold and uncomfortable loudness level for 1/3-octave bands of noise, together with age, and broadband UCL attenuation (i.e., the attenuation needed to arrive at the broadband UCL with the broadband noise burst spectrally shaped according to the narrowband UCL, see Sec. II D) for the individual hearing-impaired listeners. Mean data for the normal-hearing listeners are given at the bottom.

Listener	Age (yr)	Hearing threshold (dB SPL)					UCL (dB SPL)					Attenuation (dB)
		0.25 kHz	0.5 kHz	1 kHz	2 kHz	4 kHz	0.25 kHz	0.5 kHz	1 kHz	2 kHz	4 kHz	
a	65	64.8	57.9	48.2	54.8	55.1	109.5	105.7	96.2	98.5	96.8	30
b	67	45.0	34.7	33.9	41.4	56.1	>120	>120	177.7	116.3	>120	40
c	62	31.0	22.8	38.6	72.8	>80	>120	112.0	106.8	103.5	104.2	20
d	65	32.3	31.8	44.8	52.8	73.4	114.0	106.3	101.0	107.5	112.8	30
e	58	76.0	70.2	57.4	65.6	74.5	109.5	100.5	84.7	90.5	88.5	35
f	63	59.9	51.8	48.4	50.7	49.1	>120	113.3	112.8	115.0	117.0	30
g	53	53.5	56.0	52.1	63.8	72.1	105.7	94.3	102.3	99.0	92.0	30
h	57	45.9	58.6	59.5	57.7	48.4	78.2	82.0	89.5	82.0	75.5	40
i	52	48.5	58.7	56.5	58.7	54.9	>120	>120	119.0	117.0	>120	20
j	62	25.9	22.8	30.9	39.1	64.0	>120	>120	116.7	116.8	108.7	15
k	58	60.6	56.7	52.4	61.8	39.5	108.7	104.8	99.3	107.2	98.8	35
l	39	27.4	28.7	29.6	66.3	50.0	>120	118.2	113.0	109.2	100.0	20
m	54	47.7	50.8	62.9	66.6	69.3	>120	>120	114.2	117.7	109.7	35
n	39	42.9	38.3	49.0	45.3	24.8	97.7	95.3	91.7	93.5	85.3	20
o	60	45.8	36.7	31.9	33.1	59.7	96.0	90.2	88.0	84.8	87.8	30
p	67	31.2	20.0	8.8	25.2	49.4	>120	119.8	106.0	107.7	114.2	40
q	45	27.7	20.4	12.5	31.3	47.8	>120	114.2	100.3	101.0	105.5	20
r	65	33.0	23.3	20.9	71.7	71.7	>120	>120	>120	>120	>120	20
s	64	60.3	49.3	47.2	74.9	>80	93.3	96.7	93.0	96.3	115.7	35
t	65	65.3	65.4	52.1	61.8	49.4	>120	104.5	93.8	98.5	80.2	30
u	67	79.9	73.7	64.0	66.8	67.5	119.0	111.7	113.3	113.3	113.3	30
v	64	60.8	54.9	60.8	58.1	64.9	>120	113.3	>120	>120	113.3	25
w	41	51.6	38.3	45.8	50.3	46.5	101.5	91.3	85.3	87.8	85.2	30
x	64	38.5	38.7	43.6	75.5	>80	119.0	108.5	101.8	111.3	113.3	30
Mean normal	27	27.8	18.6	8.1	7.6	6.3	118.9	115.3	111.7	108.9	105.0	22

measurements of the auditory functions were divided over four blocks (blocks 2, 3, 5, and 6). Speech reception was measured in the fourth block. The reason for presenting this speech-reception block in between the more-demanding auditory-function blocks was to give the listeners some variation in their task.

The normal-hearing listeners performed the same tests as the hearing-impaired listeners (sessions 1 and 2) and an extra third session. This extra session was included to investigate the level dependence of the auditory functions measured in sessions 1 and 2. Auditory functions were measured at three presentation levels: 15 dB below, at the same level as, and 15 dB above the levels used in sessions 1 and 2 (determined in block 2). Session 3 consisted of nine test blocks (three blocks, each tested at three levels) of 15 min each, with breaks of 15 min in between. The first block in session 3 contained tests 2c through 3c; the second block tests 5a through 5c, and the third block tests 6a through 6d. The presentation order of the levels was counterbalanced over the listeners according to a 3×3 Latin square. Each sequence of levels was presented to four normal-hearing listeners.

1. Threshold and UCL (block 1)

Hearing thresholds and uncomfortable loudness levels (UCLs) were measured with 1/3-octave bands of noise at five center frequencies: 250, 500, 1000, 2000, and 4000 Hz. Levels for intermediate 1/3-octave bands were calculated by inter-

polation. For the determination of the hearing threshold, a fixed-frequency Békésy procedure was used with a step size of 1 dB. After 11 reversals, the threshold measurement was finished. The threshold was defined as the average of all but the first reversal.

The UCL was determined in two steps. First, the UCL of the five 1/3-octave bands of noise were measured individually. Next, the UCL was measured with a 4-s broadband noise burst, spectrally shaped according to the narrow-band UCLs. In the determination of the 1/3-octave band UCLs, the listeners were presented with noise bursts that increased in level. They had to press a button when the noise burst was experienced as uncomfortably loud. After the button was pressed, the noise level was reduced by a random amount between 21 and 31 dB. The measurement was finished after six responses. The UCL of each band was computed by averaging across the levels at which the button was pushed. For details of the threshold and UCL measurement procedure, see Noordhoek *et al.* (2000).

2. Speech intelligibility (block 4)

In this block, four intelligibility thresholds were measured: the speech-reception threshold in quiet (SRT_q), the SRT in noise (SRT_n), the SRT in noise with the speech and noise signals adapted to the midline of the dynamic range of individual listeners (SRT_a), and the speech-reception *bandwidth* threshold (SRBT). In session 1 the order of the tests was SRT_q, SRT_n, SRT_a, and SRBT. In session 2 the order

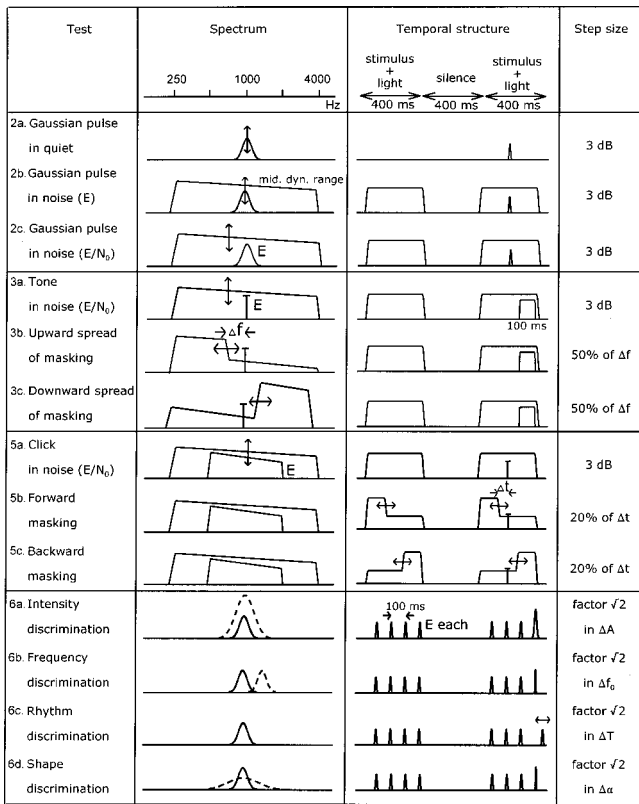


FIG. 1. Schematic representation of spectrum (second column) and temporal structure (third column) of the stimuli in the auditory-function tests as given in the first column. The parameter varied in the adaptive procedure is indicated with an arrow, or with a dashed line. The step size is given in the last column.

was SRBT, SRTa, SRTq, and SRTn, i.e., the order was reversed, except for SRTq and SRTn. Their order was fixed, because the level of the noise in the SRTn test was taken 20 dB above the measured SRTq for each listener. In the SRBT procedure, the bandwidth of the speech signal was varied. Complementary shaped bandstop noise was added to the speech stimuli. Both the speech and noise stimuli were shaped to resemble the midline of the dynamic range of the individual listener, i.e., a line halfway between hearing threshold and broadband UCL (measured in block 1). A procedure comparable to the SRT test was followed, with the important difference that the bandwidth (center frequency: 1 kHz), instead of the sound-pressure level, of the speech signal is varied adaptively. For details of the intelligibility tests see Noordhoek *et al.* (2000).

Before the speech-intelligibility measurements, two lists of 13 sentences were used to familiarize the listeners with the procedure. With these lists, a SRTq test and a SRTn test were performed.

3. Auditory functions (blocks 2, 3, 5, and 6)

a. General. The four test blocks are schematically presented in Fig. 1. Blocks 2, 3, and 5 each contain three detection tests. Block 6 contains four discrimination tests. Thresholds were determined using an adaptive two-interval forced-choice procedure (Levitt, 1971) with visual feedback. Each trial consisted of two intervals of 400 ms, each indicated by

a light, with 400 ms of silence in between. A two-down one-up procedure was applied that estimates the 70.7% correct point on the psychometric function. The threshold measurements were finished after 16 reversals. The threshold was defined as the mean (for block 2, and tests 3a and 5a) or the geometric mean (for the other tests) of the last 12 reversals. A practice run with four reversals was presented before each measurement, except in session 3.

In test 2b of session 1, the energy E of the signals (tone, click, and Gaussian pulse) to be used in all subsequent tests was determined. E was chosen as the threshold energy of the Gaussian pulse in a pink noise with a bandwidth of four octaves (250–4000 Hz). The level of the pink noise was chosen so that the $\frac{1}{3}$ -octave band centered at 1 kHz was presented halfway between the hearing threshold and the uncomfortable loudness level of each individual listener. Consequently, the level of the pink masking noise in the subsequent detection tests was varied around the middle of the dynamic range for each listener.

b. Signal-detection efficiency (block 2). The efficiency of the detection process in a listener is represented by the ratio of signal power to noise power at the output of the auditory filter required for detection (Patterson *et al.*, 1982). To determine the signal-detection efficiency without confounding it with the width of the auditory filter, temporal integration, or spectral integration, we have chosen a Gaussian pulse, which is localized in both time and frequency, as the signal in the detection-efficiency experiment.

First, the threshold for a Gaussian-windowed tone pulse was measured in quiet (2a). This test was included to be able to calculate the sensation level of the signals in the subsequent discrimination tests. Next, the threshold for a Gaussian pulse was measured in pink noise (2b). This test was included to determine the probe-signal energy E to be used in all subsequent tests. The threshold was defined as the energy level (in dB) at the detection threshold. [The energy level is the acoustic power times duration of the signal in decibels, defined as $10 \log(E/E_0)$. The reference value E_0 is 10^{-12} W s, which makes the numerical value of the energy level for a plane wave through a unit surface (1 m^2) during 1 s equal to the numerical value of the sound-pressure level.] In these tests (2a and 2b), the level of the Gaussian pulse was varied in the adaptive procedure. Finally, the threshold for a Gaussian pulse in pink noise was determined again (2c), but now the noise level was varied in the adaptive procedure. In tests 2b and 2c, the Gaussian pulse was temporally centered in the masker. The threshold in test 2c was defined as the energy of the Gaussian pulse at detection threshold, normalized by the spectral density of the pink noise at 1 kHz, i.e., E/N_0 (in dB).

c. Spectral resolution (block 3). To determine the spectral resolution without confounding it with signal-detection efficiency (Patterson *et al.*, 1982), upward spread of masking (USOM) and downward spread of masking (DSOM) were determined in two steps. In the first step the threshold for the tone in pink noise (3a) was determined. The noise level was varied in the adaptive procedure. The threshold was defined as the energy of the tone at the detection threshold, normalized by the spectral density of the noise at 1 kHz. In the

second step, two measurements were performed, one to measure USOM (3b), the other to measure DSOM (3c). The USOM masker was constructed from the noise at the threshold level of the first step of this block. The low-frequency part of the noise was amplified 10 dB, and the high-frequency part was attenuated 10 dB (see Fig. 1, 3b). To make the DSOM masker the high-frequency part of the noise was amplified 10 dB, and the low-frequency part was attenuated 10 dB (see Fig. 1, 3c). In these tests, the attenuated parts of the noise are included to limit off-frequency listening. The frequency difference Δf (in Hz) between the tone and the masker cutoff was varied in the adaptive procedure. The threshold was defined as the frequency difference at the detection threshold. The USOM masker and DSOM masker may generate a tonal sensation, because of the steep spectral slope between the low- and high-frequency part of the noise. Therefore, the tone was presented at the end of the masker to ease detection. The onset of the tone occurred 280 ms after the onset of the masker; the offset of the tone occurred 20 ms before the offset of the masker. Both the tone and the masker were gated with a 20-ms cosine-squared ramp.

d. Temporal resolution (block 5). To determine the temporal resolution without confounding it with signal-detection efficiency, forward and backward masking were determined in two steps. First, the threshold for the click in pink noise (5a) was measured. The noise level was varied in the adaptive procedure. The threshold was defined as the energy of the click at the detection threshold, normalized by the spectral density of the noise. In the second step, forward masking (5b), and backward masking (5c) were measured. The forward masker was constructed from the noise at threshold level in step 5a, by amplifying the first part of the noise by 10 dB, and by attenuating the last part by 10 dB (see Fig. 1, 5b). For the backward masker, the last part of the noise was amplified 10 dB, and the first part was attenuated 10 dB (see Fig. 1, 5c). The interval Δt (in ms) between the click and transition in the masker was varied in the adaptive procedure. The threshold was defined as the interval at the detection threshold. The attenuated part of the noise limits “off-time listening” (Moore *et al.*, 1988).

e. Discrimination (block 6). In each measurement trial, the two intervals contained four Gaussian-windowed tone pulses repeated every 100 ms (see Fig. 1). In one randomly chosen interval, all four pulses were identical (reference pulses). In the other interval, the first three pulses were equal to the corresponding reference pulses and the fourth pulse deviated. The size of the difference in the fourth, odd, pulse (in intensity, frequency, latency, or shape) was varied in the adaptive procedure.

In test 6a, intensity discrimination was measured. The amplitude factor A in Eq. (1) was increased from A_0 to $A_0 + \Delta A$, and ΔA was varied in the adaptive procedure. The threshold was defined as the just-noticeable difference in energy (in dB), i.e., $20 \log((A_0 + \Delta A)/A_0)$. In test 6b, frequency discrimination was measured. The carrier frequency of the odd pulse was $1000 \text{ Hz} + \Delta f_0$. The frequency difference Δf_0 (in Hz) was varied in the adaptive procedure. The threshold was defined as the just-noticeable difference in frequency between the odd and the reference pulse (in percent). In test

6c, rhythm discrimination was measured. The latency between the third reference pulse and the odd pulse was $100 \text{ ms} + \Delta T$, and the delay ΔT was varied in the adaptive procedure. The threshold was defined as the just-noticeable increase in delay (in ms). In test 6d, shape discrimination was measured. The shape factor of the odd pulse was $\alpha_0 + \Delta \alpha$ (i.e., the duration of the fourth pulse was shorter and its bandwidth was wider). The shape-factor difference $\Delta \alpha$ was varied in the adaptive procedure. The threshold was defined as the just-noticeable difference in shape factor between the odd and the reference pulse (in percent).

f. Integration. The temporal and spectral integration of each listener was calculated by combining the masked thresholds for the Gaussian pulse (test 2c), the tone (test 3a), and the click (test 5a). We defined the temporal integration as the masked threshold for the 100-ms tone subtracted from the masked threshold of the 2.8-ms Gaussian pulse. Spectral integration was defined as the masked threshold for the click (two octaves wide) subtracted from the masked threshold for the Gaussian pulse (1/4 octave wide). With these definitions, maximally efficient integration corresponds to 0 dB and less efficient integration corresponds to negative numbers. The click presented in pink noise approximately fulfills the condition of equal detectability across the frequency range covered by the signal, necessary for accurately measuring spectral integration (van den Brink, 1990a).

E. SII calculations

The SII values corresponding to each SRT and SRBT measurement were calculated following the ANSI $\frac{1}{3}$ -octave band procedure (ANSI, 1997). The SII replaces the older articulation index (ANSI, 1969). The band-importance function for speech material of average redundancy (Pavlovic, 1987) was used. For frequencies below 500 Hz, shallower slopes were used in the calculation of upward spread of masking, because previous calculations showed that, in a SRBT measurement, the standard SII model underestimates the upward spread of masking produced by the low-frequency noise (Noordhoek *et al.*, 1999).

For the SII procedure, the levels of speech and noise were transformed to equivalent free-field levels using the “artificial-ear-to-free-field transfer function” as derived in Noordhoek *et al.* (1999). The spectrum level of the internal noise was calculated as the observed $\frac{1}{3}$ -octave band-noise threshold (transformed to free-field level) minus the critical ratio in dB (Pavlovic, 1987).

III. RESULTS AND DISCUSSION

A. Results of sessions 1 and 2

Table II presents the average results of sessions 1 and 2 for the normal-hearing listeners and the hearing-impaired listeners. Data analysis was performed on the logarithm of the individual thresholds for eight tests: upward and downward spread of masking, forward and backward masking, and the four discrimination tests. [Data analysis was performed on the logarithms of the intensity discrimination data, because the variability is approximately independent of the logarithm of the JND in dB (Florentine, 1983)]. The average threshold

TABLE II. Average results of sessions 1 and 2 for normal-hearing listeners (NH) and hearing-impaired listeners (HI). Thresholds for the group of hearing-impaired listeners that differ significantly (t test for unequal variances, $p < 0.05$) from corresponding normal-hearing thresholds are indicated with an asterisk. “Number HI” indicates the number of hearing-impaired listeners over which the average has been calculated. “HI deviant” indicates the number of hearing-impaired listeners with a deviant threshold. Columns σ_{NH} and σ_{HI} present the standard deviation among listeners. In the last column the average individual standard error is shown. When the data analysis was performed on the logarithms of the individual thresholds, the values given in columns “NH” and “HI” represent geometric means, and the data given in parentheses in columns σ_{NH} , σ_{HI} and “Individual SE” represent the error factor: the range of plus or minus one standard deviation (or standard error) is from the geometric mean divided by the error factor to the geometric mean multiplied by the error factor.

Test	Dimension	NH	HI	Number HI	HI deviant	σ_{NH}	σ_{HI}	Individual SE
<i>Speech reception (block 4)</i>								
SRTq	dBA	22.7	56.0*	24	22	4.2	15.7	2.7
SRTn	dB S/N	-4.8	0.6*	23	23	0.9	2.5	0.8
SRTa	dB S/N	-5.0	-2.0*	23	17	0.7	2.3	1.0
SRBT	Octaves	1.35	2.07*	23	19	0.14	0.52	0.15
<i>Auditory functions</i>								
2a. Gaussian pulse in quiet	dB	-3.4	31.8*	24	23	3.2	13.5	3.9
2b. Gaussian pulse in noise (E)	dB	42.0	53.3*	24	11	6.7	8.8	2.3
2c. Gaussian pulse in noise (E/N_0)	dB	16.7	13.6*	24	3	2.7	4.2	1.7
3a. Tone in noise (E/N_0)	dB	9.3	14.2*	23	21	1.1	2.8	1.6
3b. Upward spread of masking	Hz	142	213*	23	9	(1.50)	(1.87)	(1.24)
3c. Downward spread of masking	Hz	65	63	23	4	(1.36)	(2.01)	(1.65)
5a. Click in noise (E/N_0)	dB	15.1	15.2	24	3	2.6	2.7	1.3
5b. Forward masking	ms	10.5	24.8*	23	7	(1.71)	(1.98)	(1.29)
5c. Backward masking	ms	13.5	19.7	20	5	(1.54)	(1.91)	(1.16)
Temporal integration	dB	7.4	-0.8*	23	20	2.2	5.0	1.9
Spectral integration	dB	1.7	-1.6*	24	13	1.6	3.9	1.8
6a. Intensity discrimination	dB	3.9	2.8	24	1	(1.43)	(1.74)	(1.26)
6b. Frequency discrimination	%	3.1	6.2*	23	10	(1.56)	(2.20)	(1.25)
6c. Rhythm discrimination	ms	25	26	24	1	(1.58)	(1.62)	(1.27)
6d. Shape discrimination	%	27	40	22	8	(1.63)	(1.81)	(1.47)

on test 2b has been calculated from just the thresholds measured in session 1, because these thresholds determined the signal energy E to be used in all subsequent tests. The numbers of hearing-impaired listeners over which the averages have been calculated are given in Table II, because some hearing-impaired listeners could not perform one or two tests. Additionally, the thresholds of one hearing-impaired listener on the three tests of block 3 (and therefore also on temporal integration) were left out of the data analysis, because they were considered to be severe outliers. [Severe outliers were defined as values that are more than three quartile ranges (the difference of upper and lower quartile) above the upper, or below the lower quartile.] The upper limit of the one-tailed 95%-confidence interval of the thresholds of the normal-hearing listeners was chosen as the boundary between a normal and a deviant threshold (for temporal and spectral integration: lower limit). The standard error of individual threshold values represents a reliability measure of the test. This “individual standard error,” given in Table II, is the square root of the variance of test and retest values averaged over the listeners, divided by the square root of 2 (the number of observations per listener):

$$\text{Individual SE} = \frac{\sqrt{\sum_{i=1}^n \frac{(\text{test}_i - \text{retest}_i)^2}{2n}}}{\sqrt{2}}, \quad (2)$$

where n is the total number of listeners.

Table II shows that on average the thresholds of the hearing-impaired listeners on all four speech intelligibility tests were significantly worse than the thresholds of the normal-hearing listeners. Five listeners with an elevated SRTn, had a normal SRTa. Thus, these five listeners had a normal SRT in noise when the stimuli were shaped to fit in their dynamic range. However, for 17 hearing-impaired listeners, adapting the spectrum did not result in a normal SRT in noise.

The average detection threshold for a Gaussian pulse in noise expressed as E/N_0 (test 2c) was significantly better for the hearing-impaired than for the normal-hearing listeners. This contrasts with the average detection threshold for a tone in noise which is significantly worse for the hearing-impaired than for the normal-hearing listeners. The average detection threshold for a click in noise is not significantly different for both groups of listeners.

The hearing-impaired listeners showed on average more upward spread of masking than the normal-hearing listeners, but the average downward spread of masking of hearing-impaired and normal-hearing listeners did not differ significantly. Furthermore, the hearing-impaired listeners showed on average more forward masking than the normal-hearing listeners, but the average backward masking of both groups of listeners did not differ significantly. Frequency discrimi-

TABLE III. Results on the auditory-function tests measured in session 3 for 12 normal-hearing listeners. Each test was performed at three levels relative to the level E in sessions 1 and 2: $E - 15$ dB, E , and $E + 15$ dB. Pairs of thresholds that differ significantly ($p < 0.05$) are indicated with asterisks or daggers.

Test	Dimension	$E - 15$	E	$E + 15$
2c. Gaussian pulse in noise (E/N_0)	dB	11.4*	15.4*	14.3
3a. Tone in noise (E/N_0)	dB	7.7	7.7	9.7
3b. Upward spread of masking	Hz	92*†	152*	172†
3c. Downward spread of masking	Hz	57	70	50
5a. Click in noise (E/N_0)	dB	14.3	14.5	15.8
5b. Forward masking	ms	11.3	8.2	11.3
5c. Backward masking	ms	10.0	8.9	13.4
Temporal integration	dB	3.8*	7.7*	4.6
Spectral integration	dB	-2.8*	0.9*	-1.5
6a. Intensity discrimination	dB	5.5*†	3.2*	2.3†
6b. Frequency discrimination	%	2.4	2.4	2.9
6c. Rhythm discrimination	ms	21	21	18
6d. Shape discrimination	%	29	22	20

nation is the only discrimination test on which the hearing-impaired listeners had on average a significantly higher threshold than the normal-hearing listeners: The just noticeable difference (JND) in frequency was on average 3.1% for the normal-hearing listeners, while the JND of the hearing-impaired listeners was on average 6.2%. Also noticeable is that the hearing-impaired listeners on average showed better intensity discrimination (JND of 2.8 dB) than the normal-hearing listeners (JND of 3.9 dB), although the difference was not significant.

B. Level effects (session 3)

Table III presents the thresholds of the normal-hearing listeners on the auditory-function tests at three presentation levels. For each test, the presence of a level effect was investigated with three Bonferroni-corrected t tests for matched samples ($p < 0.05$ for each set of three comparisons; Keren and Lewis, 1993). To compare the detection efficiencies for the different stimuli, the average masked thresholds for the tone, the click, and the Gaussian pulse are also presented in Fig. 2.

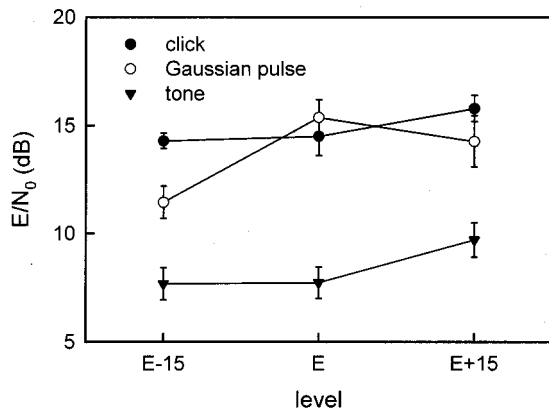


FIG. 2. Mean masked threshold for click, Gaussian pulse, and tone for 12 normal-hearing listeners at three levels 15 dB apart. Thresholds are expressed as the signal energy relative to the spectral density of the pink noise at 1 kHz. Vertical bars represent the standard error of the mean.

The signal energy E in sessions 1 and 2 differed over listeners (determined by the result of test 2b, with the noise level set at the midline of the individually measured dynamic range). For the normal-hearing listeners, the energy level E ranged from 32 to 52 dB, with an average of 42 dB. For the hearing-impaired listeners, E ranged from 36 to 72 dB, with an average of 52 dB. The range of the hearing-impaired listeners approximately overlaps the combined range of E and $E + 15$ for the normal-hearing listeners in session 3. The average signal energy at which the hearing-impaired listeners performed the tests was 10 dB higher than the average level at which the hearing-impaired listeners performed the tests. As can be seen in Table III, no significant differences were found between the thresholds at E and at $E + 15$ for the normal-hearing listeners. Therefore, it seems unlikely that significant differences in test results between the hearing-impaired and normal-hearing listeners are only a consequence of the different absolute levels at which the tests were performed. However, the increased USOM of the hearing-impaired listeners may partly be explained by the higher absolute level at which they performed the test, because the average USOM threshold of the hearing-impaired listeners tested at E (i.e., at 52 dB on average) is not significantly different from that of the normal-hearing listeners tested at $E + 15$ (i.e., at 57 dB on average). Furthermore, the higher absolute level may provide an explanation for the (insignificantly) better JND in intensity of the hearing-impaired listeners.

Many auditory functions are known to decline at low sensation levels. In the discrimination experiments, sensation levels of the signals were different for each listener. This may cause differences in performance between normal and impaired listeners. As Table III indicates, intensity discrimination was the only discrimination ability that was worse at $E - 15$ than at higher sensation levels for the normal-hearing listeners. However, on average intensity discrimination was better for the hearing-impaired than for the normal-hearing listener. Therefore, it appears that the lower sensation levels per se do not provide an explanation for the observed differences between the hearing-impaired and normal-hearing listeners.

Table III shows that the detection threshold for the Gaussian pulse in noise is level dependent. The difference between the performance of the hearing-impaired and the normal-hearing listeners appears not significant at each of the three levels measured in session 3. Thus, while the threshold for the Gaussian pulse in noise of the impaired listeners was significantly better than that of the normal listeners at the signal level E in sessions 1 and 2, it was not significantly better than the threshold of the normal listeners measured at the same level in session 3. The reason is that the average threshold of the normal-hearing listeners at signal level E in session 3 is 1.3 dB below their average threshold in sessions 1 and 2. This may be caused by a learning effect. Therefore, instead of comparing thresholds measured in different sessions, the differences among the detection thresholds of the normal-hearing listeners at the three levels in the same session will be considered. The average threshold for the Gaussian pulse in noise was 4 dB better at E

–15 than at E and 1 dB better at $E+15$ than at E (see Table III). Thus, the fact that the detection threshold for the Gaussian pulse in noise was 3 dB lower for the hearing-impaired listeners than for the normal-hearing listeners (see Table II) may be a result of the position in the dynamic range at which the detection test was presented.

C. Comparisons with the literature

1. Signal-detection efficiency

For the normal-hearing listeners, the detection threshold for the Gaussian pulse in noise is significantly higher at the intermediate level than at the lowest level (see Table III and Fig. 2). For the click and the tone, the thresholds did not significantly change with level. This is in agreement with results of Festen and Dreschler (1988), who found that the threshold for brief Gaussian-windowed tone pulses is higher at intermediate levels, and that this effect disappears both for clicklike signals (duration shorter than 0.5 ms) and for signals longer than 5 ms. Van den Brink and Houtgast (1990a) did not observe a level effect in the detection of short tones, but a level dependence of masked thresholds was also reported by Carlyon and Moore (1986), von Klitzing and Kohlrausch (1994), and Oxenham *et al.* (1997). In the last two studies, an explanation is provided in terms of the level-dependent compressive nature of the input–output function of the basilar membrane.

At the intermediate level in our experiment, the average energy level of the Gaussian pulse was 42 dB. This corresponds to a peak amplitude of 67-dB SPL. At this sound-pressure level, the basilar membrane transfer characteristic is strongly compressive. Thus, the peak amplitude of the Gaussian pulse is compressed more than the noise amplitudes. As a result, at the intermediate level E the normalized energy of the Gaussian pulse needed for detection (i.e., E/N_0) is higher than at the levels $E-15$ and $E+15$.

The average masked detection threshold for the Gaussian pulse was significantly *better* for the hearing-impaired than for the normal-hearing listeners. This finding is consistent with the idea that cochlear impairment can lead to a loss of compression. Thus, because the masked threshold of the Gaussian pulse appears to be closely related to peripheral compression (more compression leading to higher masked thresholds), it constitutes a poor measure for signal-detection efficiency. Therefore, from now on we will consider the masked threshold for the Gaussian pulse a measure for the amount of peripheral compression.

2. Integration

Van den Brink and Houtgast (1990b) investigated temporal and spectral integration in masked signal detection. They found that listeners can efficiently integrate the energy of narrow-band signals ($< \frac{1}{3}$ octave) over time, and the energy of short-duration signals (< 30 ms) over frequency. This means that the total energy of those signals determines the masked detection threshold.

The normal-hearing listeners in our study showed even lower masked thresholds for the tone than for the Gaussian pulse, especially at the intermediate level. Thus, for the

normal-hearing listeners, temporal integration (defined as the masked threshold for the tone subtracted from the masked threshold for the Gaussian pulse) is greater than maximally efficient. As mentioned previously, the higher masked threshold for the Gaussian pulse at the intermediate level is probably a consequence of peripheral compression. The fact that the tone was presented at the end of the masker, while the Gaussian pulse was temporally centered in the masker, may also have caused a difference in detectability. The hearing-impaired listeners showed on average less temporal integration (as defined in this study) than the normal-hearing listeners, probably as a result from loss of peripheral compression, in agreement with data from Oxenham *et al.* (1997).

On average the hearing-impaired listeners showed less spectral integration than the normal-hearing listeners, but for both groups of listeners the spectral integration is close to 0 dB. This means that both groups of listeners can integrate the energy of the click across frequency, in agreement with the efficient spectral integration for short-duration signals reported by van den Brink and Houtgast (1990b). The difference in spectral integration between both groups of listeners is caused by their different masked thresholds for the Gaussian pulse; their masked thresholds for the click did not differ significantly.

3. Spectral resolution

In Tables II and III, the upward spread of masking (USOM) and downward spread of masking (DSOM) are expressed as the frequency difference (in Hz) at the detection threshold between the cutoff frequency of the masker and the frequency of the tone. The spread of masking (in Hz) can be converted to a slope (in dB/octave):

$$\text{Slope (in dB/octave)} = \frac{10 \log(2)}{\log(1000 \pm \text{SOM}) - \log(1000)}, \quad (3)$$

where SOM is the amount of USOM or DSOM (in Hz). USOM is subtracted from 1000, and DSOM is added to 1000. For the normal-hearing listeners, the average USOM was 152 Hz at the intermediate level (Table III), corresponding to a slope of -42 dB/octave. The steepness of the slope increases with decreasing level. The slope of DSOM is about 100 dB/octave, independent of the level. These findings agree with the masking curves measured by Zwicker (1963).

Of the 23 hearing-impaired listeners, 11 listeners demonstrated increased spread of masking: either increased USOM (7 listeners), increased DSOM (2 listeners), or both (2 listeners). As already mentioned in Sec. IIIB, the increased USOM of the hearing-impaired listeners may partly be explained by the higher absolute level at which they performed the test. For hearing-impaired listeners, increased USOM has often been reported, and increased DSOM has occasionally been reported in the literature (for a review, see Tyler, 1986).

4. Temporal resolution

In the present study, forward masking and backward masking were measured for masker levels just 10 dB above

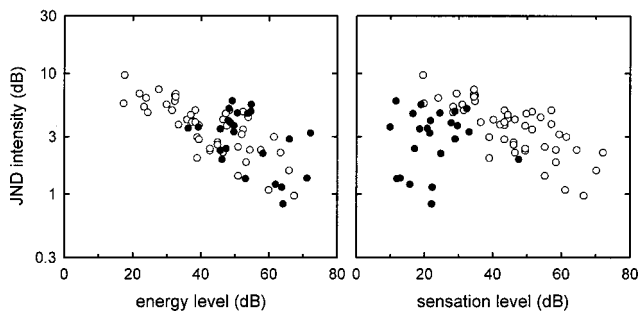


FIG. 3. Just-noticeable differences in intensity for Gaussian pulses vs the energy level of the pulses (left panel) and vs the sensation level of the pulses (right panel) for normal-hearing listeners (open circles) at three levels ($E - 15$, E , and $E + 15$) and hearing-impaired listeners (closed circles) at one level (E).

the threshold level for simultaneous masking of the same probe signal. This resulted in intervals between the click and the transition in the masker of about 10 ms at the detection threshold for normal-hearing listeners. For these conditions, the thresholds for forward and backward masking did not depend significantly on the presentation level. This result differs from literature data for larger delays between masker and probe signal for which forward and backward masking decreases as a function of masker level. This level dependence of nonsimultaneous masking becomes more pronounced with increasing masker-signal interval (Penner, 1974; Weber and Green, 1979; Oxenham and Moore, 1995). Therefore, the small intervals at threshold in the present study are probably the reason that no level effect was found in nonsimultaneous masking. Another factor that may have reduced a possible level effect is that the 20-dB step in masker level ensured that for each masker level the asymptotic threshold for long delays is about 10 dB below the fixed signal level.

On average, the hearing-impaired listeners in this study showed more forward masking than the normal-hearing listeners, in agreement with Festen and Plomp (1983), and Oxenham and Moore (1995).

5. Intensity discrimination

In Fig. 3 the just-noticeable difference (JND) in intensity is plotted against energy level and sensation level of the Gaussian-windowed tone pulses. The thresholds of the hearing-impaired listeners are averaged over sessions 1 and 2. Four data points are shown for each normal-hearing listener: the average JND of sessions 1 and 2, and the three individual JNDs measured at the three levels in session 3.

Intensity discrimination deteriorates as stimulus duration decreases (see Florentine, 1986). Therefore, the JNDs of the normal-hearing listeners in Fig. 3 for the brief tone pulses used in the present study are higher than commonly reported for stimuli of longer duration. The JNDs are in the same range as those found by van Schijndel *et al.* (1999), who also used Gaussian-windowed tone pulses. Figure 3 shows that the JND at 1 kHz decreases with increasing signal level, consistent with Rabinowitz *et al.* (1976) and Florentine *et al.* (1987). When compared at equal sensation level, the JNDs of most hearing-impaired listeners are better than those of the

normal-hearing listeners, but at equal absolute level, this difference in performance vanishes. This is consistent with Turner *et al.* (1989), Florentine *et al.* (1993), and Schroder *et al.* (1994), although some listeners in their studies did show higher JNDs at equal absolute levels.

6. Frequency discrimination

As the duration of a tonal signal decreases, frequency discrimination deteriorates (Moore, 1973; Hall and Wood, 1984; Freyman and Nelson, 1986). Therefore, the JNDs of the normal-hearing listeners obtained with the 2.8-ms Gaussian pulse are poorer than is normally reported in the literature for longer-duration stimuli. On average, the hearing-impaired listeners performed poorer than the normal-hearing listeners. This is in contrast with results by Hall and Wood (1984), and Freyman and Nelson (1987), who found that performance of most of the hearing-impaired listeners was normal for brief tones, and poorer than normal for tones of longer durations. A possible explanation is that the ERD of the shortest tones in the studies of Hall and Wood (6.3 ms) and Freyman and Nelson (8.3 ms) was still longer than the ERD of the Gaussian pulse in this study.

D. Influence of audibility on speech intelligibility

The speech intelligibility index (ANSI, 1997) has been designed to predict speech intelligibility for normal-hearing listeners, and for hearing-impaired listeners without suprathreshold deficits. For normal-hearing listeners, all conditions of equal intelligibility should result in the same SII. Thus, when the measured SRT and SRBT of the normal-hearing listeners are expressed in SII values, the model should yield identical SII values.

For the normal-hearing listeners, the average SII values for the SRT_q, SRT_n, SRT_a, and SRBT are 0.19, 0.26, 0.29, and 0.30, respectively. The SII_{SRT_q} is significantly lower than the SII for the other conditions (paired *t* tests with Bonferroni correction, $p < 0.05$; Keren and Lewis, 1993). This was also found in our previous study in which we assumed that Békésy tracking resulted in hearing thresholds that were systematically a few dB higher than the methods on which the ISO (1961) threshold is based (Noordhoek *et al.*, 2000).

When the internal noise level in the SII calculation, which represents the hearing threshold, was lowered by 4.6 dB, the differences among the four SII values were minimized. The upper two rows of Table IV show the average SII values calculated with the lowered internal noise level. For the hearing-impaired listeners, the average SII_{SRT_q} is similar to the average SII for normal-hearing listeners, but for the SRT_n, SRT_a and SRBT, the average SII for the hearing-impaired listeners is significantly higher than the average SII for the normal-hearing listeners (*t* test for unequal variances, $p < 0.05$). An elevated SII indicates that the hearing-impaired listeners needed more speech information than the normal-hearing listeners to understand 50% of the sentences. Therefore, an elevated SII suggests that suprathreshold deficits affected intelligibility. Consistent with previous results (Noordhoek *et al.*, 2000), the effect of suprathreshold deficits is most obvious for the SRBT, less obvious for the SRT_a,

TABLE IV. Average speech intelligibility index with standard deviation in parentheses for the normal-hearing listeners (NH) and the hearing-impaired listeners (HI), for four intelligibility tests. The SII was calculated according to two different procedures. Modifications with respect to the standard SII procedure (ANSI, 1997) are given in the second column. ‘‘Slopes:’’ Shallower slopes of the masking curves are used below 500 Hz (see Sec. II E). ‘‘Noise:’’ The internal noise level is lowered by 4.6 dB (see Sec. III D). ‘‘USOM, DSOM:’’ The individually measured upward and downward spread of masking is included (see Sec. III F). Results for the hearing-impaired listeners that differ significantly from the corresponding results for the normal-hearing listeners are indicated with an asterisk.

Modifications SII		SII _{SRTq}	SII _{SRTn}	SII _{SRTa}	SII _{SRBT}
NH	Slopes, noise	0.29 (0.11)	0.27 (0.02)	0.30 (0.02)	0.29 (0.03)
HI	Slopes, noise	0.27 (0.10)	0.30* (0.06)	0.32* (0.05)	0.39* (0.09)
NH	Slopes, noise, USOM, DSOM	0.29 (0.11)	0.27 (0.04)	0.30 (0.04)	0.29 (0.04)
HI	Slopes, noise, USOM, DSOM	0.27 (0.10)	0.27 (0.06)	0.30 (0.04)	0.36* (0.07)

and absent for the SRT_q. In contrast with our previous results, the effect of suprathreshold deficits now is also present in the SRT_n condition. In our previous study, we suggested that the dependence of the effect of suprathreshold deficits on condition may be related to the different spectra of speech and noise for the different conditions: when, for instance, a hearing-impaired listener suffers from excessive spread of masking, the effect on speech intelligibility will depend on the spectra of speech and noise.

For each intelligibility test, the SII of individual listeners is shown in Fig. 4 as a function of the threshold. Dashed lines represent the maximum possible SII, i.e., the SII that would have been reached if the audibility of the speech had not been influenced by the hearing threshold, upward spread of masking, and level distortion. (Since the maximum possible SII_{SRTq} is one, no dashed line has been drawn in the upper left graph). The upper limit of the one-tailed 95%-confidence interval of the SII of normal-hearing listeners is chosen as the separation between normal and higher-than-normal SII (horizontal lines). The separation between normal and deviant SRT or SRBT is indicated with a vertical line.

The horizontal and vertical lines divide the graphs in four quadrants. No data points fall in the upper left quadrant: A normal threshold never corresponds to an elevated SII. Data points in the lower left quadrant correspond to a normal threshold and a normal SII. Data points in the lower right quadrant correspond to an elevated SRT or a broader-than-normal SRBT; these result can be explained on the basis of audibility by the SII model. Data points in the upper right quadrant correspond to a deviant threshold that cannot be explained by the SII model. The higher the position of the data point above the horizontal line, the larger the speech perception deficit. The upper left graph shows that the SII model can account for all differences in SRT_q between hearing-impaired listeners and normal-hearing listeners. The other three graphs show that audibility can account for some, but not all, deviant speech thresholds found for the other tests. Therefore, in these conditions, the effects of suprathreshold deficits appear to influence speech intelligibility for part of the hearing-impaired listeners.

E. Correlations among the tests

1. Correlations among auditory functions

The data of the combined groups of hearing-impaired and normal-hearing listeners form a continuum of thresholds

on each test. Therefore, pooling the data of hearing-impaired and normal-hearing listeners will not bias the values of the correlation coefficients between each pair of tests. Table V shows correlation coefficients among 11 auditory functions for the combined group of all listeners. The masked thresholds for tone and click are not included, because they are not independent from (the included) temporal integration and spectral integration. Missing data were deleted casewise. Thirty complete cases remained: 18 hearing-impaired listeners and 12 normal-hearing listeners. Of the 55 correlation coefficients, 13 are significant at the 1% level, and 5 are significant at the 5% level. Within the group of hearing-impaired listeners, none of the auditory functions correlated significantly with age or absolute presentation level (not shown in Table V).

Because several auditory functions are correlated, a

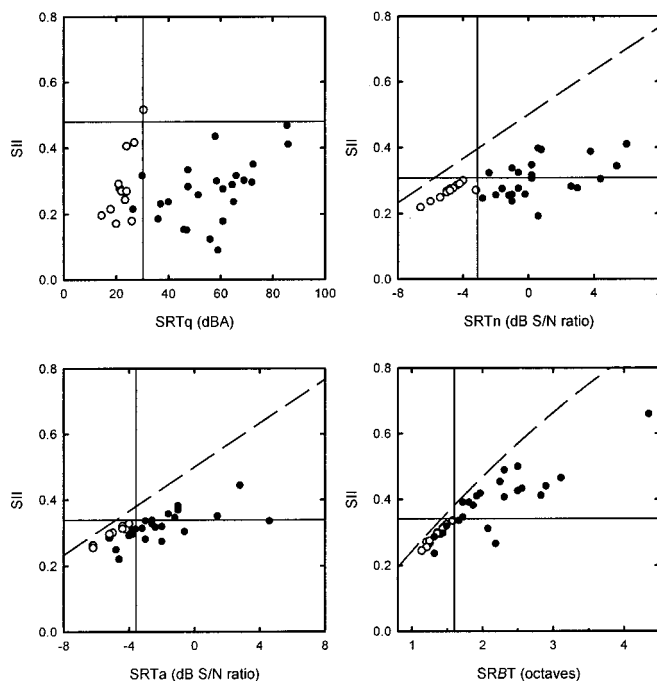


FIG. 4. Speech intelligibility index vs speech-reception threshold on the four intelligibility tests (SRT_q, SRT_n, SRT_a, SRBT) for normal-hearing listeners (open circles) and hearing-impaired listeners (closed circles). Solid lines represent the one-tailed 95%-confidence limit for the data of the normal-hearing listeners. Dashed lines represent the maximum SII as a function of SRT or SRBT.

TABLE V. Matrix of correlation coefficients among 11 auditory-function tests for 18 hearing-impaired listeners and 12 normal-hearing listeners. Underlined coefficients are significant at the 5% level; double-underlined coefficients are significant at the 1% level. Correlation coefficients were calculated from the mean thresholds of test and retest, except nine correlation coefficients in italics, which were calculated from the individual results. [The thresholds, on which the italic correlation coefficients are based, are mutually dependent within a session. For example, the noise level used in the measurements of USOM and DSOM was determined by the masked threshold for the tone in the same session. If, due to a measurement error, the masker noise level was chosen too low, this resulted in an underestimate of USOM and DSOM thresholds. Therefore, if the correlation coefficient between USOM and DSOM was calculated from the mean thresholds, it would have been artificially enhanced, because of error variance in their common reference (the masked threshold for the tone). However, the test of USOM and the retest of DSOM are independent, as well as the test of DSOM and the retest of USOM. Therefore, the correlation coefficient between USOM and DSOM was calculated as the average of the correlation coefficient between the USOM test and the DSOM retest, and the correlation coefficient between the DSOM test and the USOM retest. The other italic correlations were calculated similarly.]

Test	3b USOM	3c DSOM	5b FM	5c BM	TI	SI	6a ID	6b FD	6c RD	6d SD
2c. Gaussian pulse in noise (E/N_0)	-0.21	0.05	<u>-0.54</u>	-0.23	<u>0.69</u>	<u>0.44</u>	0.23	0.05	-0.06	-0.05
3b. Upward spread of masking		<i>0.11</i>	0.27	0.01	-0.38	-0.24	<u>-0.65</u>	0.15	-0.17	-0.05
3c. Downward spread of masking			0.13	-0.03	-0.12	0.21	<u>-0.38</u>	0.01	-0.29	-0.21
5b. Forward masking				<u>0.60</u>	<u>-0.73</u>	<u>-0.28</u>	-0.23	0.43	0.30	<u>0.52</u>
5c. Backward masking					-0.43	<u>-0.02</u>	0.21	<u>0.50</u>	<u>0.50</u>	<u>0.48</u>
Temporal integration						<u>0.47</u>	<u>0.39</u>	-0.27	-0.01	-0.32
Spectral integration							0.14	-0.11	-0.04	-0.23
6a. Intensity discrimination								0.07	<u>0.49</u>	-0.01
6b. Frequency discrimination									0.29	<u>0.53</u>
6c. Rhythm discrimination										<u>0.36</u>
6d. Shape discrimination										

principal-components analysis was applied on the matrix of correlations to reduce the 11 auditory functions to a smaller set of factors. The resulting factors are linear combinations of the auditory functions. Only factors with eigenvalues greater than one were considered significant. This resulted in three factors that can account for 68% of the total variance. A varimax rotation was performed to obtain the factors that were clearly marked by high loadings for some auditory functions. Table VI shows the normalized factor loadings and the proportion of variance accounted for by each factor. Factor loadings can be interpreted as correlations between the auditory-function tests and the auditory factors. They are important for the interpretation of the auditory factors. Forward and backward masking, frequency discrimination, and shape discrimination have the highest loadings on auditory factor 1. Upward and downward spread of masking, intensity discrimination, and rhythm discrimination have the highest loadings on auditory factor 2. The loading of rhythm dis-

TABLE VI. Factor loadings on the first three factors from a principal-components analysis on 11 auditory-function tests for the combined groups of 18 hearing-impaired listeners and 12 normal-hearing listeners. The bottom row shows the proportion of the total variance accounted for by each factor. For each test, the highest factor loading has been underlined.

Test	Factor 1	Factor 2	Factor 3
2c. Gaussian pulse in noise	-0.10	-0.10	<u>0.83</u>
3b. Upward spread of masking	0.04	<u>0.63</u>	-0.35
3c. Downward spread of masking	0.07	<u>0.72</u>	0.32
5b. Forward masking	<u>0.72</u>	0.26	-0.47
5c. Backward masking	<u>0.84</u>	-0.11	-0.10
Temporal integration	0.43	0.37	<u>0.71</u>
Spectral integration	0.02	-0.07	<u>0.79</u>
6a. Intensity discrimination	0.12	<u>-0.85</u>	0.27
6b. Frequency discrimination	<u>0.78</u>	0.07	0.08
6c. Rhythm discrimination	<u>0.56</u>	<u>-0.57</u>	-0.04
6d. Shape discrimination	<u>0.73</u>	-0.13	-0.15
Proportion of variance explained	26%	20%	22%

crimination on factor 2 is only slightly higher than its loading on factor 1. The loadings of upward and downward spread of masking on factor 2 are positive, whereas the loadings of intensity and rhythm discrimination on factor 2 are negative, corresponding to positive and negative correlations, respectively. The auditory functions that load high on factor 3 are the masked threshold for the Gaussian pulse and temporal and spectral integration. A reduction of the masked threshold for the Gaussian pulse and reduced integration are probably caused by a loss of peripheral compression (Sec. III C). Thus, auditory factor 3 is probably related to peripheral amplitude compression. The lower factor 3, the more loss of compression.

2. Correlations between speech reception and auditory functions

Table VII shows the correlation coefficients between, on the one hand, thresholds of the four intelligibility tests and corresponding speech intelligibility indices, and, on the other hand, 11 auditory functions and the three factors that resulted from a principal-components analysis on the 11 auditory functions.

Correlation coefficients were calculated for the combined groups of 24 hearing-impaired listeners and 12 normal-hearing listeners with pairwise deletion of missing data. Thirty correlations between thresholds on the four intelligibility tests (SRT_q, SRT_n, SRT_a, and SRBT) and auditory functions are significant, but only 16 correlations between SII values and auditory functions are significant ($p < 0.05$). Apparently, for half of the correlations between intelligibility thresholds and auditory functions, the underlying cause is hearing threshold elevation: Most auditory functions correlate significantly with hearing loss, and hearing loss correlates significantly with intelligibility thresholds (not shown).

TABLE VII. Matrix of correlation coefficients between, on the one hand, thresholds on the four intelligibility tests and corresponding speech intelligibility indices and, on the other hand, 11 auditory functions, and the three factors from a principal-components analysis on these auditory functions. Underlined coefficients are significant at the 5% level; double-underlined coefficients are significant at the 1% level.

	SRTq	SRTn	SRTa	SRBT	SII _{SRTq}	SII _{SRTn}	SII _{SRTa}	SII _{SRBT}
2c. Gaussian pulse in noise	<u>-0.44</u>	<u>-0.47</u>	-0.22	<u>-0.43</u>	-0.03	-0.06	-0.08	<u>-0.35</u>
3b. USOM	<u>0.40</u>	<u>0.52</u>	<u>0.49</u>	<u>0.55</u>	0.19	<u>0.36</u>	<u>0.49</u>	<u>0.57</u>
3c. DSOM	0.17	-0.07	-0.06	0.33	0.23	<u>0.36</u>	0.22	<u>0.46</u>
5b. Forward masking	<u>0.68</u>	<u>0.56</u>	<u>0.63</u>	<u>0.61</u>	0.15	<u>0.55</u>	0.25	<u>0.47</u>
5c. Backward masking	0.28	<u>0.36</u>	0.24	0.15	0.00	0.32	0.07	0.07
Temporal integration	<u>-0.76</u>	<u>-0.73</u>	<u>-0.66</u>	<u>-0.69</u>	0.00	<u>-0.42</u>	-0.23	<u>-0.57</u>
Spectral integration	<u>-0.36</u>	<u>-0.51</u>	-0.12	<u>-0.42</u>	0.11	0.03	0.09	<u>-0.37</u>
6a. Intensity discrimination	<u>-0.45</u>	-0.27	<u>-0.47</u>	<u>-0.44</u>	-0.17	-0.24	<u>-0.35</u>	<u>-0.45</u>
6b. Frequency discrimination	0.42	<u>0.49</u>	<u>0.59</u>	0.43	0.08	<u>0.66</u>	<u>0.38</u>	<u>0.43</u>
6c. Rhythm discrimination	0.15	0.05	0.15	0.04	0.19	0.25	0.15	-0.03
6d. Shape discrimination	<u>0.47</u>	<u>0.35</u>	0.19	<u>0.48</u>	0.22	0.18	0.08	0.31
Factor 1	0.46	<u>0.48</u>	0.36	<u>0.39</u>	0.19	<u>0.47</u>	0.27	0.32
Factor 2	<u>0.40</u>	0.32	0.30	<u>0.56</u>	0.22	<u>0.45</u>	<u>0.46</u>	<u>0.65</u>
Factor 3	<u>-0.54</u>	<u>-0.60</u>	<u>-0.55</u>	<u>-0.44</u>	0.04	-0.02	0.01	-0.29

Most significant correlations between SII and auditory functions are positive, suggesting that a suprathreshold speech perception deficit (i.e., elevated SII) may be caused by an elevated threshold on the auditory-function test in question. The SII correlates negatively with the threshold for the Gaussian pulse in noise, temporal integration, spectral integration (in case of the SII_{SRBT}), and intensity discrimination. It seems very unlikely that an elevated SII may be caused by *better* intensity discrimination. Table V shows that intensity discrimination has a significant negative correlation with both USOM and DSOM. Intensity discrimination, USOM, and DSOM did not correlate significantly with presentation level for the hearing-impaired listeners (not shown). Therefore, presentation level cannot be the underlying cause for the correlation between spread of masking and intensity discrimination. The role of spread of excitation in intensity discrimination may explain the correlation between spread of masking and intensity discrimination. The spread of excitation toward the higher and, to a lesser extent, the lower frequencies is important for intensity discrimination (Viemeister, 1972; Moore and Raab, 1974). Thus, intensity discrimination may profit from increased USOM or DSOM, as suggested by Florentine *et al.* (1993) and Schroder *et al.* (1994). Table VII shows that USOM has a significant positive correlation with SII_{SRTa}, and both USOM and DSOM have a significant positive correlation with SII_{SRBT}. Therefore, spread of masking may be the underlying cause for the negative correlation between intensity discrimination and SII_{SRTa} and SII_{SRBT}.

Auditory factor 3 does not correlate significantly with any of the SII values. This suggests that a loss of peripheral compression has little effect on speech perception. Auditory factor 1 only correlates significantly with SII_{SRTn}, but auditory factor 2 correlates significantly with the SII values for three tests: the SRTn, SRTa, and SRBT. Upward and downward spread of masking, and intensity discrimination have the highest loadings on factor 2. This suggests that reduced spectral resolution is the most important cause for supra-threshold speech perception deficits. Speech intelligibility

was probably affected by increased spread of masking by the noise. Furthermore, reduced spectral resolution may have interfered with the detection and discrimination of spectral features such as formants.

F. Including measured spread of masking in the SII model

The individual SII values were recalculated to investigate whether the underlying cause for the correlation between the SII and spectral resolution is the increased spread of masking by the noise. In this recalculation, the measured USOM was used instead of the SII model values for normal hearing, and the measured DSOM was used instead of no DSOM. For normal-hearing listeners, the slope of DSOM is level and frequency independent (Zwicker, 1963). Therefore, the measured slope of DSOM was used for all frequencies and levels in the SII calculations. USOM however, is level and frequency dependent. Therefore, the ratio between the measured USOM and SII-model slopes is applied as “*USOM factor*” to calculate the individual USOM for all levels and frequencies in the SII model. For hearing-impaired listeners this is probably not correct, but it is presumably closer to the real upward spread of masking than the SII model values for normal hearing.

In the standard SII model, the spectrum level for masking (Z_i) in $\frac{1}{3}$ -octave band i is calculated as

$$Z_i = 10 \log \left(10^{0.1N_i} + \sum_{k=1}^{i-1} 10^{0.1[B_k + 3.32C_k \log(0.89F_i/F_k)]} \right), \quad (4)$$

where N is the noise spectrum level, B is the larger of the noise spectrum level and the self-speech masking spectrum level, C is the slope of USOM, and F is the $\frac{1}{3}$ -octave band center frequency. The individually measured USOM and DSOM are included in the SII model by calculating the spectrum level for masking as

$$Z_i = 10 \log \left(10^{0.1N_i} + \sum_{k=1}^{i-1} 10^{0.1[B_k + 3.32(USOM \text{ factor})C_k \log(0.89F_i/F_k)]} + \sum_{k=i+1}^{18} 10^{0.1[B_k - 3.32C_D \log(0.89F_k/F_i)]} \right), \quad (5)$$

where C_D is the measured slope of DSOM.

The two bottom rows of Table IV show the average SII values recalculated with the measured spread of masking for the normal-hearing and the hearing-impaired listeners. The SII_{SRTq} is not influenced by the modification, because no noise was present in this condition. For the normal-hearing listeners, average SII values for SRTn, SRTa, and SRBT do not change, but the standard deviations are larger. The average SII values for the hearing-impaired listeners are lower than without the measured spread of masking. The average SII_{SRTn} and SII_{SRTa} now are equal to those of the normal-hearing listeners. The average SII_{SRBT} is still significantly higher ($p < 0.05$) than the SII_{SRBT} of the normal-hearing listeners, although it is closer to the normal SII_{SRBT} than is the SII_{SRBT} calculated without the measured spread of masking.

From a comparison of SII calculations with just the measured USOM and with just the measured DSOM (not shown), it can be concluded that the effect of including DSOM is negligible. Thus, the effect of including measured spread of masking shown in Table IV originates primarily from including the measured USOM.

For normal-hearing listeners, the SII predictions with the measured USOM and DSOM included in the model are less accurate (larger standard deviations in Table IV). On the other hand, the average SII values of the hearing-impaired listeners are closer to those of the normal-hearing listeners. The change in variance in SII for the hearing-impaired and normal-hearing listeners taken together is chosen as a measure of the net effect of including the measured spread of masking. The total variance in SII_{SRTn} and SII_{SRTa} did not change compared to the original SII, but the total variance in SII_{SRBT} decreased by 46%. Therefore, it is concluded that incorporating the measured spread of masking improves the SII predictions for the SRBT. This may be related to the fact that USOM was measured with the stimulus at 1 kHz, and that only in the SRBT measurement, the speech signal was restricted to the 1-kHz frequency region.

When the measured spread of masking is included in the model, the correlation coefficient between SII_{SRBT} and USOM reduces to a nonsignificant 0.21. (Because the SII calculated when including the measured spread of masking in the model and the measured spread of masking itself are mutually dependent, the correlation coefficient between USOM and SII was calculated as the average of the correlation coefficient between USOM test and SII retest, and the correlation coefficient between USOM retest and SII test. The same holds for the correlation coefficient between DSOM and the SII calculated when including the measured spread of masking in the model.) This indicates that the main underlying cause for the correlation between SII_{SRBT} and USOM is that increased upward spread of masking by the noise reduces the speech range that contributes to intelligibility. With the measured spread of masking applied in the

model, the correlation coefficient between SII_{SRBT} and DSOM (0.35) remains significant ($p < 0.01$). Therefore, the main underlying cause for the correlation between SII_{SRBT} and DSOM probably lies in reduced spectral resolution preserving less spectral detail of the speech signal, and thus reducing intelligibility.

G. Relation between suprathreshold speech perception and auditory functions

In this section, two different methods (multiple regression analysis and individual approach) are used to study the relation between suprathreshold speech perception and auditory functions. The SII [calculated with shallower slopes of the masking curves below 500 Hz (see Sec. II E) and adjusted internal noise level (see Sec. III D)] is used as a measure for the capability of a listener to understand suprathreshold speech. Because several auditory functions are correlated, not the individual auditory functions, but the three (uncorrelated) factors extracted from the 11 auditory functions (Table VI) were used as predictor variables.

Auditory factors were calculated for 18 hearing-impaired listeners and 12 normal-hearing listeners. For six hearing-impaired listeners auditory factors could not be calculated, because they could not perform all auditory-function tests. This probably indicates that the auditory function that we tried to measure is very poor. The auditory tests that could not be measured all had a high loading on factor 1. Taking this into account in the multiple regression analysis is not possible. In the individual approach, factor 1 is assumed to be elevated when a listener could not perform one or more tests that load high on this factor.

1. Multiple regression

Stepwise multiple regression was used to predict the SII for the four speech-intelligibility tests from the factors extracted from the auditory functions. An ‘‘auditory factor’’ was only included in the regression when it could account for a significant part of the variance ($p < 0.05$). SII_{SRTq} did not correlate significantly with any of the auditory factors. For the SII values corresponding to the other intelligibility thresholds, the following regression equations were obtained:

$$SII_{SRTn} = 0.021 \cdot \text{factor2} + 0.021 \cdot \text{factor1} + 0.28, \quad R^2 = 0.43, \quad (6)$$

$$SII_{SRTa} = 0.018 \cdot \text{factor2} + 0.31, \quad R^2 = 0.21, \quad (7)$$

$$SII_{SRBT} = 0.059 \cdot \text{factor2} + 0.029 \cdot \text{factor1} - 0.025 \cdot \text{factor3} + 0.36, \quad R^2 = 0.62, \quad (8)$$

where R^2 is the variance accounted for by the regression equation. Factor 2 explains 21% of the variance in SII_{SRTn} , 21% in SII_{SRTa} , and 42% in SII_{SRBT} . Factor 1 explains 22% of the variance in SII_{SRTn} , and 11% of variance in SII_{SRBT} . Finally, factor 3 explains an additional 9% of the variance in

SII_{SRBT} . Thus, although the simple correlation between SII_{SRBT} and factors 1 and 3 is not significant (see Table VII), Eq. (8) shows that the partial correlation between SII_{SRBT} and factors 1 and 3 is significant. This means that, only after the variance explained by factor 2 is taken into account, factors 1 and 3 can explain an additional part of the variance in SII_{SRBT} .

Auditory factor 2 is related to spectral resolution (see Sec. III E). Therefore, reduced spectral resolution appears to be the most important cause of suprathreshold speech perception deficits for this group of listeners. When factor 2 is accounted for, factor 1 can further reduce the variance in SII_{SRTn} and SII_{SRBT} . Auditory functions with a high loading on factor 1 were forward and backward masking, frequency discrimination, and shape discrimination. Auditory factor 3, probably related to peripheral compression, seems least important for suprathreshold speech perception. The negative contribution of factor 3 in Eq. (8) means that loss of compression results in a higher SII_{SRBT} .

At this point it should be remembered that six listeners who could not perform on one or two tests that load high on factor 1 are excluded from this multiple regression analysis. Partly because of this, the relative importance of factors 1 and 2 will change in the individual approach.

The total variance accounted for by the auditory factors is largest for SII_{SRBT} . This was expected, because all auditory factors were measured at 1 kHz, i.e., the center frequency in the SRBT test. The auditory factors can account for a greater part of the variance in SII_{SRTn} than in SII_{SRTa} . A possible explanation is that the frequency region around 1 kHz is more important in the SRTn test than in the SRTa test. In the SRTa test, the speech signal is presented above threshold in the entire frequency range from 250 to 4000 Hz. Because most hearing-impaired listeners had a high-frequency hearing loss, the high-frequency part of the speech signal was below their threshold in the SRTn test. This increases the relative importance of the 1-kHz frequency region in speech perception.

2. Individual approach

In this section, we will try to determine for each individual listener which deteriorated auditory function affects speech intelligibility in the 1-kHz frequency region. Figure 4 shows that 19 listeners had a normal SII_{SRBT} (12 normal hearing and 7 hearing impaired) and that 16 hearing-impaired listeners had an elevated SII_{SRBT} . The auditory functions in the group of 19 listeners with no speech perception deficit in the 1-kHz frequency region apparently are adequate for normal speech perception. The thresholds on the auditory-function tests can be summarized by three factors. For factors 1 and 2, the upper one-tailed 95%-confidence limit of the auditory factors in the listener group with a normal SII_{SRBT} is chosen as the separation between sound processing sufficient for speech perception, and sound processing that may cause a deficit in speech perception. For auditory factor 3, the lower one-tailed 95%-confidence limit is chosen as separation, because a lower score on factor 3 is probably related to the sound processing deficit "loss of compression."

Of the 16 listeners with an elevated SII, 6 listeners had a deviant score on factor 1, 6 listeners had a deviant score on factor 2, and only 1 listener had a deviant score on factor 3. Therefore, factor 3 seems to be least important for suprathreshold speech perception (as was also found by multiple regression in the previous section). For the 16 hearing-impaired listeners with an elevated SII_{SRBT} , the individual thresholds on six auditory functions that load high on either factor 1 or factor 2 are presented in Table VIII. Thresholds for rhythm and shape discrimination are not shown in Table VIII, because on each test only one listener had a JND above the 95%-confidence limit for normal SII. Some listeners have a slightly deviant threshold on one test, while their corresponding factor score is still normal, because they have normal thresholds on the other tests that also load high on this factor. For 4 listeners in Table VIII, the factor scores could not be calculated, because they could not perform one or two auditory-function tests. Therefore, the factor on which these tests had a high loading is assumed to be elevated.

Table VIII shows that the speech perception deficit of individual hearing-impaired listeners seems to be related either to factor 1, or to factor 2. Only one listener deviates on both factors, and one listener deviates on neither. The SII of the listener that deviates on neither factor was only just outside the 95% confidence limit. For 9 listeners, the speech perception deficit in the 1-kHz frequency region may be explained by reduced temporal resolution and/or reduced frequency discrimination (factor 1). For 5 listeners, reduced spectral resolution (factor 2) seems responsible for the speech perception deficit.

The results of the individual approach and those of the multiple regression analysis both point to factors 1 and 2 as the most important determinants of speech perception. However, the multiple-regression results identify factor 2 as the major factor, while the individual approach identifies factor 1 as the major factor. This can be partly explained from the data of the 4 hearing-impaired listeners with an elevated SII who could not perform all auditory-function tests. These 4 listeners could not be included in the multiple regression. In the individual approach, factor 1 was considered responsible for their speech perception deficit. Another difference between the two approaches that may contribute to the differences between their results is that different assumptions underlie each approach: In the individual approach we assumed that an elevated SII can be caused by one elevated factor score, independent of the other factor scores, while in multiple regression it is assumed that an elevated SII is caused by an elevation of a linear combination of the factors. A third difference is that we tried to identify the sound processing deficit for the largest possible number of hearing-impaired listeners in the individual approach, while multiple regression is based on explaining as much as possible of the variance in the SII values.

In conclusion, factor 2 (reduced spectral resolution) can explain the largest part of the variance in intelligibility of suprathreshold speech. However, to understand each individual speech perception deficit in the 1-kHz frequency range, both factor 2 (reduced spectral resolution) and factor 1

TABLE VIII. Individual SII values for the SRBT and thresholds on six auditory functions with a high loading on factor 1 (forward masking, backward masking, and frequency discrimination) or factor 2 (upward spread of masking, downward spread of masking, and intensity discrimination) for the 16 hearing-impaired listeners with a speech perception deficit in the 1-kHz frequency region (i.e., elevated SII_{SRBT}). The characters in the column “listener” correspond to the characters that identify the listeners in Table I. The row “95% limit” gives the one-tailed 95%-confidence limit for the data of listeners with a normal SII_{SRBT} (lower limit for ID, which has a negative loading on factor 2; upper limit for other tests). Bold thresholds lie beyond this 95%-confidence limit. Empty cells mean that the listener could not perform this test. An asterisk indicates that the listener has an elevated factor score. An asterisk in parentheses indicates that the factor scores could not be calculated, because the listener could not perform on one or two tests that load high on this factor.

Listener	SII_{SRBT}	Factor 1				Factor 2			
		FM (ms)	BM (ms)	FD (%)	Elevated factor	USOM (Hz)	DSOM (Hz)	ID (dB)	Elevated factor
95% limit	0.34	30	33	8.2		331	125	2.1	
o	0.35	25	19	3.0		88	61	3.0	
n	0.38	25	47	11.4		248	157	4.7	
l	0.39	11	9		(*)	291	28	3.7	
b	0.39	26	38	8.0	*	138	49	4.9	
x	0.41	116	61	5.1	*	314	56	2.2	
f	0.41			8.6	(*)	118	47	2.9	
w	0.41	28	25	3.5		464	107	2.4	*
r	0.42	20	21	8.9	(*)	338	61	5.1	
a	0.43	28	27	14.2	*	113	67	3.5	
m	0.43	31	20	2.4		345	204	1.2	*
u	0.44	33	18	7.0	*	456	48	1.1	*
i	0.45	15	9	2.5		186	161	0.8	*
k	0.47	71		16.8	(*)	271	98	5.9	
d	0.49	36	53	11.7	*	407	89	2.3	
v	0.50	19	11	5.0		348	175	3.2	*
e	0.66	23	9	4.2		483	99	1.3	*

(reduced temporal resolution and/or reduced frequency discrimination) have to be taken into account.

IV. SUMMARY AND CONCLUSIONS

Performance of 24 hearing-impaired listeners and 12 normal-hearing listeners was measured on four speech-intelligibility tests and on a set of auditory-function tests concerning detection efficiency, resolution, discrimination, and integration. Intelligibility was measured in four conditions: SRT in quiet, SRT in noise (SRTn), spectrally adapted SRT in noise (SRTa), and the novel SRBT (Noordhoek *et al.*, 1999). The SRBT is defined as the bandwidth of speech (center frequency: 1 kHz) in complementary notched noise required for a 50% intelligibility score.

All individual intelligibility thresholds were converted to speech intelligibility indices (SII), with the assumption that the SII includes the effect of audibility. The SRT in quiet could be explained from audibility for all listeners. However, deviant thresholds on the other intelligibility tests could not all be accounted for by audibility. A higher-than-normal SII required for a 50% intelligibility score was assumed to indicate the effect of suprathreshold deficits. Including the measured upward spread of masking in the SII model substantially improved the SII predictions for the SRBT, but it did not improve the SII predictions for the two SRT tests in noise. The reason for this probably lies in the fact that upward spread of masking was measured at 1 kHz, i.e., in the frequency region that is most relevant for the SRBT measurement.

The SRBT test has been developed as a research tool to identify hearing-impaired listeners suffering from a deficit in speech perception in the 1-kHz frequency region. All auditory-function tests were measured at 1 kHz. As expected, the SII_{SRBT} was most closely related to the auditory functions: 62% of the total variance in SII_{SRBT} could be explained by the thresholds on the auditory-function tests, whereas this was 43% and 21% for SII_{SRTn} and SII_{SRTa} , respectively.

The thresholds on the auditory-function tests were subjected to a principal-components analysis. This resulted in three “auditory factors,” the first factor was related to temporal resolution and frequency discrimination, the second factor was associated with spectral resolution, and the third factor was associated with peripheral compression. The auditory factor associated with spectral resolution, and the auditory factor related to temporal resolution and frequency discrimination both seemed important for suprathreshold speech perception. Reduced peripheral amplitude compression appeared least important for speech intelligibility. On an individual basis, each substantially elevated SII_{SRBT} (for 15 of the listeners) was found to be associated with a deviant value of the first and/or the second factor.

ACKNOWLEDGMENTS

This research was supported by the Foundation “Heinsius-Houbolt Fonds,” The Netherlands. The authors would like to thank Nicolle van Schijndel, Johannes Lijzenga, and Søren Buus for their very useful comments on an earlier version of this manuscript.

- ANSI (1969). ANSI S3.5-1969, "American National Standard Methods for the Calculation of the Articulation Index" (American National Standards Institute, New York).
- ANSI (1997). ANSI S3.5-1997, "American National Standard Methods for Calculation of the Speech Intelligibility Index" (American National Standards Institute, New York).
- Carlyon, R. P., and Moore, B. C. J. (1986). "Detection of tones in noise and the 'severe departure' from Weber's law," *J. Acoust. Soc. Am.* **79**, 461–464.
- Ching, T., Dillon, H., and Byrne, D. (1997). "Prediction of speech recognition from audibility and psychoacoustic abilities of hearing-impaired listeners," in *Modeling Sensorineural Hearing Loss*, edited by W. Jestaedt (Erlbaum, Hillsdale, NJ).
- Divenyi, P. L., and Haupt, K. M. (1997a). "Audiological correlates of speech understanding deficits in elderly listeners with mild-to-moderate hearing loss. II. Correlation Analysis," *Ear Hear.* **18**, 100–113.
- Divenyi, P. L., and Haupt, K. M. (1997b). "Audiological correlates of speech understanding deficits in elderly listeners with mild-to-moderate hearing loss. III. Factor representation," *Ear Hear.* **18**, 189–201.
- Dreschler, W. A., and Plomp, R. (1985). "Relations between psychophysical data and speech perception for hearing-impaired subjects. II," *J. Acoust. Soc. Am.* **78**, 1261–1270.
- Festen, J. M., and Dreschler, W. A. (1988). "Irregularities in the masked threshold of brief tones and filtered clicks," in *Basic Issues in Hearing—Proceedings of the Eighth International Symposium on Hearing*, edited by H. Duifhuis, J. W. Horts, and H. P. Wit (Academic, London), pp. 295–301.
- Festen, J. M., and Plomp, R. (1983). "Relations between auditory functions in impaired hearing," *J. Acoust. Soc. Am.* **73**, 652–662.
- Florentine, M. (1983). "Intensity discrimination as a function of level and frequency and its relation to high-frequency hearing," *J. Acoust. Soc. Am.* **74**, 1375–1379.
- Florentine, M. (1986). "Level discrimination of tones as a function of duration," *J. Acoust. Soc. Am.* **79**, 792–798.
- Florentine, M., Buus, S., and Mason, C. R. (1987). "Level discrimination as a function of level for tones from 0.25 to 16 kHz," *J. Acoust. Soc. Am.* **81**, 1528–1541.
- Florentine, M., Reed, C. M., Rabinowitz, L. D., Durlach, N. I., and Buus, S. (1993). "Intensity Perception. XIV. Intensity discrimination in listeners with sensorineural hearing loss," *J. Acoust. Soc. Am.* **94**, 2575–2586.
- Freyman, R. L., and Nelson, D. A. (1986). "Frequency discrimination as a function of tonal duration and excitation-pattern slopes in normal and hearing-impaired listeners," *J. Acoust. Soc. Am.* **79**, 1034–1044.
- Freyman, R. L., and Nelson, D. A. (1987). "Frequency discrimination of short- versus long-duration tones by normal and hearing-impaired listeners," *J. Speech Hear. Res.* **30**, 28–36.
- Glasberg, B. R., and Moore, B. C. J. (1989). "Psychoacoustic abilities of subjects with unilateral and bilateral cochlear hearing impairments and their relationship to the ability to understand speech," *Scand. Audiol. Suppl.* **32**, 1–25.
- Hall, J. W., and Wood, E. J. (1984). "Stimulus duration and frequency discrimination for normal-hearing and hearing-impaired listeners," *J. Speech Hear. Res.* **27**, 252–256.
- International Organization for Standardization (1961). ISO R226-1961, "Normal Equal-loudness Contours for Pure Tones and Normal Threshold of Hearing Under Free Field Listening Conditions" (available from American National Standards Institute, New York).
- Keren, G., and Lewis, C. (1993). *A Handbook for Data Analysis in the Behavioral Sciences* (Lawrence Erlbaum Associates, Hillsdale, NJ).
- Levitt, H. (1971). "Transformed up-down methods in psychoacoustics," *J. Acoust. Soc. Am.* **49**, 467–477.
- Moore, B. C. J. (1973). "Frequency difference limens for short-duration tones," *J. Acoust. Soc. Am.* **54**, 610–619.
- Moore, B. C. J., Glasberg, B. R., Plack, C. J., and Biswas, A. K. (1988). "The shape of the ear's temporal window," *J. Acoust. Soc. Am.* **83**, 1102–1116.
- Moore, B. C. J., and Raab, D. H. (1974). "Pure-tone intensity discrimination: Some experiments relating to the 'near-miss' to Weber's law," *J. Acoust. Soc. Am.* **55**, 1049–1054.
- Noordhoek, I. M., Houtgast, T., and Festen, J. M. (1999). "Measuring the threshold for speech reception by adaptive variation of the signal bandwidth. I. Normal-hearing listeners," *J. Acoust. Soc. Am.* **105**, 2895–2902.
- Noordhoek, I. M., Houtgast, T., and Festen, J. M. (2000). "Measuring the threshold for speech reception by adaptive variation of the signal bandwidth. II. Hearing-impaired listeners," *J. Acoust. Soc. Am.* **107**, 1685–1696.
- Oxenham, A. J., and Moore, B. C. J. (1995). "Additivity of masking in normally hearing and hearing-impaired subjects," *J. Acoust. Soc. Am.* **98**, 1921–1934.
- Oxenham, A. J., Moore, B. C. J., and Vickers, D. A. (1997). "Short-term temporal integration: Evidence for the influence of peripheral compression," *J. Acoust. Soc. Am.* **101**, 3676–3687.
- Patterson, R. D., Nimmo-Smith, D. L., Weber, D. L., and Milroy, R. (1982). "The deterioration of hearing with age: Frequency selectivity, the critical ratio, the audiogram, and speech threshold," *J. Acoust. Soc. Am.* **72**, 1788–1803.
- Pavlovic, C. V. (1987). "Derivation of primary parameters and procedures for use in speech intelligibility predictions," *J. Acoust. Soc. Am.* **82**, 413–422.
- Penner, M. J. (1974). "Effect of masker duration and masker level on forward and backward masking," *J. Acoust. Soc. Am.* **56**, 179–182.
- Plomp, R., and Mimpen, A. M. (1979). "Improving the reliability of testing the Speech Reception Threshold for sentences," *Audiology* **18**, 43–52.
- Rabinowitz, W. M., Lim, J. S., Braida, L. D., and Durlach, N. I. (1976). "Intensity perception. VI. Summary of recent data on deviations from Weber's law for 1000-Hz tone pulses," *J. Acoust. Soc. Am.* **59**, 1506–1509.
- Schroder, A. C., Viemeister, N. F., and Nelson, D. A. (1994). "Intensity discrimination in normal-hearing and hearing-impaired listeners," *J. Acoust. Soc. Am.* **96**, 2683–2693.
- Smooenburg, G. F. (1992). "Speech reception in quiet and in noisy conditions by individuals with noise-induced hearing loss in relation to their tone audiogram," *J. Acoust. Soc. Am.* **91**, 421–437.
- Turner, C. W., Zwislocki, J. J., and Filion, P. R. (1989). "Intensity discrimination determined with two paradigms in normal and hearing-impaired subjects," *J. Acoust. Soc. Am.* **86**, 109–115.
- Tyler, R. S. (1986). "Frequency resolution in hearing-impaired listeners," in *Frequency Selectivity in Hearing*, edited by B. C. J. Moore (Academic, London), pp. 309–371.
- Tyler, R. S., Summerfield, Q., Wood, E. J., and Fernandes, M. A. (1982). "Psychoacoustic and phonetic temporal processing in normal and hearing-impaired listeners," *J. Acoust. Soc. Am.* **72**, 740–752.
- van den Brink, W. A. C., and Houtgast, T. (1990a). "Efficient across-frequency integration in short-signal detection," *J. Acoust. Soc. Am.* **87**, 284–291.
- van den Brink, W. A. C., and Houtgast, T. (1990b). "Spectro-temporal integration in signal detection," *J. Acoust. Soc. Am.* **88**, 1703–1711.
- van Rooij, J. C. G. M., and Plomp, R. (1990). "Auditive and cognitive factors in speech perception by elderly listeners. II. Multivariate analyses," *J. Acoust. Soc. Am.* **88**, 2611–2624.
- van Schijndel, N. H., Houtgast, T., and Festen, J. M. (1999). "Intensity discrimination of Gaussian-windowed tones: Indications for the shape of the auditory frequency-time window," *J. Acoust. Soc. Am.* **105**, 3425–3435.
- Viemeister, V. F. (1972). "Intensity discrimination of pulsed sinusoids: The effects of filtered noise," *J. Acoust. Soc. Am.* **51**, 1265–1269.
- von Klitzing, R., and Kohlrausch, A. (1994). "Effect of masker level on overshoot in running- and frozen-noise maskers," *J. Acoust. Soc. Am.* **95**, 2192–2201.
- Weber, D. L., and Green, D. M. (1979). "Suppression effects in backward and forward masking," *J. Acoust. Soc. Am.* **65**, 1258–1267.
- Zwicker, E. (1963). "Über die Lautheit von ungedrosselten und gedrosselten Schallen," *Acustica* **13**, 194–211.

A numerical method to predict the effects of frequency-dependent attenuation and dispersion on speed of sound estimates in cancellous bone

Keith A. Wear^{a)}

U.S. Food and Drug Administration, Center for Devices and Radiological Health, HFZ-142,
12720 Twinbrook Parkway, Rockville, Maryland 20852

(Received 1 August 2000; accepted for publication 30 November 2000)

Many studies have demonstrated that time-domain speed-of-sound (SOS) measurements in calcaneus are predictive of osteoporotic fracture risk. However, there is a lack of standardization for this measurement. Consequently, different investigators using different measurement systems and analysis algorithms obtain disparate quantitative values for calcaneal SOS, impairing and often precluding meaningful comparison and/or pooling of measurements. A numerical method has been developed to model the effects of frequency-dependent attenuation and dispersion on transit-time-based SOS estimates. The numerical technique is based on a previously developed linear system analytic model for Gaussian pulses propagating through linearly attenuating, weakly dispersive media. The numerical approach is somewhat more general in that it can be used to predict the effects of arbitrary pulse shapes and dispersion relationships. The numerical technique, however, utilizes several additional assumptions (compared with the analytic model) which would be required for the practical task of correcting existing clinical databases. These include a single dispersion relationship for all calcaneus samples, a simple linear model relating phase velocity to broadband ultrasonic attenuation, and a constant calcaneal thickness. Measurements on a polycarbonate plate and 30 human calcaneus samples were in good quantitative agreement with numerical predictions. In addition, the numerical approach predicts that in cancellous bone, frequency-dependent attenuation tends to be a greater contributor to variations in transit-time-based SOS estimates than dispersion. This approach may be used to adjust previously acquired individual measurements so that SOS data recorded with different devices using different algorithms may be compared in a meaningful fashion. [DOI: 10.1121/1.1344161]

PACS numbers: 43.80.Cs, 43.80.Sh [FD]

I. INTRODUCTION

Speed of sound (SOS) in calcaneus has been demonstrated to be highly useful in the diagnosis of osteoporosis.¹⁻¹⁴ SOS measurements may be performed using two opposing coaxially aligned transducers for transmission and reception, as is done in many commercial bone sonometers. The transit time of ultrasound through a sample (e.g., calcaneus) is compared with the transit time through water. SOS may then be computed using a well-known formula which relates SOS in the sample with SOS in water, the sample thickness, and the difference in ultrasound transit times for the two measurements. In order to measure transit time, a reference point on the pulse waveform such as a zero crossing is designated. Frequency-dependent attenuation (attenuation varies approximately linearly with frequency in most tissues, including cancellous bone) and dispersion (frequency-dependent phase velocity), however, can distort waveforms, shift locations of zero crossings, and produce artifacts in SOS measurements. This is particularly troublesome for highly attenuating media such as bone.

Ambiguities in zero-crossing-based SOS measurements in cancellous bone were first reported by Laugier *et al.*¹⁵ and subsequently by Strelitzki and Evans,¹⁶ Nicholson *et al.*,¹⁷

and Wear.¹⁸ There is a considerable variety of choices for designated reference points in the literature including the leading edge (first detectable deviation from zero) of received ultrasonic pulse^{6,17,19,20} thresholding at 10% of the maximum value,¹⁷ thresholding at 3 times the noise standard deviation,²¹ first zero crossing,^{11,14,17} “specific” zero crossings,¹ first through fourth zero crossing, first and second maxima and minima,¹⁵ and zero crossing of the first negative slope.³ An unfortunate ramification of this lack of standardization is that different investigators using different transducers and analysis algorithms obtain disparate quantitative values for calcaneal SOS, impairing and often precluding meaningful comparison and/or pooling of measurements obtained from different studies.

A mathematical model was previously developed to quantitatively predict these variations for Gaussian pulses propagating through linearly attenuating, weakly dispersive media. Good agreement was shown between theoretically predicted variations and averages of experimental measurements on 24 human calcaneus samples *in vitro*.¹⁸ The aim of the present paper is to investigate the use of a numerical approach in order to model this phenomenon. This numerical technique can be used to compute corrections for previously acquired SOS data so that measurements acquired using different measurement systems and data analysis algorithms may be compared and perhaps pooled meaningfully. The nu-

^{a)}Electronic mail: kaw@cdrh.fda.gov

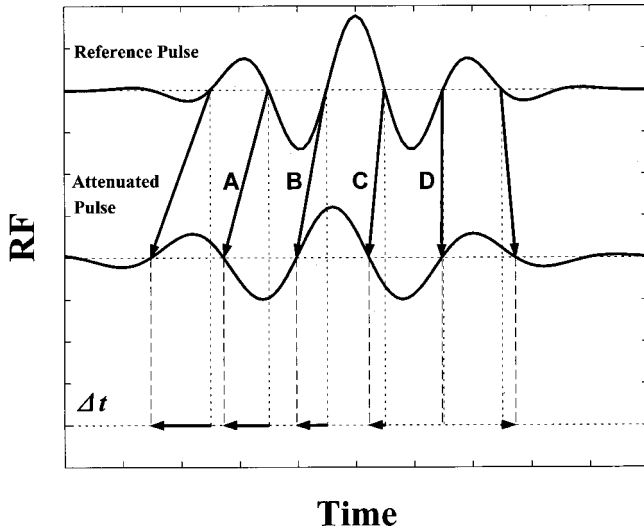


FIG. 1. Simulated waveform through water, $x(t)$ (upper), and through bone sample, $y(t)$ (lower). The four zero-crossing pair designations investigated are labeled as A, B, C, and D. The transit-time differential, Δt , (and therefore the SOS estimate) depends on which zero-crossing pair is utilized.

merical method requires several additional assumptions (see below), which were not required for the analytical model, in order to be practically useful for the task of correcting existing clinical databases. Validation experiments using measurements on a polycarbonate plate and 30 human calcaneus samples *in vitro* are described. The relative roles of frequency-dependent attenuation and dispersion in producing variations in SOS estimates are investigated.

II. THEORY

One common technique for measuring SOS in a sample (e.g., calcaneus) is as follows. Two opposing coaxially aligned broadband transducers are used: one transmitter and one receiver. Arrival times of received pulses are measured with and without the sample in the water path. SOS in a sample, c_s , is then computed from

$$c_s = \frac{c_w}{1 + \frac{c_w \Delta t}{d}}, \quad (1)$$

where d is the thickness of the sample, Δt is the difference in arrival times, and c_w is the SOS in water.

Figure 1 shows the effects of frequency-dependent attenuation and pulse reference point designation on transit time estimation. A hypothetical calibration (through water) waveform is shown in the top part of the figure. Below is the waveform corresponding to the measurement through a sample with faster SOS than water (hence, the earlier arrival time) and linear frequency-dependent attenuation (hence, the lower center frequency). The transit time differential, Δt , depends on which reference point pair is used.

In a previously developed model described in detail elsewhere¹⁸ and summarized here, the effects of attenuation and phase shifting due to differences in speeds of sound between water and sample are represented as a linear filtering process. The calibration signal through water is denoted by

$x(t)$. The impulse response of the linear filtering process is denoted by $h(t)$. The signal recorded with the sample in the water path is $y(t)$.

$$y(t) = h(t) * x(t). \quad (2)$$

The transfer function, the Fourier transform of $h(t)$, may be modeled as follows:

$$H(f) = e^{-\beta f d} e^{-i2\pi f \Delta t(f)}, \quad (3)$$

where f is frequency, β is the slope of the attenuation coefficient of the sample (sometimes referred to as normalized broadband ultrasonic attenuation or nBUA), d is the thickness of the sample, and $\Delta t(f)$ is the time delay (relative to a water calibration signal) at a given frequency due to a difference in SOS between the sample and calibration given by

$$\Delta t(f) = d \left[\frac{1}{c_s(f)} - \frac{1}{c_w} \right], \quad (4)$$

where c_w is the SOS in water (assumed to be nondispersive) and $c_s(f)$ is the frequency-dependent SOS in the dispersive medium.

The input or calibration signal, $x(t)$, may often be assumed to be a Gaussian-modulated sinusoid. The analytic signal representation is given by

$$x(t) = A e^{-t^2/2\sigma_t^2} e^{i2\pi f_0 t} e^{i\phi_0}, \quad (5)$$

where A is the amplitude, σ_t is a measure of the duration of the pulse, f_0 is the center frequency, and ϕ_0 is the initial phase.

Over a relatively narrow range of frequencies of interrogation, dispersion may be assumed to be approximately linear. This is consistent with published investigations.^{16,17,22,23}

$$c_s(f) = c_s(f_0) + b_s(f - f_0), \quad (6)$$

where $c_s(f_0)$ is the phase velocity at the center frequency and b_s is the rate of change of phase velocity with frequency.

III. NUMERICAL METHOD

Equations (1)–(6) were incorporated into a program using MATLAB (The Mathworks, Inc., Natick, MA). The program computed SOS estimates as functions of attenuation coefficient, β (nBUA), for several different zero-crossing designations on the pulse waveform. The input signal, $x(t)$, was characterized using Eq. (5) by $f_0 = 500$ kHz (typical for clinical bone sonometers), $\sigma_t = 1.1 \mu\text{s}$, and $\phi_0 = 0$. [Note that, unlike the analytical model, the numerical method did not require a Gaussian function. Any numerical representation of $x(t)$, including an digitized measurement, could have been used.] A fast Fourier transform (FFT) was computed to obtain $X(f)$.

In order to compute $Y(f) = H(f)X(f)$, it was necessary to assume values for β , d , and $\Delta t(f)$. Since the FFT corresponding to any real signal contains negative as well as positive frequency components, the attenuation transfer function had to be modified from $e^{-\beta f d}$ to $e^{-\beta|f|d}$. The program was written in the form of a loop with β ranging from 0 to 30 dB/cmMHz (typical range for human calcaneus) in steps of 1

dB/cmMHz. Sample thickness (d) was taken to be 18 mm (the average thickness for 30 calcaneus samples described below). The frequency-dependent time delay $\Delta t(f)$ is a function of the SOS in water, c_w , and the frequency-dependent phase velocity, $c_s(f) = c_s(f_0) + b(|f| - f_0)$, in the sample. Phase velocity at 500 kHz, $c_s(f_0)$, for a given sample was taken to be a function of attenuation coefficient, β . This relationship was obtained from a linear regression of experimental measurements of $c_s(f_0)$ vs β . Dispersion was characterized by $b = -26.25$ m/sMHz (the average of four values found in the literature^{16,17,22,23}). The reason for this negative dispersion is currently not well understood.²³ Note that the assumption of weak linear dispersion, which was required in the original analytical model,¹⁸ is not required for the numerical technique. Any functional form or experimental data could have been used in the numerical approach to describe dispersion. The numerical method was repeated for $b=0$ in order to investigate the importance of dispersion. The digitization rate was 320 MHz.

With the assumptions listed above, a numerical version for the transfer function, $H(f)$, could be computed. The simulated received time-domain signal, $y(t)$, was obtained from the inverse Fourier transform of the product of $H(f)$ and $X(f)$. Four SOS computations were performed for each water/sample simulated pulse waveform pair. The four computations were derived from four zero-crossing reference point pairs (A, B, C, and D) illustrated in Fig. 1.

IV. EXPERIMENT

A. Calcaneus samples

Thirty excised human calcaneus samples (genders and ages unknown) were defatted using a trichloro-ethylene solution. Since nBUA and SOS of defatted cancellous bone have been found to be only slightly different from their counterparts obtained with marrow left intact,^{19,21,24} it was assumed that defatting would not substantially affect ultrasonic measurements.

In order to isolate the effects of cancellous bone, the lateral cortical layers were sliced off leaving two parallel surfaces. This produced samples with well-defined uniform thicknesses (d) which facilitated application of the mathematical model. The thicknesses of the samples were measured using calipers and varied from 12 to 21 mm. Prior to ultrasonic interrogation, samples were vacuum degassed underwater in a desiccator. Subsequently, samples were allowed to thermally equilibrate to room temperature. Ultrasonic measurements were performed in distilled water at room temperature. The relative orientation between the ultrasound beam and the calcaneus samples was the same as with *in vivo* measurements performed with commercial bone sonometers, in which sound propagates in the mediolateral direction.

B. Ultrasound measurements

Samples were interrogated in a water tank using a Panametrics (Waltham, MA) 5800 pulser/receiver and Panametrics V301 1-in. diameter, focused (focal length=1.5 in.), broadband transducers with center frequencies of 500 kHz. A

wideband electrical excitation was applied to the transmitter. Samples were placed in the focal plane. Received signals were digitized (8 bit, 10 MHz) using a LeCroy (Chestnut Ridge, NY) 9310C Dual 400-MHz oscilloscope and stored on computer [via general purpose interface bus (GPIB)] for off-line analysis.

The through-transmission method described above was used to measure nBUA and SOS. Using two oppositely aligned transducers (one transmitter and one receiver) separated by twice the focal distance, transmitted signals were recorded both with and without the bone sample (or polycarbonate plate) in the acoustic path. The samples were larger in cross-sectional area than the receiving transducer aperture. Four to eight transmitted signals were recorded for each bone sample. The sample was translated slightly between successive measurements so that a spatial average could be obtained. Attenuation coefficient was then estimated using a log spectral difference technique.²⁵ Attenuation was characterized by the slope of a least-squares linear fit of attenuation coefficient (dB/cm) vs frequency, resulting in the normalized broadband ultrasonic attenuation²⁴ (nBUA). Since the SOS in calcaneus, approximately 1475–1650 m/s,²³ is comparable to that in distilled water at room temperature,²⁶ potential diffraction-related errors^{27–29} in this substitution technique may be ignored.²³

To measure SOS, arrival times of received broadband pulses were measured with and without the sample in the water path. Four reference point designations were used. They corresponded to the two zero crossings immediately prior and immediately following the envelope maximum (see Fig. 1—A, B, C, and D). Velocity, c_s , was computed from Eq. (1) for each of the four designations. All velocity estimates were expressed as deviations from the group velocity (velocity of the maximum of the pulse envelope). Since the variability among different bone samples tends to be much greater than the variability of repeated measurements on the same sample, only one SOS measurement for each set of four to eight recorded transmitted signals from each sample was generated. For the polycarbonate sample, six SOS measurements (each obtained from eight separate recorded transmitted signals) were performed in order to generate error bars.

Independent measurements of frequency-dependent phase velocity were performed on the calcaneus using a previously reported technique²² in order to obtain an empirical (assumed to be linear) relationship between phase velocity at 500 kHz and nBUA. This relationship was required for the numerical approach. Phase velocity measurements were also performed on the polycarbonate plate in order to obtain estimates of parameters required for the corresponding numerical technique ($c_s = 2190$ m/s, $b_s = 48$ m/sMHz). The thickness of the plate was 25.8 mm.

V. RESULTS

Figure 2 shows numerical predictions and experimental measurements for SOS in the polycarbonate plate for the four zero-crossing reference points (A, B, C, and D) utilized. Good agreement between numerical technique and experiment may be seen. Linear fits to numerical predictions and

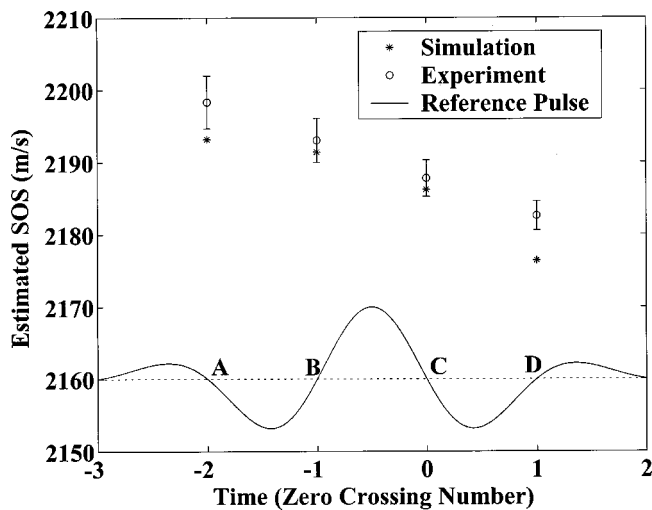


FIG. 2. Numerical and experimental results for the polycarbonate plate. Speed-of-sound (SOS) values predicted by numerical analysis are denoted by asterisks. Measurements are denoted by circles. Error bars denote standard deviations of measurements. Measurements and numerical predictions were obtained for zero crossings denoted by A, B, C, and D (see Fig. 1). The simulated calibration pulse waveform is also shown in order to clarify the relationship between the time axis and zero crossings of interest.

experimental measurements were given by SOS estimate = 2186.8 m/s – 11.1 m/s*cycle (numerical) and SOS estimate = 2190.4 m/s – 10.5 m/s*cycle (experimental) where “cycle” refers to the number of cycles (wavelengths) between the reference point location and the pulse envelope maximum. The average discrepancy between these two linear fits over the range of reference point locations considered is 3.6 m/s (0.16%). Diffraction errors may partially account for the disparity between the two.

Figure 3 shows experimental measurements of $c_s(f_0)$ vs β . The linear regression for this data is given by $c_s(f_0) = 1474.9 + 4.46\beta$ m/s (where c_s is measured in m/s and $\beta = \text{nBUA}$ is measured in dB/cmMHz). This regression formula was used in the numerical method. Typically, commercial sonometers record broadband ultrasonic attenuation,

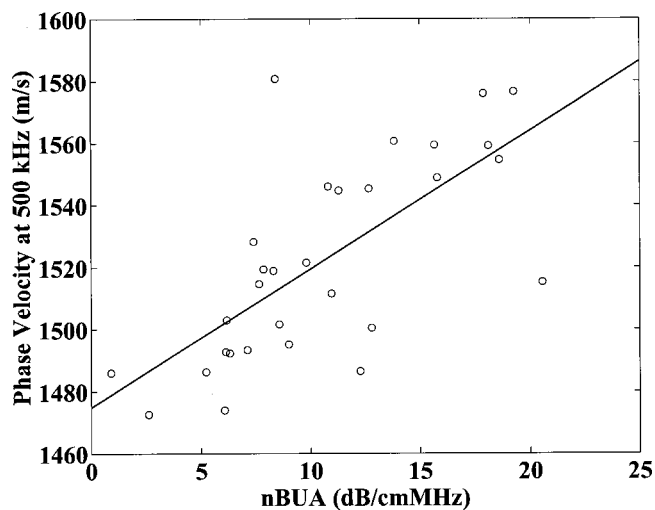


FIG. 3. Linear regression of experimental measurements of phase velocity at 500 kHz, $c_s(f_0)$, vs attenuation slope (normalized broadband ultrasonic attenuation or nBUA), β in 30 human calcaneus samples *in vitro*.

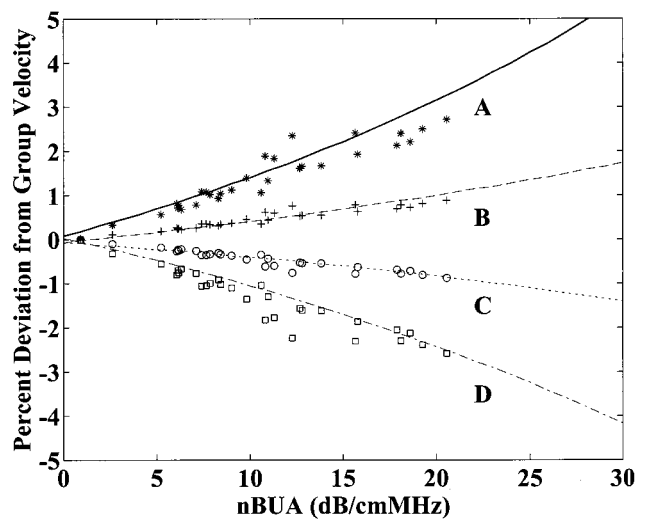


FIG. 4. Percent deviation from group velocity. Measurements for four reference point designations (A, B, C, and D; see Fig. 1). Experimental data points were generated for reference point A (asterisks), B (plus signs), C (circles), and D (squares). Predictions based on the numerical technique were also generated for reference point A (solid line), B (dashed line), C (dotted line), and D (chain dotted line). The independent variable is normalized broadband ultrasonic attenuation (also known as attenuation slope).

BUA, which is measured in dB/MHz, rather than the normalized version, $\text{nBUA} = \beta = \text{BUA}/d$. For these data, one could use an average value for d to convert BUA to nBUA.

Figure 4 shows simulated and experimental deviations from group velocity for estimates for the four zero-crossing designations. There is good agreement between theory and experiment. The average magnitude of the error between simulation and experiment was 0.15%. As reported previously by others, zero-crossing designations on the leading side of the pulse result in estimates which exceed the true group velocity while those on the trailing side result in estimates which are less than the true group velocity.

Figure 5 compares numerical computations which assume no dispersion ($b=0$, solid lines) with numerical computations which incorporate frequency-dependent attenuation and dispersion ($b = -26.25$, dashed lines). It can be seen that frequency-dependent attenuation is the factor most responsible for the disparities in SOS estimates.

VI. DISCUSSION

The effects of frequency-dependent attenuation, dispersion, and pulse reference point location on SOS measurements in a polycarbonate plate and in calcaneus have been shown to be accurately modeled using a numerical method based on a linear system theory approach. Quantitative prediction has been provided for the empirical qualitative observation made by others that magnitudes of transit-time-based SOS estimates steadily decrease as the reference point designation is moved from the leading edge to the trailing edge of the pulse waveform. Frequency-dependent attenuation is the primary source of reported variations in SOS estimates based on different reference point locations. Dispersion has a smaller effect and serves to exacerbate variations somewhat for reference points on the leading half of the pulse wave-

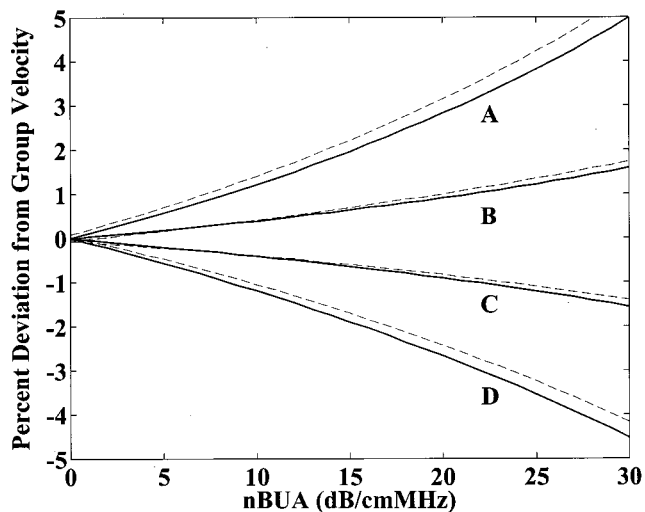


FIG. 5. Percent deviation from group velocity. Measurements for the four reference point designations. Models excluding (solid lines, $b=0$) and including (dashed lines, $b=-26.25$) dispersion are shown. The independent variable is normalized broadband ultrasonic attenuation (also known as attenuation slope).

form while mitigating them somewhat for reference points on the trailing half. Although the experimental validation provided here is limited to purely cancellous bone *in vitro*, it is likely these conclusions are relevant to *in vivo* applications.

The numerical model is in some respects more flexible than the analytical model previously described.¹⁸ In particular, assumptions of (1) Gaussian pulse shape; (2) linear dispersion; and (3) weak dispersion were required in the analytical model. These approximations were unnecessary for the numerical technique. For example, a digitized calibration pulse waveform could be measured and then used in the numerical method. Likewise, an average (not necessarily linear and not necessarily weak) frequency-dependent phase velocity could be measured and utilized in the numerical approach. In both cases, there is no need to assume a particular functional form. Moreover, in many cases the numerical approach may be far easier to implement than the analytical model which is fairly cumbersome, especially if the effects of dispersion are included.

Variations of measured velocity from one zero crossing to the next for a calcaneus with a nBUA of 20 dB/cmMHz can be on the order of 2% (30 m/s). (See Fig. 4.) This is considerable as subtle variations in SOS can convey important diagnostic information. For example, in the EPIDOS prospective study of over 5000 women,⁷ baseline SOS measurements were 1480 ± 24 m/s (mean \pm standard deviation) for subjects who experienced a hip fracture over a subsequent 2-year period compared with 1493 ± 24 m/s for subjects who did not. The difference, 13 m/s, is smaller than the differences that can occur due to different reference point designations. Thus, it would be inappropriate to compare or pool these data with data from other studies obtained using different transducers and different data analysis algorithms unless the resulting variations in SOS estimates were properly corrected.

In contrast to the analytical model,¹⁸ the numerical approach implemented here was based on assumptions of (1) a single dispersion relationship (phase velocity vs frequency) for all calcaneus samples; (2) a simple linear model relating phase velocity at 500 kHz to nBUA; and (3) an average calcaneal thickness for all samples. In reality, dispersion rates vary considerably among different samples;^{22,23} there is a lot of scatter about the average trend of the relationship between phase velocity at 500 kHz and nBUA (see Fig. 3), and there can be considerable variation in calcaneal thicknesses. While utilization of individual (rather than average) measurements of these parameters in the numerical technique would be expected to improve the level of agreement between numerical method and experiment, this detailed information on individual samples will not generally be available for previously acquired clinical databases. Therefore, these simplifying assumptions will generally be required for retroactively correcting existing data. Nevertheless, the numerical technique performs rather well.

It has previously been demonstrated that an analytical model performs well in predicting *average* variations in SOS estimates due to reference point location variations, frequency-dependent attenuation, and dispersion.¹⁸ Figure 4 shows that the numerical approach predicted these variations well for *individual* bone measurements, even though the numerical approach was based on several additional simplifying assumptions. In addition, the basic linear system approach has been shown in the current paper to be valid in another medium (polycarbonate) with considerably different acoustic properties than cancellous bone (much lower attenuation and positive rather than negative dispersion).

This result indicates promise for using this approach to adjust previously acquired individual measurements so that SOS data recorded with different devices using different algorithms may be compared in a meaningful fashion. In order to implement this technique, investigators would require the following information from manufacturers: (1) Sufficient information to reconstruct $x(t)$ [Eq. (5)]. This could be in the form of a digitized pulse waveform or a set of parameters specifying an analytic approximation (e.g., f_0, σ, ϕ_0 for a Gaussian pulse). (2) The designated reference point location for transit time measurement. In addition, investigators would have to assume a relationship between the midband phase velocity and BUA (see Sec. V) and a value for the dispersion rate (e.g., $b = -26.25$ m/sMHz, see Sec. III).

ACKNOWLEDGMENTS

The author is grateful for funding provided by the US Food and Drug Administration Office of Women's Health.

¹P. Rossman, J. Zagzebski, C. Mesina, J. Sorenson, and R. Mazess, "Comparison of speed of sound and ultrasound attenuation in the os calcis to bone density of the radius, femur and lumbar spine," *Clin. Phys. Physiol. Meas.* **10**, 353-360 (1989).

²M. B. Tavakoli and J. A. Evans, "Dependence of the velocity and attenuation of ultrasound in bone on the mineral content," *Phys. Med. Biol.* **36**, 1529-1537 (1991).

³J. A. Zagzebski, P. J. Rossman, C. Mesina, R. B. Mazess, and E. L. Madsen, "Ultrasound transmission measurements through the os calcis," *Calcif. Tissue Int.* **49**, 107-111 (1991).

⁴A. M. Schott, S. Weill-Engerer, D. Hans, F. Duboeuf, P. D. Delmas, and

- P. J. Meunier, "Ultrasound discriminates patients with hip fracture equally well as dual energy x-ray absorptiometry and independently of bone mineral density," *J. Bone Min. Res.* **10**, 243–249 (1995).
- ⁵C. H. Turner, M. Peacock, L. Timmerman, J. M. Neal, and C. C. Johnston, Jr., "Calcaneal ultrasonic measurements discriminate hip fracture independently of bone mass," *Osteoporosis Int.* **5**, 130–135 (1995).
- ⁶C. F. Njeh, R. Hodgskinson, J. D. Currey, and C. M. Langton, "Orthogonal relationships between ultrasonic velocity and material properties of bovine cancellous bone," *Med. Eng. Phys.* **18**, 373–381 (1996).
- ⁷D. Hans, P. Dargent-Molina, A. M. Schott, J. L. Sebert, C. Cormier, P. O. Kotzki, P. D. Delmas, J. M. Pouilles, G. Breart, and P. J. Meunier, "Ultrasonographic heel measurements to predict hip fracture in elderly women: The EPIDOS prospective study," *Lancet* **348**, 511–514 (1996).
- ⁸C. C. Glüer, S. R. Cummings, D. C. Bauer, K. Stone, A. Pressman, A. Mathur, and H. K. Genant, "Osteoporosis: Association of recent fractures with quantitative US findings," *Radiology* **199**, 725–732 (1996).
- ⁹M. L. Bouxsein and S. E. Radloff, "Quantitative ultrasound of the calcaneus reflects the mechanical properties of calcaneal trabecular bone," *J. Bone Min. Res.* **12**, 839–846 (1997).
- ¹⁰D. C. Bauer, C. C. Gluer, J. A. Cauley, T. M. Vogt, K. E. Ensrud, H. K. Genant, and D. M. Black, "Broadband ultrasound attenuation predicts fractures strongly and independently of densitometry in older women," *Arch. Intern. Med.* **157**, 629–634 (1997).
- ¹¹P. H. F. Nicholson, R. Muller, G. Lowet, X. G. Cheng, T. Hildebrand, P. Rueggsegger, G. Van Der Perre, J. Dequeker, and S. Boonen, "Do quantitative ultrasound measurements reflect structure independently of density in human vertebral cancellous bone?" *Bone (N.Y.)* **23**, 425–431 (1998).
- ¹²P. Thompson, J. Taylor, A. Fisher, and R. Oliver, "Quantitative heel ultrasound in 3180 women between 45 and 75 years of age: compliance, normal ranges and relationship to fracture history," *Osteoporosis Int.* **8**, 211–214 (1998).
- ¹³D. Hans, C. Wu, C. F. Njeh, S. Zhao, P. Augat, D. Newitt, T. Link, Y. Lu, S. Majumdar, and H. K. Genant, "Ultrasound velocity of cancellous cubes reflects mainly bone density and elasticity," *Calcif. Tissue Int.* **64**, 18–23 (1999).
- ¹⁴H. Trebacz and A. Natali, "Ultrasound velocity and attenuation in cancellous bone samples from lumbar vertebra and calcaneus," *Osteoporosis Int.* **9**, 99–105 (1999).
- ¹⁵P. Laugier, P. Giat, P. P. Droin, A. Saied, and G. Berger, "Ultrasound images of the os calcis: A new method of assessment of bone status," *Proceedings of the IEEE Ultrasonics Symposium*, Sponsor: Ultrasonics Ferroelectric & Frequency Control Soc., 31 Oct.–3 Nov. 1993, Baltimore, MD, edited by M. Levy and B. R. McAvoy (IEEE, New York, 1993), Vol. 2, pp. 989–992.
- ¹⁶R. Strelitzki and J. A. Evans, "On the measurement of the velocity of ultrasound in the os calcis using short pulses," *Eur. J. Ultrasound* **4**, 205–213 (1996).
- ¹⁷P. H. F. Nicholson, C. G. Lowet, C. M. Langton, J. Dequeker, and G. Van der Perre, "Comparison of time-domain and frequency-domain approaches to ultrasonic velocity measurements in cancellous bone," *Phys. Med. Biol.* **41**, 2421–2435 (1996).
- ¹⁸K. A. Wear, "The effects of frequency-dependent attenuation and dispersion on sound speed measurements: Applications in human trabecular bone," *IEEE Trans. Ultrason. Ferroelectr. Freq. Control* **47**, 265–273 (2000).
- ¹⁹C. F. Njeh and C. M. Langton, "The effect of cortical endplates on ultrasound velocity through the calcaneus: an in vitro study," *Br. J. Radiol.* **70**, 504–510 (1997).
- ²⁰C. F. Njeh, C. W. Kuo, C. M. Langton, H. I. Atrah, and C. M. Boivin, "Prediction of human femoral bone strength using ultrasound velocity and BMD: An in vitro study," *Osteoporosis Int.* **7**, 471–477 (1997).
- ²¹J. M. Alves, W. Xu, D. Lin, R. S. Siffert, J. T. Ryaby, and J. J. Kaufmann, "Ultrasonic assessment of human and bovine cancellous bone: A comparison study," *IEEE Trans. Biomed. Eng.* **43**, 249–258 (1996).
- ²²K. A. Wear, "Measurements of phase velocity and group velocity in human calcaneus," *Ultrasound Med. Biol.* **26**, 641–646 (2000).
- ²³P. Droin, G. Berger, and P. Laugier, "Velocity dispersion of acoustic waves in cancellous bone," *IEEE Trans. Ultrason. Ferroelectr. Freq. Control* **45**, 581–592 (1998).
- ²⁴C. M. Langton, C. F. Njeh, R. Hodgskinson, and J. D. Currey, "Prediction of mechanical properties of the human calcaneus by broadband ultrasonic attenuation," *Bone (N.Y.)* **18**, 495–503 (1996).
- ²⁵R. Kuc and M. Schwartz, "Estimating the acoustic attenuation coefficient slope for liver from reflected ultrasound signals," *IEEE Trans. Sonics Ultrason.* **SU-26**, 353–362 (1979).
- ²⁶D. Pierce, *Acoustics, An Introduction to Its Physical Principles and Applications* (McGraw-Hill, New York, 1981), p. 31.
- ²⁷W. A. Verhoef, M. J. T. M. Cloostermans, and J. M. Thijssen, "Diffraction and dispersion effects on the estimation of ultrasound attenuation and velocity in biological tissues," *IEEE Trans. Biomed. Eng.* **BME-32**, 521–529 (1985).
- ²⁸J. J. Kaufman, W. Xu, A. E. Chiabrera, and R. S. Siffert, "Diffraction effects in insertion mode estimation of ultrasonic group velocity," *IEEE Trans. Ultrason. Ferroelectr. Freq. Control* **42**, 232–242 (1995).
- ²⁹W. Xu and J. J. Kaufman, "Diffraction correction methods for insertion ultrasound attenuation estimation," *IEEE Trans. Biomed. Eng.* **40**, 563–570 (1993).

Acoustic nonlinearity parameter tomography for biological tissues via parametric array from a circular piston source—Theoretical analysis and computer simulations

Dong Zhang, Xi Chen, and Xiu-fen Gong^{a)}

State Key Lab of Modern Acoustics, Institute of Acoustics, Nanjing University, Nanjing 210093, China

(Received 22 December 1999; accepted for publication 16 October 2000)

The acoustic nonlinearity parameter B/A describes the nonlinear features of a medium and may become a novel parameter for ultrasonic tissue characterization. This paper presents a theoretical analysis for acoustic nonlinear parameter tomography via a parametric array. As two primary waves of different frequencies are radiated simultaneously from a circular piston source, a secondary wave at the difference frequency is generated due to the nonlinear interaction of the primary waves. The axial and radial distributions of sound pressure amplitude for the generated difference frequency wave in the near field are calculated by a superposition of Gaussian beams. The calculated results indicated that the difference frequency component of the parametric array grows linearly with distance from the piston source. It therefore provides a better source to do the acoustic nonlinearity parameter tomography because the fundamental and second harmonic signals both have a near field that goes through many oscillations due to diffraction. By using a finite-amplitude insert substitution method and a filtered convolution algorithm, a computer simulation for B/A tomography from the calculated sound pressure of the difference frequency wave is studied. For biological tissues, the sound attenuation is considered and compensated in the image reconstruction. Nonlinear parameter computed tomography (CT) images for several biological sample models are obtained with quite good quality in this study. © 2001 Acoustical Society of America. [DOI: 10.1121/1.1344160]

PACS numbers: 43.80.Cs, 43.80.Ev [WA]

I. INTRODUCTION

In clinical ultrasound diagnosis, ultrasound imaging has become a very successful modality due to its ability to provide noninvasive, real-time cross-sectional images of soft-tissue structures and blood flow without ionizing radiation. However, ultrasound identification of healthy tissues from the diseased ones is sometimes difficult. This may be due to the fact that even when tissues are pathologically different, their ultrasonic properties, such as sound velocity, attenuation, and acoustic impedance, may still be quite similar. For enhancement of the discrimination and evaluation of healthy and diseased tissues, much attention has been directed to the acoustic nonlinearity parameter B/A in the field of ultrasonic biomedicine.^{1,2}

The acoustic nonlinearity parameter B/A is an important parameter in nonlinear acoustics, which is defined as the ratio of the coefficients of the quadratic term to the linear term in the Taylor expansion of the state equation: $B/A = 2\rho_0 c_0 (\partial c / \partial p)_{o,s}$,³ where ρ_0 and c_0 are the density and velocity of the medium, p is the static pressure, and s is the entropy. Many reports have indicated that compared with linear ultrasonic parameters the acoustic nonlinearity parameter B/A could provide more information on the state of the tissues.^{4,5} Therefore, B/A becomes a novel parameter for biological tissue characterization.

The acoustic nonlinearity parameter imaging has been studied by using the phase-shift and finite-amplitude methods.⁶⁻⁹ In our laboratory, a method based on second

harmonic wave detection to image the acoustic nonlinearity parameter was proposed by using the insert-substitution method and the principle of computed tomography (CT), experimental results for several normal and pathological biological tissues were obtained successfully.^{10,11}

All these studies have been based on the assumption that the transmitted sound waves from a circular piston source are exactly plane waves, taking no account of diffraction and diffusion effects. However, the sound field of a circular piston source is complicated, especially in the near field.¹²⁻¹⁴ Our previous study indicated that the obvious fluctuation of the axial sound pressure of the second harmonics near the surface of the transmitter would increase the error of reconstruction in acoustic nonlinearity parameter imaging.¹⁵ On the other hand, Cai¹⁶ and Burov¹⁷ reported the acoustic nonlinearity parameter tomography using the diffraction effect. Although the diffraction tomography offers higher resolution compared with line-of-sight tomography, it is more difficult to carry out.

Since Westervelt¹⁸ first published the theory of the parametric array in 1963, many studies have been done in this field. The significant property of the parametric array is that it produces a much narrower beam at a relative low frequency, which can be used to obtain high resolution in acoustical imaging. Besides, the parametric field is influenced less by the edge diffraction, due to the fact that the parametric array is generated from the nonlinear interaction of two primary waves.

In this paper, the parametric sound field from a circular piston source is calculated by a superposition of Gaussian beams.¹⁹ The theoretical analysis shows that the axial sound

^{a)}Electronic mail: zligong@nju.edu.cn

pressure amplitude of the difference frequency wave in the near field is nearly proportional to the distance from the transmitter; therefore, the acoustic nonlinearity parameter tomography via the parametric array can be obtained by the conventional CT method. By using the theory of finite amplitude wave propagation, the calculated pressure amplitude of the difference frequency sound wave can be regarded as the projection data in the CT technique and the image of the acoustic nonlinearity parameter can be reconstructed by using a filtered convolution algorithm. Computer simulations of the acoustic nonlinearity parameter B/A for three sample models including some fluids and biological tissues are presented.

II. THEORY

A. The generation of a difference frequency wave

It is well-known that for a finite amplitude wave in a lossless medium, the nondimensional form of Burgers' equation can be used to describe the nonlinear propagation as follows:

$$\frac{\partial W}{\partial \sigma} - W \frac{\partial W}{\partial y} = 0, \quad (1)$$

where $W = u/u_0$, u , and u_0 are the instantaneous and peak values of particle velocity, $\sigma = \beta k u_0 x / c_0$, $k = \omega / c_0$, c_0 is the sound speed, $\beta = 1 + B/2A$ and B/A is the acoustic nonlinearity parameter, $y = \omega \tau$, $\tau = t - x/c_0$.

When two primary waves with angular frequencies ω_1 and ω_2 are radiated simultaneously from a transmitter, signals at the sum and difference frequencies will be generated due to the nonlinear interaction between the two waves. Under the boundary condition $x=0$

$$u(0, t) = u_1 \sin(\omega_1 t + \phi_1) + u_2 \sin(\omega_2 t + \phi_2). \quad (2)$$

Fenlon²⁰ gave an exact solution to Burgers' equation in a series form for a lossless medium. In the case of $p_1(0) \gg p_2(0)$ and $\omega_2 > \omega_1$, the sound pressure amplitude of sum and difference frequency signals can be written as

$$p_{\omega_1 \pm \omega_2}(x) = \frac{2p_2(0)}{\sigma \pm \varepsilon \sigma_1} J_1(\sigma_2 \pm \varepsilon \sigma_1) J_1[(\mu + 1)\sigma_1], \quad (3)$$

where $\sigma_i = \beta u_i k_i x / c_0$ ($i=1,2$), $\mu = \omega_2 / \omega_1$, $\varepsilon = u_2 / u_1$, J_1 is the Bessel function of first order, u_1 , u_2 , and $p_1(0)$, $p_2(0)$ are the peak values of particle velocities and pressure amplitude of two primary waves, respectively. When $\sigma_2 \ll 1$ and $\varepsilon \ll 1$, Eq. (3) can be simplified and the pressure amplitude for the difference frequency signal at a distance x can be expressed by

$$p_d(x) = \frac{\omega_d p_1(0) p_2(0)}{2\rho_0 c_0^3} \beta x, \quad (4)$$

where subscript 'd' denotes the difference frequency signal and $\omega_d = \omega_2 - \omega_1$.

Considering the inhomogeneity and sound attenuation of the medium, the sound pressure amplitude of the difference frequency signal after propagating a distance L can be written after modifying Eq. (4) as⁹

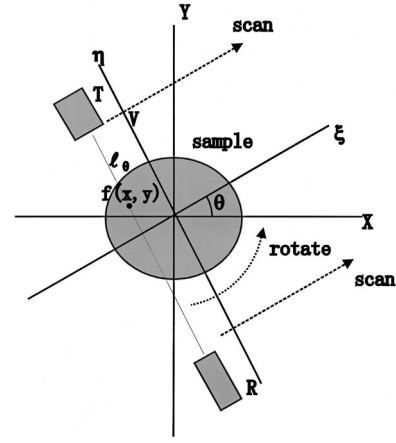


FIG. 1. The conventional computer tomography (CT) scanning system.

$$p_d(L) = \frac{\omega_d}{2} p_1(0) p_2(0) \int_0^L \beta_i(x) \times \exp \left\{ - \int_0^x [\alpha_1(l) + \alpha_2(l)] dl - \int_x^L \alpha_d(l) dl \right\} dx, \quad (5)$$

where α_1 , α_2 , and α_d are the sound attenuation coefficients of the medium at frequency ω_1 , ω_2 , and ω_d , $\beta_i(x) = \beta(x) / [\rho(x) c^3(x)]$, and l is a dummy variable.

B. Acoustic nonlinearity parameter tomography by insert substitution method

In this paper, the finite amplitude insert substitution method is utilized to image the acoustic nonlinearity parameter B/A .²¹ The sound pressures for the difference frequency wave in distilled water at a distance L before and after inserting the sample are expressed as $p_{d0}(L)$ and $p_{dx}(L)$, respectively. From Eq. (5), the ratio of $p_{dx}(L)$ to $p_{d0}(L)$ can be obtained as

$$p = \frac{p_{dx}(L)}{p_{d0}(L)} = \frac{1}{\beta_{i0} L} \int_0^L \beta_i(x) \times \exp \left\{ - \int_0^x [\alpha_1(l) + \alpha_2(l)] dl - \int_x^L \alpha_d(l) dl \right\} dx, \quad (6)$$

where β_{i0} is the value of β_i in distilled water. From Eq. (6), the two-dimensional acoustic nonlinearity parameter imaging can be reconstructed from the projection data p by the CT method.

Figure 1 shows a conventional CT scanning system. The sample rotates from 0° to 180° at a equal interval angle $\Delta\theta = \pi/K$ (K is the number of rotating steps), and at each angle $\theta_j = j \times \pi/K$ ($j=0,1,\dots,K-1$) the transmitter as well as receiver sweep step by step synchronously along one fixed direction (ξ axis). Assuming that the linear scan space is $\Delta\xi = S/N$ (S , N are the distance and step numbers of linear scan, respectively), the projection data are sampled at ξ_i

$=i \times \Delta \xi$ ($i = -N/2, -N/2+1, \dots, 0, 1, \dots, N/2$). Thus, a $K \times (N+1)$ projection data matrix will be obtained for each sample.

Theoretically, the two-dimensional projection data $p(\xi_i, \theta_j)$ can be expressed as

$$p(\xi_i, \theta_j) = \frac{1}{\beta_{i0}L} \int_L [\beta_i(x,y) - \beta_{i0}] \exp \left\{ - \int_{l_\theta} [\alpha_1(x,y) + \alpha_2(x,y)] dl' - \int_{L-l_\theta} \alpha_d(x,y) dl' \right\} dl = \frac{1}{\beta_{i0}L} \int_{-v}^v \beta_i^*(x,y) dv. \quad (7)$$

Due to the nonzero value of β_i in the surrounding homogeneous medium (distilled water), the detected signal of difference frequency component has contributions from both the reconstructed zone and the surrounding distilled water. Therefore, the reconstructed function $\beta_i(x,y)$ in Eq. (6) is replaced with $[\beta_i(x,y) - \beta_{i0}]$ in Eq. (7) to eliminate the effect of the distilled water. In Eq. (7), $\beta_i^*(x,y) = [\beta_i(x,y) - \beta_{i0}(x,y)]C(x,y)$, the η axis is perpendicular to ξ axis, and $V = L/2$. $C(x,y)$ is an attenuation matrix²² used for compensation of the sound attenuation, and it is defined as

$$C(x,y) = \frac{1}{2\pi} \int_0^{2\pi} \exp \left\{ - \int_{l_\theta} [\alpha_1(x,y) + \alpha_2(x,y)] dl - \int_{L-l_\theta} \alpha_d(x,y) dl \right\} d\theta. \quad (8)$$

Here, $\alpha_1(x,y)$ and $\alpha_2(x,y)$ can be reconstructed via conventional computed tomography, if the sound pressure amplitudes of two primary waves are also detected.

In Eq. (7), $p(\xi_i, \theta_j)$ is a line integral of $\beta_i^*(x,y)$ along the propagation path of the ultrasonic wave. Therefore, $\beta_i^*(x,y)$ image can be reconstructed by using the filtered convolution method. The overall steps of this method are as follows: First, convolve the projection data $p(\xi_i, \theta_j)$ with an $|\omega|$ function

$$g(\xi_i, \theta_j) = p(\xi_i, \theta_j) \times W_m(\xi_i) \times \Delta \xi. \quad (9)$$

Here, $W_m(\xi_i)$ is the frequency response of $|\omega|$ function. The $|\omega|$ function proposed by Shepp–Logan²³ is used in this paper. Second, use the back projection method to reconstruct $\beta_i^*(x,y)$

$$\beta_i^*(x,y) = \frac{\beta_{i0}L}{2K} \sum_{i=0}^{K-1} g(\xi_i, \theta_j). \quad (10)$$

After the image of $\beta_i^*(x,y)$ is reconstructed, the image of $[\beta_i(x,y) - \beta_{i0}]$ can be derived from dividing $\beta_i^*(x,y)$ by the attenuation matrix $C(x,y)$. After the correction of β_{i0} , the acoustic nonlinearity parameter B/A tomography can finally be obtained from $\beta_i(x,y)$.

If the sample's attenuation distribution is inhomogeneous, where the projection datum $p(\xi, \theta)$ does not equal to $p(-\xi, \theta + \pi)$, averaged projection is used and defined as

$$p_{\text{avg}}(\xi, \theta) = \frac{p(\xi, \theta) + p(-\xi, \theta + \pi)}{2}. \quad (11)$$

C. Calculation of the parametric field generated from a circular piston source using superposition of Gaussian beams

Equation (7) shows that the sound pressure amplitude of the difference frequency wave is a linear integral of the acoustic nonlinearity parameter B/A , so B/A can be reconstructed by a conventional CT method. The above discussions are under the assumption that the primary waves are planar waves. However, the acoustic beam from a transducer with finite size is always affected by edge diffraction.

For a circular piston transducer of radius a vibrating at angular frequency ω , the fundamental sound pressure at distance z from the transducer can be expressed in cylindrical coordinates as $p_1(r,z) \exp[-i(\omega t - kz)]$, with the assumption that $ka \gg 1$, where $k = \omega/c_0$. $p_1(r,z)$ satisfies the following parabolic equation:

$$2ik \frac{\partial p_1}{\partial z} + \nabla_{\perp}^2 p_1 = 0, \quad (12)$$

where ∇_{\perp}^2 is the transverse Laplace operator. In symmetric condition: $\nabla_{\perp}^2 = (1/r)(\partial/\partial r)(r[\partial/\partial r])$, the solution of this equation is¹³

$$p_1(r,z) = -i \frac{k}{z} \int_0^{\infty} \exp \left[i \frac{k(r^2 + r_1^2)}{2z} \right] J_0 \left[\frac{kr r_1}{z} \right] \times p_1(r_1, 0) r_1 dr_1, \quad (13)$$

where $p_1(r_1, 0)$ is the value of $p_1(r,z)$ at $z=0$, and J_0 is Bessel function of the zeroth order. In this paper, the plane wave approximation is used, i.e.,

$$p_1(r_1, 0) = \begin{cases} p_0 & r_1 < a \\ 0 & r_1 > a \end{cases},$$

where p_0 is the sound pressure amplitude at the surface of the transducer.

When $ka \gg 1$, Wen¹⁹ presented a new approach to express any axial symmetric beam field in a simple analytical form—the superposition of Gaussian beams. The radiation source of interest can be described by a set of Gaussian beam functions with different complex constants A_n and B_n

$$p_1(r_1, 0) = \sum_{n=1}^N A_n \exp(-B_n r_1^2). \quad (14)$$

Coefficients A_n and B_n can be calculated based on optimization theory.

From Eqs. (13) and (14), $p_1(r,z)$ can be expressed as the following:

$$p_1(r,z) = \sum_{n=1}^N \frac{A_n}{2B_n} \frac{1}{g_n(z)} \exp \left[- \frac{r^2}{g_n(z)} \right], \quad (15)$$

where $g_n(z) = (1/B_n) + i(2z/k)$.

When two primary waves with angular frequencies ω_1 and ω_2 are simultaneously radiated from a circular piston source, the first-order (linearized) pressure is given by

$$p_1(r, z) = \sum_{n=1}^N \frac{A_n}{2B_n} \frac{1}{g_{1n}(z)} \exp\left[-\frac{r^2}{g_{1n}(z)}\right] + \sum_{n=1}^N \frac{A_n}{2B_n} \frac{1}{g_{2n}(z)} \exp\left[-\frac{r^2}{g_{2n}(z)}\right], \quad (16)$$

where $g_{1n}(z) = (1/B_n) + i(2z/k_1)$, $g_{2n}(z) = (1/B_n) + i(2z/k_2)$.

Due to the nonlinear interaction of the two primary waves, the sound pressure of the generated second-order wave at the difference frequency is $p_d(r, z) \exp[-i(\omega_d t - k_d z)]$, where k_d denotes the wave number at the difference frequency ($k_d = \omega_d/c_0$, $\omega_d = \omega_2 - \omega_1$). If the nonlinearity is weak, $p_d(r, z)$ satisfies the following secondary parabolic equation:

$$\nabla_{\perp}^2 p_d + 2ik_d \frac{\partial p_d}{\partial z} = -i \frac{\beta k_1 k_2 k_d}{c_0} p_1 p_2^*, \quad (17)$$

where “*” denotes the complex conjugate.

Considering that the primary waves consist of a series of Gaussian beam functions, Eq. (17) becomes

$$\nabla_{\perp}^2 p_{dm,n} + 2ik_d \frac{\partial p_{dm,n}}{\partial z} = -i \frac{\beta k_1 k_2 k_d}{c_0} p_{1m} p_{2n}^*, \quad (18)$$

where

$$p_{1m} = \frac{A_m}{2B_m} \frac{1}{g_{1m}(z)} \exp\left[-\frac{r^2}{g_{1m}(z)}\right],$$

$$p_{2n} = \frac{A_n}{2B_n} \frac{1}{g_{2n}(z)} \exp\left[-\frac{r^2}{g_{2n}(z)}\right],$$

and $m = 1, 2, \dots, N$, $n = 1, 2, \dots, N$. The solution to Eq. (18) is

$$p_{dm,n}(r, z) = \frac{\beta k_1 k_2}{4c_0} \frac{A_m A_n^*}{B_m B_n^*} \int_{z'=0}^z \frac{1}{g_{1m}(z') g_{2n}^*(z') + i \frac{z-z'}{k_s}} \times \frac{1}{g_{1m}(z') g_{2n}^*(z') + i \frac{z-z'}{k_s}} \times \exp\left[-\frac{r^2}{g_{1m}(z') g_{2n}^*(z') + 2i \frac{z-z'}{k_s}}\right]. \quad (19)$$

TABLE I. Coefficients used in evaluating the Gaussian beam description of the parametric field of a circular piston.

N	A_n	B_n
1	11.467+0.960I	4.103+0.246I
2	0.077-0.208I	3.572-21.039I
3	-4.239-8.550I	4.472+5.165I
4	1.668+2.683I	4.383+14.964I
5	-5.008+3.237I	4.558+9.994I
6	1.075-0.689I	3.951+20.016I
7	-1.042-0.189I	2.604-10.321I
8	-2.578+3.256I	3.365-4.797I
9	-0.244-0.282I	2.089-15.884I
10	-0.174-0.228I	3.053+25.094I

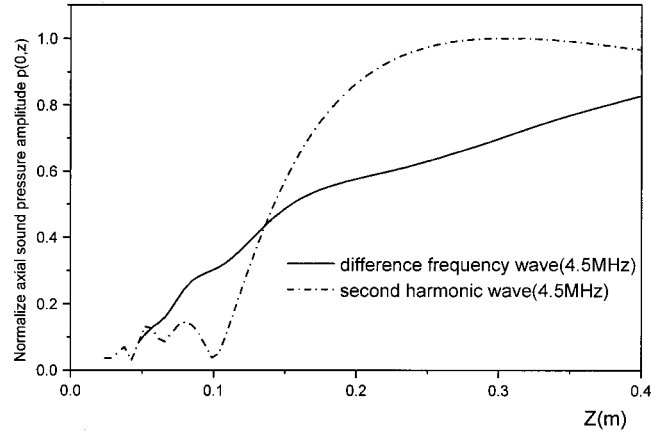


FIG. 2. The axial pressure amplitude of parametrically generated difference frequency wave.

The sound pressure of the generated difference frequency wave is therefore

$$p_d(r, z) = \sum_{m=1}^N \sum_{n=1}^N p_{dm,n}(r, z). \quad (20)$$

III. RESULTS AND DISCUSSION

A. The axial and radial sound pressure distributions of a circular piston

In this paper, a circular piston transducer with radius of 1 cm is considered as the source. Primary frequencies of $f_1 = 1$ MHz and $f_2 = 5.5$ MHz are chosen to generate a secondary wave of the difference frequency wave at 4.5 MHz. In general, for a circular piston transducer that has discontinuous surface velocity distribution, a large number of Gaussian terms are needed in the solution to achieve sufficient accuracy. In this paper, the summation of ten Gaussian beam functions is used to approximate the analytic solution of a circular piston source. Coefficients A_n and B_n are calculated from the optimization theory and are listed in Table I. These coefficients can be used in Eq. (19) and Eq. (20) to describe the axial and radial distributions of the sound pressure amplitude of the difference frequency wave.

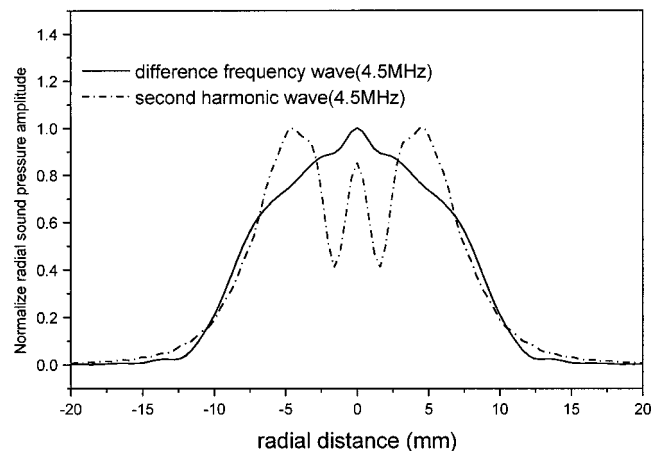


FIG. 3. The radial pressure amplitude distribution of parametrically generated difference frequency wave at $z = 8$ cm.

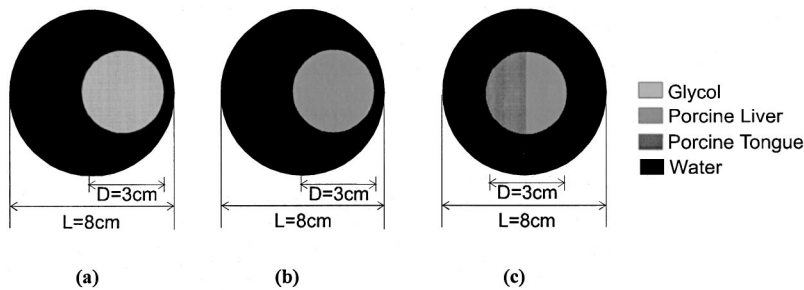


FIG. 4. The cross sections of three sample models in computer simulation.

Figure 2 shows the calculated axial sound pressure of the secondary wave at the difference frequency 4.5 MHz. For comparison, the axial sound pressure distribution of the second harmonic wave generated from a 2.25 MHz piston source of the same size is also calculated and represented by a dotted line in Fig. 2. It is clearly seen that the axial sound pressure of the wave with difference frequency is nearly proportional to the distance z in the near field, while the axial sound pressure of the second harmonic wave shows obvious fluctuation in the near field.

Figure 3 shows the radial pressure distributions of the parametrically generated wave at the difference frequency wave 4.5 MHz and the second harmonic wave 4.5 MHz at distance $z=8$ cm. It can be seen that there are no sidelobes in the radial pressure distribution of the difference frequency wave. One can draw a conclusion that the parametrically generated difference frequency wave grows linearly with the distance from the source and is less affected by the edge diffraction; it can therefore be used to obtain ultrasound imaging with higher resolution and higher accuracy.

B. Computer simulation of nonlinearity parameter tomography via parametric array

Three sample models with different combinations of liquids and biological tissues are analyzed in the present paper. The cross sections of these samples are shown in Fig. 4. For sample A, a cylindrical liquid sample (glycol) with diameter $D=3$ cm is located in a cylindrical water tank with diameter $L=8$ cm. The liquid sample is tangential with the center of the cylindrical water tank. In sample B, the liquid sample (glycol) is replaced with a biological tissue (porcine liver). Sample C is a combined sample; the internal layer consists of two half-cylindrical tissues with porcine tongue on the left and porcine liver on the right. This internal part is located at the center of a cylindrical water tank. The linear and nonlinear parameters of the liquids and biological tissues in sample A, B, and C are listed in Table II.

TABLE II. The ultrasonic parameters of some liquids and biological tissues.

Sample	Density (g/mL)	Sound velocity (m/s)	Attenuation coefficients (cm^{-1})			B/A
			1 MHz	5.5 MHz	4.5 MHz	
Water	1.00	1500	5.2 ^a
Glycol	1.11	1670	9.5 ^a
Porcine liver	1.06	1588	0.0621	0.3222	0.2797	7.3 ^b
Porcine tongue	1.05	1551	0.1715	0.8231	0.7719	6.5 ^b

^aSee Ref. 3.

^bSee Ref. 17.

When the sample is absent, the sound pressure amplitude of the difference frequency wave in water can be written as

$$p_{d0}(L) = \frac{\omega_d L P_{10} P_{20}}{4 \rho_0 c_0^3} [(B/A)_0 + 2], \quad (21)$$

where $(B/A)_0 = 5.2$ for distilled water. When the sample is inserted into the water, the pressure amplitude of the differ-

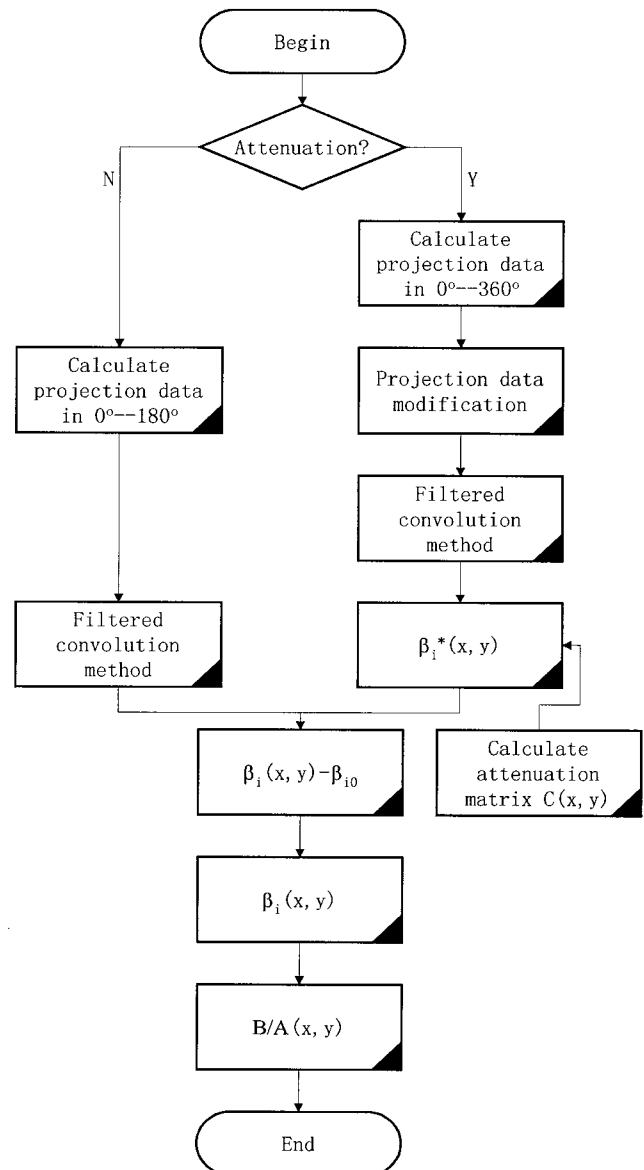


FIG. 5. The flow chart of the computer simulation of acoustic nonlinearity parameter B/A tomography.

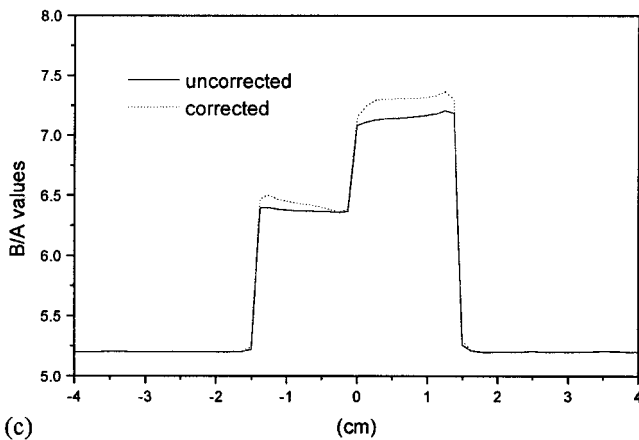
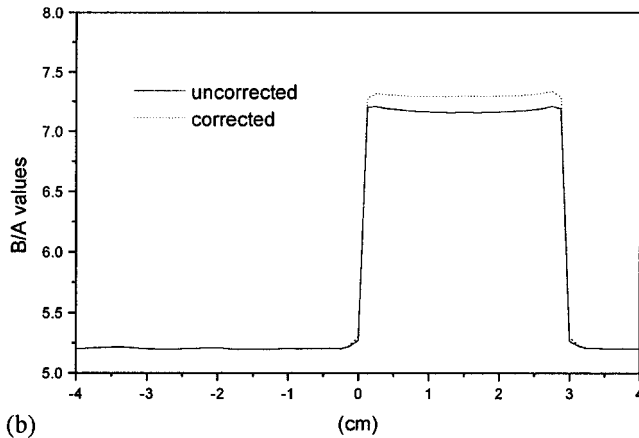
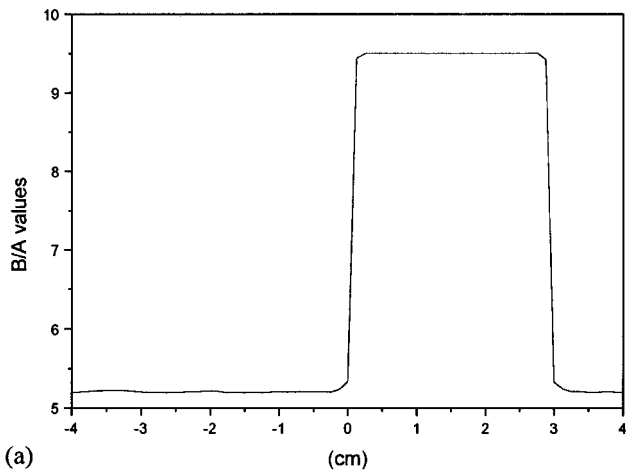


FIG. 6. The one-dimensional B/A distributions along central line for three sample models.

TABLE III. The reconstruction error for sample models.

Sample model	Reconstruction error before correction	Reconstruction error after correction
A	0.19%	...
B	0.70%	0.16%
C	1.22%	0.88%

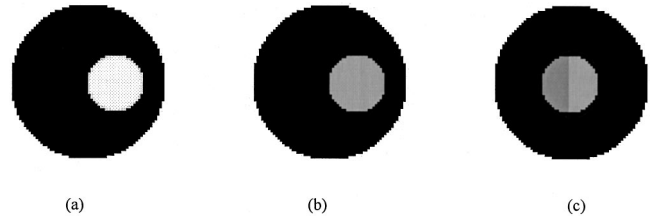


FIG. 7. The reconstructed two-dimensional B/A image for three sample models.

ence frequency wave at distance L can be expressed, according to the theory of the finite amplitude wave propagations in a layer medium, as

$$\begin{aligned}
 p_{dx}(L) = & \frac{\omega_d P_{10} P_{20}}{4 \rho_0 c_0^3} (L-x) [(B/A)_0 + 2] \\
 & + \frac{\omega_d P_{10} P_{20}}{4 \rho_x c_x^3} x [(B/A)_x + 2] \\
 & \times \frac{1 - \exp[-(\alpha_1 + \alpha_2 - \alpha_d)x]}{\alpha_1 + \alpha_2 - \alpha_d} \exp(-\alpha_d x),
 \end{aligned} \quad (22)$$

where $(B/A)_x$ is the acoustic nonlinearity parameter of the sample and $x = D \cos \theta$ is the distance that the wave has propagated through in the sample. A total transmission between the sample and the water is assumed.

Rotating from 0° to 180° with an angular step of 7.5° , scans from 24 different angles are obtained. At each angle, the transmitter and the receiver sweep an 8-cm scanning length simultaneously in one direction at a step size of 1.25 mm. A 24×65 projection data matrix is obtained for each sample. For the lossy samples, it is necessary to calculate the projection data from 0° – 360° and then obtain the projection data from 0° – 180° by using Eq. (12). Figure 5 shows the flow chart for reconstructing the acoustic nonlinearity parameter tomography. Figure 6 shows the one-dimensional images of $(B/A)_x$ along the central line of the sample models. In these figures, since glycol in sample A is lossless, it is not necessary to compensate for attenuation. For sample B and sample C, since porcine liver and porcine tongue are absorbing tissues, it is necessary to make attenuation corrections by using the attenuation matrix obtained from Eq. (8). After modification and attenuation correction for the projection data, the reconstructed one-dimensional images of acoustic nonlinearity parameter B/A are represented using dotted lines in Figs. 6(b) and (c). The reconstruction errors before and after attenuation correction are shown in Table III. Figure 7 shows the reconstructed two-dimensional B/A image for the three sample models. The different gray scales in Figs. 7(a), (b), and (c) indicate the different acoustic nonlinearity parameter values of glycol, porcine liver, and porcine tongue, respectively.

IV. CONCLUSION

In this paper, the theoretical analysis for acoustic nonlinear parameter tomography via a sound parametric array is proposed. When two primary waves are transmitted simulta-

neously from a circular piston source, a secondary wave at the difference frequency can be generated. The axial and radial sound pressure distributions of the difference frequency wave are calculated by superposition of Gaussian beams. Calculated results show that: (1) The axial sound pressure amplitude of the parametrically generated difference frequency wave is linearly proportional to the distance from the transmitter; (2) Compared with the second harmonic wave of the same frequency generated from a 2.25 MHz transducer of the same size, the parametrically generated difference frequency wave is less influenced by the edge diffraction in the near field. By using the filtered convolution method, computer simulation of B/A tomography from the calculated sound pressure of the difference frequency wave was studied. For absorbing tissue samples, the use of the modified projection data and attenuation matrix is proposed. Results of computer simulation agree well with the sample models. Further experimental studies for acoustic nonlinearity parameter tomography via a parametric array are in progress.

ACKNOWLEDGMENTS

The authors wish to thank Professor F. Dunn for his valuable comments on the manuscript and his help in preparing the final version. The authors also wish to thank the National Natural Science Foundation of China (No. 19674026 and No. 19834040) and Natural Science Foundation of Jiangsu Province (No. BK99024).

- ¹L. Bjørnø, "Characterization of biological media by means of their nonlinearity," *Ultrasonics* **4**, 254–259 (1986).
- ²T. G. Muir and E. L. Carstensen, "Prediction of nonlinear acoustic effects of biological frequencies and intensities," *Ultrasound Med. Biol.* **6**, 345–357 (1980).
- ³R. T. Beyer, "Parameter of nonlinearity in fluids," *J. Acoust. Soc. Am.* **32**, 719–721 (1960).
- ⁴W. K. Law, L. A. Frizzell, and F. Dunn, "Determination of the nonlinearity parameter B/A of biological media," *Ultrasound Med. Biol.* **11**, 307–318 (1985).
- ⁵X. F. Gong, X. Z. Liu, and D. Zhang, "Influence of tissue composition and structural features of biological media in the ultrasonic nonlinearity parameter," *Chin. J. Acoust.* **12**, 265–270 (1993).

- ⁶W. K. Law, L. A. Frizzell, and F. Dunn, "Comparison of the thermodynamic and finite amplitude methods of B/A determination in biological materials," *J. Acoust. Soc. Am.* **74**, 1295–1297 (1983).
- ⁷N. Ichida, T. Sato, and M. Linzer, "Imaging the non-linear ultrasonic parameter of a medium," *Ultrason. Imaging* **5**, 295–299 (1983).
- ⁸N. Ichida, T. Sato, H. Miwa, and K. Murakami, "Real-time nonlinear parameter tomography using impulsive pumping waves," *IEEE Trans. Sonics Ultrason.* **SU-31**(6), 635–641 (1984).
- ⁹Y. Nakagawa, W. Hou, A. Cai, N. Arnold, and G. Wade, "Nonlinear parameter imaging with finite-amplitude sound waves," *Proc. IEEE Ultrason. Symp.* **901–904** (1986).
- ¹⁰D. Zhang, X. F. Gong, and S. G. Ye, "Acoustic nonlinearity parameter tomography for biological specimens via measurements of the second harmonic wave," *J. Acoust. Soc. Am.* **99**, 2397–2402 (1996).
- ¹¹D. Zhang and X. F. Gong, "Experimental investigation of the acoustic nonlinearity parameter tomography for excised pathological biological tissues," *Ultrasound Med. Biol.* **25**(4), 593–599 (1999).
- ¹²F. Ingenito and A. O. Williams, Jr., "Calculation of second harmonic generation in a piston beam," *J. Acoust. Soc. Am.* **49**, 319–328 (1971).
- ¹³Greer S. Garrett, J. N. Tjøtta, and S. Tjøtta, "Nearfield of a large acoustic transducer. II. Parametric radiation," *J. Acoust. Soc. Am.* **74**, 1013–1020 (1983).
- ¹⁴J. Bernsten, J. N. Tjøtta, and S. Tjøtta, "Nearfield of a large acoustic transducer. IV. Second harmonic and sum frequency radiation," *J. Acoust. Soc. Am.* **75**, 1383–1391 (1984).
- ¹⁵D. Zhang, X. Chen, and X. F. Gong, "Study of the harmonic sound field from a circular piston source and the influence in the nonlinearity parameter tomography," *Chin. J. Acoust.* **18**, 272–279 (1999).
- ¹⁶V. A. Burov, I. E. Gurinovich, O. V. Rudenko, and E. Ya Tagunov, "Reconstruction of the spatial distribution of the nonlinearity parameter and sound velocity in acoustic nonlinear tomography," *Acoust. Phys.* **40**(6), 816–823 (1994).
- ¹⁷A. Cai, J. Sun, and G. Wade, "Imaging with acoustic nonlinear parameter with diffraction tomography," *IEEE Trans. Ultrason. Ferroelectr. Freq. Control* **39**(6), 708–711 (1992).
- ¹⁸P. J. Westervelt, "Parametric acoustic array," *J. Acoust. Soc. Am.* **35**, 535–537 (1963).
- ¹⁹J. J. Wen and M. A. Breazeale, "A diffraction beam field expressed as the superposition of Gaussian beams," *J. Acoust. Soc. Am.* **83**, 1752–1756 (1988).
- ²⁰F. H. Fenlon, "An extension of the Bessel-Fubini series for multiple-frequency CW acoustic source of finite amplitude," *J. Acoust. Soc. Am.* **51**, 284–289 (1972).
- ²¹X. F. Gong, Z. M. Zhu, T. Shi, and J. H. Huang, "Determination of the acoustic nonlinearity parameter in biological media using FAIS and ITD method," *J. Acoust. Soc. Am.* **86**, 1 (1989).
- ²²L. T. Chang, "A method for attenuation correction in radionuclide computed tomography," *IEEE Trans. Nucl. Sci.* **NS-26**, 2780–2789 (1979).
- ²³L. A. Shepp and B. F. Logan, "The Fourier reconstruction of a head section," *IEEE Trans. Nucl. Sci.* **NS-21**, 21–23 (1974).

Dynamic photoelastic study of the transient stress field in solids during shock wave lithotripsy

Xufeng Xi and Pei Zhong^{a)}

*Department of Mechanical Engineering and Materials Science, Duke University,
Durham, North Carolina 27708*

(Received 26 July 2000; revised 21 October 2000; accepted 10 December 2000)

Photoelastic and shadowgraph imaging techniques were used to visualize the propagation and evolution of stress waves, and the resultant transient stress fields in solids during shock wave lithotripsy. In parallel, theoretical analysis of the wavefront evolution inside the solids was performed using a ray-tracing method. Excellent agreement between the theoretical prediction and experimental results was observed. Both the sample size and geometry were found to have a significant influence on the wave evolution and associated stress field produced inside the solid. In particular, characteristic patterns of spalling damage (i.e., transverse and longitudinal crack formation) were observed using plaster-of-Paris cylindrical phantoms of rectangular and circular cross sections. It was found that the leading tensile pulse of the reflected longitudinal wave is responsible for the initiation of microcracks in regions inside the phantom where high tensile stresses are produced. In addition, the transmitted shear wave was found to play a critical role in facilitating the extension and propagation of the microcrack. © 2001 Acoustical Society of America. [DOI: 10.1121/1.1349183]

PACS numbers: 43.80.Gx, 43.35.Wa [FD]

I. INTRODUCTION

Understanding the transient mechanical interaction between an incident shock wave and the target concretion is critical for uncovering the mechanisms whereby stone comminution occurs in shock wave lithotripsy (SWL). This knowledge is needed for improving the design of shock wave lithotripters for more efficient and effective stone fragmentation with minimal tissue injury. Although significant progress has been made in understanding shock wave propagation,^{1,2} the dynamics of cavitation³ and its role in both stone comminution⁴⁻⁷ and tissue injury⁸⁻¹⁰ in SWL, limited knowledge of the transient stress field produced inside a target stone has been accumulated. The mechanical interaction between a lithotripter shock wave (LSW) and the target renal calculi has not been well elucidated.

Previous studies have identified three different modes of stone damage in SWL, namely, cavitation erosion at the anterior surface,^{4,5} spalling near the posterior surface,^{11,12} and layer separation at internal crystalline-matrix interfaces of the stone.^{13,14,16} Except for cavitation erosion, which is caused by the violent collapse of cavitation bubbles near a stone surface, both spalling and internal layer separation can be attributed to dynamic failure of the stone material under the influence of the transient stress field produced inside the stone. Because most renal calculi are brittle materials,¹⁵ they fail much more easily under tension than under compression. Hence, when a compressive wave is reflected from a pressure-release boundary such as at the posterior surface of the stone or at a crystalline-to-matrix interface, a strong reflected tensile wave will be generated, which may lead to spalling or layer separation. Using geometrical acoustics¹⁶

and finite difference methods,¹⁷ Gracewski and associates have calculated the stress/strain field in solids subjected to a spherical shock wave. The model predictions were compared to the response of strain gauges embedded in disk and sphere plaster phantoms during shock wave exposure, and reasonable agreement was obtained. The model calculation also predicted higher strain amplitudes at caustics, which are regions inside the phantom where reflected wavefronts from the concave back surface of the disk or sphere samples would fold. It was speculated that cracks are more likely to develop in these caustic regions where high tensile stresses are generated. The limitations of the strain gauge approach, however, are the low spatial and temporal resolution of the gauge,¹⁶ as well as the limited number of data points that can be collected from each sample. Therefore, the distribution of the stress field in the sample could not be determined using this experimental method.

More recently, a fracture mechanics model of stone comminution in SWL has been proposed.¹⁸ A cohesive-zone model was used to analyze the spalling mechanism, and the fragmentation process was described as a sequence of nucleation, growth, and coalescence of flaws caused by a tensile or shear stress. The accumulated damage in kidney stones in SWL was modeled using a simplified incident shock wave profile and an idealized flaw distribution in the stone material. For the potential application of such a model in SWL research, understanding of the transient stress field in the target stone is also needed.

In this work, a dynamic photoelastic imaging technique was used to characterize the LSW-stone interaction and the propagation and evolution of resultant transient stress waves inside the target stone. Epoxy stone phantoms of different geometries and sizes were fabricated to (1) identify the stress field induced by different wave components; (2) examine

^{a)}Electronic mail: pzhong@acpub.duke.edu

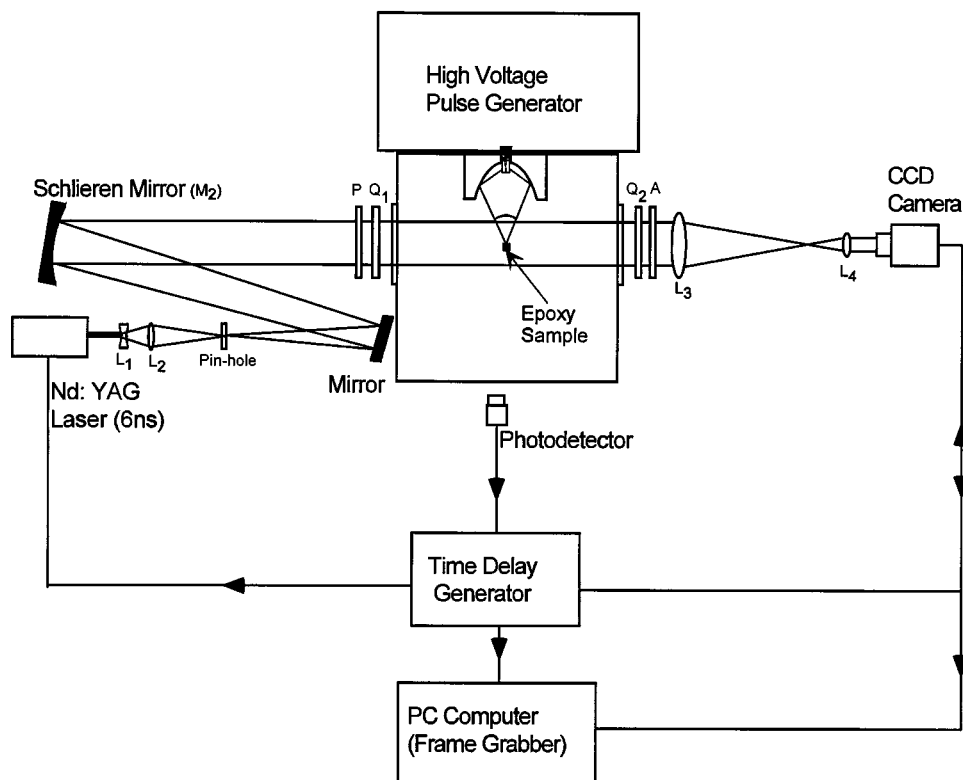


FIG. 1. Schematic diagram of the laboratory electrohydraulic shock wave lithotripter and the optical setup for shadowgraph and photoelastic imaging. *P*: polarizer; *A*: analyzer; Q_1 and Q_2 : quarter-wavelength plates. The focal lengths of the lenses and mirrors are L_1 : -50 mm, L_2 : 25.4 mm, L_3 : 300 mm, L_4 : 100 mm, M_2 : 1524 mm.

their interaction; and (3) analyze the contribution of various stress waves on microcrack initiation and extension, in relation to the spalling mechanism. To facilitate the interpretation of the experimental results, a ray-tracing method was used in parallel to determine wavefront propagation and evolution inside the phantoms. Excellent correlation between the photoelastic imaging and the ray-tracing prediction was obtained regarding the general characteristics of wavefront evolution inside the target concretion. Finally, fragmentation tests were carried out using plaster-of-Paris stone phantoms of different geometries and sizes. Comparison between the results from photoelastic imaging, ray-tracing analysis, and stone fragmentation tests allows us to identify the contribution of different stress waves to the initiation and propagation of microcracks in the target stone phantoms in SWL.

II. EXPERIMENTAL DESIGN AND METHODS

A. Lithotripter

A laboratory electrohydraulic (EH) shock wave lithotripter (80-nF capacitor), similar to an unmodified Dornier HM-3 clinical lithotripter (reflector geometry: semimajor axis $a = 138$ mm, semiminor axis $b = 78$ mm, and half-focal length $c = 114$ mm), was used in this study. The shock wave generator was placed horizontally inside a Lucite water tank ($66 \times 55 \times 48$ cm, $L \times W \times H$) with built-in optical windows on its lateral walls to facilitate high-speed imaging (Fig. 1). The pressure waveform at the focal point of the lithotripter was measured by a calibrated polyvinylidene difluoride (PVDF) membrane hydrophone (Sonic Technology), with a bandwidth of 50 MHz.¹⁹ All the experiments were carried out at an output voltage of 24 kV.

B. Dynamic photoelasticity

Photoelasticity is an experimental technique for analyzing stress or strain fields in solids with birefringent properties (i.e., photoelastic materials, such as glass and epoxy). In principle, when a photoelastic material is deformed, the electric vector of an incident polarized light beam can be resolved into two components along the axes of the principal stresses in the material due to its temporary birefringence. Because of the difference in refractive indices along the axes of the principal stresses, the two components will be retarded differentially as they propagate through the material, leading to a relative phase shift. Consequently, an interference pattern will be formed as the two components are recombined outside the material by a downstream polarizer (also called the “analyzer”). Photoelasticity is, therefore, a classic common-path interferometric technique, with the surface of the photoelastic material acting as the beam splitter.

Based on the correlation between stress and the indices of refraction for temporary birefringent materials formulated by Maxwell, in the simplest case, the stress-optic law for a plate with only variable in-plane principal stresses can be written as^{20,21}

$$\sigma_1 - \sigma_2 = \frac{Nf_\sigma}{h}, \quad (1)$$

where σ_1 , σ_2 are the principal stresses in the temporary birefringent material, N is the relative retardation (also known as the “fringe order”), $f_\sigma (= \lambda/C$, with λ being the wavelength and C the stress-optic coefficient) is the material fringe value (in units of N/m fringe) corresponding to the minimum difference in principal stresses to produce a unit change in the fringe order in a material of unit thickness, and

TABLE I. Acoustic properties of plaster-of-Paris stone phantoms and epoxy (PSM-9).

Material	P-wave speed (m/s)	S-wave speed (m/s)	Density ($\times 10^3$ kg/m ³)	Impedance Z_p ($\times 10^6$ kg/m ² -s)	Impedance Z_s ($\times 10^6$ kg/m ² -s)
PSM-9 (epoxy)	2493	1108	1.15	2.87	1.27
Stone (P/W=2.0/1.0) ^a	2478	1471	1.67	4.14	2.46

^aThe wave speeds of the stone phantoms were measured in a water-saturated state.

h is the distance traversed by the light in the stressed plate. Equation (1) applies to both static and dynamic loading conditions, except that the material-fringe value under dynamic loading (f_{σ}^{*}) is usually 10%–30% higher than that for the static case.²⁰

Dynamic photoelasticity has been widely used for transient stress analysis in fracture mechanics and geophysics.^{22,23} In this work, the dynamic photoelastic imaging technique is applied to assess qualitatively the transient stress field induced in solids exposed to lithotripter-generated shock waves.

C. High-speed photoelastic and shadowgraph imaging

To visualize shock wave propagation and the transient stress fields in solids during SWL, a high-speed imaging system combining shadowgraph and photoelastic imaging, as described in our previous study,²⁴ was employed. Briefly, a frequency-doubled Nd:YAG laser ($\lambda = 512$ nm, New Wave Research) with 6-ns pulse duration was collimated to form a parallel light beam through the beam focus of the lithotripter (Fig. 1). Two quarter-wave plates ($Q1$ and $Q2$) were placed in the light path outside the lithotripter tank, with their optical axes aligned at $+45^\circ$ and -45° , respectively, to the polarization axes of a polarizer (P) and an analyzer (A) placed nearby, which are parallel to each other. This configuration forms a bright-field circular polariscope (the fringe order $N = (2m + 1)/2$, where m is an integer) for simultaneous photoelastic and shadowgraph imaging. The image was recorded by a CCD camera (GP-MF 552, Panasonic), which was connected to a frame grabber (DT3155, Data Translation) installed on a computer (Dimension XPS M233s, Dell). To ensure accurate timing of the event, the spark discharge of the lithotripter was picked up by a fast photo detector and relayed to a multichannel time delay generator. Output TTL pulses from the delay generator were then used to trigger the Nd:YAG laser, the CCD camera, and the frame grabber, respectively. By adjusting the delay time of the trigger signals with respect to the spark discharge, a series of high-speed photoelastic and shadowgraph images can be recorded at various stages of the shock wave propagation in water, as well as the propagation and evolution of the stress waves in a target concretion. To visualize the transient stress field in the target concretion, epoxy blocks (PSM-9, Measurements Groups, Inc., $C = 10.5$ kPa/fringe/m) of different geometries and sizes were prepared and used as stone phantoms. Their acoustic properties were determined by a through-transmission ultrasound technique,¹⁴ and were found to be quite similar to the acoustic properties of the plaster-of-Paris stone phantoms (Table I).

D. Stone fragmentation tests

Stone phantoms of various geometries and sizes were fabricated by thoroughly mixing plaster-of-Paris powder with water (2:1 ratio by weight) in a $20 \times 20 \times 3$ -cm baking pan. After the mixture was cured and let dry in air at room temperature overnight, the large slab formed was cut into small blocks and ground to the desired shape and size. Previous studies showed that these phantoms have similar physical properties compared to renal calculi, in particular, struvite stones.^{14,25} Before the fragmentation test, each phantom was rehydrated in water for at least 10 min until no visible bubbles could be observed to come out from the sample. The front surface of the phantom was then aligned perpendicular to the lithotripter axis with the center of the specimen coinciding with F_2 . The specimen was subsequently exposed to the lithotripter shock waves at a pulse repetition rate of 1 Hz until spalling was produced. At this moment, the experiment was stopped, and the total number of shocks delivered was recorded. For each phantom configuration, five samples were treated. After the experiment, the thickness of the spalled piece was measured, and its damage pattern was documented photographically.

III. THEORETICAL ANALYSIS OF STRESS WAVEFRONT PROPAGATION AND EVOLUTION IN SOLIDS DURING SWL

To facilitate the interpretation of photoelastic images, the propagation and evolution of the wavefronts of stress waves generated inside a target concretion by the impingement of an LSW were analyzed using ray-tracing methods. For simplicity, plane wave incidence was assumed, which was found to be quite reasonable (see Figs. 7 and 8). When

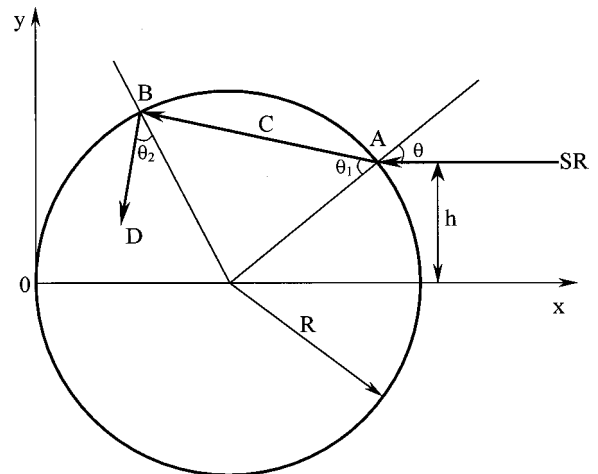


FIG. 2. Propagation of an incident source ray (SR) inside a solid disk of radius R .

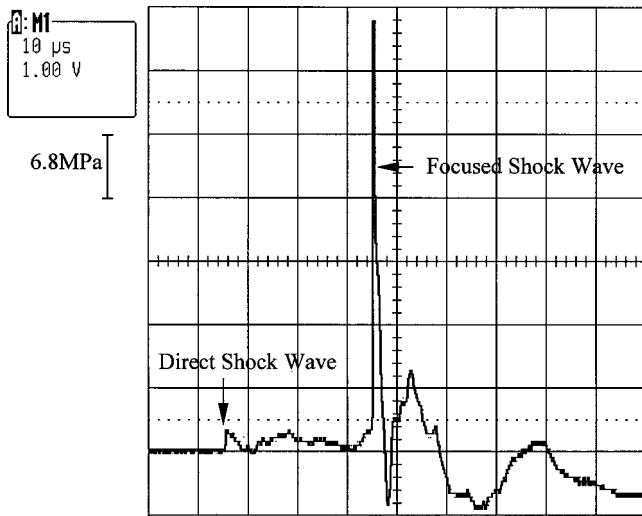


FIG. 3. Typical pressure waveform produced at F_2 by the laboratory lithotripter at 24 kV.

the LSW encounters the solid boundary, both wave reflection and refraction occur. In general, longitudinal (or P) and transverse (or S) stress waves are generated inside the solid (assumed to be homogeneous and isotropic), while part of the incident LSW will be reflected back into water. The direction and position of the new wavefronts were determined by applying Snell's law and Huygen's principle at the boundary, as depicted in Fig. 2. The ray-tracing method used in this study is similar to that described by Ting and Lee,²⁶ therefore, details will not be given here. Interested readers should consult the original paper.

IV. RESULTS AND DISCUSSION

A. Pressure waveform

Two shock waves, separated temporarily by a time delay of approximately 30 μs , were detected at F_2 after each spark discharge of the experimental lithotripter (Fig. 3). The first one (referred as the direct shock wave hereafter) is a spherical shock wave with a peak positive pressure of 2.3 MPa, emanating directly from the spark discharge at F_1 . The second one, formed by the reflection of a large portion of the spherical shock wave from the ellipsoidal reflector, is a focused shock wave with a peak positive pressure of 46.7 MPa,

a shock front rise time of 32 ns, and a positive pulse duration of 2.3 μs , respectively. These values are comparable to the measurements of the pressure waveform of a Dornier HM-3 lithotripter, which has a -6-dB beam size of $120 \times 15\text{ mm}$ along and transverse to the shock wave axis at F_2 , respectively.²⁷ Due to the properties of the membrane hydrophone, the negative tail of the pressure waveform was not well resolved.

B. Ray-tracing analysis

Assuming that an incident shock wave P_I first strikes a cylindrical epoxy sample ($D = 14\text{ mm}$, $T = 12.7\text{ mm}$) at $t = 0\ \mu\text{s}$, Fig. 4(a) illustrates the predicted wavefront position of the resultant transient stress waves inside the sample at $t = 4\ \mu\text{s}$. As shown, part of the P_I wave is reflected back toward the source in water, marked as P_R , and the other part refracted into the epoxy sample. Due to oblique incidence, both longitudinal (P_T) and transverse (S) waves are generated in the epoxy sample. The following wave speeds are used in the model calculation: 2493 m/s and 1108 m/s for P_T and S waves in epoxy, and 1500 m/s for P_I and P_R waves in water, respectively. Since the P_T wave travels faster than the P_R and S waves, a longitudinal head wave H_{TR} that connects P_T and P_R and a shear head wave H_{TS} which connects P_T and S are generated in the water and the epoxy sample, respectively. The positions of the head waves are drawn manually for the purpose of illustration. The corresponding photoelastic image, shown in Fig. 4(b), demonstrates an excellent correlation between the ray-tracing prediction and the wavefront position revealed by the isochromatic fringe pattern.

Using the ray-tracing model, a representative sequence of the propagation and evolution of the stress waves (P and S) inside the cylindrical epoxy sample was constructed. As shown in Fig. 5, several interesting features were predicted. First, because the velocity of P_T is higher than P_I , the refracted (or transmitted) P_T wave spreads out divergently inside the epoxy sample. In contrast, the transmitted S wave converges in the epoxy sample because its propagation speed is lower than P_I . Second, when the P_T wave encounters the lateral and posterior surface of the epoxy sample, both reflected longitudinal (P_{TR}) and shear (S_{TR}) waves are generated. Due to the concave geometry of the surface, both P_{TR}

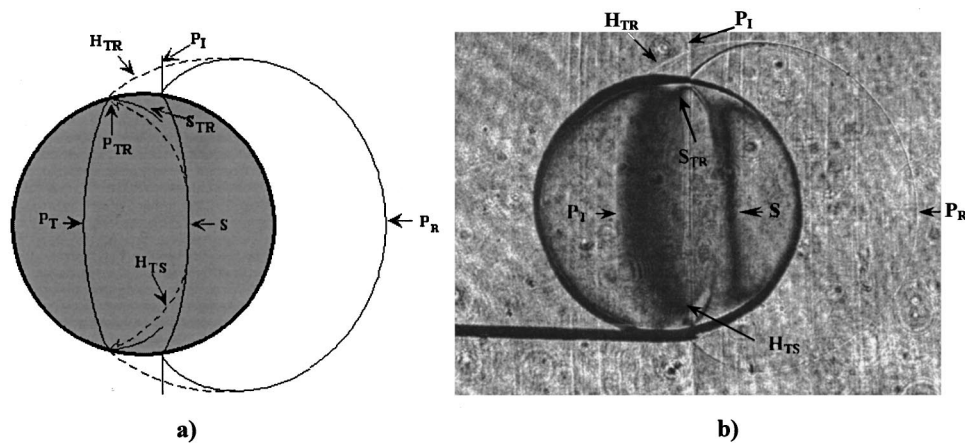


FIG. 4. (a) Theoretical (ray-tracing) prediction of the temporal distribution of different stress wavefronts generated in an epoxy disk ($D = 14\text{ mm}$) 4 μs after a plane shock wave incidence; (b) Corresponding photoelastic image of the same epoxy disk 4 μs after impingement of a direct shock wave on its front surface.

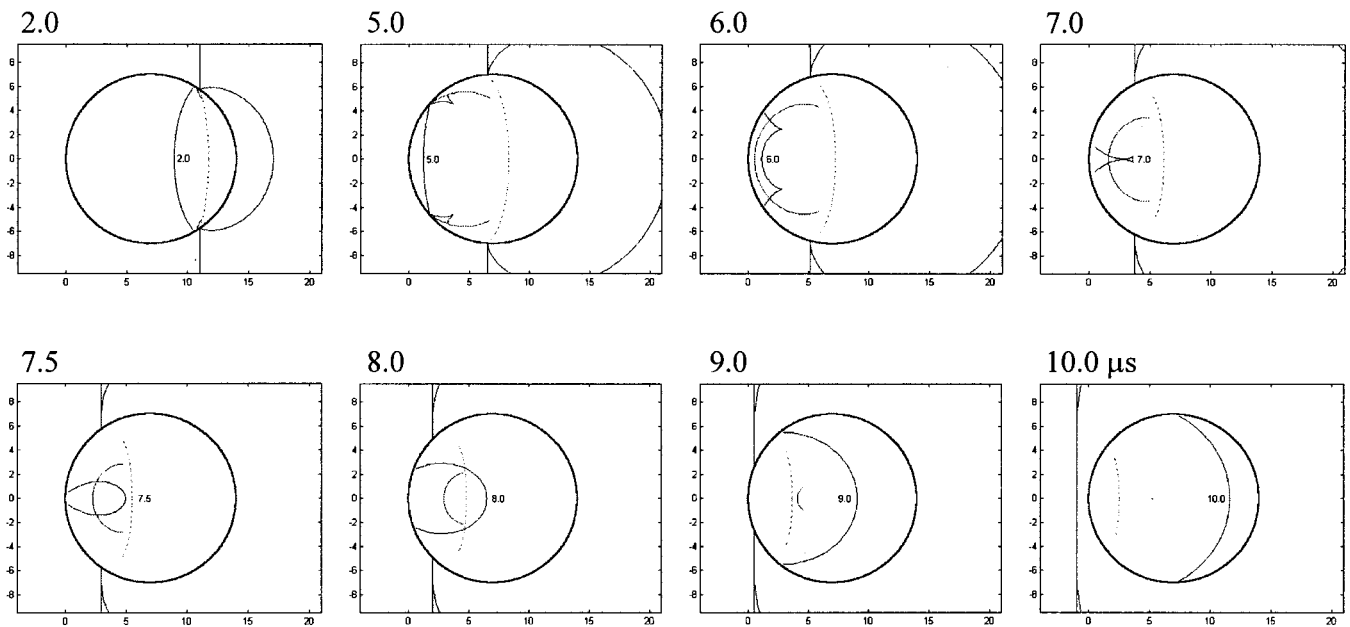


FIG. 5. Theoretical prediction of the propagation and evolution of different stress wavefronts in a cylindrical sample ($D=14$ mm) after a plane wave incidence.

and S_{TR} waves are focused toward the symmetry axis of the sample along the incident shock wave direction. Although not shown, a similar pattern of wave generation at the boundary will occur as a result of shear wave incidence. Moreover, wave interaction inside the epoxy sample could be predicted. For example, the wavefront of P_{TR} reflected from the upper and the lower boundaries of the sample, respectively, could be seen to cross each other between $t=7.0$ and $7.5 \mu\text{s}$, which may lead to a localized stress concentration and initiate damage.

To illustrate the effect of sample geometry on stress wave propagation and evolution in the target concretion during SWL, the ray-tracing model was applied to a rectangular

epoxy sample of comparable dimension ($13 \times 13 \times 12.7$ mm, $L \times H \times T$). As shown in Fig. 6, because of the normal incidence of the P_I wave, only a P_T wave was generated at the front surface of the rectangular sample, and the transmitted wavefront remained planar. In addition, shear waves were generated by wave diffraction at the edges of the sample as the incident shock wave swept by. Although the wavefronts of the shear waves also remained planar, they propagated obliquely toward the posterior surface of the sample and crossed each other after $t=8.7 \mu\text{s}$. For completeness, the head waves which connect the transmitted longitudinal and shear waves were also drawn in this sequence.

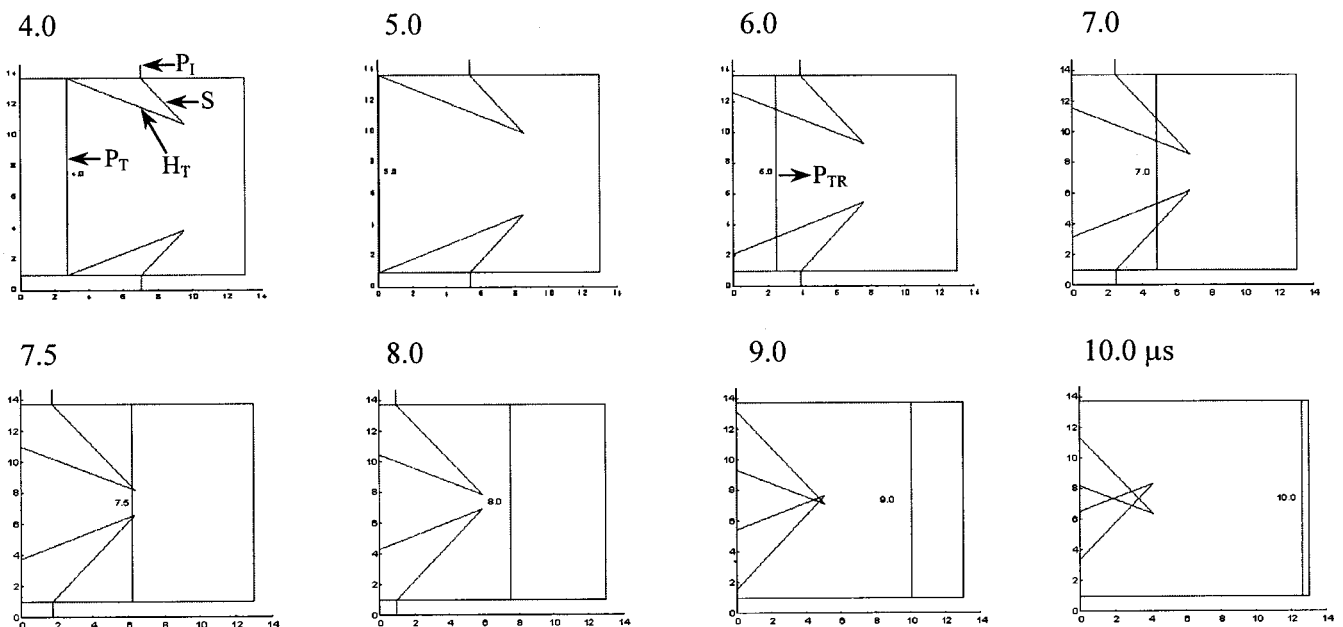


FIG. 6. Theoretical prediction of the propagation and evolution of different stress wavefronts in a rectangular sample ($13 \times 13 \times 12.7$ mm, $L \times W \times T$) after a plane wave incidence.

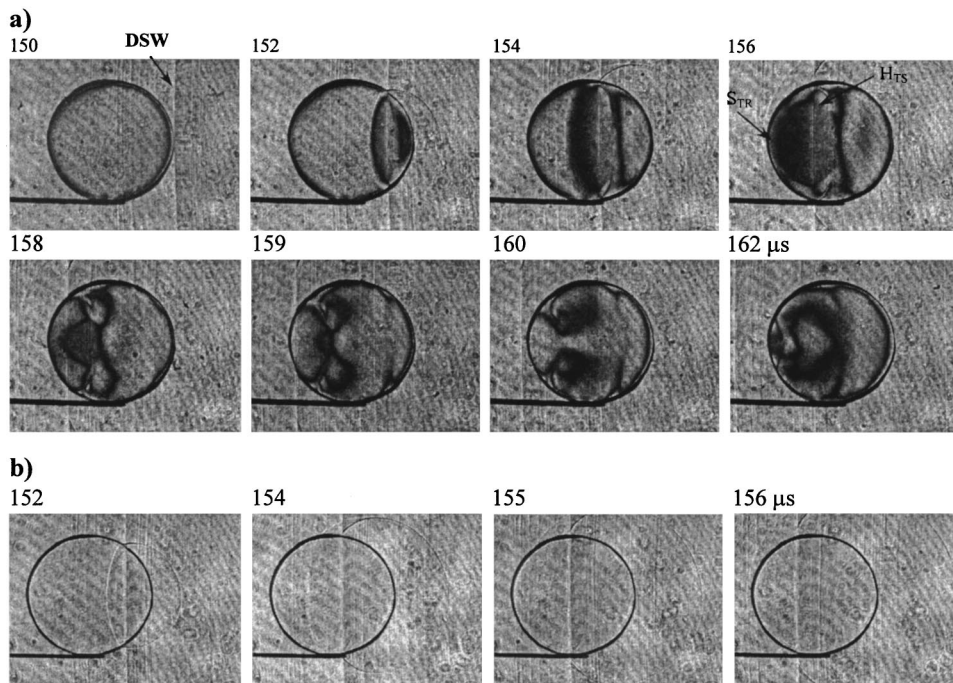


FIG. 7. Direct shock wave (DSW) incidence on a cylindrical epoxy sample ($D = 14$ mm): (a) photoelastic image, and (b) shadowgraph image.

C. Photoelastic and shadowgraph images

1. Direct shock wave

A typical sequence of the photoelastic images of the transient stress field in the cylindrical epoxy sample induced by the impingement of the direct shock wave (DSW) is shown in Fig. 7(a). Shadowgraph images of the same event were also recorded by the optical system without the polarizer, analyzer, and the two quarter-wave plates, and some selected shadowgraph images are shown in Fig. 7(b). For convenience, time zero for the experimental sequence ($t' = 0$) was chosen to coincide with the spark discharge, which was registered by a photo detector. In comparison, $t' = 150 \mu\text{s}$ in the photoelastic and shadowgraph image sequence corresponds to $t = 0 \mu\text{s}$ in the ray-tracing analysis (Fig. 5), which is the moment when the DSW first contacts the sample surface. Because the radius of curvature of the incident DSW at this moment is about 33 times that of the epoxy sample, the wavefront appears to be planar.

As shown earlier in Fig. 4, there is an excellent correlation between the wavefront profiles of various stress waves predicted by the ray-tracing method and that visualized experimentally by photoelastic imaging. This general correlation can be observed most clearly in the early stage of stress wave propagation inside the sample when individual wavefronts are separated from each other, and no wave interaction has occurred. For instance, an excellent match between the wavefront profiles at $t = 2 \mu\text{s}$ in Fig. 5 and that at $t' = 152 \mu\text{s}$ in Fig. 7(a) can be observed. As noted earlier, at $t' = 154 \mu\text{s}$ [also shown in Fig. 4(b)] the reflected P_R wave, transmitted longitudinal (P_T) and shear (S) waves, and head waves (H_{TR} and H_{TS}) can be clearly identified. When the P_T wave encountered the lateral and posterior surface of the epoxy sample, both reflected longitudinal (P_{TR}) and shear (S_{TR}) waves were induced. The P_{TR} wave, which is out of phase with the P_T wave, could not be identified clearly from the image, presumably due to superposition with the remain-

ing portion of the incident P_T wave. It is interesting to note that during the period $t' = 159\text{--}160 \mu\text{s}$, the transmitted S wave interacted with the reflected S_{TR} wave, producing temporarily a stress-free region near the horizontal symmetry axis of the sample. It is speculated that this was caused by the destructive interference of the two shear waves. After $t' = 160 \mu\text{s}$, the fringe pattern could not be related to any individual stress waves; rather, it represents the overall stress field integrated from that induced by various wave components reverberating inside the sample. On the other hand, for the shadowgraph images shown in Fig. 7(b), only the P_T wave inside the epoxy sample could be observed because of the weak strength of the DSW.

Similarly, the characteristics of the stress waves induced in a rectangular epoxy sample by the DSW, as shown in Fig. 8, were found to correlate very well with the ray-tracing prediction (see Fig. 6). All together, these results indicate that the ray-tracing method can be used to provide an accurate qualitative description of stress wave propagation and evolution in a target concretion. This observation has particular implication for applying the ray-tracing method to analyze stress wave propagation and evolution in kidney stones of various acoustic properties, size, and geometry, where photoelastic model studies are difficult to implement.

2. Focused shock wave

The general pattern of the stress wave propagation in the epoxy samples induced by the focused shock wave (FSW), as shown in Figs. 9 and 10, was quite similar to that from the DSW except that the order of the isochromatic fringes was much higher. The highest order of the isochromatic fringe was observed in frame $t' = 191 \mu\text{s}$ of Fig. 9(a) and in frame $t' = 192 \mu\text{s}$ of Fig. 10(a) for the cylindrical and rectangular samples, respectively. This occurred after the leading component of the P_T wave was reflected from the posterior surface of the sample. Subsequently, the order of the isochro-

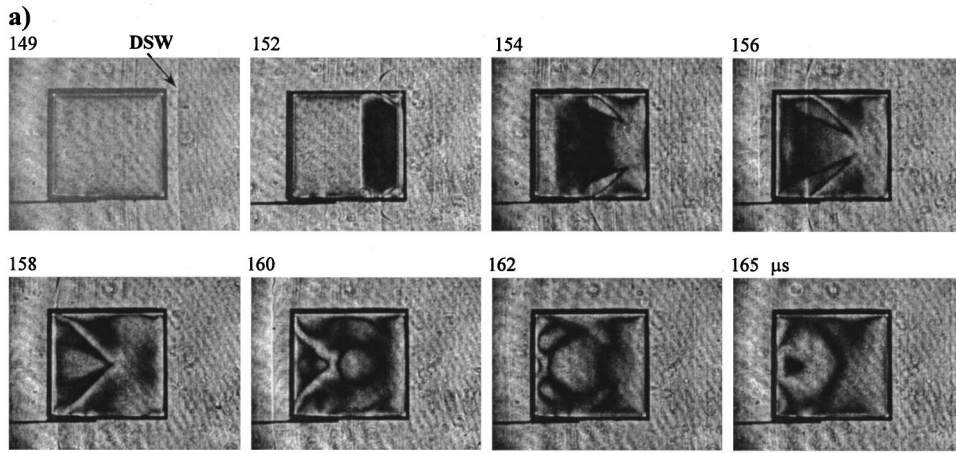
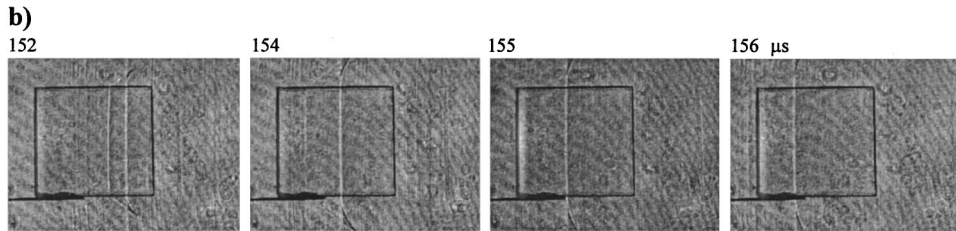


FIG. 8. Direct shock wave (DSW) incidence on a rectangular epoxy sample (14×14 mm, $L \times W$): (a) photoelastic image, and (b) shadowgraph image.



matic fringes decreased gradually as the stress waves reverberated inside the epoxy sample. Following the trailing tensile pressure of the FSW, cavitation bubbles were formed outside the sample. Aggregation of the bubbles on the solid surface was observed later in the growth period, with the aggregated bubbles reaching a maximum size at around $t' = 550$ to $600 \mu\text{s}$. This was followed by the violent inertial

collapse of the bubbles near the solid surface, with either the formation of high-speed microjet impinging towards the boundary or strong secondary shock wave emission [see frame $t' = 730 \mu\text{s}$ in Fig. 9(a) and frame $t' = 810 \mu\text{s}$ in Fig. 10(a)]. Both consequences could cause cavitation erosion on the impacted surfaces.^{4,5,7,28} It should be noted that because the FSW is much stronger than the DSW, both the P_T and S

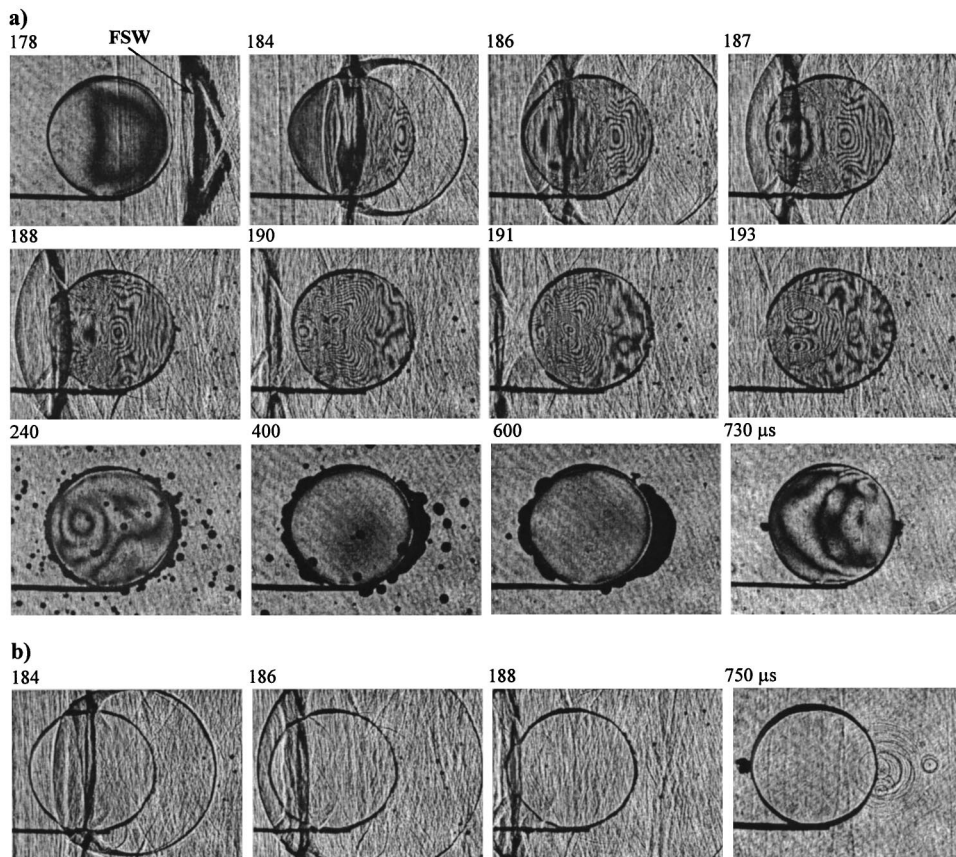


FIG. 9. Focused shock wave (FSW) incidence on a cylindrical epoxy sample ($D = 14$ mm): (a) photoelastic image, and (b) shadowgraph image.

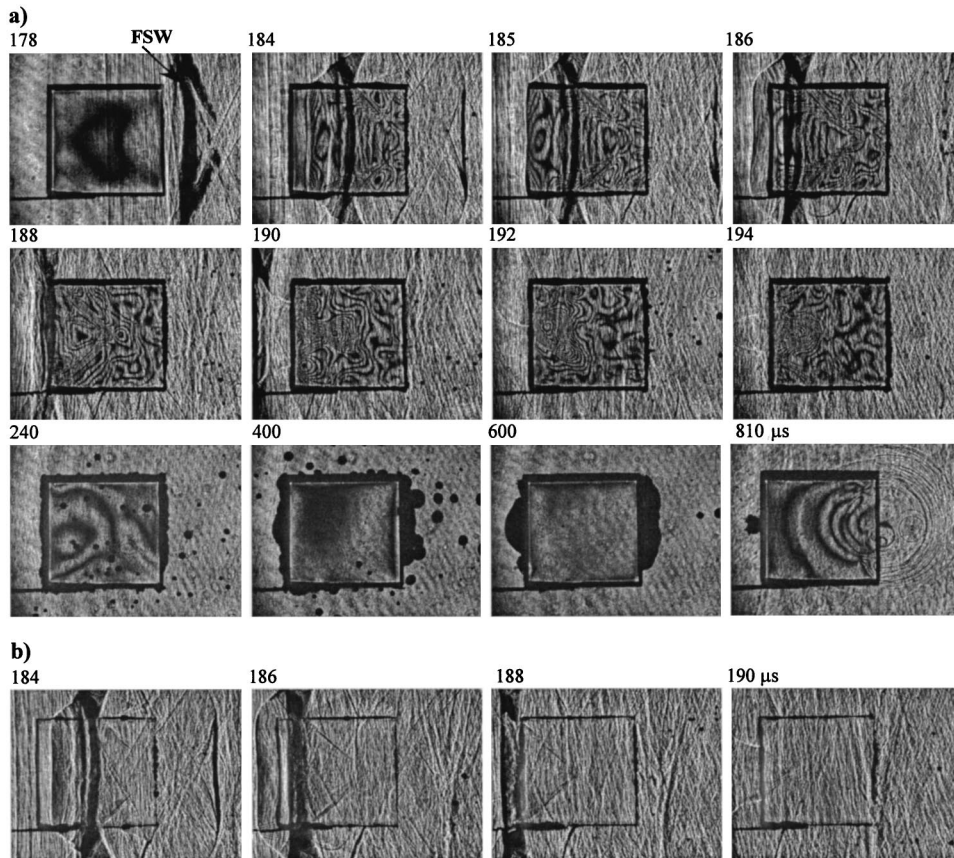


FIG. 10. Focused shock wave (FSW) incidence on a rectangular epoxy sample (14×14 mm, L×W): (a) photoelastic image, and (b) shadowgraph image.

waves induced in the cylindrical and rectangular samples can be observed in the shadowgraph images [Figs. 9(b) and 10(b)].

3. Effects of sample geometry and size on stress field

From Figs. 9 and 10, it is clear that the geometry of the epoxy sample has a significant influence on the characteristics of the stress wave propagation and resultant transient stress field induced inside the sample. For a quantitative comparison, the highest order of the isochromatic fringes induced by various wave components in different samples was measured and summarized in Table II. In the cylindrical sample, which has a divergent effect on the P_T wave, the order of the isochromatic fringes is lower than that in the rectangular sample, in which the transmitted P_T wave is nearly planar. In contrast, the opposite effect was observed for the S wave. In the rectangular sample, shear waves were induced at both the top and bottom surfaces and propagated diagonally as plane waves. In comparison, in the cylindrical sample the transmitted S wave was generated at the front surface and focused toward the horizontal symmetry axis of the sample. Due to focusing, the order of the isochromatic

fringes associated with the S wave is higher in the cylindrical sample than in the rectangular one. Furthermore, after reflection of the P_T wave from the posterior surface, the highest order of the isochromatic fringes was found to be higher in the cylindrical sample than that in the rectangular one, presumably due to the much stronger focusing effect of the cylindrical boundary. This finding suggests that it might be easier to produce spalling damage in cylindrical stones than in their rectangular counterparts, as shown later.

To further examine the effect of wave reflection on the transient stress field, two long samples (50×13×12.7 mm, L×H×T mm), with otherwise similar geometry and dimension compared to the cylindrical and rectangular samples used in previous experiments, were prepared. As shown in Figs. 11(a) and (b), without significant contribution from wave reflection from the posterior surface, the highest order of the isochromatic fringes in the long samples is much lower compared to their short counterparts. Moreover, the isochromatic fringe patterns produced in disks of different diameters were compared [Fig. 11(c)]. Although the stress distribution is similar, the highest order of the isochromatic fringe is much higher in smaller samples. This might be caused by the lesser attenuation in smaller samples due to shorter wave propagation distance.

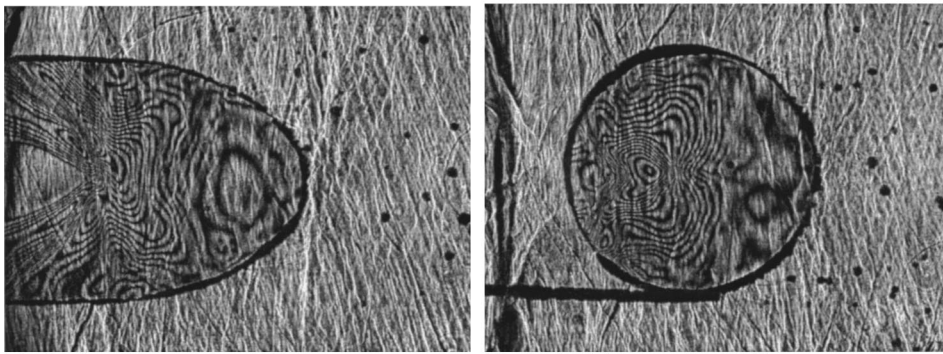
TABLE II. Comparison of fringe orders in samples of different geometries.

Sample shape	The highest order induced by P_T	The highest order induced by S	The highest order induced in the sample
Rectangular	13/2	9/2	31/2
Cylindrical	7/2	15/2	35/2

D. Stone fragmentation

1. General damage patterns

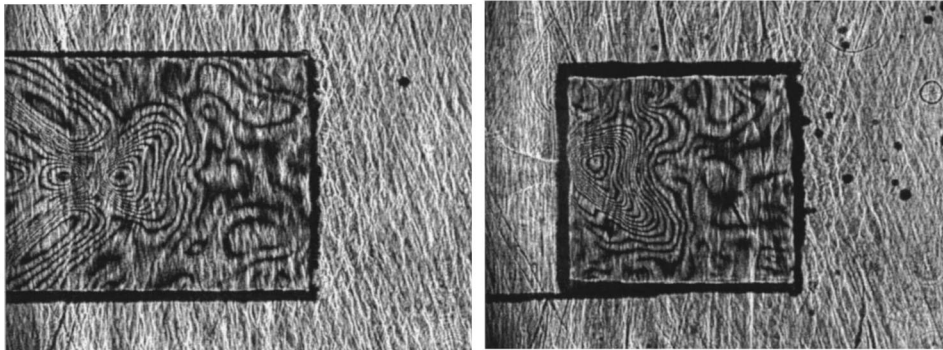
Two primary damage patterns of the stone phantoms were observed. First, on the anterior surface of the stone phantom a small damage crater with numerous minute pits



The highest fringe order: $25/2$

The highest fringe order: $35/2$

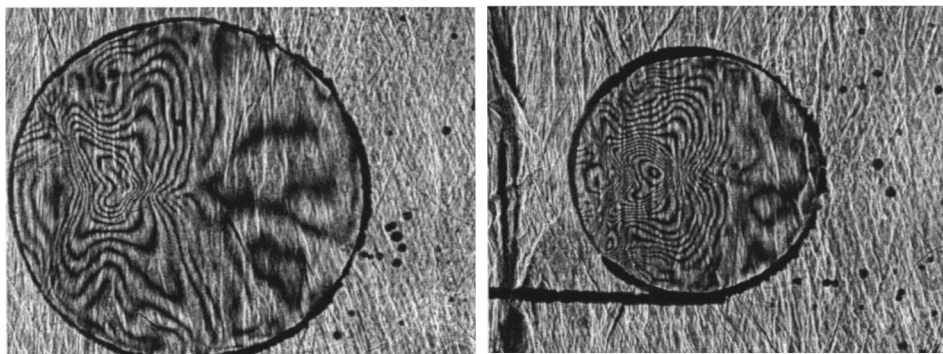
a)



The highest fringe order: $21/2$

The highest fringe order: $31/2$

b)



The highest fringe order: $21/2$

The highest fringe order: $35/2$

c)

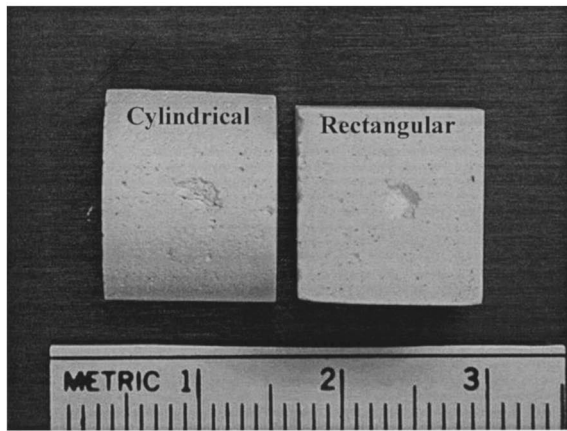
FIG. 11. Effects of sample shape and size on stress field. Photoelastic images of (a) 50-mm long bar with semi-cylindrical head (left) and 14-mm diameter disk (right); (b) 50-mm long rectangular bar (left) and 14-mm-long rectangular disk (right); and (c) 20-mm diameter disk (left) and 14-mm diameter disk (right). Sample material: epoxy. Cross-section area of the rectangular bar is 12.7×12.7 mm (L×W), and the thickness of the disk is 12.7 mm.

was produced at the site of shock wave entrance [Fig. 12(a)]. This damage pattern is characteristic of cavitation erosion, caused by the violent collapse of cavitation bubbles near a solid boundary.^{4,5} Second, near the posterior surface of the stone phantom a transverse crack was produced, breaking the phantom into two large pieces along a fracture plane perpendicular to the incident LSW [Fig. 12(b)]. In the cylindrical sample, an additional longitudinal crack was formed parallel to the symmetry axis of the incident LSW, splitting the back piece into two parts. We speculated that both the longitudinal and transverse cracks were due to spalling, which is the failure of brittle materials primarily under reflected tensile waves.²⁹

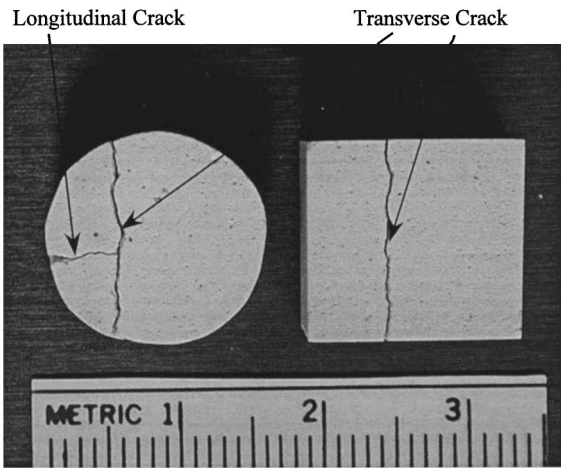
2. Effects of different stress waves on spalling damage

One common theory of spalling damage in SWL is that

when the leading compressive component of the P_T wave is reflected from the posterior surface of the stone, a reflected tensile wave will be generated due to the decrease in acoustic impedance from the stone material to the surrounding fluid.^{11,30} This reflected tensile wave, propagating backwards into the stone, will first superimpose with the remaining portion of the incident compressive component of the P_T wave and lead to a mutual reduction of their respective amplitudes. Subsequently, as the reflected tensile wave propagates further into the stone and superimposes with the trailing tensile component of the P_T wave, a much stronger tensile stress will be produced. If the superimposed tensile stress exceeds the tensile failure strength of the stone material, crack formation will be initiated. Under repeated shock wave impact, individual cracks will extend and coalesce with each other, eventually leading to spalling damage.¹⁸ Theoretically, if the tensile stress of either the incident LSW or the reflected P_T



a)

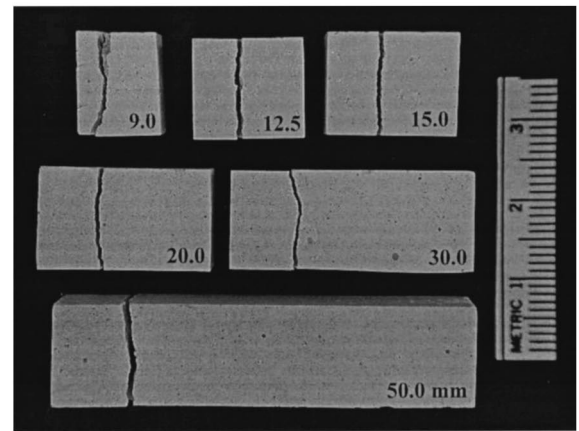


b)

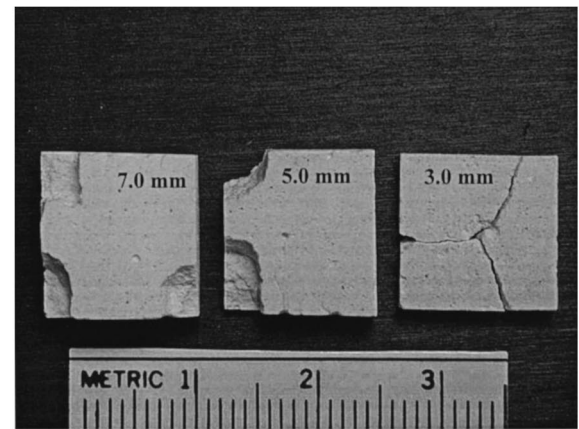
FIG. 12. Representative damage modes of the plaster-of-Paris stone phantoms after shock wave exposure. (a) cavitation erosion at the anterior surface of the stone phantom facing the incident LSW; and (b) spalling near the posterior surface of the stone phantom (the LSW propagates from right to left).

wave is strong enough (or the stone material is very fragile), multiple fracture planes perpendicular to the symmetry axis of the incident LSW could be produced.³¹

To test this theory, a series of cylindrical plaster-of-Paris samples with the same rectangular cross-sectional area (12.7×12.7 mm) but different lengths was prepared and exposed to the LSWs. The longitudinal axis of the sample was aligned with the incident shock wave (normal incidence), so that only P waves would be produced near the longitudinal axis of the phantom. This was confirmed by plotting the wavefront position of P_T , P_{TR} , and S waves in the rectangular phantoms using the ray-tracing method. The advantage of this arrangement is that it provides an idealized configuration to test the effect of the reflected tensile wave on spalling damage. It was found that in long phantoms (9 to 50 mm) the transverse crack could be produced consistently [Fig. 13(a)]. However, in short phantoms (3, 5, and 7 mm) only corner fractures or longitudinal cracks were observed [Fig. 13(b)]. The 7.0-mm-long phantoms appear to be in the transition region; sometimes a transverse crack was produced, while at other times only corner fractures were ob-



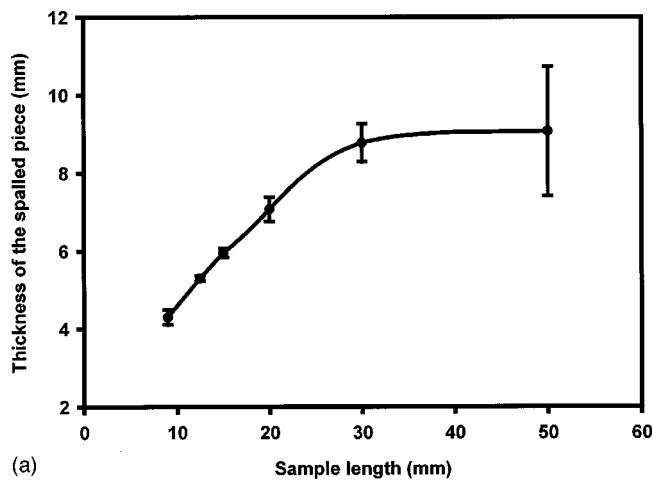
a)



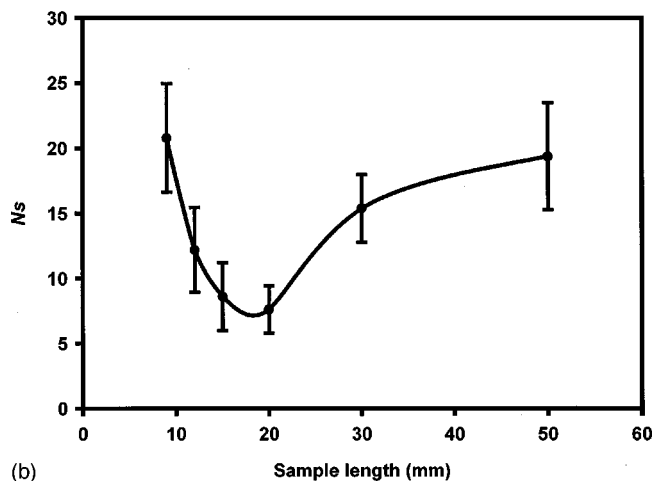
b)

FIG. 13. Damage patterns of rectangular stone phantoms (12.7×12.7 mm, H×T) of different length. (a) transverse crack formation in samples longer than 9 mm (LSW propagates from right to left); and (b) corner fracture and longitudinal crack formation in samples shorter than 7 mm (images show the posterior surface of the sample).

served. One interpretation of the result is that there is an optimal distance, d_o , from the posterior surface of the phantom where constructive superposition of the reflected P_{TR} wave and the tensile component of the incident P_T wave yields the strongest tensile stress inside the phantom. This optimal distance can be estimated by $d_o = c_p \times \Delta t / 2$, where c_p is the P wave speed in the phantom material and Δt is the time interval between the peak positive and peak negative pressure of the LSW. Based on the pressure waveform in Fig. 3, Δt is estimated to be around $3.0 \mu\text{s}$. Hence, for the plaster-of-Paris stone phantoms used in this study, d_o would be about 3.8 mm. This predicted value is very close to the thickness of the spalling piece of the 9-mm phantom. Furthermore, as the sample becomes longer the thickness of the spalling piece was found to increase as well [Fig. 14(a)]. This may be due to pulse broadening as a result of wave scattering from inhomogeneities as the P_T wave propagates inside the phantom.³² Consequently, Δt and thus d_o will increase as the sample length increases. The number of shocks needed to produce the transverse crack (N_S), however, was not found to increase monotonically with the sample length, but rather achieved a minimal value in the 20-mm-long phantoms [Fig. 14(b)].



(a)



(b)

FIG. 14. The correlation between sample length and (a) the thickness of the spalled piece, and (b) the number of shocks needed to produce the transverse crack (N_s). Stone phantoms are rectangular samples of the same cross section area (12.7×12.7 mm, H \times T) but different length.

To determine the origin of the transverse crack, several additional 15-mm-long samples were exposed to about half to two-thirds of the number of shock waves that are needed to produce spalling damage; therefore, no apparent transverse cracks were produced. The samples were then cut along their longitudinal axis using a diamond saw, and the exposed internal surface was examined under an optical microscope. It was found that microcracks were initiated near the longitudinal axis of the sample and oriented parallel to the reflected P_{TR} wavefront (Fig. 15). The tensile stress associated with the P_{TR} wavefront, which presumably is the strongest along the longitudinal axis, could initiate the microcrack. In fact, microcrack opening due to tensile stress normal to the crack length is the most predominant damage mode (opening mode) for the failure of brittle materials.³² Upon further shock wave impact, the microcrack will extend outwards to the lateral surface of the phantom, which eventually leads to the formation of the transverse crack. Using spherical plaster-of-Paris stone phantoms, Dahake and Gracewski have reported similar observations of internal microcrack formation near caustic lines before spalling damage was produced.¹⁷

Considering that the attenuation (both geometrical

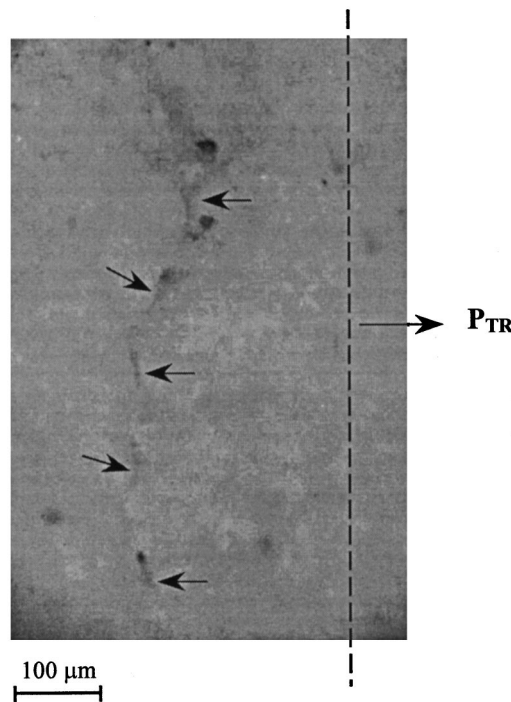


FIG. 15. Micrograph showing the formation of microcracks (indicated by small arrowheads) near the longitudinal axis of a rectangular sample. The microcracks were formed in a plane parallel to the reflected P_{TR} wavefront (indicated by a dashed line).

spreading and wave scattering) of the P_T and P_{TR} waves inside the phantom will increase with the distance they propagate inside the material, the pressure amplitudes at both the P_T and P_{TR} wavefronts should be larger in small samples. Therefore, one would expect that N_s would decrease monotonically as the sample length shortens. However, the results of N_s vs sample length [see Fig. 14(a)] showed otherwise, indicating that other stress waves (especially shear wave) may also contribute to the formation of the transverse crack. To assess this possibility, the wavefront position of the S wave at the moment when it passed through the transverse plane in which the microcrack was initiated was determined for samples of various lengths using the ray-tracing method. Three representative examples are plotted in Fig. 16. It was found that the longer the sample, the deeper the S wave would propagate toward the longitudinal axis of the sample, which increases its chance to interact with the microcrack initiated by the P_{TR} wave. Since the wavefront of the S wave is approximately parallel to the plane of the microcrack surface, the shear stress associated with the S wave could open up the microcrack tip and further facilitate its extension and propagation along the transverse plane. This is the second predominant damage mode (sliding mode) for the failure of brittle materials.³² The interaction of the S wave with microcracks initiated by the P_{TR} wave could explain the reduction in N_s as the sample length increases from 9 to 20 mm [see Fig. 14(b)]. On the other hand, the gradual increase in N_s as the sample becomes longer than 30 mm might be due to the much higher attenuation of the P_T , P_{TR} , and S waves in long samples, even though the S wave could reach closer to the longitudinal axis.

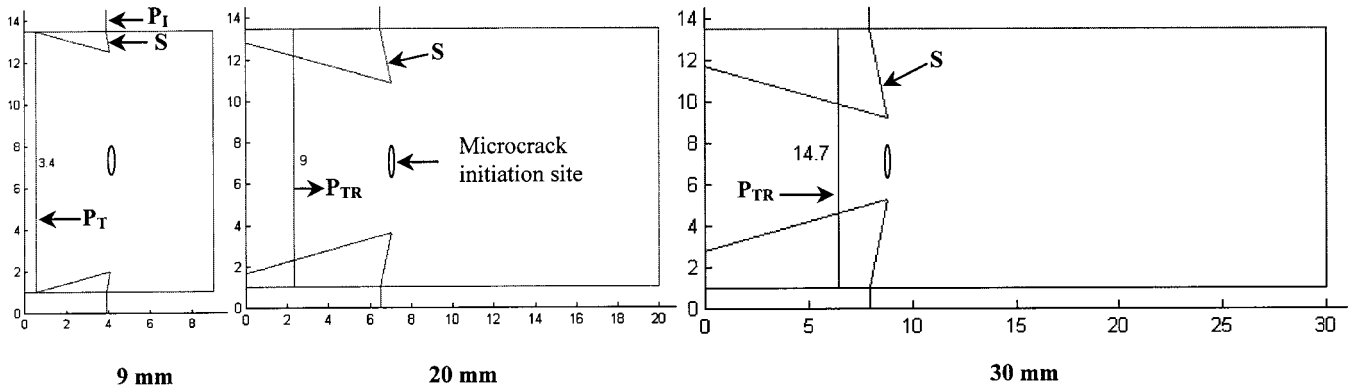
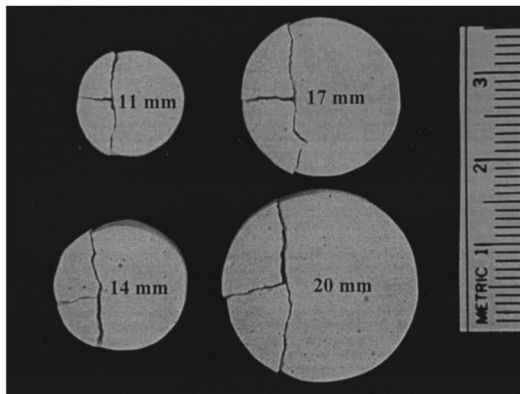


FIG. 16. Theoretical (ray-tracing) prediction of the distribution of stress wavefronts in rectangular samples of different length as the transmitted S wave passes through the transverse plane where the microcracks were initiated.

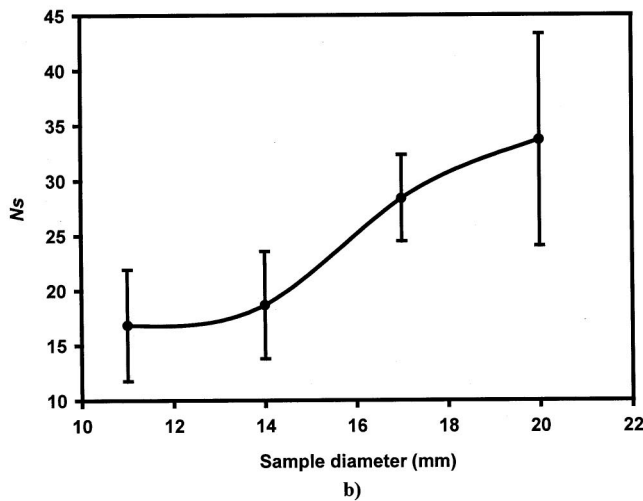
3. Effects of size and geometry on spalling damage

The effects of stone size and geometry on spalling damage were examined by using circular phantoms of the same thickness (12.7 mm) but different diameters, and by comparing the fragility of cylinders with rectangular vs circular cross sections. It was found that although the damage pattern was similar in circular samples of different diameters [Fig. 17(a)], the value of N_S increased monotonically with the

sample size [Fig. 17(b)]. This is presumably due to the higher stress concentration produced by the incident LSW in smaller cylindrical samples [see Fig. 11(c)]. Furthermore, the relative position of the transverse crack (determined by the ratio between the distance from the transverse crack to the back pole and the sample diameter) was found to be about 0.31 and almost independent of the sample size (Table III). To provide a theoretical insight on this experimental observation, the ray-tracing method was used to determine the geometrical foci of the reflected P_{TR} and S_{TR} waves, respectively. The results for the 20-mm-diameter cylindrical phantom are shown in Fig. 18, in which the position of the wavefront is normalized by the sample diameter. The caustics on the symmetry axis were calculated based on the methods described by Gracewski and associates.¹⁶ It was found that the caustic of the reflected P_{TR} wave on the horizontal axis of the cylindrical sample is about 0.29, very close to the value measured experimentally. In contrast, the caustic of the reflected S_{TR} wave on the horizontal axis of the cylindrical sample was found to be about 0.35. These calculations indicated that the transverse crack in the cylindrical sample was initiated by the reflected P_{TR} wave. Similar values were obtained for cylindrical samples of 11 to 17 mm in diameter. It is also interesting to note in Fig. 18 that the transverse crack did not extend along the profile of the P_{TR} wave, which diverges after passing its focus. Instead, the transverse crack extended along a direction almost parallel to the profile of the transmitted S wave (indicated by the dashed line in Fig. 18). This finding again supports the claim that the S wave helps to extend and propagate the microcrack initiated by the P_{TR} wave. It should be noted that although the microcrack was not initiated at the caustic of the reflected shear wave, its extension in the early stage could also be facilitated by the reflected shear wave.³³ In addition, because the P_{TR} wave is



a)



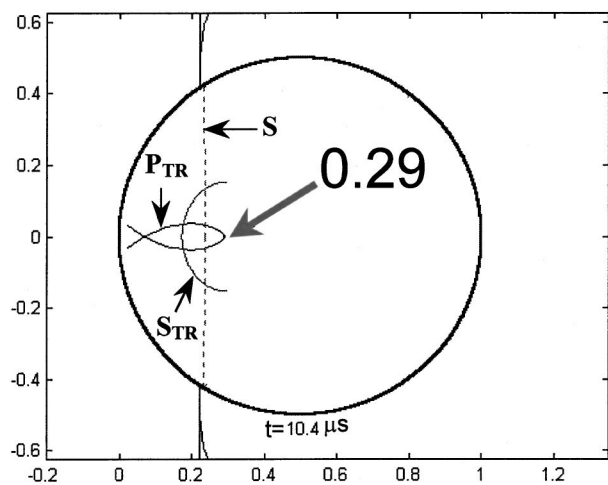
b)

FIG. 17. Spalling in cylindrical phantoms of different diameters; (a) general damage patterns, and (b) the correlation between sample diameter and the number of shocks needed to produce the transverse crack (N_S).

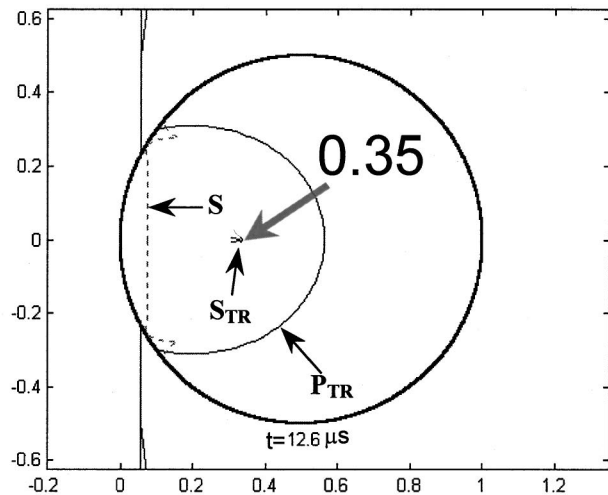
TABLE III. The relative position of the transverse crack in cylindrical samples.

Sample diameter (mm)	11	14	17	20
Relative position	0.314	0.318	0.300	0.306
Std. dev.	0.014	0.011	0.008	0.023

Relative position=Distance from the transverse crack to the backpole/ Sample diameter.



a)



b)

FIG. 18. Theoretical (ray-tracing) prediction of the focusing position of the (a) reflected P_{TR} wave, and (b) reflected S_{TR} wave in a plaster-of-Paris disk sample ($D=20$ mm).

reflected from a pressure-release boundary, the incident waveform will be inverted, yielding a leading tensile wave followed by a weak compressive wave. When the P_{TR} waves reflected from the upper and lower surface of the samples with circular cross section cross each other along the horizontal symmetry axis of the phantom [see frame $t=7\ \mu\text{s}$ in Fig. 5 and Fig. 18(a)], much stronger tensile stresses will be produced. This explains the formation of the longitudinal crack in the samples with circular cross sections [see Fig. 12(b) and Fig. 17(a)].

To assess the effect of stone geometry on spalling damage, fragmentation tests were carried out using cylindrical samples with circular (14 mm in diameter and 12.7 mm thick) and rectangular ($14\times 14\times 12.7$ mm, $L\times H\times T$) cross sections of similar sizes. The number of shocks needed to break the cylindrical samples with circular cross sections (20.0 ± 5.51 , mean value \pm s.d.) was found to be about two-thirds of that with the rectangular cross sections (30.67 ± 9.03). This finding is consistent with the results of stress concentration revealed by photoelastic imaging (see Fig. 11), which confirms the focusing effect of the cylindrical boundary on the reflected P_{TR} wave. In addition, the S wave induced in the cylindrical sample is transversely continuous across the sample. Therefore, it could help to extend the microcrack induced by the reflected P_{TR} wave from the very beginning after the initiation of the microcrack. In contrast, in the rectangular phantom the S wave was generated at the lateral edges and would only shift slightly towards the longitudinal axis as it propagated inside the phantom (see Fig. 16). Therefore, the interaction of the S wave with the microcrack would occur at a much later stage of the crack propagation. This, combined with the fact that the reflected P_{TR} wave is much weaker in the rectangular phantom, contributes to the increased number of shocks needed to produce a transverse crack in a rectangular sample than a circular sample of similar size.

V. SUMMARY

Using a dynamic photoelastic imaging technique, the transient stress fields produced in solids of different geometries and sizes exposed to LSWs were investigated. Various stress waves (both P and S) induced by the impact of the LSWs could be identified and their general pattern of propagation and evolution inside the solid were found to be predictable by a simple ray-tracing model. In addition, the effects of various stress waves on spalling damage was analyzed, and the primary findings can be summarized as follows:

- (1) Spalling, in the form of transverse and longitudinal crack formation near the posterior surface of the stone, is initiated by the reflected tensile wave. The location of the microcrack depends on stone geometry and size, and is influenced by the temporal profile of the LSW.
- (2) The transmitted shear stress wave can help to extend and propagate the microcracks initiated by the reflected tensile wave. This enhancement is most effective when the shear wavefront is parallel to the crack length.

ACKNOWLEDGMENTS

This work was supported in part by NIH through Grants Nos. RO1-DK52985 and PO1-DK20543.

¹E. Steiger, "Full wave modeling of lithotripter fields," in Proceedings of the 16th International Congress on Acoustics and the 135th Meeting of Acoustic Society of America **4**, 2795–2796 (1998).

²M. A. Averkiou and R. O. Cleveland, "Modeling of an electrohydraulic lithotripter with the KZK equation," J. Acoust. Soc. Am. **106**, 102–112 (1999).

³C. C. Church, "A theoretical study of cavitation generated by an extracorporeal shock wave lithotripter," J. Acoust. Soc. Am. **86**, 215–227 (1989).

⁴A. J. Coleman, J. E. Saunders, L. A. Crum, and M. Dyson, "Acoustic cavitation generated by an extracorporeal shockwave lithotripter," Ultrasound Med. Biol. **13**, 69–76 (1987).

⁵L. A. Crum, "Cavitation microjets as a contributory mechanism for renal

- calculi disintegration in ESWL," J. Urol. (Baltimore) **140**, 1587–1590 (1988).
- ⁶W. Sass, M. Braunlich, H. P. Dreyer, E. Matura, W. Folberth, H. G. Preismeyer, and J. Seifert, "The mechanisms of stone disintegration by shock waves," *Ultrasound Med. Biol.* **17**, 239–243 (1991).
- ⁷P. Zhong, C. J. Chuong, and G. M. Preminger, "Propagation of shock waves in elastic solids caused by the impact of cavitation microjets. II. Application to extracorporeal shock wave lithotripsy," J. Acoust. Soc. Am. **94**, 29–36 (1993).
- ⁸M. Delius, M. Jordan, H. Liebich, and W. Brendel, "Biological effects of shock waves: Effect of shock waves on the liver and gallbladder wall of dogs—administration rate dependence," *Ultrasound Med. Biol.* **16**, 459–466 (1990).
- ⁹M. Delius, "Minimal static excess pressure minimises the effect of extracorporeal shock waves on cells and reduces it on gallstones," *Ultrasound Med. Biol.* **23**, 611–617 (1997).
- ¹⁰P. Zhong, Y. F. Zhou, and S. L. Zhu, "Dynamics of bubble oscillation in constrained media and mechanisms of vessel rupture in SWL," *Ultrasound Med. Biol.* **27**, 119–134 (2001).
- ¹¹C. Chaussy, E. Schmiedt, D. Jocham, V. Walther, W. Brendel, B. Forssmann, and W. Hepp, *Extracorporeal Shock Wave Lithotripsy: New Aspects in the Treatment of Kidney Stone Disease*, edited by C. Chaussy (Karger, Basel, 1982).
- ¹²C. J. Chuong, P. Zhong, H. J. Arnott, and G. M. Preminger, "Stone damage modes during piezoelectric shock wave lithotripsy," in *Shock Wave Lithotripsy II: Urinary and Biliary*, edited by J. E. Lingeman and D. M. Newman (Plenum, New York, 1989), Chap. 20, pp. 103–106.
- ¹³S. R. Khan, R. L. Hackett, and B. Finlayson, "Morphology of urinary stone particles resulting from ESWL treatment," J. Urol. (Baltimore) **136**, 1367–1372 (1986).
- ¹⁴C. J. Chuong, P. Zhong, and G. M. Preminger, "Acoustic and mechanical properties of renal calculi: Implication in shock wave lithotripsy," J. Endourology **7**, 437–444 (1993).
- ¹⁵P. Zhong, C. J. Chuong, and G. M. Preminger, "Characterization of fracture toughness of renal calculi using a microindentation technique," J. Mater. Sci. Lett. **12**, 1460–1462 (1993).
- ¹⁶S. M. Gracewski, G. Dahake, Z. Ding, S. J. Burns, and E. C. Everbach, "Internal stress wave measurements in solids subjected to lithotripter pulses," J. Acoust. Soc. Am. **94**, 652–661 (1993).
- ¹⁷G. Dahake and S. M. Gracewski, "Finite difference predictions of P - SV wave propagation inside submerged solids. II. Effect of geometry," J. Acoust. Soc. Am. **102**, 2138–2145 (1997).
- ¹⁸M. Lokhandwalla and B. Sturtevant, "Fracture mechanics model of stone comminution in ESWL and implications for tissue damage," *Phys. Med. Biol.* **45**(7), 1923–1940 (2000).
- ¹⁹Reference shock wave hydrophone system™ User's Manual, Sonics Industries, Hatboro, PA (1997).
- ²⁰C. P. Burger, "Photoelasticity," in *Hand Book on Experimental Mechanics*, edited by A. S. Kobayashi (VCH, New York, 1993), Chap. 5, pp. 165–266.
- ²¹W. F. Riley and J. W. Dally, "A photoelastic analysis of stress wave propagation in a layered model," *Geophysics* **31**, 881–889 (1966).
- ²²A. Kuske, "Photoelastic research on dynamic stresses," *Exp. Mech.* **6**, 105–112 (1966).
- ²³I. M. Daniel and R. L. Marino, "Wave propagation in a layered model due to point source loading in a high-impedance medium," *Geophysics* **36**, 517–532 (1971).
- ²⁴X. F. Xi and P. Zhong, "Improvement of stone fragmentation during shock wave lithotripsy using a combined EH/PEAA shock wave generator—*In vitro* experiments," *Ultrasound Med. Biol.* **26**, 457–467 (2000).
- ²⁵C. J. Chuong, P. Zhong, and G. M. Preminger, "A comparison of stone damage caused by different modes of shock wave generation," J. Urol. (Baltimore) **148**, 200–205 (1992).
- ²⁶T. C. T. Ting, E. H. Lee, "Wave-front analysis in composite materials," *J. Appl. Mech.* **91**, 497–504 (1969).
- ²⁷A. J. Coleman and J. E. Saunders, "A survey of the acoustic output of commercial extracorporeal shock wave lithotripters," *Ultrasound Med. Biol.* **15**, 213–227 (1989).
- ²⁸A. Philipp and W. Lauterborn, "Cavitation erosion by single laser-produced bubbles," *J. Fluid Mech.* **361**, 75–116 (1998).
- ²⁹H. Kolsky, *Stress Waves in Solids* (Dover, New York, 1963).
- ³⁰K. Kambe, M. Kuwahara, S. Orikasa, and K. Takayama, "Mechanism of fragmentation of urinary stones by underwater shock wave," *Urol. Int.* **43**, 275–281 (1988).
- ³¹J. S. Rinehart, *Stress Transients in Solids* (Hyperdynamics, Santa Fe, NM, 1975).
- ³²B. Lawn, *Fracture of Brittle Solids* (Cambridge University Press, Cambridge, UK, 1993); M. T. Carnell and D. C. Emmony, "A Schlieren study of the interaction between a lithotripter shock wave and a simulated kidney stone," *Ultrasound Med. Biol.* **21**, 721–724 (1995).
- ³³J. F. Silva-Gomes and S. T. S. Al-Hassani, "A note on times to fracture in solid perspex spheres due to point explosive loading," *Int. J. Mech. Sci.* **18**, 543–545 (1976).

Characteristics of whistles from the acoustic repertoire of resident killer whales (*Orcinus orca*) off Vancouver Island, British Columbia

F. Thomsen^{a)} and D. Franck

Zoologisches Institut und Zoologisches Museum, Arbeitsbereich Ethologie, Universität Hamburg,
Martin-Luther-King-Platz 3, D-20146 Hamburg, Germany

J. K. B. Ford

Vancouver Aquarium, Marine Science Centre, P.O. Box 3232, Vancouver, British Columbia V6B 3X8,
Canada

(Received 9 May 2000; revised 18 December 2000; accepted 22 December 2000)

The acoustic repertoire of killer whales (*Orcinus orca*) consists of pulsed calls and tonal sounds, called whistles. Although previous studies gave information on whistle parameters, no study has presented a detailed quantitative characterization of whistles from wild killer whales. Thus an interpretation of possible functions of whistles in killer whale underwater communication has been impossible so far. In this study acoustic parameters of whistles from groups of individually known killer whales were measured. Observations in the field indicate that whistles are close-range signals. The majority of whistles (90%) were tones with several harmonics with the main energy concentrated in the fundamental. The remainder were tones with enhanced second or higher harmonics and tones without harmonics. Whistles had an average bandwidth of 4.5 kHz, an average dominant frequency of 8.3 kHz, and an average duration of 1.8 s. The number of frequency modulations per whistle ranged between 0 and 71. The study indicates that whistles in wild killer whales serve a different function than whistles of other delphinids. Their structure makes whistles of killer whales suitable to function as close-range motivational sounds. © 2001 Acoustical Society of America. [DOI: 10.1121/1.1349537]

PACS numbers: 43.80.Ka, 43.80.Lb, 43.80.Jz [WA]

I. INTRODUCTION

Odontocete social sounds are generally of two fundamental physical types: pulsed sounds, often referred to as pulsed calls, and tonal sounds, referred to as whistles (Popper, 1980). Generally one of each type, or both types of sounds, play an important role in the acoustic communication of most odontocete species (Herman and Tavolga, 1980; Evans, 1990; Tyack, 1998). Whistles are important in the underwater communication of most members of the dolphin family (Herman and Tavolga, 1980; Evans, 1990; Richardson *et al.*, 1995; Tyack, 1998).

For killer whales (*Orcinus orca*), the emphasis of acoustic studies has been on pulsed vocalizations and their relation to social organization, genealogy, and behavior (Ford and Fisher, 1983; Ford, 1989, 1991; Bain, 1986; Hoelzel and Osborne, 1986; Strager, 1996; Deecke *et al.*, 1999). Killer whales off British Columbia have stable, pod-specific repertoires of stereotyped discrete pulsed calls (Ford and Fisher, 1983; Ford, 1989, 1991). Ford (1989) suggests that discrete calls are used to maintain contact between group members and serve as indicators of group affiliation (Ford, 1989, 1991).

The whistles of killer whales have received little study and their function in killer whale underwater communication remains completely unclear. Schevill and Watkins (1966) recorded sounds of a captive subadult male collected from the

waters off British Columbia and found no whistle emissions from this animal. Since then, whistles have been described by Steiner *et al.* (1979) and Awbrey *et al.* (1982) from killer whales off Newfoundland and the Antarctic respectively. Dahlheim and Awbrey (1982) reported an average frequency of 5 kHz and an average duration of 2.3 s of whistles from captive individuals collected from different locations. Ford and Fisher (1983) and Hoelzel and Osborne (1986) reported whistles from wild killer whales off the coast of British Columbia. Ford (1989) noted a frequency range between 1.5 kHz and 18 kHz with the most energy between 6 and 12 kHz. Whistle durations ranged from 50 ms to 10–12 s. These reports gave valuable basic information on some parameters of whistles. However, no detailed quantitative characterization of whistles from wild killer whales has been undertaken to date. There is no information on fine-scale physical characteristics of this sound class nor on general structural characteristics; for example, the complexity of these sounds indicated by duration and number of frequency modulations. Therefore, an interpretation of possible functions of whistles in killer whale underwater communication has been impossible.

Here we report our findings from a study of the structure of whistles from wild killer whales off Vancouver Island, British Columbia. Parameters of whistles from groups of individually known killer whales are presented. Results of a fine-scale waveform analysis are described, as are investigations on dominant carrier frequencies of whistles in this

^{a)}Electronic mail: frank.thomsen@gkss.de

population. Based on our results, possible functions of whistles for the communication in wild killer whales will be discussed.

II. METHODS

A. Study population

We studied killer whales from the northern community of resident killer whales off Vancouver Island, British Columbia. Resident killer whales live in stable matrilineal groups of 2 to 14 animals and feed primarily on fish (Bigg *et al.*, 1990; Ford *et al.*, 1998, 2000). The northern resident community ranges from mid-Vancouver Island north to southeastern Alaska (Bigg *et al.*, 1990; Ford *et al.*, 2000). In 1996/1997 the northern resident community comprised approximately 215 individuals in 33 matrilines (Ford *et al.*, 2000; Graeme Ellis, personal communication).

B. Data collection

Acoustic recordings and surface behavioral observations were made in western Johnstone Strait and adjacent waters, British Columbia (50° 30' N, 126° 35' W). The study was conducted between July 1 and October 13, 1996 and July 11 and October 17, 1997. Most of the data were obtained from two 20-m motorvessels on 3–9 (average 4.5) h long commercial whale-watching excursions based from Telegraph Cove (northern Vancouver Island). Additionally some recordings were obtained from small (<2 m) outboard powered inflatables and motorboats. A total of 222 excursions were undertaken in 1996 and 1997 with more than 1000 h spent at sea. Killer whales were observed on 196 excursions with approximately 200 h observation time. Underwater sounds were recorded with a Bruel and Kjaer 8101 hydrophone in 1996, and an Offshore Acoustics hydrophone in 1997 (sensitivity: greater than -180 dB *re*: 1 V/ μ Pa). Recordings were made on Sony 60-, 90- and 120-min digital audio tapes using Sony TCD-D8 (1996) and Sony TCD-D7 (1997) DAT recorders (system frequency response: 20 Hz–20 kHz ± 1 dB). Simultaneous voice recordings of behavioral observations were made on a separate track of the same tape. Killer whale individuals were identified by natural markings on the dorsal fin and back (Ford *et al.*, 1994). A total of 167 recordings with a total length of 40 h were obtained.

C. Behavior categories

Based on surface behavior observations, the activities of killer whales were classified into two long-range and two short-range categories (modified from Ford, 1989; Barrett-Lennard *et al.*, 1996).

Long-range categories were defined as the distance between observed animals of more than one body length. One is foraging. During foraging whales were usually dispersed over a wide area. Nondirectional swimming, irregular diving patterns, and varying swimming speeds with short periods of high speed swimming at the surface indicated foraging ac-

tivities. Another category is slow traveling, loosely organized groups on a consistent course of 3 to 6 km/h. Short-range categories were defined by the distance between observed animals of less than one body length. One category is social traveling by a closely knit group on a consistent course at 3 to 6 km/h. During social traveling whales engaged sporadically in interactions such as body contact or in activities such as flipper or fluke slapping. A second category is socializing. Socializing whales group together, often in body contact, and engage in social displays and interactions such as breaching, flipper and fluke slapping, chasing each other, rolling over each other, and sexual interactions. During socializing killer whales made little or no consistent progress.

D. Acoustic analysis

The selection of whistles was done with the bioacoustics software, RTS, version 2.0 (Engineering Design, Inc.). To avoid aliasing, a Frequency Device 901 low-pass filter set at 20-kHz corner frequency was used before the signal was digitized. The signal was then sampled at 50 kHz (16 bit), giving a real-time spectrogram with a range of 0–20 kHz. The dynamic range was set at 42 dB. A continuous color-enhanced 512 point spectrographic display with a 98-Hz frequency resolution and a simultaneous waveform display, both in a 4-s window, were viewed. The recordings were then re-played and killer whale sounds were classified into the categories listed below (modified from Ford, 1989):

Pulsed calls are sounds made up of pulses generated at a high rate. In spectrographic analysis, these pulses are resolved as sidebands equivalent to the pulse repetition rate (Watkins, 1967). Repetition rates range from 2.5 to 4 kHz. The main energy is usually between 1 and 6 kHz. Pulsed calls are further divided into discrete calls, which are calls that are repetitive, remain stable over years, and are pod specific (Ford and Fisher, 1983; Ford, 1989, 1991); variable calls are calls that are nonrepetitive with a variety of forms such as squeaks, squawks, grunts, and growls. Variable calls were usually rich in sidebands and low in frequency (1–4 kHz).

Whistles are sounds based on a tonal format, generally with a continuous waveform which appears in spectrographic analysis as a narrow-band tone with or without harmonics. Ford (1989) reported frequencies between 1.5 and 18 kHz with the most energy between 6 and 12 kHz.

Problems seldom arose in distinguishing discrete calls from whistles. However, problems sometimes occurred in distinguishing higher pitched variable calls from whistles. If doubts were present from spectrographic analysis as to whether to assign a sound to the call or whistle category, the decision was made aurally. Whistles sound soft-high pitched “whistlelike,” whereas pulsed calls generally sound harsh, metallic, and screamlike.

A total of 200 whistles were selected for further analysis. We chose 50 whistles randomly from each of the 4 behavior categories. Whistles were then digitized directly with the bioacoustics-software SIGNAL, version 3.0 (Engineering Design, Inc.). High-resolution color spectrograms were calculated using a Hanning Window and a 512 point FFT (over-

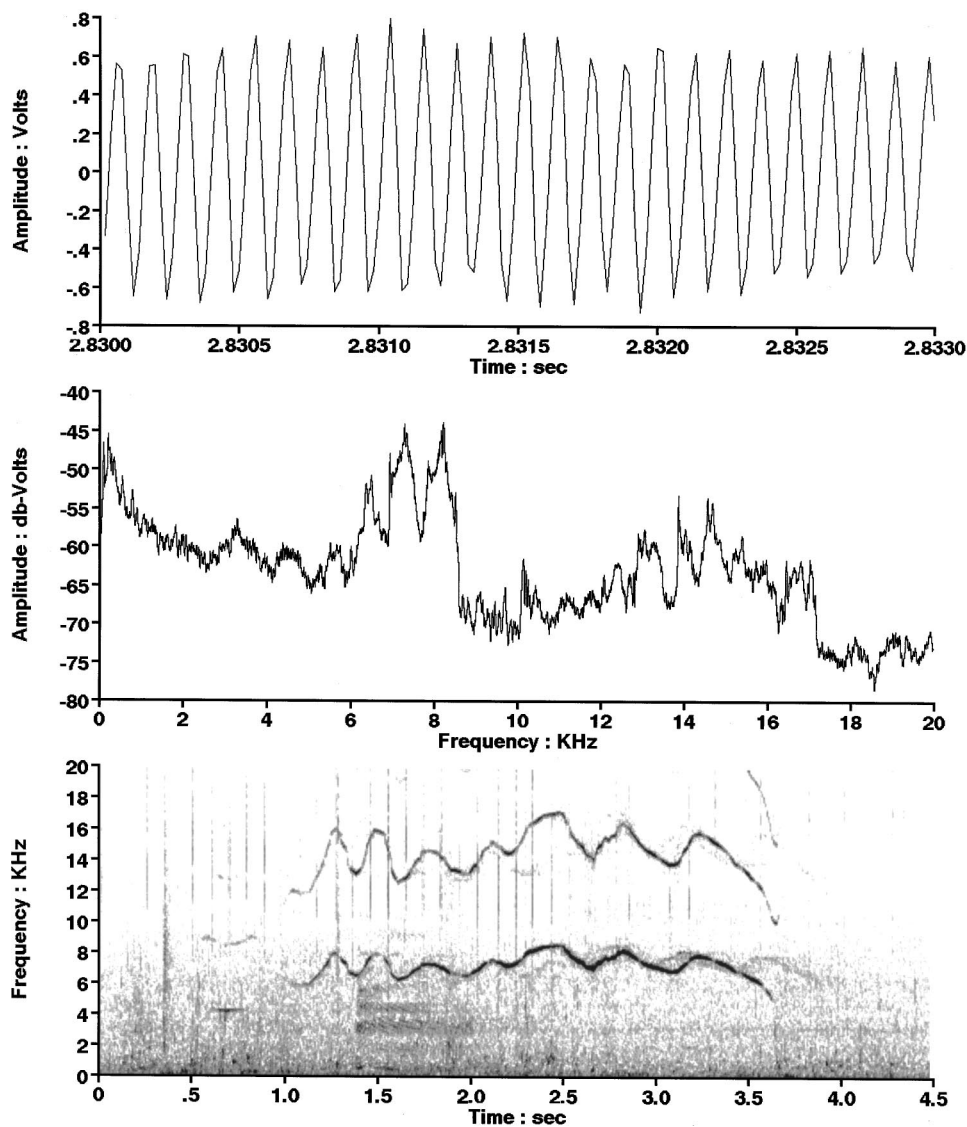


FIG. 1. Spectrogram (below), power-spectrum (mid), and section (3 ms, above) of the time waveform of a whistle with harmonics. The whistle starts at 4 kHz rises up to 8 kHz and ends after 3 s at 5 kHz. This whistle has a dominant frequency between 7 and 8 kHz. Vertical lines in the spectrogram: sonar-clicks. Spectrogram: DF=98 Hz, DT=10.2 ms, FFT=512 points. The oscillogram above shows a continuous waveform of 8 kHz.

lap: 50%). Based on visual inspection of the spectrogram, sections of interest were analyzed in detail. We performed a waveform analysis and selected several 3-ms long sections of the signal to investigate fine-scale temporal patterns. These sections were then printed. Whistles were then categorized in the classes below. The following parameters were measured for each whistle with cursors directly from the spectrographic display: *start frequency (sf)*; *end frequency (ef)*; *minimum frequency (min.f)*; *maximum frequency (max.f) of the fundamental or the carrier frequency*; *frequency range (max.f-min.f)*; *duration (dur.)*; *number of inflection points (frequency modulations, fm)*. The number of inflection points was defined as a change in slope of the spectrographic contour from negative to positive and vice versa (Steiner, 1981). Additionally the *dominant frequency (df)* was calculated for each whistle using a power spectrum analysis. Power spectra were performed with 32 768 FFT points, frequency resolution of 1.2 Hz, and a time resolution of 818 ms. The dominant frequency was indicated by the main peak in the power spectrum display and was measured with cursors directly from the screen.

III. RESULTS

A. Delectability of whistles

All observations in the field indicate that whistles have a relatively short range of delectability. Regardless of the observed behavior of the whales, whistles were recorded only when whales were relatively close to the recording vessel (<500 m). Whistle recordings of the highest quality were obtained from whales swimming directionally toward the hydrophone at a distance not exceeding 300 m. As whales passed the boat, whistles dropped in volume, quickly indicating a directional effect.

B. Characteristics of whistles

The majority of whistles were tones of a fundamental frequency and harmonics which were integer multiples of the fundamental. The main energy of these sounds was concentrated in the fundamental frequency. The fundamental often showed considerable modulations. The waveform of this sound was continuous (Fig. 1). Sporadically some of the whistles showed higher energy not in the fundamental but in

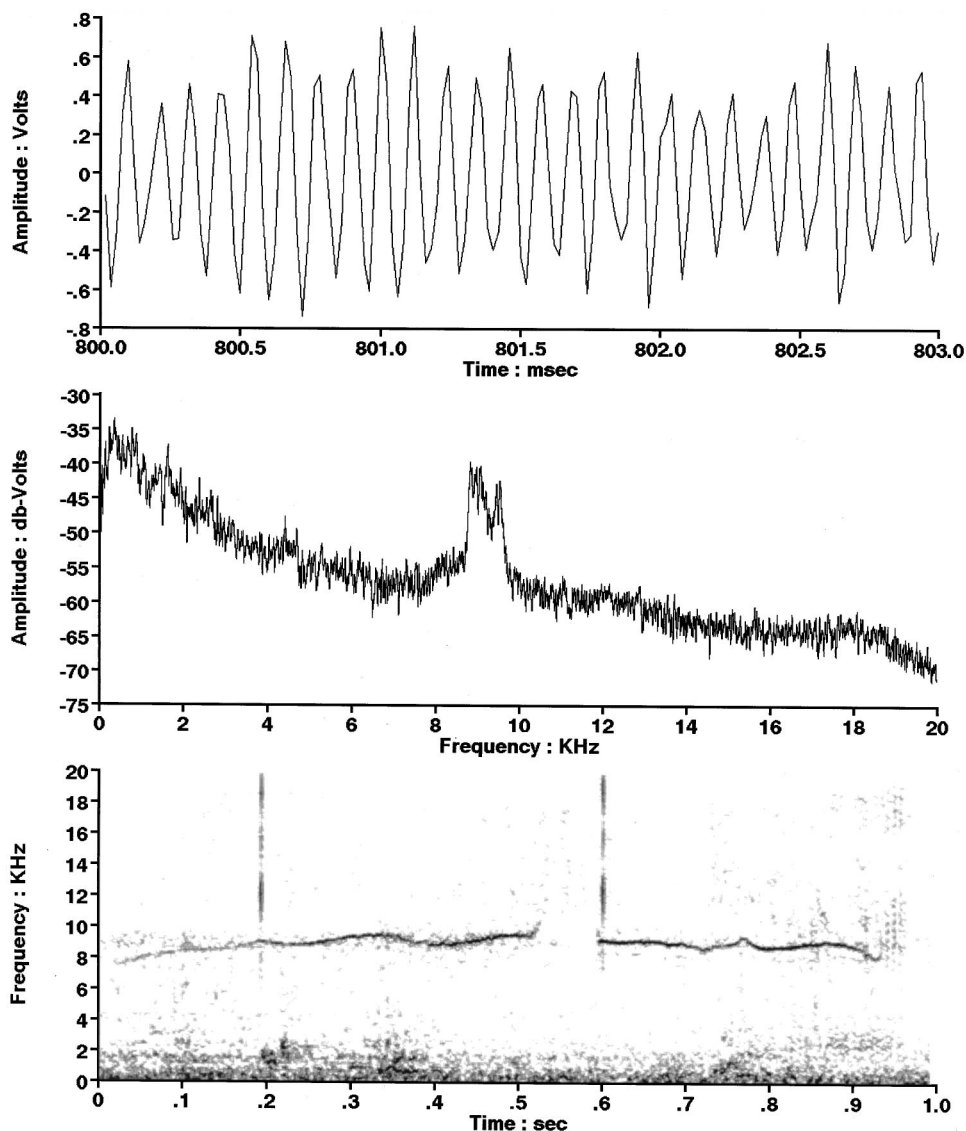


FIG. 2. Spectrogram (below), power-spectrum (mid), and section (3 ms, above) of the time waveform of whistle without harmonics. The whistle starts at 8 kHz and ends at 8 kHz. Duration is 0.9 s. Vertical lines in the spectrogram: sonar clicks. Spectrogram: DF=98 Hz, DT=10.2 ms, FFT=512 points. The oscillogram above shows a continuous waveform of 9 kHz.

one of the higher harmonics. Power spectrum analysis showed a major peak at the level of this enhanced harmonic. The waveform of these sounds showed a high degree of amplitude modulation (Fig. 2). Tones without harmonics were present but rare (Fig. 3).

C. Whistle Parameters

From the 200 selected whistles 180 (90%) were tones with harmonics, 7 (3.5%) were tones with enhanced harmonics, and 13 (6.5%) were tones without harmonics.

The average minimum frequency was 5.4 ± 1.9 kHz (\pm s.d., range 2.4–12.8 kHz). The average maximum frequency was 9.9 ± 2.4 kHz (range 3.6–16.7 kHz). The frequency range of the whistles averaged 4.5 ± 2.2 kHz (range 0.5–10.2 kHz). The dominant frequency averaged 8.3 ± 2.8 kHz (range 3–18.5 kHz). Whistles had an average duration of 1.8 ± 2 s (range 0.06–18.3 s). The average number of frequency modulations was 5 ± 7.8 . The maximum number of frequency modulations in one whistle was 71. Some of the whistles had no frequency modulations.

IV. DISCUSSION

The results of this study show that whistles of northern resident killer whales are physically more complex than previously described. Earlier descriptions which defined whistles as pure tones with little or no harmonic structure (Ford, 1989) should be revised. Our results indicate that pure tones are absent from the acoustic repertoire of killer whales. Whistles without harmonics are rare and are always frequency modulated and therefore not pure. Most whistles emitted by northern resident killer whales are tonal sounds of a fundamental frequency with the addition of several harmonics. It is very likely that most whistles of other killer whale populations are also tones with several harmonics. Published spectrograms of killer whale whistles which are undoubtedly tones without harmonics can be found only in Ford and Fisher (1983). Other published spectrograms of whistles are either difficult to interpret because the frequency range is too limited and possible additional harmonics are therefore not visible (Steiner, 1979; Dahlheim and Awbrey, 1982) or the spectrograms clearly show harmonics (Awbrey, 1982; Hoelzel and Osborne, 1986; Bowles *et al.*, 1988).

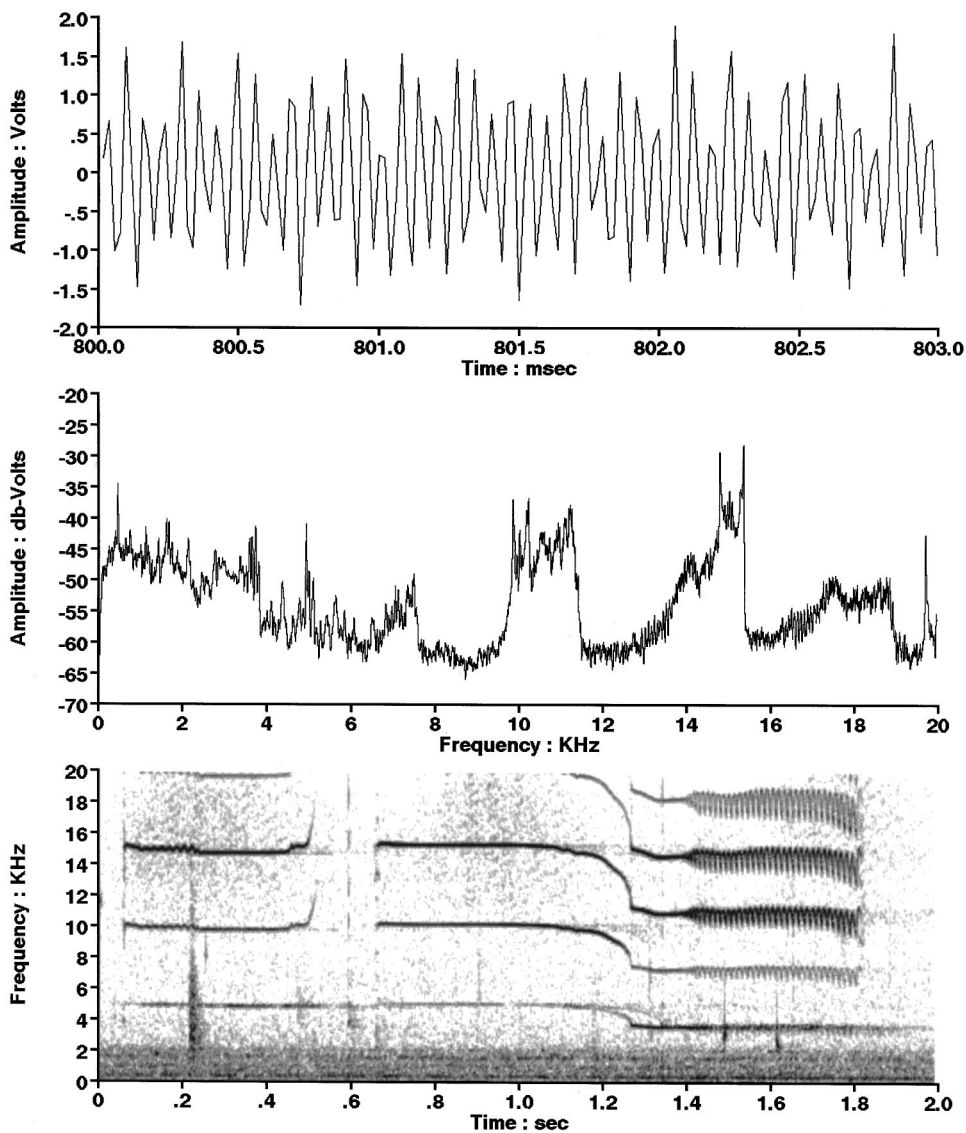


FIG. 3. Spectrogram (below), power-spectrum (mid), and sections (3 ms, above) of the time waveform of a whistle with enhanced higher harmonic. This whistle starts at 5 kHz and falls down to 3 kHz. Duration is 1.8 s. Spectrogram shows a harmonic structure with emphasis on the third harmonic (15 kHz). Vertical lines in the spectrogram: sonar clicks. Spectrogram: DF=98 Hz, DT=10.2 ms, FFT=512 points. The oscillogram above shows a continuous waveform with amplitude modulation.

Therefore most killer whale whistles appear to be structurally similar to those of other delphinids which in most cases show several harmonics (spectrograms in: Lilly and Miller, 1961; Busnel and Dziedzic, 1966, 1968; Caldwell and Caldwell, 1971; Caldwell *et al.*, 1973, 1990; Sjare and Smith, 1986; dos Santos, 1990; Schultz and Corkeron, 1994).

Some of the whistles in our data set contained more energy in higher harmonics and not in the fundamental. This enhancement of higher harmonics has also been described for bottlenose dolphin whistles (Saprykin *et al.*, 1977) and might be the result of pulsation. Pulsed signals are resolved in spectrographic analysis in discrete harmonic bands. The interval between the harmonic bands indicates the pulse repetition rate. The harmonic band where most of the energy is concentrated represents the carrier frequency of the pulsed signal (Schevill and Watkins, 1966; Watkins, 1967; Gerhardt, 1998). Therefore whistles with the most energy concentrated in higher harmonics might be interpreted as pulsed rather than continuous signals. The results of fine-scale waveform analysis are difficult to interpret in our case. On the one hand, the waveform of these whistles never went to zero for consecutive A/D samples and therefore indicated a

continuous sound. On the other hand, recordings obtained from the wild contain noise in the background which might distort the waveform slightly and make it difficult to identify distinctive intervals of zero amplitude. However, if these sounds are pulsed, they are very likely to be perceived as a single tone by the receiver since intervals between harmonic bands exceeded 1 kHz in every case and the temporal resolution of killer whales is limited to pulses with a repetition rate slightly above 1 kHz (Szymanski *et al.*, 1998).

Alternatively enhancement of higher harmonics can be caused by filtering mechanisms in the sound production complex or by sound production in two independent sites, as described for songbirds (Bradbury and Vehrencamp, 1998; Gerhardt, 1998). The site of sound production in delphinids is proposed to be localized pairwise in the upper nasal passages (Au, 1993; Cranford *et al.*, 1996, 1998). It is therefore likely that enhancement of higher harmonics is the result of a biphonation with different energy on different frequencies rather than pulsation.

Whistles of northern resident killer whales have a greater frequency range and a higher dominant frequency than those described by Dahlheim and Awbrey (1982). The

average duration of the whistles is similar. However, whistles exceeding 18 s were not described by Dahlheim and Awbrey (1982) or by Ford (1989). In general, whistles of northern resident killer whales are much more complex than those described for other delphinids. They are comparably longer in duration and contain a greater number of frequency modulations. Whistles from other dolphin species have an average duration from 0.13 s (*Sousa chinensis*) to 1.3 s (*Tursiops truncatus*) (Matthews *et al.*, 1999). The average number of frequency modulations per whistle ranges between 0.04 (*Peponocephala electra*) and 3.43 (*Stenella frontalis*) (Matthews *et al.*, 1999).

It has been hypothesized that in some dolphin species, whistles are acoustic signatures that are used as long-range contact signals among group members when out of sight (Caldwell *et al.*, 1990; Tyack, 1998). To fulfill such a task such signals should be comparably simple in structure and loud, suitable to carry over several hundred meters underwater. In fact source levels of bottlenose dolphin whistles are estimated to be as high as 173 dB *re*: 1 μ Pa @ 1 m giving them a range of at least 1 km (Richardson *et al.*, 1995). Our results indicate that whistles in northern resident killer whales have a different function in underwater communication than those of other delphinids. Our observation that the whistles of northern resident killer whales are short-range sounds are confirmed by recent studies of Miller and Tyack (1999), who measured a consistently "soft" source level of 138 dB *re*: 1 μ Pa @ 1 m of whistles from northern resident killer whales. Observations in the field, as well as investigations on the behavioral context, suggest that northern resident killer whales use whistles mostly during close-range interactions (Ford, 1989; Thomsen *et al.*, in preparation). Structurally more variable and complex signals are suitable to carry information on various motivational states of the signaller at close range (Morton, 1977; Owings and Morton, 1998). Thus their structure makes whistles of northern resident killer whales suitable to coordinate interactions at close range.

V. CONCLUSIONS

This study shows that whistles of killer whales are physically diverse signals with the majority being harmonical sounds. Parameter measurements indicate that they are much more complex than whistles described for other delphinids. Finally, observations during this study indicate that whistles in resident killer whales are mostly close-range sounds.

ACKNOWLEDGMENTS

We are especially grateful to Jim Borrowman and Bill and Donna Mackay for their support of this study. Thanks to Dave Tyre, Brian Sylvester, and Wayne Garton for their help in the field. Steve Wischniowski and Rolf Hicker kindly provided space on their boats for sound recordings. Dave Briggs, Helena Symonds, Paul Spong, Rob Williams, and several others from the Johnstone Strait killer whale research community provided important information on whale locations. Many thanks to Professor Dr. Andreas Elepfandt and

Dr. Karl-Heinz Frommolt (Humboldt-University, Berlin) for their cooperation. Frank Thomsen would like to thank members of the Animal Behavior working group at the University of Hamburg, especially Cord Crasselt, Ralf Wanker, Masoud Yasserli, and Ingo Schlupp for their help. The study was partly funded by a graduate scholarship of the University of Hamburg and by a scholarship of the German Academic Exchange Fund (Bonn). We would like to thank Ralf Wanker for comments on an earlier draft of this paper.

- Au, W. W. L. (1993). *The Sonar of Dolphins* (Springer, New York).
- Awbrey, F. T., Thomas, J. A., Evans, W. E., and Leatherwood, S. (1982). "Ross Sea killer whale vocalizations: Preliminary description and comparison with those of some northern hemisphere killer whales," *Rep. Int. Whal. Commn.* **32**, 667–670.
- Bain, D. E. (1986). "Acoustic behaviour of *Orcinus*: Sequences, periodicity, behavioral correlates and an automated technique for call classification," in *Behavioral Biology of Killer Whales*, edited by B. C. Kirkeveld and J. S. Lockard (Alan R. Liss, Inc., New York), pp. 335–371.
- Barrett-Lennard, L. G., Ford, J. K. B., and Heise, K. A. (1996). "The mixed blessing of echolocation: differences in sonar use by fish-eating and mammal-eating killer whales," *Anim. Behav.* **51**, 553–565.
- Bigg, M. A., Olesiuk, P. F., Ellis, G. M., and Ford, J. K. B. (1990). "Social organization and genealogy of resident killer whales (*Orcinus orca*) in the coastal waters of British Columbia and Washington State," *Rep. Int. Whaling Comm Spec. Issue No.* **12**, 383–405.
- Bowles, A. E., Young, W. G., and Asper, E. D. (1988). "Ontogeny of stereotyped calling of a killer whale calf, *Orcinus orca*, during her first year," in *Rit Fiskeildar, Vol. XI: North Atlantic Killer Whales*, edited by J. Sigurjonsson and S. Leatherwood (Reykjavik), pp. 251–275.
- Bradbury, J. W., and Vehrencamp, S. L. (1998). *Principles of Animal Communication* (Sinauer Associates, Sunderland).
- Busnel, R. G., and Dziedziec, A. (1966). "Acoustic signals of the pilot whale *Globicephala melaena* and of the porpoises *Delphinus delphis* and *Phocoena phocoena*," in *Whales, Dolphins and Porpoises*, edited by K. S. Norris (University of California Press, Berkeley), pp. 607–646.
- Busnel, R. G., and Dziedziec, A. (1968). "Caracteristiques physiques des signaux acoustiques de *Pseudorca crassidens* Owen (Cetace Odontocete)," *Mammalia* **32**, 1–5.
- Caldwell, M. C., and Caldwell, D. K. (1971). "Statistical evidence for individual signature whistles in Pacific whitesided dolphins *Lagenorhynchus obliquidens*," *Cetology* **3**, 1–9.
- Caldwell, M. C., Caldwell, D. K., and Miller, J. F. (1973). "Statistical evidence for individual signature whistles in the spotted dolphin (*Stenella plagiodon*)," *Cetology* **16**, 1–21.
- Caldwell, M. C., Caldwell, D. K., and Tyack, P. L. (1990). "Review of the signature-whistle hypothesis for the Atlantic bottlenose dolphin," in *The Bottlenose Dolphin*, edited by S. Leatherwood and R. R. Reeves (Academic, San Diego), pp. 199–234.
- Cranford, T. W., Amundin, M., and Norris, K. S. (1996). "Functional morphology and homology in the odontocete nasal complex: implications for sound generation," *J. Morphol.* **229**, 223–283.
- Cranford, T. W., Van Bonn, W. G., Chaplin, M. S., Carr, J. A., Carder, D. A., Kamolnick, T., and Ridgway, S. H. (1998). "High-speed video endoscopy of Delphinid sonar signal generators" Abstract, The World Marine Mammal Science Conference, Society for Marine Mammalogy & European Cetacean Society, Monaco, 20–24 January 1998, Society for Marine Mammalogy, p. 30.
- Dahlheim, M. E., and Awbrey, F. (1982). "A classification and comparison of vocalizations of captive killer whales (*Orcinus orca*)," *J. Acoust. Soc. Am.* **72**, 661–670.
- Deecke, V. B., Ford, J. K. B., and Spong, P. (1999). "Quantifying complex patterns of bioacoustic variations: use of neural networks to compare killer whale (*Orcinus orca*) dialects," *J. Acoust. Soc. Am.* **105**, 2499–2507.
- dos Santos, M. E., Caporin, G., Moreira, H. O., Ferreira, A. J., and Coelho, J. L. B. (1990). "Acoustic behavior in a local population of bottlenose dolphins," in *Sensory Abilities of Cetaceans*, edited by T. Kastelein and J. Thomas (Plenum, New York), pp. 585–598.
- Evans, P. G. H. (1990). *The Natural History of Whales and Dolphins* (Facts on File, New York).
- Ford, J. K. B. (1989). "Acoustic behaviour of resident killer whales (*Orci-*

- nus orca*) off Vancouver Island, British Columbia," *Can. J. Zool.* **67**, 727–745.
- Ford, J. K. B. (1991). "Vocal traditions among resident killer whales (*Orcinus orca*) in coastal waters of British Columbia," *Can. J. Zool.* **69**, 1454–1483.
- Ford, J. K. B., and Fisher, H. D. (1983). "Group-specific dialects of killer whales (*Orcinus orca*) in British Columbia," in *Communication and Behavior of Whales*, edited by R. Payne (AAAS Selected Symp), Vol. 76, pp. 129–161.
- Ford, J. K. B., Ellis, G. M., and Balcomb, K. C. (1994). *Killer Whales—the Natural History and Genalogy of Orcinus orca in British Columbia and Washington State* (UBC Press, Vancouver).
- Ford, J. K. B., Ellis, G. M., Barrett-Lennard, L. G., Morton, A. B., Palm, R. S., and Balcomb, K. C., III (1998). "Dietary specialization in two sympatric populations of killer whales (*Orcinus orca*) in coastal British Columbia and adjacent waters," *Can. J. Zool.* **76**, 1456–1471.
- Ford, J. K. B., Ellis, G. E., and Balcomb, K. C. III (2000). *Killer Whales*, 2nd ed. (UBC Press, Vancouver).
- Gerhardt, H. C. (1998). "Acoustic signals of animals: recording, field measurements, analysis and description," in *Animal Acoustic Communication—Sound Analysis and Research Methods*, edited by S. L. Hopp, M. L. Owren, and C. S. Evans (Springer, New York), pp. 1–25.
- Herman, L. M., and Tavolga, W. N. (1980). "The communication systems of cetaceans," in *Cetacean Behavior: Mechanisms and Functions*, edited by L. M. Herman (Wiley, New York), pp. 149–209.
- Hoelzel, A. R., and Osborne, R. W., (1986). "Killer whale call characteristics: implications for cooperative foraging strategies," in *Behavioral Biology of Killer Whales*, edited by B. C. Kirkevold and J. S. Lockard (Alan R. Liss, New York), pp. 373–403.
- Lilly, J. C. and Miller, A. M. (1961). "Vocal exchanges between dolphins," *Science* **134**, 1873–1876.
- Matthews, J. N., Rendell, L. E., Gordon, J. C. D., and MacDonald, D. W. (1999). "A review of frequency and time parameters of cetacean tonal calls," *Bioacoustics* **10**, 47–71.
- Miller, P. J. O., and Tyack, P. L. (1999). "Source levels of resident killer whale sounds measured with two beamforming arrays towed in series," Abstracts of the 13th Biennial Conference on the Biology of Marine Mammals, Wailea, Maui, Hawaii, p. 126.
- Morton, E. S. (1977). "On the occurrence and significance of motivation-structural rules in some bird and mammal sounds," *Am. Nat.* **111**, 855–869.
- Owings, H. O., and Morton, E. S., (1998). *Animal Vocal Communication: A New Approach* (Cambridge University Press, Cambridge).
- Popper, A. N. (1980). "Sound emission and detection by delphinids," in *Cetacean Behavior: Mechanisms and Functions*, edited by L. M. Herman (Wiley, New York), pp. 1–52.
- Richardson, W. J., Green, Jr., Ch. R., Charles, I., and Thompson, D. H. (1995). *Marine Mammals and Noise* (Academic, New York).
- Saprykin, V. A., Vereshchagin, V. I., Dokukin, A. Y., Kovtunenkov, S. V., and Pavlovich, I. K. (1977). "Investigation of the structure of the spectrum of communication signals of dolphins," *Biofizika* **22**, 149–153.
- Schevill, W. E., and Watkins, W. A. (1966). "Sound structure and directionality in *Orcinus* (killer whale)," *Zoologica* **51**, 71–76.
- Schultz, K. W., and Corkeron, P. J. (1994). "Interspecific differences in whistles produced by inshore dolphins in Moreton Bay, Queensland, Australia," *Can. J. Zool.* **72**, 1061–1068.
- Sjare, B. L., and Smith, T. G. (1986). "The vocal repertoire of white whales, *Delphinapterus leucas*, summering in Cunningham Inlet, Northwest Territories," *Can. J. Zool.* **64**, 407–415.
- Steiner, W. W. (1981). "Species-specific differences in pure tonal whistle vocalizations of five western North Atlantic dolphin species," *Behav. Ecol. Sociobiol.* **9**, 241–246.
- Steiner, W. W., Hain, J. H., Winn, H. E., and Perkins, P. J. (1979). "Vocalizations and feeding behavior of the killer whale (*Orcinus orca*)," *J. Mammal.* **60**, 823–827.
- Strager, H. (1995). "Pod-specific call repertoires and compound calls of killer whales, *Orcinus orca* Linnaeus, 1758, in the waters of northern Norway," *Can. J. Zool.* **73**, 1037–1047.
- Szymanski, M. D., Supin, A. Y., Bain, D. E., and Henry, K. R. (1998). "Killer whale (*Orcinus orca*) auditory evoked potentials to rhythmic clicks," *Marine Mammal Sci.* **14**, 676–692.
- Thomson, F., Franck, D., and Ford, J. K. B. (2000). "Discrete and variable whistles as close-range acoustic signals in wild killer whales (*Orcinus orca*)" (submitted).
- Tyack, P. (1998). "Acoustic communication under the sea," in *Animal Acoustic Communication—Sound Analysis and Research Methods*, edited by S. L. Hopp, M. J. Owren, and C. S. Evans (Springer, New York), pp. 163–219.
- Watkins, W. A. (1967). "The harmonic interval: fact or artifact in spectral analysis of pulse trains," in *Marine Bioacoustics, Vol. 2.*, edited by W. N. Tavolga (Pergamon, New York), pp. 15–43.

Neural representation of sound amplitude by functionally different auditory receptors in crickets^{a)}

Kazuo Imaizumi^{b)} and Gerald S. Pollack

Department of Biology, McGill University, Montreal, Quebec H3A 1B1, Canada

(Received 18 September 2000; revised 11 December 2000; accepted 13 December 2000)

The physiological characteristics of auditory receptor fibers (ARFs) of crickets, a model system for studying auditory behaviors and their neural mechanisms, are investigated. Unlike auditory receptor neurons of many animals, cricket ARFs fall into three distinct populations based on characteristic frequency (CF) [Imaizumi and Pollack, *J. Neurosci.* **19**, 1508–1516 (1999)]. Two of these have CFs similar to the frequency component of communication signals or of ultrasound produced by predators, and a third population has intermediate CF. Here, sound-amplitude coding by ARFs is examined to gain insights to how behaviorally relevant sounds are encoded by populations of receptor neurons. ARFs involved in acoustic communication comprise two distinct anatomical types, which also differ in physiological parameters (threshold, response slope, dynamic range, minimum latency, and sharpness of tuning). Thus, based on CF and anatomy, ARFs comprise four populations. Physiological parameters are diverse, but within each population they are systematically related to threshold. The details of these relationships differ among the four populations. These findings open the possibility that different ARF populations differ in functional organization. © 2001 Acoustical Society of America. [DOI: 10.1121/1.1348004]

PACS numbers: 43.80.Lb, 43.64.Pg [WA]

I. INTRODUCTION

Auditory information is often represented across populations of receptor neurons with different properties. One approach toward understanding the neural coding of acoustic stimuli is to reveal how each neuron responds to a relevant stimulus and how neurons within a population are organized. Crickets provide a favorable model for studying auditory systems, in particular how sound frequency is analyzed. Behavioral experiments show that the field cricket, *Teleogryllus oceanicus*, classifies sounds into two distinct frequency bands (Wytenbach *et al.*, 1996). One of these, centered at 4–5 kHz, is used for acoustic communication and the other, centered at 20–50 kHz, is used to detect echolocation sounds produced by bats (Moiseff *et al.*, 1978; Hennig and Weber, 1997; Nolen and Hoy, 1986). Despite the dual nature of auditory behavior, cricket auditory receptor fibers (ARFs) fall into three distinct populations based on their characteristic frequency (CF) (Imaizumi and Pollack, 1999). Two of these, low-frequency (CF \approx 3–5.5 kHz) and ultrasound ARFs (CF \geq 18 kHz), are apparently involved in acoustic communication and predator detection, respectively. The role of the third group, midfrequency ARFs (CF=10–12 kHz), is not yet clear. The population sizes of these groups are unbalanced. In particular, low-frequency ARFs are more than four times as numerous as ultrasound ARFs (Imaizumi and Pollack, 1999; Pollack and Faulkes, 1998). However, the behaviors mediated by these two ARF populations, finding mates

and escaping from predators (e.g., echolocating bats), are presumably equally important for crickets (Wytenbach *et al.*, 1996). In order to understand how acoustic signals are represented by populations of these afferents, we examine how responses of single ARFs within each population vary with sound amplitude. Amplitude is an important feature of acoustic stimuli, which serves to signal the distance and, via interaural level comparison, the direction of a sound source.

Rate-level functions have been extensively studied for mammalian auditory-nerve fibers (ANFs), usually with the goal of exploring the relationships between the mechanics of the basilar membrane and neural responses (Sachs and Abbas, 1974; Sachs *et al.*, 1989; Yates, 1990; Yates *et al.*, 1990). Rate-level functions have also been applied to study how a population of ANFs encodes complex sounds, such as vowels (Sachs and Young, 1979, 1980; Le Prell *et al.*, 1996). We use spike count-level functions (hereafter, spike-level functions) to investigate how different populations of cricket ARFs encode sound amplitude.

Parts of this study have been published in abstract form (Imaizumi and Pollack, 1997, 1998a).

II. METHODS

A. Animals

Adult virgin female crickets, *Teleogryllus oceanicus*, aged 14–23 days after the final molt, were used. They were cultured under crowded conditions on a 12-h light/dark cycle, at 25–28 °C, and fed water and cat chow (Ralston Purina, St. Louis, MO) *ad libitum*.

B. Physiological recording and staining

Experiments were performed in a sound-attenuating chamber at 20–23 °C. We used two different recording techniques, whole tympanal nerve (WTN) and single-unit record-

^{a)}Portions of this work were presented in “Physiological properties of auditory receptors in the Australian field cricket *Teleogryllus oceanicus*,” Society for Neuroscience Abstract **23**, 1571, New Orleans, LA, October 1997, and “The physiological organization of cricket auditory receptors responding to different behavioral relevant frequency ranges,” Society for Neuroscience Abstract **24**, 156, Los Angeles, CA, November 1998.

^{b)}Present address: W.M. Keck Center for Integrative Neuroscience, UCSF, San Francisco, CA 94143-0732. Electronic mail: kazuo@phy.ucsf.edu

ings. For WTN recording, animals were fixed vertically after removal of the head, wings, and mid- and hind-legs. The stump of the neck was covered by a mixture of rosin and bees wax (1:1 by weight). The tibia was held flexed against the femur. The leg nerve was exposed by removing the anterior femoral cuticle, placed on a silver-wire hook electrode, and covered with a mixture of petroleum jelly and mineral oil (1:1 by weight). The prothoracic spiracles, which form part of the auditory system in crickets, were neither occluded nor forced open. A chlorided silver ground wire was inserted into the abdomen. For single-unit recordings, crickets were waxed on a platform ventral side up. The prothoracic ganglion was exposed by ventral dissection and kept moist with modified TES ringer [140 mM NaCl, 10 mM KCl, 7 mM CaCl₂, 4 mM NaHCO₃, 1 mM MgCl₂, 5 mM d-trehalose dihydrate, 5 mM n-tris (hydroxymethyl) methyl-2-aminoethane sulfonic acid] (Strausfeld *et al.*, 1983). The prothoracic ganglion was stabilized on a silver platform, and a chlorided silver ground wire was inserted into the abdomen. Recordings were made with glass micropipettes in the leg nerve near its entry into the prothoracic ganglion. The sites of single-unit recordings varied by up to 1 mm along the length of the leg nerve, which may affect our measurements of latency. However, the error this would introduce is only ca. 0.5 ms, given the mean conduction velocity of ARFs, ~2 m/s (Pollack and Faulkes, 1998).

The tips of micropipettes were filled with one of the following aqueous solutions: 3 M KCl (resistance, 10–40 M Ω), 2%–4% Lucifer Yellow CH (Aldrich, Milwaukee, WI) (resistance, 100–300 M Ω), 2.5–25 mM Alexa 488 or 568 hydrazide (Molecular Probes, Eugene, OR) (resistance, 150–1000 M Ω). Axon terminals of ARFs were filled with fluorescent dyes by constant negative current injection (1–10 nA). Ganglia containing dye-filled ARFs were washed with modified TES ringer, fixed, and dehydrated with 4% formaldehyde in 0.1 M phosphate buffer (pH 7.3) for 10–30 min, 4% formaldehyde in methanol for 1 h, and 100% ethanol for 15 min (Atkins and Pollack, 1987). The ganglion was cleared with methyl salicylate and mounted on a depression slide. Stained ARFs were observed with an epifluorescence microscope (Leica Microsystems, Wetzlar, Germany). Well-stained specimens were further analyzed with a confocal microscope (Leica Microsystems). Reconstructions of ARF terminals were made by combining serial optical sections in the horizontal plane. Drawings were made by projecting film negatives of these reconstructions with a photo enlarger. The detailed anatomy of ARFs and their organization will appear in a separate paper.

C. Acoustic stimulation

Sound stimuli were generated by a National Instruments (Austin, TX) AT-MIO-64F5 input–output board (resolution: 12 bits, digital-to-analog update rate: 250 kHz) driven by software written using LAB WINDOWS/CVI (National Instruments). After power amplification (Amcron) and computer-controlled attenuation (Mike Walsh Electronics, San Dimas, CA), stimuli were delivered ipsilateral to the recording side through separate loud speakers for frequencies ≤ 10 kHz (InterTAN, Toronto, Canada), and frequencies > 10 kHz

(Matsushita Electrical Industrial, Osaka, Japan). The distance between the speakers and the animal was 37 cm. Sound level (*re* 20 μ Pa) was calibrated with a 1/4-in. 4135 condenser microphone and 2610 measuring amplifier (Brüel & Kjær, Denmark). Responses were examined at CF and several other frequencies for as long as recordings could be held. Stimuli at a given frequency were usually presented at 45–100 dB SPL; in 3-dB increments from 45–51 dB SPL, and in 5-dB increments from 55–100 dB SPL (or up to 90 dB SPL in the early experiments). For a few low-threshold neurons, stimuli were presented down to 40 dB SPL. In some recordings, sound levels from below threshold to 100 dB SPL were tested in 2-dB increments. Each stimulus was presented three times (5–10 times in several cases). Stimuli were 30 ms in duration (including 5-ms rise and fall times) and were presented at 2 pulses/s. The search stimulus used was either 4.5 kHz (or 5 kHz) at 80 dB SPL or bandpass-filtered white noise (3–50 kHz) at 90 dB SPL. Background noise level between 2 and 40 kHz was less than 30 dB SPL, measured with a 1/2-in 4134 condenser microphone, 2610 measuring amplifier (Brüel & Kjær), and 3550 filter (Krohn-Hite, Avon, MA).

D. Data analysis

Responses were stored on magnetic tape for off-line analysis. Recordings were digitized at a sampling rate of 10 kHz and analyzed using the computer program SWEEPS (Pollack, 1997). WTN recordings were bandpass filtered (100–1000 Hz), full-wave rectified, and integrated over a 40-ms time window beginning at stimulus onset. For single-unit recordings, the number of spikes was counted in a 50-ms time window beginning at stimulus onset, except for two ARFs with unusually long latency, for which the time window began 10 ms after stimulus onset.

We first determined CF as described previously (Imaizumi and Pollack, 1999). Curves relating ARF responses to sound level were fit by nonlinear models using SIGMA PLOT 4.0 (SPSS, Chicago, IL), in which the Marquardt–Levenberg algorithm was used. Several physiological parameters are derived from spike-level function at CF [Fig. 1(A)] which we examined for 136 ARFs. A sigmoid model was used with three, four, or five free parameters

$$y = d + a / \{1 + \exp[-(x - b)/c]\}^e,$$

where y is the number of spikes, d is the minimum asymptote (4th parameter), a is the maximum asymptote, x is sound level, b is sound level at 50% of maximum response, c is a slope factor, and e is an asymmetry factor (5th parameter). Because we corrected spike counts for spontaneous activity (see below), the minimum asymptote “ d ” is expected to be zero, and in most cases it was not a free parameter. In some recordings, however, including minimum asymptote d as a free parameter improved the fit. The choice of the number of parameters was determined by an F test for the overall goodness of fit. We employed mostly a three-parameter sigmoid model.

In order to examine the driven response to sound, spontaneous spike counts in a 50-ms time window immediately prior to each sound stimulus were subtracted from the raw

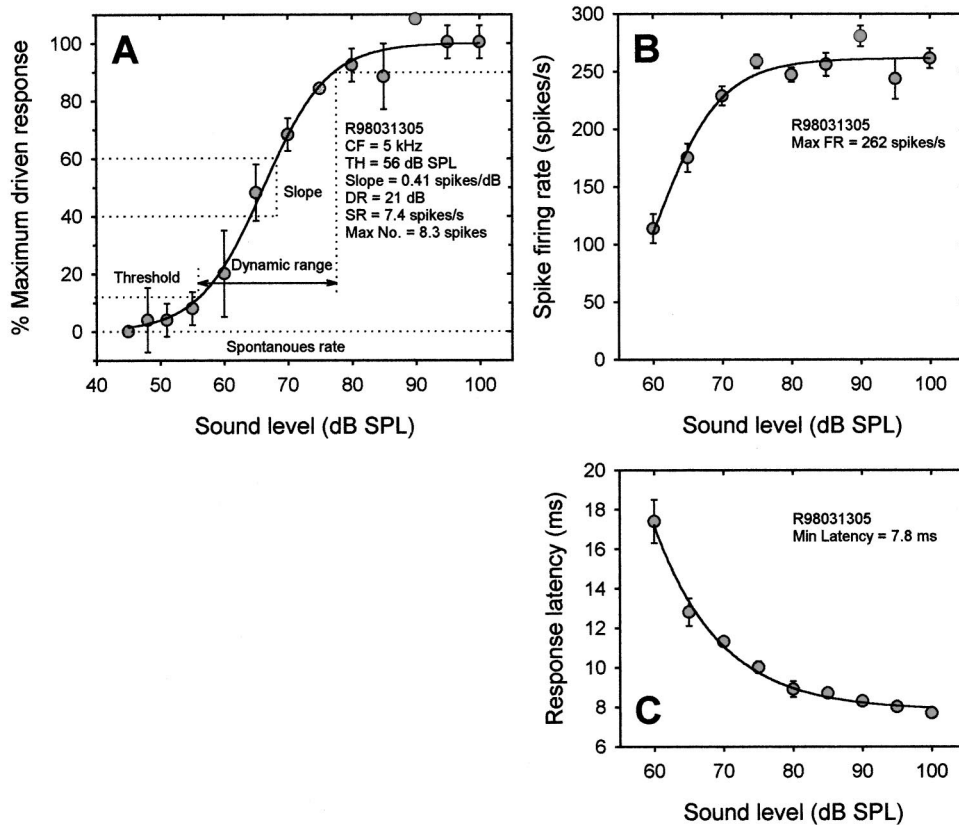


FIG. 1. Physiological parameters derived from responses of a single auditory receptor fiber (ARF) with characteristic frequency (CF) of 5 kHz. Data points represent mean (\pm s.d.) of three presentations of the stimulus at each sound level. ARF identification and physiological parameters are shown inside the graphs. (A) Spike-level function. Normalized driven response is plotted as a function of sound level. Threshold (TH) was estimated as dB SPL at CF at which the ARF produced one spike above the minimum asymptote. Response slope (Slope) was measured for the portion of the curve spanning 40%–60% of the maximum response. Dynamic range (DR) was calculated as dB range from threshold to 90% of the maximum response. Spontaneous rate (SR) was measured as number of spikes per s in the absence of sound stimulus. Maximum number of spikes (Max No.) was estimated as maximum asymptote. This curve was fit with a three-parameter sigmoid model. (B) Instantaneous-rate level function. Instantaneous firing rate is plotted as a function of sound level. Maximum firing rate (Max FR) was estimated as maximum asymptote. Curve was fit using a three-parameter hill model for this ARF. (C) Latency-level function. Response latency is plotted as a function of sound level. Minimum latency was estimated as minimum asymptote. Curve was fit using a three-parameter single exponential decay model. See Secs. II and III for further explanation.

data. Threshold was estimated as the sound level at CF at which an ARF produced one spike above minimum asymptote. Response slope was measured as the slope of the fitted curve from 40% to 60% of the maximum response. Dynamic range was determined as the sound-level range from threshold to 90% of the maximum response. Spontaneous rate was measured from recordings 2 to 41 s (mostly 6–12.5 s) in duration without sound stimulation. Maximum number of spikes was estimated as maximum asymptote. For 13 ARFs, we lost recordings before completing the spike-level function over the entire sound-level range (up to 100 dB SPL or 90 dB SPL for the early experiments). In these cases, response slope, dynamic range, and maximum response were not estimated. However, because the overall curve fit was significant by an F test ($p < 0.05$), threshold was estimated.

Some ARFs had sloping-saturation responses similar to those found in vertebrate ANFs (Sachs and Abbas, 1974; Sachs *et al.*, 1980; Köppl and Yates, 1999). For these ARFs, spike-level functions were fit to a double logistic model (Nizami and Schneider, 1997). The model worked well both for cricket ARFs and cat ANFs (Imaizumi and Nizami, unpublished observations). Definitions of physiological parameters for ARFs with sloping-saturation responses were the

same as for other ARFs. For some ARFs, there was little or no indication of response saturation within the sound-level range we tested (upper limit: 100 dB SPL). In these cases, the uncertainty of the estimate of maximum asymptote was high; that is, the goodness of fit, as reflected by the least-squares error, depended only weakly on the precise value of the asymptote. The curve-fitting program we used (SIGMA PLOT 4.0) expresses this uncertainty in terms of the t statistic and its associated probability value; low p indicates low uncertainty (Glantz and Slinker, 1990). For the two sloping-saturation ARFs for which the results of this test were not significant, response slope and dynamic range were also excluded from the results.

Instantaneous firing rate was calculated as the inverse of the average interspike interval: number of spikes minus one divided by response duration. Instantaneous-rate level function was fit by either a three- or four-parameter (as determined by F test) gompertz growth model (Draper and Smith, 1983). We employed mostly a three-parameter gompertz model

$$y = a \exp\{-\exp[-(x-b)/c]\},$$

where y is the instantaneous firing rate, a is the maximum

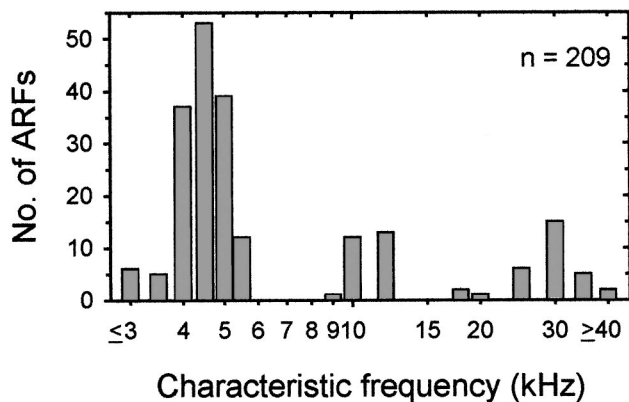


FIG. 2. The distributions of CFs of 209 ARFs. CFs of 86 of these ARFs were reported previously (Imaizumi and Pollack, 1999). CFs of 3 kHz and lower and 40 kHz and higher are expressed as ≤ 3 and ≥ 40 , respectively. ARFs fall into three distinct populations based on CF. However, anatomical evidence (see Fig. 6) shows that the low-frequency population includes two distinct ARF types. Anatomy was not determined for all ARFs, and so these two types are not distinguished in Figs. 2, 3, and 4, which include our entire data set. Proportions of low-frequency (CF ~ 3 –5.5 kHz), midfrequency (CF = 9–12 kHz), and ultrasound ARFs (CF ≥ 18 kHz) are 73%, 12%, and 15%, respectively.

asymptote, x is sound level, b is sound level at 50% of maximum firing rate, and c is a slope factor. For a four-parameter gomperz model, the minimum asymptote d was added

$$y = d + a \exp\{-\exp[-(x - b)/c]\}.$$

In a few cases a three-parameter hill model was also employed [Fig. 1(B)]. We also estimated minimum response latency of the first response spike (see Sec. III for a detailed description), using a three-parameter single exponential decay model [Fig. 1(C)]. The model is

$$y = d + a \exp(-cx),$$

where y is response latency, d is minimum response latency, a is maximum latency, c is a slope factor, and x is sound level. Estimates of maximum firing rate and minimum latency were accepted only for cases where uncertainty of the estimate of maximum or minimum asymptote, respectively, was low as indicated by the t statistic. Five estimates of maximum firing rate, and 12 of minimum latency, were excluded by this criterion.

III. RESULTS

We determined CFs of 209 ARFs, 86 of which were included in an earlier paper (Imaizumi and Pollack, 1999). As in the previous study, ARFs fall into three distinct populations based on CF (Fig. 2). Low-frequency ARFs (~ 3 –5.5 kHz) comprise the largest population (73%), while midfrequency (9–12 kHz) and ultrasound ARFs (≥ 18 kHz) are less numerous (12% and 15%, respectively). However, we found two distinct anatomical types among low-frequency ARFs, as described later. Therefore, based on both CF and anatomy, ARFs are recognized as comprising four populations rather than three.

A. Spike-level functions of cricket ARFs

Figure 3 illustrates spike-level functions at CF for nine ARFs representing the three ARF populations that were previously identified (Imaizumi and Pollack, 1999) on the basis of CF alone. Spike-level functions were monotonic, except for a single ARF (data not shown), and were in most cases sigmoid. However, as judged by visual inspection, 20 ARFs [e.g., Figs. 3(A) and (E)] showed sloping saturation at CF, similar to that found in vertebrate ANFs (Sachs and Abbas, 1974; Sachs *et al.*, 1980; Köppl and Yates, 1999). Sixteen of these had CF of 4–5 kHz, three had CF of 10–12 kHz, and one had CF of 35 kHz.

B. Distributions of physiological parameters

In general, insect ARFs have been considered to be similar in physiological parameters (Rheinlaender, 1975; Römer, 1976; Kalmring *et al.*, 1978; Oldfield, 1983, 1984; Römer *et al.*, 1998). However, as Fig. 3 suggests, cricket ARFs may have a wide range of physiological parameters. Distributions of physiological parameters derived from spike-level and instantaneous-rate level functions are illustrated in Fig. 4. Indeed, cricket ARFs differ not only in threshold but also in response slope, dynamic range, and maximum response.

Threshold is one parameter that can be compared directly with behavior. Many low-frequency ARFs have thresholds between 50 and 60 dB SPL [Fig. 4(A)]. However, eight low-frequency ARFs had lower thresholds, 35–45 dB SPL at CF (and one had exceptionally low threshold), and six ultrasound ARFs also had low thresholds, less than 55 dB SPL at CF. Given the behavioral thresholds of crickets (e.g., 45–50 dB SPL for orientation towards communication signals: Pollack and Plourde, 1982; Schmitz, 1985; Doolan and Pollack, 1985, and ~ 55 dB SPL for orientation away from bat-like sounds: Nolen and Hoy, 1986), thresholds of many ARFs appear to be high. To examine the possibility of sampling bias, we measured responses of the entire ARF population using WTN recordings. Figure 5 illustrates WTN responses at 5 and 30 kHz. The slope of the WTN response increases at 55–60 dB SPL for 5-kHz stimuli and at 75–80 dB SPL for 30-kHz stimuli (Fig. 5), as would be expected if large numbers of ARFs were recruited at these sound levels (see also Fig. 9). These results are thus consistent with the clustering of threshold at 50–65 dB SPL for frequency ARFs and at 65–80 dB SPL for ultrasound ARFs [Fig. 4(A)].

However, two cautions are necessary. First, the number of low-threshold ARFs may be underestimated. As we show later (Fig. 8), low-threshold ARFs have higher spontaneous activity, and this made estimation of CF during the course of the experiments more difficult. As a precaution, we measured spike-level functions at a number of frequencies near the apparent CF. This was not necessary for high-threshold ARFs, for which CF was unambiguous. Due to the limited duration of recordings (mean: 3.9 min; range: 1–19 min), we sometimes lost the recording before all spike-level functions were completed. Thus, our sample of low-threshold ARFs may underestimate the relative size of this group. The other caution is that threshold, especially for high-threshold ultra-

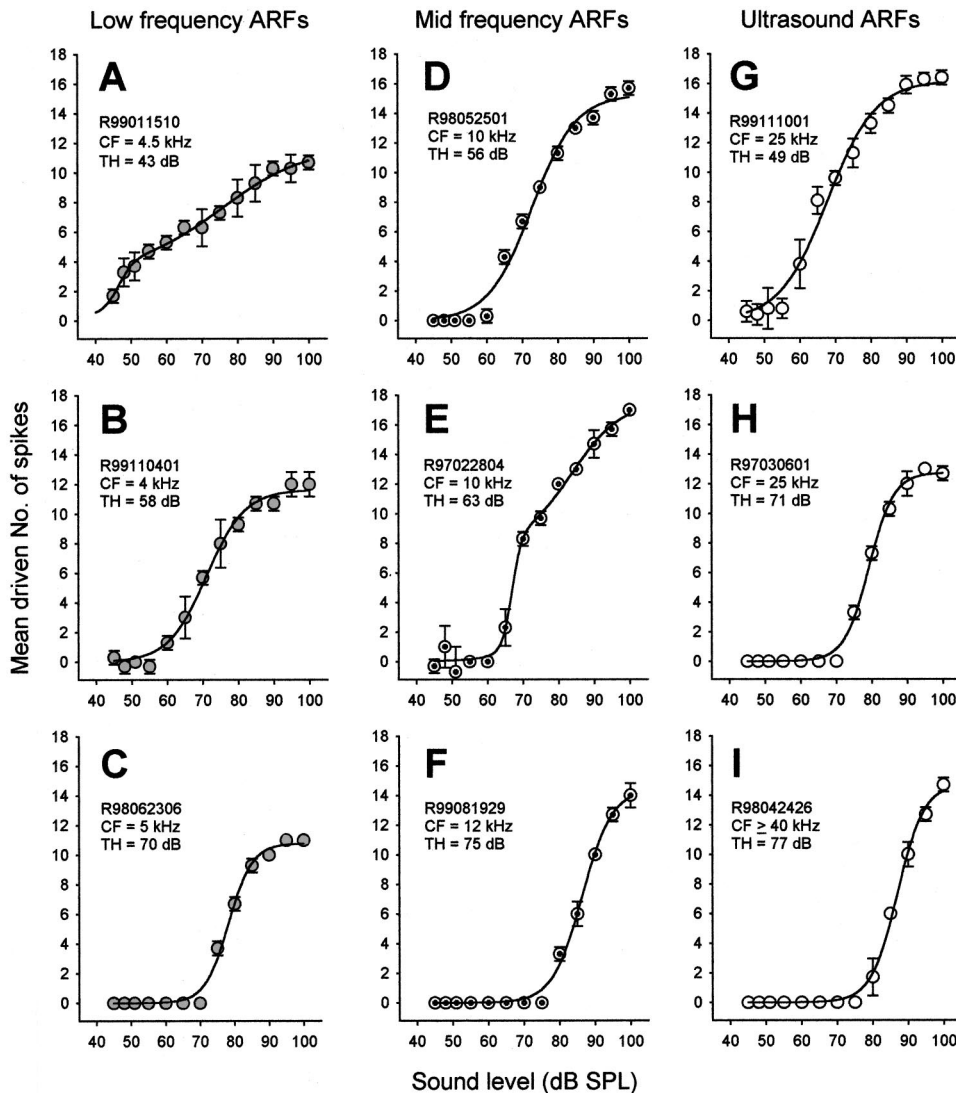


FIG. 3. Spike-level functions of 9 ARFs from three populations are illustrated. Data points represent mean (\pm s.d.) of three stimulus presentations for most cases [eight presentations for (G)]. (A)–(C), (D)–(F), and (G)–(I) represent low-frequency, mid-frequency, and ultrasound ARFs, respectively. ARF identifications, CFs, and THs (thresholds) are shown on the left of each curve. For all except (A) and (E), curve fits were made using a three-parameter sigmoid model. For sloping-saturation types (A) and (E), a double logistic model (Nizami and Schneider, 1997) was used.

sound ARFs, may have been measured at other than the “true” CF. Many ARFs have additional sensitivity peaks at frequencies other than CF (Imaizumi and Pollack, 1999). Thus, the true CFs of some of the ultrasound ARFs might be outside the frequency range that we examined (2–40 kHz, 3–40 kHz in the early experiments). However, these high-threshold ultrasound ARFs are not spontaneously active. As we show later, high-threshold ARFs in other populations, as well as ultrasound ARFs, have low spontaneous rates (Fig. 8); thus, threshold of ultrasound ARFs are likely to be high regardless of their true CF.

C. Low-frequency ARFs comprise two anatomically different types

Intracellular staining of 137 ARFs (92 low-frequency ARFs, 21 midfrequency ARFs, and 24 ultrasound ARFs) reveals two distinct anatomical types (Imaizumi and Pollack, 1996, 1998b; Pollack and Imaizumi, 1999). Horizontal reconstructions of axon terminals of representative ARFs are illustrated in Fig. 6. One type projects near the midline of the prothoracic ganglion (Medial Termination; MT type) and the other, which has large bifurcating branches, terminates more laterally (Bifurcation; BC type). MT types occur among all

three ARF populations, while BC types occur only among low-frequency ARFs. For the remainder of this paper we use the terms MT and BC to distinguish between these low-frequency ARFs. Of the 92 low-frequency ARFs we stained, 51 were BC types, and 41 were MT types.

D. Different ARF populations differ in physiological parameters

Given the differences in probable behavioral roles of the different ARF populations, it seemed possible that they might differ in physiological parameters. Figure 7 compares the physiological properties among the four different ARF populations as defined by both CF and anatomy. For low-frequency ARFs, only anatomically identified ARFs were included in the analysis. Because midfrequency and ultrasound ARFs are anatomically homogeneous (Fig. 6), we included all physiological data for these ARFs in our analysis, even if anatomical evidence was not available.

BC types differ significantly from midfrequency ARFs in dynamic range, maximum number of spikes, and maximum firing rate. MT types differ significantly from midfrequency ARFs in response slope, spontaneous rate, maximum

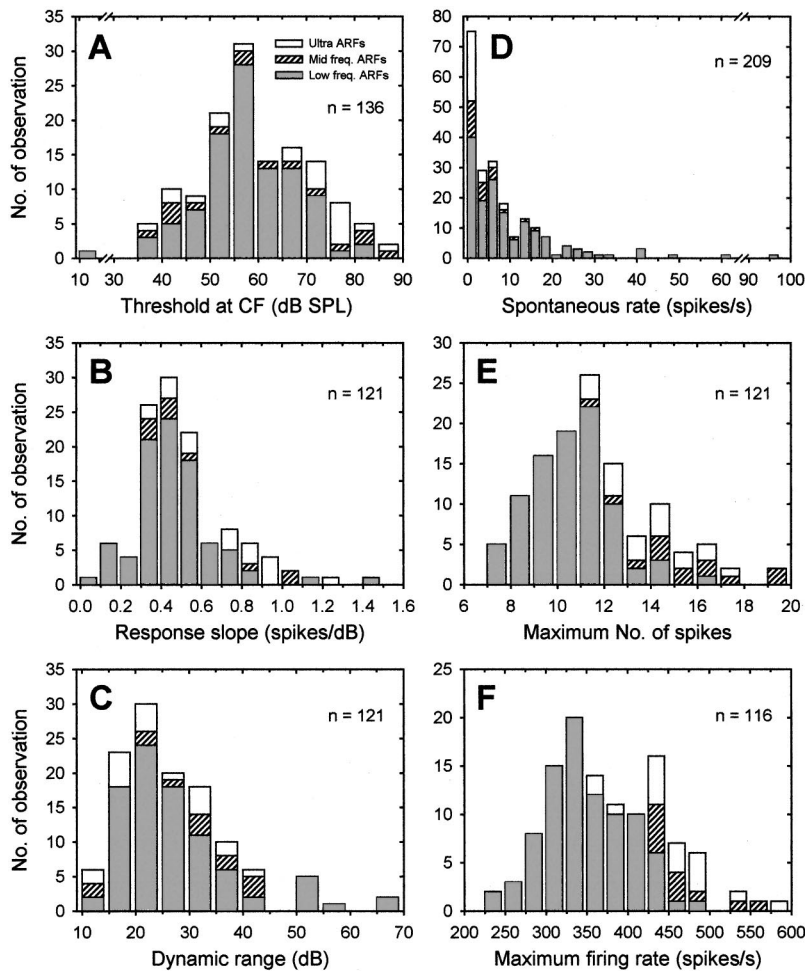


FIG. 4. Distributions of physiological parameters. Different populations of ARFs, based on CF, are indicated by different fill patterns. As in Fig. 2, we include ARFs for which anatomy was not determined, and thus the two types of low-frequency ARFs are not distinguished. (A) Threshold at CF. Note the break on *abscissa*. (B) Response slope. (C) Dynamic range. (D) Spontaneous rate. Note the break on *abscissa*. (E) Maximum number of spikes. (F) Maximum firing rate.

number of spikes, and maximum firing rate. BC types differ significantly from ultrasound ARFs in response slope, spontaneous rate, maximum number of spikes, and maximum firing rate, while MT types differ significantly from ultrasound ARFs in all parameters. However, midfrequency ARFs differ significantly from ultrasound ARFs only in spontaneous rate

[Fig. 7(D)], although the significance is weak ($p=0.049$).

Of particular interest is the difference between BC and MT types, both of which are, based on CF, presumably involved in acoustic communication (Imaizumi and Pollack, 1999). Their anatomical differences suggest that they may provide inputs to different central neurons. They differ physiologically as well. MT types have lower threshold, wider dynamic range, and higher maximum response than BC types [Figs. 7(A), (C), (E)], whereas BC types have steeper response slope than MT types [Fig. 7(B)].

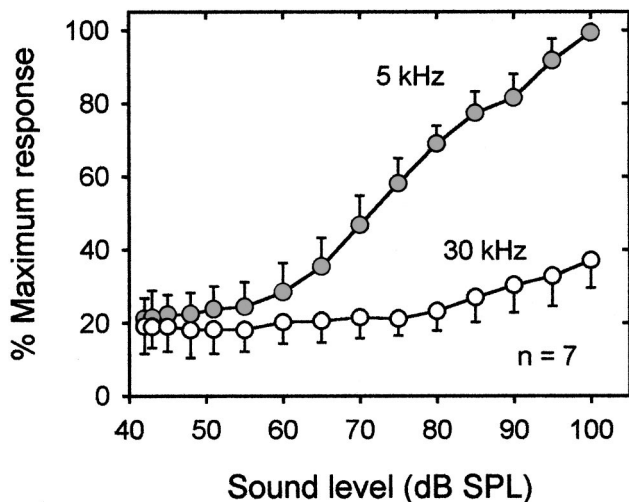
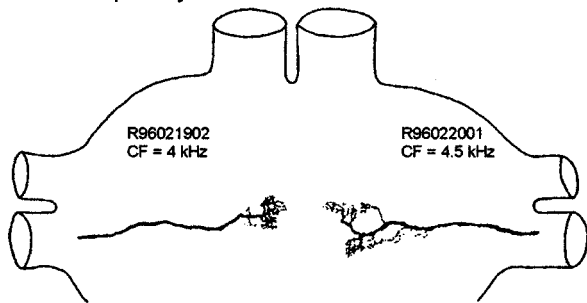


FIG. 5. Response of the whole tympanal nerve to increasing sound level. The responses were normalized to the maximum response at 5 kHz. Stimulus frequencies are shown beside curves. Five kHz represents low frequency, illustrated by filled circles, while 30 kHz represents ultrasound, illustrated by open circles. Points are means and s.d. of seven experiments.

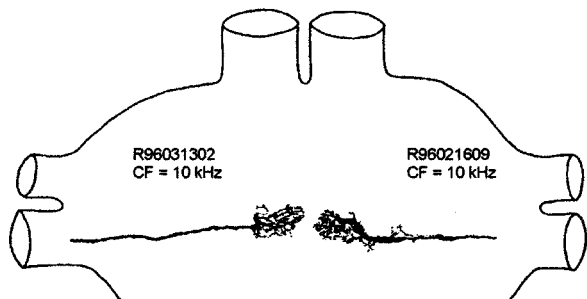
E. Relationships between threshold and other physiological parameters

Sound amplitude is a behaviorally important parameter of acoustic signals. As sound amplitude increases ARFs with different thresholds will be recruited, and the nature of the summed sensory input will depend on how other physiological parameters of ARFs vary systematically with threshold. We examined these relationships separately for the four ARF populations. In all cases, response slope increases with increasing threshold, while dynamic range decreases (Fig. 8). Spontaneous rate decreases with increasing threshold, although the relationship is not significant for BC low-frequency ARFs [Figs. 8(A3)–(D3)]. There are no significant relationships between threshold and maximum responses (either spike counts or firing rate) for most populations (data

Low frequency ARFs



Mid frequency ARFs



Ultrasound ARFs

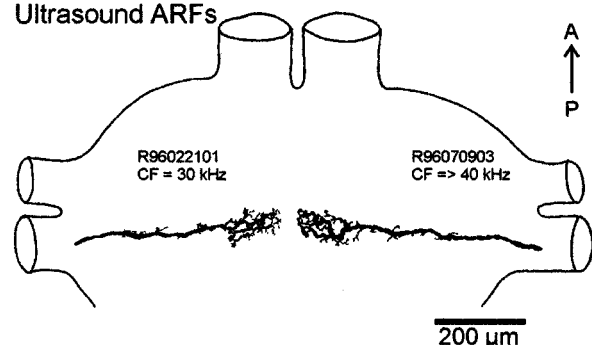


FIG. 6. Anatomy of axon terminals of six different ARFs in the prothoracic ganglion. Axon terminals were stained with either Lucifer Yellow or Alexa 488 or 568 by constant negative current injection. Horizontal reconstructions were prepared from optical sections made using confocal microscopy. There are two types of ARFs, medial termination (MT type) and bifurcation (BC type). MT types occur in all populations, while BC types occur only among low-frequency ARFs. For low-frequency ARFs, MT and BC types are illustrated on the *left* and *right*, respectively. ARF identifications and CFs are shown above drawing of axon terminals. Orientation of ganglion is illustrated by an arrow (A: anterior; P: posterior). Scale bar is given at the *bottom*.

not shown). However, only for MT types, maximum firing rate increases significantly with threshold ($r^2=0.147$, $p=0.048$; data not shown).

F. Response latency

In general, response latency of auditory neurons decreases with increasing sound level, and is also a potential carrier of information concerning sound amplitude to central neurons. Response latency is usually measured as the delay between stimulus onset and the first post-onset spike. However, for auditory neurons with spontaneous activity, the first spike is not always sound elicited. We excluded spontaneous spikes from the measurements by using the latency of WTN

responses as a guide. WTN response were recorded at the femur, which is several millimeters closer to the spike initiating zone in the tibia than the site of single-unit recordings in the leg nerve near its entry into the prothoracic ganglion. Consequently, WTN response latency is shorter than single-unit response latency (2–4 ms shorter, in general, as indicated by simultaneous recordings, Imaizumi, unpublished observations; see also Pollack and Faulkes, 1998). We therefore consider spikes occurring before the WTN responses as spontaneous. WTN response latency was measured as the time from stimulus onset to the first conspicuous peak in averaged WTN traces ($n=5$) at each sound level (Fig. 9). Because of low signal-to-noise ratio at low sound levels, we measured latencies of WTN response at ≥ 70 dB SPL (we used WTN response latency at 70 dB SPL as the lower limit for latency for all sound levels ≤ 70 dB SPL). Figure 10 summarizes the results from seven experiments. Minimum latency was estimated as the minimum asymptote of a non-linear model fit to the data [Fig. 1(C), see Sec. II].

BC low-frequency ARFs have the shortest minimum latency [Fig. 11(A)]. Minimum latency does not differ significantly between the other three populations. The relationship between threshold and minimum latency also differs among the populations. For MT low- and midfrequency ARFs, minimum latency decreases with increasing threshold [Figs. 11(C), (D)], whereas BC low-frequency and ultrasound ARFs have similar minimum latencies regardless of threshold [Figs. 11(B), (E)].

G. Frequency selectivity of different ARF populations

Our previous results showed that frequency selectivity, as reflected by the quality factor ($Q_{75\%}$), was similar among the three ARF populations we recognized based on CF (Imaizumi and Pollack, 1999). $Q_{75\%}$ was calculated as best frequency divided by bandwidth at 75% of the maximum response in isolevel curves (Imaizumi and Pollack, 1999). The higher the $Q_{75\%}$, the more sharply the ARF is tuned. However, when the anatomical distinction among low-frequency ARFs is taken into account, differences in frequency selectivity are apparent. Although $Q_{75\%}$ does not differ among the four populations at sound levels from 0 to <5 dB SPL above threshold (Mann-Whitney U test adjusted by the sequential Bonferroni technique; Rice, 1989), MT types are more sharply tuned to CF than the other three ARF populations at sound levels from 5 to <10 dB SPL above threshold (Fig. 12).

H. Parallel and nonparallel spike-level functions in cricket ARFs

Spike-level functions at different frequencies for a given receptor neuron may be related to the biophysical properties of the structures conducting sound energy to receptor neurons. In mammals, rate-level functions of single ANFs may show nonparallel responses at different frequencies because of nonlinearity of the input–output function of the basilar membrane (Sachs and Abbas, 1974; Yates *et al.*, 1990; Cooper and Yates, 1994). In contrast, in insects, previous studies of spike-level functions for single ARFs have shown

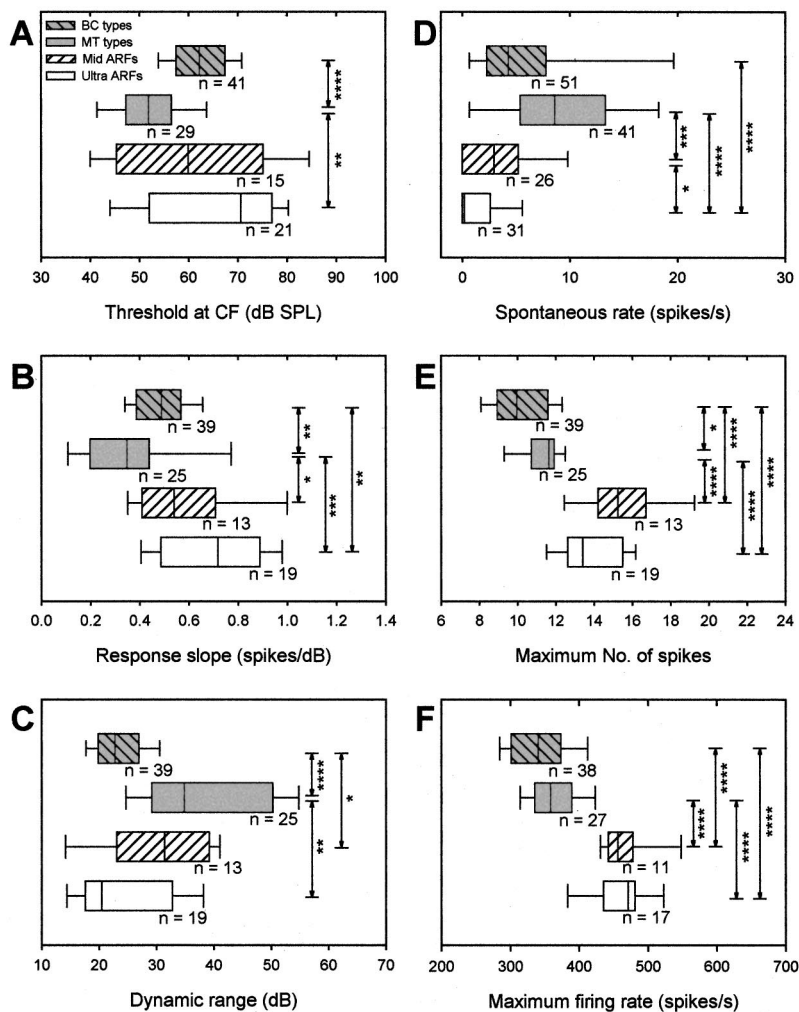


FIG. 7. Comparisons of physiological parameters among different ARF populations. Different ARF populations are illustrated with different fill patterns. Box plots illustrate medians (vertical lines), quartiles (box widths), and 10th and 90th percentiles (whiskers). Sample sizes are shown under each box. Significant differences between ARF populations are illustrated by bars and asterisks. Number of asterisks corresponds to the probabilities (*: $p < 0.05$, **: $p < 0.01$, ***: $p < 0.001$, ****: $p < 0.0001$) determined by Mann-Whitney U test, adjusted, for multiple comparisons using the sequential Bonferroni technique (Rice, 1989).

parallel responses at different frequencies (Suga, 1960; Rheinlaender, 1975; Römer, 1976; Oldfield, 1982, 1984, 1985; Oldfield *et al.*, 1986). However, we found both parallel and nonparallel responses in single cricket ARFs. Figure 13 illustrates some representative examples. Although the number of frequencies at which spike-level functions were measured in a single ARF was limited (range, 1–13), many ARFs appeared to respond in a parallel manner [Figs. 13(A), (B)], while a small number appeared to respond in a nonparallel manner [Figs. 13(C), (D)]. Additional indications of nonparallel responses are evident in previously published isolevel curves (Fig. 3 of Imaizumi and Pollack, 1999). Figures 13(B) and (D) also demonstrate that the midfrequency and ultrasound ARFs respond robustly to the carrier frequency of communication signals (4.5 kHz) (see also Imaizumi and Pollack, 1999).

IV. DISCUSSION

A. Cricket ARFs may differ from other insect ARFs

In insects, physiological parameters of spike-level functions have been studied in bushcrickets and locusts (Rheinlaender, 1975; Römer, 1976; Kalrning *et al.*, 1978; Oldfield, 1983, 1984; Römer *et al.*, 1998). These studies suggested that insect ARFs are stereotyped (similar response slope and dynamic range) except for threshold. A previous study on

crickets also produced similar results (Oldfield *et al.*, 1986). However, we demonstrate that these parameters of cricket ARFs vary considerably. This discrepancy may result from differences in recording techniques. Oldfield *et al.* (1986) made intracellular recordings directly from cell bodies after removing the anterior tympanal membrane and immersing the inner ear in Ringer solution. These procedures did not alter frequency sensitivity at low frequencies, but they did alter neuronal threshold by up to 30 dB, in particular >10 kHz. It appears possible that these procedures affected the biomechanics of the inner ear.

In many ARFs, spike-level functions appear to be parallel at different frequencies. In several other insects, parallel spike-level functions were also found (Suga, 1960; Rheinlaender, 1975; Römer, 1976; Oldfield, 1983, 1984, 1985; Oldfield *et al.*, 1986). However, we also find that some ARFs show nonparallel responses at different frequencies. Hutchings and Lewis (1981) also reported nonparallel responses of cricket ARFs, but in their case the responses of a single ARF were monotonic and nonmonotonic at different frequencies, which we never observed. Previous studies showed that insect tympanal membranes, including those of crickets, respond linearly at different frequencies (Paton *et al.*, 1977; Breckow and Sipple, 1985). However, the recent discovery of otoacoustic emissions in locusts and moths suggests that insect ears may not respond in an entirely linear manner

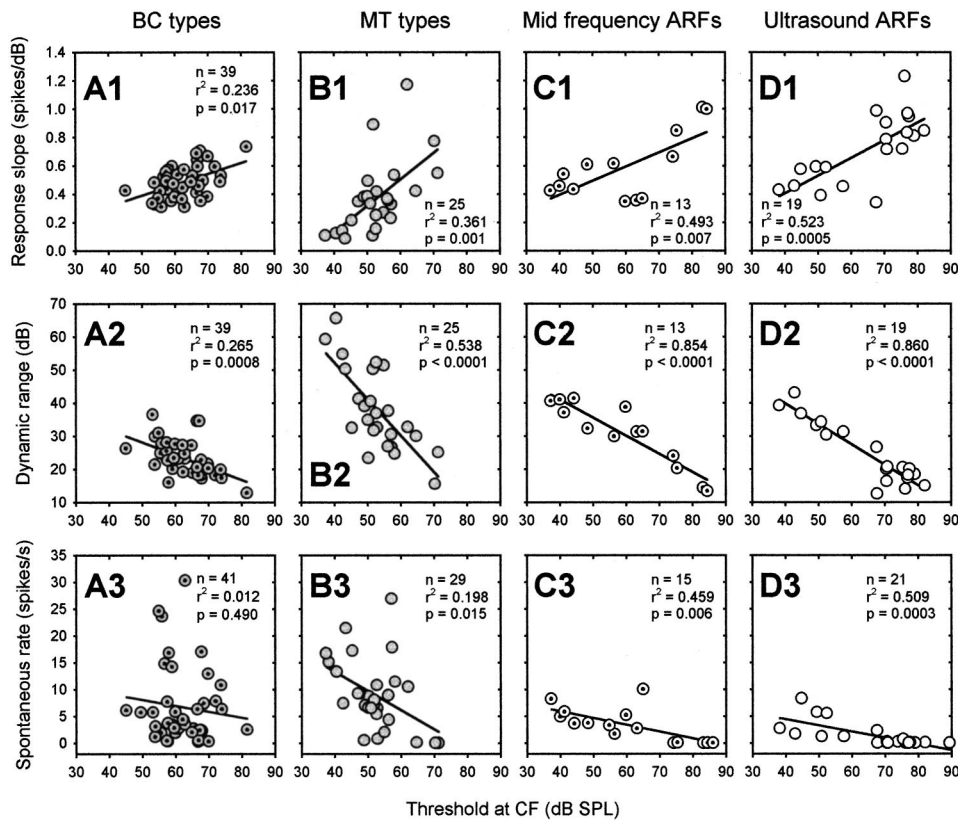


FIG. 8. Linear relationships between threshold and three other physiological parameters. Regression lines were computed by least-squares analysis. Sample sizes, r^2 values (coefficient of determination), and probabilities are shown inside each graph. Threshold is linearly related to response slope, dynamic range, and spontaneous rate for all populations, except for spontaneous rate in BC types (A3). There is no relationship between threshold and maximum number of spikes or firing rate for most populations (data not shown). However, only for MT types, threshold is related weakly to maximum firing rate ($r^2=0.147$, $p=0.048$; data not shown).

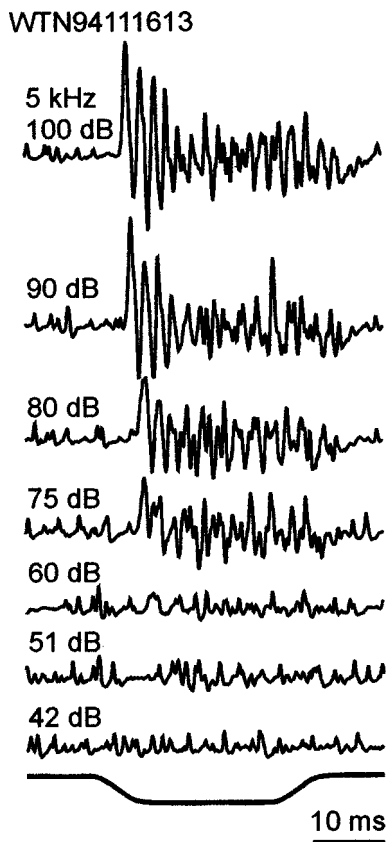


FIG. 9. Extracellular recordings from the whole tympanal nerve in one animal. Traces are averages of five repetitions. Stimulus level is shown at the left. Stimulus monitor and time scale are illustrated below. First peaks are not clear at low sound levels (≤ 60 dB SPL) because of low signal-to-noise ratio, while the first peaks are clear at high sound levels (≥ 75 dB SPL).

(Kössl and Boyan, 1998; Coro and Kössl, 1998). Unlike the situation in these insects, auditory receptors of crickets are not directly attached to the tympanal membrane; rather, they are situated between a tracheal branch and a covering membrane (for a recent review, see Yager, 1999). Moreover, in addition to acting directly on the external surface of the tympanum, sound reaches the inner surface via tracheal tubes, crossing a phase-shifting partition if the sound is contralateral (Michelsen, 1998). Although there currently is no evidence that these complex structures of the cricket inner ear

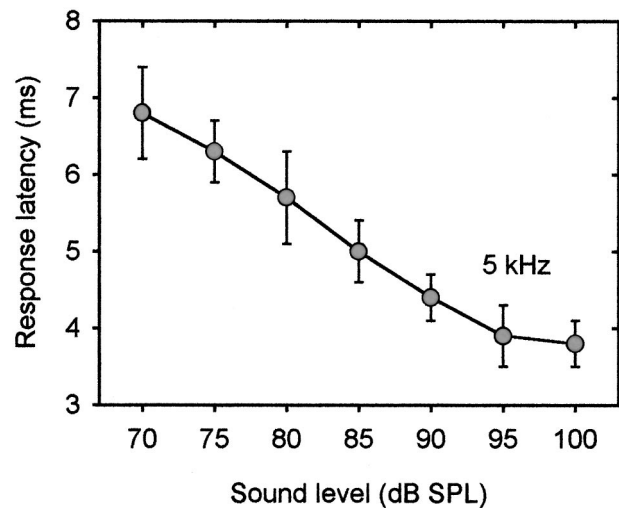


FIG. 10. Response latency in whole tympanal nerve recordings. Response latency of the entire ARF population was measured from the first clear peak of the averaged recording traces. Latencies (mean \pm s.d.) were averaged from seven different experiments except for 70 and 75 dB SPL, at which averages were made from five experiments.

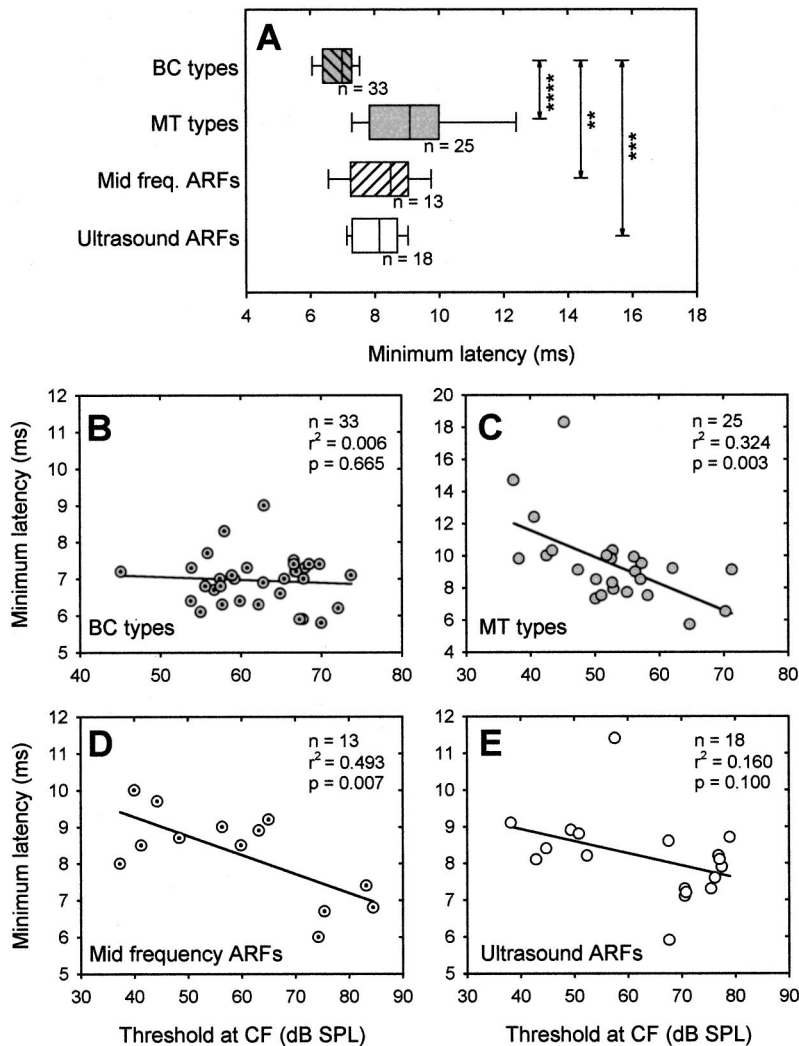


FIG. 11. Minimum response latency in single-unit recordings. Minimum latency was estimated from latency-level function [Fig. 1(C)]. (A) Comparison of minimum latency among four different ARF populations. Minimum latency is the shortest for BC types. Sample sizes are shown under the box. Different ARF populations are illustrated with different fill patterns. See the caption of Fig. 7 for explanation of box plots and statistical tests. (B)–(E) Linear relationship between threshold and minimum latency in each population. Sample sizes, r^2 values, and probabilities are shown inside each graph.

are related to nonlinearity, reassessment of the mechanical response of the cricket tympanal membrane and associated inner structures might be illuminating.

Another conspicuous property of spike-level functions in cricket ARFs is the occurrence of sloping-saturation responses, which has not been reported previously for insects. In mammalian ANFs, the shapes of rate-level functions, including sloping saturation, may be largely accounted for by the nonlinear mechanics of the basilar membrane (Sachs and Abbas, 1974; Yates, 1990; Yates *et al.*, 1990, 1992). According to this view, ANFs with sloping-saturation responses are not discrete types, as had first been proposed by Sachs and Abbas (1974). Rather, whether an ANF has a sigmoid or sloping-saturation curve is determined by whether the curve spans the sound level at which mechanical nonlinearities appear (Yates *et al.*, 1990). The origin of sloping-saturation responses in crickets is not known.

B. A small number of ARFs drives central neurons and behavior at threshold

Despite considerable variation, thresholds are clustered around 50–65 dB SPL for low-frequency ARFs, and around 65–80 dB SPL for ultrasound ARFs [Fig. 4(A)]. Thus, it appears that relatively few ARFs are highly sensitive and, at

near-threshold levels (ca. 40–45 dB SPL for low frequencies and 50–55 dB SPL for ultrasound), central neurons and behavior may be driven by only a small number of ARFs. In other words, crickets may use the lower envelope principal; sensory thresholds are determined by the class of lowest-threshold neurons without being influenced by the existence of less sensitive neurons for a given stimulus (Barlow, 1995; see also Parker and Newsome, 1998).

C. Four different ARF populations differ in physiological organization

In crickets, sound-amplitude coding by ARFs may serve several functions. One is to estimate distances of conspecific males (Cade, 1981) and closely approaching echolocating bats (Nolen and Hoy, 1986). Another is to compute interaural level difference for sound-amplitude discrimination (Doherty, 1985) and for sound localization (Moiseff *et al.*, 1978; Schmitz *et al.*, 1983).

To understand how a population of ARFs codes sound amplitude, it is necessary to know how the response properties of individual ARFs are organized within the population. We find that cricket ARFs comprise four different populations, based on physiology (CF) and anatomy. Within each population, threshold is linearly related to other physiologi-

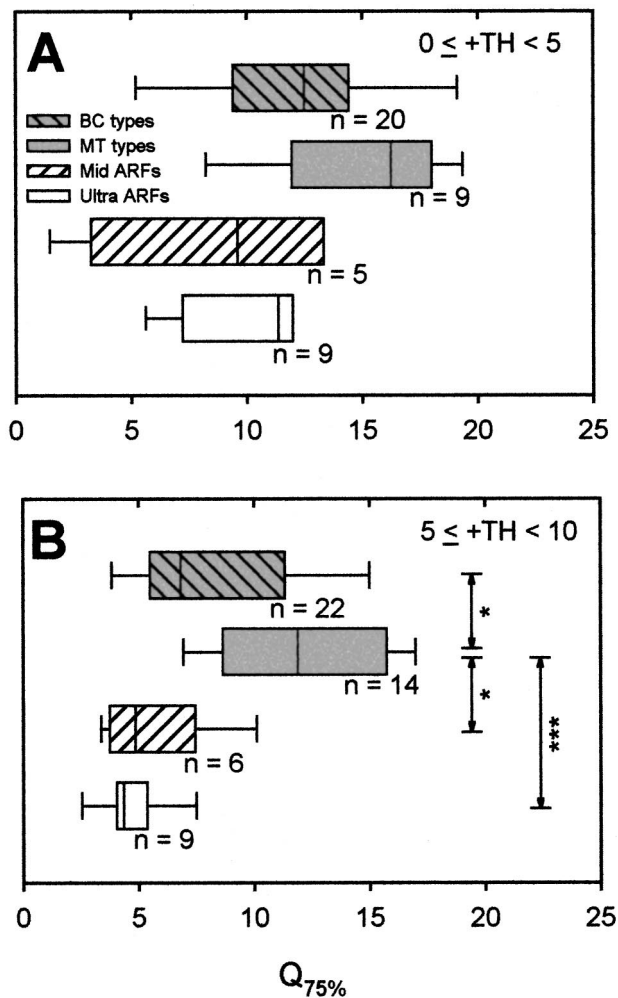


FIG. 12. Frequency selectivity ($Q_{75\%}$) of four ARF populations. $Q_{75\%}$ was calculated as best frequency divided by bandwidth at 75% of the maximum response (Imaizumi and Pollack, 1999). The higher the $Q_{75\%}$, the more sharply the ARF is tuned. MT types are more sharply tuned to CF than other populations. These significant differences are not due to a fortuitous difference in the particular sound levels above threshold within the sound-level range compared (MT types vs BC types; $p = 0.685$ by Mann-Whitney U test, MT types vs midfrequency ARFs; $p = 0.458$, MT types vs ultrasound ARFs; $p = 0.186$). Stimulus level above threshold (+TH) is shown at the top right. Different populations are illustrated with different fill patterns. Sample sizes are given at the bottom of box plots. See the caption of Fig. 7 for explanation of box plots and statistics.

cal parameters. However, the details of these relationships differ among the different ARF populations.

Figure 14 illustrates a highly simplified scheme of normalized spike counts (*top row*) and response latency (*bottom row*) for each population, based on the observed relationships between threshold and response slope, dynamic range, and minimum latency. Threshold is linearly related to other physiological parameters in all four populations. However, for BC low-frequency ARFs, the differences in these parameters across the population are so small that, provisionally, we neglect them. Therefore, BC low-frequency ARFs are stereotyped, and differ from the other three populations physiologically as well as anatomically. The first spikes from different ARFs are separated at higher sound levels for MT low-frequency and midfrequency ARFs, whereas for BC low-frequency and ultrasound ARFs the first spike timing is

coincident at higher sound levels. Three of the four ARF populations, BC and MT low-frequency and ultrasound ARFs, thus exhibiting distinct relationships between threshold and other parameters (response slope, dynamic range, and minimum latency). The organization of the fourth population, midfrequency ARFs, is intermediate to those of MT types and ultrasound ARFs. Therefore, the four different ARF populations may have four different physiological organizations.

In mammalian ANFs, threshold and other parameters are also related. However, the natures of the relationships differ, in most cases, from those we have described. In crickets, response slope increases, and dynamic range decreases with increasing threshold, whereas the converse is true in mammals (Schalk and Sachs, 1980; Winter *et al.*, 1990; Yates *et al.*, 1992). In mammals, these relationships are accounted for by the biomechanics of the basilar membrane. It is not known what mechanisms might account for the relationships in crickets.

D. Behavioral roles of cricket ARFs

Low-frequency and ultrasound ARFs are likely to be involved in intraspecific communication and predator detection, respectively. The behavioral role of midfrequency ARFs is unclear. The similarity of physiological properties of midfrequency and ultrasound ARFs (Figs. 7, 8, 11, 12) suggests that the former might also be involved in predator detection. Some midfrequency ARFs have additional sensitivity peaks at higher sound frequencies including ultrasound (Imaizumi and Pollack, 1999). However, the physiological organization of midfrequency ARFs is somewhat different from that of ultrasound ARFs (Fig. 14). Midfrequency ARFs may be involved in acoustic communication as well as predator detection (Imaizumi and Pollack, 1999). Cricket songs contain higher harmonics, which enhance the recognition and localization of the signals (Latimer and Lewis, 1986).

The population sizes of midfrequency and ultrasound ARFs are small (Fig. 2). For both populations, response slope, maximum number of spikes, and maximum firing rate are high. Steep response slope may facilitate high-resolution sound-amplitude discrimination, which may be suitable for sound localization based on inputs from small numbers of ARFs. High spike counts and firing rate may also, through temporal summation, allow these ARFs to provide powerful inputs to central neurons, despite their small numbers. Presumably, these mechanisms facilitate predator detection by small populations of ARFs.

Low-frequency ARFs are over-represented, comprise two distinct anatomical types (BC and MT types), and may play different roles in acoustic communication. The lower threshold, wider dynamic range, and sharper tuning of MT types are suitable for processing songs of distant conspecific mates, although their shallow response slope may not be ideal for sound-amplitude discrimination. This may be related to the relatively poor acuity of phonotaxis at low sound levels (Schmitz, 1985). Based on anatomy, MT types are good candidates for providing direct inputs to AN1 (see also Hennig, 1988), which in turn sends information to the brain.

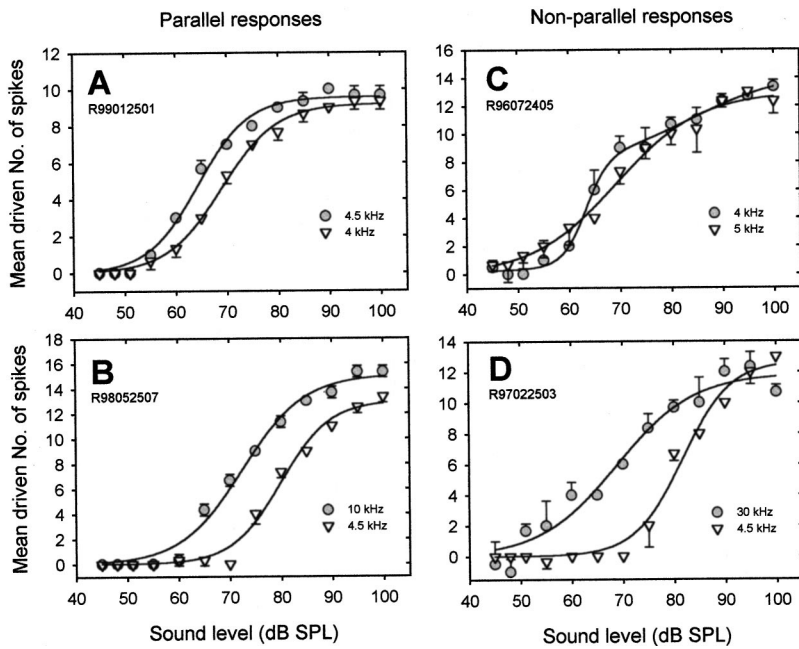


FIG. 13. Parallel and nonparallel spike-level functions of single ARFs. ARF identifications are shown at the top left. Stimulus frequencies are given at the bottom right by the different markers. Data points represent mean (\pm s.d.) of three presentations of the stimulus at each sound level. (A) Parallel responses in low-frequency ARF with CF of 4.5 kHz. (B) Parallel responses in mid-frequency ARF with CF of 10 kHz. This mid-frequency ARF also responds robustly at the carrier frequency of cricket songs (4.5 kHz). (C) Nonparallel responses in low-frequency ARF. Spike-level function at CF of 4.5 kHz for this ARF was not available. Note the difference in response shape at the two frequencies; sloping saturation at 4 kHz and sigmoid at 5 kHz. (D) Nonparallel responses in ultrasound ARF with CF of 30 kHz. This ultrasound ARF also responds robustly at 4.5 kHz.

An ascending pathway is required for phonotaxis (Pollack and Hoy, 1981), and AN1, in particular, is involved in sound recognition and localization (Schildberger, 1984; Schildberger and Hörner, 1988). MT types, as the probable source of song-related inputs to AN1 (Hennig, 1988), would thus appear to be crucial for acoustic communication. By contrast, the behavioral role of BC types is less clear. Anatomical evidence suggests that BC types may make few, if any,

contacts with ON1 (Pollack and Imaizumi, 1999) and, as AN1's dendrites are in the same region as ON1's, extensive direct input from BC types to AN1 seems unlikely. Thus, it is less likely that BC types directly influence ascending information. Moreover, thresholds of most BC types (55–65 dB) are higher than that of behavior (45–50 dB SPL, Pollack and Plourde, 1982; Schmitz, 1985; Doolan and Pollack, 1985). However, because of their steep response slope,

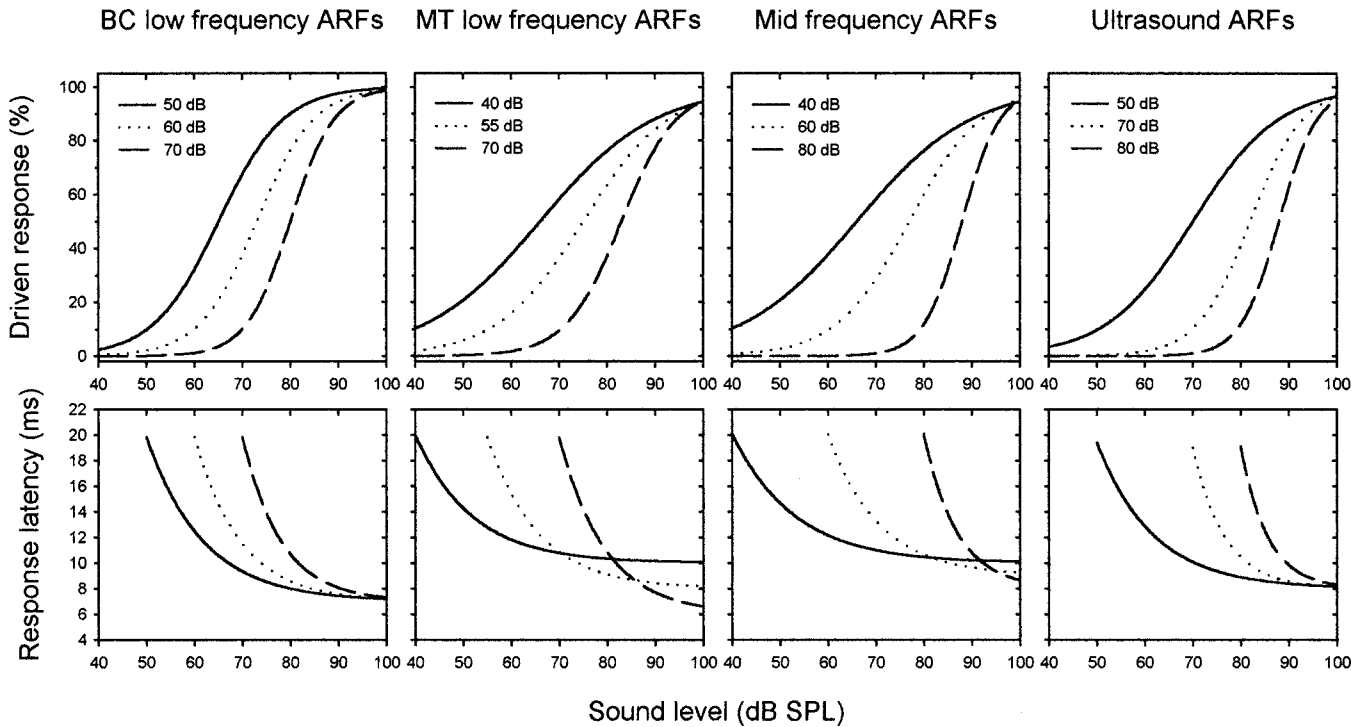


FIG. 14. Scheme of physiological organization in four different ARF populations. Top row illustrates normalized spike-level functions. Spike counts were normalized to maximum response after subtraction of spontaneous rate from the raw data. Hence, spontaneous rate and maximum number of spikes are not considered in this scheme. Threshold and saturation were set as \sim 10% and 90% of the normalized response, although, in the actual data analysis, threshold varied from 5% to 14% because of the difference in maximum responses. Bottom row illustrates latency-level functions. Shapes of the functions were based on the observations. Three representative ARFs, with different thresholds illustrated by different dashed lines, were schematized. The values of threshold chosen are based on the distribution of threshold within each population.

which is well suited for sound-amplitude discrimination and thus for sound localization [Fig. 7(B)], BC types may participate in increasing the accuracy of orientation at suprathreshold levels. Indeed, phonotaxis improves substantially with increasing stimulus levels (Schmitz, 1985), at which BC types would be recruited. The target neuron(s) of BC types is not yet known, and so the pathway by which they might influence phonotaxis is unclear. Nevertheless, the anatomical differences between BC and MT types suggest that auditory input pertaining to intraspecific signals is separated into different pathways at the earliest level of neural processing. These different pathways may, at least partially, account for the large population size of low-frequency ARFs.

E. Minimum latency

BC types have significantly shorter minimum latency than the other three ARF populations. Minimum latency is accounted for mainly by conduction delay between the spike initiating site and the recording point (acoustic delay between the speaker and the ear is only ~ 1.1 ms). Somata of ARFs are tonotopically arrayed in the inner ear; low-frequency-tuned somata are situated proximally, and high-frequency-tuned somata are distal (Oldfield *et al.*, 1986). Therefore, conduction path length differs for ARFs with different CFs. However, the length of the array of somata is only ~ 270 – 400 μm (Young and Ball, 1974; Imaizumi, 2001). Given the mean conduction velocity of ARFs, ca. 2 m/s (Pollack and Faulkes, 1998), the differences in conduction delay due to soma position would be < 0.2 ms, which is less than the 1–2 ms we observed between BC types and the other ARF populations (Fig. 11).

Conduction velocity is proportional to the square root of axon diameter. Thus, ARFs with shorter minimum latency (BC low-frequency ARFs) might have larger axon diameters. The soma sizes of ARFs vary according to position within the ear; somata of proximal and distal cells are larger than those of cells situated in the middle of the array (Young and Ball, 1974; Imaizumi, 2001). If we assume (as seems reasonable) that axon diameter varies with soma size, then it seems possible that the proximal-most receptor neurons correspond to the BC low-frequency ARFs (Imaizumi, 2001). However, this reasoning also predicts that ultrasound ARFs (distal) should have higher conduction velocities, and shorter minimum latencies, than receptor neurons situated in the middle of the array. As we discuss above, differences in conduction distance among the ARF types will have only a very small effect on minimum latency. Minimum latencies of ultrasound ARFs, however, were not shorter than those of MT low-frequency ARFs. It seems likely that other factors, in addition to conduction velocity, might contribute to differences in minimum latency. One possibility is the latency of spike initiation.

The minimum latency for ultrasound ARFs is longer than for BC types. Because ultrasound ARFs are involved in avoidance behavior, their minimum latency might be expected to be shorter than that of other ARFs. In locusts, too, high-frequency (including ultrasound) sensitive ARFs are presumably involved in negative phonotaxis (Robert, 1989; Dawson *et al.*, 1997), and yet have smaller diameter axons,

and thus presumably lower conduction velocities, than low-frequency sensitive ARFs (Halex *et al.*, 1988). In crickets, the longer minimum latency for ultrasound ARFs is compensated at the central neuron level. AN2, a command neuron for negative phonotaxis (Nolen and Hoy, 1984), has a large axon diameter (Atkins and Pollack, 1986; Wohlers and Huber, 1985), and sends information to the brain at high velocity.

ACKNOWLEDGMENTS

We thank Ifty (Lance) Nizami (Boys Town National Research Hospital, Omaha, NE) for his generous and invaluable advice on a double logistic function, Ron Chase for his comments on an early version of manuscript, and Axel Michelsen and an anonymous reviewer for their comments, which greatly improved our manuscript. This work was supported by grants from the National Sciences and Engineering Research Council of Canada and the Whitehall Foundation to G.S.P. and by a Government of Canada Award to K.I.

- Atkins, G., and Pollack, G. S. (1986). "Age-dependent occurrence of an ascending axon on the omega neuron of the cricket, *Teleogryllus oceanicus*." *J. Comp. Neurol.* **243**, 527–534.
- Atkins, G., and Pollack, G. S. (1987). "Correlations between structure, topography arrangement, and spectral sensitivity of sound-sensitive interneurons in crickets." *J. Comp. Neurol.* **266**, 398–412.
- Barlow, H. (1995). "The neuron doctrine in perception," in *The Cognitive Neurosciences*, edited by M. S. Gazzaniga (MIT Press, Cambridge, MA), pp. 415–435.
- Breckow, J., and Sipple, M. (1985). "Mechanics of the transduction of sound in the tympanal organ of adults and larvae of locusts." *J. Comp. Physiol. A* **157**, 619–629.
- Cade, W. H. (1981). "Field cricket spacing, and the phonotaxis of crickets and parasitoid flies to clumped and isolated cricket songs." *Z. Tierpsychol.* **55**, 365–375.
- Cooper, N. P., and Yates, G. K. (1994). "Nonlinear input–output functions derived from the responses of guinea-pig cochlear nerve fibers: Variations with characteristic frequency." *Hear. Res.* **78**, 221–234.
- Coro, F., and Kössl, M. (1998). "Distortion-product otoacoustic emissions from the tympanic organ in two noctuid moths." *J. Comp. Physiol. A* **183**, 525–531.
- Dawson, J. W., Dawson-Scully, K., Robert, D., and Robertson, R. M. (1997). "Forewing asymmetries during auditory avoidance in flying locusts." *J. Exp. Biol.* **200**, 2323–2335.
- Doherty, J. A. (1985). "Phonotaxis in the cricket, *Gryllus bimaculatus* De-Geer: Comparisons of choice and no-choice paradigms." *J. Comp. Physiol. A* **157**, 279–289.
- Doolan, J. M., and Pollack, G. S. (1985). "Phonotactic specificity of the cricket *Teleogryllus oceanicus*: Intensity-dependent selectivity for temporal parameters of the stimulus." *J. Comp. Physiol. A* **157**, 223–233.
- Draper, N. R., and Smith, H. (1983). *Applied Regression Analysis* (Wiley, New York).
- Glantz, S. A., and Slinker, B. K. (1990). *Primer of Applied Regression and Analysis of Variance* (McGraw-Hill, New York).
- Halex, H., Kaiser, W., and Kalmring, K. (1988). "Projection areas and branching patterns of the tympanal receptor cells in migratory locusts, *Locusta migratoria* and *Schistocerca gregaria*." *Cell Tissue Res.* **253**, 517–528.
- Hennig, R. M. (1988). "Ascending auditory interneurons in the cricket *Teleogryllus commodus* (Walker): Comparative physiology and direct connections with afferents." *J. Comp. Physiol. A* **163**, 135–143.
- Hennig, R. M., and Weber, T. (1997). "Filtering of temporal parameters of the calling song by cricket females of two closely related species: A behavioral analysis." *J. Comp. Physiol. A* **180**, 621–630.
- Hutchings, M., and Lewis, B. (1981). "Response properties of primary auditory fibers in the cricket *Teleogryllus oceanicus* (Le Guillou)." *J. Comp. Physiol. A* **143**, 129–134.

- Imaizumi, K., and Pollack, G. S. (1996). "Anatomy and physiology of auditory receptors in the Australian field cricket *Teleogryllus oceanicus*," Soc. Neurosci. Abstr. **22**, 1082.
- Imaizumi, K., and Pollack, G. S. (1997). "Physiological properties of auditory receptors in the Australian field cricket *Teleogryllus oceanicus*," Soc. Neurosci. Abstr. **23**, 1571.
- Imaizumi, K., and Pollack, G. S. (1998a). "The physiological organization of cricket auditory receptors responding to different behavioral relevant frequency ranges," Soc. Neurosci. Abstr. **24**, 156.
- Imaizumi, K., and Pollack, G. S. (1998b). "Functional organization of axon terminals of auditory receptor fibers in Australian field cricket *Teleogryllus oceanicus*," 5th International Congress of Neuroethology. 50.
- Imaizumi, K., and Pollack, G. S. (1999). "Neural coding of sound frequency by cricket auditory receptors," J. Neurosci. **19**, 1508–1516.
- Imaizumi, K. (2001). "Peripheral representation of sound frequency in cricket auditory system: Beyond tonotopy," Ph.D. thesis (McGill Univ., Montreal, Canada).
- Kalmring, K., Lewis, B., and Eichendorf, A. (1978). "The physiological characteristics of the primary sensory neurons of the complex tibial organ of *Decticus verrucivorus* L. (Orthoptera, Tettigoniidae)," J. Comp. Physiol. A **127**, 109–121.
- Köpl, C., and Yates, G. (1999). "Coding of sound pressure level in the barn owl's auditory nerve," J. Neurosci. **19**, 9674–9686.
- Kössl, M., and Boyan, G. S. (1998). "Otoacoustic emissions from a non-vertebrate ear," Naturwissenschaften **85**, 124–127.
- Latimer, W., and Lewis, D. B. (1986). "Song harmonic content as a parameter determining acoustic orientation behavior in the cricket *Teleogryllus oceanicus* (Le Guillou)," J. Comp. Physiol. A **158**, 583–591.
- Le Prell, G., Sachs, M., and May, B. (1996). "Representation of vowel-like spectra by discharge rate responses of individual auditory-nerve fibers," Aud. Neurosci. **2**, 275–288.
- Michelsen, A. (1998). "Biophysics of sound localization in insects," in *Comparative Hearing: Insects*, edited by R. R. Hoy, A. N. Popper, and R. R. Fay (Springer, New York), pp. 18–62.
- Moiseff, A., Pollack, G. S., and Hoy, R. R. (1978). "Steering responses of flying crickets to sound and ultrasound: Mate attraction and predator avoidance," Proc. Natl. Acad. Sci. U.S.A. **75**, 4052–4056.
- Nizami, L., and Schneider, B. (1997). "Auditory dynamic range derived from the mean rate-intensity function in the cat," Math. Biosci. **141**, 1–28.
- Nolen, T. G., and Hoy, R. R. (1984). "Initiation of behavior by single neurons: The role of behavioral context," Science **226**, 992–994.
- Nolen, T. G., and Hoy, R. R. (1986). "Phonotaxis in flying crickets. I. Attraction to the calling song and avoidance of bat-like ultrasound are discrete behaviors," J. Comp. Physiol. A **159**, 423–439.
- Oldfield, B. P. (1982). "Tonotopic organization of auditory receptors in Tettigoniidae (Orthoptera: Ensifera)," J. Comp. Physiol. A **147**, 461–469.
- Oldfield, B. P. (1983). "Central projections of primary auditory fibers in Tettigoniidae (Orthoptera: Ensifera)," J. Comp. Physiol. A **151**, 389–395.
- Oldfield, B. P. (1984). "Physiology of auditory receptors in two species of Tettigoniidae (Orthoptera: Ensifera). Alternative tonotopic organizations of the auditory organ," J. Comp. Physiol. A **155**, 689–696.
- Oldfield, B. P. (1985). "The tuning of auditory receptors in bushcrickets," Hear. Res. **17**, 27–35.
- Oldfield, B. P., Kleindienst, H. U., and Huber, F. (1986). "Physiology and tonotopic organization of auditory receptors in the cricket *Gryllus bimaculatus* DeGeer," J. Comp. Physiol. A **159**, 457–464.
- Parker, A. J., and Newsome, W. T. (1998). "Sense and the single neuron: Probing the physiology of perception," Annu. Rev. Neurosci. **21**, 227–277.
- Paton, J. A., Capranica, R. R., Dragsten, P. R., and Webb, W. W. (1977). "Physical basis for auditory frequency analysis in field crickets (Gryllidae)," J. Comp. Physiol. A **119**, 221–240.
- Pollack, G. S. (1997). "SWEEPS: A program for the acquisition and analysis of neurophysiological data," Comput. Methods Programs Biomed. **53**, 163–173.
- Pollack, G. S., and Faulkes, Z. (1998). "Representation of behaviorally relevant sound frequencies by auditory receptors in the cricket *Teleogryllus oceanicus*," J. Exp. Biol. **201**, 155–163.
- Pollack, G. S., and Hoy, R. R. (1981). "Phonotaxis in flying crickets: Neural correlates," J. Insect Physiol. **27**, 41–45.
- Pollack, G. S., and Imaizumi, K. (1999). "Neural analysis of sound frequency in insects," BioEssays **21**, 295–303.
- Pollack, G. S., and Plourde, N. (1982). "Directionality of acoustic orientation in flying crickets," J. Comp. Physiol. A **146**, 207–215.
- Rheinlaender, J. (1975). "Transmission of acoustic information at three neuronal levels in the auditory system of *Decticus verrucivorus* (Tettigoniidae, Orthoptera)," J. Comp. Physiol. **97**, 1–53.
- Rice, W. R. (1989). "Analyzing tables of statistical tests," Evolution (Lawrence, Kans.) **43**, 223–225.
- Robert, D. (1989). "The auditory behavior of flying locusts," J. Exp. Biol. **147**, 279–301.
- Römer, H. (1976). "Die Informationsverarbeitung tympanaler Rezeptorelemente von *Locusta migratoria* (Acrididae, Orthoptera)" ["Information processing by tympanal receptors in *Locusta migratoria* (Acrididae, Orthoptera)"], J. Comp. Physiol. **109**, 101–122.
- Römer, H., Spickermann, M., and Bailey, W. (1998). "Sensory basis for sound intensity discrimination in the bushcricket *Requena verticalis* (Tettigoniidae, Orthoptera)," J. Comp. Physiol. A **182**, 595–607.
- Sachs, M. B., and Abbas, P. J. (1974). "Rate versus level functions for auditory-nerve fibers in cats: Tone-burst stimuli," J. Acoust. Soc. Am. **56**, 1835–1847.
- Sachs, M. B., and Young, E. D. (1979). "Encoding of steady-state vowels in the auditory nerve: Representation in terms of discharge rate," J. Acoust. Soc. Am. **66**, 470–479.
- Sachs, M. B., and Young, E. D. (1980). "Effects of nonlinearities on speech encoding in the auditory nerve," J. Acoust. Soc. Am. **68**, 858–875.
- Sachs, M. B., Winslow, R. L., and Sokolowski, B. H. A. (1989). "A computational model for rate-level functions from cat auditory-nerve fibers," Hear. Res. **41**, 61–70.
- Sachs, M. B., Woolf, N. K., and Sinnott, J. M. (1980). "Response properties of neurons in the avian auditory system: Comparisons with mammalian homologues and consideration of the neural encoding of complex stimuli," in *Comparative Studies of Hearing in Vertebrates*, edited by A. N. Popper and R. R. Ray (Springer, New York), pp. 323–353.
- Schalk, T. B., and Sachs, M. B. (1980). "Nonlinearities in auditory-nerve fiber responses to bandlimited noise," J. Acoust. Soc. Am. **67**, 903–913.
- Schildberger, K. (1984). "Temporal selectivity of identified auditory neurons in the cricket brain," J. Comp. Physiol. A **155**, 171–185.
- Schildberger, K., and Hörner, M. (1988). "The function of auditory neurons in cricket phonotaxis. I. Influence of hyperpolarization of identified neurons on sound localization," J. Comp. Physiol. A **163**, 621–631.
- Schmitz, B. (1985). "Phonotaxis in *Gryllus campestris* L. (Orthoptera, Gryllidae). III. Intensity dependence of the behavioral performance and relative importance of tympana and spiracles in directional hearing," J. Comp. Physiol. A **156**, 165–180.
- Schmitz, B., Scharstein, H., and Wendler, G. (1983). "Phonotaxis in *Gryllus campestris* L. (Orthoptera, Gryllidae). II. Acoustic orientation of female crickets after occlusion of single entrances," J. Comp. Physiol. A **152**, 257–264.
- Strausfeld, N. J., Seyan, H. S., Wohlers, D., and Bacon, J. P. (1983). "Lucifer yellow histology," in *Functional Neuroanatomy*, edited by N. J. Strausfeld (Springer, Berlin), pp. 132–155.
- Suga, N. (1960). "Peripheral mechanism of hearing in locust," Jpn. J. Physiol. **10**, 533–546.
- Winter, I. M., Robertson, D., and Yates, G. K. (1990). "Diversity of characteristic frequency rate-intensity functions in guinea pig auditory nerve fibers," Hear. Res. **45**, 191–202.
- Wohlers, D. W., and Huber, F. (1985). "Topographical organization of the auditory pathway within the prothoracic ganglion of the cricket *Gryllus campestris* L.," Cell Tissue Res. **239**, 555–565.
- Wytenbach, R. A., May, M. L., and Hoy, R. R. (1996). "Categorical perception of sound frequency by crickets," Science **273**, 1542–1544.
- Yager, D. D. (1999). "Structure, development, and evolution of insect auditory systems," Microsc. Res. Tech. **47**, 380–400.
- Yates, G. K. (1990). "Basilar membrane nonlinearity and its influence on auditory nerve rate-intensity functions," Hear. Res. **50**, 145–162.
- Yates, G. K., Winter, I. M., and Robertson, D. (1990). "Basilar membrane nonlinearity determines auditory nerve rate-intensity functions and cochlear dynamic range," Hear. Res. **45**, 203–220.
- Yates, G. K., Johnstone, B. M., Patuzzi, R. B., and Robertson, D. (1992). "Mechanical preprocessing in the mammalian cochlea," Trends Neurosci. **15**, 57–61.
- Young, D., and Ball, E. (1974). "Structure and development of the auditory system in the prothoracic leg of the cricket *Teleogryllus commodus* (Walker). Adult structure," Z. Zellforsch. Mikrosk. Anat. **147**, 293–312.

Erratum: “Thermal diffusion and mixture separation in the acoustic boundary layer” [J. Acoust. Soc. Am. 106, 1794–1800 (1999)]

G. W. Swift and P. S. Spoor

Condensed Matter and Thermal Physics Group, Los Alamos National Laboratory, Los Alamos, New Mexico 87545

(Received 13 November 2000; accepted for publication 14 November 2000)

[DOI: 10.1121/1.1348007]

In the first paragraph of Sec. IV, the statement “...while the total mass flux density $\overline{\rho u}$ remains zero” is wrong. In the situation we are considering, with sealed reservoirs at the ends of the channel, the total time-averaged *mole* flux is zero, as the mole flux of the heavy component in one direction equals that of the light component in the other direction. Hence, nonzero net mass must flow in the direction that the heavy component flows.

It is easy to show that this net time-averaged second-order mass flux is

$$\dot{M}_2 = \dot{M}_{H,2}(1 - m_L/m_H) \quad (46a)$$

when the mole fluxes are equal and opposite, and that the

time-averaged second-order mass flux of the heavy component is

$$\dot{M}_{H,2} \equiv A \langle \overline{\rho c u} \rangle_2 = \frac{A \rho_m}{2} \text{Re}[\langle c_1 \widetilde{u}_1 \rangle] + c_m \dot{M}_2. \quad (46b)$$

These equations should replace Eq. (46) in the manuscript. Equations (48) and (49) give expressions for $\rho_m \text{Re}[\langle c_1 \widetilde{u}_1 \rangle]/2$, not for $\langle \overline{\rho c u} \rangle_2$.

Finally, by combining Eqs. (46a) and (46b) to eliminate \dot{M}_2 and solving for $\dot{M}_{H,2} \equiv m_H \dot{N}_{H,2}$, we arrive at Eq. (52), which is correct as written.

We are grateful to Drew Geller for bringing this error to our attention.